The fate of melts within the slow-spreading lower oceanic crust : New insights from Atlantis Bank (Southwest Indian Ridge)

Marine Boulanger

UNIVERSITE DE LORRAINE

École doctorale SIReNA

Centre de Recherches Pétrographiques et Géochimiques

THESE DE DOCTORAT

présentée et soutenue publiquement le 21 février 2020 pour l'obtention du titre de

Docteur de l'Université de Lorraine (mention Géosciences), par

Marine Boulanger

Le devenir des liquides au sein de la croûte océanique des dorsales à expansion lente

Nouveaux apports de l'étude d'Atlantis Bank (dorsale Sud-Ouest Indienne)

Composition du jury

Directeurs de thèse

Dr. Lydéric France - Maître de conférences - Université de Lorraine (France)

Prof. Dr. Jürgen Koepke - Professeur - Université Leibniz de Hanovre (Allemagne)

Dr. Raphaël Pik - Directeur de recherches - CRPG (France)

Rapporteurs

Prof. Katharine Cashman - Professeure - Université de Bristol (Royaume Uni)

Dr. Marguerite Godard - Directrice de Recherches - Géosciences Montpellier (France)

Examinateurs

Dr. Mathilde Cannat - Directrice de Recherches - IPGP (France)

Dr. Johan Lissenberg - Chargé d'enseignements - Université de Cardiff (Royaume Uni)

Invité

Dr. Olivier Namur - Professeur adjoint - Université Catholique de Leuven (Belgique)

CRPG-CNRS Université de Lorraine
15 rue Notre Dames des Pauvres 54500 Vandœuvre-lès-Nancy

UNIVERSITE DE LORRAINE

Graduate school SIReNA

Centre de Recherches Pétrographiques et Géochimiques

THESE DE DOCTORAT

presented and defended publicly the 21st of February 2020 for the title of

Doctor of philosophy from the University of Lorraine (in Earth Science)

by Marine Boulanger

The fate of melts within the slow-spreading lower oceanic crust

New insights from Atlantis Bank (Southwest Indian Ridge)

Composition of the jury

Supervisors

Dr. Lydéric France - Associate professor - Université de Lorraine (France)

Prof. Dr. Jürgen Koepke - Professor - Leibniz Universität Hannover (Germany)

Dr. Raphaël Pik - Senior researcher - CRPG (France)

Principal examiners

Prof. Katharine Cashman - Professor - University of Bristol (United Kingdom)

Dr. Marguerite Godard - Senior researcher - Géosciences Montpellier (France)

Defense examiners

Dr. Mathilde Cannat - Senior researcher - IPGP (France)

Dr. Johan Lissenberg - Senior Lecturer - Cardiff University (United Kingdom)

Invitee

Dr. Olivier Namur - Associate professor - Katholieke Universiteit Leuven (Belgium)

CRPG-CNRS Université de Lorraine
15 rue Notre Dames des Pauvres 54500 Vandœuvre-lès-Nancy

"Ses pensées se cognaient, s'entassaient ou bien s'écartaient les unes des autres. Comme les plaques de l'écorce terrestre qui s'ingénient à déraper sur le machin glissant et chaud qu'il y a en dessous. Sur le manteau en fusion. C'est terrible cette histoire de plaques qui déconnent dans tous les sens à la surface de la Terre. Impossible de tenir en place. La tectonique des plaques, voilà comment ça s'appelle. Eh bien lui, c'était la tectonique des pensées. Les glissades perpétuelles et parfois, inévitablement, la bousculade. Avec les emmerdements qu'on sait. Quand les plaques s'écartent, éruption volcanique. Quand les plaques se heurtent, éruption volcanique aussi."

Fred Vargas, *Debout les morts*

doi:10.1242/jcs.033340

Remerciements

Acknowledgments - Danksagungen

Si j'en suis là aujourd'hui, à (enfin) écrire les remerciements qui s'imposent en cette fin de thèse, c'est avant tout grâce aux différentes personnes que j'ai pu rencontrer durant tout mon parcours scolaire et universitaire, et à celles aussi qui m'ont soutenu depuis toujours. De même, je pense qu'on s'accorde souvent à dire que malgré le caractère très personnel du projet de thèse, sans toutes les personnes qui nous accompagnent durant ces (presque) 3 années, la conduite d'un tel projet serait beaucoup plus ardue, sinon impossible. Je ne remercierais donc jamais assez toutes ces personnes, mais je vais quand même essayer dans les quelques lignes qui suivent.

Merci à celui qui m'a aidé à trouver mon tout premier stage en laboratoire, puis mon stage de master, et qui a repris le flambeau en tant que directeur lors de cette thèse: Raphaël Pik. Au final c'est grâce à toi que j'ai pu mettre un premier pied dans la recherche, et que j'ai pu initier tout mon parcours jusqu'à cette thèse. I also would like to thank a lot Jürgen Koepke, second director who also wasted a lot of time dealing with administrative nightmares regarding this thesis. I am really glad I had the opportunity to work with you and the Hannover team. Despite tight schedules, few unexpected experimental issues and some bad German weather, I did enjoy all my stays in Hannover which really helped and forged me scientifically. Enfin, je voudrais remercier chaleureusement le dernier "chef" (déso) Lydéric France. Merci de m'avoir intégrée dans la team Oldoinyo Lengai en me proposant de bosser avec toi pour mon futur projet master. Ce volcan était le "Graal" pour moi et je rêvais de pouvoir bosser dessus un jour, et c'est arrivé beaucoup plus tôt que prévu! Donc merci infiniment pour ça, et surtout pour m'avoir réitéré ta confiance avec ce projet de thèse. Je suis consciente de la chance que j'ai eu de pouvoir vivre ces 3 années, et la jeune chercheuse que je suis te doit beaucoup. I also would like to thank Katharine Cashman, Marguerite Godard, Mathilde Cannat, Johan Lissenberg and Olivier Namur who accepted to be part of the jury and to evaluate this work. And I would like to seize the opportunity to apologize for the 1.2 kg of paper you received each.

Ma thèse est basée sur 3 petites boîtes de lames minces et ces petites boîtes, enfin leur contenu, a été en grande partie confectionné par Christophe Nevado et Doriane Delmas. Merci à eux et aussi pour m'avoir secouru lors de mes passages intempestifs à Montpellier. De même, je tiens aussi à remercier chaleureusement les personnes m'ayant aidé pour le volet analytique de cette thèse et avec qui j'ai pu échanger lors de mes allers-retours Nancy - Clermont-Ferrand - Montpellier -

Hanovre. Merci donc à Fabrice Barou des analyses EBSD et à Olivier Bruguier des analyses laser à Montpellier. Un grand merci également à Jean-Luc Devidal avec qui j'ai réalisé toute la partie EPMA à Clermont-Ferrand, mais pas que, puisque tu étais déjà impliqué dans le projet de master. I also express my grateful thanks to Chao Zhang, without whom none of the experimental project in Hannover would have been possible. I didn't help simplify your already (very) tight schedule, but you always took the time and helped me a great deal.

Merci à Benoît Ildefonse pour avoir fait partie du comité de suivi de thèse, et pour les diverses discussions EBSD ou encore missions océaniques. Merci également à Olivier Namur d'avoir accepté de faire partie du comité de suivi dès la première année de thèse, et d'avoir toujours manifesté beaucoup d'enthousiasme pour le projet et mes avancées. I also would like to thank Kathy Faak whom I met during the first Leg of the Oman Drilling Project onboard Chikyu, in 2017. Thank you for the coffees at sunrise on the helideck, with Mount Fuji in the background (definitely in my top 5 of the best moments during the PhD!), and for the support and encouragements especially during these 4 weeks of crazy shifts.

Let's stay a little longer in Germany, with my great thanks to the Institut members with whom I was lucky to spend a few months, the Hannover team in general and its director François Holtz. Special thanks to Dominik Mock, another gabbro maniac from the fast-spreading side of the force, Insa Kassens, without whom I would have been (completely) lost when landing in Hannover, but also Sarah, Lena, Yvonne, Stefan, Dachuan, Lennart, Philipp and all the others, for welcoming me and helping me during my stays.

Revenons maintenant à Nancy, avec un grand merci général aux personnes du CRPG. Je ne pourrais pas citer tout le monde, mais dans le désordre merci Bruno pour le soutien logistique et acoustique en cette fin de thèse. Merci infiniment à Cati et Aurélie, et toute l'équipe administrative plus généralement pour leur aide en lien avec mes pérégrinations scientifiques françaises ou plus internationales. Merci à Guillaume Caro de m'avoir encadré pour mon tout premier stage recherche au CRPG, et à Aimeryc qui m'a appris la chimie de salle blanche (meilleure stagiaire!). Merci à David pour les discussions océaniques et déformation, ou encore merci au bout du couloir du 4ème pour le teasing pré-rendu et surtout pré-soutenance!

Merci maintenant à quelqu'un qui m'a beaucoup aidé, et qui a rapporté à Nancy sa bonne humeur "alla genovese", Carlotta Ferrando. Merci pour ton accueil à Montpellier, pour les discussions gabbros (Marine-type vs. Carlotta-type), etc. J'espère qu'on pourra bosser encore un petit bout de temps ensemble. Autre post-doc de la "team Lydé" qui a toujours été de bon conseil et avec qui on aura eu quelques sueurs froides à Barcelone: merci Céline! Merci aussi à Gaëlle, qui a fini sa thèse alors que je commençais à peine la mienne, à Papache évidemment, et puis tous les autres thésards qui ont accompagné ce début de thèse, et notamment Paul, Rémi ou encore Yumi. Merci

aux autres anciens dans la barre d'erreur du 3ème, à savoir P'tit Seb, Nina et bien sûr le Big Seb ou plutôt Parrain. Une "cohabitation" plus ou moins détendue (tu le cherches bien), mais on ne va pas se mentir, c'était quand même très cool de passer les presque trois ans de thèse en ta compagnie.

Au tour de mes géniaux, les seuls et uniques, co-bureaux. Tout d'abord "Daaaaaave", enfin Dr David Bekaert, déjà parti vers l'infini depuis un petit bout de temps avec ses histoires de xénon; futur Dr Guillaume Florin, l'expatrié qui nous a bien manqué, et qui nous a aussi bien nargué au pays des kangourous avec ses histoires de plages de sable blanc et d'hiver estival (et Aurélie aussi!); et puis Dr Apo Mariotti, avec qui nous avons beaucoup partagé le bureau pendant ces derniers mois de thèse. Sans ton soutien et nos hakas improvisés de motivation, je ne pense pas que j'aurais aussi "bien" vécu la fin de thèse. Merci à vous pour ces trois ans, c'est important de pouvoir partager ces moments de thèse (aussi difficiles que géniaux parfois) et je suis très heureuse d'avoir pu les partager avec vous. Et j'espère avoir un peu contribué à vous faire apprécier / découvrir certains coins de Lorraine...

Et puis plus ou moins par étage, merci à tous les autres thésards ou étudiants, notamment Vin... Valentin, Jazote, Delphine et Marion, la dream team du 4ème, Jatlab, Arbia, Toitoine, Mathieu, Cécile, Florian, Mathis... Merci pour l'aide aux pots de thèse, et puis juste merci de former un groupe aussi éclectique que sympathique avec qui c'était sympa de se retrouver entre autres chaque midi, et tous les autres moments que nos thèses / projets respectifs nous ont accordé ! J'ai déjà écrit trois tartines donc je finis rapidement en remerciant Pierre Faure (merci pour l'accueil clermontois!), et sans tous les nommés je remercie aussi les anciens du master T&P et de Géol. J'ai failli oublier! Merci aux Bobs et à Marcel. Et puis merci énormément aussi à Camille, j'ai hâte que ce soit mon tour de pouvoir assister à ta thèse, future Dr Collin.

Enfin, je ne saurais finir ces remerciements sans exprimer tout mon amour et ma gratitude envers ma famille, qui m'a toujours soutenu et qui a toujours cru en moi tout au long de ces années. Ce n'est pas vraiment le genre de la maison, donc je ne m'attarderais pas trop même s'il y aurait beaucoup à dire. Merci à tous, à mamie et papy, à mes grands-mères, à mes oncles et tantes ou encore cousins que je n'ai pas assez vus au cours de ces trois ans. Papa et maman, merci infiniment pour tout. Bon, initialement, vous vous demandiez quand même dans quoi je me lançais avec ces histoires de géologie, mais vous m'avez toujours fait confiance et avez cru en moi quand j'en avais le plus besoin. Et Arthur aussi (mon mollusque préféré), en espérant avoir pu te montrer que ça vaut le coup de s'accrocher, même si je ne me fais pas beaucoup de soucis pour toi.

Merci à tous.

A mes parents

Résumé étendu

Contexte

Les océans recouvrent près des deux tiers de la surface de la Terre, et leur géométrie varie en fonction des mouvements des plaques tectoniques. La croûte qui compose le plancher océanique est formée au niveau des zones de divergence des plaques ou dorsales médio-océaniques. Ces zones concentrent plus de 60% de la production annuelle de magma sur Terre, dont près de la moitié reste piégé en profondeur au sein de la croûte océanique (***Fisher and Schmincke, 1984***). La morphologie des dorsales ainsi que la structure et la composition de la croûte océanique sont fonction de la vitesse d'expansion des plaques tectoniques. Les dorsales dites lentes (vitesses d'expansion $<$ 40mm/an) représentent près de la moitié des dorsales médio-océaniques, et sont caractérisées par un afflux de magma limité en provenance du manteau en comparaison avec les dorsales dites rapides (***Dunn, 2015***). En conséquence, l'extension au niveau des dorsales lentes est en partie accommodée par une accrétion magmatique discontinue et intermittente, mais également par une déformation cassante de la croûte (e.g., ***Carbotte et al., 2015***). La croûte océanique des dorsales lentes est très hétérogène (***Figure A***), et ses caractéristiques dépendent de la balance entre ces deux mécanismes d'accommodation de l'extension. Dans ce contexte, la localisation des magmas et leurs modes d'évolution au sein de la croûte sont fondamentaux pour la compréhension des processus d'accrétion de la croûte océanique.

L'observation de liquides magmatiques au niveau des dorsales lentes par méthodes sismiques est compliquée par la nature éphémère et sporadique des réservoirs magmatiques. Seules quelques études ont pu identifier de petits réservoirs situés entre 2 et 10 km de profondeur (e.g., ***Canales et al., 2017; Jian et al., 2016; Singh et al., 2006; Sinha et al., 1997***). La principale caractéristique de ces réservoirs de une taille relativement restreinte, est qu'ils sont majoritairement constitués de bouillie cristalline ou mush ($<$20% de liquides, ***Lissenberg et al., 2019***). Ces observations sont cohérentes avec celles effectuées lors de forages de croûte océanique *in situ,* ou lors de l'étude d'ophiolites : les liquides se mettent en place sous forme de petites intrusions ou sills dans la croûte, et peuvent s'empiler jusqu'à former des unités de plusieurs centaines de mètres d'épaisseur lors d'un même pulse magmatique dans un segment actif (e.g., ***Dick et al., 2019, 2000; Godard et al., 2009; Sanfilippo and Tribuzio, 2013***). L'hétérogénéité de la croûte résulte de l'épaisseur variable des unités magmatiques formées, de

leur degré d'évolution, mais aussi des proportions de lithologies mantelliques incorporées dans chaque unité (e.g., ***Basch et al., 2019; Drouin et al., 2009; Ferrando et al., 2018***). Cependant, bien qu'en apparence très hétérogène, les descriptions de différentes sections de croûte inférieure *in situ* ou ophiolitique suggèrent une continuité des processus de mise en place et d'évolution des magmas impliqués dans l'accrétion océanique des dorsales lentes (***Dick et al., 2019***).

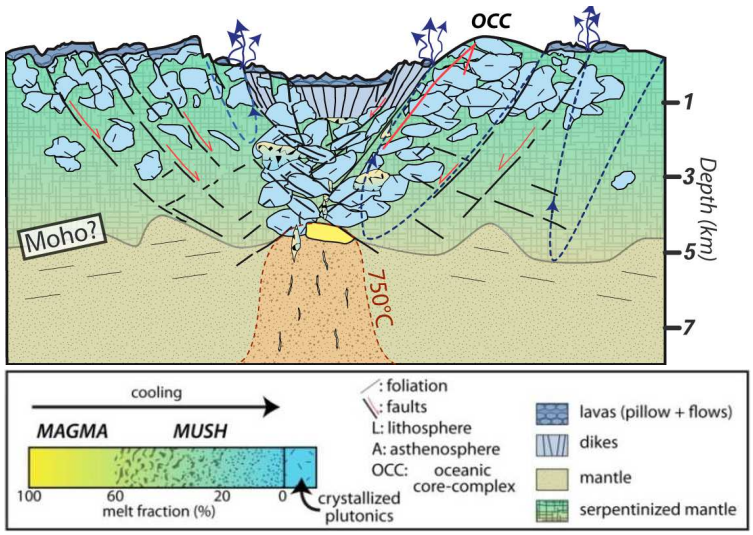

Figure A: Coupe transversale d'une structure représentative d'une dorsale médio-océanique à expansion lente (France & Bouilhol, in prep.)

Les processus d'accrétion magmatique dépendent des modes de migration des liquides, qui peut se faire soit par intrusion (***e.g., Grimes et al., 2008; Kelemen and Aharonov, 1998***), soit par écoulement poreux au travers de la charpente cristalline du mush qui constitue les réservoirs magmatiques. Plusieurs moteurs de cet écoulement poreux sont décrits: (1) un contraste de densité entre le liquide et la matrice cristalline du mush (minéraux cumulatifs plus denses que le liquide dans un système tholéiitique), liquide qui tend à percoler vers le haut de la colonne, (2) une compaction de la matrice cristalline qui force l'expulsion du liquide interstitiel, plus ou moins assisté par (3) une déformation plastique des structures et en particulier dans des zones en extension comme les dorsales lentes (***Lissenberg et al., 2019***). Le mode de migration des liquides est fondamental car il impacte les processus de différenciation des liquides. Plusieurs processus peuvent être impliqués dans la différenciation des magmas tholéiitiques mis en place au niveau des dorsales médio-océaniques. Les plus classiques sont les processus de cristallisation à l'équilibre et de cristallisation fractionnée (***Grove and Brown, 2018***). Ils supposent un système fermé et une évolution sans contamination, sans apports ou sans extractions de liquide. L'équilibre du système est complet et continu pendant la cristallisation à l'équilibre, ou seulement instantané dans le cas de la cristallisation fractionnée avec une séparation efficace des minéraux du liquide une fois formés (e.g., ***Allègre and Minster, 1978***).

Les séquences de cristallisation classiques impliquent la formation d'olivines, puis de plagioclases et de clinopyroxènes, principaux minéraux constitutifs des cumulats gabbroïques de base de croûte, ainsi que d'autres minéraux plus accessoires comme le spinel, ou les oxydes, amphiboles ou apatites en fin de séquence (e.g., ***Villiger et al., 2007***). Ces processus de cristallisation sont toutefois remis en cause par la présence de mush dans les systèmes magmatiques, soit en bordure de chambre où la cristallisation est favorisée (***Langmuir, 1989***), soit dans l'ensemble du réservoir comme décrit précédemment (***Lissenberg et al., 2019 - Figure B***).

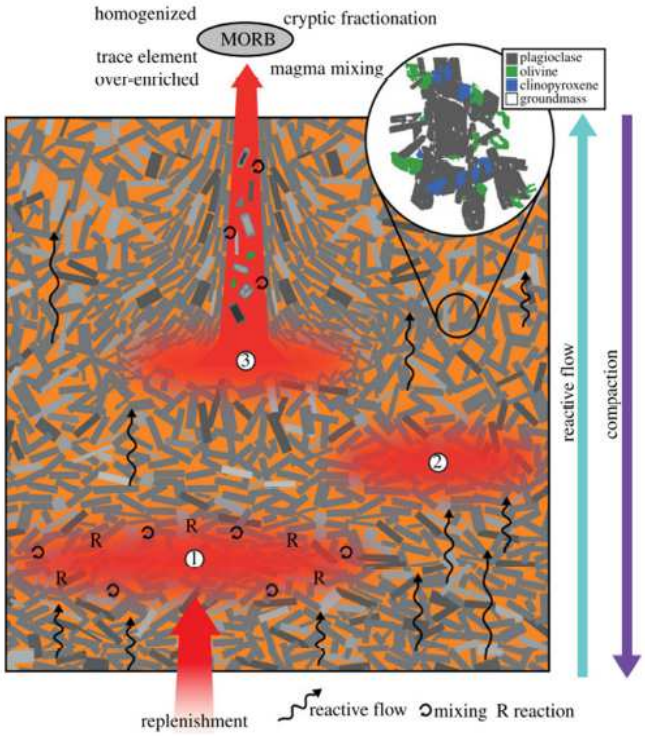

Figure B : Représentation schématique d'un mush de croûte inférieure océanique (Lissenberg et al., 2019). Formation de la lentille 1 par recharge d'un liquide primaire; Formation de la lentille 2 par ségrégation du liquide interstitiel; Lentille 3 alimentant une éruption de MORB.

Dans le cas d'un mush, la migration de liquides plus ou moins évolués par flux poreux implique la création de déséquilibres entre ce liquide et la matrice cristalline qu'il traverse et avec laquelle il réagit. Ces réactions liquide-mush provoquent une dissolution variable des minéraux dans le liquide dont la composition change, et la cristallisation d'une nouvelle génération de minéraux (e.g., ***Liang, 2003; Yang et al., 2019***). Les réactions liquide-mush peuvent conduire à la formation de textures caractéristiques de type dissolution-précipitation, ainsi qu'au développement de signatures géochimiques particulières dans les minéraux recristallisés ***(Lissenberg and MacLeod, 2016***). Par exemple, pour des signatures en éléments majeurs équivalentes, des enrichissements plus importants en éléments incompatibles sont observés par rapport ce qui est attendu par simple cristallisation à l'équilibre ou fractionnée, de

même qu'un fractionnement plus important entre terres rares légères et terres rares lourdes (e.g., ***Coogan et al., 2000***).

Ces signatures, ainsi que les textures qualifiées de "réactives" ont été observées dans un grand nombre d'échantillons crustaux de dorsales lentes, et dans leurs analogues ophiolitiques (e.g., ***Lissenberg and MacLeod, 2016; Sanfilippo et al., 2015***). Cela implique que les processus de réaction en flux poreux sont généralisés et quasi omniprésents au cours de l'évolution des liquides magmatiques dans la croûte. Peu d'études de pétrologie expérimentale se sont attachées à reproduire ces processus (***Kvassnes and Grove, 2008; Yang et al., 2019***), mais des modélisations numériques sont possibles. Les principaux modèles utilisés n'intègrent pas de contraintes thermodynamiques fortes comme les modèles existant pour les processus de cristallisation, mais permettent de modéliser l'évolution des compositions en éléments traces. C'est le cas de l'Assimilation-Cristallisation Fractionnée (***DePaolo, 1981***) ou du Plate Model (***Vernières et al., 1997***). Ces modèles dépendent fortement des paramètres d'entrée fixés (coefficients de partage) et des réactions formulées par l'utilisateur afin de reproduire les gammes de variation des compositions des minéraux analysés *in situ*. Dans les modèles existants, les réactions considérées sont variables d'une étude à l'autre mais des similarités existent pour les paramètres intégrés : il s'agit le plus souvent de l'assimilation d'une matrice cristalline constituée d'olivines et plagioclases, par un liquide relativement primitif pour le système. Dans la majorité des cas la cristallisation est prédominante par rapport à l'assimilation, ce qui provoque la fermeture progressive de la porosité du mush au cours de la réaction (***Coogan et al., 2000; Gao et al., 2007; Kvassnes, 2003; Leuthold et al., 2018; Lissenberg and Dick, 2008; Sanfilippo et al., 2014***). Ces études sont jusqu'à présent ponctuelles, car étudient les réactions liquide-mush à l'échelle d'un ou plusieurs échantillons sans les replacer dans le contexte plus global d'évolution des liquides magmatiques à l'échelle d'un réservoir ou d'un système crustal. Qu'elle est alors la contribution des réactions liquide-mush par rapport aux processus de cristallisation classiques dans la différenciation magmatique et dans l'accrétion crustale au niveau des dorsales lentes?

Objectifs de l'étude et méthodologie

Cette étude vise à mieux contraindre l'implication des processus de migration en flux poreux des liquides dans la croûte inférieure des dorsales lentes : leur impact sur la différenciation des liquides et sur l'évolution des réservoirs magmatiques. L'étude est basée sur un système océanique en particulier, celui du corps complexe océanique Atlantis Bank situé sur la dorsale sud-ouest indienne (32°S, 57°E - ***Fisher and Sclater, 1983***). Une des particularités des dorsales lentes est que l'extension à l'axe peut être accommodée de manière symétrique ou bien asymétrique. Dans le cas d'une extension asymétrique, une grande faille de détachement se

forme dans un des flancs de la dorsale et accommode la quasi-totalité de l'extension. Cette faille donne alors naissance à un corps complexe océanique (ou OCC de l'anglais oceanic core complex), portion de croûte inférieure exhumée à la surface du plancher océanique et formant un dôme composé de roches mantelliques et / ou de roches plutoniques cristallisées en profondeur (e.g., ***Cannat et al., 2019; Escartín et al., 2003; Ildefonse et al., 2007***).

Atlantis Bank se situe à 90 km au sud d'un segment de la dorsale sud-ouest indienne où l'extension mesurée est d'environ 14 mm/an (***Hosford et al., 2003***), le long de la faille transformante Atlantis II. C'est un des OCCs les plus étudiés et le plus grand de tous (40 km de long pour 30 km de large et ~5 km de hauteur à partir de la base de la vallée transformante). Le sommet de la structure est formé d'un plateau de 4 km de large par 8,5 km de long à ~700 m de profondeur sous la surface de l'océan indien (***Dick et al., 2019***). Trois forages profonds ont été réalisés dans ce plateau par le consortium international IODP : le puits 735B, le plus ancien et le plus profond (1508 mbsf - meters below seafloor; ***Dick et al., 2000***), le puits 1105A (158 mbsf; ***Casey et al., 2007***) et le puits U1473A, le plus récent foré dans Atlantis Bank (810 mbsf; ***MacLeod et al., 2017***). Les forages ont permis l'échantillonnage *in situ* de sections hétérogènes de croûte âgées de ~12 Ma (***Rioux et al., 2016***). Les lithologies gabbroïques qui les composent couvrent la quasi-totalité de la gamme modale attendue par évolution de magmas tholéiitiques (troctolites, gabbros à olivine, gabbros *sensu stricto*, gabbros à oxydes, etc.), et sont plus ou moins affectés par des processus d'altération et de déformation plastique (***Dick et al., 2019a; Dick et al., 2019b***). Ces sections quasi continues de croûte océanique constituent une fenêtre inédite sur les roches cristallisées en profondeur. En effet, elles conservent les marqueurs des processus magmatiques se produisant dans les réservoirs magmatiques.

Deux approches complémentaires ont été suivies lors de cette thèse : (1) l'étude d'échantillons naturels provenant des forages IODP 735B et U1473A réalisés dans Atlantis Bank, et (2) une étude de pétrologie expérimentale visant à reproduire les processus de cristallisation à l'équilibre et de cristallisation fractionnée propre au système magmatique d'Atlantis Bank. Pour l'étude des échantillons naturels, des outils d'observation pétrologique et d'analyses géochimiques *in situ* à haute résolution des éléments majeurs (microsonde électronique Cameca SX100 - LMV Clermont-Ferrand) et des éléments traces (spectrométrie de masse sur ThermoFinnigan Element2 XR couplé à un système d'ablation laser - Géosciences Montpellier) ont été utilisés. Différentes échelles ont été considérées afin de traquer les processus de différenciation au niveau de l'échantillon (étude de la variabilité à petite échelle grâce à un échantillonnage ponctuel ciblé) de même qu'au niveau d'un ou de plusieurs réservoirs magmatiques (étude de la variabilité à grande échelle avec des échantillonnages stratégiques sur plusieurs centaines de mètres de carotte). L'étude de pétrologie expérimentale quant à elle visait

à compléter et vérifier les modèles thermodynamiques à disposition pour une meilleure quantification des processus de cristallisation classiques et leurs signatures géochimiques. Les expériences ont été réalisées en autoclave à l'Institut de Minéralogie de Hanovre (Allemagne). Les produits de ces expériences y ont également été préparés, étudiés par imagerie au MEB (microsonde électronique à balayage JEOL JSM-7671F) et analysés pour les éléments majeurs avec une microsonde électronique Cameca SX100. Certains échantillons spécifiques ont été analysés par spectrométrie de masse (ThermoFinnigan Element XR) couplée à un système d'ablation laser au LMV (Clermont-Ferrand).

Apports de cette étude

Chapitre 3 : migration des liquides et interactions dans la croûte océanique de dorsales lentes

La première partie décrivant les résultats de cette thèse est consacrée à l'étude de figures pétrographiques récurrentes observées dans les différentes carottes forées à Atlantis Bank. Des variations de tailles de grains sont observées à intervalles réguliers avec la présence de gabbros à grains fins (~0.5 mm) soit sous forme de litages, soit sous forme de patches irréguliers dans les gabbros encaissants à plus gros grains. ***Bloomer et al. (1991)*** ont étudié ces structures dans le puits 735B, et les interprètent toutes deux comme résultant d'une cristallisation hétérogène en bordure d'une grande chambre magmatique de forme irrégulière formant à elle seule les ~1508 m du puits. Cette conclusion est discutable car, d'une part, de plus récentes études proposent que la portion de croûte échantillonnée dans le puits 735B résulte de l'accrétion de plusieurs réservoirs magmatiques (de 3 à 5 réservoirs), et d'autre part, le modèle proposé ne tient pas compte d'un éventuel impact des réactions en flux poreux lors de la différenciation du réservoir. Ici, les litages et les patches de gabbros à grains fins ont été étudiés séparément. L'étude des patches irréguliers du puits U1473A a été menée par ***Ferrando et al. (submitted),*** et les conclusions de ce projet mené en parallèle de cette thèse y sont brièvement exposés. Les patches de grains fins sont interprétés comme des poches de ségrégation des liquides les plus différenciés, ayant réagi lors de leur migration dans le mush avec les minéraux plus primitifs de la charpente cristalline. En effet, les signatures géochimiques des minéraux à grains fins et des bordures de minéraux dans l'encaissant à gros grains sont similaires, et portent les traces des réactions liquide-mush.

La seconde étude dédiée aux litages, et conduite dans le cadre de cette thèse, s'est focalisée sur une portion de 1,35 m de gabbros lités du puits IODP U1473A. Un échantillonnage à très haute résolution (1 échantillon tous les 5 cm en moyenne) a permis d'établir un profil géochimique en roches totales et en analyses *in situ* (éléments majeurs et éléments traces), ainsi que la caractérisation microstructurale de zones clefs de la section par EBSD (Electron BackScatter Diffraction, Géosciences Montpellier). Le litage est caractérisé par une rythmicité importante (lits de 20 cm de large en moyenne), et présente des contacts ignés intrusifs de la lithologie à grains fins dans celle à gros grains, plus différenciée. Cette observation est confirmée par les données microstructurales qui décrivent une fabrique magmatique dans les lits à grains fins d'autant plus forte que l'on se rapproche des contacts avec l'encaissant à gros grains, marquant la présence d'un flux magmatique lors de leur emplacement. L'étude géochimique a quant à elle permit d'établir trois étapes d'évolution des litages impliquant des réactions en flux poreux (***Figure C***). La première étape intervient au cours de l'évolution de la lithologie à gros grains avant intrusion des lits à grains fins. Une migration des liquides interstitiels dans le mush a provoqué des enrichissements en éléments incompatibles, modélisés par AFC. La deuxième étape est liée à l'intrusion du magma parent des gabbros à grains fins dans la lithologie à gros grains : le liquide plus primitif a percolé dans la porosité résiduelle du mush à gros grains et a tamponné les compositions proches des contacts.

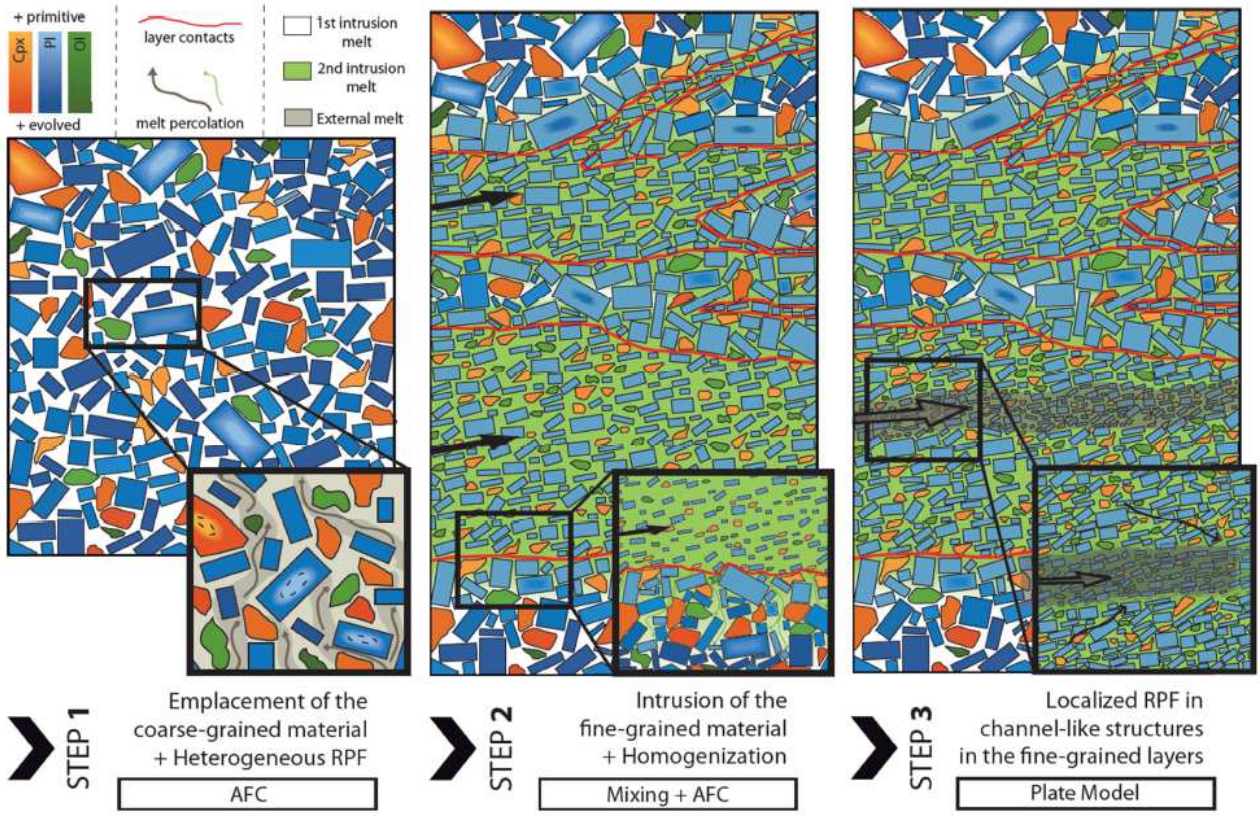

Figure C : Modèle schématique de formation de la séquence litée échantillonnée dans le forage U1473A.

Enfin la troisième étape correspond au tout dernier évènement de percolation des liquides interstitiels dans le mush des lits à grains fins. Cette percolation est focalisée dans des structures de type chenaux. Elle se caractérise au niveau géochimique par une chromatographie des éléments traces incompatibles, qui aboutit à des fractionnements très importants entre terres rares légères et terres rares lourdes dans les minéraux analysés (modélisé grâce au Plate Model). Enfin, la géométrie des contacts montre que la structure est relativement restreinte dans l'espace, et semble être la conséquence d'une intrusion secondaire dans une colonne de mush. Ces résultats impliquent que les réactions liquides-mush observées, qui sont en partie la conséquence directe d'un évènement intrusif dans la croûte, sont potentiellement récurrentes dans les réservoirs de base de croûte puisque le principal mode de mise en place des liquides se fait par empilement et recoupement de séquences intrusives. L'étude des variations de taille de grains a donc permis de montrer l'implication forte des réactions liquide-mush dans l'évolution des lithologies crustales, présentes soit en bordure d'intrusion ou au sein même du mush. Ces réactions impactent à la fois les compositions, mais également les textures et les structures des échantillons considérés. De plus, le liquide résultant de ces réactions semble pouvoir être collecté et donc potentiellement migrer sur de grandes distances dans la croûte et être extrudé.

Chapitre 4 : Développement en plusieurs étapes d'un réservoir magmatique de dorsale lente

La deuxième partie de cette thèse est consacrée à l'étude à plus grande échelle d'une section crustale continue de ~250 m de long échantillonnée dans le puits IODP 735B, soit une unité précédemment décrite comme étant une intrusion individuelle dans la croûte (***Dick et al., 2000***). L'étude se base sur une compilation de données en roche totale existante et sur un échantillonnage haute résolution des différentes lithologies de la section (échantillonnage tous les ~6 m en moyenne). Deux sous-unités se distinguent: une unité inférieure plus primitive, et plus hétérogène en matière de lithologies rencontrées (alternance de troctolites primitives et de gabbros à olivine plus évolués) et de compositions; et une unité supérieure très homogène de gabbros à olivine. L'unité inférieure est interprétée comme une zone d'empilement de sills présentant une fabrique magmatique et une déformation plastique non négligeable. L'unité supérieure quant à elle est interprétée comme un mush homogène présentant des évidences de différenciation progressive et de percolation des liquides de plus en plus évolués vers le haut de l'unité (***Figure D***).

Dans les deux cas, une évolution de liquide primitif par cristallisation fractionnée ne permet pas d'expliquer les gammes de composition géochimiques, ni les compositions modales des échantillons. De plus, des évidences texturales de réactions en flux poreux sont présentes tout au long de la section. Différents modèles AFC appliqués aux deux sous-unités montrent que

la quasi-totalité des gammes de variations géochimiques peuvent être expliquées par la présence de réactions liquide-mush au cours de la différenciation. Les observations pétrographiques des échantillons (textures, compositions modales) et leurs gammes de variations géochimiques *in situ* en éléments traces ont servi à quantifier les paramètres régissant ces réactions (minéraux et proportions en jeu, balance entre assimilation et cristallisation). Un lien a également pu être établi entre les liquides magmatiques de l'unité inférieure et les liquides évoluant dans le mush de l'unité supérieure. Ces liquides hybrides proviennent des réactions liquide-mush mis en évidence dans l'unité inférieure, et semblent progressivement être collectés et différences vers le haut de la séquence. Cette étude a permis d'établir un modèle de mis en place et d'évolution complet d'un réservoir magmatique, et montre l'omniprésence des réactions en flux poreux et leur impact sur la différenciation des liquides magmatiques mis en place dans la croûte.

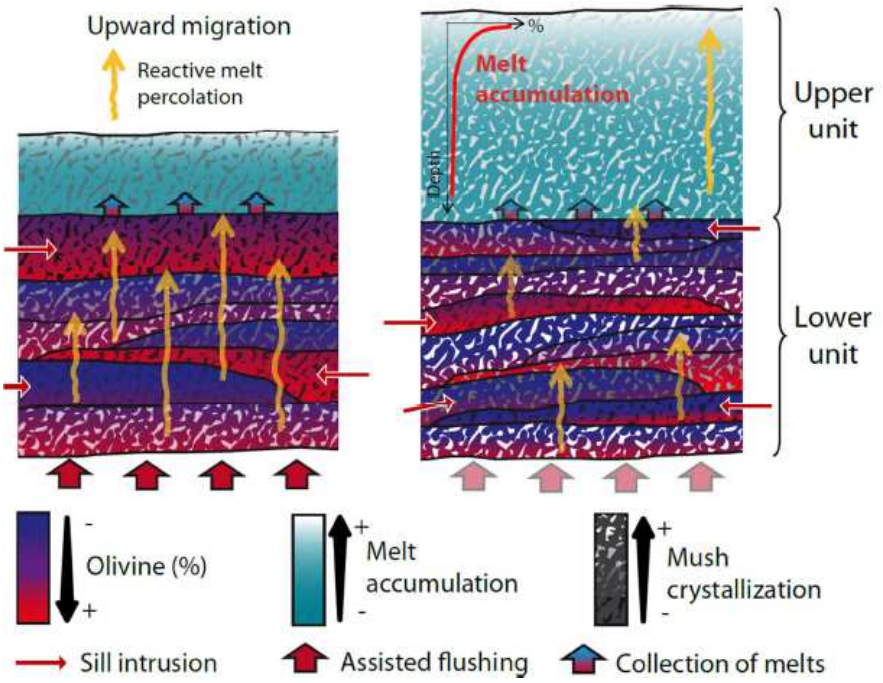

Figure D : Modèle de formation du réservoir magmatique correspondant à la séquence échantillonnée dans le puits IODP 735B.

Ce premier modèle de réservoir magmatique décrit à cette échelle a plusieurs implications pour l'accrétion crustale des dorsales à expansion lente, que ce soit concernant (1) le rôle de la dynamique de migration des liquides et des réactions en jeu dans l'acquisition des signatures géochimiques cumulatives des lithologies gabbroïques (modèle de "melt flushing" s'ajoutant aux processus de compaction, de densité et de déformation) ou (2) l'assimilation des cumulats les plus primitifs formés dans les réservoirs et les questions relatives à l'origine et la composition des magmas parents injectés dans la croûte à Atlantis Bank. Mais ce modèle a également des implications plus larges pour l'accrétion crustale des dorsales océaniques à

expansion lentes avec (3) la question de l'applicabilité du modèle à d'autres sections de croûte inférieure que celle échantillonnée pour cette étude. Ce dernier point est abordé plus en détail dans le chapitre suivant.

Chapitre 5 : Implications pour l'évolution des magmas des dorsales à expansion lente

Cette partie est consacrée à l'étude des similarités entre forages océaniques et les implications à plus grande échelle des modèles établis lors des études à haute résolution développées précédemment. Cette partie présente également de nouvelles données géochimiques *in situ* en éléments majeurs et en éléments traces, analysées dans des échantillons provenant d'une section de ~400 m du puits IODP U1473A. Le chapitre commence avec une synthèse des modèles développés, en les replaçant dans une séquence d'évolution de réservoir magmatique de croûte inférieure. Le détail des caractéristiques communes établies entre les forages *in situ* réalisés à Atlantis Bank (forages IODP 735B et U1473A) mais également à Atlantis Massif est ensuite présenté. Atlantis Massif est un corps complexe océanique situé sur la dorsale Atlantique (30°N) formé il y a ~2 Ma, dans lequel le puits IODP U1309D a été foré (~1400 mbsf - ***Blackman et al., 2006***). À la différence d'Atlantis Bank, des lithologies plus primitives sont trouvées dans la section (comme les troctolites riches en olivines) qui contient une majorité de gabbros *sensu stricto*, de même que des fragments de roches mantelliques assimilées (***Drouin et al., 2009; Ferrando et al., 2018***). Malgré ces différences, des points communs concernant les processus de différenciation et la dynamique de mise en place et de migration des liquides ont été observés. Les réactions liquide-mush semblent omniprésentes dans les cumulats gabbroïques de croûte inférieure. Les réactions les mieux documentées dans la littérature sont celles observées dans des échantillons provenant d'Atlantis Bank (puits IODP 735B, voir ci-dessus). Concernant les nouvelles données *in situ* acquises pour les échantillons du puits U1473A, les réactions établies au cours de l'étude du réservoir de 735B pour l'unité supérieure permettent d'expliquer, à première vue, les gammes de composition en éléments traces de la section. Concernant le puits U1309D, la majorité des réactions en flux poreux établies sont relatives aux processus d'assimilation de lithologies d'origine mantellique, et ne permettent pas pour l'instant d'établir la même importance des réactions liquides-mush dans la différenciation des lithologies gabbroïques.

L'autre point commun entre les différentes sections *in situ* forées à Atlantis Bank et Atlantis Massif concerne les modes de mise en place de magmas, et de formation des réservoirs magmatiques dans la croûte. Tout ou partie du modèle de réservoir établit au chapitre 4 semble s'appliquer aux différentes sections *in situ*. Pour Atlantis Bank, les caractéristiques structurales et géochimiques observées dans le puits U1473A et dans le reste du puits 735B ressemblent aux

caractéristiques décrites pour l'unité supérieure du modèle de réservoir, de par leur relative homogénéité et le caractère plus évolué des lithologies. Les quelques divergences observées (présence de gabbros à oxydes, signatures géochimiques plus hétérogènes) sont probablement dues à des évènements magmatiques ou de déformation secondaires. Pour le forage IODP U1309D, la dynamique d'accrétion précédemment établie par accumulation de sills primitifs dans la séquence (***Godard et al., 2009; Grimes et al., 2008***), et le caractère plus hétérogène des unités laissent penser à un mode d'évolution des réservoirs se rapprochant de celui observé pour l'unité inférieure du réservoir de 735B. La seule exception concerne une section précédemment décrite par ***Suhr et al. (2008)***, qui comporte à la fois une unité inférieure hétérogène et une unité supérieure homogène interprétées ici comme faisant part d'un même réservoir, tel que décrit dans 735B.

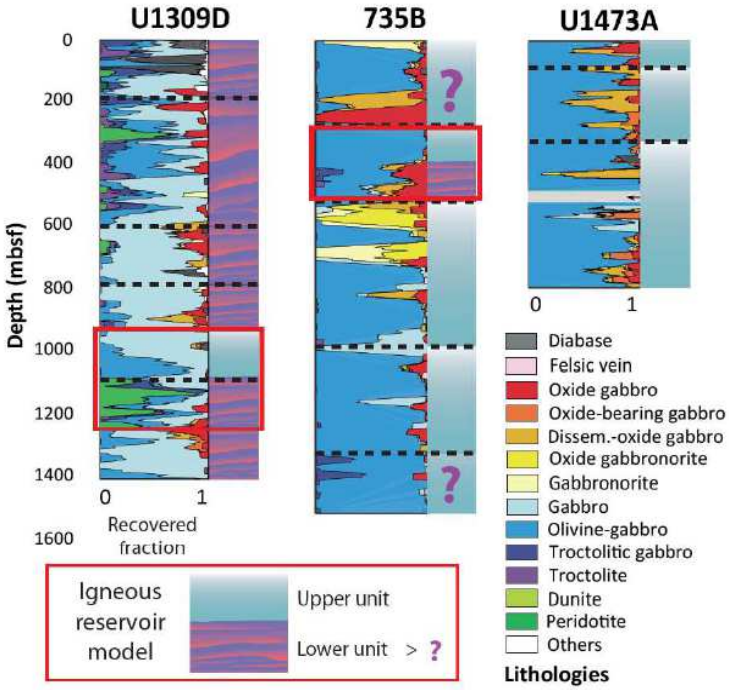

Figure E : Schéma de synthèse des comparaisons établies entre le modèle de réservoir magmatique établit au chapitre 4, et les sections in situ forées à Atlantis Bank (IODP 735B et U1473A) et à Atlantis Massif (IODP U1309D).

En conclusion, les études à haute résolution menées lors de cette thèse à différentes échelles sur des échantillons naturels permettent de mieux comprendre la dynamique d'accrétion crustale au niveau des dorsales à expansion lente. Elles permettent également pour la première fois d'établir des comparaisons directes entre les séquences gabbroïques forées dans deux corps complexes distincts, Atlantis Bank (dorsale Sud-Ouest indienne) et Atlantis Massif (dorsale médio-atlantique, ***Figure E***).

Chapitre 6 : Contraintes expérimentales sur l'évolution des magmas tholéiitiques à Atlantis Bank

Pour finir, le dernier chapitre de ce manuscrit présente les résultats des études de pétrologie expérimentale réalisées au cours de cette thèse. Deux projets distincts ont été menés, le premier concernant la reproduction des processus de cristallisation à l'équilibre et de cristallisation fractionnée d'une composition de diabase primitive échantillonnée au sein même d'Atlantis Bank (puits U1473A - ***MacLeod et al., 2017b***), et considérée comme analogue du liquide primitif susceptible d'alimenter les réservoirs de base de croûte. Les expériences ont été réalisées en autoclave à 2 kbar, pour des températures allant de 1200 à 1070°C, et pour des conditions redox fixées à QFM0. Le deuxième projet visait à déterminer de nouveaux coefficients de partage d'éléments traces pour les principaux minéraux constitutifs des échantillons gabbroïques, à savoir olivine, plagioclase et clinopyroxene. Ces coefficients de partage ont été déterminés en reproduisant l'expérience réalisée à 1100°C au cours du premier projet, avec les mêmes conditions et à partir de la même composition de départ dopée à 300 ppm en divers éléments traces. Contrairement au premier projet, au cours duquel seules des analyses *in situ* des éléments majeurs étaient nécessaires (par microsonde électronique), le deuxième projet nécessitait également de pouvoir analyser les éléments traces dans les produits des expériences par ablation laser. Afin d'optimiser la taille des cristaux formés, la méthode dite de "temperature cycling" a été appliqué pour la première fois sur un système de type tholéiitique (***Erdmann and Koepke, 2016***). Tous les résultats obtenus ont ensuite été comparés à des expériences similaires de la littérature (e.g., ***Berndt et al., 2005; Feig et al., 2006; Villiger et al., 2007***), mais aussi aux résultats de modélisations thermodynamiques de cristallisation pour le même système, et à des modèles de détermination de coefficients de partage de la littérature (e.g., ***Sun et al., 2017; Wood and Blundy, 1997***). Que ce soit pour les étapes de cristallisation ou pour les coefficients de partage obtenus, les résultats sont globalement similaires aux modèles préétablis. Quelques variations sont toutefois à noter, tel que le degré de cristallinité observé à une température donnée pour les expériences de cristallisation, ou encore l'impact de la présence d'eau sur les coefficients de partage et qui n'est pas pour m'instant prit en compte dans la plupart des modèles. À terme, les expériences réalisées au cours de cette thèse vont permettre d'affiner les modèles de cristallisation, et de vérifier les paramètres clefs que sont les coefficients de partage utilisés pour tracer l'évolution des signatures géochimiques au cours de la différenciation magmatique.

Abstract

Oceanic crust covers about two-thirds of the Earth's surface and is built along oceanic spreading ridges, accounting for more than 60% of the Earth's yearly magma budget. Yet, processes of magma emplacement and evolution within the crust are not sufficiently constrained, and especially at slow-spreading ridges that represent more than half of the 55 000 km-long ridge system (spreading rates <40 mm/y). Since the early 80's, several drilling operations were conducted by an international consortium (the current International Ocean Discovery Project) and provide the scientific community with an invaluable opportunity to study *in situ* lower oceanic crust samples. Oceanic Core Complexes (OCCs) exhume deep mantle and gabbroic sequences thanks to the development of long-lived detachment faults at the ridge axes during asymmetric spreading. The largest OCC and one of the most thoroughly studied is Atlantis Bank on the Southwest Indian Ridge (32°S, 57°E). In total, three deep Holes were drilled in the structure: ODP Hole 735B during Leg 118 and 176 (1500 m-long), IODP Hole 1105A during Leg 179 (157 m-long) and IODP Hole U1473A during Exp. 360 (800 m-long). The results of their study regarding magmatic accretion are consistent with what has been found during the studies of other OCCs (e.g., Atlantis Massif on the Mid-Atlantis Ridge) or fossil portions of oceanic crust from ophiolites (e.g. the Ligurian and Alpine ophiolites). The heterogeneous character of the slow-spreading oceanic crust is directly related to the modes of melt emplacement and migration within the crustal reservoirs. The current vision of the magmatic systems involves a predominance of mushy magma reservoirs, with the implication of reactive porous flow processes during differentiation of the gabbroic crustal lithologies in addition to simple crystallization processes.

During my PhD thesis I conducted high-resolution petrographic, structural and geochemical studies of gabbroic cumulate sections from the two deepest drilled holes of Atlantis Bank, i.e. Hole 735B and Hole U1473A. The new resulting igneous reservoir models and associated evolution processes provide new constraints on magmatic accretion at slow-spreading ridges. The coupled experimental study of simple crystallization processes aimed at better constraining those processes in order to better characterize, in the future, the balance between crystallization and melt-rock reactions in the evolution of the studied gabbro lithologies.

The results of the study of a layered gabbro sequence from Hole U1473A indicate that layers originally formed by intrusion of a crystal-bearing magma into a solidifying coarse-grained, more evolved mush. Melt-rock reactions are widespread, occurred at all stages of formation of the layers, and contrasting melt dynamics due to variable focusing of the porous flow impacted the geochemical signatures and textures of the reacted gabbros. In addition, among the two main types of systematic grain size variations described in gabbro cumulates at Atlantis Bank, layering likely represent contacts between magma reservoirs within the crust. The geometry and the different steps of formation of a major igneous reservoir have been established thanks to the study of a 250 m-long section from Hole 735B. The section was previously described as a single intrusion due to its characteristic large-scale whole rock upward differentiation trends. In details, the lower half of the reservoir formed by sills stacking, and was impacted by successive replenishment events that assimilated the primitive cumulates initially crystallized in the sills. In contrast, the upper half of the reservoir constitutes a homogeneous unit that evolved by progressive percolation of melts collected from the lower units, and by accumulation of evolved melts towards the top of the section. We additionally show that melt-rock reactions triggered by a global upward porous melt flow in the reservoir constitute the main processes governing magma differentiation. We infer that the principal driving force for the upward percolation of melts through the entire section is a "melt flushing" process caused by successive replenishment of the reservoir. Comparison of the geochemical and structural characteristics defining the igneous reservoir model with other sections of *in situ* lower crust from Atlantis Bank and Atlantis Massif, reveal that all or part of the model can apply to those sections. This led to the broader conclusion that the model could initiate new perspectives regarding the formation and evolution of the lower slow-spreading crust outside of the Atlantis Bank system.

Finally, the experimental study help constraining simple crystallization processes under lower crustal conditions. The results confirm that crystallization alone cannot account for the formation of the lower crust gabbroic lithologies, and paves the way for further characterization of melt-rock reactions and the quantification of their involvement in magma accretion at slow-spreading ridges.

Résumé

La croûte océanique, qui recouvre environ les deux tiers de la surface de la Terre, est formée au niveau des dorsales océaniques où plus de 60% du budget magmatique annuel de la Terre se concentre qui représentent plus de 60 % du budget annuel du magma de la Terre. Pour autant, les processus de mise en place et d'évolution des magmas dans la croûte ne sont pas encore suffisamment contrains, et tout particulièrement au niveau des dorsales à expansion lente qui comptent pour plus de la moitié des 55 000 km du système de dorsales (taux d'expansion <40 mm/an). Depuis le début des années 1980, de nombreuses opérations de forages ont été menées par un consortium international (l'actuel International Ocean Discovery Project), et ont fourni à la communauté scientifique une occasion inestimable d'étudier des échantillons *in situ* de croûte inférieure océanique. Les Cores Complexes Océaniques (OCCs) sont le lieu d'exhumation de séquences gabbroïques profondes, grâce au développement de grandes failles de détachements à l'axe de la ride lors d'épisodes d'extension asymétrique. Le plus grand OCC et l'un des plus étudiés est celui d'Atlantis Bank sur la dorsale Sud-Ouest Indienne (à 32°S, 57°E). Au total, trois forages profonds y ont été réalisés: le puits ODP 735B pendant les Leg 118 et 176 (1500 m de long), le puits IODP 1105A pendant le Leg 179 (157 m de long) et le puits IODP U1473A pendant l'Expédition 360 (800 m de long). Les résultats de leur étude concernant l'accrétion magmatique sont en accord avec les résultats des études d'autres OCCs (e.g., Atlantis Massif sur la dorsale Atlantique) ou des reliques de croûte océanique provenant d'ophiolites (e.g., les ophiolites Ligurienne ou Alpines). Le caractère hétérogène de la croûte océanique de dorsales lentes est directement relié aux modes de mise en place et de migration des liquides dans les réservoirs crustaux. La vision actuelle des systèmes magmatiques implique une prépondérance des réservoirs sous forme de bouillie cristalline, ou mush, et la participation de processus de flux poreux réactifs pendant la différenciation des lithologies gabbroïques crustales, en plus des processus de cristallisation simples.

Pendant ma thèse j'ai mené des études pétrographiques, structurales et géochimiques à haute-résolution de sections gabbroïques cumulatives provenant des deux forages les plus profonds d'Atlantis Bank, i.e. les puits ODP 735B et IODP U1473A. Les nouveaux modèles de réservoir igné et les processus magmatiques associés ont permis d'établir de nouvelles contraintes sur l'accrétion magmatique aux dorsales lentes. L'étude de pétrologie expérimentale couplée des processus de cristallisation simple visait à mieux contraindre ces processus afin de

pouvoir, dans le futur, mieux caractériser l'implication relative de la cristallisation et des processus d'interactions liquides-roches dans l'évolution des lithologies gabbroïques étudiées.

Les résultats de l'étude des gabbros lités du puits IODP U1473A montrent que ces litages sont en premier lieu formés par intrusion d'un magma cristallin dans un mush à gros grains plus différencié. Des interactions liquides-roches se sont produites à toutes les étapes de formation du litage, et des dynamiques de percolation contrastées dues à une focalisation variable du flux poreux ont impacté les signatures géochimiques et les textures des gabbros concernés. De plus, parmi les deux types de variations systématiques des tailles de grain décrites dans les gabbros d'Atlantis Bank, les litages représentent vraisemblablement un contact entre différents réservoirs de la croûte. La géométrie et les différentes étapes de formation d'un réservoir igné principal ont été établies grâce à l'étude d'une section de 250 m de long provenant du puits 735B. La section avait été précédemment décrite comme une intrusion unique du fait de ses tendances progressives d'évolution vers le haut en compositions de roches totales. Dans le détail, la moitié inférieure du réservoir a été formée par accumulation de sills et a été impactée par des épisodes successifs de recharge qui ont assimilé les cumulas les plus primitifs initialement cristallisés dans ces sills. A l'inverse, la moitié supérieure du réservoir constitue une unité homogène ayant évolué par percolation progressive des liquides collectés depuis la partie basse du réservoir, et par accumulation des liquides évolués vers le haut de la section. Nous montrons également que les interactions liquides-roches induites par le flux poreux global ascendant constituent les processus principaux gouvernant la différenciation magmatique. Nous proposons que la principale force motrice du flux poreux ascendant au travers de la section soit un processus de vidange des liquides causé par la recharge en continu du réservoir. La comparaison des caractéristiques géochimiques et structurales qui décrivent le modèle de réservoir igné avec celles d'autres sections in situ de croûte inférieure provenant d'Atlantis Bank et Atlantis Massif montre que tout ou partie du modèle peut être appliqué à ces sections. Cela a conduit à la conclusion plus large que le modèle pourrait ouvrir de nouvelles perspectives concernant la formation et l'évolution de la croûte inférieure de dorsales lentes en dehors du système d'Atlantis Bank. Enfin, l'étude de pétrologie expérimentale aide à contraindre les processus de cristallisation simple dans des conditions typiques de base de croûte. Les résultats confirment que la cristallisation seule ne peut expliquer la formation des lithologies gabbroïques de base de croûte, et ouvrent la voie à une caractérisation ultérieure plus précise des interactions liquides-roches et à une quantification de leur implication dans l'accrétion magmatique au niveau des dorsales à expansion lente.

Zusammenfassung

Die ozeanische Kruste bedeckt etwa zwei Drittel der Erdoberfläche und wird entlang Mittelozeanischer Rücken gebildet, auf die mehr als 60% des jährlichen Magmabudgets der Erde entfallen. Dennoch sind die Prozesse der Magmenbewegung und -entwicklung innerhalb der Kruste bislang noch nicht ausreichend erforscht, insbesondere an langsam spreizenden Rücken (Ausbreitungsraten <40 mm/y), die mehr als die Hälfte des 55000 km langen globalen Rückensystems ausmachen. Seit Anfang der 80er Jahre wurden mehrere Bohrungen von einem internationalen Konsortium (dem aktuellen International Ocean Discovery Project) durchgeführt, die der wissenschaftlichen Gemeinschaft die unschätzbare Gelegenheit bieten, Proben der unteren ozeanischen Kruste *in situ* zu untersuchen. Aufgrund langlebiger tektonischer Störungen an den Spreizungsachsen infolge von asymmetrischer Spreizung, können durch Ozeanische Kernkomplexe (Oceanic Core Complexes; OCCs) tiefliegende gabbroide Sequenzen exhumiert werden. Der größte und einer der am gründlichsten untersuchten OCCs ist Atlantis Bank am Südwestindischen Rücken (32°S, 57°E). Insgesamt wurden hier drei Tiefbohrungen durchgeführt: ODP Bohrloch 735B während der Expeditionen 118 und 176 (1500 m lang), IODP Bohrloch 1105A während der Expedition 179 (157 m lang) und IODP Bohrloch U1473A während der Expedition 360 (800 m lang). Die Ergebnisse der Untersuchungen zur magmatischen Akkretion an diesen Bohrkernen stehen im Einklang mit dem, was vorherige Studien an anderen OCCs (z.B. Atlantis-Massif am Mittelatlantischen Rücken) oder fossilen Teilen der ozeanischen Kruste aus Ophiolithen (z.B. den ligurischen und alpinen Ophiolithen) bereits herausfanden. Der heterogene Charakter der langsam spreizenden ozeanischen Kruste steht in direktem Zusammenhang zu den Modi der Schmelzeinlagerung und -migration in den krustalen Magmenreservoiren. Die aktuelle Ansicht über die magmatischen Systeme geht von einem dominanten Reservoir von Kristallbrei aus, wobei neben einfachen Kristallisationsprozessen auch reaktives Fließen von Schmelze durch den Porenraum bei der Differenzierung der gabbroiden Krustenlithologien eine Rolle spielt. Während meiner Doktorarbeit habe ich hochauflösende petrographische, strukturelle und geochemische Studien an gabbroiden Kumulatsequenzen aus den beiden tiefsten Bohrungen an Atlantis Bank, Bohrloch 735B und Bohrloch U1473A, durchgeführt. Die neuen Modelle der magmatischen Reservoire und die damit verbundenen Bildungsprozesse lassen neue Schlüsse für die Akkretion von Magmen an langsam spreizenden Rücken zu. Gleichzeitig durchgeführte einfache Kristallisationsexperimente zielten darauf ab, diese Prozesse besser nachzuvollziehen, um in Zukunft das Gleichgewicht zwischen Kristallisation und Schmelz-Gesteins-Reaktionen in der Entwicklung der untersuchten Gabbros besser charakterisieren zu können.

Die Ergebnisse der Studie an lagigen Gabbros aus Bohrloch U1473A geben Hinweise darauf, dass deren Lagen ursprünglich durch das Eindringen eines kristallhaltigen Magmas in einen verfestigenden, grobkörnigen und weiter entwickelten Kristallbrei gebildet wurden. Schmelz-Gesteins-Reaktionen traten in allen Phasen der Lagenbildung auf, zudem wirkte sich die unterschiedliche Bewegung von Schmelze durch variable Fokussierung des porösen Fließens auf die geochemischen Signaturen und Texturen der reagierenden Gabbros aus. Die systematischen Korngrößenvariationen, die in den Gabbros von Atlantis Bank beschrieben werden, stellen darüberhinaus vermutlich Kontakte zwischen verschiedenen Magmenreservoiren innerhalb der Kruste dar. Die Geometrie und die Entwicklung eines großen magmatischen Reservoirs wurden durch die Untersuchung eines 250 m langen Abschnitts aus Bohrloch 735B ermittelt. Der Abschnitt wurde zuvor aufgrund seines charakteristischen aufwärts gerichteten Differentiationstrends im Gesteinschemismus als eine einzelne Intrusion beschrieben. Die detaillierte Untersuchung zeigt, dass die untere Hälfte des Reservoirs in übereinanderliegenden kleinen Magmenkammern (sills) gebildet wurde, die zudem durch aufeinanderfolgende Magmenzuflüsse in die bereits kristallisierten sills beeinflusst wurden. Im Gegensatz dazu stellt die obere Hälfte des Reservoirs eine homogene Einheit dar, die sich durch fortschreitende Perkolation der aus den unteren Einheiten gesammelten Schmelzen und durch Akkumulation der entwickelten Schmelzen zum oberen Teil des Abschnitts hin entwickelte. Unsere Studie zeigt außerdem, dass Schmelz-Gesteins-Reaktionen, die durch eine übergeordnete, nach oben gerichtete poröse Schmelzbewegung im Reservoir hervorgerufen werden, die Hauptkomponente bei der Magmendifferenzierung darstellen. Daraus lässt sich ableiten, dass die treibende Kraft für die aufwärtsgerichtete Perkolation von Schmelzen über den gesamten Abschnitt ein "Ausspülen" von Schmelze ist, das durch den sukzessiven Zufluss von Schmelzen in das magmatische Reservoir verursacht wird. Vergleicht man andere Abschnitte der *in situ* beprobten unteren Kruste von Atlantis Bank und Atlantis Massif mit den geochemischen und strukturellen Charakteristika, die das Modell eines magmatischen Reservoirs beschreiben, zeigt sich, dass dieses Modell ganz oder zumindest teilweise auch auf andere Bereiche von Atlantis Bank und das Atlantis Massif zutreffen kann. Dies führte zu der Schlussfolgerung, dass das Modell neue Sichtweisen für die Bildung und Entwicklung der unteren langsam spreizenden Kruste jenseits von Atlantis Bank eröffnen könnte. Die experimentelle Studie hilft dabei, einfache Kristallisationsprozesse der unteren Kruste abzuleiten. Ihre Ergebnisse bestätigen, dass die Bildung der gabbroiden Lithologien der unteren Kruste nicht allein durch einfache Kristallisation erklärt werden kann, und ebnen den Weg für die weitere Charakterisierung von Schmelz-Gesteins-Reaktionen und eine exaktere Quantifizierung von deren Einfluss auf die Akkretion von Magma an langsam spreizenden Rücken.

TABLE OF CONTENTS

Introduction

The oceanic crust covers about 70% of the Earth's surface and is produced at spreading ridges. The characteristics of the crust and the processes involved during its accretion vary as a function of the spreading rate at the ridge axis (***Coogan, 2014***). Slow-spreading ridges (spreading rates < 40 mm/y) account for about 50% of the global 55 000 km-long ridge system (***Dunn, 2015***). The oceanic crust formed at those ridges does not fit the historical model that was depicted during the Penrose Conference, and the well-stratified ensemble of successive mantle, gabbroic and finally extrusive basalt lithologies (from bottom to top - Conference Participants, 1973). In contrast, at slow-spreading ridges a more complex interplay between magmatic processes and deformation is at stake, leading to the formation of a very heterogeneous crust in depth (***Cannat, 1996, 1993***). This heterogeneity has been identified for example during campaigns of (sub)seafloor seismic imaging, with the observation of interleaved mantle-inherited lithologies and magmatic components. The lesser development of the magmatic component of the crust at slow-spreading ridges is mainly the result of a lower mantle melt supply at the ridge axis (***Carbotte et al., 2015; Dick et al., 2003; Dunn, 2015***). Only few seismic studies were able to identify either the presence of melts within the crust or the occurrence of only localized, discontinuous and ephemeral magma reservoirs (***Canales et al., 2017; Jian et al., 2016; Seher et al., 2010; Singh et al., 1999***). The development and evolution of magma reservoirs and associated processes which govern magma differentiation at depth are still questioned. Yet, they are fundamental for the understanding of the structure and composition of the oceanic crust.

The modes of melt migration involved in the formation and evolution of the reservoirs are key in the understanding of magma differentiation. Magma emplacement by intrusions within the crust during large magmatic events is usually inferred from the study of long *in situ* section of lower crust or ophiolites (***Dick et al., 2019; Godard et al., 2009; Sanfilippo and Tribuzio, 2013***). In addition, magma storage models in the oceanic crust progressively shifted from the large melt-rich magma chambers towards the current models of more complex, mush-dominated magma reservoirs (***Lissenberg et al., 2019***). As a consequence, melt migration by porous flow is considered as a leading process within the lower crust. It is likely facilitated in an extensional context where deformation applies. Evidences for nearly ubiquitous melt-rock reactions are found in lower crust samples from various localities. These are markers of the occurrence of reactive porous flow during the lithologies formation (***Lissenberg and MacLeod, 2016***). Their quantification mainly at the scale of individual samples, helped for example confirm the presence of assimilated mantle relicts within deep sections of lower crust (***Ferrando et al., 2018***), or infer that mush assimilation and/or reworking must happen at variously scales during the development of the lower crust reservoirs (e.g. ***Leuthold et al., 2018; Sanfilippo et al., 2015***).

The study of *in situ* samples of the lower oceanic crust from slow-spreading ridges is facilitated by the presence of Oceanic Core Complexes (OCCs) at the ridges axis in several locations. OCCs are the result of the formation of low-angle and long-lived detachment faults that exhume deep sections of the crust at the seafloor during asymmetric spreading. Overall, asymmetric accretion would account for about half of extension along ridges in some areas (***Escartín et al., 2008; Ildefonse et al., 2007***). Expeditions led by the ODP/IODP consortium sampled by drilling long *in situ* sections of lower oceanic crust in two different OCCs, Atlantis Bank (Southwest Indian Ridge) and Atlantis (Mid-Atlantic Ridge). Both sets of samples show distinctive characteristics of structure, composition and also proportions of the gabbroic lithologies recovered. These characteristics are difficult to reconcile with a single integrated model of formation of slow-spreading oceanic crust (***Blackman et al., 2006; MacLeod et al., 2017***). Their study, however, converge toward models of heterogeneous magmatic systems, where lithologies form thanks to complex interplays between large magmatic events (3 to 5 intrusion events identified at Atlantis Bank by ***Dick et al., 2000***), and different stages of replenishment, percolation or infiltration of melts. Adding to this complexity, deformation likely plays a role in the organization and interconnection of the magmatic structures (***Dick et al., 2019***).

The aim of this PhD project was to identify and to quantify magmatic processes occurring at different stages of evolution of the slow-spreading ridge magmatic system. To do so, I combined two different levels of observation: 1/ at the scale of individual samples with high-resolution petrographic and geochemical studies, and 2/ at the scale of the reservoirs with an integration of the high-resolution observations to the description of the *in situ* sections considered. The project focuses on the largest ever discovered OCC that is one of the most thoroughly studied OCCs since its discovery in the late 70's: the Atlantis Bank OCC on the Southwest Indian Ridge (32°S, 57°E). Four ODP/IODP campaigns made it possible to drill three holes in the structure, separated by only few kilometers (***Casey et al., 2007; Dick et al., 2000; MacLeod et al., 2017***). The two deepest ODP Hole 735B and IODP Hole U1473A were sampled for this study and gave us the invaluable opportunity to combine the two levels of observation described above on almost entirely preserved and continuous sections of lower crust. I implemented two different approaches for the study of the Atlantis Bank magmatic system.

1/ Structural, petrographic and geochemical studies were conducted on natural gabbroïc samples of lower crust from ODP Hole 735B and IODP Hole U1473A. The sampling strategy was mostly based on previous descriptions of the structural and geochemical characteristics of the holes, in order to target different levels of the magmatic reservoirs. The structures sampled are:

- A well-defined grain size layering from the main layered sequence of Hole 1473A (***MacLeod et al., 2017***); it represents one type of the systematic grain size variations identified in both Hole 735B and Hole U1473A.
- An entire tectono-magmatic unit of ODP Hole 735B that presents whole rock upward geochemical differentiation signatures; it was previously characterized as a single intrusion by ***Dick et al. (2000)***.
- The most primitive and preserved gabbroic lithologies of two different units; these lithologies were identified by ***MacLeod et al. (2017)*** in IODP Hole U1473A.

2/ A complementary, experimental petrology study was conducted to better characterize the simple crystallization processes that act under conditions compatible with the lower crust at Atlantis Bank. Such crystallization of MORB-type melts characteristic of Atlantis Bank are presumed to take part in magma differentiation, at least partly and concomitantly with melt-rock reactions associated with reactive porous flow. An attempt to determine Rare Earth Element partition coefficients is also presented. This aimed at finding more accurate values for parameters that are commonly used in numerical modeling of magmatic crystallization/interaction processes.

The manuscript is organized in six main chapters, two of them being dedicated to the literature review of the scientific question and of the object studied. In order of appearance:

Chapter 1.

Overview of the magmatic system and associated evolution processes for the slow-spreading lower oceanic crust. A special focus is also given on the geochemical tracers used to quantify magma differentiation and on the numerical models available for the study of lower crust samples.

Chapter 2.

Synthesis of relevant models of OCCs formation during asymmetric spreading, and importance of the study of OCCs for the understanding of the lower slow-spreading oceanic crust accretion. In addition, I propose a description of the main features that characterize the Atlantis Bank OCC, plus a description of the three *in situ* sections drilled at Atlantis Bank (including the main results of their study).

Chapter 3.

Determination of the main melt migration processes that are involved in the formation of characteristic grain size variations and were identified at Atlantis Bank, and identification of their impact on the geochemical signatures of the gabbro cumulate sequence. I present the context of the study of the layered series sampled in IODP Hole U1473A, that is further

developed in the second part of the chapter in the form of an article submitted to *Geochemistry, Geophysics, Geosystems*.

Chapter 4.

Structural, petrographic and geochemical study of the tectono-magmatic unit from ODP Hole 735B that was previously characterized as an intrusion by ***Dick et al. (2000)***, and development of a new integrated model of formation and evolution of a lower crust igneous reservoir. This chapter is presented in the form of an article that has been accepted for submission in the special issue of *Frontiers in Earth Science* "Magma-rock and magma-mush interactions as fundamental processes of magmatic differentiation".

Chapter 5.

Review of the main findings of the studies on natural samples and comparison of the newly developed igneous reservoir model with other portions of long *in situ* sections drilled in OCCs. The comparison is based on new geochemical data for the two units sampled in IODP Hole U1473A, and on published data and descriptions of Holes 735B and U1473A for Atlantis Bank and Hole U1309D for Atlantis Massif.

Chapter 6.

Presentation of the results of the experimental petrology studies and perspectives on the implications of these results for the lower crust magmatic system at Atlantis Bank. The first part of the chapter aims at contextualizing the purpose of the experimental petrology studies. The second part is dedicated to the study of crystallization processes. Finally, the third part deals with the determination of partition coefficients.

I finally conclude with a short synthesis of the main outcomes of this thesis and I present the perspectives offered by the new models of magmatic accretion developed herein.

CHAPTER I.

Migration and evolution of melts within the slow-spreading lower oceanic crust

The role of magmatic processes in building the lower crust structure and in defining its composition

1 The magmatic system below (ultra)slow-spreading ridges

1.1 The oceanic spreading ridges system and characteristics of slow- to ultra-slow spreading ridges

Oceanic crust covers about 70% of the Earth's surface. The accretion of the oceanic crust at spreading ridges is a key process in the understanding of Earth's dynamics. The magma budget of spreading ridges represents more than 60% of the total magma production per year. Magma can be emplaced within the lower oceanic crust (intrusive fraction - 50% of the Earth magma budget; ***Fisher and Schmincke, 1984***), or extruded as Mid Oceanic Ridge Basalts (MORB) at the ridge axis and trapped within the crust as dikes. Two end member models of spreading ridges can be distinguished with regards to the expansion rate at the ridge axis, i.e. how fast the two diverging tectonic plates separate and the oceanic crust forms (*Figure 1.1*).

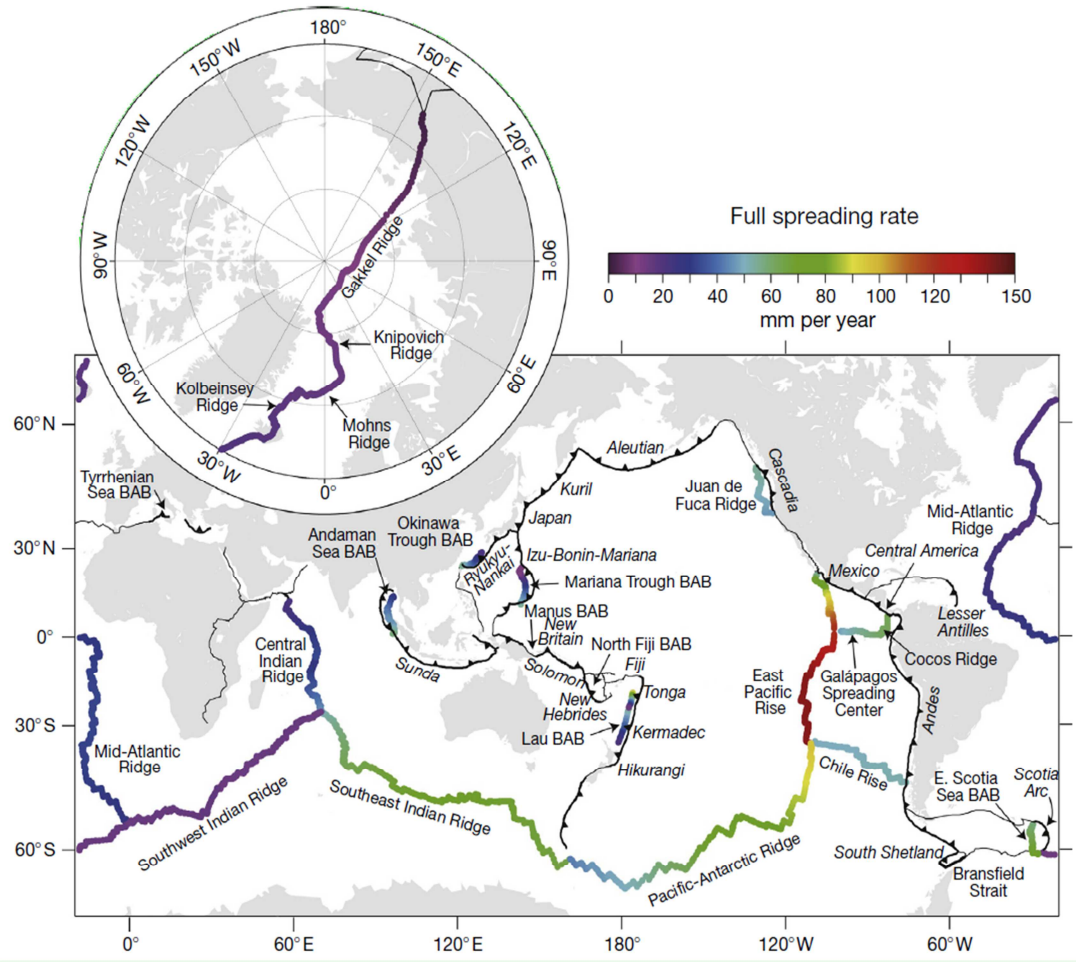

Figure 1.1 - Mid-ocean ridges, active back-arc basins (BAB) and subduction zones worldwide (Dunn, 2015)

Fast-spreading ridges have spreading rates higher than 8 cm/y (such as the East Pacific Rise with an expansion rate of about 14 cm/y), while slow- to ultra-slow spreading ridges have expansion rates lower than 4 cm/y (such as the Southwest Indian Ridge with a maximum expansion rate along the axis of ~1.8 cm/y). This difference in spreading rates leads to variability in spreading ridges morphology, structure, and composition. Unlike the continuous symmetric and narrow relief of fast-spreading ridges, the emblematic morphology at slow-spreading ridges resembles to a rift system, with an axial graben flanked by elevated and fractured plateaus that may extend several tens of kilometers away from the ridge axis. The slower the spreading rate, the rougher and more irregular the topography (*Figure 1.2* - ***Buck et al., 2005***). The different morphologies expressed at the ridge surface are the result of critical differences in the processes of accretion of the crust and accommodating the extensional deformation at depth.

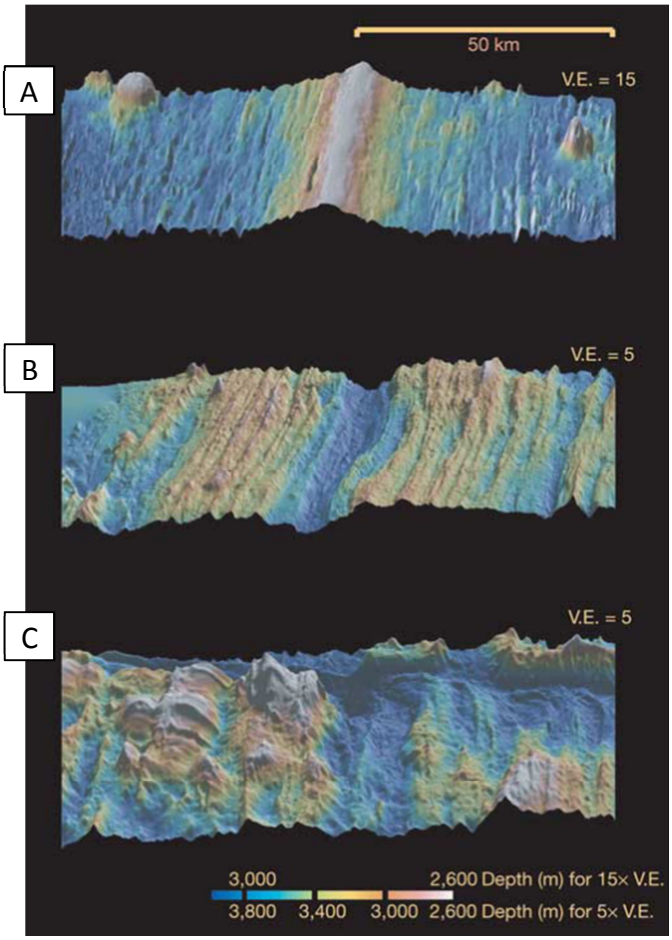

Figure 1.2 - Shaded relief images of bathymetry over three representative sections of the mid-ocean ridge system (Buck et al., 2005). Each image shows ~40 km sections along the ridge axis and ~110 km across the axis. (a) East Pacific Rise - fast-spreading ridge (>8 cm/y); (b) Southeast Indian Ridge, intermediate spreading ridge; (c) Mid-Atlantic Ridge, slow-spreading ridge (<4 cm/y).

Compared to the architecture of fast-spreading environments where steady-state active magma reservoirs are identified all along the ridge (e.g. ***Detrick et al., 1987; Nicolas et al., 1988; Sinton and Detrick, 1992***), there is no long-lived and continuous active magmatic systems along the axis at slow-spreading centers. Instead, the presence of variably starved segments and the heterogeneously distributed magma supply below the ridges are identified especially at ultra-slow spreading ridges (***Dick et al., 2003; Carbotte et al., 2015***). Compared to fast-spreading environments, magmas are also emplaced in a cooler, thinner crust but within a thicker lithosphere (***Dick et al., 2003***). This model is consistent with that developed by ***Cannat (1993)*** for magma-poor slow-spreading centers. Indeed, their model predicts the consequence of a thick lithosphere on the magmatic system with the formation of short-lived magma reservoirs. The model also emphasizes the strong influence of brittle deformation on the accreted crust structure with the exhumation of deep lithologies by faulting. In total, more than 50% of extension is accommodated by faulting in some sections along slow-spreading ridges (***Dunn, 2015*** and references therein). The balance between accommodation of extension by brittle deformation and magmatic processes is thought to be directly controlled by axial ridge melt supply that varies in space and time. Thus, melt supply potentially controls the thickness, the structure and the rheological properties of the crust (e.g. ***Cannat, 1993; Tucholke and Lin, 1994***). In this context, the localization of magmas is fundamental in the understanding of magmatic accretion processes, hence formation of the crust.

1.2 Magma localization and migration below the (ultra-) slow spreading ridges

1.2.1 Localization and morphology of magma reservoirs at slow-spreading ridges

1.2.1.1 Localization of melts within the lower crust: contribution of seismic studies

The inherent characteristics of slow-spreading ridges control the fate of melts extracted from the mantle then emplaced within the crust. The average magma volume accreted is smaller than the volume accreted in fast-spreading ridges due to lower regional melt supply (***Rubin and Sinton, 2007***). The direct consequence of a lower supply is the localization of the thermal boundary layer above the upwelling mantle. Thus, melts incorporated within the crust crystallize within the lithospheric mantle instead of a completely developed crust (***Cannat, 1993***). Compared to the ridge architecture at fast environments, there is no steady state magmatic system below the ridge. Rather, there are intermittent magmatic events that involve larger volumes of magmas, which variably agglomerate along magmatic segments at shallow levels (< 5 kmbsf) and are separated by amagmatic segments of thinner crust (***Carbotte et al.,***

2015; Dick et al., 2003; Dick et al., 1991). This also means that compared to the fast-spreading crust a large portion of the slow-spreading oceanic crust is composed of mantle-derived lithologies, as confirmed by the presence of mantle-derived peridotites outcropping on the sea floor in numerous locations (*Figure 1.3b* - ***Cannat, 1993; Cannat et al., 2006; Dick et al., 2019b***).

The localization of melts below modern slow-spreading ridges is arduous to determine as a result of the ephemeral and sporadic nature of the magma reservoirs. Nonetheless, a few seismic imaging studies show the presence of melts at different localities below the slow-spreading Mid Atlantic Ridge (MAR) and the ultra-slow spreading Southwest Indian Ridge (SWIR). ***Sinha et al. (1997)*** describe an anomalous melt body located 2 to 3km below the hot spot-influenced Reykjanes ridge segment of the MAR. ***Magde et al. (2000)*** and ***Dunn et al. (2005)*** studied the same portion of the MAR at around 35°N. ***Magde et al. (2000)*** inferred the presence of pipe-like structures (<10 km wide) down to depths of 4 km that feed shallower intrusive bodies and eruptions. Deeper below this structure, at depth of 4 to 10 km, ***Dunn et al. (2005)*** defined a "bull's eye" structure that contains ~5% melt. This structure is also interpreted as a plumbing system which focuses melts and feeds the crust, but the previous pipe-like structure is then reconsidered as partially molten dikes intruded within the crust (***Dunn et al., 2005***). Below the Lucky Strike volcano and hydrothermal vent field (at 37°N), a 3 to 4 km wide and up to 7 km along-axis axial magma chamber has been described at about 3 to 3.5 km depth, as described by ***Singh et al. (2006)***. Again and similarly to what has been found at 35°N, ***Seher et al. (2010)*** identify a zone of low velocities underlying the former axial magma chamber

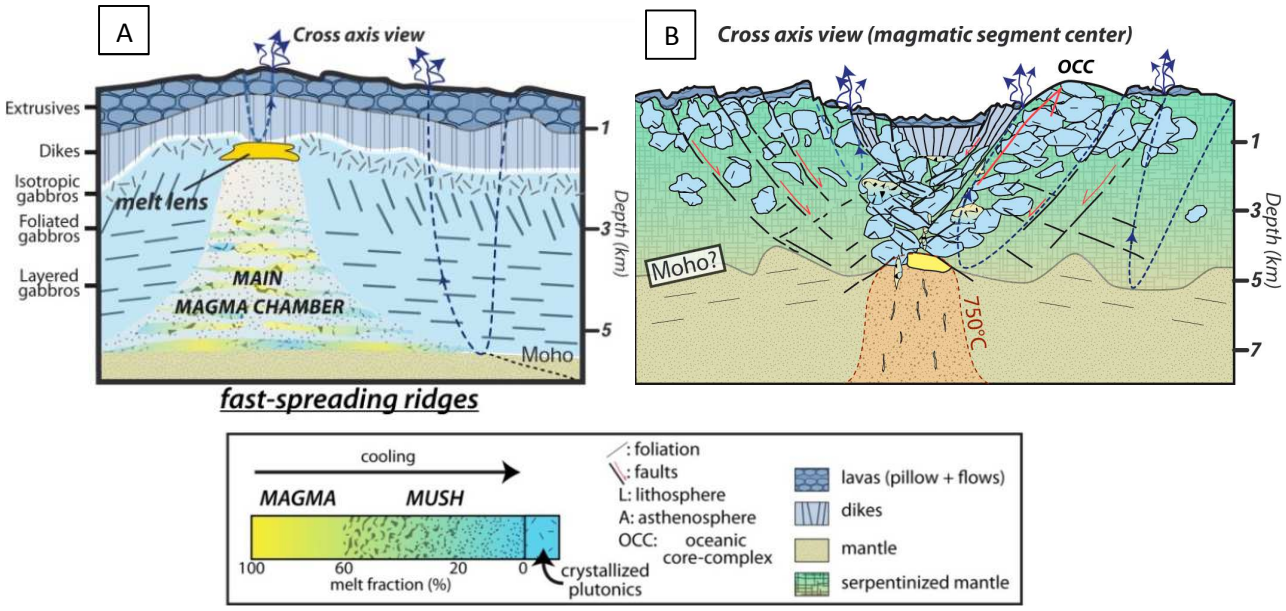

Figure 1.3 - Cross section of representative oceanic crust structure at fast-spreading ridges and slow-spreading ridges. Note the difference in scale of depth for each model. Figure from France & Bouilhol, in prep (a- is modified from France et al., 2009, and b- from Pomerol et al., 2000).

reflector. This zone contains low amount of melts (probably < 1%) and is interpreted as the magma supply system of the chamber.

More recently, ***Jian et al. (2016)*** discovered close to the Gallieni Fracture Zone an axial magma chamber below the ultra-slow SWIR at 4 to 9km depth below seafloor (*Figure 1.4a*). Finally, ***Canales et al. (2017)*** imaged multiple magmatic sills at different stages of crystallization between 2 and 10 km depth below the Rainbow hydrothermal field of the MAR (36°N; *Figure 1.4b*). Sill length varies between 0.1 and ~1.4 km long, but the majority is 200 to 400 m long. They intrude ultramafic rocks that lack any strong serpentinization. This last occurrence of intruded magma differs from the previously observed magma bodies, and translates a potentially different mode of magma emplacement below the ridge axis.

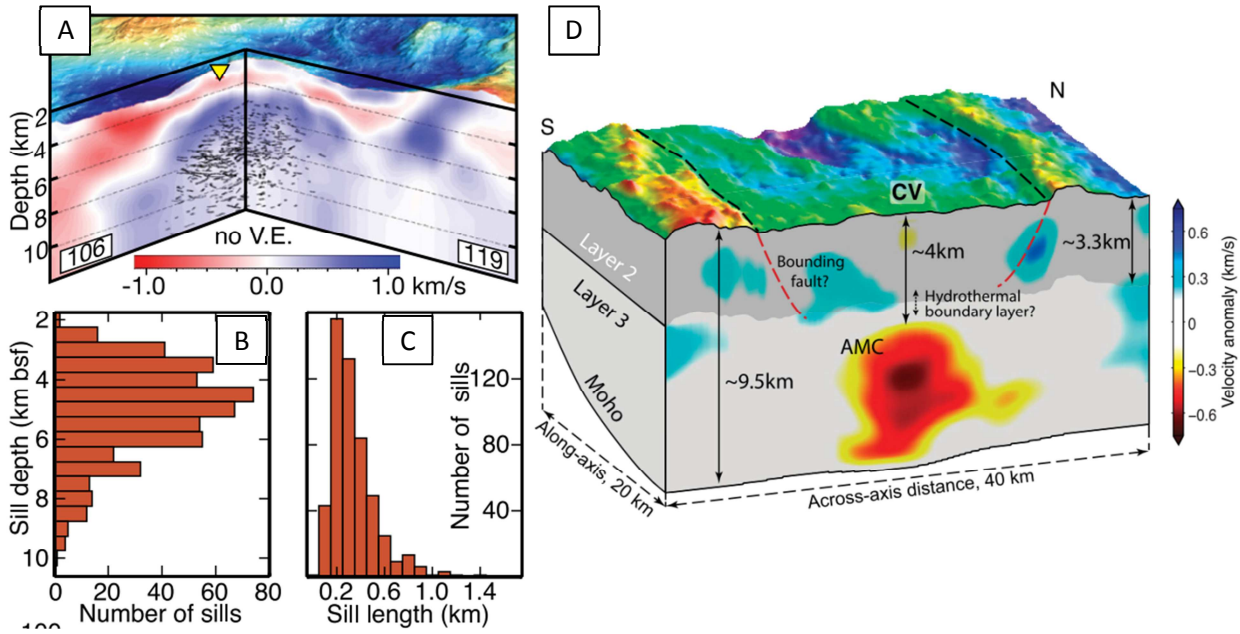

Figure 1.4 - Seismic imaging of lower oceanic crust magma reservoirs at slow-spreading ridges. (a) Three-dimensional distribution of sills within the Rainbow massif (inverted triangle: Rainbow hydrothermal field) shown against the relative P-wave velocity (Vp - km/s), (b) distribution of the sills in depth and (c) distribution of the sills length (Canales et al., 2017); (d) Block diagram presenting the bathymetry and the final velocity anomaly containing the axial magma chamber (AMC) located below the Southwest Indian Ridge (Jian et al., 2017)

1.2.1.2 Genesis and architecture of the slow-spreading lower crust magma reservoirs

Early studies describing models of magma emplacement at slow-spreading ridges, described above as areas of lower melt supply and thicker oceanic crust, involved the emplacement of short-lived small intrusions (***Dick et al., 1991***) and the absence of steady-state eruptible melt lens within the crust (***Sinton and Detrick, 1992***). ***Sinton and Detrick (1992)*** argue for the development of "dike-like mush zones [...] forming small sill-like intrusive bodies". The sills have a length of 1 to 2 km and their thickness vary from tens to hundreds of meters (*Figure 1.5*). The model had foreseen the structure of the crust and notably the sills that have

been described below the Rainbow hydrothermal field on the MAR (***Canales et al., 2017***). Similarly, the magma-poor ocean ridge model developed by ***Cannat (1996, 1993)*** emphasizes the generation of dike intrusions in thick lithosphere. Melts in this model get mostly trapped within the lithospheric mantle thereby forming a heterogeneous lower crust (the so-called "Plum pudding model").

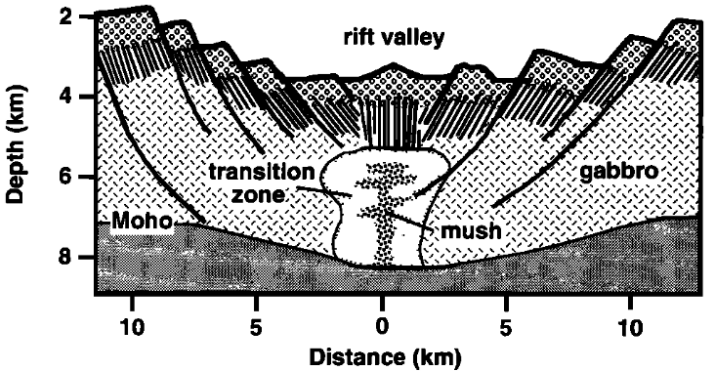

Figure 1.5 - Interpretative model of a magma chamber beneath a slow-spreading (low magma supply) ridge like the Mid-Atlantic Ridge, from Sinton & Detrick (1992).

The input from long *in situ* sections of modern lower crust sampled at Oceanic Core Complexes (OCCs - *see Chapter II*) enabled to precise the modes of magma emplacement in magmatically robust segments of slow-spreading ridges. The drilled cores and the results of site surveys confirmed the heterogeneous character of the crust, with the presence of coexisting gabbroic and mantle lithologies at the seafloor and within the OCCs (e.g. ***Blackman et al., 2006, 2004b; Dick et al., 2019; Macleod et al., 1998; MacLeod et al., 2017***). The detailed study of the Atlantis Massif Oceanic Core Complex (MAR - 30°N) *in situ* section highlighted that the structure was built by multiple magma sill injections of a common parental MORB-type melt (***Godard et al., 2009***). The age constraints given by ***Grimes et al. (2008)*** indicate that the cored cumulate sequence formed during two main magma events over a minimum period of 100 to 200 ka, and corresponds to the two main, ~600 m-long structural units. The repartition of ages with depth also suggests that the sills intruded at random depths below the ridge axis, forming a >1.4 km-thick sequence (*Figure 1.6*). Hence, magma accretion at this location occurred by formation of short-lived intrusions that evolved individually, albeit being part of first-order magmatic pulses (similar to the model of ***Kelemen et al., 2007***). These intrusions emplaced within the lithospheric mantle that was partly incorporated in the structure, and impregnated or assimilated within the lenses (***Drouin et al., 2010, 2009; Ferrando et al., 2018; Suhr et al., 2008***).

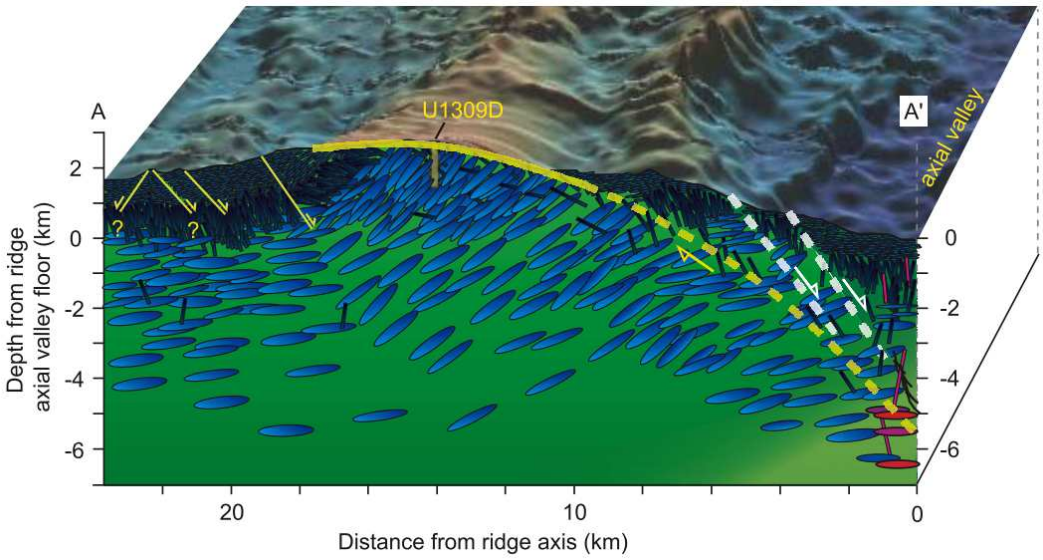

Figure 1.6 - Schematic model of on-axis sill emplacement.
The trace of the detachment fault is shown as curved, dashed yellow line that becomes more steeply dipping below the rift valley and roots near the zone of active intrusion. The intrusive crust in the footwall of the detachment fault comprises a series of small-scale sills (shown in blue), which intrude one another to ultimately construct the plutonic crust. The red sills and dikes beneath the ridge axis represent active zones of intrusion, Grimes et al. (2008).

These findings contrast to some extent with the model of magma emplacement and evolution deduced from the studies of the Atlantis Bank OCC (SWIR - 32°S, 57°E) and its three deep-drilled *in situ* sections. The OCC is the largest magmatic core complex found at slow-spreading ridges (>40% of the size of the Kane Massif, i.e. the second biggest magmatic center studied). It is described as a batholith by ***Dick et al. (2019)***. The structure is characterized at depth by the presence of ~200 m thick tectono-magmatic units that formed by the emplacement of "numerous small igneous bodies often with crosscutting relationships" during distinct magmatic events (***Dick et al., 2019***). ***Natland et al. (2002)*** develop a large-scale model of formation of the tectono-magmatic units, with the supposed emplacement of large funnel-like reservoirs that intrude one another as the structure progressively migrates away from the ridge and is exhumed (*Figure 1.7*).

The main differences with the model defined for Atlantis Massif is the lack of mantle lithology slivers in the structure, likely reflecting the thicker character of the magmatic section linked to more robust magma input from the mantle (e.g. ***Dick et al., 2000; Dick et al., 2019; MacLeod et al., 2017***). The gabbroic sections are also in average more evolved than the Atlantis Massif section, with an initial crystallization of 40% from an equivalent primary mantle melt required to obtain the Atlantis Bank gabbros parental melts. In order to explain this contrasting compositions, ***Dick et al. (2019)*** infer the same hypothesis as formulated by ***Dick et al. (2000)***. They propose that a missing primitive cumulate is likely to lie at the bottom of the structure, at the location of the highly focused mantle melt flow (*Figure 1.8*), and that the rest of the section

likely evolved by upward and lateral migration of interstitial melts. Melts migration was likely enhanced by continuous deformation and migration by diapirism of the interconnected mushy magma reservoirs towards the direction of extension (***Dick et al., 2019; Natland et al., 2002***). Such interconnected reservoirs, allowing large-scale migration of evolved melts through the crust, reflect rapid emplacement of large volumes of magma with sufficiently low cooling rates. The main unit boundaries then represent "breaks into the cooling cycle due to intrusion of a new hot unit into older colder unit with minimum porosity and permeability" (***Dick et al., 2019***).

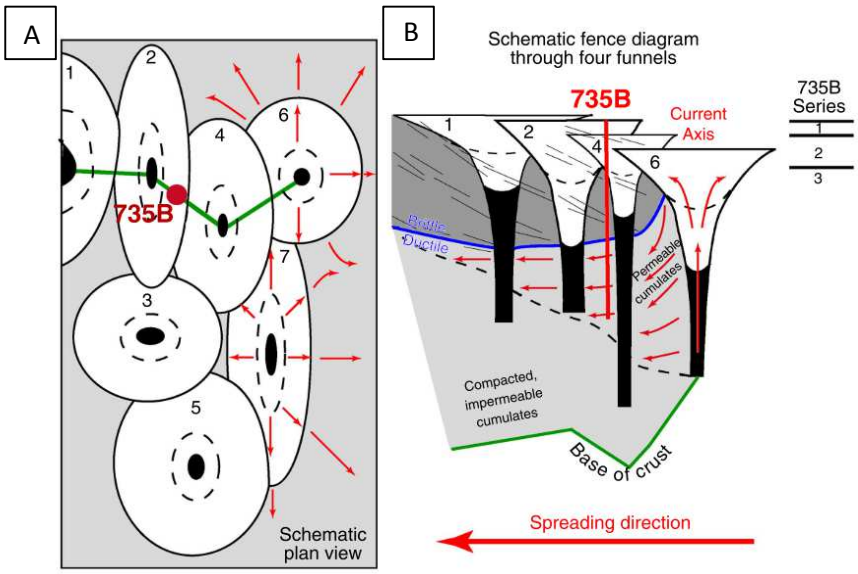

Figure 1.7 - Simplified conceptual diagrams showing models of emplacement of plutons deduced from ODP Hole 735B observations. (a) plan view and (b) a fence diagram cross section of the possible relationships between shallow plutons (white, funnel shaped, numbered in order of intrusion), underplated olivine gabbro (gray), and primitive cumulates (black) frozen in column-like conduits in the vicinity of ODP Hole 735B. Red arrows give hypothetical directions of migration of ferrobasaltic magmas as they are expelled from the funnel-shaped plutons beneath the brittle-ductile transition that deepens with distance away from the center of spreading.

The study of ophiolite analogues for slow-spreading oceanic crust enables to add more precise constraints on the 3D development of the magmatic lower crust. The study of the Canadian Appalachians ophiolites by ***Bédard (2015)*** predicted the findings of ***Dick et al. (2019)*** with evidences for magma pondings at the base of the crust and favorable emplacement of magmas by sill intrusions (see above). Another example is the study of the transition between the lithospheric mantle and the magmatic crust conducted by ***Sanfilippo and Tribuzio (2013, 2011)***. The authors specified for example the mode of migration of MORB-type melts: first, migration occurs by channeling and impregnation; then by gabbroic diking in the lithospheric mantle, before the onset of sill formation and building of the larger gabbroic plutons.

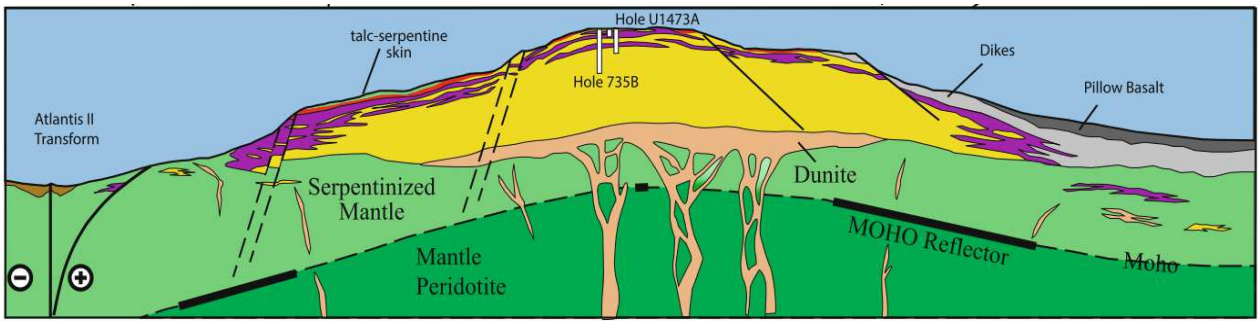

Figure 1.8 -East-West cross-section of Atlantis Bank through Hole 735B based on the seafloor geology and ODP and IODP drill cores. Subsurface geology at depth including dunite and basal cumulates, and the location of crust-mantle boundary is somewhat arbitrary. Heavy black lines show the Moho reflectors. Best guess model for Moho and crust-mantle boundary are shown. Dick et al., 2019 (and references therein).

Altogether, despite the observed heterogeneity of the slow-spreading lower oceanic crust sections from modern ridges or relict systems in ophiolites, latest models of magma accretion below magmatically robust segments suggest continuity in the processes involved in the formation of the crust (e.g. melt migration and differentiation processes).

1.2.2 Magma storage and related melt migration processes

Melt migration by intrusions or by porous flow are the two end members for magma migration processes that have been considered either in the studies of extraction and migration of melts in the mantle (e.g. ***Ahern and Turcotte, 1979; Daines and Pec, 2015; Kelemen et al., 1997; Nicolas, 1990***), or in the studies of melt migration within the fast-spreading lower crust (e.g. ***Kelemen and Aharonov, 1998***; ***Korenaga and Kelemen, 1998***). Once melt bodies are emplaced, the modality of melt migration within the cooling magma bodies has a fundamental control on the evolution of magma, and the composition and structure of the lower crust. For example, the migration by intrusion or by focused flow, also named "hydrofracturing" in ***Nicolas (1990)*** or ***Kelemen and Aharonov (1998)***, is considered to account for the formation of the layered gabbros from fast-spreading ridges lower crust (see ***Kelemen and Aharonov, 1998***). The migration by porous flow and the related reactions between a circulating melt and the surrounding rocks - or mush - have been identified in various localities and contexts, as well as in fast- and slow-spreading environments (***Lissenberg and MacLeod, 2016*** and references therein, *see I.2.2.3.*). Such processes are increasingly considered to be key during differentiation of magma. Their occurrence supports the model of accumulation of melts within mushy reservoirs as the prevalent magma storage structure within the lower crust.

Within mushy magma reservoirs, the differentiation of melts is closely related to the internal migration capacity of these melts. Differentiation has been studied for example by ***Cashman et al. (2017)*** and ***Jackson et al. (2018),*** who modeled the chemical differentiation and

dynamic evolution of a large continental magma reservoir. They show that in such porous dynamic environment, magma evolution is strongly constrained by reactive porous migration, and that percolating melts can likely be remobilized from the mush and feed eruptions. In oceanic environments, ***Lissenberg et al. (2019)*** present the state of the art related to melt-rock reactions, and investigate the consequences of such mush-dominated magma plumbing systems on accretion modes and composition of the lower crust (*Figure 1.9*). Porous migration of melts results from a combined effect of melt buoyancy and crystal matrix compaction, potentially enhanced by deformation in an extensional context. The buoyancy hypothesis is supported by ***Lissenberg et al. (2019)*** who show that crystallizing mineral assemblages are always denser than their conjugate melt during fractional crystallization from a primitive oceanic composition (*Figure 1.10*). The upward melt flow generated by buoyancy could then participate into reorganization of the crystal matrix, and aid compaction, as inferred in continental mush reservoirs (***Jackson et al., 2018***).

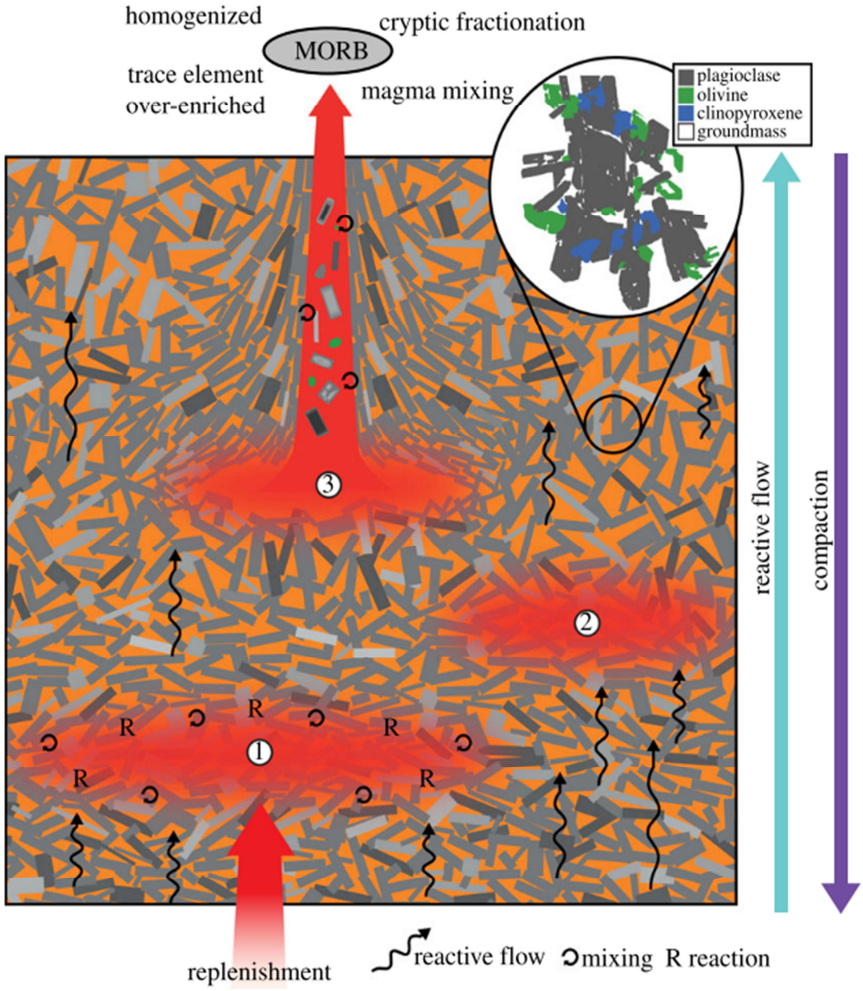

Figure 1.9 - Schematic of a lower oceanic crustal mush (Lissenberg et al., 2019). Formation of melt lens 1 by replenishment of the mush by primary melt; Formation of melt lens 2 by segregation of interstitial melts in the mush; Melt lens 3 feeding eruptions of MORB.

Most of the literature dedicated to compaction focuses on the mantle and the feasibility of extraction after few percent of melting to feed the accreting crust. Therefore, literature mainly focuses on the properties of olivine-rich lithologies (e.g. ***Holtzman et al., 2003; Mckenzie, 1984***). Within the crust, compaction is usually argued to explain adcumulates formation of large layered intrusions in continental environments (***Meurer and Boudreau, 2009; Namur and Charlier, 2012; Tegner et al., 2009; Irvine, 1980***). However, other studies, such as those of ***Higgins (1991)*** and more recently ***Holness et al. (2017)*** challenge this vision. ***Higgins (1991)*** considers that compaction was not sufficient enough to produce the textures observed in the Sept Iles layered intrusion. His proposition is supported by the general observations and modeling of ***Vigneresse et al. (1996),*** or ***Daines and Pec (2015),*** which show that gravity driven flow generated by compaction is not sufficient to segregate large volumes of melt over geological timescales. ***Holness et al. (2017)*** show that no conclusive evidence for compaction can be identified from textures in adcumulates of the Skaergaard intrusion (East Greenland). The authors rather argue that compaction would preferably impact slowly cooled intrusions crystallizing abundant dense minerals. The other process commonly evoked for the formation of adcumulate and the expulsion of liquids from the crustal mushes is magmatic deformation (***Higgins, 1991***; ***Namur et al., 2015*** and references therein). Both mechanisms of compaction and deformation are especially appropriate when dealing with oceanic crust and oceanic mushes, as (1) the formation of long-lived slowly cooled mushes is ensured by either continuous magma supply below fast-spreading ridges, or the large volumes of magma emplaced in magmatically robust segments of slow-spreading ridges, (2) the thickness of the magmatic system and mushes is sufficient enough for gravity to drive compaction (rather applicable to fast-spreading ridges), and (3) both magmatic accretion and deformation occur synchronously in an extensional tectonic context (***Lissenberg et al., 2019)***.

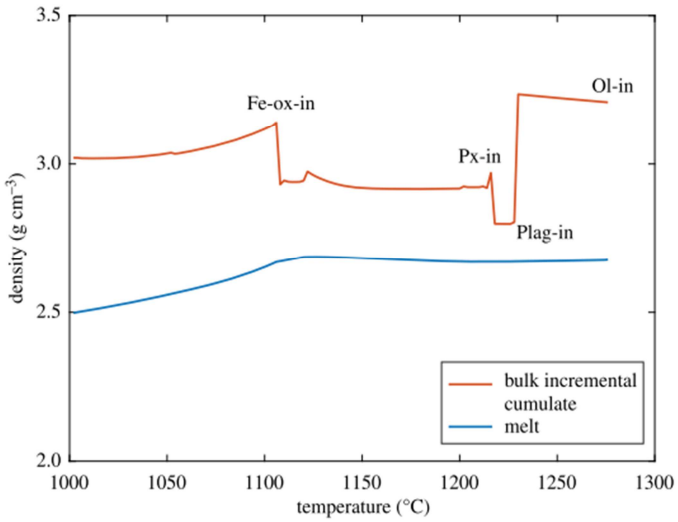

Figure 1.10 - Density evolution of a primary MORB during progressive fractional crystallization, and bulk density of the conjugated cumulate produced at each step (Lissenberg et al., 2019)

Evidences of deformation in the presence of melt in lithologies from the lower oceanic crust are widespread at slow-spreading ridges. For example slightly deformed minerals (tapered plagioclase twins, kink bands in olivines) are most likely to occur when the melt fraction doesn't exceeds 20% (***Ildefonse et al., 1992; Lissenberg et al., 2019; Mckenzie, 1984; Meurer and Boudreau, 2009***). Such phenomenon at different melt fractions can lead to both the complete reorganization of crystals within the much and the formation of layered lithologies within the crust. It has been observed in fast-spreading environment (at the bottom of the crust in the Moho transition zone; ***Higgie and Tommasi, 2012; Jousselin et al., 2012***) and potentially in slow-spreading environment too (***Bédard, 2015***; ***Thy and Dilek, 2000*** and modal layering from the SWIR). Another consequence from deformation applied to a mushy reservoir is the segregation of melts which tend to concentrate (e.g. ***Rosenberg, 2001; Vigneresse et al., 1996***). This process has been heavily investigated for the focusing of melt flows within the mantle that is exacerbated by the interaction between the circulating melt and the lithology being crosscut (*Figure 1.11*).

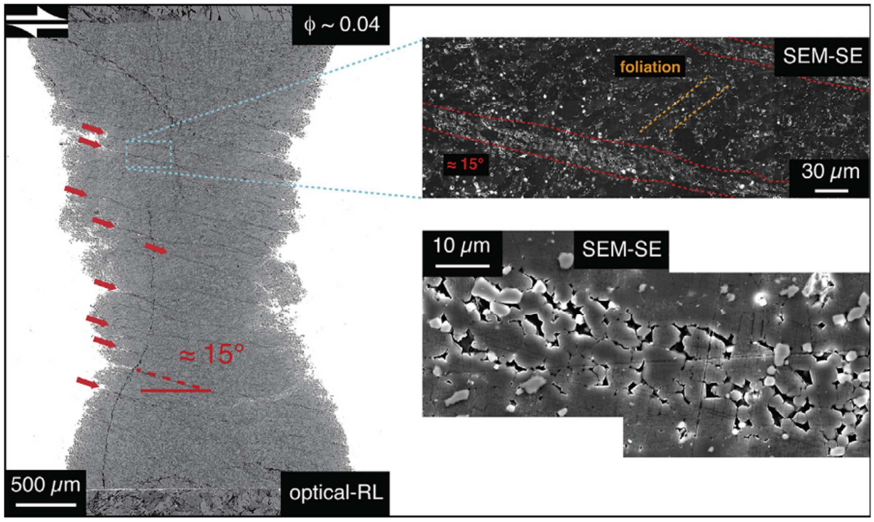

Figure 1.11 - Melt-rich bands produced during stress-driven segregation (olivine: medium gray; chromite: light; quenched melt: dark). Reflected light (RL) and secondary electron microscope (SEM-SE) images of a sample deformed in torsion (Daines & Pec, 2015)

The ultimate step of the melt focusing process is fracturing of the surrounding lithologies and expulsion of the melts (***Daines and Pec, 2015; Kelemen et al., 1995; Lambart et al., 2009; Pec et al., 2015***). ***Lissenberg et al. (2019)*** argue that such processes of magma focusing are inevitable in mushy magma reservoirs of the lower oceanic crust. At fast-spreading ridges, it is required to allow primitive melts from the lower part of the crust to be rapidly remobilized in sufficient amounts to feed dikes and lavas in the upper crust. Potentially, this also applies to a lesser extent at slow-spreading ridges, where dikes are often considered as key structures for the formation of the crust (*see II.1.* - e.g. ***Cannat et al., 2019; Dick et al., 2008; Dunn et al., 2005b; Olive et al., 2010***).

Overall, at slow-spreading oceanic ridges where large volumes of magma emplace and evolve (*Figure 1.12*), mush dominated systems develop and likely form the main type of magma reservoir of the lower oceanic crust. This statement, which is based on numerous observations and models, is compatible with the ability of the melts to be extracted from the crust, especially in a context where extension plays a significant role and can enhance melt segregation within the mush. It also implies that the two melt migration end member processes of focused flow and porous flow occur within the lower crust, and can influence the differentiation of magma.

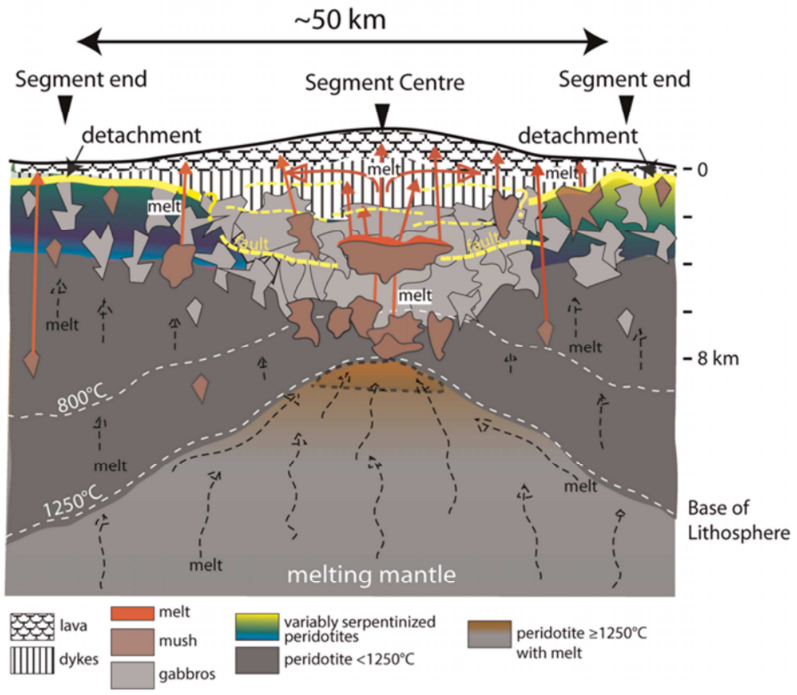

Figure 1.12 - Along-axis section of idealized magmatic spreading segment at slow-spreading ridges based on studies summurized in Carbotte et al. (2015) and modified from Cannat et al. (1995). Strong focusing of mantle melts leads to thick crust/thin axial lithosphere at center and thin crust/thick axial lithosphere at ends of each principal segment. Both vertical and lateral magma transport during dyking may occur.

2 Magma evolution at slow-spreading ridges: constraints from petrographic, geochemical and experimental studies

One of the key questions to address to understand lower crustal accretion at slow-spreading ridges is how magmas evolve once emplaced within the crust. This depends on several parameters, one of them being composition of the melts that intrude the crust. Another one is the evolution of these melts during the different reactions that lead to the formation of crustal rocks. This evolution depends in turn on the physical conditions of storage and / or migration of melts that crystallize. Key parameters are therefore the temperature evolution of the magma reservoirs and the pressure conditions within these reservoirs, and some intrinsic characteristics like the melt fraction, or the capacity of migration and interactions of the melts stored.

2.1 Origin of the crustal melts and models of evolution within the lower crust

2.1.1 Origin of crustal melts and crystallization depth

Melts that intrude the oceanic crust are extracted from the underlying upper mantle at the ridge axis. The mantle starts melting when the upper mantle adiabatically upwelled in response to extension intersects the solidus of the lithologies (***Langmuir et al., 1992***). The composition of the primary melts resulting from this process depends on the composition of the mantle itself, which is potentially heterogeneous and contains diversely fusible lithologies. It is also a function of the amount of melt generated which progressively lead to the formation of a depleted mantle source (***White and Klein, 2014*** and references therein). Processes of mixing and hybridation within mantle or crustal magma reservoirs are also presumably involved into the evolution of MORB. Such processes would explain the discrepancy between the relative homogeneous compositions of MORBs compared to basalts from other tectonic settings. It also explains the stronger variability and the more primitive compositions recorded in melt inclusions of MORB phenocrysts or minerals from lower crust cumulates, formed before complete aggregation of melts (***White and Klein, 2014*** and references therein; ***Lambart et al., 2019***). In addition, the primary melt composition is likely modified by crystallization processes or interactions during migration within the crust (e.g. ***O'Hara, 1968; Rubin et al., 2009, 2001***). Such reactions are usually inferred to account for the relative variability of MORB compositions recovered along the spreading ridges: MORB compositions can be found in equilibrium with mantle lithologies but they can also be much more evolved, presenting variable degrees of depletion (e.g. ***Gale et al., 2013; O'Hara, 1968***).

At some point during their ascent, mantle melts eventually start crystallizing within the cooling lithosphere. Below the Lucky Strike volcano where the magmatic plumbing has been characterized by seismic imaging (*see 1.2.1*), the crystallization pressures recorded in olivine-hosted melt inclusions range between 0.3 and 3 kbar (***Wanless et al., 2015***). The authors determined that even though 50% of the melt inclusions reflect crystallization within the axial magma chamber (depths of 3 to 4 km), ~35% of these inclusions originate from crystallization deeper than this main magma reservoir (i.e. between 4 and 9.9 kmbsf). ***Wanless et al. (2015)*** conclude that a significant amount of crystallization must occur within the lower crust and the upper mantle, which is in agreement with recent findings of ***Bennett et al. (2019)*** who determined a maximum depth of 16.4 km for plagioclase crystallization below the ultra-slow spreading Gakkel ridge. This result also seems to agree with numerous studies conducted on MORB or clinopyroxene crystals, as well as experimental investigations of primary MORB crystallization.

The depth at which melts start to crystallize is a function of the spreading rate at the ridge axis. Crystallization beneath slow-spreading ridges is considered to start at higher pressure compared to fast-spreading environments (e.g. ***Coogan, 2014***; ***Herzberg, 2004***; ***Jenner and O'Neill, 2012***; ***Villiger et al., 2007a***). The pressures recorded at slow-spreading ridges range between ~0 and 8 kbar (*Figure 1.13* - ***Lissenberg and Dick, 2008; Coogan, 2014*** and references therein), such as at the Atlantis II Fracture Zone on the SWIR (***Villiger et al., 2007a***). However, the high pressure hypothesis is difficult to completely reconcile with the observed lithosphere structure and composition. For example, the upper mantle lack the presence of abundant fractionation products of MORB (***Lissenberg and Dick, 2008***). In addition, one must be careful when considering indications of high pressure evolution deduced from MORB studies, as many models rely on phase equilibria and MORB petrogenesis which only consider differentiation by simple crystallization processes.

2.1.2 Evolution of tholeiitic magmas by simple crystallization processes

The determination of the crystallization pressure, as well as many other studies of MORB evolution, relies on the major assumption that the main processes involved in the lower crust accretion are equilibrium and fractional crystallization. Since the work of ***O'Hara (1968b)***, experimental investigations, thermodynamic modeling of phase equilibrium and diverse petrological observations inferred an evolution for MORB by low pressure fractional crystallization of gabbroic lithologies (olivine, plagioclase, clinopyroxene) at relatively dry

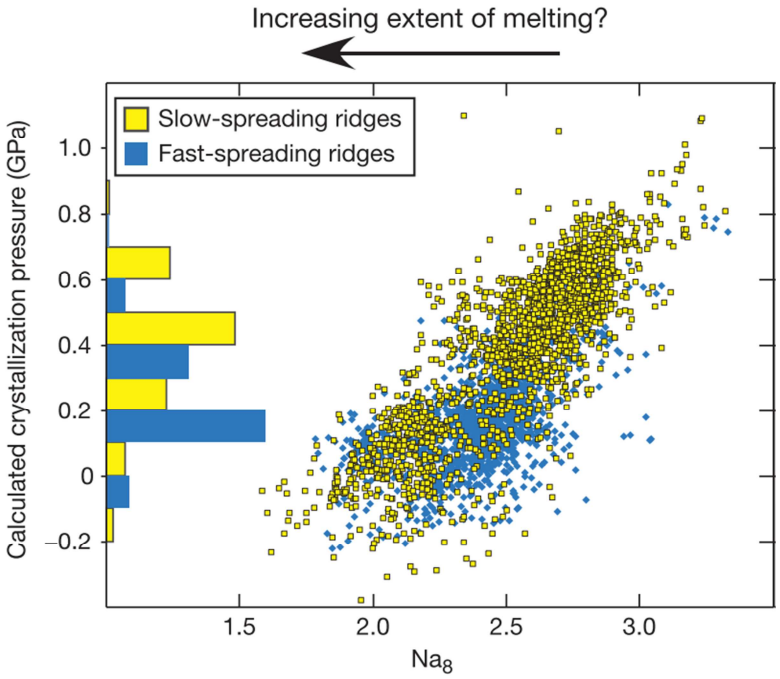

Figure 1.13 - Crystallization pressure of MORB glasses determined by the approach of Villiger et al. (2007) correlated to the Na8 compositional parameter (Na at 8% MgO). Slow-spreading ridges: <40 mm/y; Fast-spreading ridges: >60 mm/y (Coogan 2014)

conditions (***Grove et al., 1992; Grove and Brown, 2018; Herzberg, 2004; O'Hara and Herzberg, 2002; Villiger et al., 2007***). Although the slow-spreading lower oceanic crust does not resemble to the classical layered oceanic crust as described in the Penrose model (Conference Participants, 1973), it is composed of lithologies which crystallize from primary tholeiitic melts. Such series have been for example described in the first long *in situ* section sampled in the lower magmatic crust exposed at the Atlantis Bank Oceanic Core Complex (*see Chapter II.*). ***Dick et al. (1991)*** describe all the associated lithologies from troctolites, olivine gabbros and gabbros to more evolved gabbros containing oxides, and felsic rocks. The only missing cumulates of the series are the primitive dunites and wehrlites found in other slow-spreading oceanic crust section (e.g. at Atlantis Massif on the MAR, ***Blackman et al., 2006***).

The first-order compositional evolution recorded in the lithologies compares to fractional crystallization trends determined by numerical modeling (*Figure 1.14* **- *Coogan, 2014*** and references therein). However, numerous deviations from the classical evolution path have been encountered since the first studies of lower oceanic crust samples. The typical example deals with the saturation of clinopyroxenes that depends on the crystallization pressure, the composition of the evolving melt and the crystallization model considered. The classic low-pressure fractional crystallization sequence is the following (***Grove et al., 1992***; and references therein):

$$\begin{aligned} &\textit{olivine} \pm \textit{spinel} \rightarrow \textit{olivine} + \textit{plagioclase} \\ &\rightarrow \textit{olivine} + \textit{plagioclase} + \textit{clinopyroxene} \\ &\rightarrow \textit{plagioclase} + \textit{clinopyroxene} + \textit{orthopyroxene} + \textit{FeTi oxides} \end{aligned} \quad (1)$$

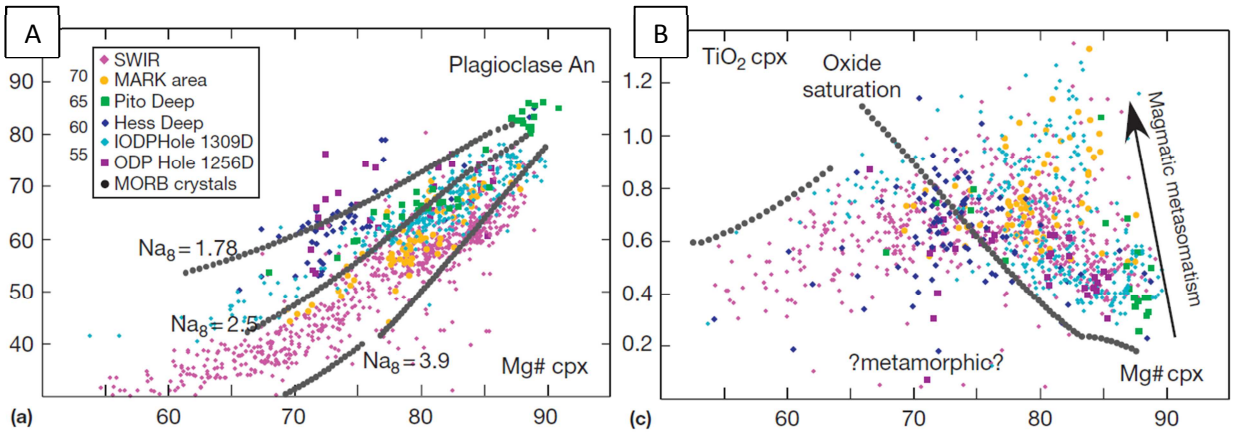

Figure 1.14 - Variations in the major element composition of minerals in oceanic gabbros (Coogan 2014). (a) Plagioclase An content versus clinopyroxene Mg#. Grey symbols: fractional crystallization modeling by MELTS (Ghiorso & Sack, 1995). (b) Mg#-Ti in clinopyroxene with fractional crystallization modeling by MELTS.

Here, clinopyroxenes start crystallizing at low pressure and saturate ~40 °C below the temperature of saturation of olivines and plagioclases (***Kelemen and Aharonov, 1998; Villiger et al., 2007***). At higher pressure, the saturation temperature of clinopyroxene increases, minerals start to crystallize earlier before or together with plagioclase and have more primitive compositions than recorded at lower pressure (marked by higher Mg# for instance, molar ratio $\mathrm{Mg}/[\mathrm{Mg} + \mathrm{Fe}] \times 100$). This principle is the basis of most of the barometers described above. Many Mg-rich clinopyroxenes were sampled in oceanic gabbros (***Ross and Elthon, 1997; Coogan et al., 2000; Dick et al., 2002***) suggesting deep crystallization of the minerals. Nevertheless the textures of those samples, such as the presence of interstitial clinopyroxenes or clinopyroxene oikocrysts, rather indicate crystallization at low pressures. The explanation given by ***Lissenberg and Dick (2008)***, which has also been proposed in other oceanic gabbro studies (e.g. ***Coogan et al., 2000***), is that processes other than fractional crystallization are involved during the evolution of the magma reservoir: the melt-rock reaction processes.

The consideration of equilibrium and fractional crystallization implies also crystallization of magmas in a relatively closed system, without any "external" modification of the melt. The composition of the melt then only changes due to progressive removal of elements incorporated in the crystallizing minerals that form homogeneously in the chamber. Yet, the models of progressive crystallization from the walls to the center of the magma chamber entail the creation of an internal zonation of the structure and melt composition. Moreover, compared to the first models of oceanic magma chamber, such as the "Infinite onion" model of ***Cann (1974)***, the current oceanic magma "chamber" models are rather considered as mush-dominated systems (*Figure 1.15* - ***Lissenberg et al., 2019; Sinton and Detrick, 1992***).

In addition a significant proportion of the melts tend to migrate by porous flow through such differentiating (open) systems. In slow-spreading environments, the propensity of melt migration and the interconnection between the different evolving systems are also enhanced due to the strong influence of deformation (*see I.1.2.*). In such context, additional magmatic processes are required and have been taken into account to comprehend the structure and the composition of slow-spreading lower oceanic crust samples.

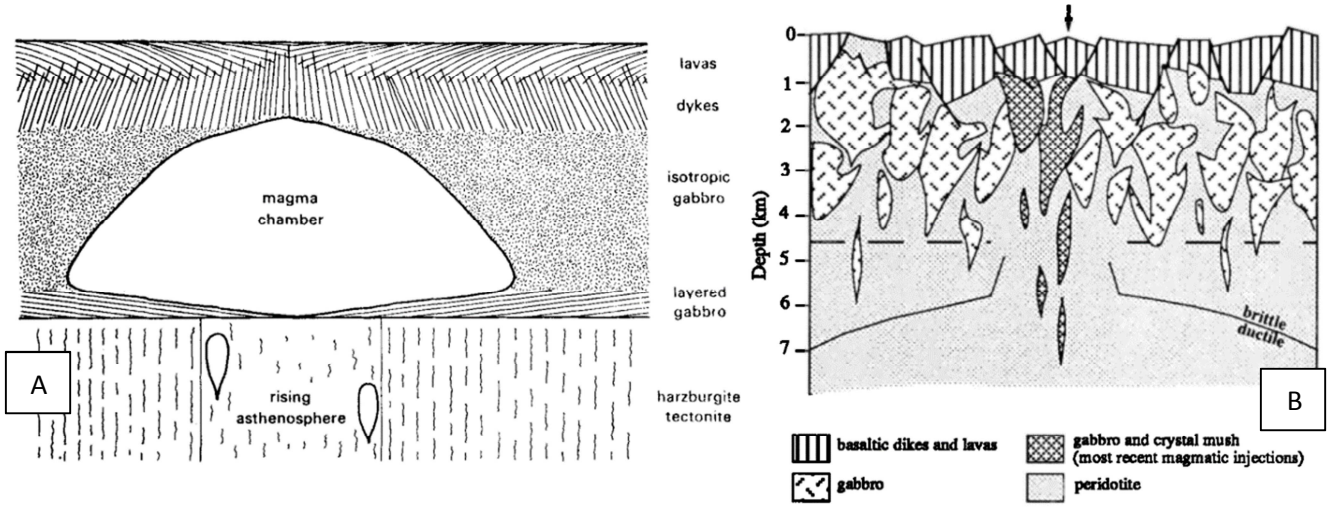

Figure 1.15 - Models of magma reservoirs developed for slow-spreading ridges. (a) "Infinite onion" model in which an ever-present magma chamber generates the lower oceanic crust through crystals plating in margins (Cann, 1974). (b) "Plum pudding" model in which teh lower oceanic crust at slow-spreading ridges is constructed from a number of nested plutons that may crystallize within the mantle or the crust (Cannat, 1993). Definitions from Coogan (2014)

2.1.3 Magma reservoir maturation and associated crystallization processes

Fractional and equilibrium crystallization were the two principal processes taken into account when dealing with crystallization of tholeiitic melts. The two models imply crystallization in homogeneous closed system, and crystallization of minerals with compositions continuously equilibrated with the melt in the case of equilibrium crystallization. In the fractional crystallization model, this equilibrium is instantaneous only at the moment of crystallization of the minerals that are progressively extracted from the system (usually by crystal settling). This prevents any interaction between the different phases (e.g. ***Allègre and Minster, 1978; Bowen, 1928; Grove and Brown, 2018***). On the contrary, reaction and reequilibration between phases are allowed during equilibrium crystallization as minerals stay in the main crystallizing system (***Shaw, 1970***). However, most of the magma reservoirs evolve as open systems with periodic replenishment and melt extraction via eruptions, as well as potential magma chamber wall assimilation (*Figure 1.16a* - e.g. ***DePaolo, 1981; O'Hara, 1977***).

In addition to perturbations linked to the open system character of the chambers, the equilibrium condition that is assumed for the entire magma reservoir is challenged as a result of its own evolution in time (***Marsh, 1996***). ***Langmuir (1989)*** re-emphasizes the role of the localization of crystallization, which happens where heat loss is focused (i.e. along the magma chamber margins rather than homogeneously within the magma body). This transition zone forms a mush at the edge of the main magma body, from which evolved liquids can return and mix with the main homogenous magma reservoir. This process is called *in situ* crystallization by ***Langmuir (1989)*** (*Figure 1.16b*) or boundary layer fractionation by ***Nielsen and DeLong (1992)***. The only difference between the two models is the crystallization process considered within the mush, the former using equilibrium crystallization and the latter using fractional crystallization.

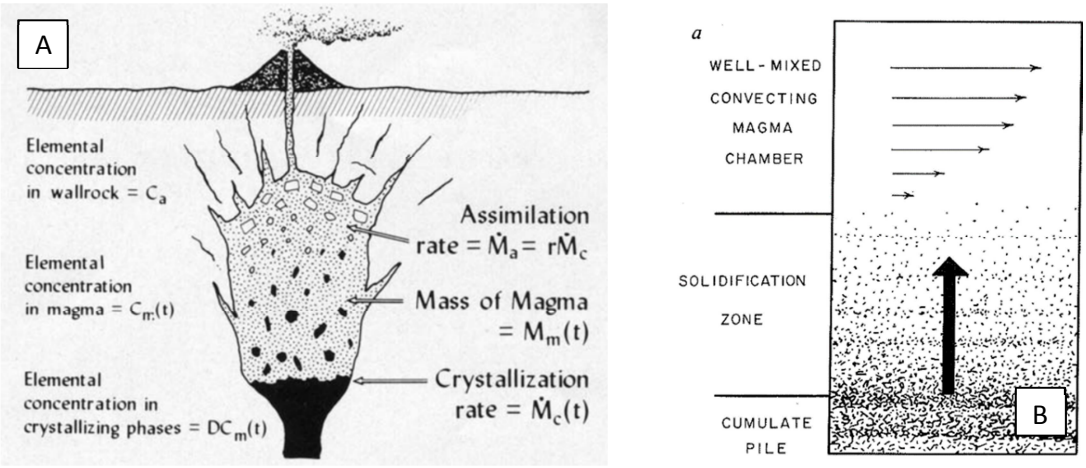

Figure 1.16 - Models of magma chamber evolution and crystallization. Model for assimilation and fractional crystallization in a magma chamber (DePaolo, 1981); (b) Schematic diagram of in situ crystallization (Langmuir, 1989)

In oceanic environment and especially at fast-spreading ridges, steady-state magma chambers continuously feed the crust, and need gradual replenishment to stay active (*Figure 1.17*). This would also be the case, albeit to a much lesser extent in segments described as magmatically robust at slow-spreading ridges (*see Figure 1.12*). A model that combines both the replenished-tapped magma chambers model (***O'Hara and Mathews, 1981***) and the *in situ* crystallization model previously considered for oceanic crust magma differentiation (e.g. ***Ross and Elthon, 1997***) was proposed by ***Coogan and O'Hara (2015)***. The authors also compared this model to *in situ* crystallization in a closed system applied to an oceanic context. Their results show that both models manage to reproduce the variability of compositions recorded in MORBs, with the former being able to reproduce most of the variability observed in incompatible element contents. Hence, a complex interplay between processes of crystallization and other changes in the crystallizing melt composition must be taken into account when studying gabbroic samples from the oceanic lower crust, as they potentially record the same processes as MORBs do.

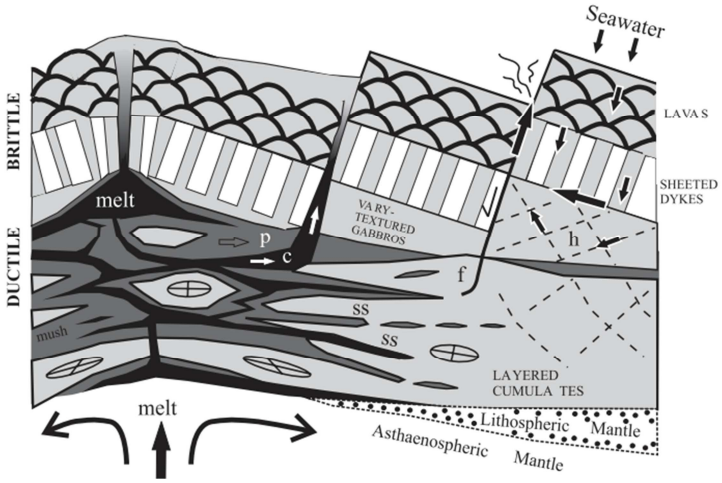

Figure 1.17 - Schematic cross-section of a ridge experiencing distributed deformation during a magmatic pulse (from ***Bédard, 2015****). Strain circles are shown for the case where mantle is flowing faster than crust. h: seawater penetrating deeper along brittle-ductile shear zones (dashed lines). ss: formation of the sheeted sill zone by injection of overpressured magma into cooler, partly consolidated distal cumulate rocks during phases of high axial melt flux from the mantle. Percolation flow (p) and channel flow (c) migration of evolved melt located in the pores of partly consolidated gabbros towards low-pressure sinks.*

Another consequence of the presence of mushes in magma chambers is the development of reactions between the crystallized phases and the liquid. At a later stage of development of the magma reservoirs, such postcumulus processes were asserted for the evolution in the lower oceanic crust where melt migration by porous flow is substantial (*see I.1.2.*). The main consequence of porous flow in a crystal mush is to put together a melt in disequilibrium with the minerals forming the architecture of the reservoir (***Blackman et al., 2011; Dick et al., 2000***). As a result, minerals can start dissolving in the melt and newly formed minerals can crystallize from this melt, which composition progressively changes due to the progressive assimilation during migration (e.g. ***Kvassnes and Grove, 2008***). Melt evolution is then far from being controlled by simple crystallization processes (and especially equilibrium crystallization). The formation of the gabbroic lithologies is rather controlled by multistep crystallization. The textural and geochemical consequences of reactive porous flow in lower oceanic crust samples and crustal xenoliths are nearly ubiquitous, as described by ***Lissenberg and MacLeod (2016)*** and ***Lissenberg et al.*** (***2019*** - and references therein). However, reactive textures are not always present as expected when dissolution-precipitation occurs (e.g. ***Lissenberg and MacLeod, 2016***). Many authors assumed that such processes take place in the lower slow-spreading oceanic crust since the first studies of (long) in situ sections sampled in modern crust, and also in ophiolites (e.g. ***Blackman et al., 2011***; ***Coogan et al., 2000***; ***Dick et al., 2002, 2000***; ***Elthon et al., 1992***; ***Leuthold et al., 2018***; ***Lissenberg and Dick, 2008***; ***Meyer et al., 1989***).

Finally, at the very end of the crystallization of the magma reservoir, processes of trapped melt crystallization can lead to further muddling of the geochemical signatures (***Natland and Dick, 2001***). The trapped melt crystallization process (e.g. ***Bédard, 1994; Meyer***

et al., 1989) involves the formation of accessory phases, the development of zoned minerals, and the increase in incompatible elements concentrations during crystallization before complete solidification of the rock. As extraction is more efficient in oceanic environments, trapped melt crystallization does not seem to play a role as strong as it does in continental environment. However, it has been considered in oceanic crust studies such as that of ***Ross and Elthon (1997)***.

2.2 Geochemical signatures and evolution of melts within the lower crust

The reaction sequence that led to the formation of the igneous rocks recovered from the lower section of the slow-spread crust is a complex interplay between potentially several steps of crystallization and reworking, especially in a context where magma reservoirs are rather expected to evolve as open systems. In order to constrain the different steps of this reaction sequence, the geochemical signatures recorded in rocks and minerals are a precious indicator. Their study in the lower crust samples from modern slow-spreading ridges or ophiolites provides important information on the development of the lower crust magma reservoirs.

2.2.1 Geochemical tracers of crustal evolution processes

As opposed to incompatible trace elements, major and minor element compositions in the gabbroic sequences considered here seem to be mainly controlled by the cotectic assemblages. Their evolution generally fit the progressive differentiation trend expected by crystallization of theoleiitic magmas (*see I.2.1.2*). Experimental investigations such as by ***Berndt et al. (2005)***, ***Villiger et al. (2007)*** and ***Feig et al. (2010, 2006)*** studied simple crystallization processes and detailed the changes of mineral assemblages and compositions with temperature, pressure, or water content of the magma. In general, the differentiation is characterized by a progressive loss of Mg in the olivine, and Ca incorporation in plagioclases then preferentially in clinopyroxenes. In opposite, in melt, Fe and alkaline contents increase during crystallization, until the stability field of oxides is reached allowing crystallization, inducing a drop in Fe-Ti contents and a large increase in silica content. These major element evolution trends can vary with any change in the cotectic assemblage crystallized. For example, higher pressures induce an increase of the stability field of clinopyroxene that as a result start to crystallize earlier in the sequence (*see I.2.1.2.*). As the composition of the minerals directly depends on the composition of the melt from which they crystallize, such variations in the crystallization sequence induce variations in the mineral compositions. Clinopyroxene crystallized at higher pressure will be more enriched in Mg compared to their low-pressure counterparts. However, variations in the

melt composition are not only induced by the proportions of the crystallized phases but can also be affected by mixing or incorporation of external components (*see I.2.1.3.*).

The study of trace element compositions in igneous lithologies is another way to monitor the processes that led to the formation of igneous rocks. As described by ***Blundy and Wood (2003)***, trace elements are interesting as they are strongly diluted which prevent them from influencing the crystallization sequence. Hence, they behave passively during the various processes of magma evolution, and are usually considered to follow Henry's Law. The amount of trace elements incorporated in the lattice of minerals depends on the composition of the liquid, and pressure, temperature and redox conditions. Trace elements evolution is linked to the proportion of phases that crystallized from the primary melt. This evolution is mainly governed by "the behavior of an element on its preference, or possibility, to enter a specific lattice site of the different coexisting phases, such as crystals, metals and liquids", i.e. the partitioning of the element as described by ***Goldschmidt (1937)***. This partitioning is characterized by the partition coefficients of an element between melt and minerals, which is the ratio of concentrations between the two phases. If the considered elements are preferentially incorporated in minerals, it is described as compatible (partition coefficient $Kd > 1$). On opposite if the elements are more concentrated in the melt, this element is incompatible with a $Kd < 1$. Following magma differentiation, incompatible elements will be progressively enriched in the melt. Consequently, the incompatible element composition of minerals progressively increases. In contrast, compatible elements are promptly incorporated in minerals as soon as they start to crystallize and their composition in the melt exponentially decreases (*Figure 1.18*). Compatible elements are then good indicators of processes occurring early in the differentiation when they vary the most, whereas incompatible elements are better suited for tracking later processes as their concentration increases.

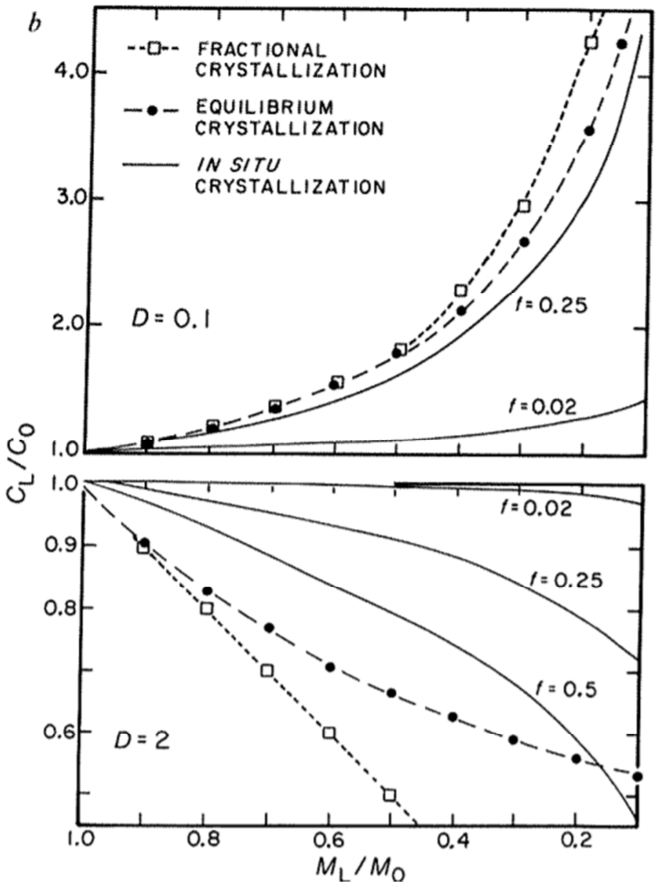

Figure 1.18 - Comparison for two values of mineral/melt partition coefficients (incompatible, D = 0.1; compatible D = 2) of in situ crystallization with equilibrium crystallization and fractional crystallization. f =proportion of the liquid which returns in the magma chamber during in situ crystallization. The evolution of the liquid compositions in the magma chamber (C_L/C_0) is shown as a function of the fraction of the magma chamber solidified (M_L/M_0). Langmuir (1989)

The incompatible Rare Earth Elements (REE) are particularly suited for the study of differentiation processes, as they have very similar geochemical behavior but their degree of incompatibility slightly vary between each other and as a function of the mineral considered (*Figure 1.19*). The composition in REE gradually increases during crystallization but vary with the process considered (e.g. stronger enrichments during fractional crystallization compared to equilibrium or in situ crystallization, *see Figure 1.18*). In addition, the slight difference of incompatibility between minerals imply that the development of variable fractionations between Light REE (i.e. La) and Heavy REE (i.e. Lu) in the lithologies is a record of variations in the crystallization sequence, of mixing or assimilation of external components. Thus, enrichment and fractionation in REE are key in tracking the various processes potentially ongoing during differentiation.

In order to study the signature of the various crystallization processes that likely led to the formation of the different lower crustal lithologies, an important parameter to take into account is the preservation of the igneous geochemical signatures directly resulting from those processes. During subsolidus cooling of igneous rocks, reequilibration of the compositions by diffusion can occur and likely disrupt the primary magmatic signature (e.g ***Chakraborty, 2008*** and references therein). Some elements are more sensitive to this process than others, depending on the considered mineral and on the ability of the elements to migrate within the crystal structure (= diffusivity constant). The diffusion coefficient, which describes the diffusion process, is strongly dependent on the temperature of the system; the higher the temperature the higher the diffusion coefficient and the faster the diffusion (e.g. ***Chakraborty, 2008***). As a consequence, reequilibration by diffusion is often critical for some minerals in slowly cooled systems such as the lower oceanic crust magma reservoirs studied here (*see I.2.2.2.2.*).

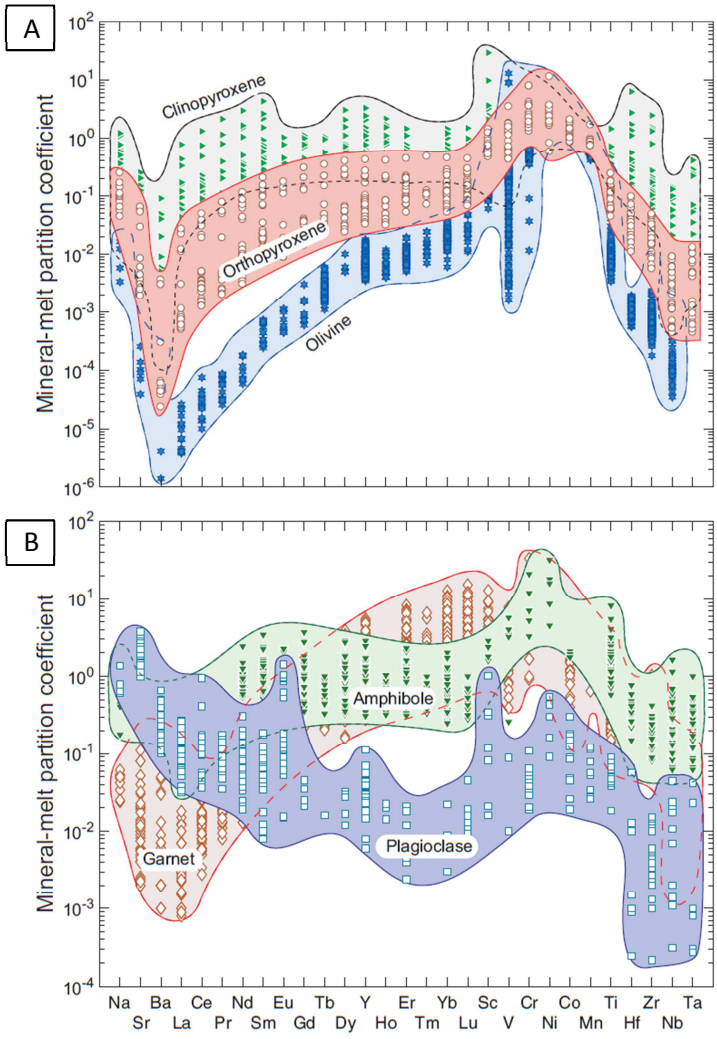

Figure 1.19 - Experimentally determined partition coefficients mineral / melt for (a) olivine, orthopyroxene, clinopyroxene and (b) plagioclase, amphibole and garnet (compilation from Sun, 2018).

2.2.2 Prediction of the lower crust signatures by numerical modeling

The complexity of the oceanic lower crust system result of the combination of different processes potentially affecting the geochemical trace element signatures during the lithologies evolution steps. An overview of the numerical modeling of the processes previously described (*see I.2.1.3*) is given below.

2.2.2.1 Crystallization and melt-rock reaction models

Equilibrium and fractional crystallization

Equilibrium and fractional crystallization are the first two simple crystallization models developed for the behavior of trace elements and the evolution of their concentrations in rocks (e.g. ***Allègre and Minster, 1978*** and references therein). Equilibrium crystallization ideally happens when a melt evolve by cooling in a closed system maintaining continuous equilibrium between melt and minerals. In contrast fractional crystallization occurs in the same conditions but with only instantaneous equilibrium between the melt and the crystallizing minerals, that are progressively removed from the system. The composition of the melt for a given element is predicted for the two reactions by the following equations:

Equilibrium (or batch) crystallization	Fractional (or Rayleigh) crystallization
(simple mass balance between the phases)	(based on the Rayleigh distillation law)
$C^l = C_0^l.[F.(1-K_d)+K_d]^{-1}$	$C^l = C_0^l.F^{(K_d-1)}$

with

F: fraction of melt remaining after crystallization

C^l : concentration of the considered element in the melt

C_0^l : initial concentration of the considered element in the melt

K_d : equivalent bulk partition coefficient of the crystallizing phases

These equations work on the assumption that the bulk partition coefficient of the crystallized phases remains constant during crystallization, i.e. that the mineral assemblage remains the same during crystallization with partition coefficients for each phases that do not change. Other models based on the equation of fractional crystallization are presented in ***Allègre and Minster (1978)*** for example for multisequence fractional crystallization (change of the mineral assemblage during crystallization) and defined as follow :

Multisequence fractional crystallization

$$C^l = C_0^l . f_1^{K_{d,1}-K_{d,2}} . f_2^{K_{d,2}-K_{d,3}} \dots f_n^{K_{d,n}-1}$$

with

$f_1, \dots f_n$: degrees of crystallization at the end of each step

$K_{d,1}, \dots K_{d,n}$: bulk partition coefficient during each step

The approach considered when using the previous models implies to constrain the crystallization sequence for the studied system thanks to petrographic observations, such as the mineral assemblages and textures of the lithologies. Other parameters, for example the minerals composition or the temperature, can be implemented with appropriate partition coefficients, but they are usually considered constant (***Allègre and Minster, 1978*** - *see I.2.2.1*). The accuracy of the models also depend on the available coefficients determined experimentally or predicted by partitioning models, and that need to be constrained for the parameters considered during differentiation (*see I.2.2.2.2*).

Thermodynamic modeling has been developed and implemented in different programs such as MELTS (from ***Ghiorso and Sack, 1995*** to ***Gualda and Ghiorso, 2015***), Comagmat (e.g. ***Ariskin and Barmina, 2004***) or Petrolog (***Danyushevsky and Plechov, 2011***). Models such as MELTS (or rhyolite-MELTS) enable to calculate phase equilibrium for a multi-component silicate liquid. MELTS is based on standard state thermodynamic laws, and is calibrated on experimentally determined equilibrium between coexisting minerals (e.g. olivine, pyroxene, feldspar, oxide or spinel) and silicate liquids over broad ranges of composition, temperature, pressure and oxygen fugacity (***Ghiorso and Sack, 1995***). MELTS enable to model both equilibrium and fractional crystallization, along with other processes such as assimilation. The temperature range for MELTS varies between 500 and 2000°C, with pressures ranging from 0 to 2 GPa. It also allows to specify an oxygen buffer during crystallization with addition or not of water, to get as close as possible to the supposed natural conditions of magma crystallization. As a result, the model determines at each temperature step the composition and proportion of the residual liquid after crystallization. The composition and the relative proportion of minerals crystallized are also determined as well as associated thermodynamic parameters, such as the molar Gibbs free energy of the liquid and phases in equilibrium. The calculation of trace element contents evolution during differentiation can then be determined by relying on the crystallization sequence established and by implementing the appropriate partition coefficients.

In situ crystallization and trapped melt crystallization

In situ crystallization developed initially by ***Langmuir*** (***1989*** - *see I.2.1.3*) enable to model trace element evolutions in a more complex system, where minerals are not completely extracted from the system but rather form a mush where crystallization occurs. This model suppose the progressive mixing between the melt present in the main magma chamber with a fraction of the more evolved residual melt present in the mush. The process is described by the following equation (***Langmuir, 1989***), which consider equilibrium crystallization of the melt present in the mush:

In situ crystallization

$$C_l = C_0 . \left(\frac{M_L}{M_0}\right)^{f_A(E-1)/(f_A-1)}$$

with

C_L : concentration of the considered element in the magma chamber

C_0 : initial concentration of the considered element in the magma chamber

$E = \frac{C_F}{C_L}$ with

C_F : concentration of the interstitial melt returning in the magma chamber

M_L : mass of liquid in the magma chamber

M_0 : initial mass of the magma chamber

f_A : proportion of the interstitial liquid returning in the magma chamber

An alternative similar model is the "boundary layer fractionation" of ***Nielsen and DeLong (1992)***, which includes the modeling of phase equilibrium and trace element partitioning. The crystallization process in the boundary layer fractionation is not equilibrium but fractional crystallization, with a solidification zone migrating progressively inward during the solidification of the magma chamber. Both models of in situ crystallization and boundary layer fractionation then only represent processes occurring when a large portion of melt still remains in the main magma chamber. Compared to equilibrium and fractional crystallization, the main effect of this localized crystallization is to produce higher fractionation between incompatible elements at similar enrichments (*Figure 1.20*).

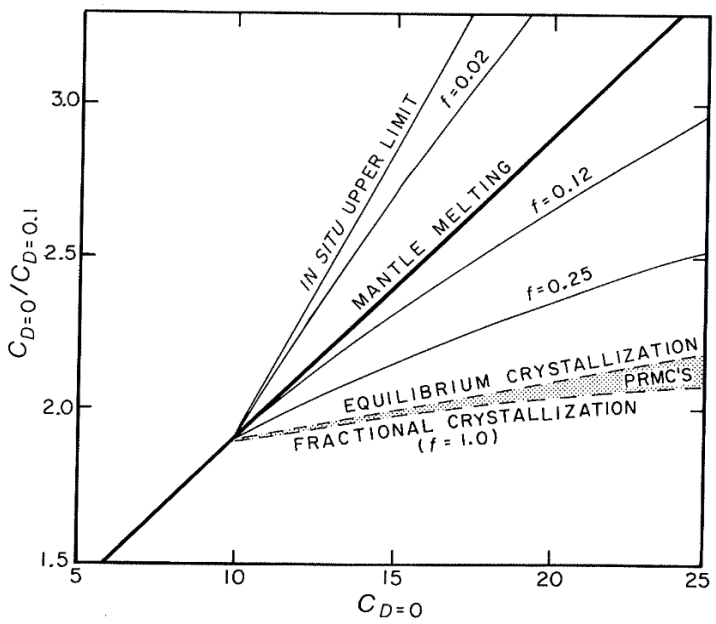

Figure 1.20 - Plot of the ratio of a highly incompatible element with D=0 to a moderately incompatible element with D=0.1 against the abundance of the highly incompatible element, to compare periodically replenished magma chambers (PRMC's - between the equilibrium and fractional crystallization curves), in situ crystallization and partial melting of the mantle. f: proportion of the liquid which returns in the magma chamber during in situ crystallization (Langmuir, 1989)

On opposite close to the solidus point of the system, melts can get trapped due to porosity closure within the crystallizing mush (e.g. ***Meyer et al., 1989; Morse, 1979***). Trapped melt crystallization can lead to the formation of more differentiated, newly formed minerals or crystal cumulate overgrowths, with marked major and trace element zoning patterns (***Barnes, 1986***). Such trapped melt evolution has been evoked for the occurrence of "late stage" minerals such as amphibole in rather primitive oceanic cumulates (e.g. ***Borghini and Rampone, 2007; Coogan et al., 2001; Natland et al., 1991***). The presence of trapped melt has also been raised to explain the discrepancy between enriched whole-rock compositions that fail to be mass balanced by *in situ* mineral compositions (***Ross and Elthon, 1997***). The modeling proposed for example by ***Barnes (1986)***, ***Bédard (1994)*** or used later by ***Charlier et al. (2005)*** consists in a mass balance equation based on the bulk composition of the lithologies, the composition and proportion of the minerals in the studied sample. The difference between the bulk composition of the cumulate phases and the whole rock composition describes the trapped melt component of the rock.

Reactive porous flow and melt-rock reactions

As described earlier, the evolution of lower oceanic crust reservoirs is increasingly considered as being governed by mush-related processes. Even though the processes described above may take place locally, the inner dynamic of mushy magma reservoirs and its impact on melt and cumulate evolution has been considered by several authors (e.g. ***Coogan et al., 2000;***

Ferrando et al., 2018; Lissenberg and MacLeod, 2016; Sanfilippo et al., 2015 - *see I.2.2.3*). Melt in equilibrium with the mush crystals (from which they crystallize in open system) migrates and is replaced by a melt in disequilibrium with the same minerals. Hence, the crystals start to dissolve and the composition of the percolating melt progressively changes. The melt then precipitates or overgrows minerals with a composition that will exhibit the melt-rock reaction signature. To model and predict the evolution of trace element concentrations during such dissolution-precipitation process (***Liang, 2003***), two main models are used.

The first model was initially developed by ***DePaolo (1981)*** to describe the evolution of a magma chamber that assimilates an external component and differentiates by fractional crystallization. This external component as described by ***DePaolo (1981)*** can be assimilated wall rocks or recharge magmas. The external components in our case are the preexisting crystals of the mush assimilated by the percolating melt. The Assimilation-Fractional Crystallization or AFC model for a considered element is described by the following equation:

Assimilation-Fractional Crystallization (AFC)

$$C_{AFC} = C_0.F^{-z} + \frac{r}{r+1}.(1-F^{-z}).\frac{C_a}{z}$$

with

C_{AFC} : concentration of the liquid in instantaneous equilibrium with the crystallizing minerals

C_0 : concentration of the percolating reactive liquid

C_a : concentration of the assimilated equivalent surrounding mush

F : fraction of residual melt in the system after reaction

$r = \frac{M_A}{M_C}$: ratio assimilated mass (M_A) on crystallizing mass (M_C)

$z = \frac{r+K_d+1}{r-1}$ with K_d the global partition coefficient of the crystallized phases ($K_d = \sum_1^n x_i.K_{d,i}$ with x_i the proportion of phase *i* crystallized and $K_{d,i}$ the partition coefficient between phase *i* and the melt)

No additional impact such as diffusion or migration during the reaction is considered here and no thermodynamic constrains are applied to the system. The main mechanism which governs the reaction is the partitioning of the considered element(s) between melt and crystals. Similarly to the other models described above, at each step of the reaction the global partition coefficient is considered constant as well as the composition of the assimilated component, with the assumption that crystals remain in instantaneous equilibrium with the residual melt.

However dissolution-precipitation processes lead to progressive variations in the melt composition during the reaction. The migration of the elements between the two interacting phases in disequilibrium is controlled by the partitioning of the considered elements in a boundary layer (e.g. ***Dohmen et al., 2003; Wang et al., 2013***). Thus, the capacity of migration of the reactive melt can influence its composition during the reaction. A chromatographic fractionation of the elements may add to the chemical variation related to magma/rock interactions; this chromatographic effect has been first described for mantle rocks (***Navon and Stopler, 1985***). The behavior of trace elements during the reaction varies with their ability to be exchanged with the percolated lithology. The slightly incompatible elements and compatible elements are further exchanged with the solid phase and equilibrate more rapidly with the surrounding lithology, in contrary to the strongly incompatible elements. As a result, the more incompatible elements migrate faster within the porous flow than the less incompatible and compatible ones (*Figure 1.21*).

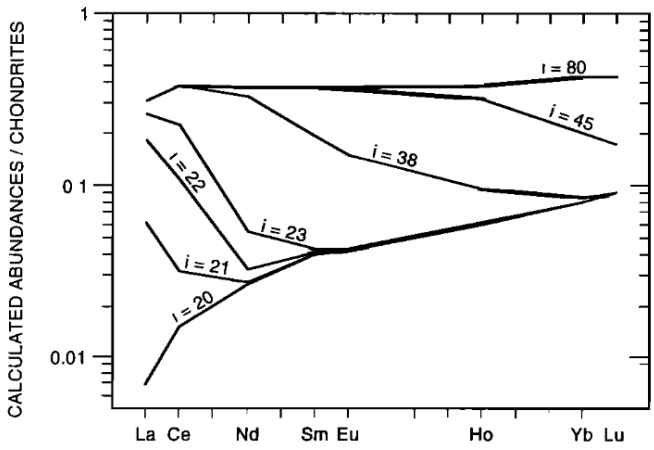

Figure 1.21 - Simulation of the standard one-dimensional porous flow model with the plate model, reproducing the chromatographic fractionation of rare earth elements (REE) during infiltration of a LREE-enriched fluid in LREE-depleted peridotites, without fluid-rock reaction. Result for the peridotite compositions in the upper cell of the model after variable increment number (i). Vernières et al. (1997)

The "Plate model" first developed by ***Vernières et al. (1997)*** combines both the dissolution-precipitation and the chromatographic effect during transport for the modeling of reactive porous flow. The "Percol 0D" model is independent of time and distance. It considers as column made of reactive cells through which the melt percolates from the bottom and reacts with the equivalent mush / rock. The initial porosity of the cells controls the amount of melt reacting by dissolution-precipitation due to local equilibrium constrains. Dissolution and precipitation are applied successively in representative micro volumes of rocks, in which the amount of both reactions can be parameterized according to their localization in the reactive column. The modal proportions of the dissolved and precipitated material, in addition to the associated partition coefficients for each element governing the reaction are set by the operator.

The initial porosity of the matrix, and the dissolution and crystallization rates are also defined by the user to shape the reaction being modeled in the different areas in the column.

Similarly to the AFC model and to other models of trace elements behavior during magmatic evolution, the plate model does not directly take into account any thermodynamic consideration. On one hand, the proportion of minerals being assimilated in the melt induces a progressive change in the major element contents of the melt. On the other hand, the proportion of minerals precipitated during the reaction depends of melt major element composition, which is not considered at each reaction increment. The MELTS model described earlier enables to model major element variations for an Assimilation-Fractional Crystallization scenario, but does not enable to directly track the variations in trace element concentrations during the reaction.

2.2.2.2 Input parameters and preservation of the geochemical signatures

Partition coefficients

The evolution of magmatic systems modeled by the implementation of the various models described above requires different input parameters, for example the starting composition (parental melt) or the composition of the minerals involved during dissolution or crystallization. Trace elements concentrations during differentiation are also strongly dependent on the partition coefficient between silicate melt and the different minerals involved in the reactions (*see I.2.2.1.*). These partition coefficients depend on the composition of the system, the pressure (in particular for pressures > 3GPa, e.g. ***Taura et al., 1998***), the temperature and the redox conditions. During magma differentiation those parameters vary, thus considering constant partition coefficient through the reactions would likely deviate the potential chemical variability induced by changes of the trace elements partitioning behavior (***Blundy and Wood, 2003***).

In order to account for temperature and composition variations during the differentiation process, the best approach is therefore to implement the partition coefficient calculation at each step of evolution of the system. The partitioning of trace elements can be predicted based on the Lattice Strain Model, which describes the facility for an ion to enter a crystal lattice depend on its charge in radius (***Onuma et al., 1968***). The partition coefficients values K_d as a function of the ionic radius of the ions considered are described by a parabola in the logarithmic scale (*Figure 1.22a*). This parabola can be described by the Brice equation (***Brice, 1975***):

Partition coefficient determination based on the Lattice Strain Model

$$D_i = D_0 \times \exp\left(\frac{-4\pi E_s N_A \left(\left(\frac{r_0}{2}\right)(r_0 - r_i)^2 - \left(\frac{1}{3}\right)(r_0 - r_i)^3\right)}{RT}\right)$$

with

D_i : partition coefficient of the considered element

D_0 : ideal partition coefficient for the best-fit ion radius r_0 in the crystal site

r_i : ion radius of the considered element

E_s : effective Young's modulus of the crystal site (describing the elastic response of the crystal site)

R : ideal gaz constant, T : temperature of the system, N_A : Avogadro's number

Several models to predict partition coefficients are available for different minerals such as olivine, plagioclase and clinopyroxene, which are the three main phases constituting the gabbroic sequence considered here. The models developed and compared with experimental data for olivines (e.g. ***Beattie, 1994***; ***Stead et al., 2017***; ***Sun and Liang, 2013***), plagioclases (e.g. ***Sun et al., 2017***) and clinopyroxenes (e.g. ***Sun and Liang, 2013; Wood and Blundy, 1997***) are able to predict the evolution of the elements partitioning with variations of temperature and compositions. As shown in *Figure 1.22b*, a general decrease of the temperature triggers an increase of the partition coefficients, whereas the increase of water content of the melt induces a decrease of partitioning.

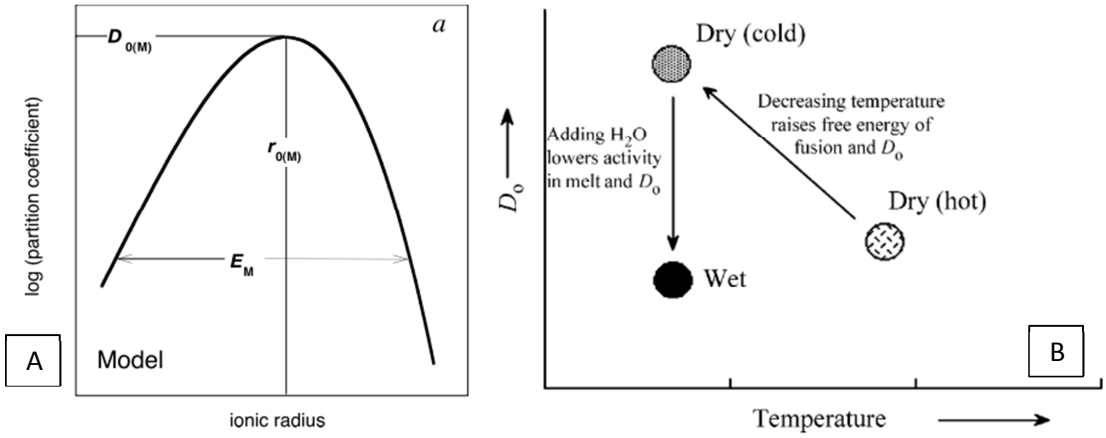

Figure 1.22 - (a) Cartoon illustrating the Lattice Strain model of trace element partitioning and partition coefficient variations with ionic radius(M : crystal lattice site considered - Blundy & Wood, 2003). (b) Schematic illustration of the combined effects of increasing H_2O content of the melt and decreasing temperature on partition coefficients. Decreasing temperature raises D0 because the entropy of fusion (ΔS_f) is positive, while adding H_2O decreases D0 because it lowers the activities of all other components in the melt (Wood & Blundy, 1997)

For Rare Earth Elements (REE), the partition coefficients are higher for clinopyroxene (at around 10^{-1} from La to Yb, *Figure 1.23c)*) and decrease for plagioclase (between 10^{-1} for La and 10^{-2} for Lu, *Figure 1.23b)*) and olivine (below 10^{-2} and down to 10^{-5} for La, *Figure 1.23a)*). During tholeiitic MORB differentiation, REE will thus have stronger affinity for clinopyroxene than olivine or plagioclase. The fractionation of REE between each other that is caused by the partitioning in the different minerals is also variable between the three phases. Depending on the ionic radius of the ideal cation to which trace elements substitutes, LREE partition coefficient can be either higher relative to HREE partition coefficient (e.g., Pl) or lower (e.g., Cpx, Ol). This variable behavior will likely influence the chemical evolution of the melt depending on which minerals are involved in the dissolution and crystallization processes.

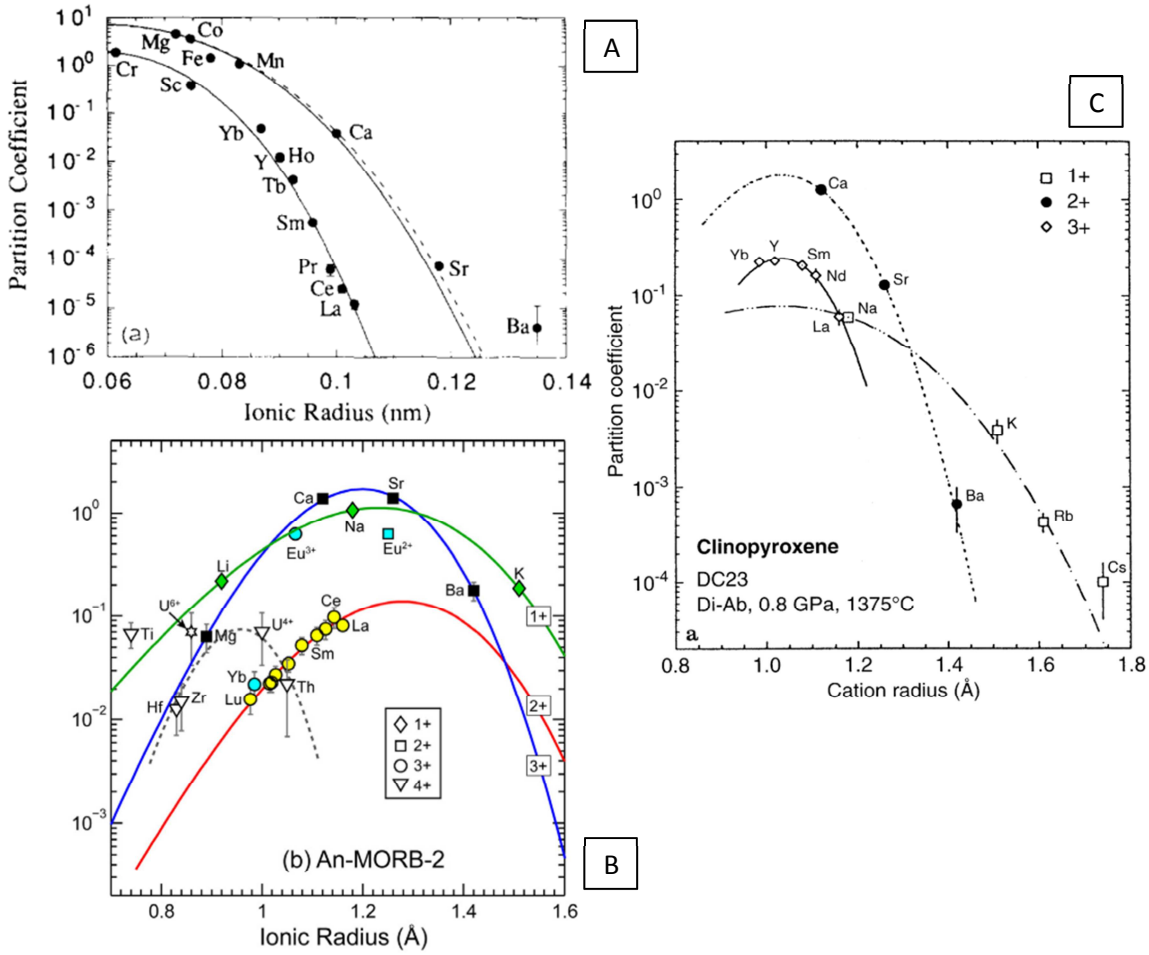

Figure 1.23 - Diagrams showing Lattice Strain Models fits to experimental data on (a) olivine-melt (Beattie ,1994), (b) plagioclase-melt (Sun et al., 2017) and (c) clinopyroxene-melt (Wood & Blundy, 1997) partitioning.

Reequilibration by diffusion

To track the effect of the different processes occurring in magma reservoirs thanks to the geochemical signature in major and trace elements of the igneous lithologies, it is important to take into account potential reequilibration events during and after crystallization. Reequilbration by diffusion may partially or totally overprint the initial contents and compositional variability in the minerals, and create new gradients within minerals due to partial reequilibration between crystals and melts or between the crystallized phases. Diffusion represents the motion of a particle relative to the motion of other particles in a defined region of particles (***Onsager, 1945***). The homogenization of concentrations is the consequence of this random process in the medium studied, whenever a compositional gradient exists in a single or between different phases. The evolution of the concentrations by diffusion is described by the Fick's laws (in one dimension):

Fick's 1st law (1D)

$$J = -D\frac{\partial C}{\delta x}$$

Fick's 2nd law (1D)

$$\frac{\partial C}{\delta t} = -\frac{\partial J}{\delta x} = D\frac{\partial^2 C}{\partial x^2}$$

with

J: flux of particles in the solid

C: concentration of the considered element

$\frac{\partial C}{\delta x}$: compositional gradient & $\frac{\partial^2 C}{\delta x^2}$: gradient of the compositional flux

D: diffusion coefficient of the considered element

The diffusion coefficient characterizes the ability of an atom to jump from one site to another in mineral lattices. It varies from one element to another and depends on the phase that is considered, but also on the pressure of the system, the oxygen fugacity and the composition of the mineral. In addition, diffusion coefficients are strongly dependent on the temperature; the higher the temperature, the faster the diffusion. Cooling has an impact on the compositions recorded in minerals if diffusion is fast enough to reequilibrate the element concentrations before the decrease in temperature makes diffusion inefficient. Some elements are more impacted by diffusion and are often reequilibrated in gabbroic plutons. Despite the variability in the diffusion coefficients determined by different studies, in general olivine presents the higher diffusion coefficients for major elements (for example Fe and Mg) but also for trace elements such as REE (e.g. ***Cherniak, 2010; Dohmen and Chakraborty, 2007; Spandler and O'Neill, 2010***). Hence the conservation of the primary magmatic composition in olivine crystals can be challenged. On opposite for plagioclase and clinopyroxene, the diffusion of major and trace

elements is slower compared to olivine (e.g. ***Cherniak, 2010b, 2003; Cherniak and Liang, 2007; Faak et al., 2013; Spandler et al., 2007; Spandler and O'Neill, 2010; Van Orman et al., 2001; Zhang et al., 2010***). For example, the slow coupled diffusion in plagioclase of Na + Si and Ca + Al (***Grove et al., 1984; Morse, 1984***) ensures the preservation of any zoning directly linked to the formation of the minerals. This characteristic also explains the common use of clinopyroxene compositions in major and trace elements for the study of lower oceanic crust samples (*see I.2.2.3* below), as diffusion is unlikely to have reset the initial magmatic signature of the samples.

2.2.3 Pervasive melt-rock reactions in the slow-spreading lower oceanic crust

2.2.3.1 Determination and description of characteristic geochemical signatures

Observations on ophiolites representative of slow-spread lower oceanic crust in the Canadian Appalachians, the Alps and Corsica, and the Apennines (e.g. ***Bédard, 2015, 1991; Lagabrielle et al., 2015; Lagabrielle and Cannat, 1990; Lagabrielle and Lemoine, 1997; Renna et al., 2016; Sanfilippo et al., 2017; Sanfilippo and Tribuzio, 2013, 2011; Tribuzio et al., 2000***) may precise the relationship between the lithosphere and the intruding magmas. Evidences of progressive assimilation of mantle lithologies by mantle melts migrating by diffuse or channelized flow were identified (e.g. ***Sanfilippo and Tribuzio, 2011***), in addition to the presence of gabbroic bodies crosscutting associations of plagioclase peridotites, dunites, olivine-

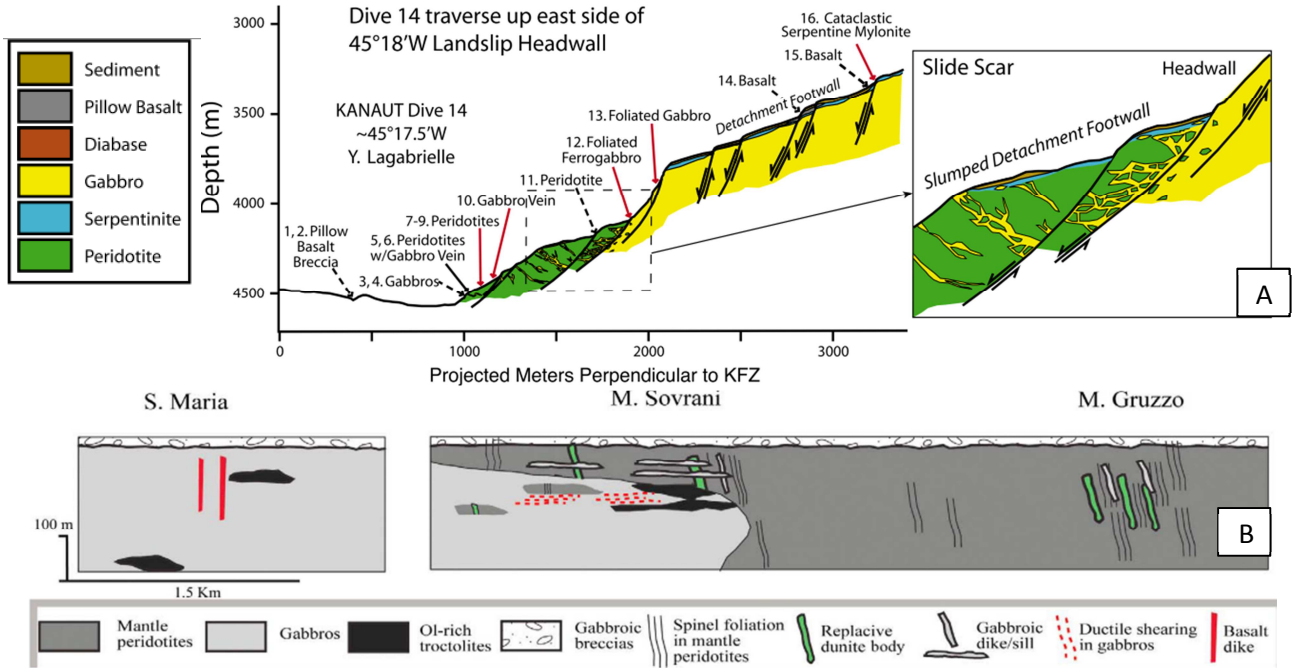

Figure 1.24 - (a) Interpretation of observations from Nautile traverses up the southern wall of the Kane Transform bordering the Kane Megamullion by Lagabrielle (Dick et al., 2008). (b) Paleotectonic reconstruction of Scogna-Rocchetta Vara ophiolite in the Middle Jurassic (exaggerated scales for dunite bodies, gabbroic dykes and sills. (Sanfilippo & Tribuzio, 2011).

rich troctolites and troctolites *sensu stricto* (e.g. ***Lagabrielle et al., 2015***). Very similar associations have been found in modern crust sampled at the Atlantis Massif Core Complex on the MAR (***Blackman et al., 2004; Godard et al., 2009***) or in other dredged oceanic core complexes (e.g. ***Coogan et al., 2004; Dick et al., 2008; Macleod et al., 1998; Sanfilippo et al., 2019*** - *Figure 1.24*). In addition to the reactive textures observed in the samples, the geochemical signature of ophiolitic primitive cumulates reveal their likely inheritance from mantle lithologies (e.g. ***Basch et al., 2018; Drouin et al., 2010, 2009; Ferrando et al., 2018; Sanfilippo et al., 2014; Suhr et al., 2008***).

The primitive cumulates share similar characteristics with impregnated mantle rocks from modern oceanic crust and ophiolites (e.g. ***Borghini and Rampone, 2007; Dick, 1989; Rampone et al., 2008***). The samples usually show Fe-Ni-rich olivines, high An plagioclase cores (molar Ca/[Ca + Na + K] × 100) or highly magnesian clinopyroxenes with both high Cr and Ti contents. While the major element contents of the different phases are relatively coherent with evolution by simple crystallization processes, trace elements are in disequilibrium and especially the incompatible elements. The samples present enrichments in the most

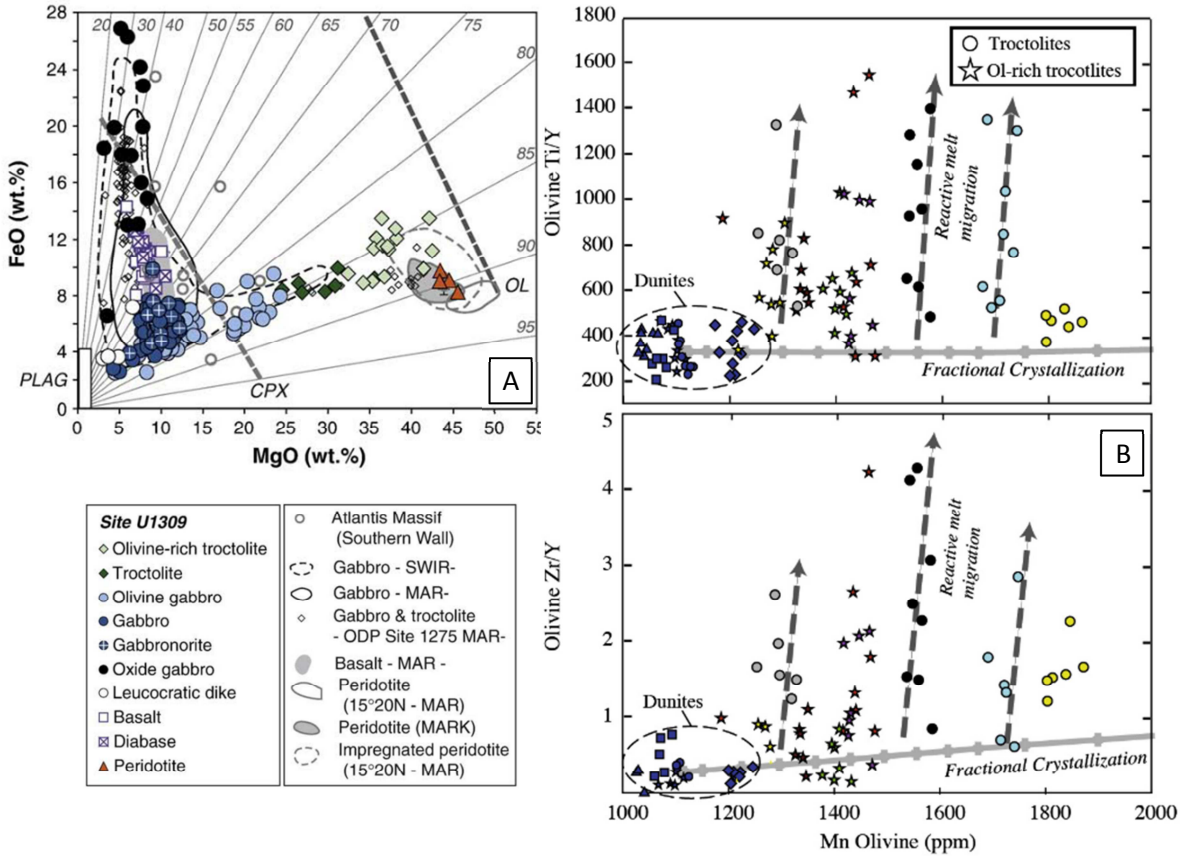

Figure 1.25 - (a) Composition in wt% of the different rock types recovered at Site U1309 (MAR) in FeO (total) versus MgO and comparison with the compositional ranges of gabbros and basalts from mid-ocean ridges (Godard et al., 2009 and references therein). (b) Mn (ppm) versus Ti/Y and Zr/Y ratios in the olivines from dunites and lower crustal samples from the Alpine Jurassic ophiolites (Sanfilippo et al., 2014). Blue symbols: dunites. For troctolites and Ol-rich troctolites each color represents one sample.

incompatible trace elements compared to the compositions expected by crystallization at similar major element contents. These enrichments are generally interpreted as evidence for melt-rock reaction involvement (*Figure 1.25*). The decoupling between major and trace element compositions of minerals and whole-rocks together with the minerals reactive textures are not only witnessed in the most primitive components of the lower crust. More evolved lithologies interpreted as crystallized in crustal magmatic reservoirs like olivine gabbros have similar features (***Meyer et al., 1989***).

Many studies have reported Ti over enrichments in clinopyroxenes of gabbroic rocks, together with strong enrichments in the most incompatible trace elements (*Figure 1.26* - e.g. ***Bédard et al., 2000; Coogan et al., 2000; Dick et al., 2002; Gao et al., 2007; Lissenberg et al., 2013; Lissenberg and MacLeod, 2016; Ross and Elthon, 1997, 1993***). ***Ross and Elthon (1997)*** considered the boundary layer fractionation model (*see I.2.2.2.1*) to explain the major element contents of their samples from the MAR. They also determined the proportion of trapped melt in the samples that could account for the enriched REE composition of plagioclases and clinopyroxenes. The calculated amount of trapped melt is variable depending on the element considered and decreases from ~20% for La and Ce, to 10% for the HREE and less than 5% for Y or Ti. This highlights the stronger enrichments in the more incompatible elements, and that trapped melt alone cannot account for the formation of the corresponding samples. Other features such as the lack of textural evidence for trapped melt crystallization or major element zoning in minerals also preclude this hypothesis, as shown by ***Coogan et al. (2000)*** on the same samples as ***Ross and Elthon, 1997***, or ***Gao et al. (2007)*** on samples from the Atlantis Bank OCC. Instead, the process of melt migration within a crystal matrix has been considered by many authors as key in understanding the geochemical signatures of oceanic gabbro cumulates over the past decades.

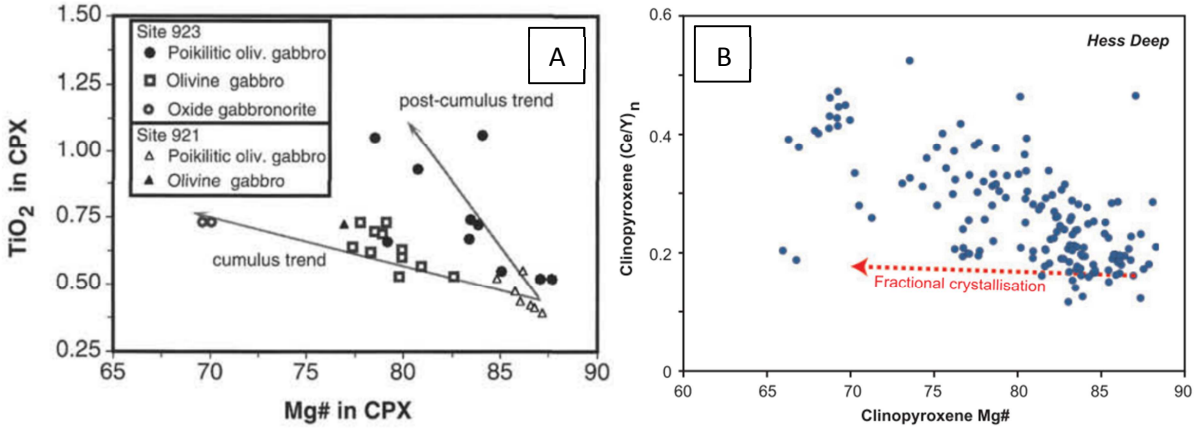

Figure 1.26 - (a) Mg# versus TiO_2 (wt%) in clinopyroxene in Leg 153 gabbroic rocks. "Cumulus trend" consistent with fractional crystallization, "post-cumulus trend" defined by samples in which clinopyroxene has intercumulus or poikilitic textures (Ross & Elthon, 1997). (b) Relationship between Mg# and chondrite-normalized Ce/Y ratio for the lower crustal section exposed at Hess Deep. Red arrow: Fractional crystallization trend calculated by MELTS (Lissenberg & MacLeod, 2016).

In the lower oceanic crust, mineral compositions deviating from the equilibrium or fractional crystallization evolution trends were considered as a potential consequence of such reactive melt migration within magma reservoirs (e.g. ***Bédard et al., 2000; Dick et al., 2002; Gao et al., 2007; Kvassnes et al., 2004; Natland and Dick, 2001***). The main geochemical characteristics of crustal rocks which were subject to melt-rock reactions are reviewed in ***Lissenberg and MacLeod (2016)***. Clinopyroxenes usually present high Mg# compared to the expected values for a tholeiitic suite (***Grove et al., 1992***). Together with the sample texture (evidence for crystallization of clinopyroxene after olivine and plagioclases) and the high Ti contents of the same crystals, crystallization of such minerals at high pressure from primitive melt is excluded (*see I.2.1.1*). On the opposite, high Mg# clinopyroxenes can be explained by reaction of an olivine-plagioclase matrix interacting with a percolating melt, which composition is buffered by the primitive matrix and from which "primitive" clinopyroxenes can crystallize (***Lissenberg and Dick, 2008***). Another characteristic of clinopyroxenes is their combined high composition in Cr and Ti (*Figure 1.27*). In the case of fractional crystallization, during differentiation Cr contents (compatible behavior) should decrease when the Ti contents (incompatible behavior) should increase. Again, assimilation of a more primitive cumulate component (rich in Cr and Mg) by a moderately differentiated melt at clinopyroxene saturation would explain such compositions (***Lissenberg and MacLeod, 2016*** and references therein; ***Leuthold et al., 2018***). Minerals (especially the rims) also present enrichments in the most incompatible trace elements, which is a rather ubiquitous signature in the lower curst of various oceanic settings (***Coogan, 2014; Lissenberg and MacLeod, 2016*** and references therein). During fractional or in situ crystallization an increase of the incompatible element contents of the melt is also expected, but in natural samples the magnitude of the enrichments and fractionations between the more to less incompatible elements is several times higher than expected (e.g. ***Coogan et al., 2000; Gao et al., 2007; Leuthold et al., 2018; Lissenberg et al., 2013***).

Coogan and O'Hara (2015) explained the trace element fractionation by diffusion. The diffusion speed of each REE progressively decreases from the Heavy REE to the Light REE, the latter would appear more "enriched" in the rims of the minerals compared to the heavy REE that would already be equilibrated with the lower concentrations present in the core of the same minerals. However, diffusion is usually slow enough in clinopyroxene to preclude such process (*see I.2.2.2.2.*) and ***Lissenberg and MacLeod (2016)*** shows that typical reactive melt migration signatures described in representative samples kept their primary magmatic features. Their reasoning relies on the study of a coarse grained clinopyroxene, large enough to prevent complete reequilibration of the compositions by diffusion, in which a zonation in the fastest diffusive species Mg and Fe is observed. Hence, no significant reequilibration occurred and the joint typical melt-rock reaction signatures in minor trace elements cannot be explained by diffusion. Such fractionation and enrichment in the most incompatible trace elements is the main geochemical tracer considered to track the occurrence of reactive melt migration, but also used to quantify the reactions.

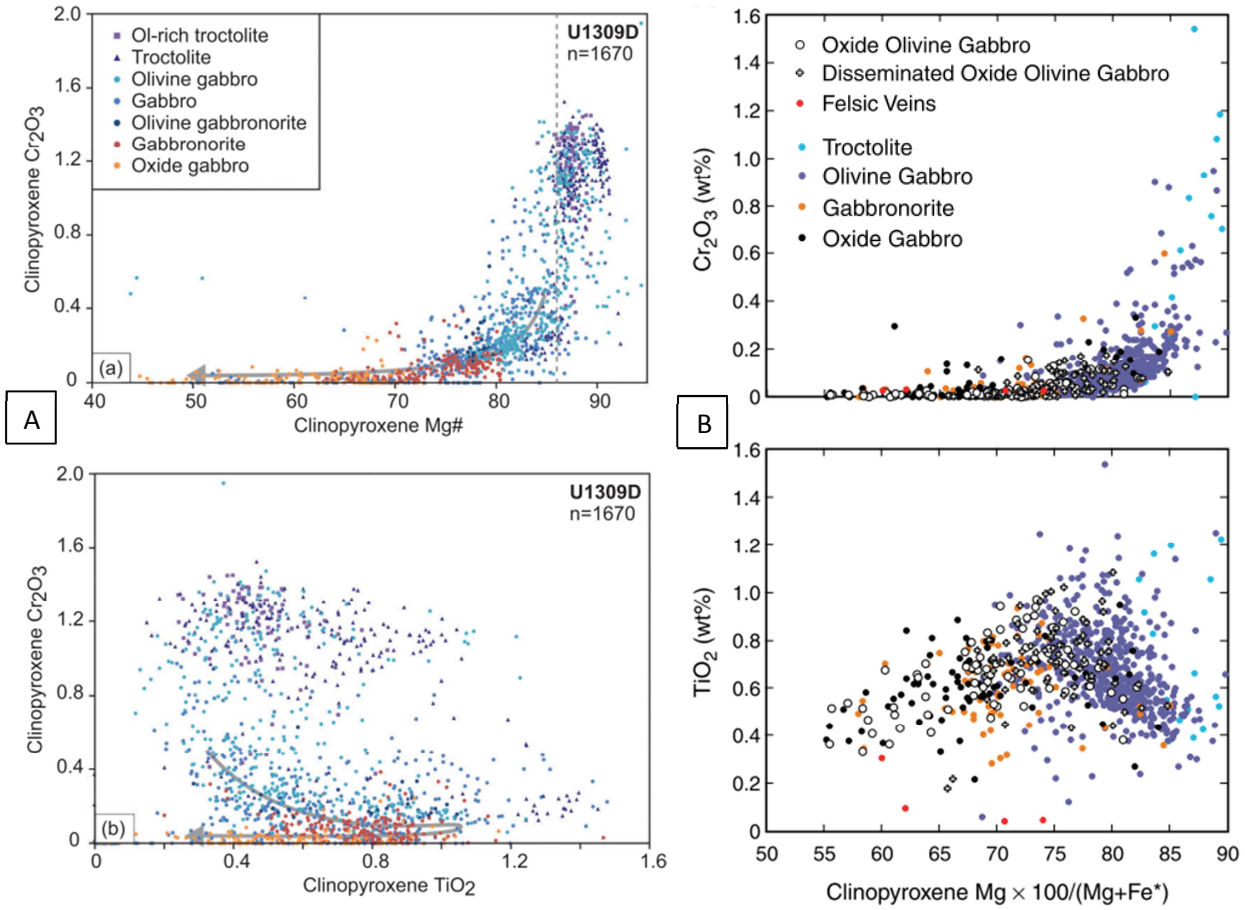

Figure 1.27 - (a) Mg-Ti-Cr relationships in clinopyroxene from gabbroic rocks from IODP Hole U1309D at Atlantis Massif (MAR). Top: Mg# - Cr_2O_3 (wt%). Dashed grey line separates a population of high-Mg# clinopyroxenes. Bottom: TiO_2 - Cr_2O_3 (wt%). Grey arrow: mark schematic fractional crystallization trend of clinopyroxene in equilibrium with MORB undergoing fractional crystallization at low pressure (Lissenberg & MacLeod, 2016 and reference therein). (b) TiO_2 and Cr_2O_3 (wt%) concentrations in Hole 735B clinopyroxenes at Atlantis Bank (SWIR) plotted against the molar ratio of Mg and Mg + Fe (Dick et al., 2002).Note the difference in color coding for the two studies.

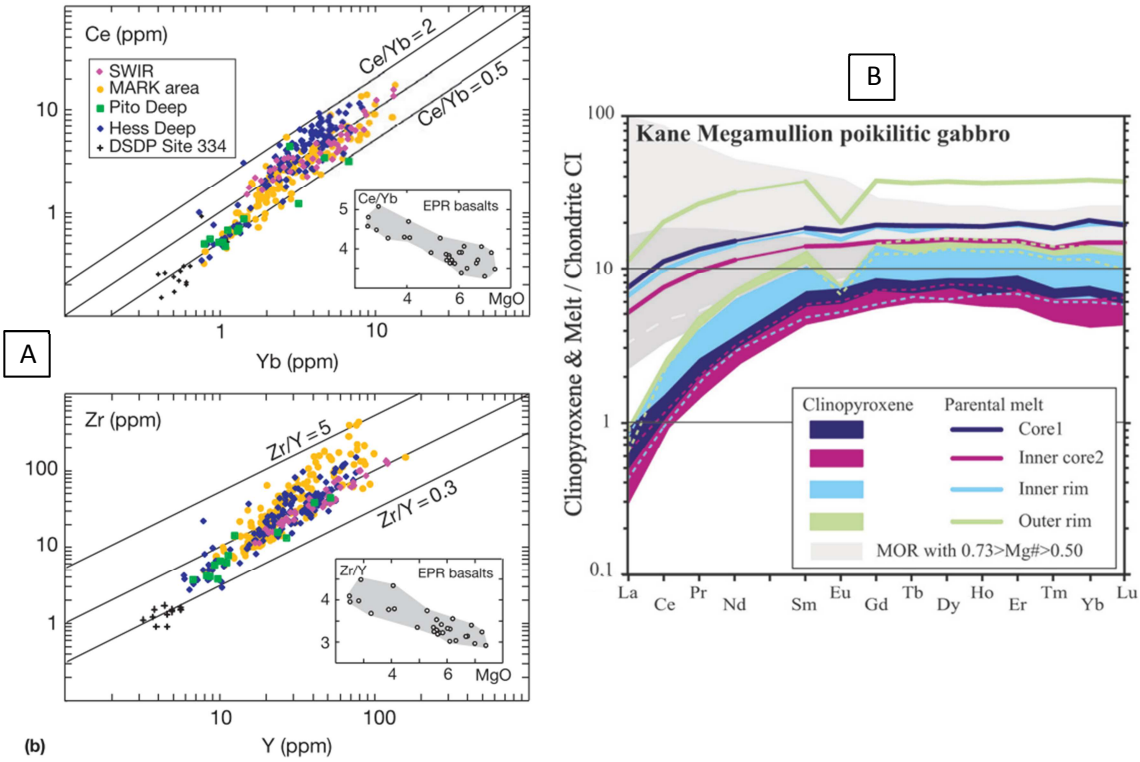

Figure 1.28 - Variations in trace element abundances in clinopyroxene in oceanic gabbros for (a) Ce versus Yb and (b) Zr versus Y, both showing a general increase in more-to-less incompatible element ratios with increasing incompatible element abundances (Coogan 2014 and references therein). (c) Chondrite normalized REE compositions of equilibrium melts with clinopyroxenes for Kane Megamullion poikilitic gabbros, compared with MORB compositions (Leuthold et al., 2018 and references therein).

2.2.3.2 Modeling of melt-rock reactions associated with reactive porous flow (RPF) and experimental determination

Modeling of melt-rock reaction processes was used both in studies of mantle impregnation or incorporation within lower crustal lithologies, and in studies of lower crust gabbroic lithologies differentiation. The models are based on a common principle that the reactions involve assimilation of a crystal phase by a melt from which a new generation of minerals that contain the RPF signatures crystallizes. In the following, I consider (1) modeling of reactions involving mantle lithologies and (2) modeling of reactions occurring during the evolution of the lower slow-spread oceanic crust.

Mantle assimilation and primary melt interactions with mantle lithologies

Melt interactions with lithologies from mantle origin are key in understanding the very first step of formation of the oceanic crust, the feasibility of melt migration and extraction from the mantle, and the evolution of their compositions before emplacement within the crust. Both the composition in major elements and in trace elements of melts are impacted by reactive

porous flow processes involving mantle lithologies, even though modeling of their evolution by melt-rock reactions are usually considered separately.

For example, ***Borghini and Rampone (2007)*** used the AFC model (*see 2.2.2.1*) to emphasize the implication of RPF in the very last step of formation of MORB-type primitive olivine-rich cumulates present as intrusions within the Erro-Tobbio mantle peridotite of the Ligurian ophiolite (Italy). Their models reproduce Zr enrichments relative to other REE in clinopyroxenes from the olivine-rich troctolites with a favored reaction:

$$olivine + melt1 \rightarrow clinopyroxene + plagioclase + melt2 \quad (2)$$

The reaction follows a first step of *in situ* fractional crystallization before the onset of RPF that constrains the trace element composition of the reactive melt. Assimilation of 100% olivine and crystallization of 10% clinopyroxene and 90% plagioclase, with ratios Mass assimilated/Mass crystallized of 0.9 and 0.95, are required to fit the clinopyroxene compositions analyzed in the troctolites. However, no strong constraints are given for the selection of the assimilated mass composition, and most of the trace element signatures are explained by crystallization processes (*in situ* crystallization of trapped melts). In that case, RPF is inferred to occur at a small-scale and is not the main process involved in the formation of the lithologies.

The same AFC model was used by ***Sanfilippo et al. (2014)*** to explain the variable incompatible element signatures found in olivines of olivine-rich troctolites and troctolites from the mantle-crust transition of slow-spreading ocean lithosphere preserved in the Alpine Jurassic ophiolites. The reaction considers assimilation of a troctolitic matrix (40% olivine and 60% plagioclase) and crystallization of a gabbroic assemblage (30% olivine, 50% plagioclase and 20% clinopyroxene):

$$olivine + plagioclase + melt1 \rightarrow olivine + plagioclase + clinopyroxene + melt2 \quad (3)$$

The ratios Mass assimilated/Mass crystallized tested are of 0.85, 0.9 and 0.95 (similar to the model of ***Borghini and Rampone, 2007***), but the reactive melt is taken here as the melt in equilibrium with minerals presenting the lowermost degree of reaction within the samples, and the compositions of the assimilated and crystallized phase are the minerals compositions analyzed in one of the troctolite samples. Reaction (3) occurred during infiltration of olivine and plagioclase crystal mushes at the base of the crust by a melt that previously reacted within the mantle, and constitutes the main process leading to the formation of the studied olivine-rich troctolites (*Figure 1.29*).

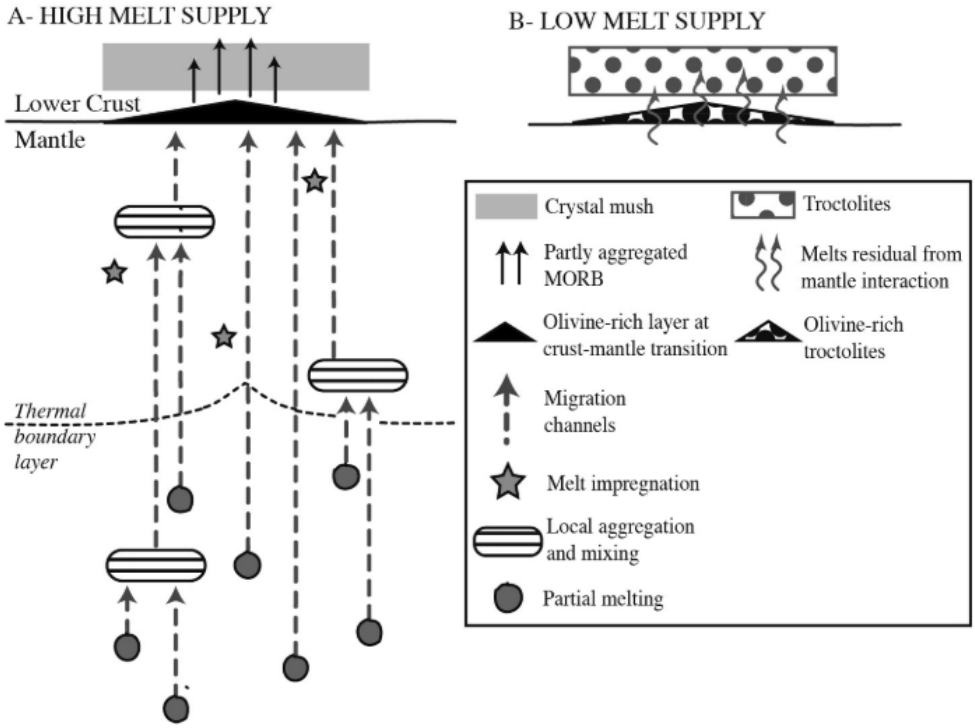

Figure 1.29 - Schematic cartoon showing the early magmatic processes that occurred in the oceanic lithopshere (Sanfilippo et al., 2014 - modified after Grove et al., 1992 and Collier & Kelemen, 2010).

On opposite to what has been described above in ophiolites, the AFC model failed to reproduce the REEs mineral contents of olivine-rich troctolites sampled in the long *in situ* section drilled in the Atlantis Massif OCC on the MAR (***Ferrando et al., 2018***). A more complex model involving a two steps reaction, with evolution of compositions controlled by a chromatic effect during element transport within the migrating melts, has been proposed by ***Ferrando et al. (2018)*** who implemented the Plate Model (*see 2.2.2.1*).

The reactions they considered are the following:

$$pyroxene + melt1 \rightarrow olivine1 + melt2 \quad (4)$$

$$olivine2 + melt1 + melt2\ (\pm\ olivine1) \rightarrow olivine3 + clinopyroxene + plagioclase + melt3 \quad (5)$$

The olivine-rich troctolites formation is here the consequence of assimilation of a mantle harzburgite by a primary MORB melt, now trapped within the gabbroic cumulate sequences emplaced within the lower crust (reaction (4) and (5)). Contrary to the previous AFC models, the composition of the reactants are taken as the composition of lithologies and equivalent melts sampled along slow-spreading ridges, also the reactions are strongly constrained by textural and

microstructural observations. The authors managed to reproduce in their study the incompatible element contents of the olivine and clinopyroxene, but also the Ni and Mg# contents of the olivine from the studied olivine-rich troctolites. This general evolution of the lithologies is similar to other reactions involving assimilation of mantle lithologies inferred for the formation of the olivine-rich troctolites from IODP Hole U1309D in studies that did not directly implemented numerical models (***Suhr et al., 2008; Drouin et al., 2009***).

Altogether, these few examples emphasize that there is no consensus on the reaction involved in the formation of lithologies presenting anomalous trace element contents compared to simple crystallization processes. The models depend on the samples (usually enriched in olivines) and their relationship with their surroundings (mantle or crustal). However, reactive porous flow processes and associated melt-rock reactions at various scales play a role in the formation and / or evolution of lithologies involving mantle precursors in the deeper part of the oceanic crust (e.g. ***Sanfilippo et al., 2015a***). The most recent models developed for the interactions between inherited mantle lithologies and primary melts attempt to integrate thermodynamic constrains on the assimilation-crystallization process, and investigate their feasibility within the lower crust (e.g. ***Ferrando et al., 2018b; Basch et al., 2019***).

Quantification of melt-rock reactions associated with RPF during the evolution of slow-spread crustal lithologies

The Plate Model was never applied to constrain the evolution of gabbroic cumulates from the lower oceanic crust outside of the context described above, but the AFC model was applied several times (e.g. ***Coogan et al., 2000; Kvassnes, 2003; Gao et al., 2007b***) to fit the trace element contents of clinopyroxenes in gabbros from lower oceanic crust sections. The same assimilated material was considered by ***Coogan et al. (2000)*** and ***Gao et al. (2007a)***, i.e. clinopyroxenes with the most primitive composition analyzed in the samples from the MAR for the former (reaction (6)), or the core composition of the single clinopyroxene from ODP Hole 735 (Atlantis Bank, SWIR) studied in ultra-high resolution by the latter (reaction (7)). Similarly, the composition of the reactive melt in both cases is the equilibrium melt with the minerals, which are at the same time assimilated (e.g. ***Sanfilippo et al., 2014***), which raises the question of the feasibility of such a process that involve primarily disequilibrium.

$$clinopyroxene1 + melt1 \rightarrow clinopyroxene2 + melt2 \quad (6)$$

$$clinopyroxene1 + melt1 \rightarrow plagioclase + clinopyroxene2 + melt2 \quad (7)$$

Whereas ***Coogan et al. (2000)*** only considers crystallization of clinopyroxene, (Gao *et al.*, 2007a) include crystallization of plagioclase and clinopyroxene in various amounts in the

reaction (from 0 to 40% clinopyroxene and the rest as plagioclase), both with ratios Mass assimilated/Mass crystallized between 0.5 and 0.9. Another parameter not yet described but which has its importance in the outcomes of the models are the trace elements partition coefficients. Partition coefficients are sensible to several parameters (see *2.2.2.2*), and especially the composition of the minerals. In the case of the models described above, ***Coogan et al. (2000)*** is the only one to consider the compositional parameter, by using the models of ***Wood and Blundy (1997)*** to calculate a partition coefficient for clinopyroxene based on the average composition of the minerals analyzed in the samples. Both studies conclude that their AFC models are useful as they confirm that melt-rock reactions and RPF are necessary to explain the evolution of the lithologies, but the uncertainty in the input parameters preclude any further constrain on the actual processes that occurred during differentiation or on the scale at which they proceeded.

AFC has also been applied to slow-spread lower oceanic crust samples by ***Kvassnes (2003)*** to reproduce trace element contents of clinopyroxenes from ODP Hole 735B gabbros. Instead of a reaction focusing on clinopyroxene, the author modeled assimilation of a typical olivine gabbro from Atlantis Bank by a depleted MORB mantle composition, and further crystallization of an olivine gabbro assemblage (15% olivine, 35% clinopyroxene and 50% plagioclase - reaction (8)).

$$\textit{olivine1} + \textit{plagioclase1} + \textit{clinopyroxene1} + \textit{melt1} \rightarrow \textit{olivine 2} + \textit{plagioclase2} + \textit{clinopyroxene2} + \textit{melt2} \quad (8)$$

The *in situ* trace element contents of clinopyroxenes used by ***Kvassnes (2003)*** cover the entire compositional range of the lithologies sampled in hole 735B and come from lithologies that do not always similar to the olivine gabbros involved in the reaction. Thus, even though the trends obtained by AFC (with ratios Mass assimilated/Mass crystallized of 0.5, 0.8 and 0.9) fit well the natural compositions, it rather demonstrates that AFC occurred during the formation of the lithologies but do not enable to constrain precisely the processes involved.

Another approach was conducted by ***Lissenberg and Dick (2008)*** to test the implication of RPF on the evolution of gabbroic lithologies from the Kane Megamullion (MAR). The authors modeled the evolution of melt composition in major elements during assimilation of a troctolitic assemblage and crystallization of a gabbro assemblage (reaction (9)). The reaction is strongly constrained by the crystallization sequence deduced from the texture of the samples studied, and the presence or lack of evidences for dissolution and/or recrystallization of the minerals.

$$\textit{olivine1} + \textit{plagioclase1} + \textit{melt1} \rightarrow \textit{plagioclase2} + \textit{clinopyroxene} + \textit{melt2} \quad (9)$$

The authors modeled the evolution of the melt composition by adding "manually" different fractions of the troctolite assemblage and removing various fractions of the gabbro assemblage considered. As the reaction is supposed to have occurred in an open system, and hence is not balanced, the volume of melt involved is not constrained nor taken into account in the model. Plagioclase and olivine with average compositions of troctolites from the Kane Megamullion (with An 80 and Fo 88, respectively) are assimilated in various proportions (plagioclase:olivine as 85:15, 80:20 and 67:33). The two reactive melts are taken as more evolved than the melt in equilibrium with the assimilated matrix, falling along a low-pressure olivine-plagioclase-clinopyroxene cotectic. The crystallized assemblage is made of 44% clinopyroxene and 56% plagioclase (relative abundances in gabbroic bands found at Kane), with the composition of the minerals taken as the average compositions of the gabbroic bands sampled in the area. The main differences with the previous models is that ***Lissenberg and Dick (2008)*** considered two stages of evolution during the reaction, the first one characterized by predominant assimilation over crystallization (ratio Mass assimilated/Mass crystallized of 2) and the second with predominant crystallization (ratio Mass assimilated/Mass crystallized of 0.75). This sequence of the reaction is closer to what is expected during the early stages of assimilation by over dissolution and suppression of crystallization (see ***Liang, 2003***; ***Lissenberg and Dick, 2008*** and references therein). Consequently to their model, the authors manage to explain the presence of highly magnesian clinopyroxenes without involving high-pressure crystallization of MORB-type melts (see *2.1.1*).

Finally, other studies involve for example hybrid melts and initial mixing between mantle-derived melts and anatectic melt resulting from partial melting of gabbroic cumulates (producing Cr- and incompatible elements-poor melt with high Mg# - ***Leuthold et al., 2018***). In general, no real consensus exists on the reactive melt composition and the initial assimilated matrix composition, nor on the proportions of the crystallized phases that might vary from on case to the other. A few experimental studies proved that during such assimilation - crystallization processes a percolating melt can efficiently assimilate surrounding crystals, leading to variations in melt composition from which a new generation of minerals may crystallize (e.g. ***Kvassnes and Grove, 2008; Liang, 2003; Yang et al., 2019***). However, other studies are required to improve or to go further the various scenarios proposed in the literature. In addition, systematic consideration of the sample textures (*Figure 1.30*) and modal contents are key to constrain the reactions involved during melt-rock reactions associated to RPF. As illustrated in *Figure 1.31*, even though olivine and plagioclase have low contents in REEs compared to clinopyroxenes, their implication in AFC strongly influence the evolution of melts and minerals in equilibrium. Crystallization of clinopyroxenes always leads to enrichments in REEs and strong fraction between more to les incompatible elements (represented by the La/Lu

ratio). On opposite, reactions involving assimilation of olivine and crystallization plagioclase (depending on the assimilation / crystallization ratio) can lead to a decrease in the REE contents and strong decrease in the La/Lu ratios. Thus, the mineral assemblages involved in RPF processes need to be tightly constrained by geochemical and textural observations in order to get closer to the actual reactions involved in these lithologies formation.

Such melt-rock interactions associated to RPF lead to a progressive differentiation of the melts, thus potentially also lead to modify the reactions involved at the different steps of evolution of the system (i.e. at decreasing melt fraction, e.g. ***Mathez, 1995***). As melts rise upward in the system and differentiate they can eventually form oxide-rich melts, and react with gabbroic mushes leading to the formation of oxide gabbros within the crust (***Dick et al., 2000*** or ***Natland and Dick, 2001***). Other reactions might involve highly differentiated compositions, reaction of clinopyroxenes and formation of amphiboles, or crystallization of reversely zoned plagioclases with high An contents (e.g. ***Lissenberg and MacLeod, 2016***), but further studies have to be conducted to quantify these "late-stage" reactive melt migration processes.

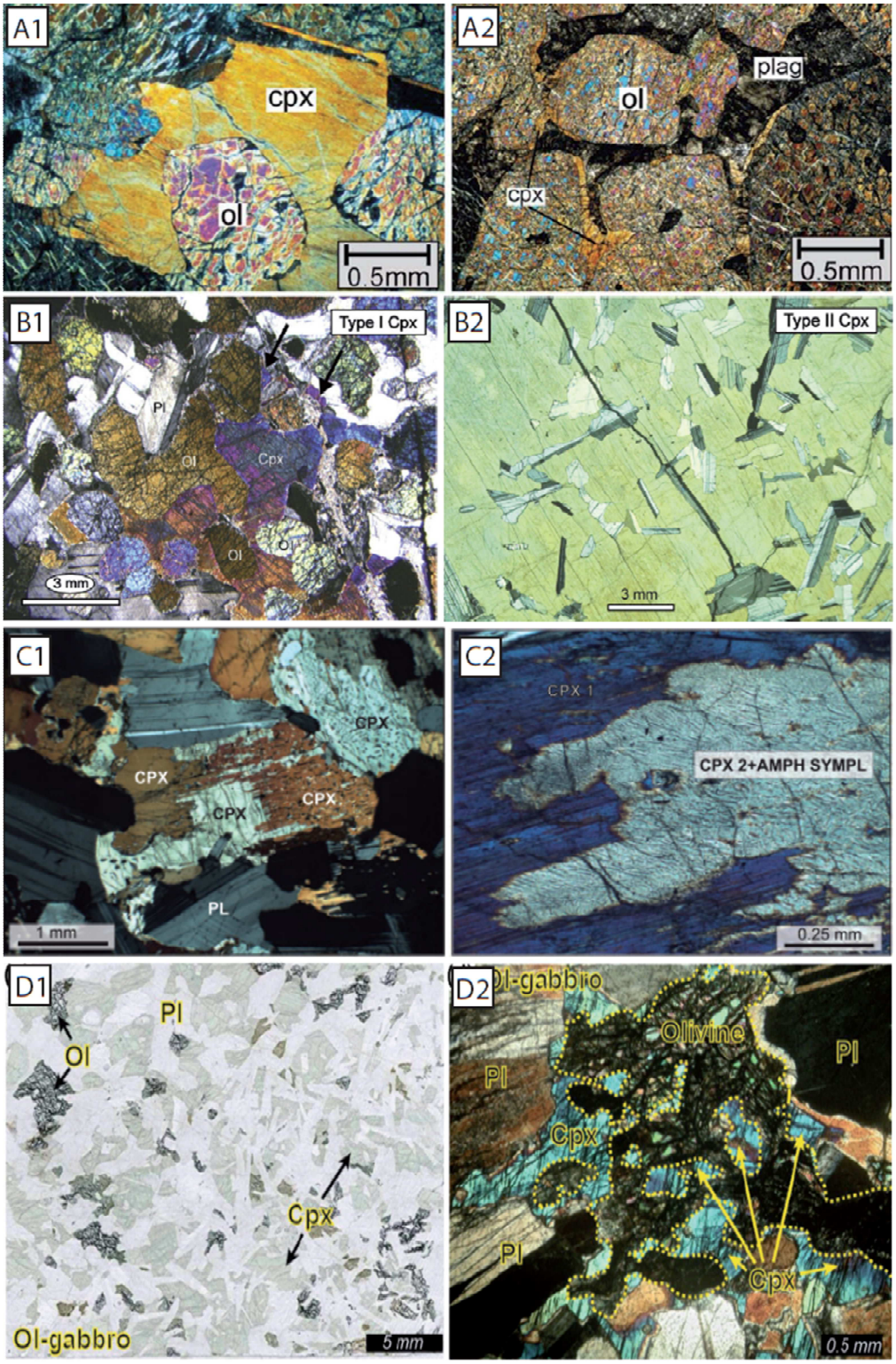

Figure 1.30 - Reactive textures found in oceanic lower crust samples. (a1) Coarse mm-size anhedral clinopyroxene (cpx) between rounded cumulus olivine (ol) and (a2) thin "vermicular" cpx between cumulus olivine and anhedral plagioclase (plag) from the ET troctolites (Borghini & Rampone, 2007). Photomicrographs of (b1) type 1 cpx oikocryst and (b2) resorbed plagioclase in type 2 cpx oikocryst in gabbros from the Kane Megamullion (Lissenberg & Dick, 2008). (c1) and (c2): photomicrographs of cpx textures associated with RPF (from ODP Hole 735B, SWIR). (c1) Irregular, ragged grain boundaries between a series of cpx crystals in olivine gabbro. (c2) Examples of cpx-brown amphibole symplectites replacing cpx (Lissenberg & MacLeod, 2016). (d1) Thin section image of an olivine gabbro with subhedral ol, anhedral plag and poikilitic cpx. (d2) olivine with irregular shape and rounded grain-boundaries against cpx in an olivine gabbro (Sanfilippo et al., 2015).

Overall the characteristic geochemical signatures interpreted as resulting from reactive melt migration in the lower crust are coherent with large scale considerations for melts migration occurring in oceanic magma reservoirs. As first specified by ***Sinton and Detrick (1992)*** and reviewed in ***Lissenberg et al. (2019)***, crystal mush is the dominant magma reservoir type in the lower oceanic crust, making reactive melt migration a critical model for the understanding of the accretion processes.

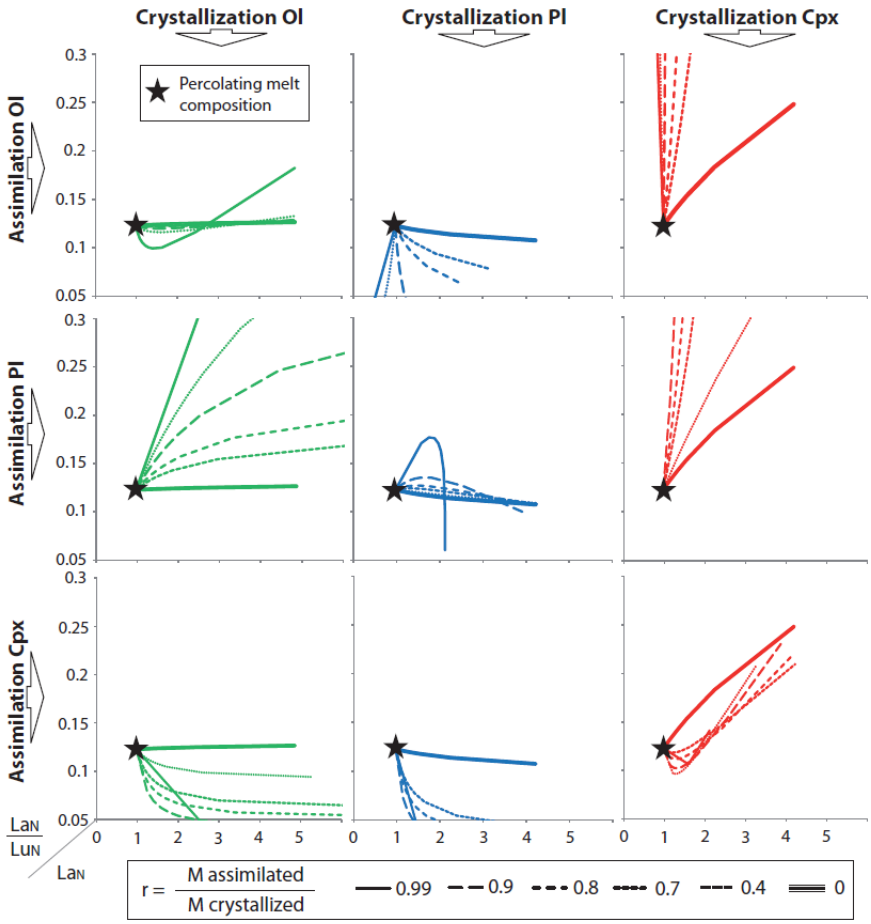

Figure 1.31 - Influence of the mineral assemblage considered on the evolution of clinopyroxene compositions after Assimilation-Fractional Crystallization. End-member models for Assimilation-Fractional Crystallization (AFC - DePaolo, 1981), considering 100% assimilation or crystallization of olivine (Ol), plagioclase (Pl) or clinopyroxene (Cpx). The reactive melt composition is a primitive MORB average for the Atlantis Bank area (see Chapter 5).

3 Conclusions

In a few decades the models of slow-spread oceanic crust magma reservoirs dramatically changed, from initial magma chambers composed of melts towards mushy magma storage models. As detailed above, the associated differentiation processes considered during accretion also evolved, and reactive porous flow processes now appear to be one of the predominant controls over magma differentiation. However some issues remain unresolved that we aimed at

elucidating during this PhD thesis, and from which the main outcomes are compiled in the rest of this manuscript:

- What are the main petrographic and geochemical characteristics of lithologies expected after evolution by relatively simple crystallization processes, i.e. equilibrium and fractional crystallization? The answers to this question for a given site or system study (and for fixed parameters like composition, pressure or redox conditions) are essential if we are to quantify additional complex processes in the natural rock record. Both an experimental approach and numerical modeling were implemented to constrain simple crystallization processes for the Atlantis Bank system (Chapter 6).
- What are the impacts of the main melt percolation processes on magma evolution during crustal accretion, and at which spatial or chronological scale do they occur relative to each other? The characterization and quantification of magmatic processes recorded in common magmatic structures found in lower slow-spread crust sections aim to help understand magma differentiation systematics and the main events that lead to the lower crust formation (Chapter 3).
- At the scale of an entire tectono-magmatic unit described in the lower crust, how do magma reservoirs form and evolve, and what are the main processes involved in their accretion and in the differentiation of magmas they contain? Understanding the structuration of the reservoirs and the modes of melt migration involved is key to determine to which extent melt-rock reactions potentially govern differentiation, at which step of evolution, and where in the reservoir they do occur (Chapter 4).

At the first order the lower slow-spread oceanic crust appears highly heterogeneous, but continuity in the processes involved in its formation is often hypothesized to explain the similar geochemical or petrographic characteristics observed in various lower crustal sections. If intrusion and porous migration of melts are the two major processes governing the evolution of the lower crust, can a different balance between porous or intrusive regimes explain the discrepancies of lower crust structures observed? Can the magma reservoir model elaborated in Chapter 5 for one lower crustal section be applied to other lower crust sections and lead to the elaboration of a uniformed model of formation and evolution of the magmatic lower oceanic crust at slow-spreading ridges (Chapter 5)?

CHAPTER II.

Oceanic Core Complexes and the Atlantis Bank OCC

Relevance of their study for the comprehension of the slow-spreading lower oceanic crust formation

1 Asymmetric spreading and the formation of Oceanic Core Complexes

The study of modern oceanic crust is challenging because of its inaccessibility, the average depth of the seafloor being at 3000m below the sea surface. One way to avoid this problem is to study fossil oceanic crust preserved in ophiolites on which were based several studies and oceanic crust models (e.g. ***Bédard, 1991; Boudier et al., 1996; France et al., 2009; Jansen et al., 2018; Kelemen et al., 1997; Lagabrielle and Cannat, 1990; MacLeod and Yaouancq, 2000; Nicolas et al., 1988; Sanfilippo and Tribuzio, 2011***). Different techniques have been developed for the study of modern crust but few allow collecting samples, such as dredging, in situ sampling thanks to manned submersible or ROV (Remotely Operated underwater Vehicle), and drilling. In addition, the sampling of modern lower crust accreted at about 4km depth below the seafloor (or 4000 mbsf - meters below seafloor) requires the ability to drill as deep. However, the deepest hole drilled during an Expedition lead by the International Ocean Discovery Program (IODP) in the so called oceanic "hard rocks" reaches less than 2km.

As reported earlier (*see I.1.1.*), brittle deformation is a fundamental component of the accommodation of the extension at the slow- to ultra-slow spreading ridge axis, where the low magma supply cannot accommodate the entire extension. Another characteristic of slow-spreading ridges directly linked to the consequences of deformation on the crust and ridge structures, is the occurrence of asymmetric spreading along the ridge axis (e.g. ***Parnell-Turner et al., 2018***). Asymmetric spreading is linked to the development of a long-lived detachment fault in one flank of the ridge that accommodates the majority of the extension at the ridge axis. The first evidences for the presence of such faults were found during seafloor explorations in the 90's, with the discovery of tectonic breccia and topographic breaks imaged on the seafloor associated with exposures of deep plutonic or mantle derived rocks (***Cannat, 1995; Dick et al., 1991***). Almost all of the topographic highs present well-defined corrugations and striations oriented parallel to the spreading direction on the planar surface at the top of the domal structure (*Figure 2.32* - ***Cann et al., 1997; Cannat, 1995; Cannat et al., 1997; MacLeod et al., 2009***). The highs were interpreted as being the consequence of the uplift of mafic rocks tectonically emplaced at the seafloor next to the ridge axis, exhumed in the footwall of a detachment fault. Such structures are named Oceanic Core Complexes (OCCs) and represent an invaluable opportunity to study the evolution of mantle rocks and the formation of the lower oceanic crust at slow-spreading ridges.

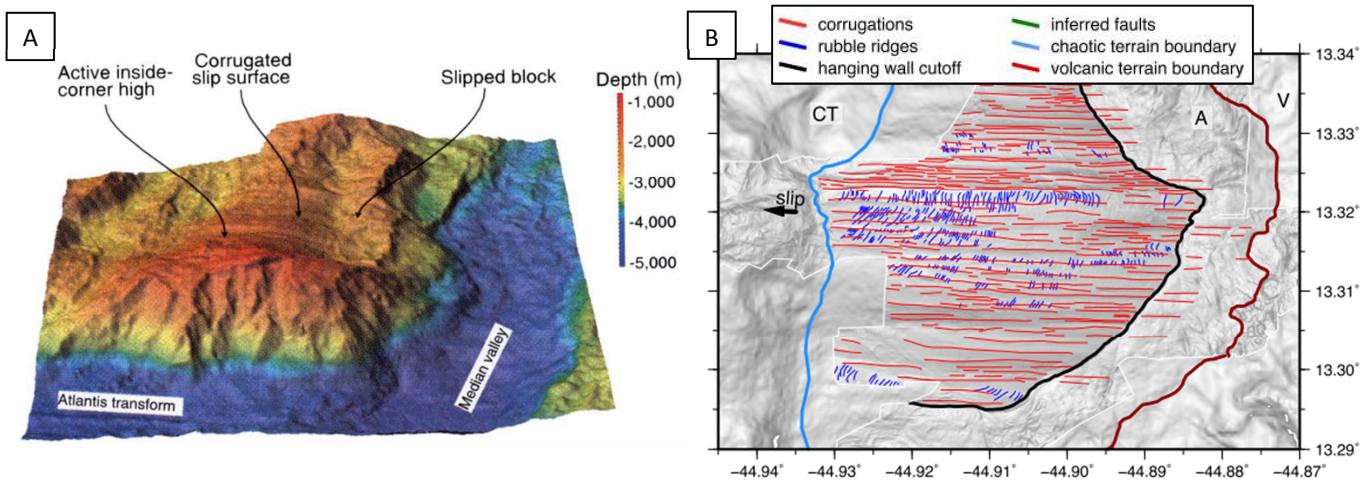

Figure 2.32 - Footwall of detachment faults presenting corrugations and striations. (a) Three-dimensional shaded relief image of the bathymetry of the active inside-corner high (Atlantis Massif Oceanic Core Complex) and corrugated surface at the eastern ridge-transform intersection (Cann et al., 1997); (b) Bathymetric slope maps with interpretation of seafloor features from the MAR (Parnell-Turner et al., 2018).

A great diversity of lithologies can be found constituting the OCCs, with various proportions of mantle dominated to gabbroic-rich material (***Cannat et al., 2006***). One of the main issues is to understand how the same mechanism of detachment faulting developed to form OCCs in such diverse environments. Similarly to the hypotheses of ***Dick et al. (2000)*** and ***Tucholke et al. (1998)***, ***Escartín et al. (2003)*** have proposed that the formation of the detachment fault rely on the presence at depth of a rheological boundary at a rather shallow level, which constitutes the root of the fault (*Figure 2.33*). ***Escartín et al. (2003)*** classified the structures into two types: the "hot" detachments which root in a melt-rich zone or a magma chamber, and the "cold" detachments which root in an alteration front. This model of formation involving the presence of a rheological discontinuity at depth is consistent with observations of the heterogeneous lithologies constituting the OCCs in magmatic or amagmatic slow-spreading ridges segments.

It doesn't however preclude the synchronicity of magmatism and exhumation, as many undeformed and deformed diabase dikes are found within the shear zone of the detachments indicating the occurrence of magmatism at different steps of the faulting. Diking is one of the main processes investigated for the formation and evolution of the detachment fault involving magmatism, as it is assumed that the presence of dikes creates major structural weaknesses within the crust. According to the models of ***Buck et al. (2005)*** or ***Tucholke et al. (2008)***, the amount of dike formed to accommodate the extension controls the transition between symmetric (*see Chapter 1*) and asymmetric ridge geometry. The model of ***Buck et al. (2005)*** which doesn't take into account temperature variations in the crust, predicts the creation of asymmetrical ridges when less than 50% of the extension is accommodated by diking. ***Tucholke et al. (2008)***, with a model that includes heat extraction by advection and conduction, better

quantify this threshold between 30 to 50% of the total extension. Those results are not inconsistent but nethertheless questioned by the results of ***John and Cheadle (2010)*** and references therein, who studied the accommodation of extension on 3 of the most studied OCCs (two on the MAR, one on the SWIR). Their results suggest that the detachment could accommodate from 60% to 100% of the total spreading at the ridge axis, leaving almost no component for accommodation by diking. ***Tucholke et al. (2008)*** raise the question of the unevenly repartition in depth of magmas emplaced below the ridge, that can reinforce the rheological heterogeneity of the crust without the requirement of dike formation. Hence, the localization in depth of magmas is crucial information if we are to understand OCC's formation, as it can strongly influence the occurrence and location of such structures along slow-spreading ridges. This idea is reinforced by the study of ***Cannat et al., (2019)*** on a volcanic portion of the eastern part of the SWIR, who also proposed that the amount of magma supplied to the ridge axis directly influence the rheology of the crust and the modes of spreading at the ridge axis, with for example different capacities of strain localization which favor or not detachment faulting.

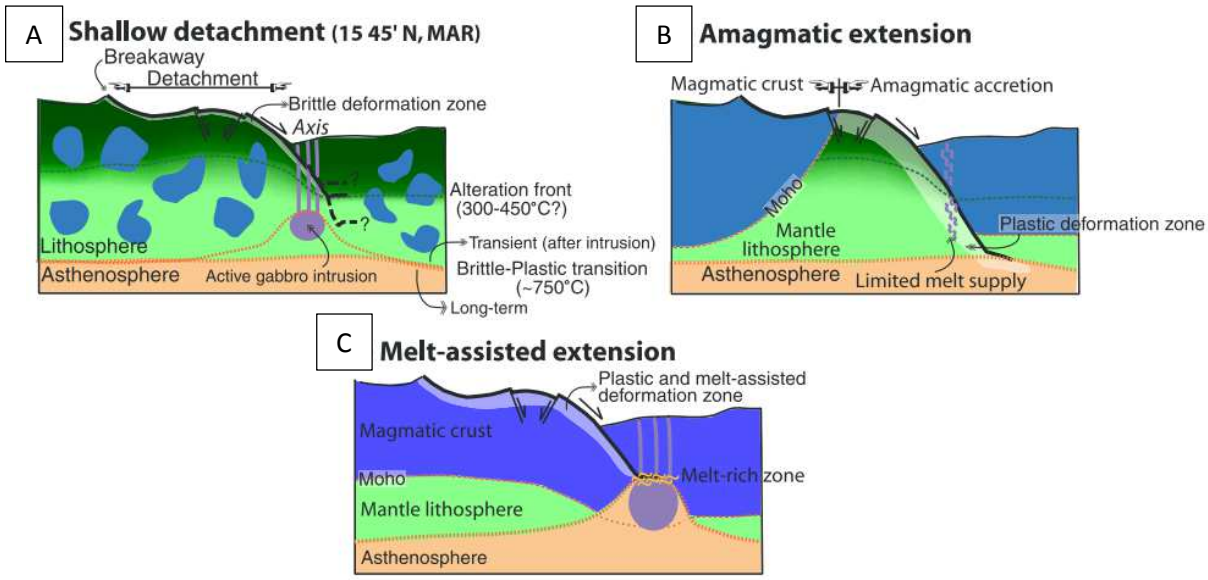

Figure 2.33 - Proposed model for oceanic core complexes depending on the localization of the detachment fault rooting within the lithosphere (Escartin et al., 2003 and references therein). (a) "cold" detachment rooting in the shallow lithosphere at the rheological boundary created by the alteration front; (b) Model of detachment rooting at the base of the lithosphere during amagmatic extension; (c) "hot" detachment rooting at or near a melt-rich zone near the ridge axis.

In the case of the exhumation of large gabbroic bodies constituting the main portion of some OCCs, alternative models of formation were proposed. The model developed by ***Ildefonse et al. (2007)*** embraces both the need of a rheological discontinuity at depth for the rooting of the detachment fault, and the heterogeneous nature of the lower crust at slow-spreading ridges discussed above (named the "Plum pudding" model and based on the model of ***Cannat, 1996***).

In their model, the authors propose that the arrival of a large magma intrusion within peridotites enhances fluid circulation around the magma body triggering intense serpentinization, and eventually drastically modifies the mechanical behavior of the mantle lithologies (*Figure 2.34*).

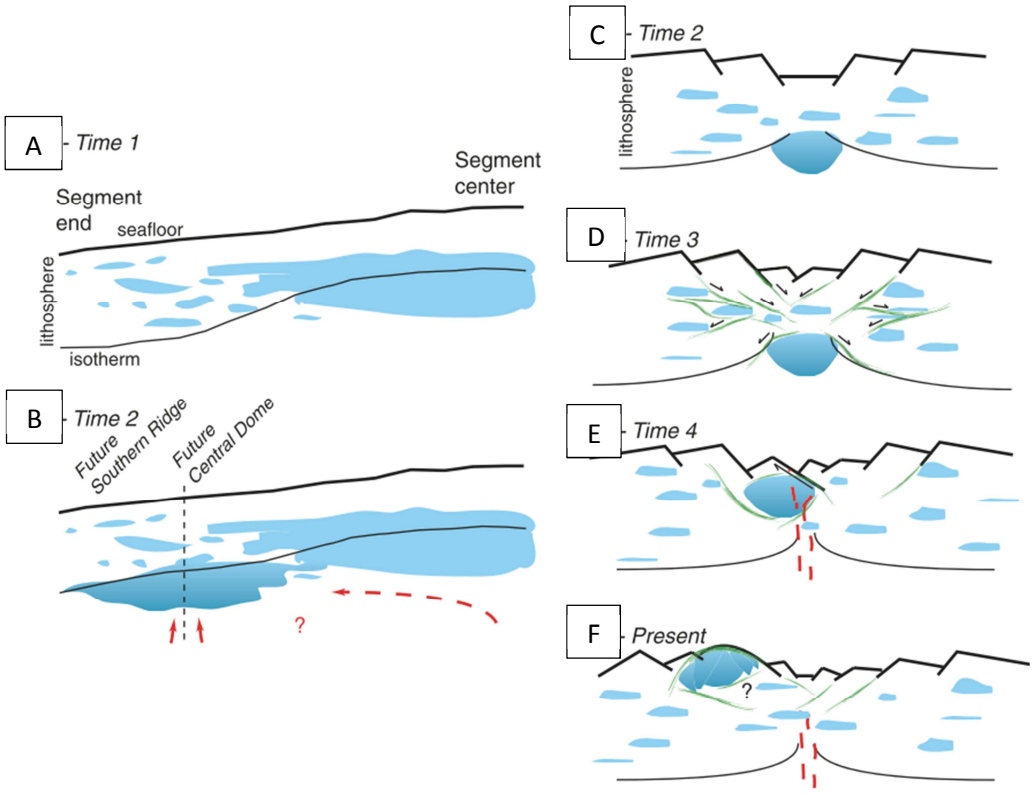

Figure 2.34 - Sketch of revised model for oceanic core complex formation (Ildefonse et al., 2007). (a - b) Along-axis sections. (c - f) Spreading-parallel cross sections. Blue: gabbro intrusions.

The relative proportion of asymmetric spreading with regard to symmetric spreading is significant, as exposed by ***Escartín et al. (2008)*** who gathered bathymetric data for ~2500 km along the northern part of the MAR, and from which they estimated that asymmetric accretion dominates for ~50% of the ridge length (*Figure 2.35*). In addition, according to ***Smith et al. (2006)*** detachment dynamics would occur for more than 35% of the ridge in another area of the MAR, and ***Okino et al. (2004)*** recognizes that up to 70% of the total area of both ridge flanks of the Australian-Antarctic discordance are composed of detachment surfaces.

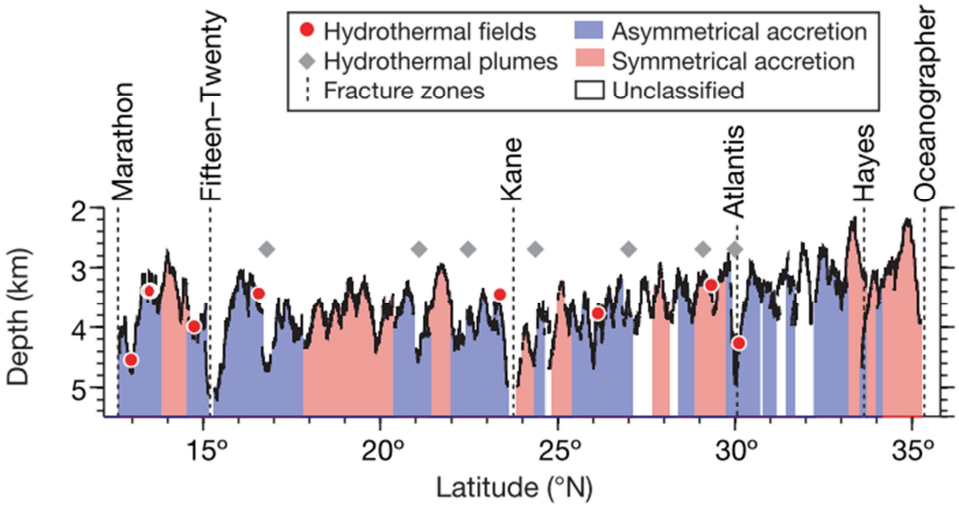

Figure 2.35 - Along-axis distribution of asymmetrical and symmetrical ridges section, and correlation with the bathymetric profile and hydrothermal activity on the Mid-Atlantic Ridge (Escartin et al., 2008)

2 The Atlantis Bank OCC

Among the >172 OCCs that have been reported in ***Ciazela et al. (2015)***, one in particular has been quite extensively studied by drilling and dredging: the Atlantis Bank Core Complex, on the Atlantis II Transform Fault of the Southwest Indian Ridge.

2.1 Morphology and crust structure around Atlantis Bank

The Atlantis Bank OCC is located along the SWIR, on the eastern flank of the Atlantis II Transform fault at 57°E (***Fisher and Sclater, 1983***). The SWIR is classified as an ultraslow-spreading ridge with a full spreading rate of 14 mm/yr. Locally at the ridge segment NE of the Atlantis II Transform, the spreading is asymmetric with spreading rates of 8.5 mm/yr to the S and 5.5 mm/yr to the N (***Hosford et al., 2003***). The eastern flank of the Atlantis II Transform presents an uplifted block that rises to about 700 m below the sea surface and located about 95 km south of the ridge axis: the Atlantis Bank OCC (*Figure 2.36* - ***Dick et al., 1991b***).

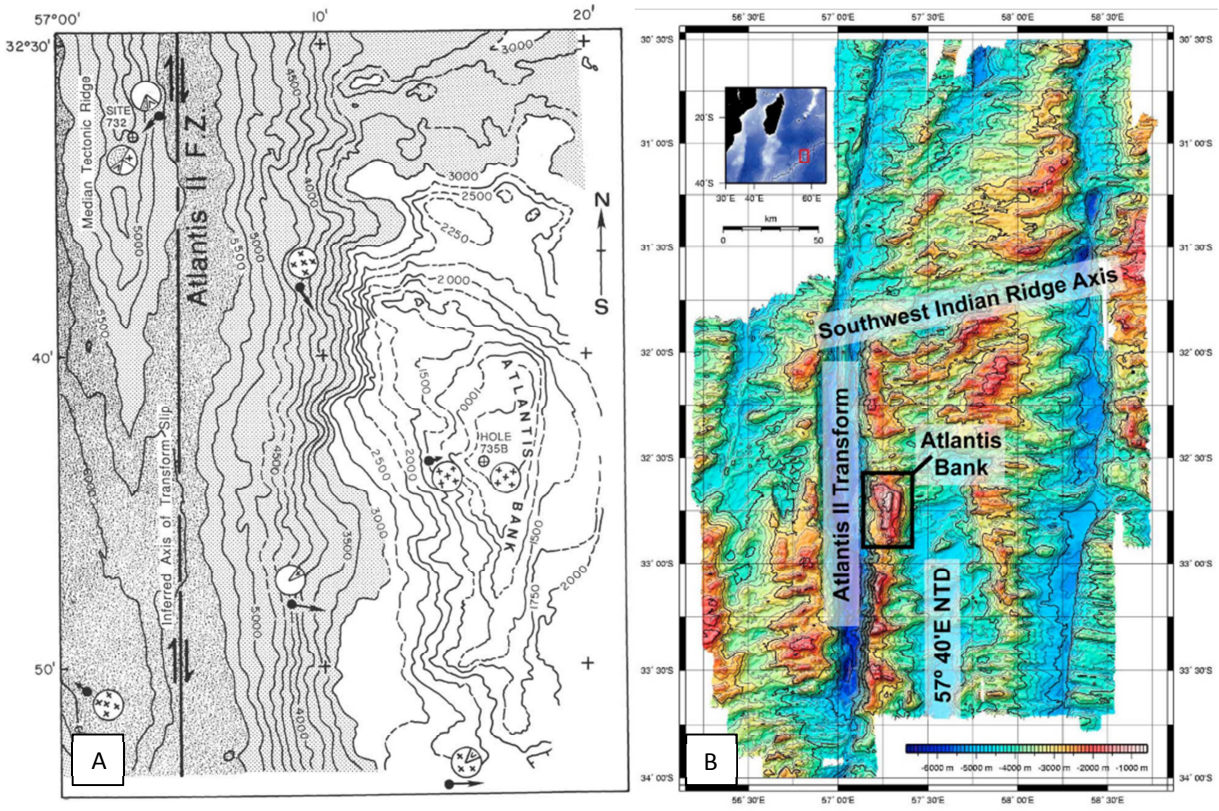

Figure 2.36 - Bathymetric maps showing the Atlantis Bank OCC on the Atlantis II Fracture Zone (SWIR). (a) Hand-contoured bathymetric map of the eastern transverse ridge, showing location of Site 735 and Hole 735B (Dick et al., 1991b); (b) Bathymetric map of the Atlantis Bank region (Miranda & John, 2010)

The Atlantis II Fracture Zone was first described during a preliminary survey by ***Fisher and Sclater (1983)***. The same area was later studied in more details thanks to SeaBeam echo sounding, seismic reflection, magnetics and gravity profiles as reported in ***Dick et al. (1991)***. The aim of the survey was to prepare drilling operations for the ODP Leg 118. The objectives of the drilling expedition were to reach the lower crust and shallow mantle into the not-yet-named Oceanic Core Complex, but also aimed at testing if drilling plutonic rocks was possible (***Natland and Dick, 2001***). The geological and geophysical survey enables to describe the "*shallow platform [...] at the crest of the eastern wall of the Atlantis II Fracture Zone*" presenting "*exposures of foliated and massive gabbros locally covered by sediments drifts*" on top of an uplifted block, and named for the first time in the 1991 paper Atlantis Bank. Since then several other surveys collected narrow-beam echo soundings, multibeam, magnetics and gravity data in addition to seafloor samples (remotely operative vehicle, submersible dives, dredging) and sub-seafloor samples by seabed rock coring (*Figure 2.37* - ***Arai et al., 2000; Dick et al., 1999; Dick et al., 1991b; Kinoshita et al., 1999; Macleod et al., 1998; Matsumoto et al., 2002***).

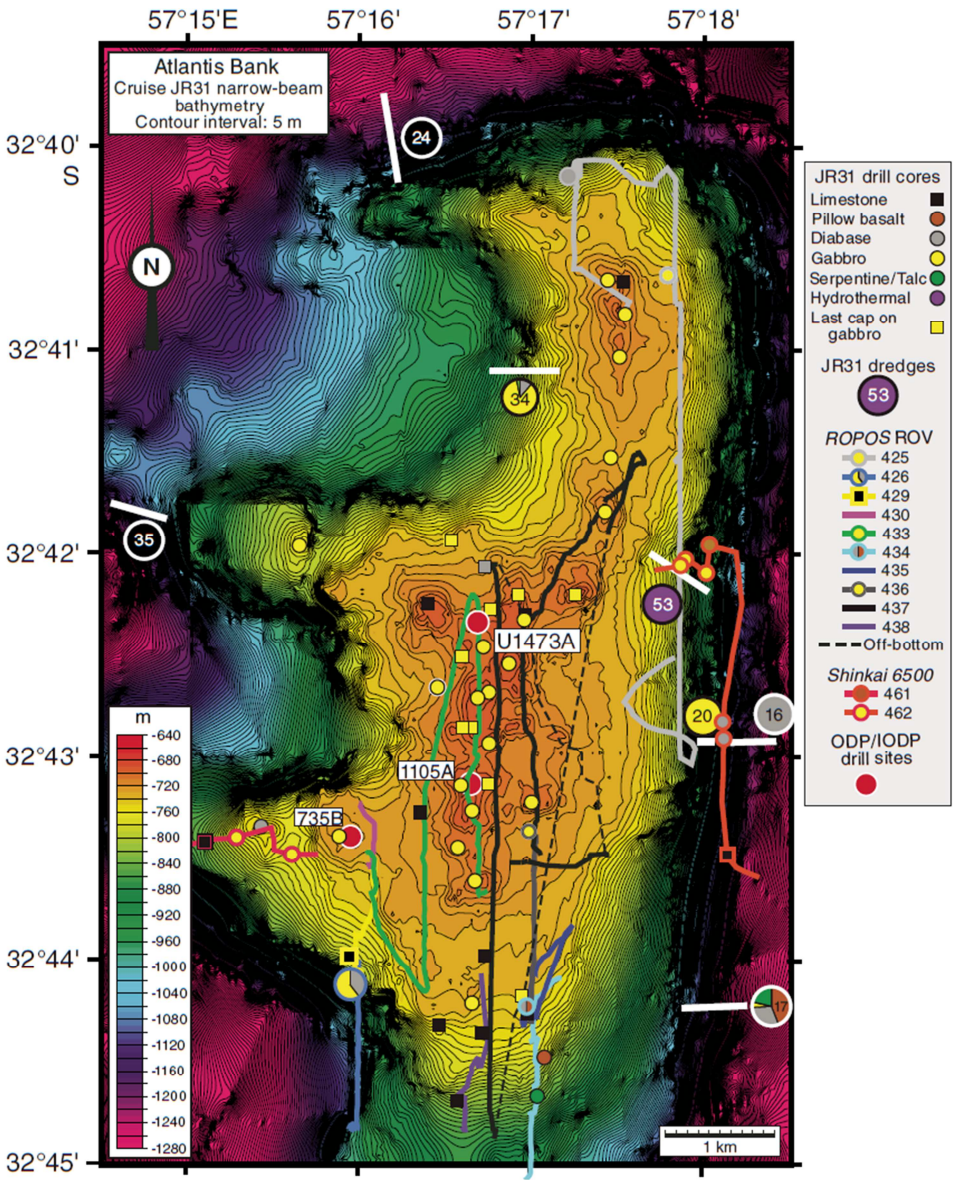

Figure 2.37 - High-resolution contoured narrow-beam bathymetry map of Atlantis Bank wave-cut platform (Dick et al., 1999), showing ROV and submersible dive tracks plus locations of shallow and deep drill holes (MacLeod et al., 1998) from MacLeod et al. (2017)

The bank is ~40km long for ~30 km wide, with an approximate height of 5000 m (from the bottom depth of the transform wall at ~5700 m below sea level). The wave-cut platform at the top of the OCC (with a surface of ~25 km^2) is bordered to the east by two large transform-parallel east-dipping normal faults that drop the seafloor from 700 m to 4300 m below sea level (***Baines et al., 2003; Dick et al., 1991b***). Unlike other OCCs, recognized primarily thanks to a corrugated surface indicating the presence of a low-angle detachment fault footwall, the flat surface of AB present mainly gabbroic outcrops with some limestones, sometimes ripple marked, and carbonate cemented pebble conglomerates which suggest that at some point the OCC was exhumed above sea level (***Dick et al., 2016b***).

The mechanisms involved in the ~2 km uplift of the Atlantis Bank lithologies can be described as a consequence of a ~1 km flexural uplift due to detachment faulting, in addition to transform-parallel normal faulting on the eastern flank of the structure (Baines *et al.*, 2003). This last mechanism is assumed to result from a change in the spreading direction (of about 10°) at the ridge axis between ca. 19.5 Ma and 7 Ma (***Baines et al., 2008; Dick et al., 1991; Hosford et al., 2003***). In addition, ***Baines et al. (2008)*** quantified the rate of detachment faulting thanks to magnetic data (ages and polarity) and Pb/U zircon ages. The half-spreading rate during the detachment was about 14.1 ±1.8/1.5 km/Myr during 2 My. This timing is consistent with a regional increase of the asymmetric spreading rate along the segment axis north of AB (***Baines et al., 2007***). Concerning the crust structure in the vicinity of Atlantis Bank, ***Muller (1997)*** first conducted a wide-angle seismic survey at the Atlantis II Fracture Zone. Together with geochemical data from dredged basalts and drilled plutonic rocks, they concluded that the crustal thickness below AB is 4 to 5 ±1 km beneath the seafloor.

Together with the seismic model that predicts an uplift of ~1 km for the upper crust instead of the ~3 km uplift observed in AB, ***Baines et al. (2008)*** concluded that the limit between magmatic rocks and mantle peridotites was ~2 kmbsf, underlined by 2 to 3 km of serpentinized mantle (*Figure 2.38*). The Moho, as proposed in other models of slow-spread oceanic crust, would there represent a serpentinization front rather than a transition between mantle and crustal lithologies. This hypothesis is in good agreement with the very heterogeneous nature of the slow-spread crust (*see I.1.2.*), also observed in the area around AB by ***Muller et al. (2000)***, which precludes the formation of a continuous and homogeneous stratified gabbroic crust at the ridge axis and hence the presence of a clear Moho discontinuity as described in fast-spreading environments (***Coogan, 2014*** and references therein).

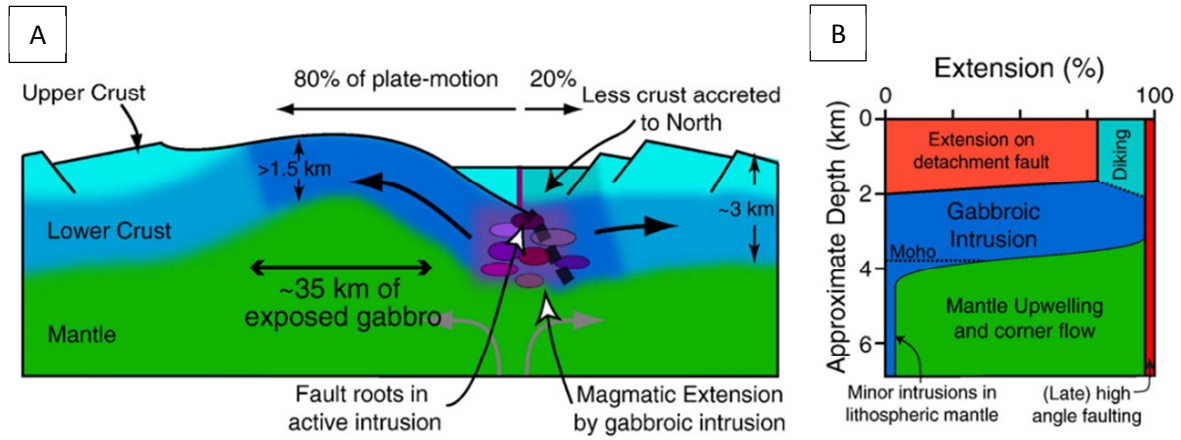

Figure 2.38 - Lithosphere structure at Atlantis Bank. (a) Cartoon of asymmetric spreading and the distribution of crustal accretion during detachment faulting at AB. Darker shaded crust: accreted during active detachment faulting. (b) Schematic model of how extensional strain was accommodated with depth during detachment faulting (Baines et al., 2008)

2.2 The lower crust exhumed at Atlantis Bank

2.2.1 Mapping and sampling of the lower crust

As mentioned above, the Atlantis Bank area has been heavily studied and a large collection of samples were recovered, from the surface and shallow depth (by dredging, submersible diving and sea floor coring) and from inside of the OCC thanks to deep drilling conducted by the ODP/IODP consortium.

Shallow sampling enabled to collect different types of igneous rocks thanks to the favorable localization of the OCC, in an area of great current activity which prevent any significant sedimentation on top of the structures. Mainly mantle lithologies were recovered on the west side of the OCC, with variably altered peridotite near the bottom of the Atlantis II Transform fault valley and talc-serpentine peridotites at the contact of the OCC on its southwest side. Basalts can be found in different places around the OCC, for example in the form of pillow basalt at the top of the crust on the east and north sides of the OCC. On the northwestern most corner of the OCC basalts form dikes intruding peridotite and gabbro, or on top of the OCC on the east part of the structure intruding gabbros (***Macleod et al., 1998; Dick et al., 2008, 2016a***). The core of the OCC itself is almost exclusively composed of gabbroic lithologies (*Figure 2.39* - ***Coogan et al., 2001; Dick et al., 2016a***).

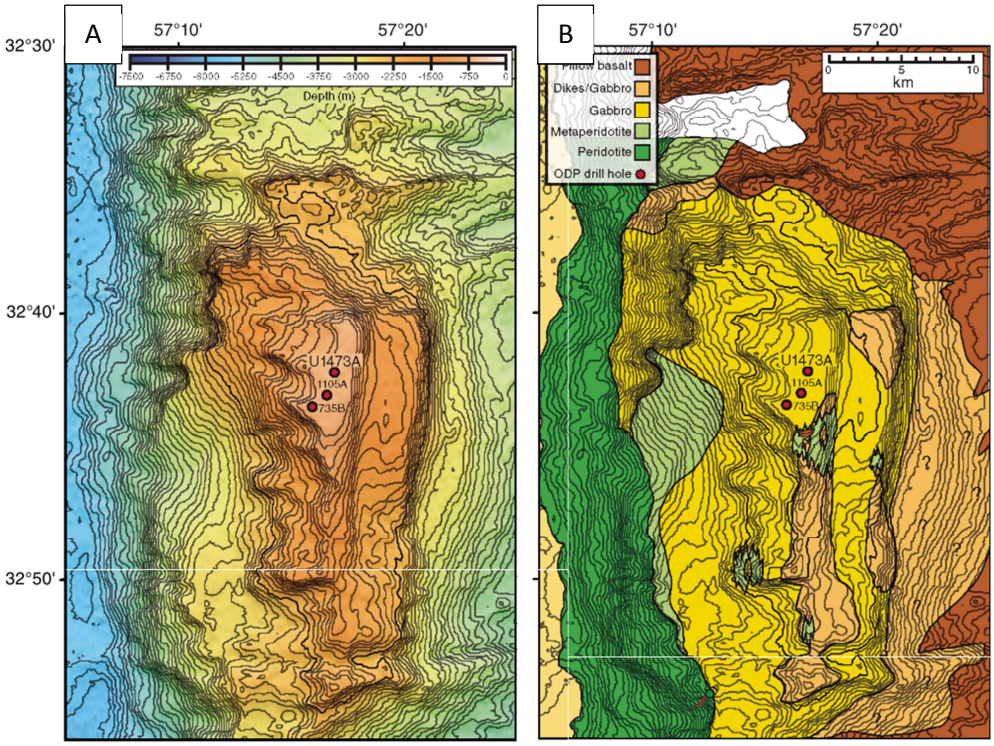

Figure 2.39 - Bathymetric and geological map of the Atlantis Bank OCC. (a) Bathymetry of the Atlantis Bank area, with ODP/IODP drill sites marked. (b) Summary of mapping of the same area, with geological interpretation by H.J.B. Dick based on site survey results (Dick et al., 2016)

Atlantis Bank is also one of the only two OCCs where very deep drilled holes were realized by the ODP / IODP consortium (*Figure 2.40*), the other being the Atlantis Massif OCC located along the MAR. The first drilling operations were conducted in 1987 with ODP Leg 118, during which about 500 mbsf were drilled in ODP Hole 735B. The same Hole was reoccupied 10 years later during Leg 176 and deepened the hole to 1508 mbsf, which makes of Hole 735B the second deepest ever drilled into oceanic "hard rocks". During the second expedition, the recovery rate reached 86.3% of the total section and the rates were close to 100% for the non-fractured lithologies. The second Hole drilled during Leg 179 in Atlantis Bank is Hole 1105A.

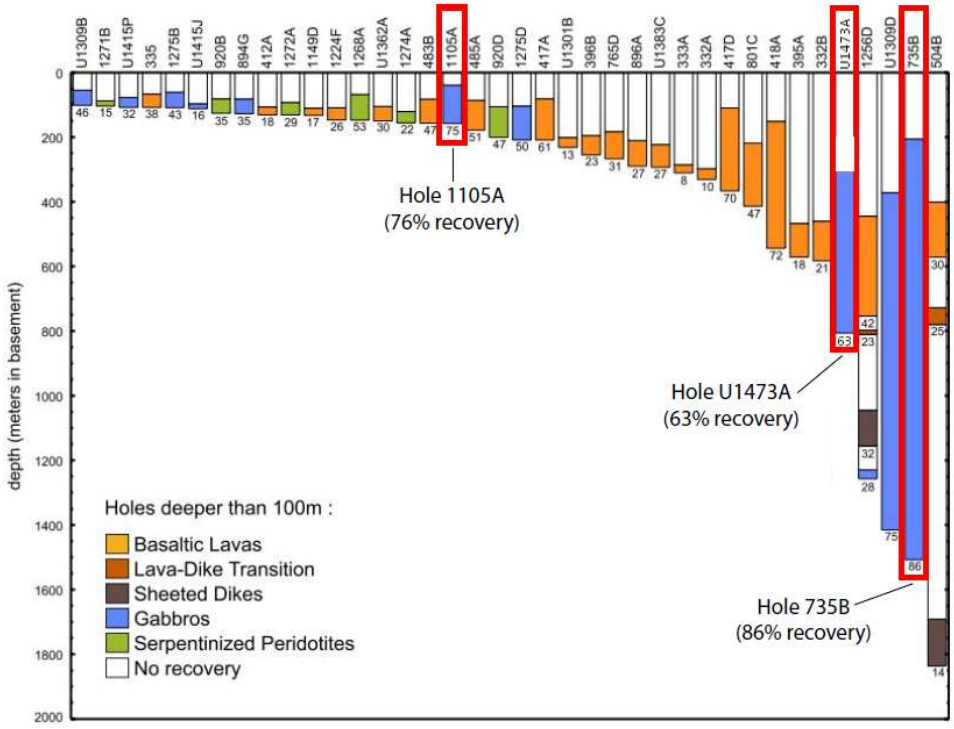

Figure 2.40 - Compilation chart showing holes drilled >100m in intact crust and tectonically exposed lower crust and upper mantle from 1974 to 2013 (in addition Hole U1473A drilled in 2015). For each hole are indicated the hole number and the recovery (in percent) for each lithology (modifies from Ildefonse et al., 2014).

The hole locates 1.2 km east-northeast of Hole 735B and was initially planned as an engineering operation to test drilling tools, but was eventually able to drill and sample the OCC down to 158 mbsf (***Pettigrew et al., 1999; Casey et al., 2007***). The last and most recently drilled Hole within AB is IODP Hole U1473A realized during Expedition 360 (2015-2016), and is the deepest ever drilled during a single expedition. The hole is located 2.2 km north-northeast of Hole 735B and 1.4 km north of Hole 1105A, and reaches a total depth of 789.7 mbsf with an average 59% recovery (i.e. ~470 m of cores recovered, ***Dick et al., 2016b***). The deepest 200 m of the hole were associated with recovery rates close to 100%, and the hole has been deepened to 808.5 mbsf during technical Expedition 362T (***Blum et al., 2017***)

2.2.2 Description of the three ODP/IODP drilled cores from Atlantis Bank

Hole 735B is the oldest and also the most extensively studied hole drilled at Atlantis Bank (***Dick et al., 2000***). The drilled cores are mainly composed of gabbroic lithologies, which is coherent with the surface samples collected at the top of the OCC. Other minor lithologies are present such as the more differentiated felsic veins (0.5% of the recovered rocks), in addition to 2 diabase dikes present in the upper 500 m of the hole. Within the main gabbroic type composed mostly of plagioclase (Pl - up to 60%) and clinopyroxene (Cpx), different lithologies have been distinguished according to their model contents of olivine (Ol), (Ox) and orthopyroxene (Opx). Olivine gabbros compose the majority of the section (~68%), followed by the different classes of gabbros containing oxides (23%), and finally troctolites (5%) and gabbros *sensu stricto* (4% - *Figure 2.41*). Microgabbros showing intrusive or irregular contacts with the gabbroic lithologies are also present at various depths within the sequence and are described as a subtype. According to their whole rock compositions, the lithologies recovered are cumulates and are the typical products expected after MORB differentiation. Whole rock compositions are rather evolved and the most primitive dunites are missing from the section (***Dick et al., 2000***). The lithologies are also heterogeneously distributed with depth, even though the oxide gabbro content tend to increase towards the top of the section in the upper 500m of the Hole, where they compose for example more than 90% of the rock recovered at about ~200 mbsf.

Lithology	Proportion	Mineral(s)
Disseminated oxide gabbro	[1%; 2%]	Fe-Ti oxide
Oxide bearing gabbro	[2%; 5%]	Fe-Ti oxide
Oxide gabbro	[5%; 50%]	Fe-Ti oxide
Gabbronorite	> 5%	Opx
Gabbro	> 95%	Pl (>10%) + Cpx (>10%)
Olivine bearing gabbro	[1%; 5%]	Ol
Olivine gabbro	> 5%	Ol & Pl & Cpx
Olivine-rich gabbro	> 70%	Ol
Troctolite	> 95 %	Ol (>10%) + Pl (>10%)

Table 2.1 - Lithologies classification used during Expedition 360 following the Streikeisen (1974) classification (after MacLeod et al., 2017)

Together with the presence of the different lithologies enumerated earlier (*Table 2.1*), the igneous contact characteristics, the local variations in grain size, and the local presence of layering were the main criteria used to define 12 units in Hole 735B. Despite the extreme small scale geochemical and textural variability recorded in the section resulting from various intrusive events (***Dick et al., 2000***), three main categories of rocks can be established. First, the oxide-poor olivine gabbros (including troctolites) represent the main early stage gabbroic cumulate(s) emplaced within the crust.

Those lithologies represent together about 78% of the samples recovered and have Ol contents covering the entire modal range from olivine-bearing gabbros to troctolites. Second, microgabbro cumulates (oxide-poor lithologies, including troctolites) crosscut the former. Finally, the gabbros containing oxides and associated gabbronorites are late stage intrusive lithologies often associated with deformation. The reaction textures and the geochemical compositions of the oxide gabbro samples together with their structure show that the amount of reaction that lead to their formation seems to be controlled by the efficiency of melt percolation, and increase proportionally with the amount of deformation of the samples (***Dick et al., 2000; Dick et al., 1991***). Other reactive and melt percolation textures show that such interaction of various types of melts with a preexisting crystal matrix can occur, for example with the presence of troctolites locally transformed into gabbros (***Dick et al., 1991***).

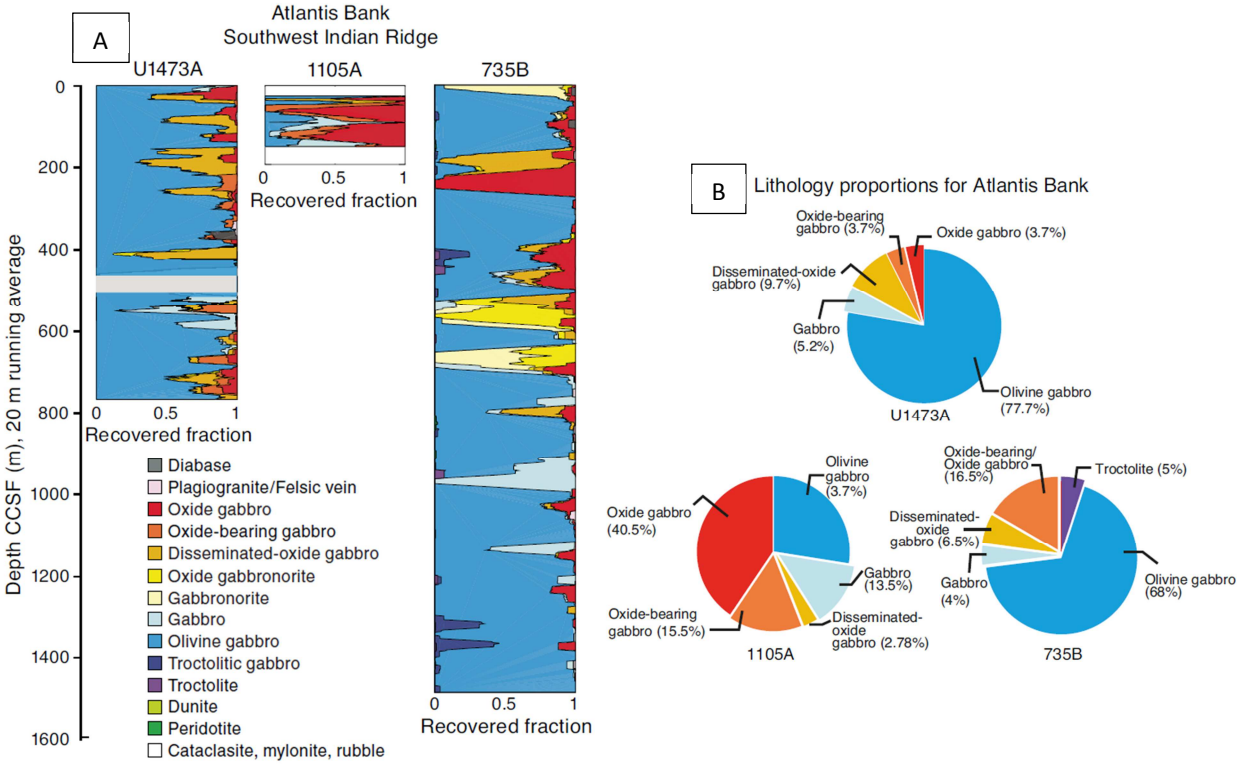

Figure 2.41 -Lithological characteristics of ODP Hole 735B and IODP Hole 1105A and Hole U1473A. (a) Comparison of the lithostratigraphic variations of the three holes drilled at Atlantis Bank (Holes U1473A, 1105A and 735B). Relative abundances of rocks are averaged over 20 m. In Hole 735B oxide gabbro includes both oxide gabbro and oxide-bearing gabbro. Gray bar = drilled interval; (b) Main lithologies proportions (vol%) for each hole (MacLeod et al., 2017)

Despite the very heterogeneous character of the cumulate lithologies even at a very small scale, whole rock major element compositions enabled to describe 4 to 5 different units presenting at first sight continuous upward differentiation trends, the upper two units being the most primitive of the hole (i.e., starting at the highest #Mg value, where #Mg=molar Mg/[Mg+Fe_{tot}], and with high #Mg values indicating more primitive samples related to lower #Mg values - *Figure 2.42*).

Dick et al., (2000) and ***Robinson et al. (2000)*** interpreted these trends as the signatures of individual intrusions emplaced within the crust, potentially subdivided into two main magma stages between the two upper rather primitive intrusions and the two to three lower more differentiated intrusions. Overall however, the bulk composition of Atlantis Bank is too evolved to be in equilibrium with the mantle (***Dick et al., 2000; Coogan et al., 2001***). This is at odds with other crustal sections sampled at slow-spreading ridges that present average compositions much closer to a primary magma composition, as pointed out by ***Dick et al., 2000*** (and references therein). The last authors hypothesized about the presence of a missing primitive cumulate not sampled by the drilling of Hole 735B, which either is present elsewhere in the OCC or is trapped within the mantle below the ridge axis. A sampling bias has also been recognized thanks to whole rock compositions of the crustal section sampled in IODP Hole U1309D at the Atlantis Massif OCC on the MAR (***Godard et al., 2009***). The issue at Atlantis Massif is nevertheless the opposite as the bulk composition of Hole U1309D is too depleted in trace elements to mass balance the composition of basalts from the area and reproduces the estimated composition of primary MORB-type melts. In that case, the bulk composition of Hole U1309D would be biased by 1/ assimilation of preexisting olivine-rich lithologies of potential mantle origin, 2/ the underestimation of oxide lithologies due to a sampling bias and 3/ by not considering the more evolved component of the crust in the calculation, i.e. the minor leucrocratic gabbros. The latter was also emphasized by ***Hart et al. (1999)*** for Hole 735B, and estimated that up to 10% of the most differentiated component were not considered in the bulk composition.

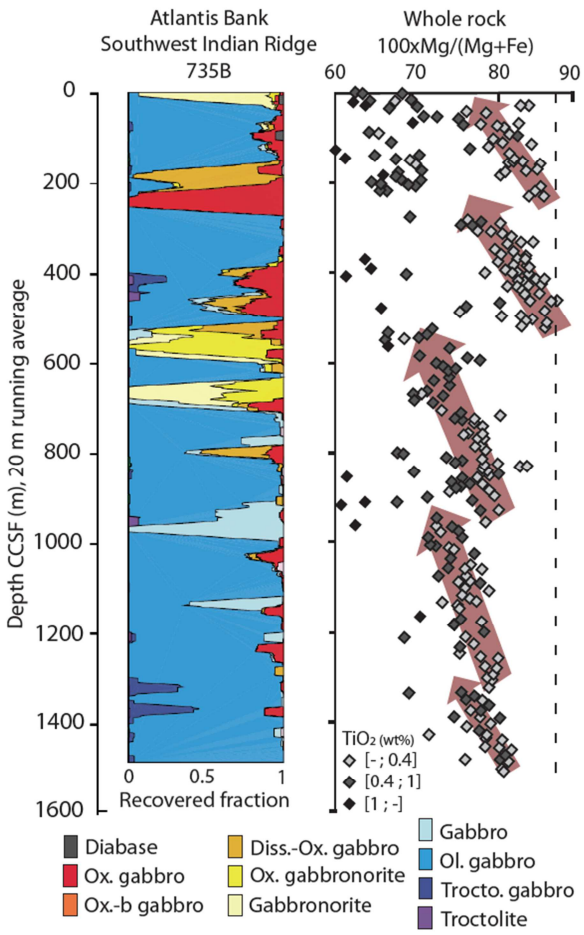

Figure 2.42 - Comparison between the lithostratigraphic variations of Hole 735B (see legend Figure 2.10.) and the corresponding shipboard XRF whole rock gabbro Mg# trends interpreted by (and modified from) Dick et al. (2000)

The second Hole 1105A was first studied by ***Pettigrew et al. (1999)*** during IODP Leg 179 followed by a synthesis of ***Casey et al. (2007),*** and later re-described during Expedition 360 (***MacLeod et al., 2017a***). Drilled cores from Hole 1105A contrary to Hole 735B are mainly composed of gabbros containing oxides (3% disseminated-oxide gabbro, 15.4% oxide-bearing gabbro, 40% oxide gabbros), olivine gabbros only represent 27.2% and gabbros 13.4% of the total recovered lithologies. Four major lithologic units were determined based mainly on the presence and amount of the oxide lithologies. The gabbroic rocks at Hole 1105A are of cumulate origin which is similar to Hole 735B, and the early cumulate products of the MORB differentiation sequence are missing from the section (***Casey et al., 2007***). The correlation between the presence of oxides and the deformation background of the samples established for 735B is not as clearly observed in Hole 1105A, with oxide lithologies which do not present crystal-plastic deformation evidences and are not necessarily associated with felsic veins (***MacLeod et al., 2017b***). The textures of the oxide lithologies and other gabbroic lithologies also present evidence for reaction of the minerals with melt (***MacLeod et al., 2017b***).

The lithologies recovered in Hole U1473A during the last expedition at Atlantis Bank are very similar to the lithologies from Holes 735B and 1105A (*Figure 2.41*). Most of the cores are composed of gabbros (76.5% Olivine gabbros, 9.5% disseminated-oxide gabbros, 5.1% gabbros sensu stricto, 3.7% oxide gabbros and 3.7% oxide-bearing gabbros), with some felsic veins (1.5%) and a total of seven diabase dikes through the section. Compared to Hole 735B, no troctolite (the most primitive lithologies) was recovered (***MacLeod et al., 2017a***) but the same slight increase in oxide contents of the gabbros is also observed towards the top of U1473A. Grain-size variations are also observed in the cores of olivine gabbros, with fine-grained areas (equivalent to the microgabbros described in Hole 735B) present in mostly irregular domains with intrusive contacts with the host rock. Grain-size layering is also observed at various depth within Hole U1473A, with occurrence of up to 7 layers per 5 m of cores at ~595 mbsf.

Eight major lithologic units were distinguished in Hole U1473A based on the same criteria as for the determination of the 12 major units of Hole 735B, in addition to the whole rock composition variations with depth. The same differentiation sequence is observed as in the two other drilled cores at Atlantis Bank, with first the formation of the main gabbroic lithologies (except the most primitive troctolites lacking in U1473A), followed by the formation of the oxide lithologies likely by interactions of late-stage melt with the former lithologies. In addition, frequent assimilation evidences have been reported at two different levels of evolution. The first level corresponds to reaction between melt and mush crystals at a relatively early stage of evolution, with assimilation and/or crystallization of olivine, plagioclase or clinopyroxene. The second level potentially corresponds to a late stage phase of reaction between evolved melts and clinopyroxene crystals, producing amphibole and oxides (***MacLeod et al., 2017a*** and references therein).

The structural description of the three sections drilled at AB highlight the occurrence of a "down-temperature history" of the deformation, with a complex interplay between magmatic processes and different steps of deformation (***Casey et al., 2007; Dick et al., 2000; MacLeod et al., 2017a***). Localized discrete shear and fault zones, and several major fault zones are observed throughout the sections. For example, 2 large zones of continuous high intensity of the crystal-plastic deformation between ~150 and ~250 mbsf and between ~300 and ~400 mbsf, and 7 major fault zones were identified in the upper half of Hole U1473A (***MacLeod et al., 2017a***). A large part of the cores still preserve their initial magmatic textures, and for instance about 42% of gabbros from Hole U1473A are identified as undeformed or show moderate overprint of crystal-plastic deformation (***MacLeod et al., 2017a***). Both Hole 735B and U1473A present a downhole decrease in intensity of the crystal-plastic deformation with almost no deformation at the bottom of Hole 735B (*Figure 2.43*).

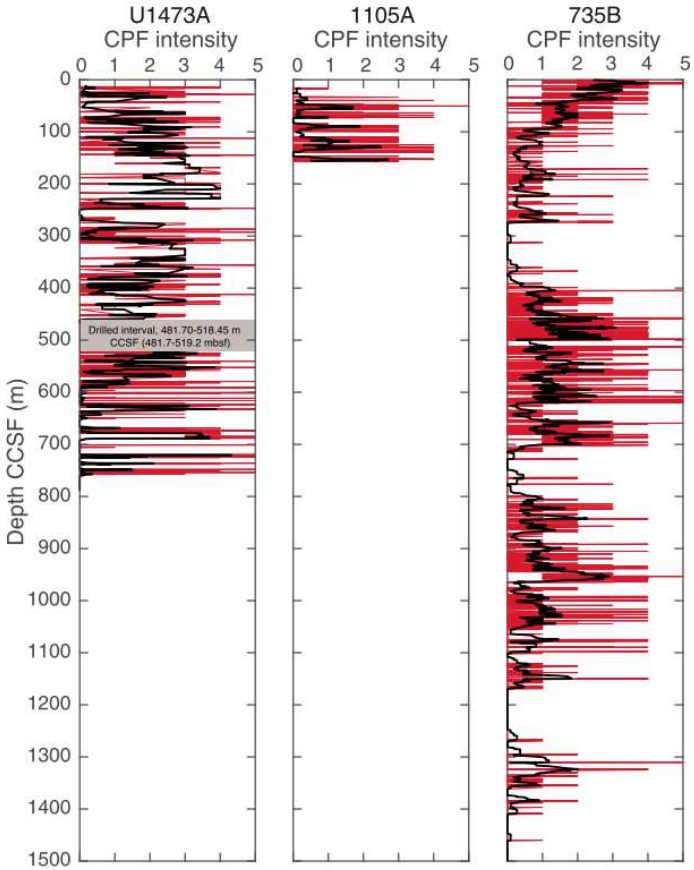

Figure 2.43 - Comparison of crystal-plastic fabric intensity between Holes U1473A, 1105A and 735B (MacLeod et al., 2017). 0 = undeformed, 1 = foliated, 2 = porphyroclastic, 3 = protomylonitic, 4 = mylonitic, 5 = ultramylonitic. Red lines ! raw data, black line = 5-cell thickness-corrected running averages of intensity.

This observation can be potentially connected to the decrease of the oxide gabbro content toward the bottom of both sections. Indeed, a strong link exist between the presence of oxide minerals and the localization of the crystal-plastic deformation, even though the modal content in oxide of the lithologies is not correlated to the intensity of the deformation (see above - ***MacLeod et al., 2017a***). Both opposite models are proposed to explain this association, 1/ the initial presence of weaker oxide minerals which focus the deformation or 2/ the migration, emplacement and reaction of late-stage Fe-Ti-rich melts migrating through the sequence and focusing within more permeable deformed areas (***Casey et al., 2007; Dick et al., 2000; MacLeod et al., 2017a; Natland and Dick, 2001***). Usually in the gabbroic sections, a progressive transition from magmatic fabrics to crystal-plastic fabrics (CPF) can be observed. In Hole 735B, magmatic foliation and zones of crystal-plastic deformation are strongly associated, and generally share a common orientation with fabrics having E-W strike and dipping toward the ridge axis (***Dick et al., 2000***). Hole U1473A share the same characteristics with however a strong variability in the distribution of the dip magnitude of the CPF, with the majority having a dip lower than 50°.

This strong association between magmatic and crystal-plastic fabrics might be the result of the presence of magmatic structures such as grain size layering, or already formed magmatic textures such as well-developed foliation of the gabbros, that potentially act as favored sites of nucleation for the deformation (***MacLeod et al., 2017a***). Overall, the structural features recorded in the sections show a continuum of deformation as the lower crust is exhumes at AB, with evolving strain field through time as shown by the variety of deformation type from magmatic to brittle identified in the cores (***MacLeod et al., 2017a***).

The continuity between the different Holes is difficult to establish. The only formulated assumption is that the sequence recovered from Hole 1105A presenting a very high amount of oxide gabbros would correspond to Units III and IV of Hole 735B, which also present very high amount of these lithologies (***Casey et al., 2007***). Still, strong similarities exist between the structure and composition of ODP Hole 735B and IODP Hole 1105A and U1473A. The main plutonic section is composed of olivine gabbros crosscut by (mostly deformed) gabbros containing oxides, within lithologic units characterized by distinct or partially continuous geochemical trends with a width of few hundred meters (*Figure 2.42*). The strong heterogeneity between the cores suggests that there is no continuity between the magma bodies present in the different sections recovered, but the magmatic processes at stake during the formation of the ~11 Ma gabbroic body from Atlantis Bank (***Dick et al., 1991a***) were likely similar through the entire structure, with a complex interplay between various magmatic processes and deformation (***MacLeod et al., 2017a*** and references therein).

CHAPTER III.

Melt migration and interactions in the slow-spreading lower oceanic crust

Study of recurrent petrographic variations found in the lower oceanic crust sections sampled at Atlantis Bank OCC

- PART 1 -

General introduction

1 Occurrence and significance of grain size variations found in deep drilled sections of lower crust from the Atlantis Bank OCC

Despite the dissimilarities observed between the long in situ sections of lower oceanic crust sampled in ODP Hole 735B and in IODP Hole U1473A (see Chapter 2), both present similar and recurrent petrographic variations within the gabbros (***Bloomer et al., 1991; Dick et al., 2019; MacLeod et al., 2017***). These variations take the form of fine-grained material patches (also described as microgabbros) inside the main coarse-grained olivine gabbros, or alternation of fine- and coarse-grained layers of olivine gabbros (*Figure 3.44*). Only subtle modal changes are associated with these discrete structures. Although well-defined layering only accounts for a small fraction of the core sections, less than ~2 % according to ***Dick et al. (2000)*** in the lower 600 m of Hole 735B, layers *sensus lato* (layering and patchy gabbros) are scarce but found in almost every units described in Hole 735B, and on average patchy gabbros are present every 3.5 m in Hole U1473A. Layered structures are weakly to moderately developed in two different units of Hole U1473A (Unit II and Unit VII, ***MacLeod et al., 2017***), with a maximum density of 7 layers in a 5 m-long section (*Figure 3.45*). Layers *sensu lato* are generally characterized by sharp contacts presenting fine and coarse grains interlocking and forming sutured boundaries, and only 10% present gradational transition between layers. Most of the layers do not present a magmatic fabric, but if present, foliation tends to be parallel to the layer boundaries (***Dick et al., 2019, 2000; MacLeod et al., 2017***).

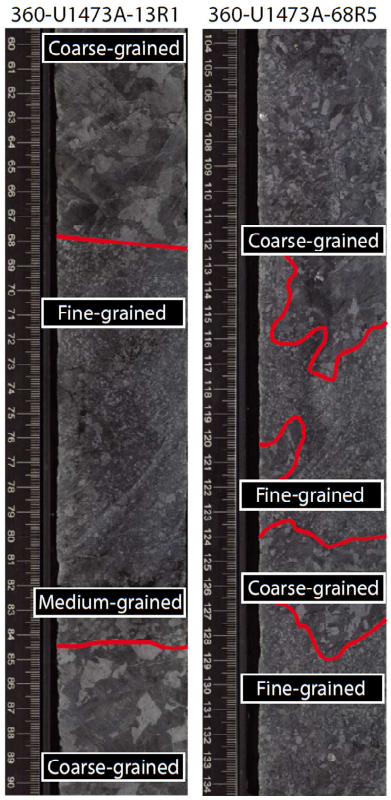

Figure 3.44 - Left : Grain size igneous layering showing planar and sharp contacts between coarse- and fine-grained olivine gabbros. Right: Irregular to patchy "layers". Red lines: igneous contacts. Modified from MacLeod et al. (2017).

In Hole 735B, the distinction between layering and patchy olivine gabbros is difficult to extract from the core descriptions as both have been usually described together, and the exact repartition and amount of both is unclear. A "rhythmic layering" has been described as a minor feature in two units at the bottom of the Hole (Unit X and XI), whereas "microgabbros" have been described as minor intrusive features in 4 different units (Unit II, VI, X and XII - ***Dick et al., 2000***). In addition in regards of the descriptions provided in ***Bloomer et al. (1991)***, patchy gabbros characterized by curved or irregular boundaries appears to be the predominant type of grain size variations in the section. In Hole U1473A, about 50% of the layering is characterized by planar contacts, the rest being patchy gabbros (with curved, wavy or irregular boundaries - ***MacLeod et al., 2017***). The latter has been observed locally in Unit VII, while the textures of the entire Unit V and VI are characterized as patchy. On opposite layering *sensus stricto* was described mainly in Unit II and VII, and some rare layering have been observed in unit IV (***MacLeod et al., 2017***). The observed amount of these features and especially of the layered sequences is potentially lowered compared to their actual amount. Layering is indeed often overprinted by crystal-plastic deformation; the rheological discontinuities created by the layers tend to act as a pre-existing anisotropy that focuses deformation (e.g. ***MacLeod et al., 2017***).

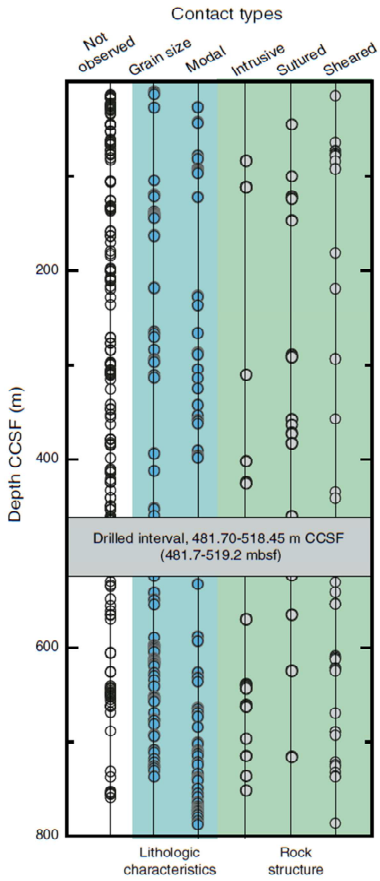

Figure 3.45 - Variations in contact type with depth, Hole U1473A (MacLeod et al., 2017).

Altogether, the frequency of grain size variations through the two long in situ sections from Atlantis Bank and their similar characteristics (even though they are not ubiquitous in both core sections) translate the occurrence of recurrent magmatic processes that are potentially key in the comprehension of magmatic accretion in the slow-spreading lower oceanic crust.

2 Development of models for magma reservoir formation and dynamics based on the study of grain size variations

2.1 Grain size variations in ODP Hole 735B and IODP Hole U1473A

Bloomer et al. (1991) considered together layering and patchy gabbros to determine a model of formation of ODP Hole 735B section. The authors suggested that the lithologies have formed by *in situ* crystallization along the margins of a magma chamber, as no distinct modal changes associated to the grain size variations nor evidences for density crystal sorting were found. As a consequence, the sudden grain size changes are either explained by the occurrence of crystal-mush intrusions or by changes of the conditions of crystallization during the formation of the lithologies (***Bloomer et al., 1991***).

The authors found no evidence for post-cumulus reequilibration, mixing between the adjacent lithologies or variable intercumulus liquid contents that might explain the relative homogeneity of compositions of the coarse- and fine-grained lithologies. They deduced that the relative homogeneity of the sequences is a first order magmatic signal. According to ***Bloomer et al. (1991),*** the coarse- and the fine-grained lithologies have crystallized from liquids with similar compositions, with the fine-grained one being intrusive in a local sense. Eventually, ***Bloomer et al. (1991)*** concluded that the global section has formed within an irregularly shaped magma chamber, where crystal density was possibly redistributed along the margins by local slumping or by the development of crystal-rich plumes (*Figure 3.46*). They explained the presence of grain size variations (both patchy gabbros and layering) by local thermal perturbations occurring during crystallization localized along these irregular margins. However, this vision is now challenge for example by the absence of evidence for the presence of large magma chambers within the slow-spread crust (e.g. ***Dick et al., 2019; Lissenberg et al., 2019*** and references therein).

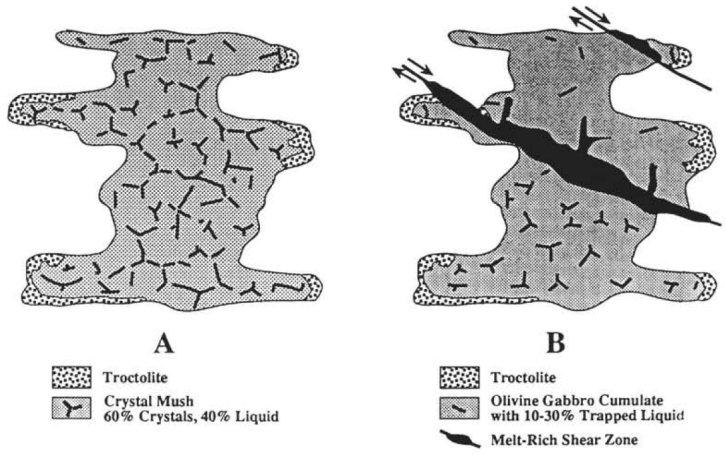

Figure 3.46 - Schematic model for the crystallization of gabbros at Hole 735B. (from Bloomer et al., 1991)

During IODP Expedition 360 that drilled Hole U1473A, both the main layered sequence located at ~590 mbsf and patchy gabbros from the lower ~400 m of the hole were sampled. ***Ferrando et al. (in prep.)*** conducted a high resolution geochemical study of the patchy gabbro samples (see details in *Appendix 1.1*). Minerals chemistry analyzed on profiles across contacts between the coarse-grained olivine gabbros and patches of fine-grained material show systematically that the latter crystallized from a more differentiated melt modified after melt-rock interactions. Both disequilibrium textures and strong incompatible trace element enrichments found in the two lithologies suggest that their evolution was constrained by melt-rock reactions in a reactive porous flow (e.g. ***Coogan et al., 2000; Lissenberg and MacLeod, 2016; Sanfilippo and Tribuzio, 2013***). Numerical modeling was conducted using the Assimilation-Fractional Crystallization equation of ***DePaolo (1981)*** in order to reproduce the

enriched geochemical signatures and confirm the melt-rock reaction hypothesis. Modeling also enables to constrain the reaction(s) that took place during the formation of the lithologies. The model results show that different extents of assimilation of a troctolitic crystal matrix by a percolating primitive melt (and consecutive crystallization of a gabbroic assemblage) were necessary to reproduce the compositional range of the patchy olivine gabbros. ***Ferrando et al. (in prep.)*** established an integrated model of formation of the patchy gabbros. In the model, the first step corresponds to the formation of a coarse-grained heterogeneous mush composed of crystal-poor and crystal-rich areas. The mush evolves in open system through which melts continuously percolate and react with the pre-existing crystal matrix. At some point, interstitial melts present within crystal-rich areas migrate towards and segregate within crystal-poor zones to form the fine-grained patches (*Figure 3.47*).

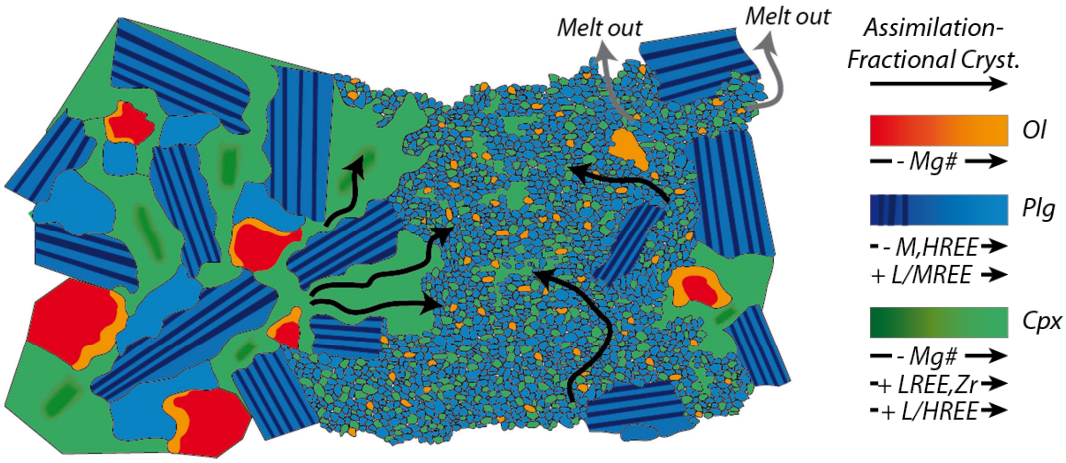

Figure 3.47 - Model of crystal mush evolution and formation of patchy olivine gabbros (from Ferrando et al., in prep. - Appendix 3.1)

The counterpart of the previous project is the study of the layered series from IODP Hole U1473A, and more specifically of section 65R5 which presents the highest layer intensity of the hole.

2.2 Background on layering in igneous systems

The term "layering" should be used with caution as for many petrologists it recalls large stratified intrusions and related igneous processes. In the following I shortly review different layering types (that are not limited to the consideration of stratified intrusions), and their possible origin. For ***Irvine (1981)*** the definition of layering is restricted to cumulate stratification and is mainly based on large layered intrusion descriptions. ***McBirney and Nicolas (1997)*** and more recently ***Namur et al. (2015)*** rather define layering based on structural and / or petrographic features as a "succession of layers characterized by contrasted mineral modes and / or mineral textures, including grain size and orientation and, locally, changing mineral

compositions". In this perspective, the interlayered series studied herein are layered, but do not compare directly with large bodies of layered gabbros reported at fast-spreading ridges nor in large layered intrusions.

As a petrographic feature, layering has been heavily studied in various plutonic bodies and always brings key information on the igneous and structural processes involved in magma reservoir evolution (e.g. ***Holness et al., 2007; Naslund and McBirney, 1996; Nicolas et al., 1988***). Following the numerous studies of large basaltic layered intrusions, a great variety of formation models has been proposed for layering and is reviewed in ***Namur et al. (2015)***. It relies on the early studies of ***McBirney and Nicolas (1997)*** and ***Boudreau and McBirney (1997)***, in which those processes are grouped in two categories: dynamic and non-dynamic magmatic processes.

Dynamic magmatic processes involve for example movements of magmas and instabilities within the magma chamber, or separation of magma(s) and / or crystals (immiscibility, crystal settling, etc., ***Namur et al., 2015***). The former has been widely described in continental environments, such as the occurrence of avalanches of material from instable crystallizing walls of magma chambers which produced some of the layers of the Skaergaard layered series according to ***McBirney and Nicolas (1997)***. Another common dynamic process is replenishment of the chamber, which modifies the liquid line of descent after magma hybridized through mixing with the recharge melt. It thus modifies the mode of the crystallizing phases that accumulate in the chamber, as proposed in the Bushveld Complex and in the Sept Iles Intrusion (e.g. ***Holness et al., 2017; Namur et al., 2010***). These processes generally lead to the formation of modal layering.

Non-dynamic magmatic processes concern all changes of intensive parameters of crystallization (such as temperature, pressure, redox, etc., and following nucleation and growth rate), and processes affecting the crystal mush once emplaced such as compaction or chemical diffusion (***Namur et al., 2015*** and references therein). Non-dynamic layering is usually expressed by grain size and compositional or cryptic layering (modal or chemical). In the Kap Edvard Holm Layered Gabbro Complex (20 km southwest of the Skaergaard Intrusion) the local quench of an intruding liquid produced a grain size layering, with the formation of fine-grained gabbro horizons at the contacts between the intrusion and the surrounding cumulate rock (***Tegner et al., 1993***). In more recent studies (i.e. ***Hepworth et al., 2018***), sills intrusion tend to be shown as one of the process linked to emplacement of large continental layered intrusions. Another example of non-dynamic process is compaction and associated melt migration which contributed to the formation of layering in the Skaergaard intrusion (as described by ***Boudreau and McBirney (1997)***, and ***Namur et al., 2013***).

Beyond magmatic processes, deformation can also lead to the formation of layered sequences. In a domain in extension like mid-ocean ridges, it is thus crucial to quantify the interplay between magmatic and deformation processes if we are to understand the formation of layering, and more generally the building of the lower oceanic crust. Layered gabbros commonly described in ophiolitic lower crust formed at fast-spreading centers might result from ductile deformation within thick cumulates subject to extension (***Quick and Denlinger, 1993***). Also, ***Jousselin et al. (2012)*** and ***Higgie and Tommasi (2012)*** proposed that deformation in the presence of melt at the Moho Transition Zone governs the formation of layering in the Samail ophiolite. Alternatively as mentioned above, crystal-plastic deformation can also overprint the initial magmatic layering that may have acted as a favored planar anisotropy to nucleate deformation, as very often described in slow-spread lower oceanic crust (***MacLeod et al., 2017***).

In any case whether the origin of the layering is purely magmatic (dynamic and non-dynamic) or related to deformation, the characterization of the processes involved provides essential information linked to the magmatic system. The details of the study of the layered series from IODP Hole U1473A are given in the following part of the chapter.

- PART 2 -

Insight from Atlantis Bank interlayered series at IODP Hole U1473A (Southwest Indian Ridge)

This part of Chapter IV is an article initially submitted in June 2019 at *Geochemistry, Geophysics, Geosystems*. It has been reviewed by Laurence Coogan and two anonymous reviewers. The version presented below is the last resubmitted to *G³* in November 2019.

Supplementary materials submitted together with the article are reported in Appendix and comprise:

- Appendix 1.2: A text file documenting details on
  - the EBSD and whole rock analyses analytical methods (Text S1 and S2) and an estimation of the impact of the ablation spot size on the trace element measurements (Text S3)
  - additional figures illustrating examples of EBSD concatenated maps (Figure S1), examples of reactive textures found in the studied section (Figure S2), temperature-constrained models for fractional crystallization (Figure S3)
  - whole rock compositions (Table S1)
  - reference values used for data treatment and representation (Table S4) and input parameters of the numerical models applied to the studied system (Table S5)
- Appendix 1.3 and 1.4: Tables containing
  - minerals *in situ* analyses for major elements (Table S2)
  - minerals *in situ* analyses for trace elements (Table S3)

MELT MIGRATION AND INTERACTIONS IN THE LOWER OCEANIC CRUST: INSIGHTS FROM ATLANTIS BANK INTERLAYERED SERIES AT IODP HOLE U1473A (SOUTHWEST INDIAN RIDGE)

Marine Boulanger[1,2], Lydéric France[1], Carlotta Ferrando[1], Benoît Ildefonse[3], Biswajit Ghosh[4], Alessio Sanfilippo[5], Tomoaki Morishita[6], Chuan-Zhou Liu[7], Jürgen Koepke[2] and Olivier Bruguier[3]

[1]Centre de Recherches Pétrographiques et Géochimiques, Université de Lorraine, CNRS, Vandœuvre-lès-Nancy, France.

[2]Institut für Mineralogie, Leibniz Universität Hannover, Callinstrasse 3, D-30167 Hannover, Germany.

[3]Géosciences Montpellier, CNRS, Université de Montpellier, Université des Antilles, Montpellier, France.

[4]Department of Geology, University of Calcutta, Kolkata West Bengal 700019, India.

[5]Dipartimento di scienze della Terra, Università degli studi di Pavia, Pavia 27100, Italy.

[6]College of Science and Engineering, Kanazawa University, Kanazawa Ishikawa 920-1192, Japan.

[7]State Key Laboratory of Lithospheric Evolution, Institute of Geology and Geophysics, Chinese Academy of Sciences, Beijing 100029, China.

Key Points:

- At slow-spreading ridges, igneous layering in the lower crust records intrusive events of crystal-bearing magmas
- At lower crustal levels, melt migration proceeds by intrusion and reactive porous flow
- Melt migration modes strongly influence the chemical compositions of melts, crystal matrices, and crustal lithologies

Abstract

Magma migration and evolution processes are key to understanding the development and evolution of oceanic magma reservoirs. To provide new quantitative constraints on these processes, we applied a high-resolution approach to study an interlayered section of the lower oceanic crust sampled at the slow-spreading Southwest Indian Ridge. The section is characterized by grain-size layering of olivine gabbros that is representative of other layered structures described at the Atlantis Bank oceanic core complex. The textures and fabrics of the layers and the nature of their contacts indicate their formation by intrusion of a crystal-bearing magma into a solidifying mush. Based on in-situ measurements and numerical modeling, we determined the evolution of the two lithologies. Petrographic observations and in-situ incompatible trace element signatures indicate that the fine- and coarse-grained lithologies record the reactive porous migration of interstitial melts. Within the first-emplaced lithology (coarse-grained gabbro), widespread porous melt migration occurred heterogeneously at the sample scale, producing mineral compositions highly enriched in incompatible elements. The intrusive fine-grained lithology records a late stage event of localized melt percolation in channel-like structures, which lead to a strong rare earth element fractionation. In addition to these already intricate signatures, we highlight the occurrence of interactions at the contacts between layers. This layered section likely represents a contact between two larger magma bodies emplaced within the lower crust during accretion, and thus demonstrates that these two main melt migration processes, i.e., intrusion and porous flow, govern magmatic evolution within the lower oceanic crust.

1 Introduction

Accretion processes that occur at mid-ocean ridges and build the oceanic crust (70% of the Earth's surface) are the most common magmatic processes on Earth. However, our knowledge of those igneous processes remains limited, mainly because of limited access to oceanic crust samples, especially samples from the lower oceanic crust. At oceanic spreading centers, the main igneous processes responsible for lower crustal accretion have typically been ascribed to equilibrium and fractional crystallization of mantle melts. Both have been characterized and quantified in natural samples (***Natland and Dick, 2001; O'Hara, 1965; Ross and Elthon, 1997; Sanfilippo and Tribuzio, 2013***), reproduced experimentally (***Feig et al., 2010; Villiger et al., 2007***) and constrained by numerical modeling (***Coogan et al., 2001; Meyer et al., 1989***). During recent decades, comprehensive petrological studies have highlighted that melt migration within mantle and crustal sequences, which triggers melt-rock reactions (MRR) during reactive porous flow (RPF), exerts a major control on both lower and upper crustal

compositions (e.g., ***Bédard et al., 2000; Collier and Kelemen, 2010; Coogan et al., 2000; Dick et al., 1991; Drouin et al., 2009; Ferrando et al., 2018; Gao et al., 2007; Leuthold et al., 2018; Lissenberg and MacLeod, 2016; Sanfilippo et al., 2015; Suhr et al., 2008***). Therefore, RPF must be considered alongside other igneous processes involved in oceanic accretion, such as in-situ crystallization (***Coogan and O'Hara, 2015; Langmuir, 1989***), magma cycling through crustal magma chambers (***O'Neill and Jenner, 2012***), and contamination by anatexis of magma chamber roof rocks (***France et al., 2014***).

The modalities of melt migration and storage within the accreting crust at slow-spreading ridges remain poorly constrained. Only a few seismic imaging studies have reported molten bodies in contexts where magma input from the mantle is considered relatively low (e.g., ***Rubin and Sinton, 2007***). For example, along the mid-Atlantic ridge (MAR), ***Sinha et al., (1997)*** revealed the presence of a crustal magma body at 2–3 km depth below the Reykjanes Ridge. ***Canales et al. (2017)*** showed the presence of multiple magma sills stacked at different stages of crystallization between 2 and 10 km depth below the Rainbow ultramafic massif, also on the MAR. Similarly, ***Jian et al. (2016)*** discovered an axial magma chamber at 4–9 km depth below the ultra-slow southwest Indian ridge (SWIR).

Melt migration in cooling magma bodies emplaced within the crust exerts a fundamental control on differentiation processes and on the thermal regime of the crust. Two main types of melt migration in oceanic crust have emerged from studies at fast- and slow-spreading ridges (***Lissenberg et al., 2019***, and references therein): migration by focused flow or magmatic intrusions (e.g., ***Dunn et al., 2005; Kelemen and Aharonov, 1998***), and migration by porous flow (e.g., ***Blackman et al., 2011; Dick et al., 2000***). Evidences of reaction between a percolating melt and the surrounding rock or mush have been identified in various localities in fast- and slow-spreading environments (e.g., ***Lissenberg and MacLeod, 2016*** and references therein). For example, some olivine-rich troctolites recovered in fossil oceanic crust (e.g., ***Basch et al., 2019; Sanfilippo et al., 2014***) and drilled in the Atlantis Massif oceanic core complex (OCC) on the MAR (e.g., ***Drouin et al., 2010, 2009; Ferrando et al., 2018***) result from the interaction of a percolating melt with an olivine-rich matrix, possibly of mantle origin. This argues for reactive migration of melts in mantle domains, or through the deeper and more primitive portions of the crust as proposed by ***Renna et al. (2016)***. At Atlantis Bank (SWIR), some of evolved oxide-rich lithologies have been interpreted as the consequence of interactions between gabbroic rocks and late-stage melts (***Dick et al., 2000; MacLeod et al., 2017; Natland et al., 1991***), and common evidences for extraction of interstitial liquids at crustal levels were also found (***Lissenberg and MacLeod, 2016,*** and references therein).

Here, we focus on discrete layered structures in olivine gabbro from the slow-spread lower oceanic crust that have the potential to document key processes linked to melt migration. Layering *sensu stricto* has been heavily studied in various plutonic bodies from continental and oceanic environments, and provides key information on the igneous and structural processes involved in magma body accretion. Layering can originate from processes occurring in a magmatic body such as crystal settling (e.g., ***Namur et al., 2015*** and references therein) or can be linked to intrusive events (e.g., ***Tegner et al., 1993***). Furthermore, in extensive domains like mid-ocean ridges, deformation of magma bodies can lead to the formation of layered sequences in the lower crust (e.g., ***Higgie and Tommasi, 2012; Jousselin et al., 2012; Quick and Denlinger, 1993***). Alternatively, crystal-plastic deformation can overprint initial magmatic layering that once acted as a favored planar anisotropy to nucleate deformation, as often described in slow-spreading lower oceanic crust (***MacLeod et al., 2017***). Layering in gabbros typical of the lower crust formed at fast-spreading ridges represents about a third to half of the total crustal thickness (e.g., ***Kelemen et al., 1997; Nicolas et al., 1996***). In slow-spreading environments, layering has been described in both ophiolites (Corsican, Alpine, and Ligurian ophiolites: ***Lagabrielle et al., 2015; Sanfilippo and Tribuzio, 2013, 2011***), and in present day oceanic crust (at OCCs from slow-spreading ridges: ***Blackman et al., 2006; Dick et al., 2000***).

OCCs at slow-spreading ridges represent exhumation of lower crust and mantle sections by detachment faulting during asymmetric spreading, and provide an invaluable opportunity to study deep crustal sections (e.g., ***Cann et al., 1997; Escartín et al., 2008; Ildefonse et al., 2007; Lagabrielle et al., 2015***). Layering is rather sparse in those areas, with only localized meter-thick layered intervals, mainly related to variations in grain size, with planar to curved contacts, as described during drilling expeditions conducted at the Atlantis Massif OCC (MAR, IODP Exp. 304/305, ***Blackman et al., 2006b***) and at the Atlantis Bank OCC (SWIR, ODP Leg 176, ***Dick et al., 1999***; and IODP Exp. 360, ***MacLeod et al., 2017***).The Atlantis Bank OCC is along the SWIR, on the eastern wall of the Atlantis II Transform fault (*Figure 3.48*). The OCC formed as a consequence of 3 km of uplift of lower crustal gabbros (***Dick et al., 1991***), which resulted from the offset of a detachment fault (of about 1 km) from transform-parallel normal faults during a period of change in the spreading direction at the ridge axis ~19.5 Ma (***Baines et al., 2003***). Based on magnetic data (ages and polarity) and U/Pb zircon ages, ***Baines et al. (2008)*** have quantified the half-spreading rate during detachment faulting to have been about 14.1 +1.8/–1.5 km/Myr.

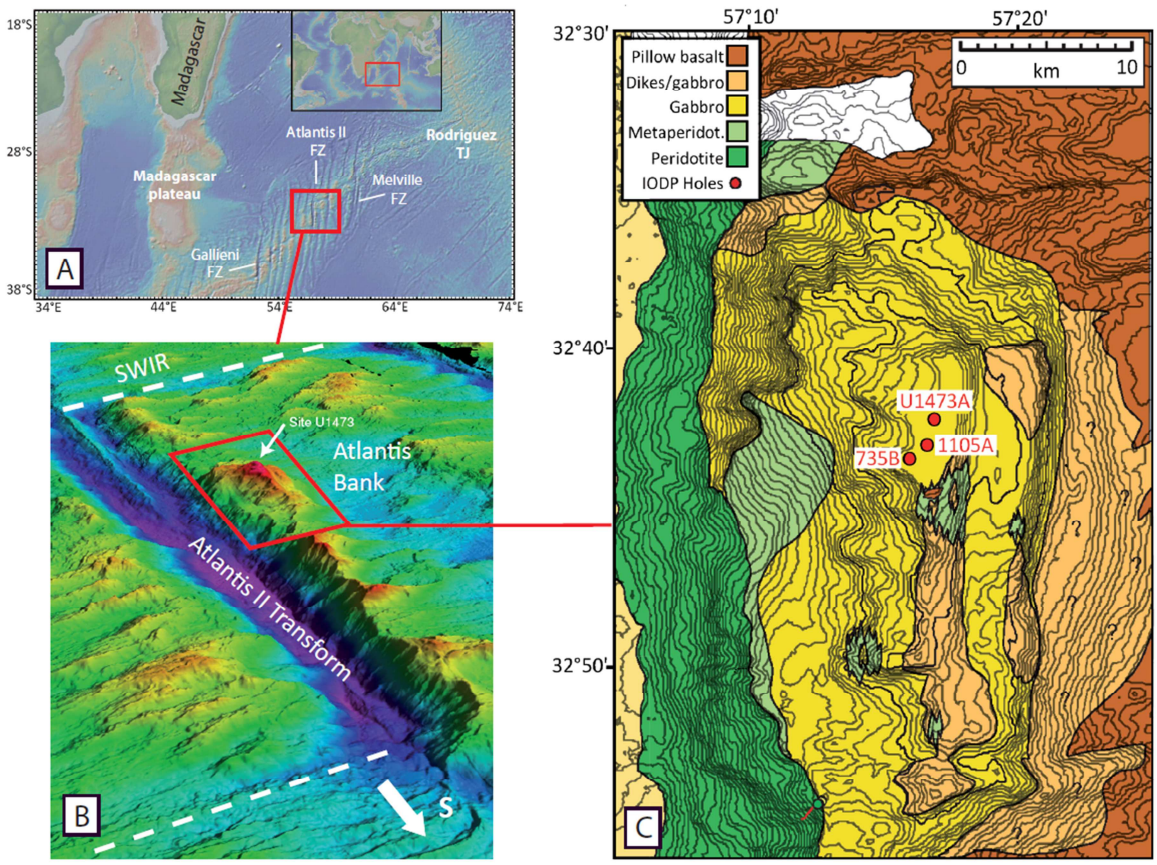

*Figure 3.48 - (**a**) Location map of the Atlantis II Fracture Zone, (**b**) 3D bathymetric map of the Atlantis II Fracture Zone and location of the Atlantis Bank OCC (MacLeod et al., 2017), and (**c**) geological map of the Atlantis Bank OCC and location of ODP/IODP Holes 735B, 1105A, and U1473A (modified from Dick et al., 2016).*

In total, three deep holes were drilled by ODP and at Atlantis Bank: the first and deepest is ODP Hole 735B (total depth 1,508 m below the sea floor, mbsf); the second is ODP Hole 1105A, 1.4 km north of hole 735B and drilled to <200 mbsf; and the last, drilled during IODP Exp. 360, is Hole U1473A (809 mbsf), 2.2 km north-northeast of hole 735B. These cores share very similar petrographic features and present the same highly variable lithological assemblages. Lithologies range from primitive troctolites to more differentiated oxide gabbros, with olivine gabbros representing 68% of ODP Hole 735B and 76.5% of IODP Hole U1473A (*Figure 3.49*; ***Dick et al., 2002; MacLeod et al., 2017***). Together with modal mineralogy, grain size, texture, magnetic susceptibility, geochemical composition, and lithological distribution, the presence of layering constitutes one of the main parameters used to identify lithological units. In Hole U1473A, eight units were described (*Figure 3.49a*; ***MacLeod et al., 2017***). Sparse layering occurs in almost every lithological unit. In most cases, layering is characterized by contrasted grain size, ranging from fine- to coarse-grained material, with sub-parallel and sub-horizontal contacts. Relatively intense layering is present in two units (*Figure 3.49a*): Unit II with a strong crystal-plastic deformation background, between 100 and 175 mbsf (up to four layers per 10 m), and Unit VII, between 578 and 642 mbsf (up to seven layers per 10 m).

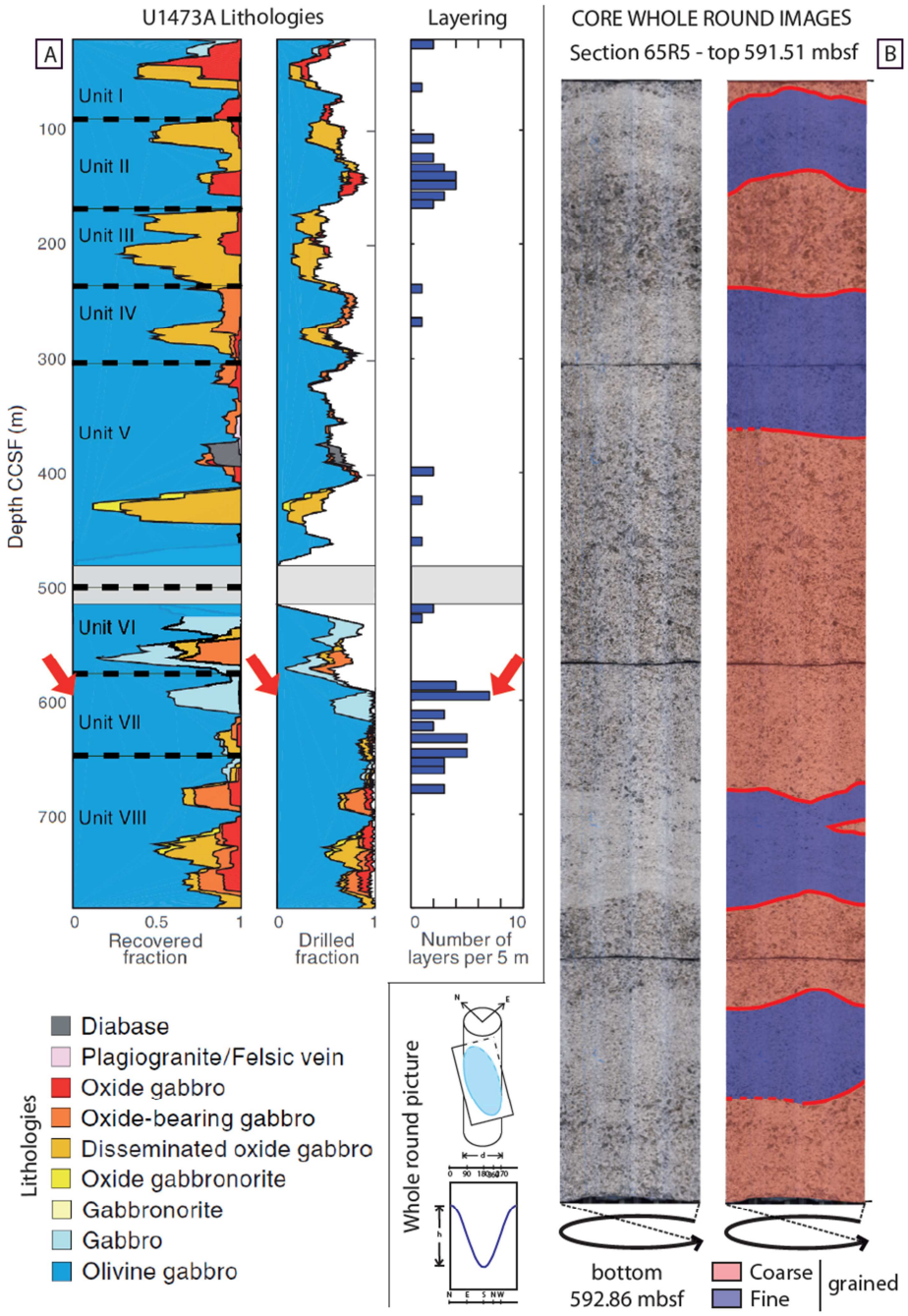

*Figure 3.49 - (**a**) Lithostratigraphic variations of IODP Hole U1473A (modified from MacLeod et al., 2017). Relative abundances are averaged over 20 m, dashed lines represent unit boundaries, and the histogram documents the number of igneous layers identified every 5 m. Red arrows indicate the depth of section U1473A-65R5 (~592–593 mbsf, shown in (**b**)). (**b**) Whole round scans of section U1473A-65R5 (top and bottom depths indicated on both sides). Red lines indicate boundaries between coarse- and fine-grained layers.*

In this study, we focus on a layered sequence from the main layered unit of hole U1473A, sampled at around 590 mbsf (*Figure 3.49b*; Unit VII in ***MacLeod et al., 2017***). We conducted high resolution petrologic, geochemical, and structural studies of this sequence to identify the origin of the layering and discuss melt crystallization, migration, and interaction within t he lower crust.

2 Analytical methods

2.1 Electron backscatter diffraction (EBSD)

Details on EBSD measurements and data processing are presented in the supplementary materials (Text S1).

Intragrain misorientation is quantified as the angle between the crystallographic orientation of a particular pixel within a grain and the average orientation of all pixels of the same grain (Mis2Mean parameter). The grain orientation spread (GOS) is the average of the Mis2Mean and the average GOS quantifies the grains misorientation per sample. The fabric strength and distribution density of the principle crystallographic axes are determined by calculating the J index (e.g., ***Mainprice and Silver, 1993***) of the orientation distribution function (ODF); J varies from 1 for a random distribution to infinity for a single perfectly uniform crystal. We calculated the ODF using the "de la Vallee Poussin" kernel with a half-width of 10° (***Mainprice et al., 2014***). The symmetry of the minerals crystal preferred orientations (CPOs) are evaluated by calculating the BA (for plagioclase) and BC indexes (for olivine and clinopyroxene - ***Mainprice et al., 2014; Satsukawa et al., 2013***). The indexes are based on three other indexes P, G and R (Point, Girdle and Random), calculated using the eigenvalues of the orientation tensor that represent the distribution of the crystallographic axes or poles to crystallographic planes in each pole figure (***Satsukawa et al., 2013***). BA and BC indexes represent the relative weight of the fabrics defined by [100] and (010) for the former and [010] and [001] for the latter.

For non-equigranular samples, coarse grains are overrepresented when calculating pole figures from the orientations of each pixel. To avoid this bias, we instead used the average orientations of the grains (one-point-per-grain data, 1PPG) to calculate the ODF. In this study, we used individual EBSD maps of coarse-grained samples for misorientation data, but not to determine orientations and fabrics due to the small number of grains analyzed (less than 20 olivine (ol) grains and less than 50 plagioclase (pl) grains without considering recrystallized grains at grain boundaries). To increase the number of minerals analyzed, 1PPG data for eight coarse-grained material maps were concatenated with the Channel 5 software suite and similarly processed as an individual map (*Figure S1*).

2.2 Whole-rock major and trace element analyses

Major and trace elements concentrations were measured by the Service d'Analyses des Roches et des Minéraux (CRPG, Nancy, France) via inductively coupled plasma optical emission spectrometry and inductively coupled plasma mass spectrometry (ICP-MS), respectively. Each layer of the section (four finer- and three coarser-grained lithologies) was analyzed for whole-rock major and trace element compositions (*Table S1*). Details on analytical protocols and data are given in supplementary materials (*Text S2* and *Table S1*).

2.3 Electron probe microanalysis (EPMA)

In-situ major element contents of minerals were quantified by EPMA at the Laboratoire Magmas et Volcans (Clermont-Ferrand, France) with a Cameca SX100 equipped with four wavelength dispersive X-ray spectrometers. Analyses for all minerals were performed with a 15 kV accelerating potential and a focused beam using a 15 nA beam current. On-peak and background counting times were 10 or 20 s (see details and calibration standards for each element in *Table S2*). The data and associated analytical errors are available in supplementary materials.

2.4 Laser ablation inductively coupled plasma mass spectrometry (LA-ICP-MS)

In-situ trace element contents of minerals were analyzed with a ThermoFinnigan Element2 XR ICP-MS coupled with a Microlas-GeoLas Q+ housing a Lambda-Physik CompEx 102 excimer laser at Géosciences Montpellier (AETE-ISO regional facility of the OSU OREME, Montpellier University, France). Signal acquisition was performed in time-resolved acquisition mode, counting 2 min for blanks and 1 min for sample measurements. The laser frequency was 8 Hz with an energy density of ~12–15 J·cm^2. Ablation was performed in He gas, which was mixed with Ar before entering the plasma. Clinopyroxene (cpx) was analyzed with a laser spot size of 77 µm, whereas a spot size of 102 µm was used for ol and pl. Data were processed using the GLITTER software (***van Achterbergh et al., 2001***; *Table S3*). All measured concentrations were calibrated to the synthetic glass NIST 612 using the values of ***Pearce et al., (1997)***. Internal standards used for the minerals were ^{43}Ca for cpx and ^{29}Si for pl and ol.

The averaged values (and associated 2SD values) obtained by LA-ICP-MS analyses of the standard reference basalt BIR-1G are available in Supplementary *Table S3*, together with all trace element data and associated analytical errors.

3 Results on the layered series of IODP Hole U1473A

3.1 Petrography and microstructures

In IODP Hole U1473A, the interlayered series (as named by the IODP Expedition 360 Science Party; ***MacLeod et al., 2017***) is defined by grain size variations, and only a few series present weak variations in modal mineralogy. Contacts are locally slightly diffuse or gradational (~10%), but are generally sub-planar and sharp. The layering fabric is commonly overprinted by crystal plastic deformation, preventing any reliable study of the magmatic processes. Locally, deformation is too intense to identify if any initial magmatic (mineralogical or textural) heterogeneity was present before deformation (***MacLeod et al., 2017***).

We focus on the interval at ~592–593 mbsf in Unit VII of IODP Hole U1473A, where the layer frequency is highest (section 65R5, *Figure 3.49b*). The 1.35-m-long section 65R5 shows successive fine- (average grain size ~0.5 mm) and coarse-grained (average grain size ~5 mm) layers of olivine gabbros with average thickness of 20 cm. Fine-grained layers are granular and coarse-grained layers are granular to subophitic. Some reactive textures are observed in the section, with cpx intergrowths and resorbed pl boundaries in the coarse-grained lithologies, and locally resorbed pl and cpx grain boundaries in the fine-grained layers (Figure S2). The majority of the contacts between layers are sharp and planar, and some are locally weakly diffuse at the bottom of the section, with the presence of "slabs" of coarse-grained material trapped within the fine-grained layers (described as "coarse in fine" hereafter). There is no systematic change in modal mineralogy between the layers, which contain on average 60% pl, 28% cpx, 8% ol, 3% orthopyroxene, and about 1% accessory minerals (ilmenite, brown amphibole, and sulfides–mostly pyrites with some chalcopyrites and pentlandite) as quantified by EBSD measurements.

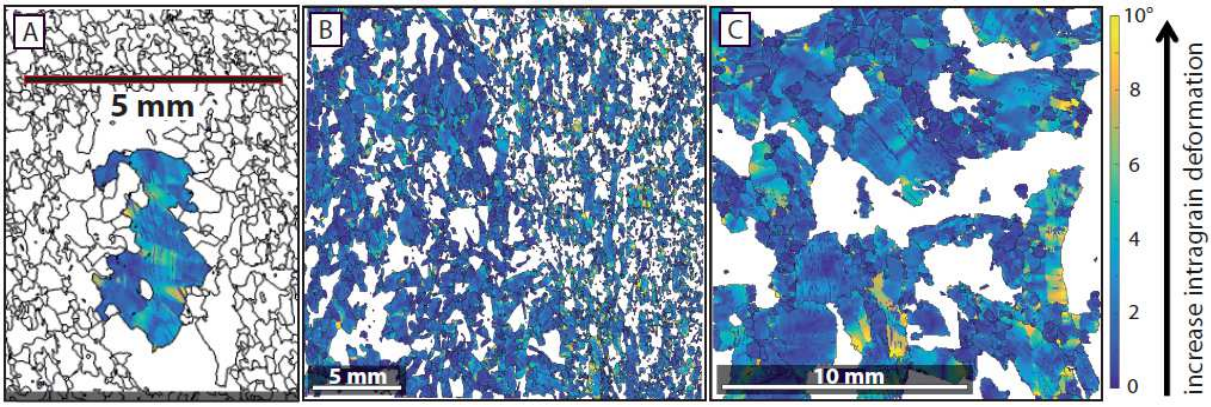

*Figure 3.50 - Grain misorientation maps (deviation of each pixel from the average orientation of all pixels within a grain) describing the deformation of pl grains in section U1473A-65R5. (**a**) A single coarse-grained pl crystal located at a lithological contact at ~80 cm below the top of the section. Deformed pl twins are visible. (**b**) A fine-grained lithology that transitions to a finer grained area to the right at ~3 cm below the top of the section. The average GOS for the fine-grained area to the left is 0.32° and is 0.54° for the finer-grained lithology to the right. (**c**) A coarse-grained lithology at ~76 cm below the top of the section. The average GOS in this area is 0.37°.*

The average GOS (see section 2.1) is 0.32° for pl and 1.11° for ol over the entire section, indicating that grains in fine- and coarse-grained layers are weakly deformed. When present at the layer contacts, cpx and pl locally show minor recrystallization (*Figure 3.50**Erreur ! Source du renvoi introuvable.**a*). Although still weak, pl grains are slightly more deformed in finer-grained areas of the fine-grained layers (*Figure 3.50b*). No fabric can be identified in coarse-grained layers at the sample scale because the average grain size is too large relative to the core (~6 cm in diameter). In contrast, well-developed fabrics can be described both macroscopically and microscopically in fine-grained layers. These fabrics are parallel to the contacts between layers and are marked by a shape preferred orientation of pl laths (*Figure 3.51*). CPOs of pl and ol in the fine-grained layers have average J indexes of 2.3 and 1.36, respectively. Foliation is defined by the (010) plane of pl, ol and cpx, and lineations are marked by the [100] axis of pl and the [001] axis of ol and cpx. Hence, the BA-index for pl and the BC-index for ol and cpx represent the relative weight of lineation over foliation of the considered fabric. For pl, a BA-index close to 0 characterizes a perfect Axial-B fabric and translates the predominance of the foliation in the fabric (***Satsukawa et al., 2013***). Similarly for ol and cpx, the predominance of the foliation is described by BC-indexes close to 0. The average BA index of the fine-grained material is of 0.36 for pl and the average BC index is of 0.38 for ol (*Figure 3.51a*). Only one contact shows a distinctly irregular contact, with a mm-thick portion of fine-grained material that crosscuts the sharp contact at ~30° (*Figure 3.51c*). This portion of fine-grained ol gabbro presents the same fabric as other fine-grained areas, but the fabric is sub-parallel to the walls of the structure, as highlighted by pl and ol CPOs (J indexes of 5.66 and 4.32 respectively, BA index of 0.37 for pl and BC index of 0.18, *Figure 3.51c*). At the scale of the section, the eight concatenated maps of coarse-grained layers (see section 2.1) show a weak pl CPO with a subhorizontal foliation (J index of 1.44 and BA index of 0.37 - *Figure 3.51b*). No significant ol or cpx fabric is observed in those maps.

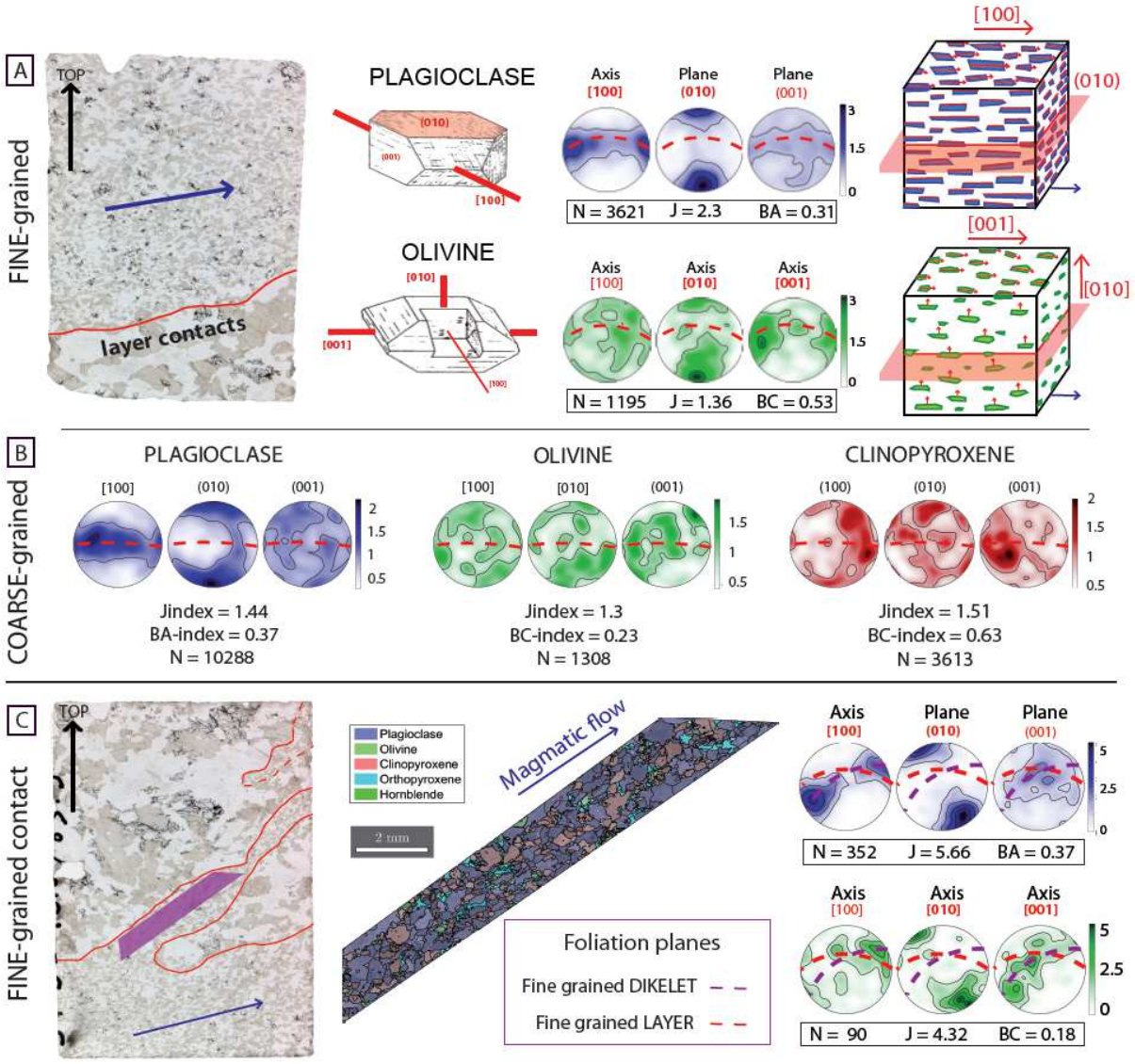

*Figure 3.51 - Petrographic observations and EBSD measurements for samples (**a**) U1473A-65R5-91cm, (**b**) concatenated maps of coarse-grained samples, and (**c**) U1473A-65R5-79.8cm.*
*(**a**) From left to right: natural-light photomicrograph of a contact between fine- (top) and coarse-grained (bottom) lithologies; crystallographic characteristics of pl and ol crystals (red lines, crystallographic axes; red surfaces, crystallographic planes); pl and ol CPOs analyzed in the fine-grained material (red dashed lines, orientation of the foliation plane as defined by pl [100] preferred orientation; N, number of grains considered; J, BA and BC indexes, see section 2.1); and 3D schematic diagrams representing the orientation of pl and ol crystals (and their crystallographic characteristics) within a magmatic flow as described by the blue arrows.*
*(**b**) CPOs of pl, ol, and cpx analyzed in the concatenated maps of the coarse-grained samples.*
*(**c**) From left to right: natural-light photomicrograph of a contact between fine- (bottom) and coarse-grained (top) lithologies (purple area, surface analyzed separately to obtain CPOs within the incursion of fine-grained material); mineralogical map corresponding to the purple area; pl and ol CPOs (purple dashed lines, orientation of the foliation plane as described by pl [100] planes, compared with the foliation plane described by pl in the rest of the fine-grained layer below the contact in red dashed lines).*

3.2 Whole rock compositions

The Mg# (molar ratio of Mg/[Mg + Fe_{tot}] × 100) of the layers in section 65R5 ranges from 76.3 to 79.3, whereas the Ca# (molar ratio of Ca/[Ca + Na] × 100) varies slightly between 72.3 and 74.7. When compared with whole-rock major and minor element compositions of ODP Hole 735B (***Dick et al., 2000***) and of other samples from U1473A (***MacLeod et al., 2017***), our data fall within the compositional range of ol gabbros from Atlantis Bank (Mg# between 62 and 84 and Ca# between 56 and 83). The studied samples are nevertheless more primitive than the average bulk composition of the three ODP-IODP Holes drilled at Atlantis Bank (average respective Mg# and Ca# of 71 and 69.7 for IODP Hole U1473A, 73 and 70.3 for ODP Hole 735B, and 53 and 65.6 for ODP Hole 1105A).

The compositions of the fine- and coarse-grained layers are very similar, and span a relatively narrow range compared to the variability observed in ol gabbros from holes 735B or U1473A. They present strong positive Sr and Eu anomalies and their rare earth element (REE) contents vary within the range of ol gabbros from ODP Hole 735B (*Figure 3.52b*). The REE compositions of coarse- and fine-grained layers are depleted relative to primitive mid-ocean ridge basalt (MORB), with the most incompatible elements (light REEs) being the most depleted. In detail, fine-grained layers have higher Mg#, are enriched in compatible elements (e.g., Cr), and are depleted in incompatible elements (e.g., Y and REE) compared to the coarse-grained layers (see *Figure 3.52* and *Table S1* for details).

3.3 Mineral compositions

In-situ measurements in the following sections are described as core and rim points in reference to grain boundaries; no intermediate points were analyzed in the minerals.

3.3.1 Major and minor elements

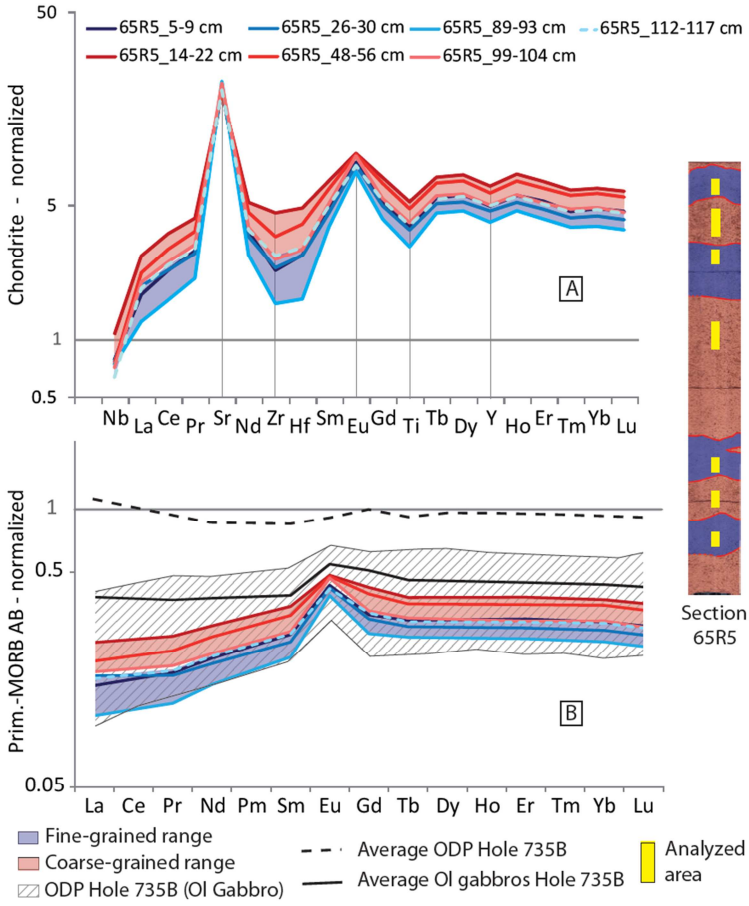

*Figure 3.52 - Whole-rock (**a**) spider diagram normalized to chondrite (McDonough & Sun, 1995) and (**b**) REE profiles normalized to the average of the most primitive MORBs sampled on the Atlantis Bank section of the SWIR (Table S3; from Coogan et al., 2004) for each layer sampled in section U1473A-65R5. Red and blue shaded areas correspond to fine- and coarse-grained ol gabbros, respectively. The hatched domain in (**b**) corresponds to the compositional range of ol gabbros from ODP Hole 735B (Dick et al., 2002), with the solid black line representing the average composition of ol gabbros and the dashed black line the average composition of the entire ODP Hole 735B.*

Pl compositions are homogeneous along the section (*Figure 3.53a*). Anorthite (An) contents of pl (molar Ca/[Ca + Na + K] × 100) range from 56.6 to 62.4 in the fine-grained layers and vary within 53.4–70.4 in the coarse-grained layers. In the fine-grained layers, some pl display inverse zoning with higher An contents at the rims (up to 75.8) than in pl cores (as low as 58.9). This is the only clear zoning observed for major or minor elements throughout the entire section. Cpx Mg# range between 77.6 and 84.4 in the fine-grained layers, slightly higher than in coarse-grained Cpx (75.2–83.2). Cpx TiO_2 contents are on average higher in the coarse-grained layers (0.40–1.34 wt%) than in the fine-grained layers (0.46–1 wt%, *Table S2*), with no systematic core-to-rim variations.The NiO contents of ol are rather homogeneous throughout the section, and range between 0 and 0.15 wt% (average 0.08 ± 0.02 wt%) in both fine- and coarse-grained layers. Contrastingly, ol Forsterite (Fo) contents are generally higher in the fine-grained layers (72.2–77.4) than in the coarse-grained layers (73.2–76.5, *Figure 3.53c*), even though the ranges are similar, and no systematic core-to-rim variations are observed.

Overall, mineral major and minor element compositions display small variations throughout the studied section (*Figure 3.53*, *Table S2*), and no systematic compositional zoning is present.

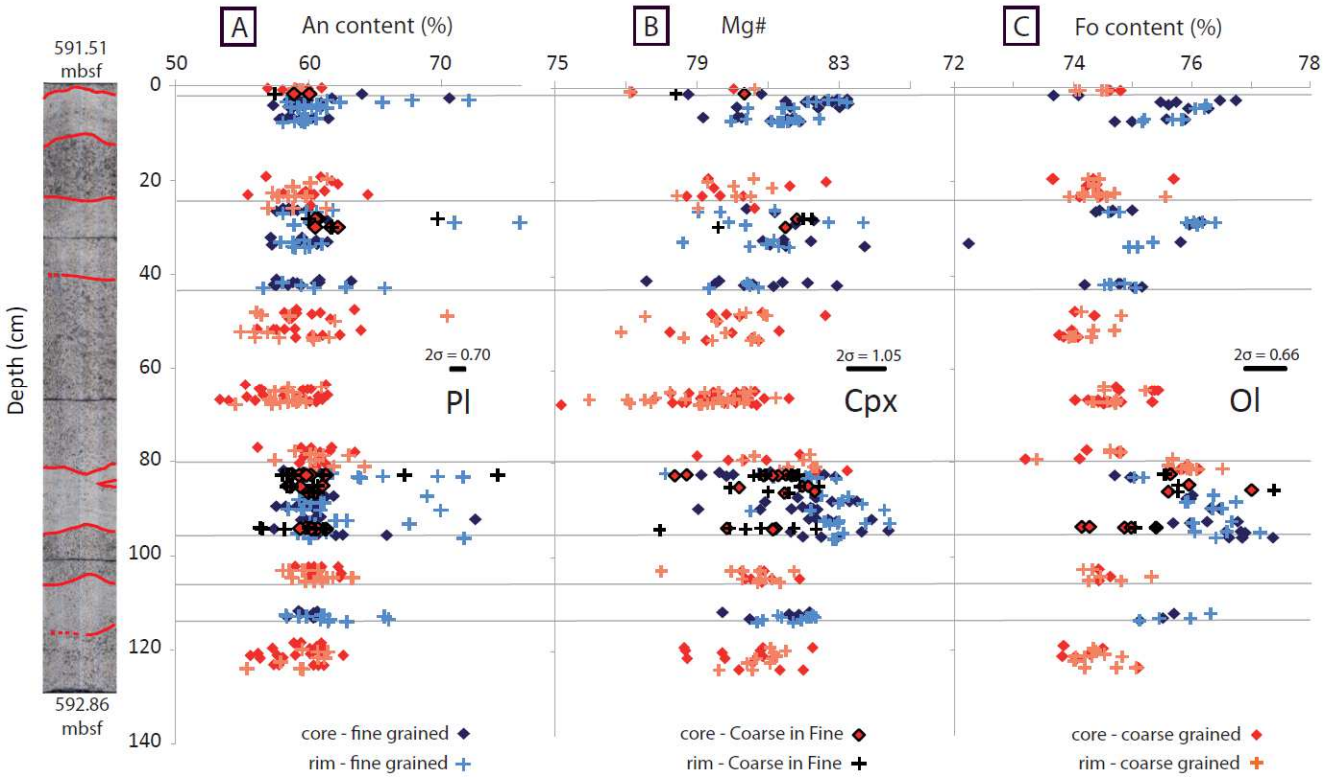

*Figure 3.53 - Depth profiles (cm from the top of the section) of (**a**) pl An content, (**b**) cpx Mg#, and (**c**) ol Fo content. Blue points represent analyses of fine-grained material, red points coarse-grained material, and black points coarse-grained material trapped within fine-grained layers ("coarse in fine"). Reported errors correspond to propagated 2σ errors on the considered elements.*

3.3.2 Trace elements

Mineral-specific REE contents are on average higher and are more variable in the coarse- than in the fine-grained layers (*Figure 3.54* and *Figure 3.55*). The best example of this is cpx Ce contents, which average 1.87 ± 0.46 ppm in the fine-grained layers and 2.96 ± 1.17 ppm in the coarse-grained layers. In a single sample located at ~20 cm depth, cpx Ce contents vary by a factor of ~6 (i.e., from 1.15 to 6.45 ppm, *Figure 3.55b*).

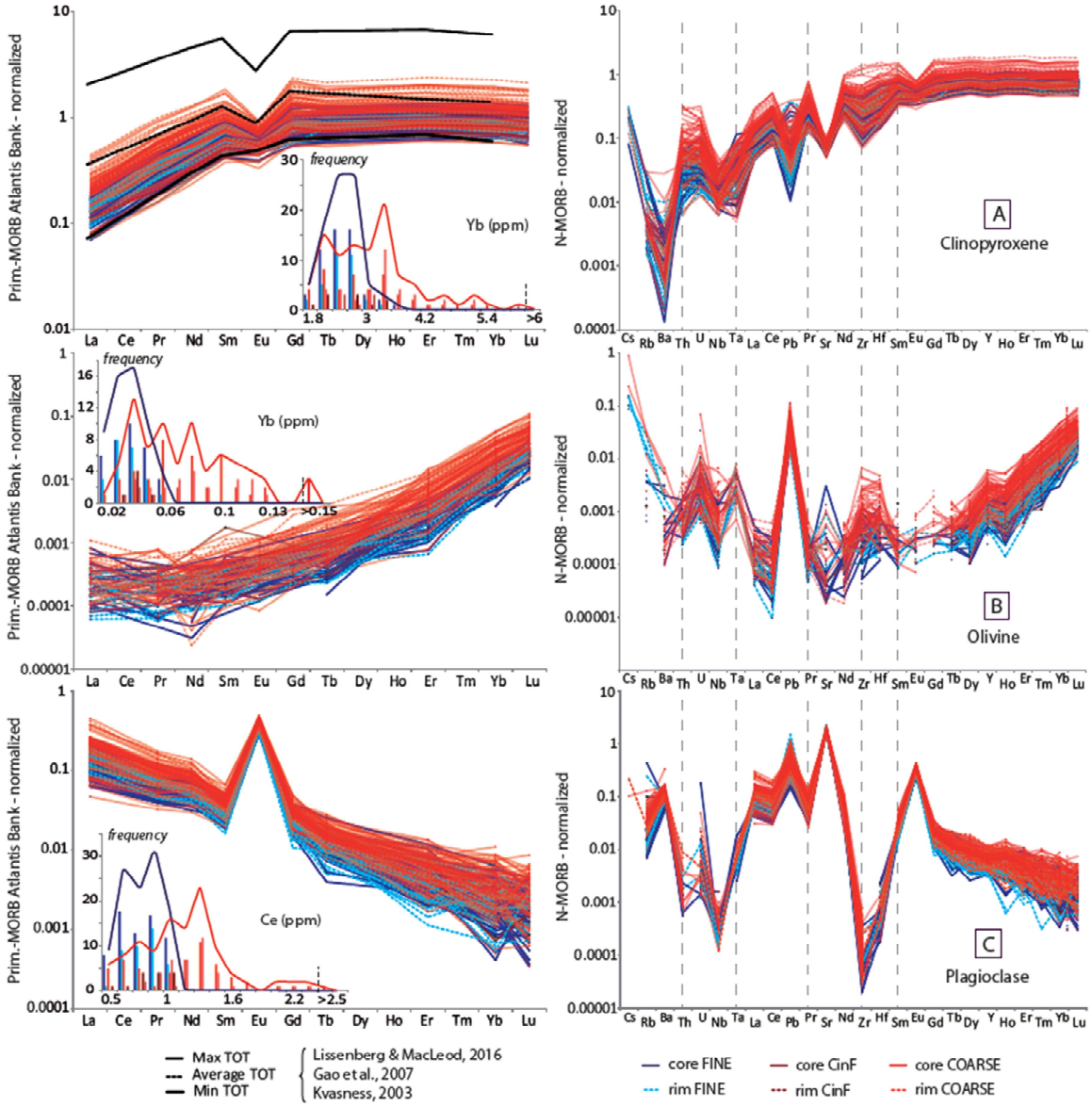

*Figure 3.54 - REE (left, normalized to the most primitive MORB observed in Atlantis Bank by Coogan et al., 2004, Table S4) and trace element (right, normalized to the average N-MORB composition of Gale et al., 2013, Table S4) concentration diagrams for (**a**) cpx, (**b**) ol, and (**c**) pl from section 65R5. Solid and dashed lines indicate crystal cores and rims, respectively. The black lines in (**a**) correspond to the maximum, average, and minimum values of in-situ cpx compositions from Atlantis Bank (Gao et al., 2007; Lissenberg & MacLeod, 2016; Kvasness, 2003). Histograms indicate the compositional distribution of the most abundant REE in pl and ol, and that of the most fractionated REE in cpx.*

In addition to the distinction between fine- and coarse-grained materials, the compositions of coarse-grained layers are not homogeneous throughout the section. Indeed, the middle of the coarse-grained layer at ~63 cm from the top of the section stands out from the general pattern described above. The minimum compositional values of that layer (e.g., 2.49 ppm Ce in cpx and 0.45 ppm La in pl) are higher than in any other layer of the studied section (0.94 ppm Ce in cpx and 0.13 ppm La in pl; *Figure 3.55*).

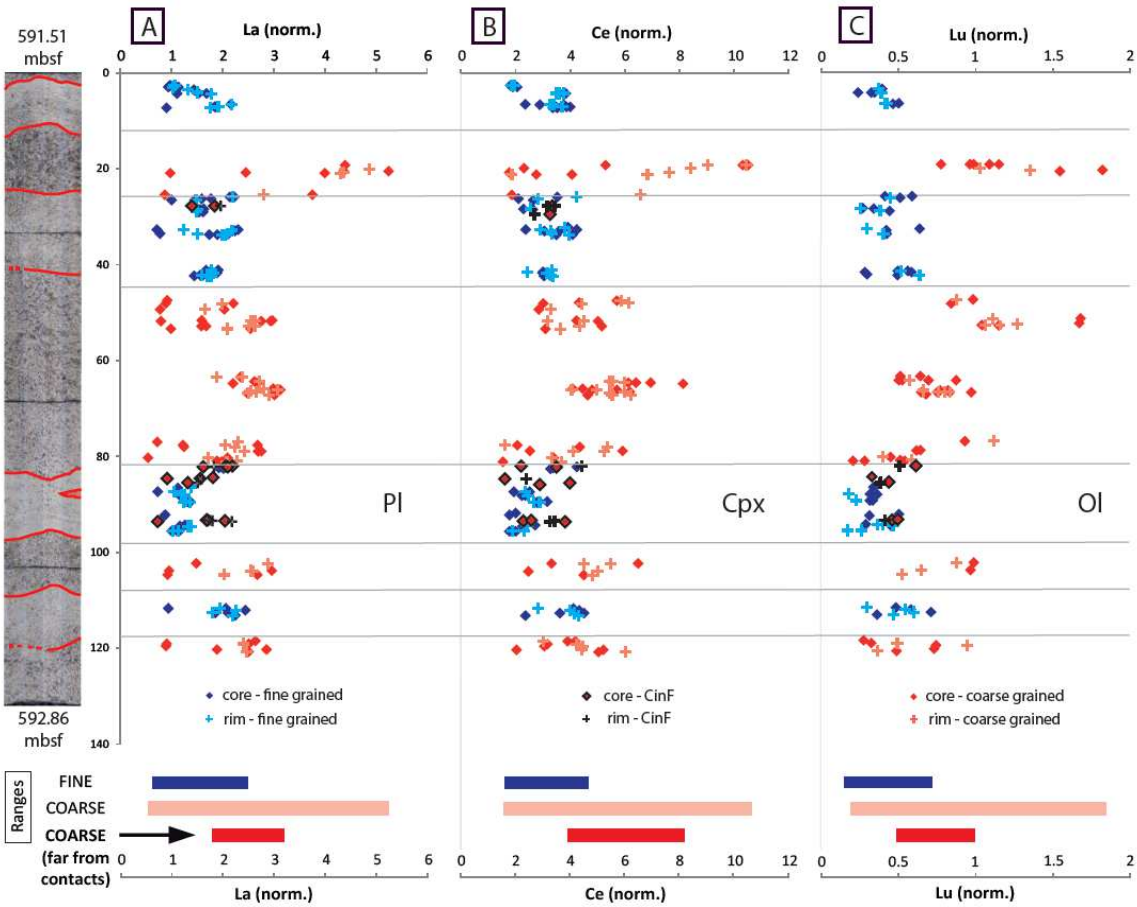

*Figure 3.55 - Depth profiles (cm from the top of the section) of the chondrite-normalized (McDonough & Sun, 1995) concentrations of (**a**) La in pl, (**b**) Ce in cpx, and (**c**) Lu in ol. Symbols are as described in Figure 6. The compositional ranges of each lithology throughout the section are represented by the colored boxes at the bottom of the figure. The compositional range describing the coarse-grained lithology far from any lithological contacts (dark red) corresponds to the two samples from ~63 cm depth.*

Finally, the ratios of more to less incompatible trace elements in cpx vary with depth and within each layer. The average La/Lu ratio is lower in the fine- than in the coarse-grained layers (0.99 and 1.25, respectively). La/Lu in the fine-grained layers tends to very low values and ranges between 0.46 and 1.5. The minimum La/Lu value of the coarse-grained layer at ~63 cm depth is again higher than in the rest of the section (1.19 compared to 0.59, respectively).

4 Discussion

4.1 Origin of layering

The first step in this study was to determine if the observed layering resulted from solid-state deformation or magmatic processes. Microscopic observations and EBSD data enable us to discard crystal-plastic deformation. Strong evidence of crystal-plastic deformation such as extensive recrystallization or intra-grain deformation are absent in both lithologies, and internal deformation as determined by EBSD is low (average GOS of 0.3 for pl, *Figure 3.50*). The pl fabric

of both fine- and coarse-grained layers is a classical axial-B CPO (average BA indexes of 0.36 and 0.37, respectively, *Figure 3.51*).This CPO is characteristic of fabrics formed by crystal alignment during magmatic flow (***Jousselin et al., 2012; Morales et al., 2011; Satsukawa et al., 2013***). In the fine-grained layers, ol CPO (*Figure 3.51a*) with respect to the reference frame defined by the pl grains is also consistent with crystal alignment during magmatic flow. No fabric was detected for ol or cpx in the coarse-grained lithologies even after merging of the EBSD maps, and only pl attests to the magmatic fabric in these layers. The granular to subophitic textures and grain size layering of the ol-gabbros further indicate the magmatic origin of the layering.

Contacts between layers are sharp and sutured, with nested fine- and coarse-grained minerals. No significant variations in modal mineralogy are observed between layers that are homogeneous in grain size, except for a few randomly distributed extra-fine-grained areas and lenticular enclaves of coarse-grained material within fine-grained layers near lithological contacts. The fabric in fine-grained layers is globally sub-horizontal, but is locally parallel to contacts near layer margins. For example, in the sutured contact at 80 cm from the top of section 65R5 (*Figure 3.51c*), the contact is not straight and presents a structure similar to a vein of fine-grained material intruding the coarse-grained layer. The magmatic fabric within this fine-grained incursion is as described in fine-grained materials elsewhere, except for a difference of orientation; instead of being sub-horizontal and parallel to the main layer boundary, the foliation there is sub-parallel to the margins of the vein (*Figure 3.51c*) and the lineation follows the same orientation. Conversely, the fabric and orientation of the coarse-grained lithology remains unchanged near this structure and other contacts in the section.

Hence, the layering has likely formed by intrusion of the fine-grained material into the coarse-grained lithology. This model explains both the fabric in the fine-grained layers, which is controlled by the geometry of the contacts due to orientation of the crystals in the flowing magma, and the presence of coarse-grained enclaves trapped during emplacement. The sutured contacts and the lack of strong intra-grain deformation preclude an origin by compaction of a heterogeneous mush, and in this case indicate that the coarse-grained material was not fully solidified as it accommodated the intrusion without fracturing. The geochemical composition of the lithologies further support this model and discard an origin of the fine-grained layers by their segregation from the coarse-grained mush, as the latter presents more differentiated signatures (lower whole rock Mg# or higher REE contents, *see section 3.2*). In addition, the average pl CPOs of the fine- and coarse-grained lithologies are not identical, but sub-parallel to each other. This can be explained by moderate compaction of the layers in the same strain field and in the presence of melt, thus allowing movement of the crystals without deforming them and the superimposition of a similar fabric in both lithologies.

4.2 Constraints on the parental magmas and interactions between layers

Whole-rock incompatible element contents show that both the coarse- and fine-grained layers record a strong cumulative component (positive Sr and Eu anomalies, and depletion in incompatible elements relative to primitive MORB; *Figure 3.52a*). In addition, the coarse-grained layers are more enriched in incompatible elements than the fine-grained layers (*Figure 3.52b*), suggesting that the coarse-grained lithology formed from a more evolved melt or contained more interstitial liquid than the fine-grained layers.

Interactions between the two lithologies may have occurred once the fine-grained material began intruding the coarse-grained lithology (see below). To avoid misinterpreting any imprint of such processes near lithological contacts, we first compare the fine-grained material with only the samples from ~63 cm from the top of the section, i.e., the central part of the thickest coarse-grained layer, which is the farthest from any contact. A key difference between the lithologies is that the minimum observed incompatible element contents in ol, pl, and cpx are notably higher in the coarse-grained samples (*Figure 3.55*). The most depleted values of a given sample are of particular interest as they constrain the composition of the most primitive magma from which the minerals crystallized. This difference between the central coarse-grained layer and the fine-grained layers therefore leads us to suggest that both layers crystallized from distinct parental magmas that were at different stages of evolution.

To better illustrate the difference between the parental magmas of the two lithologies, we calculated the composition of melts in equilibrium with the most depleted and most enriched cpx in both lithology (*Figure 3.56*). These results show that the melt in equilibrium with the most primitive cpx in the coarse-grained layer cannot be reproduced by fractional crystallization of the melt in equilibrium with the most primitive cpx in the fine-grained layers. For example, REE fractionations are notably higher in the fine-grained equilibrium melt, and continually increase during fractional crystallization (average initial value of $La_N/Sm_N = 1.3$, see *Figure 3.56*; the subscript 'N' denotes normalization to primitive MORB), whereas the value for the coarse-grained material only reaches $La_N/Sm_N = 1.1$. This suggests that the two lithologies formed from distinct parental melts that evolved under different conditions and followed different crystallization paths, at least before emplacement at their current location, and that the coarse-grained material cannot have evolved directly from a melt similar to the more primitive parental melt of the fine-grained material.

As presented in section 3.3.2, the coarse-grained materials are not homogeneous from one layer to the next. Notably, the minimum incompatible element contents observed in coarse-grained minerals near the contacts of the thickest coarse-grained layer (~40–80 cm from the top) are similar to those of neighboring fine-grained layers, whereas the minimum contents in

the middle of this layer (~63 cm from the top of the section) are much higher (*Figure 3.55*). Small enclaves of coarse-grained material integrated into the fine-grained layers record the same depleted signatures as coarse-grained minerals near contacts.

Diffusion between layers during subsolidus re-equilibration might explain these variations. However, our samples require that this process would have somehow only affected the coarse-grained layers, as no combined increase in incompatible trace element contents is recorded near the contacts in the fine-grained lithology. In addition, cm-scale compositional variations across contacts and the heterogeneous compositions of minerals in the coarse-grained layers preclude the diffusion hypothesis. For example, ol Fo contents are quite different on either side of the contact at 80 cm depth from the top of the section (*Figure 3.53*). Although Fe and Mg are the fastest-diffusing elements in ol, we do not observe cm-scale diffusion profiles at the contacts between the lithologies. As other major and trace elements in pl or cpx diffuse more slowly, diffusion at such a scale cannot explain the geochemical variations observed in the coarse-grained layers near lithological contacts.

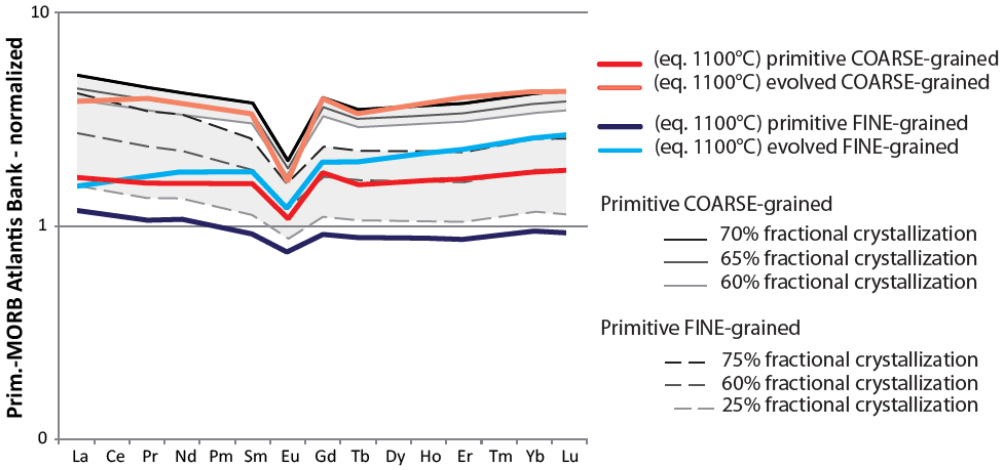

Figure 3.56 - REE contents of liquids in equilibrium with cpx in coarse- and fine-grained layers in section 65R5. Purple and blue thick lines indicate liquids in equilibrium with the most primitive and most evolved fine-grained cpx, respectively, and red and orange thick lines indicate liquids in equilibrium with the most primitive and most evolved coarse-grained cpx, respectively. Dashed and solid lines represent fractional crystallization models calculated after different percentages of crystallization from the least evolved fine-grained (purple line) and coarse-grained compositions (red line), respectively. REE contents are normalized to the average primitive MORB composition of the Atlantis Bank section of the SWIR from Coogan et al. (2004). The equilibrium melts were calculating using partition coefficients from Wood and Blundy (1997) at 1100 °C, the average equilibrium temperature (1095 ± 19 °C) determined for both lithologies using the REE-in-pl-cpx thermometer of Sun and Liang (2017).

The compositional evolution of the coarse-grained layers near contacts more likely results from a homogenization (or mixing) process at the time of the intrusion. The homogenization process might be related to percolation of the less-evolved melt (depleted in incompatible elements) from the intruding crystal-bearing magma through the residual porosity present in the almost solidified coarse-grained material. As a consequence, the infiltrating melt could have hybridized with any residual melt in the coarse-grained material, forming new

minerals and recording the homogenized compositions at the margins of the coarse-grained layers. The middle of the thickest coarse-grained layer (~63 cm depth, *Figure 3.55*) seems un-homogenized, suggesting that residual permeability was limited in the coarse-grained mush and that the intruding melt was unable to migrate farther than 10–20 cm within the solidifying mush.

4.3 Magmatic evolution of both lithologies

4.3.1 Divergence from simple crystallization processes

The parental melts that formed the coarse- and fine-grained layers likely underwent various magmatic processes after emplacement, which may include equilibrium or fractional crystallization. Although the variability of mineral major element compositions remains limited in both lithologies (*Figure 3.53*), incompatible element concentrations vary drastically between layers and sometimes within a single sample.

In the coarse-grained layers, REE concentrations vary greatly at the scale of a single thin section, with strong associated enrichment factors reaching 5.95 for cpx Ce contents at ~20 cm depth (*Figure 3.55*). However, if we exclude areas effected by homogenization and consider only the more primitive value recorded in the central coarse-grained layer, the enrichment factors are lower (2.34 for Ce). Furthermore, the associated fractionations between different REEs are rather constant throughout the entire section. To test whether the observed geochemical signatures can be reproduced by simple equilibrium and fractional crystallization of a typical primitive MORB, we applied the equations referenced in ***Allègre and Minster (1978)***. We used partition coefficients for ol, pl and cpx calculated at 1100 °C (*Table S4*), and modal proportions fixed by MELTS (***Ghiorso and Gualda, 2015; Gualda and Ghiorso, 2015***) modeling of fractional crystallization from a primitive MORB equivalent, taken as the diabase dike U1473A-65R5 composition (*Table S5*). The results show that a Ce enrichment factor of about 2.3 is attained after 65% equilibrium crystallization and after 60% fractional crystallization. Such extensive crystallization seems unlikely considering the subtle variations of the major element compositions of the minerals; the expected cpx Mg# from MELTS after 60% fractional crystallization is 73, whereas the lowest observed value (in the sample at ~20 cm depth) is 79. In addition, the expected fractionations between more and less incompatible REEs for both equilibrium (La_N/Sm_N = 1.65) and fractional crystallization (La_N/Sm_N = 1.28) are beyond the range observed in our samples (La_N/Sm_N = 1.08–1.13). Therefore, neither equilibrium nor fractional crystallization can explain the enrichment in incompatible elements observed in the coarse-grained lithology.

No strong variability or enrichments in REEs were observed in the fine-grained lithology, with a maximum enrichment factor of 1.8 for Ce in cpx in a single thin section. This may be related to an analytical bias due to the large size of the ablation spot compared to the size of the minerals analyzed. We estimated the compositional impact if only a small fraction of an enriched rim (with a similar enrichment as that in the coarse-grained material) was included in an analysis of a grain with a core composition equivalent to the less differentiated compositions of our samples (details in *Text S3*). The results show that less than 25% of the volume analyzed needs to comprise such hypothetical enriched rims to produce the upper bound of the compositional ranges of our samples. If such enriched rims were present, it is unlikely that almost none of our measurements would show significant traces of such compositions. More importantly, fine-grained cpx present stronger fractionations between light and heavy REEs with lower La/Lu values (La/Lu = 0.46–1.5) compared to cpx in the coarse-grained lithology (La/Lu = 0.99-1.25). Such REE fractionations cannot be explained by the potential analytical bias discussed above. We modeled the amount of crystallization required to reproduce the REE composition of the most evolved cpx by fractional crystallization of the least evolved cpx composition. The La content is reproduced after 25% crystallization, but 60% crystallization is required to account for Sm content and heavy REE contents. This discrepancy again indicates that fractional crystallization alone cannot explain the data.

The models of REE evolution by equilibrium and fractional crystallization developed above depend on the partition coefficients considered, and we explore here the potential impact of partition coefficient variations on the mineral trace element compositions. Two parameters strongly influence partition coefficient values: mineral composition and crystallization temperature. To incorporate mineral composition, we only determined partition coefficients using the compositionally dependent models of ***Wood and Blundy (1997)*** for cpx, ***Sun et al., (2017)*** for pl, and ***Sun and Liang (2014, 2013)*** for ol (*Table S4*). The partition coefficients were then used to calculate the melt compositions in equilibrium with the minerals in our samples, and average coefficients for each mineral were determined for the crystallization models. To test the control of temperature on the REE enrichments and fractionations during fractional crystallization, we used different sets of coefficients determined at 900, 1000, 1100, and 1200 °C. The results of the fractional crystallization models vary significantly with crystallization temperature (*Figure S3*). However, none of the models reproduce both the observed incompatible element enrichments and fractionations, further confirming that simple crystallization models cannot explain the geochemical signatures observed in our samples.

Similar conclusions are reached by considering the TiO_2 contents of cpx, as they are higher than expected after fractional crystallization in both lithologies, with strong enrichments developed at rather constant Mg#. Comparison of our data with cpx compositions produced by experimental petrology leads to the same conclusion. Equilibrium and fractional crystallization of typical tholeiitic melts produces cpx with TiO_2 contents lower than 0.6 wt% (***Villiger et al., 2007***; *Figure 3.57*). Even cpx crystallization from MORB-type melts enriched in Ti produces lower cpx TiO_2 contents at similar Mg# (***Koepke et al., 2018***), as Ti is preferentially incorporated into oxides in such melts. ***Ross and Elthon (1997)*** also described anomalous REE fractionations and incompatible element enrichments in cpx in samples from the MAR, and argued for the occurrence of "postcumulus crystal growth from or interaction with evolving intercumulus melts" to explain their data ('post-cumulus trend' in *Figure 3.57*).

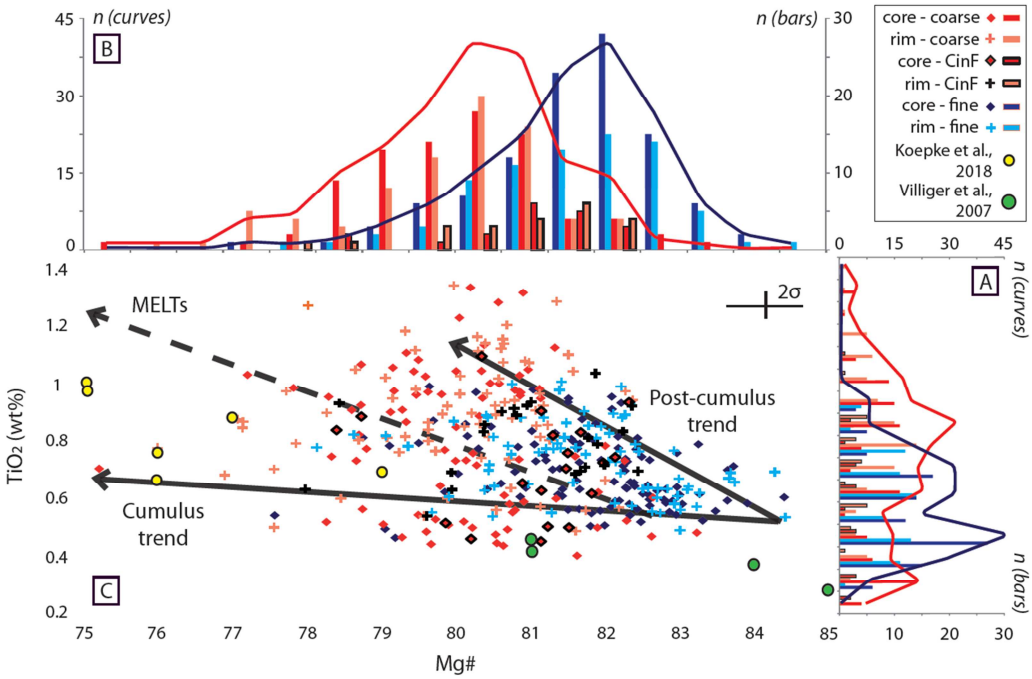

*Figure 3.57 - TiO_2 (wt%) versus Mg# of cpx from section 65R5 (**c**) and corresponding histograms for TiO_2 content (**a**) and Mg# (**b**) of the analyzed grains. Darker colors represent the cores of minerals and lighter colors their rims. The cumulus and post-cumulus trends are defined by Ross and Elthon (1997) and the fractional crystallization trend is from our MELTS model (Table S5). Results from equilibrium crystallization experiments on late-stage MORBs from Koepke et al. (2018), representing evolution under different water activities and redox conditions of Fe-Ti-rich melts, and results from equilibrium and fractional crystallization experiments on a tholeiitic magma from Villiger et al. (2007) are reported for comparison.*

Simple crystallization processes therefore fail to reproduce the incompatible element contents of the layered lithologies. As mentioned in section 4.2, subsolidus re-equilibration by diffusion at the cm-scale is unlikely in our samples, but grain-scale diffusion is rather common in such samples (e.g., ***Coogan & O'Hara, 2015***). The main effect of grain-scale diffusion and re-equilibration would be a smoothing of the initial magmatic signatures and a reduction of any potential core-to-rim variations in the samples. However, our samples record highly variable

compositions with strong incompatible element enrichments and fractionations in the coarse- and fine-grained layers, respectively. If grain-scale re-equilibration occurred, those signatures might represent a minimum estimate of the initial enrichment and fractionation recorded in the samples, which nonetheless cannot be reproduced by simple crystallization processes. Other processes must therefore be considered to explain the development of our layered section.

4.3.2 Arguments for the occurrence of Reactive Porous Flow (RPF), and related modeling

At Atlantis Bank (ODP Hole 735B), extreme trace element, and especially REE, enrichments and fractionations were highlighted by ***Gao et al.*** (***2007***; enrichment factors up to 2.7) and ***Lissenberg and MacLeod*** (***2016*** ; enrichment factors up to 20 in a single cpx grain). In both studies, the textures and compositions were attributed to melt-rock reactions between mushy cumulate lithologies and a percolating reactive melt. The same mineral textures interpreted as reactive textures in the previous studies are observed in the fine- and coarse-grained layers studied herein, such as resorbed cpx and pl grain boundaries (*Figure S3*). In addition, other crystallization processes have failed to reproduce the strong REE enrichments and fractionations in both the fine- and coarse-grained layers. The petrographic and geochemical characteristics of the studied gabbros thus suggest the occurrence of RPF in the layered section.

To confirm the implication of RPF in the formation of the layers and to constrain the parameters governing the processes for each lithology, we applied two numerical models to our system: the assimilation-fractional crystallization (AFC) model (***DePaolo, 1981***) and the plate model (***Vernières et al., 1997***). Both models consider a coupled evolution by crystallization of a percolating melt and assimilation of the percolation matrix. The plate model additionally accounts for a chromatographic effect induced by migration of the reactive melt, and differential trace element transport due to their variable incompatibilities. This process induces stronger fractionations between more and less incompatible elements, but not necessarily higher enrichments. ***Gao et al. (2007)*** and ***Lissenberg and MacLeod (2016)*** reproduced the REE fractionations and enrichments in their Atlantis Bank samples by AFC modeling, making AFC a suitable candidate for modeling the compositions recorded in our coarse-grained material, in which similar enrichments are observed. On the other hand, we applied the plate model to the fine-grained lithology because the main evidence for the occurrence of RPF in the fine-grained layers is the strong fractionation of light to heavy REEs.

Both models require the selection of input parameters consistent with the processes considered. In our models, the REE contents of the cumulate minerals are taken as the least differentiated ol, pl, and cpx compositions from the coarse-grained layers for the AFC model, and those from the fine-grained layers for the plate model. The composition of the percolating melt is difficult to constrain, but as only pl and cpx seem to be strongly impacted by the reaction, we selected a primitive melt composition from the Atlantis Bank area to interact with those two minerals: the diabase dike IODP 360-U1473A, 42R1 sampled in Hole U1473A at 382 mbsf. Temperature and pressure are not directly considered in either model, but can be implemented by tuning the partition coefficients selected for each mineral involved in the process; we used the partition coefficients determined at 1100 °C (*Table S4*).

4.3.2.1 AFC model applied to the coarse-grained lithology

Taking into account the documented chronology of emplacement and the fact that only the coarse-grained lithology is notably enriched in incompatible trace elements, this step of reaction most likely occurred before the emplacement of the fine-grained material. To avoid any potential interference from the homogenization reaction linked to the intruding event, we first consider only the samples located in the middle of the thickest layer (i.e., at ~63 cm from the top of the section; *see section 4.2*).

We modeled the reaction between the percolating melt and an equivalent primitive cumulate which modal mineralogy was obtained after 20% fractional crystallization of the primitive MORB-type melt from the area (obtained from the MELTS model, *Table S5*). Some of the compositional variability can be explained by fractional crystallization from the most primitive composition recorded in the samples, but RPF is required to reproduce all the data (*Figure 3.58a*). Different assimilation/crystallization ratios (r) are required to reproduce the entire range of fractionation represented by the Ce_N/Yb_N ratio of the equilibrium melts (*Figure 3.58a*), from a predominantly assimilation regime ($r = 0.9–0.99$) to more crystallization-driven regimes ($r = 0.8–0.7$). This variation likely indicates either heterogeneous percolation at the sample scale, with assimilation being favored in areas of preferential reactive melt circulation, or changes in porosity as the reaction proceeded. Porosity variations may eventually result in the closing of the porosity of the mush preventing further infiltration of the external melt, and favor larger amounts of crystallization.

To reproduce the entire range of parental melt compositions of the coarse-grained material, including areas affected by homogenization, we also modeled a simple mixing process between the most evolved melt compositions produced by AFC and three extremum liquids from the fine-grained layers (lower La/Lu ratios for variable Ce contents - *Figure 3.58b*). The results show that most of the data can be reproduced by such process, except for some rare Ce-rich melts that require further crystallization (*Figure 3.58b*). The formation of the coarse-grained lithology is therefore the consequence of the complex interplay between crystallization processes and at least two steps of reaction with percolating melts: first by AFC, and then by mixing after intrusion of the fine-grained lithology. This last step implies that the intruded lithology was not fully crystallized at the time of the intrusion. The first step of RPF linked to the evolution of the coarse-grained mush strongly impacted the REE composition of the minerals, which was then partially erased after the intrusion event. The lack of systematic zoning in the incompatible trace element contents then either reflects heterogeneous percolation and the uneven distribution of RPF signatures in the samples, or is the consequence of the additional homogenization process, which erased the initial signatures.

*Figure 3.58 - (**a**) Ce_N/Yb_N ratio versus Ce_N of liquids in equilibrium with cpx from the central layer of section 65R5 (N = normalized to primitive MORB composition of the Atlantis Bank area, from Coogan et al., 2004). Orange curve: fractional crystallization (FC) from the liquid in equilibrium with the least evolved cpx analyzed. Red curve: FC from the composition of the percolating reactive liquid, a primitive diabase sampled in Hole U1473A (Table S1). Black curves: assimilation-fractional crystallization (AFC) modeling reactive porous flow in the central coarse-grained layer for different ratios of mass assimilated/mass crystallized (r). (**b**) Ce_N/Yb_N ratio versus Ce_N of liquids in equilibrium with cpx from all coarse-grained layers of section 65R5. Gray curves are mixing curves between extremum compositions from the fine-grained range (blue points in the gray shaded area) and the most evolved compositions of the central layer after FC and AFC. The mixing curves are compared to FC from the least evolved (or most homogenized) composition of the coarse-grained material (orange curve) and AFC between the same composition and the reactive percolating diabase liquid (black curves).*

*(**c**) La_N/Lu_N ratio versus La_N of liquids in equilibrium with cpx from all fine-grained layers of section 65R5. Light-blue points: liquids in equilibrium with cpx present in three localized areas of extra-fine-grained material within the fine-grained layers. Solid orange curves: FC from the liquid in equilibrium with the least evolved cpx analyzed in the section (light blue) and with the least evolved cpx outside of the extra-fine-grained area (dark blue). Dashed orange curves: FC of only cpx from the light and dark blue compositions. Red curve: FC of the percolating reactive liquid (diabase).*

*(**d**) La_N/Lu_N ratio versus La_N of liquids in equilibrium with cpx from all fine-grained layers of section 65R5. Grey and black trends: plate model of reactive percolation associated with a chromatographic effect during transport for different modal compositions of the dissolved phases (see legend for details). For all sections, values in % represent the percentage of crystallization of the melt involved in the FC or AFC models.*

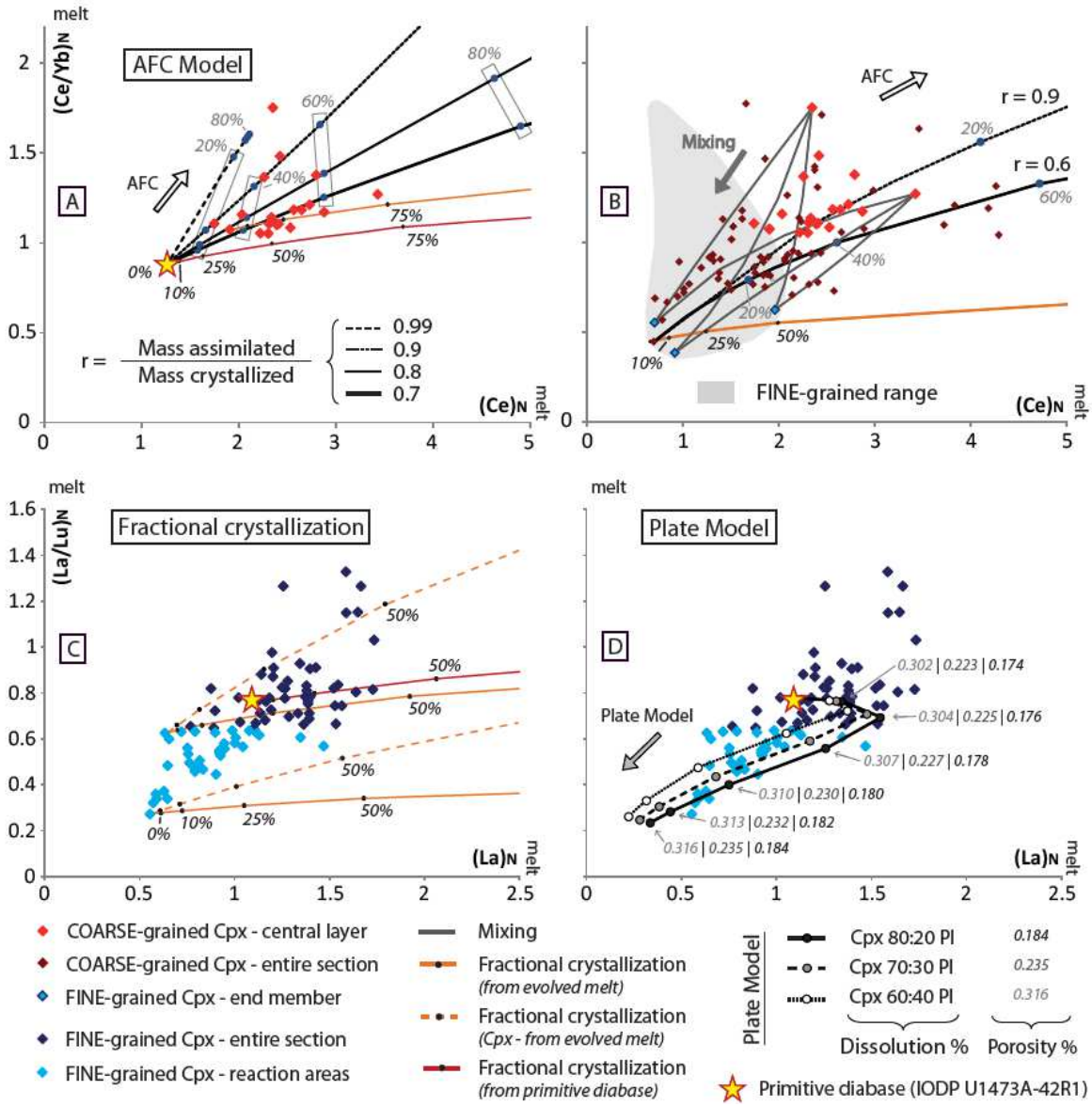

4.3.2.2 Plate model applied to the fine-grained lithology

According to our model, the fractionated signatures of the fine-grained material formed during the last stage of formation of the layered sequence. The specific locations of the minerals presenting these signatures indicate that the process leading to their formation was localized in three main areas of lighter color and finer grain size within the fine-grained material (*Figure 3.59*).

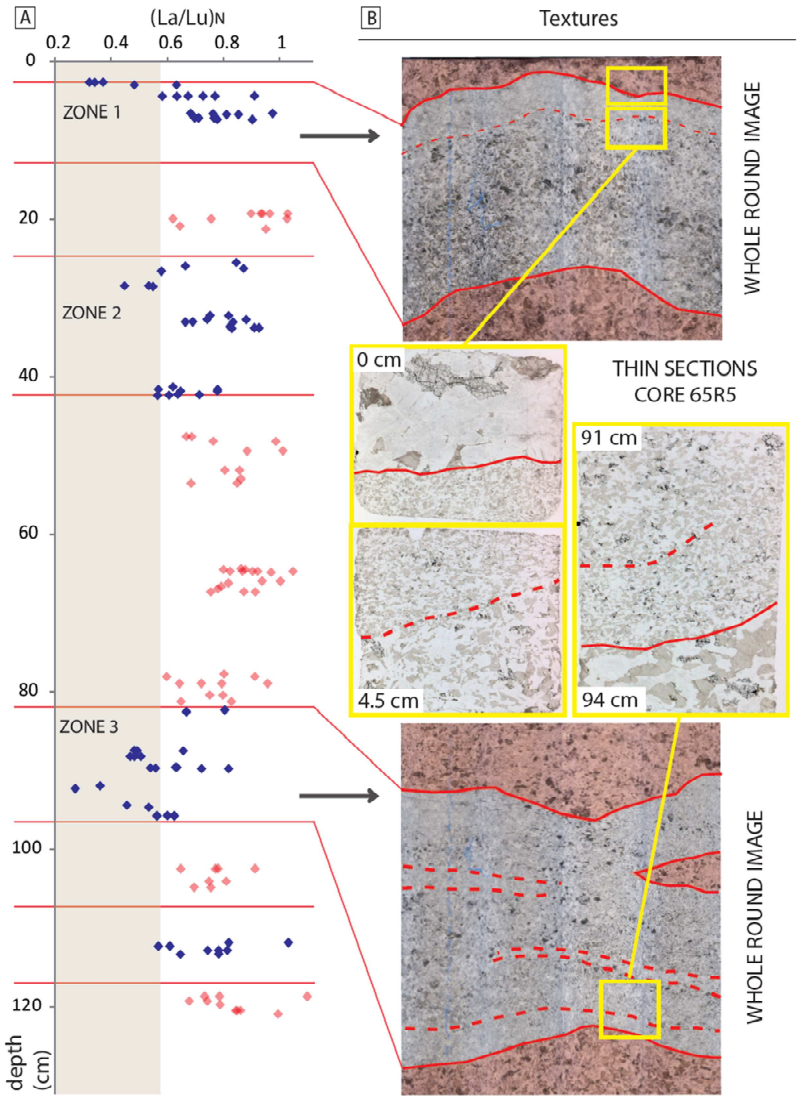

*Figure 3.59 - (**a**) La/Lu ratio of the liquids in equilibrium with cpx analyzed in the fine-grained-layers, normalized to the average primitive MORB composition of the Atlantis Bank area. Analyses of the coarse- (red) and fine-grained (blue) layers are represented. Red lines: layer contacts. The colored vertical band highlights the three extra-fine-grained zones presenting strong LREE fractionations. (**b**) Textural details are presented for zones 1 and 3, which are characterized by finer grained bands present within the fine-grained layers. Top and bottom: whole round scans centered on zone 1 and zone 3, respectively (contacts between finer grained material and the surrounding lithology represented by red dashed lines). Center: Photomicrographs of the corresponding thin sections. Areas in red correspond to the coarse-grained layers enclosing the fine-grained layers considered.*

To test how melt-rock reactions proceeded in these extra-fine-grained areas we applied the plate model, which combines both dissolution-precipitation and the chromatographic effect during melt percolation. The model considers a column of reactive cells in which the initial porosity controls the amount of reacting melt, which percolates from the bottom of the column where the reaction is the most complete. During melt percolation, dissolution and precipitation are applied successively in representative microvolumes of rock in which the extents of both reactions (and associated mineral proportions) can be parameterized according to their location in the column. The reaction considered is as follows:

$$cpx1 + pl1 + melt1 \rightarrow cpx2 + pl2 + melt2$$

Cpx and pl are dissolved in our model in proportions (cpx:pl) of 80:20, 70:30, and 60:40 (solid, dashed, and dotted lines, respectively, in *Figure 3.58d*), and the crystallizing cpx:pl assemblage is 30:70.The reactions result in a significant decrease of the La/Lu ratio, accompanied by a decrease in the La content of the liquid in equilibrium with the crystallizing minerals (*Figure 3.58d*). The La/Lu ratio decreases with increased cpx removal from the system (i.e., where the reaction is stronger at the bottom of the column). The porosity of the system increases with the degree of reaction for all three models and is consistent with the decreasing La content of the melt. Moreover, the porosity of the system is higher when a greater proportion of pl is dissolved because pl is the dominant phase of the percolated ol gabbro mush considered.

Beyond the three extra-fine-grained areas, fractional crystallization from a melt in equilibrium with the most depleted cpx in the fine-grained lithology is a good candidate to explain the evolution of the fine-grained lithology (dark blue points in *Figure 3.58c*), highlighting that the intruding melt mainly crystallized by fractional crystallization. On the other hand, the equilibrium melts with lower La_N/Lu_N values (0.3–0.6, blue dots in *Figure 3.59*) from the three extra-fine-grained areas cannot be reproduced by fractional crystallization (*Figure 3.58c*), and are well explained by the plate model (*Figure 3.58d*). The REE signatures of the three extra-fine-grained areas are therefore the consequence of evolution by reactive porous flow associated with a chromatographic component. Variations of the dissolved assemblages likely account for the local heterogeneities of the modal compositions throughout the section, or may be linked to the compositional evolution of the melt during the reaction and thus its ability to dissolve the minerals encountered. We interpret these areas as channels of porous flow of liquids through the lithology (*Figure 3.60*, Step 3). To create such localized flow, the rest of the fine-grained material was most likely at an advanced stage of crystallization, with this final step of RPF occurring during the last stage of formation of the section. This model would also explain the stronger deformation in the extra-fine-grained areas, with reinforcement of the pre-existing fabric by magmatic deformation in areas of localized melt flow.

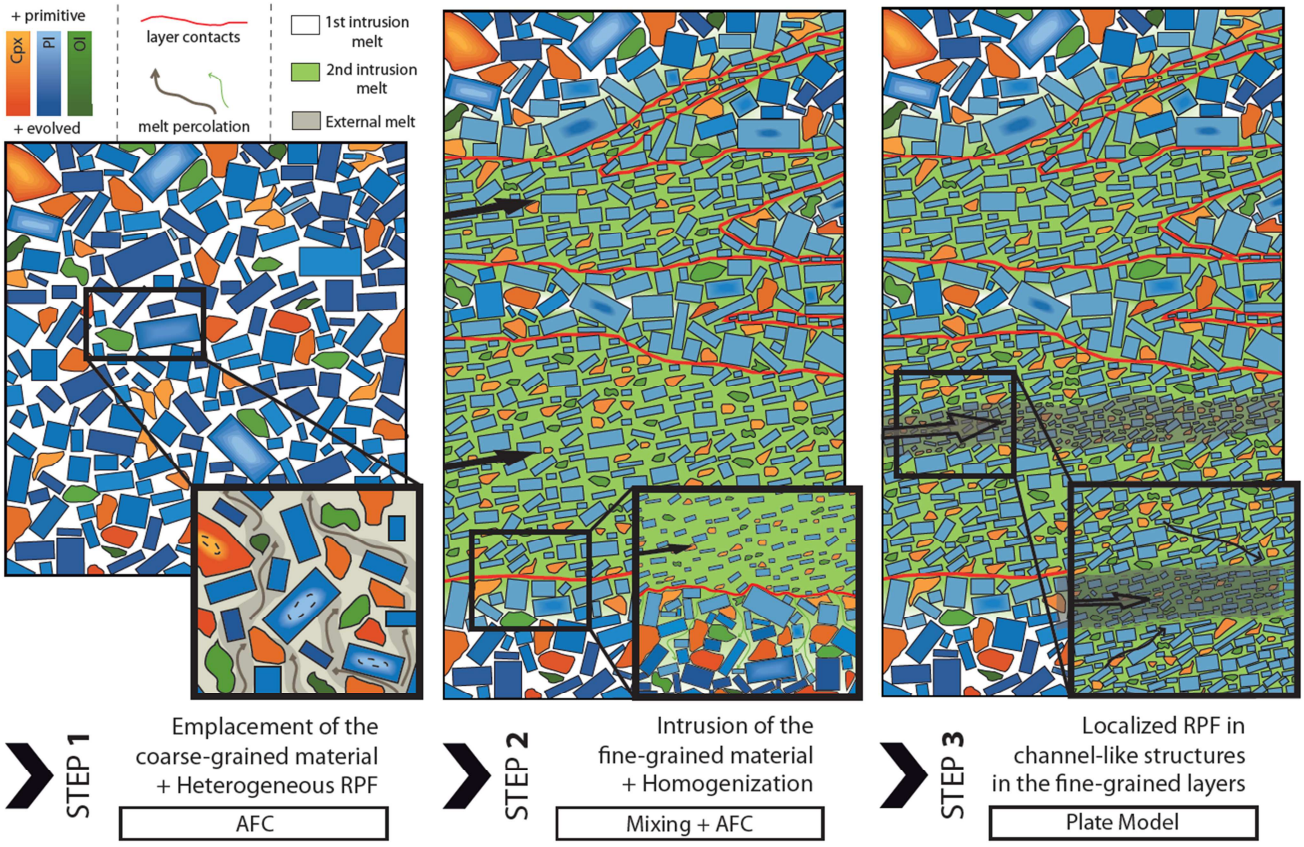

Figure 3.60 - Schematic model of formation of the layered section U1473A-65R5. Step 1: crystallization of the coarse-grained mush and widespread but heterogeneous reactive percolation of a primitive melt (darker areas and gray arrows in the outset enlarged view) resulting in incompatible trace element enrichment of the minerals. Step 2: intrusion of a crystal-bearing magma within the coarse-grained mush that is already at an advanced stage of solidification. Liquid from the intruding magma (green) infiltrates the coarse-grained material and undergoes fractional crystallization and mixing with any residual melt trapped in porosity (white). Step 3: localization of the porous flow within channel-like structures in the fine-grained material (darker area) forms extra-fine-grained domains that progressively transition to the fine-grained material. Incompatible element contents become strongly fractionated in those domains due to a chromatographic effect during melt migration.

4.4 Implications for melt migration processes during the evolution of lower crustal magma reservoirs

Similar grain size variations between fine-grained micrograbbros and coarser-grained ol gabbros were reported by ***Bloomer et al. (1991)*** in IODP Hole 735B. They observed both discrete layers with sharp intrusive relationships and irregular patchy pods of mixed microgabbros and ol gabbros. They also reported the same equigranular texture for the finer grained lithology and the same modal compositional range for the ol gabbro, but only 25–30% of the grain size variations are associated with a similar type of layering as observed in our study. They inferred two main processes for the formation of the layering and the patchy structures: (1) changes of crystallization conditions and subsequent nucleation and growth rates, and (2) the occurrence of intrusions of crystal mushes or the redistribution of crystal density by

development of crystal-rich plumes or local slumps of material, both occurring at the border of an irregularly shaped magma chamber. Interestingly, they also qualified the finer grained lithology as "intrusive in a local sense", as in the model developed herein, and hypothesized that the distinct lithologies potentially had initially different cumulus compositions now "erased by intermingling of intercumulus liquids and re-equilibration", a process very similar to the homogenization process implemented here. Despite the differences with the final model developed herein, the similarity between the characteristic structures of Hole 735 and U1473A indicate that our conclusions are pertinent to the evolution of magmatic reservoirs at Atlantis Bank.

The whole-round core images allow unique estimation of the relative dip direction of any structure observed in the cores, and of the successive layering (*Figure 3.61a, b*). A planar contact is represented by a sinusoidal trace on the whole-round image, with the dip direction given by the azimuth of the sinusoid minimum (*Figure 3.61a*). The whole round image of section 65R5 shows that the successive layers are heterogeneously organized, with the two fine-grained layers at the top of the section displaying subparallel margins (~2–12 cm and ~26–44 cm depth in the section), the third pinching towards the front of the core (~80–98 cm depth), and the fourth pinching towards the back of the core (~109–118 cm depth, *Figure 3.61b*). It is also clear from the whole-round images that the two fine-grained layers at the top of the section merge together backward of the core, and that the central coarse-grained layer also pinches backward. These structural features indicate that the lateral extent of the layers described herein is not at the scale of several meters, but rather likely represent an interfingered contact between two larger intrusions (*Figure 3.61b-d*).

The exact lateral extent of the structure and the size of the intrusive bodies are difficult to establish. Such an intrusion of a more primitive magma into a mush recalls geophysical observations of magma sills stacked at various depths and different stages of crystallization, with thicknesses ranging from tens to hundreds of meters (***Canales et al., 2017***). However, our interpretation tentatively shows that such regular layering is not ubiquitous at IODP Hole U1473A (*Figure 3.49a*) because the number of magma bodies emplaced in the accreting crust was likely limited (e.g., ***Dick et al., 2000***) and because such structures are poorly preserved due to subsequent overprinting due to plastic deformation (***MacLeod et al., 2017***).

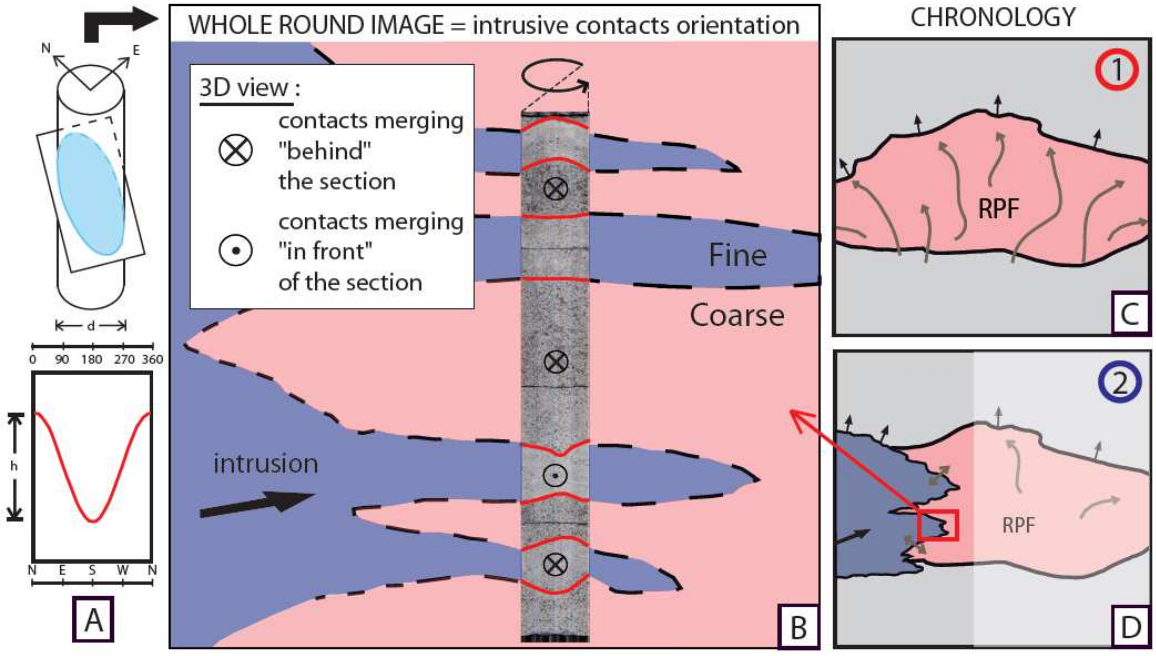

Figure 3.61 - Integrated model of the formation of the layered series in section U1473A-65R5. (a) Interpretation scheme of the geometric features present in the whole-round scan of a drilled core (here, schematically, a plane crosscutting the core). (b) Interpretation of the layered geometry of the section and the contacts between the two crosscutting lithologies. (c) First step of formation: crystallization of the initial mush (formation of the coarse-grained lithology, red) and subsequent reactive percolation (RPF, gray arrows). Black arrows: melts escaping from the open-system mush due to buoyancy, compaction, and/or deformation. (d) Second step of formation: intrusion of the second crystal-bearing magma, leading to the formation of the fine-grained lithology (purple). Double gray arrows: interactions and homogenization at the contact of the two lithologies.

5 Conclusions

This study is the first high-resolution petrographic, microstructural, and geochemical study of a layered olivine gabbro section from the slow-spreading lower oceanic crust sampled at Atlantis Bank. Our study emphasizes the importance of melt migration and interaction processes during magma emplacement at the ridge axis. We show that melt migration by reactive porous flow and intrusion was involved in the formation of this layered section, the latter being directly responsible for the formation of the layered structure. Combined petrographic observations and geochemical analyses enabled us to use numerical models to quantify the melt-rock reactions linked to reactive porous flow. We propose that reactive porous flow is ubiquitous during the formation of the section, although at different scales, and left a significant geochemical imprint on the samples. During the first formation step of the sequence, widespread melt migration occurred heterogeneously (at the sample scale) by widespread reactive porous flow, whereas the last step of evolution of the olivine gabbro layers occurred as the localized migration of interstitial melts in small-scale channel-like structures. The models used to quantify the reactions illustrate that the consequences of reactive porous flow are

dependent on the distribution and efficiency of migration. In addition, we highlight that interactions and related homogenization between the crystallizing mush and the intrusive crystal-bearing magma occurred during the intrusion event, overprinting the already intricate geochemical signatures of the section. Such a complex superposition of geochemical signatures from various and successive magmatic processes was only resolved by our high-resolution approach because the section was preserved from subsequent alteration or crystal-plastic deformation. Finally, although the grain-size variations described here are not ubiquitous along the drilled core, similar observations have been reported elsewhere and in other drilled cores from Atlantis Bank. The magmatic and fluid percolation processes described herein therefore likely represent a key process in the formation of the lower crust at this location.

Acknowledgments

We express our warm thanks to the various people involved at different technical stages in this work: Christophe Nevado and Doriane Delmas (Geosciences Montpellier) for their high quality thin sections, and Jean-Luc Devidal (LMV) and Fabrice Barou (Geosciences Montpellier) for their assistance during EPMA and EBSD measurements, respectively. This research used data provided by the International Ocean Discovery Program (IODP). We gratefully acknowledge the Captain and shipboard crew of IODP Expedition 360 for their assistance in data collection at sea. We wish to thank the Scientific Party of IODP Expedition 360 for fruitful discussions during the cruise and post-cruise meeting. This study also benefited from discussions with David Jousselin (CRPG), and Kathi Faak (RUB), and from thorough reviews by Laurence Coogan, two anonymous reviewers, and the editor Marie Edmonds. We thank Robert Dennen for English phrasing improvements. This research was supported by CNRS-INSU and IODP-France. MB's PhD project was funded by the French ministry of research (MESRI). This is CRPG contribution number XXXX.

CHAPTER IV.

Multi-stage development of a magma reservoir at a slow-spreading center

New high-resolution structural and geochemical characterization of a preserved primitive portion of ODP Hole 735B, Atlantis Bank (Southwest Indian Ridge)

MUSHY MAGMA RESERVOIR EMPLACEMENT AND EVOLUTION AT SLOW-SPREADING CENTERS

Marine Boulanger[1,2], Lydéric France[1], Jeremy Deans[3], Carlotta Ferrando[1]

[1]Centre de Recherches Pétrographiques et Géochimiques, Université de Lorraine, CNRS, Vandœuvre-lès-Nancy, France.

[2]Institut für Mineralogie, Leibniz Universität Hannover, Callinstr. 3, D-30167 Hannover, Germany.

[3]School of Biological, Environmental, and Earth Sciences, University of Southern Mississippi, Hattiesburg, MS, USA

Keywords: Atlantis Bank, lower oceanic crust, magma intrusion, reactive porous flow, Assimilation-Fractional Crystallization

---

This draft article has been accepted for submission at *Frontiers in Earth Science* (submission deadline January 20), as part of the special research topic "*Magma-rock and magma-mush interactions as fundamental processes of magmatic differentiation*".

Supplementary materials to be submitted together with the article are reported in Appendix 2 and comprise:

- Appendix 2.1: Mineral *in situ* major element compositions (Table S1)
- Appendix 2.2: Mineral *in situ* trace element contents (Table S2)
- Appendix 2.3: Details on the modeling of fractional crystallization by MELTS and normalization values for the graphic representations involving Rare Earth Elements (Table S3)
- Appendix 2.4: Details on the Assimilation-Fractional Crystallization models described in this Chapter (Table S4)

Abstract

Several ODP-IODP expeditions drilled Oceanic Core Complexes (OCCs) interpreted as exhumed portions of lower crust close to the ridge axis, opening potential for providing further constraints on magmatic processes involved in the formation of the slow-spread lower oceanic crust. We focus on a ~250 m thick plutonic section of ODP Hole 735B presenting the most primitive lithologies sampled at Atlantis Bank OCC (Southwest Indian Ridge) and interpreted as a single crustal intrusion. We combined detailed structural and petrographic constraints with whole rock and *in situ* mineral analyses in order to quantify processes of emplacement, crystallization and melts migration within the lower crust. The lower half of the unit presents alternations between olivine gabbros and troctolites showing intrusive contacts and magmatic deformation. Such structures and most primitive lithologies are lacking in the upper half rather uniform gabbroic sequence. Whole rock compositions highlight the cumulative character of both lower and upper units and a great compositional variability in the lower sequence, whereas the upper sequence is homogeneous and differentiates upsection. *In situ* analyses of mineral phases document magma emplacement processes and the ubiquity of reactive porous flow processes during differentiation. We propose that the whole section constitutes a single magmatic reservoir, in which the lower unit is formed by stacked primitive sills and was subject to repeated recharge of primitive melts. Recharges led to partial assimilation of the crystallizing primitive cumulates present within the sills, and hybridization with interstitial melts. Hybrid melts were progressively collected in the overlying mushy part of the reservoir, whereas the sills' residual hybrid melts differentiated by reactive porous flow processes under a predominant crystallization regime. Similarly in the upper unit, hybrid melts evolution was governed by upward reactive porous flow and progressive differentiation and accumulation of evolved melts at the top of the reservoir. We suggest that the overall upward porous flow result from a "melt flushing" process triggered by the continuous recharge of the reservoir. Our results eventually provide the community with a unique model for magma reservoir formation in the lower slow-spread oceanic crust, that all or part can be applied to other in situ sections.

1 Introduction

Slow-spreading ridges represent more than 50% of the global oceanic ridge system (spreading rates <40 mm year^{-1}, ***Dunn, 2015***) and are characterized by the heterogeneity of both the oceanic crust structure and composition they generate. Most of this heterogeneity can be linked to uneven repartition and strength of the mantle melt supply below the ridge axis (e.g., ***Tucholke and Lin, 1994; Dunn et al., 2005; Rubin and Sinton, 2007; Dunn, 2015*** and references therein). It results in the formation of intermittent and discontinuous magma reservoirs within the crust (e.g. ***Carbotte et al., 2015; Dick et al., 2003***), contrasted reservoirs geometry, and variable depths of melt emplacement which can range between 2 and 16 km depth below seafloor (***Bennett et al., 2019; Canales et al., 2017; Dunn et al., 2005; Singh et al., 2006***). Thus, the characterization of an igneous reservoir model potentially applicable to various sections of magmatic lower crust appears unlikely, even though the dynamics of igneous reservoirs and magmatic processes involved in their evolution are crucial to understand slow-spreading lower oceanic crust accretion. The common thread running through all processes that potentially govern magma accretion at spreading ridges is the importance of the type of melt migration involved. Among them, reactive porous flow and associated melt-rock reactions tend to be considered as ubiquitous during the evolution of magma reservoirs, since crystal-mushes constitutes the principal medium of the magma plumbing systems (***Lissenberg et al., 2019*** and references therein).

Long *in situ* sections of lower slow-spreading oceanic crust have been sampled by deep drilling in Oceanic Core Complexes (OCCs). These structures form during asymmetric spreading at the ridge axis and associated exhumation of both lower oceanic crust and upper mantle (e.g., ***Ciazela et al., 2015; Escartín et al., 2003; Ildefonse et al., 2007***). Two of the drilled holes reach more than 1400 mbsf (meters below sea floor), one in the Atlantis Massif OCC on the Mid-Atlantic Ridge (MAR, IODP Hole U1309D), and the other in the Atlantis Bank OCC on the Southwest Indian Ridge (SWIR, ODP Hole 735B). Their study enabled to precise the modes of magma emplacement and evolution at these locations. The crust appears highly heterogeneous in both structures and lack any systematic downhole variations in modal compositions, or lateral continuity as evidence at Atlantis Bank (***Blackman et al., 2006; Dick et al., 2000; Dick et al., 2019***). Thanks to whole rock compositions and together with the lack of modal downhole variations, ***Godard et al., (2009)*** interpreted the cumulate sequence sampled in Atlantis Massif as the result of multiple magma injections related to a common parental melt. Upward differentiation trends with wavelength >200 m have been identified in ODP Hole 735B based on whole rock major element compositions (***Dick et al., 2000***), and in situ mineral compositions (***Dick et al., 2002***); those are interpreted as the result of cyclic intrusion that differentiated in

situ during upward percolation of melts (***Dick et al., 2000***). Despite the disparities between the ODP Hole 735B and IODP Hole U1309D, similar type of magma emplacement by along-axis intrusions have been inferred by the authors that suggest a continuity of processes for the accretion of the lower slow-spreading oceanic crust (***Dick et al., 2019a***). In particular, detailed studies of individual samples collected in drilled cores from both Atlantis Massif and Atlantis Bank enabled to find evidence for extensive melt-rock or melt-mush reactions (in olivine rich troctolites from Hole U1309D, ***Drouin et al., 2009; Ferrando et al., 2018; Suhr et al., 2008;*** or in gabbroic samples from Hole 735B ***Dick et al., 2002***; ***Natland and Dick, 2001; Robinson et al., 2000***).

Here we combine a structural, petrographic and high-resolution geochemical study of a ~250 m section from ODP Hole 735B characterized as a single intrusion by ***Dick et al. (2000)***. We aim at reconstructing the different steps of evolution of a magma reservoir and the impact of RPF processes within such reservoir of the slow-spread lower oceanic crust sampled at Atlantis Bank.

2 Geological setting

The Atlantis Bank OCC locates on the eastern flank of the Atlantis II Transform Fault ~ 95 km south of the ultra-slow SWIR (***Dick et al., 1991*** - *Figure 4.62*). The ~2 km uplift of lower crust lithologies at Atlantis Bank is the consequence of a ~1 km flexural uplift due to detachment faulting, exacerbated by transform-parallel normal faulting on the eastern flank of the structure. The latter event is linked to a change of spreading direction at the ridge axis between 19.5 and ~12 Ma (***Baines et al., 2003***). The OCC is mainly composed of gabbroic lithologies, bordered to the East by extrusive lithologies (dikes and pillow lavas) and to the West by mantle lithologies affected by variable degrees of serpentinization (***Dick et al., 2000; MacLeod et al., 2017***). The top of the structure forms a 30 km-large and 40-km long horizontal platform at ~700 m depth below sea level, in which three deep holes have been drilled by the ODP/IODP consortium (***MacLeod et al., 2017***).

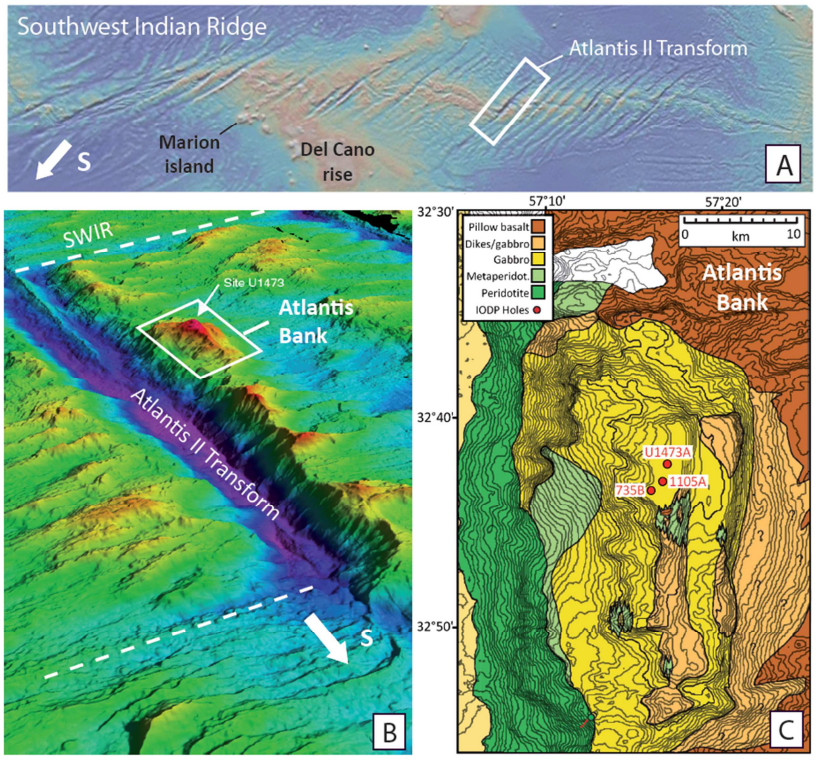

Figure 4.62. (a) Location map of the Atlantis II Transform on the Southwest Indian Ridge (b) 3D bathymetric map of the Atlantis II Transform and location of the Atlantis Bank Oceanic Core Complex (IODP Publications), and (c) geological map of the Atlantis Bank OCC and location of ODP Holes 735B and 1105A, and IODP Hole U1473A (modified from Dick et al., 2016).

The oldest, deepest and most studied so far is the ODP Hole 735B that reached a total depth of 1508 m, and in which ~1300 m of gabbroic lithologies were recovered. The drilled cores are composed of 68% olivine gabbros, 23% of oxide and oxide-bearing gabbros, in addition to 5% troctolites and 4% gabbros *sensu stricto*. Some minor lithologies such as diabase dikes and felsic veins were also recovered (***Dick et al., 2000***). Whole rock and *in situ* major element compositions both present three to five upward differentiation trends (*Figure 4.63*). Each trend has been interpreted as the signature of individual intrusions, potentially crosscutting each other, and emplaced during large magmatic events (***Dick et al., 2002, 2000***). In this study we focus on the second unit from the top, which is among the two more primitive ones (Mg# = molar ratio $Mg/[Mg+Fe_{tot}]x100$ of Ti-poor lithologies ranging between 74.5 and 86.8). The unit is the less altered and less deformed of the drilled core, and present the entire range of rocks recovered in Hole 735B.

The intrusion has been described as two separate units during IODP Leg 118 & Leg 176 (***Dick et al., 2000; Dick et al., 1991***). The upper Unit V is a massive olivine gabbro unit of 108.3 m long. The lower Unit VI is described as a "lower compound olivine gabbro" of 153.6 m long including more than 200 distinct intervals. In details, Unit VI is composed of 4 intersected subunits of olivine gabbros or troctolites, crosscut by various amounts of synkinematic oxide gabbros (***Dick et al., 2000***). The intrusion is bordered at the top by a 50.5 m-long massive oxide gabbro unit (Unit IV) and at the bottom by a 63 m-long gabbronorite and oxide gabbronorite unit (Unit VII). Oxide-rich lithologies are often associated with strain localization areas and are interpreted as a consequence of late-stage synkinematic differentiation, caused by expulsion of evolved liquids from crystallizing gabbro bodies that emplace and impregnate other gabbroic protoliths (***Dick et al., 2000; Natland et al., 1991***).

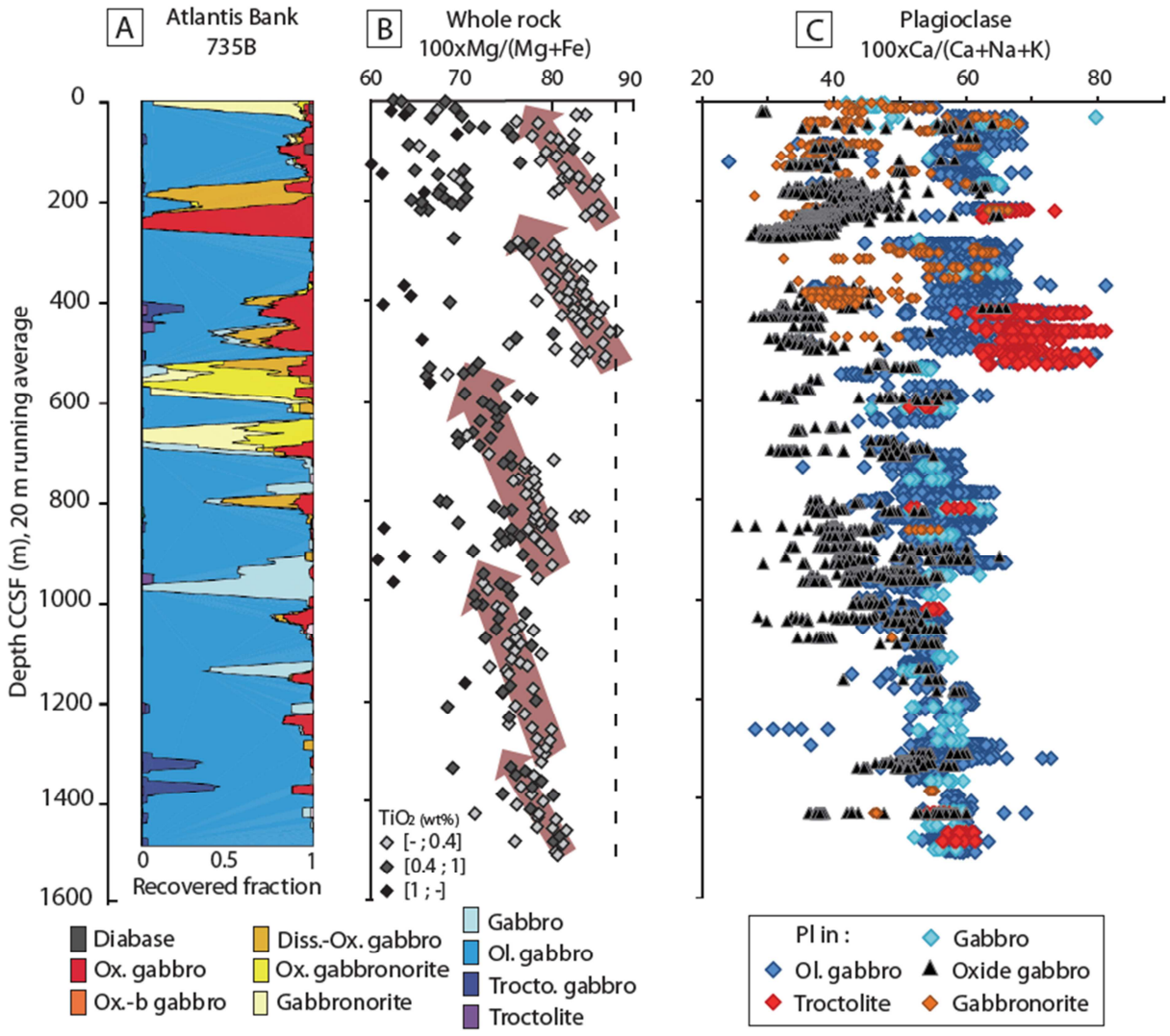

Figure 4.63. Comparison between (a) the lithostratigraphic variations of Hole 735B with relative abundances averaged over 20 m (from Dick et al., 2016), (b) the corresponding shipboard XRF whole rock gabbro Mg# trends (modified from Dick et al., 2000) and (c) in situ plagioclase An content (data from Dick et al., 2002).

3 *Methods*

The structure and textures of Unit V and VI from ODP Hole 735B were re-described at the Kochi Core Center, where the Atlantis Bank drilled cores are stored. Magmatic fabrics are defined by a shape preferred orientation of igneous phases like plagioclase, pyroxene, and/or olivine with no to little internal crystal-plastic strain and no recrystallization. Crystal-plastic fabrics are defined by a shape preferred orientation of porphyroclasts and neoblasts with internal crystal-plastic strain. The level development of each fabric type is based on a ranking system plotted as a thickness corrected running average developed by the Shipboard Scientific Party (***Dick et al., 1999***). Magmatic fabrics range from no alignment, rank of 0, to almost all phases are aligned, rank of 3. Crystal-plastic fabrics range from no alignment, rank of 0, to porphyroclastic (close to equal proportion of porphyroclasts and noeblasts), rank of 3, to ultramylonite, rank of 5. Contacts are defined by changes in mineral proportion, grain size, and/or sheared contacts. Contacts used here were defined and delineated by the Shipboard Scientific Party (1999). In total, 50 new gabbroic lithologies (olivine gabbros and troctolites) were resampled following a strategy based on the available whole rock data (*Figure 4.63*), in order to cover the entire range of compositions covered by the targeted section. The mineral mode of each sample was determined thanks to thin section scans processed using the ImageJ software.

Major element contents of minerals from 33 samples were quantified by Electron Probe Micro Analyzer (EPMA) at Laboratoire Magmas et Volcans (Clermont-Ferrand, France) with a Cameca SX100 equipped with 4 wavelengths dispersive X-ray spectrometers (WDS). Analyses were performed with a 15kV accelerating potential and a focused beam using a 15nA beam current. Counting times were of 10 or 20s (see details and calibration standards for each element in *Table S1*) on peak and also for background. The data and associated analytical errors are available in supplementary materials.

In-situ trace elements of 24 samples were analyzed with a ThermoFinnigan Element2 XR (eXtended Range - ICP-MS) coupled with a laser ablation (LA) system Téledyne G2 at Géosciences Montpellier (AETE-ISO regional facility of the OSU OREME, Montpellier University, France). Signal acquisition was made in Time Resolved Acquisition, counting 120 s for the background, and 60 s for the sample measurement. The frequency of the laser was of 10 Hz, with an energy density of ~6.2 J.cm^2. Ablation experiments were conducted under helium which was mixed with argon before entering the plasma. Clinopyroxenes (cpx) were analyzed with a laser spot size of 77 µm, while a spot size of 102 µm was used for olivines (ol) and plagioclases (pl). Data were processed using the GLITTER software (***Van Achterberg et al., 2001*** - *Table S2*). All measured concentrations were calibrated using the synthetic glass NIST 612 with the values of

Pearce et al. (1997). The internal standards used for the minerals are 43Ca for cpx, and 29Si for pl and ol. An average of the values analyzed by LA-ICP-MS for the standard reference basalt BIR-1G is available in Supplementary Materials (*Tables S1 and S2*), together with all trace elements data and associated analytical errors.

4 Results

Despite the first order relative continuity of compositions suggested by the whole rock geochemical trends (e.g. Mg# - *Figure 4.63*), the section can be divided in two distinct units based on structural, lithological and geochemical criteria. In the following we refer to the Upper Unit and to the Lower Unit, which correspond to the ensemble formed by Unit V and Unit VI as described by ***Dick et al., (2000)***.

4.1 *Structure and petrographic variations of the selected intrusion*

The Lower unit is heterogeneous and presents numerous igneous contacts recovered at different depths all along the section, between ~ 395 mbsf and 530 mbsf. The subunit's thickness ranges from meters to tens of meters. The presence and rank of crystal-plastic and magmatic fabrics are highly variable with depth and are recorded in all lithologies (*Figure 4.64a*). The more primitive lithologies representing the primary magmatic background of the sequence show magmatic fabrics whose intensity varies along the section. Textures are subophitic to granular with grain size varying from medium to coarse-grained; lithologies range from the more primitive troctolites and ol rich gabbros to modal compositions with less olivine in ol gabbros and gabbros (*Figure 4.64b*). The transition between lithologies is gradational within each subunits that are separated of each other by igneous contacts. In general, the modal composition in ol tends to decrease (from 69% to 0%) and proportions of interstitial cpx increase (from 1% to 64%) towards the top of each subunit. Sparse evidences for weak compaction are present such as intragrain deformation, for example, tapered twins in pl and subgrain development in ol. Minerals presenting reaction and dissolution textures are common in this Lower unit, for example rounded ol grains in poikilitic pl, and cpx in the troctolites, dissolved pl crystals in poikilitic cpx, and pl crystals with ragged grain boundaries and complex zoning in ol gabbros(*Figure 4.65c-d*).

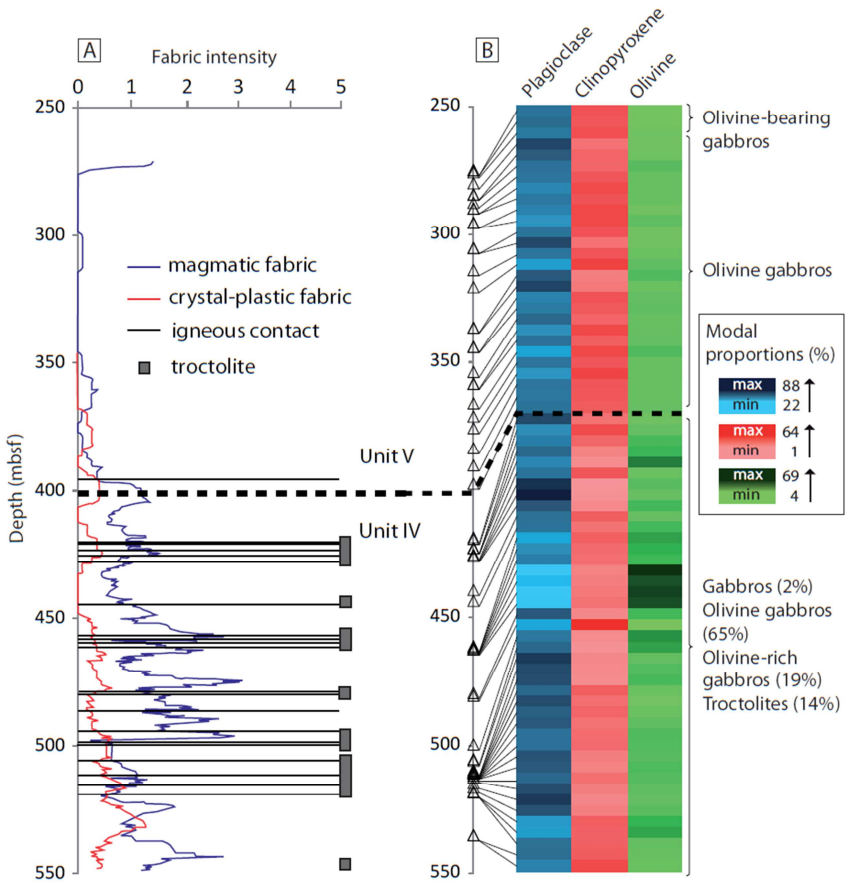

Figure 4.64. (a) Downhole evolution of the fabric intensity. Red line is magmatic fabric intensity; blue line is crystal-plastic intensity. The fabric intensity is a qualitative scale developed by Shipboard Scientific Party (1999) and the intensity is plotted as a thickness-corrected running average. The horizontal black lines represent igneous contacts (Natland & Dick, 2002, their Table 1). The gray boxes are the location of troctolites. (b) Location at depth of the samples collected in Unit V and VI (Dick et al., 2000) with their corresponding modal compositions. The proportions of each lithology are presented on the right side of the diagram. The black dotted line represents the transition between the Lower and the Upper unit.

The Upper unit is homogeneous and generally lacks the common intrusive features and the marked magmatic fabrics of the Lower unit (*Figure 4.64a*). The Upper unit is composed of ol gabbros with an average 60% pl, 30% cpx and 10% ol. At the very top of the unit at ~ 275 mbsf the ol proportions decrease down to 4% with the presence of more differentiated ol bearing gabbros (*Figure 4.64b*). The initial description by ***Dick et al. (2000)*** characterized these last samples as felsic veins, due to the presence of several areas of conjugated veins filed with felsic material crosscutting the primary gabbroic lithology. Closer to the veins, minerals present interaction textures with amphiboles rims around cpx, completely dissolved ol grains and strong zoning of the pl. Similar lithologies have been reported from Atlantis Bank IODP Hole U1473A; those are referred as "*felsic rocks with diffused boundaries (vein-D)*" by ***Nguyen et al. (2018)***, and interpreted as felsic melts infiltration into solidifying gabbros. In the rest of the Upper unit ubiquitous evidences for dissolution and interactions with melts are found. Cpx intergrowths are common, and pl crystals with dissolved grain boundaries and complex zoning together with symplectite textures in cpx (*Figure 4.65a-b*).

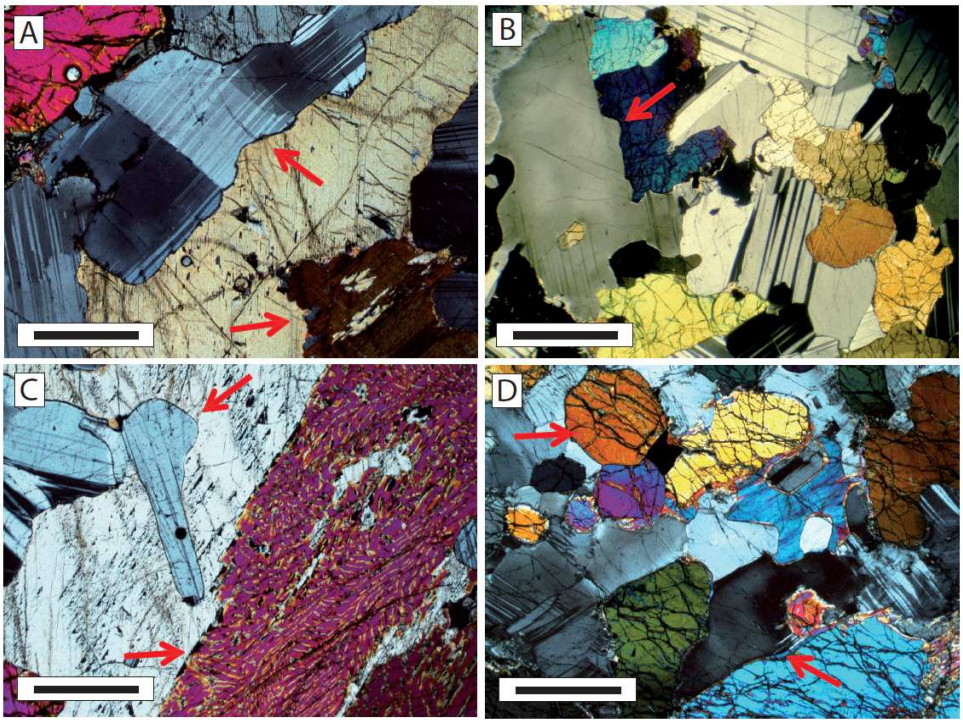

Figure 4.65. Microphotographs in polarized light on samples from the Upper unit (a and b) and from the Lower unit (c and d) presenting reactive textures. Scale bar: 500 µm. (a) Sample 735B-60R4-115 cm: Plagioclase grain presenting dissolved grain boundaries (top red arrow) and clinopyroxenes intergrowth (bottom arrow). (b) Sample 735B-72R3-0 cm: Plagioclase grain presenting complex zoning and dissolved grain boundaries. (c) Sample 735B-81R5-7 cm: Plagioclase grain with dissolved grain boundaries (top arrow) engulfed in a clinopyroxene crystal presenting symplectite textures (bottom arrow). (d) Sample 735B-83R7-130 cm: Rounded-shape olivine crystals (top arrow) and plagioclase presenting complex zoning (bottom arrow).

4.2 Whole rock and in situ geochemical compositions of the intrusion

The whole rock compositions used herein for the Upper and Lower units are from the ***Shipboard Scientific Party - Leg 118 (1989), Dick et al. (1999), Dick et al. (1991), Hart et al. (1999), Hertogen et al. (2002), Holm (2002)*** and ***Niu et al. (2002)***. Both units present samples with weak to strong cumulative signatures in Rare Earth Elements (depletion in LREE relative to MREE and HREE, and positive Eu anomalies), a cumulate character of the lithologies already identified by ***Dick et al. (2000, 1991)***. Compatible element contents (e.g., Cr) and Mg# recorded in the Lower unit reach higher values compared to the Upper unit, which highlights a more primitive character of the considered lithologies below ~400 mbsf (*Figure 4.66*). Compositions are also more heterogeneous in the Lower unit, with for example variation ranges in Cr contents of ~3500 ppm in the Lower unit and of only ~750 ppm in the Upper unit. The Upper unit presents a progressive upward differentiation trend in Mg# (ranging between 82.8 and 67) and relatively constant compositions through depth in compatible and incompatible trace elements, except in the very top ~50 m of the unit where the Cr contents decrease (*Figure 4.66b*).

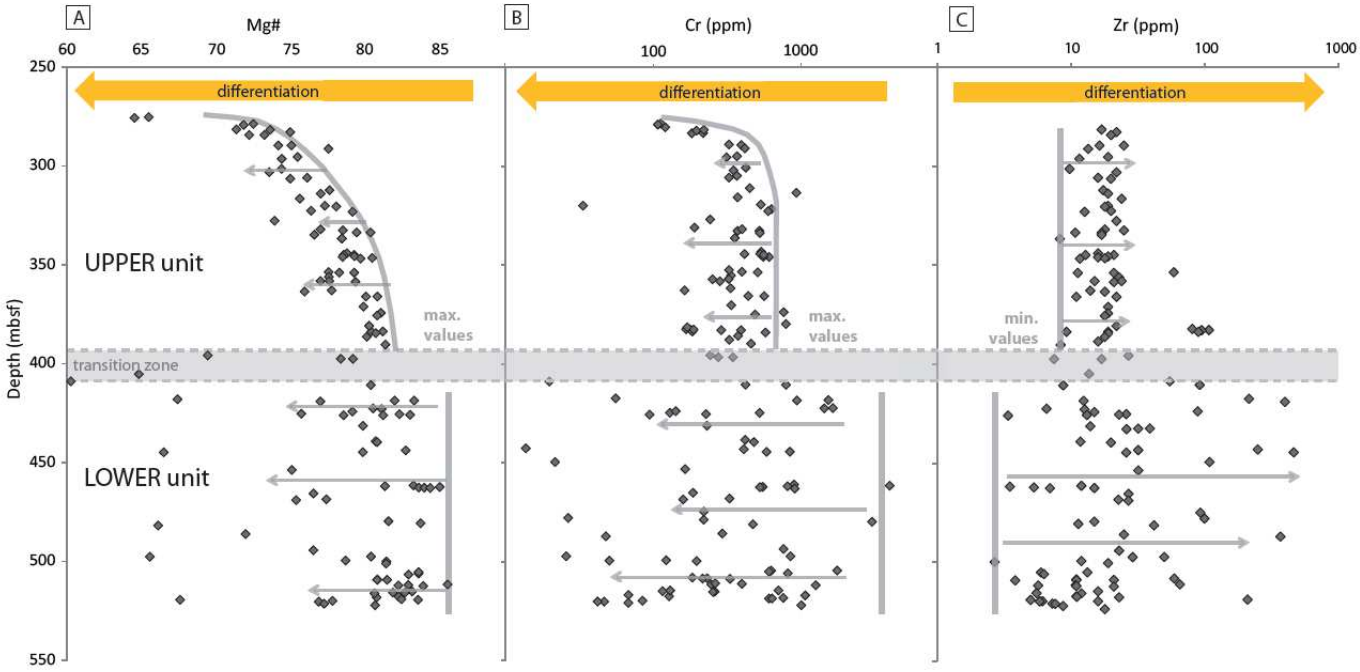

Figure 4.66. Downhole evolution of whole rock Mg# (a) - molar ratio Mg/[Mg+Fe_{tot}]x100), Cr content (b) - in ppm) and Zr content (c)- in ppm) in Hole 735B Unit V and VI. Grey trends represent the more primitive values (maximum or minimum values) and grey arrows the schematic extent of differentiation at a given depth.

In situ major and trace element compositions of the samples collected along the section (*Figure 4.64*) are consistent with whole rock data, and provide further key information for our understanding of this igneous system. The maximum *in situ* An content of pl (An content = molar ratio Ca/[Ca+Na+K] x 100), and of Mg# and Cr contents of cpx are higher in the Lower unit compared to the corresponding maximum values in the Upper unit (*Figure 4.67*). Those differentiation tracers are also heterogeneous in the Lower unit regardless of the lithology considered (troctolite or ol gabbro). In addition, the compositional variability recorded in a single sample or at the same depth is much greater in the Lower unit compared to the Upper one. For example, the cpx Cr contents range between 0.85 and 0.2 wt% at 462 mbsf (variation of 0.65 percentage points), when on average at a single depth the contents only vary of 0.17 percentage points in the Upper unit. However in the upper ~20 m of the section, the cpx Mg# and Cr contents and the pl An content drop toward the top of the unit (*Figure 4.67*). The compositions fall down to 61.9 Mg#, 0.007 wt% Cr, and 10.4 An content in the felsic rocks with diffused boundaries. No clear systematic zoning of the mineral is observed in the Lower unit in major and compatible elements, whereas in the Upper unit a normal zoning in Mg# and An content is observed in the upper 20 m of the section (*Figure 4.67*).

Minerals incompatible element contents are in average more enriched in the rims of the minerals, such as Ti in cpx and La in pl (*Figure 4.68*). Although they display lower initial values, the cpx Ti contents increase to higher contents for a given Mg# in the most primitive minerals of the Lower unit (with Mg# > 85, up to 1.8 wt% TiO_2) compared to the minerals in the Upper one

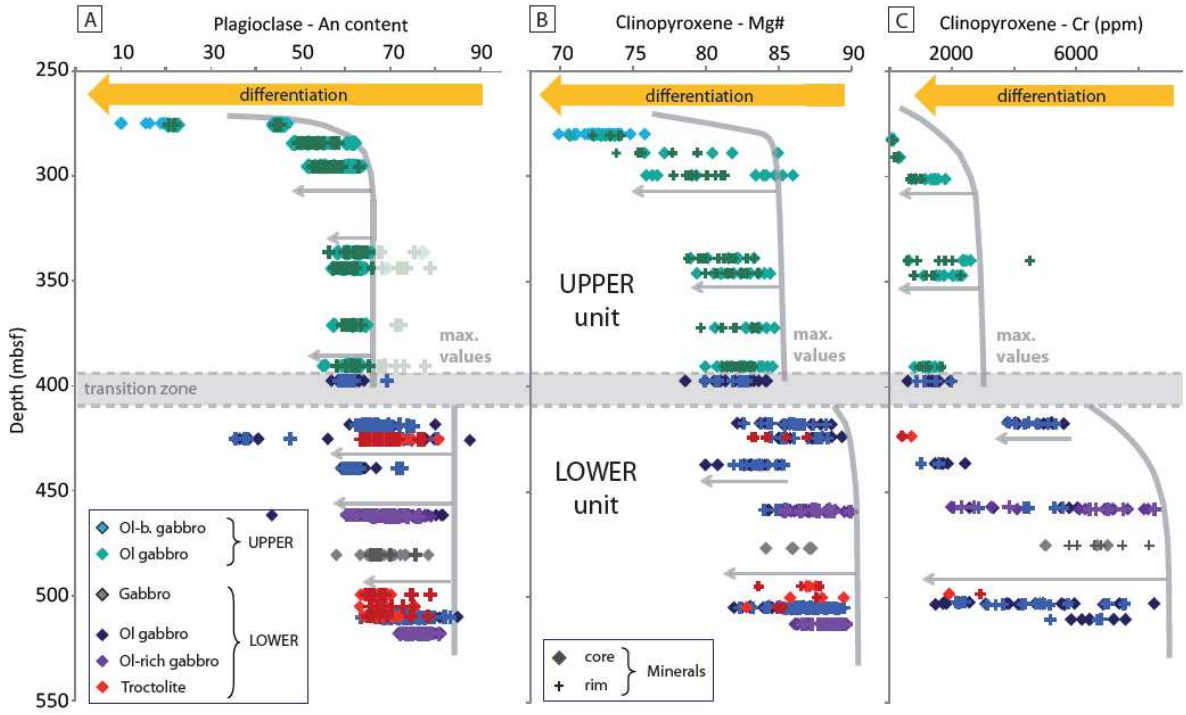

Figure 4.67. Downhole composition evolution along Hole 735B Unit V and VI of in situ (a) plagioclase An content, (b) clinopyroxene Mg# and (c) clinopyroxene Cr content (in ppm). Grey trends represent the maximum values and grey arrows the schematic extent of differentiation at a given depth.

(*Figure 4.68a*). On opposite, Rare Earth Elements (REE) content in pl varies within similar ranges of compositions for Upper and Lower units despite significant differences in the minerals' major element contents (*Figure 4.68b*). For example, the pl La_N content ranges between 0.58 and 4.35 in the Lower Unit for an average minerals An content of 69.3, and ranges between 0.58 and 4.6 in the Upper unit for an average minerals An content of 55.4. In the same minerals, fractionation between more to less incompatible REEs (described for example by the ratio La_N/Sm_N) tend to high values with La_N/Sm_N ranging between 0.88 and 7.9.

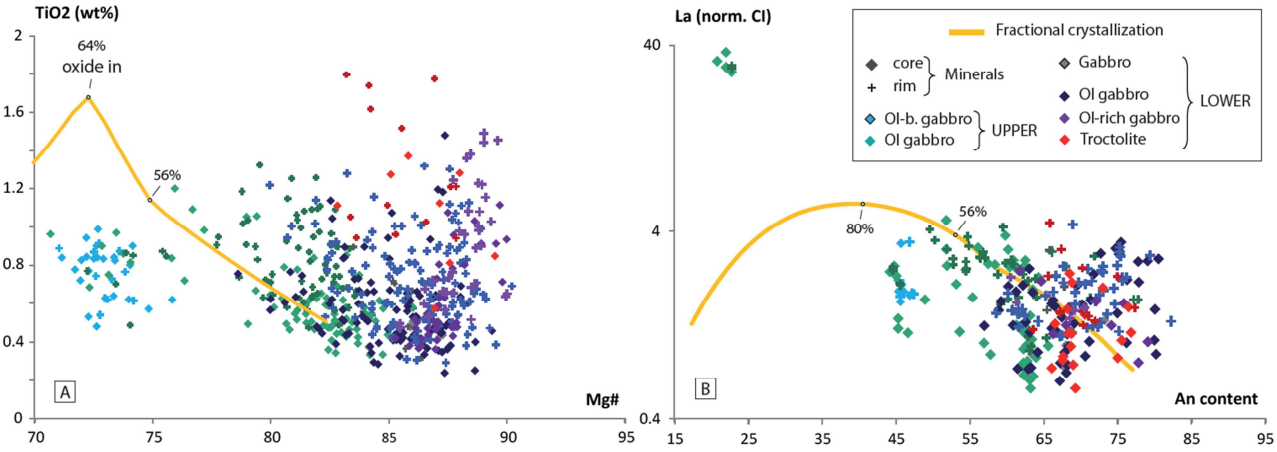

Figure 4.68. (a) TiO_2 concentrations in clinopyroxenes plotted against the minerals' Mg#. (b) Chondrite-normalized La concentrations in plagioclases plotted against the minerals' An contents. Normalization values after McDonough & Su, (1995). The orange trend correspond to the evolution by fractional crystallization of an average primitive MORB composition for the Atlantis Bank area determined by MELTS (details in the supplementary materials - Table S3).

5 Discussion

5.1 Model of emplacement and evolution of the magma reservoir

A two-step evolution model emerges from the combined observation of structure, textures and geochemical compositions of the gabbroic sequence. In the Lower unit (~125 m thick), the variability in the compositions recorded in the hole, together with the presence of 20 intrusive contacts and the associated magmatic fabrics, indicate that the Lower unit most likely formed from emplacement of in average 6 m thick sills stacked at the bottom of the intrusion. It could also explain the presence of magmatic fabrics preferentially localized in the Lower unit. Indeed as described in ***Boulanger et al. (submitted)***, magmatic fabric can be related to intrusive events as a consequence of magmatic deformation during magma emplacement. This hypothesis is reinforced by the progressive transition from ol rich lithologies to ol gabbros observed within the ~5 m thick subunits, indicating a progressive magma evolution from bottom to top of the sills. The degree of differentiation within each unit seems to vary from one subunit to the other according to the variable ranges of compositions recorded in the samples. In addition, the cumulative character of the lithologies and textures indicative of subtle compaction indicates that melt at some point was extracted from the crystallizing mushes.

The Upper unit is a massive ol gabbro sequence lacking any particular structure. The most primitive mineral compositions are very homogeneous through the section, and indicate crystallization during a common magmatic event. At the top of the unit, the presence of more evolved ol bearing gabbros and more differentiated geochemical signatures of the cumulates indicate a progressive differentiation towards the top of the sequence. In contrast to the whole rock compositions, the *in situ* analysis of minerals do not display this progressive evolution toward the top of the unit, and rather show a constant higher bound on more than 100 m thick. Only the very upper part of the Upper unit record more evolved compositions. We interpret these contrasted signatures as the sign of an increase of the amount of evolved interstitial melt accumulation in the reservoir towards the top of the Upper unit. Both units were built thanks to very distinct magma reservoir dynamics (*Figure 4.69*). On one hand the Lower unit formed by stacking of primitive sills, and on the other hand the homogeneous Upper unit formed during a single magmatic event, with progressive melt evolution and accumulation towards the top of the unit. However in spite of the disparities listed above, the two units are part of the same broad differentiation trend at the scale of the entire Hole 735B, suggesting that the magmatic events that lead to their formation were linked, as suggested by ***Dick et al., (2000)***. Melt extraction evidence in the Lower unit and the overall more differentiated character of the Upper unit suggests that the primary melt that fed the Upper reservoir was collected from the Lower one.

Another similarity between the two units is the common, if not ubiquitous, occurrence of reactive textures regardless of the lithology considered (*Figure 4.65*). The same type of textures have been previously described in Hole 735B and in other gabbroic sections sampled in modern slow-spread oceanic crust. They have been interpreted as the result of RPF processes, and assimilation of crystals during percolation of melt(s) through the porosity of a mush (***Lissenberg et al., 2019*** and references therein). To test this hypothesis, we modeled the evolution by fractional crystallization (FC) at crustal pressure (0.2 GPa) of a primary melt composition thanks to the rhyolite-MELTS model (***Ghiorso and Gualda, 2015; Gualda and Ghiorso, 2015*** - details in the supplementary materials *Table S3*). Cpx Ti contents and Mg# expected after FC are both lower than the actual content of the minerals from both the Lower and the Upper unit (*Figure 4.68a*). Both these signatures have already been interpreted as evidences for the occurrence of MRR in lower oceanic crust section (e.g. ***Lissenberg and Dick, 2008*** for the Mg# and ***Leuthold et al., 2018*** for the Ti contents). Hence, the geochemical signatures of the studied igneous unit support this hypothesis and are consistent with an evolution by RPF. Hereafter we quantify the MRR that govern the evolution of both Upper, and Lower units by RPF.

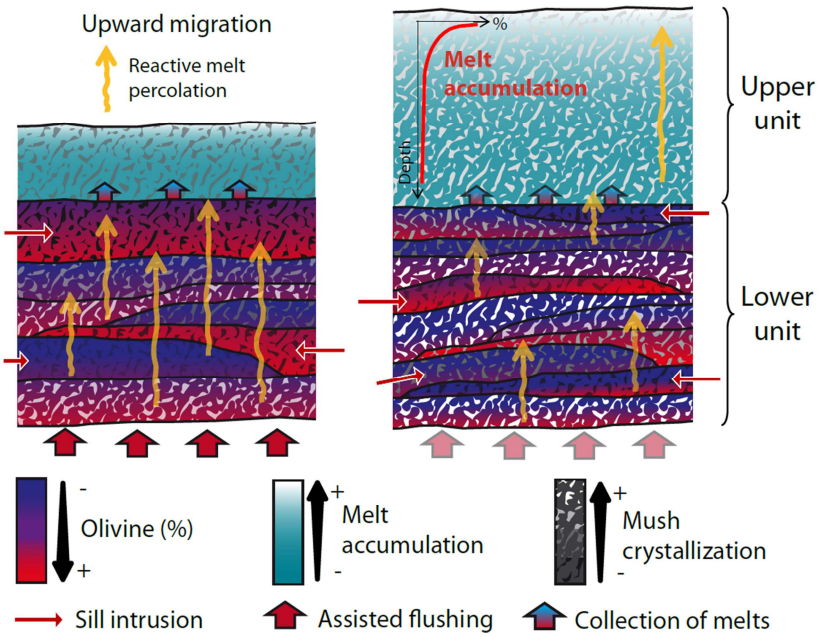

Figure 4.69. Model of formation of the magma reservoir implying the intrusion of sills in the Lower unit, and progressive extraction and collection of the melts in the Upper unit of the reservoir. Widespread occurrence of reactive textures suggests the implication of reactive porous flow processes in both units, and accumulation of melts at the top of the intrusion.

5.1.1 Evolution of melts within the Lower unit

The widespread involvement of MRR in the evolution of the Lower unit is supported by the pervasive reactive textures found in the samples, and by the major and minor element

compositional trends that fail to be reproduced by simple FC models. In order to better constrain the reactions involved, and the extent of RPF in the sequence, we modeled the evolution of the minerals REE contents after both FC and MRR. We focused on the pl compositions as this mineral is the most abundant in all samples (58% in average - *Figure 4.64b*), and pl is less subject to post-crystallization reequilibration than ol due to slower diffusion of the REE (e.g. ***Cherniak, 2003; Spandler and O'Neill, 2010***).

The evolution by FC is based on the crystallization sequence given by the MELTS model described above (and in supplementary materials *Table S3*). Two initial REE contents were considered, first the average composition of primitive MORB-type melts from the AB area (also used for the MELTS modeling), and second the average composition of the pl equilibrium melts which present the lower La contents and La/Sm ratios of the unit, i.e. the most primitive signatures. The global partition coefficient of the crystallized mass was calculated for each increment of fractionation, and was then used to determine the composition of the crystallizing minerals. For each temperature step of the MELTS model, minerals REE partition coefficients were calculated thanks to the models of ***Sun and Liang (2014, 2013)*** for ol, ***Sun et al. (2017)*** for pl and ***Wood and Blundy (1997)*** for cpx. The results for both initial melts show that evolution by FC fails to reproduce the REE compositional ranges of pl, and more specifically the progressive increase of fractionation between more to less incompatible REE that we quantify with the La/Sm ratio (*Figure 4.70a*).

To test the hypothesis of RPF, and to better constrain the reactions involved, we applied the assimilation-fractional crystallization model (AFC equation from ***DePaolo, 1981***). The model reproduces an evolution by assimilation of a preexisting crystal matrix by a disequilibrium melt, and simultaneous crystallization of a new generation of minerals. The input parameters are the composition of the percolating melt, the composition and proportion of assimilated phases, and the proportion of the minerals crystallized during the reaction. The modal compositions of the assimilated and crystallized compounds were strongly constrained thanks to the reactive textures and the modal compositions of the lithologies recovered in the Lower unit. The general reaction considered is as follow:

$$Ol1 + Pl1 + melt1 \rightarrow Ol2 + Pl2 + Cpx + melt2$$

The composition of the assimilated phases was taken as the composition of the minerals (with ~1:1 ol and pl) determined by MELTS after 12% FC. In addition, we used the partition coefficients calculated for ol, pl and cpx analyzed in the Lower unit. The same two melt REE compositions considered in the FC models were used as the reactive melt composition in the AFC model.

A first general AFC model considering the percolation of a melt with the composition of the average equilibrium melts through a troctolitic mush manages to reproduce the compositional range recorded in the samples, and especially the increase of fractionation between more to less incompatible REEs (*Figure 4.70c*). The ratios Mass assimilated / Mass crystallized considered varies between 0.5 and 0.99. Such variations potentially highlight a progressive change of the RPF process parameters. A decrease of the ratio might reflect a progressive closure of the crystal matrix porosity during the reaction, and the promotion of crystallization over assimilation due to a decrease of the disequilibrium melt flow. The variations might also reflect the heterogeneous character of the reaction in space, and the presence of areas with enhanced percolation or areas of preferred crystallization. However, even though an average AFC model manages to reproduce the compositional range of the Lower unit, we showed that the modal compositions of the lithologies recovered are highly heterogeneous. This contrasts with the idea of a common process involved in the formation of all the lithologies of the Lower unit. The type of reactive textures encountered is also correlated to the modal composition of the sample considered. For example, the ol crystals which present the more advanced dissolution textures are found in the ol rich lithologies, together with poikilitic pl and cpx (*Figure 4.65*). Altogether, results of modeling and the reaction history recorded in the textures of the samples suggest that the different steps of assimilation and crystallization are decoupled during the reaction.

An alternative model is that the initial primitive melt involved in the reaction has the composition of the average primitive melt from the AB area. In that case, pl with the lower La_N contents and the lower La_N/Sm_N ratios analyzed in the unit cannot be reproduced by the previous average AFC reaction. In agreement with the assimilation and crystallization decoupling hypothesis suggested above, a first step of intensive ol and pl assimilation, and secondary pl crystallization is possible and enables to reproduce the most depleted and fractionated compositions (*Figure 4.70b*). This assumption is supported by the presence of troctolites in the sequence which present heavily dissolved ol crystals and poikilitic pl enclosing the latter, with modal contents of pl reaching ~90%. The second step of evolution of the unit would then correspond to the reaction initially presented, i.e. reaction of the troctolitic matrix with the average equilibrium melt of the section (i.e., Figure 9b and then Figure 9c). The exact composition of the initial reactive melt is arduous to determine, and the previous results suggest that the reaction sequence is likely specific to each lithology sampled. However in general, the evolution of the Lower unit is governed by RPF processes and the reaction between a primitive melt and a troctolitic crystal matrix.

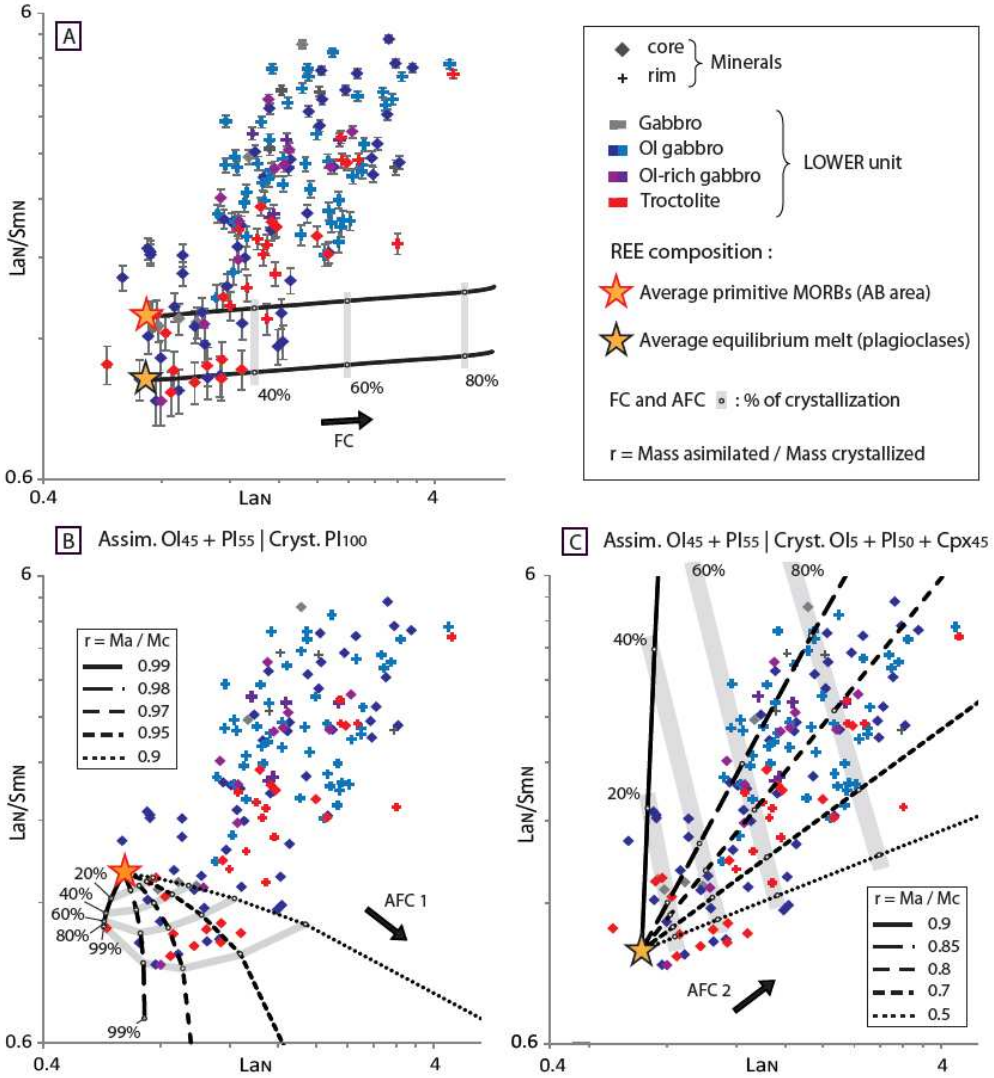

Figure 4.70. La_N/Sm_N ratio versus La_N analyzed in plagioclases from the Lower unit of ODP Hole 735B (N = normalized to primitive MORB composition of the Atlantis Bank area, from Coogan et al., 2004). (a) Modeling of the plagioclase compositions expected after Fractional Crystallization (FC) from two different parental melts, the average primitive MORB of the Atlantis Bank area (star with red), and the melt in equilibrium with the plagioclase presenting the more depleted La compositions and the lower La/Sm ratios (star with black rim). The error bars on the sample analyses represent a 1σ error on the values. (b) Modeling of the plagioclase compositions expected after Assimilation-Fractional Crystallization (AFC1) of a troctolitic matrix (45% Olivine + 55% Plagioclase) by the average primitive MORB-type melt (star with red rim) with crystallization of plagioclase exclusively. (c) Modeling of the plagioclase compositions expected after Assimilation-Fractional Crystallization (AFC2) of a troctolitic matrix (45% Olivine + 55% Plagioclase) by the melt in equilibrium with the more depleted plagioclases (star with black rim) with crystallization of a gabbroic assemblage (5% Olivine + 50% Plagioclase + 55% Clinopyroxene).
Details in Table S3 and S4

5.1.2 Origin and evolution of melts within the Upper unit

The geochemical continuity of compositions of the 250 m thick sequence, and the evidences for melt extraction observed in the Lower unit suggest that melt(s) were extracted from this unit and collected to form the homogeneous Upper sequence. The stage of evolution at which this extraction occurs can be inferred thanks to the geochemical characteristics of the Upper unit. Mineral major element compositions of the upper sequence are more differentiated,

with, for example, maximum pl An content of 63 recorded in the Upper unit, while the more primitive An contents recorded in the Lower unit are up to 87.7. After an evolution by FC of the primitive MORB determined by MELTS, a pl An content of 63 would correspond to 50% crystallization. However, we determined earlier that RPF is the dominant process during the evolution of the Lower unit, which precludes the collection of a melt in the upper reservoir that only experienced FC during its evolution. In addition, there is a decoupling between the minerals major element contents and the REE contents of the same minerals. For example, the most depleted pl La contents in the Upper unit are similar to those in the Lower unit (*Figure 4.71b*). The only difference in terms of REE compositions between the parental melts of the two units is the slightly stronger fractionation (represented by the La/Sm ratio) recorded in the Upper one. We proposed earlier (see 5.1.1.) that assimilation and crystallization might be chronologically decoupled in the Lower unit with crystallization following assimilation, leading to the formation of lithologies with a large range of modal compositions. This decoupling was already considered by ***Lissenberg and Dick (2008)*** for the oceanic environment, based on the work of ***Edwards and Russell (1998)*** or ***Reiners et al. (1995)***. A major consequence of this decoupling is the potential increase of the melt fraction in the system during the first step of reaction by predominant assimilation that would favor remobilization of melts.

The general reaction sequence established for the evolution of the Lower unit involves assimilation of ol and pl, and crystallization of mainly pl and cpx. We tested if the first step of predominant assimilation of a troctolitic matrix by a primitive MORB-type melt could lead to the formation of a melt with a composition consistent with the one that fed the Upper unit. We determined by mass balance the theoretical compositions of hybrid melts resulting from such an assimilation step. To proceed, we used the composition of the average primitive MORB from which variable fractions of ol and pl were added (= assimilation), and variable fractions of cpx were removed (= crystallization). The compositions of the minerals used for calculations are the average compositions of minerals from the Lower unit. This RPF model results in a hybrid melt composition that is, for example, enriched in Mg, and depleted in Ca (*Figure 4.71a*). In order to check if this hybrid melt can account for the melt that fed the Upper unit, we run MELTS models using the corresponding hybrid melt major element composition, and compared the obtained minerals compositions to the ones of the natural samples. The rationale behind this comparison is to check if the first phases to crystallize in the Upper unit (i.e., the most primitive ol and pl) can crystallize from this hybrid melt; further differentiation (by FC, or MRR-RPF) within this Upper unit will be tested in the following section. The best fit to the compositions of the natural samples was obtained by addition of 30% of a troctolitic matrix (30% pl and 70% ol) with the primitive MORB melt, and a removal of 10% cpx (fractional crystallization of the hybrid melt at 1100°C, 2 kbar, and [H_2O] = 0.2 wt%). The model shows that the compositions of ol and pl

crystallizing from the hybrid melt are Fo_{74} and An_{63}, respectively, when the corresponding compositions in natural samples from the Upper unit are Fo_{76} and An_{63}. The model therefore perfectly matches the composition of the first phases to crystallize in the Upper unit (i.e., the most primitive ol and pl). The cpx that likely formed after further evolution of the Upper unit melts are enriched in Mg in natural samples (Mg# = 85) in comparison to those obtained by modelling the direct crystallization of the hybrid melt with MELTS (Mg# = 79). This discrepancy in cpx composition highlights that the Upper unit experienced further differentiation (by FC, or MRR-RPF); those processes will be quantified in the next section. The associated evolution of the hybrid melts REE contents expected after such predominant assimilation stage would explain the decoupling observed between major and trace elements in the section. Assimilation of REE-poor materials (ol+pl), together with the small fraction of cpx crystallized, imply relatively stable REE contents of the melt during the reaction despite the simultaneous significant changes in the major element contents of the melt. This effect could also explain the relatively constant range of La compositions at variable An contents from the Lower and the Upper unit. For example, at low An contents the La concentrations in the pl is very low compared to the contents expected after FC (down to 0.58 La_N - *Figure 4.68b*). However, the exact initial melt REE composition involved in the formation of the Upper unit is difficult to determine. The construction of the Lower unit by several sill intrusions and recharge implies a potential great variability of melt compositions present at the same time within the unit. In addition, variable extents of mixing between those melts are likely.

We then constrain the evolution of melts collected in the Upper reservoir following their extraction from the Lower unit. We first modeled evolution by FC (following the method used for FC in 5.1.1) of two different starting compositions in REE. The first one is the melt in equilibrium with the most primitive pl of the Upper unit (lower La contents and lower La/Sm ratios), and the second is a melt composition resulting from the general AFC model applied to the Lower unit. Both FC models fail to reproduce the compositional range recorded in the Upper unit, and especially the increase of fractionation between more to less incompatible REE that we quantify with the La/Sm ratio (*Figure 4.71c*). We then applied two AFC models involving interactions between the latter melts, and a troctolitic matrix with the following reaction:

$$Ol + Pl1 + melt1 \rightarrow Pl2 + Cpx + melt2$$

The AFC model involving the equilibrium melt reproduces the entire compositional range of the Upper unit, with ratios Mass assimilated / Mass crystallized varying between 0.6 and 0.92 (AFC1 - *Figure 4.71c*). However, a contribution of melts that previously experienced various step of evolution in the Lower unit, and that display more enriched and fractionated signatures cannot be excluded. RPF processes involving such melts (e.g., AFC2 in *Figure 4.71c*)

also reproduce part of the compositional range recorded in the Upper unit. Overall, RPF processes are the predominant processes governing the evolution of the Upper reservoir, and shape the rock textures, crystal morphologies and compositions, and the modal proportions of rocks. The occurrence of RPF during the formation of the Upper unit also explain the major element compositions of the cpx that present high Mg#. Indeed cpx Mg# tends to increase during MRR as the Mg content of the melt increase by assimilation of ol (***Lissenberg and Dick, 2008***).

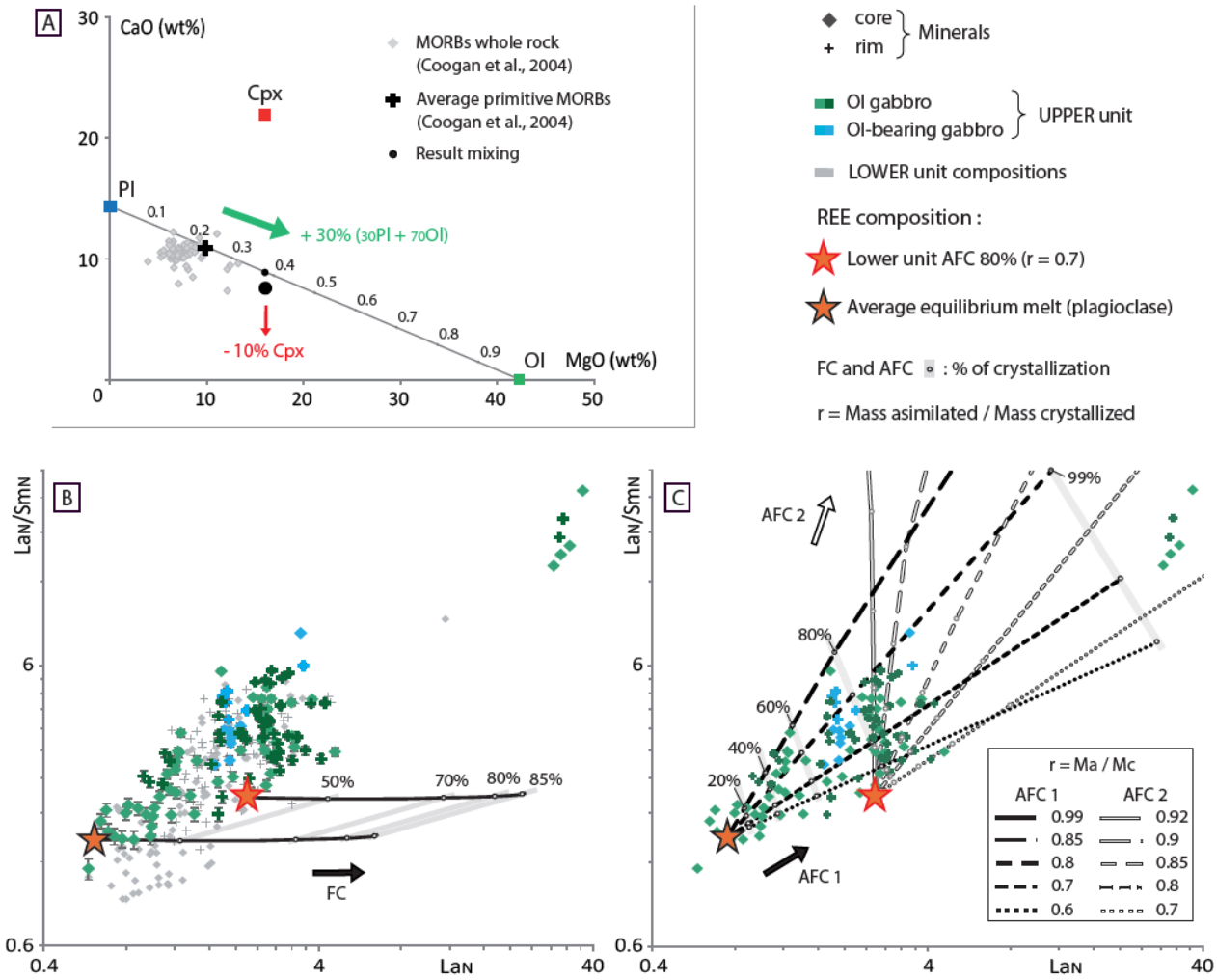

Figure 4.71. (a) Evolution of the composition in CaO (wt%) and MgO (wt%) of a primitive MORB-type melt after 1/ assimilation of a troctolitic component with 40% Plagicolase (Pl) and 60% Olivine (Ol) (green arrow), and 2/ crystallization of clinopyroxene (Cpx) (red arrow). Black line: Mixing line between the Pl and Ol end member compositions. (b) and (c) La_N/Sm_N ratio versus La_N analyzed in plagioclases from the Upper unit of ODP Hole 735B (N = normalized to primitive MORB composition of the Atlantis Bank area, from Coogan et al., 2004). (b) Modeling of the plagioclase compositions expected after Fractional Crystallization (FC) from two different parental melts, the melt in equilibrium with the plagioclase presenting the more depleted La compositions and the lower La/Sm ratios (star with black rim), and a residual melt obtained with the second AFC model (star with red rim - AFC2 in Figure 9). The error bars on the sample analyses represent a 1σ error on the values. The grey symbols represent the composition of the plagioclase analyzed in the Lower unit. (c) Modeling of the plagioclase compositions expected after Assimilation-Fractional Crystallization (AFC) of a troctolitic matrix (45% Olivine + 55% Plagioclase) by the equilibrium melt (AFC1) and the residual melt (AFC2) with crystallization of a gabbro assemblage (55% Plagioclase and 45% Clinopyroxene). Details in Table S3 and S4

5.2 Implications for the slow-spread lower oceanic crust

5.2.1 Importance of melt recharge and RPF in the acquisition of the cumulative signature: the melt flushing process

The model of magma reservoir formation and related modes of melt migration presented herein emphasize the critical role of reactive porous flow for the differentiation of melts emplaced within the crust. This is in agreement with early findings of oceanic systems being dominated by crystal mushes (***Detrick et al., 1987; Sinton and Detrick, 1992***), and with recent developments on igneous systems structure and especially in oceanic environments, where crystal mushes are considered to be the principal magma storage medium (e.g., ***Canales et al., 2017***; ***Lissenberg et al., 2019*** and references therein). Porous migration of melts through crystal mushes can be triggered by different processes, such as melt buoyancy and compaction, likely acting simultaneously and enhanced by deformation (e.g. ***Meurer and Boudreau, 1989***). The strong cumulative character of the lithologies recovered in the section studied herein, and from lower oceanic crustal sections suggests that strong compaction acted during the lithologies formation. However, similarly to what have been recently reported for continental layered intrusions (***Holness et al., 2017***), only very limited mineral imprint of crystal-plastic deformation linked to compaction can be observed (*see 4.1*).

In the Atlantis Bank section studied herein, both Lower and Upper parts of the reservoir evolved through reactive porous flow. In both cases too, their evolution involve the repeated inputs of primitive melts in the Lower unit, and of the identified hybrid melt in the Upper unit. We suggest that, driven by these continuous recharges within the mush, the melt mass was likely forced to percolate, and migrates in a similar way as the process of mush rejuvenation triggering eruptions in continental settings (e.g., ***Bachmann and Bergantz, 2003; Szymanowski et al., 2017***). In the two previous sections, the percolation process has been shown to be associated with intense RPF with reactions that eventually consume the melt. We therefore suggest here that the cumulative character of the studied plutonic rocks is acquired thanks to a continuous recharge of the system coupled to a melt consuming RPF reaction, a process we call here "*melt flushing*". Melt flushing doesn't require compaction of the system or melt extraction assisted by deformation; instead it implies a progressive closure of the melt porosity by incremental crystallization of continuously refreshed interstitial melt.

5.2.2 Hidden primitive cumulates assimilated by reactive porous flow processes

The average bulk compositions of the lower crust section drilled at Atlantis Bank and the other long *in situ* section drilled at the Atlantis Massif OCC (MAR - IODP Hole U1309D) are considered as one of their main differences. The estimated bulk composition of the crust at Hole U1309D is close to the composition of primary MORB magmas (average bulk crust Mg# of 76, ***Godard et al., 2009***). This has led ***Godard et al. (2009)*** to suggest that primary MORB melts were trapped within the lower crust, and no significant fraction of evolved melt escaped the magmatic system sampled at Atlantis Massif. At Atlantis Bank, ***Dick et al. (2000)*** or ***Kvassnes (2003)*** suggest that the average bulk composition of the cumulate sequence from ODP Hole 735B (and later from IODP Hole U1473A, ***Dick et al., 2019***) is too evolved and cannot compensate the composition of MORBs from the area towards the composition of primary MORB melts (bulk Mg# of 73 for Hole 735B and of 71 for Hole U1473A, ***MacLeod et al., 2017***). The authors infer the presence of a significant mass of "missing" primitive cumulates lying either out of the section or further deep in the OCC. The cumulate sequences drilled at Atlantis Bank would then represent already differentiated melts originating from a first step of crystallization at depth. This model would also explain the major lack of primitive lithologies drilled at Atlantis Bank such as dunite, or troctolites which are only found very locally in Hole 735B (***Dick et al., 2000; MacLeod et al., 2017***).

In the igneous reservoir model, the formation of the Lower unit involves intrusion of liquids with primitive compositions relative to the compositions considered for the Atlantis Bank system (i.e., average of the most primitive MORB sampled in the area). These melts initially crystallize ol+pl, and thus form primitive cumulate assemblages within the lower crust. However, these assemblages tend to be almost entirely transformed during the RPF reactions. Likewise, the Upper unit presents the same progressive reincorporation of its most primitive compounds by infiltrating melts, even though the recharge melts already endured a first step of reaction (*Figure 4.69*). Hence, the igneous reservoir model presented herein seems to confirm the hypothesis formulated by ***Dick et al. (2019)***, in which some of the gabbros sampled at Atlantis Bank "initially crystallized from primitive melts but were later hybridized to evolved compositions". The lack of the most primitive cumulates expected after crystallization of primitive MORB-type melts (e.g., ***Grove et al., 1992; O'Hara, 1968***) would then not result only from differentiation of already evolved melts, but also due to their assimilation by percolating melts. The amount of missing primitive cumulate to be found in the lower crust at Atlantis Bank would as a consequence be overestimated without considering this assimilation process.

5.2.3 To what extent can the igneous reservoir model be applied to other sections of slow-spreading oceanic crust?

The long in situ sections of lower oceanic crust sampled at Atlantis Massif (MAR - IODP Hole U1309D) and at Atlantis Bank (SWIR - ODP Hole 735B and IODP Hole U1473A) appear highly dissimilar (e.g. ***Blackman et al., 2006; Dick et al., 2019; MacLeod et al., 2017***). Even within the same oceanic core complex at Atlantis Bank, no obvious correlation can be established between the two drilled sections despite their relative spatial proximity (~2.2 km). However, at Atlantis Bank, both Holes present tectono-magmatic units characterized by geochemical upward differentiation trends (***Dick et al., 2019***) similar to the trends initially described by ***Dick et al. (2000)*** characterizing the intrusion studied herein. In addition, numerous evidences for reactive porous flow processes are found in all three sections, and are now considered as key in the evolution of the lower crust (e.g., ***Drouin et al., 2010, 2009; Ferrando et al., 2018a; Lissenberg and MacLeod, 2016; Suhr et al., 2008***; this study). Altogether these similarities reflect a continuity of magmatic processes during accretion (e.g., ***Dick et al., 2019*** and references therein), hence suggesting that all or part of the igneous reservoir model can apply to other crustal sections.

Godard et al. (2009) proposed that the gabbroic sequence sampled at Hole U1309D was the result of multiple sill injections. In agreement with the age distribution with depth, ***Grimes et al. (2008)*** favored a model of construction of the lower crust section by dispersed and randomly distributed sill injections. This model suggest that the gabbroic cumulate sequence of Hole U1309D compare to the Lower unit of the igneous reservoir model proposed herein, albeit a first order compositional dissimilarities between the sections. The major difference between Holes U1309D and 735B is also the occurrence of highly primitive lithologies (ol rich troctolites) at Site 1309, which are interpreted as incorporated slivers of mantle into the plutonic series (***Drouin et al., 2010, 2009; Ferrando et al., 2018b; Suhr et al., 2008***). However, mantle incorporation within the lower crust after accretion by multiple sill injections has already been proposed for example by ***Sanfilippo and Tribuzio (2013)***, and only rather suggest that the limit between gabbroic and mantle lithologies lay closer to the section drilled at Atlantis Massif.

Suhr et al. (2008) studied in details one of these primitive portions in Hole U1309D between 1194 and 1242 mbsf, the same as ***Drouin et al. (2010, 2009)*** and ***Ferrando et al. (2018)***, in addition to the overlying unit (up to ~850 mbsf). They explain the formation of the ol rich troctolites from the lower ~50 m of the sequence by intrusion of discrete batches of progressively more evolved melt into an ol rich troctolite of mantle origin (***Drouin et al., 2010, 2009; Suhr et al., 2008***). The study of the rest of the unit is not as developed and is explained by differentiation within a "single magmatic cycle" (***Suhr et al., 2008***). In addition to these two

distinct modes of evolution, comparison between geochemical signatures and the repartition of igneous contacts with depth show that the unit presents actually striking similarities with the intrusion of Hole 735B studied herein. Below a transition zone at about 1090 mbsf, the whole rock Mg# or the plagioclase An contents are rather constant despite their variability at depth, similar to the signatures of the Lower unit. Numerous igneous contacts are also present and separate lithologies ranging from ol rich troctolites to gabbros and gabbronorites. In contrast above ~1090 mbsf, the lithologies present increasingly differentiated signatures towards the top of the sequence, with for example whole rock Mg# of ~80 at 1090 mbsf down to ~70 at 850 mbsf (*Figure 4.72* - ***Godard et al., 2009***). Together, the disappearance of the igneous contacts in the upper ~150 m presenting mainly more evolved ol gabbros, gabbronorites and gabbros suggests that this sequence compare to the Upper unit of the reservoir model.

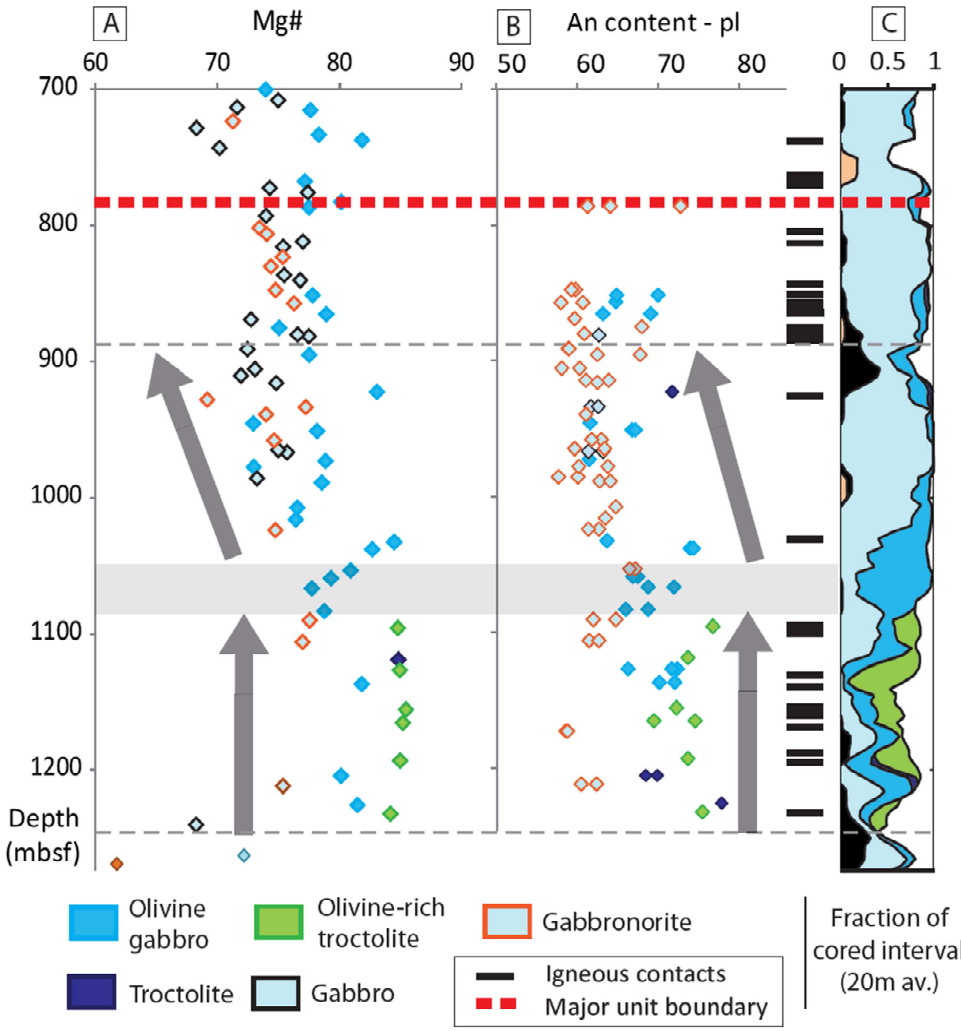

Figure 4.72. (a) Downhole whole rock Mg# evolution of Hole U1309D. Whole rock data, major structural unit boundary and igneous contacts are from Blackman et al. (2006). (b) Downhole in situ An contents of plagioclases from Suhr et al. (2008). (c) Lithostratigraphic variations with relative recovered abundances averaged over 20 m (modified after Blackman et al., 2006).The dotted grey lines represent the limits of the section potentially explained by the igneous reservoir model presented herein. Grey arrows: upward differentiation trends.

Even though the textural variability of the samples and the detailed processes involved during the evolution of melts within the sequence are unknown (e.g. impact of the mantle assimilation, origin of the gabbros and gabbronorites), we propose that the igneous reservoir model likely apply to this sequence of Hole U1309D, located between ~850 and ~1200 mbsf. The exact extent of application of the igneous reservoir model to all examples of lower slow-spreading oceanic crust sections is at the moment difficult to establish. Yet this comparison between two different OCCs from distinct spreading centers enabled by the igneous reservoir model suggest that this model potentially paves the way for the development of new perspectives on the understanding of magma reservoir processes at slow-spreading ridges.

6 Conclusions

We combined high-resolution in situ analyses together with detailed petrographic and structural characterization of a preserved magmatic unit from ODP Hole 735B. The study enabled to establish a first integrated evolution model of a slow-spread lower oceanic crust igneous reservoir. Both melt emplacement processes by intrusion and migration by reactive porous flow contributed to its accretion, and strongly influenced the architecture and composition of the reservoir. The principal characteristics of evolution of the igneous reservoir emphasized by the model are as follows:

(1) The lower half of the reservoir represents the initial emplacement of magmas within the slow-spreading crust by repetitive intrusions and sills stacking during a major magmatic event (~20 sills stacked over ~125 m);
(2) The continuous recharge of the lower half of the reservoir has led to assimilation of early primitive cumulates and to the formation of hybrid melts, which were progressively collected in an overlying mush constituting the upper half of the reservoir;
(3) The upper half of the reservoir has formed by upward differentiation and progressive accumulation of evolved melts towards to the top of the mushy magmatic unit.
(4) The general upward reactive porous flow that causes melt-rock reactions and constrains melts differentiation is a result of a "*melt flushing*" process triggered by the continuous recharge of the reservoir.

Geochemical modeling of *in situ* incompatible trace element contents enabled to enlighten the strong and ubiquitous involvement of reactive porous flow processes in the evolution of the intrusion, and to add further constraints on melt-rock reactions that occurred during the evolution of both units. Eventually, the first successful comparison of the new igneous reservoir model with another lower slow-spreading crust section suggests that the model open new perspectives for the comprehension of magma accretion at slow-spreading oceanic centers.

CHAPTER V.

Implications for magma evolution at slow-spreading ridges

Perspectives of the models established at different scales and comparison between ODP/IODP Holes drilled at Atlantis Bank (SWIR) and Atlantis Massif (MAR)

1 Overview on the main findings, and application to magma reservoir evolution

The different aspects of the work exposed in the previous chapters shed new light on the reactions ongoing during differentiation of gabbroic bodies emplaced within the lower oceanic crust. The impact of reactive porous flow processes during formation and evolution of a magma reservoir was determined at different scales, from the sample-scale to the scale of a given igneous reservoir (~250 m-thick). The reactions involved are now better quantified, thanks to high-resolution studies of the main first order heterogeneities observed at IODP Hole U1473A: grain size igneous contacts (*Chapter 3,* and *Appendix 1.1*), and to the study of the tectono-magmatic unit of ODP Hole 735B (*Chapter 4*). The quantification of the reactions also suggests that changes in melt migration dynamics are key in the development of distinct geochemical signatures. This is particularly true for the layered series, in which the first step of RPF was widespread at the scale of the core (m-scale) but heterogeneous at the sample scale (cm-scale), whereas the second step of RPF occurred in channel-like structures that focused the porous flow. At the scale of an entire reservoir (few hundreds of m), we consider RPF as the main process implicated in the evolution of the lithologies despite very different architectures of the lower and upper part of the reservoir. Altogether, this suggests that RPF and associated melt-rock reactions are indeed ubiquitous during accretion as they occur at all stages of formation of the reservoirs and are recorded in very different types of structures.

The high-resolution studies of samples from Hole U1473A not only lead to a better definition of reactive porous flow processes, but also helped understanding magma reservoirs architecture, and evolution of crystal mushes. We hypothesize that the layered series, resulting from the intrusion of a crystal-bearing magma within a solidifying mush, represent a contact between two larger magma bodies. The presence of layers thus demonstrates movements of magmas by intrusion that occur in a rather shallow part of the magmatic crust at Atlantis Bank (e.g., ***Dick et al., 2019; Natland et al., 2002***). The igneous reservoir model based on the study of the intrusion from ODP Hole 735B confirms the broad implication of intrusive magma displacement in the formation of the crust, and enabled to refine the size of the structures formed (i.e., sills of ~6 meters thick in average building the Lower unit of the reservoir). It also enables us to draw broader conclusions for magma migration dynamics of mush-dominated reservoirs.

First, a general upward porous flow is inferred to explain the progressively more evolved geochemical signatures found towards the top of the tectono-magmatic units as described in the lower crust at Atlantis Bank by ***Dick et al. (2019)***. Together with the evidences for progressive replenishment of sills-stacked unit, and for continuous collection of melts that are transferred to

the upper homogeneous unit, the model suggests that constant arrival of external melts, and the associated "*melt flushing*" process is a driving force for porous melt migration in the mushy magma reservoirs. This also tentatively explains the strong apparent cumulate signatures observed in the gabbroic lithologies studied (e.g., strong Eu and Sr positive anomalies, important depletion of LREE comparative to MREE) despite the lack of ubiquitous compaction evidences.

Second, at Atlantis Bank, the composition of the gabbroic lithologies is too evolved to balance the composition of MORBs from the area into a primary melt in equilibrium with the mantle (***Dick et al., 2000, 2019a***). The authors suggest the presence of a missing primitive cumulate lying out of the drilled section. We show in our model that the parental melts supposed to be at the origin of the intrusion are rather primitive compared to other melts sampled in the area (i.e., the most primitive MORB melts from Atlantis Bank segment; ***Coogan et al., 2004***). Hence, the initial primitive cumulates crystallized in the reservoirs tend to be re-assimilated by new incoming melts in the system. These melts can be more primitive as demonstrated in the model, but can also potentially be more evolved as the general melt dynamics governed by reactive porous flow suggest significant displacement of evolved melts within the crust. The displacement of such evolved melt and reaction with more primitive sequences could potentially be one of the reasons for the moderately differentiated bulk composition of Holes 735B and U1473A.

A synthesis of the models proposed herein is presented in *Figure 5.73*.

Figure 5.73 - Synthesis of the different models of magma reservoir emplacement and evolution resulting from the work developed in Chapter 3 and 4 on the Atlantis Bank in situ sections, including the work of Ferrando et al. (in prep.) that is presented in appendix of this manuscript. (a) Igneous reservoir model based on the study of ODP Hole 735B intrusion (Chapter 4). (b) Models of magma mush evolution based on the study of systematic grain size variations found in IODP Hole U1473A (Chapter 3). Left: igneous layering development possibly materializing the contact between two larger mushy intrusions. Right: magma mush heterogeneity as identified by the study of patchy olivine gabbros (Ferrando et al., in prep.)

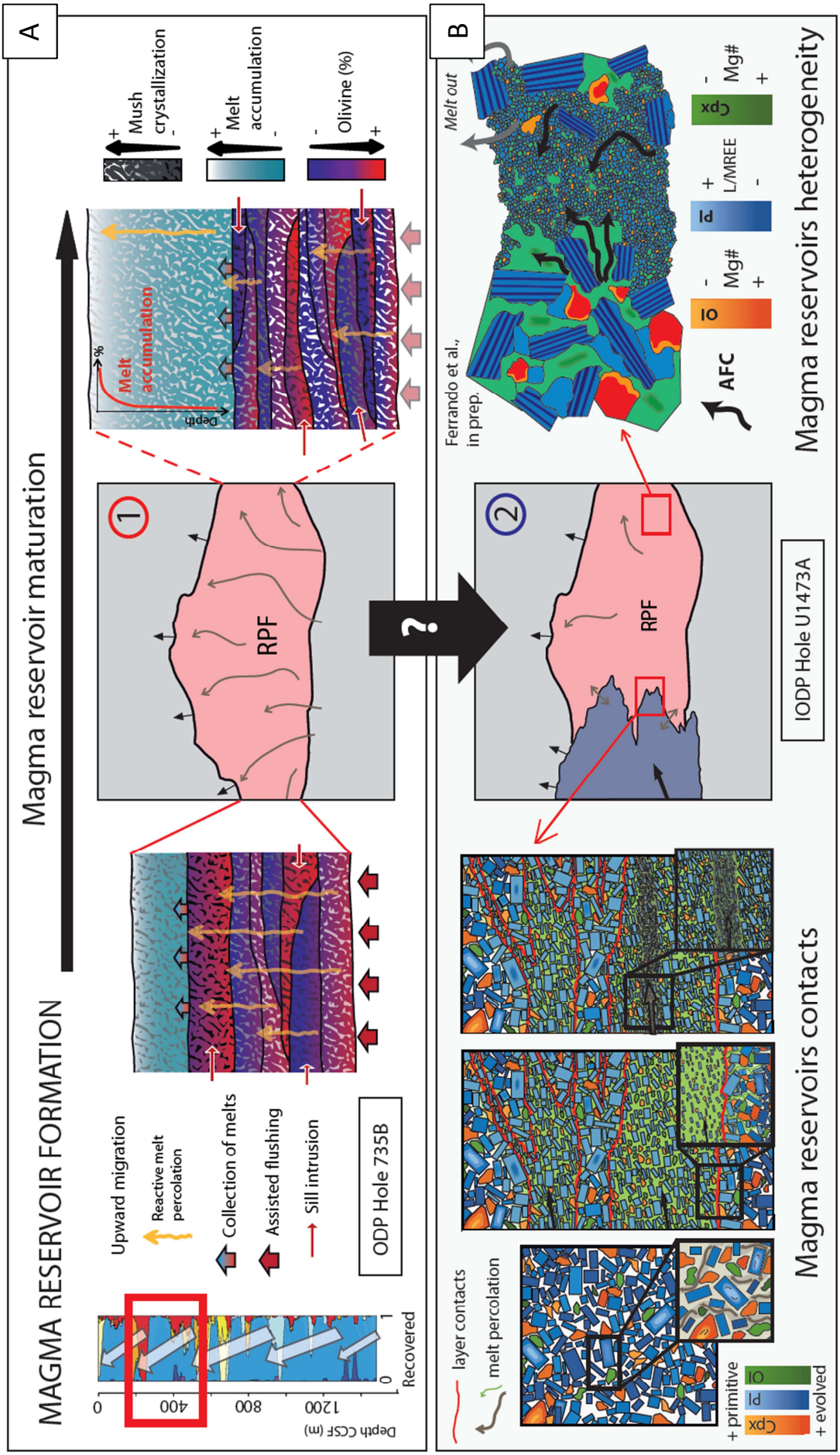
A
MAGMA RESERVOIR FORMATION
Magma reservoir maturation
Depth CCSF (m)
Recovered
ODP Hole 735B
Upward migration
Reactive melt percolation
Collection of melts
Assisted flushing
Sill intrusion
Mush crystallization
Melt accumulation
Olivine (%)
Melt accumulation
Depth
RPF
1
2
?
B
Melt out
Ferrando et al., in prep.
AFC
Ol
Mg#
Pl
L/MREE
Cpx
IODP Hole U1473A
Magma reservoirs heterogeneity
Magma reservoirs contacts
layer contacts
melt percolation
+ primitive
+ evolved

2 Characterization of other long in situ sections drilled in OCCs

2.1 Sections from the Atlantis Bank OCC

A detailed description of the geological setting and of the formation of the OCC is available in *Chapter 2*.

2.1.1 New characterization of a 300 m-long section from IODP Hole U1473A

IODP Hole U1473A is the last of the sections drilled in OCCs, and the last drilled in the Atlantis Bank OCC during IODP Exp. 360. I conducted a high-resolution study of samples from a ~350 m-long section of the bottom of the hole. The following aims at describing the first order structural and petrographic features of the section considered, but a more complete description of the 809 m-long Hole U173A is given in *Chapter 2*.

The study focused on the second and deepest tectono-magmatic unit, which is also the least altered and the least deformed of the hole. The recovery from ~580 mbsf to the bottom of the hole is of about 96% which is one of the highest ever obtained during drilling operations. Similarly to other units described in Hole 735B, the unit is characterized by a first order upward differentiation trend (e.g., Mg# decreases upsection - *Figure 5.74*). The unit is mainly composed of olivine gabbros and some gabbros, with additional crosscutting oxide gabbros *sensu lato* and felsic veins. Our sampling which was conducted during Exp. 360 on the bottom ~350 m of the hole (described as units V to VIII in ***MacLeod et al., 2017***), is focused on the least evolved lithologies free of any deformation or alteration (i.e., mostly olivine gabbros, and gabbros). All units are characterized by the presence of coarse-grained subophitic to granular olivine gabbros, some displaying patchy textures (mainly in Unit V and VI, some are also found in Unit VII). Unit VII is characterized by frequent grain size layering, and Unit VIII on opposite is rather homogeneous compared to the three others. In total, 20 of the olivine gabbro samples collected were considered for minerals *in situ* major and trace elements measurements. The sampling rate for the section is of 1 sample every ~15 m, considering the gap of recovery between 460 and 525 mbsf. I compare hereafter the available whole rock data (shipboard data from ***MacLeod et al., 2017***) with new *in situ* mineral analyzes obtained following the same analytical methods as described in Chapter 3 and Chapter 4 (analyses available in *Appendix 3.1* and *3.2*).

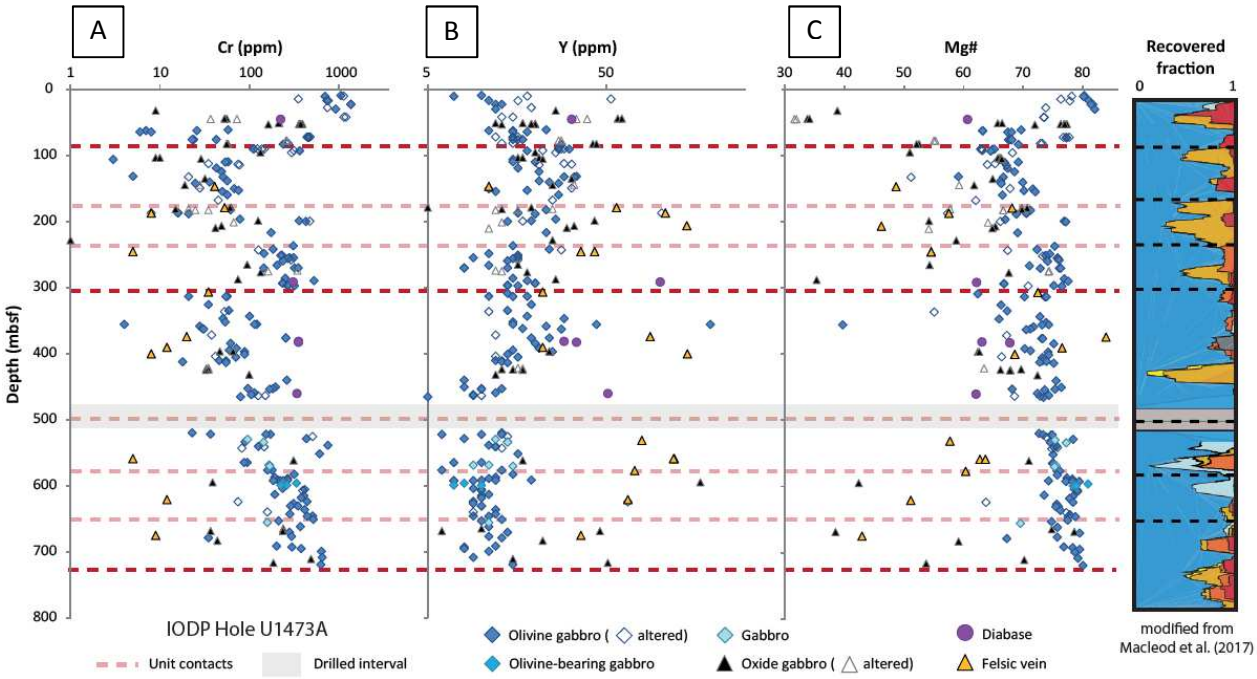

Figure 5.74 - Whole rock compositions in (a) Cr, (b) Y and (c) Mg# content as a function of depth, IODP Hole U1473A. The main dashed dark red lines represent geochemical unit boundaries based on Cr and Ni data. Modified from MacLeod et al. (2017). The light red dashed lines highlight the limits between the 8 units defined in MacLeod et al. (2017).

Whole rock compositions of Hole U1473A are similar to those of Hole 735B, except for the most primitive lithologies found in the latter (troctolites) that are lacking in the cores of Hole U1473A. When plotted against depth, whole rock Mg# or concentrations in Cr and Y enable to distinguish three main geochemical units as described by the Mg# and the compatible elements contents of the lithologies (contacts located at ~60, 300 and 700 mbsf - ***MacLeod et al., 2017***). In details, the main geochemical units present second order disruptions of the geochemical trends, some corresponding to the boundaries of the lithostratigraphic units (e.g. at ~570 mbsf and the transition between Unit VI and VII, also highlighted by a slope failure in the Y variations with depth for olivine gabbros - *Figure 5.74*).

In situ element contents of minerals from samples collected in the lower ~350 m of the hole shed new light on the variability and the potential processes implicated in the evolution of the unit. Despite the relative homogeneity of the plagioclase An contents and clinopyroxene Mg# with depth, some tendencies are observed such as the slight decrease towards the top of the unit of both these parameters (*Figure 5.75*). An inverse zoning in the plagioclases An content located between ~550 and 700 mbsf is also observed similarly to what can be found locally in the intrusion of Hole 735B between ~330 and 400 mbsf (*Chapter 4*). This inverse zoning is restricted to the very rim (~5-10 µm) of plagioclase grains. In comparison, minerals minor elements and trace elements present stronger variability with depth. The compositional ranges in Cr of clinopyroxene and in REEs of plagioclase and clinopyroxene expand with depth, especially in the lower 50 m of the section (*Figure 5.75* and *Figure 5.76*).

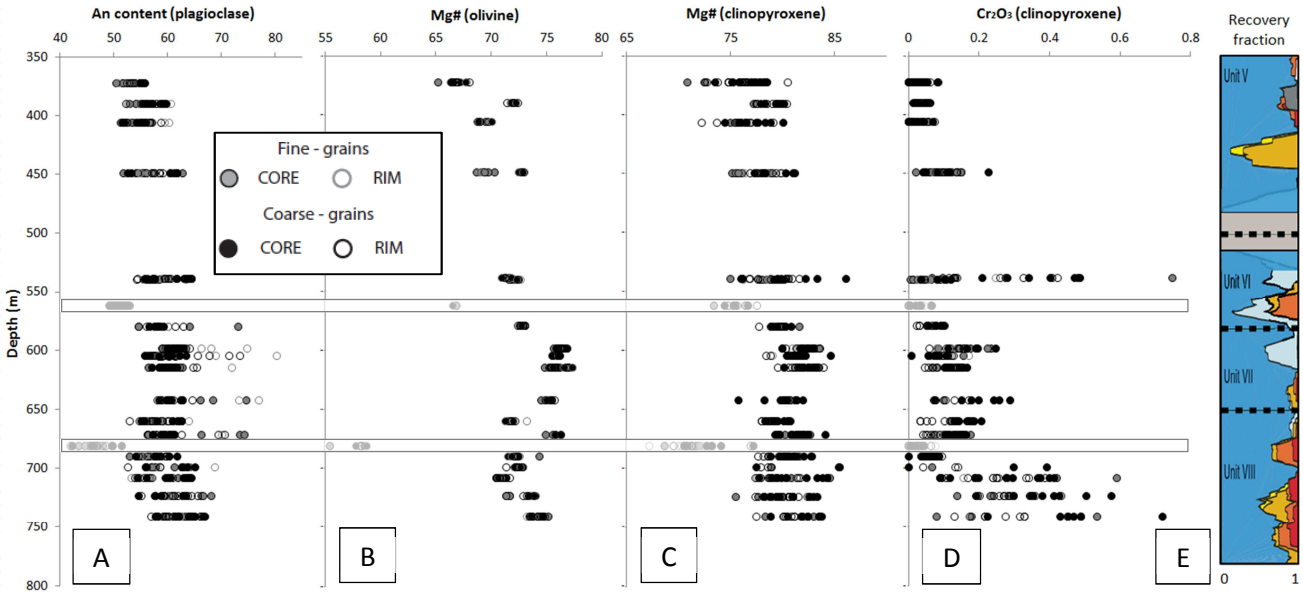

Figure 5.75 - In situ plagioclase An contents (a), olivine (b) and clinopyroxene (c) Mg#, and Cr_2O_3 (in wt%) contents of clinopyroxene (d) with depth. The lithostratigraphic column (e) represents the proportions of olivine gabbros (analyzed samples) compared to other lithologies of the considered section. The samples behind the shadowed boxes are either overprinted by strong alteration (at ~560 mbsf) or strong deformation (at ~680 mbsf), and hence are excluded from the discussion. In situ major element data available in Appendix 3.1 (Table S1).

Clinopyroxenes Cr signatures of the bottom part of the section (below 700 mbsf) potentially translate the more primitive character of the parental melts from which evolved the lithologies. The more depleted *in situ* REEs values recorded in the samples are rather constant through the entire section, and appear even slightly more evolved (higher contents) in the bottom 50 m of the section. As both compatible and incompatible elements are not equally sensible to magmatic processes at different stages of evolution of the lithologies (see Chapter 1), the signatures described above are not irreconcilable. Some interstitial minerals ("Fine - grains" in the legend and description in *Appendix 3.3*) and rims of the minerals on opposite show the highest incompatible trace element compositions of the section, with enrichment factors of Ce in clinopyroxenes of up to ~7 in the sample located at 700 mbsf (*Figure 5.76*). According to the previous developments (Chapter 3 and 4) and the interpretation of similar signatures found in the literature (e.g., ***Gao et al., 2007; Lissenberg and MacLeod, 2016***), a first order interpretation is the implication of RPF processes during differentiation of the sequence and especially between 700 and 750 mbsf. This would also mean that the melt-rock reactions involved or their efficiency vary with depth, and for example are progressively attenuated towards the top of the sequence where REEs enrichment factors in individual samples decrease.

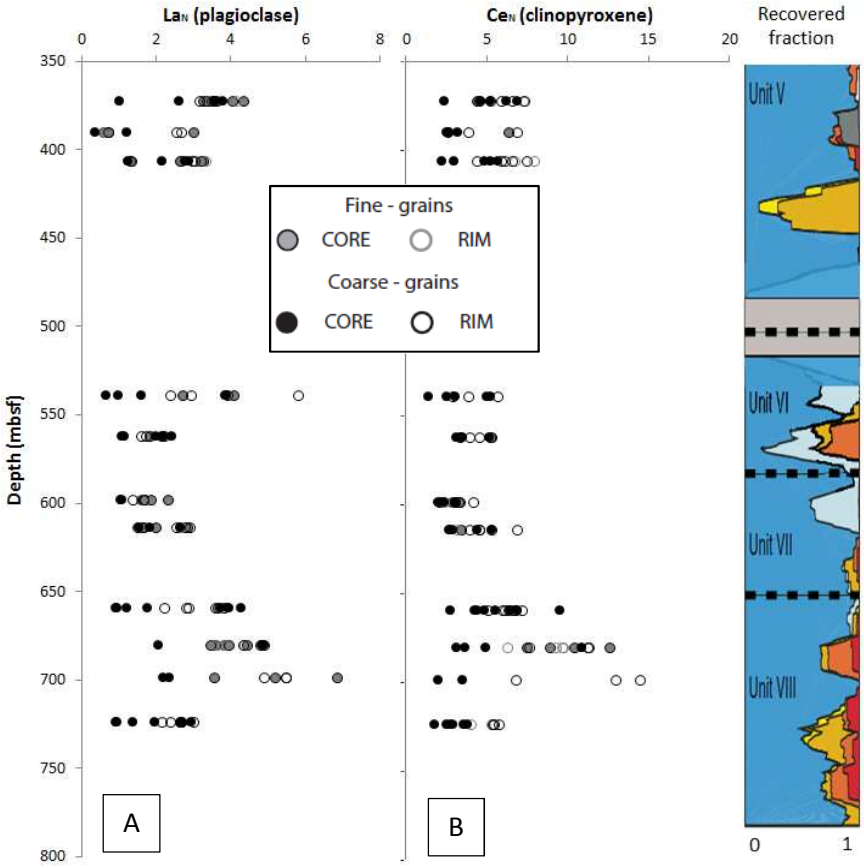

Figure 5.76 - In situ plagioclase La content (a) and clinopyroxene Ce content (b) analyzed in samples from IODP Hole U1473A. As the textures of the samples are non equigranular, we indicate the difference between fine-grained rather interstitial minerals and other coarser grained minerals in the samples. In situ trace element data available in Appendix 3.2 (Table S2).

Minerals *in situ* compositions obtained for the section of Hole U1473A were compared with the compositions of Hole 735B intrusion presented in Chapter 4 (*Figure 5.77*). The values fall exactly within the same compositional ranges in major, minor and trace elements. In detail, the compositions compare specifically with the compositions of the upper part of the intrusion, i.e. the homogeneous overlying mushy reservoir that evolved by progressive upward differentiation constrained by RPF processes (*Figure 5.73*). This finding is consistent with the rather homogeneous character of the lithologies observed in Hole U1473A, despite the presence of some grain size layering and patchy gabbros. This also confirms the implication of melt-rock reactions associated to RPF in the evolution of the section. Indeed, the same geochemical signatures found in the upper unit of the intrusion were reproduced by an AFC model involving assimilation of a troctolitic matrix by hybrid melts, and crystallization of secondary plagioclase and clinopyroxene crystals. Further descriptions of the samples texture and modal composition are required to confirm the implication of the same process, or to redefine the reaction involved in the formation of each lithology or subunits.

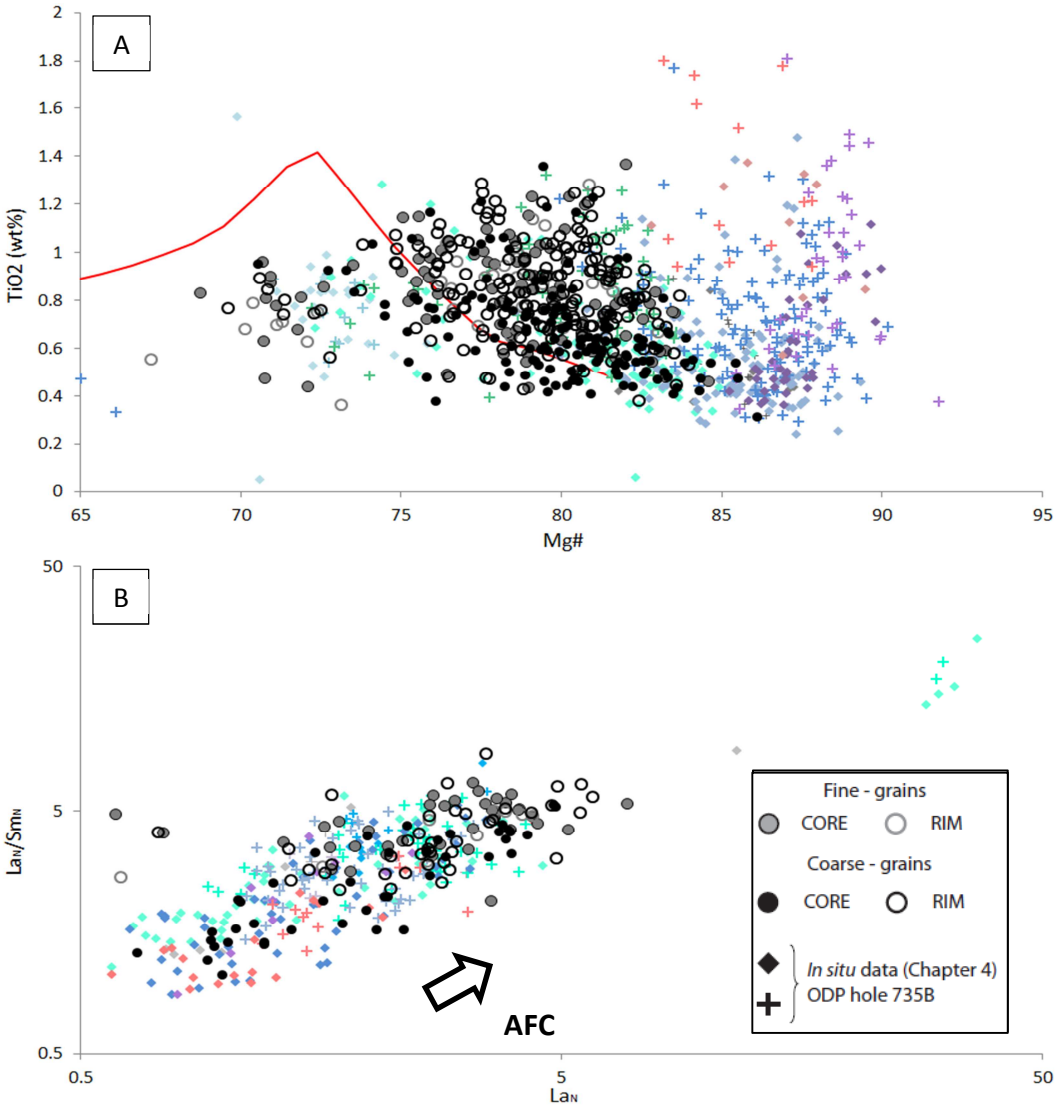

Figure 5.77 - Comparison between in situ mineral compositions of plagioclase and clinopyroxene analyzed in the bottom ~350 m of Hole U1473A, and the compositions analyzed for the study of Hole 735B intrusion. Red: troctolites, purple: olivine-rich gabbro, dark blue: olivine gabbro (lower unit) and light blue: olivine gabbro (upper unit). (a) TiO_2 concentrations in clinopyroxenes plotted against the minerals Mg#. The red trend corresponds to the evolution by fractional crystallization of an average primitive MORB composition for the Atlantis Bank area determined by MELTS (see Chapter 4). (b) La_N/Sm_N ratio versus La_N analyzed in plagioclases (N = normalized to the average primitive MORB composition of the Atlantis Bank area).

2.1.2 Available data and models based on ODP Hole 735B

Whole rock compositions of ODP Hole 735B enable to characterize a series of geochemical upward differentiation trends with depth (e.g., Mg#), as emphasized by ***Dick et al., (2000)***.). The second shallowest unit, and also the most primitive of the section, is the intrusion on which the reservoir model of Chapter 4 is based. A number of second order slope discontinuities are also observed, as shown by all geochemical tracers including Cr and Y (e.g., at about 1200 mbsf - *Figure 5.78*). ***Dick et al. (2019)*** proposed a model of formation by accretion

of numerous small igneous bodies during separated magmatic events, based on recent descriptions of Hole U1473A and previous deductions from studies of Hole 735B. The large distinct magmatic events are represented by shifts towards more primitive compositions upsection (e.g., boundary at ~510 mbsf in Hole 735B - *Figure 5.78*).

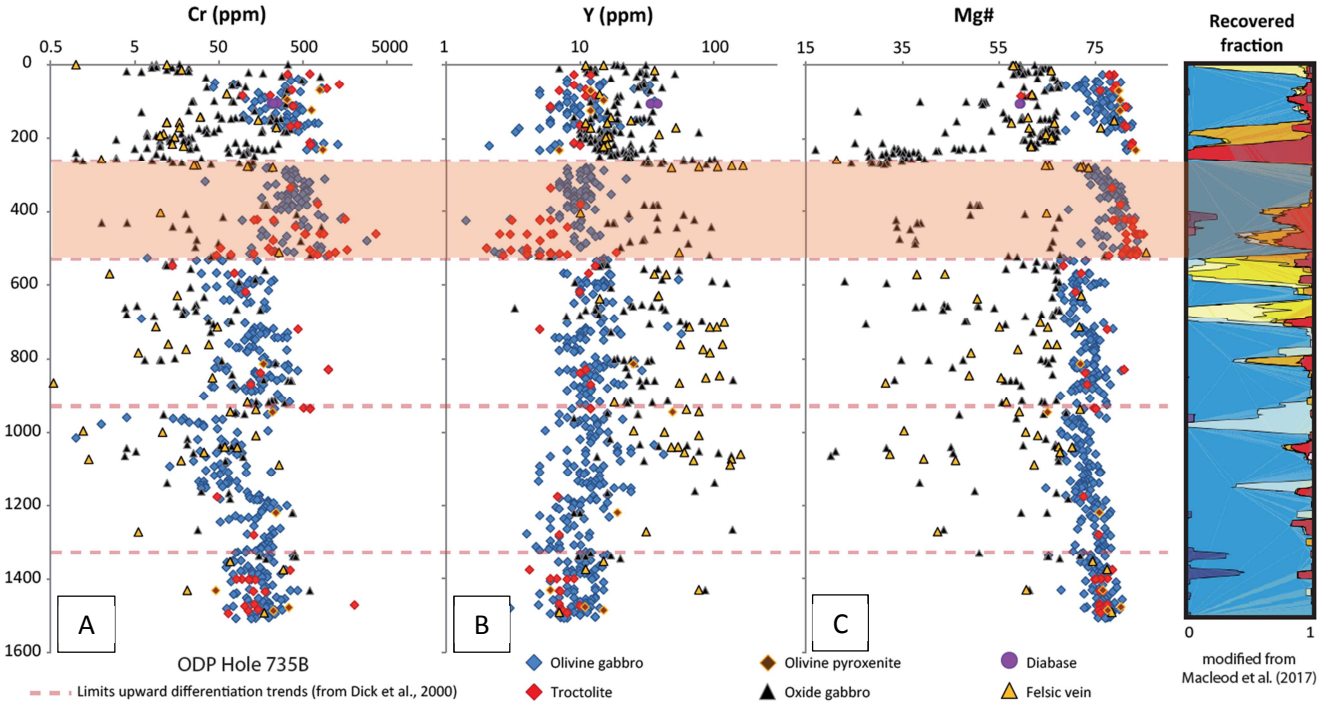

Figure 5.78 - Whole rock compositions in (a) Cr, (b) Y and (c) Mg# content as a function of depth, ODP Hole 735B. The dashed red lines represent the approximate unit boundaries between sections presenting upward differentiation trends in Mg# as described by Dick et al. (2000). The orange area corresponds to the localization of the intrusion studied in Chapter 4. Data from Shipboard Scientific Party - Leg 118 (1989), Dick et al. (1991), Dick et al. (1999), Hart et al. (1999), Hertogen et al. (2002), Holm et al. (2002) and Niu et al. (2002).

Except for the most primitive lithologies that are not found in Hole U1473A, the compositions (whole rock and minerals) of the two deep drilled *in situ* sections from Atlantis Bank are rather similar. In addition, the petrographic description of the main lithostratigraphic units shows that they are also rather homogeneous with depth, apart from the presence of localized layered sequences and the patchy gabbros. ***MacLeod et al. (2017)*** proposed a comparison between the bottom two units of Hole 735B and the entire Hole U1473A (*Figure 5.79*). There are indeed some similarities between the downhole variations of the two sections (proportions between the thickness of the upper and lower units, second order slope failures at about one third from the bottom of the hole). However, the differences observed between both holes (variable unit thickness and lithologies recovered) call for further determination of 3D models to determine the lateral extension of the tectono-magmatic units and to understand the lateral variability of the OCCs.

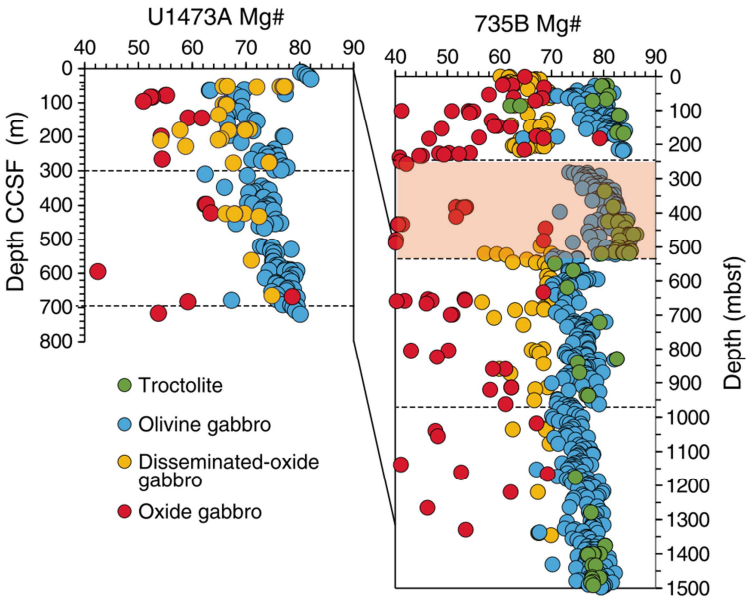

Figure 5.79 - Comparison of downhole variation in Mg#, Holes U1473A and 735B (from MacLeod et al., 2017). The orange area in the downhole plot of 735B corresponds to the localization of the intrusion studied in Chapter 4.

2.2 IODP Hole U1309D from the Atlantis Massif OCC

2.2.1 Geological settings

IODP Hole U1309D is the second deepest long *in situ* section drilled in an OCC after ODP Hole 735B. The hole reaches 1415 mbsf within the Atlantis Massif OCC, that locates on the western flank of the Atlantis Fracture Zone, at 30°N on the MAR (***Blackman et al., 2006***). The structure is about one eighth the size of the Atlantis Bank OCC, with ~15 km long for ~10 km wide (~40 km long for ~30 km wide at Atlantis Bank), and formed during the last ~2 My. The surface of the dome structure is characterized by a well-defined corrugated surface that represents the preserved footwall of the detachment fault (*Figure 5.80a*). At this location, the half-spreading rate of the ridge axis is of 12 mm/y (***Blackman et al., 2004*** and references therein). Gravity anomalies likely indicate that unaltered ultramafic rocks are lying several hundreds of meters below the seafloor, and also that the distribution of lower crustal lithologies and upper mantle rocks is uneven within the OCC (***Blackman et al., 2006, 2004***). The Central Dome, in which hole U1309D has been drilled, is covered by angular rubble fragment of metabasalts that cap serpentinized peridotite and metagabbroic rocks (*Figure 5.80b*).

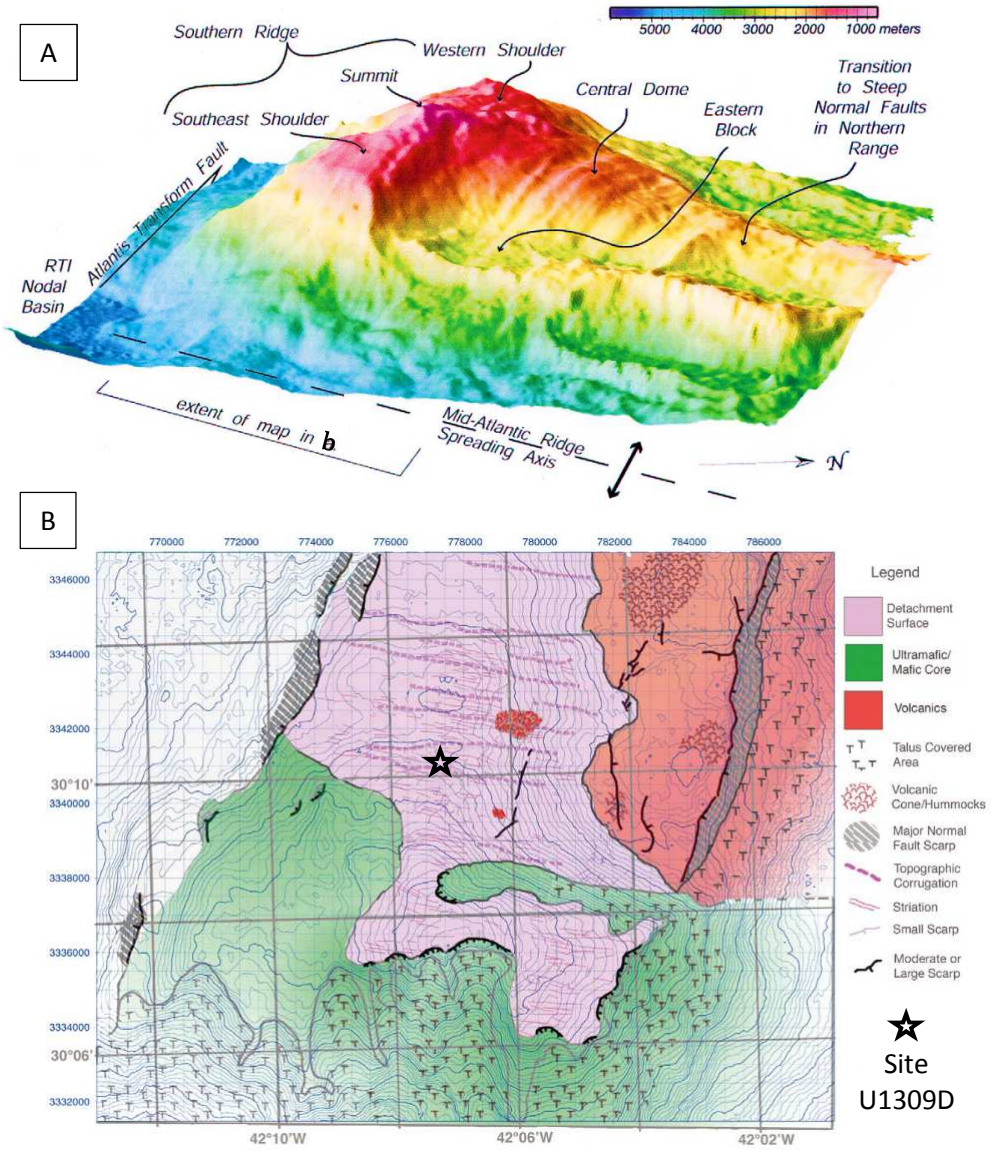

Figure 5.80 - Atlantis Massif at the eastern Mid-Atlantic Ridge - Atlantis Transform Fault intersection (Blackman et al., 2004). (a) Large-scale morphology of the Atlantis Massif from WSW-looking perspective shows major morphotectonic features. (b) Morphotectonic map of Atlantis Massif. Blue contours are at intervals of 50 m with bold contours every 250 m (shallowest at 1000 m).

2.2.2 Description of the section and comparison of the accretion models of the magmatic crust at Atlantis Massif and Atlantis Bank

The total 1043 m of cores recovered from Hole U1309D (75% recovery rate below ~20 mbsf) were drilled during IODP Exp. 304 and 305. Compared to the sections drilled at Atlantis Bank, the most abundant rock type is gabbro (including gabbronorites - 55.7%), followed by olivine gabbro (25.5%) and gabbros with oxides (7%). The cores contain about 8% of olivine-rich lithologies (troctolites and olivine-rich troctolites *sensu lato*), and notably peridotites

(~0.3%), which constitutes one of the main difference with the sections drilled at Altantis Bank (***Blackman et al., 2006***). The description of the relationship between lithologies highlights that in general gabbros are intrusive within olivine-rich lithologies, with sharp intrusive contacts above ~650 mbsf, and more diffuse contacts deeper in the section. Olivine gabbros locally grade to troctolite, and gabbros with oxides are present in the form of patches dispersed within usually undeformed coarse-grained gabbro. Oxide gabbros sometimes occur as dikelets or layers within other rock types and associated with ductile deformation (***Blackman et al., 2006***). ***Godard et al., (2009)*** deduced from the strong lithology variations lacking downhole systematic associated with intrusive contacts, that the section is composed of a series of interfingered units (varying in thickness from few cm to m - *Figure 5.81*).

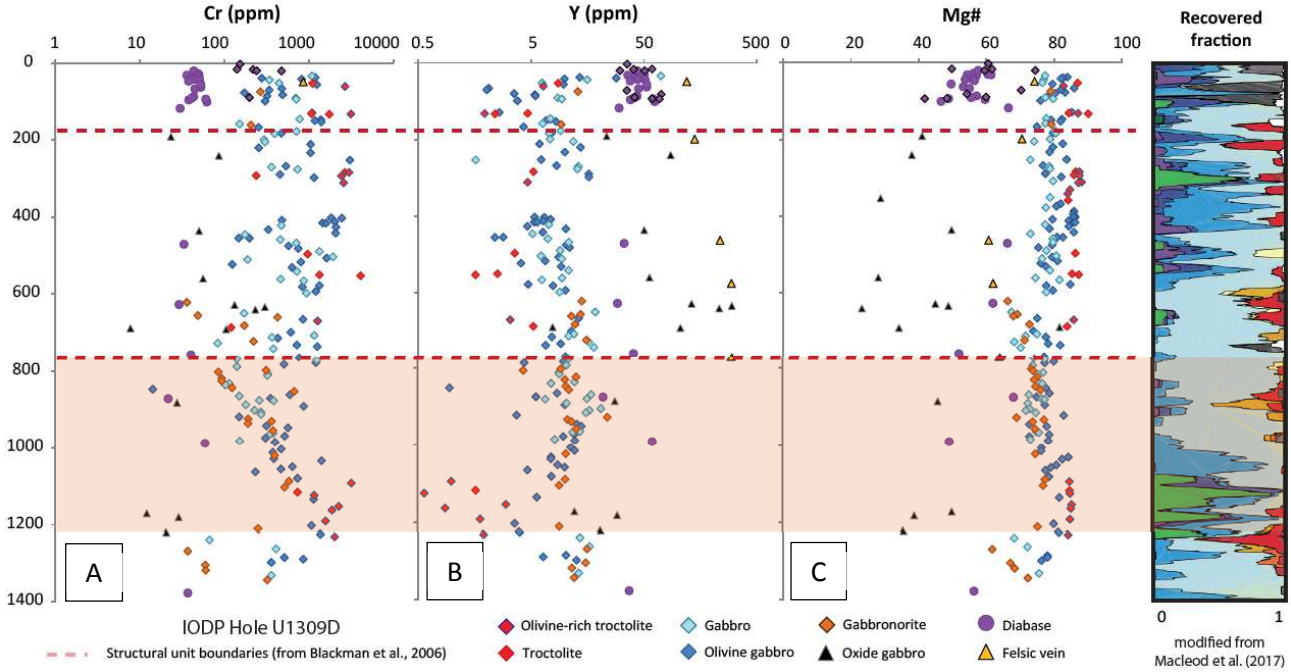

Figure 5.81 - Whole rock compositions in (a) Cr, (b) Y and (c) Mg# content as a function of depth, IODP Hole U1309D. The dashed red lines represent two major structural unit boundaries (Blackman et al., 2006). Data from Godard et al. (2009). The box corresponds to the section studied by Suhr et al. (2008) and discussed below.

Whole rock compositions suggest that the plutonic units share the same parental melt with the diabases and MORBs sampled in the area (***Godard et al., 2009***). The average composition of the section is more primitive that the Atlantis Bank sections (***MacLeod et al., 2017***), even though the compositional range covered by the lithologies of both OCCs are similar when considering only whole rock data (*Figure 5.82*). No clear upward differentiation trend can be identified with depth in the whole rock compositions for Hole U1309D unlike what is observed in Holes 735B and U1473A. These contrasting results lead authors to suggest that the mechanisms for lower crust formation at slow-spreading ridges vary significantly, from one ridge segment to the other but also potentially along-axis (e.g., ***Dick et al., 2019; MacLeod et al.,***

2017). ***MacLeod et al. (2017)*** inferred the implication of variable melt supply and location below the ridge axis, acting together with the tectonic activity in controlling the thermal regime and lower crust structure. The authors also suspected the potential difference of stratigraphic level sampled or exposed within the different OCCs. Atlantis Massif would represent a deeper portion of lower crust closer to the transition with the lithospheric mantle. This seems to be in agreement with the fact that a large contribution to the lower crust at Atlantis Massif comes from the mantle. Indeed, many authors highlight the presence of olivine-rich lithologies that originate from assimilation of olivine-rich precursors of likely mantle origin (***e.g. Drouin et al., 2010, 2009; Ferrando et al., 2018; Suhr et al., 2008***).

Dick et al. (2019) took a step further in the discussion and hypothesized that the Atlantis Bank section formed within a massive, slowly cooled gabbroic body where large scale melt migration through the (entire) structure was possible. On opposite, previous work from ***Godard et al. (2009)*** or ***Grimes et al. (2008)***, hypothesized that the crustal section at Atlantis Massif formed by more infrequent and independently cooled small intrusions preventing large scale redistribution of the more evolved melts in the sequence. Regarding the detailed modes of emplacement and evolution of the crustal lithologies apart from the mantle-inherited ones, very few studies detailed the processes involved.

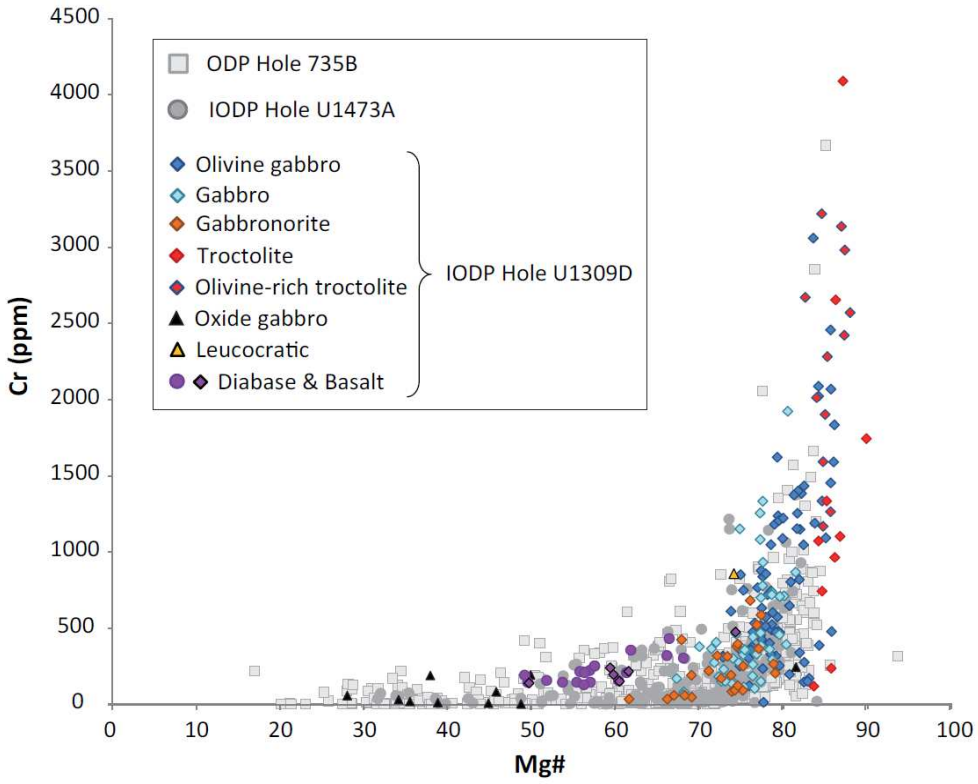

Figure 5.82 -Comparison of the geochemistry (Mg# and Cr contents) of rocks recovered from hole 735B and U1473A, with details on the composition of rocks from hole U1309D. Data from Macleod et al. (2017), Godard et al. (2009) and the compilation of data detailed in Figure 5.6.

As described in Chapter 4, ***Suhr et al. (2008)*** conducted an in situ geochemical study of a ~400 m long section from IODP Hole U1309D, between ~850 and ~1240 mbsf. The authors also focused on an interval between 1194 and 1242 mbsf, similar to the one studied by ***Drouin et al. (2010, 2009)*** and ***Ferrando et al. (2018)***. These last ~50 m are characterized by interleaved olivine-rich troctolites associated with more evolved lithologies like olivine gabbros, gabbros and gabbronorites, and present several intrusive contacts. ***Suhr et al., (2008)*** first order interpretation is that the upper part of the unit (850 - 1090 mbsf) results from upward differentiation within a single magmatic unit that is also visible in ***Godard et al. (2009)*** whole rock synthesis, whereas the lower ~50 m sequence formed by intrusion of discrete magma batches within a primitive troctolitic lithology. The authors stated that the poor spatial resolution of their data unabled to fully reconstruct the formation and evolution sequence of the section, which requires additional processes than simple differentiation by fractional crystallization in the upper unit (***Suhr et al., 2008***). We combined the minerals *in situ* major element data of ***Suhr et al. (2008)*** with the data reported by ***Miller et al. (2009)*** for the considered section (*Figure 5.83*). The results show, as proposed by ***Suhr et al. (2008)***, that the ~400 m-long section can be divided into two different subunits, characterized by contrasting structures and geochemical signatures. It also confirms the statements established at the end of Chapter 4, that in our view those two subunits are associated in a single igneous reservoir. The

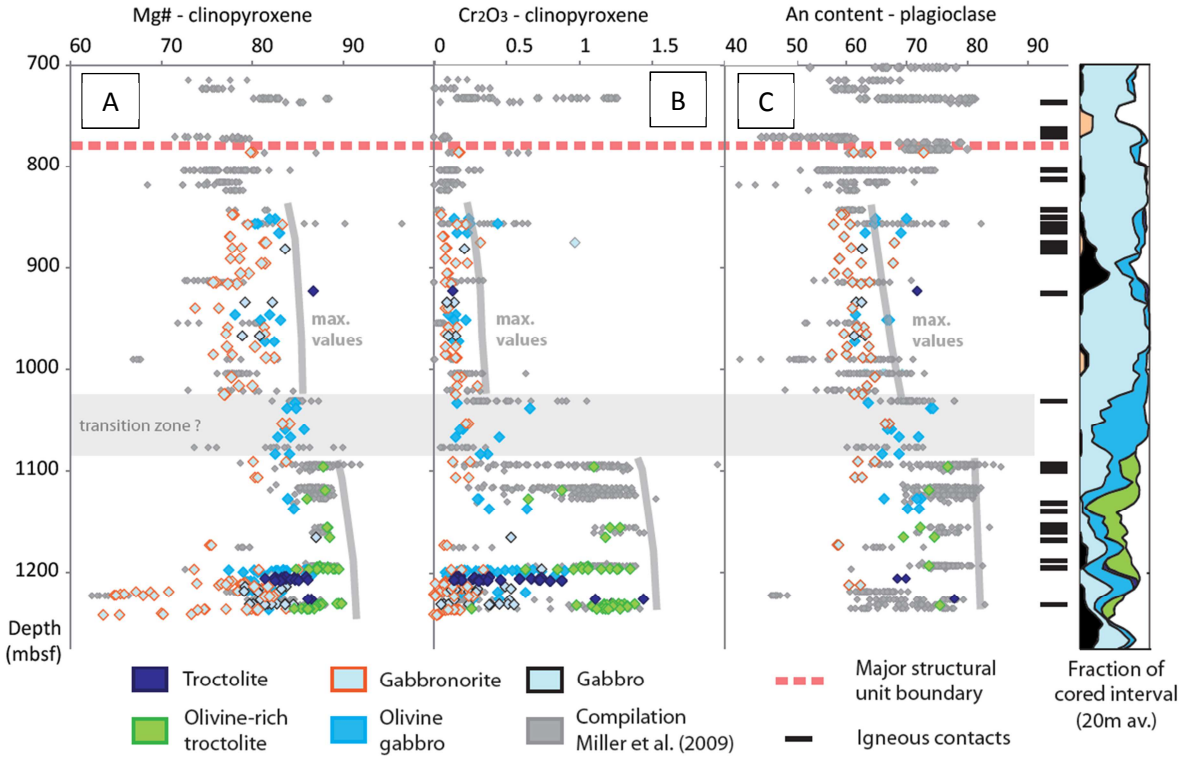

Figure 5.83 - Minerals in situ major and minor element contents in (a) Mg# and (b) Cr of clinopyroxenes, and (c) An of plagioclases from IODP Hole U1309D. Data points in grey from Miller et al. (2009), colored data points representing averages per sample of the minerals analyzed from Suhr et al. (2008). Major structural unit boundary, igneous contacts and (d) lithostratigraphic column from Blackman et al. (2006).

upper rather homogeneous subunit (between ~850 and ~1090 mbsf) is mainly composed of gabbros (including gabbronorites) and olivine gabbros, in addition to crosscutting oxide gabbros in the upper half of the sequence. In contrast, the lower subunit is made of interleaved gabbros and olivine gabbros with more primitive troctolites and olivine-rich troctolites, separated by numerous igneous contacts. The lower 50m of the subunit contains olivine-rich troctolites interpreted as mantle relicts crosscut and partially assimilated by basaltic melt percolation (***Drouin et al., 2010, 2009; Ferrando et al., 2018; Suhr et al., 2008***). Geochemically, the upper subunit present a progressive upward differentiation trend in whole rock Mg# and Cr contents (*Figure 5.81*) but rather constant and homogeneous minerals *in situ* contents (*Figure 5.83*). The lower subunit is instead more primitive, present more dispersed values in depth all along the section (e.g., clinopyroxene Cr contents between 1.5 and almost 0 wt%), and display no sign of progressive differentiation upsection.

3 Continuity of processes within the slow-spread lower oceanic crust: inputs from the new igneous reservoir model

In the following, based on previous descriptions from literature (*see 2.*), I aim at tentatively applying the models deduced from the high-resolution studies conducted during my PhD thesis to other portions of long *in situ* sections drilled at OCCs.

3.1 Differentiation governed by reactive porous flow processes

The results of this study (*Chapter 3* and *4*) are in agreement with recent considerations of melt-rock reactions as one of the main processes leading to differentiation of magmas in the lower slow-spreading lower oceanic crust (e.g., ***Lissenberg and MacLeod, 2016***; ***Lissenberg et al., 2019*** and references therein). Experimental constraints and numerical modeling for equilibrium or fractional crystallization show that the expected geochemical signatures related to those processes are usually at odds with the natural trend (*Chapter 1*). One of the characteristic signatures is the Ti content of clinopyroxene, which is higher than expected after fractional crystallization for minerals with the most primitive Mg#, as illustrated in *Figure 5.84.* for both ODP Hole 735B and IODP Hole U1309D.

At Atlantis Bank, the three high resolution projects conducted herein on 1/ the layered series of Hole U1473A, 2/ the most common intrusive contact type observed at Hole U1473A (coarse-grained - fine-grained igneous contacts that are observed in average every 3.5 m in the hole; ***Ferrando et al., in prep***; *Appendix 1.1*), and 3/ the 250 m thick intrusion sequence from Hole 735B show that MRR processes happened at all steps of formation of the lithologies. RPF

processes are key in the evolution of the lithologies in the proposed magmatic reservoir model, and control both the modal and geochemical signatures of plutonic rocks. ***Kvassnes (2003)*** and ***Dick et al. (2019)*** presented clinopyroxene trace element compositions of 8 different samples from Hole 735B, which they explain by *in situ* crystallization and / or AFC. The new data obtained here for the ~400 m-long section of Hole U1473A enable to confirm that RPF not only occurs at a local cm-scale but also at the scale of an entire hm-unit. The comparison of the new data with our magmatic reservoir model established in Chapter 4 reveals that the two main units of U1473A are similar to the Upper unit of the reservoir model. Hence, the processes identified at Hole 735B are likely widespread during accretion of the lower slow-spreading oceanic crust at Atlantis Bank. At Atlantis Massif, several lines of evidence for melt-rock reactions associated to assimilation of mantle lithologies already existed (*see 2.2.2*). The comparison between the magmatic reservoir model and the ~400 m-long section of Hole U1309D also implicates the involvement of RPF during the evolution of the reservoir(s), even if the exact magnitude and impact of the processes is yet to be determined. Similarly in the rest of the section, the exact implication of RPF is unclear, which is mainly due to a lack of data and detailed studies on the gabbroic portions of the cores. In general in the three long in situ sections of lower crust considered, ubiquitous evidence for RPF are found at all scales and at all steps of formation of the lithologies. It confirms that mush-dominated magma reservoirs are present in the crust and that RPF processes likely control a very large part of differentiation at slow-spreading ridges.

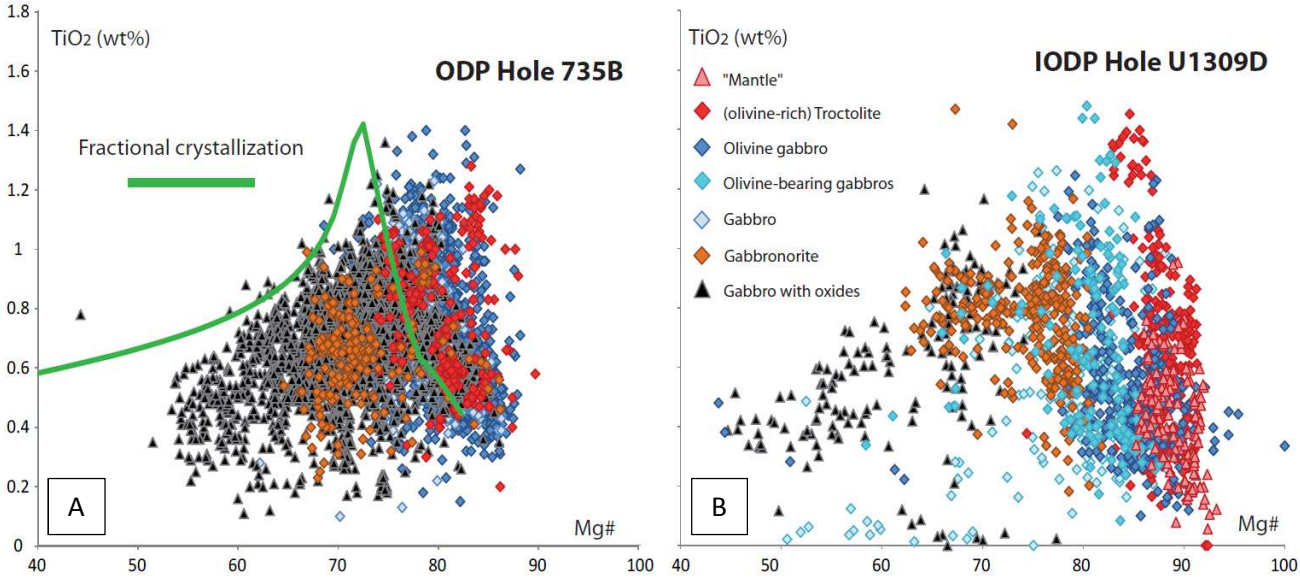

Figure 5.84 - Clinopyroxene TiO_2 contents (wt%) versus Mg# of samples from (a) ODP Hole 735B (data from Dick et al., 2002) and (b) from IODP Hole U1309D (Miller et al., 2009). The green trend represents fractional crystallization modeling of an average primitive MORB melt from the Atlantis Bank area modeled by MELTS.

3.2 Magma reservoir dynamics: a hidden link between the Atlantis Bank and the Atlantis Massif OCCs?

The direct comparison between Atlantis Bank (ODP Hole 735B and IODP Hole U1473A) and Atlantis Massif (IODP Hole U1309D) seems hazardous as both sections present strong dissimilarities. The proportions of the lithologies encountered are different in both structures, the holes' structure and microstructures are also contrasting (much more deformed at Atlantis Bank), not to mention the geochemical discrepancies with an average more primitive section sampled at Atlantis Massif (*Figure 5.85*). However, the new model of magma reservoir formation and evolution presented in Chapter 4, and complemented by the more detailed observations presented in Chapter 3 and in *Appendix 1.1* (***Ferrando et al., in prep.***) possibly pave the way for new interpretations on lower crust accretion processes.

Figure 5.85 - Comparison between long in situ sections drilled at Atlantis Massif (a - IODP Hole U1309D) and Atlantis Bank (b - ODP Hole 735B and c - IODP Hole U1473A). Left: Running average (20 m) of lithologies. Center: Whole rock Mg# with depth. Right: Localization and dip of igneous contacts described in the cores. Red dashed lines: main structural unit boundaries as described by Blackman et al. (2006), Dick et al. (2000) and MacLeod et al. (2017), respectively. Whole rock data from Godard et al. (2009 - IODP Hole U1309D), compilation as described in Chapter 4 of the present thesis for ODP Hole 735B, and from MacLeod et al. (2017 - IODP Hole U1473A).

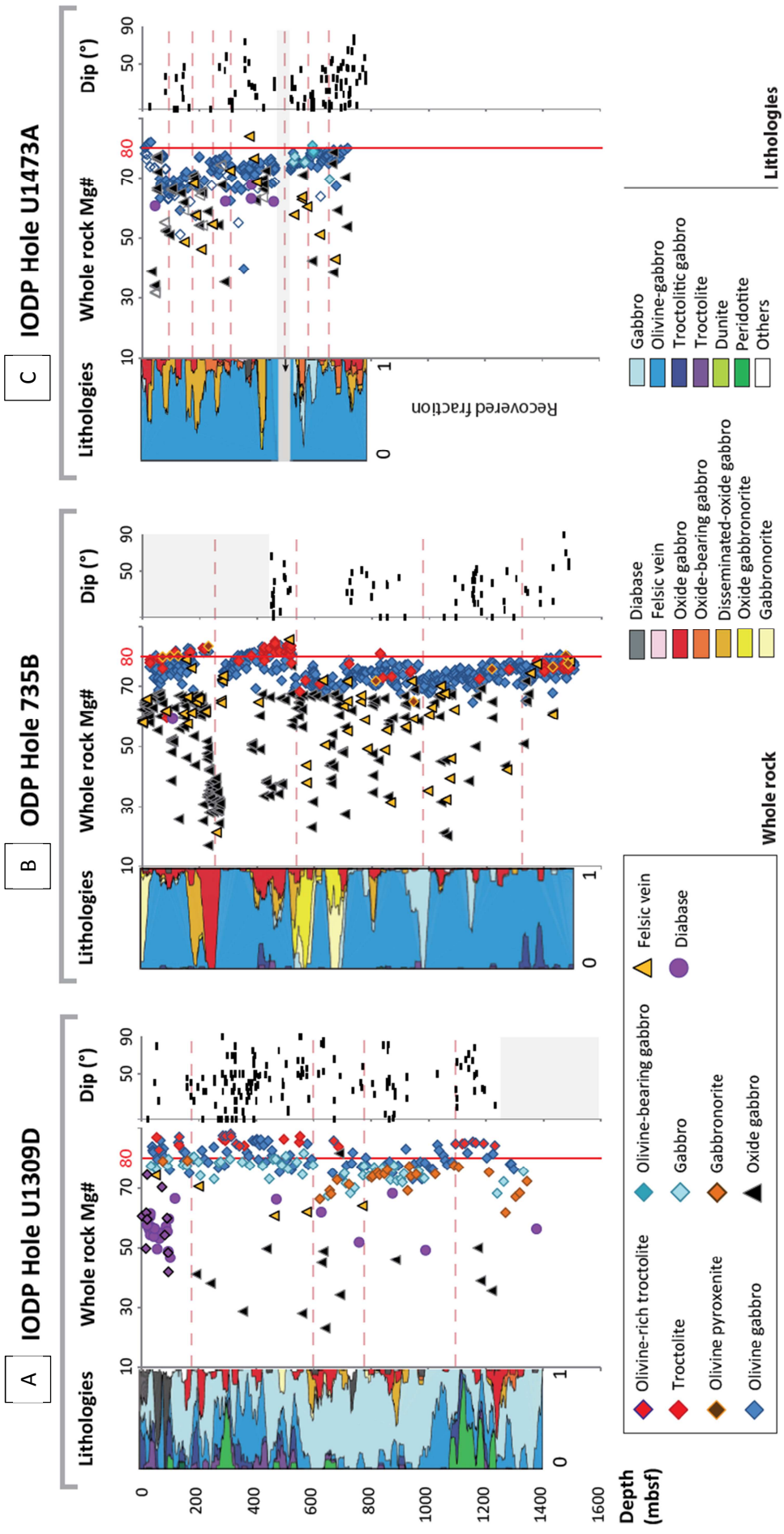
A
IODP Hole U1309D
B
ODP Hole 735B
C
IODP Hole U1473A
Lithologies
Whole rock Mg#
Dip (°)
Recovered fraction
Depth (mbsf)
0
200
400
600
800
1000
1200
1400
1600
10
30
50
70
80
90
0
1
Olivine-rich troctolite
Troctolite
Olivine pyroxenite
Olivine gabbro
Olivine-bearing gabbro
Gabbro
Gabbronorite
Oxide gabbro
Felsic vein
Diabase
Whole rock
Diabase
Felsic vein
Oxide gabbro
Oxide-bearing gabbro
Disseminated-oxide gabbro
Oxide gabbronorite
Gabbronorite
Gabbro
Olivine-gabbro
Troctolitic gabbro
Troctolite
Dunite
Peridotite
Others
Lithologies

The comparison between the proportion and location of the lithologies, the presence (or lack) of igneous contacts, and the available whole rock and minerals *in situ* analyzes available for the section of Hole U1309D detailed by ***Suhr et al. (2008)*** show that the section present very similar characteristics with the intrusion of Hole 735B studied in Chapter 4. Between ~850 and ~1050 mbsf the relative scarcity of igneous contacts, the presence of more evolved lithologies with rather homogeneous compositions, and the progressive differentiation observed in whole rock compositions towards the top of the sequence strongly recall the characteristics observe in the Upper unit of the intrusion studied in Hole 735B. Similarly, between ~1050 and ~1250 mbsf the section present numerous igneous contacts between interleaved primitive (troctolites and olivine-rich troctolites) and more evolved lithologies (gabbros *sensus lato* and olivine gabbros) as found in the Lower unit of the 735B intrusion. In addition, the compositional ranges are wider and record the most primitive signatures of the sequence, with a sharp transition towards the upper subunit and no systematic variations with depth.

We propose here that this section of Hole U1309D has formed thanks to the same complete scenario as proposed in the igneous reservoir model (*Figure 5.86*). The lower subunit would represent stacked interlocking sills, and the upper subunit an overlying reservoir which collected melts from the lower sills, and which progressively evolved upsection. In details a few differences can be observed between the reservoirs of Hole 735B and Hole U1309D. First, the lower subunit present alternations between gabbroic and olivine-rich lithologies interpreted as assimilated mantle, which are not found in Hole 735B. These observations however are not incompatible with the model developed here, since slivers of mantle lithologies can be trapped during accretion of gabbroic sequences by multiple sill intrusions (***Sanfilippo and Tribuzio, 2013***). More detailed descriptions of the cores are required, but such relationships are rather consistent with the model proposed in Chapter 4.

For the rest of IODP Hole U1309D, the comparison between the igneous reservoir model and the sections is more arduous. The compilation of microprobe data by ***Miller et al. (2009)*** show that the mineral signatures of the upper subunit is very specific to this section, located between ~850 and ~1090 mbsf. Above it, minerals major and minor element contents (e.g., plagioclase An content, clinopyroxene Mg# or Cr contents - *see Appendix 3.4*) rather compare to those found in the lower subunit between ~1090 and ~1150 mbsf. Together with previous models of accretion developed by ***Grimes et al. (2008)*** or ***Godard et al. (2009)***, we propose that the rest of the section drilled at Atlantis Massif formed by multiple sill injections similarly to the Lower unit of the igneous reservoir model.

We also explored possible correspondences between the magmatic reservoir model presented in Chapter 4, and the rest of Holes 735B and U1473A. Hole U1473A lack troctolites, and many of the intrusive contacts described in Hole U1473A are actually contacts between coarse grained olivine gabbros and finer grained patchy olivine gabbros that are interpreted as evidences of local melt migration (***Ferrando et al., in prep.***; *Appendix 1.1*). In addition to the upward differentiation trends in whole rock Mg# or other differentiation indexes, the whole rock and minerals in situ compositional ranges (*Figure 5.77*) are very similar to those of the section between ~250 and 550 mbsf of ODP Hole 735B. Overall, these observations rather suggest that an accretion model similar to the Upper unit of our magmatic reservoir model presented in Chapter 4 may apply to those sections (*Figure 5.86*).

Conclusions for the comparison between the section located between ~250 and 550 mbsf (equivalent to the igneous reservoir model) and the rest of the Hole 735B are not as straightforward. On one hand, some of the whole rock geochemical signatures recorded in depth are close to those of the Lower unit of the igneous reservoir model (e.g., Mg# above or close to 80 between 0 and ~250 mbsf, and between ~1300 mbsf and the bottom of the hole), and are conjugated with the presence of the primitive lithologies (troctolitic gabbros and troctolites, *Figure 5.85*). However some differences remain, and for example the "coarser grained" troctolites from the bottom of the Hole (>1300 mbsf) have been described as "chemically and texturally distinct" from the troctolites sampled in the Lower unit of the igneous reservoir model (***Dick et al., 2000***). On the other hand, all units have been described as composed of rather homogeneous olivine gabbro sections, all presenting relatively progressive differentiation trends upsection. In addition except for the two units described above, the ranges of compositions of the units are similar to the one of the Upper unit of the igneous reservoir model. Overall, I suggest that most of the section compare to the Upper unit of the reservoir model based on the second unit of Hole 735B. In addition, the shallowest and the deepest units either potentially represent sections equivalent to the Upper unit of the reservoir model crosscut by more primitive intrusions, or an hybrid reservoir type between the two end member dynamics (sills-stacked and homogeneous percolation). Further descriptions and geochemical study of the Hole would help confirm or revise the attempted comparisons, and which are summarized in *Figure 5.86*.

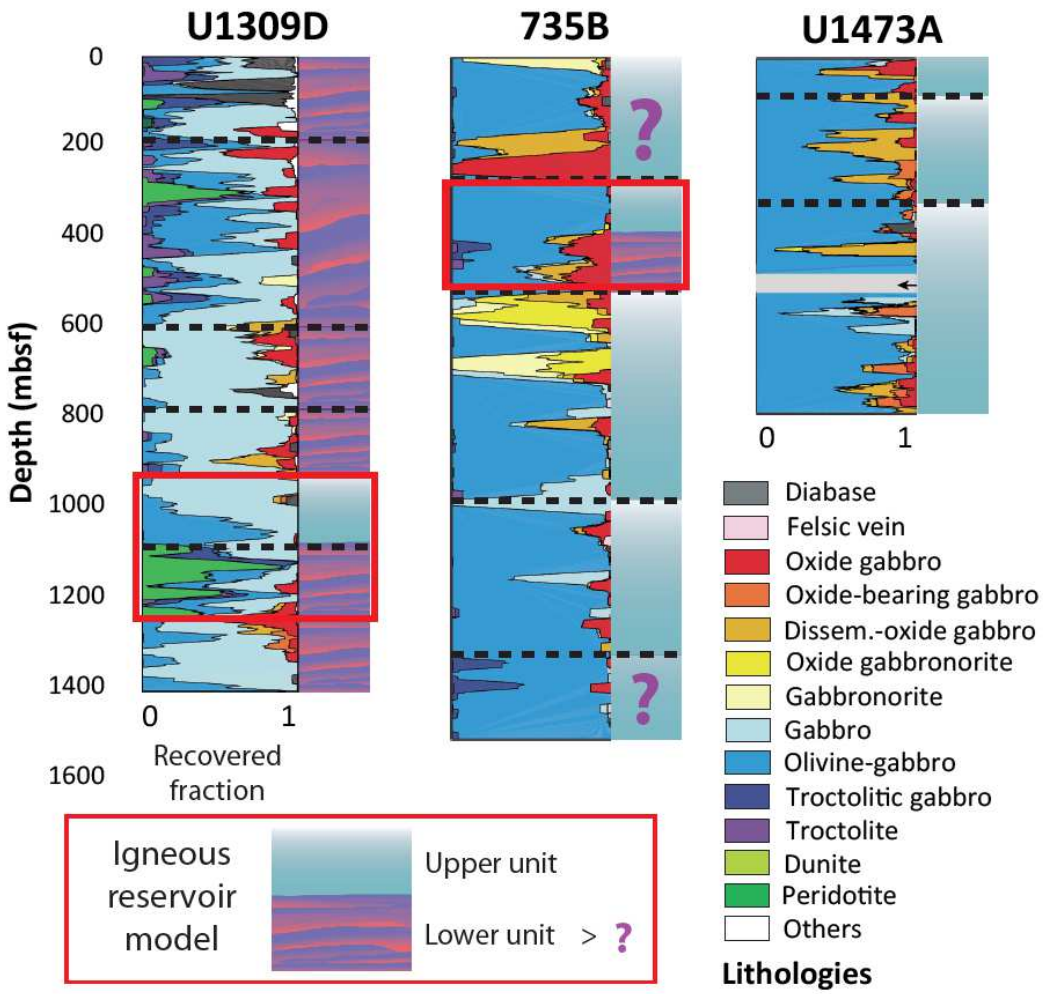

Figure 5.86 - Synthesis of the comparisons established between the igneous reservoir model (based on the second unit from the top described in ODP Hole 735B - Chapter 4), the ~400 m-long section described by Suhr et al. (2008) in IODP Hole U1309D, and the rest of the cumulate sequences drilled at the Atlantis Bank and the Atlantis Massif OCCs. Lithostratigraphic columns from MacLeod et al. (2017) and magmatic reservoir model as described in Chapter 4.

CHAPTER VI.

Experimental constraints on the evolution of tholeiitic magmas at Atlantis Bank

Liquid line of descent for equilibrium crystallization and fractional crystallization, and new experimental determination of Rare Earth Elements partition coefficients for the Atlantis Bank system

- PART 1 -

General introduction

The models for magma migration and storage in the lower slow-spreading oceanic crust developed above are based on 1/ the structure of the sequences studied, on 2/ the petrographic characteristics and 3/ geochemical signatures of the samples analyzed. We are now able to propose more specific constraints on processes involved in the formation and evolution of magma reservoirs during crustal accretion, with a new model that can potentially be applied more generally to magma accretion at slow-spreading ridges. A majority of the samples geochemical signatures fails to be explained by simple crystallization processes, and are more coherent with an evolution partly controlled by processes associated to reactive porous flow. Numerical models together with petrographic observations enabled to first order determine the parameters of the melt-rock reactions at stake during magma evolution. This is the case for instance with the determination of the type of assimilated crystal matrix and reactive melt composition at stake for the AFC processes involved in the igneous reservoir model. Overall, one of the main outcomes from this work is that RPF is strongly involved at all stages of formation of the lower crust lithologies. However, the exact share of those processes compared to simple crystallization, and the type of interaction mechanisms are still to be questioned.

Details on the processes involved and their feasibility in the lower crust system are usually lacking, even though strong petrographic constraints are implemented in the models. RPF processes are usually determined by considering numerical models that reproduce the geochemical variability and / or evolution tendencies found in natural samples. In contrast and in addition to eventual reactive textures found in the samples, deviations of the natural compositions from the geochemical differentiation trends determined by numerical modeling for simple crystallization processes guide the search for alternative models to implement in the evolution of the lithologies. The main questions arising are how are constrained the models of simple crystallization and RPF processes, and are they applicable here to the Atlantis Bank system. As mentioned earlier, even though RPF seems preponderant, the exact share between both types of processes is yet to be determined and can potentially be constrained thanks to a precise understanding of the reactions ongoing during differentiation.

Experimental studies enable to reproduce igneous processes under controlled conditions, with only variations of few known parameters which allow constraining their effect on the system. Direct studies of melt-rock reactions for mantle lithologies are numerous (e.g. ***Borghini et al., 2018; Daines and Kohlstedt, 1994; Lambart et al., 2009***), but only ***Kvassnes and Grove (2008)*** and ***Yang et al. (2019)*** focused on interactions applied to gabbroic crustal cumulates. ***Kvassnes and Grove (2008)*** studied the behavior of mineral pairs from oceanic lower crust samples (olivine-plagioclase and clinopyroxene-plagioclase) during melting experiments, as they tried to constrain the impact of reheating by replenishment within the crust. ***Yang et al. (2019)*** more recently studied the reaction between MORB melts with troctolite at lower crust conditions, which is one the main reaction considered in the literature (*see Chapter 1*) and in the igneous reservoir model established in this thesis. The results of their experiments show that such reaction lead to the formation of melts and cumulates with similar compositions and textures as those witnessed in natural samples (e.g. reacted troctolites containing high-Mg clinopyroxenes, some with poikilitic textures engulfing resorbed plagioclase or olivine grains). Experimental studies of simple crystallization of tholeiitic to calc-alkaline systems are much more common, and are done for variable conditions of pressure or water contents. The experimental systems considered are not always appropriate for the study of Atlantis Bank due to different starting melt compositions, inadequate pressure of crystallization which does not reflect crystallization pressures in the lower crust, or different water contents or redox conditions (see details below). However, most of the numerical models described above consider thermodynamic laws that are calibrated on these experiments.

Ideally, and in order to answer the questions established in the previous paragraphs, all three main types of crystallization and melt-rock processes are to be tested experimentally under conditions consistent with the Atlantis Bank lower crust. In the following, I show the results of equilibrium crystallization and for the first time fractional crystallization experimentally determined for Atlantis Bank (Part 2), together with new trace elements partition coefficients determined for the system (Part 3). Crystallization was conducted at single pressure and redox conditions (2 kbar and QFM), for two different initial water contents ("nominally dry" and 1.5 wt% H_2O) and at temperatures between 1200 and 1030°C. Partitioning experiments were done for one step of temperature at 1100°C, based on the results of the crystallization experiments. All experiments and associated preparations were conducted at the Institut für Mineralogie of the Leibniz Universität Hannover (Germany) as part of the cotutelle project of the PhD thesis.

- PART 2 -

Experimental constraints on equilibrium and fractional crystallization of a tholeiitic MORB-type melt from Atlantis Bank

This project has been conducted at the Institut für Mineralogie of the Leibniz Universität Hannover, Germany. Three different stays for a total duration of about 9 months were necessary to obtain the results presented in the following sections. This work has been realized in close collaboration with Chao Zhang (now at the Northwest University of Xi'an, China), and with the help of the Petrology group from the Institut.

1 Introduction

Many experimental studies detail phase equilibrium and the evolution of melts by simple crystallization processes (e.g. ***Berndt et al., 2005; Feig et al., 2010, 2006; Grove et al., 1992; Koepke et al., 2018; Nandedkar et al., 2014; Neave et al., 2019; Sisson and Grove, 1993; Toplis and Carroll, 1995; Villiger et al., 2004, 2007***). The majority of the studies focus on equilibrium crystallization for a range of composition and conditions, but only few report fractional crystallization experiments (***Nandedkar et al., 2014; Neave et al., 2019; Villiger et al., 2007***). However, the textures and the common cumulative geochemical signatures of natural igneous rocks rather suggest the involvement of fractional crystallization during their evolution (e.g., ***Dick et al., 2000; Villiger et al., 2007***). In addition, the few studies that compared equilibrium and fractional crystallization for similar starting composition and conditions show that both processes lead to significantly different liquid lines of descent, phase relationship and evolution of melt compositions (***Villiger et al., 2007, 2004***). The limited data set available for tholeiitic systems is partly due to the fact that before the development of rapid quench equipment (***Berndt et al., 2002a*** and references therein), especially at moderate pressures, basaltic systems tend to form quench crystals upon cooling that disrupt the experiment products. Fractional crystallization experiments are also difficult to implement. One of the most common technique used to reproduce fractional crystallization is the stepwise approach (e.g., ***Nandedkar et al., 2014; Neave et al., 2019; Villiger et al., 2007, 2004***). It involves the synthesis of a new starting melt composition between each temperature increment of the experiments, when equilibrium crystallization experiments only involve crystallization of the same starting melt at different temperatures.

The conditions of crystallization are also crucial for the evolution of melts, in addition to the initial basaltic melt composition considered. A typical example is the phase relationship between plagioclase and clinopyroxene, which is of fundamental relevance for oceanic crust systems (***Coogan, 2014*** and references therein). For example, at dry conditions and moderate to low pressure ($<$ 4 kbar) the typical tholeiitic crystallization sequence starts with crystallization of olivine, followed by plagioclase and finally clinopyroxene (e.g., ***Grove et al., 1992***). The increase of pressure for the same dry condition results in an increase of the stability of clinopyroxene, which crystallizes earlier in the sequence and bear as a result more primitive composition (i.e. more magnesian, ***Grove et al., 1992; O'Hara, 1968***). This principle is the basis of the majority of the barometers used to determine the depth of crystallization of MORB melts and cumulates within the lower oceanic crust (***Villiger et al., 2007a*** and references therein). However, the melt water content has also a strong influence on the same phase equilibrium at pressure $>$1 kbar as shown for example by ***Feig et al. (2006)***. The authors show that the

stability of plagioclase is suppressed at H_2O in melt >3 wt%, leading to early crystallization of clinopyroxene before plagioclase. More systematic calibration of the effect of pressure and melt H_2O are given by ***Husen et al. (2016),*** who also demonstrate that even addition of small amounts of H_2O in melts strongly influence the cotectic melt composition: the effect of an addition of 0.4 wt% of H_2O in a melt is equivalent to an increase of 1 to ~3 kbar in pressure during crystallization. However, most of the crystallization experiments of basaltic systems were initially conducted at dry conditions, as no evidence for the presence of large amount water was detected in the natural rock record before the development of new analytical techniques (***Berndt et al., 2005*** and references therein). Even if water was actually added to the melt, some studies reproduced water saturated conditions that are not always representative of crustal systems (***Feig et al., 2006*** and references therein). Finally, the other main parameter controlling phase equilibria during crystallization of basaltic melts is the oxygen fugacity and the redox conditions applied to the system, which control the oxidation state of iron and the ratio Fe^{2+}/Fe^{3+} of the melt. Whereas the water content of the melt rather influence the saturation curves of silicate minerals, the oxygen fugacity or fO_2 has a major effect on oxide minerals and to a lesser extent on the most mafic phases (i.e. olivine and pyroxene, ***Koepke et al., 2018*** and references therein). At high fO_2, oxides and orthopyroxene are stable and crystallize from MORB-type melts, thus removing Fe from the melt which differentiate following a calc-alkaline trend. In contrast at low fO_2 the same minerals are not stable, and the melt follow a tholeiitic differentiation trend (at an equivalent QFM buffer - ***Berndt et al., 2005***).

Equilibrium and particularly fractional crystallization were long considered as the main processes governing magma differentiation of basaltic melts in the lower oceanic crust, in addition to other processes of magma mixing, assimilation of external components (such as mantle lithologies) or melt-rock reactions within mushy magma reservoirs. The last type of magma storage structure within the crust and associated occurrence of reactive porous flow (RPF) processes are observed in almost every lower crust sections from slow-spreading ridges. Hence, the quantification of the balance between RPF and simple crystallization processes turned into a key issue for the understanding of magma accretion in those environments. To this end, precise constraints on crystallization processes are required to identify the diverging petrographic or geochemical characteristics that would be potentially associated to melt-rock reactions. According to the above discussion, such constraints are only accurate if the conditions applied during crystallization are close to the alleged conditions of the natural system. In this study we focus on the magmatic system described at the Atlantis Bank Oceanic Core Complex (Southwest Indian Ridge). We quantified the results of equilibrium and fractional crystallization of typical MORB-type melts from the area, which are characterized by elevated Na and Ti compared to MORB from other spreading centers. The crystallization experiments were

conducted at two different initial water contents in order to study the effect of water on the phase equilibrium and evolution of the melt composition, and under a constrained fO_2 at QFM buffer. We ultimately tried to compare the results of the crystallization experiments with the results of thermodynamic numerical modeling of the same processes, and to the natural rock record of the Atlantis Bank area.

2 Methods

Four different suites of experiments were performed at 0.2 GPa, two of them corresponding to equilibrium crystallization and the others to fractional crystallization. A total of 6 temperature steps were investigated between 1200°C and 1030 °C. For the equilibrium crystallization experiments, the starting composition at each temperature step was the same initial melt composition, i.e. a synthetic reproduction of a diabase dike sampled in IODP Hole U1473A. The same approach as described by ***Villiger et al. (2007, 2004)*** was used here to approximate fractional crystallization. The stepwise approach consists in analyzing the residual melt composition of each experiment, which is then reproduced and used as the starting melt composition of the next experiment. For both types of crystallization experiments, one series was conducted under "nominally dry" conditions (~0.5 wt%) and the second with an initial H_2O content (~1.5 wt%).

2.1 Starting material

The initial starting material of the crystallization experiments is a synthetic reproduction of a diabase dike sampled in a long *in situ* section of lower oceanic crust drilled at Atlantis Bank (SWIR). In details, the diabase sampled in core 360-U1473A-42R1 is a ~3 m thick micrograbbro that intrudes olivine gabbros. The whole rock composition of the diabase is similar to the composition of the most primitive MORBs sampled in the Atlantis Bank area, and lacks any evidence of a significant cumulative character of the rock (e.g., high Ni contents translating olivine accumulation, *Figure 6.87*). Similar diabases or microgabbros from ODP Hole 735B have been interpreted by ***Dick et al. (2000)*** as feeding melt conduits emplaced through the crystallizing reservoirs of the crust. In details, the diabase is composed of olivine, plagioclase and some clinopyroxene phenocrysts embedded in a microgranular olivine gabbro matrix, also containing accessory minerals (orthopyroxene, oxide, sulphide, amphibole and spinel - ***Toussaint et al., in prep.***).

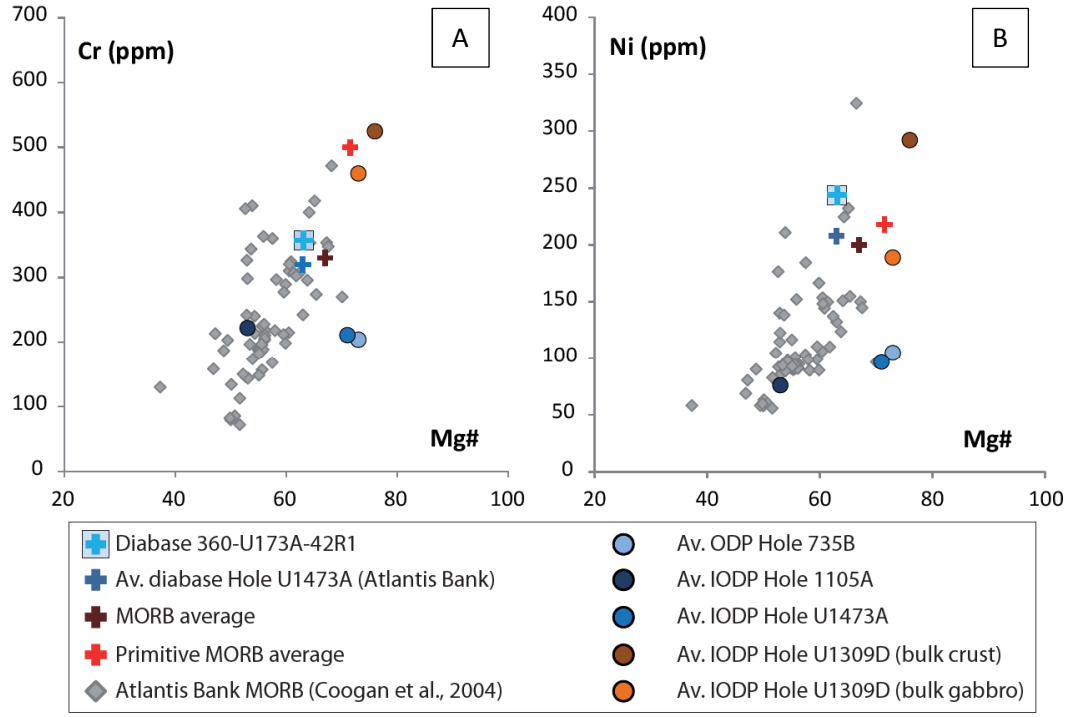

Figure 6.87 - Whole rock composition of the primitive diabase dike 360-U1473A-42R1 in (a) Cr and (b) Ni in ppm versus Mg# (molar ratio Mg / Mg + Fetot). Grey symbols represent the composition of individual MORB samples collected in the vicinity of Atlantis Bank from Coogan et al. (2004). The average compositions from MacLeod et al. (2017) and references therein represent the average compositions of MORB-type melts (global average, primitive average and equivalent melts sampled at Atlantis Bank - average diabases) and of lower crustal sections drilled in the Atlantis Bank OCC (Holes 735B, 1105A and U1473A) and in the Atlantis Massif OCC (Hole U1309D).

All starting materials (*Table 6.2*) were synthetized following the same procedure. A mix of oxide and carbonate powders was homogenized by grounding in an agate mortar, and melted three times at 1 atm and 1600°C during 2 to 3 hours. The large Pt crucibles were dipped into clear water bowls at room temperature to proceed to the quenching of the melts after each melting sequence. The resulting glasses were then powdered in an agate disc or bowl mill before the next step of melting or before being used in the experiments. After the final melting step, the homogeneity of the synthetic glasses and their composition were checked before crushing by electron microprobe analyses on randomly selected pieces of glass. The same synthetic glass composition SG-01 was used for all temperature steps of the equilibrium crystallization experiments, and two different synthetic glass compositions were prepared for the fractional crystallization experiments at each temperature step, one for the "nominally dry" series and the other for the water-bearing series.

Table 6.2- Starting material compositions.

Sample	SiO_2	TiO_2	Al_2O_3	FeO	MnO	MgO	CaO	Na_2O	K_2O	P_2O_5	Total	Mg#
SG-01	48.59	1.50	16.19	9.85	0.17	8.93	11.40	3.06	0.20	0.12	100	61.8
SG-04	49.45	1.64	16.95	9.77	0.23	6.46	11.90	3.25	0.22	0.13	100	54.1
SG-05	49.44	1.56	16.95	9.65	0.22	7.11	11.87	2.94	0.20	0.06	100	56.8
SG-06	48.86	1.97	16.01	12.72	0.26	5.71	10.67	3.32	0.24	0.24	100	44.5
SG-07	49.76	1.58	17.16	9.47	0.20	6.67	12.02	2.78	0.21	0.13	100	55.7
SG-08	47.03	3.01	13.00	19.72	0.42	3.91	9.01	3.35	0.40	0.19	100	26.1
SG-09	50.38	1.80	16.14	11.56	0.26	5.28	11.27	2.86	0.25	0.19	100	44.9
SG-11	49.50	2.72	14.13	16.67	0.39	3.59	8.95	3.31	0.38	0.36	100	27.7
SG-12	50.94	1.92	16.48	12.95	0.22	4.41	9.65	2.99	0.26	0.19	100	37.8

2.2 Experimental setup

Crystallization experiments were performed thanks to a large-volume internally heated pressure vessel (IHPV) in Fe-presaturated $Au_{80}Pd_{20}$ capsules in order to minimize iron loss by diffusion from the melt into the capsule at high temperature (*see 2.4*). The capsules were filled with 40 or 80 mg of starting material powder and, for water-bearing experiments, by 0.6 or 1.2 mg of distilled water using a microsyringe. The two "nominally dry" capsules or the two capsules with water were then placed together within the IHPV equipped with a rapid quench system, using a mixture of Ar and H_2 as pressure medium (details in ***Berndt et al., 2002*** and references therein). Dry experiments rather correspond to "nominally dry" conditions as it has been shown that perfectly dry starting compositions are difficult to load into the capsules (e.g. ***Berndt et al., 2005; Feig et al., 2006***), with initial compositions estimated at ~0.5 wt% H_2O. As described in ***Feig et al. (2006)***, the water can result from the reaction between the air present in the capsule and the hydrogen used to control the fO_2 of the experiments. Water can also come from the ambient moisture of the air during the preparation of the capsules, or formed after a potential release of oxygen from the iron present in the capsules at low fO_2 and reaction with hydrogen. The hydrogen partial pressures were determined according to the water content and composition of the starting material in order to reach the QFM buffer for all experiments (procedure by ***Scaillet et al., 1995***). Experiments were performed at 2 kbar (approximate crustal pressure at mid-ocean ridges, e.g. ***Feig et al., 2006; Grove et al., 1992***) at temperatures of 1200, 1150, 1125, 1100, 1070 and 1030°C to construct phase diagrams for the early crystallization sequences. The experiments lasted 24 to 48h, with temperature continuously measured with four S-type thermocouples.

2.3 Analytical methods

The capsules resulting from the experiments were prepared and mounted in epoxy resin. The samples were then carbon coated for BSE imaging with a JSM-7671F scanning electron microprobe (SEM), and analysis of melt and minerals phases with a Cameca SX100 electron probe micro analyzer (EPMA). An accelerating voltage of 15 kV was used for all measurements. Beam current was of 15 nA for minerals and 10 nA for glass, with a beam size of 5 µm for glass, 2 µm for plagioclases and a focused beam for olivines, clinopyroxenes and oxides. Analyses were normalized to standards measurements during each session (values from ***Jarosewich et al., 1980***). In addition, the water content of the residual melts for some of the experiments was approximated by the "by-difference" method (***Devine et al., 1995***) thanks to the analysis of water-bearing MORB glasses composition (reference compositions in ***Berndt et al., 2002***).

2.4 Loss of iron

Feig et al. (2010) observed an increase of iron diffusion into $Au_{80}Pd_{20}$ capsules with decreasing fO_2 at temperatures above 1020°C, which means that iron loss must be taken into account especially at a QFM oxygen buffer as considered in this study. In order to minimize iron loss by diffusion during the experiments, the capsules were pre-saturated at ~0.25 wt% Fe and then loaded with 40 mg to 80 mg of the starting glass powder. The majority of the experiments analyzes where also carried whenever possible close to the center of the capsules, to avoid potential greater iron loss of the material at the contact with the $Au_{80}Pd_{20}$ capsules. The amount of iron considered to be lost from the melt has been determined by mass balance calculation for each experiment. This parameter is particularly sensible for the fractional crystallization experiments as the starting melt composition of each run is the composition of the residual melt from the previous experiment. The maximum iron loss recorded is of 6.73 wt% for experiment MB-19 (at 1030°C), and is on average of 1.79 wt% for the fractional crystallization experiments. The final melt iron content for each experiment was corrected with the iron value given by the mass balance calculation.

2.5 Calculation of oxygen fugacity

Both fO_2 and water content of the experiments are coupled, as the balance between the water content of the system and the oxygen buffer is controlled by the water dissociation equilibrium detailed in ***Botcharnikov et al. (2005)*** and ***Scaillet et al. (1995)***. The initial oxygen buffer at the beginning of the experiments was constrained by applying an initial pressure of H_2 mixed with Ar in the IHPV. The H_2 pressure required to reach the QFM buffer was calculated

thanks to the composition of the starting material, the expected initial water content in the capsules, the temperature and the pressure of the experiments. The calculation of the oxygen fugacity of the experiments is based on the method used by ***Feig et al. (2010, 2006)*** who conducted crystallization experiments for similar compositions and with the same apparatus at the Institut für Mineralogie of the Leibniz Universität Hannover. However, the water content of the melt progressively changes during crystallization and is higher at the end of the experiments, and additional data are required for the "nominally dry" experiments above 1100°C, and for the 4 experiments at 1030°C. In the following, I am leaving out for now consideration of variations in oxygen fugacity during the experiments, and only consider the starting fO2 buffered at QFM.

3 Results

The parameters of crystallization for each run are available in the following *Table 6.3* together with the proportions of each phase present in the run products.

Table 6.3 - Experimental run conditions, phase assemblage and associated proportions

Run	Crystallization series	Initial H2O content (wt%)	Starting mat.	Pressure (kbar)	T (°C)	Time (h)	Phases (Nb)	Glass (%)	Ol (%)	Pl (%)	Cpx (%)	Ox (%)
MB-01	Equilibrium Fractional	"nominally dry"	SG-01	2.03	1200	42	1	100	-	-	-	-
MB-02	Equilibrium Fractional	1.5	SG-01	2.03	1200	42	1	100	-	-	-	-
MB-03	Equilibrium Fractional	1.5	SG-01	2.09	1150	42	2	100	-	-	-	-
MB-04	Equilibrium Fractional	"nominally dry"	SG-01	2.02	1150	24	3	91.1	5.5	3.4	-	-
MB-05	Equilibrium	"nominally dry"	SG-01	2.05	1125	48	4	53.6	9.1	26.1	11.2	-
MB-06	Equilibrium	1.5	SG-01	2.04	1125	93	2	94.8	5.2	-	-	-
MB-07	Fractional	"nominally dry"	SG-04	2.05	1125	48	4	69.3	1.7	21.6	7.4	-
MB-08	Fractional	1.5	SG-05	2.04	1125	93	2	99.8	0.2	-	-	-
MB-09	Equilibrium	"nominally dry"	SG-01	1.99	1100	24	4	44.8	11.7	28.4	15.1	-
MB-10	Equilibrium	1.5	SG-01	2.01	1100	25	4	81.7	7.7	6.5	4.1	-
MB-11	Fractional	"nominally dry"	SG-06	1.97	1100	25	4	56.7	5.4	27.6	10.3	-
MB-12	Fractional	1.5	SG-07	2.01	1100	25	4	75.8	3.1	14.9	6.2	-
MB-13	Equilibrium	"nominally dry"	SG-01	2.00	1070	32	4	36.4	12	30.7	20.9	-
MB-14	Equilibrium	1.5	SG-01	1.92	1070	36	4	-	17.5	54.1	25.1	3.3
MB-15	Fractional	"nominally dry"	SG-08	2.00	1070	32	3	96.7	-	-	1.4	1.9
MB-16	Fractional	1.5	SG-09	1.92	1070	36	3	84	-	5.8	10.2	-
MB-17	Equilibrium	"nominally dry"	SG-01	2.07	1030	25	5	23.7	13	35.6	26.8	0.9
MB-18	Equilibrium	1.5	SG-01	2.05	1030	49	4	59.5	9.1	14.1	17.3	-
MB-19	Fractional	"nominally dry"	SG-11	2.07	1030	25	4	54.8	-	24.6	15.7	4.9
MB-20	Fractional	1.5	SG-12	2.05	1030	49	4	83.8	1.2	11.3	3.7	-

3.1 Achievement of equilibrium

A certain number of the criteria enumerated in ***Berndt et al. (2005)*** suggest that both equilibrium and fractional crystallization experiments achieved near-equilibrium conditions. First, within each run the composition of the phases and the crystal distribution in the capsules are homogeneous (*Figure 6.88*). The composition of the phases also vary systematically for each series and follow evolution trends that are coherent with evolutions determined during previous crystallization experiments. Only runs with successful quenching were acknowledge, and if the quenching procedure failed or if quench crystal were detected in the experiments another identical run was performed (e.g., for MB-14 and MB-16). The next step not yet conduced would be to determine mineral-mineral and mineral-melt (with corrected iron loss values) partitioning coefficients and verify the equilibrium condition and the validity of the iron loss corrections.

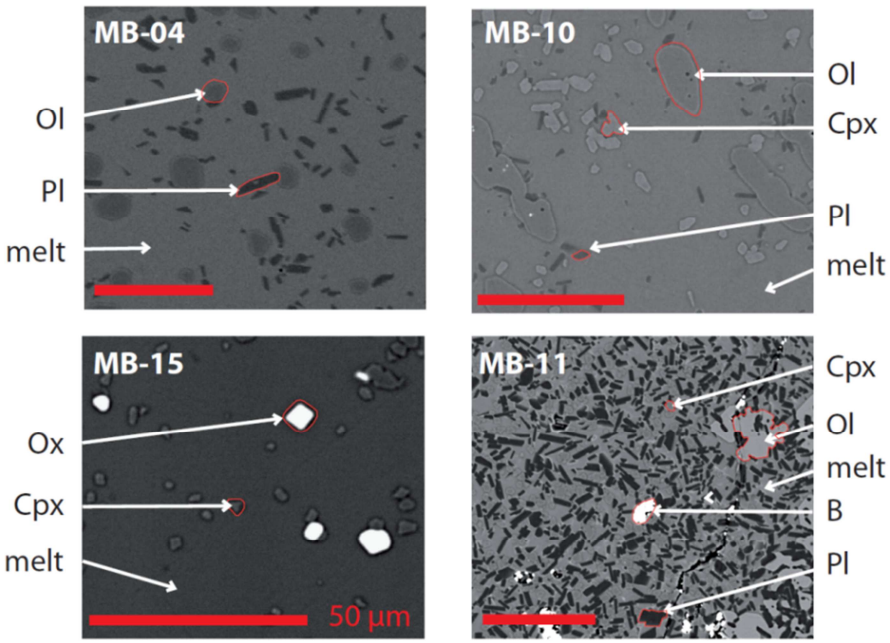

Figure 6.88 - Backscattered electron images of experimental products for run (see Table 6.2 for details on the experimental conditions). Ol: olivine, Pl: plagioclase, Cpx: clinopyroxene, Ox: oxide, B: bubble. All red scales represent 50 µm.

3.2 Phase relations

The type of crystallization involved (equilibrium or near-fractional) and the initial water content of the series ("nominally dry" or with 1.5 wt% H_2O) both have an effect on the saturation temperatures of the minerals, the amount of crystallization achieved in the system and the proportion of the different phases crystallized (*Figure 6.89*). Olivine is the liquidus phase for the water-bearing experiments and appears between 1150 and 1125°C, when it appears between 1200 and 1150°C for the "dry" ones. Those temperatures are equivalent to the liquidus determined at 2 kbar by ***Berndt et al. (2005)*** for a primitive MORB composition at

QFM, and almost 100°C lower than the olivine liquidus of ***Feig et al. (2006)*** for their low-water experiments (diabase composition from ODP Hole 735B). For the "dry" experiments olivine together with plagioclase starts to crystallize before 1150°C. Thus, the water content of the melt suppresses the crystallization of olivine by 25°C and of plagioclase by 50°C. Clinopyroxene appears together with plagioclase at 1100°C in the water-bearing experiments, and earlier at 1125°C in the "dry" experiments. Oxides are the last minerals to appear only in the "dry" experiments. Their saturation temperature is of about 1030°C during equilibrium crystallization, and occurs before 1070°C in the near-fractional experiments. Hence, the water content of the series is not the only parameter to influence the crystallization of oxides, the type of crystallization involved also plays a role. By comparison, oxide saturation temperature determined by ***Berndt et al. (2005)*** is of 950 °C and ***Feig et al. (2006)*** only observe crystallization of magnetite below ~1100°C.

The presence of water results in a decrease of the plagioclase and clinopyroxene saturation temperatures of about 50°C, as described before, and in lower proportion of the minerals crystallized within similar temperature interval as for the "dry" experiments. The proportions of phases crystallized also change as a function of the crystallization process considered (*Figure 6.89*). At similar water content of the starting melt, fractional crystallization leads to a higher decrease of the melt fraction with temperature. This effect is due to the cumulate amount of plagioclase crystallized in the systems which is higher for fractional crystallization. For example at 1030°C, about 36% of plagioclase formed during the equilibrium crystallization series, while in total 49% formed by fractional crystallization. In contrast though, the amount of clinopyroxene is higher for the equilibrium crystallization series (27% against 19% obtained by fractional crystallization).

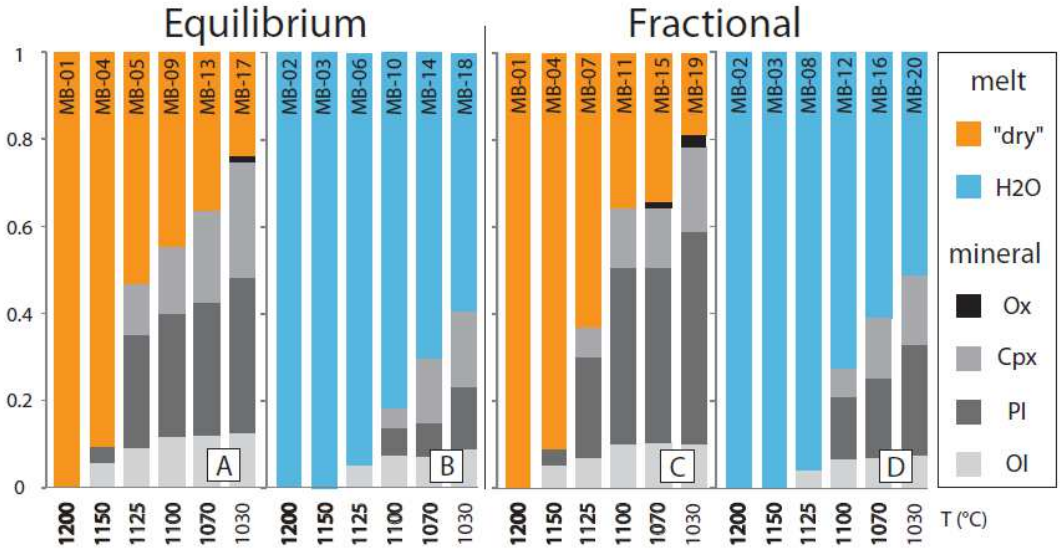

Figure 6.89 - Relative minerals and melt proportions in the products of the four experimental series for equilibrium (a and b) and fractional crystallization (cumulative phase proportions - c and d), and at "nominally dry" (orange melt phase, a and c) and water-bearing conditions (blue melt phase, b and d). See Table 6.2 for details.

3.3 Phase chemistry

The average compositions of melts and crystallized phases for each experimental run are available in *Appendix 4.1*.

Olivine

The evolution trend in Fo contents are similar for both equilibrium crystallization series, but are shifted of about 10 points towards higher values for the water-bearing experiments (*Figure 6.90a*). Similarly for the fractionation experiments, the olivine Fo contents are higher for the water-bearing series, with a steeper decrease of the Fo contents for the fractionation experiment at 1100°C (64.4 against 78.8 at water-bearing conditions). These higher Fo contents observed for water-bearing experiments can be the results of the higher melt fraction of the runs due to the presence of water in the systems (e.g. ***Feig et al., 2006***). As the fO_2 also controls the melt content in Fe^{2+}, this parameter potentially also influences the olivines Fo content: increases in the fO_2 would result in an increase of the olivine Fo content (***Berndt et al., 2005***). The range of compositions observed are similar to those of ***Berndt et al. (2005)*** for the B1 experiments at QFM, and of ***Feig et al. (2006)*** for the low-water experiments.

Plagioclase

The An content of plagioclases varies as a function of temperature, water content of the melt, and crystallization process considered, but is independent on the fO_2 (***Feig et al., 2010***). As already evidenced in other studies (***Feig et al., 2006*** and references therein), the higher the water content the higher the plagioclase An content. The values range between 81.8 and 67.5 for the water-bearing series and between 72 and 50.5 for the "dry" series (*Figure 6.89b*). There is a progressive decrease of the An content with temperature for all series, of about 0.2 mol%/°C at most for the dry fractional crystallization series. For the same initial water content of the starting material, fractional crystallization result in plagioclase with lower An contents which can be explained by the higher total amount of crystals formed in these series compared to the equilibrium crystallization series. The compositional range described here are consistent with the ranges obtained by ***Berndt et al. (2005)*** for the low-water experiments (between 0.5 and 1 wt% H_2O) at QFM, but also with those of ***Feig et al. (2006)*** at 2 kbar and for water contents $<$2.8 wt% H_2O.

Clinopyroxene

Classically, clinopyroxene Mg# increases with the increase of water content of the system (***Feig et al., 2010, 2006***; and references therein). The processes involved are the same as for the effect of water on olivine (see above). For the water-bearing experiments, clinopyroxene Mg# vary between 79.4 and 70.4 whereas they vary between 80.3 and 60.7 for the "dry"

experiments. For all four crystallization series, the clinopyroxene Mg# decreases with temperature (*Figure 6.89c*). This decrease is more important during fractional crystallization, potentially due to the higher cumulate amount of clinopyroxenes crystallized compared to equilibrium crystallization. The only exception to this evolution is the increase in Mg# of the equilibrium crystallization series under "dry" conditions at 1030°C, the temperature at which the first oxide minerals appear in the system. Thus, the crystallization of Fe-Ti oxide potentially leads to a decrease in Fe content of the melt and likely to an associated increase in the Mg# of the clinopyroxene, even though this effect is not observed for the fractional crystallization series under "dry" conditions where larger amounts of Fe-Ti oxide formed. In contrast, the TiO_2 contents tend to record the crystallization of oxide in the fractional crystallization experiments, due to the incorporation of Ti in oxides and subsequent removal from the melt. As a consequence, instead of a gradual increase in the minerals concentrations, clinopyroxenes present a decrease from 1.23 wt% TiO_2 at 1070°C to 0.85 wt% TiO_2 at 1030°C.

Overall, the clinopyroxene compositions analyzed in our experiments present significant differences with the compositions reported for similar experiments in the literature. The Mg# of clinopyroxenes from ***Feig et al. (2006)*** obtained for experiments conducted at 2 kbar and low-water contents are higher than 80 mol%, which is the higher bound of the compositional ranges obtained herein. Crystallization of the primitive MORB at QMF and 2 kbar from ***Berndt et al. (2005)*** leads to the formation above 1100°C of clinopyroxene with Mg# $>$ 80, and below 1100°C of clinopyroxenes with Mg# between 74.8 and 77.6. This last range corresponds to the compositional range for the water-bearing series and the equilibrium crystallization series for "dry" conditions. Finally, the most striking difference betweeen the clinopyroxene compositions of our experiments and the compositions of ***Berndt et al. (2005)*** and ***Feig et al. (2006)*** is the Ti content of the minerals. When our compositions range between 0.8 and 1.8 wt% TiO_2, those of the last two studies are lower than 0.8 wt% for temperatures above 1030 °C.

Fe-Ti oxides

The Fe-Ti oxide compositions of the "dry" experiments are often contaminated during analyzed by the glass, due to the small size of those minerals in our runs. Two groups of oxides can be distinguished in our experiments, Ti-poor with ~16 wt% TiO_2 and Ti-rich with ~41% TiO_2. Both are present in the fractional experiment at 1070°C and in the equilibrium experiment at 1030°C, but only the Ti-poor type are present in the fractional experiment at 1030°C. In comparison, no oxides are stable above 950°C in the experiments of ***Berndt et al. (2005)*** at QFM, and a majority of magnetite are observed by ***Feig et al. (2006)*** in their experiments. For the last study this is a consequence of the low Ti content of the starting material compared to ours, and also compared to the composition of the natural sample on which it is based.

Residual melt composition

Overall and as expected during evolution of melt by crystallization, the Mg# decreases with the temperature due to the crystallization of olivine and clinopyroxene. The Mg# is higher for the residual of the water-bearing experiments as a consequence of the suppressed liquidi of all minerals and the high melt fraction preserved in the runs (*Figure 6.89e*). The decrease in melt Mg# is more important for the fractional crystallization experiments due to the higher proportion of minerals crystallized. The appearance of oxides in the system does not seem to strongly affect the residual melt Mg#, at the exception of the slope disruption starting at the saturation temperature of the minerals at 1070°C for the "dry" fractional crystallization series. The silica content of the residual melt slightly increases compared to the composition of the starting material for all series. In details, the SiO_2 content of the "dry" experiments first drop between 1050 and 1100°C (by about 1 to 1.5 point %), and then increases. The higher increase is recorded for fractional crystallization likely due to the onset of oxide formation at 1100°C. No such drop is observed during crystallization of the water-bearing system. Finally, the TiO_2 content of the residual melt strongly depends on the phase equilibrium of the systems and the (lack of) crystallization of Fe-Ti oxides. The strong increase in Ti during the first 3 temperature steps of the "dry" series represent the high amount of crystals formed compared to the water-bearing experiments, which melt Ti content only slightly increases during crystallization. Then, even though the amount of minerals formed during each run does not exceed 5%, the residual melt content in Ti significantly drops from ~3.5 to 2.5 wt% for the "dry" fractional series and from ~3.7 to 2.5 wt% for the "dry" equilibrium crystallization series.

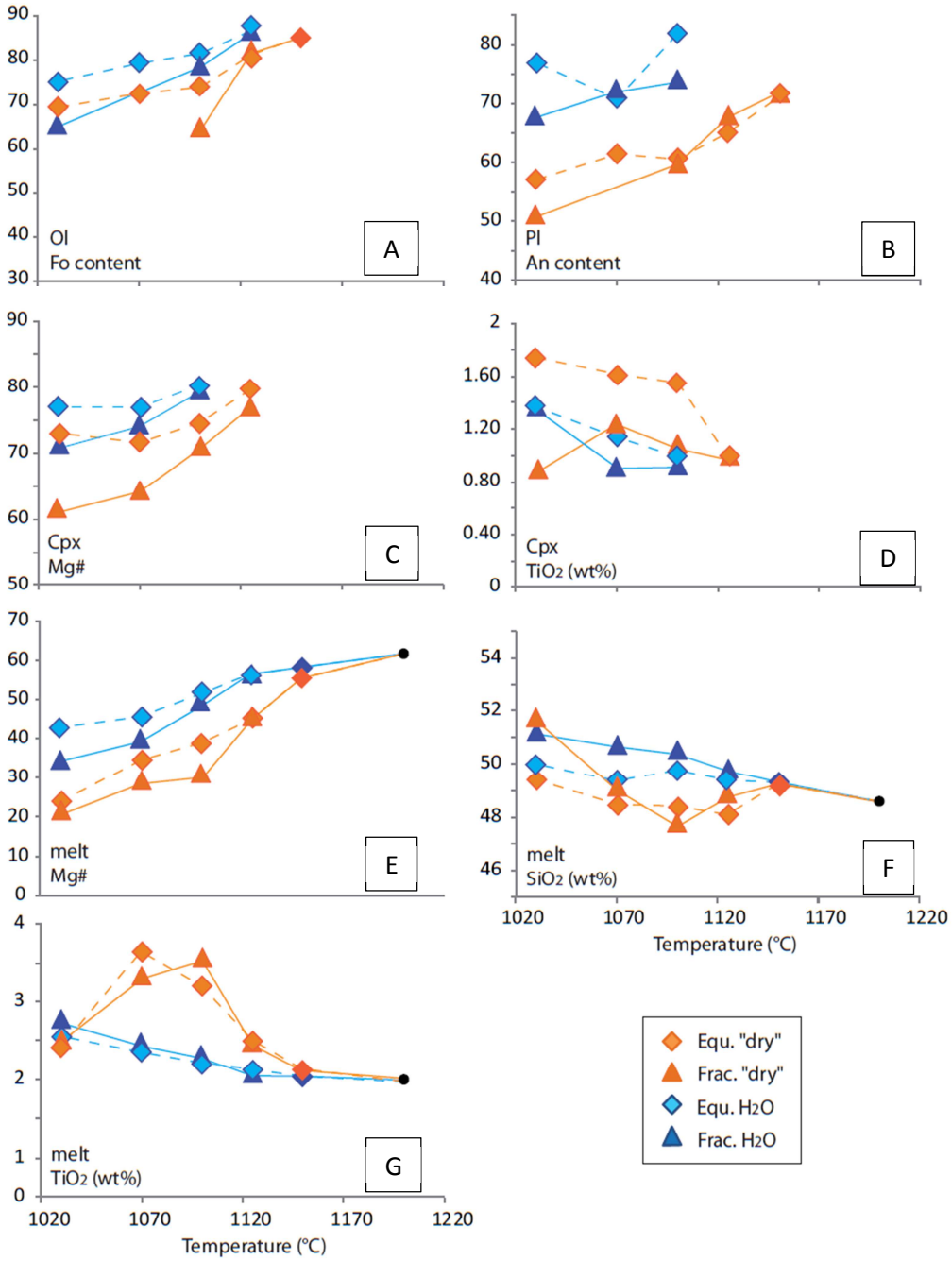

Figure 6.90 - Evolution of selected components of olivines (a), plagioclases (b), clinopyroxenes (c and d) and melts (e, f and g) during crystallization shown against temperature. Dotted lines represent evolution of the equilibrium crystallization series and solid lines of the fractional crystallization series.

4 Discussion

The aim of the discussion developed hereafter is to give a first comparison of the experimental results with some of the previous experimental studies for similar systems, with MELTS modeling for the same starting composition and conditions except for variable water contents, and with the natural record of the Atlantis Bank area. Some early perspectives on the implication of the results for the lower oceanic crust system are also tentatively given.

Evolution of melt fractions during crystallization

The results of the experiments show variations in the proportion of phases crystallized at each temperature step, mainly as a function of the initial water content of the glass and also to a lesser extent as a function of the crystallization process involved. I compared the data with the results of the equilibrium crystallization experiments of ***Feig et al. (2006)*** for the lowest water contents at 2 kbar (equivalent to ~0.7 and ~1.5 wt% H_2O), with the results of ***Berndt et al. (2005)*** for the equilibrium crystallization of a primitive MORB at QFM and 2 kbar, and with the results of both equilibrium and fractional crystallization of a primitive mantle-derived tholeiitic melt at 7 kbar from ***Villiger et al. (2007)***. The results show that the melt fractions obtained for the "dry" series fit well the results of ***Berndt et al. (2005)*** and ***Villiger et al. (2007)***, but that the water-bearing series present higher melt fractions of about ~20 percentage points (*Figure 6.91a*) due to the lowering of the liquids temperature of about 50 °C. The conclusions of the comparison with the MELTS models at different water contents are similar (*Figure 6.91b*), i.e. the residual melt fractions of the water-bearing experiments are much higher that the fractions

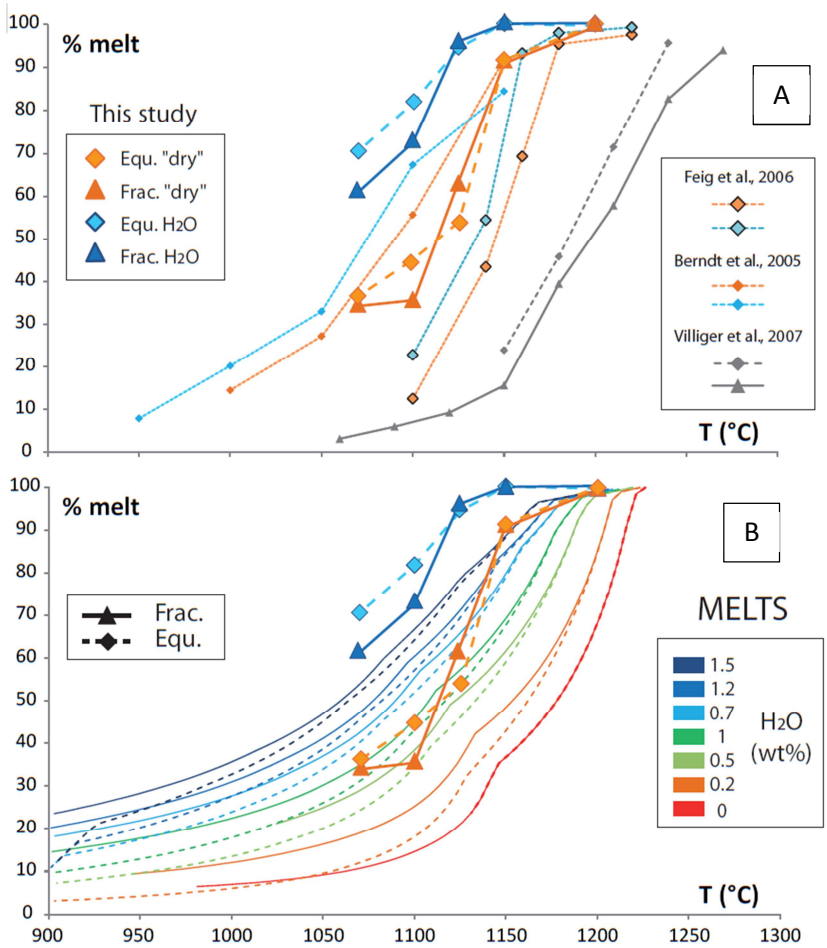

Figure 6.91 - Melt fractions in the run products as a function of temperature for the four experimental series. (a) Comparison with the results of the previous experimental studies of Feig et al. (2006), Berndt et al. (2005) and Villiger et al. (2007). (b) Comparison with MELTS modeling of fractional and equilibrium crystallization of the starting composition SG-01 at 2 kbar, QFM and different initial water contents.

expected during crystallization of melt with up to 1.5 wt% H_2O. Similarly the "dry" crystallization series fell within the variation range of the models, but present melt fractions rather identical to what is expected for crystallization of water-bearing melts (between 0.5 and 1.5 wt% H_2O). Also, the effect of the crystallization process involved in the evolution of the melts does not seem to impact the results of the experiments as much as what is described by ***Villiger et al. (2007)***, with systematic higher melt fractions for their equilibrium series of up to 15 percentage points (*Figure 6.91a*). Variations in the melt fractions during differentiation have potentially a strong impact on the global differentiation of the systems and the crust composition (e.g. ***Neave et al., 2019***). One of the potential direct consequences on the lower oceanic crust system is the effect on the efficiency of melt extraction or melt migration dynamics within the reservoirs, which as described previously is key in the understanding of the reservoirs evolution.

Compositional evolution trends of melts

In the perfect systems considered here where crystallization is the only process ongoing, the evolution of the minerals composition and of the melt from which they crystallize is dependent on phase equilibrium relations and on the proportion of minerals crystallized in the system. The crystallization sequences of the equilibrium and fractional series are globally similar and function of the water content of the melt (*Figure 6.89*). The main difference between the equilibrium and fractional series at the same initial water content is the earlier crystallization of oxides for the "dry" fractional crystallization experiments, as evidence by the drop in Ti content of the melt at ~30 in Mg# (*Figure 6.92*). The evolution in the melt Ti contents predicted by the MELTS models are consistent with the observed variations in Ti of the residual melts, even though the equivalent initial water contents of the water-bearing experiments would correspond to a range between 1.2 and 0.7 wt% H_2O instead of the ~1.5 wt% as initially added to the glass. Compared to the range of compositions of natural MORB-type melts collected in the vicinity of Atlantis Bank, the experimental melts are all depleted in Ti relative to MORBs with similar Mg#. Hence, the Ti enrichment of melts during differentiation are then potentially underestimated by modeling, but still simple crystallization processes seems at odds with the natural melt compositions. Comparatively, the melts Ca# (molar ratio Ca / Ca + Na) are higher than the composition of MORBs which are better fitted by the MELTS models at similar Mg#. The experiments show here that the loss of Ca or/together with the enrichment of Na during differentiation is potentially overestimated by the models. As a result, even though the models reproduce most of the MORB compositions of the area, this tentatively confirms that crystallization alone cannot account for the variability of MORBs as it seems to be also suggested by the discussions on Ti.

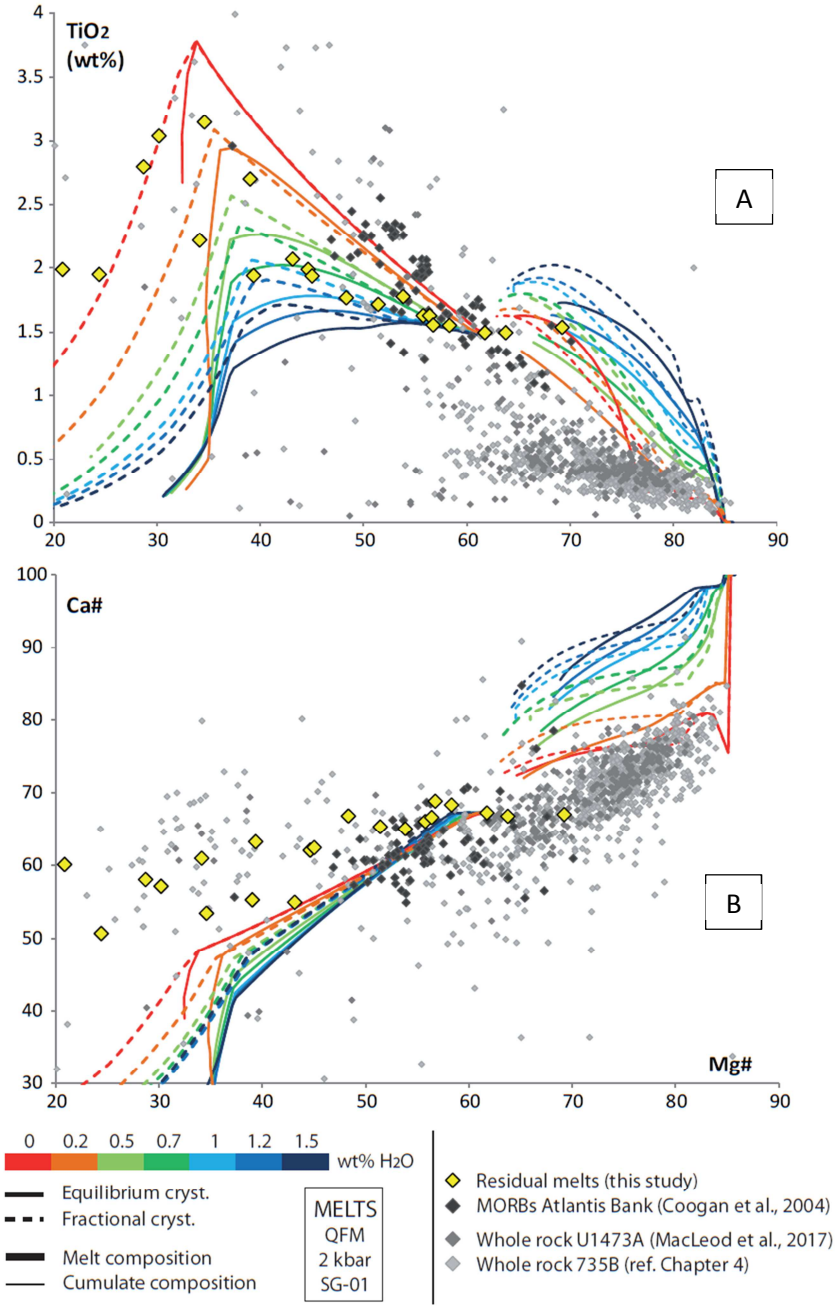

Figure 6.92 - Equivalent whole rock compositions in Mg# versus (a) TiO_2 (wt%) and (b) Ca# of melts and cumulates from the Atlantis Bank area (grey diamonds), compared with the compositions of residual melts from the crystallization experiments and MELTS models for the same system.

Finally, and despite a potential sampling bias of MORBs at Atlantis Bank, the comparison between MORBs and both the experimental results and the MELTS models show that MORB only sampled a quite narrow range in Mg# compared to the potential variability of melt compositions during differentiation (between ~70 and ~45 in Mg#, *Figure 6.92*). If considering that only crystallization processes are involved in the differentiation of melts, such Mg# range would be obtained for equivalent remaining melt fractions superior to 50% in the MELTS models, and superior to 70% for the experiments, after crystallization of the primitive melt considered.

Composition of minerals and cumulate assemblages

In addition to the composition of melts presented in *Figure 6.92*, whole rock composition of gabbroic samples from ODP Hole 735 and IODP Hole U1473A are represented (light gray symbols), together with the evolution trends of the cumulate compositions obtained by MELTS modeling. The results strikingly show that for both Ti and Ca#, all the natural compositions fell below the compositional range predicted by the models, even though the Mg# seems to match the observed variability of the samples (except for the oxide gabbros with Mg#<60, ***MacLeod et al., 2017***). These discrepancies can for example either result from the fact that natural rocks are not pure cumulates but might contain variable fraction of "melt", or because minerals forming the cumulates have different compositions than those expected by simple crystallization processes. *Figure 6.93* shows that the composition of minerals expected during simple equilibrium or fractional crystallization modeled by MELTS are rather consistent with the results of the experiments under "dry" or water-bearing conditions. However, the compositional range obtained by the two methods tends to higher An contents of plagioclase for similar Mg# of clinopyroxene compared to the minerals from the natural rock record.

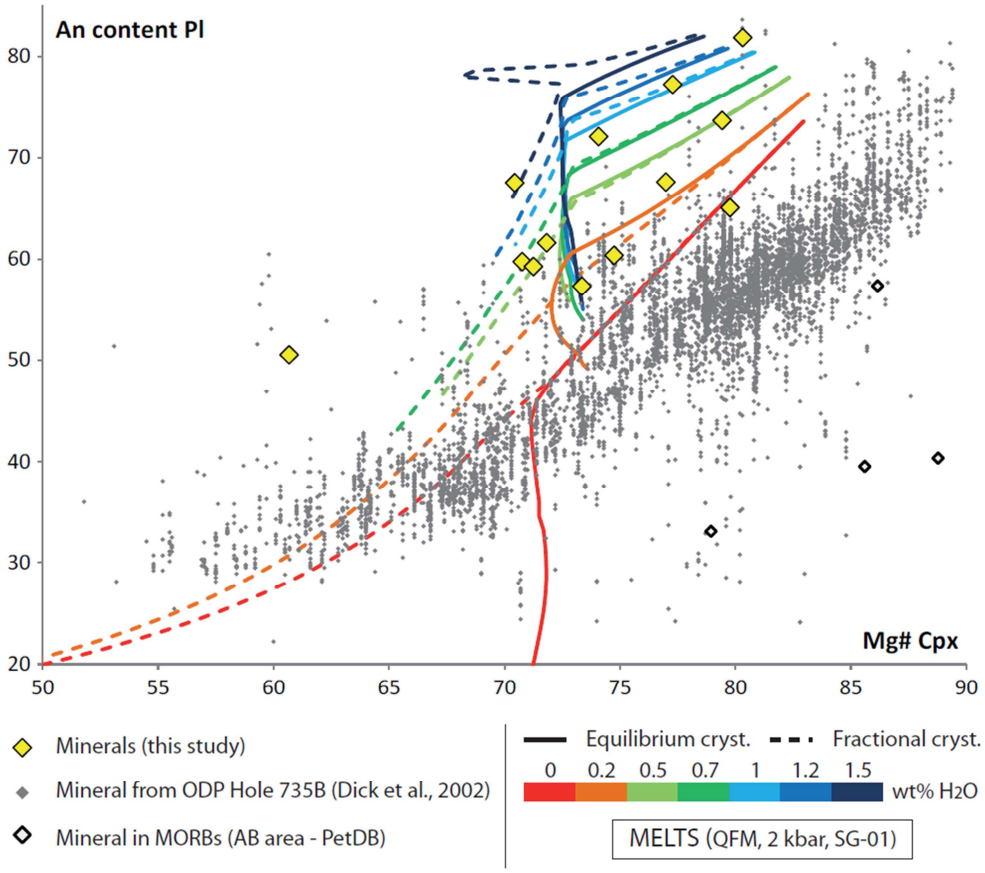

Figure 6.93 - In situ Mg# of clinopyroxenes versus An content of plagioclases analyzed in single samples from ODP Hole 735B (grey points - Dick et al., 2002), in MORBs from the Atlantis Bank area (PetDB), and from the experimental charges analyzed in this study (yellow diamonds). Comparison with covariations of the minerals composition during equilibrium and fractional crystallization determined by MELTS.

The gap between the compositions expected by crystallization and the natural rock record is greater for cumulates and lower crustal rocks than for MORBs found at the seafloor. This confirms that crystallization is not the only process to be considered for the formation of gabbroic cumulate, and is at least significantly perturbed by additional processes of melt-rock reactions. It also potentially highlights that compared to MORBs, lower crustal lithologies are more impacted by melt-rock reactions during differentiation. The geochemical tracers are different between the two sample types, but if true this observation would mean that melts involved in RPF do not contribute significantly to the geochemistry of MORBs from the area.

5 Conclusion

The experiments conducted for both equilibrium and fractional crystallization show conclusive results. A few parameters are still to be constrained and verified in more details, such as the final H_2O content of the residual melts and the potential variability of fO_2 associated in the four different series. The first description of the results demonstrate that water as a major effect on the phase equilibrium, and the type of crystallization process considered impact both phase equilibrium (earlier appearance of oxides during fractional crystallization) and the proportion of phases crystallized. As a result, variations in the evolution of melt compositions can be distinguished between the four crystallization series. The evolution tendencies during crystallization described herein are coherent with previous experimental crystallization studies of similar basaltic systems. However in details, significant differences can be observed such as the composition and liquidus of oxides, or the composition of the phases crystallized. In addition, the final results of our experiments show that at first glance, thermodynamic models of crystallization predict geochemical differentiation trends for major elements that are not always consistent with the experimental ones. More work is required to understand the origin of such discrepancies that are essential if we are to determine the share of crystallization processes on the differentiation of crustal lithologies.

- PART 3 -

Determination of Rare Earth Elements partition coefficients at 2 kbar and 1100°C

This project has been conducted together with the crystallization experiments described in Part 2 at Institut für Mineralogie of the Leibniz Universität Hannover. A previous introduction on the importance of the partition coefficients for the comprehension of the behavior of Rare Earth Elements as geochemical tracers in natural systems is given in Chapter 1. The following aims at 1/ emphasizing the main point on the discussion about partition coefficients, 2/ describing the experimental setup and results, and 3/ establishing a first comparison between the partition coefficients obtained experimentally and those determined for the same systems thanks to partition coefficient models.

1 Introduction

REE help identify and constrain melt-rock reactions associated to reactive porous flow processes (e.g., ***Boulanger et al., submitted; Coogan et al., 2000; Ferrando et al., 2018; Gao et al., 2007; Leuthold et al., 2018; Lissenberg and MacLeod, 2016*** - see chapter 1). Their behavior during magma differentiation is dependent on their distribution between melt and crystals, which is described by the partition coefficients Kd. As described in Chapter 1, partition coefficients change with the mineral considered and their composition, with temperature, pressure, or the redox conditions applied to the system. ***Ferrando (2017)*** established ranges of variations of the partition coefficients given in the literature for olivine, plagioclase and clinopyroxene in basaltic melts at temperatures varying between 1100°C and 1300°C. The data shows that coefficients can vary by one order of magnitude for the same element and mineral, and that for some elements such as Tm no value is referenced in the literature. *Figure 6.94* shows examples of REE partition coefficients for olivine, plagioclase and clinopyroxene used in numerical modeling of melt-rock reactions described in Chapter 1 (section 2.2.3.2.): the study of the layered series and AFC modeling presented in this PhD manuscript (***Boulanger et al., submitted*** - Chapter 3, determined at 1100°C), in ***Gao et al. (2007)*** with partition coefficients from experimental studies and natural sample analyses, and other coefficients of ***Bédard (2001)***

which are used in different studies including REE numerical models (***Kvassnes, 2003; Lissenberg et al., 2013; Lissenberg and MacLeod, 2016***). The figure shows that the magnitude of the coefficients can vary a lot but also the difference of partitioning between light REE and heavy REE. For olivine, the partitioning of La is ~3 orders of magnitudes weaker than the partitioning of Lu for the coefficients used in this study, and is of ~1 order of magnitude weaker in the data set of ***Bédard (2001)***. This difference of partitioning implies potentially strong differences in the fractionation between more to less incompatible elements during crystallization of the considered mineral. Yet, these fractionation signatures are critical in the

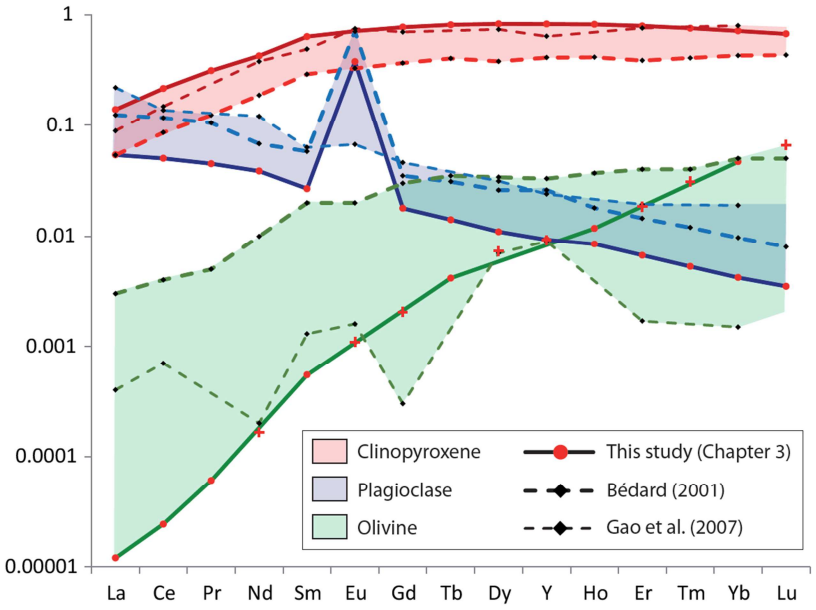

Figure 6.94 - Examples of REE partition coefficients in clinopyroxene (red), plagioclase (blue) and olivine (green) used in numerical models of melt-rock reactions. Solid lines: partition coefficients calibrated for the average mineral compositions analyzed in the layered series (Chapter 3) after the models of Wood and Blundy (1997) for clinopyroxene, Sun et al. (2017) for plagioclase and Sun (2017) for olivine at 1100°C. Large dotted lines: partition coefficients from Bédard (2001) used as modeling parameters for exemple by Kvassnes (2003) and Lissenberg et al. (2013). Narrow dotted line: partition coefficients compiled by Gao et al. (2007).

understanding of melt-rock reactions as detailed in Chapter 3 and 4.

Partition coefficients can be determined by experimental petrology, or can be estimated thanks to models based on the Lattice Strain Model (***Onuma et al., 1968***) and calibrated on experimentally determined coefficients. Experimental petrology provides partition coefficients that are preferably only applicable for similar systems, i.e. similar compositions and crystallization parameters (e.g., temperature or pressure). In addition and as emphasized for example by ***Nielsen et al. (2017)***, the published partition coefficients are often presented as averages of the analyzed products of the experimental runs, and may carry a bias linked to the inclusion of incorrect values. This in turn has consequences on the partitioning models which are calibrated on these values. Hence, the precision of the geochemical models for differentiation of magmatic systems and the quantification of the processes involved might be limited by the

consideration of inappropriate coefficients and by systematic errors on the partition coefficient models.

In order to clear this uncertainty and with the eventual idea of using partition coefficients calibrated for the system we study herein (the Atlantis Bank lower crust igneous reservoirs), we determined new sets of partition coefficients for olivine, plagioclase and clinopyroxene crystallized from typical MORB-type melts of the Atlantis Bank area.

2 Experimental and analytical methods

Partition coefficients were determined for the 1100°C temperature step of the crystallization experiments (see Part II), for nominally dry and water-bearing conditions of both the equilibrium and fractional crystallization series (i.e. 4 experiments in total). This temperature step was selected due to the high proportions of residual melt in each experiment after crystallization of all three main mineral phases, i.e. olivine, plagioclase and clinopyroxene. The same starting powders and experimental methods as those of the crystallization experiments were used, except that 1/ the starting powders were doped in trace elements and that 2/ we used a temperature cycling method to enlarge the size of melt pools and crystals. The starting materials needed to be enriched in trace elements as they are synthetic glasses which did not contain any REE, unlike starting materials made from natural rocks. In addition, analysis of trace elements can be challenging due to their low concentrations in the plagioclase and olivine. In order to be able to analyze correctly REE in those two minerals, one possibility is to enrich the melt from which they crystallize to obtain olivine and plagioclase with higher REE contents. The other possibility to facilitate the REE analysis is to increase the mineral size of the experimental products. The temperature cycling method as presented by ***Erdmann and Koepke (2016)*** enables to enlarge the size of the crystals during an experimental run thanks to small variations in temperature (*Figure 6.95*). Small increases of temperature lead to preferential dissolution of small crystals. Then during the cooling steps, crystallization focuses on already

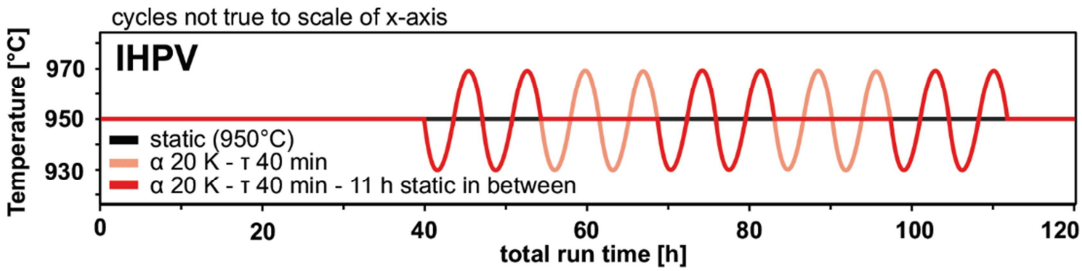

Figure 6.95 - Simplified experimental temperature profiles tested by Erdmann and Koepke (2016) in IHPV experiments for two different amplitudes and periods (red lines), and compared to static temperature experiments (black line).

existing minerals which progressively widen.

The same method of temperature cycling applied for the crystallization of a high silica system by ***Erdmann and Koepke (2016)*** was tested here for the first time on a basaltic system. The targeted temperature was of 1100°C, and successive instantaneous increases or decreases by +10°C or -10°C (variations of 20°C in total). The description of the temperature cycling applied to the systems is given in *Figure 6.96*).

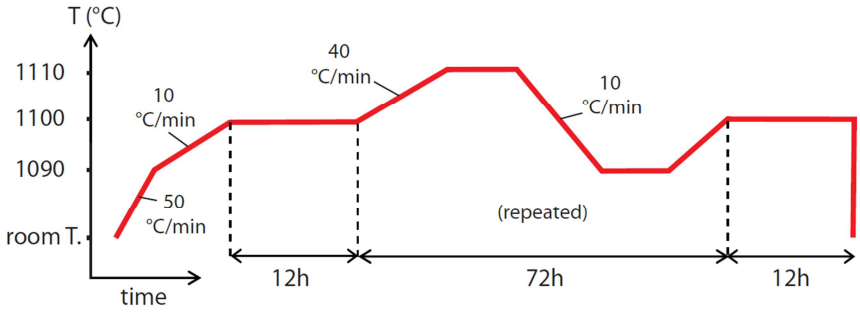

Figure 6.96 - Parameters of the temperature cycling programmed for the partition coefficient experiments. Indicative axes not to scale. The increases or decreases of temperature would appear instantaneous with a correct time scale.

Trace elements doping of the glass to ~300 ppm (*Table 6.4*) was realized by adding a high-purity standard solution (in HNO_3 4%) to the starting glass powder in a large-volume Pt crucible. The mixture was put to evaporate on a heating plate at 90°C, before an additional step of melting at 1600°C for 2 hours to obtain a homogenous glass composition. Four different capsules were then prepared following the same method as presented in Part 2 with the starting glasses SG-01, SG-06 and SG-07 enriched in trace elements. Experiments were then performed in two different runs with the same conditions as those used for the 1100 °C temperature step of the crystallization project, except for the application of the temperature cycling method to the system.

Table 6.4 - Elements present in the standard solution used to enriched the starting glass powders SG-01, SG-06 and SG-07 in trace elements (solution "High-purity standards" Cat. # ICP-MS-68B-A)

Al	Cd	Cu	**Ho**	**Lu**	K	Se	**Tm**
As	Ca	**Dy**	in	Mg	**Pr**	Na	U
Ba	**Ce**	Er	Fe	Mn	Re	Sr	V
Be	Cs	**Eu**	**La**	**Nd**	Rb	**Tb**	Yb
Bi	Cr	**Gd**	Pb	Ni	**Sm**	Tl	**Yb**
B	Co	Ga	Li	P	Sc	Th	Zn

The same analytical methods as detailed in Part 2 for imaging (SEM) and major elements analysis (EPMA) of the experimental products were used. Trace elements analysis was conducted at LMV in Clermont-Ferrand (France) with a Thermo Element XR coupled with a laser excimer 193nm Resonetics M-50E. Ablation spot size varied at a function of the size of the phases analyzed, between 40 and 20 µm. A laser frequency of 2 to 4 Hz was used with an energy

density of 2.9 J.cm^{-1}. Data were processed using the GLITTER software (***van Achterbergh et al., 2001***), and all measured concentrations were calibrated to the synthetic glass NIST 610 using the values of ***Pearce et al., (1997)***.

3 Results

The major and trace elements composition of melts and crystallized phases for each experimental run are available in *Appendix 4.3* and *4.4*.

Table 6.5 - Average in situ major element compositions of the different phases analyzed in MBPC-fd, MBPC-fw, MBPC-ed and MBPC-ew.

Run	Phase	SiO_2	TiO_2	Al_2O_3	FeO	MnO	MgO	CaO	Na_2O	K_2O	P_2O_5	Cr_2O_3	NiO	Total	Mg# /An
MBPC ed	Melt	49.24	2.42	15.93	12.14	0.29	5.24	10.03	4.02	0.36	0.33	-	-	100	43.5
MBPC ed	Ol	38.99	0.05	0.05	19.83	0.36	40.21	0.42	0.03	0.01	-	0.01	0.05	100	78.3
MBPC ed	Pl	51.51	0.18	30.24	0.94	0.02	0.23	13.41	3.36	0.11	-	-	-	100	68.4
MBPC ed	Cpx	50.23	1.11	4.29	7.43	0.14	15.14	21.02	0.41	0.00	-	0.22	0.02	100	78.4
MBPC ew	Melt	52.10	2.71	15.90	8.93	0.29	5.89	9.65	3.54	0.43	0.52	0.02	0.02	100	54.0
MBPC ew	Ol	38.95	0.06	0.20	17.86	0.46	41.72	0.64	0.03	0.01	0.04	0.01	0.03	100	80.6
MBPC ew	Pl	51.62	0.10	29.69	0.61	0.07	0.32	13.26	4.02	0.07	0.22	0.02	0.01	100	64.3
MBPC ew	Cpx	50.82	1.05	3.34	6.61	0.28	16.66	20.34	0.32	0.00	0.35	0.20	0.05	100	81.8
MBPC fd	Melt	48.84	2.15	15.14	14.51	0.39	4.97	9.77	3.69	0.29	0.26	-	-	100	37.9
MBPC fd	Ol	38.11	0.05	0.04	23.42	0.44	37.47	0.39	0.01	0.01	-	0.02	0.06	100	74.0
MBPC fd	Pl	51.67	0.10	30.33	0.81	0.01	0.22	13.30	3.45	0.09	-	-	-	100	67.7
MBPC fd	Cpx	50.60	0.88	3.77	9.02	0.20	15.34	19.45	0.37	0.00	-	0.35	0.01	100	75.2
MBPC fw	Melt	49.97	1.69	17.48	7.86	0.15	6.95	11.82	3.38	0.26	0.42	0.02	0.01	100	61.1
MBPC fw	Ol	39.43	0.01	0.06	14.17	0.27	45.66	0.31	0.01	0.01	0.01	0.02	0.04	100	85.2
MBPC fw	Cpx	49.70	0.99	5.09	4.78	0.13	16.06	22.01	0.30	0.01	0.38	0.53	0.02	100	85.7

3.1 Textures and major element compositions of the experimental runs

The results of the experiments show that temperature cycling helped form larger crystals in all four runs of crystallization of the basaltic composition. The size of the minerals is >20 µm in both experiments for the fractional crystallization series and up to few hundreds of µm for the water-bearing experiments (MBPC-fd and MBPC-fw, *Figure 6.97*). The impact of temperature cycling on the products of the equilibrium crystallization series is more limited, with minerals that barely reach 20 µm in size (MBPC-ed and MBPC-ew, *Figure 6.97*). In addition, the minerals in the four runs tend to form aggregates of similar minerals that grow apart from one another. In details, as witnessed in particular in the fractional crystallization series, olivine crystals are more rounded than in the products of experiments conducted at constant temperature and present dissolution textures as described by ***Xing et al. (2017 -*** *Figure 6.97e****)***. This is not completely surprising as temperature cycling involves a step of dissolution during the

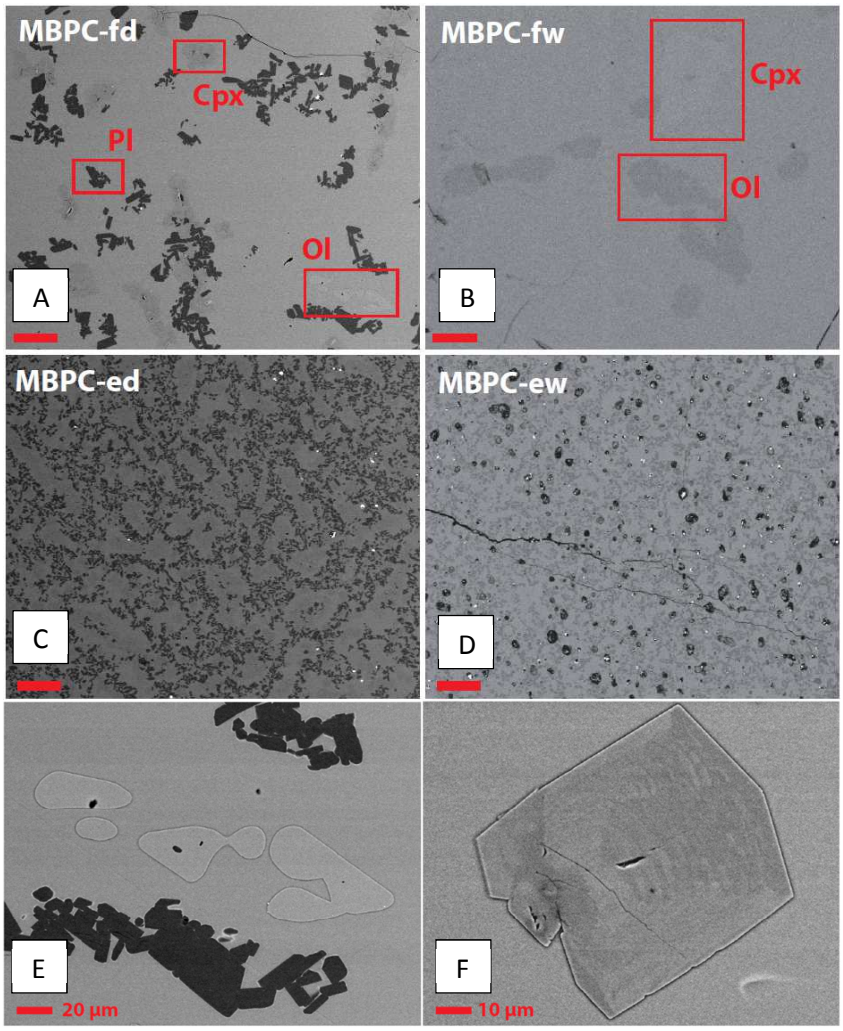

Figure 6.97 - Backscattered electron images of the run products of the partition coefficients experiments. From a to d, results of the experiment under temperature cycling conditions. fd: "dry" fractional crystallization series, fw: water-bearing fractional crystallization series, ed: "dry" equilibirum crystallization series, ew: water-bearing equilibrium crystallization series. The red scales represent 100 µm. e and f, example of disequilibrium textures found in run MBPC-fd. e) Olivine crystal with resorbed and rounded boundaries, f) clinopyroxene crystal with growth zonation.

increase of temperature, which preferentially applies to small crystals but also inevitably to larger ones too.

The composition of olivine and plagioclase are globally homogeneous within each crystal, but as illustrated in *Figure 6.97f* some of the clinopyroxene crystals from the fractional crystallization series under "dry" conditions present small compositional heterogeneities as observed on the BSE image. Analyses show that these variations correspond to jumps of <2 percentage points in Mg# between the light and darker grey bands. Also compared to the results of the crystallization experiments at constant temperature, the proportions and compositions of the phases are here different. On average, both olivine Fo contents and clinopyroxene Mg# are higher for the partitioning experiments. Theses variations can either result from 1/ the

temperature cycling that involves crystallization of minerals in cycles of dissolution and re-crystallization, or 2/ they can be the result of the addition of trace elements in the starting material, the only two parameters that are different from the experimental crystallization series.

3.2 REE analyses and partition coefficients

All phases present in the experimental runs were analyzed successfully for major element compositions, yet the small sizes of the crystals and melt pools in the two equilibrium crystallization series (<20 μm) prevented us from getting usable trace element measurements. In these two last runs, no partition coefficient was determined for the water-bearing equilibrium crystallization experiment, and only partition coefficients for clinopyroxene was determined for the "dry" equilibrium crystallization experiment. The measured coefficients and their expected values calculated thanks to the major element composition of the minerals are available in *Table 6.6*. Plagioclase was the most difficult phase to analyze in the run products because of the size and the elongated shape of the crystals, and because of the presence of inclusions within the minerals (usually of melt). For olivine, the very low REE contents of the minerals, despite the doping of the starting material at 300 ppm, prevented us from obtaining compositions higher than the detection limit with laser ablation spot sizes < 40 μm. The scatter in the partition coefficients selected for each run is relatively limited, so only the average partition coefficients will be discussed below.

Table 6.6 - REE partition coefficients based on the experimental products at 1100°C. (a) Average partition coefficients based on the REE in situ analyses by LA-ICP-MS. (b) Expected partition coefficients calculated thanks to the models of Wood and Blundy (1997) for clinopyroxene, Sun et al. (2017) for plagioclase and Sun (2017) for olivine based on the major element compositions of all three minerals.

(a) Kd - Experimental runs

Run	Kd(min)	La	Ce	Pr	Nd	Sm	Eu	Gd	Tb	Dy	Ho	Er	Tm	Yb	Lu
MBPC fd	Cpx	0.0731	0.1210	0.1931	0.2864	0.4844	0.4811	0.6424	0.6657	0.7129	0.6944	0.6837	0.6436	0.6343	0.6263
MBPC fw	Cpx	0.0751	0.1271	0.2047	0.3045	0.4917	0.4828	0.6351	0.6468	0.6854	0.6608	0.6452	0.5886	0.5690	0.5471
MBPC ed	Cpx	0.0950	0.1638	0.2325	0.3275	0.4949	0.4993	0.5685	0.5983	0.6116	0.5942	0.5632	0.5396	0.5049	0.4983
MBPC fd	Ol	0.0003	-	0.0001	0.0010	0.0007	0.0007	0.0024	0.0033	0.0060	0.0100	0.0154	0.0263	0.0397	0.0594
MBPC fw	Ol	0.0005	0.0003	0.0004	-	0.0009	0.0006	0.0021	0.0024	0.0046	0.0068	0.0117	0.0185	0.0280	0.0422
MBPC ed	Ol	-	0.0020	0.0026	0.0099	-	0.0041	0.0176	0.0045	0.0102	0.0097	0.0157	0.0244	0.0375	0.0569
MBPC fd	Pl	0.0538	0.0375	0.0311	0.0279	0.0176	0.2254	0.0142	0.0090	0.0062	0.0055	0.0043	0.0029	0.0025	0.0018

(b) Kd - REE partitioning models (Wood & Blundy, 1997; Sun, 2017 and Sun & Liang, 2017)

Run	Kd(min)	La	Ce	Pr	Nd	Sm	Eu	Gd	Tb	Dy	Ho	Er	Tm	Yb	Lu
MBPC ed	Cpx	0.1308	0.2023	0.2930	0.3983	0.5896	0.6600	0.7145	0.7486	0.7597	0.7491	0.7229	0.6870	0.6467	0.6058
MBPC fd	Cpx	0.1098	0.1721	0.2527	0.3481	0.5272	0.5958	0.6512	0.6887	0.7055	0.7016	0.6822	0.6529	0.6184	0.5824
MBPC fw	Cpx	0.1539	0.2363	0.3399	0.4589	0.6714	0.7477	0.8054	0.8397	0.8481	0.8325	0.8002	0.7577	0.7109	0.6641
MBPC ew	Cpx	0.1274	0.1975	0.2867	0.3907	0.5809	0.6515	0.7065	0.7415	0.7538	0.7445	0.7195	0.6847	0.6452	0.6050
MBPC ed	Ol	0.0000	0.0000	0.0000	0.0000	0.0002	0.0004	0.0008	0.0015	0.0026	0.0044	0.0068	0.0100	0.0137	0.0178

MBPC fd	Ol	0.0000	0.0000	0.0000	0.0000	0.0002	0.0004	0.0008	0.0015	0.0027	0.0045	0.0070	0.0102	0.0140	0.0182
MBPC fw	Ol	0.0000	0.0000	0.0000	0.0000	0.0002	0.0004	0.0007	0.0014	0.0025	0.0041	0.0064	0.0093	0.0128	0.0167
MBPC ew	Ol	0.0000	0.0000	0.0000	0.0001	0.0003	0.0007	0.0013	0.0025	0.0045	0.0076	0.0117	0.0171	0.0234	0.0306
MBPC ed	Pl	0.0378	0.0352	0.0315	0.0271	0.0188	0.0155	0.0125	0.0099	0.0077	0.0060	0.0047	0.0037	0.0030	0.0024
MBPC fd	Pl	0.0393	0.0366	0.0327	0.0281	0.0196	0.0161	0.0130	0.0103	0.0080	0.0062	0.0049	0.0038	0.0031	0.0025
MBPC ew	Pl	0.0392	0.0365	0.0326	0.0280	0.0195	0.0161	0.0130	0.0103	0.0080	0.0062	0.0048	0.0038	0.0031	0.0025

4 Discussion on the REE partition coefficients and conclusions

Some differences are observed between the products of the simple crystallization experiments and the products of the partition coefficient experiments as established above, even though the major element compositions of the starting material and the pressure and redox conditions are considered similar. To better understand the reasons for these differences new experiments would potentially be required, in order to verify the effect of trace element enrichments or temperature cycling on the run products. For example, crystallization experiments of the starting glasses without trace elements could be attempted with temperature cycling. The other way around, experiments of crystallization of the enriched starting glasses under static temperature could be completed. In the following, I will only discuss the values of the experimental partition coefficients and compare them with the expected values calculated with the partitioning models used in the rest of the manuscript for the crystallization and melt-rock reaction models.

In order to simplify this preliminary discussion on the results, I will consider here that the successive dissolution and re-precipitation steps that formed the minerals did not influence the REE partitioning between melt and crystals. As presented in *Figure 6.98*, most of the average plagioclase REE partition coefficients fell close to the calculated coefficients thanks to the model of ***Sun et al. (2017)***. The only exception is for the Eu value that is completely underestimated by the model. The Eu partition coefficient identified thanks to the grey line corresponds to the value determined by ***Laubier et al. (2014)*** at the QFM buffer for basaltic and basaltic-andesitic melts. The experimental value determined herein is much closer to the value of ***Laubier et al. (2014),*** and the difference between the two could be explained by small variations in the redox conditions or simply because of differences in the composition of the systems considered.

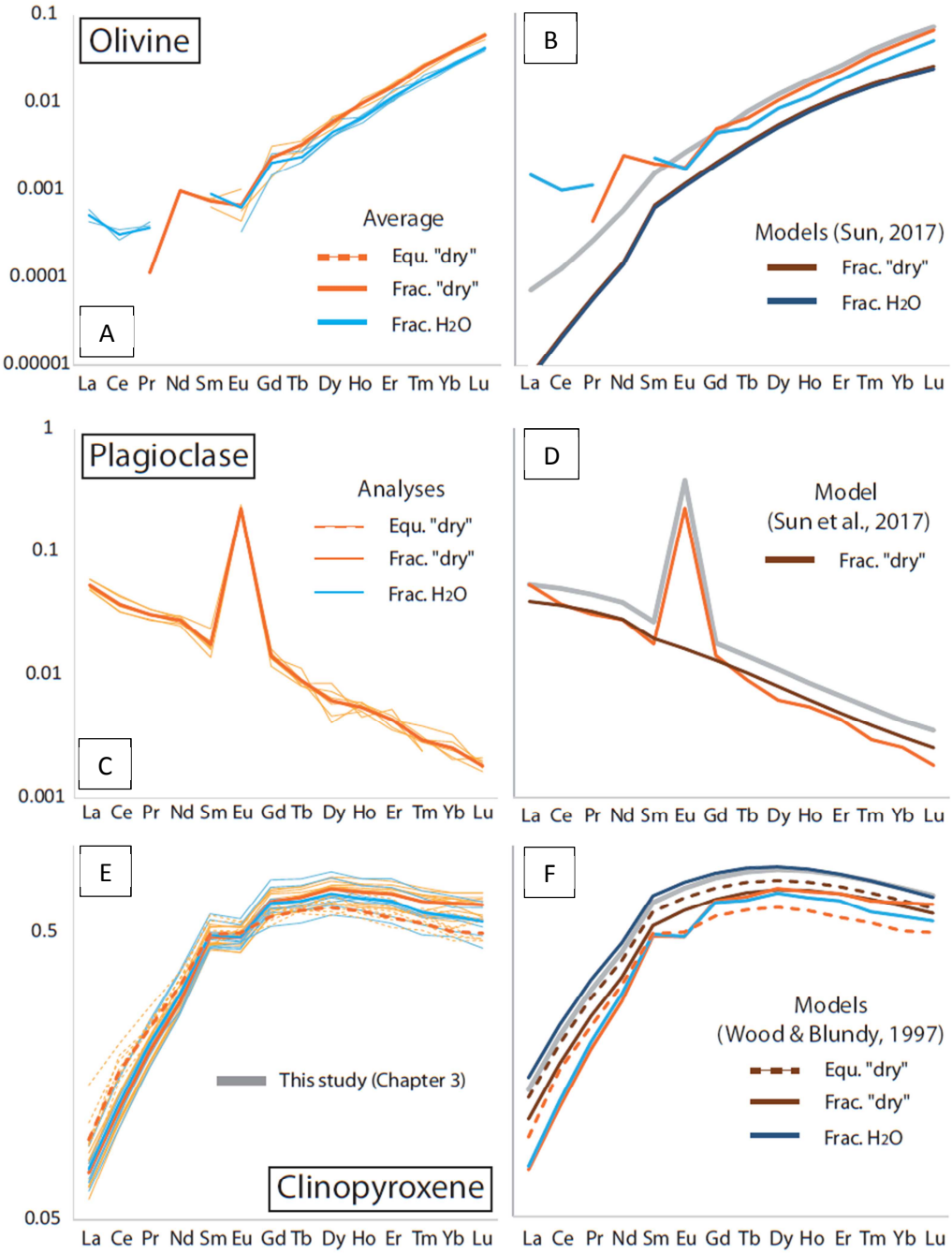

Figure 6.98 - REE partition coefficients for olivine (a and b), plagioclase (c and d) and clinopyroxene (e and f) determined in the experimental runs for the water-bearing fractional crystallization series (blue solid line), "dry" fractional crystallization series (orange solid line) and "dry" equilibrium crystallization series (orange dotted line). Left (a, c and e): average values of the coefficients (large lines) and coefficients obtained for each mineral REE analysis. ight (b, d and f): comparison between the average values of the coefficients determined experimentally and coefficients calculated thanks to the average major element composition of the minerals (same model as described in Table 6.5). The REE partition coefficients determined at 1100°C for the layered series studied in Chapter 1 and present in Figure 6.5 is given for comparison (large grey solid line; b, d and f).

In comparison, the partition coefficients determined for olivine and clinopyroxene are quite different from the calculated values. For olivine, the partition coefficients determined for the fractional crystallization series are higher than the calculated values for similar mineral compositions. I tested if a ~10 °C temperature difference in the models could explain the systematic underestimation of the values, but it does not involve an increase by half an order of magnitude of the coefficients. In addition, the gap between the values obtained for the water-bearing experiment and the "dry" experiment is not reproduced by the models. This difference in the partition coefficients could be a consequence of the presence of water in the system, and for example associated variations in the redox conditions of crystallization. However, the values are very close to each other and more systematic experiments should be performed to confirm an eventual effect of water on the system. For clinopyroxenes, this effect seems to be the opposite, with a slight overestimation of the partition coefficients for both the water-bearing fractional crystallization series and for the "dry" equilibrium crystallization series. Similarly, a change of $\pm$ 10 °C of the temperature in the models does not lead to a decrease of the calculated coefficients, hence variations of temperature during the cycling method are not responsible for these differences. The best fit of the model with the partition coefficient is for the heavy REE of the "dry" fractional crystallization series. However here, the coefficients for the light REE (from La to Nd here) are slightly overestimated. Finally, the coefficients determined for both fractional crystallization experiments are almost identical, and show lower coefficients for Eu that, if accurate, are not reproduced in the models.

In the end, further examination of the reliability of the partition coefficients and additional constrain on the exact parameters (e.g., water content of melts at the end of the run, see Part 2) can be implemented in the discussion on the significance of the coefficients started above. At first glance, the values are coherent between each other and fall within the range of values found in the literature (cf. ***Ferrando, 2017***). The small differences found between the experimentally determined values and the calculated coefficients indicate that systematic shifts in the result of the models are potentially implemented in the differentiation models which use such calculated coefficients. In order to quantify the potential differences in the results of differentiation models, such as the models developed in this manuscript (Chapter 3 and 4 mainly), the two different sets of coefficients determined experimentally and recalculated could be implemented in the REE models.

Conclusion

The objective of this thesis was to bring new constraints on the evolution of melts within the slow-spreading lower oceanic crust. Different aspects of the magmatic systems were investigated: 1/ emplacement and maturation of the igneous reservoirs, 2/ modes of melt migration involved in the evolution of these reservoirs, and 3/ characterization of magmatic processes involved in the differentiation of melts and feedback of these processes on the structure and composition of the reservoirs. To address these points, I studied gabbroic rocks from long *in situ* sections of lower oceanic crust exhumed at the Atlantis Bank Oceanic Core Complex. In addition, I carried out a complementary experimental petrology to reproduce simple crystallization processes of a melt that is typical of the Atlantis Bank magmatic system. The ultimate aim of these approaches was to quantify the role of reactive porous flow and associated melt-rock reactions in oceanic crust accretion.

The two studies of natural samples from Atlantis Bank highlight that the impact of melt percolation is ubiquitous on the geochemical signatures of gabbroic rocks, and can also be found in their petrographic characteristics. Melt-rock reactions occurred at all stages of evolution of the igneous systems: before and after the intrusion event that formed the layered series, and at every step of formation of the igneous reservoir, as described in Chapter 4. Even though the characterization of the associated melt dynamics still has to be clarified, the new data for the lower two units of Hole U1473A seems to confirm this statement in another portion of lower crust. In addition, I show that the result of melt-rock reactions is dependent on the type of porous melt migration involved. Localized porous flow evidenced within the layered sequence leads to distinctive geochemical signatures compared to more pervasive percolation. In the igneous reservoir model, the contrasted compositions of the two units result from two different types of melt-rock reactions that are likely to be attributed to the contrasted melt dynamics implicated in their formation.

The characterization of the tectono-magmatic unit from Hole 735B enabled us to construct an integrated model of formation and evolution of a lower crust magma reservoir. This model, which is the first to describe the different steps of formation of an entire tectono-magmatic unit, reveals the contrasted melt migration dynamics involved in the formation of single reservoirs: whereas the lower part of the reservoir formed by sills-stacked and successive episodes of replenishment and percolation, the upper homogeneous part formed by progressive collection of hybrid melts from the former. In both cases though, differentiation was governed by upsection reactive porous melt migration. Broader implications for magmatic processes and accretion can also be extracted from the model, such as 1/ the assimilation of the most primitive cumulates that crystallized within the reservoir, and 2/ the "melt-flushing" process considered as the potentially main driving force for the general upward melt flow through the section.

Despite the first order heterogeneity of the crust and the discrepancies of the lower *in situ* sections from OCCs, I corroborate the implication of similar processes in the evolution of the igneous reservoirs both at Atlantis Bank and Atlantis Massif. Beyond the detailed magmatic processes (i.e. melt-rock reactions), I propose that all or part of the igneous reservoir model can apply to these sections. This conclusion results from direct comparison of the main features defining the two parts of the reservoir model with structural, petrographic and geochemical characteristics described in the natural rock record. The link that is drawn between Atlantis Bank and Atlantis Massif is also one of the first links to be revealed between lower crust sections and between two OCCs that are usually considered to be significantly different.

To finish with, and to go a step further into the quantification of magmatic processes governing differentiation at slow-spreading ridges, I attempted to identify the limits of the models commonly used in petrologic studies. To do so, experimental petrology studies are particularly useful as they enable us to precisely quantify the main processes at play during differentiation, e.g. the crystallization processes studied herein. They show here that even though no striking first-order differences are identified between the expected (modeled) and the obtained results for crystallization, small variations can be found. The consideration of these differences in numerical modeling can lead to systematic propagation of bias that impacts the quantification of the processes. Similar conclusions can be drawn for the partitioning project, so that both projects pave the way for further development on the understanding of the balance between processes within the lower crust.

In summary:

- Melt-rock reactions are ubiquitous and occur at all stages of the igneous reservoirs formation. They impact the geochemical signatures, textures, and mineral modes of the rock considered.
- The signatures of melt-rock reactions can vary as a function of melt dynamics, i.e. more diffuse or localized porous flow.
- I build a unique integrated model of formation and evolution of an entire tectono-magmatic unit / igneous reservoir of the lower slow-spreading oceanic crust.
- I show that the most primitive cumulates formed in the reservoir are almost entirely reprocessed; also, "melt flushing" by progressive recharges of the reservoir is likely a main driving force for the upward porous melt flow.
- All or part of the igneous reservoir model applies to other long *in situ* sections of lower crust recovered at Atlantis Bank and Atlantis Massif.
- The early characterization of crystallization processes for the Atlantis Bank system paves the way for new quantification of magmatic processes during accretion.

Finally and in the continuity of the work detailed in this manuscript, a few prospects on additional work are presented below.

Regarding the igneous reservoir model, additional descriptions and detailed sampling of the transitions zones between 1/ the lower and upper units of the reservoir, and 2/ the reservoir and surrounding units of Hole 735B, could help clarifying the modes of magma migration within the structure, as well as the potential impact of the formation and evolution of the reservoirs on the lower crust sections studied. The comparison of the reservoir model with other sections of lower crust from Holes U1473A, 735B and U1309D could also benefit from additional descriptions and targeted sampling. It would enable us to confirm or specify the reservoir model, and to characterize the magmatic processes associated with reservoir formation. Especially, new high-resolution studies of the gabbros from Hole U1309D, with particular focus on the ~400 m-long section described at the end of Chapter 4 and in Chapter 5, seems crucial. Also, the study of ophiolites that are representative of slow-spreading lower oceanic crust in the light of the new models could help validate our findings. This would bring new constraints on the 3D spatial resolution of the reservoirs structure.

In order to pursue the detailed characterization of magmatic processes end-members for the Atlantis Bank system, additional experimental petrology studies are required. This is also true when it comes to better characterize the parameters involved in the acquisition of the geochemical signatures of differentiation. We could continue the crystallization sequences established in Chapter 6, and complete the sequences down to lower temperatures. Additional experiments could also be used to confirm the first results of the partition coefficient experiments, and to help understanding the impact of the experimental techniques on the final products of crystallization. An important counterpart of the study not addressed here is the better quantification of the mechanisms at stake during melt-rock reactions. Only very few experimental studies have investigated melt-rock reactions within gabbros. However, such studies are key for our understanding of the balance between simple crystallization and interactions during the evolution of the reservoirs. New experimental petrology studies could be based on the reactions described herein since the latter have been calibrated thanks to geochemical and textural characteristics of the natural rock record.

At last, other leads for broader additional investigations and contextualization of the results of this thesis could be attempted: from the implementation of integrated numerical models of magma reservoirs for the studied system (e.g., the Magma Chamber Simulator, ***Bohrson et al., 2014***) to the consideration of the potential impact of the models established here for the global comprehension of mushy magma reservoirs present within the crust.

References

118, S. S. P. L. (1989). Shipboard Scientific Party 2 HOLE 735A. *Proceedings of the Ocean Drilling Program, Scientific Results* **118**, 89–222.

A

Ahern, J. & Turcotte, D. (1979). Magma migration beneath an ocean ridge. *Earth and Planetary Science Letters* **45**, 115–122.

Allègre, C. J. & Minster, J. F. (1978). Quantitative models of trace element behavior in magmatic processes. *Developments in Petrology* **5**, 1–25.

Arai, S., Dick, H. J. B. & Party, and S. (2000). *Cruise Report, Mode 2000 (Kairei/Kaiko KR00-06)*. .

Ariskin, A. A. & Barmina, G. S. (2004). COMAGMAT: Development of a magma crystallization model and its petrological applications. *Geochemistry International* **42**, s1–s157.

B

Bachmann, O. & Bergantz, G. W. (2003). Rejuvenation of the Fish Canyon magma body: A window into the evolution of large-volume silicic magma systems. *Geology* **31**, 789–792.

Baines, A. G., Cheadle, M. J., Dick, H. J. B., Scheirer, A. H., John, B. E., Kusznir, N. J. & Matsumoto, T. (2003). Mechanism for generating the anomalous uplift of oceanic core complexes: Atlantis Bank, southwest Indian Ridge. *Geology* **31**, 1105–1108.

Baines, A. G., Cheadle, M. J., John, B. E. & Schwartz, J. J. (2008). The rate of oceanic detachment faulting at Atlantis Bank, SW Indian Ridge. *Earth and Planetary Science Letters* **273**, 105–114.

Barnes, S. J. (1986). The effect of trapped liquid crystallization on cumulus mineral compositions in layered intrusions. *Contributions to Mineralogy and Petrology* **93**, 524–531.

Basch, V., Rampone, E., Crispini, L., Ferrando, C., Ildefonse, B. & Godard, M. (2018). From mantle peridotites to hybrid troctolites: Textural and chemical evolution during melt-rock interaction history (Mt. Maggiore, Corsica, France). *Lithos*. Elsevier B.V **323**, 4–23.

Basch, V., Rampone, E., Crispini, L., Ferrando, C., Ildefonse, B. & Godard, M. (2019). Multi-stage Reactive Formation of Troctolites in Slow-spreading Oceanic Lithosphere (Erro–Tobbio, Italy): a Combined Field and Petrochemical Study. *Journal of Petrology* **60**, 873–906.

Beattie, P. (1994). Systematics and energetics of trace-element partitioning between olivine and silica melts: implications for the nature of mineral/melt partitioning. *Chemical Geology* **17**,

57–71.

Bédard, J. H. (1991). Cumulate Recycling and Crustal Evolution in the Bay of Islands Ophiolite Author (s): Jean H . Bédard Source : The Journal of Geology , Vol . 99 , No . 2 (Mar ., 1991), pp . 225-249 Published by : The University of Chicago Press Stable URL : http://www. **99**, 225–249.

Bédard, J. H. (1994). A procedure for calculating the equilibrium distribution of trace elements among the minerals of cumulate rocks , and the concentration of trace elements in the coexisting liquids. *Chemical Geology* **118**, 143–153.

Bédard, J. H. (2001). Parental magmas of the nain plutonic suite anorthosites and mafic cumulates: A trace element modelling approach. *Contributions to Mineralogy and Petrology* **141**, 747–771.

Bédard, J. H. (2015). Ophiolitic Magma Chamber Processes, a Perspective from the Canadian Appalachians. *Layered Intrusions*, 1–748.

Bédard, J. H., Hébert, R., Berclaz, A. & Varfalvy, V. (2000). Syntexis and the genesis of lower oceanic crust. *Special Paper of the Geological Society of America* **349**, 105–119.

Bennett, E. N., Jenner, F. E., Millet, M.-A., Cashman, K. V. & Lissenberg, C. J. (2019). Deep roots for mid-ocean-ridge volcanoes revealed by plagioclase-hosted melt inclusions. *Nature*. Springer US **572**, 235–239.

Berndt, J., Koepke, J. & Holtz, F. (2005). An experimental investigation of the influence of water and oxygen fugacity on differentiation of MORB at 200 MPa. *Journal of Petrology* **46**, 135–167.

Berndt, J., Liebske, C., Holtz, F., Freise, M., Nowak, M., Ziegenbein, D., Hurkuck, W. & Koepke, J. (2002a). A combined rapid-quench and H2-membrane setup for internally heated pressure vessels: Description and application for water solubility in basaltic melts. *American Mineralogist* **87**, 1717–1726.

Berndt, J., Liebske, C., Holtz, F., Freise, M., Nowak, M., Ziegenbein, D., Hurkuck, W. & Koepke, J. (2002b). A combined rapid-quench and H2-membrane setup for internally heated pressure vessels: Description and application for water solubility in basaltic melts. *American Mineralogist* **87**, 1717–1726.

Blackman, D. K. *et al.* (2004a). Geology of the Atlantis Massif (Mid-Atlantic Ridge, 30°N): Implications for the evolution of an ultramafic oceanic core complex. *Marine Geophysical Research* **23**, 443–469.

Blackman, D. K. *et al.* (2011). Drilling constraints on lithospheric accretion and evolution at

Atlantis Massif, Mid-Atlantic Ridge 30N. *Journal of Geophysical Research: Solid Earth* **116**, 1–25.

Blackman, D. K., Ildefonse, B., John, B. E., Ohara, Y., Miller, D. J. & MacLeod, C. J. (2006a). Expedition 304/305 summary. *Proceedings of the IODP, 304/305* **304**.

Blackman, D. K., Ildefonse, B., John, B., Ohara, Y., Miller, D. J. & Macleod, C. J. (2006b). Site U1309. *Proceedings of the IODP, 304/305* **304**.

Blackman, D. K., John, B. E., Ildefonse, B., Ohara, Y., MacLeod, C. J. & Miller, D. J. (2004b). Oceanic core complex Formation, Atlantis Massif. *Integrated Ocean Drilling Program*.

Bloomer, S. H., Meyer, P. S., Dick, H. J. B., Ozawa, K. & Natland, J. H. (1991). Textural and mineralogic variations in gabbroic rocks from Hole 735B. *Proceedings of the Ocean Drilling Program*.

Blum, P. *et al.* (2017). Hole U1473A remediation operations, Expedition 362T. .

Blundy, J. & Wood, B. (2003). Partitioning of trace elements between crystals and melts. *Earth and Planetary Science Letters* **210**, 383–397.

Bohrson, W. A., Spera, F. J., Ghiorso, M. S., Brown, G. A., Creamer, J. B. & Mayfield, A. (2014). Thermodynamic model for energy-constrained open-system evolution of crustal magma bodies undergoing simultaneous recharge, assimilation and crystallization: The magma chamber simulator. *Journal of Petrology* **55**, 1685–1717.

Borghini, G., Francomme, J. E. & Fumagalli, P. (2018). Melt-dunite interactions at 0.5 and 0.7 GPa: experimental constraints on the origin of olivine-rich troctolites. *Lithos*. Elsevier B.V **323**, 44–57.

Borghini, G. & Rampone, E. (2007). Postcumulus processes in oceanic-type olivine-rich cumulates: The role of trapped melt crystallization versus melt/rock interaction. *Contributions to Mineralogy and Petrology* **154**, 619–633.

Botcharnikov, R. E., Koepke, J., Holtz, F., McCammon, C. & Wilke, M. (2005). The effect of water activity on the oxidation and structural state of Fe in a ferro-basaltic melt. *Geochimica et Cosmochimica Acta* **69**, 5071–5085.

Boudier, F., Nicolas, A. & Ildefonse, B. (1996). Magma chambers in the Oman ophiolite: fed from the top and and the bottom. *Earth and Planetary Science Letters* **144**.

Boudreau, A. E. & McBirney, A. R. (1997). The Skaergaard Layered Series. Part III. Non-dynamic Layering. *Journal of Petrology* **38**, 1003–1020.

Boulanger, M. *et al.* (submitted). Melt migration and interactions in the lower oceanic crust:

insights from Atlantis Bank interlayered series at IODP Hole U1473A (Southwest Indian Ridge). *Geochemistry, Geophysics, Geosystems*.

Bowen, N. L. (1928). *The evolution of the igneous rocks*. .

Brice, J. C. (1975). Some thermodynamic aspects of the growth of strained crystals. *Journal of Crystal Growth* **28**, 249–253.

Buck, W. R., Lavier, L. L. & Poliakov, A. N. B. (2005). Modes of faulting at mid-ocean ridges. *Nature* **434**, 719–723.

C

Canales, J. P., Dunn, R. A., Arai, R. & Sohn, R. A. (2017). Seismic imaging of magma sills beneath an ultramafic-hosted hydrothermal system. *Geology* **45**, 451–454.

Cann, J. R. (1974). A Model for Oceanic Crystal Structure Developed. *Geophysical Journal of the Royal Astronomical Society* **39**, 169–187.

Cann, J. R., Blackman, D. K., Smith, D. K., McAllister, E., Janssen, B., Mello, S., Avgerinos, E., Pascoe, A. R. & Escartin, J. (1997). Corrugated slip surfaces formed at ridge-transform intersections on the mid-Atlantic ridge. *Nature*.

Cannat, M. (1993). Emplacement of mantle rocks in the seafloor at mid-ocean ridges. *Journal of Geophysical Research: Solid Earth* **98**, 4163–4172.

Cannat, M. (1995). Thin crust, ultramafic exposures, and rugged faulting patterns at the Mid-Atlantic Ridge (22??-24??N). *Geology* **23**, 49–52.

Cannat, M. (1996). How thick is the magmatic crust at slow spreading oceanic ridges ? Melt Migration in the Axial Lithosphere of Slow Spreading Ridges : Constraints from Ultramafic and Gabbroic Samples. *Journal of Geophyscial Research* **101**, 2847–2857.

Cannat, M., Lagabrielle, Y., Bougault, H., Casey, J., de Coutures, N., Dmitriev, L. & Fouquet, Y. (1997). Ultramafic and gabbroic exposures at the Mid-Atlantic Ridge: geological mapping in the 15°N region. *Tectonophysics* **279**, 193–213.

Cannat, M., Sauter, D., Lavier, L., Bickert, M., Momoh, E. & Leroy, S. (2019). On spreading modes and magma supply at slow and ultraslow mid-ocean ridges. *Earth and Planetary Science Letters*. Elsevier B.V. **519**, 223–233.

Cannat, M., Sauter, D., Mendel, V., Ruellan, E., Okino, K., Escartin, J., Combier, V. & Baala, M. (2006). Modes of seafloor generation at a melt-poor ultraslow-spreading ridge. *Geology* **34**, 605–608.

Carbotte, S. M., Smith, D. K., Cannat, M. & Klein, E. M. (2015). Tectonic and magmatic segmentation of the Global Ocean Ridge System: a synthesis of observations. *Geological Society, London, Special Publications* **420**, 249–295.

Casey, J. F., Banerji, D. & Zarian, P. (2007). Leg 179 Synthesis: Geochemistry, Stratigraphy, and Structure of Gabbroic Rocks Drilled in ODP Hole 1105A, Southwest Indian Ridge. *Proceedings of the Ocean Drilling Program, 147 Scientific Results* **179**.

Cashman, K. V., Sparks, R. S. J. & Blundy, J. D. (2017). Vertically extensive and unstable magmatic systems: A unified view of igneous processes. *Science* **355**.

Chakraborty, S. (2008). Diffusion in Solid Silicates: A Tool to Track Timescales of Processes Comes of Age. *Annual Review of Earth and Planetary Sciences* **36**, 153–190.

Charlier, B., Vander Auwera, J. & Duchesne, J. C. (2005). Geochemistry of cumulates from the Bjerkreim-Sokndal layered intrusion (S. Norway). *Lithos* **83**, 255–276.

Cherniak, D. J. (2003). REE diffusion in feldspar. *Chemical Geology* **193**, 1–17.

Cherniak, D. J. (2010a). REE diffusion in olivine. *American Mineralogist* **95**, 362–368.

Cherniak, D. J. (2010b). Cation Diffusion in Feldspars. *Reviews in Mineralogy and Geochemistry* **72**, 691–733.

Cherniak, D. J. & Liang, Y. (2007). Rare earth element diffusion in natural enstatite. *Geochimica et Cosmochimica Acta* **71**, 1324–1340.

Ciazela, J., Koepke, J., Dick, H. J. B. & Muszynski, A. (2015). Mantle rock exposures at oceanic core complexes along mid-ocean ridges. *Geologos* **21**, 207–231.

Collier, M. L. & Kelemen, P. B. (2010). The case for reactive crystallization at mid-ocean ridges. *Journal of Petrology* **51**, 1913–1940.

Coogan, L. A. (2014). *The Lower Oceanic Crust*. *Treatise on Geochemistry: Second Edition*. Elsevier Ltd.

Coogan, L. A., MacLeod, C. J., Dick, H. J. B., Edwards, S. J., Kvassnes, A., Natland, J. H., Robinson, P. T., Thompson, G. & O'Hara, M. J. (2001). Whole-rock geochemistry of gabbros from the Southwest Indian Ridge: Constraints on geochemical fractionations between the upper and lower oceanic crust and magma chamber processes at (very) slow-spreading ridges. *Chemical Geology* **178**, 1–22.

Coogan, L. A. & O'Hara, M. J. (2015). MORB differentiation: In situ crystallization in replenished-tapped magma chambers. *Geochimica et Cosmochimica Acta*. Elsevier Ltd **158**, 147–161.

Coogan, L. A., Saunders, A. D., Kempton, P. D. & Norry, M. J. (2000). Evidence from oceanic

gabbros for porous melt migration within a crystal mush beneath the Mid-Atlantic Ridge. *Geochemistry, Geophysics, Geosystems* **1**.

Coogan, L. A., Thompson, G. M., MacLeod, C. J., Dick, H. J. B., Edwards, S. J., Hosford Scheirer, A. & Barry, T. L. (2004). A combined basalt and peridotite perspective on 14 million years of melt generation at the Atlantis Bank segment of the Southwest Indian Ridge: Evidence for temporal changes in mantle dynamics? *Chemical Geology* **207**, 13–30.

D

Daines, M. J. & Kohlstedt, D. L. (1994). The transition from porous to channelized flow due to melt/rock reaction during melt migration. *Geophysical Research Letters* **21**, 145–148.

Daines, M. J. & Pec, M. (2015). Migration of Melt. *The Encyclopedia of Volcanoes* 49–64.

Danyushevsky, L. V. & Plechov, P. (2011). Petrolog3: Integrated software for modeling crystallization processes. *Geochemistry, Geophysics, Geosystems* **12**.

DePaolo, D. J. (1981). Trace element and isotopic effects of combined wallrock assimilation and fractional crystallization. *Earth and Planetary Science Letters* **53**, 189–202.

Detrick, R. S., Buhl, P., Vera, E., Mutter, J., Orcutt, J., Madsen, J. & Brocher, T. (1987). Multi-channel seismic imaging of a crustal magma chamber along the East Pacific Rise. *Nature* **326**, 35–41.

Devine, J. D., Gardner, J. E., Brack, H. P., Layne, G. D. & Rutherford, M. J. (1995). Comparison of microanalytical methods for estimating H2O contents of silicic volcanic glasses. *American Mineralogist* **80**, 319–328.

Dick, H. J. B. (1989). Abyssal peridotites, very slow spreading ridges and ocean ridge magmatism. *Geological Society Special Publication* **42**, 71–105.

Dick, H. J. B. *et al.* (1991a). Tectonic Evolution of the Atlantis I I Fracture Zone. *proceedings of the Ocean Drilling Program, Scientific Results* **118**, 359–398.

Dick, H. J. B. *et al.* (2000). A long gabbro section in the ocean crust: Results of leg 176 drilling, Southwest Indian Ridge. *JOIDES Journal* **24**, 11-14+30.

Dick, H. J. B. *et al.* (2002). 10 . Primary silicate mineral chemistry of a 1.5-km section of very slow spreading lower ocean crust: ODP Hole 753B, Southwest Indian Ridge. *Proceedings of the Ocean Drilling Program: Scientific Results* **176**, 1–61.

Dick, H. J. B. *et al.* (2019a). Dynamic accretion beneath a slow-spreading ridge segment: IODP Hole U1473A and the Atlantis Bank Core Complex. *Solid Earth*.

Dick, H. J. B., Kvassnes, A. J. S., Robinson, P. T., Macleod, C. J. & Kinoshita, H. (2019b). The Atlantis Bank Gabbro Massif , Southwest Indian Ridge. Progress in Earth and Planetary Science **9**.

Dick, H. J. B., Lin, J. & Schouten, H. (2003). An ultraslow-spreading class of ocean ridge. *Nature* **426**, 405–412.

Dick, H. J. B., Macleod, C. J. & Blum, P. and the E. 360 S. (2016a). *Expedition 360 Scientific Prospectus Southwest Indian Ridge Lower Crust and Moho The nature of the lower crust and Moho at slower spreading ridges (SloMo-Leg 1). International Ocean Discovery Program*.

Dick, H. J. B., Macleod, C. J., Blum, P. & the Expedition 360 Scientists (2016b). *Expedition 360 Preliminary report: Southwest Indian Ridge lower crust and Moho*. .

Dick, H. J. B., Meyer, P. S., Bloomer, S., Kirby, S., Stakes, D. & Mawer, C. (1991b). Lithostratigraphic Evolution of an In-Situ Section of Oceanic Layer 3. *Proceedings of the Ocean Drilling Program, 118 Scientific Results* **118**.

Dick, H. J. B., Natland, J. H., Miller, D. J. & Al., E. (1999). Site 735. *Proceedings of the Ocean Drilling Program* **176**.

Dick, H. J. B., Tivey, M. A. & Tucholke, B. E. (2008). Plutonic foundation of a slow-spreading ridge segment: Oceanic core complex at Kane Megamullion, 23°30′N, 45°20′W. *Geochemistry, Geophysics, Geosystems* **9**.

Dohmen, R. & Chakraborty, S. (2007). Fe-Mg diffusion in olivine II: Point defect chemistry, change of diffusion mechanisms and a model for calculation of diffusion coefficients in natural olivine. *Physics and Chemistry of Minerals* **34**, 409–430.

Dohmen, R., Chakraborty, S., Palme, H. & Rammensee, W. (2003). Role of element solubility on the kinetics of element partitioning: In situ observations and a thermodynamic kinetic model. *Journal of Geophysical Research: Solid Earth* **108**, 1–15.

Drouin, M., Godard, M., Ildefonse, B., Bruguier, O. & Garrido, C. J. (2009). Geochemical and petrographic evidence for magmatic impregnation in the oceanic lithosphere at Atlantis Massif, Mid-Atlantic Ridge (IODP Hole U1309D, 30°N). *Chemical Geology*. Elsevier B.V. **264**, 71–88.

Drouin, M., Ildefonse, B. & Godard, M. (2010). A microstructural imprint of melt impregnation in slow spreading lithosphere: Olivine-rich troctolites from the Atlantis Massif, Mid-Atlantic Ridge, 30??N, IODP Hole U1309D. *Geochemistry, Geophysics, Geosystems* **11**, 1–21.

Dunn, R. A. (2015). *Crust and Lithospheric Structure - Seismic Structure of Mid-Ocean Ridges*. *Treatise on Geophysics: Second Edition*. Elsevier B.V.

Dunn, R. A., Lekić, V., Detrick, R. S. & Toomey, D. R. (2005). Three-dimensional seismic structure of the Mid-Atlantic Ridge (35°N): Evidence for focused melt supply and lower crustal dike injection. *Journal of Geophysical Research B: Solid Earth* **110**, 1–17.

E

Edwards, B. R. & Russell, J. K. (1998). Time scales of magmatic processes: New insights from dynamic models for magmatic assimilation. *Geology* **26**, 1103–1106.

Elthon, D., Stewart, M. & Ross, D. K. (1992). Compositional trends of minerals in oceanic cumulates. *Journal of Geophysical Research* **97**.

Erdmann, M. & Koepke, Jü. (2016). Experimental temperature cycling as a powerful tool to enlarge melt pools and crystals at magma storage conditions. *American Mineralogist* **101**, 960–969.

Escartín, J., Mével, C., MacLeod, C. J. & McCaig, A. M. (2003). Constraints on deformation conditions and the origin of oceanic detachments: The Mid-Atlantic Ridge core complex at 15°45′N. *Geochemistry, Geophysics, Geosystems* **4**.

Escartín, J., Smith, D. K., Cann, J., Schouten, H., Langmuir, C. H. & Escrig, S. (2008). Central role of detachment faults in accretion of slow-spreading oceanic lithosphere. *Nature* **455**, 790–794.

F

Faak, K., Chakraborty, S. & Coogan, L. A. (2013). Mg in plagioclase: Experimental calibration of a new geothermometer and diffusion coefficients. *Geochimica et Cosmochimica Acta*. Elsevier Ltd **123**, 195–217.

Feig, S. T., Koepke, J. & Snow, J. E. (2006). Effect of water on tholeiitic basalt phase equilibria: An experimental study under oxidizing conditions. *Contributions to Mineralogy and Petrology* **152**, 611–638.

Feig, S. T., Koepke, J. & Snow, J. E. (2010). Effect of oxygen fugacity and water on phase equilibria of a hydrous tholeiitic basalt. *Contributions to Mineralogy and Petrology* **160**, 551–568.

Ferrando, C. (2017). Transport de magma et processus d ' assimilation- précipitation dans la croute océanique inférieure hétérogène : contraintes microstructurales et pétro-géochimiques de forages océaniques Présentée par Carlotta FERRANDO. .

Ferrando, C., Godard, M., Ildefonse, B. & Rampone, E. (2018a). Melt transport and mantle

assimilation at Atlantis Massif (IODP Site U1309): Constraints from geochemical modeling. *Lithos*. Elsevier B.V. **323**, 24–43.

Ferrando, C., Godard, M., Ildefonse, B. & Rampone, E. (2018b). Melt transport and mantle assimilation at Atlantis massif (IODP site U1309): Constraints from geochemical modeling. *Lithos*. Elsevier B.V.

Fisher, R. L. & Sclater, J. G. (1983). Tectonic evolution of the Southwest Indian Ocean since the Mid-Cretaceous: plate motions and stability of the pole of Antarctica/Africa for at least 80 Myr. *Geophysical Journal of the Royal Astronomical Society* **73**, 553–576.

Fisher, R. V & Schmincke, H.-U. (1984). *Pyroclastic rocks*. .

France, L., Ildefonse, B. & Koepke, J. (2009). Interactions between magma and hydrothermal system in Oman ophiolite and in IODP Hole 1256D: Fossilization of a dynamic melt lens at fast spreading ridges. *Geochemistry, Geophysics, Geosystems* **10**, 1–30.

France, L., Koepke, J., MacLeod, C. J., Ildefonse, B., Godard, M. & Deloule, E. (2014). Contamination of MORB by anatexis of magma chamber roof rocks: Constraints from a geochemical study of experimental melts and associated residues. *Lithos*. Elsevier B.V. **202–203**, 120–137.

G

Gale, A., Dalton, C. A., Langmuir, C. H., Su, Y. & Schilling, J. G. (2013). The mean composition of ocean ridge basalts. *Geochemistry, Geophysics, Geosystems* **14**, 489–518.

Gao, Y., Hoefs, J., Hellebrand, E., von der Handt, A. & Snow, J. E. (2007a). Trace element zoning in pyroxenes from ODP Hole 735B gabbros: Diffusive exchange or synkinematic crystal fractionation? *Contributions to Mineralogy and Petrology* **153**, 429–442.

Gao, Y., Hoefs, J., Hellebrand, E., von der Handt, A. & Snow, J. E. (2007b). Trace element zoning in pyroxenes from ODP Hole 735B gabbros: Diffusive exchange or synkinematic crystal fractionation? *Contributions to Mineralogy and Petrology* **153**, 429–442.

Ghiorso, M. S. & Gualda, G. A. R. (2015). An H<inf>2</inf>O–CO<inf>2</inf> mixed fluid saturation model compatible with rhyolite-MELTS. *Contributions to Mineralogy and Petrology*. Springer Berlin Heidelberg **169**.

Ghiorso, M. S. & Sack, R. O. (1995). Chemical mass transfer in magmatic processes IV. A revised and internally consistent thermodynamic model for the interpolation and extrapolation of liquid-solid equilibria in magmatic systems at elevated temperatures and pressures. *Contributions to Mineralogy and Petrology* **119**, 197–212.

Godard, M. *et al.* (2009). Geochemistry of a long in-situ section of intrusive slow-spread oceanic lithosphere: Results from IODP Site U1309 (Atlantis Massif, 30°N Mid-Atlantic-Ridge). *Earth and Planetary Science Letters*. Elsevier B.V. **279**, 110–122.

Goldschmidt, V. M. (1937). Distribution of. *Journal of the chemical society* **The sevent**, 655–673.

Graham Baines, A., Cheadle, M. J., Henry Dick, J. B., Scheirer, A. H., John, B. E., Kusznir, N. J. & Matsumoto, T. (2007). Evolution of the Southwest Indian ridge from 55°45′E to 62°E: Changes in plate-boundary geometry since 26 Ma. *Geochemistry, Geophysics, Geosystems* **8**.

Grimes, C. B., John, B. E., Cheadle, M. J. & Wooden, J. L. (2008). Protracted construction of gabbroic crust at a slow spreading ridge: Constraints from 206Pb/238U zircon ages from Atlantis Massif and IODP Hole U1309D (30°N, MAR). *Geochemistry, Geophysics, Geosystems* **9**.

Grove, T. L., Baker, M. B. & Kinzler, R. J. (1984). Coupled CaAl-NaSi diffusion in plagioclase feldspar: Experiments and applications to cooling rate speedometry. *Geochimica et Cosmochimica Acta* **48**, 2113–2121.

Grove, T. L. & Brown, S. M. (2018). Magmatic processes leading to compositional diversity in igneous rocks: Bowen (1928) revisited. *American Journal of Science* **318**, 1–28.

Grove, T. L., Kinzler, R. J. & Bryan, W. B. (1992). Fractionation of mid-ocean ridge basalt (MORB). In: Morgan, J. P., Blackman, D. K. & Sinton, J. M. (eds) *Mantle flow and melt generation at Mid-Ocean Ridges*. Washington, D. C.: AGU, 281–310.

Gualda, G. A. R. & Ghiorso, M. S. (2015). MELTS-Excel: A Microsoft Excel-based MELTS interface for research and teaching of magma properties and evolution. *Geochemistry, Geophysics, Geosystems* **16**, 315–324.

H

Hart, S. R., Blusztajn, J., Dick, H. J. B., Meyer, P. S. & Muehlenbachs, K. (1999). The fingerprint of seawater circulation in a 500-meter section of ocean crust gabbros. *Geochimica et Cosmochimica Acta* **63**, 4059–4080.

Hepworth, L. N., O'Driscoll, B., Gertisser, R., Daly, J. S. & Emeleus, C. H. (2018). Linking in situ crystallization and magma replenishment via sill intrusion in the Rum Western Layered Intrusion, NW Scotland. *Journal of Petrology* **59**, 1605–1642.

Hertogen, J., Emmermann, R., Robinson, P. T. & Erzinger, J. (2002). Lithology, mineralogy, and

geochemistry of the lower ocean crust, ODP Hole 735B, Southwest Indian Ridge. *Proceedings of the Ocean Drilling Program, 176 Scientific Results* **176**.

Herzberg, C. (2004). Partial crystallization of mid-ocean ridge basalts in the crust and mantle. *Journal of Petrology* **45**, 2389–2405.

Higgie, K. & Tommasi, A. (2012). Feedbacks between deformation and melt distribution in the crust-mantle transition zone of the Oman ophiolite. *Earth and Planetary Science Letters* **359–360**, 61–72.

Higgins, M. D. (1991). The origin of laminated and massive anorthosite, Sept Iles layered intrusion, Québec, Canada. *Contributions to Mineralogy and Petrology* **106**, 340–354.

Holm, P. M. (2002). Data report: On the composition of the lower ocean crust—major and trace element analyses of gabbroic rocks from Hole 735B, 500-1500 mbsf. *Proceedings of the Ocean Drilling Program, 176 Scientific Results* **176**, 1–13.

Holness, M. B., Cawthorn, R. G. & Roberts, J. (2017a). The thickness of the crystal mush on the floor of the Bushveld magma chamber. *Contributions to Mineralogy and Petrology*. Springer Berlin Heidelberg **172**, 1–20.

Holness, M. B., Hallworth, M. A., Woods, A. & Sides, R. E. (2007). Infiltration metasomatism of cumulates by intrusive magma replenishment: The wavy horizon, Isle of Rum, Scotland. *Journal of Petrology* **48**, 563–587.

Holness, M. B., Vukmanovic, Z. & Mariani, E. (2017b). Assessing the role of compaction in the formation of adcumulates: A microstructural perspective. *Journal of Petrology* **58**, 643–674.

Holtzman, B. K., Groebner, N. J., Zimmerman, M. E., Ginsberg, S. B. & Kohlstedt, D. L. (2003). Stress-driven melt segregation in partially molten rocks. *Journal of Petrology* **51**, 9–19.

Hosford, A., Tivey, M., Matsumoto, T., Dick, H., Schouten, H. & Kinoshita, H. (2003). Crustal magnetization and accretion at the Southwest Indian Ridge near the Atlantis II fracture zone, 0-25 Ma. *Journal of Geophysical Research: Solid Earth* **108**, 1–23.

Husen, A., Almeev, R. R. & Holtz, F. (2016). The Effect of H2O and Pressure on Multiple Saturation and Liquid Lines of Descent in Basalt from the Shatsky Rise. *Journal of Petrology* **57**, 309–344.

I

Ildefonse, B. *et al.* (2007). Oceanic core complexes and crustal accretion at slow-speading ridges. *Geology* **35**, 623–626.

Ildefonse, B., Sokoutis, D. & Mancktelow, N. S. (1992). Mechanical interactions between rigid particles in a deforming ductile matrix. Analogue experiments in simple shear flow. *Journal of Structural Geology* **14**, 1253–1266.

Irvine, T. (1980). Magmatic infiltration metasomatism, double diffusive fractional crystallization and adcumulus growth in the Muskox Intrusion and other layered intrusions. *Physics of Magmatic Processes* 325–383.

Irvine, T. N. (1982). Terminology for Layered Intrusions. *Journal of Petrology* **23**, 127–162.

J

Jackson, M. D., Blundy, J. & Sparks, R. S. J. (2018). Chemical differentiation, cold storage and remobilization of magma in the Earth's crust. *Nature*. Springer US **564**, 405–409.

Jansen, M. N., Lissenberg, C. J., Klaver, M., de Graaff, S. J., Koornneef, J. M., Smeets, R. J., MacLeod, C. J. & Davies, G. R. (2018). Isotopic variation in Semail Ophiolite lower crust reveals crustal-level melt aggregation. *Geochemical Perspectives Letters* 37–42.

Jarosewich, E., Nelen, J. A. & Norbers, J. A. (1980). Reference Samples for Electron Microprobe Analysis. *Geostandards Newsletter* **4**, 43–47.

Jenner, F. E. & O'Neill, H. S. C. (2012). Analysis of 60 elements in 616 ocean floor basaltic glasses. *Geochemistry, Geophysics, Geosystems* **13**, 1–11.

Jian, H., Singh, S. C., Chen, Y. J. & Li, J. (2016). Evidence of an axial magma chamber beneath the ultraslow-spreading Southwest Indian Ridge. *Geology* **44**, G38356.1.

John, B. E. & Cheadle, M. J. (2010). Deformation and Alteration Associated With Oceanic and Continental.pdf. *University of Wyoming* 175–205.

Jousselin, D., Morales, L. F. G., Nicolle, M. & Stephant, A. (2012). Gabbro layering induced by simple shear in the Oman ophiolite Moho transition zone. *Earth and Planetary Science Letters*. Elsevier B.V. **331–332**, 55–66.

K

Kelemen, P. B. & Aharonov, E. (1998). Periodic formation of magma fractures and generation of layered gabbros in the lower crust beneath oceanic spreading ridges. *Geophysical Monograph Series* **106**, 267–289.

Kelemen, P. B., Hirth, G., Shimizu, N., Spiegelman, M. & Dick, H. J. (1997a). A review of melt

migration processes in the adiabatically upwelling mantle beneath oceanic spreading ridges. *Philosophical Transactions of the Royal Society A: Mathematical, Physical and Engineering Sciences* **355**, 283–318.

Kelemen, P. B., Kikawa, E. & Miller, D. J. (2007). Leg 209 Summary - Processes in a 20-km-Thick Conductive Boundary Layer beneath the Mid-Atlantic Ridge, 14°–16°N. *Proceedings of the Ocean Drilling Program, Scientific Results* **209**, 1–38.

Kelemen, P. B., Koga, K. & Shimizu, N. (1997b). Geochemistry of gabbro sills in the crust-mantle transition zone of the Oman ophiolite: implications for the origin of the oceanic lower crust. *Earth and Planetary Science Letters* **146**, 475–488.

Kelemen, P. B., Shimizu, N. & Salters, V. J. M. (1995). Extraction of mid-ocean-ridge basalt from the upwelling mantle by focused flow of melt in dunite channels. *Nature* **375**.

Kinoshita, J., Dick, H. J. B. & JAMSTEC/WHOI, and S. P. (1999). Deep see diving expedition in SW Indian Ridge. *Eos, Transactions of the American Geophysical Union* **80**.

Koepke, J., Botcharnikov, R. E. & Natland, J. H. (2018). Crystallization of late-stage MORB under varying water activities and redox conditions: Implications for the formation of highly evolved lavas and oxide gabbro in the ocean crust. *Lithos*. Elsevier B.V. **323**, 58–77.

Korenaga, J. & Kelemen, P. (1998). Melt migration through the oceanic lower crust: a constraint from melt percolation modeling with finite solid diffusion. *Earth and Planetary Science Letters* **156**, 1–11.

Kvassnes, A. J. S. (2003). The evolution of oceanic gabbros : in situ and ancient examples. .

Kvassnes, A. J. S. & Grove, T. L. (2008). How partial melts of mafic lower crust affect ascending magmas at oceanic ridges. *Contributions to Mineralogy and Petrology* **156**, 49–71.

Kvassnes, A. J. S., Strand, A. H., Moen-Eikeland, H. & Pedersen, R. B. (2004). The Lyngen Gabbro: The lower crust of an Ordovician Incipient Arc. *Contributions to Mineralogy and Petrology* **148**, 358–379.

L

Lagabrielle, Y. & Cannat, M. (1990). Alpine jurassic ophiolites resemble the modern central Atlantic basement. *Geology* **18**, 319–322.

Lagabrielle, Y. & Lemoine, M. (1997). Alpine, Corsican and Apennine ophiolites: the slow-spreading ridge model. *Earth and Planetary Science* 909–920.

Lagabrielle, Y., Vitale Brovarone, A. & Ildefonse, B. (2015). Fossil oceanic core complexes

recognized in the blueschist metaophiolites of Western Alps and Corsica. *Earth-Science Reviews*. Elsevier B.V. **141**, 1–26.

Lambart, S., Didier, A. E., Ae, L. & Schiano, P. (2009a). An experimental study of focused magma transport and basalt-peridotite interactions beneath mid-ocean ridges: implications for the generation of primitive MORB compositions. *Contributions to Mineralogy and Petrology*.

Lambart, S., Koornneef, J. M., Millet, M. A., Davies, G. R., Cook, M. & Lissenberg, C. J. (2019). Highly heterogeneous depleted mantle recorded in the lower oceanic crust. *Nature Geoscience*. Springer US **12**, 482–486.

Lambart, S., Laporte, D. & Schiano, P. (2009b). An experimental study of focused magma transport and basalt-peridotite interactions beneath mid-ocean ridges: Implications for the generation of primitive MORB compositions. *Contributions to Mineralogy and Petrology* **157**, 429–451.

Langmuir, C. H. (1989). Geochemical consequences of in situ crystallization. *Nature* **340**, 199–205.

Langmuir, C. H., Klein, E. M. & Plank, T. (1992). Petrological systematics of mid-ocean ridge basalts: Constraints on melt generation beneath ocean ridges BT - … melt generation at mid-ocean …. *Geophysical Monograph Series* **71**, 183–280.

Laubier, M., Grove, T. L. & Langmuir, C. H. (2014). Trace element mineral/melt partitioning for basaltic and basaltic andesitic melts: An experimental and laser ICP-MS study with application to the oxidation state of mantle source regions. *Earth and Planetary Science Letters*. Elsevier B.V. **392**, 265–278.

Leuthold, J., Lissenberg, C. J., O'Driscoll, B., Karakas, O., Falloon, T., Klimentyeva, D. N. & Ulmer, P. (2018). Partial Melting of Lower Oceanic Crust Gabbro: Constraints From Poikilitic Clinopyroxene Primocrysts. *Frontiers in Earth Science* **6**.

Liang, Y. (2003). Kinetics of crystal-melt reaction in partially molten silicates: 1. Grain scale processes. *Geochemistry, Geophysics, Geosystems* **4**.

Lissenberg, C. J. & Dick, H. J. B. (2008). Melt-rock reaction in the lower oceanic crust and its implications for the genesis of mid-ocean ridge basalt. *Earth and Planetary Science Letters* **271**, 311–325.

Lissenberg, C. J. & MacLeod, C. J. (2016). A reactive porous flow control on mid-ocean ridge magmatic evolution. *Journal of Petrology* **57**, 2195–2220.

Lissenberg, C. J., MacLeod, C. J., Howard, K. A. & Godard, M. (2013). Pervasive reactive melt migration through fast-spreading lower oceanic crust (Hess Deep, equatorial Pacific

Ocean). *Earth and Planetary Science Letters*. Elsevier **361**, 436–447.

Lissenberg, J. C., MacLeod, C. J. & Bennett, E. N. (2019). Consequences of a crystal mush-dominated magma plumbing system: A mid-ocean ridge perspective. *Philosophical Transactions of the Royal Society A: Mathematical, Physical and Engineering Sciences* **377**.

M

Macleod, C. J. *et al.* (1998). Geological mapping of slow-spread lower ocean crust: a deep-towed video and wireline rock drilling survey of Atlantis Bank (ODP Site 735, SW Indian Ridge). *InterRidge News* **7**, 39–43.

MacLeod, C. J. *et al.* (2017a). Site U1473. *Proceedings of the Ocean Drilling Program* **360**.

MacLeod, C. J. *et al.* (2017b). Hole 1105A redescription. *Proceedings of the Ocean Drilling Program* **360**.

MacLeod, C. J., Searle, R. C., Murton, B. J., Casey, J. F., Mallows, C., Unsworth, S. C., Achenbach, K. L. & Harris, M. (2009). Life cycle of oceanic core complexes. *Earth and Planetary Science Letters*. Elsevier B.V. **287**, 333–344.

MacLeod, C. J. & Yaouancq, G. (2000). A fossil melt lens in the Oman ophiolite: Implications for magma chamber processes at fast spreading ridges. *Earth and Planetary Science Letters* **176**, 357–373.

Magde, L. S., Barclay, A. H., Toomey, D. R., Detrick, R. S. & Collins, J. A. (2000). Crustal magma plumbing system within a segment of the slow-spreading MAR, 35°N. *Earth and Planetary Science Letters* **79**, 799.

Mainprice, D., Bachmann, F., Hielscher, R. & Schaeben, H. (2014). Descriptive tools for the analysis of texture projects with large datasets using MTEX : strength, symmetry and components. *Geological Society, London, Special Publications* **409**, 251–271.

Mainprice, D. & Silver, P. G. (1993). Interpretation of SKS-waves using samples from the subcontinental lithosphere. *Physics of the Earth and Planetary Interiors* **78**, 257–280.

Marsh, B. D. (1996). Solidification Fronts and Magmatic Evolution. *Mineralogical Magazine* **60**, 5–40.

Mathez, E. A. (1995). Magmatic metasomatism and formation of the Merensky reef, Bushveld Complex. *Contributions to Mineralogy and Petrology* **119**, 277–286.

Matsumoto, T., Dick, H. J. B. & Party, and S. (2002). *Investigation of Atlantis Bank and the SW Indian Ridge from 568E to 588E: Peliminary Report (Tokyo).* .

McBirney, A. R. & Nicolas, A. (1997). The Skaergaard Layered Series. Part II. Magmatic flow and dynamic layering. *Journal of Petrology* **38**, 569–580.

Mckenzie, D. (1984). The generation and compactation of partially molten rock. *Journal of Petrology* **25**, 713–765.

Meurer, W. P. & Boudreau, A. E. (1989). Compaction of Igneous Cumulates Part II: Compaction and the Development of Igneous Foliations. *The Journal of Geology* **106**, 293–304.

Meyer, P. S., Dick, H. J. B. & Thompson, G. (1989). Cumulate gabbros from the Southwest Indian Ridge, 54°S-7°16' E: implications for magmatic processes at a slow spreading ridge. *Contributions to Mineralogy and Petrology* **103**, 44–63.

Miller, D. J. *et al.* (2009). Data report: microprobe analyses of primary mineral phases from Site U1309, Atlantis Massif, IODP Expedition 304/305. *Proceedings of the IODP, 304/305*. Integrated Ocean Drilling Program.

Morales, L. F. G., Boudier, F. & Nicolas, A. (2011). Microstructures and crystallographic preferred orientation of anorthosites from Oman ophiolite and the dynamics of melt lenses. *Tectonics* **30**.

Morse, S. A. (1979). Kiglapait geochemistry II: Petrography. *Journal of Petrology* **20**, 591–624.

Morse, S. A. (1984). Cation diffusion in plagioclase feldspar. *Science* **225**, 504–505.

Muller, M. R. (1997). Thin crust beneath ocean drilling program borehole 735B at the Southwest Indian Ridge? *Earth and Planetary Science Letters* **148**, 93–107.

Muller, M. R., Minshull, T. A. & White, R. S. (2000). Crustal structure of the Southwest Indian Ridge. *Journal of Geophyscial Research* **105**, 25809 – 25828.

N

Namur, O. *et al.* (2015). Igneous layering in basaltic magma chambers. *Layered Intrusions*, 1–748.

Namur, O. & Charlier, B. (2012). Efficiency of compaction and compositional convection during mafic crystal mush solidification: The Sept Iles layered intrusion, Canada. *Contributions to Mineralogy and Petrology* **163**, 1049–1068.

Namur, O., Charlier, B., Toplis, M. J., Higgins, M. D., Liégeois, J. P. & vander Auwera, J. (2010). Crystallization sequence and magma chamber processes in the ferrobasaltic Sept Iles layered intrusion, Canada. *Journal of Petrology* **51**, 1203–1236.

Namur, O., Humphreys, M. C. S. & Holness, M. B. (2013). Lateral reactive infiltration in avertical gabbroic crystal mush, skaergaard intrusion, east greenland. *Journal of Petrology* **54**, 985–1016.

Nandedkar, R. H., Ulmer, P. & Müntener, O. (2014). Fractional crystallization of primitive, hydrous arc magmas: An experimental study at 0.7 GPa. *Contributions to Mineralogy and Petrology* **167**, 1–27.

Naslund, H. R. & McBirney, A. R. (1996). Mechanisms of Formation of Igneous Layering. *Developments in Petrology* **15**, 1–43.

Natland, J. H. & Dick, H. J. B. (2001a). Formation of the lower ocean crust and the crystallization of gabbroic cumulates at a very slowly spreading ridge. *Journal of Volcanology and Geothermal Research* **110**, 191–233.

Natland, J. H. & Dick, H. J. B. (2001b). A brief narrative history of ODP Hole 735B. *Proceedings of the Ocean Drilling Program, 176 Scientific Results* **176**.

Natland, J. H., Dick, H. J. B., Miller, D. J. & Von Herzen, R. P. (2002). Stratigraphy and composition of gabbros drilled in ODP Hole 735B, SWIR: A synthesis of geochemical data. *Proceedings of the Ocean Drilling Program* **176**, 1–69.

Natland, J. H., Meyer, P. S., Dick, H. J. B. & Bloomer, S. H. (1991). Magmatic oxides and sulfides in gabbroic rocks from Hole 735B and the later development of the liquid line of descent. *Proceedings of the Ocean Drilling Program, Scientific Results* **118**, 75–111.

Navon, O. & Stopler, E. (1985). Geochemical consequences of melt percolation: the upper mantle as a chromatographic melt column. *journal of geology* **93**.

Neave, D. A., Namur, O., Shorttle, O. & Holtz, F. (2019). Magmatic evolution biases basaltic records of mantle chemistry towards melts from recycled sources. *Earth and Planetary Science Letters*. Elsevier B.V. **520**, 199–211.

Nguyen, D. K. *et al.* (2018). *Occurrence of felsic rocks in oceanic gabbros from iodp hole 1473a: Implications for evolved melt migration in the lower oceanic crust*. *Minerals*.

Nicolas, A. (1990). Melt extraction from mantle peridotites: hydrofracturing and porous flow, with consequences for oceanic ridge activity. In: Ryan, M. P. (ed.) *Magma transport and storage*. New York, 159–174.

Nicolas, A., Boudier, F. & Ildefonse, B. (1996). Variable crustal thickness in the Oman ophiolite: Implication for oceanic crust. *Journal of Geophysical Research: Solid Earth* **101**, 17941–17950.

Nicolas, A., Reuber, I. & Benn, K. (1988). A new magma chamber model based on structural studies in the Oman ophiolite. *Tectonophysics* **151**, 87–105.

Nielsen, R. L. & DeLong, S. E. (1992). A numerical approach to boundary layer fractionation: application to differentiation in natural magma systems. *Contributions to Mineralogy and Petrology* **110**, 355–369.

Nielsen, R. L., Ustunisik, G., Weinsteiger, A., Ill, T., Johnston, A. & Kent, A. J. R. (2017). Geochemistry, Geophysics, Geosystems. *Geochemistry Geophysics Geosystems* 3359–3384.

Niu, Y., Gilmore, T., Mackie, S., Greig, A. & Bach, W. (2002). Mineral chemistry, whole-rock compositions, and petrogenesis of Leg 176 gabbros: data and discussion. *Proceedings of the Ocean Drilling Program, 176 Scientific Results* **176**.

O

O'Hara, M. J. (1965). Primary magmas and the origin of basalts. *Scottish Journal of Geology* **1**, 19–40.

O'Hara, M. J. (1968a). Are Ocean Floor Basalts Primary Magma? *Nature* **220**, 683–686.

O'Hara, M. J. (1968b). The bearing of phase equilibria studies in synthetic and natural systems on the origin and evolution of basic and ultrabasic rocks. *Earth-Science Reviews*. Elsevier Publishing Company **4**, 69–133.

O'Hara, M. J. (1977). Geochemical evolution during fractional crystallisation of a periodically refilled magma chamber. *Nature* **266**, 503–507.

O'Hara, M. J. & Herzberg, C. (2002). Interpretation of trace element and isotope features of basalts: relevance of field relations, petrology, major element data, phase equilibria, and magma chamber modeling in basalt petrogenesis. *Geochimica et Cosmochimica Acta* **66**, 2167–2191.

O'Hara, M. J. & Mathews, R. E. (1981). Geochemical evolution in an advancing, periodically replenished, periodically tapped, continuously fractionated magma chamber. *Journal of the Geological Society* **138**, 237–277.

O'Neill, H. S. C. & Jenner, F. E. (2012). The global pattern of trace-element distributions in ocean floor basalts. *Nature*. Nature Publishing Group **491**, 698–704.

Okino, K., Matsuda, K., Christie, D. M., Nogi, Y. & Koizumi, K. I. (2004). Development of oceanic detachment and asymmetric spreading at the Australian-Antarctic Discordance. *Geochemistry, Geophysics, Geosystems* **5**.

Olive, J. A., Behn, M. D. & Tucholke, B. E. (2010). The structure of oceanic core complexes controlled by the depth distribution of magmaemplacement. *Nature Geoscience*. Nature Publishing Group **3**, 491–495.

Onsager, L. (1945). Theories and Problems of Liquid Diffusion. *Annals of the New York Academy of Sciences* **46**, 241–265.

Onuma, N., Higuchi, H., Wakita, H. & Nagasawa, H. (1968). Trace element partition between two pyroxenes and the host lava. *Earth and Planetary Science Letters* **5**, 47–51.

P

Parnell-Turner, R., Escartín, J., Olive, J. A., Smith, D. K. & Petersen, S. (2018). Genesis of corrugated fault surfaces by strain localization recorded at oceanic detachments. *Earth and Planetary Science Letters*. Elsevier B.V. **498**, 116–128.

Pearce, N. J. G., Perkins, W. T., Westgate, J. A., Gorton, M. P., Jackson, S. E., Neal, C. R. & Chenery, S. P. (1997). A compilation of new and published major and trace element data for NIST SRM 610 and NIST SRM 612 glass reference materials. *Geostandards Newsletter* **21**, 115–144.

Pec, M., Holtzman, B. K., Zimmerman, M. & Kohlstedt, D. L. (2015). Reaction infiltration instabilities in experiments on partially molten mantle rocks. *Geology* **43**, 575–578.

Pettigrew, T. L., Casey, J. F., Miller, D. J. & Al., E. (1999). Hammer drill site (1104 and 1106) and site 1105. *Proceedings of the Ocean Drilling Program* **179**.

Q

Quick, J. E. & Denlinger, R. P. (1993). Ductile deformation and the origin of layered gabbro in ophiolites. *Journal of Geophysical Research: Solid Earth* **98**, 14015–14027.

R

Rampone, E., Piccardo, G. B. & Hofmann, A. W. (2008). Multi-stage melt-rock interaction in the Mt. Maggiore (Corsica, France) ophiolitic peridotites: Microstructural and geochemical evidence. *Contributions to Mineralogy and Petrology* **156**, 453–475.

Reiners, P. W., Nelson, B. K. & Ghiorso, M. S. (1995). Assimilation of felsic crust by basaltic magma: Thermal limits and extents of crustal contamination of mantle-derived magmas. *Geology* **23**, 563–566.

Renna, M. R., Tribuzio, R. & Ottolini, L. (2016). New perspectives on the origin of olivine-rich troctolites and associated harrisites from the Ligurian ophiolites (Italy). *Journal of the Geological Society* **173**, 916–932.

Robinson, P. T. *et al.* (2000). Lower oceanic crust formed at an ultra-slow-spreading ridge: Ocean Drilling Program Hole 735B, Southwest Indian Ridge. *Geological Society of America* 75–86.

Rosenberg, C. L. (2001). Deformation of partially molten granite: A review and comparison of experimental and natural case studies. *International Journal of Earth Sciences* **90**, 60–76.

Ross, D. K. & Elthon, D. (1997). Cumulus and postcumulus crystallization in the oceanic crust: major- and trace-element geochemistry of Leg 153 gabbroic rocks. *Proceedings of the Ocean Drilling Program, Scientific Results* **153**, 333–353.

Ross, K. & Elthon, D. (1993). Cumulates from strongly depleted mid-ocean-ridge basalt. *Nature* **365**, 826–829.

Rubin, K. H. & Sinton, J. M. (2007). Inferences on mid-ocean ridge thermal and magmatic structure from MORB compositions. *Earth and Planetary Science Letters* **260**, 257–276.

Rubin, K. H., Sinton, J. M., MacLennan, J. & Hellebrand, E. (2009). Magmatic filtering of mantle compositions at mid-ocean-ridge volcanoes. *Nature Geoscience*. Nature Publishing Group **2**, 321–328.

Rubin, K. H., Smith, M. C., Bergmanis, E. C., Perfit, M. R., Sinton, J. M. & Batiza, R. (2001). Geochemical heterogeneity within mid-ocean ridge lava flows: Insights into eruption, emplacement and global variations in magma generation. *Earth and Planetary Science Letters* **188**, 349–367.

S

Sanfilippo, A., Dick, H. J. B., Marschall, H. R., Lissenberg, C. J. & Urann, B. (2019). Emplacement and High-Temperature Evolution of Gabbros of the 16.5°N Oceanic Core Complexes (Mid-Atlantic Ridge): Insights Into the Compositional Variability of the Lower Oceanic Crust. *Geochemistry, Geophysics, Geosystems* **20**, 46–66.

Sanfilippo, A., Morishita, T., Kumagai, H., Nakamura, K., Okino, K., Hara, K., Tamura, A. & Arai, S. (2015a). Hybrid troctolites from mid-ocean ridges: Inherited mantle in the lower crust. *Lithos* **232**, 124–130.

Sanfilippo, A. & Tribuzio, R. (2011). Melt transport and deformation history in a nonvolcanic ophiolitic section, northern Apennines, Italy: Implications for crustal accretion at slow

spreading settings. *Geochemistry, Geophysics, Geosystems* **12**, 1–34.

Sanfilippo, A. & Tribuzio, R. (2013). Building of the deepest crust at a fossil slow-spreading centre (Pineto gabbroic sequence, Alpine Jurassic ophiolites). *Contributions to Mineralogy and Petrology* **165**, 705–721.

Sanfilippo, A., Tribuzio, R., Ottolini, L. & Hamada, M. (2017). Water, lithium and trace element compositions of olivine from Lanzo South replacive mantle dunites (Western Alps): New constraints into melt migration processes at cold thermal regimes. *Geochimica et Cosmochimica Acta*. Elsevier Ltd **214**, 51–72.

Sanfilippo, A., Tribuzio, R. & Tiepolo, M. (2014). Mantle-crust interactions in the oceanic lithosphere: Constraints from minor and trace elements in olivine. *Geochimica et Cosmochimica Acta*. Elsevier Ltd **141**, 423–439.

Sanfilippo, A., Tribuzio, R., Tiepolo, M. & Berno, D. (2015b). Reactive flow as dominant evolution process in the lowermost oceanic crust: evidence from olivine of the Pineto ophiolite (Corsica). *Contributions to Mineralogy and Petrology*. Springer Berlin Heidelberg **170**, 1–12.

Satsukawa, T., Ildefonse, B., Mainprice, D., Morales, L. F. G., Michibayashi, K. & Barou, F. (2013). A database of plagioclase crystal preferred orientations (CPO) and microstructures-implications for CPO origin, strength, symmetry and seismic anisotropy in gabbroic rocks. *Solid Earth* **4**, 511–542.

Scaillet, B., Pichavant, M. & Roux, J. (1995). Experimental crystallization of leucogranite magmas. *Journal of Petrology* **36**, 663–705.

Seher, T., Crawford, W. C., Singh, S. C., Cannat, M., Combier, V. & Dusunur, D. (2010). Crustal velocity structure of the Lucky Strike segment of the Mid-Atlantic Ridge at 37°n from seismic refraction measurements. *Journal of Geophysical Research: Solid Earth* **115**, 1–28.

Shaw, D. M. (1970). Trace element fractionation during anatexis. *Geochimica et Cosmochimica Acta* **34**, 237–243.

Singh, S. C. *et al.* (2006). Discovery of a magma chamber and faults beneath a Mid-Atlantic Ridge hydrothermal field. *Nature* **442**, 1029–1032.

Singh, S. C., Collier, J. S., Harding, A. J., Kent, G. M. & Orcutt, J. A. (1999). Seismic evidence for a hydrothermal layer above the solid roof of the axial magma chamber at the southern East Pacific Rise. *Geology* 219–222.

Sinha, M. C., Navin, D. A., Macgregor, L. M., Constable, S., Peirce, C., White, A., Heinson, G. & Inglis, M. A. (1997). Evidence for accumulated melt beneath the slow-spreading Mid-Atlantic

Ridge. *Philosophical Transactions of the Royal Society A: Mathematical, Physical and Engineering Sciences* **355**, 233–253.

Sinton, J. M. & Detrick, R. S. (1992). Mid-ocean ridge magma chambers. *Journal of Geophysical Research* **97**, 197–216.

Sisson, T. W. & Grove, T. L. (1993). Experimental investigations of the role of H2O in calc-alkaline differentiation and subduction zone magmatism. *Contributions to Mineralogy and Petrology* **113**, 143–166.

Smith, D. K., Cann, J. R. & Escartín, J. (2006). Widespread active detachment faulting and core complex formation near 13°N on the Mid-Atlantic Ridge. *Nature* **442**, 440–443.

Spandler, C. & O'Neill, H. S. C. (2010). Diffusion and partition coefficients of minor and trace elements in San Carlos olivine at 1,300°C with some geochemical implications. *Contributions to Mineralogy and Petrology* **159**, 1–28.

Spandler, C., O'Neill, H. S. C. & Kamenetsky, V. S. (2007). Survival times of anomalous melt inclusions from element diffusion in olivine and chromite. *Nature* **447**, 303–306.

Stead, C. V., Tomlinson, E. L., McKenna, C. A. & Kamber, B. S. (2017). Rare earth element partitioning and subsolidus exchange behaviour in olivine. *Chemical Geology*. Elsevier B.V **475**, 1–13.

Suhr, G., Hellebrand, E., Johnson, K. & Brunelli, D. (2008). Stacked gabbro units and intervening mantle: A detailed look at a section of IODP Leg 305, Hole U1309D. *Geochemistry, Geophysics, Geosystems* **9**.

Sun, C., Graff, M. & Liang, Y. (2017). Trace element partitioning between plagioclase and silicate melt: The importance of temperature and plagioclase composition, with implications for terrestrial and lunar magmatism. *Geochimica et Cosmochimica Acta*. Elsevier Ltd **206**, 273–295.

Sun, C. & Liang, Y. (2013). The importance of crystal chemistry on REE partitioning between mantle minerals (garnet, clinopyroxene, orthopyroxene, and olivine) and basaltic melts. *Chemical Geology*. Elsevier B.V. **358**, 23–36.

Sun, C. & Liang, Y. (2014). An assessment of subsolidus re-equilibration on REE distribution among mantle minerals olivine, orthopyroxene, clinopyroxene and garnet in peridotites. *Chemical Geology*.

Szymanowski, D., Wotzlaw, J. F., Ellis, B. S., Bachmann, O., Guillong, M. & Von Quadt, A. (2017). Protracted near-solidus storage and pre-eruptive rejuvenation of large magma reservoirs. *Nature Geoscience* **10**, 777–782.

T

Taura, H., Yurimoto, H., Kurita, K. & Sueno, S. (1998). Pressure dependence on partition coefficients for trace elements between olivine and the coexisting melts. *Physics and Chemistry of Minerals* **25**, 469–484.

Tegner, C., Thy, P., Holness, M. B., Jakobsen, J. K. & Lesher, C. E. (2009). Differentiation and compaction in the Skaergaard intrusion. *Journal of Petrology* **50**, 813–840.

Tegner, C., Wilson, J. R. & Brooks, C. K. (1993). Intraplutonic Quench Zones in the Kap-Edvard-Holm-Layered-Gabbro-Complex, East Greenland. *Journal of Petrology* **34**, 681–710.

Thy, P. & Dilek, Y. (2000). Magmatic and tectonic controls on the evolution of oceanic magma chambers at slow-spreading ridges: Perspectives from ophiolitic and continental layered intrusions. *Special Paper 349: Ophiolites and oceanic crust: new insights from field studies and the Ocean Drilling Program* 87–104.

Toplis, M. J. & Carroll, M. R. (1995). An experimental study of the influence of oxygen fugacity on fe-ti oxide stability, phase relations, and mineral-melt equilibria in ferro-basaltic systems. *Journal of Petrology* **36**, 1137–1170.

Tribuzio, R., Tiepolo, M. & Thirlwall, M. F. (2000). Origin of titanian pargasite in gabbroic rocks from the Northern Apennine ophiolites (Italy): Insights into the late-magmatic evolution of a MOR-type intrusive sequence. *Earth and Planetary Science Letters* **176**, 281–293.

Tucholke, B. E., Behn, M. D., Buck, W. R. & Lin, J. (2008). Role of melt supply in oceanic detachment faulting and formation of megamullions. *Geology* **36**, 455–458.

Tucholke, B. E. & Lin, J. (1994). A geological model for the structure of rdige segments in slow spreading ocean crust. *Journal of Geophyscial Research* **99**, 11,937-11,958.

Tucholke, B. E., Lin, J. & Kleinrock, M. C. (1998). Megamullions and mullion structure defining oceanic metamorphic core complexes on the Mid-Atlantic Ridge. *Journal of Geophysical Research: Solid Earth* **103**, 9857–9866.

V

van Achterbergh, E., Ryan, C. G., Jackson, S. E. & Griffin, W. L. (2001). Data reduction software for LA-ICP-MS. *Laser Ablation ICP-MS in Earth Science*, 239–243.

Van Orman, J. A., Grove, T. L. & Shimizu, N. (2001). Rare earth element diffusion in diopside: Influence of temperature, pressure, and ionic radius, and an elastic model fordiffusion in

silicates. *Contributions to Mineralogy and Petrology* **141**, 687–703.

Vernières, J., Godard, M. & Bodinier, J.-L. (1997). A plate model for the simulation of trace element fractionation during partial melting and magma transport in the Earth's upper mantle. *Journal of Geophysical Research: Solid Earth* **102**, 24771–24784.

Vigneresse, J. L., Barbey, P. & Cuney, M. (1996). Rheological transitions during partial melting and crystallization with application to felsic magma segregation and transfer. *Journal of Petrology* **37**, 1579–1600.

Villiger, S., Müntener, O. & Ulmer, P. (2007a). Crystallization pressures of mid-ocean ridge basalts derived from major element variations of glasses from equilibrium and fractional crystallization experiments. *Journal of Geophysical Research: Solid Earth* **112**, 1–18.

Villiger, S., Ulmer, P. & Müntener, O. (2007b). Equilibrium and fractional crystallization experiments at 0.7 GPa; the effect of pressure on phase relations and liquid compositions of tholeiitic magmas. *Journal of Petrology* **48**, 159–184.

Villiger, S., Ulmer, P., Müntener, O. & Thompson, A. B. (2004). The liquid line of descent of anhydrous, mantle-derived, tholeiitic liquids by fractional and equilibrium crystallization - An experimental study at 1·0 GPa. *Journal of Petrology* **45**, 2369–2388.

W

Wang, C., Liang, Y., Xu, W. & Dygert, N. (2013). Effect of melt composition on basalt and peridotite interaction: Laboratory dissolution experiments with applications to mineral compositional variations in mantle xenoliths from the North China Craton. *Contributions to Mineralogy and Petrology* **166**, 1469–1488.

Wanless, V. D., Shaw, A. M., Behn, M. D., Soule, S. A., Escartín, J. & Hamelin, C. (2015). Magmatic plumbing at Lucky Strike volcano based on olivine-hosted melt inclusion compositions. *Geochemistry Geophysics Geosystems* 126–147.

White, W. M. & Klein, E. M. (2014). *Composition of the Oceanic Crust*. *Treatise on Geochemistry: Second Edition*. Elsevier Ltd.

Wood, B. J. & Blundy, J. D. (1997). A predictive model for rare earth element partitioning between clinopyroxene and anhydrous silicate melt. *Contributions to Mineralogy and Petrology* **129**, 166–181.

X

Xing, C. M., Wang, C. Y. & Tan, W. (2017). Disequilibrium growth of olivine in mafic magmas revealed by phosphorus zoning patterns of olivine from mafic–ultramafic intrusions. *Earth and Planetary Science Letters* **479**, 108–119.

Y

Yang, A. Y., Wang, C., Liang, Y. & Lissenberg, C. J. (2019). Reaction between MORB magma and lower oceanic crust: An experimental study. *Geochemistry Geophysics Geosystems*.

Zhang, X., Ganguly, J. & Ito, M. (2010). Ca-Mg diffusion in diopside: Tracer and chemical inter-diffusion coefficients. *Contributions to Mineralogy and Petrology* **159**, 175–186.

Appendix

Appendix

Appendix 1

(84 pages)

Appendix 2

(76 pages)

Appendix 3

(46 pages)

Appendix 4

(12 pages)

Appendix 1

Melt migration and interactions in the slow-spreading lower oceanic crust (CHAPTER 3)

- **Appendix 1.1**: Ferrando et al. (in prep.) - "Migration and segregation of melts through the lower oceanic crust recovered in the 800m-deep Hole U1473A (Atlantis Bank OCC, 57°E, Southwest Indian Ridge)"
  28 PAGES

- **Appendix 1.2**: A text file documenting details on
  - the EBSD and whole rock analyses analytical methods (*Text S1* and *S2*) and an estimation of the impact of the ablation spot size on the trace element measurements (*Text S3*)
  - additional figures illustrating examples of EBSD concatenated maps (*Figure S1*), examples of reactive textures found in the studied section (*Figure S2*), temperature-constrained models for fractional crystallization (*Figure S3*)
  - whole rock compositions (*Table S1*)
  - reference values used for data treatment and representation (*Table S4*) and input parameters of the numerical models applied to the studied system (*Table S5*)

  11 PAGES

- **Appendix 1.3**: minerals *in situ* analyses for major elements of olivine (6p), plagioclase (12p) and clinopyroxene (10p - *Table S2*), from IODP Hole U1473A (~590 mbsf).
  28 PAGES

- **Appendix 1.4**: minerals *in situ* analyses for trace elements of olivine (4p), plagioclase (6p) and clinopyroxene (7p - *Table S3*), from IODP Hole U1473A (~590 mbsf).
  17 PAGES

Appendix 1.1

Migration and segregation of melts through the lower oceanic crust recovered in the 800m-deep Hole U1473A (Atlantis Bank OCC, 57°E, Southwest Indian Ridge)

Carlotta Ferrando[a,b,*], Lyderic France[a], Marine Boulanger[a], Alessio Sanfilippo[b], Valentin Basch[b], Riccardo Tribuzio[b]

[a] CRPG, UMR 7358 CNRS - Université de Lorraine, 54501 Vandœuvre-lès-Nancy, France

[b] Dipartimento di Scienze della Terra e dell'Ambiente - Università degli Studi di Pavia, I-27100 Pavia, Italy

(in preparation; to be submitted to CMP)

*Corresponding Author
Carlotta Ferrando
PostDoc
Centre de Recherches Pétrographiques et Géochimiques (UMR 7358 - CNRS)
Université de Lorraine
15 Rue Notre Dame des Pauvres, 54500 Vandœuvre-lès-Nancy

Tel. Office: +33 (0) 3 83 59 42 42
Email: ferrando@crpg.cnrs-nancy.fr ou ottaferrando@gmail.com

ABSTRACT

Oceanic Core Complexes (OCCs) at slow- to ultraslow- spreading ridges provide a unique access to lower sections of the modern oceanic crust. In situ sampling of OCC reveal that the slow-spreading oceanic crust is constructed by a complex history of multiple and successive magma injections. In order to better quantify the processes that contribute to the building of ultraslow-spreading oceanic crust, we investigate olivine gabbro recovered during IODP Expedition 360 in the 810 m deep Hole U1473A at the Atlantis Bank (SWIR, 57°E).

U1473A olivine gabbros display intense grain size variability throughout the Hole from fine- to coarse-grained with sharp (rare) to irregular contacts (common). At irregular contacts, the grain boundaries of coarser grained plagioclase [Plg] and clinopyroxene [Cpx] are resorbed against the finer grained olivine gabbros, suggesting partial dissolution by a melt that crystallized the fine-grained material. Relicts of partially dissolved coarse-grained Plg are also embayed in fine-grained domains. Minerals chemical composition vary away from contacts between different grain sizes. Coarser grained minerals have more primitive composition (Mg#Olivine[Ol] = 72-74 mol%; Mg#Cpx = 80-86 mol%) compared to the finer grained (Mg#Ol = 71-72 mol%; Mg#Cpx = 78-80 mol%). Coarse-grained Cpx have primitive cores and more evolved rims, which are in chemical equilibrium with fine-grained. Cpx display significant enrichments in the most incompatible elements (from Zr = 10 ppm and Ce/Y = 0.2 in coarse-crystal cores, to Zr = 100 ppm and Ce/Y = 0.5 in fine-grained), associated to reactive porous flow. Fine-grained Cpx show the most significant enrichments in LREE, suggesting crystallization of segregated reacted melt.

Structural, microstructural and chemical constraints point to a multi-process origin of these grain size variations: (i) crystallization of primitive coarse-grained olivine gabbro mush, (ii) reactive porous flow driven by a MORB-type melt migrating and partially assimilating the pre-existing coarse-grained matrix, (iii) segregation of the reacted melt, which crystallizes the fine-grained olivine gabbro. The widespread occurrence of grain size variations in olivine gabbro from IODP Hole U1473A indicates that melt migration and reactive porous flow are primary and fundamental processes in the formation of the ultraslow-spreading oceanic crust.

TOT WORDS: 8000

TOT Fig.: 14

INTRODUCTION

-beneath ultra-slow ridges no magma chamber but crystal magma mush predominate

-melts produced in the mantle migrate through the mush reacting with crystal matrix; compaction lead to extraction of melt that erupt/segregate

-compaction seen in deformed coarse minerals

-during compaction/extraction melt react and can be modified

-Atlantis Bank is characterized by gabbroic sequence that was drilled during 3 IODP Expeditions: gabbroic sequence formed by multiple injections and different sills are identified by chemical trends. Gabbros show poikilitic cpx that partially dissolves plg + grain size variations that may indicate migration of melts --> we study gabbros from AB

-Most studies focused on single minerals (one cpx), here we took samples from the latest drilled Hole U1473A; samples come from different depths and record grain size variations

-we aim at understanding the origin of such grain size variations and provide new constraints on magma transport through the lower oceanic crust

GEOLOGICAL SETTING AND IODP HOLE U1473A

Fig. 1: Location AB

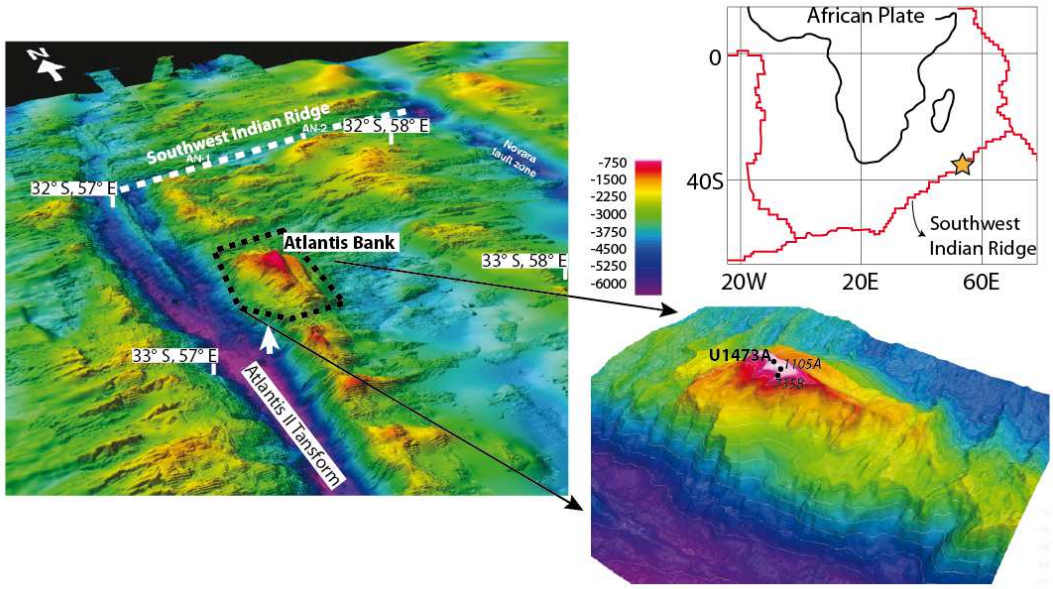

Fig.2: lithology and sample location

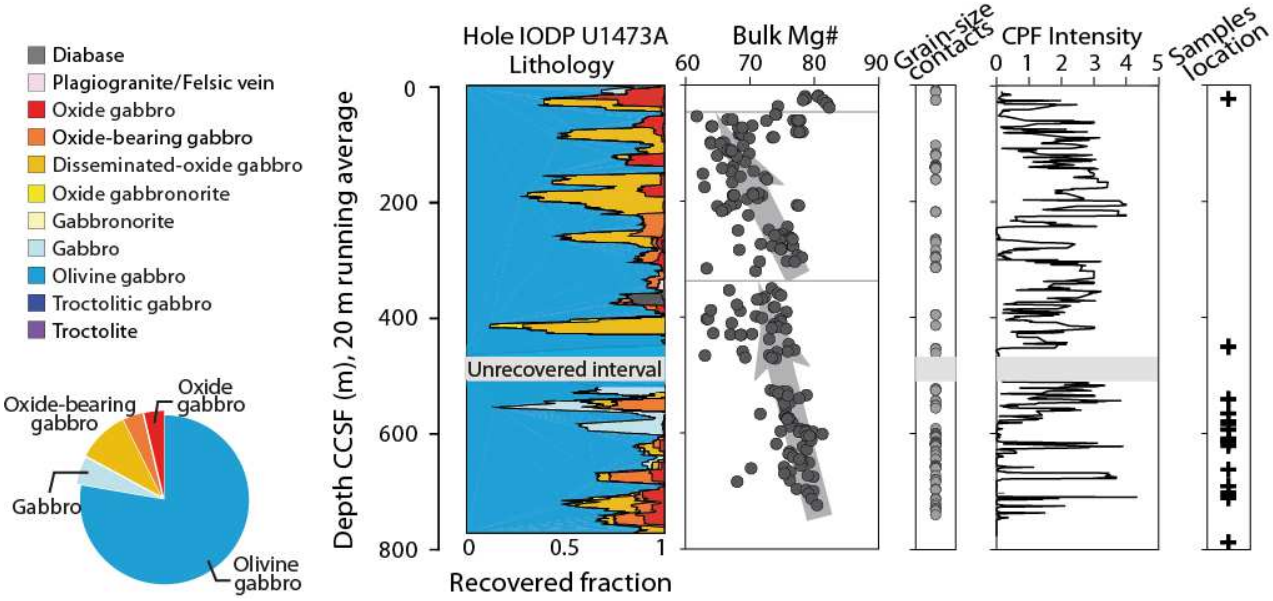

Atlantis Bank, located at 57° E along the ultraslow-spreading SWIR, is a 5 km-high local dome on the eastern wall of the Atlantis II Transform (Fig. 1). This raised dome is an Oceanic Core Complex (OCC) exposing massive gabbro on the seafloor interpreted to result from initial uplift by detachment faulting at the ridge-transform intersection, and subsequently offset during a period of change in the spreading direction (e.g., Dick et al. 1991b; MacLeod et al. 2000; Baines et al. 2008).

IODP Hole U1473A was drilled during IODP Expedition 360 (MacLeod et al. 2017) into the flat summit of the OCC, 2.2 km north northeast of 1508-m deep Hole 735B (ODP Leg 118 and IODP Leg 176, e.g., Dick et al. 1991a, 2000). This borehole penetrated 809 meters below sea floor (mbsf) recovering a section of lower oceanic crust (Fig. 2) mainly composed of olivine gabbros (76.5 %), less abundant disseminated-oxide gabbro (containing 1–2% oxide; 9.5% of recovery) and gabbro (*sensu stricto*; 5% of recovery), and minor oxide gabbro (>5% oxide; 7.5% of recovery) and felsic veins (1.5%). Two chemical discontinuities were identified downhole by Shipboard whole-rock analyses (at ~60–90 mbsf and 300 mbsf, MacLeod et al. 2017). They separate three principal chemical units where variations in Mg# (increase downhole; Fig. 2), Ca#, and Cr and Ni concentrations result from fractional crystallization of the basaltic melts supplied to the system, similar to chemical trends observed throughout the nearby ODP Hole 735B (Dick et al. 2000).

Grain-size of olivine gabbros is highly variable ranging from coarse- to medium- and fine-grained. Primary contacts between intervals of different grain-sizes are copious (121 contacts according to MacLeod et al., 2017; ~one contact every 3.9 m of recovered core) and were identified throughout Hole U1473A at different depths (Fig. 2). Grain-size variations are mostly irregular and patchy with variable thickness of fine- (or medium-) and coarse-grained intervals (MacLeod et al., 2017). Sparsely, the grain-size contacts are sharp, planar and subparallel boundaries that define local igneous layering (Dick et al., 2019; Boulanger et al., submitted). Grain-size contacts are most abundant in the deepest chemical unit (300-800 mbsf; Fig. 2).

Primary structures and textures are often overprinted by ubiquitous crystal-plastic deformation (CPF). The intensity of CPF decreases downhole: between 550 and 800 mbsf primary grain-size variations are well preserved (Fig. 2).

IRREGULAR GRAIN-SIZE VARIATIONS IN OLIVINE GABBROS

Fig. 3: grain size variation and example of thin section

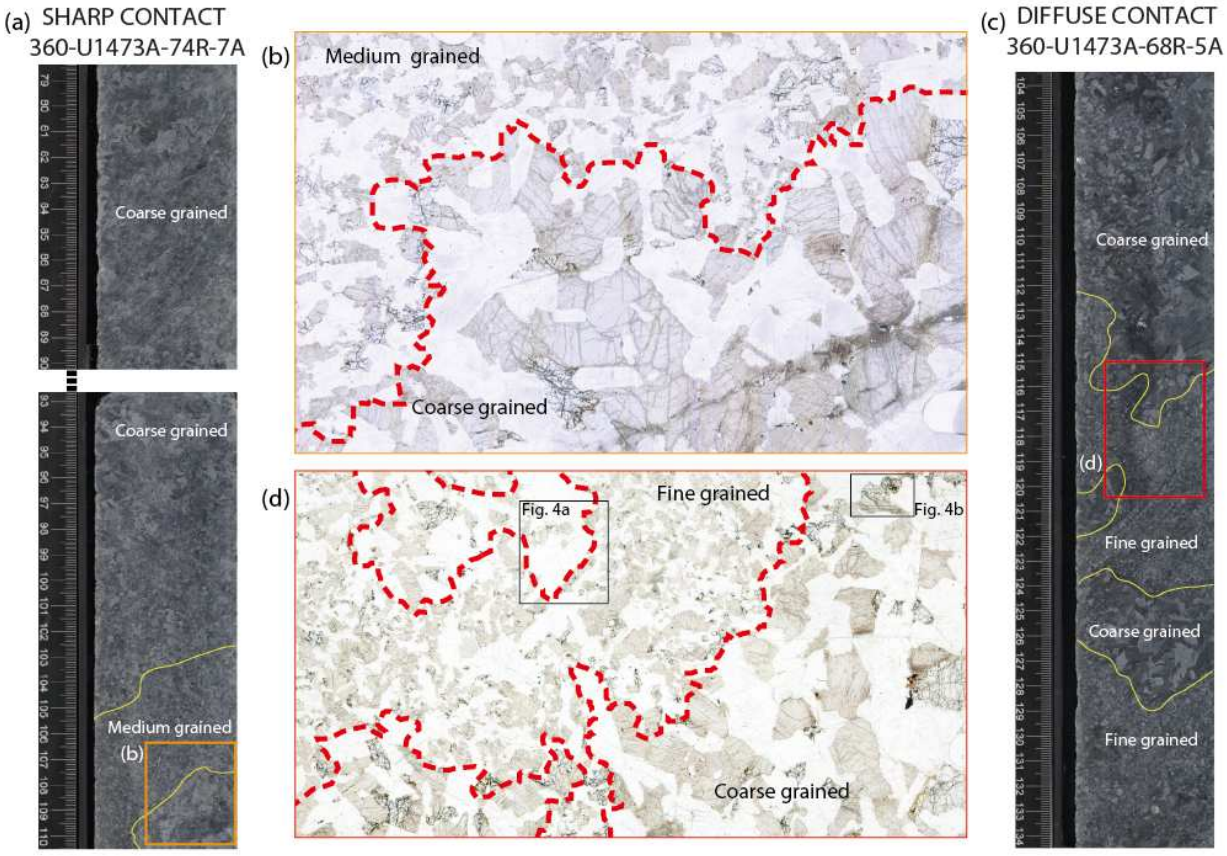

Irregular and patchy grain-size variations are distinguished from igneous layering by *(i)* the presence of rather small intervals of fine- to medium-grained olivine gabbro within coarse-grained thick intervals, or *(ii)* preserved patchy coarse-grained embayed in fine-grained olivine gabbro. Based on these structural occurrences, we distinguished two end-members of irregular grain-size variations in olivine gabbros.

Sharp grain-size contacts are characterized by variably thick (<20 cm) intervals of medium-grained olivine gabbro in contact with coarse-grained interval up to ~60 cm-thick (Fig. 3a). Fine-grained domains are minor and often absent. Contacts are sharp but wavy and lobate (Fig. 3b).

Diffuse grain-size contacts present medium- to fine-grained intervals up to 50 cm-thick, but locally reaching only 2-3 cm-thick, in contact with coarse-grained intervals. The coarse-grained olivine gabbro can be embayed within the finer-grained intervals in levels of less than 10 cm thickness (Fig. 3c). Coarse-grained intervals also appear as 1 to 2 cm-thick patchy levels. Sparsely single crystals of coarse-grained olivine, plagioclase or clinopyroxene are isolated within fine-grained olivine gabbro. The contacts are often difficult to delineate as the medium- to fine-grained minerals locally appear to crystallize between the coarser-grained minerals (Fig. 3d).

The downhole distribution of sharp and diffuse grain-size contacts is homogeneous (Fig. 2 and Table 1).

SAMPLING AND ANALYTICAL METHODS

We sampled medium- to fine- and coarse-grained olivine gabbros displaying irregular grain-size contacts at variable depths throughout Hole U1473A. A total of 28 samples were selected: 16 samples across the grain-size contacts and 6 couples (12 samples) within single grain-size intervals, each sampled at 2 to ~20 cm distance from their respective grain-size contact (Table 1). Overall, samples were selected in the least deformed interval of the hole and within the deepest chemical unit (Fig. 2). Exception was made for one sample from 24 mbsf (360-U1473A-4R-2W, 19-27) and a couple of fine- and coarse-grained olivine gabbros each sampled at ~5 cm distance from their contact located at 450 mbsf (360-U1473A-50R-1W, 73-80 and 360-U1473A-50R-1W, 92-97).

157 *In situ* mineral major and trace element analyses were performed across grain-size contacts
158 at increasing distance from the contact.

159 Minerals major element analyses were performed by Electron Probe Micro Analyser
160 (EPMA) at Geosciences Montpellier (University of Montpellier), using a CAMECA SX100
161 equipped with five wavelength-dispersive X-ray spectrometers (WDS). Analyses were done
162 with 20 kV accelerating potential, 10 nA beam current and 30 s counting times for all
163 elements measured. Natural minerals and synthetic oxides are used as standards.

164 Trace element compositions were determined at Geosciences Montpellier, using a Thermo
165 Scientific Element 2XR (eXtended Range) high resolution - Inductively Coupled Plasma
166 Mass Spectrometry (ICPMS). The ICP-MS is coupled with laser ablation (LA) system, a
167 Microlas (Geolas Q+) automated platform with a 193 nm Excimer Compex 102 laser from
168 LambdaPhysik. The laser energy density was set to 12–15 J cm^2 and repetition rate at 10 Hz
169 for analyses of olivine and 8 Hz for plagioclase and clinopyroxene. The laser spot size was set
170 to 77-85 μm. Data were reduced with the GLITTER software package (Van Achterbergh et
171 al., 2001), using the linear fit to ratio method. Concentrations were calibrated against the
172 NIST 612 rhyolitic glass using the values given in Pearce et al. (1997). ^{29}Si for olivine and
173 ^{43}Ca for plagioclase and clinopyroxenes were used for internal standardization relative to
174 EPMA data. The precision and accuracy of the LA-ICP-MS analyses together with the values
175 obtained for standard reference basalt BIR-1G are reported in Supplementary Material.

176

177 **TEXTURES OF OLIVINE GABBRO**

178 *Fig. 4: Textures*

179

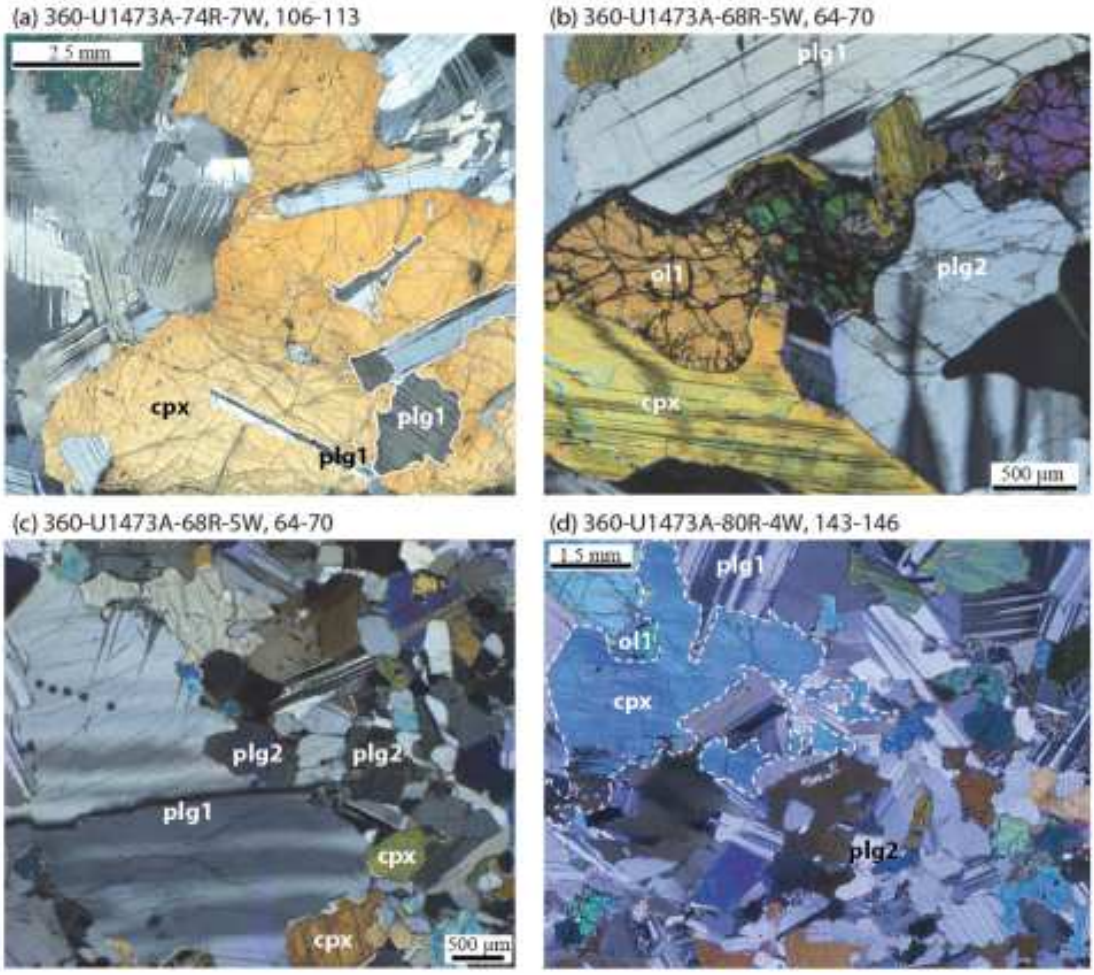

180

181 Olivine gabbros from Hole U1473A contain cumulus assemblages of subhedral to anhedral
182 olivine (0.2–1 mm in fine- to medium-grained and 2-8 mm in coarse-grained), euhedral and
183 subhedral to lath shaped plagioclase (0.2–1 mm in fine- to medium-grained and 1.5-10 mm in
184 coarse-grained), and poikilitic to interstitial clinopyroxene (0.2–1.5 mm in fine- to medium-
185 grained and 2-15 mm in coarse-grained) enclosing plagioclase ± olivine. These textural
186 features are at first order indicative of an olivine–plagioclase–clinopyroxene crystallization
187 sequence.

188 Textures of coarse-grained olivine gabbro are predominantly subophitic with subhedral
189 tabular plagioclase partly or fully enclosed within poikilitic clinopyroxene (Fig.4a).
190 Plagioclase chadacrysts and coarse-grained crystals display magmatic twins, and also show
191 mechanical twins and local undulose extinction indicative of incipient crystal plastic
192 deformation. They have lobate grain boundaries against clinopyroxene. Clinopyroxenes occur
193 as large oikocryst embaying plagioclase ± olivine and show little to no undulose extinction,

thus indicating that they are slightly deformed to undeformed. Olivines are deformed showing kink bands and display lobate contacts against adjacent interstitial clinopyroxene and finer-grained plagioclase (Fig. 4b).

Medium- to fine-grained olivine gabbros are characterized by granular textures (Fig. 4c). Plagioclases are euhedral to subhedral and show less deformation than coarse-grained plagioclase, as evidenced by the scarce occurrence of mechanical twins (Fig. 4c, 4d). Clinopyroxenes are mainly undeformed; they occur as subhedral crystals and locally as poikilitic crystals enclosing subhedral plagioclase (Fig. 4d) ± olivine. Olivines are subhedral and undeformed.

The textural relationships in coarse-grained olivine gabbro suggest that original subhedral coarse-grained olivine and plagioclase were partly corroded by a melt that concomitantly or subsequently crystallized the poikilitic clinopyroxene. Textures of medium- to fine-grained intervals indicate synchronous crystallization of olivine, plagioclase, and clinopyroxene in absence of dissolution-precipitation processes.

At grain-size contacts coarse-grained plagioclase displays lobate grain boundaries against medium- to fine-grained minerals (Fig. 4c). Poikilitic coarse-grained clinopyroxene can be found in optical continuity with fine-grained clinopyroxene (Fig. 4d). These textural features suggest that coarse-grained intervals were partially dissolved by a melt that crystallized the fine-grained olivine gabbro. Locally, clinopyroxene in fine-grained intervals within the first ~2 mm from the grain-size contact appears to grow on the rim of pre-existing coarse-grained clinopyroxene, while plagioclase always form new fine-grained nucleus. For these reasons, we identified two generations of plagioclase and olivine: we refer to coarse-grained partly corroded crystals as olivine 1 (ol 1) and plagioclase 1 (plg 1), and to fine-grained subhedral crystals as olivine 2 (ol 2) and plagioclase 2 (plg 2).

MINERAL COMPOSITIONS

Representative major, minor and trace element compositions of olivine, plagioclase and clinopyroxene are reported in Table 2. In the following, we first present the overall mineral compositions of medium- to fine-grained and coarse-grained crystals, and second we compare mineral compositions across sharp and diffuse irregular grain-size contacts.

224

225 **Major and minor elements**

226 *Fig. 5: Major ol, plg, cpx;*

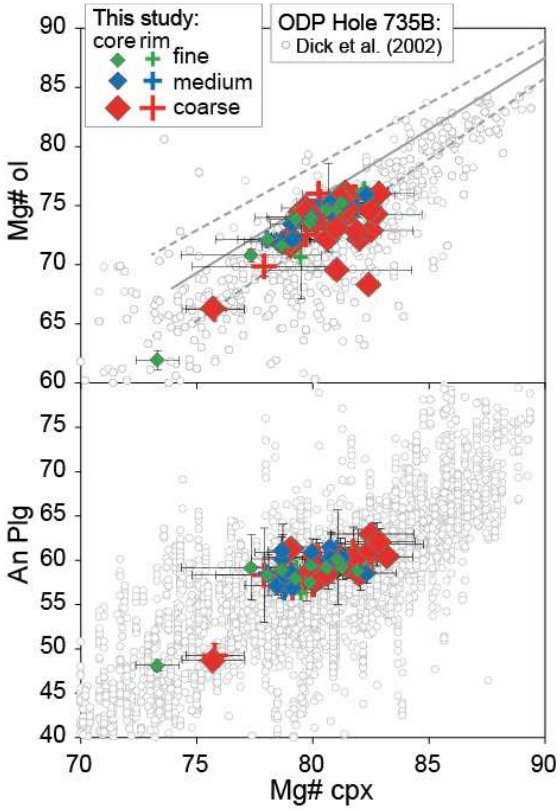

227

228

229 *Fig. 6: Mg# vs Cr203 and Ni in Cpx;*

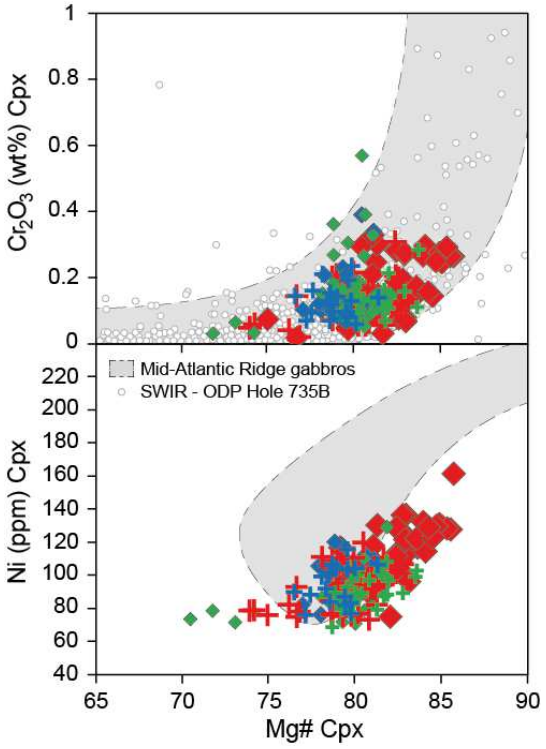

230

231

232 *Fig. 7: Mg# vs TiO2 in Cpx*

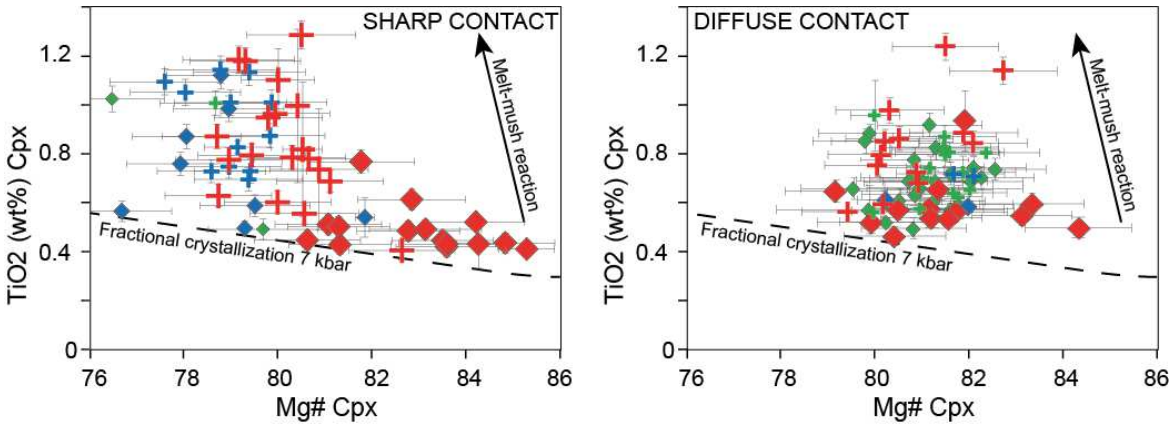

233

234

235 Minerals from olivine gabbros in Hole U1473A have major element compositions
236 comparable with compositions of olivine, plagioclase and clinopyroxene from ODP Hole
237 735B (Dick et al. 2002; Fig. 5).

238 Olivine crystals have no systematic core-to-rim chemical variations. Overall, they have
239 homogeneous compositions within single grain-size intervals, but vary with no systematic
240 correlations throughout the Hole. Coarse-grained olivine have Mg# ranging from 66 to 76

241 (Fig. 5), rather low compatible elements (Ni = 375-680 ppm, Co = 180-222 ppm) and high
242 moderately incompatible elements (Mn = 2314-3402 ppm, Zn = 84-155 ppm), and low Ca
243 contents (Ca = 165-563 ppm). Medium- to fine-grained olivine reach more evolved major and
244 minor element compositions (Mg# = 61-76, Mn = 2230-3710 ppm, Zn = 81-145 ppm, Ca =
245 105-482 ppm), but similar to slightly higher contents of compatible elements (Ni = 389-751
246 ppm, Co = 185-265 ppm) compared to coarse-grained olivine.

247 Plagioclase have overall homogeneous compositions with, at first order, no systematic
248 core-to-rim variations. An contents range from 55 to 68 (Fig. 5). Chemical heterogeneity
249 between medium- to fine-grained and coarse-grained plagioclase is exclusively observed at
250 the scale of a single sample, as detailed in the following section.

251 Clinopyroxene have the most heterogeneous composition among all phases in olivine
252 gabbros from Hole U1473A (Fig. 5, 6, 7). They have a wide compositional range of Mg# (72-
253 86), and Cr_2O_3 and Ni contents comparable with the lowermost values of clinopyroxene from
254 ODP Hole 735B (Dick et al. 2002) and from the oceanic crust at the Mid-Atlantic Ridge
255 (MAR; Ross and Elthon 1993, 1997; Coogan et al. 2000; Nonnotte et al. 2005; Lissenberg
256 and Dick 2008; Dick et al. 2010; Ferrando et al. 2018; Sanfilippo et al. 2018) (Fig. 6). Cores
257 of coarse-grained clinopyroxene have Mg# ranging between 79 and 86 (Fig. 5), Cr_2O_3 (Fig.
258 6), Al_2O_3 and TiO_2 contents in the ranges 0.03-0.33 wt%, 2.39-3.48 wt% and 0.39-0.72 wt%,
259 respectively. They have Ni contents varying from 75 to 161 ppm (Fig. 6). Rims of coarse-
260 grained clinopyroxene have lower Mg# (76-82), Al_2O_3 (1.91-3.32 wt%) and Ni contents (73-
261 140 ppm), similar Cr_2O_3 contents (0.05-0.31; Fig. 6) and higher TiO_2 contents (0.53-1.28
262 wt%) compared to their relative cores. At a given Mg# of olivine, cores of coarse-grained
263 clinopyroxene have Mg# higher compared to the predicted composition of clinopyroxene in
264 equilibrium with adjacent coarse-grained olivine (Fig. 5). Cores and rims of medium- to fine-
265 grained clinopyroxene share similar compositions that are characterized by Mg# varying in
266 the range 76-84, Cr_2O_3 contents between 0.05 and 0.57 wt% (Fig. 6), Al_2O_3 and TiO_2 contents
267 in the ranges 1.63-3.28 wt% and 0.43-1.12 wt%, respectively. Ni contents (68-129 ppm) are
268 overall lower than those in coarse-grained clinopyroxene. Compositions of fine-grained
269 clinopyroxenes are comparable to rims of coarse-grained clinopyroxene as shown in Figure 7a
270 for clinopyroxenes in a representative sample of sharp grain-size contact. Ni contents of
271 medium- to fine-grained clinopyroxene progressively decrease from cores (Ni = 71-129 ppm)
272 to their rims having the lowest Ni contents (Ni = 68-115 ppm).

Sample 360-U1473A-83R-4W, 118-124 cm displays the most evolved mineral compositions (Mg# ol = 61-66, An plg = 48-51, Mg# cpx = 72-76) among all minerals in olivine gabbro from this study (Fig. 5), testifying the local variability in mineral compositions throughout the hole.

Trace elements

Fig. 8: REE phases;

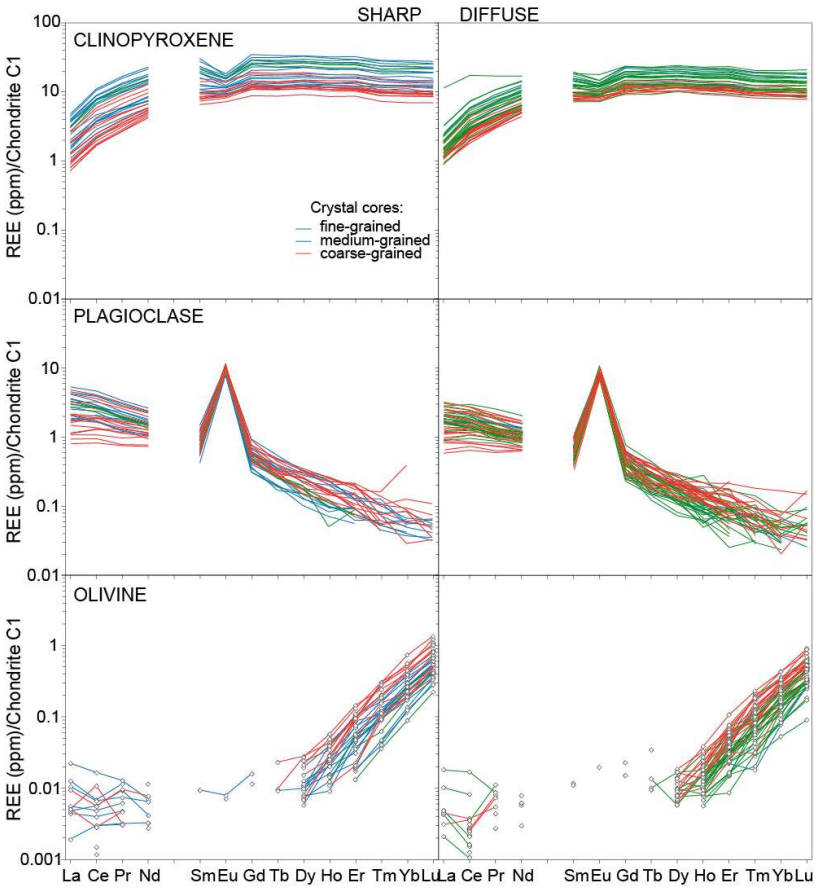
SHARP
DIFFUSE
CLINOPYROXENE
PLAGIOCLASE
OLIVINE
REE (ppm)/Chondrite C1
Crystal cores:
fine-grained
medium-grained
coarse-grained
La Ce Pr Nd Sm Eu Gd Tb Dy Ho Er Tm Yb Lu

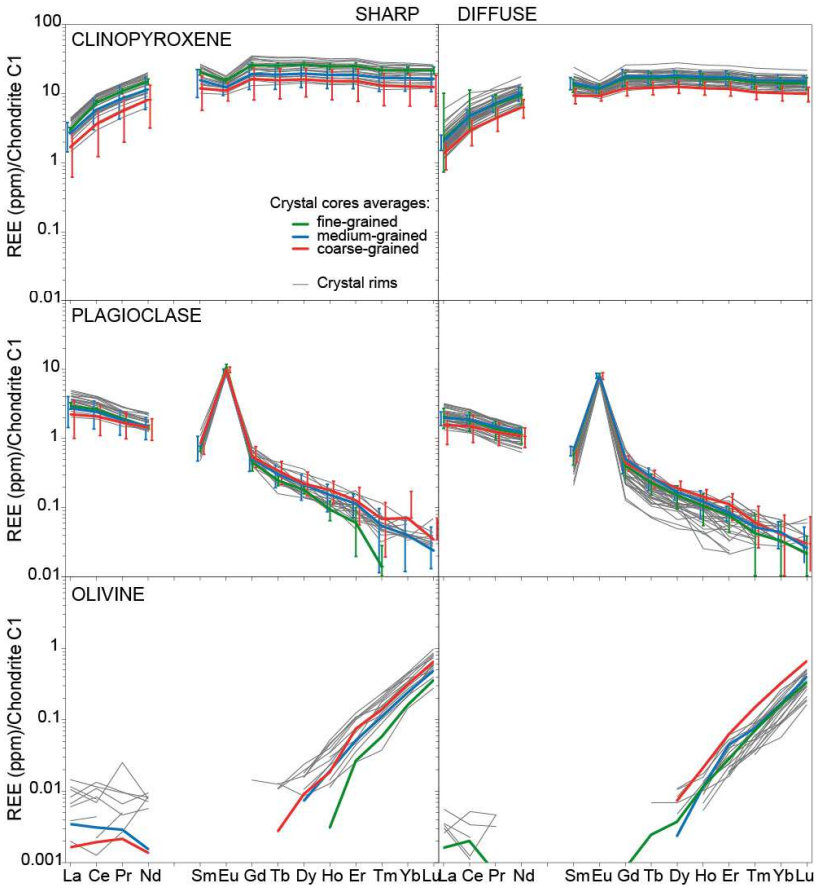
SHARP
DIFFUSE
CLINOPYROXENE
PLAGIOCLASE
OLIVINE
REE (ppm)/Chondrite C1
Crystal cores averages:
fine-grained
medium-grained
coarse-grained
Crystal rims
La Ce Pr Nd Sm Eu Gd Tb Dy Ho Er Tm Yb Lu

280

281 *Fig. 9: Spectra; Fig?? supplementary: Ce/Y versus Y/Cr dans les Cpx*

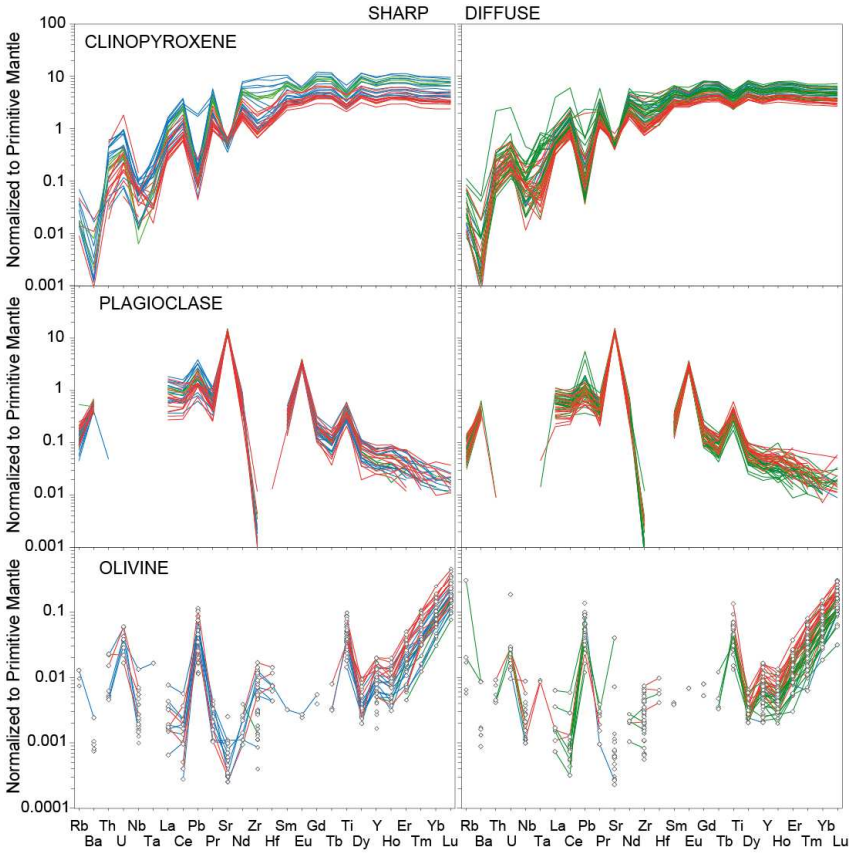

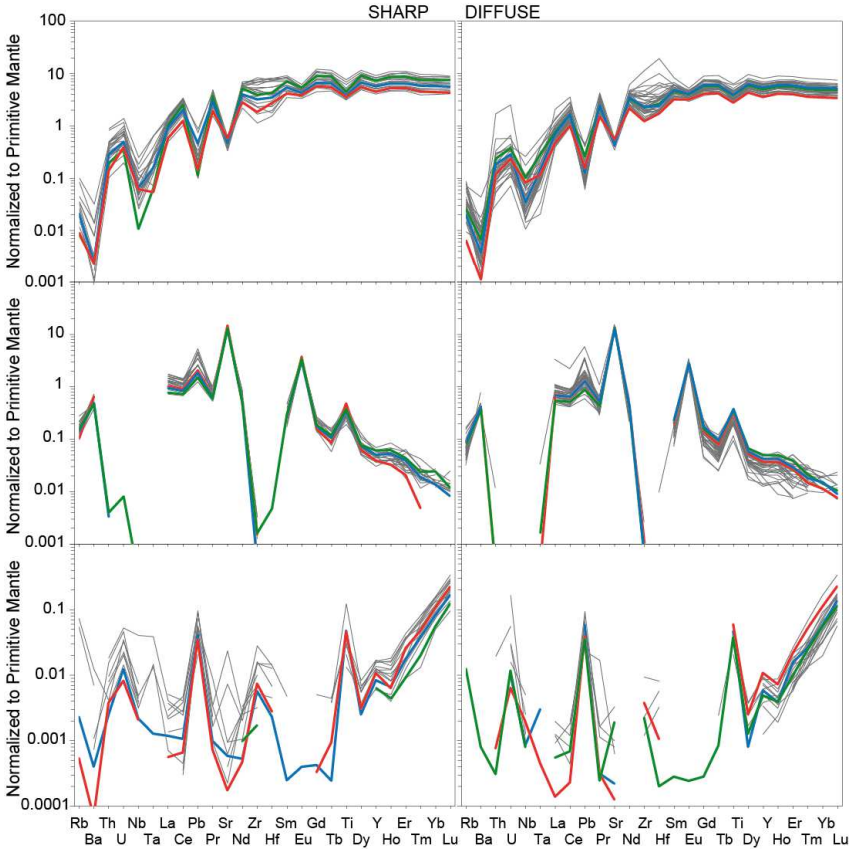

282

Olivines are on average depleted in lithophile trace elements. They have Yb_N (N=values normalized to chondrites, after Sun and McDonough, 1989) ranging from 0.02 to 0.72, coupled to strong depletion in M (medium) - REE (Dy_N = 0.005–0.028) and scattered L (light) - REE (Fig. 8). These REE contents result in strong normalized H (heavy) - REE to M-REE fractionations (Dy_N/Yb_N = 0.02–0.12, Fig. 8). Olivines display strong enrichments in the most incompatible High Field Strength Elements (HFSE), such as Ti and Zr-Hf (Zr = 0.003-0.31 ppm), relative to the neighboring trace elements (Fig. 9). These enrichments and the H-REE to M-REE fractionations of the studied olivines are similar to those observed in olivines from reactive gabbroic rocks from ophiolitic massifs (e.g., Dy_N/Yb_N = 0.04–0.15 and Zr = 0.01-0.43 ppm in olivines from Alpine ophiolites; Sanfilippo et al. 2014; Rampone et al. 2016; Basch et al. 2018) and oceanic crustal sequences (e.g., Dy_N/Yb_N = 0.04–0.11 and Zr = 0.02-0.20 ppm in olivines from Atlantis Massif OCC; Drouin et al. 2009; Ferrando et al. 2018). Cores of coarse-grained olivine have high trace elements composition (Yb_N = 0.14 - 0.72 and Zr = 0.01-0.19 ppm) compared to cores of medium- to fine-grained olivine (Yb_N = 0.02 - 0.39 and Zr = 0.003-0.14 ppm). All rims have trace element contents that fall within the compositional range of olivine cores, although showing the highest trace element contents (Yb_N = 0.04-0.54 and Zr = 0.004-0.31; Fig. 8, 9).

Plagioclases display strong Eu positive anomalies (Eu/Eu* = 10-31; Fig. 8). REE contents vary between coarse- and medium- to fine-grained plagioclase (Ce_N = 0.65-4.66). They are overall comparable with compositions of plagioclase in olivine gabbros from the Kane area (MAR (MARK area), Ce_N = 0.47-5.42; Coogan et al. 2000b,a). Trace element patterns show positive anomalies in Sr and Ti relative to neighboring elements, and negative anomalies in Zr (Fig. 9). Cores of coarse-grained plagioclase have flat L-REE (Ce_N = 0.65-4.11 and Ce_N/Nd_N = 1.0-1.6) and rather high M-REE (Sm_N = 0.34-1.27). Cores of medium- to fine-grained plagioclase have higher L-REE (Ce_N = 0.96-4.66 and Ce_N/Nd_N = 1.13-2.18) compared to coarse-grained crystals and show variable M-REE to the lowest values among all plagioclases from this study (Sm_N = 0.26-1.46). The increase of L-REE coupled with the decrease of M-REE lead to progressive stronger REE fractionations from coarse- (Ce_N/Sm_N = 1.28-3.64) to finer-grained plagioclase (Ce_N/Sm_N = 1.32-5.48). Rims of plagioclase display the strongest L-REE to M-REE fractionations (Ce_N/Sm_N = 2.37-9.80; Fig. 8).

Clinopyroxenes have flat patterns for M-REE and H-REE (Yb_N = 6.93-34.35), and variable depletion in L-REE (Fig. 8). Their REE contents are similar, but reach more evolved compositions compared to the composition of clinopyroxenes in olivine gabbros from the

316 MARK area (Yb_N = 7.22-10.85; Coogan et al. 2000b,a). All clinopyroxenes are distinguished
317 by moderate negative anomalies in Ti, while contents of Zr-Hf are significantly variable from
318 depleted to enriched relative to neighbor trace elements (Zr_N/Nd_N = 0.42-1.85). Strong
319 fractionation relative to neighboring elements is also observed for Sr, Pb and Ba on extended
320 trace element patterns (Fig. 9). Cores of coarse-grained have low trace elements contents with
321 Yb_N, Ce_N, Y_N and Zr ranging in the intervals 6.93-17.08, 1.67-6.44, 7.47-17.35 and 7.39-
322 40.29 ppm, respectively. They have strong fractionations in L-REE to Y (Ce_N/Y_N = 0.18-0.43)
323 and no to little Eu negative anomalies (Eu/Eu* = 0.81-1.02). The depletion in Zr contents
324 result in Zr_N/Nd_N ranging between 0.42 and 0.89. Cores of medium- to fine-grained
325 clinopyroxenes are characterized by higher trace elements contents (Yb_N = 8.60-28.38, Ce_N =
326 2.27-17.42, Y_N = 8.06-28.35 and Zr = 9.83-101.07 ppm), lower L-REE to Y fractionations
327 (Ce_N/Y_N = 0.23-0.87) compared to coarse-grained crystals (Fig. 8, 9). The high Zr contents
328 lead to higher values of Zr_N/Nd_N that reach positive anomalies (0.42-1.17). Their Eu negative
329 anomaly is pronounced (Eu/Eu* = 0.55-0.84). All rims have compositions similar to medium-
330 to fine-grained crystal cores, reaching the highest trace element contents. They have almost
331 flat REE and most pronounced negative Eu anomaly (Fig. 8, 9).

332

333 **Mineral compositions across contacts**

334 *Fig. 10: Ol, Plg, Cpx compositions across contact*

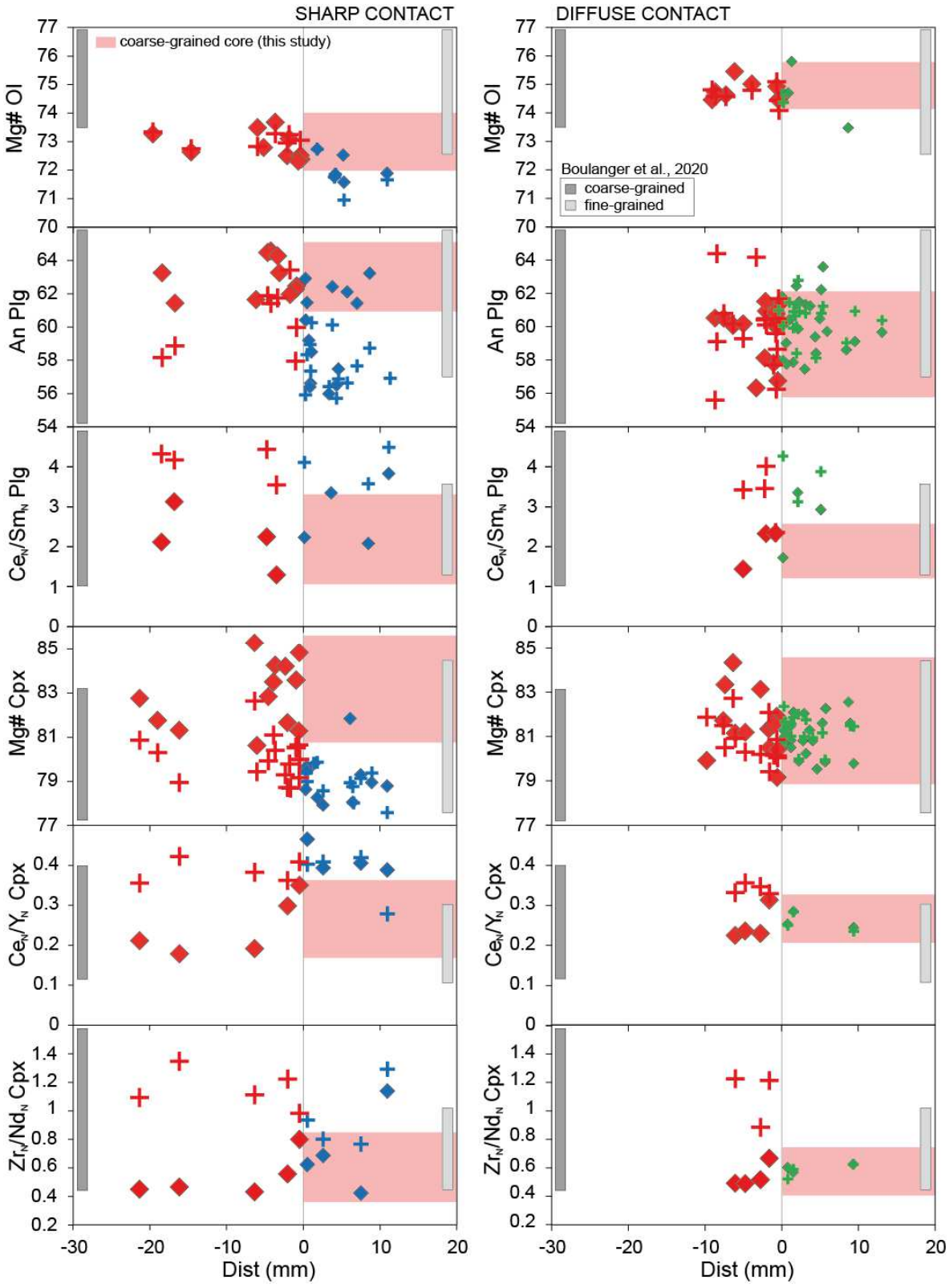

335

336

337

338

EQUILIBRIUM TEMPERATURES

Fig. Supplementary: Plot of Kd to calculate T; example of two samples of diffusive/ fine-coarse and sharp/fine-coarse

Equilibrium temperatures between the mineral pairs plagioclase-clinopyroxene and olivine-clinopyroxene were obtained to investigate temperatures of magmatic processes recorded in olivine gabbros from Hole U1473A. Temperatures were determined using two geothermometers based on partitioning of REE between the two mineral pairs considered. The geothermometer from Sun et al. (2017) was used for plagioclase-clinopyroxene, while the geothermometer from Sun and Liang (2014) for olivine-clinopyroxene.

Equilibrium temperatures between plagioclase and clinopyroxene range in the interval 1050-1160°C with no systematic variations observed between temperatures calculated using compositions of crystals cores and those using crystals rims. Also, plagioclase-clinopyroxene equilibrium temperatures of coarse-grained intervals overlap with temperatures of medium- to fine-grained intervals. The highest equilibrium temperatures correspond to crystallization temperatures of the two mineral phases (~1150°C) and may represent temperatures at which melt-rock interactions occurred (see in the discussion). The lowest temperatures likely mark the closure of the system.

Equilibrium temperatures between olivine and clinopyroxene are overall lower than 1000°C, thus suggesting chemical re-equilibration of olivine under subsolidus conditions (Sun and Liang 2014). The latter is further supported by the H-REE to M-REE strong fractionations and the low Ca contents in olivine from this study (e.g., Coogan et al. 2005; Sun and Liang 2014). Thus, equilibrium temperatures and the geochemical signature of olivine in the olivine gabbros from Hole U1473A indicate that the primary magmatic composition of olivine was modified during cooling of the crustal sequence. For this reason, only plagioclase and clinopyroxene compositions were considered in the discussion of our study.

DISCUSSION

Reactive melt migration recorded in olivine gabbro

Fig. 11: Equilibrium melts

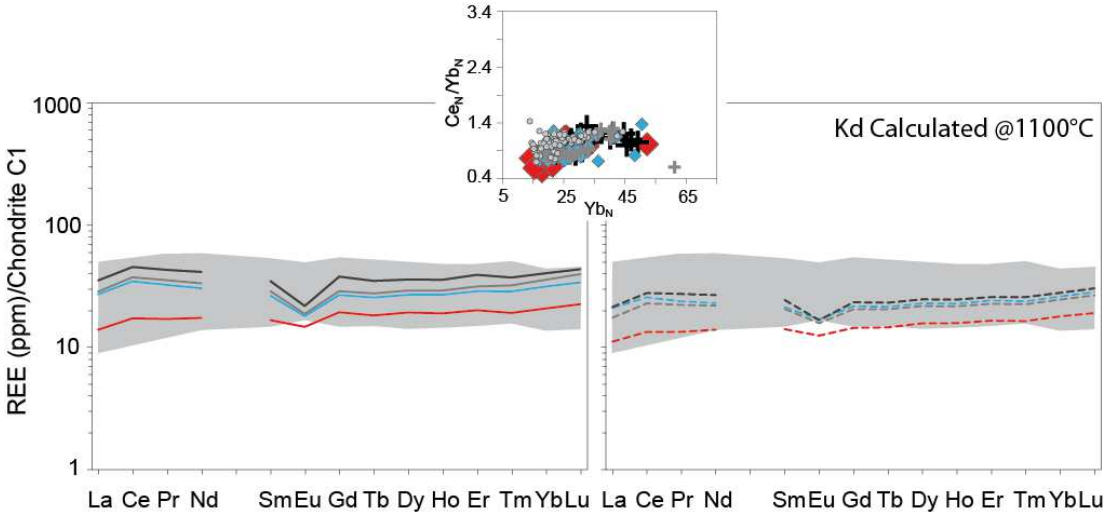

Textures of olivine gabbros from Hole U1473A and major compositions of rock-forming minerals, at first order, appear to form during a process of fractional crystallization responsible for the typical olivine–plagioclase–clinopyroxene crystallization sequence at low pressure conditions (e.g., Villiger et al. 2007). Major and trace elements composition of cores of coarse-grained crystals indicate that coarse-grained intervals formed after crystallization of an N-MORB in equilibrium with the primitive end-member compositions of MORBs from the SWIR (Coogan et al. 2004). This N-MORB has on average Mg# ~62 and low trace element contents (Yb_N = 15.6; Fig. 11). Conversely, cores of medium- to fine- grained crystals and all rims are in equilibrium with a more evolved melt with Mg# ~53 and high trace elements contents (average evolved MORB from the SWIR: Yb_N = 25.05; Coogan et al. 2004).

These compositions may support the formation of olivine gabbros from Hole U1473A after continuous fractional crystallization leading to progressive differentiation of an N-MORB from coarse-grained intervals to rims and finer-grained olivine gabbros. However, the occurrence of poikilitic clinopyroxene embaying corroded plagioclase ± olivine and the strong enrichments in the most incompatible elements toward the crystal rims, such as Zr in clinopyroxene, point to melt-rock interactions widely described in the oceanic crust (e.g., Coogan et al. 2000b; Gao et al. 2007; Lissenberg and Dick 2008; Suhr et al. 2008; Drouin et al. 2009; Lissenberg and MacLeod 2016; Ferrando et al. 2018; Lissenberg et al. 2019; Boulanger et al., submitted). In the following, we provide evidences of such reactive process and support our discussion with geochemical modelling.

Textural and geochemical evidences

The corroded grain boundaries of coarse-grained olivine and plagioclase against poikilitic clinopyroxene indicate that a pre-existing crystal matrix of troctolitic composition (olivine + plagioclase) was partially dissolved by a melt that crystallized clinopyroxene. Disequilibrium textures are coupled with high Mg# in cores of coarse-grained clinopyroxene documenting olivine partial dissolution (e.g., Coogan et al. 2000b; Lissenberg and Dick 2008; Drouin et al. 2009; Sanfilippo et al. 2013, 2015; Ferrando et al. 2018; Basch et al. 2019). Moreover, the progressively stronger enrichments in Zr and Ti contents from cores to rims of coarse-grained clinopyroxene cannot be explained by a simple fractional crystallization process. Such compositions have been reproduced experimentally after reaction between a troctolitic crystal matrix and a percolating primitive MORB (i.e., Ti contents, Yang et al. 2019), and they are documented in gabbroic oceanic crustal series as resulting from melt-rock interactions in a porous flow process (e.g., Gao et al. 2007; Lissenberg et al. 2013; Lissenberg and MacLeod 2016; Basch et al. 2018; Ferrando et al. 2018). The absence of Eu anomalies in cores of coarse-grained clinopyroxene indicate that they likely crystallized prior (or slightly prior) to plagioclase, thus representing the first products of melt-rock interactions in olivine gabbros from Hole U1473A.

The finer-grained olivine gabbro likely crystallized after the formation of the coarse-grained matrix, as evidenced by the occurrence of coarse-grained plagioclase with corroded grain boundaries at contact with finer-grained minerals. This textural feature also suggests that the parental melt of finer-grained olivine gabbro was in chemical disequilibrium with the coarse-grained troctolitic matrix. In sharp irregular contacts, where chemical heterogeneity between grain-size intervals is best preserved, the finer-grained crystals have compositions similar to those of rims of coarse-grained minerals. Finer-grained clinopyroxene and rims of coarse-grained clinopyroxene share similar enrichments in the most incompatible elements, thus indicating that the finer-grained olivine gabbro formed after the reacted and modified MORB within the coarse-grained intervals. Yet, L-REE to M-REE fractionations in plagioclase, which are negligible in cores of coarse-grained crystals, are instead significant in finer-grained crystals. The decrease in M-REE and H-REE in plagioclase could be related to subsolidus re-equilibration during cooling of the system (e.g., Coogan and O'Hara 2015) that is favored in fine-grained crystals. However, strong Ce_N/Sm_N fractionations were observed in reacted plagioclase from a single sample of olivine gabbro from Hole U1473A (parallel study of reactive porous flow by Sanfilippo et al., submitted). Thus, alternatively, plagioclase in

finer-grained olivine gabbro could have crystallized after a reacted and modified MORB. The increase in Ce_N/Sm_N fractionations is strictly related to reaction in a progressively cooling system, which is in turns controlled by the composition of the migrating melt to evolved and cooler compositions.

Textures and mineral compositions point to disequilibrium and reaction of a pre-existing troctolitic matrix with a MORB-type melt. The reactive porous flow process leads to the progressive differentiation and trace elements over-enrichments in the migrating melt, as testified by the systematic evolution of mineral major and trace element compositions from more primitive cores of coarse-grained crystals to more evolved rims of coarse-grained crystals and the finer-grained olivine gabbro. The composition of the percolating melt can be estimated by the first products of crystallization and, therefore, from the composition of cores of coarse-grained clinopyroxene that are in equilibrium with primitive MORBs from the SWIR (Coogan et al., 2004; Fig. 11).

In order to test whether the observed selective enrichments in the most incompatible elements in clinopyroxene and the geochemical signature of plagioclase result from melt-rock interactions in the studied olivine gabbros, we performed Assimilation Fractional Crystallization (AFC) models (using the equation of DePaolo 1981). Two reactions were modeled: *(i)* assimilation of the troctolitic crystal matrix and crystallization of olivine gabbro (AFC1), and *(ii)* assimilation of olivine gabbro resulting from the previous AFC1 and crystallization of gabbro during the closure of the system (AFC2).

Geochemical modelling: AFC of a primitive N-MORB through a troctolitic mush

Fig. 12: AFC Model

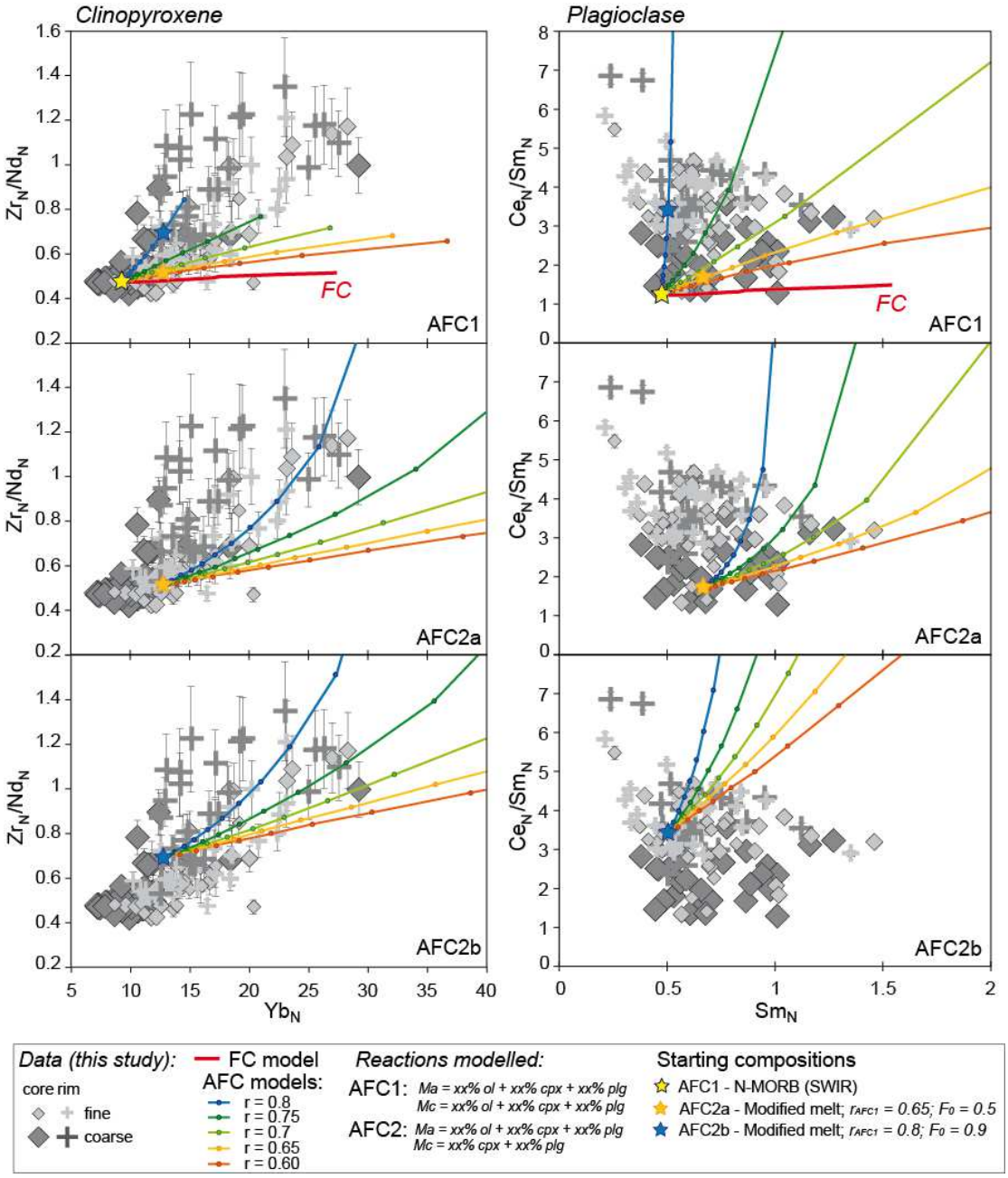

448

449 The melt-rock interaction process described above was modelled assuming the following
450 reaction (AFC1):

451 38 vol% ol_1 + 62 vol% plg_1 + $melt_1$ = 10 vol% ol_2 + 60 vol% plg_2 + 30 vol% cpx + $melt_2$

452 where ol_1 (olivine) and plg_1 (plagioclase) constitute the pre-existing troctolitic crystal matrix
453 (Ma -assimilated mass), $melt_1$ is the migrating melt before reactive crystallization, and ol_2 +
454 plg_2 + cpx (clinopyroxene) are the olivine gabbro-forming minerals (Mc - crystallized mass)
455 in equilibrium with the reacted and modified $melt_2$.

456 The occurrence of large poikilitic clinopyroxene in the coarse-grained intervals suggests
457 that the percolated matrix was a crystal mush with more than 30 vol% occupied by melt
458 between heterogeneously distributed crystals of plagioclase and olivine (e.g., Coogan et al.,
459 2000b). Starting modal and bulk composition of the assimilated troctolitic crystal matrix was
460 determined after fractional crystallization of primitive N-MORB (~20% fractionation; starting
461 melt from Coogan et al., 2004). The composition of $melt_1$ corresponds to the computed melt
462 in equilibrium with the average REE composition of clinopyroxene cores in U1473A coarse-
463 grained olivine gabbros.

464 The results of the AFC1 modelling are reported in Figure 12a,b in terms of Yb_N vs
465 Zr_N/Nd_N in clinopyroxene and Sm_N vs Ce_N/Sm_N in plagioclase. For comparison, the trend of
466 fractional crystallization is also showed and clearly demonstrates that it fails to explain the
467 strong enrichments in incompatible elements concentrations of the analyzed phases.
468 Computed trends of AFC1 show the compositions of clinopyroxene and plagioclase in
469 equilibrium with modified melt during the reactive process ($melt_2$) at decreasing melt mass (F
470 = 0.95–0.05). We set five different Ma/Mc (r values in the model, r = 0.6-0.8) representing
471 different extents of the reactive process. These AFC models succeed in reproducing most of
472 the range of geochemical compositions of plagioclase and clinopyroxene in olivine gabbros
473 from Hole U1473A. The models also show that Zr_N/Nd_N fractionations in clinopyroxene and
474 Ce_N/Sm_N in plagioclase increase progressively during the reaction and explain the observed
475 trace element enrichments from coarse- to finer-grained minerals.

476 In-sample trace elements composition across single grain-size contacts were considered
477 separately to understand the significance of different Ma/Mc of the AFC1 models.
478 Compositions of single samples fall along a single trend of Ma/Mc (Fig. Supplementary
479 Material). Because samples were selected at different depths throughout the hole, the AFC1
480 models indicate that melt-rock interactions have local different extents of troctolite crystal
481 mush assimilation. This is likely due to variable porosity and melt vol% of the pre-existing
482 crystal mush.

483 It should be noted that our AFC1 fails to reproduce the most Zr enriched concentrations in
484 rims of coarse-grained clinopyroxene and some medium- to fine-grained clinopyroxene. We
485 infer that these compositions are the result of the decrease of temperature during the closure
486 of the system as be detailed in the following.

487

Closure of the system: crystallization of crystal rims and finer-grained gabbro

Fig. 13: YbvsNi in Cpx

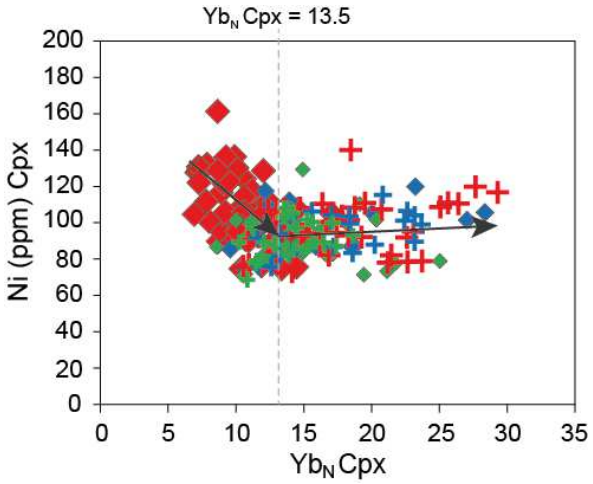

Significant enrichments in highly incompatible elements characterize the rims of coarse-grained and medium- to fine-grained clinopyroxene. These enrichments are coupled with constant Ni at decreasing Mg# and increasing REE in clinopyroxene, as opposite to cores of coarse-grained crystals that show decreasing Ni as REE increase (Fig. 13). Because Ni partitioning is significantly higher in olivine than in clinopyroxene ($^{ol/melt}Kd_{Ni} \approx 10$ and $^{cpx/melt}Kd_{Ni} \approx 3.8$; Le Roux et al. 2011), variations of Ni contents in clinopyroxene can be used to trace crystallization of olivine. Concomitant crystallization of olivine and clinopyroxene lead to decreasing Ni in clinopyroxene as magmatic crystallization proceeds, as observed in cores of coarse-grained clinopyroxene (Fig. 13). When olivine crystallization ceases, Ni concentration in the melt cannot be preferentially controlled by olivine and thus Ni concentrations in clinopyroxene do not vary or slightly increase during crystallization. Also, during melt crystallization and AFC processes, melt differentiation occurs at decreasing temperature. At temperatures 1150°-1200°C olivine ceases to crystallize and only crystals of plagioclase and pyroxenes (±ilmenite) form (e.g., Villiger et al. 2007). In light of this, constant Ni contents in the rims of analyzed clinopyroxene could result from the crystallization of the reacted and evolved melt undersaturated in olivine.

Some medium- to fine- grained clinopyroxene and most clinopyroxene rims precipitated from a common melt that partially dissolved the olivine gabbro and crystallize plagioclase and clinopyroxene. To test this hypothesis, we performed AFC models to reproduce the geochemical evolution of clinopyroxene and plagioclase in the reaction (AFC2):

511 $ol_2 + plg_2 + cpx + melt_2 = plg_3 + cpx_2 + melt_3$

512 where $ol_2 + plg_2 + cpx$ constitute the olivine gabbro formed during AFC1, $plg_3 + cpx_2$ are
513 crystal rims of plagioclase and clinopyroxene, respectively, precipitated from the reacted
514 $melt_3$.

515 We considered the variation in Ni vs Yb_N contents in clinopyroxene to constrain the
516 change in olivine saturation in the melt, and thus to pinpoint the melt composition at which
517 olivine ceases to crystallize. Ni in clinopyroxene remains relatively constant from $Yb_N = 13.5$
518 (Fig. 13) as Yb_N increases. The latter is in equilibrium with a melt having Yb_N = 23.5-23.8.
519 We selected this melt composition and the corresponding bulk rock composition from the
520 output of AFC1. These starting compositions were chosen from two AFC1 models:

521 *(i) AFC2a* uses bulk rock and melt compositions from AFC1 run with r = 0.65; $melt_2$ with
522 Yb_N =23.5-23.8 was reproduced after 45% crystallization of N-MORB during reaction 1;

523 *(ii) AFC2b* uses bulk rock and melt compositions from AFC1 run with r = 0.8; $melt_2$ with Yb_N
524 =23.5-23.8 was reproduced after 80% crystallization of N-MORB during reaction 1.

525 The results of the AFC2 models are reported in Figure 12c,d,e,f. The compositions of
526 plagioclase and clinopyroxene rims are reproduced by AFC2 at Ma/Mc relatively high. The
527 results of these models indicate that enrichments in the most incompatible elements can be
528 recorded in precipitated phases at decreasing temperature and porosity of the system, thus
529 suggesting the last melt crystallization and closure of the system.

530

531 **Formation of fine grained olivine gabbro**

532 **Temporal reconstruction from migration to segregation of melts**

533 *Fig. 14: sketch*

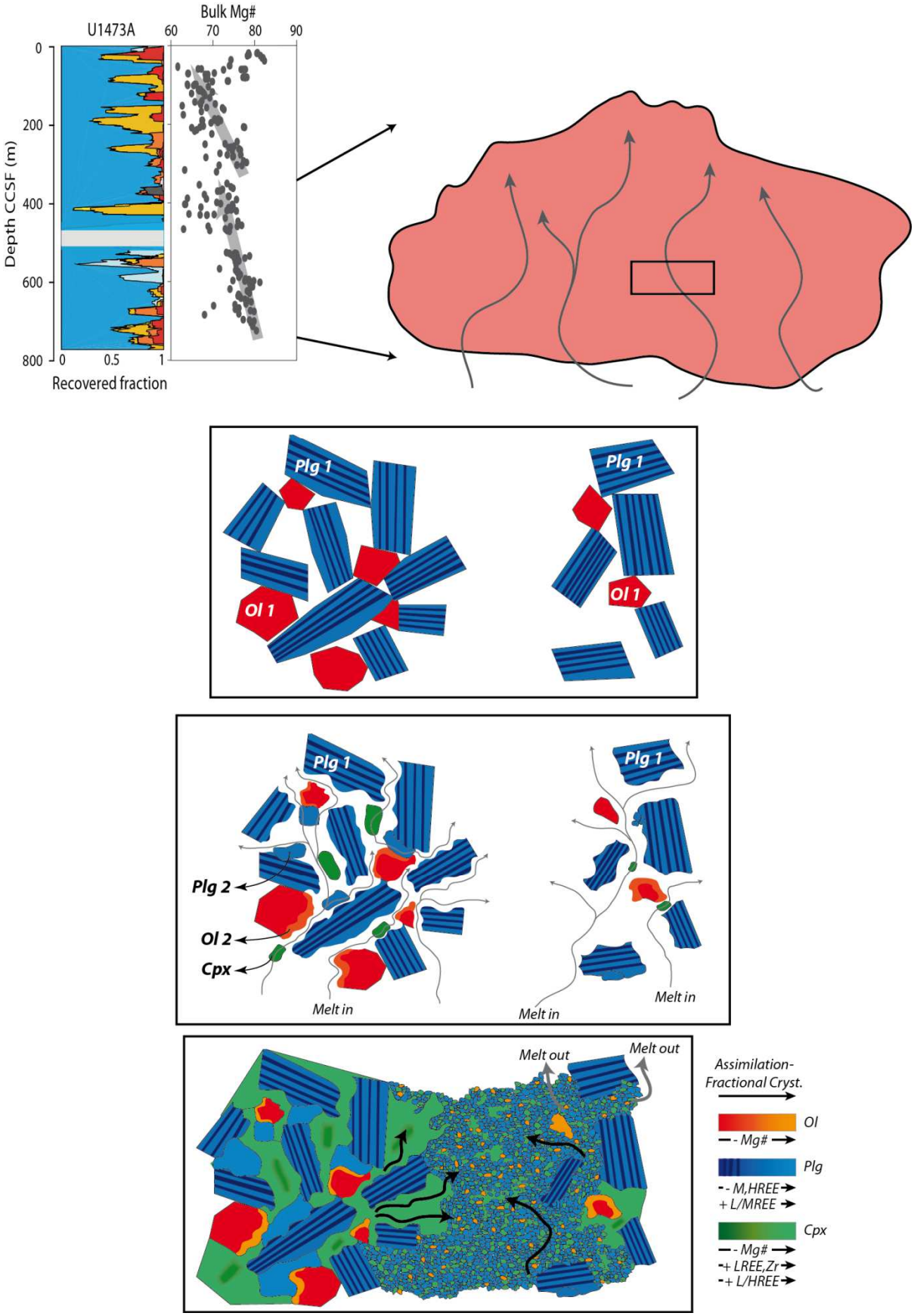
U1473A
Bulk Mg#
60
70
80
90
0
200
400
600
800
Depth CCSF (m)
0
0.5
1
Recovered fraction
Plg 1
Ol 1
Plg 1
Ol 1
Plg 1
Plg 2
Ol 2
Cpx
Melt in
Plg 1
Melt in
Melt in
Melt out
Melt out
Assimilation-
Fractional Cryst.
Ol
- Mg# →
Plg
- M,HREE →
+ L/MREE →
Cpx
- Mg# →
+ LREE,Zr →
+ L/HREE →

534

Textures and mineral geochemical compositions coupled with AFC models are consistent with the formation of olivine gabbros from Hole U1473A after migration of MORB melts through a crystal-mush. The geochemical evolution and the enrichments in incompatible elements from coarse-grained crystals to their relative rims and medium- to fine-grained olivine gabbro intervals suggest that they formed during a continuous process of melt-rock interaction and crystals precipitation. New crystal cores formed during concomitant crystallization of olivine + plagioclase + clinopyroxene, while crystal rims precipitated from a more evolved melt undersaturated in olivine.

Sharp irregular contacts are characterized by distinct compositions of coarse- and medium- to fine-grained crystals, while diffuse irregular contacts show similar compositions of coarse- and fine-grained olivine gabbro. The latter is the result of pervasive melt migration and embayment of coarse-grained intervals, while the former resulted from local crystallization of migrating melt between preserved intervals of coarse-grained olivine gabbro.

We propose the following scenario for the formation of olivine gabbros in Hole U1473A:

1: formation of troctolitic crystal mush with heterogeneous distribution of crystals (Fig. 14a)

2: melt migration in the crystal mush: partial dissolution of olivine+plagioclase and concomitant crystallization of coarse-grained olivine gabbro (Fig. 14b)

3: continuous melt-rock interactions in porous flow process and crystallization of medium- to fine- grained olivine gabbro (Fig. 14b)

4: crystallization of reacted melt in fine-grained intervals corresponding to low crystal modal contents in the starting mush. Locally high volumes of melt were generated during the reaction and pervasively crystallized the fine-grained olivine gabbro also modifying the composition of coarse-grained minerals. Where less melt was produced, rather thin fine-grained intervals formed between preserved coarse-grained olivine gabbro (Fig. 14c).

Appendix 1.2

Geochemistry, Geophysics, Geosystems

Supporting Information for

Melt migration and interactions in the lower oceanic crust: insights from Atlantis Bank interlayered series at IODP Hole U1473A (Southwest Indian Ridge)

M. Boulanger[1,2], L. France[1], C. Ferrando[1], B. Ildefonse[3], B. Ghosh[4], A. Sanfilippo[5], T. Morishita[6], C.-Z. Liu[7], J. Koepke[2] and O. Bruguier[3]

[1]Centre de Recherches Pétrographiques et Géochimiques, CNRS, Université de Lorraine, Vandœuvre-lès-Nancy, France.

[2]Intitut für Mineralogie, Leibniz Universität Hannover, Callinstrasse 3, D-30167 Hannover, Germany.

[3]Géosciences Montpellier, CNRS, Université de Montpellier, Université des Antilles, Montpellier, France.

[4]Department of Geology, University of Calcutta, Kolkata West Bengal 700019, India.

[5]Dipartimento di scienze della Terra, Università degli studi di Pavia, Pavia 27100, Italy.

[6]College of Science and Engineering, Kanazawa University, Kanazawa Ishikawa 920-1192, Japan.

[7]State Key Laboratory of Lithospheric Evolution, Institute of Geology and Geophysics, Chinese Academy of Sciences, Beijing 100029, China.

Contents of this file

Additional Supporting Information (Files uploaded separately)

Table S2. Plagioclase, clinopyroxene and olivine in-situ major elements concentrations in wt% (section U1473A-65R5 - this study). The error average (2σ and %) and the counting time for each element are indicated at the top of each section.

Table S3. Plagioclase, clinopyroxene and olivine in-situ trace elements concentrations in ppm (section U1473A-65R5 - this study). The analytical error average (1σ) and 2SD on BIR analyses for each element is indicated at the top and bottom of each section, respectively.

Introduction

The supporting information includes:

- analytical method for the EBSD measurements - **Text S1**
- details on the whole rock analyses procedure conducted at Service d'Analyse des Roches et des Minéraux (SARM - CRPG, Nancy) and the compositions obtained - **Text S2 and Table S1**
- calculation of the impact of the ablation spot size on the concentrations analyzed in the fine-grained layers - **Text S3**
- in-situ major elements and trace elements compositions measured in plagioclase (Pl), olivine (Ol) and clinopyroxene (Cpx) from the layered Ol-gabbro section U1473A-65R5 studied here - additional **Table S2** and **Table S3**
- reference values used in this study for data treatments and representation - **Table S4**
- compositional and thermodynamic parameters used in the magma evolution models applied to our system, i.e. the fractional crystallization model using the rhyolite-MELTS software, the Assimilation-Fractional Crystallization (AFC) model using the equation of *DePaolo* (1981) and the Plate model after *Vernières et al.* (1997) - **Table S5**
- supporting figures to illustrate additional issues presented in the article,
  - Examples of EBSD concatenated maps of coarse-grained samples - **Figure S1**
  - Reactive texture examples found in the coarse- and the fine-grained lithologies - **Figure S2**
  - Simple fractional crystallization models conducted for different temperatures - **Figure S3**

Text S1. Analytical methods - EBSD measurments

Crystallographic orientations were measured by Electron BackScatter Diffraction (EBSD) at Géosciences Montpellier, France. We used the CamScan X500FE Crystal Probe facility equipped with the EBSD HKL Oxford/Nordlys and EDS X-MaxN 20mm^2 detectors, and the AZtecHKL (Oxford) software. Crystal preferred orientations (CPO) and misorientations were obtained for 8 thin sections of coarse-grained, 6 thin sections of fine-grained, and 7 thin sections of mixed fine- and coarse-grained lithologies (5 of which presenting sharp contacts between layers) for olivine (Ol), plagioclase (Pl), clinopyroxene (Cpx), and orthopyroxene (Opx). The choice of the measurement step size was adjusted to the sample grain size and to the size of the area analyzed; it varied between 12 and 45 µm (25 µm on average). We obtained indexation rates of 97.8 % on average (ranging from 91 to 99.5 %).

Post-acquisition data processing, performed with the Channel 5 (Oxford) software suite, and with MTEX, a free toolbox for Matlab (Bachmann et al., 2010; Mainprice et al., 2014), includes (1) the automatic removal of isolated pixels surrounded by pixels indexed for another phase, and the filling of non-indexed pixels which have at least 5 neighbors with the same orientation with the Tango software of the Channel 5 software suite, (2) the calculation of grain boundaries based on a threshold value of 10° between adjacent pixels of the same phase, (3) the removal of small grains with an average diameter smaller than 5 pixels, (4) the filtering of the 178°-~~1~~80° misorientations which characterize Pl or Cpx twins (otherwise detected as grain boundaries) and, (5) the correction of Ol crystal systematic indexation errors due to the Ol hexagonal pseudosymmetry.

Bachmann, F., Hielscher, R., & Schaeben, H. (2010). Texture Analysis with MTEX – Free and Open Source Software Toolbox. SSP 160, 63–68. doi:10.4028/www.scientific.net/SSP.160.63

Mainprice, D., Bachmann, F., Hielscher, R., Schaeben, H. (2014). Descriptive tools for the analysis of texture projects with large datasets using MTEX: strength, symmetry and components. Geological Society, London, Special Publications. doi:10.1144/SP409.8

Text S2. Analytical methods - Whole rock analyses (SARM, Nancy)

For each sample, ~ 200 mg of rock powder was fused together with $LiBO_2$ and subsequently dissolved in a diluted HNO_3 solution. The major element oxide contents were measured by Inductively Coupled Plasma-Atomic Emission Spectrometry (ICP-AES) following the method of *Govindaraju & Mevelle* (1987). Related uncertainties are better than 5% for values >0.5 wt% and better than 15% for values >0.01wt%. Trace element concentrations were measured by ICP-MS following the method of *Carignan et al*. (2001). Related uncertainties were usually better than 10% for most trace elements whose concentrations are higher than the detection limits by more than 10 times, but were likely >25% for those with concentrations similar to the detection limits. Analytical accuracy and reproducibility were monitored by repeat analyses of five geochemical reference standards (see details in *Carignan et al*. 2001).

Carignan, J., Hild, P., Mevelle, G., Morel, J., Yeghicheyan, D. (2001). Routine Analyses of Trace Elements in Geological Samples using Flow Injection and Low Pressure On-Line Liquid Chromatography Coupled to ICP-MS: A Study of Geochemical Reference Materials BR, DR-N, UB-N, AN-G and GH. Geostandards Newsletter 25, 187-198.

Govindaraju, K. & Mevelle, G. (1987). Fully automated dissolution and separation methods for inductively coupled plasma atomic emission spectrometry rock analysis. Application to the determination of rare earth elements. Plenary lecture. Journal of Analytical Atomic Spectrometry 2, 615-621.

Text S3. Calculation of the spot size influence on the enrichment values

The spot size used for the ablation measurements are fairly large compared to the size of the crystals in the fine-grained material (average 0.5 mm). We discuss here the impact of a 70 µm ablation spot size (diameter used for the analyses of Cpx) on the composition analyzed and the possible averaging of enrichments if present in the minerals.

We consider the case in which the fine and the coarse-grained lithologies record the same enrichment in trace elements. In the case of Cpx Ce contents, the hypothetical composition of the fine-grained minerals' rims would reach ~8 ppm (higher composition recorded in the middle of the central coarse-grained layer). The lowest core composition of the same minerals would be at ~1.09 ppm (lower bound of the fine-grained range). We calculated the final composition we would obtain if during our measurements the rim signal would be diluted by analyzing at the same time various proportions of cores. If the volume analyzed (the 70 µm spot) includes 76% of "core" and 24% of "rim", the final composition would reach 2.76 ppm which is the highest value recorded in the fine-grained lithology. This means that if there was a systematic zoning pattern with enriched rim compositions in trace elements, we would miss it in almost every measurements which seems unlikely. The variability in composition recorded in the fine-grained material is then much lower than the variability and enrichments found in the coarse-grained layers despite the analytical limit of our method.

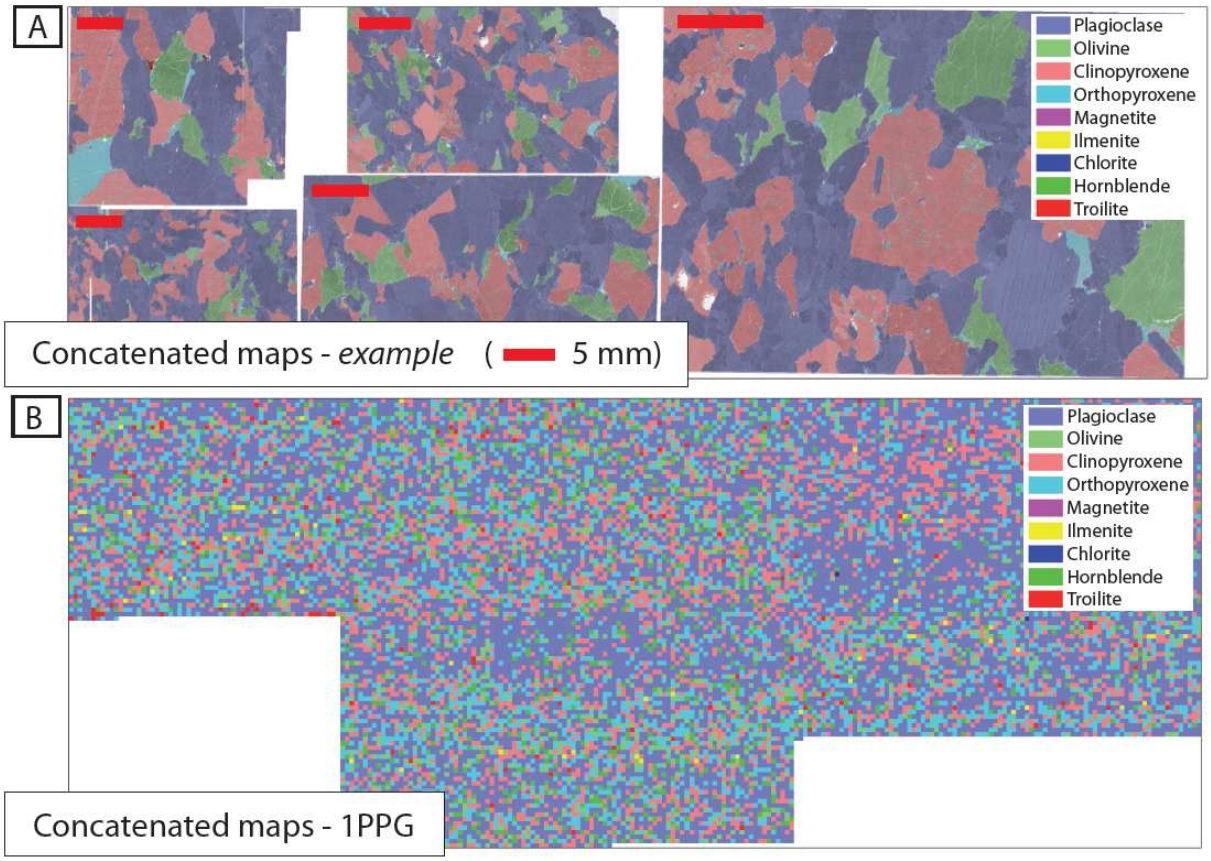

Figure S1. (a) Example of 5 concatenated superimposed phase and contrast maps for coarse-grained samples. As the step size for each map analyzed was initially different, a single step size was redefined for all the maps before concatenation. (b) Phase map representation of the final concatenated data set for all analyzed coarse-grained samples (8 in total). The 1PPG data were used (one-point-per-grain - average value per grain of each parameter instead of one value per each pixel analyzed), which result in the speckled map.

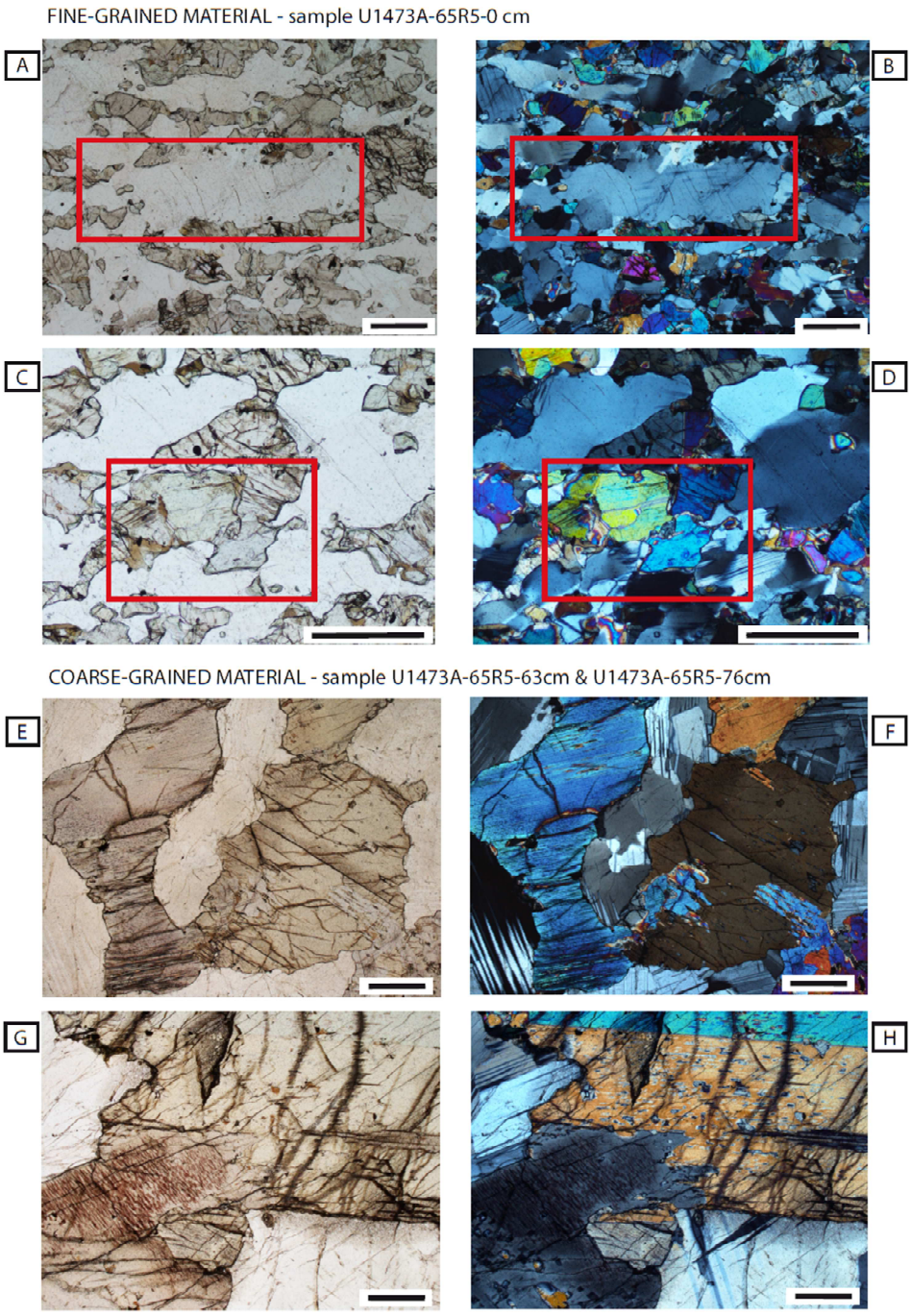

Figure S2. Photomicrographs of the reactive textures identified in section 65R5. Resorbed grain boundaries of a Pl crystal (a and b) and of Cpx crystals (c and d) observed in a finer grained area of the top fine-grained layer. Intergrowths of Cpx crystals from coarse-grained layers.

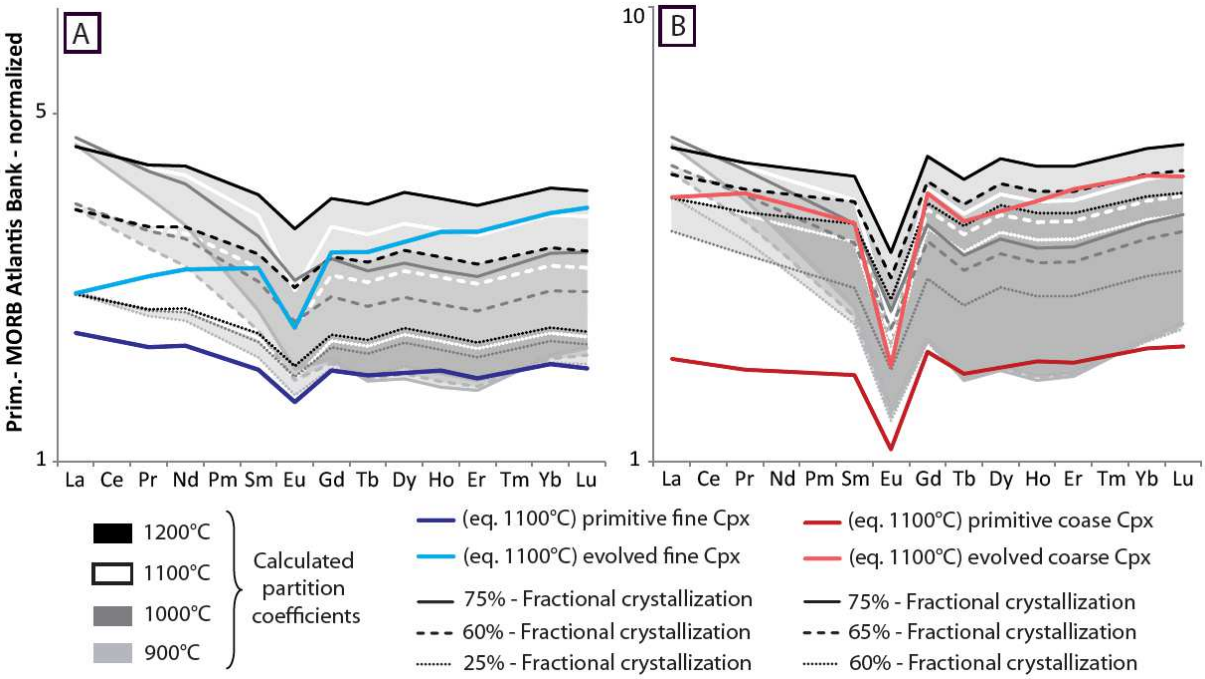

Figure S3. Rare Earth Elements diagrams of the liquids in equilibrium with Cpx crystals analyzed in section 65R5, and evolution of the equilibrium melts by fractional crystallization for (a) the fine-grained lithology and (b) the coarse-grained lithology. Dark lines represent the least evolved compositions analyzed, and light colored lines the most evolved compositions. The different dashed lines represent the amount of fractional crystallization modeled from the least evolved composition. The color of each line represents the temperature set for each model (from 900°C to 1200°C). The normalization value is an average primitive MORB composition for the Atlantis Bank section of the SWIR from *Coogan et al*. (2004).

Sample	Reference	SiO_2 %	Al_2O_3 %	Fe_2O_3 %	MnO %	MgO %	CaO %	Na_2O %	K_2O %	TiO_2 %	P_2O_5 %	PF %	Total %	As ppm	Ba ppm	Be ppm	Bi ppm	Cd ppm	Ce ppm	Co ppm
65R5_5-9	1602244	50.03	16.70	5.70	0.11	10.20	13.21	2.59	< L.D.	0.29	< L.D.	0.41	99.23	< L.D.	2.9861	< L.D.	< L.D.	0.0721	1.4072	47.3616
65R5_14-22	1602245	49.94	15.88	6.34	0.12	10.81	13.22	2.47	< L.D.	0.38	< L.D.	0.10	99.26	0.2546	2.2695	0.1055	< L.D.	0.0753	2.1907	45.3068
65R5_26-30	1602246	50.35	17.43	5.23	0.10	9.44	13.38	2.74	< L.D.	0.27	< L.D.	0.17	99.11	0.3028	< L.D.	0.0921	< L.D.	0.0674	1.4132	40.9492
65R5_48-56	1602247	49.42	16.01	6.65	0.12	10.83	12.66	2.52	< L.D.	0.35	< L.D.	0.08	98.65	0.2204	2.888	0.0928	< L.D.	0.0843	1.8175	47.8738
65R5_89-93	1602248	50.17	17.81	4.68	0.09	9.08	13.67	2.74	< L.D.	0.22	< L.D.	0.22	98.69	< L.D.	< L.D.	< L.D.	< L.D.	0.0629	0.9884	42.2826
65R5_99-104	1602249	50.38	17.42	5.96	0.11	10.03	12.85	2.72	< L.D.	0.30	< L.D.	-0.04	99.73	< L.D.	< L.D.	0.1119	< L.D.	0.0575	1.5593	45.5873
65R5_112-117	1602250	50.15	16.48	6.06	0.11	10.87	13.11	2.52	< L.D.	0.29	< L.D.	0.04	99.62	< L.D.	2.5834	0.0945	< L.D.	0.0689	1.5087	48.1545
(continued)	Reference	Cr ppm	Cs ppm	Cu ppm	Dy ppm	Er ppm	Eu ppm	Ga ppm	Gd ppm	Ge ppm	Hf ppm	Ho ppm	In ppm	La ppm	Lu ppm	Mo ppm	Nb ppm	Nd ppm	Ni ppm	Pb ppm
65R5_5-9	1602244	240.9694	< L.D.	109.7287	1.3978	0.8398	0.4692	12.3643	1.0325	1.1616	0.2847	0.3075	0.0275	0.4077	0.1147	< L.D.	0.1903	1.6701	133.0747	< L.D.
65R5_14-22	1602245	214.2656	< L.D.	54.6441	1.7677	1.0616	0.5225	12.398	1.3858	1.1756	0.4992	0.3961	0.0313	0.6486	0.1457	< L.D.	0.2569	2.3687	126.4331	< L.D.
65R5_26-30	1602246	241.2492	< L.D.	85.8049	1.2821	0.7636	0.4554	12.6827	0.9871	1.1141	0.2831	0.2834	0.0255	0.4524	0.1039	< L.D.	0.1863	1.5764	112.1422	< L.D.
65R5_48-56	1602247	209.0515	< L.D.	68.0155	1.6458	0.9795	0.5165	12.3269	1.2915	1.2074	0.4114	0.3645	0.0292	0.5294	0.1358	< L.D.	0.182	2.1023	133.8263	< L.D.
65R5_89-93	1602248	237.4662	< L.D.	85.7359	1.1514	0.6798	0.4194	13.086	0.8446	1.1797	0.168	0.2563	0.0231	0.296	0.0919	< L.D.	0.1795	1.26	114.1079	< L.D.
65R5_99-104	1602249	188.4661	< L.D.	52.762	1.4074	0.8215	0.5067	13.1455	1.0779	1.1278	0.304	0.3095	0.0268	0.472	0.1132	< L.D.	0.1734	1.7553	119.2076	< L.D.
65R5_112-117	1602250	246.5456	< L.D.	118.16	1.367	0.8115	0.4514	12.1653	1.0539	1.1139	0.3121	0.3034	0.0265	0.4387	0.1121	< L.D.	0.1545	1.7062	143.6405	< L.D.
(continued)	Reference	Pr ppm	Rb ppm	Sc ppm	Sb ppm	Sm ppm	Sn ppm	Sr ppm	Ta ppm	Tb ppm	Th ppm	Tm ppm	U ppm	V ppm	W ppm	Y ppm	Yb ppm	Zn ppm	Zr ppm	
65R5_5-9	1602244	0.2692	< L.D.	38.57	< L.D.	0.7359	< L.D.	144.8489	0.7682	0.1976	< L.D.	0.115	< L.D.	136.0816	88.6119	7.7915	0.7759	25.0561	8.7595	
65R5_14-22	1602245	0.3985	< L.D.	40.55	< L.D.	0.9941	< L.D.	138.7078	0.3818	0.2523	0.0148	0.148	< L.D.	156.2442	42.8725	9.8772	0.9855	28.6509	17.451	
65R5_26-30	1602246	0.2611	< L.D.	37.5	< L.D.	0.6792	< L.D.	151.7924	0.6048	0.1845	< L.D.	0.1065	< L.D.	137.5738	66.4604	7.3525	0.7092	22.6042	9.0565	
65R5_48-56	1602247	0.3403	< L.D.	37.94	< L.D.	0.9031	< L.D.	142.6096	0.4229	0.2355	< L.D.	0.1392	< L.D.	144.2431	48.1109	9.093	0.9282	30.5057	13.139	
65R5_89-93	1602248	0.1941	< L.D.	36.83	< L.D.	0.5758	< L.D.	159.78	0.7729	0.1646	< L.D.	0.0951	< L.D.	134.9823	88.2593	6.4256	0.6271	19.5413	5.8955	
65R5_99-104	1602249	0.2901	< L.D.	34.34	< L.D.	0.7595	< L.D.	156.418	0.5787	0.2023	< L.D.	0.1182	< L.D.	136.0418	66.2916	7.8726	0.7847	27.4818	10.0185	
65R5_112-117	1602250	0.2746	< L.D.	37.79	< L.D.	0.739	< L.D.	144.4093	0.5382	0.1942	< L.D.	0.1144	< L.D.	139.259	63.5337	7.8359	0.7658	26.1004	10.4536	

Table S1. Whole rock compositions of the Ol-gabbro layers sampled in section U1473A-65R5.

A/ Partition coefficients for Ol, Pl and Cpx (Dmin/liq)

Mineral	Temperature (°C)	Reference	La	Ce	Pr	Nd	Sm	Eu	Gd	Tb	Dy	Y	Ho	Er	Tm	Yb	Lu
Ol	-	*Beattie et al.*, 1994	1.20E-05	2.42E-05	6.05E-05	1.65E-04	5.49E-04	1.10E-03	2.05E-03	4.15E-03	7.30E-03	9.20E-03	1.18E-02	1.85E-02	3.10E-02	4.69E-02	6.60E-02
Pl	1100	*Sun et al.,* 2017	*5.39E-02*	*5.02E-02*	*4.49E-02*	*3.86E-02*	*2.68E-02*	*3.78E-01*	*1.79E-02*	*1.41E-02*	*1.10E-02*	*9.30E-03*	*8.50E-03*	*6.70E-03*	*5.30E-03*	*4.20E-03*	*3.50E-03*
Cpx	1100	*Wood & Blundy*, 1997	*1.39E-01*	*2.16E-01*	*3.13E-01*	*4.27E-01*	*6.36E-01*	*7.14E-01*	*7.75E-01*	*8.14E-01*	*8.30E-01*	*8.26E-01*	*8.21E-01*	*7.95E-01*	*7.58E-01*	*7.16E-01*	*6.73E-01*
Ol		*Sun & Liang*, 2013	7.46E-08	3.51E-07	1.50E-06	5.79E-06	5.03E-05	1.17E-04	2.61E-04	5.50E-04	1.10E-03	1.65E-03	2.01E-03	3.37E-03	5.22E-03	7.57E-03	1.03E-02
Pl	900	*Sun et al.*, 2017	2.91E-03	2.68E-03	2.36E-03	1.97E-03	1.29E-03	1.03E-03	8.01E-04	6.09E-04	4.52E-04	3.72E-04	3.37E-04	2.53E-04	1.92E-04	1.49E-04	1.17E-04
Cpx		*Wood & Blundy*, 1997	2.60E-01	4.51E-01	7.24E-01	1.08E+00	1.82E+00	2.14E+00	2.41E+00	2.61E+00	2.73E+00	2.75E+00	2.74E+00	2.69E+00	2.58E+00	2.44E+00	2.29E+00
Ol		*Sun & Liang*, 2013	2.39E-07	9.97E-07	3.79E-06	1.32E-05	9.67E-05	2.11E-04	4.41E-04	8.77E-04	1.67E-03	2.42E-03	2.90E-03	4.66E-03	6.97E-03	9.82E-03	1.31E-02
Pl	1000	*Sun et al.*, 2017	1.40E-02	1.30E-02	1.15E-02	9.80E-03	6.63E-03	5.38E-03	4.27E-03	3.32E-03	2.52E-03	2.11E-03	1.92E-03	1.48E-03	1.15E-03	9.05E-04	7.28E-04
Cpx		*Wood & Blundy*, 1997	1.55E-01	2.57E-01	3.95E-01	5.67E-01	9.15E-01	1.06E+00	1.18E+00	1.27E+00	1.32E+00	1.33E+00	1.33E+00	1.30E+00	1.26E+00	1.19E+00	1.13E+00
Ol		*Sun & Liang*, 2013	6.48E-07	2.43E-06	8.40E-06	2.67E-05	1.69E-04	3.49E-04	6.90E-04	1.31E-03	2.37E-03	3.35E-03	3.96E-03	6.14E-03	8.93E-03	1.23E-02	1.60E-02
Pl	1100	*Sun et al.*, 2017	*5.39E-02*	*5.02E-02*	*4.49E-02*	*3.86E-02*	*2.68E-02*	*2.21E-02*	*1.79E-02*	*1.41E-02*	*1.10E-02*	*9.28E-03*	*8.52E-03*	*6.67E-03*	*5.28E-03*	*4.24E-03*	*3.46E-03*
Cpx		*Wood & Blundy*, 1997	*1.00E-01*	*1.58E-01*	*2.35E-01*	*3.28E-01*	*5.08E-01*	*5.81E-01*	*6.42E-01*	*6.86E-01*	*7.11E-01*	*7.16E-01*	*7.15E-01*	*7.03E-01*	*6.79E-01*	*6.49E-01*	*6.16E-01*
Ol		*Sun & Liang*, 2013	1.53E-06	5.26E-06	1.67E-05	4.91E-05	2.74E-04	5.39E-04	1.02E-03	1.84E-03	3.21E-03	4.43E-03	5.18E-03	7.80E-03	1.11E-02	1.49E-02	1.91E-02
Pl	1200	*Sun et al.,* 2017	1.72E-01	1.61E-01	1.45E-01	1.26E-01	8.99E-02	7.51E-02	6.15E-02	4.94E-02	3.90E-02	3.34E-02	3.08E-02	2.45E-02	1.97E-02	1.61E-02	1.33E-02
Cpx		*Wood & Blundy,* 1997	6.85E-02	1.05E-01	1.50E-01	2.04E-01	3.06E-01	3.46E-01	3.79E-01	4.03E-01	4.17E-01	4.19E-01	4.19E-01	4.12E-01	3.99E-01	3.83E-01	3.65E-01

B/ Rare Earth Elements - normalization values

Type	Reference	La	Ce	Pr	Nd	Sm	Eu	Gd	Tb	Dy	Y	Ho	Er	Tm	Yb	Lu
Diabase U1473A-42R1	This study	3.01	10.24	-	10.64	3.87	1.4	5.77	-	7	29	-	4.19	-	3.8	0.59
CI Chondrite	*McDonough & Sun* 1995	0.237	0.613	0.0928	0.457	0.148	0.0563	0.199	0.0361	0.246	1.57	0.0546	0.16	0.0247	0.161	0.0246
Prim. MORB Atlantis Bank	from *Coogan et al.*, 2004	2.76	8.11	1.59	8.43	2.88	1.08	3.27	0.66	4.26		0.94	2.78	0.46	2.65	0.41

C/ Trace elements reference values - normalization values

Type	Reference	La	Ce	Pr	Nd	Sm	Eu	Gd	Tb	Dy	Y	Ho	Er	Tm	Yb	Lu
MORB	*Gale et al.*, 2013	5.21	14.86	2.24	12.03	3.82	1.36	4.99	0.9	6.08	36.8	1.28	3.79	-	3.63	0.53

Type	Reference	Li	V	Cs	Rb	Ba	Th	U	Nb	Ta	Pb	Sr	Zr	Hf
MORB	*Gale et al.*, 2013	6.5	309	0.034	2.88	29.2	0.404	0.119	5.24	0.34	0.57	129	116.9	2.79

Table S4. Reference values used in this study. (a) Partition coefficient sets of rare earth elements (and Y) calculated at different temperature conditions and for the mineral compositions analyzed in the section. Normalization values for (b) rare earth elements and (c) extended trace elements diagrams.

A/ MELTs parameters

Starting composition

Label ID	depth (mbsf)	SiO_2	Al_2O_3	TiO_2	Fe_2O_3t	MgO	MnO	CaO	Na_2O	K_2O	P_2O_5*	Cr	total
Diabase from U1473A (42R1)	381.6	48.723	15.489	1.480	10.686	9.225	0.167	10.980	3.059	0.049	0.108	0.035	100

* from Godard et al., 2009

Conditions

N°	P (bar)	Start T (°C)	Stop T (°C)	Inc. T (°C)	Start. comp.	H2O (wt%)	deltaQFM	Liquidus (°C)	Mode
2	2000	1300	900	5	Diabase	0.5	0	1233.4	Fractional

B/ AFC modeling

Percolating liquid composition	La	Ce	Pr	Nd	Sm	Eu	Gd	Tb	Dy	Ho	Er	Tm	Yb	Lu
Diabase from U1473A (42R1)	3.01	10.24	-	10.64	3.87	1.40	5.77	-	7.00	-	4.19	-	3.80	0.59
Mush composition	La	Ce	Pr	Nd	Sm	Eu	Gd	Tb	Dy	Ho	Er	Tm	Yb	Lu
Equivalent prim. - Coarse	0.479	1.721	0.324	2.002	0.834	0.453	1.226	0.231	1.683	0.356	1.011	0.147	0.974	0.142
Partition coefficients	La	Ce	Pr	Nd	Sm	Eu	Gd	Tb	Dy	Ho	Er	Tm	Yb	Lu
Pl	0.0539	0.0502	0.0449	0.0386	0.0268	0.3780	0.0179	0.0141	0.0110	0.0085	0.0067	0.0053	0.0042	0.0035
Cpx	0.139	0.216	0.313	0.427	0.636	0.714	0.775	0.814	0.830	0.821	0.795	0.758	0.716	0.673
Ol	1.20E-05	2.42E-05	6.05E-05	1.65E-04	5.49E-04	1.10E-03	2.05E-03	4.15E-03	7.30E-03	1.18E-02	1.85E-02	3.10E-02	4.69E-02	6.60E-02

Crystallization steps

F (%)	0.0	0.1	0.2	0.2	0.3	0.3	0.4	0.6	0.8	1.0

Ratio Assimilated / Fractionated

r	0.7	0.8	0.9	0.99

Mineral proportions	Pl	Ol	Cpx
%	50	11	39

C/ Plate Model

Percolating liquid composition	La	Ce	Pr	Nd	Sm	Eu	Gd	Tb	Dy	Ho	Er	Tm	Yb	Lu
Diabase from U1473A (42R1)	3.01	10.24	-	10.64	3.87	1.40	5.77	-	7.00	-	4.19	-	3.80	0.59
Mush composition	La	Ce	Pr	Nd	Sm	Eu	Gd	Tb	Dy	Ho	Er	Tm	Yb	Lu
Equivalent prim. - Fine	0.174	0.673	0.162	1.193	0.586	0.358	0.844	0.178	1.291	0.274	0.776	0.112	0.737	0.104
Partition coefficients	La	Ce	Pr	Nd	Sm	Eu	Gd	Tb	Dy	Ho	Er	Tm	Yb	Lu
Pl	0.0539	0.0502	0.0449	0.0386	0.0268	0.3780	0.0179	0.0141	0.0110	0.0085	0.0067	0.0053	0.0042	0.0035
Cpx	0.139	0.216	0.313	0.427	0.636	0.714	0.775	0.814	0.830	0.821	0.795	0.758	0.716	0.673
Ol	1.20E-05	2.42E-05	6.05E-05	1.65E-04	5.49E-04	1.10E-03	2.05E-03	4.15E-03	7.30E-03	1.18E-02	1.85E-02	3.10E-02	4.69E-02	6.60E-02

(continued)

Mineral proportion & dissolution / crystallization ratio				Dissolution proportions			Crystallization proportions			
		F (diss.)	**f (cryst.)**	**Ol**	**Pl**	**Cpx**	**Ol**	**Pl**	**Cpx**	**Ma/Mc**
M_360_fineV_cpx-V	Zone 1	0.06	0.96	0	0.2	0.8	0	0.7	0.3	0.1
	Zone 2	0.06	0.94	0	0.2	0.8	0	0.7	0.3	
	Zone 3	0	1	0	0.2	0.8	0	0.7	0.3	
M_360_fineV_cpx1-V	Zone 1	0.06	0.96	0	0.3	0.7	0	0.7	0.3	0.1
	Zone 2	0.06	0.94	0	0.3	0.7	0	0.7	0.3	
	Zone 3	0	1	0	0.3	0.7	0	0.7	0.3	
M_360_fineV_cpx2-V	Zone 1	0.06	0.96	0	0.4	0.6	0	0.7	0.3	0.1
	Zone 2	0.06	0.94	0	0.4	0.6	0	0.7	0.3	
	Zone 3	0	1	0	0.4	0.6	0	0.7	0.3	

Table S5. Modeling parameters used in this study. (a) Rhyolite-MELTs parameters used to model the fractional crystallization of an equivalent primitive melt composition for our system (whole rock analysis of the primitive diabase 42R1 sampled in Hole U1473A). (b) Parameters used in the modeling of the Assimilation-Fractional Crystallization of an equivalent primitive mush representative of the coarse-grained material (see 6.6.2 for details) and a percolating reactive liquid, taken as the whole rock composition of the primitive diabase dike found in Hole U1473A. (c) Parameters used in the Plate modeling. The assimilated lithology is an equivalent primitive mush representative of the fine-grained lithology, the same reactive liquid as for the AFC model is considered.

Appendix 1.3

In situ major elements concentrations in wt% analysed by EPMA on a Cameca SX100 in LMV (Clermont-Ferrand, Frar

Mineral	Sample	Area	Point	Depth (mbsf)	Layer type	Grain area	SiO2	Al2O3	TiO2	CaO	Na2O	MnO	MgO	FeO	Cr2O3	NiO	Total
						ox	0.418	0.024	0.042	0.040	0.024	0.065	0.423	0.384	0.045	0.048	
						%	1.1	277.8	255.3	101.6	254.6	19.6	1.1	1.7	362.6	58.4	
Ol			Counting time (s)				10	10	10	10	10	10	10	10	20	20	
Ol		C	3 / 1 .	592.280	Coarse	core	38.09	0.00	0.00	0.07	0.00	0.37	38.26	23.30	0.00	0.10	100.1
Ol		C	3 / 2 .	592.280	Coarse	rim	38.18	0.02	0.00	0.04	0.00	0.32	38.12	22.79	0.02	0.09	99.5
Ol		F	9 / 1 .	592.285	Coarse	core	38.36	0.03	0.00	0.05	0.04	0.34	38.72	22.96	0.02	0.12	100.5
Ol		F	9 / 2 .	592.285	Coarse	rim	38.22	0.02	0.00	0.03	0.00	0.29	38.63	22.92	0.04	0.11	100.2
Ol	360_65R5_76	F	10 / 1 .	592.285	Coarse	core	38.34	0.03	0.00	0.04	0.02	0.37	38.54	22.76	0.00	0.06	100.1
Ol		F	10 / 2 .	592.285	Coarse	rim	38.47	0.00	0.06	0.04	0.01	0.35	38.26	22.84	0.00	0.06	100.0
Ol		G	21 / 1 .	592.299	Coarse	core	38.33	0.00	0.00	0.07	0.00	0.43	38.45	23.51	0.00	0.04	100.8
Ol		G	21 / 2 .	592.299	Coarse	rim	38.52	0.02	0.00	0.01	0.01	0.28	38.96	22.05	0.00	0.09	99.9
Ol		E	27 / 1 .	592.300	Coarse	core	38.06	0.00	0.04	0.02	0.00	0.42	37.72	24.20	0.00	0.13	100.5
Ol		E	27 / 2 .	592.300	Coarse	rim	38.30	0.00	0.03	0.04	0.00	0.33	37.82	24.12	0.03	0.08	100.7
Ol		B	5 / 1 .	591.795	Fine	core	38.69	0.03	0.00	0.00	0.01	0.31	39.55	21.90	0.00	0.10	100.6
Ol		B	5 / 2 .	591.795	Fine	rim	38.36	0.00	0.01	0.01	0.03	0.32	39.64	21.52	0.01	0.13	100.0
Ol		B	5 / 3 .	591.795	Fine	rim	38.61	0.00	0.02	0.03	0.00	0.30	39.18	21.86	0.00	0.09	100.0
Ol		C	13 / 1 .	591.794	Fine	core	38.30	0.00	0.02	0.04	0.00	0.24	39.37	21.72	0.00	0.09	99.7
Ol	360_65R5_27	C	13 / 2 .	591.794	Fine	rim	38.38	0.00	0.00	0.02	0.00	0.29	39.30	21.61	0.00	0.08	99.7
Ol		C	16 / 1 .	591.794	Fine	core	38.57	0.02	0.04	0.05	0.00	0.27	39.56	21.84	0.00	0.09	100.3
Ol		C	16 / 2 .	591.794	Fine	rim	38.42	0.01	0.02	0.00	0.00	0.24	39.34	21.87	0.00	0.03	99.9
Ol		A	23 / 1 .	591.800	Fine	core	38.32	0.00	0.00	0.02	0.00	0.37	39.36	21.83	0.01	0.07	100.0
Ol		A	23 / 2 .	591.800	Fine	rim	38.36	0.00	0.05	0.03	0.00	0.31	39.41	21.77	0.00	0.10	100.0
Ol		G	35 / 1 .	591.715	Coarse	core	38.35	0.01	0.07	0.06	0.00	0.33	38.56	23.33	0.03	0.09	100.7
Ol		G	35 / 2 .	591.715	Coarse	rim	38.32	0.00	0.03	0.04	0.02	0.29	38.41	23.34	0.05	0.10	100.5
Ol		F	39 / 1 .	591.717	Coarse	rim	37.93	0.00	0.01	0.07	0.00	0.30	38.47	23.37	0.00	0.08	100.1
Ol		E	40 / 1 .	591.717	Coarse	core	37.95	0.01	0.03	0.09	0.00	0.26	38.20	23.37	0.00	0.04	99.8
Ol	360_65R5_18	Bis	23 / 1 .	591.703	Coarse	core	38.04	0.00	0.00	0.07	0.02	0.31	38.35	23.29	0.02	0.06	100.1
Ol		Bis	23 / 2 .	591.703	Coarse	rim	38.42	0.01	0.05	0.06	0.03	0.33	38.57	23.51	0.02	0.09	100.9
Ol		Bis	23 / 3 .	591.703	Coarse	rim	38.39	0.00	0.02	0.05	0.03	0.38	38.57	23.22	0.02	0.11	100.7
Ol		Bis	25 / 1 .	591.703	Coarse	core	38.81	0.01	0.07	0.03	0.03	0.32	39.11	22.07	0.04	0.07	100.4
Ol		Bis	25 / 2 .	591.703	Coarse	core	38.32	0.01	0.03	0.07	0.02	0.34	38.05	23.90	0.00	0.06	100.7
Ol		Bis	25 / 3 .	591.703	Coarse	core	38.46	0.05	0.00	0.01	0.00	0.44	37.69	23.60	0.00	0.06	100.3
Ol		D	23 / 1 .	591.993	Coarse	core	38.56	0.03	0.00	0.05	0.01	0.32	38.39	23.27	0.00	0.08	100.6
Ol	360_65R5_46	D	23 / 3 .	591.993	Coarse	rim	38.48	0.01	0.00	0.02	0.00	0.31	38.88	23.02	0.00	0.05	100.7
Ol		A	30 / 1 .	591.985	Coarse	core	38.08	0.01	0.03	0.03	0.00	0.30	38.36	23.68	0.02	0.07	100.5
Ol		A	30 / 2 .	591.985	Coarse	rim	38.48	0.00	0.03	0.05	0.03	0.36	37.97	23.25	0.01	0.06	100.1
Ol		C	4 / 4 .	592.466	Fine	core	39.25	0.00	0.00	0.00	0.00	0.29	40.04	20.60	0.00	0.06	100.2
Ol		C	5 / 1 .	592.466	Fine	core	39.20	0.00	0.00	0.04	0.00	0.29	40.16	21.27	0.00	0.04	101.0
Ol		C	5 / 3 .	592.466	Fine	rim	38.73	0.02	0.00	0.04	0.00	0.31	40.05	21.73	0.00	0.12	100.9
Ol		A	8 / 1 .	592.466	Fine	core	39.06	0.00	0.00	0.03	0.00	0.25	39.85	21.16	0.07	0.09	100.4
Ol		A	8 / 2 .	592.466	Fine	core	39.03	0.00	0.00	0.04	0.00	0.34	39.76	21.28	0.03	0.09	100.5

Mineral	360_65R5_94	Area	Point	Depth (mbsf)	Layer type	Grain area	SiO2	Al2O3	TiO2	CaO	Na2O	MnO	MgO	FeO	Cr2O3	NiO	Total
Ol		B	12 / 1 .	592.456	Fine	core	38.44	0.00	0.00	0.08	0.02	0.32	40.19	21.21	0.02	0.06	100.2
Ol		B	12 / 2 .	592.456	Fine	rim	38.83	0.00	0.02	0.06	0.00	0.37	40.06	20.78	0.04	0.10	100.1
Ol		D	15 / 1 .	592.453	Fine	core	38.74	0.00	0.01	0.07	0.03	0.36	39.99	21.45	0.07	0.04	100.6
Ol		D	15 / 2 .	592.453	Fine	rim	38.63	0.01	0.00	0.02	0.01	0.29	39.33	21.79	0.04	0.06	100.1
Ol		D	15 / 3 .	592.453	Fine	core	38.85	0.00	0.09	0.02	0.00	0.29	40.51	21.49	0.00	0.10	101.2
Ol		D	15 / 4 .	592.453	Fine	rim	38.71	0.00	0.13	0.02	0.02	0.36	40.07	21.47	0.00	0.11	100.7
Ol		A	18 / 1 .	592.354	Coarse in	core	38.54	0.01	0.00	0.03	0.01	0.29	39.47	21.99	0.04	0.08	100.4
Ol		A	18 / 2 .	592.354	Coarse in	rim	38.76	0.00	0.00	0.02	0.00	0.30	39.00	21.93	0.01	0.07	100.1
Ol		C	25 / 1 .	592.365	Coarse in	core	38.35	0.00	0.00	0.05	0.01	0.34	40.02	20.96	0.06	0.08	99.8
Ol		C	25 / 2 .	592.365	Coarse in	rim	38.47	0.01	0.02	0.01	0.01	0.37	40.36	20.67	0.04	0.10	100.0
Ol	360_65R5_83	B	26 / 1 .	592.369	Coarse in	core	37.81	0.01	0.02	0.07	0.00	0.29	38.87	22.07	0.02	0.05	99.1
Ol		B	26 / 2 .	592.369	Coarse in	rim	38.27	0.03	0.00	0.01	0.00	0.33	39.24	22.04	0.05	0.12	100.0
Ol		E	31 / 1 .	592.376	Fine	core	38.41	0.00	0.01	0.05	0.01	0.28	39.46	21.92	0.00	0.08	100.2
Ol		E	31 / 2 .	592.376	Fine	rim	38.48	0.01	0.05	0.03	0.00	0.35	39.64	21.53	0.00	0.08	100.1
Ol		D	9 / 1 .	592.432	Fine	core	38.80	0.00	0.01	0.05	0.00	0.34	40.12	21.31	0.03	0.11	100.7
Ol		D	9 / 2 .	592.432	Fine	rim	38.97	0.02	0.03	0.06	0.00	0.29	39.80	21.29	0.00	0.06	100.4
Ol		D	9 / 3 .	592.432	Fine	core	38.58	0.00	0.01	0.02	0.01	0.31	39.54	21.64	0.02	0.11	100.2
Ol		F	13 / 1 .	592.435	Fine	core	38.55	0.02	0.00	0.02	0.00	0.31	39.30	22.20	0.00	0.12	100.5
Ol		F	13 / 2 .	592.435	Fine	rim	38.25	0.00	0.01	0.06	0.00	0.30	39.19	21.74	0.05	0.08	99.6
Ol		F	13 / 3 .	592.435	Fine	core	38.62	0.00	0.04	0.03	0.02	0.33	39.25	21.80	0.00	0.07	100.1
Ol		F	13 / 4 .	592.435	Fine	rim	38.87	0.03	0.06	0.05	0.00	0.33	39.07	21.64	0.02	0.10	100.0
Ol	360_65R5_91	B	17 / 1 .	592.443	Coarse in	core	38.53	0.03	0.01	0.05	0.00	0.37	38.35	23.47	0.00	0.08	100.8
Ol		B	17 / 2 .	592.443	Coarse in	core	38.56	0.00	0.01	0.00	0.00	0.36	38.55	23.44	0.00	0.10	101.0
Ol		A	20 / 1 .	592.445	Coarse in	core	38.56	0.02	0.01	0.05	0.00	0.32	38.69	22.83	0.01	0.11	100.5
Ol		A	20 / 2 .	592.445	Coarse in	rim	38.41	0.02	0.03	0.03	0.04	0.34	39.01	22.36	0.00	0.11	100.2
Ol		A	20 / 3 .	592.445	Coarse in	core	38.68	0.02	0.00	0.03	0.00	0.31	39.05	22.40	0.00	0.10	100.5
Ol		A	20 / 4 .	592.445	Coarse in	rim	38.21	0.02	0.00	0.07	0.01	0.36	38.57	22.50	0.06	0.09	99.7
Ol		A	21 / 4 .	592.445	Coarse in	core	38.68	0.00	0.01	0.10	0.00	0.31	38.42	22.54	0.02	0.10	100.1
Ol		D	3 / 1 .	592.313	Coarse	core	38.94	0.00	0.02	0.02	0.00	0.34	39.68	22.08	0.02	0.08	101.1
Ol		D	3 / 2 .	592.313	Coarse	rim	38.72	0.00	0.06	0.04	0.00	0.32	39.16	21.82	0.02	0.04	100.1
Ol		D	3 / 3 .	592.313	Coarse	rim	38.68	0.00	0.05	0.03	0.00	0.30	39.04	22.15	0.01	0.01	100.2
Ol		D	3 / 4 .	592.313	Coarse	core	38.33	0.04	0.06	0.02	0.00	0.36	39.05	21.72	0.01	0.07	99.5
Ol		C	5 / 1 .	592.321	Coarse	core	38.80	0.03	0.00	0.02	0.00	0.34	39.54	22.16	0.05	0.05	100.9
Ol		C	5 / 2 .	592.321	Coarse	rim	38.80	0.02	0.01	0.06	0.01	0.30	39.37	21.89	0.01	0.10	100.5
Ol	360_65R5_79g	C	5 / 3 .	592.321	Coarse	core	38.31	0.02	0.00	0.05	0.00	0.33	39.47	21.74	0.02	0.11	100.0
Ol		C	5 / 4 .	592.321	Coarse	rim	38.05	0.00	0.01	0.06	0.02	0.27	39.36	21.79	0.00	0.11	99.6
Ol		A	8 / 1 .	592.320	Coarse	core	38.51	0.05	0.00	0.04	0.00	0.35	39.38	21.99	0.01	0.03	100.3
Ol		A	8 / 2 .	592.320	Coarse	rim	38.65	0.02	0.00	0.01	0.00	0.34	39.41	21.94	0.00	0.05	100.4
Ol		A	8 / 3 .	592.320	Coarse	rim	38.33	0.02	0.03	0.04	0.00	0.33	39.38	22.06	0.02	0.07	100.2
Ol		A	8 / 4 .	592.320	Coarse	core	38.24	0.00	0.03	0.03	0.04	0.32	39.23	22.20	0.01	0.07	100.1
Ol		A	8 / 5 .	592.320	Coarse	rim	38.06	0.00	0.02	0.02	0.00	0.35	39.62	21.32	0.00	0.09	99.5
Ol		C	16 / 1 .	592.332	Coarse in	core	38.37	0.01	0.02	0.07	0.00	0.37	39.62	22.38	0.00	0.07	100.8

Mineral		Area	Point	Depth (mbsf)	Layer type	Grain area	SiO2	Al2O3	TiO2	CaO	Na2O	MnO	MgO	FeO	Cr2O3	NiO	Total
Ol		C	16 / 2 .	592.332	Coarse in	rim	38.40	0.00	0.00	0.00	0.00	0.32	38.97	22.19	0.02	0.08	100.0
Ol	360_65R5_79f	C	16 / 3 .	592.332	Coarse in	rim	38.63	0.00	0.00	0.04	0.00	0.35	39.45	22.40	0.07	0.09	100.9
Ol		F	2 / 1 .	592.334	Fine	core	38.34	0.00	0.01	0.00	0.04	0.34	38.66	22.99	0.00	0.09	100.4
Ol		E	5 / 1 .	592.338	Fine	core	38.22	0.00	0.00	0.04	0.00	0.40	38.88	22.67	0.00	0.12	100.3
Ol		E	5 / 2 .	592.338	Fine	rim	38.12	0.00	0.02	0.04	0.00	0.25	38.83	22.79	0.00	0.09	100.1
Ol		E	5 / 3 .	592.338	Fine	core	38.21	0.00	0.03	0.04	0.00	0.33	38.68	22.69	0.00	0.12	100.0
Ol		E	5 / 4 .	592.338	Fine	rim	38.07	0.00	0.03	0.08	0.00	0.35	38.63	22.39	0.00	0.06	99.5
Ol		D	20 / 1 .	592.627	Fine	core	38.35	0.00	0.14	0.05	0.03	0.29	39.40	22.25	0.00	0.14	100.4
Ol		D	20 / 2 .	592.627	Fine	rim	38.47	0.01	0.02	0.01	0.01	0.34	39.49	21.50	0.02	0.05	99.8
Ol		A	3 / 1 .	592.637	Fine	core	38.11	0.02	0.03	0.10	0.00	0.34	39.30	22.38	0.03	0.09	100.2
Ol	360_65R5_111	A	3 / 2 .	592.637	Fine	rim	38.75	0.02	0.00	0.03	0.00	0.31	39.34	21.87	0.03	0.06	100.3
Ol		A	3 / 3 .	592.637	Fine	rim	38.23	0.00	0.02	0.02	0.01	0.39	39.17	22.34	0.00	0.04	100.2
Ol		B	6 / 1 .	592.642	Fine	core	38.57	0.00	0.00	0.04	0.00	0.26	39.25	22.91	0.00	0.07	101.0
Ol		B	6 / 2 .	592.642	Fine	rim	38.01	0.00	0.00	0.07	0.00	0.39	38.69	22.45	0.02	0.08	99.6
Ol		E	9 / 1 .	592.533	Coarse	core	38.39	0.00	0.01	0.01	0.01	0.36	38.41	23.17	0.01	0.07	100.4
Ol		E	9 / 2 .	592.533	Coarse	rim	38.26	0.00	0.00	0.05	0.01	0.40	38.52	23.51	0.05	0.10	100.8
Ol		E	9 / 3 .	592.533	Coarse	rim	37.96	0.00	0.00	0.01	0.00	0.34	38.17	23.16	0.04	0.09	99.7
Ol		A	16 / 1 .	592.549	Coarse	core	38.28	0.01	0.06	0.06	0.00	0.27	38.21	22.89	0.00	0.07	99.7
Ol	360_65R5_102	A	16 / 2 .	592.549	Coarse	rim	38.68	0.01	0.00	0.06	0.00	0.30	38.78	22.36	0.00	0.07	100.2
Ol		A	16 / 3 .	592.549	Coarse	rim	37.95	0.00	0.02	0.04	0.00	0.34	38.52	23.21	0.03	0.07	100.1
Ol		D	20 / 1 .	592.557	Coarse	core	38.33	0.00	0.01	0.09	0.00	0.33	38.11	23.00	0.00	0.08	99.9
Ol		D	20 / 2 .	592.557	Coarse	rim	38.12	0.02	0.03	0.03	0.00	0.38	38.83	22.92	0.02	0.08	100.3
Ol		D	20 / 3 .	592.557	Coarse	rim	38.29	0.00	0.02	0.05	0.00	0.38	38.30	23.28	0.01	0.04	100.3
Ol		F	13 / 1 .	591.536	Fine	core	38.44	0.00	0.00	0.03	0.01	0.31	39.83	21.21	0.00	0.05	99.8
Ol		F	14 / 1 .	591.536	Fine	core	38.60	0.00	0.00	0.04	0.00	0.31	39.64	21.43	0.00	0.10	100.1
Ol		E	18 / 1 .	591.540	Fine	core	38.54	0.00	0.00	0.01	0.00	0.32	39.17	22.05	0.00	0.11	100.2
Ol		E	19 / 5 .	591.540	Fine	core	38.84	0.00	0.00	0.07	0.02	0.30	38.98	22.28	0.00		100.4
Ol		C	20 / 1 .	591.546	Fine	core	38.77	0.03	0.00	0.06	0.00	0.33	39.05	22.13	0.00	0.09	100.4
Ol	360_65R5_2	C	20 / 2 .	591.546	Fine	rim	38.57	0.01	0.04	0.00	0.00	0.31	39.27	21.53	0.02	0.08	99.8
Ol		C	20 / 3 .	591.546	Fine	rim	38.49	0.00	0.00	0.04	0.00	0.33	39.31	21.52	0.00	0.10	99.8
Ol		B	28 / 1 .	591.553	Fine	core	38.60	0.01	0.08	0.02	0.00	0.38	39.48	21.91	0.00	0.10	100.5
Ol		B	28 / 2 .	591.553	Fine	rim	39.04	0.00	0.00	0.04	0.03	0.36	39.34	21.72	0.00	0.05	100.5
Ol		B	28 / 3 .	591.553	Fine	core	38.56	0.00	0.04	0.04	0.01	0.39	39.63	21.59	0.00	0.09	100.3
Ol		B	28 / 4 .	591.553	Fine	rim	38.70	0.01	0.00	0.03	0.00	0.28	39.45	21.68	0.00	0.07	100.2
Ol		A	31 / 1 .	591.576	Fine	rim	38.57	0.00	0.03	0.07	0.00	0.32	39.03	22.63	0.03	0.06	100.6
Ol		A	31 / 2 .	591.576	Fine	rim	38.47	0.00	0.00	0.02	0.00	0.27	38.71	21.71	0.00	0.08	99.2
Ol		A	31 / 3 .	591.576	Fine	core	38.61	0.00	0.03	0.01	0.01	0.30	39.03	22.19	0.02	0.07	100.2
Ol		D	34 / 1 .	591.577	Fine	core	38.70	0.02	0.02	0.05	0.00	0.35	38.89	21.68	0.07	0.10	99.7
Ol		D	34 / 2 .	591.577	Fine	rim	38.60	0.00	0.03	0.04	0.01	0.33	39.01	22.02	0.00	0.10	100.1
Ol		D	34 / 3 .	591.577	Fine	rim	38.70	0.02	0.00	0.02	0.02	0.34	39.13	21.89	0.00	0.08	100.1
Ol	360_65R5_4	D	34 / 4 .	591.577	Fine	rim	38.70	0.00	0.00	0.00	0.00	0.39	39.24	21.91	0.02	0.09	100.3
Ol		B	37 / 1 .	591.581	Fine	core	37.96	0.01	0.01	0.01	0.00	0.29	38.55	22.62	0.01	0.10	99.5

Mineral		Area	Point	Depth (mbsf)	Layer type	Grain area	SiO2	Al2O3	TiO2	CaO	Na2O	MnO	MgO	FeO	Cr2O3	NiO	Total
Ol		B	37 / 2 .	591.581	Fine	rim	38.11	0.01	0.07	0.05	0.01	0.37	38.64	22.40	0.03	0.09	99.6
Ol		B	37 / 3 .	591.581	Fine	core	38.12	0.01	0.00	0.04	0.01	0.38	38.24	22.71	0.02	0.08	99.5
Ol		C	1 / 1 .	592.718	Coarse	core	38.03	0.00	0.00	0.03	0.00	0.30	37.84	23.62	0.02	0.11	99.9
Ol		C	2 / 1 .	592.718	Coarse	rim	38.30	0.03	0.00	0.02	0.00	0.33	38.34	23.44	0.00	0.10	100.5
Ol		C	3 / 1 .	592.718	Coarse	rim	38.69	0.00	0.00	0.05	0.00	0.27	38.18	23.59	0.00	0.05	100.8
Ol		A	6 / 1 .	592.713	Coarse	core	37.98	0.00	0.01	0.06	0.03	0.38	38.50	23.37	0.00	0.10	100.3
Ol	360_65R5_117	A	6 / 2 .	592.713	Coarse	rim	38.52	0.01	0.03	0.06	0.04	0.36	38.45	23.06	0.01	0.11	100.5
Ol		B	9 / 1 .	592.706	Coarse	core	38.30	0.00	0.00	0.03	0.04	0.32	38.39	23.29	0.00	0.04	100.3
Ol		B	9 / 2 .	592.706	Coarse	rim	38.20	0.00	0.00	0.02	0.00	0.40	38.09	23.00	0.00	0.01	99.7
Ol		D	12 / 1 .	592.701	Coarse	rim	38.64	0.00	0.01	0.02	0.01	0.28	38.23	23.25	0.00	0.06	100.5
Ol		D	12 / 2 .	592.701	Coarse	core	38.46	0.02	0.02	0.06	0.01	0.30	38.56	23.22	0.00	0.07	100.6
Ol		E	15 / 1 .	592.695	Coarse	core	38.50	0.00	0.01	0.05	0.00	0.32	37.82	23.56	0.00	0.07	100.3
Ol		B	18 / 1 .	592.742	Coarse	core	37.85	0.00	0.00	0.08	0.00	0.32	38.61	22.50	0.00	0.04	99.3
Ol		B	18 / 2 .	592.742	Coarse	rim	37.90	0.01	0.00	0.04	0.00	0.25	38.49	22.55	0.05	0.02	99.2
Ol		B	18 / 3 .	592.742	Coarse	rim	38.23	0.00	0.01	0.03	0.00	0.33	38.37	23.46	0.04	0.08	100.5
Ol		B	18 / 4 .	592.742	Coarse	rim	38.46	0.03	0.02	0.00	0.00	0.30	38.28	22.78	0.02	0.11	99.9
Ol	360_65R5_120	A	25 / 1 .	592.727	Coarse	rim	38.35	0.00	0.06	0.05	0.00	0.37	37.50	23.10	0.01	0.04	99.4
Ol		A	25 / 2 .	592.727	Coarse	rim	38.00	0.00	0.02	0.08	0.06	0.32	37.45	23.08	0.00	0.09	98.9
Ol		E	29 / 1 .	592.722	Coarse	core	38.01	0.00	0.00	0.02	0.00	0.36	37.98	23.34	0.00	0.09	99.8
Ol		D	31 / 1 .	592.719	Coarse	core	37.95	0.00	0.01	0.07	0.00	0.33	37.86	23.34	0.00	0.10	99.6
Ol		D	31 / 2 .	592.719	Coarse	rim	38.29	0.03	0.00	0.09	0.00	0.32	38.49	22.76	0.01	0.05	99.9
Ol		D	31 / 3 .	592.719	Coarse	rim	38.40	0.01	0.03	0.05	0.07	0.31	38.21	23.24	0.01	0.13	100.3
Ol		A	1 / 1 .	592.024	Coarse	rim	38.19	0.03	0.00	0.07	0.00	0.31	38.79	23.11	0.00	0.04	100.4
Ol		A	2 / 1 .	592.024	Coarse	core	38.08	0.00	0.02	0.05	0.02	0.30	37.56	23.26	0.00	0.07	99.3
Ol		A	3 / 1 .	592.024	Coarse	rim	38.36	0.00	0.00	0.02	0.02	0.41	37.98	22.95	0.00	0.07	99.8
Ol		H	11 / 1 .	592.034	Coarse	core	38.59	0.00	0.01	0.08	0.00	0.36	37.71	23.55	0.00	0.14	100.4
Ol		G	11 / 2 .	592.035	Coarse	rim	38.00	0.00	0.07	0.06	0.02	0.32	38.00	23.42	0.00	0.14	99.9
Ol	360_65R5_51	D	12 / 1 .	592.038	Coarse	core	37.97	0.00	0.00	0.04	0.01	0.27	37.67	23.52	0.00	0.08	99.5
Ol		D	12 / 2 .	592.038	Coarse	rim	38.19	0.01	0.02	0.05	0.00	0.33	38.04	23.46	0.00	0.09	100.1
Ol		D	12 / 3 .	592.038	Coarse	rim	38.18	0.00	0.02	0.03	0.00	0.36	38.03	23.49	0.04	0.09	100.1
Ol		C	16 / 1 .	592.039	Coarse	rim	38.04	0.00	0.03	0.02	0.00	0.39	37.85	23.40	0.00	0.10	99.8
Ol		C	16 / 2 .	592.039	Coarse	core	38.10	0.01	0.00	0.07	0.00	0.39	38.05	23.33	0.01	0.08	100.0
Ol		C	16 / 3 .	592.039	Coarse	rim	38.20	0.00	0.00	0.02	0.02	0.30	37.94	23.08	0.00	0.07	99.6
Ol		B	22 / 1 .	592.404	Fine	rim	38.57	0.01	0.03	0.03	0.00	0.33	39.29	21.38	0.02	0.09	99.7
Ol		B	22 / 2 .	592.404	Fine	core	38.54	0.00	0.01	0.05	0.01	0.33	39.67	21.43	0.00	0.09	100.0
Ol		B	22 / 3 .	592.404	Fine	core	38.28	0.01	0.00	0.04	0.02	0.31	39.37	21.47	0.01	0.07	99.5
Ol		B	22 / 4 .	592.404	Fine	rim	38.68	0.00	0.03	0.00	0.01	0.30	39.39	21.27	0.00	0.08	99.7
Ol		B	22 / 5 .	592.404	Fine	core	38.30	0.02	0.00	0.04	0.00	0.29	39.79	21.71	0.01	0.08	100.2
Ol		E	30 / 1 .	592.391	Fine	rim	38.42	0.02	0.00	0.03	0.00	0.33	39.12	21.82	0.00	0.10	99.8
Ol	360_65R5_87	E	30 / 2 .	592.391	Fine	rim	38.26	0.03	0.00	0.05	0.02	0.33	39.10	21.82	0.00	0.04	99.5
Ol		D	34 / 1 .	592.390	Fine	rim	38.65	0.00	0.00	0.04	0.01	0.32	39.85	21.21	0.01	0.13	100.2
Ol		D	34 / 2 .	592.390	Fine	rim	38.51	0.00	0.04	0.00	0.02	0.34	39.31	21.86	0.00	0.08	100.1

Mineral		Area	Point	Depth (mbsf)	Layer type	Grain area	SiO2	Al2O3	TiO2	CaO	Na2O	MnO	MgO	FeO	Cr2O3	NiO	Total
Ol		D	34 / 3 .	592.390	Fine	rim	38.45	0.05	0.00	0.00	0.00	0.30	39.30	21.91	0.01	0.07	100.0
Ol		F	37 / 1 .	592.384	Fine	core	38.62	0.00	0.03	0.00	0.02	0.35	39.20	21.82	0.07	0.09	100.1
Ol		F	37 / 2 .	592.384	Fine	core	38.43	0.03	0.00	0.03	0.00	0.35	39.23	21.76	0.06	0.10	99.9
Ol		A	1 / 1 .	591.925	Fine	core	38.24	0.00	0.00	0.02	0.04	0.32	38.35	22.76	0.00	0.08	99.8
Ol		A	2 / 1 .	591.925	Fine	rim	38.30	0.00	0.06	0.03	0.00	0.35	38.47	22.97	0.00	0.08	100.2
Ol		A	2 / 2 .	591.925	Fine	core	38.15	0.00	0.00	0.06	0.00	0.36	38.42	22.71	0.00	0.10	99.7
Ol		A	2 / 3 .	591.925	Fine	rim	38.56	0.02	0.00	0.04	0.00	0.36	38.67	22.78	0.00	0.08	100.5
Ol	360_65R5_39	E	7 / 1 .	591.928	Fine	rim	38.43	0.00	0.00	0.03	0.03	0.32	38.46	22.99	0.02	0.11	100.3
Ol		E	7 / 2 .	591.928	Fine	core	38.52	0.03	0.02	0.04	0.00	0.33	38.18	23.35	0.00	0.08	100.5
Ol		E	7 / 3 .	591.928	Fine	rim	38.20	0.01	0.00	0.10	0.01	0.38	38.26	22.94	0.00	0.09	99.9
Ol		C	10 / 1 .	591.934	Fine	core	38.18	0.00	0.01	0.07	0.00	0.33	38.62	22.59	0.01	0.01	99.7
Ol		C	10 / 2 .	591.934	Fine	rim	38.19	0.00	0.00	0.04	0.00	0.29	38.67	22.62	0.00	0.09	99.9
Ol		B	13 / 1 .	591.932	Fine	core	38.52	0.00	0.03	0.00	0.00	0.34	38.80	22.51	0.00	0.08	100.3
Ol		A	16 / 2 .	591.848	Fine	rim	38.48	0.00	0.01	0.03	0.00	0.34	38.64	22.69	0.00	0.08	100.2
Ol		A	16 / 3 .	591.848	Fine	rim	38.65	0.00	0.01	0.01	0.00	0.35	38.71	22.55	0.02	0.08	100.3
Ol	360_65R5_32	C	21 / 1 .	591.840	Fine	core	38.02	0.02	0.05	0.00	0.03	0.35	36.61	24.72	0.01	0.11	99.8
Ol		B	24 / 1 .	591.837	Fine	core	38.62	0.01	0.01	0.05	0.00	0.31	39.20	21.98	0.03	0.06	100.2
Ol		B	24 / 2 .	591.837	Fine	rim	38.27	0.01	0.00	0.02	0.00	0.35	38.43	22.07	0.00	0.08	99.2
Ol		B	4 / 1 .	591.769	Fine	core	38.40	0.02	0.00	0.02	0.00	0.34	38.40	22.88	0.01	0.08	100.1
Ol		B	4 / 2 .	591.769	Fine	core	38.15	0.01	0.01	0.02	0.00	0.34	38.49	22.54	0.00	0.07	99.6
Ol		B	4 / 3 .	591.769	Fine	core	38.20	0.01	0.02	0.03	0.00	0.32	37.97	22.92	0.01	0.07	99.5
Ol	360_65R5_23	A	8 / 1 .	591.773	Fine	core	38.37	0.00	0.02	0.03	0.00	0.31	37.97	23.00	0.00	0.13	99.8
Ol		A	8 / 2 .	591.773	Fine	rim	38.46	0.00	0.04	0.03	0.05	0.30	38.34	22.75	0.00	0.09	99.9
Ol		A	8 / 3 .	591.773	Fine	core	38.22	0.01	0.01	0.07	0.02	0.37	38.26	22.81	0.01	0.06	99.7
Ol		A	8 / 4 .	591.773	Fine	rim	38.36	0.00	0.03	0.05	0.02	0.31	38.14	22.85	0.00	0.10	99.8
Ol		D	16 / 1 .	591.515	Coarse	rim	38.19	0.01	0.00	0.02	0.00	0.40	38.19	22.81	0.00	0.06	99.6
Ol		D	16 / 2 .	591.515	Coarse	core	38.16	0.01	0.04	0.08	0.02	0.35	38.21	22.60	0.00	0.05	99.4
Ol		D	16 / 3 .	591.515	Coarse	rim	38.18	0.01	0.01	0.04	0.00	0.37	38.11	23.44	0.00	0.09	100.2
Ol	360_65R5_0	B	18 / 1 .	591.515	Coarse	rim	38.24	0.00	0.00	0.09	0.00	0.34	38.37	23.09	0.02	0.05	100.1
Ol		B	18 / 2 .	591.515	Coarse	core	38.22	0.03	0.02	0.07	0.02	0.32	38.18	22.83	0.02	0.08	99.6
Ol		B	18 / 3 .	591.515	Coarse	rim	38.52	0.00	0.00	0.08	0.02	0.34	38.00	23.32	0.03	0.08	100.3
Ol		F	26 / 1 .	591.526	Fine	core	38.10	0.02	0.00	0.04	0.00	0.37	37.87	23.23	0.00	0.07	99.6
Ol		F	26 / 2 .	591.526	Fine	core	38.32	0.03	0.00	0.02	0.01	0.42	37.77	23.64	0.00	0.11	100.3
Ol		A	29 / 1 .	591.733	Coarse	rim	38.54	0.00	0.05	0.07	0.00	0.36	38.39	22.82	0.00	0.06	100.2
Ol		A	29 / 2 .	591.733	Coarse	core	38.64	0.02	0.01	0.05	0.00	0.34	38.01	22.92	0.02	0.06	100.0
Ol		A	29 / 3 .	591.733	Coarse	rim	38.38	0.00	0.04	0.02	0.00	0.29	37.91	23.25	0.02	0.11	99.9
Ol		A	29 / 4 .	591.733	Coarse	rim	38.44	0.00	0.05	0.04	0.00	0.34	38.11	23.01	0.00	0.11	100.0
Ol		B	35 / 1 .	591.741	Coarse	core	38.41	0.00	0.09	0.05	0.00	0.41	37.96	23.23	0.00	0.05	100.1
Ol		B	35 / 2 .	591.741	Coarse	rim	37.95	0.01	0.00	0.00	0.00	0.35	37.92	22.89	0.00	0.06	99.2
Ol	360_65R5_21	B	35 / 3 .	591.741	Coarse	rim	38.29	0.00	0.00	0.05	0.00	0.28	38.12	22.90	0.06	0.12	99.7
Ol		B	35 / 4 .	591.741	Coarse	rim	38.23	0.01	0.03	0.04	0.00	0.27	38.91	22.17	0.00	0.07	99.6
Ol		C	37 / 1 .	591.740	Coarse	core	38.34	0.00	0.01	0.03	0.01	0.38	38.03	22.89	0.00	0.09	99.7

Mineral		Area	Point	Depth (mbsf)	Layer type	Grain area	SiO2	Al2O3	TiO2	CaO	Na2O	MnO	MgO	FeO	Cr2O3	NiO	Total
Ol		C	37 / 2 .	591.740	Coarse	rim	38.31	0.02	0.00	0.04	0.00	0.32	37.88	23.47	0.00	0.06	100.0
Ol		C	37 / 3 .	591.740	Coarse	rim	38.31	0.01	0.00	0.00	0.00	0.37	38.00	23.19	0.02	0.09	100.0
Ol		N2	3 / 1 .	592.153	Coarse	core	38.58	0.00	0.04	0.03	0.00	0.29	38.86	22.28	0.03	0.05	100.1
Ol		N2	4 / 1 .	592.153	Coarse	core	38.53	0.01	0.01	0.03	0.00	0.34	39.17	22.52	0.06	0.12	100.7
Ol		N2	7 / 1 .	592.153	Coarse	rim	38.53	0.03	0.00	0.05	0.00	0.36	38.33	22.99	0.00	0.10	100.3
Ol		N2	8 / 1 .	592.153	Coarse	core	38.58	0.02	0.00	0.06	0.00	0.31	38.51	22.85	0.05	0.12	100.4
Ol	360_65R5_63A	N2	9 / 1 .	592.153	Coarse	core	38.46	0.01	0.00	0.02	0.00	0.31	39.08	22.45	0.00	0.10	100.4
Ol		N2	10 / 1 .	592.153	Coarse	rim	38.25	0.00	0.02	0.04	0.00	0.34	38.63	22.35	0.00	0.05	99.6
Ol		N3	43 / 1 .	592.145	Coarse	core	38.01	0.01	0.00	0.08	0.00	0.25	38.51	22.97	0.00	0.04	99.8
Ol		N3	44 / 1 .	592.145	Coarse	rim	38.34	0.02	0.01	0.04	0.02	0.35	38.33	23.02	0.00	0.08	100.1
Ol		E	30 / 1 .	592.178	Coarse	core	38.88	0.02	0.05	0.05	0.05	0.42	39.04	22.37	0.00	0.00	100.7
Ol		E	31 / 1 .	592.178	Coarse	core	38.41	0.00	0.03	0.04	0.01	0.38	38.37	22.66	0.05	0.10	99.9
Ol		E	32 / 1 .	592.178	Coarse	rim	38.41	0.00	0.00	0.05	0.15	0.33	37.96	23.03	0.03	0.07	99.8
Ol		E	33 / 1 .	592.178	Coarse	core	38.51	0.01	0.00	0.04	0.00	0.42	38.06	22.78	0.03	0.11	99.9
Ol		E	34 / 1 .	592.178	Coarse	rim	38.30	0.02	0.02	0.00	0.00	0.35	38.19	23.18	0.00	0.10	100.1
Ol		E	35 / 1 .	592.178	Coarse	rim	38.20	0.03	0.01	0.02	0.00	0.34	38.13	22.68	0.00	0.12	99.5
Ol		E	43 / 1 .	592.182	Coarse	core	38.59	0.00	0.02	0.04	0.00	0.38	37.99	22.78	0.03	0.13	99.9
Ol	360_65R5_63B	E	44 / 1 .	592.182	Coarse	rim	38.83	0.00	0.00	0.02	0.01	0.32	37.90	22.55	0.00	0.02	99.6
Ol		G	75 / 1 .	592.178	Coarse	core	38.58	0.00	0.00	0.10	0.00	0.41	38.06	22.66	0.00	0.05	99.8
Ol		G	77 / 1 .	592.178	Coarse	core	38.87	0.01	0.00	0.05	0.02	0.35	38.23	23.07	0.01	0.09	100.6
Ol		G	78 / 1 .	592.178	Coarse	rim	38.29	0.03	0.00	0.06	0.09	0.45	37.85	22.55	0.00	0.10	99.3
Ol		H	83 / 1 .	592.174	Coarse	core	38.65	0.03	0.01	0.04	0.07	0.36	38.54	23.46	0.00	0.04	101.1
Ol		H	84 / 1 .	592.174	Coarse	core	38.58	0.02	0.01	0.02	0.15	0.44	37.69	23.12	0.00	0.15	100.0
Ol		H	85 / 1 .	592.174	Coarse	core	38.60	0.00	0.01	0.06	0.02	0.40	38.68	23.30	0.03	0.08	101.1
Ol		H	86 / 1 .	592.174	Coarse	rim	38.71	0.00	0.00	0.04	0.01	0.33	38.13	22.66	0.00	0.08	99.9

Calibration standards							Wollastonite (San Carlos)	Al2O3	TiMnO3	Wollastonite	Albite	TiMnO3	Forsterite	Fayalite	Cr2O3	NiO	

In situ major elements concentrations in wt% analysed by EPMA on a Cameca SX100 in LMV (Clermont-Ferrand, France)

Mineral	Sample	Area	Point	Depth (mbsf)	Layer type	Grain area	SiO2	Al2O3	TiO2	CaO	Na2O	K2O	MnO	MgO	FeO	Total
						2 sigma	0.496	0.317	0.060	0.300	0.094	0.035	0.034	0.028	0.061	
						%	0.9	1.1	77.4	2.4	2.1	60.9	298.0	91.3	24.7	
Pl			Counting time (s) - per element				10	10	10	10	10	10	10	10	20	
Pl		C	1 / 1 .	592.280	Coarse	core	53.22	29.43		12.51	4.22	0.08	0.01		0.30	99.8
Pl		C	2 / 1 .	592.280	Coarse	rim	53.30	29.14		12.01	4.55	0.09	0.02		0.28	99.4
Pl		C	6 / 1 .	592.280	Coarse	core	53.01	29.70		12.29	4.44	0.07	0.04		0.30	99.8
Pl		C	7 / 1 .	592.280	Coarse	core	53.92	29.60		12.15	4.55	0.04	0.02		0.20	100.5
Pl		C	8 / 1 .	592.280	Coarse	core	53.91	28.89	0.10	11.88	5.05	0.10	0.02	0.04	0.28	100.3
Pl		B	13 / 1 .	592.287	Coarse	core	53.34	29.40		12.10	4.47	0.04	0.00		0.20	99.5
Pl		B	13 / 2 .	592.287	Coarse	rim	53.58	29.60		12.24	4.43	0.07	0.01		0.18	100.1
Pl		B	14 / 1 .	592.287	Coarse	core	52.94	29.51		12.39	4.21	0.07	0.00		0.30	99.4
Pl		B	14 / 2 .	592.287	Coarse	rim	53.26	29.44		12.41	4.41	0.09	0.03		0.25	99.9
Pl		A	17 / 1 .	592.290	Coarse	core	53.18	29.33		12.69	4.47	0.03	0.00		0.22	99.9
Pl	360_65R5_76	A	17 / 2 .	592.290	Coarse	rim	53.13	29.77		12.51	4.37	0.04	0.00		0.25	100.1
Pl		A	18 / 1 .	592.290	Coarse	core	52.88	29.65		12.88	4.07	0.03	0.00		0.32	99.8
Pl		A	18 / 2 .	592.290	Coarse	rim	52.68	29.71		13.24	4.26	0.05	0.00		0.25	100.2
Pl		G	23 / 1 .	592.299	Coarse	rim	53.47	29.60		12.38	4.44	0.05	0.02		0.38	100.3
Pl		G	23 / 2 .	592.299	Coarse	core	53.48	29.60		12.40	4.41	0.06	0.00		0.30	100.3
Pl		D	24 / 1 .	592.299	Coarse	core	53.51	29.14		12.23	4.55	0.03	0.06		0.19	99.7
Pl		E	28 / 1 .	592.300	Coarse	core	53.48	29.44		12.09	4.48	0.06	0.00		0.26	99.8
Pl		E	28 / 2 .	592.300	Coarse	rim	54.36	28.89		11.81	4.79	0.06	0.02		0.17	100.1
Pl		E	29 / 1 .	592.300	Coarse	core	53.38	29.39		12.50	4.47	0.06	0.00		0.18	100.0
Pl		E	30 / 1 .	592.300	Coarse	core	53.30	29.50		12.75	4.46	0.06	0.01		0.26	100.4
Pl		E	30 / 2 .	592.300	Coarse	rim	53.38	29.39		12.40	4.45	0.03	0.03		0.25	99.9
Pl		D	1 / 1 .	591.788	Coarse in Fine	core	53.40	29.40		12.61	4.46	0.07	0.01		0.20	100.1
Pl		D	2 / 1 .	591.788	Coarse in Fine	rim	53.45	29.45		12.20	4.47	0.03	0.05		0.30	100.0
Pl		D	3 / 1 .	591.788	Coarse in Fine	core	53.38	29.47		12.56	4.49	0.06	0.00		0.17	100.1
Pl		D	3 / 2 .	591.788	Coarse in Fine	rim	51.24	31.07		14.24	3.40	0.03	0.00		0.17	100.2
Pl		B	9 / 1 .	591.795	Coarse in Fine	core	53.22	29.48		12.58	4.34	0.03	0.02		0.30	100.0
Pl		B	9 / 2 .	591.795	Coarse in Fine	rim	49.72	31.80		15.31	2.69	0.01	0.01		0.24	99.8
Pl		B	10 / 1 .	591.795	Coarse in Fine	core	53.40	29.24		12.46	4.44	0.06	0.01		0.23	99.8
Pl		B	10 / 2 .	591.795	Coarse in Fine	rim	50.50	31.06		14.44	3.25	0.03	0.00		0.32	99.6
Pl	360_65R5_27	C	15 / 1 .	591.794	Coarse in Fine	rim	53.40	29.72		12.14	4.42	0.05	0.00		0.28	100.0
Pl		C	15 / 2 .	591.794	Coarse in Fine	core	53.39	29.76		12.48	4.33	0.03	0.00		0.26	100.2
Pl		C	18 / 1 .	591.794	Coarse in Fine	core	53.07	29.49		12.38	4.43	0.06	0.05		0.31	99.8
Pl		A	24 / 1 .	591.800	Coarse in Fine	core	53.68	29.23		12.21	4.46	0.03	0.01		0.19	99.8
Pl		A	24 / 2 .	591.800	Coarse in Fine	rim	53.86	28.96		12.23	4.68	0.05	0.00		0.24	100.0
Pl		E	27 / 1 .	591.805	Coarse in Fine	core	53.14	29.49		12.43	4.45	0.05	0.00		0.20	99.8
Pl		E	28 / 1 .	591.805	Coarse in Fine	core	52.90	30.09		12.45	4.26	0.01	0.00		0.25	100.0
Pl		E	29 / 1 .	591.805	Coarse in Fine	core	52.82	29.58		12.91	4.32	0.02	0.02		0.25	99.9
Pl		E	29 / 2 .	591.805	Coarse in Fine	rim	52.50	29.84		12.82	4.35	0.06	0.01		0.17	99.7

Mineral	Sample	Area	Point	Depth (mbsf)	Layer type	Grain area	SiO2	Al2O3	TiO2	CaO	Na2O	K2O	MnO	MgO	FeO	Total
Pl		M	33 / 1 .	591.718	Coarse	core	52.86	29.54		12.87	4.25	0.07	0.01		0.26	99.9
Pl		M	33 / 2 .	591.718	Coarse	rim	53.44	28.97		11.85	4.55	0.06	0.00		0.27	99.1
Pl		K	37 / 1 .	591.712	Coarse	core	53.14	29.78		12.88	4.36	0.07	0.00		0.33	100.6
Pl		K	37 / 2 .	591.712	Coarse	rim	53.65	29.30		12.34	4.49	0.05	0.00		0.27	100.1
Pl	360_65R5_18	L	41 / 1 .	591.719	Coarse	core	53.05	29.49		12.87	4.27	0.08	0.00		0.31	100.1
Pl		L	41 / 2 .	591.719	Coarse	rim	53.53	29.44		12.19	4.68	0.05	0.00		0.23	100.1
Pl		Bis	26 / 1 .	591.703	Coarse	core	53.54	29.55		12.54	4.40	0.06	0.00		0.26	100.3
Pl		Bis	26 / 2 .	591.703	Coarse	rim	52.86	29.88		12.73	4.38	0.06	0.00		0.29	100.2
Pl		Bis	26 / 3 .	591.703	Coarse	core	54.44	28.72		11.65	4.85	0.07	0.00		0.21	99.9
Pl		E	17 / 1 .	592.004	Coarse	core	53.78	29.36		12.06	4.66	0.04	0.01		0.20	100.1
Pl		E	18 / 1 .	592.004	Coarse	core	53.38	29.42		12.13	4.69	0.08	0.00		0.22	99.9
Pl		E	19 / 1 .	592.004	Coarse	core	52.97	29.73		12.55	4.28	0.05	0.02		0.25	99.8
Pl		E	19 / 2 .	592.004	Coarse	rim	53.07	29.68		12.50	4.22	0.03	0.02		0.21	99.7
Pl		C	21 / 1 .	591.991	Coarse	core	53.18	29.52		12.62	4.41	0.10	0.00		0.28	100.1
Pl		C	21 / 2 .	591.991	Coarse	rim	54.19	28.66		11.73	4.94	0.08	0.03		0.29	99.9
Pl		C	21 / 3 .	591.991	Coarse	core	54.22	28.98		12.04	4.61	0.07	0.01		0.28	100.2
Pl	360_65R5_46	C	21 / 4 .	591.991	Coarse	core	53.55	29.07		11.83	4.62	0.10	0.03		0.25	99.5
Pl		D	25 / 1 .	591.993	Coarse	core	53.28	29.50		12.45	4.47	0.07	0.00		0.25	100.0
Pl		D	25 / 2 .	591.993	Coarse	rim	50.83	31.54		14.40	3.31	0.05	0.00		0.34	100.5
Pl		D	25 / 3 .	591.993	Coarse	core	54.00	29.36		12.13	4.56	0.09	0.00		0.25	100.4
Pl		D	25 / 4 .	591.993	Coarse	rim	53.94	28.91		11.81	4.57	0.07	0.03		0.29	99.6
Pl		D	25 / 5 .	591.993	Coarse	rim	54.12	29.20		12.01	4.65	0.07	0.00		0.23	100.3
Pl		A	28 / 1 .	591.985	Coarse	core	53.85	29.30		12.09	4.60	0.05	0.00		0.22	100.1
Pl		A	28 / 2 .	591.985	Coarse	core	52.63	29.78		13.04	4.12	0.04	0.03		0.34	100.0
Pl		A	28 / 3 .	591.985	Coarse	rim	54.21	28.49		11.45	4.91	0.06	0.02		0.28	99.4
Pl		C	1 / 1 .	592.466	Fine	core	53.84	29.41		12.27	4.37	0.02	0.00		0.21	100.1
Pl		C	2 / 1 .	592.466	Fine	rim	53.72	29.36		12.47	4.54	0.05	0.00		0.20	100.3
Pl		C	3 / 1 .	592.466	Fine	core	52.31	30.52		13.30	3.79	0.01	0.06		0.20	100.2
Pl		C	3 / 2 .	592.466	Fine	core	53.60	29.80		12.26	4.38	0.02	0.02		0.21	100.3
Pl		C	3 / 3 .	592.466	Fine	core	53.39	29.75		13.00	4.26	0.05	0.00		0.22	100.7
Pl		A	9 / 1 .	592.466	Fine	core	53.24	29.47		12.30	4.43	0.00	0.03		0.19	99.7
Pl		A	9 / 2 .	592.466	Fine	rim	53.53	29.76		12.46	4.53	0.05	0.00		0.20	100.5
Pl	360_65R5_94	A	9 / 3 .	592.466	Fine	core	52.59	29.96		13.10	4.41	0.01	0.00		0.25	100.3
Pl		A	9 / 4 .	592.466	Fine	rim	50.89	31.44		14.46	3.16	0.01	0.00		0.21	100.2
Pl		B	13 / 1 .	592.456	Fine	core	53.47	29.53		12.62	4.44	0.03	0.00		0.25	100.4
Pl		B	13 / 2 .	592.456	Fine	rim	54.20	29.47		12.21	4.63	0.03	0.00		0.17	100.7
Pl		B	14 / 1 .	592.456	Fine	core	53.88	29.68		12.55	4.66	0.01	0.01		0.20	101.0
Pl		B	14 / 2 .	592.456	Fine	rim	53.16	29.37		12.29	4.57	0.04	0.00		0.20	99.6
Pl		D	17 / 1 .	592.453	Fine	core	53.71	29.25		12.04	4.91	0.03	0.00		0.25	100.2
Pl		D	17 / 2 .	592.453	Fine	rim	53.29	29.73		12.73	4.42	0.03	0.02		0.25	100.5
Pl		A	20 / 1 .	592.354	Coarse in Fine	core	53.42	29.28		12.11	4.71	0.06	0.00		0.28	99.9
Pl		A	20 / 2 .	592.354	Coarse in Fine	rim	52.61	29.51		12.31	4.45	0.01	0.01		0.29	99.2

Mineral		Area	Point	Depth (mbsf)	Layer type	Grain area	SiO2	Al2O3	TiO2	CaO	Na2O	K2O	MnO	MgO	FeO	Total
Pl		A	20 / 3 .	592.354	Coarse in Fine	core	52.94	29.48		12.48	4.35	0.07	0.03		0.26	99.6
Pl		A	20 / 4 .	592.354	Coarse in Fine	rim	53.21	29.40		12.34	4.39	0.04	0.03		0.22	99.6
Pl		D	22 / 1 .	592.357	Coarse in Fine	core	53.21	29.32		12.15	4.69	0.07	0.00		0.21	99.6
Pl		D	22 / 2 .	592.357	Coarse in Fine	rim	54.00	29.39		12.12	4.69	0.03	0.00		0.15	100.4
Pl		D	22 / 3 .	592.357	Coarse in Fine	core	53.34	29.35		12.35	4.64	0.03	0.00		0.20	99.9
Pl		D	22 / 4 .	592.357	Coarse in Fine	rim	53.17	29.26		12.10	4.75	0.02	0.06		0.21	99.6
Pl	360_65R5_83	C	23 / 1 .	592.365	Coarse in Fine	core	53.09	29.26		12.46	4.48	0.05	0.02		0.16	99.5
Pl		C	23 / 2 .	592.365	Coarse in Fine	rim	53.33	29.49		12.52	4.51	0.05	0.02		0.32	100.2
Pl		B	28 / 1 .	592.369	Coarse in Fine	core	53.39	29.37		12.45	4.48	0.02	0.00		0.23	100.0
Pl		B	28 / 2 .	592.369	Coarse in Fine	rim	53.32	29.41		12.30	4.52	0.01	0.00		0.21	99.8
Pl		B	28 / 3 .	592.369	Coarse in Fine	core	53.22	29.32		12.19	4.46	0.05	0.00		0.15	99.4
Pl		B	28 / 4 .	592.369	Coarse in Fine	rim	53.16	29.52		12.57	4.49	0.01	0.04		0.19	100.0
Pl		F	30 / 1 .	592.374	Fine	core	52.98	29.40		12.54	4.53	0.03	0.00		0.20	99.7
Pl		F	30 / 2 .	592.374	Fine	rim	53.29	29.65		12.25	4.51	0.04	0.03		0.22	100.0
Pl		E	33 / 1 .	592.376	Fine	core	53.22	29.53		12.37	4.54	0.02	0.00		0.42	100.1
Pl		E	33 / 2 .	592.376	Fine	core	53.44	29.46		12.53	4.59	0.03	0.01		0.27	100.3
Pl		E	33 / 3 .	592.376	Fine	rim	51.38	31.00		14.08	3.49	0.03	0.00		0.19	100.2
Pl	360_65R5_91	E	5 / 1 .	592.428	Fine	rim	53.91	29.77		12.71	4.30	0.00	0.00		0.26	100.9
Pl		E	7 / 1 .	592.428	Fine	core	53.23	29.45		12.44	4.40	0.02	0.01		0.18	99.7
Pl		E	7 / 2 .	592.428	Fine	core	53.09	29.39		12.50	4.46	0.03	0.03		0.19	99.7
Pl		E	7 / 3 .	592.428	Fine	rim	52.35	29.51		12.78	4.29	0.03	0.00		0.27	99.2
Pl		E	7 / 4 .	592.428	Fine	core	53.23	29.67		12.51	4.42	0.04	0.02		0.17	100.1
Pl		E	7 / 5 .	592.428	Fine	rim	52.68	30.13		13.01	4.24	0.01	0.00		0.14	100.2
Pl		D	11 / 1 .	592.432	Fine	core	53.31	29.59		12.30	4.63	0.01	0.00		0.26	100.1
Pl		D	11 / 2 .	592.432	Fine	rim	52.83	29.28		12.58	4.58	0.05	0.01		0.30	99.6
Pl		D	11 / 3 .	592.432	Fine	core	50.10	31.77		14.83	3.08	0.02	0.02		0.24	100.1
Pl		D	11 / 4 .	592.432	Fine	core	53.26	29.64		12.36	4.56	0.03	0.00		0.18	100.0
Pl		F	12 / 1 .	592.435	Fine	core	53.05	29.85		12.65	4.47	0.04	0.01		0.27	100.3
Pl		F	12 / 2 .	592.435	Fine	rim	51.25	30.81		13.84	3.64	0.05	0.04		0.33	99.9
Pl		F	12 / 3 .	592.435	Fine	core	52.63	29.67		12.54	4.55	0.02	0.00		0.18	99.6
Pl		F	12 / 4 .	592.435	Fine	rim	53.40	29.66		12.41	4.46	0.04	0.01		0.23	100.2
Pl		B	18 / 1 .	592.443	CinF	core	53.92	29.26		12.33	4.55	0.05	0.03		0.21	100.3
Pl		B	18 / 2 .	592.443	CinF	rim	53.12	29.61		12.33	4.51	0.04	0.00		0.32	99.9
Pl		B	18 / 3 .	592.443	CinF	core	52.88	29.28		12.48	4.51	0.08	0.01		0.25	99.5
Pl		B	18 / 4 .	592.443	CinF	rim	54.12	28.89		11.79	4.98	0.09	0.01		0.25	100.1
Pl		A	22 / 1 .	592.445	CinF	core	53.61	29.62		12.21	4.59	0.03	0.03		0.29	100.4
Pl		A	22 / 2 .	592.445	CinF	rim	53.87	28.98		11.69	4.93	0.05	0.00		0.27	99.8
Pl		A	22 / 3 .	592.445	CinF	core	53.44	29.32		12.19	4.33	0.05	0.00		0.22	99.5
Pl		A	22 / 4 .	592.445	CinF	rim	52.83	29.78		12.45	4.36	0.01	0.00		0.21	99.6
Pl		C	25 / 1 .	592.446	CinF	core	53.22	29.35		12.21	4.43	0.03	0.03		0.20	99.5
Pl		C	25 / 2 .	592.446	CinF	rim	52.89	29.57		12.60	4.37	0.04	0.00		0.20	99.7
Pl		C	25 / 3 .	592.446	CinF	core	52.41	29.72		12.72	4.40	0.05	0.00		0.26	99.6

Mineral	Sample	Area	Point	Depth (mbsf)	Layer type	Grain area	SiO2	Al2O3	TiO2	CaO	Na2O	K2O	MnO	MgO	FeO	Total
Pl		C	25 / 4 .	592.446	CinF	rim	53.29	29.50		12.44	4.44	0.06	0.00		0.30	100.0
Pl		C	25 / 5 .	592.446	CinF	rim	53.47	29.34		12.32	4.85	0.07	0.00		0.23	100.3
Pl		D	4 / 1 .	592.313	Coarse	core	53.54	29.33		12.17	4.57	0.05	0.01		0.27	99.9
Pl		D	4 / 2 .	592.313	Coarse	rim	52.07	30.17		12.99	3.98	0.03	0.04		0.21	99.5
Pl		D	4 / 3 .	592.313	Coarse	core	53.14	29.62		12.64	4.40	0.04	0.00		0.24	100.1
Pl		D	4 / 4 .	592.313	Coarse	rim	52.87	29.72		12.80	4.31	0.06	0.04		0.16	100.0
Pl		C	6 / 1 .	592.321	Coarse	core	52.86	30.02		12.68	4.35	0.05	0.04		0.26	100.3
Pl		C	6 / 2 .	592.321	Coarse	rim	53.64	29.23		12.56	4.57	0.06	0.04		0.17	100.3
Pl	360_65R5_79g	A	9 / 1 .	592.320	Coarse	core	53.02	29.49		12.39	4.40	0.08	0.03		0.23	99.6
Pl		A	9 / 2 .	592.320	Coarse	rim	53.02	29.58		12.15	4.42	0.05	0.04		0.23	99.5
Pl		A	9 / 3 .	592.320	Coarse	core	52.57	29.73		12.41	4.42	0.05	0.01		0.26	99.5
Pl		B	11 / 1 .	592.328	Fine	core	54.08	29.32		11.84	4.69	0.05	0.00		0.20	100.2
Pl		B	11 / 2 .	592.328	Fine	rim	52.88	29.78		12.87	4.38	0.04	0.00		0.22	100.2
Pl		B	11 / 3 .	592.328	Fine	rim	53.23	29.63		12.31	4.58	0.01	0.00		0.14	99.9
Pl		D	13 / 1 .	592.330	CinF	core	53.27	29.40		12.11	4.51	0.03	0.00		0.19	99.5
Pl		D	13 / 2 .	592.330	CinF	rim	53.75	29.03		12.16	4.75	0.05	0.00		0.22	100.0
Pl		D	13 / 3 .	592.330	CinF	core	53.50	29.30		12.10	4.67	0.03	0.06		0.17	99.8
Pl		D	13 / 4 .	592.330	CinF	rim	53.06	29.64		12.31	4.80	0.04	0.00		0.24	100.1
Pl		A	15 / 1 .	592.336	Fine	core	53.18	29.39		12.47	4.63	0.06	0.02		0.32	100.1
Pl		A	15 / 2 .	592.336	Fine	rim	52.90	29.92		12.67	4.39	0.04	0.00		0.23	100.1
Pl		A	15 / 3 .	592.336	Fine	core	52.91	29.99		12.70	4.33	0.07	0.01		0.22	100.2
Pl		A	15 / 4 .	592.336	Fine	rim	52.05	30.17		13.07	4.09	0.03	0.00		0.26	99.7
Pl		C	18 / 1 .	592.332	CinF	core	53.19	29.51		12.33	4.29	0.01	0.00		0.21	99.5
Pl		C	18 / 2 .	592.332	CinF	rim	49.66	32.00		14.93	2.84	0.04	0.00		0.37	99.8
Pl		C	18 / 3 .	592.332	CinF	core	53.18	29.42		12.36	4.48	0.06	0.00		0.24	99.7
Pl		C	18 / 4 .	592.332	CinF	rim	51.52	30.80		13.95	3.75	0.02	0.00		0.26	100.3
Pl		B	20 / 1 .	592.332	CinF	core	53.18	29.18		11.92	4.49	0.04	0.00		0.18	99.0
Pl		B	20 / 2 .	592.332	CinF	rim	52.93	29.92		12.67	4.42	0.07	0.03		0.22	100.2
Pl		B	20 / 3 .	592.332	CinF	core	53.01	29.36		12.36	4.54	0.06	0.00		0.23	99.6
Pl	360_65R5_79f	B	20 / 4 .	592.332	CinF	rim	53.93	29.28		11.89	4.71	0.06	0.03		0.16	100.0
Pl		B	20 / 5 .	592.332	CinF	rim	53.19	29.17		11.80	4.54	0.04	0.00		0.23	99.0
Pl		F	4 / 1 .	592.334	Fine	core	53.22	29.64		12.24	4.49	0.05	0.03		0.24	99.9
Pl		F	4 / 2 .	592.334	Fine	rim	50.96	30.84		14.31	3.42	0.03	0.03		0.19	99.8
Pl		F	4 / 3 .	592.334	Fine	core	53.14	29.30		12.37	4.36	0.05	0.00		0.21	99.4
Pl		F	4 / 4 .	592.334	Fine	rim	52.94	29.50		12.35	4.54	0.05	0.00		0.17	99.5
Pl		F	4 / 5 .	592.334	Fine	rim	52.20	30.31		13.43	3.88	0.03	0.03		0.22	100.1
Pl		E	7 / 1 .	592.338	Fine	core	52.56	29.24		12.16	4.41	0.02	0.00		0.22	98.6
Pl		E	7 / 2 .	592.338	Fine	rim	51.74	30.25		13.27	4.13	0.02	0.04		0.39	99.9
Pl		E	7 / 3 .	592.338	Fine	rim	52.68	29.87		12.80	4.42	0.04	0.00		0.19	100.0
Pl		E	7 / 4 .	592.338	Fine	core	53.49	29.71		12.69	4.37	0.04	0.04		0.21	100.5
Pl		E	7 / 5 .	592.338	Fine	rim	53.14	29.55		12.27	4.56	0.03	0.00		0.20	99.8
Pl		A	14 / 1 .	592.336	Fine	rim	50.49	31.79		14.87	3.25	0.02	0.00		0.25	100.7

Mineral		Area	Point	Depth (mbsf)	Layer type	Grain area	SiO2	Al2O3	TiO2	CaO	Na2O	K2O	MnO	MgO	FeO	Total
Pl		B	17 / 1 .	592.332	CinF	rim	51.52	30.90		13.73	3.71	0.01	0.00		0.26	100.1
Pl		D	22 / 1 .	592.627	Fine	core	53.72	29.17		12.34	4.66	0.03	0.00		0.25	100.2
Pl		D	22 / 2 .	592.627	Fine	rim	52.92	29.54		12.64	4.44	0.04	0.03		0.23	99.8
Pl		D	22 / 3 .	592.627	Fine	core	53.31	29.55		12.55	4.48	0.03	0.00		0.27	100.2
Pl		D	22 / 4 .	592.627	Fine	rim	52.70	29.32		12.80	4.47	0.05	0.00		0.16	99.5
Pl		D	22 / 5 .	592.627	Fine	rim	53.71	29.21		11.93	4.67	0.07	0.03		0.19	99.8
Pl		C	24 / 1 .	592.631	Fine	rim	53.31	29.43		12.29	4.66	0.03	0.05		0.33	100.1
Pl		C	24 / 2 .	592.631	Fine	rim	53.14	29.30		12.34	4.64	0.05	0.02		0.29	99.8
Pl		C	27 / 1 .	592.631	Fine	core	53.16	29.71		12.28	4.59	0.06	0.00		0.17	100.0
Pl		C	27 / 2 .	592.631	Fine	rim	53.39	29.15		12.18	4.76	0.06	0.01		0.22	99.8
Pl		C	27 / 3 .	592.631	Fine	rim	53.13	29.39		12.57	4.63	0.05	0.03		0.28	100.1
Pl	360_65R5_111	C	27 / 4 .	592.631	Fine	core	52.97	29.76		12.57	4.53	0.06	0.01		0.32	100.2
Pl		C	27 / 5 .	592.631	Fine	rim	51.75	30.58		13.81	3.97	0.02	0.01		0.17	100.3
Pl		A	1 / 1 .	592.637	Fine	core	53.10	29.12		12.04	4.71	0.05	0.00		0.16	99.2
Pl		A	2 / 1 .	592.637	Fine	rim	51.43	30.63		13.60	3.83	0.06	0.00		0.31	99.9
Pl		A	2 / 2 .	592.637	Fine	core	53.35	29.01		12.13	4.74	0.02	0.03		0.14	99.4
Pl		A	2 / 3 .	592.637	Fine	rim	53.15	29.41		12.75	4.38	0.04	0.03		0.25	100.0
Pl		A	2 / 4 .	592.637	Fine	core	53.04	29.70		12.48	4.45	0.05	0.00		0.22	99.9
Pl		A	5 / 1 .	592.637	Fine	rim	53.30	29.65		12.61	4.46	0.03	0.03		0.29	100.4
Pl		B	7 / 1 .	592.642	Fine	core	52.96	29.59		12.57	4.54	0.04	0.00		0.23	99.9
Pl		B	7 / 2 .	592.642	Fine	rim	52.27	30.23		12.86	4.17	0.04	0.01		0.18	99.8
Pl		B	7 / 3 .	592.642	Fine	core	52.90	29.61		12.72	4.55	0.06	0.00		0.26	100.1
Pl		B	7 / 4 .	592.642	Fine	rim	52.74	29.79		12.76	4.38	0.06	0.05		0.22	100.0
Pl		E	10 / 1 .	592.533	Coarse	core	52.95	29.49		12.69	4.57	0.04	0.04		0.33	100.1
Pl		E	10 / 2 .	592.533	Coarse	rim	52.93	29.33		12.49	4.43	0.06	0.01		0.27	99.5
Pl		E	10 / 3 .	592.533	Coarse	rim	53.12	29.25		12.42	4.64	0.04	0.03		0.23	99.7
Pl		C	13 / 1 .	592.533	Coarse	core	53.52	29.51		12.09	4.62	0.05	0.03		0.21	100.0
Pl		C	13 / 2 .	592.533	Coarse	rim	53.33	29.58		12.55	4.67	0.05	0.00		0.18	100.4
Pl		C	13 / 3 .	592.533	Coarse	core	52.08	29.78		12.78	4.25	0.06	0.00		0.28	99.2
Pl		C	13 / 4 .	592.533	Coarse	core	52.93	29.31		12.48	4.54	0.08	0.01		0.23	99.6
Pl		C	13 / 5 .	592.533	Coarse	rim	53.15	29.13		12.26	4.75	0.07	0.01		0.21	99.6
Pl		B	14 / 2 .	592.550	Coarse	rim	52.61	29.60		12.83	4.49	0.07	0.02		0.25	99.9
Pl		B	14 / 3 .	592.550	Coarse	rim	52.21	29.87		13.05	4.19	0.01	0.00		0.30	99.6
Pl		B	14 / 4 .	592.550	Coarse	core	52.54	29.28		12.52	4.53	0.07	0.02		0.21	99.2
Pl		B	14 / 5 .	592.550	Coarse	rim	53.28	29.53		12.33	4.73	0.08	0.01		0.24	100.2
Pl		E	1 / 1 .	592.533	Coarse	core	53.01	29.87		12.60	4.42	0.06	0.05		0.21	100.2
Pl		E	4 / 1 .	592.533	Coarse	rim	53.15	28.96		12.09	4.45	0.09	0.03		0.38	99.1
Pl	360_65R5_102	C	12 / 1 .	592.533	Coarse	rim	53.49	29.22		12.15	4.83	0.03	0.00		0.44	100.1
Pl		A	18 / 1 .	592.549	Coarse	core	52.45	29.55		12.90	4.25	0.05	0.02		0.30	99.5
Pl		A	18 / 2 .	592.549	Coarse	rim	52.84	29.80		12.61	4.36	0.04	0.02		0.23	99.9
Pl		A	18 / 4 .	592.549	Coarse	rim	52.41	29.49		13.01	4.12	0.06	0.02		0.28	99.4
Pl		A	18 / 5 .	592.549	Coarse	core	52.92	29.66		12.47	4.45	0.06	0.00		0.18	99.7

Mineral		Area	Point	Depth (mbsf)	Layer type	Grain area	SiO2	Al2O3	TiO2	CaO	Na2O	K2O	MnO	MgO	FeO	Total
Pl		A	18 / 6 .	592.549	Coarse	rim	52.39	29.78		12.89	4.34	0.08	0.00		0.24	99.7
Pl		A	18 / 7 .	592.549	Coarse	rim	53.38	29.19		12.00	4.60	0.09	0.02		0.23	99.5
Pl		D	22 / 1 .	592.557	Coarse	core	53.23	28.99		12.24	4.46	0.07	0.00		0.21	99.2
Pl		D	22 / 2 .	592.557	Coarse	rim	53.63	29.13		12.23	4.51	0.07	0.01		0.19	99.8
Pl		D	22 / 3 .	592.557	Coarse	core	52.43	29.73		12.95	4.29	0.06	0.00		0.28	99.7
Pl		D	22 / 4 .	592.557	Coarse	rim	52.48	29.90		12.62	4.53	0.05	0.03		0.25	99.9
Pl		D	22 / 5 .	592.557	Coarse	rim	53.08	29.35		12.60	4.37	0.11	0.00		0.25	99.8
Pl		F	1 / 1 .	591.536	Fine	core	53.35	29.65		12.34	4.54	0.03			0.23	100.1
Pl		F	2 / 1 .	591.536	Fine	core	50.90	31.38		14.22	3.27	0.02			0.22	100.0
Pl		F	3 / 1 .	591.536	Fine	rim	51.50	31.15		14.14	3.69	0.03			0.28	100.8
Pl		F	4 / 1 .	591.536	Fine	core	52.86	29.94		12.88	4.38	0.05			0.15	100.3
Pl		F	5 / 1 .	591.536	Fine	rim	49.83	31.82		15.08	3.20	0.05			0.23	100.2
Pl		F	16 / 1 .	591.536	Fine	rim	53.09	29.99		12.79	4.43	0.03			0.22	100.5
Pl		E	17 / 1 .	591.540	Fine	core	53.79	29.52		11.96	4.67	0.04			0.24	100.2
Pl		E	17 / 2 .	591.540	Fine	rim	52.95	29.30		12.08	4.73	0.03			0.23	99.3
Pl		E	17 / 3 .	591.540	Fine	core	53.73	29.64		12.21	4.47	0.05			0.22	100.3
Pl		E	17 / 4 .	591.540	Fine	core	53.22	29.53		12.15	4.57	0.07			0.17	99.7
Pl		C	21 / 1 .	591.546	Fine	core	53.48	29.32		12.12	4.70	0.03			0.30	100.0
Pl		C	21 / 2 .	591.546	Fine	rim	53.15	29.38		12.28	4.39	0.02			0.19	99.4
Pl		C	21 / 3 .	591.546	Fine	rim	53.48	29.34		12.21	4.52	0.05			0.18	99.8
Pl		C	21 / 4 .	591.546	Fine	core	53.28	29.69		12.49	4.39	0.05			0.28	100.2
Pl		C	21 / 5 .	591.546	Fine	core	53.77	29.35		12.16	4.66	0.02			0.20	100.2
Pl		G	23 / 1 .	591.541	Fine	rim	51.61	30.53		13.69	3.94	0.05			0.14	100.0
Pl	360_65R5_2	G	23 / 2 .	591.541	Fine	core	53.24	29.44		12.50	4.60	0.02			0.18	100.0
Pl		G	23 / 3 .	591.541	Fine	rim	52.62	29.77		12.69	4.20	0.05			0.24	99.6
Pl		G	23 / 4 .	591.541	Fine	core	53.01	29.54		12.48	4.59	0.06			0.14	99.8
Pl		G	23 / 5 .	591.541	Fine	core	53.29	29.64		12.13	4.57	0.01			0.16	99.8
Pl		A	25 / 1 .	591.551	Fine	core	53.62	28.95		11.78	4.81	0.04			0.21	99.4
Pl		A	25 / 2 .	591.551	Fine	rim	53.25	29.37		12.18	4.61	0.03			0.21	99.6
Pl		A	25 / 3 .	591.551	Fine	rim	53.20	29.28		11.98	4.62	0.06			0.23	99.4
Pl		A	25 / 4 .	591.551	Fine	core	52.94	29.60		12.40	4.56	0.05			0.23	99.8
Pl		A	25 / 5 .	591.551	Fine	core	53.13	29.14		12.20	4.52	0.02			0.17	99.2
Pl		A	25 / 6 .	591.551	Fine	core	52.86	29.18		12.17	4.61	0.04			0.29	99.1
Pl		D	27 / 2 .	591.553	Fine	rim	53.22	30.11		12.76	4.41	0.05			0.18	100.7
Pl		D	27 / 3 .	591.553	Fine	core	53.94	29.41		11.99	4.67	0.05			0.20	100.3
Pl		D	27 / 4 .	591.553	Fine	rim	53.12	29.91		12.33	4.44	0.08			0.21	100.1
Pl		D	27 / 5 .	591.553	Fine	core	53.71	29.31		12.09	4.63	0.04			0.19	100.0
Pl		B	30 / 1 .	591.553	Fine	core	53.13	29.65		12.29	4.55	0.06			0.23	99.9
Pl		B	30 / 2 .	591.553	Fine	rim	53.50	29.26		12.41	4.69	0.04			0.22	100.1
Pl		B	30 / 3 .	591.553	Fine	core	53.09	29.37		12.59	4.45	0.02			0.27	99.8
Pl		B	30 / 4 .	591.553	Fine	rim	52.82	29.68		12.44	4.39	0.04			0.33	99.7
Pl		A	33 / 1 .	591.576	Fine	core	52.97	29.39		12.45	4.49	0.05			0.25	99.6

Mineral		Area	Point	Depth (mbsf)	Layer type	Grain area	SiO2	Al2O3	TiO2	CaO	Na2O	K2O	MnO	MgO	FeO	Total
Pl		A	33 / 2 .	591.576	Fine	rim	53.34	29.36		12.27	4.54	0.05			0.23	99.8
Pl		A	33 / 3 .	591.576	Fine	rim	52.76	29.95		12.42	4.46	0.02			0.25	99.9
Pl		A	33 / 4 .	591.576	Fine	core	53.18	29.26		12.21	4.85	0.04			0.28	99.8
Pl		A	33 / 5 .	591.576	Fine	core	53.33	29.12		11.87	4.60	0.02			0.27	99.2
Pl		A	33 / 6 .	591.576	Fine	core	53.47	29.35		12.24	4.78	0.04			0.19	100.1
Pl		D	36 / 1 .	591.577	Fine	core	53.42	29.33		12.27	4.72	0.04			0.24	100.0
Pl		D	36 / 2 .	591.577	Fine	rim	53.05	29.35		12.54	4.71	0.02			0.37	100.0
Pl	360_65R5_4	D	36 / 3 .	591.577	Fine	core	52.66	29.66		12.92	4.46	0.04			0.21	99.9
Pl		D	36 / 4 .	591.577	Fine	core	53.82	29.17		12.04	4.79	0.09			0.16	100.1
Pl		D	36 / 5 .	591.577	Fine	rim	53.09	29.29		12.34	4.51	0.06			0.29	99.6
Pl		B	39 / 1 .	591.581	Fine	core	53.80	29.37		12.14	4.86	0.02			0.31	100.5
Pl		B	39 / 2 .	591.581	Fine	rim	53.40	29.41		12.23	4.68	0.05			0.24	100.0
Pl		B	39 / 3 .	591.581	Fine	core	54.01	29.09		12.02	4.82	0.05			0.26	100.2
Pl		B	39 / 4 .	591.581	Fine	rim	53.66	29.37		12.19	4.55	0.04			0.21	100.0
Pl		C	41 / 1 .	591.583	Fine	core	53.65	29.41		12.06	4.82	0.01			0.24	100.2
Pl		C	41 / 2 .	591.583	Fine	core	53.11	29.26		12.11	4.57	0.05			0.22	99.3
Pl		C	41 / 3 .	591.583	Fine	rim	53.06	29.69		12.46	4.61	0.06			0.26	100.1
Pl		C	41 / 4 .	591.583	Fine	rim	53.06	29.13		12.21	4.82	0.07			0.27	99.6
Pl		C	5 / 1 .	592.718	Coarse	core	53.21	29.88		12.46	4.31	0.08			0.24	100.2
Pl		C	5 / 2 .	592.718	Coarse	rim	52.86	29.76		12.69	4.50	0.06			0.16	100.0
Pl		C	5 / 3 .	592.718	Coarse	core	53.30	29.54		12.31	4.49	0.02			0.30	100.0
Pl		A	8 / 1 .	592.713	Coarse	core	52.97	29.67		12.62	4.40	0.04			0.29	100.0
Pl		A	8 / 2 .	592.713	Coarse	core	53.51	29.69		12.33	4.45	0.11			0.29	100.4
Pl		A	8 / 3 .	592.713	Coarse	core	53.47	29.49		12.48	4.47	0.07			0.18	100.2
Pl		B	11 / 1 .	592.706	Coarse	core	53.05	29.87		12.35	4.49	0.06			0.25	100.1
Pl		B	11 / 2 .	592.706	Coarse	rim	52.84	29.60		12.59	4.33	0.06			0.39	99.8
Pl	360_65R5_117	B	11 / 3 .	592.706	Coarse	rim	53.18	29.55		12.43	4.41	0.06			0.22	99.8
Pl		B	11 / 4 .	592.706	Coarse	core	53.98	28.98		11.82	4.83	0.05			0.19	99.8
Pl		D	14 / 1 .	592.701	Coarse	core	53.17	29.85		12.47	4.43	0.07			0.21	100.2
Pl		D	14 / 2 .	592.701	Coarse	core	53.13	29.79		12.15	4.56	0.09			0.23	99.9
Pl		D	14 / 3 .	592.701	Coarse	core	52.80	29.78		12.45	4.37	0.04			0.21	99.7
Pl		D	14 / 4 .	592.701	Coarse	rim	53.42	29.59		12.33	4.62	0.02			0.21	100.2
Pl		E	17 / 1 .	592.695	Coarse	core	53.77	29.66	0.09	12.04	4.50	0.04	0.00	0.00	0.32	100.4
Pl		E	17 / 2 .	592.695	Coarse	core	52.21	29.38	0.02	12.54	4.38	0.09	0.02	0.02	0.23	98.9
Pl		E	17 / 3 .	592.695	Coarse	core	53.54	29.23	0.05	12.14	4.65	0.05	0.01	0.02	0.24	99.9
Pl		B	20 / 1 .	592.742	Coarse	core	53.62	29.27		12.07	4.90	0.07			0.19	100.1
Pl		B	20 / 2 .	592.742	Coarse	rim	54.14	28.90		11.35	5.01	0.07			0.20	99.7
Pl		B	20 / 3 .	592.742	Coarse	rim	53.24	29.28		12.17	4.54	0.08			0.18	99.5
Pl		B	20 / 4 .	592.742	Coarse	core	52.99	29.47		12.40	4.38	0.06			0.27	99.6
Pl		C	22 / 1 .	592.742	Coarse	core	52.68	29.27		12.49	4.45	0.11			0.24	99.2
Pl		C	22 / 2 .	592.742	Coarse	rim	53.35	29.28		12.10	4.51	0.04			0.27	99.6
Pl		C	24 / 1 .	592.742	Coarse	core	53.84	29.37		11.91	4.76	0.07			0.15	100.1

Mineral		Area	Point	Depth (mbsf)	Layer type	Grain area	SiO2	Al2O3	TiO2	CaO	Na2O	K2O	MnO	MgO	FeO	Total
Pl	360_65R5_120	C	24 / 2 .	592.742	Coarse	core	53.08	29.79		12.76	4.45	0.05			0.22	100.3
Pl		A	28 / 1 .	592.727	Coarse	core	53.15	29.16		12.08	4.74	0.11			0.25	99.5
Pl		A	28 / 2 .	592.727	Coarse	core	53.59	29.00		11.69	4.94	0.08			0.27	99.6
Pl		A	28 / 3 .	592.727	Coarse	rim	53.44	29.15		11.85	4.71	0.06			0.23	99.4
Pl		E	30 / 1 .	592.722	Coarse	core	51.98	29.86		12.88	4.20	0.08			0.25	99.2
Pl		E	30 / 2 .	592.722	Coarse	core	54.10	28.72		11.67	5.10	0.06			0.24	99.9
Pl		E	30 / 3 .	592.722	Coarse	core	53.24	29.35		12.02	4.57	0.09			0.25	99.5
Pl		E	30 / 4 .	592.722	Coarse	core	53.20	29.32		11.82	4.75	0.07			0.25	99.4
Pl		D	33 / 1 .	592.719	Coarse	core	53.82	28.54		11.62	4.96	0.07			0.23	99.2
Pl		D	33 / 2 .	592.719	Coarse	core	52.29	29.20		12.55	4.44	0.07			0.27	98.8
Pl		D	33 / 3 .	592.719	Coarse	rim	52.69	29.63		12.52	4.35	0.05			0.28	99.5
Pl		B	7 / 1 .	592.027	Coarse	core	53.59	28.75		11.91	4.69	0.06			0.33	99.3
Pl		B	7 / 2 .	592.027	Coarse	rim	54.05	28.29		11.14	5.01	0.07			0.31	98.9
Pl		B	7 / 3 .	592.027	Coarse	core	54.38	28.61		11.47	4.88	0.12			0.21	99.7
Pl		B	7 / 4 .	592.027	Coarse	core	53.99	28.60		11.84	4.81	0.09			0.27	99.6
Pl		B	7 / 5 .	592.027	Coarse	rim	54.38	28.75		11.55	4.97	0.08			0.40	100.1
Pl		E	10 / 1 .	592.028	Coarse	core	53.08	29.38		12.17	4.63	0.07			0.43	99.7
Pl		E	10 / 2 .	592.028	Coarse	core	53.86	29.42		12.14	4.90	0.06			0.24	100.6
Pl		E	10 / 3 .	592.028	Coarse	rim	53.80	28.61		11.73	4.85	0.08			0.26	99.3
Pl		E	10 / 4 .	592.028	Coarse	core	52.16	29.87		13.07	4.03	0.06			0.26	99.5
Pl	360_65R5_51	D	14 / 1 .	592.038	Coarse	rim	53.57	28.74		11.46	4.93	0.07			0.25	99.0
Pl		D	14 / 2 .	592.038	Coarse	rim	52.54	29.42		12.48	4.28	0.05			0.34	99.1
Pl		D	14 / 3 .	592.038	Coarse	core	52.51	29.63		12.72	4.20	0.06			0.30	99.4
Pl		C	18 / 1 .	592.039	Coarse	core	52.62	29.78		12.73	4.46	0.05			0.23	99.9
Pl		C	18 / 2 .	592.039	Coarse	rim	52.66	29.38		12.70	4.57	0.06			0.32	99.7
Pl		C	18 / 3 .	592.039	Coarse	core	53.04	29.22		12.61	4.56	0.04			0.24	99.7
Pl		C	18 / 4 .	592.039	Coarse	rim	52.88	29.30		12.45	4.49	0.05			0.36	99.5
Pl		C	18 / 5 .	592.039	Coarse	rim	53.74	28.92		12.06	4.83	0.04			0.23	99.8
Pl		F	21 / 1 .	592.044	Coarse	core	53.11	29.51		12.57	4.55	0.06			0.28	100.1
Pl		F	21 / 2 .	592.044	Coarse	rim	52.29	29.59		12.53	4.49	0.07			0.22	99.2
Pl		F	21 / 3 .	592.044	Coarse	core	53.37	29.50		12.14	4.61	0.07			0.21	99.9
Pl		B	24 / 1 .	592.404	Fine	core	53.16	29.40		12.43	4.57	0.04			0.19	99.8
Pl		B	24 / 2 .	592.404	Fine	rim	53.36	29.21		12.20	4.76	0.04			0.26	99.8
Pl		A	26 / 1 .	592.406	Fine	core	53.30	29.69		12.39	4.49	0.02			0.16	100.1
Pl		A	26 / 2 .	592.406	Fine	rim	50.18	30.98		14.44	3.41	0.03			0.24	99.3
Pl		A	26 / 3 .	592.406	Fine	core	53.11	29.63		12.69	4.51	0.05			0.24	100.2
Pl		A	26 / 4 .	592.406	Fine	core	53.53	29.37		12.03	4.87	0.05			0.21	100.1
Pl		A	26 / 5 .	592.406	Fine	rim	52.50	29.96		12.62	4.46	0.02			0.32	99.9
Pl		C	29 / 1 .	592.405	Fine	core	52.96	29.37		12.42	4.71	0.06			0.13	99.6
Pl		C	29 / 2 .	592.405	Fine	rim	53.05	29.11		12.32	4.60	0.07			0.17	99.3
Pl		C	29 / 3 .	592.405	Fine	core	53.32	29.27		12.32	4.84	0.03			0.16	99.9
Pl		C	29 / 4 .	592.405	Fine	core	53.42	29.27		12.56	4.53	0.05			0.18	100.0

Mineral	360_65R5_87	Area	Point	Depth (mbsf)	Layer type	Grain area	SiO2	Al2O3	TiO2	CaO	Na2O	K2O	MnO	MgO	FeO	Total
Pl		C	29 / 5 .	592.405	Fine	core	53.28	29.46		12.38	4.71	0.05			0.20	100.1
Pl		C	29 / 6 .	592.405	Fine	rim	52.70	28.94		12.37	4.59	0.05			0.22	98.9
Pl		E	32 / 1 .	592.391	Fine	core	53.08	29.55		12.08	4.52	0.01			0.18	99.4
Pl		E	32 / 2 .	592.391	Fine	rim	52.85	29.66		12.57	4.59	0.03			0.17	99.9
Pl		E	32 / 3 .	592.391	Fine	core	52.97	29.59		12.44	4.46	0.04			0.21	99.7
Pl		E	32 / 4 .	592.391	Fine	rim	53.06	29.61		12.48	4.37	0.02			0.15	99.7
Pl		E	32 / 5 .	592.391	Fine	rim	52.74	29.63		12.56	4.44	0.03			0.13	99.5
Pl		F	39 / 1 .	592.384	Fine	core	52.76	30.05		12.58	4.36	0.04			0.30	100.1
Pl		F	39 / 2 .	592.384	Fine	rim	53.36	29.23		12.42	4.67	0.06			0.24	100.0
Pl		F	39 / 3 .	592.384	Fine	core	52.30	29.76		12.70	4.31	0.03			0.37	99.4
Pl		A	4 / 1 .	591.925	Fine	core	53.69	29.64		11.87	4.56	0.04			0.12	99.9
Pl		A	4 / 2 .	591.925	Fine	core	52.45	30.09		13.14	4.20	0.03			0.32	100.2
Pl		A	4 / 3 .	591.925	Fine	core	52.96	29.53		12.40	4.37	0.05			0.32	99.6
Pl		D	6 / 1 .	591.922	Fine	core	53.40	29.49		12.52	4.40	0.06			0.17	100.0
Pl		D	6 / 2 .	591.922	Fine	core	53.91	28.98		11.83	4.78	0.06			0.27	99.8
Pl		D	6 / 3 .	591.922	Fine	rim	53.48	28.85		11.97	4.74	0.07			0.25	99.4
Pl		E	9 / 1 .	591.928	Fine	core	53.45	29.49		12.40	4.44	0.03			0.16	100.0
Pl		E	9 / 2 .	591.928	Fine	core	53.33	29.40		12.16	4.61	0.05			0.21	99.8
Pl		E	9 / 3 .	591.928	Fine	rim	53.22	29.21		12.15	4.56	0.04			0.45	99.6
Pl	360_65R5_39	C	12 / 1 .	591.934	Fine	core	53.18	29.12		12.14	4.55	0.05			0.20	99.3
Pl		C	12 / 2 .	591.934	Fine	rim	53.04	29.35		12.46	4.50	0.02			0.20	99.6
Pl		C	12 / 3 .	591.934	Fine	core	53.50	29.48		11.80	4.78	0.07			0.23	99.8
Pl		C	12 / 4 .	591.934	Fine	rim	51.31	30.40		13.43	3.84	0.05			0.39	99.4
Pl		C	12 / 5 .	591.934	Fine	core	53.25	29.61		12.58	4.48	0.06			0.20	100.2
Pl		C	12 / 6 .	591.934	Fine	rim	54.06	28.97		11.91	5.00	0.06			0.24	100.2
Pl		B	15 / 1 .	591.932	Fine	core	53.47	29.15		11.74	4.74	0.06			0.14	99.3
Pl		B	15 / 2 .	591.932	Fine	core	53.58	29.27		12.12	4.73	0.06			0.23	100.0
Pl		B	15 / 3 .	591.932	Fine	core	54.01	28.85		11.55	4.73	0.04			0.27	99.5
Pl		B	15 / 4 .	591.932	Fine	rim	52.58	29.68		12.89	4.18	0.06			0.25	99.6
Pl		A	18 / 1 .	591.848	Fine	core	53.31	29.75		12.42	4.50	0.04			0.27	100.3
Pl		A	18 / 2 .	591.848	Fine	core	54.02	28.77		11.70	4.79	0.05			0.34	99.7
Pl		A	18 / 3 .	591.848	Fine	rim	53.45	29.59		12.17	4.50	0.05			0.30	100.1
Pl		A	18 / 4 .	591.848	Fine	core	53.25	29.27		12.53	4.59	0.05			0.23	99.9
Pl		A	18 / 5 .	591.848	Fine	rim	53.49	29.61		11.90	4.54	0.04			0.15	99.7
Pl		D	20 / 1 .	591.846	Fine	core	52.61	29.54		12.50	4.47	0.02			0.24	99.4
Pl		D	20 / 2 .	591.846	Fine	rim	53.13	29.50		12.53	4.56	0.06			0.30	100.1
Pl		D	20 / 3 .	591.846	Fine	core	53.92	29.35		12.16	4.62	0.04			0.25	100.3
Pl		D	20 / 4 .	591.846	Fine	rim	52.87	29.44		12.07	4.61	0.09			0.29	99.4
Pl		C	23 / 1 .	591.840	Fine	core	52.89	29.55	0.05	12.61	4.39	0.01	0.02	0.00	0.27	99.8
Pl	360_65R5_32	C	23 / 2 .	591.840	Fine	core	52.22	29.66	0.07	12.56	4.49	0.02	0.00	0.01	0.25	99.3
Pl		C	23 / 3 .	591.840	Fine	rim	53.39	29.68	0.06	12.66	4.44	0.05	0.00	0.01	0.21	100.5
Pl		B	26 / 1 .	591.837	Fine	core	53.58	29.45		12.15	4.56	0.06			0.23	100.0

Mineral		Area	Point	Depth (mbsf)	Layer type	Grain area	SiO2	Al2O3	TiO2	CaO	Na2O	K2O	MnO	MgO	FeO	Total
Pl		B	26 / 2 .	591.837	Fine	rim	53.47	29.27		11.94	4.76	0.06			0.23	99.7
Pl		B	26 / 3 .	591.837	Fine	rim	53.48	29.35		12.24	4.69	0.06			0.26	100.1
Pl		B	26 / 4 .	591.837	Fine	core	52.78	29.62		12.50	4.49	0.03			0.28	99.7
Pl		E	27 / 1 .	591.832	Fine	core	53.84	29.05		11.77	4.83	0.06			0.34	99.9
Pl		E	27 / 2 .	591.832	Fine	rim	53.32	29.49		12.39	4.58	0.07			0.24	100.1
Pl		E	27 / 3 .	591.832	Fine	core	53.73	29.59		12.26	4.60	0.02			0.20	100.4
Pl		D	1 / 1 .	591.765	Coarse	rim	52.95	29.25		12.55	4.32	0.08			0.18	99.3
Pl		D	2 / 1 .	591.765	Coarse	rim	52.97	29.08		11.97	4.59	0.06			0.23	98.9
Pl		D	2 / 2 .	591.765	Coarse	core	53.21	29.45		12.43	4.50	0.09			0.27	99.9
Pl		D	2 / 3 .	591.765	Coarse	rim	53.61	28.95		11.75	4.85	0.08			0.57	99.8
Pl		D	2 / 4 .	591.765	Coarse	core	53.27	29.18		12.33	4.44	0.08			0.24	99.5
Pl		B	6 / 1 .	591.769	Fine	core	53.68	29.28		11.86	4.60	0.07			0.25	99.7
Pl		B	6 / 2 .	591.769	Fine	core	53.03	29.32		12.15	4.82	0.05			0.23	99.6
Pl		B	6 / 3 .	591.769	Fine	core	53.06	29.06		12.07	4.69	0.05			0.25	99.2
Pl	360_65R5_23	B	6 / 4 .	591.769	Fine	rim	52.40	29.57		12.86	4.34	0.07			0.48	99.7
Pl		A	10 / 1 .	591.773	Fine	core	53.14	29.64		12.37	4.53	0.09			0.24	100.0
Pl		A	10 / 2 .	591.773	Fine	rim	53.08	29.21		12.29	4.53	0.04			0.30	99.5
Pl		A	10 / 3 .	591.773	Fine	core	53.15	29.08		12.33	4.48	0.05			0.20	99.3
Pl		A	10 / 4 .	591.773	Fine	rim	52.94	29.33		12.49	4.45	0.06			0.22	99.5
Pl		C	13 / 1 .	591.776	Fine	core	53.31	29.09		12.01	4.62	0.08			0.20	99.3
Pl		C	13 / 2 .	591.776	Fine	core	53.13	29.36		12.26	4.65	0.02			0.18	99.6
Pl		C	13 / 3 .	591.776	Fine	rim	53.89	29.16		11.87	4.68	0.08			0.24	99.9
Pl		C	13 / 4 .	591.776	Fine	core	53.19	28.99		12.13	4.87	0.08			0.30	99.6
Pl		E	15 / 1 .	591.513	Coarse	rim	53.22	29.42		12.14	4.65	0.03			0.31	99.8
Pl		E	15 / 2 .	591.513	Coarse	core	53.48	29.18		12.23	4.62	0.08			0.25	99.8
Pl		D	17 / 1 .	591.515	Coarse	core	53.09	29.33		12.31	4.52	0.03			0.25	99.5
Pl		D	17 / 2 .	591.515	Coarse	rim	53.24	29.53		12.27	4.57	0.06			0.35	100.0
Pl		D	17 / 3 .	591.515	Coarse	core	53.34	29.55		12.19	4.52	0.09			0.22	99.9
Pl		B	20 / 1 .	591.515	Coarse	core	52.83	29.57		12.75	4.49	0.03			0.23	99.9
Pl		B	20 / 2 .	591.515	Coarse	core	53.17	29.03		11.73	4.86	0.06			0.42	99.3
Pl		B	20 / 3 .	591.515	Coarse	rim	53.20	29.15		12.03	4.51	0.07			0.26	99.2
Pl	360_65R5_0	C	22 / 1 .	591.519	Coarse	core	53.63	29.63		12.04	4.77	0.07			0.25	100.4
Pl		C	22 / 2 .	591.519	Coarse	core	53.37	29.31		12.07	4.63	0.09			0.24	99.7
Pl		C	22 / 3 .	591.519	Coarse	rim	53.41	29.26		12.22	4.68	0.08			0.24	99.9
Pl		A	24 / 1 .	591.523	CinF	core	53.33	29.55		12.17	4.46	0.01			0.30	99.8
Pl		A	24 / 2 .	591.523	CinF	rim	54.02	29.03		11.78	4.80	0.03			0.18	99.8
Pl		A	24 / 3 .	591.523	CinF	core	53.57	29.09		12.06	4.61	0.05			0.25	99.6
Pl		F	28 / 1 .	591.526	Fine	core	52.35	29.67		12.97	4.02	0.01			0.62	99.6
Pl		F	28 / 2 .	591.526	Fine	core	53.57	29.77		12.19	4.66	0.03			0.21	100.4
Pl		A	31 / 1 .	591.733	Coarse	core	53.23	29.00		12.27	4.53	0.03			0.37	99.4
Pl		A	31 / 2 .	591.733	Coarse	rim	53.78	28.87		11.84	4.82	0.08			0.28	99.7
Pl		A	31 / 3 .	591.733	Coarse	core	53.22	29.33		12.32	4.27	0.05			0.34	99.5

Mineral		Area	Point	Depth (mbsf)	Layer type	Grain area	SiO2	Al2O3	TiO2	CaO	Na2O	K2O	MnO	MgO	FeO	Total
Pl		E	34 / 1 .	591.739	Coarse	core	52.55	29.55		12.36	4.42	0.07			0.25	99.2
Pl		E	34 / 2 .	591.739	Coarse	rim	53.52	28.90		11.87	4.75	0.06			0.22	99.3
Pl		E	34 / 3 .	591.739	Coarse	core	52.99	28.93		11.88	4.70	0.06			0.20	98.7
Pl		B	36 / 1 .	591.741	Coarse	rim	53.66	29.15		11.72	4.71	0.05			0.27	99.6
Pl		B	36 / 2 .	591.741	Coarse	core	54.10	28.75		11.27	4.97	0.05			0.28	99.4
Pl	360_65R5_21	B	36 / 3 .	591.741	Coarse	core	53.21	29.28		12.27	4.47	0.08			0.28	99.6
Pl		B	36 / 4 .	591.741	Coarse	core	52.59	29.27		12.48	4.48	0.07			0.27	99.2
Pl		C	39 / 1 .	591.740	Coarse	core	51.85	30.24		13.30	4.02	0.05			0.20	99.7
Pl		C	39 / 2 .	591.740	Coarse	rim	53.43	29.06		12.12	4.73	0.04			0.35	99.7
Pl		C	39 / 3 .	591.740	Coarse	core	53.17	29.59		12.22	4.53	0.07			0.24	99.8
Pl		D	41 / 1 .	591.740	Coarse	core	52.89	29.54		12.45	4.58	0.09			0.28	99.8
Pl		D	41 / 2 .	591.740	Coarse	rim	53.31	29.20		12.36	4.71	0.05			0.31	99.9
Pl		D	41 / 3 .	591.740	Coarse	core	53.30	29.29		12.41	4.63	0.06			0.25	99.9
Pl		D	41 / 4 .	591.740	Coarse	rim	53.34	29.14		12.33	4.53	0.07			0.21	99.6
Pl		D	41 / 6 .	591.740	Coarse	core	53.12	29.31		12.32	4.45	0.07			0.25	99.5
Pl		D	41 / 7 .	591.740	Coarse	rim	53.12	29.06		12.27	4.53	0.05			0.30	99.3
Pl		N4	15 / 1 .	592.156	Coarse	core	53.52	29.84	0.07	12.09	4.46	0.11	0.00	0.00	0.21	100.3
Pl		N4	16 / 1 .	592.156	Coarse	rim	53.60	29.60	0.06	11.98	4.58	0.10	0.00	0.08	0.18	100.2
Pl		N1	32 / 1 .	592.158	Coarse	core	54.16	28.93	0.10	11.36	4.41	0.15	0.00	0.04	0.51	99.7
Pl		N5	37 / 1 .	592.154	Coarse	core	54.12	29.24	0.04	11.59	4.88	0.14	0.00	0.01	0.21	100.2
Pl		N5	38 / 1 .	592.154	Coarse	core	53.78	29.40	0.07	11.80	4.97	0.09	0.00	0.01	0.31	100.4
Pl		N5	39 / 1 .	592.154	Coarse	core	53.58	29.56	0.06	12.01	4.32	0.10	0.00	0.03	0.23	99.9
Pl	360_65R5_63A	N5	40 / 1 .	592.154	Coarse	rim	53.97	29.49	0.08	11.81	4.74	0.14	0.00	0.02	0.24	100.5
Pl		N5	41 / 1 .	592.154	Coarse	rim	53.61	29.70	0.08	12.03	4.64	0.15	0.01	0.03	0.22	100.5
Pl		N5	42 / 1 .	592.154	Coarse	core	53.03	29.73	0.07	12.20	4.41	0.14	0.02	0.02	0.21	99.8
Pl		N3	46 / 1 .	592.145	Coarse	rim	54.16	29.75	0.10	12.09	4.64	0.16	0.02	0.01	0.25	101.2
Pl		N3	47 / 1 .	592.145	Coarse	core	53.87	29.33	0.12	11.58	5.09	0.13	0.00	0.02	0.26	100.4
Pl		N3	48 / 1 .	592.145	Coarse	rim	53.13	29.83	0.17	12.24	4.25	0.13	0.00	0.01	0.34	100.1
Pl		N3	49 / 1 .	592.145	Coarse	core	52.62	29.60	0.07	12.33	4.20	0.15	0.01	0.03	0.31	99.3
Pl		A	57 / 1 .	592.170	Coarse	rim	53.35	29.65	0.05	12.21	4.54	0.11	0.00	0.02	0.32	100.2
Pl		A	58 / 1 .	592.170	Coarse	core	53.28	29.95	0.07	12.33	4.35	0.09	0.00	0.04	0.27	100.4
Pl		B	68 / 1 .	592.175	Coarse	core	53.82	29.52	0.10	11.80	4.59	0.11	0.01	0.04	0.22	100.2
Pl		B	69 / 1 .	592.175	Coarse	rim	53.56	29.94	0.05	12.44	4.52	0.15	0.00	0.01	0.24	100.9
Pl		B	70 / 1 .	592.175	Coarse	core	53.91	29.68	0.08	12.04	4.52	0.12	0.00	0.03	0.27	100.7
Pl		B	71 / 1 .	592.175	Coarse	rim	54.10	29.83	0.08	11.92	4.61	0.10	0.01	0.00	0.23	100.9
Pl		B	72 / 1 .	592.175	Coarse	rim	54.58	29.60	0.04	11.88	4.44	0.13	0.00	0.02	0.18	100.9
Pl		B	73 / 1 .	592.175	Coarse	core	53.87	29.44	0.05	11.94	4.46	0.13	0.02	0.02	0.28	100.2
Pl		B	80 / 1 .	592.177	Coarse	rim	53.98	29.92	0.05	11.97	4.61	0.14	0.00	0.02	0.21	100.9
Pl		B	81 / 1 .	592.177	Coarse	core	53.77	29.81	0.05	12.00	4.41	0.09	0.00	0.13	0.28	100.5
Pl		B	82 / 1 .	592.173	Coarse	rim	53.91	29.54	0.10	11.96	4.54	0.14	0.00	0.02	0.23	100.4
Pl		B	83 / 1 .	592.173	Coarse	core	53.24	29.89	0.06	12.35	4.26	0.13	0.00	0.02	0.29	100.2
Pl		C	4 / 1 .	592.169	Coarse	core	54.75	29.06	0.07	11.24	4.61	0.23	0.00	0.02	0.21	100.2

Mineral		Area	Point	Depth (mbsf)	Layer type	Grain area	SiO2	Al2O3	TiO2	CaO	Na2O	K2O	MnO	MgO	FeO	Total
Pl		C	9 / 1 .	592.169	Coarse	core	53.95	29.37	0.12	11.67	4.57	0.13	0.00	0.03	0.34	100.2
Pl		C	11 / 1 .	592.169	Coarse	core	53.65	29.81	0.09	12.07	4.70	0.14	0.00	0.11	0.45	101.0
Pl	360_65R5_63B	D	22 / 1 .	592.171	Coarse	core	54.32	29.06	0.19	11.22	4.91	0.13	0.01	0.02	0.31	100.2
Pl		D	23 / 1 .	592.171	Coarse	rim	54.19	29.45	0.04	11.73	4.76	0.16	0.04	0.07	0.28	100.7
Pl		D	24 / 1 .	592.171	Coarse	core	54.29	29.85	0.11	11.98	4.69	0.10	0.00	0.01	0.17	101.2
Pl		E	38 / 1 .	592.178	Coarse	rim	54.20	29.32	0.09	11.55	4.69	0.13	0.00	0.03	0.27	100.3
Pl		E	39 / 1 .	592.178	Coarse	core	55.06	29.14	0.06	11.23	5.33	0.12	0.00	0.01	0.23	101.2
Pl		E	40 / 1 .	592.178	Coarse	core	53.87	29.54	0.14	11.90	4.45	0.10	0.02	0.11	0.39	100.5
Pl		E	41 / 1 .	592.178	Coarse	rim	54.10	29.71	0.05	12.05	4.40	0.12	0.02	0.10	0.32	100.9
Pl		E	51 / 1 .	592.182	Coarse	core	53.10	29.88	0.06	12.31	4.43	0.14	0.00	0.05	0.34	100.3
Pl		E	52 / 1 .	592.182	Coarse	rim	54.83	28.82	0.13	11.16	5.06	0.13	0.01	0.02	0.32	100.5
Pl		E	53 / 1 .	592.182	Coarse	core	53.87	29.71	0.08	12.16	4.28	0.14	0.01	0.03	0.23	100.5
Pl		E	54 / 1 .	592.182	Coarse	rim	54.19	29.86	0.06	11.64	4.72	0.13	0.01	0.04	0.25	100.9
Pl		F	62 / 1 .	592.179	Coarse	rim	54.20	29.38	0.09	11.60	4.57	0.15	0.01	0.01	0.16	100.2
Pl		F	63 / 1 .	592.179	Coarse	core	54.01	29.64	0.08	11.72	5.01	0.12	0.02	0.04	0.22	100.9
Pl		F	65 / 1 .	592.179	Coarse	core	54.60	29.07	0.09	11.36	5.24	0.15	0.00	0.03	0.19	100.7
Pl		G	79 / 1 .	592.178	Coarse	core	53.54	29.71	0.07	12.20	4.23	0.11	0.03	0.03	0.23	100.1
Pl		G	80 / 1 .	592.178	Coarse	rim	53.48	29.53	0.08	11.88	4.46	0.12	0.00	0.00	0.30	99.9
Pl		H	82 / 1 .	592.174	Coarse	rim	54.05	29.44	0.07	11.84	4.49	0.12	0.02	0.05	0.35	100.4
Pl		I	90 / 1 .	592.167	Coarse	core	53.15	30.05	0.06	12.25	4.18	0.10	0.01	0.01	0.25	100.1

Calibration standards	Wollastonite (San Carlos)	Al2O3	TiMnO3	Wollastonite	Albite	Orthose	TiMnO3	Forsterite	Fayalite

In situ major elements concentrations in wt% analysed by EPMA on a Cameca SX100 in LMV (Clermont-Ferrand, Frar

Mineral	Sample	Area	Point	Depth (mbsf)	Layer type	Grain area	SiO2	Al2O3	TiO2	CaO	Na2O	K2O	MnO	MgO	FeO	Cr2O3	NiO	Total
						2 sigma	0.489	0.091	0.090	0.345	0.056	0.020	0.060	0.270	0.226	0.063	0.038	
						%	0.9	3.5	11.7	1.7	14.8	314.1	30.6	1.7	3.3	64.2	231.6	
Cpx			Counting time (s)				10	10	10	10	10	10	10	10	20	10	10	
Cpx		B	11 / 1 .	592.287	Coarse	core	52.56	3.01	0.62	20.55	0.43	0.00	0.18	16.15	6.36	0.08	0.00	99.9
Cpx		B	11 / 2 .	592.287	Coarse	rim	52.69	2.77	0.56	21.73	0.42	0.00	0.21	15.85	6.13	0.14	0.05	100.5
Cpx		A	16 / 1 .	592.290	Coarse	core	52.86	2.55	0.51	18.24	0.33	0.01	0.22	17.60	8.33	0.03	0.01	100.7
Cpx		A	16 / 2 .	592.290	Coarse	rim	51.46	2.80	1.15	22.11	0.35	0.03	0.25	14.89	6.38	0.08	0.00	99.5
Cpx	360_65R5_76	D	25 / 1 .	592.299	Coarse	core	52.61	2.62	0.50	18.87	0.29	0.00	0.24	17.35	7.78	0.12	0.00	100.4
Cpx		D	25 / 2 .	592.299	Coarse	rim	51.58	3.05	1.16	21.92	0.45	0.01	0.20	15.15	6.63	0.04	0.00	100.2
Cpx		D	25 / 3 .	592.299	Coarse	rim	51.93	2.64	0.66	21.01	0.33	0.00	0.22	16.39	6.41	0.10	0.00	99.7
Cpx		D	26 / 1 .	592.299	Coarse	core	51.29	2.93	1.04	21.77	0.41	0.01	0.19	14.88	6.49	0.12	0.02	99.1
Cpx		D	26 / 2 .	592.299	Coarse	core	51.84	2.75	1.05	21.83	0.36	0.01	0.16	15.21	6.37	0.07	0.00	99.6
Cpx		D	4 / 1 .	591.788	Coarse in Fin	core	52.76	2.69	0.61	21.26	0.40	0.00	0.13	16.22	6.43	0.11	0.00	100.6
Cpx		D	4 / 2 .	591.788	Coarse in Fin	rim	52.32	2.58	0.71	22.02	0.44	0.00	0.25	15.81	6.19	0.13	0.00	100.5
Cpx		D	4 / 3 .	591.788	Coarse in Fin	rim	52.01	2.69	0.83	22.47	0.42	0.00	0.21	15.76	6.07	0.06	0.00	100.5
Cpx		B	6 / 1 .	591.795	Fine	core	52.50	2.80	0.73	21.90	0.40	0.00	0.15	15.61	6.00	0.13	0.00	100.2
Cpx		B	7 / 1 .	591.795	Fine	rim	52.91	2.24	0.69	22.93	0.36	0.01	0.17	15.69	5.46	0.15	0.00	100.6
Cpx	360_65R5_27	C	14 / 2 .	591.794	Fine	rim	52.50	2.60	0.60	21.57	0.31	0.01	0.21	16.11	7.22	0.11	0.04	101.2
Cpx		C	14 / 3 .	591.794	Fine	rim	52.96	2.50	0.63	21.95	0.33	0.00	0.14	16.15	6.02	0.14	0.03	100.8
Cpx		A	22 / 1 .	591.800	Fine	core	52.36	2.84	0.50	20.87	0.38	0.00	0.16	16.40	6.50	0.19	0.06	100.2
Cpx		A	22 / 2 .	591.800	Fine	rim	53.25	2.17	0.62	19.50	0.32	0.00	0.26	17.21	7.49	0.11	0.03	100.9
Cpx		E	25 / 1 .	591.805	Coarse in Fin	core	52.67	2.69	0.75	20.53	0.38	0.00	0.20	16.23	6.57	0.05	0.01	100.1
Cpx		E	25 / 2 .	591.805	Coarse in Fin	rim	53.41	2.68	0.54	18.46	0.37	0.00	0.19	17.56	8.02	0.10	0.03	101.3
Cpx		N	34 / 1 .	591.718	Coarse	core	52.84	2.48	0.40	20.16	0.34	0.00	0.16	17.26	6.93	0.09	0.02	100.7
Cpx		N	34 / 2 .	591.718	Coarse	rim	52.19	2.69	0.96	20.16	0.37	0.00	0.22	16.29	7.24	0.08	0.00	100.2
Cpx		P	36 / 1 .	591.709	Coarse	core	52.78	2.84	0.60	21.62	0.40	0.00	0.17	16.35	6.12	0.12	0.00	101.0
Cpx	360_65R5_18	P	36 / 2 .	591.709	Coarse	rim	51.91	3.14	1.18	19.78	0.37	0.01	0.22	15.85	7.37	0.05	0.03	99.9
Cpx		O	42 / 1 .	591.722	Coarse	core	53.52	2.44	0.54	15.90	0.29	0.00	0.22	18.52	8.52	0.16	0.03	100.1
Cpx		O	42 / 2 .	591.722	Coarse	rim	51.91	2.68	0.57	21.51	0.39	0.00	0.16	15.34	6.36	0.02	0.00	98.9
Cpx		Bis	27 / 1 .	591.703	Coarse	core	51.84	2.87	1.10	21.71	0.47	0.02	0.22	14.92	6.93	0.07	0.00	100.1
Cpx		Bis	27 / 2 .	591.703	Coarse	rim	51.87	2.99	1.12	21.76	0.42	0.00	0.17	15.16	6.50	0.06	0.00	100.0
Cpx		E	16 / 1 .	592.004	Coarse	core	53.15	2.49	0.48	18.96	0.37	0.03	0.18	17.13	7.83	0.04	0.02	100.6
Cpx		E	16 / 2 .	592.004	Coarse	rim	52.55	2.62	0.54	20.22	0.42	0.00	0.22	16.69	7.64	0.11	0.02	101.0
Cpx		C	20 / 1 .	591.991	Coarse	core	52.61	2.83	0.47	21.67	0.44	0.00	0.20	16.21	6.08	0.15	0.02	100.7
Cpx		C	20 / 2 .	591.991	Coarse	rim	52.13	2.79	1.07	22.08	0.44	0.00	0.21	15.33	6.42	0.05	0.00	100.5
Cpx		D	22 / 1 .	591.993	Coarse	core	52.71	2.70	0.50	19.60	0.30	0.00	0.23	16.56	7.28	0.04	0.01	99.9
Cpx		D	22 / 3 .	591.993	Coarse	rim	53.16	2.49	0.50	14.89	0.29	0.01	0.34	18.66	9.62	0.11	0.03	100.1
Cpx	360_65R5_46	F	26 / 1 .	591.989	Coarse	core	52.60	3.03	0.77	19.20	0.33	0.00	0.21	16.33	7.35	0.16	0.02	100.0
Cpx		F	26 / 2 .	591.989	Coarse	rim	51.84	2.71	0.89	21.90	0.43	0.01	0.20	15.14	6.66	0.20	0.02	100.0
Cpx		F	26 / 4 .	591.989	Coarse	core	52.08	2.99	1.04	19.62	0.40	0.01	0.25	15.77	7.28	0.24	0.00	99.7
Cpx		F	26 / 6 .	591.989	Coarse	rim	52.86	2.67	0.88	22.09	0.39	0.01	0.17	15.18	6.40	0.09	0.05	100.7

Mineral		Area	Point	Depth (mbsf)	Layer type	Grain area	SiO2	Al2O3	TiO2	CaO	Na2O	K2O	MnO	MgO	FeO	Cr2O3	NiO	Total
Cpx		B	27 / 1 .	591.985	Coarse	core	51.76	2.81	0.97	22.18	0.37	0.00	0.19	15.15	6.40	0.11	0.00	99.9
Cpx		B	27 / 2 .	591.985	Coarse	rim	51.71	3.15	1.14	21.85	0.44	0.02	0.19	15.10	6.57	0.09	0.02	100.2
Cpx		C	4 / 1 .	592.466	Fine	core	52.42	2.58	0.52	20.43	0.41	0.01	0.17	16.66	6.31	0.11	0.00	99.6
Cpx		C	4 / 2 .	592.466	Fine	rim	52.74	2.49	0.63	22.02	0.39	0.02	0.14	15.73	5.81	0.10	0.02	100.1
Cpx		C	4 / 5 .	592.466	Fine	core	52.69	2.54	0.51	20.03	0.32	0.01	0.17	17.35	6.79	0.10	0.01	100.5
Cpx		C	4 / 6 .	592.466	Fine	rim	52.65	2.65	0.58	21.84	0.40	0.01	0.19	16.06	5.90	0.11	0.04	100.4
Cpx	360_65R5_94	A	7 / 1 .	592.466	Fine	core	52.89	2.63	0.61	22.18	0.40	0.00	0.20	15.83	5.78	0.11	0.01	100.6
Cpx		A	7 / 2 .	592.466	Fine	core	53.38	2.52	0.62	19.81	0.33	0.00	0.21	17.21	6.50	0.13	0.00	100.7
Cpx		B	11 / 1 .	592.456	Fine	core	53.26	2.56	0.56	21.70	0.34	0.03	0.23	16.25	6.52	0.11	0.00	101.5
Cpx		B	11 / 2 .	592.456	Fine	core	52.88	2.51	0.70	21.73	0.43	0.01	0.18	16.04	5.59	0.04	0.02	100.1
Cpx		D	16 / 1 .	592.453	Fine	core	52.90	2.38	0.60	18.48	0.42	0.03	0.21	17.92	5.91	0.07	0.03	98.9
Cpx		D	16 / 2 .	592.453	Fine	rim	52.79	2.46	0.64	21.59	0.38	0.00	0.21	16.27	5.89	0.11	0.00	100.3
Cpx		A	19 / 1 .	592.354	Coarse in Fin	core	52.66	2.87	0.72	21.80	0.41	0.00	0.19	15.51	6.08	0.07	0.01	100.3
Cpx		A	19 / 2 .	592.354	Coarse in Fin	rim	52.24	2.52	0.79	20.18	0.38	0.00	0.20	16.49	6.50	0.11	0.03	99.4
Cpx		A	19 / 5 .	592.354	Coarse in Fin	core	52.37	2.55	0.74	21.34	0.38	0.00	0.22	15.97	6.19	0.14	0.00	99.9
Cpx		A	19 / 6 .	592.354	Coarse in Fin	rim	52.63	2.54	0.69	22.19	0.42	0.00	0.21	15.72	5.97	0.15	0.00	100.5
Cpx		D	21 / 1 .	592.357	Coarse in Fin	core	53.01	2.46	0.46	15.47	0.27	0.00	0.22	19.51	8.59	0.08	0.04	100.1
Cpx		D	21 / 2 .	592.357	Coarse in Fin	rim	52.79	2.24	0.63	17.23	0.24	0.00	0.24	18.55	8.29	0.09	0.04	100.3
Cpx	360_65R5_83	C	24 / 1 .	592.365	Coarse in Fin	core	51.40	2.86	0.93	21.31	0.38	0.01	0.21	16.19	6.20	0.03	0.02	99.5
Cpx		C	24 / 2 .	592.365	Coarse in Fin	rim	52.32	2.58	0.93	19.54	0.35	0.01	0.25	16.87	7.05	0.08	0.00	100.0
Cpx		B	27 / 2 .	592.369	Coarse in Fin	core	52.72	2.52	0.70	18.10	0.39	0.02	0.24	17.55	7.11	0.13	0.00	99.5
Cpx		B	27 / 3 .	592.369	Coarse in Fin	rim	52.65	2.39	0.68	20.05	0.34	0.03	0.24	17.16	6.90	0.15	0.04	100.6
Cpx		F	29 / 1 .	592.374	Fine	core	52.38	2.77	0.58	20.29	0.40	0.00	0.18	16.62	6.36	0.16	0.00	99.7
Cpx		F	29 / 3 .	592.374	Fine	rim	52.40	2.42	0.63	21.83	0.39	0.00	0.15	15.95	6.03	0.10	0.02	99.9
Cpx		E	32 / 2 .	592.376	Fine	core	52.85	2.63	0.63	19.74	0.41	0.00	0.22	16.95	6.51	0.19	0.00	100.1
Cpx		E	32 / 3 .	592.376	Fine	rim	53.05	2.37	0.62	21.69	0.34	0.02	0.24	16.31	5.84	0.04	0.01	100.5
Cpx		E	8 / 1 .	592.428	Fine	core	52.72	2.44	0.62	22.23	0.38	0.02	0.19	15.82	5.90	0.12	0.00	100.4
Cpx		E	8 / 2 .	592.428	Fine	rim	53.06	2.30	0.56	21.98	0.41	0.00	0.24	15.80	5.76	0.07	0.00	100.2
Cpx		E	8 / 3 .	592.428	Fine	core	52.40	2.79	0.66	21.88	0.47	0.00	0.14	15.45	6.00	0.11	0.00	99.9
Cpx		E	8 / 4 .	592.428	Fine	rim	52.99	2.52	0.63	21.78	0.42	0.00	0.19	15.71	5.91	0.13	0.04	100.3
Cpx		E	8 / 7 .	592.428	Fine	core	52.45	2.57	0.66	21.80	0.44	0.00	0.23	15.45	5.90	0.18	0.02	99.7
Cpx		E	8 / 8 .	592.428	Fine	rim	53.01	2.29	0.55	21.43	0.33	0.02	0.18	16.65	6.24	0.08	0.00	100.8
Cpx		D	10 / 1 .	592.432	Fine	core	53.04	2.55	0.55	21.80	0.44	0.00	0.19	15.85	5.84	0.18	0.04	100.4
Cpx		D	10 / 3 .	592.432	Fine	rim	52.95	2.14	0.53	22.56	0.31	0.00	0.19	16.04	5.28	0.07	0.00	100.1
Cpx		D	10 / 4 .	592.432	Fine	rim	52.80	2.20	0.65	22.14	0.36	0.01	0.17	15.82	5.48	0.11	0.02	99.7
Cpx		D	10 / 6 .	592.432	Fine	core	53.04	2.26	0.58	22.88	0.31	0.02	0.16	15.91	5.44	0.08	0.04	100.7
Cpx		D	10 / 8 .	592.432	Fine	core	52.43	2.55	0.59	21.85	0.35	0.03	0.22	15.88	5.87	0.06	0.01	99.8
Cpx		D	10 / 9 .	592.432	Fine	rim	52.81	2.41	0.60	22.00	0.38	0.00	0.20	15.68	5.74	0.12	0.03	100.0
Cpx		F	14 / 1 .	592.435	Fine	core	52.18	3.02	0.61	22.26	0.39	0.01	0.20	15.59	5.87	0.20	0.00	100.3
Cpx		F	14 / 3 .	592.435	Fine	rim	53.01	2.23	0.55	21.23	0.38	0.01	0.16	16.43	6.11	0.15	0.00	100.2
Cpx	360_65R5_91	F	14 / 5 .	592.435	Fine	core	52.80	2.37	0.64	22.14	0.40	0.00	0.23	15.84	5.80	0.15	0.01	100.4
Cpx		B	19 / 1 .	592.443	Coarse in Fin	core	52.69	2.79	0.50	20.57	0.32	0.01	0.18	16.39	6.75	0.08	0.02	100.3

Mineral		Area	Point	Depth (mbsf)	Layer type	Grain area	SiO2	Al2O3	TiO2	CaO	Na2O	K2O	MnO	MgO	FeO	Cr2O3	NiO	Total
Cpx		B	19 / 2 .	592.443	Coarse in Fin	rim	52.26	2.60	0.89	20.45	0.36	0.00	0.18	16.42	6.95	0.07	0.07	100.2
Cpx		B	19 / 4 .	592.443	Coarse in Fin	rim	52.66	2.84	0.71	22.54	0.44	0.01	0.20	15.38	6.13	0.14	0.04	101.0
Cpx		B	19 / 6 .	592.443	Coarse in Fin	core	53.46	2.71	0.51	16.73	0.33	0.04	0.24	18.09	8.13	0.14	0.01	100.3
Cpx		B	19 / 7 .	592.443	Coarse in Fin	rim	52.07	2.62	0.69	20.68	0.42	0.00	0.24	16.02	7.17	0.08	0.00	100.0
Cpx		A	21 / 1 .	592.445	Coarse in Fin	core	52.46	2.67	0.45	19.95	0.37	0.00	0.21	16.54	6.85	0.08	0.02	99.6
Cpx		A	21 / 2 .	592.445	Coarse in Fin	rim	52.80	2.51	0.85	19.61	0.33	0.00	0.22	17.23	7.49	0.12	0.03	101.2
Cpx		A	21 / 3 .	592.445	Coarse in Fin	rim	52.18	2.53	0.83	20.92	0.39	0.00	0.20	16.33	7.11	0.09	0.00	100.6
Cpx		A	21 / 9 .	592.445	Coarse in Fin	rim	51.80	2.63	0.92	22.52	0.44	0.00	0.15	15.42	5.89	0.10	0.01	99.9
Cpx		C	24 / 1 .	592.446	Coarse in Fin	core	52.17	2.66	0.62	21.98	0.40	0.00	0.20	15.42	6.39	0.10	0.05	100.0
Cpx		C	24 / 3 .	592.446	Coarse in Fin	rim	52.65	2.37	0.63	16.60	0.28	0.02	0.23	18.36	9.24	0.17	0.02	100.5
Cpx		D	2 / 1 .	592.313	Coarse	core	52.32	2.82	0.52	21.85	0.41	0.00	0.25	16.09	6.17	0.12	0.00	100.5
Cpx		D	2 / 3 .	592.313	Coarse	rim	52.18	2.80	0.94	22.22	0.37	0.01	0.19	15.75	6.01	0.08	0.02	100.5
Cpx		D	2 / 4 .	592.313	Coarse	rim	52.06	2.77	0.97	22.34	0.36	0.00	0.21	15.57	5.98	0.12	0.00	100.4
Cpx		D	2 / 6 .	592.313	Coarse	rim	51.83	2.66	1.04	22.23	0.45	0.02	0.19	15.44	6.22	0.18	0.03	100.2
Cpx		C	7 / 1 .	592.321	Coarse	core	52.02	2.61	0.48	19.85	0.31	0.00	0.25	17.31	6.22	0.14	0.01	99.2
Cpx		C	7 / 2 .	592.321	Coarse	rim	52.78	2.53	0.48	18.82	0.36	0.00	0.21	17.02	6.84	0.10	0.03	99.1
Cpx	360_65R5_79g	C	7 / 4 .	592.321	Coarse	rim	52.40	2.58	0.81	21.25	0.36	0.01	0.20	15.64	6.40	0.04	0.00	99.7
Cpx		C	7 / 5 .	592.321	Coarse	core	52.15	2.66	0.94	22.09	0.45	0.01	0.18	15.82	6.04	0.10	0.00	100.4
Cpx		B	10 / 1 .	592.328	Fine	core	52.26	2.63	0.99	19.75	0.41	0.02	0.19	16.42	7.47	0.12	0.00	100.2
Cpx		B	10 / 2 .	592.328	Fine	rim	51.85	2.76	1.00	22.15	0.40	0.00	0.16	15.25	6.21	0.07	0.02	99.9
Cpx		B	10 / 4 .	592.328	Fine	core	52.14	2.53	0.82	21.02	0.41	0.00	0.16	15.82	6.47	0.08	0.02	99.4
Cpx		B	10 / 5 .	592.328	Fine	rim	53.05	2.24	0.77	16.57	0.25	0.00	0.19	18.27	9.12	0.10	0.06	100.6
Cpx		B	10 / 6 .	592.328	Fine	core	52.11	2.80	0.98	21.57	0.38	0.00	0.28	15.43	6.44	0.13	0.00	100.1
Cpx		B	10 / 7 .	592.328	Fine	rim	51.89	2.71	1.00	21.70	0.40	0.00	0.17	15.26	6.49	0.19	0.01	99.8
Cpx		D	12 / 1 .	592.330	Coarse in Fin	core	52.24	2.79	0.50	20.52	0.42	0.01	0.19	16.38	6.62	0.10	0.00	99.8
Cpx		D	12 / 2 .	592.330	Coarse in Fin	rim	52.39	2.69	0.69	21.64	0.39	0.00	0.16	15.88	6.35	0.13	0.02	100.3
Cpx		D	12 / 3 .	592.330	Coarse in Fin	rim	51.86	2.66	0.91	21.89	0.39	0.00	0.19	15.32	6.50	0.04	0.00	99.8
Cpx		D	12 / 4 .	592.330	Coarse in Fin	rim	51.92	2.70	1.03	21.69	0.44	0.02	0.12	15.13	5.98	0.08	0.04	99.1
Cpx		D	12 / 5 .	592.330	Coarse in Fin	core	52.75	2.53	0.88	17.44	0.30	0.00	0.22	17.65	8.50	0.09	0.03	100.4
Cpx		D	12 / 6 .	592.330	Coarse in Fin	rim	51.87	2.88	0.92	21.80	0.41	0.00	0.19	15.29	6.42	0.16	0.01	99.9
Cpx		A	14 / 1 .	592.336	Fine	core	52.63	2.66	0.78	15.38	0.31	0.01	0.22	18.60	8.75	0.18	0.02	99.5
Cpx		A	14 / 2 .	592.336	Fine	rim	52.22	2.51	0.72	22.35	0.39	0.00	0.21	15.16	5.88	0.08	0.06	99.5
Cpx		A	14 / 3 .	592.336	Fine	core	52.67	2.19	0.64	22.45	0.42	0.00	0.13	15.40	5.79	0.07	0.01	99.8
Cpx		A	14 / 4 .	592.336	Fine	core	53.00	2.51	0.68	17.18	0.33	0.00	0.23	18.10	8.05	0.04	0.04	100.1
Cpx		A	14 / 5 .	592.336	Fine	rim	52.65	2.61	0.79	22.14	0.39	0.00	0.21	15.37	5.85	0.15	0.01	100.2
Cpx		A	14 / 6 .	592.336	Fine	rim	52.13	2.53	0.90	21.99	0.41	0.00	0.20	15.48	6.41	0.11	0.02	100.2
Cpx		C	17 / 3 .	592.332	Coarse in Fin	core	51.81	2.51	0.82	20.98	0.40	0.00	0.18	15.75	6.46	0.14	0.02	99.1
Cpx		B	19 / 1 .	592.332	Coarse in Fin	core	52.66	2.46	0.83	17.29	0.33	0.00	0.20	17.59	8.64	0.11	0.00	100.1
Cpx		B	19 / 2 .	592.332	Coarse in Fin	rim	52.27	2.80	0.90	21.38	0.48	0.01	0.22	15.45	6.63	0.12	0.00	100.2
Cpx		B	19 / 3 .	592.332	Coarse in Fin	core	52.02	2.62	0.90	21.02	0.47	0.04	0.21	15.40	6.38	0.08	0.02	99.1
Cpx	360_65R5_79f	B	19 / 4 .	592.332	Coarse in Fin	core	52.47	2.51	0.83	22.04	0.41	0.01	0.19	15.25	6.10	0.06	0.00	99.9
Cpx		B	19 / 5 .	592.332	Coarse in Fin	core	52.65	2.48	0.65	20.23	0.41	0.00	0.17	16.42	6.92	0.07	0.00	100.0

Mineral		Area	Point	Depth (mbsf)	Layer type	Grain area	SiO2	Al2O3	TiO2	CaO	Na2O	K2O	MnO	MgO	FeO	Cr2O3	NiO	Total
Cpx		B	19 / 6 .	592.332	Coarse in Fin	rim	52.23	2.43	0.81	21.20	0.41	0.00	0.24	15.89	6.31	0.08	0.00	99.6
Cpx		F	3 / 1 .	592.334	Fine	core	52.27	2.43	0.73	22.06	0.37	0.00	0.23	15.68	5.89	0.15	0.00	99.8
Cpx		F	3 / 2 .	592.334	Fine	core	52.29	2.52	0.77	22.02	0.41	0.01	0.18	15.78	6.00	0.12	0.00	100.1
Cpx		F	3 / 4 .	592.334	Fine	core	52.81	2.62	0.71	21.83	0.44	0.01	0.22	15.92	6.13	0.12	0.00	100.8
Cpx		F	3 / 5 .	592.334	Fine	rim	52.74	2.42	0.82	21.85	0.39	0.00	0.18	15.83	6.17	0.10	0.01	100.5
Cpx		F	3 / 6 .	592.334	Fine	core	52.08	2.55	0.72	21.62	0.38	0.02	0.21	15.49	6.20	0.15	0.04	99.4
Cpx		F	3 / 7 .	592.334	Fine	rim	52.69	2.44	0.69	21.75	0.42	0.00	0.16	15.99	6.17	0.08	0.03	100.4
Cpx		E	6 / 1 .	592.338	Fine	core	52.56	2.41	0.74	21.85	0.37	0.01	0.17	16.00	6.05	0.18	0.05	100.3
Cpx		E	6 / 2 .	592.338	Fine	rim	52.45	2.42	0.73	21.68	0.42	0.00	0.14	15.58	6.08	0.19	0.02	99.7
Cpx		E	6 / 3 .	592.338	Fine	core	53.38	2.07	0.59	22.01	0.34	0.00	0.17	16.17	5.94	0.08	0.03	100.8
Cpx		E	6 / 6 .	592.338	Fine	core	53.13	2.59	0.62	19.49	0.29	0.05	0.13	16.83	7.57	0.15	0.02	100.8
Cpx		E	6 / 7 .	592.338	Fine	rim	52.35	2.41	0.76	22.49	0.33	0.02	0.17	15.58	5.72	0.09	0.06	99.9
Cpx		D	21 / 3 .	592.627	Fine	core	52.08	2.53	0.82	21.94	0.44	0.00	0.24	15.90	6.15	0.12	0.01	100.2
Cpx		D	21 / 5 .	592.627	Fine	core	52.36	2.52	0.87	19.09	0.36	0.00	0.22	17.56	7.98	0.10	0.03	101.1
Cpx		D	21 / 6 .	592.627	Fine	rim	51.58	2.71	0.89	21.31	0.38	0.02	0.20	15.97	6.14	0.09	0.00	99.3
Cpx		D	21 / 7 .	592.627	Fine	rim	52.26	2.63	0.55	20.05	0.38	0.00	0.20	16.77	6.89	0.09	0.03	99.8
Cpx		C	26 / 2 .	592.631	Fine	core	51.71	2.56	0.86	22.12	0.41	0.01	0.18	15.82	6.24	0.08	0.00	100.0
Cpx		C	26 / 3 .	592.631	Fine	rim	52.33	2.50	0.89	22.31	0.38	0.00	0.16	15.64	6.08	0.12	0.03	100.4
Cpx		C	26 / 4 .	592.631	Fine	core	52.11	2.68	0.79	21.57	0.35	0.02	0.17	15.85	6.37	0.16	0.00	100.0
Cpx		C	26 / 6 .	592.631	Fine	rim	51.90	2.74	0.93	22.09	0.44	0.00	0.26	15.49	5.92	0.07	0.01	99.8
Cpx		C	26 / 7 .	592.631	Fine	rim	51.54	2.80	0.99	22.20	0.39	0.00	0.18	15.76	6.08	0.04	0.03	100.0
Cpx		C	26 / 8 .	592.631	Fine	core	52.28	2.66	0.80	21.78	0.42	0.00	0.22	15.58	6.16	0.05	0.03	99.9
Cpx		C	26 / 9 .	592.631	Fine	rim	51.74	2.65	0.97	22.00	0.44	0.00	0.17	15.44	6.29	0.12	0.02	99.8
Cpx	360_65R5_111	C	26 / 10 .	592.631	Fine	rim	52.09	2.58	0.88	21.90	0.37	0.01	0.21	15.56	6.00	0.12	0.00	99.7
Cpx		A	4 / 3 .	592.637	Fine	core	52.13	2.83	0.93	20.52	0.37	0.00	0.22	16.29	6.59	0.13	0.01	100.0
Cpx		A	4 / 4 .	592.637	Fine	rim	52.00	2.70	0.85	21.06	0.34	0.00	0.17	16.25	6.38	0.09	0.04	99.8
Cpx		A	4 / 6 .	592.637	Fine	core	52.23	2.68	0.59	22.01	0.42	0.00	0.20	15.58	6.04	0.12	0.03	99.9
Cpx		A	4 / 7 .	592.637	Fine	core	52.09	2.61	0.61	21.89	0.38	0.00	0.20	15.61	6.35	0.15	0.00	99.9
Cpx		A	4 / 8 .	592.637	Fine	rim	52.22	2.53	0.88	19.55	0.30	0.02	0.18	16.86	7.11	0.09	0.00	99.7
Cpx		B	8 / 2 .	592.642	Fine	core	52.80	2.62	0.54	21.62	0.38	0.00	0.19	16.07	6.14	0.08	0.02	100.4
Cpx		B	8 / 3 .	592.642	Fine	rim	52.34	2.59	0.78	21.08	0.35	0.00	0.26	16.00	6.82	0.07	0.03	100.3
Cpx		B	8 / 4 .	592.642	Fine	core	52.51	2.54	0.95	22.12	0.40	0.00	0.16	15.71	6.11	0.10	0.02	100.6
Cpx		B	8 / 5 .	592.642	Fine	rim	52.27	2.54	0.90	21.90	0.44	0.00	0.13	15.53	6.19	0.13	0.01	100.0
Cpx		B	8 / 6 .	592.642	Fine	core	52.10	2.49	0.85	21.15	0.30	0.00	0.22	16.15	6.99	0.17	0.01	100.4
Cpx		B	8 / 7 .	592.642	Fine	core	52.03	2.54	0.79	20.64	0.34	0.02	0.23	16.50	6.61	0.13	0.02	99.8
Cpx		E	11 / 1 .	592.533	Coarse	core	51.49	3.23	1.31	22.28	0.46	0.00	0.21	14.82	6.24	0.06	0.02	100.1
Cpx		E	11 / 2 .	592.533	Coarse	rim	51.34	3.20	1.34	22.50	0.41	0.00	0.22	15.04	6.72	0.06	0.02	100.8
Cpx		E	11 / 4 .	592.533	Coarse	rim	52.48	2.73	0.55	21.31	0.37	0.00	0.19	16.10	6.41	0.09	0.03	100.2
Cpx		E	11 / 5 .	592.533	Coarse	rim	51.86	3.02	1.27	18.54	0.36	0.00	0.23	16.80	8.44	0.08	0.06	100.6
Cpx		C	12 / 4 .	592.533	Coarse	core	52.32	2.73	0.71	20.66	0.37	0.00	0.18	16.14	7.07	0.06	0.03	100.2
Cpx		C	12 / 5 .	592.533	Coarse	rim	51.90	2.70	0.94	21.24	0.41	0.00	0.13	15.81	6.71	0.12	0.07	100.0
Cpx		C	12 / 8 .	592.533	Coarse	core	51.76	2.79	0.98	21.53	0.35	0.00	0.22	15.50	6.57	0.08	0.04	99.8

Mineral		Area	Point	Depth (mbsf)	Layer type	Grain area	SiO2	Al2O3	TiO2	CaO	Na2O	K2O	MnO	MgO	FeO	Cr2O3	NiO	Total
Cpx		C	12 / 9 .	592.533	Coarse	rim	51.61	2.79	1.11	22.03	0.41	0.03	0.19	15.26	6.67	0.05	0.02	100.1
Cpx	360_65R5_102	B	15 / 1 .	592.550	Coarse	core	52.38	2.56	0.47	22.12	0.41	0.00	0.19	15.57	6.71	0.06	0.01	100.5
Cpx		B	15 / 2 .	592.550	Coarse	rim	51.51	2.79	1.08	22.14	0.38	0.00	0.16	15.23	6.40	0.09	0.02	99.8
Cpx		B	15 / 1 .	592.550	Coarse	core	52.49	2.72	0.50	19.51	0.39	0.00	0.23	16.88	6.65	0.01	0.01	99.4
Cpx		B	15 / 2 .	592.550	Coarse	rim	52.37	2.67	0.88	21.72	0.40	0.01	0.17	15.20	6.46	0.06	0.00	99.9
Cpx		B	15 / 3 .	592.550	Coarse	core	51.60	2.80	1.13	21.76	0.48	0.00	0.27	15.11	6.58	0.09	0.00	99.8
Cpx		B	15 / 4 .	592.550	Coarse	rim	51.11	2.85	1.16	21.48	0.42	0.02	0.22	15.41	6.75	0.17	0.05	99.6
Cpx		B	15 / 7 .	592.550	Coarse	core	51.57	2.65	0.98	21.88	0.36	0.00	0.21	15.26	6.33	0.13	0.01	99.4
Cpx		B	15 / 8 .	592.550	Coarse	rim	51.19	2.64	0.96	22.23	0.37	0.00	0.21	15.18	6.30	0.10	0.00	99.2
Cpx		D	21 / 1 .	592.557	Coarse	core	51.94	2.84	0.73	21.63	0.45	0.00	0.18	15.35	6.49	0.12	0.03	99.7
Cpx		D	21 / 3 .	592.557	Coarse	rim	51.63	2.59	0.73	20.66	0.40	0.02	0.26	16.14	6.88	0.06	0.00	99.4
Cpx		D	21 / 4 .	592.557	Coarse	rim	51.17	2.98	1.28	21.82	0.37	0.00	0.22	15.44	6.31	0.06	0.03	99.7
Cpx		F	6 / 1 .	591.536	Fine	core	52.32	2.35	0.60	21.26	0.40	0.02	0.16	16.48	6.19	0.10		99.9
Cpx		F	7 / 1 .	591.536	Fine	rim	52.30	2.35	0.60	21.88	0.29	0.00	0.23	15.68	5.85	0.18		99.4
Cpx		F	8 / 1 .	591.536	Fine	rim	52.43	2.38	0.49	22.14	0.39	0.02	0.27	15.81	5.77	0.20		99.9
Cpx		F	11 / 1 .	591.536	Fine	core	52.82	2.31	0.61	22.14	0.37	0.00	0.15	15.76	5.64	0.20		100.0
Cpx		F	12 / 1 .	591.536	Fine	core	52.54	2.30	0.54	21.82	0.47	0.00	0.22	15.90	5.82	0.17		99.8
Cpx		E	19 / 1 .	591.540	Fine	core	52.67	2.52	0.58	21.74	0.41	0.01	0.15	15.54	5.83	0.09		99.5
Cpx		E	19 / 2 .	591.540	Fine	rim	52.89	2.49	0.58	20.77	0.36	0.02	0.18	15.96	6.19	0.20		99.6
Cpx		E	19 / 3 .	591.540	Fine	core	52.95	2.48	0.56	19.66	0.39	0.00	0.21	17.00	6.88	0.07		100.2
Cpx		E	19 / 4 .	591.540	Fine	rim	52.86	2.34	0.57	22.01	0.39	0.01	0.17	15.73	6.01	0.13		100.2
Cpx		E	19 / 6 .	591.540	Fine	core	52.40	2.66	0.64	21.63	0.40	0.00	0.17	15.71	6.03	0.15		99.8
Cpx		C	22 / 2 .	591.546	Fine	core	52.45	2.27	0.79	22.43	0.39	0.01	0.17	15.65	5.61	0.16		99.9
Cpx	360_65R5_2	G	24 / 1 .	591.541	Fine	core	52.90	2.47	0.57	18.71	0.35	0.00	0.25	17.64	6.87	0.07		99.8
Cpx		G	24 / 2 .	591.541	Fine	rim	52.44	2.53	0.57	22.38	0.40	0.00	0.18	15.70	5.65	0.15		100.0
Cpx		G	24 / 3 .	591.541	Fine	core	52.52	2.36	0.63	21.60	0.39	0.01	0.19	15.97	5.91	0.10		99.7
Cpx		D	26 / 1 .	591.553	Fine	core	52.14	2.73	0.77	21.89	0.44	0.00	0.13	15.35	6.15	0.13		99.7
Cpx		D	26 / 2 .	591.553	Fine	rim	52.00	2.45	0.86	22.02	0.42	0.01	0.18	15.26	6.19	0.08		99.4
Cpx		D	26 / 3 .	591.553	Fine	rim	52.78	2.29	0.72	19.86	0.34	0.00	0.18	16.64	7.21	0.08		100.1
Cpx		D	26 / 5 .	591.553	Fine	core	51.72	2.73	0.86	20.60	0.41	0.02	0.21	15.76	6.97	0.18		99.4
Cpx		D	26 / 6 .	591.553	Fine	rim	52.27	2.52	0.77	22.21	0.35	0.00	0.26	15.84	6.45	0.09		100.8
Cpx		B	29 / 2 .	591.553	Fine	core	52.50	2.60	0.58	22.18	0.35	0.00	0.17	15.64	5.70	0.11		99.8
Cpx		B	29 / 3 .	591.553	Fine	rim	52.04	2.51	0.75	20.18	0.39	0.00	0.22	16.34	6.51	0.06		99.0
Cpx		B	29 / 4 .	591.553	Fine	core	52.16	2.46	0.81	21.32	0.39	0.00	0.18	15.87	6.03	0.10		99.3
Cpx		A	32 / 2 .	591.576	Fine	core	52.80	2.33	0.46	18.27	0.33	0.00	0.17	17.05	7.98	0.10		99.5
Cpx		A	32 / 4 .	591.576	Fine	rim	51.89	2.46	0.85	22.11	0.44	0.01	0.16	15.29	6.08	0.09		99.4
Cpx		A	32 / 6 .	591.576	Fine	core	52.44	2.52	0.82	20.50	0.35	0.00	0.17	15.94	7.04	0.09		99.9
Cpx		A	32 / 7 .	591.576	Fine	rim	52.41	2.35	0.76	22.72	0.40	0.00	0.19	15.48	5.88	0.09		100.3
Cpx		D	35 / 2 .	591.577	Fine	core	52.92	2.35	0.80	20.66	0.34	0.00	0.19	16.50	6.65	0.16		100.6
Cpx		D	35 / 4 .	591.577	Fine	core	51.85	2.83	0.87	21.87	0.37	0.00	0.18	15.59	6.23	0.17		100.0
Cpx		D	35 / 5 .	591.577	Fine	core	52.05	2.48	0.81	21.28	0.37	0.00	0.16	15.71	6.25	0.13		99.2
Cpx		D	35 / 6 .	591.577	Fine	core	51.47	2.82	0.97	20.16	0.37	0.00	0.22	16.55	7.25	0.09		99.9

Mineral		Area	Point	Depth (mbsf)	Layer type	Grain area	SiO2	Al2O3	TiO2	CaO	Na2O	K2O	MnO	MgO	FeO	Cr2O3	NiO	Total
Cpx	360_65R5_4	D	35 / 7 .	591.577	Fine	rim	52.28	2.48	0.89	20.03	0.42	0.00	0.21	16.39	7.12	0.08		99.9
Cpx		B	38 / 1 .	591.581	Fine	core	52.09	2.65	0.56	22.05	0.44	0.00	0.25	15.48	6.08	0.10		99.7
Cpx		B	38 / 3 .	591.581	Fine	rim	52.00	2.53	0.81	22.23	0.33	0.00	0.22	15.44	6.09	0.09		99.7
Cpx		B	38 / 4 .	591.581	Fine	rim	51.69	2.56	0.76	21.77	0.40	0.01	0.16	15.29	6.35	0.12		99.1
Cpx		B	38 / 5 .	591.581	Fine	core	51.64	2.51	0.79	21.85	0.41	0.00	0.24	15.30	6.37	0.09		99.2
Cpx		B	38 / 8 .	591.581	Fine	rim	52.16	2.41	0.87	22.21	0.43	0.00	0.21	15.35	6.85	0.10		100.6
Cpx		C	40 / 1 .	591.583	Fine	core	52.06	2.72	0.70	22.26	0.44	0.02	0.19	15.36	6.30	0.15		100.2
Cpx		C	40 / 3 .	591.583	Fine	rim	51.99	2.69	0.81	20.69	0.37	0.01	0.19	16.22	6.66	0.09		99.7
Cpx		C	40 / 4 .	591.583	Fine	rim	51.90	2.51	0.79	22.50	0.31	0.01	0.22	15.24	6.23	0.04		99.7
Cpx		C	40 / 5 .	591.583	Fine	core	51.89	2.68	0.66	21.85	0.45	0.00	0.22	15.59	6.26	0.10		99.7
Cpx		C	40 / 6 .	591.583	Fine	rim	52.62	2.51	0.65	21.07	0.37	0.00	0.25	15.69	6.32	0.08		99.6
Cpx		C	40 / 8 .	591.583	Fine	rim	51.78	2.63	0.81	21.95	0.42	0.02	0.28	15.42	6.26	0.12		99.7
Cpx		C	4 / 2 .	592.718	Coarse	core	51.78	2.61	0.95	22.18	0.31	0.00	0.21	15.29	6.34	0.09		99.7
Cpx		C	4 / 4 .	592.718	Coarse	core	51.84	2.70	0.96	19.44	0.39	0.02	0.18	16.39	7.39	0.08		99.4
Cpx		C	4 / 5 .	592.718	Coarse	rim	52.30	2.64	0.93	21.53	0.42	0.00	0.17	15.61	6.68	0.06		100.3
Cpx		C	4 / 7 .	592.718	Coarse	rim	51.60	2.85	1.20	22.31	0.40	0.00	0.19	15.08	6.44	0.11		100.2
Cpx		C	4 / 8 .	592.718	Coarse	core	53.08	2.38	0.56	15.65	0.26	0.00	0.21	18.81	9.05	0.11		100.1
Cpx		C	4 / 9 .	592.718	Coarse	rim	52.28	2.60	0.81	20.48	0.37	0.00	0.18	16.08	6.67	0.01		99.5
Cpx		A	7 / 1 .	592.713	Coarse	core	51.50	2.79	1.03	21.24	0.43	0.01	0.19	15.71	6.64	0.12		99.6
Cpx		A	7 / 2 .	592.713	Coarse	rim	51.87	2.48	0.80	21.79	0.35	0.00	0.20	15.64	6.43	0.07		99.6
Cpx		A	7 / 3 .	592.713	Coarse	core	51.80	2.92	0.58	18.86	0.37	0.00	0.19	17.18	7.32	0.11		99.3
Cpx	360_65R5_117	A	7 / 4 .	592.713	Coarse	core	51.73	2.77	0.95	19.80	0.39	0.03	0.24	16.46	6.95	0.08		99.4
Cpx		B	10 / 1 .	592.706	Coarse	core	52.66	2.35	0.52	17.77	0.34	0.01	0.20	17.80	8.07	0.06		99.8
Cpx		B	10 / 2 .	592.706	Coarse	rim	52.08	2.57	0.92	21.59	0.37	0.00	0.22	15.73	6.51	0.13		100.1
Cpx		D	13 / 3 .	592.701	Coarse	core	52.53	2.63	0.56	21.28	0.40	0.00	0.20	15.81	6.70	0.10		100.2
Cpx		D	13 / 4 .	592.701	Coarse	rim	51.88	2.76	1.10	22.08	0.38	0.00	0.15	15.36	6.22	0.12		100.0
Cpx		D	13 / 5 .	592.701	Coarse	core	52.37	2.41	0.82	18.29	0.30	0.01	0.22	17.14	8.27	0.04		99.9
Cpx		E	16 / 1 .	592.695	Coarse	core	51.80	2.41	0.73	22.21	0.39	0.00	0.17	15.63	6.01	0.10		99.5
Cpx		E	16 / 3 .	592.695	Coarse	rim	51.78	2.59	0.85	20.64	0.34	0.00	0.23	16.08	6.69	0.13		99.3
Cpx		E	16 / 4 .	592.695	Coarse	core	52.73	2.23	0.73	17.51	0.33	0.00	0.23	17.77	8.59	0.13		100.3
Cpx		E	16 / 5 .	592.695	Coarse	core	52.05	2.61	0.97	21.81	0.38	0.01	0.22	15.35	6.47	0.06		99.9
Cpx		B	19 / 1 .	592.742	Coarse	core	51.33	3.19	1.33	19.93	0.44	0.03	0.21	15.80	6.96	0.01		99.2
Cpx		C	21 / 1 .	592.742	Coarse	core	51.62	3.22	0.78	21.88	0.47	0.00	0.19	15.17	5.94	0.02		99.3
Cpx		C	21 / 2 .	592.742	Coarse	rim	52.41	2.56	0.84	19.77	0.33	0.00	0.23	16.80	7.66	0.07		100.7
Cpx	360_65R5_120	C	23 / 2 .	592.742	Coarse	core	52.24	2.66	0.60	21.54	0.39	0.00	0.12	16.02	6.55	0.10		100.2
Cpx		C	23 / 3 .	592.742	Coarse	rim	51.82	2.82	1.01	22.20	0.41	0.00	0.17	14.81	6.37	0.10		99.7
Cpx		A	26 / 3 .	592.727	Coarse	core	51.60	2.74	1.00	21.50	0.39	0.01	0.23	15.27	6.56	0.05		99.3
Cpx		A	26 / 4 .	592.727	Coarse	rim	51.39	2.82	0.90	21.72	0.42	0.02	0.18	15.45	6.43	0.10		99.4
Cpx		A	26 / 5 .	592.727	Coarse	rim	51.45	2.77	0.96	20.68	0.37	0.00	0.20	16.00	6.95	0.08		99.5
Cpx		A	4 / 1 .	592.024	Coarse	core	51.15	3.01	1.12	22.29	0.40	0.00	0.24	15.34	6.28	0.08		99.9
Cpx		B	8 / 1 .	592.027	Coarse	core	52.66	2.45	0.51	16.86	0.30	0.00	0.27	18.27	9.05	0.02		100.4
Cpx		B	8 / 2 .	592.027	Coarse	rim	52.30	2.40	0.68	15.74	0.30	0.01	0.23	18.36	9.83	0.09		99.9

Mineral		Area	Point	Depth (mbsf)	Layer type	Grain area	SiO2	Al2O3	TiO2	CaO	Na2O	K2O	MnO	MgO	FeO	Cr2O3	NiO	Total
Cpx		E	9 / 1 .	592.028	Coarse	core	51.56	2.91	1.04	21.74	0.44	0.02	0.24	15.05	6.71	0.10		99.8
Cpx		E	9 / 2 .	592.028	Coarse	rim	51.74	2.62	0.89	21.40	0.42	0.00	0.19	15.24	6.87	0.09		99.5
Cpx	360_65R5_51	C	17 / 1 .	592.039	Coarse	rim	52.07	2.82	1.05	18.03	0.37	0.00	0.21	17.32	8.38	0.10		100.4
Cpx		C	17 / 2 .	592.039	Coarse	core	51.38	3.18	1.28	20.02	0.47	0.00	0.23	15.62	6.72	0.08		99.0
Cpx		C	17 / 4 .	592.039	Coarse	rim	51.35	3.04	1.14	21.99	0.45	0.00	0.25	15.24	6.52	0.11		100.1
Cpx		F	20 / 1 .	592.044	Coarse	rim	51.55	2.81	1.11	21.77	0.44	0.00	0.20	14.98	6.91	0.08		99.8
Cpx		F	20 / 2 .	592.044	Coarse	core	52.49	2.58	0.46	16.27	0.36	0.03	0.21	18.81	8.77	0.17		100.1
Cpx		F	20 / 4 .	592.044	Coarse	rim	51.79	2.47	0.63	21.84	0.40	0.00	0.25	15.12	6.43	0.07		99.0
Cpx		F	20 / 5 .	592.044	Coarse	core	51.79	3.12	0.55	20.82	0.45	0.01	0.22	16.05	6.82	0.20		100.0
Cpx		F	20 / 6 .	592.044	Coarse	rim	52.17	2.61	0.56	21.30	0.41	0.00	0.23	15.21	6.55	0.13		99.2
Cpx		B	23 / 1 .	592.404	Fine	core	52.52	2.40	0.73	20.57	0.36	0.00	0.13	16.39	6.43	0.06		99.6
Cpx		B	23 / 3 .	592.404	Fine	core	52.29	2.46	0.70	21.08	0.40	0.02	0.18	16.51	6.34	0.09		100.0
Cpx		B	23 / 4 .	592.404	Fine	rim	52.34	2.49	0.69	22.26	0.37	0.00	0.18	15.91	5.29	0.12		99.6
Cpx		A	25 / 2 .	592.406	Fine	core	53.40	2.23	0.63	19.06	0.26	0.00	0.22	17.65	7.06	0.03		100.5
Cpx		A	25 / 3 .	592.406	Fine	core	52.32	2.41	0.49	16.97	0.31	0.02	0.27	18.37	8.68	0.09		99.9
Cpx		A	25 / 4 .	592.406	Fine	rim	52.31	2.50	0.64	19.14	0.34	0.00	0.21	16.95	7.31	0.09		99.5
Cpx		A	25 / 5 .	592.406	Fine	core	52.08	2.65	0.64	21.25	0.41	0.00	0.19	15.74	5.99	0.12		99.1
Cpx		C	28 / 2 .	592.405	Fine	core	52.35	2.55	0.59	21.87	0.45	0.04	0.20	15.55	6.01	0.07		99.6
Cpx		C	28 / 3 .	592.405	Fine	core	52.75	2.39	0.69	19.53	0.35	0.00	0.19	17.16	7.27	0.09		100.4
Cpx		C	28 / 4 .	592.405	Fine	core	52.40	2.71	0.77	21.84	0.43	0.01	0.22	15.54	6.01	0.05		100.0
Cpx		C	28 / 5 .	592.405	Fine	rim	52.31	2.54	0.76	21.95	0.37	0.02	0.15	15.52	5.99	0.10		99.7
Cpx	360_65R5_87	E	31 / 2 .	592.391	Fine	core	52.30	2.72	0.52	22.12	0.41	0.00	0.22	15.83	5.66	0.14		99.9
Cpx		E	31 / 3 .	592.391	Fine	rim	52.60	2.28	0.67	22.07	0.41	0.00	0.16	15.66	5.46	0.13		99.4
Cpx		E	31 / 4 .	592.391	Fine	core	52.29	2.54	0.64	19.13	0.33	0.00	0.18	16.97	7.13	0.10		99.3
Cpx		D	35 / 1 .	592.390	Fine	rim	52.18	2.42	0.67	21.64	0.33	0.02	0.16	16.23	5.94	0.08		99.6
Cpx		D	35 / 2 .	592.390	Fine	core	52.65	2.46	0.56	20.72	0.30	0.01	0.18	16.65	5.87	0.13		99.5
Cpx		D	35 / 3 .	592.390	Fine	core	52.77	2.51	0.59	22.10	0.39	0.00	0.13	15.90	5.89	0.09		100.4
Cpx		F	38 / 1 .	592.384	Fine	core	52.03	2.66	0.56	21.82	0.40	0.00	0.24	15.74	5.98	0.06		99.5
Cpx		F	38 / 3 .	592.384	Fine	core	52.80	2.23	0.65	20.46	0.36	0.00	0.14	16.90	6.44	0.11		100.1
Cpx		F	38 / 4 .	592.384	Fine	core	52.96	2.30	0.55	18.74	0.33	0.00	0.22	17.52	6.94	0.07		99.6
Cpx		F	38 / 5 .	592.384	Fine	rim	51.85	2.58	0.63	21.63	0.36	0.00	0.24	16.01	5.81	0.04		99.1
Cpx		F	38 / 6 .	592.384	Fine	core	52.21	2.50	0.73	22.03	0.37	0.00	0.18	15.69	6.02	0.13		99.9
Cpx		A	3 / 4 .	591.925	Fine	core	51.59	2.61	0.91	22.28	0.38	0.00	0.19	15.42	5.99	0.10		99.5
Cpx		A	3 / 5 .	591.925	Fine	core	51.92	2.57	0.70	21.91	0.41	0.00	0.16	15.38	6.26	0.14		99.5
Cpx		A	3 / 6 .	591.925	Fine	rim	52.77	2.33	0.70	19.11	0.32	0.00	0.18	17.22	7.47	0.12		100.2
Cpx		D	5 / 3 .	591.922	Fine	core	52.72	2.42	0.54	14.88	0.26	0.01	0.20	19.02	9.81	0.13		100.0
Cpx		D	5 / 4 .	591.922	Fine	rim	51.85	2.57	0.88	21.86	0.37	0.00	0.21	15.38	6.67	0.09		99.9
Cpx		D	5 / 5 .	591.922	Fine	core	52.16	2.65	0.81	20.63	0.38	0.01	0.24	15.68	7.15	0.05		99.8
Cpx		E	8 / 2 .	591.928	Fine	rim	51.87	2.66	0.81	21.57	0.40	0.00	0.22	15.44	6.67	0.05		99.7
Cpx		E	8 / 3 .	591.928	Fine	core	52.41	2.53	0.65	20.80	0.38	0.00	0.15	16.26	6.98	0.14		100.3
Cpx	360_65R5_39	E	8 / 4 .	591.928	Fine	core	52.45	2.39	0.79	18.22	0.34	0.00	0.18	17.67	8.12	0.07		100.2
Cpx		C	11 / 3 .	591.934	Fine	core	52.29	2.66	0.75	21.84	0.35	0.00	0.21	15.47	6.39	0.10		100.1

Mineral		Area	Point	Depth (mbsf)	Layer type	Grain area	SiO2	Al2O3	TiO2	CaO	Na2O	K2O	MnO	MgO	FeO	Cr2O3	NiO	Total
Cpx		C	11 / 4 .	591.934	Fine	rim	52.50	2.51	0.78	22.15	0.36	0.04	0.21	15.59	7.23	0.15		101.5
Cpx		B	14 / 1 .	591.932	Fine	core	52.35	2.42	0.76	22.49	0.43	0.00	0.22	15.64	5.72	0.09		100.1
Cpx		B	14 / 3 .	591.932	Fine	core	51.89	2.59	0.77	20.56	0.34	0.00	0.23	15.89	6.95	0.09		99.3
Cpx		B	14 / 4 .	591.932	Fine	rim	52.09	2.47	0.75	22.21	0.42	0.00	0.24	15.40	6.55	0.08		100.2
Cpx		A	17 / 3 .	591.848	Fine	core	52.42	2.57	0.71	18.17	0.37	0.02	0.21	18.08	6.27	0.10		98.9
Cpx		A	17 / 4 .	591.848	Fine	rim	52.58	2.56	0.77	21.34	0.34	0.00	0.20	16.19	6.51	0.12		100.6
Cpx		A	17 / 5 .	591.848	Fine	core	52.03	2.67	0.94	21.99	0.41	0.00	0.22	15.29	6.19	0.10		99.8
Cpx		D	19 / 2 .	591.846	Fine	rim	52.74	2.63	0.54	19.45	0.36	0.00	0.19	16.67	7.21	0.09		99.9
Cpx		D	19 / 3 .	591.846	Fine	rim	52.64	2.70	0.77	21.61	0.41	0.02	0.24	15.57	6.38	0.08		100.4
Cpx		D	19 / 4 .	591.846	Fine	core	52.31	2.53	0.73	21.62	0.39	0.01	0.21	15.52	6.46	0.05		99.8
Cpx	360_65R5_32	C	22 / 1 .	591.840	Fine	core	52.21	2.76	0.83	21.76	0.41	0.01	0.17	15.28	6.38	0.09		99.9
Cpx		C	22 / 2 .	591.840	Fine	core	52.34	2.69	0.61	20.37	0.38	0.00	0.22	16.09	6.57	0.14		99.4
Cpx		C	22 / 3 .	591.840	Fine	rim	51.89	2.69	0.65	21.91	0.41	0.00	0.19	15.33	6.43	0.09		99.6
Cpx		B	25 / 2 .	591.837	Fine	core	51.71	2.69	0.93	22.29	0.49	0.01	0.22	15.26	5.88	0.13		99.6
Cpx		B	25 / 3 .	591.837	Fine	core	53.01	2.57	0.60	18.88	0.38	0.00	0.24	17.55	7.40	0.11		100.7
Cpx		B	25 / 4 .	591.837	Fine	rim	53.04	2.39	0.82	16.10	0.30	0.00	0.20	18.42	8.92	0.06		100.2
Cpx		E	28 / 1 .	591.832	Fine	core	52.39	2.67	0.63	21.96	0.43	0.00	0.17	15.58	6.33	0.13		100.3
Cpx		E	28 / 2 .	591.832	Fine	rim	51.34	2.63	0.88	21.90	0.42	0.01	0.17	15.38	6.36	0.11		99.2
Cpx		D	3 / 2 .	591.765	Coarse	rim	51.77	2.77	1.02	19.66	0.38	0.02	0.25	16.35	7.72	0.06		100.0
Cpx		D	3 / 4 .	591.765	Coarse	core	53.10	2.67	0.43	18.37	0.30	0.00	0.23	17.47	7.48	0.05		100.1
Cpx		B	5 / 3 .	591.769	Fine	rim	52.24	2.43	0.77	21.85	0.41	0.00	0.16	15.45	6.37	0.14		99.8
Cpx	360_65R5_23	B	5 / 4 .	591.769	Fine	core	52.50	2.42	0.63	17.99	0.34	0.00	0.23	17.45	7.58	0.11		99.2
Cpx		A	9 / 4 .	591.773	Fine	rim	51.95	2.32	0.82	18.16	0.29	0.00	0.25	17.06	8.05	0.12		99.0
Cpx		A	9 / 5 .	591.773	Fine	rim	52.73	2.30	0.55	14.56	0.23	0.00	0.28	19.48	8.86	0.10		99.1
Cpx		C	12 / 2 .	591.776	Fine	core	51.65	2.59	0.73	21.91	0.41	0.00	0.22	15.34	6.33	0.11		99.3
Cpx		E	14 / 3 .	591.513	Coarse	rim	51.84	2.77	1.07	21.59	0.45	0.00	0.21	15.40	6.59	0.04		100.0
Cpx		E	14 / 4 .	591.513	Coarse	core	51.15	3.31	1.22	21.84	0.45	0.00	0.15	14.77	6.56	0.06		99.5
Cpx		C	21 / 1 .	591.519	Coarse	core	51.18	3.21	1.03	22.32	0.44	0.01	0.26	14.04	7.39	0.01		99.9
Cpx	360_65R5_0	C	21 / 2 .	591.519	Coarse	rim	51.75	2.37	0.84	21.48	0.42	0.00	0.17	14.88	7.86	0.01		99.8
Cpx		A	23 / 1 .	591.523	Coarse in Fin	rim	51.71	2.67	0.93	19.44	0.30	0.00	0.30	16.52	8.10	0.02		100.0
Cpx		A	23 / 2 .	591.523	Coarse in Fin	core	51.77	2.96	1.09	21.20	0.42	0.02	0.22	15.64	6.82	0.05		100.2
Cpx		F	27 / 2 .	591.526	Fine	core	52.43	2.30	0.81	17.31	0.33	0.01	0.23	17.75	8.53	0.06		99.8
Cpx		F	27 / 3 .	591.526	Fine	core	52.48	2.29	0.78	19.29	0.33	0.01	0.23	16.91	7.15	0.14		99.6
Cpx		E	33 / 1 .	591.739	Coarse	core	53.17	2.53	0.44	17.95	0.30	0.00	0.21	17.79	8.10	0.10		100.6
Cpx		E	33 / 2 .	591.739	Coarse	rim	52.29	2.53	0.60	18.07	0.35	0.02	0.17	16.96	8.30	0.05		99.3
Cpx		D	40 / 1 .	591.740	Coarse	core	51.92	2.64	0.88	21.78	0.44	0.01	0.19	15.24	6.66	0.08		99.8
Cpx	360_65R5_21	D	40 / 2 .	591.740	Coarse	core	51.83	2.77	1.06	19.59	0.40	0.00	0.19	16.14	7.77	0.12		99.9
Cpx		D	40 / 3 .	591.740	Coarse	rim	51.77	2.63	0.89	22.10	0.40	0.00	0.21	15.14	6.52	0.10		99.8
Cpx		D	40 / 4 .	591.740	Coarse	rim	51.91	2.72	0.85	21.01	0.36	0.02	0.22	15.77	6.98	0.11		99.9
Cpx		D	40 / 5 .	591.740	Coarse	core	52.02	2.57	0.97	19.69	0.41	0.01	0.23	16.13	7.57	0.08		99.7
Cpx		N2	14 / 1 .	592.153	Coarse	rim	51.81	2.69	0.92	20.74	0.39	0.01	0.18	16.38	7.07	0.09	0.00	100.3
Cpx		N4	17 / 1 .	592.156	Coarse	core	51.87	2.72	0.97	21.36	0.48	0.03	0.14	15.55	7.09	0.05	0.00	100.2

Mineral		Area	Point	Depth (mbsf)	Layer type	Grain area	SiO2	Al2O3	TiO2	CaO	Na2O	K2O	MnO	MgO	FeO	Cr2O3	NiO	Total
Cpx		N4	19 / 1 .	592.156	Coarse	core	51.44	2.99	1.08	21.04	0.41	0.01	0.16	15.71	7.23	0.07	0.00	100.1
Cpx		N4	20 / 1 .	592.156	Coarse	rim	51.92	2.72	0.76	20.74	0.39	0.03	0.17	16.05	7.50	0.05	0.00	100.3
Cpx		N4	21 / 1 .	592.156	Coarse	core	52.06	2.67	0.73	21.11	0.42	0.01	0.16	16.10	7.12	0.14	0.03	100.5
Cpx	360_65R5_63A	N4	22 / 1 .	592.156	Coarse	rim	51.75	2.53	0.90	19.08	0.37	0.03	0.15	16.65	8.24	0.02	0.00	99.7
Cpx		N4	23 / 1 .	592.156	Coarse	rim	52.02	2.60	0.86	21.66	0.44	0.01	0.14	15.39	6.72	0.07	0.01	99.9
Cpx		N4	25 / 1 .	592.156	Coarse	core	51.53	2.74	0.96	21.22	0.07	0.02	0.25	15.63	7.20	0.11	0.03	99.7
Cpx		N1	27 / 1 .	592.158	Coarse	core	51.77	2.27	0.95	21.32	0.37	0.01	0.09	15.69	7.75	0.00	0.06	100.2
Cpx		N1	29 / 1 .	592.158	Coarse	core	52.20	2.45	0.77	21.02	0.40	0.01	0.19	15.84	7.60	0.02	0.00	100.5
Cpx		N5	34 / 1 .	592.154	Coarse	rim	52.09	2.43	0.80	20.73	0.00	0.02	0.21	16.09	7.34	0.08	0.02	99.8
Cpx		N5	35 / 1 .	592.154	Coarse	core	51.90	2.40	0.61	21.67	0.52	0.03	0.18	15.65	6.70	0.15	0.05	99.8
Cpx		N5	36 / 1 .	592.154	Coarse	core	51.49	2.80	0.95	21.84	0.49	0.01	0.15	15.49	6.75	0.08	0.00	100.0
Cpx		A	51 / 1 .	592.170	Coarse	core	51.80	2.60	0.91	20.62	0.37	0.01	0.15	15.97	7.44	0.10	0.00	99.9
Cpx		A	52 / 1 .	592.170	Coarse	rim	51.61	2.91	1.02	21.26	0.42	0.01	0.21	15.59	6.92	0.00	0.00	99.9
Cpx		A	53 / 1 .	592.170	Coarse	core	52.79	2.63	0.73	21.50	0.50	0.00	0.20	15.65	6.98	0.07	0.01	101.0
Cpx		A	54 / 1 .	592.170	Coarse	rim	51.96	2.56	0.80	19.73	0.00	0.01	0.13	16.30	7.87	0.04	0.01	99.4
Cpx		A	55 / 1 .	592.170	Coarse	core	51.83	2.92	0.98	18.64	0.45	0.02	0.24	16.13	8.19	0.02	0.00	99.4
Cpx		B	61 / 1 .	592.175	Coarse	rim	52.57	2.57	0.76	21.86	0.37	0.00	0.18	15.45	7.01	0.11	0.00	100.9
Cpx		B	64 / 1 .	592.175	Coarse	core	51.65	2.61	0.86	21.81	0.44	0.00	0.18	15.12	7.02	0.13	0.06	99.8
Cpx		B	76 / 1 .	592.177	Coarse	core	51.80	2.77	0.90	20.09	0.35	0.00	0.16	16.22	7.87	0.07	0.02	100.2
Cpx		B	77 / 1 .	592.177	Coarse	rim	51.43	2.77	0.92	21.30	0.31	0.02	0.16	15.49	6.96	0.12	0.02	99.5
Cpx		B	78 / 1 .	592.177	Coarse	rim	51.71	2.63	0.97	18.69	0.27	0.01	0.21	16.93	8.65	0.13	0.00	100.2
Cpx		B	79 / 1 .	592.177	Coarse	core	51.74	2.66	0.92	20.07	0.00	0.01	0.16	16.04	7.73	0.08	0.05	99.4
Cpx		C	1 / 1 .	592.169	Coarse	core	51.67	2.75	0.90	21.58	0.52	0.02	0.15	15.50	7.29	0.12	0.07	100.5
Cpx		C	2 / 1 .	592.169	Coarse	rim	52.15	2.52	0.86	21.40	0.44	0.02	0.18	15.49	7.06	0.05	0.00	100.2
Cpx		C	3 / 1 .	592.169	Coarse	core	52.81	2.61	0.58	21.42	0.50	0.02	0.14	15.55	6.54	0.10	0.02	100.3
Cpx		C	6 / 1 .	592.169	Coarse	core	52.36	2.77	0.74	21.45	0.62	0.00	0.20	15.68	6.31	0.06	0.00	100.2
Cpx		C	7 / 1 .	592.169	Coarse	rim	52.73	2.56	0.60	18.62	0.48	0.01	0.16	17.08	7.67	0.11	0.00	100.0
Cpx		D	12 / 1 .	592.171	Coarse	rim	52.70	2.40	0.81	20.85	0.37	0.02	0.15	16.23	7.04	0.06	0.00	100.6
Cpx		D	13 / 1 .	592.171	Coarse	core	51.78	2.76	0.96	21.57	0.45	0.01	0.16	15.27	7.03	0.13	0.02	100.1
Cpx		D	15 / 1 .	592.171	Coarse	core	52.68	2.53	0.75	19.60	0.38	0.01	0.16	16.98	7.46	0.11	0.00	100.7
Cpx		D	16 / 1 .	592.171	Coarse	rim	52.78	2.23	0.77	15.43	0.00	0.01	0.23	18.53	10.43	0.08	0.02	100.5
Cpx		D	17 / 1 .	592.171	Coarse	rim	52.25	2.49	0.87	17.86	0.00	0.01	0.16	17.65	9.36	0.07	0.02	100.7
Cpx	360_65R5_63B	D	25 / 1 .	592.171	Coarse	core	51.97	2.66	0.85	21.74	0.28	0.02	0.14	15.43	6.87	0.20	0.00	100.1
Cpx		D	26 / 1 .	592.171	Coarse	rim	52.30	2.52	0.70	18.45	0.29	0.00	0.23	16.99	8.76	0.15	0.01	100.4
Cpx		E	46 / 1 .	592.182	Coarse	core	52.11	2.60	0.49	20.82	0.42	0.01	0.15	16.55	7.06	0.18	0.04	100.4
Cpx		E	47 / 1 .	592.182	Coarse	rim	51.38	2.63	0.95	21.38	0.40	0.02	0.17	15.52	7.29	0.04	0.00	99.8
Cpx		E	49 / 1 .	592.182	Coarse	rim	52.29	2.61	0.81	21.04	0.45	0.01	0.13	15.56	7.34	0.09	0.02	100.3
Cpx		E	50 / 1 .	592.182	Coarse	core	53.12	2.31	0.70	15.70	0.28	0.01	0.24	17.52	10.29	0.04	0.01	100.2
Cpx		F	55 / 1 .	592.179	Coarse	rim	51.41	2.87	0.98	21.73	0.00	0.00	0.17	14.97	6.90	0.09	0.00	99.1
Cpx		F	56 / 1 .	592.179	Coarse	core	52.39	2.73	1.05	21.09	0.41	0.00	0.19	15.65	7.35	0.10	0.00	101.0
Cpx		F	58 / 1 .	592.179	Coarse	core	52.10	2.72	0.44	21.05	0.39	0.00	0.22	16.13	6.94	0.14	0.00	100.1
Cpx		F	59 / 1 .	592.179	Coarse	rim	51.86	2.48	0.81	20.61	0.36	0.01	0.15	16.09	7.48	0.14	0.04	100.0

Mineral	Area	Point	Depth (mbsf)	Layer type	Grain area	SiO2	Al2O3	TiO2	CaO	Na2O	K2O	MnO	MgO	FeO	Cr2O3	NiO	Total
Cpx	F	60 / 1 .	592.179	Coarse	rim	52.25	2.63	0.86	18.57	0.27	0.01	0.17	16.85	8.90	0.14	0.01	100.6
Cpx	F	61 / 1 .	592.179	Coarse	core	52.14	2.55	0.64	19.32	0.35	0.02	0.20	16.98	7.67	0.13	0.00	100.0
Cpx	G	71 / 1 .	592.178	Coarse	core	52.76	2.36	0.74	16.93	0.27	0.01	0.16	18.35	9.05	0.00	0.01	100.6
Cpx	G	73 / 1 .	592.178	Coarse	rim	51.78	2.71	0.74	21.23	0.55	0.02	0.15	15.67	6.84	0.00	0.00	99.7
Cpx	G	74 / 1 .	592.178	Coarse	core	51.86	3.00	0.52	20.24	0.31	0.02	0.15	16.32	7.23	0.06	0.03	99.7
Cpx	I	91 / 1 .	592.167	Coarse	core	51.95	2.96	1.02	19.18	0.47	0.00	0.17	16.61	7.59	0.05	0.00	100.0
Cpx	I	93 / 1 .	592.167	Coarse	rim	51.99	2.67	0.85	21.51	0.40	0.00	0.19	15.99	6.59	0.05	0.00	100.2
Cpx	I	95 / 1 .	592.167	Coarse	rim	52.59	2.56	0.79	18.99	0.32	0.02	0.19	16.94	8.59	0.06	0.03	101.0
Cpx	I	96 / 1 .	592.167	Coarse	core	51.48	3.00	1.00	21.12	0.46	0.01	0.15	15.85	6.86	0.08	0.05	100.0

Calibration standards	Wollastonite (San Carlos)	Al2O3	TiMnO3	Wollastonite	Albite	Orthose	TiMnO3	Forsterite	Fayalite	Cr2O3	NiO

Appendix 1.4

In situ trace elements concentrations in ppm analysed by La-ICP-MS on Thermo Fisher Element XR in GM (Montpellier, France)

Mineral	Sample	Area	Point	Depth (mbsf)	Layer type	Grain area	La	Ce	Pr	Nd	Sm	Eu	Gd	Tb	Dy	Y	Ho	Er	Tm	Yb	Lu
Ol		Analitycal error average				1 sigma	0.0003	0.0004	0.00018	0.001	0.00056	0.0002	0.0013	0.0003	0.0011	0.0035	0.0004	0.0024	0.0007	0.005	0.0013
Ol		C	mb_2	591.546	Fine	core	<0.00049	<0.00044	0.0003	<0.0013	<0.00092	0.00048	<0.0035	<0.00046	<0.00049	0.0356	0.00041	0.0063	0.00142	0.0204	0.0097
Ol	360_65R5_2	C	mb_3	591.546	Fine	rim	<0.00047	0.00128	<0.00031	0.0018	0.00117	0.00063	<0.0036	<0.00046	0.002	0.0226	0.0005	0.0034	0.00268	0.0245	0.0092
Ol		B	mb_4	591.553	Fine	core	<0.00071	0.00094	<0.00033	<0.0014	<0.00136	<0.00044	<0.0031	0.00052	<0.0021	0.0366	0.00114	0.0064	0.00259	0.0302	0.008
Ol		B	mb_5	591.553	Fine	rim	<0.00051	<0.00053	<0.00030	<0.00146	<0.00211	<0.00042	<0.0021	<0.00048	<0.00	0.0254	0.00091	0.005	0.00188	0.0262	0.0096
Ol		B	mb_6	591.553	Fine	core	<0.00076	<0.00089	<0.00045	<0.0026	<0.0012	<0.00047	<0.0064	<0.00069	<0.00080	0.008	<0.00	<0.0032	0.00113	0.0101	0.0059
Ol		B	mb_7	591.553	Fine	core	0.00187	0.00403	0.00071	0.0031	<0.00	<0.00052	<0.0042	<0.00096	<0.0026	0.0253	<0.00	0.0045	0.00103	0.018	0.0085
Ol	360_65R5_4	A	mc_1	591.576	Fine	rim	0.00059	0.00097	0.00035	<0.00055	<0.00067	<0.00030	0.00108	<0.00009	0.00095	0.0385	0.0007	0.0072	0.00229	0.0306	0.01057
Ol		A	mc_2	591.576	Fine	core	0.00063	0.00035	0.00011	<0.00043	<0.00023	0.00027	<0.00092	0.00022	0.00213	0.0444	0.00219	0.0094	0.00379	0.0411	0.01237
Ol		D	mc_3	591.577	Fine	core	0.00226	0.00329	0.00041	0.00154	0.00081	<0.00013	0.00166	0.00026	0.003	0.0495	0.00255	0.0081	0.00278	0.0331	0.01145
Ol		D	mc_4	591.577	Fine	rim	0.00032	0.00064	<0.00012	<0.00059	<0.00024	<0.00016	0.00133	0.00016	0.00174	0.025	0.00079	0.0057	0.00145	0.043	0.01014
Ol		G	ba_1	591.715	Coarse	core	0.00082	0.00388	0.00126	0.0032	<0.00	0.00116	<0.0045	<0.00084	0.009	0.1777	0.0045	0.0297	0.0112	0.149	0.0448
Ol		G	ba_2	591.715	Coarse	rim	0.00093	0.00432	0.00097	<0.0028	<0.0010	<0.00040	<0.0035	0.00116	0.0043	0.1343	0.00258	0.0325	0.0103	0.124	0.0333
Ol		Bis	ba_7	591.711	Coarse	rim	<0.00070	0.00096	<0.00034	<0.0029	<0.00070	<0.00075	<0.0047	<0.00071	0.0065	0.1232	0.00347	0.0289	0.0103	0.115	0.0253
Ol	360_65R5_18	E	ba_8	591.717	Coarse	core	<0.00040	<0.00045	0.00035	<0.0019	<0.00069	0.00087	<0.0022	<0.00060	0.0076	0.1657	0.00644	0.0323	0.0107	0.1229	0.038
Ol		Bis	ba_9	591.703	Coarse	core	<0.00062	<0.00077	0.00054	<0.0032	<0.00074	<0.00068	<0.0040	<0.00082	0.0052	0.0949	0.00257	0.0221	0.0082	0.104	0.0243
Ol		Bis	ba_10	591.703	Coarse	core	<0.00077	0.00223	<0.00060	<0.0029	<0.00111	0.00058	<0.0041	<0.00096	0.0054	0.079	0.00264	0.0159	0.0081	0.109	0.0237
Ol		Bis	ba_11	591.703	Coarse	core	<0.00080	<0.00080	<0.00052	<0.0036	<0.0020	<0.0010	<0.0049	0.0011	<0.0021	0.0807	0.0037	0.0156	0.0054	0.095	0.0283
Ol		Bis	ba_12	591.703	Coarse	core	<0.00041	0.00163	<0.00021	<0.00194	0.00051	<0.00044	<0.0026	0.00126	0.003	0.0531	0.00114	0.0116	0.00554	0.0658	0.0191
Ol		Bis	ba_13	591.703	Coarse	core	<0.00049	<0.00036	<0.00021	<0.00192	<0.00042	<0.00039	<0.0022	0.0006	0.0046	0.1057	0.00351	0.029	0.00663	0.0952	0.0268
Ol		B	mj_1	591.769	Fine	core	0.00028	0.00038	<0.00019	<0.00051	<0.00032	<0.00018	<0.00098	<0.00023	0.00169	0.0243	0.00053	0.0067	0.0024	0.0321	0.01017
Ol	360_65R5_2	B	mj_2	591.769	Fine	core	0.00028	0.00025	<0.00016	<0.00053	<0.00113	<0.00025	<0.00107	<0.00017	0.00211	0.0251	0.00135	0.0076	0.00334	0.0396	0.0145
Ol		A	mj_3	591.773	Fine	core	<0.00020	0.00074	0.00023	<0.00064	0.00032	<0.00017	<0.0014	0.00035	<0.00	0.0496	0.00127	0.0095	0.00357	0.045	0.01259
Ol		A	mj_4	591.773	Fine	rim	0.00017	0.00012	0.0001	<0.00018	<0.00091	0.00031	<0.00109	0.00023	0.00165	0.0362	0.00093	0.0048	0.00335	0.0279	0.01108
Ol		B	ca_1	591.795	Fine	core	0.00033	0.00045	<0.00009	0.0004	<0.00035	0.00013	<0.00069	0.00029	0.00158	0.0264	0.00059	0.0043	0.00187	0.0216	0.00839
Ol	360_65R5_27	B	ca_2	591.795	Fine	rim	<0.00030	0.00118	<0.00023	<0.0015	<0.00117	<0.00035	<0.0011	0.00039	<0.00047	0.0234	0.00036	0.0028	0.0013	0.0341	0.0062
Ol		C	ca_3	591.794	Fine	core	<0.00028	0.00069	<0.00017	<0.00092	0.00079	<0.00019	<0.00072	0.00024	<0.00063	0.0185	<0.00027	0.0028	0.00204	0.0275	0.00664
Ol		A	ca_6	591.800	Fine	core	0.00051	0.00066	0.00017	0.0031	<0.00176	<0.00033	<0.00121	<0.00023	0.00056	0.029	0.00036	0.0067	0.00134	0.0291	0.0109
Ol	360_65R5_32	A	ca_7	591.800	Fine	rim	0.0004	0.00049	<0.00009	<0.00134	<0.00083	<0.00036	<0.0012	0.00057	<0.00061	0.0158	0.00027	0.0072	0.00132	0.0202	0.0094
Ol		A	mi_1	591.848	Fine	core	0.00049	0.00068	<0.00009	<0.00	0.0004	<0.00022	<0.00088	0.00017	0.00076	0.0387	0.0003	0.0057	0.00322	0.0313	0.01047
Ol		A	mi_2	591.848	Fine	rim	0.00082	0.00223	0.00011	<0.00	<0.00	0.00013	0.00074	0.00015	0.00209	0.0347	0.00059	0.0084	0.00231	0.0319	0.00991
Ol		C	mi_3	591.840	Fine	core	0.00133	0.00196	<0.00022	0.00095	<0.00091	0.00023	<0.0021	0.00016	0.00114	0.0255	0.0005	0.008	0.00155	0.0293	0.0104
Ol		B	mi_4	591.837	Fine	core	0.00025	<0.00032	0.00012	<0.00094	<0.00040	<0.00031	<0.00136	<0.00031	0.003	0.0427	0.0017	0.0115	0.00285	0.0322	0.0157
Ol		B	mi_5	591.837	Fine	rim	0.00038	0.00247	0.00048	0.0023	0.0005	0.00051	0.0017	0.00015	0.002	0.0282	0.00073	0.0056	0.00112	0.0199	0.0073
Ol	36(	A	mh_1	591.925	Fine	core	0.00125	0.00307	0.00041	0.00156	0.00056	0.00039	0.00156	0.00031	0.0041	0.0487	0.00132	0.0065	0.0027	0.039	0.01224
Ol		A	mh_2	591.925	Fine	rim	0.00091	0.00295	0.00053	0.0019	<0.00	<0.00062	<0.0023	<0.00043	0.0022	0.051	0.00172	0.0079	0.00248	0.0498	0.0128
Ol		A	mh_3	591.925	Fine	core	0.00051	0.00118	<0.00015	<0.00	<0.00032	<0.00	<0.00066	<0.00021	<0.00116	0.046	0.00158	0.0112	0.00394	0.0511	0.0138
Ol		E	mh_4	591.928	Fine	core	<0.00032	<0.00019	0.00043	<0.00060	<0.00	0.00014	<0.0018	0.00018	<0.00134	0.0318	0.00129	0.0073	0.00243	0.0187	0.00697
Ol		E	mh_5	591.928	Fine	core	0.00098	0.00158	<0.00009	<0.0014	<0.00094	<0.00037	<0.0025	0.00033	<0.00099	0.0504	0.00245	0.0079	0.00434	0.0521	0.0144
Ol		C	mh_6	591.934	Fine	core	0.00073	0.00173	0.00037	0.00144	0.00065	<0.00017	0.0016	0.00047	0.00124	0.0525	0.00179	0.0136	0.00294	0.0433	0.01217

Mineral	Sample	Area	Point	Depth (mbsf)	Layer type	Grain area	La	Ce	Pr	Nd	Sm	Eu	Gd	Tb	Dy	Y	Ho	Er	Tm	Yb	Lu
Ol		C	mh_7	591.934	Fine	rim	<0.00030	<0.00025	<0.00017	<0.00085	<0.00	<0.00	<0.00149	0.00029	0.00251	0.0501	0.00139	0.0115	0.00294	0.0479	0.0157
Ol		B	mh_8	591.932	Fine	core	<0.00031	<0.00052	<0.00022	<0.00126	<0.00077	<0.00040	<0.00187	<0.00041	0.0025	0.025	<0.00040	0.0038	0.00273	0.0234	0.00734
Ol	360_65R5	D	bf_2	591.993	Coarse	core	0.00104	0.00146	0.00016	0.00193	0.00108	<0.00020	0.0025	<0.00028	0.0056	0.0869	0.0022	0.0166	0.00539	0.0701	0.0207
Ol		A	bf_3	591.985	Coarse	core	0.00038	0.00148	0.0005	0.0021	<0.00083	<0.00026	<0.0014	0.0004	0.0026	0.0976	0.00375	0.0151	0.00383	0.0799	0.0242
Ol		A	bf_4	591.985	Coarse	rim	0.00075	0.00161	<0.00021	<0.00089	0.00153	<0.00031	0.0013	0.0003	0.0077	0.0848	0.00228	0.0165	0.00557	0.0658	0.0215
Ol		C	md_1	592.039	Coarse	core	0.00028	0.00057	0.0002	<0.00069	0.00133	0.00026	<0.00064	0.00035	0.0037	0.1262	0.00358	0.0403	0.00757	0.0962	0.0283
Ol		C	md_2	592.039	Coarse	rim	0.00061	0.00277	0.00046	0.00153	<0.00052	<0.00013	<0.00036	0.00048	0.0055	0.0968	0.00365	0.0231	0.00658	0.0803	0.0285
Ol	360_65R5_51	D	md_3	592.038	Coarse	core	0.00134	0.00242	0.00024	0.00245	0.00202	<0.00	<0.00074	0.00054	0.0041	0.1054	0.00347	0.0244	0.00619	0.0926	0.0256
Ol		D	md_4	592.038	Coarse	rim	0.00155	0.00504	0.0006	0.006	0.00093	<0.00	0.0046	0.00042	0.0065	0.121	0.00364	0.0264	0.00837	0.1028	0.0262
Ol		G	md_5	592.035	Coarse	rim	0.00028	0.00057	0.00018	<0.00049	0.00044	0.00028	0.00126	0.00044	0.0071	0.1243	0.00346	0.026	0.00793	0.1122	0.0312
Ol		H	md_6	592.034	Coarse	core	0.00023	0.00058	<0.00009	<0.00	0.00036	0.00009	<0.00134	0.00031	0.0111	0.2008	0.00606	0.0381	0.0104	0.154	0.0411
Ol		A	md_7	592.024	Coarse	rim	<0.00025	0.00058	0.00011	0.00105	0.00044	<0.00026	<0.0016	0.00033	0.0045	0.0902	0.00336	0.0227	0.00705	0.1038	0.0273
Ol		A	md_8	592.024	Coarse	core	<0.00034	<0.00036	<0.00017	0.00045	<0.00152	<0.00029	<0.0013	0.0003	0.0054	0.1604	0.0034	0.0335	0.0098	0.146	0.0413
Ol	360_65R5_7	C	cb_1	592.280	Coarse	core	<0.00034	0.00061	0.00021	<0.00098	<0.00064	<0.00032	<0.00163	<0.00027	0.00063	0.0737	0.00211	0.0121	0.00561	0.0767	0.0229
Ol		C	cb_2	592.280	Coarse	rim	0.0005	0.0019	0.00018	<0.00110	<0.00096	<0.00025	0.0013	0.00049	0.0026	0.0603	0.00251	0.0108	0.00522	0.0702	0.0275
Ol		G	cb_3	592.299	Coarse	core	<0.00079	0.00099	<0.00030	<0.0020	<0.00191	<0.00048	<0.0027	<0.00047	<0.0013	0.0466	0.00043	0.006	0.0027	0.0514	0.0158
Ol		E	cb_4	592.300	Coarse	core	0.00144	0.00099	0.00046	<0.0019	0.00135	<0.00027	<0.00114	<0.00028	0.0022	0.0394	0.00193	0.0069	0.00223	0.0438	0.0152
Ol		D	bd_Olv1	592.313	Coarse	rim	0.00051	<0.00054	0.00056	<0.00138	<0.00	<0.00046	<0.0025	<0.00035	0.0021	0.0352	0.00034	0.0043	0.00174	0.031	0.0099
Ol	360_65R5_79g	D	bd_Olv2	592.313	Coarse	core	0.00119	0.00035	0.00037	<0.00104	<0.00071	0.00044	<0.0023	<0.00022	0.0033	0.023	0.00102	0.0068	0.00209	0.0217	0.01106
Ol		C	bd_Olv3	592.321	Coarse	core	<0.00058	0.00051	<0.00029	<0.0020	<0.00094	0.00052	<0.0027	0.0006	<0.00133	0.0207	0.00051	<0.0018	0.00233	0.0224	0.00692
Ol		A	bd_Olv4	592.320	Coarse	core	<0.00032	0.004	0.00032	0.0018	0.00054	<0.00027	<0.0017	0.00038	0.0032	0.0267	0.00095	0.0073	0.00367	0.0331	0.0126
Ol		A	bd_Olv5	592.320	Coarse	rim	0.00185	0.0028	0.00052	<0.0024	<0.00147	<0.00080	<0.0027	<0.00058	<0.00073	0.0327	0.00116	0.0058	0.00294	0.0331	0.0144
Ol		C	bd_Opx4	592.321	Coarse	core	<0.00110	<0.00132	<0.00099	0.0038	<0.0048	<0.00119	<0.0074	<0.00122	<0.0034	0.0304	0.00142	0.0099	<0.00096	0.0341	0.0133
Ol		C	bd_Opx5	592.321	Coarse	core	<0.0016	<0.0012	<0.00107	0.0065	<0.00229	<0.00125	0.0112	<0.0015	<0.0042	0.0188	<0.00	<0.0032	<0.00084	0.0155	0.0051
Ol	360_6	C	bd_Olv6	592.332	Coarse in F	core	<0.00028	<0.00033	0.00026	<0.00141	<0.00076	<0.00020	<0.0018	<0.00027	0.0031	0.0469	0.00123	0.0053	0.00193	0.0442	0.0151
Ol		C	bd_Olv7	592.332	Coarse in F	rim	0.00108	0.00178	<0.00015	<0.00121	<0.00033	<0.00029	<0.0014	0.00031	0.0035	0.0477	0.00111	0.009	0.00348	0.0473	0.0125
Ol		A	ce_1	592.354	Coarse in F	core	0.00087	0.00106	0.00068	0.00108	<0.00067	<0.00028	<0.0016	0.00042	0.0031	0.0385	0.001	0.0064	0.00236	0.0298	0.00809
Ol	360_65R5_83	C	ce_2	592.365	Coarse in F	rim	<0.00028	<0.00032	0.00061	<0.00076	<0.00067	0.00014	<0.0013	0.00021	0.0032	0.0271	0.00062	0.0095	0.00281	0.0225	0.0095
Ol		C	ce_3	592.365	Coarse in F	core	<0.00026	<0.00043	0.00051	0.00094	<0.00079	<0.00027	<0.0015	0.0002	0.0018	0.0541	0.00072	0.0076	0.00255	0.0388	0.0108
Ol		B	ce_4	592.369	Coarse in F	rim	<0.00026	0.00029	0.00041	0.00094	<0.00056	<0.00023	<0.00128	0.00043	<0.00083	0.0315	0.00078	0.0042	0.00217	0.032	0.0094
Ol		E	ce_5	592.376	Fine	core	0.00041	<0.00036	<0.00015	<0.00091	<0.00074	<0.00011	<0.0013	<0.00022	<0.00036	0.0222	0.00044	0.0034	0.00109	0.03	0.00834
Ol		B	mg_2	592.404	Fine	core	0.00028	0.00035	<0.00010	0.00026	0.00032	<0.00021	0.00115	0.00019	0.00167	0.0291	0.00081	0.0035	0.00135	0.0266	0.00823
Ol	360_65R5_87	B	mg_3	592.404	Fine	core	0.00022	0.00054	0.00016	<0.00060	<0.00028	<0.00012	<0.00091	<0.00016	0.00141	0.0164	0.00045	0.0045	0.00169	0.0197	0.00779
Ol		B	mg_4	592.404	Fine	rim	0.00048	0.00069	0.00009	<0.00064	0.00095	<0.00032	<0.00147	<0.00016	<0.00	0.0155	0.00017	0.00184	0.00126	0.021	0.00562
Ol		E	mg_5	592.391	Fine	core	0.00043	0.00082	<0.00019	<0.00185	<0.00073	<0.00031	<0.00150	<0.00	0.00056	0.0176	0.00028	0.0032	0.0007	0.0152	0.00896
Ol		D	mg_6	592.390	Fine	core	<0.00021	0.00019	<0.00014	<0.00052	<0.00	0.00016	<0.00104	<0.00013	0.00139	0.0136	0.00046	0.0035	0.00083	0.0162	0.00781
Ol		D	mg_7	592.390	Fine	rim	<0.00032	0.00041	<0.00012	0.00106	0.00049	<0.00029	<0.0019	0.00054	<0.00067	0.0118	<0.00029	0.0039	0.00106	0.0137	0.00441
Ol		A	cf_1	592.445	Coarse in F	core	0.0004	<0.00040	<0.00025	0.0026	<0.00053	<0.00024	<0.0022	<0.00037	0.0016	0.0393	0.00068	0.0105	0.00246	0.0302	0.0113
Ol		A	cf_2	592.445	Coarse in F	rim	<0.00033	0.00061	<0.00022	0.0027	<0.00048	<0.00033	<0.0014	<0.00025	0.00091	0.0275	0.0008	0.009	0.00208	0.0362	0.0102
Ol		B	cf_3	592.443	Coarse in F	core	<0.00056	<0.00068	0.00049	<0.0010	0.005	<0.00061	<0.0029	0.00043	0.0014	0.0341	0.00129	0.0036	0.00058	0.0246	0.0122
Ol	R5_91	F	cf_4	592.435	Fine	core	<0.00056	<0.00083	<0.00020	<0.0015	<0.00161	<0.00043	<0.0024	<0.00047	0.0054	0.0188	<0.00021	<0.0009	0.00179	0.018	0.0077

Mineral	360_65	Area	Point	Depth (mbsf)	Layer type	Grain area	La	Ce	Pr	Nd	Sm	Eu	Gd	Tb	Dy	Y	Ho	Er	Tm	Yb	Lu
Ol		D	cf_5	592.432	Fine	core	0.00078	<0.00037	<0.00017	<0.00103	0.00061	<0.00033	<0.00085	0.00038	0.0021	0.0364	0.0009	0.0067	0.00209	0.0336	0.0124
Ol		D	ma_1	592.453	Fine	rim	0.00064	0.00067	0.00015	0.0023	<0.00037	0.00044	<0.0013	0.0005	0.00137	0.029	0.00076	0.0082	0.00163	0.026	0.00984
Ol		D	ma_2	592.453	Fine	rim	0.00048	0.00046	<0.00028	<0.00181	<0.00062	<0.00052	<0.0023	<0.00030	0.00133	0.0192	<0.00042	0.0039	0.00122	0.0321	0.00901
Ol	360_65R5_94	D	ma_3	592.453	Fine	core	<0.00051	0.00155	0.00023	0.0027	<0.00188	<0.00046	<0.0019	<0.00036	<0.0019	0.021	<0.00	0.0021	0.00177	0.032	0.00712
Ol		B	ma_4	592.456	Fine	core	<0.00032	0.00034	<0.00011	<0.00077	<0.00044	<0.00026	<0.00122	0.00032	0.0032	0.0482	0.00166	0.006	0.00403	0.0471	0.01107
Ol		B	ma_5	592.456	Fine	rim	0.00022	<0.00021	<0.00020	<0.00087	<0.00126	<0.00	<0.00151	<0.00016	0.00099	0.0357	0.00132	0.0103	0.00282	0.0321	0.01145
Ol		C	ma_7	592.466	Fine	rim	<0.00029	0.00138	0.00049	<0.00106	<0.00058	<0.00021	0.00101	<0.00025	<0.00090	0.0201	0.00044	0.003	0.00148	0.018	0.0064
Ol		C	ma_8	592.466	Fine	rim	<0.00028	0.0017	<0.00021	<0.00124	<0.00044	<0.00031	<0.00104	<0.00030	0.0016	0.0136	0.00104	0.0042	0.00092	0.0138	0.0042
Ol		D	cc_2	592.557	Coarse	rim	<0.00051	0.00088	0.00037	0.0036	0.0032	<0.00033	<0.0026	<0.00043	<0.0017	0.0379	0.00078	0.0039	0.00275	0.0566	0.0129
Ol	360_65R5_102	A	cc_3	592.549	Coarse	core	0.00031	0.00052	<0.00032	<0.00193	0.00056	<0.00025	0.0043	0.00057	0.0062	0.0836	0.00142	0.0143	0.00485	0.0762	0.0238
Ol		A	cc_4	592.549	Coarse	rim	<0.00036	0.00064	0.00029	<0.00146	<0.0014	<0.00040	0.0028	<0.00027	0.0023	0.0347	0.00091	0.0106	0.00281	0.0501	0.016
Ol		E	cc_5	592.533	Coarse	rim	<0.00036	0.00061	0.00022	0.0049	<0.00091	<0.00028	<0.0018	<0.00039	<0.0018	0.0877	0.00233	0.0168	0.00525	0.0687	0.0215
Ol		E	cc_6	592.533	Coarse	core	<0.00043	0.00053	0.00057	<0.0013	<0.00083	<0.00035	<0.0017	<0.00045	0.0053	0.1033	0.00246	0.0194	0.0089	0.0924	0.0243
Ol		D	cd_1	592.627	Fine	core	0.00077	0.00097	0.00051	0.0007	0.00101	0.00024	<0.00077	0.0002	0.00081	0.0301	0.00064	0.0089	0.00178	0.0272	0.01193
Ol		D	cd_2	592.627	Fine	rim	<0.00018	0.00106	<0.00013	<0.00021	0.0009	<0.00020	<0.00055	0.00036	0.00189	0.0232	0.00084	0.0043	0.00181	0.0308	0.00724
Ol		C	cd_3	592.631	Fine	core	<0.00019	0.00027	<0.00010	0.00048	0.00174	<0.00015	<0.00089	0.00035	0.00216	0.0518	0.00139	0.0112	0.00396	0.0508	0.0143
Ol	360_65R5_111	C	cd_4	592.631	Fine	rim	0.00019	0.00111	<0.00011	<0.00049	0.00029	0.00036	<0.00094	<0.00005	0.00225	0.044	0.00092	0.0098	0.00375	0.0449	0.01336
Ol		A	cd_5	592.637	Fine	core	0.00064	0.00039	0.0001	0.00102	0.00088	<0.00015	0.00105	<0.00018	0.00231	0.0492	0.00057	0.0111	0.00443	0.0447	0.0175
Ol		A	cd_6	592.637	Fine	rim	0.0003	0.00057	0.00031	<0.00093	0.00057	<0.00008	<0.00082	0.00038	0.00112	0.0329	0.00093	0.0085	0.0029	0.037	0.0147
Ol		B	cd_7	592.642	Fine	core	<0.00025	<0.00042	<0.00017	<0.00096	<0.00106	<0.00025	<0.0015	0.0001	<0.00057	0.0351	0.00114	0.0123	0.00278	0.0307	0.0089
Ol		B	cd_8	592.642	Fine	rim	0.00086	0.00029	<0.00012	<0.00064	0.00038	<0.00028	<0.00106	<0.00014	0.00083	0.0334	0.00103	0.0077	0.00278	0.028	0.01158
Ol		E	me_1	592.695	Coarse	core	<0.00030	0.00291	0.00039	0.00075	<0.00	<0.00027	<0.00134	<0.00010	0.0007	0.0256	0.00044	0.0022	0.00115	0.0278	0.0068
Ol		D	me_2	592.701	Coarse	core	<0.00055	0.00229	<0.00022	<0.00136	<0.0012	<0.00078	<0.0029	<0.00034	<0.00137	0.0273	<0.00026	<0.00093	0.0022	0.034	0.008
Ol		D	me_3	592.701	Coarse	rim	<0.00025	0.00123	<0.00011	<0.00104	<0.00065	<0.00027	<0.0018	<0.00028	0.00218	0.0267	0.00073	0.0115	0.00199	0.0414	0.01214
Ol	360_65R5_117	B	me_4	592.706	Coarse	core	<0.00028	<0.00024	<0.00018	<0.00084	<0.00061	<0.00029	<0.0018	<0.00007	0.0041	0.0578	0.00151	0.0129	0.00415	0.0554	0.0183
Ol		B	me_5	592.706	Coarse	rim	0.00077	0.00218	0.00031	0.00131	<0.00085	<0.00015	<0.0015	<0.00018	0.0018	0.0732	0.00214	0.0149	0.00432	0.0729	0.0232
Ol		A	me_6	592.713	Coarse	core	<0.00025	<0.00031	<0.00016	<0.00083	<0.00104	<0.00026	<0.00128	<0.00035	0.0035	0.0751	0.00219	0.016	0.00374	0.058	0.018
Ol		C	me_7	592.718	Coarse	core	<0.00033	0.00139	<0.00015	<0.00069	<0.00043	<0.00018	<0.00178	0.00027	0.00242	0.0398	0.00147	0.0091	0.00235	0.0405	0.01201
Ol		C	me_8	592.718	Coarse	rim	0.0003	0.00093	<0.00019	0.0036	<0.00104	0.00037	<0.0016	<0.00034	0.0025	0.0361	0.0006	0.0039	0.0011	0.0324	0.00898
Ol		E	xa_1	592.178	Coarse	core	<0.00030	0.00181	0.00033	0.00034	0.00073	0.00034	0.00159	0.00056	0.00475	0.097	0.0033	0.0206	0.00631	0.0884	0.0239
Ol		E	xa_2	592.178	Coarse	core	0.00061	0.0011	0.00027	0.0022	0.00082	0.00045	<0.00066	0.00035	0.0049	0.0804	0.0028	0.0161	0.00496	0.0779	0.0185
Ol		E	xa_3	592.178	Coarse	rim	0.00066	0.00212	0.00022	0.00137	<0.00050	<0.00024	0.00331	<0.00028	0.00482	0.0901	0.00291	0.0175	0.00588	0.0711	0.01869
Ol		E	xa_4	592.178	Coarse	rim	0.00099	0.00176	0.00022	0.00152	<0.00073	<0.00029	<0.00112	0.00056	0.00326	0.0708	0.00267	0.0201	0.00552	0.0645	0.0205
Ol	360_65R5_63B	E	xa_5	592.182	Coarse	core	0.00043	0.00121	0.00023	0.00189	0.00069	0.00041	<0.0012	<0.00040	0.00225	0.0522	0.00146	0.0106	0.00335	0.0569	0.0167
Ol		G	xa_6	592.178	Coarse	core	0.0005	<0.00078	<0.00017	<0.00041	<0.00018	0.00035	<0.00083	<0.00025	0.00249	0.0567	0.00137	0.0087	0.0046	0.0554	0.01596
Ol		G	xa_7	592.178	Coarse	rim	0.00295	0.00751	0.0009	0.0056	0.00085	<0.00031	0.0057	0.00044	0.0071	0.109	0.00308	0.0223	0.00591	0.0781	0.0197
Ol		G	xa_8	592.178	Coarse	core	0.00032	0.00042	<0.00009	<0.00051	<0.00042	<0.00016	<0.00079	<0.00023	0.00419	0.0901	0.00285	0.0219	0.00581	0.0745	0.0205
Ol		H	xa_9	592.174	Coarse	core	0.00041	0.00266	0.0002	0.00114	<0.00054	<0.00025	0.00106	<0.00031	0.00435	0.0867	0.00297	0.0221	0.00569	0.0699	0.01895
Ol		H	xa_10	592.174	Coarse	core	0.00139	0.00404	0.00032	0.00303	<0.00043	0.00052	0.003	0.00042	0.0084	0.1176	0.00278	0.0181	0.00636	0.057	0.0202
Ol		H	xa_11	592.174	Coarse	rim	0.00218	0.00542	0.00069	0.00293	0.0012	0.00049	0.0025	0.00066	0.0062	0.0942	0.00239	0.0181	0.00607	0.0635	0.0163
Ol		N2	xb_1	592.153	Coarse	rim	<0.00025	0.00095	0.0005	0.0002	<0.00027	0.0005	0.0017	0.00041	0.0046	0.0637	0.00179	0.015	0.00278	0.0474	0.01405

Mineral	360_65R5_63A	Area	Point	Depth (mbsf)	Layer type	Grain area	La	Ce	Pr	Nd	Sm	Eu	Gd	Tb	Dy	Y	Ho	Er	Tm	Yb	Lu
Ol		N2	xb_2	592.153	Coarse	core	<0.00037	0.00131	0.0003	0.0027	<0.0010	<0.00036	<0.0022	<0.00032	<0.00038	0.0672	0.00191	0.0118	0.00385	0.0611	0.0124
Ol		N2	xb_3	592.153	Coarse	core	0.00158	0.00231	0.00119	0.0025	<0.00126	<0.00018	<0.0017	<0.00035	0.00248	0.0552	0.00121	0.0075	0.00298	0.0388	0.0129
Ol		N2	xb_4	592.153	Coarse	core	<0.00026	0.00163	0.00017	0.00055	0.00148	<0.00024	0.0012	0.00041	0.0034	0.0607	0.00188	0.0112	0.00324	0.0449	0.0171
Ol		N2	xb_5	592.153	Coarse	core	<0.00039	0.00035	0.00026	0.0017	<0.00111	0.00098	<0.0022	<0.00033	0.0036	0.0727	0.00226	0.019	0.00469	0.0718	0.0215
Ol		N3	xb_6	592.145	Coarse	core	0.00077	0.00149	0.00018	0.00085	<0.00042	0.00014	<0.0015	<0.00026	0.0043	0.0633	0.00198	0.013	0.00449	0.0559	0.0158
Ol		N3	xb_7	592.145	Coarse	core	0.00068	0.00162	<0.00021	0.00131	<0.00096	<0.00041	<0.0023	<0.00032	0.0021	0.0616	0.00199	0.0136	0.00523	0.0522	0.01263
			Average (N = 42)				0.58	1.74	0.34	2.22	1.02	0.49	1.43	0.31	2.30	1.56	0.50	1.47	0.22	1.56	0.22
BIR			2SD				0.04	0.16	0.02	0.16	0.11	0.04	0.34	0.04	0.34	0.16	0.08	0.21	0.04	0.16	0.04
			Preferred values ("GeoRem" Jochum et al., 2007)				0.609	1.89	0.37	2.37	1.09	0.517	1.85	0.35	2.55	14.3	0.56	1.7	0.24	1.64	0.25

In situ trace elements concentrations in ppm analysed by La-ICP-MS on Thermo Fisher Element XR in GM (Montpellier, France)

Mineral	Sample	Area	Point	Depth (mbsf)	Layer type	Grain area	La	Ce	Pr	Nd	Sm	Eu	Gd	Tb	Dy	Y	Ho	Er	Tm	Yb	Lu
Pl		Analitycal error average				1 sigma	0.02	0.037	0.006	0.03	0.01	0.019	0.01	0.001	0.006	0.011	0.001	0.004	0.0006	0.003	0.0004
Pl		F	mb_15	591.536	Fine	core	0.249	0.521	0.0813	0.356	0.095	0.346	0.08	0.0074	0.0311	0.198	0.0098	0.0093	0.00095	0.0061	0.00095
Pl		F	mb_16	591.536	Fine	rim	0.252	0.502	0.0746	0.365	0.0818	0.358	0.0449	0.0054	0.0336	0.166	0.0047	0.0047	0.00086	0.005	0.0006
Pl		F	mb_17	591.536	Fine	core	0.231	0.468	0.0653	0.297	0.0671	0.31	0.07	0.0072	0.0284	0.1578	0.0065	0.0105	<0.00	0.0067	0.00052
Pl		E	mb_18	591.540	Fine	core	0.223	0.48	0.0708	0.311	0.0629	0.349	0.0572	0.007	0.0346	0.1407	0.0059	0.0154	<0.00	0.0072	0.00119
Pl		E	mb_19	591.540	Fine	rim	0.245	0.515	0.0649	0.348	0.06	0.311	0.063	0.0037	0.0222	0.1258	0.00072	0.0065	<0.00058	0.0032	0.001
Pl		E	mb_20	591.540	Fine	core	0.269	0.532	0.0759	0.296	0.073	0.346	0.055	0.0054	0.0293	0.1281	0.00159	0.0104	0.00121	0.0063	<0.00079
Pl	360_65R5_2	C	mb_21	591.546	Fine	core	0.259	0.614	0.0879	0.427	0.077	0.374	0.065	0.0079	0.0335	0.177	0.0056	0.0078	0.00132	0.0075	0.00081
Pl		C	mb_22	591.546	Fine	rim	0.315	0.691	0.0993	0.433	0.0658	0.376	0.078	0.0071	0.0526	0.18	0.0046	0.0063	0.0018	0.0109	<0.00116
Pl		C	mb_23	591.546	Fine	core	0.342	0.65	0.0757	0.344	0.094	0.348	0.07	0.0077	0.0272	0.132	0.00177	0.0099	0.00072	0.0039	<0.00067
Pl		A	mb_24	591.551	Fine	core	0.259	0.578	0.0861	0.487	0.098	0.403	0.125	0.0166	0.0626	0.336	0.0096	0.0325	0.0026	0.0166	0.00143
Pl		A	mb_25	591.551	Fine	rim	0.356	0.698	0.1047	0.466	0.079	0.372	0.066	0.0093	0.0329	0.207	0.0036	0.0198	0.00246	0.0061	<0.00083
Pl		D	mb_26	591.553	Fine	core	0.364	0.78	0.1019	0.397	0.077	0.324	0.066	0.0071	0.0308	0.1442	0.0042	0.0053	<0.00105	<0.0031	<0.00059
Pl		D	mb_27	591.553	Fine	rim	0.421	0.865	0.1096	0.426	0.115	0.37	0.078	0.0077	0.0274	0.1408	0.004	0.0203	0.00119	0.0054	<0.00046
Pl		D	mb_28	591.553	Fine	core	0.403	0.89	0.105	0.426	0.071	0.355	0.0501	0.0026	0.0367	0.1085	0.0035	0.0082	<0.00	0.0034	0.00144
Pl		B	mb_29	591.553	Fine	core	0.264	0.698	0.0955	0.46	0.062	0.337	0.078	0.0059	0.0368	0.145	0.005	0.008	0.0019	0.0091	0.00137
Pl		B	mb_30	591.553	Fine	core	0.4	0.839	0.0994	0.435	0.073	0.347	0.058	0.0049	0.0323	0.1303	0.003	0.0089	0.00136	<0.0037	<0.00033
Pl		A	mc_9	591.576	Fine	core	0.513	0.935	0.1196	0.546	0.0949	0.405	0.0686	0.009	0.0384	0.1763	0.0078	0.014	0.00199	0.0042	0.00059
Pl		A	mc_10	591.576	Fine	rim	0.516	0.925	0.112	0.436	0.0816	0.417	0.0525	0.0075	0.0284	0.1196	0.00339	0.0031	0.00068	0.0018	0.00029
Pl	360_65R5_4	B	mc_12	591.581	Fine	rim	0.456	0.856	0.1064	0.457	0.0744	0.401	0.0556	0.00603	0.0349	0.1396	0.00499	0.0133	0.00147	0.0071	0.00106
Pl		B	mc_13	591.581	Fine	core	0.438	0.854	0.1037	0.434	0.0785	0.394	0.0547	0.0069	0.0323	0.1218	0.00477	0.0075	0.0007	0.0023	0.00034
Pl		B	mc_14	591.581	Fine	rim	0.452	0.831	0.1051	0.396	0.0574	0.381	0.053	0.00411	0.0246	0.1248	0.00439	0.0051	<0.00062	0.0066	0.00097
Pl		B	mc_15	591.581	Fine	core	0.444	0.867	0.1012	0.435	0.0767	0.429	0.0541	0.00565	0.0327	0.1252	0.00432	0.0109	0.00127	0.0038	<0.00044
Pl		C	mc_17	591.583	Fine	core	0.215	0.562	0.0849	0.415	0.1	0.364	0.076	0.008	0.0396	0.183	0.0061	0.0156	<0.00	0.0063	0.0005
Pl		C	mc_18	591.583	Fine	rim	0.417	0.833	0.1142	0.446	0.0791	0.382	0.072	0.00608	0.0356	0.1603	0.007	0.0118	0.00175	0.0046	0.00081
Pl		M	ba_BIR3	591.718	Coarse	rim	1.037	2.271	0.26	1.047	0.136	0.498	0.102	0.0124	0.0379	0.177	0.0047	0.0071	<0.00077	0.0041	<0.00038
Pl		M	ba_Plag2	591.718	Coarse	core	0.582	1.515	0.1878	0.798	0.14	0.507	0.122	0.0148	0.0728	0.292	0.0109	0.0282	0.00289	0.0137	0.00201
Pl		L	ba_Plag3	591.719	Coarse	core	0.232	0.694	0.1016	0.5	0.112	0.47	0.112	0.0178	0.084	0.382	0.0116	0.0234	0.00188	0.0291	<0.00093
Pl	360_65R5_18	L	ba_Plag4	591.719	Coarse	rim	1.022	2.14	0.243	1.001	0.151	0.462	0.116	0.014	0.0613	0.312	0.0067	0.0125	0.0014	0.0066	0.00121
Pl		L	ba_Plag5	591.719	Coarse	core	0.948	2.015	0.2265	0.844	0.133	0.427	0.106	0.0131	0.0512	0.268	0.0083	0.011	0.00071	0.0146	<0.00092
Pl		Bis	ba_Plag6	591.703	Coarse	core	1.042	2.142	0.261	0.895	0.099	0.501	0.093	0.0115	0.0467	0.193	0.0065	0.0107	0.00073	0.0054	0.00178
Pl		K	ba_Plag7	591.712	Coarse	rim	1.156	2.084	0.224	0.902	0.11	0.463	0.092	0.0111	0.0458	0.22	0.0061	0.0148	0.0018	0.013	0.00089
Pl		J	ba_Plag9	591.715	Coarse	core	1.036	2.247	0.256	1.064	0.13	0.483	0.126	0.0126	0.0617	0.228	0.0095	0.0128	<0.00121	0.0032	0.00211
Pl		J	ba_Plag1	591.715	Coarse	core	1.244	2.534	0.276	1.181	0.194	0.465	0.156	0.0137	0.071	0.326	0.012	0.0209	0.005	0.0159	0.00151
Pl		D	mj_8	591.765	Coarse	core	0.891	1.721	0.2191	0.986	0.165	0.507	0.145	0.0135	0.0733	0.309	0.0104	0.0231	0.00156	0.0143	0.00188
Pl		D	mj_9	591.765	Coarse	core	0.2066	0.489	0.0739	0.402	0.1004	0.498	0.0963	0.0106	0.0616	0.309	0.0131	0.025	0.00224	0.0076	0.00078
Pl		D	mj_10	591.765	Coarse	rim	0.666	1.398	0.1831	0.822	0.126	0.532	0.1086	0.0126	0.0658	0.253	0.0097	0.0194	0.00246	0.018	0.00092
Pl		B	mj_11	591.769	Fine	core	0.508	1.005	0.1312	0.548	0.0933	0.45	0.0798	0.0085	0.0382	0.1867	0.0073	0.0126	0.00203	0.0075	0.00132
Pl		B	mj_12	591.769	Fine	core	0.529	1.026	0.128	0.581	0.1065	0.455	0.0791	0.00838	0.0368	0.2034	0.0084	0.0128	0.00163	0.0044	0.0011
Pl	13	B	mj_13	591.769	Fine	core	0.518	1.037	0.1383	0.604	0.1138	0.45	0.0835	0.0098	0.0458	0.215	0.00709	0.0136	0.00103	0.0082	<0.00030

Mineral	360_65R5_2	Area	Point	Depth (mbsf)	Layer type	Grain area	La	Ce	Pr	Nd	Sm	Eu	Gd	Tb	Dy	Y	Ho	Er	Tm	Yb	Lu
Pl		B	mj_14	591.769	Fine	rim	0.521	1.009	0.1314	0.572	0.1036	0.448	0.07	0.0102	0.0486	0.2117	0.0107	0.0113	0.0006	0.0066	0.00089
Pl		A	mj_15	591.773	Fine	core	0.378	0.768	0.0994	0.431	0.0655	0.388	0.0742	0.00601	0.0299	0.1503	0.00323	0.0164	0.00131	0.0051	0.00142
Pl		A	mj_16	591.773	Fine	core	0.421	0.865	0.1073	0.458	0.093	0.395	0.084	0.0065	0.0242	0.1545	0.0065	0.0177	0.00154	0.0033	0.00068
Pl		C	mj_17	591.776	Fine	core	0.2384	0.63	0.097	0.459	0.1005	0.409	0.0804	0.0111	0.0558	0.212	0.00606	0.0121	0.00053	0.00109	0.00113
Pl		C	mj_18	591.776	Fine	rim	0.352	0.734	0.0964	0.431	0.0766	0.442	0.0639	0.00689	0.0267	0.1432	0.0047	0.0087	<0.00053	0.0051	0.00065
Pl		C	mj_19	591.776	Fine	core	0.345	0.706	0.0881	0.423	0.0621	0.389	0.0606	0.008	0.0313	0.1221	0.00365	0.0094	0.00113	0.0046	0.00022
Pl		D	ca_10	591.788	Coarse in F	core	0.332	0.78	0.1012	0.485	0.085	0.371	0.0678	0.00898	0.0389	0.1595	0.00719	0.0141	0.00139	0.0039	0.00035
Pl		D	ca_11	591.788	Coarse in F	rim	0.465	0.907	0.1093	0.438	0.0736	0.385	0.0726	0.00864	0.0283	0.1258	0.00709	0.0079	0.00066	0.0044	0.00129
Pl		D	ca_12	591.788	Coarse in F	core	0.438	0.864	0.1077	0.472	0.0738	0.347	0.0688	0.0082	0.0263	0.1639	0.0069	0.0132	0.00163	0.0104	0.00075
Pl	360_65R5_27	B	ca_13	591.795	Fine	core	0.372	0.751	0.0952	0.404	0.058	0.351	0.077	0.0064	0.0265	0.1432	0.0054	0.006	0.00093	0.0082	0.00054
Pl		B	ca_14	591.795	Fine	rim	0.357	0.716	0.0907	0.384	0.0642	0.354	0.0543	0.0077	0.0337	0.1347	0.00499	0.0127	0.00136	0.0077	0.00072
Pl		B	ca_15	591.795	Fine	core	0.348	0.684	0.0787	0.366	0.0572	0.336	0.0547	0.00627	0.0218	0.1091	0.00319	0.0078	0.00079	0.0026	<0.00033
Pl		C	ca_16	591.794	Fine	core	0.388	0.721	0.0937	0.419	0.0718	0.359	0.0644	0.0075	0.0319	0.1581	0.007	0.0057	<0.00041	0.0062	<0.00043
Pl		A	ca_17	591.800	Fine	rim	0.354	0.715	0.0955	0.426	0.0762	0.373	0.0568	0.0072	0.044	0.171	0.00429	0.0126	0.00212	0.0076	0.00055
Pl		A	ca_18	591.800	Fine	core	0.366	0.725	0.0944	0.489	0.096	0.407	0.0742	0.011	0.0495	0.2138	0.0072	0.0239	0.00118	0.0078	0.00047
Pl		A	ca_19	591.800	Fine	core	0.384	0.737	0.0888	0.415	0.0688	0.356	0.0442	0.0053	0.0343	0.1294	0.00447	0.0054	0.00094	0.0086	0.0006
Pl		A	mi_9	591.848	Fine	core	0.45	0.933	0.1098	0.455	0.0796	0.4	0.0658	0.00626	0.0258	0.1317	0.00475	0.012	0.00038	0.0068	0.0006
Pl		A	mi_10	591.848	Fine	rim	0.488	0.996	0.1162	0.478	0.0907	0.394	0.0796	0.0092	0.0364	0.1369	0.00496	0.0126	0.00095	0.0047	0.00085
Pl		A	mi_11	591.848	Fine	core	0.413	0.946	0.1117	0.476	0.0843	0.401	0.078	0.00657	0.0337	0.151	0.0047	0.0121	0.0016	0.0047	0.00015
Pl		A	mi_12	591.848	Fine	rim	0.473	0.992	0.1209	0.487	0.095	0.397	0.0698	0.0077	0.0355	0.1311	0.00472	0.0099	0.00148	0.0038	<0.00018
Pl		D	mi_13	591.846	Fine	core	0.1848	0.45	0.0643	0.369	0.08	0.438	0.0763	0.0087	0.0494	0.236	0.0082	0.0161	0.00145	0.0124	0.00152
Pl	360_65R5_32	D	mi_14	591.846	Fine	rim	0.357	0.776	0.1069	0.489	0.0912	0.431	0.0735	0.00658	0.0327	0.1512	0.00552	0.0062	<0.00014	0.0055	<0.00022
Pl		D	mi_15	591.846	Fine	core	0.503	0.892	0.1149	0.476	0.0849	0.41	0.0638	0.00744	0.0383	0.1525	0.00498	0.0098	0.00051	0.0029	0.00031
Pl		D	mi_16	591.846	Fine	rim	0.496	0.928	0.1148	0.496	0.0658	0.394	0.0647	0.0088	0.0347	0.1573	0.0067	0.0103	0.00057	0.0035	<0.00
Pl		C	mi_17	591.840	Fine	rim	0.517	0.897	0.1113	0.542	0.0878	0.427	0.0623	0.0075	0.0227	0.124	0.00357	0.0078	0.00086	0.0041	0.00035
Pl		C	mi_18	591.840	Fine	core	0.532	0.952	0.1241	0.603	0.1093	0.451	0.0816	0.008	0.0478	0.1938	0.0068	0.015	0.0018	0.0038	0.00069
Pl		B	mi_19	591.837	Fine	core	0.547	1.037	0.1369	0.595	0.1057	0.435	0.0854	0.0087	0.0452	0.207	0.0076	0.0164	0.00134	0.0058	0.00101
Pl		B	mi_20	591.837	Fine	rim	0.519	0.964	0.125	0.51	0.0772	0.469	0.0708	0.0075	0.044	0.1884	0.007	0.0125	0.00064	0.0052	0.00036
Pl		B	mi_21	591.837	Fine	core	0.1706	0.384	0.0649	0.314	0.0746	0.466	0.0687	0.0097	0.0433	0.237	0.00754	0.0183	0.00238	0.015	0.0018
Pl		B	mi_22	591.837	Fine	rim	0.295	0.672	0.0981	0.5	0.1115	0.462	0.1039	0.0121	0.0576	0.247	0.0095	0.0156	0.00155	0.0097	0.00145
Pl		A	mh_14	591.925	Fine	core	0.418	0.867	0.116	0.523	0.1015	0.418	0.073	0.0112	0.0474	0.1985	0.0084	0.0289	0.00149	0.0036	0.00014
Pl		D	mh_15	591.922	Fine	core	0.398	0.821	0.1139	0.563	0.1093	0.443	0.102	0.0106	0.0581	0.215	0.0079	0.0138	0.00185	0.0098	0.0012
Pl		D	mh_16	591.922	Fine	rim	0.424	0.838	0.1068	0.483	0.0856	0.399	0.0738	0.0082	0.0397	0.1753	0.0063	0.0179	0.00172	0.0016	<0.00024
Pl		D	mh_17	591.922	Fine	core	0.454	0.89	0.1121	0.488	0.0695	0.4	0.0603	0.0068	0.0265	0.1344	0.00418	0.0141	0.00131	0.007	0.00034
Pl		E	mh_18	591.928	Fine	core	0.449	0.873	0.1114	0.515	0.0981	0.427	0.116	0.0079	0.0444	0.218	0.0062	0.0137	0.00139	0.0052	<0.00036
Pl		E	mh_19	591.928	Fine	rim	0.433	0.869	0.1053	0.492	0.0725	0.433	0.0711	0.0061	0.0241	0.1564	0.00344	0.004	0.00113	0.0071	<0.00
Pl	360_65R5_39	C	mh_21	591.934	Fine	rim	0.42	0.892	0.1099	0.502	0.0766	0.396	0.0441	0.0079	0.0318	0.1675	0.00435	0.0072	0.00123	0.0043	0.00061
Pl		C	mh_22	591.934	Fine	core	0.343	0.802	0.1138	0.552	0.1262	0.413	0.0954	0.0105	0.0585	0.253	0.008	0.0163	0.00333	0.0113	0.00099
Pl		C	mh_23	591.934	Fine	rim	0.403	0.874	0.1142	0.55	0.0752	0.441	0.0637	0.0104	0.0395	0.1836	0.0065	0.0112	0.0023	0.0067	0.00109
Pl		B	mh_24	591.932	Fine	core	0.406	0.831	0.1031	0.439	0.0779	0.398	0.0741	0.0054	0.0308	0.1416	0.0055	0.008	0.001	0.0022	0.00052
Pl		B	mh_25	591.932	Fine	core	0.384	0.852	0.0995	0.461	0.0817	0.379	0.0707	0.0083	0.0346	0.1601	0.007	0.0226	0.00223	0.0056	<0.00033

Mineral		Area	Point	Depth (mbsf)	Layer type	Grain area	La	Ce	Pr	Nd	Sm	Eu	Gd	Tb	Dy	Y	Ho	Er	Tm	Yb	Lu
Pl		B	mh_26	591.932	Fine	core	0.371	0.838	0.104	0.465	0.079	0.429	0.086	0.00507	0.0436	0.1537	0.0047	0.0181	0.00122	0.0041	<0.00021
Pl		B	mh_27	591.932	Fine	rim	0.377	0.848	0.1022	0.411	0.0723	0.359	0.0445	0.0055	0.0181	0.106	0.00293	0.0059	<0.00041	0.005	0.00075
Pl		A	bf_10	591.985	Coarse	core	0.218	0.532	0.0857	0.402	0.099	0.468	0.091	0.011	0.0676	0.346	0.0104	0.0253	0.00396	0.0195	0.00348
Pl		C	bf_11	591.991	Coarse	core	0.525	1.106	0.1366	0.586	0.098	0.45	0.102	0.009	0.0426	0.17	0.0076	0.0189	0.00199	0.0083	<0.00029
Pl	360_65R5_46	C	bf_12	591.991	Coarse	core	0.212	0.534	0.0753	0.391	0.074	0.426	0.086	0.0105	0.0434	0.233	0.0071	0.0161	0.00228	0.0043	0.00211
Pl		C	bf_13	591.991	Coarse	rim	0.471	0.964	0.1264	0.504	0.073	0.427	0.075	0.0071	0.035	0.154	0.0055	0.0117	0.0011	0.0041	<0.00038
Pl		E	bf_14	592.004	Coarse	core	0.482	0.976	0.119	0.482	0.09	0.453	0.0555	0.0058	0.0259	0.147	0.0062	<0.0025	0.00046	0.0077	0.00046
Pl		E	bf_15	592.004	Coarse	rim	0.392	0.954	0.1198	0.551	0.104	0.462	0.087	0.0087	0.035	0.174	0.005	0.0165	0.00151	0.0068	0.00162
Pl		E	bf_16	592.004	Coarse	core	0.185	0.513	0.0686	0.336	0.086	0.448	0.0453	0.0087	0.0449	0.202	0.0077	0.0132	0.0009	0.0082	0.00062
Pl		B	md_12	592.027	Coarse	core	0.705	1.371	0.167	0.75	0.138	0.498	0.098	0.0126	0.0732	0.267	0.0093	0.0161	0.0028	0.0196	0.00126
Pl		B	md_13	592.027	Coarse	rim	0.626	1.377	0.194	0.796	0.113	0.543	0.101	0.0071	0.045	0.207	0.0107	0.0073	0.00078	0.0089	0.00025
Pl		B	md_14	592.027	Coarse	core	0.378	0.793	0.0998	0.515	0.113	0.473	0.086	0.0117	0.0418	0.175	0.0078	0.0046	<0.00092	0.0089	<0.00048
Pl		E	md_15	592.028	Coarse	core	0.697	1.446	0.1724	0.812	0.139	0.479	0.089	0.0112	0.0523	0.212	0.0082	0.0195	0.0011	0.0093	0.00086
Pl		E	md_16	592.028	Coarse	core	0.654	1.463	0.1807	0.765	0.114	0.482	0.105	0.0094	0.034	0.195	0.0102	0.0193	0.00078	0.0067	<0.00064
Pl	360_65R5_51	E	md_17	592.028	Coarse	rim	0.608	1.256	0.1521	0.7	0.109	0.482	0.116	0.0114	0.0641	0.222	0.008	0.0094	0.00233	0.0042	0.00234
Pl		E	md_18	592.028	Coarse	core	0.189	0.459	0.0743	0.314	0.0697	0.478	0.108	0.0088	0.0816	0.301	0.0133	0.0331	0.00347	0.0225	0.00243
Pl		C	md_19	592.039	Coarse	core	0.377	1.029	0.1563	0.666	0.134	0.429	0.119	0.0087	0.0569	0.284	0.0115	0.0221	0.00167	0.0045	0.00066
Pl		C	md_20	592.039	Coarse	rim	0.594	1.26	0.169	0.723	0.143	0.467	0.109	0.0158	0.0644	0.251	0.012	0.022	0.00263	0.006	0.00031
Pl		C	md_21	592.039	Coarse	rim	0.623	1.307	0.1549	0.717	0.117	0.524	0.089	0.0071	0.0424	0.224	0.0056	0.0239	0.00134	0.0064	0.00162
Pl		C	md_22	592.039	Coarse	core	0.398	0.999	0.1281	0.634	0.107	0.491	0.098	0.0096	0.0488	0.197	0.0061	0.0128	<0.00076	0.0051	<0.00054
Pl		F	md_23	592.044	Coarse	core	0.235	0.586	0.0899	0.49	0.115	0.483	0.115	0.0163	0.0702	0.335	0.0105	0.0253	0.00246	0.0187	0.00167
Pl		F	md_24	592.044	Coarse	rim	0.498	0.979	0.1361	0.638	0.143	0.478	0.113	0.0109	0.0508	0.269	0.0094	0.0274	<0.00	0.0191	0.00115
Pl		F	md_25	592.044	Coarse	core	0.604	1.165	0.1522	0.636	0.096	0.494	0.088	0.0105	0.0507	0.23	0.007	0.0131	0.00122	0.0169	0.00177
Pl		C	cb_7	592.280	Coarse	rim	0.547	1.159	0.1452	0.648	0.14	0.455	0.091	0.0131	0.0696	0.282	0.0124	0.017	0.00178	0.0127	0.00063
Pl		C	cb_8	592.280	Coarse	core	0.172	0.397	0.0566	0.294	0.096	0.457	0.0501	0.0101	0.0715	0.329	0.0135	0.0286	0.0053	0.0218	0.00201
Pl		B	cb_9	592.287	Coarse	rim	0.487	1.064	0.1358	0.69	0.152	0.437	0.127	0.0124	0.0488	0.249	0.0059	0.0165	0.00103	0.0124	0.00055
Pl	360_65R5_76	B	cb_10	592.287	Coarse	core	0.291	0.749	0.1071	0.591	0.13	0.456	0.137	0.0159	0.094	0.373	0.0158	0.0371	0.0013	0.0101	<0.00077
Pl		B	cb_11	592.287	Coarse	core	0.637	1.255	0.1648	0.776	0.139	0.483	0.125	0.0143	0.058	0.398	0.0162	0.0326	0.003	0.0092	0.00066
Pl		A	cb_12	592.290	Coarse	core	0.296	0.779	0.113	0.583	0.118	0.459	0.121	0.0147	0.0491	0.279	0.0116	0.009	<0.00072	0.0162	0.00258
Pl		A	cb_13	592.290	Coarse	rim	0.532	1.18	0.1473	0.695	0.146	0.455	0.094	0.0129	0.0631	0.335	0.0114	0.02	0.0038	0.0082	0.00064
Pl		E	cb_14	592.300	Coarse	rim	0.577	1.143	0.1503	0.625	0.106	0.464	0.085	0.0084	0.0646	0.194	0.0085	0.0083	0.00125	0.0013	<0.00041
Pl		E	cb_15	592.300	Coarse	core	0.639	1.313	0.1574	0.713	0.107	0.453	0.104	0.013	0.0571	0.229	0.0079	0.0184	<0.00114	0.011	0.0015
Pl		E	cb_16	592.300	Coarse	core	0.654	1.319	0.158	0.72	0.098	0.474	0.157	0.0141	0.0441	0.259	0.0083	0.0162	0.0024	0.0077	0.00258
Pl		A	bd_Plag1	592.320	Coarse	core	0.449	1.069	0.1425	0.627	0.105	0.429	0.116	0.0091	0.0452	0.2134	0.0065	0.014	0.00256	0.0079	<0.00054
Pl		A	bd_Pla2	592.320	Coarse	rim	0.539	1.07	0.1315	0.544	0.093	0.396	0.094	0.0062	0.0221	0.1448	0.00267	0.015	<0.00079	0.0096	<0.00
Pl		C	bd_Plag4	592.321	Coarse	core	0.469	1.098	0.1267	0.511	0.1008	0.383	0.06	0.0075	0.0288	0.1465	0.00411	0.0121	0.00232	0.0042	<0.00038
Pl		C	bd_Plag5	592.321	Coarse	rim	0.494	1.142	0.1356	0.512	0.084	0.377	0.081	0.007	0.0416	0.1614	0.0048	0.0059	<0.00083	0.0031	0.00272
Pl	360_65R5_79g	D	bd_Plag6	592.313	Coarse	core	0.498	1.121	0.1443	0.554	0.0941	0.409	0.0786	0.0089	0.0405	0.1841	0.0061	0.024	0.00141	0.0107	0.00091
Pl		D	bd_Plag7	592.313	Coarse	rim	0.406	0.954	0.111	0.517	0.0947	0.372	0.0631	0.0051	0.0371	0.137	0.00337	0.0127	0.00084	0.0079	0.00078
Pl		D	bd_Plag8	592.313	Coarse	core	0.1292	0.368	0.0512	0.25	0.0566	0.358	0.0601	0.0085	0.05	0.2099	0.0113	0.0191	0.00172	0.0095	0.00111
Pl		D	bd_Plag9	592.330	Coarse in F	core	0.52	1.004	0.1219	0.494	0.0767	0.374	0.084	0.0076	0.0412	0.1614	0.0059	0.0091	<0.00105	0.0061	<0.00042

Mineral		Area	Point	Depth (mbsf)	Layer type	Grain area	La	Ce	Pr	Nd	Sm	Eu	Gd	Tb	Dy	Y	Ho	Er	Tm	Yb	Lu
Pl	360_65R5_79f	D	bd_Plag1	592.330	Coarse in F	core	0.489	0.986	0.1188	0.48	0.0694	0.387	0.0647	0.007	0.0319	0.1598	0.0074	0.0098	<0.00050	0.0057	<0.00056
Pl		A	bd_plag1	592.336	Fine	core	0.479	0.987	0.1171	0.5	0.09	0.397	0.086	0.0055	0.041	0.1877	0.0039	0.0123	<0.00096	0.0121	0.0006
Pl		B	bd_plag1	592.332	Coarse in F	core	0.385	0.864	0.1152	0.509	0.1008	0.39	0.101	0.0128	0.0432	0.217	0.0072	0.0108	<0.00063	0.0038	0.00148
Pl		B	bd_Plag1	592.332	Coarse in F	rim	0.435	0.897	0.1096	0.476	0.0886	0.371	0.0801	0.0072	0.0442	0.1908	0.0063	0.0152	0.00215	0.0056	<0.00058
Pl		B	bd_Plag1	592.332	Coarse in F	core	0.499	1.006	0.1259	0.474	0.0812	0.362	0.051	0.0049	0.0325	0.1386	0.007	0.0142	0.00062	0.0044	<0.00059
Pl		F	bd_Plag1	592.334	Fine	core	0.457	0.974	0.1227	0.532	0.0821	0.387	0.0781	0.0103	0.0475	0.1909	0.0057	0.0212	0.001	0.0141	<0.00056
Pl		A	ce_7	592.354	Coarse in F	core	0.43	0.78	0.0999	0.501	0.08	0.346	0.093	0.0099	0.0463	0.213	0.0072	0.0098	0.00156	0.0051	0.00074
Pl		D	ce_8	592.357	Coarse in F	core	0.371	0.752	0.0973	0.459	0.08	0.36	0.071	0.009	0.0369	0.165	0.0042	0.016	<0.00053	0.0037	0.0005
Pl	360_65R5_83	D	ce_9	592.357	Coarse in F	core	0.218	0.516	0.0785	0.391	0.089	0.392	0.088	0.0113	0.0587	0.242	0.01	0.012	<0.00082	0.0069	0.00097
Pl		D	ce_10	592.357	Coarse in F	rim	0.372	0.727	0.1067	0.385	0.096	0.369	0.0628	0.0071	0.0298	0.164	0.0066	0.0104	<0.00	0.0072	0.0003
Pl		C	ce_11	592.365	Coarse in F	core	0.314	0.694	0.0944	0.463	0.0712	0.349	0.109	0.0102	0.0412	0.189	0.0069	0.0141	0.00221	0.0019	0.00066
Pl		C	ce_12	592.365	Coarse in F	rim	0.359	0.744	0.1034	0.435	0.0666	0.347	0.083	0.0105	0.0439	0.188	0.0052	0.0307	0.00076	0.0129	0.00075
Pl		F	ce_13	592.374	Fine	rim	0.329	0.666	0.0843	0.36	0.0691	0.345	0.0478	0.0064	0.0351	0.1293	0.00269	0.012	0.00072	0.0024	<0.00041
Pl		E	ce_15	592.376	Fine	core	0.267	0.564	0.0722	0.363	0.0602	0.328	0.074	0.006	0.0393	0.159	0.0045	0.0178	0.00174	<0.0011	0.00044
Pl		B	mg_11	592.404	Fine	core	0.312	0.702	0.0848	0.393	0.0607	0.347	0.0507	0.0069	0.0201	0.1016	0.00492	0.0097	0.00135	0.00134	0.00053
Pl		B	mg_12	592.404	Fine	rim	0.305	0.708	0.0838	0.341	0.0522	0.335	0.0538	0.00328	0.0241	0.0995	0.00307	0.0112	0.00041	0.0057	<0.00050
Pl		C	mg_13	592.405	Fine	core	0.316	0.668	0.0916	0.414	0.0946	0.341	0.0539	0.0078	0.037	0.145	0.00433	0.0068	0.001	0.0037	0.00035
Pl		C	mg_14	592.405	Fine	rim	0.324	0.67	0.0886	0.431	0.085	0.356	0.0588	0.0067	0.0396	0.158	0.00527	0.0114	0.00114	<0.0032	0.00107
Pl		C	mg_15	592.405	Fine	core	0.329	0.675	0.0912	0.428	0.0782	0.373	0.0568	0.00712	0.0356	0.158	0.00702	0.0162	0.00155	0.0056	0.00094
Pl	360_65R5_87	C	mg_16	592.405	Fine	rim	0.295	0.638	0.0888	0.411	0.0637	0.374	0.0589	0.00505	0.039	0.1374	0.0056	0.0072	0.00133	0.0088	0.00055
Pl		C	mg_17	592.405	Fine	core	0.325	0.665	0.0882	0.384	0.0599	0.362	0.0718	0.0067	0.0345	0.1246	0.0051	0.0097	0.0013	0.0025	0.00057
Pl		E	mg_18	592.391	Fine	rim	0.298	0.598	0.0772	0.356	0.0646	0.343	0.0803	0.0083	0.0359	0.1264	0.0052	0.0163	0.00154	0.0066	0.0007
Pl		E	mg_19	592.391	Fine	core	0.288	0.58	0.083	0.362	0.0729	0.356	0.0589	0.0066	0.0319	0.168	0.0069	0.0123	0.00056	0.0068	<0.00051
Pl		E	mg_20	592.391	Fine	core	0.276	0.6	0.08	0.378	0.0676	0.332	0.0744	0.0084	0.036	0.165	0.0058	0.0138	0.00058	0.0051	0.00028
Pl		E	mg_21	592.391	Fine	rim	0.284	0.58	0.0851	0.371	0.0786	0.349	0.0683	0.0069	0.0321	0.148	0.00387	0.0105	0.00084	0.0048	0.0003
Pl		F	mg_22	592.384	Fine	rim	0.249	0.543	0.0742	0.314	0.0647	0.339	0.0486	0.00537	0.0251	0.137	0.0059	0.007	0.00016	0.0032	0.0006
Pl		F	mg_23	592.384	Fine	core	0.174	0.413	0.0625	0.3	0.0768	0.314	0.0587	0.0112	0.043	0.207	0.00678	0.0129	0.00146	0.0058	0.00103
Pl		F	mg_24	592.384	Fine	core	0.269	0.586	0.0798	0.386	0.0674	0.344	0.0612	0.00542	0.029	0.138	0.0065	0.01	0.00076	0.0021	0.00034
Pl		C	cf_9	592.446	Coarse in F	rim	0.517	0.946	0.1224	0.517	0.095	0.444	0.119	0.0105	0.0337	0.192	0.0048	0.0077	0.00095	0.0069	0.00042
Pl		C	cf_10	592.446	Coarse in F	core	0.1739	0.385	0.066	0.328	0.108	0.423	0.082	0.0171	0.0758	0.335	0.0117	0.0304	0.0034	0.0177	<0.00092
Pl		A	cf_11	592.445	Coarse in F	core	0.486	0.988	0.1279	0.544	0.115	0.393	0.086	0.0109	0.0435	0.22	0.0087	0.0069	0.0007	<0.00118	0.00111
Pl	360_65R5_91	A	cf_12	592.445	Coarse in F	rim	0.427	0.829	0.1026	0.463	0.071	0.393	0.054	0.0087	0.0363	0.1349	0.0036	0.0127	0.00248	0.0089	0.00027
Pl		B	cf_13	592.443	Coarse in F	core	0.4	0.821	0.1091	0.417	0.087	0.418	0.055	0.0092	0.0345	0.1219	0.0039	0.0124	<0.00100	0.0057	<0.00037
Pl		B	cf_14	592.443	Coarse in F	core	0.404	0.891	0.111	0.502	0.088	0.384	0.068	0.0074	0.0429	0.1569	0.0052	0.0227	0.00057	0.0084	0.00092
Pl		B	cf_15	592.443	Coarse in F	rim	0.412	0.844	0.1019	0.454	0.0749	0.395	0.0668	0.0047	0.0295	0.1424	0.0049	0.0137	0.00136	0.0134	0.00054
Pl		F	cf_16	592.435	Fine	core	0.2022	0.473	0.0665	0.302	0.0543	0.322	0.076	0.0078	0.0345	0.15	0.0081	0.0102	0.00129	0.0121	0.00125
Pl		D	cf_17	592.432	Fine	core	0.2088	0.437	0.0624	0.263	0.074	0.364	0.065	0.0062	0.0338	0.194	0.0057	0.0199	0.00092	<0.00	0.00135
Pl		C	ma_13	592.466	Fine	core	0.239	0.516	0.0682	0.303	0.056	0.355	0.05	0.0048	0.0141	0.1102	0.00343	0.006	0.00046	0.0027	<0.00
Pl		C	ma_14	592.466	Fine	rim	0.245	0.53	0.071	0.318	0.0586	0.317	0.035	0.0064	0.0297	0.117	0.0049	<0.00	<0.00	<0.0042	<0.00044
Pl		C	ma_16	592.466	Fine	core	0.264	0.556	0.071	0.316	0.0681	0.327	0.076	0.00349	0.0301	0.1105	0.0055	0.0081	<0.00079	0.0038	<0.00051
Pl		A	ma_17	592.466	Fine	core	0.274	0.535	0.0733	0.373	0.0685	0.348	0.073	0.0092	0.0458	0.173	0.0052	0.0122	0.00068	0.0083	0.00174

Mineral		Area	Point	Depth (mbsf)	Layer type	Grain area	La	Ce	Pr	Nd	Sm	Eu	Gd	Tb	Dy	Y	Ho	Er	Tm	Yb	Lu
Pl	360_65R5_94	A	ma_18	592.466	Fine	rim	0.267	0.529	0.071	0.37	0.091	0.34	0.065	0.0088	0.0488	0.1517	0.0068	0.0139	<0.00092	0.0051	<0.00
Pl		A	ma_19	592.466	Fine	core	0.264	0.494	0.0683	0.315	0.0637	0.333	0.055	0.0068	0.0253	0.1368	0.0059	0.0057	<0.00033	0.0038	0.00017
Pl		B	ma_20	592.456	Fine	core	0.277	0.575	0.089	0.41	0.0623	0.368	0.08	0.0104	0.0435	0.188	0.0053	0.014	0.00113	0.0064	0.00059
Pl		B	ma_21	592.456	Fine	rim	0.33	0.602	0.075	0.34	0.0463	0.363	0.05	0.0049	0.0213	0.1124	0.00086	<0.0037	0.00063	0.003	<0.00052
Pl		B	ma_22	592.456	Fine	core	0.313	0.609	0.0952	0.466	0.0652	0.41	0.071	0.0118	0.0386	0.195	0.0068	0.0143	0.00121	0.0063	<0.00018
Pl		B	ma_23	592.456	Fine	rim	0.314	0.612	0.0735	0.399	0.055	0.407	0.092	0.006	0.0352	0.162	0.0071	0.0099	0.00059	0.0048	0.00045
Pl		D	ma_24	592.453	Fine	core	0.3	0.563	0.0808	0.339	0.0593	0.36	0.063	0.0055	0.0262	0.1219	0.0064	0.0109	0.0009	<0.0022	0.00162
Pl		E	cc_11	592.533	Coarse	rim	0.685	1.297	0.1387	0.7	0.135	0.482	0.095	0.0095	0.0521	0.207	0.0091	0.0171	0.0009	<0.00	0.00135
Pl		E	cc_12	592.533	Coarse	core	0.353	0.883	0.1341	0.728	0.146	0.47	0.127	0.0184	0.087	0.369	0.0181	0.0214	0.0049	0.0232	0.0019
Pl	360_65R5_102	B	cc_13	592.550	Coarse	rim	0.614	1.18	0.1275	0.682	0.102	0.43	0.082	0.0136	0.0546	0.204	0.006	0.0077	0.00052	0.007	<0.00051
Pl		B	cc_14	592.550	Coarse	rim	0.608	1.255	0.1592	0.672	0.12	0.435	0.1	0.008	0.0388	0.207	0.0053	0.0181	0.00092	0.0051	<0.00058
Pl		A	cc_15	592.549	Coarse	core	0.227	0.529	0.0829	0.462	0.113	0.474	0.109	0.0124	0.082	0.361	0.0121	0.0291	0.0026	0.0133	0.00181
Pl		A	cc_16	592.549	Coarse	rim	0.604	1.28	0.1513	0.798	0.11	0.478	0.106	0.0161	0.102	0.38	0.0142	0.0223	0.0038	0.0209	0.0023
Pl		A	cc_17	592.549	Coarse	core	0.703	1.396	0.1863	0.858	0.189	0.52	0.16	0.0127	0.091	0.376	0.012	0.0367	0.0031	0.0129	<0.00099
Pl		D	cc_18	592.557	Coarse	core	0.636	1.252	0.1583	0.619	0.096	0.485	0.103	0.0101	0.0455	0.204	0.0076	0.0068	0.0037	0.0164	0.00115
Pl		D	cc_19	592.557	Coarse	core	0.22	0.592	0.0817	0.499	0.088	0.472	0.088	0.0118	0.0503	0.296	0.0107	0.0225	0.00188	0.0185	0.0014
Pl		D	cc_20	592.557	Coarse	rim	0.482	1.042	0.1422	0.698	0.111	0.46	0.108	0.0124	0.0423	0.219	0.0044	0.021	0.0029	0.0061	0.00098
Pl		B	cd_11	592.642	Fine	core	0.534	1.08	0.133	0.566	0.0847	0.385	0.0859	0.0097	0.047	0.206	0.0068	0.0134	0.00219	0.0066	0.00066
Pl		B	cd_12	592.642	Fine	rim	0.522	1.087	0.1238	0.534	0.0993	0.357	0.0777	0.0094	0.0489	0.1827	0.0057	0.0148	0.00187	0.0081	0.00089
Pl		A	cd_13	592.637	Fine	rim	0.428	0.908	0.1178	0.534	0.117	0.376	0.0852	0.0063	0.0421	0.218	0.0084	0.0204	0.00161	0.0129	0.00135
Pl	360_65R5_111	A	cd_14	592.637	Fine	core	0.441	0.935	0.119	0.533	0.094	0.381	0.101	0.01	0.0476	0.205	0.0073	0.017	0.00135	0.005	0.00134
Pl		A	cd_15	592.637	Fine	core	0.5	1.005	0.1199	0.574	0.1059	0.401	0.0883	0.0094	0.0376	0.209	0.0075	0.0142	0.00143	0.0131	0.00083
Pl		C	cd_16	592.631	Fine	core	0.58	1.044	0.1364	0.594	0.089	0.399	0.088	0.0072	0.0586	0.222	0.0075	0.016	0.00113	0.0045	<0.00027
Pl		C	cd_17	592.631	Fine	rim	0.535	1.035	0.1234	0.546	0.0849	0.419	0.0921	0.0085	0.0523	0.198	0.0099	0.012	0.00072	0.0097	0.0009
Pl		D	cd_18	592.627	Fine	core	0.49	0.978	0.1084	0.524	0.0749	0.406	0.0736	0.0056	0.0338	0.1431	0.0057	0.0166	0.0013	0.004	0.00116
Pl		D	cd_19	592.627	Fine	core	0.223	0.551	0.0842	0.385	0.0906	0.398	0.0758	0.0076	0.0579	0.207	0.0079	0.02	0.00169	0.0097	0.00134
Pl		D	cd_20	592.627	Fine	rim	0.464	0.912	0.1065	0.47	0.0687	0.393	0.0776	0.0061	0.0291	0.1179	0.00398	0.0101	0.00075	0.0014	0.00126
Pl		E	mf_1	592.695	Coarse	core	0.627	1.136	0.1517	0.689	0.1171	0.506	0.127	0.0105	0.0446	0.1815	0.00632	0.015	0.00104	0.006	0.00014
Pl		D	mf_2	592.701	Coarse	core	0.596	1.132	0.1481	0.644	0.1123	0.45	0.1046	0.0094	0.04	0.1782	0.00656	0.014	0.00092	0.0049	<0.00031
Pl		D	mf_3	592.701	Coarse	core	0.2158	0.574	0.0898	0.469	0.0822	0.458	0.085	0.0136	0.05	0.252	0.009	0.0154	0.00127	0.0102	0.00185
Pl	360_65R5_117	D	mf_4	592.701	Coarse	rim	0.57	1.109	0.1269	0.47	0.0856	0.446	0.0779	0.00624	0.0269	0.1299	0.00212	0.0094	0.00091	0.0049	0.00033
Pl		B	mf_5	592.706	Coarse	core	0.2126	0.492	0.0837	0.447	0.1161	0.516	0.111	0.01018	0.0671	0.265	0.01	0.0193	0.00316	0.0138	0.00137
Pl		A	mf_7	592.713	Coarse	core	0.678	1.257	0.1583	0.653	0.1259	0.476	0.111	0.00963	0.0355	0.1541	0.00534	0.0112	0.00149	0.0044	0.00042
Pl		A	mf_8	592.713	Coarse	core	0.449	0.738	0.0775	0.339	0.064	0.396	0.061	0.0062	0.0337	0.139	0.0035	0.0092	<0.00253	0.0111	<0.00076
Pl		C	mf_10	592.718	Coarse	core	0.59	1.331	0.1587	0.651	0.0836	0.411	0.1004	0.0094	0.0384	0.1691	0.0091	0.0141	0.00166	0.0118	0.00074
Pl		C	mf_11	592.718	Coarse	rim	0.584	1.307	0.146	0.618	0.1071	0.408	0.0831	0.0068	0.046	0.1659	0.00391	0.0116	0.00129	0.0062	0.0004
Pl		C	mf_12	592.718	Coarse	core	0.595	1.22	0.1333	0.521	0.0675	0.333	0.0512	0.00541	0.0244	0.1323	0.00456	0.008	0.00076	0.0015	0.00025
Pl		B	xa_16	592.175	Coarse	rim	0.63	1.515	0.1894	0.789	0.1336	0.515	0.113	0.01011	0.0577	0.271	0.0098	0.0163	0.00167	0.01	<0.00035
Pl		C	xa_18	592.169	Coarse	rim	0.666	1.497	0.1791	0.758	0.109	0.467	0.084	0.00985	0.0487	0.2215	0.00811	0.0171	0.00142	0.0086	0.00108
Pl		C	xa_19	592.169	Coarse	core	0.709	1.563	0.1906	0.765	0.1433	0.468	0.117	0.01239	0.0659	0.273	0.00968	0.023	0.00245	0.0131	0.00234
Pl		D	xa_20	592.171	Coarse	core	0.742	1.61	0.1939	0.788	0.122	0.504	0.106	0.01031	0.0541	0.2423	0.00924	0.0185	0.00191	0.0118	0.00172

Mineral		Area	Point	Depth (mbsf)	Layer type	Grain area	La	Ce	Pr	Nd	Sm	Eu	Gd	Tb	Dy	Y	Ho	Er	Tm	Yb	Lu
Pl	360_65R5_63B	D	xa_21	592.171	Coarse	rim	0.729	1.504	0.175	0.708	0.1164	0.499	0.089	0.01005	0.0493	0.2016	0.0062	0.0177	0.00099	0.0065	0.00089
Pl		D	xa_22	592.171	Coarse	core	0.711	1.477	0.1797	0.693	0.112	0.476	0.0906	0.0116	0.042	0.2236	0.0083	0.0257	0.00366	0.0081	<0.00068
Pl		E	xa_23	592.178	Coarse	core	0.707	1.57	0.1934	0.809	0.1271	0.5	0.099	0.0127	0.0563	0.263	0.0096	0.0217	0.00223	0.0098	0.00095
Pl		E	xa_24	592.178	Coarse	rim	0.593	1.351	0.1669	0.662	0.1189	0.473	0.093	0.00962	0.0373	0.1849	0.00561	0.0136	0.00273	0.0087	<0.00044
Pl		E	xa_25	592.178	Coarse	core	0.589	1.367	0.165	0.686	0.119	0.484	0.098	0.00929	0.0505	0.2082	0.00827	0.0159	0.001	0.0074	0.00061
Pl		E	xa_26	592.182	Coarse	core	0.715	1.674	0.2101	0.828	0.147	0.501	0.117	0.0135	0.0686	0.268	0.0107	0.0172	0.00289	0.0105	0.00095
Pl		E	xa_27	592.182	Coarse	rim	0.689	1.562	0.1771	0.755	0.135	0.482	0.103	0.0112	0.0517	0.254	0.0092	0.0174	0.00147	0.0095	0.00151
Pl		H	xa_31	592.174	Coarse	rim	0.604	1.361	0.163	0.651	0.1068	0.468	0.082	0.0093	0.0478	0.2162	0.00925	0.0114	0.00168	0.008	<0.00030
Pl		N3	xb_14	592.145	Coarse	rim	0.446	1.163	0.1454	0.618	0.1175	0.441	0.109	0.0095	0.0459	0.2254	0.01	0.0206	0.00077	0.0036	0.00126
Pl	360_65R5_63A	N3	xb_16	592.145	Coarse	rim	0.564	1.311	0.1647	0.657	0.124	0.467	0.0934	0.0092	0.0577	0.224	0.0097	0.0182	0.0015	0.0089	0.00146
Pl		N3	xb_17	592.145	Coarse	core	0.558	1.312	0.1646	0.625	0.1069	0.463	0.103	0.0104	0.0436	0.2095	0.0079	0.0112	0.00153	0.0129	0.001
Pl		N4	xb_19	592.156	Coarse	core	0.64	1.424	0.1687	0.683	0.0998	0.439	0.0966	0.0088	0.0442	0.1869	0.0087	0.0113	<0.00051	<0.00	0.00097
Pl		N1	xb_20	592.158	Coarse	core	0.523	1.338	0.1792	0.774	0.134	0.442	0.115	0.0104	0.053	0.2018	0.0104	0.0139	0.00092	0.0035	<0.00050
Pl		N5	xb_21	592.154	Coarse	core	0.622	1.369	0.1611	0.619	0.12	0.447	0.0871	0.0086	0.0479	0.201	0.0085	0.0184	0.00165	0.0053	0.00039
Pl		N5	xb_22	592.154	Coarse	rim	0.644	1.371	0.1568	0.605	0.101	0.444	0.081	0.0087	0.0293	0.1858	0.0049	0.0146	0.00145	0.0028	0.00128
		Average (N = 42)					0.58	1.74	0.34	2.22	1.02	0.49	1.43	0.31	2.30	1.56	0.50	1.47	0.22	1.56	0.22
BIR		2SD					0.04	0.16	0.02	0.16	0.11	0.04	0.34	0.04	0.34	0.16	0.08	0.21	0.04	0.16	0.04
		Preferred values ("GeoRem" Jochum et al., 2007)					0.609	1.89	0.37	2.37	1.09	0.517	1.85	0.35	2.55	14.3	0.56	1.7	0.24	1.64	0.25

In situ trace elements concentrations in ppm analysed by La-ICP-MS on Thermo Fisher Element XR in GM (Montpellier, France)

Mineral	Sample	Area	Point	Depth (mbsf)	Layer type	Grain area	La	Ce	Pr	Nd	Sm	Eu	Gd	Tb	Dy	Y	Ho	Er	Tm	Yb	Lu
Cpx		Analitycal error average				1 sigma	0.017	0.080	0.021	0.160	0.087	0.025	0.160	0.026	0.190	1.040	0.040	0.120	0.018	0.113	0.017
Cpx		F	mb_31	591.536	Fine	core	0.2058	1.112	0.33	3.03	1.673	0.558	3.13	0.617	4.6	25.91	0.995	2.78	0.4	2.54	0.364
Cpx		F	mb_32	591.536	Fine	rim	0.2036	1.121	0.347	2.86	1.731	0.567	3.19	0.64	4.45	24.85	0.983	2.78	0.399	2.279	0.365
Cpx		F	mb_33	591.536	Fine	core	0.1962	1.188	0.354	3.09	1.737	0.618	2.99	0.628	4.58	26.27	0.996	2.92	0.41	2.536	0.377
Cpx		E	mb_34	591.540	Fine	core	0.1984	1.259	0.354	2.88	1.629	0.588	2.63	0.517	3.78	20.77	0.822	2.33	0.321	2.069	0.295
Cpx		E	mb_35	591.540	Fine	core	0.2048	1.166	0.337	2.66	1.433	0.507	2.37	0.486	3.39	18.63	0.733	2.1	0.294	1.889	0.256
Cpx		D	mb_36	591.553	Fine	core	0.37	2.191	0.599	4.54	2.087	0.663	3.28	0.613	4.48	24.42	0.962	2.68	0.395	2.428	0.368
Cpx		D	mb_37	591.553	Fine	rim	0.351	2.202	0.59	4.43	2.143	0.693	3.23	0.627	4.44	24.31	0.958	2.78	0.382	2.53	0.367
Cpx		D	mb_38	591.553	Fine	core	0.386	2.215	0.554	4.43	2.18	0.654	3.04	0.61	4.42	24.23	0.982	2.65	0.35	2.41	0.37
Cpx		D	mb_39	591.553	Fine	rim	0.359	2.152	0.563	4.43	2.12	0.64	3.08	0.606	4.4	23.2	0.911	2.44	0.35	2.29	0.32
Cpx		B	mb_40	591.553	Fine	core	0.385	2.352	0.563	3.91	1.82	0.616	2.72	0.517	3.67	20.06	0.766	2.16	0.326	2.2	0.31
Cpx		B	mb_41	591.553	Fine	rim	0.369	2.3	0.573	4.08	2.04	0.648	2.92	0.518	3.79	20.21	0.788	2.23	0.295	2.108	0.295
Cpx		F	mb_44	591.536	Fine	rim	0.2228	1.197	0.353	3.08	1.835	0.62	3.36	0.643	4.68	26.6	1.016	2.86	0.421	2.6	0.399
Cpx		A	mc_19	591.576	Fine	core	0.319	1.445	0.369	2.822	1.449	0.527	2.253	0.478	3.51	19.68	0.76	2.177	0.31	2.056	0.292
Cpx		A	mc_20	591.576	Fine	rim	0.401	1.992	0.512	4	1.937	0.614	2.93	0.582	4.24	24.46	0.927	2.576	0.376	2.396	0.353
Cpx		D	mc_21	591.577	Fine	core	0.362	1.77	0.494	3.89	1.96	0.6	3.33	0.575	4.19	22.29	0.858	2.5	0.356	2.26	0.339
Cpx		D	mc_22	591.577	Fine	rim	0.389	2.077	0.549	4.16	2.003	0.62	2.916	0.598	4.25	23.77	0.883	2.508	0.356	2.273	0.337
Cpx		D	mc_23	591.577	Fine	core	0.454	2.306	0.644	4.67	2.269	0.696	3.25	0.676	4.83	26.4	1.005	2.91	0.402	2.661	0.367
Cpx		B	mc_24	591.581	Fine	core	0.451	2.369	0.614	4.57	2.188	0.707	3.2	0.651	4.81	27.5	1.028	2.93	0.427	2.725	0.387
Cpx		B	mc_25	591.581	Fine	core	0.461	2.139	0.526	4.01	1.935	0.636	2.796	0.605	4.41	24.31	0.926	2.708	0.384	2.436	0.371
Cpx		B	mc_26	591.581	Fine	rim	0.439	2.269	0.594	4.53	2.212	0.687	3.22	0.648	4.79	26.28	1.011	2.91	0.41	2.547	0.376
Cpx		B	mc_27	591.581	Fine	core	0.471	2.452	0.649	4.78	2.393	0.732	3.4	0.691	5.01	28.49	1.08	3.11	0.428	2.93	0.404
Cpx		C	mc_28	591.583	Fine	core	0.436	2.165	0.544	3.83	1.73	0.59	2.573	0.54	4	22.68	0.887	2.481	0.361	2.311	0.333
Cpx		C	mc_29	591.583	Fine	core	0.42	2.062	0.524	3.96	1.944	0.646	2.94	0.62	4.4	24.89	0.896	2.589	0.336	2.325	0.336
Cpx		N	bb_1	591.718	Coarse	core	0.224	1.084	0.279	2.265	1.218	0.479	2.073	0.425	3.15	17.35	0.645	1.928	0.262	1.833	0.259
Cpx		N	bb_2	591.718	Coarse	rim	0.898	4.69	1.03	6.97	2.8	0.723	4.12	0.764	5.42	30.3	1.196	3.42	0.474	3.19	0.468
Cpx		P	bb_4	591.709	Coarse	rim	0.977	5.16	1.276	9.09	4.16	0.946	6.5	1.193	8.78	47.39	1.881	5.51	0.75	4.99	0.74
Cpx		P	bb_5	591.709	Coarse	core	0.289	1.414	0.36	2.99	1.599	0.553	2.68	0.518	3.87	20.47	0.823	2.35	0.327	1.943	0.309
Cpx		Bis	bb_6	591.703	Coarse	core	1.174	6.33	1.501	10.58	5.31	1.009	7.38	1.224	8.75	52.59	1.903	5.66	0.775	5.22	0.726
Cpx		Bis	bb_7	591.703	Coarse	core	1.111	6.45	1.441	10.35	4.92	0.961	6.81	1.211	8.55	51.15	1.842	5.68	0.781	4.82	0.753
Cpx	360_65R5_2																				
Cpx	360_65R5_4																				

Mineral	360_65R5_18	Area	Point	Depth (mbsf)	Layer type	Grain area	La	Ce	Pr	Nd	Sm	Eu	Gd	Tb	Dy	Y	Ho	Er	Tm	Yb	Lu
Cpx		Bis	bb_8	591.703	Coarse	core	0.716	3.25	0.675	4.48	2.159	0.632	3.46	0.702	5.3	30.96	1.171	3.57	0.514	3.35	0.488
Cpx		Bis	bb_9	591.703	Coarse	rim	1.067	5.55	1.314	9.32	4.11	0.903	6.28	1.208	8.59	47.43	1.814	5.32	0.784	4.98	0.706
Cpx		Bis	bb_10	591.703	Coarse	rim	1.223	6.4	1.584	10.84	4.88	0.99	7.74	1.419	10.32	58.24	2.212	6.67	0.92	6.05	0.868
Cpx		O	bb_11	591.722	Coarse	core	0.358	1.69	0.376	2.73	1.226	0.361	1.841	0.356	2.73	15.02	0.578	1.683	0.249	1.551	0.225
Cpx		O	bb_12	591.722	Coarse	rim	0.799	4.19	1.01	7.38	3.3	0.804	5.11	0.94	6.86	37.66	1.513	4.07	0.593	3.89	0.545
Cpx		O	bb_13	591.722	Coarse	rim	0.222	1.142	0.303	2.57	1.559	0.56	2.53	0.499	3.73	20.28	0.783	2.28	0.316	2.01	0.309
Cpx		O	bb_14	591.722	Coarse	core	0.538	2.492	0.573	3.81	1.846	0.518	2.95	0.542	4.21	22.61	0.888	2.55	0.34	2.37	0.346
Cpx		D	mj_20	591.765	Coarse	core	0.2296	1.141	0.308	2.36	1.38	0.487	1.951	0.418	3.05	16.78	0.654	1.833	0.256	1.708	0.247
Cpx		D	mj_21	591.765	Coarse	rim	0.754	4.04	1.062	7.66	3.51	0.862	4.63	0.927	6.54	35.6	1.365	3.82	0.54	3.58	0.519
Cpx	360_65R5_23	B	mj_22	591.769	Fine	core	0.417	2.165	0.546	4.02	1.857	0.591	2.7	0.561	4.01	22.21	0.841	2.42	0.347	2.28	0.328
Cpx		B	mj_23	591.769	Fine	rim	0.452	2.596	0.707	5.3	2.54	0.749	3.63	0.753	5.45	29.25	1.101	3.1	0.463	3.04	0.424
Cpx		A	mj_24	591.773	Fine	core	0.248	1.293	0.327	2.528	1.204	0.427	1.796	0.385	2.83	15.73	0.611	1.71	0.249	1.699	0.244
Cpx		A	mj_25	591.773	Fine	rim	0.32	1.732	0.462	3.55	1.712	0.572	2.47	0.526	3.73	20.88	0.807	2.34	0.322	2.05	0.317
Cpx		C	mj_26	591.776	Fine	core	0.318	1.623	0.424	3.25	1.648	0.606	2.47	0.551	3.88	22	0.828	2.43	0.334	2.13	0.335
Cpx		D	ca_20	591.788	Coarse in	rim	0.37	1.94	0.518	4.08	1.963	0.618	2.72	0.592	4.28	23.2	0.895	2.47	0.345	2.28	0.318
Cpx		D	ca_21	591.788	Coarse in	core	0.411	2.05	0.53	3.89	1.97	0.618	2.88	0.589	4.53	24.65	0.958	2.72	0.413	2.59	0.351
Cpx		D	ca_22	591.788	Coarse in	rim	0.399	2.103	0.556	4.02	1.94	0.65	2.65	0.584	4.32	23.58	0.922	2.62	0.37	2.39	0.348
Cpx	360_65R5_27	B	ca_23	591.795	Fine	core	0.31	1.613	0.42	3.34	1.682	0.581	2.64	0.551	4.09	23.22	0.925	2.64	0.37	2.44	0.363
Cpx		C	ca_24	591.794	Fine	rim	0.299	1.565	0.445	3.46	1.767	0.601	3.06	0.666	4.84	27.41	1.048	2.99	0.426	2.75	0.426
Cpx		C	ca_25	591.794	Fine	core	0.312	1.404	0.366	3.05	1.67	0.566	2.55	0.59	4.48	24.91	0.969	2.79	0.394	2.494	0.378
Cpx		E	ca_26	591.805	Coarse in	core	0.395	2	0.56	4.53	2.28	0.648	3.6	0.727	5.57	29.92	1.163	3.53	0.488	3.06	0.464
Cpx		E	ca_27	591.805	Coarse in	rim	0.342	1.65	0.442	3.59	1.9	0.566	2.97	0.603	4.46	24.56	0.957	2.91	0.416	2.78	0.421
Cpx		A	mi_23	591.848	Fine	core	0.395	2.143	0.529	3.7	1.714	0.569	2.25	0.488	3.58	19.91	0.761	2.171	0.329	2.056	0.307
Cpx		A	mi_24	591.848	Fine	rim	0.453	2.423	0.617	4.3	2.003	0.685	2.65	0.587	4.2	22.98	0.88	2.47	0.372	2.42	0.331
Cpx		A	mi_25	591.848	Fine	core	0.465	2.507	0.631	4.55	2.174	0.725	2.9	0.617	4.32	23.57	0.908	2.59	0.364	2.48	0.346
Cpx		D	mi_27	591.846	Fine	rim	0.405	2.039	0.54	4.01	1.971	0.653	2.74	0.581	4.19	22.56	0.893	2.52	0.361	2.233	0.324
Cpx		C	mi_28	591.840	Fine	core	0.429	1.873	0.485	3.67	1.759	0.583	2.76	0.601	4.34	25.01	0.925	2.65	0.406	2.52	0.378
Cpx		C	mi_29	591.840	Fine	rim	0.435	2.015	0.526	4.15	2.031	0.634	2.85	0.618	4.64	25.9	0.954	2.84	0.403	2.48	0.391
Cpx	360_65R5_32	C	mi_30	591.840	Fine	core	0.473	2.203	0.614	4.73	2.357	0.71	3.37	0.715	5.44	30.22	1.16	3.29	0.46	2.96	0.457
Cpx		B	mi_31	591.837	Fine	core	0.308	1.454	0.402	3.12	1.594	0.538	2.35	0.515	3.72	20.56	0.792	2.23	0.324	2.071	0.297
Cpx		B	mi_32	591.837	Fine	rim	0.363	1.785	0.484	3.82	1.868	0.561	2.65	0.529	3.88	21.28	0.828	2.37	0.311	2.086	0.298

Mineral		Area	Point	Depth (mbsf)	Layer type	Grain area	La	Ce	Pr	Nd	Sm	Eu	Gd	Tb	Dy	Y	Ho	Er	Tm	Yb	Lu
Cpx		B	mi_33	591.837	Fine	core	0.533	2.602	0.722	5.52	2.5	0.761	3.53	0.785	5.47	30.05	1.138	3.27	0.452	2.84	0.425
Cpx		E	mi_34	591.832	Fine	core	0.513	2.405	0.612	4.54	2.023	0.682	2.99	0.635	4.67	26.21	0.991	2.96	0.421	2.69	0.394
Cpx		E	mi_35	591.832	Fine	rim	0.48	2.327	0.606	4.49	2.143	0.669	2.96	0.631	4.44	25.74	0.99	2.74	0.395	2.57	0.384
Cpx		A	mh_2	591.925	Fine	core	0.348	1.84	0.522	4.12	2.046	0.649	2.14	0.616	4.44	25.04	0.972	2.697	0.388	2.493	0.379
Cpx		A	mh_3	591.925	Fine	rim	0.279	1.484	0.422	3.43	1.722	0.55	1.86	0.525	3.76	20.54	0.786	2.202	0.304	1.955	0.2915
Cpx		D	mh_5	591.922	Fine	rim	0.379	2.041	0.578	4.49	2.147	0.681	2.42	0.653	4.76	25.78	0.979	2.81	0.399	2.54	0.376
Cpx	360_65R5_39	E	mh_6	591.928	Fine	core	0.362	1.814	0.488	3.83	1.814	0.577	2.05	0.569	3.84	22.12	0.84	2.406	0.348	2.196	0.323
Cpx		E	mhStd_16	591.928	Fine	rim	0.36	1.933	0.542	4.22	2.063	0.658	2.39	0.618	4.5	25.11	0.945	2.594	0.38	2.41	0.355
Cpx		C	mh_9	591.934	Fine	core	0.334	1.863	0.526	4.09	1.944	0.627	2.5	0.612	4.35	23.96	0.932	2.691	0.378	2.46	0.35
Cpx		C	mh_10	591.934	Fine	rim	0.36	2.07	0.591	4.67	2.298	0.71	2.84	0.67	4.85	26.53	1.021	2.9	0.401	2.57	0.388
Cpx		B	mh_11	591.932	Fine	core	0.355	2	0.559	4.42	2.137	0.672	2.68	0.628	4.46	24.55	0.924	2.54	0.367	2.34	0.348
Cpx		B	mh_12	591.932	Fine	rim	0.341	2.02	0.564	4.26	2.26	0.602	2.7	0.594	4.24	23.12	0.901	2.54	0.367	2.02	0.32
Cpx		B	bf_18	591.985	Coarse	rim	0.709	3.59	0.916	7.25	3.53	0.916	5.45	1.138	8.48	45.4	1.837	5.27	0.711	4.52	0.654
Cpx		B	bf_19	591.985	Coarse	core	0.737	3.5	0.833	6.74	3.48	0.876	5.04	1.076	7.97	43.19	1.679	4.77	0.686	4.29	0.666
Cpx		F	bf_20	591.989	Coarse	core	0.574	2.653	0.626	4.35	2.019	0.624	3.07	0.623	4.69	26.93	0.996	2.92	0.44	2.63	0.39
Cpx	360_65R5_46	F	bf_21	591.989	Coarse	rim	0.786	3.76	0.934	6.97	3.12	0.852	4.33	0.882	6.87	37.52	1.427	4.02	0.565	3.72	0.536
Cpx		C	bf_22	591.991	Coarse	rim	0.487	2.72	0.692	5.3	2.51	0.726	3.49	0.735	5.32	28.2	1.107	3.12	0.445	2.83	0.394
Cpx		C	bf_23	591.991	Coarse	core	0.429	1.847	0.42	3.2	1.46	0.543	2.277	0.461	3.52	19.16	0.773	2.13	0.312	2.003	0.286
Cpx		E	bf_24	592.004	Coarse	rim	0.372	2.025	0.495	3.5	1.782	0.576	2.293	0.508	3.7	20.65	0.779	2.28	0.314	2.218	0.31
Cpx		E	bf_25	592.004	Coarse	core	0.323	1.749	0.43	3.24	1.691	0.526	2.228	0.503	3.46	19	0.765	2.09	0.305	1.949	0.271
Cpx		B	md_26	592.027	Coarse	core	0.519	2.598	0.622	4.69	2.225	0.581	3.38	0.654	4.91	26.96	1.023	2.89	0.408	2.684	0.391
Cpx		B	md_27	592.027	Coarse	rim	0.413	1.95	0.492	3.6	1.797	0.506	2.632	0.513	3.85	22.63	0.816	2.331	0.324	2.079	0.319
Cpx		E	md_28	592.028	Coarse	core	0.629	3.079	0.765	5.73	2.78	0.765	4.25	0.805	5.98	32.18	1.247	3.56	0.494	3.34	0.461
Cpx	360_65R5_51	E	md_29	592.028	Coarse	rim	0.531	2.768	0.715	5.27	2.599	0.704	3.63	0.743	5.48	30.32	1.1	3.29	0.472	2.99	0.425
Cpx		C	md_30	592.039	Coarse	core	0.648	3.165	0.823	6.68	3.31	0.824	5.04	0.969	6.94	39.37	1.491	4.3	0.581	3.81	0.562
Cpx		C	md_31	592.039	Coarse	rim	0.546	2.655	0.689	5.38	2.61	0.684	3.95	0.756	5.55	30.37	1.141	3.19	0.465	3.07	0.443
Cpx		F	md_32	592.044	Coarse	core	0.449	1.899	0.462	3.41	1.698	0.599	2.648	0.568	4.19	23.8	0.924	2.634	0.402	2.438	0.37
Cpx		F	md_33	592.044	Coarse	rim	0.485	2.227	0.557	4.35	2.248	0.701	3.55	0.702	5.24	30.1	1.128	3.23	0.453	2.89	0.437
Cpx		B	cb_17	592.287	Coarse	rim	0.2084	0.996	0.292	2.48	1.449	0.525	2.76	0.546	4.11	22.72	0.893	2.54	0.378	2.252	0.352
Cpx		B	cb_18	592.287	Coarse	core	0.331	1.266	0.306	2.52	1.31	0.477	2.584	0.49	3.7	20.25	0.8	2.258	0.31	2.034	0.307
Cpx		A	cb_19	592.290	Coarse	rim	0.674	3.3	0.819	6.56	3.21	0.824	5.47	1.044	7.87	43.09	1.682	4.91	0.709	4.36	0.677

Mineral		Area	Point	Depth (mbsf)	Layer type	Grain area	La	Ce	Pr	Nd	Sm	Eu	Gd	Tb	Dy	Y	Ho	Er	Tm	Yb	Lu
Cpx	360_65R5_76	A	cb_20	592.290	Coarse	core	0.503	2.668	0.669	5.17	2.43	0.638	3.84	0.744	5.54	32.03	1.181	3.52	0.47	3.15	0.494
Cpx		D	cb_21	592.299	Coarse	rim	0.501	2.514	0.647	4.72	2.38	0.69	3.59	0.74	5.45	30.42	1.155	3.43	0.486	3.16	0.466
Cpx		D	cb_22	592.299	Coarse	core	0.368	1.547	0.337	2.715	1.481	0.508	2.5	0.497	3.69	20.41	0.767	2.238	0.341	2.106	0.323
Cpx		D	cb_23	592.299	Coarse	rim	0.583	3.22	0.8	6.19	3.05	0.807	4.83	0.955	6.83	37.22	1.48	4.06	0.564	3.86	0.563
CPx		D	cb_24	592.299	Coarse	core	0.712	3.63	0.898	6.96	3.44	0.857	5.09	0.977	7.33	40.12	1.608	4.16	0.627	3.71	0.557
Cpx	360_65R5_79g	D	be_1	592.313	Coarse	rim	0.399	2.038	0.477	3.44	1.613	0.571	2.453	0.48	3.51	19.14	0.722	2.139	0.322	2.15	0.305
Cpx		D	be_2	592.313	Coarse	core	0.405	2.086	0.514	3.65	1.833	0.597	2.765	0.538	3.91	21.61	0.848	2.459	0.361	2.264	0.344
Cpx		C	be_3	592.321	Coarse	core	0.1968	0.942	0.2477	1.979	1.089	0.42	1.74	0.372	2.708	15.08	0.592	1.676	0.2423	1.551	0.2279
Cpx		C	be_4	592.321	Coarse	rim	0.4	2.261	0.564	3.88	1.854	0.561	2.631	0.507	3.84	20.33	0.814	2.281	0.312	2.139	0.325
Cpx		B	be_5	592.332	Fine	core	0.48	2.604	0.681	5.33	2.649	0.703	4.23	0.801	5.8	32.93	1.274	3.53	0.483	3.08	0.455
Cpx	360_65R5_79f	D	be_6	592.330	Coarse in	core	0.288	1.353	0.343	2.634	1.348	0.47	2.301	0.468	3.5	19.17	0.771	2.176	0.31	1.958	0.293
Cpx		D	be_7	592.330	Coarse in	rim	0.531	2.714	0.711	5.59	2.65	0.725	4.45	0.821	5.84	31.43	1.266	3.33	0.502	3.03	0.505
Cpx		A	be_8	592.336	Fine	core	0.353	2.012	0.513	3.85	1.877	0.533	2.9	0.549	4.07	21.82	0.877	2.452	0.36	2.308	0.327
Cpx		B	be_10	592.332	Coarse in	core	0.389	2.144	0.567	4.26	2.122	0.6	3.49	0.673	4.78	25.41	1.027	2.88	0.412	2.54	0.378
Cpx		F	be_11	592.334	Fine	core	0.36	2.07	0.534	3.93	2.007	0.58	3.16	0.607	4.43	23.59	0.93	2.699	0.365	2.37	0.342
Cpx	360_65R5_83	D	ce_16	592.357	Coarse in	core	0.2228	0.985	0.253	2.201	1.192	0.408	2.091	0.437	3.33	17.71	0.689	1.973	0.298	1.813	0.273
Cpx		D	ce_17	592.357	Coarse in	rim	0.284	1.468	0.392	3.12	1.524	0.512	2.57	0.526	3.96	21.62	0.856	2.377	0.339	2.172	0.342
Cpx		C	ce_18	592.365	Coarse in	core	0.478	2.445	0.641	4.99	2.498	0.69	3.64	0.743	5.44	29.48	1.103	3.13	0.431	2.76	0.441
Cpx		B	ce_19	592.369	Coarse in	core	0.327	1.77	0.487	3.93	2.064	0.574	3.27	0.66	4.88	26.98	1.051	2.97	0.427	2.629	0.409
Cpx		B	mg_25	592.404	Fine	core	0.307	1.936	0.495	3.69	1.836	0.644	2.47	0.511	3.83	20.15	0.767	2.23	0.321	2.107	0.295
Cpx		B	mg_26	592.404	Fine	core	0.271	1.759	0.442	3.23	1.566	0.57	2.17	0.445	3.23	17.37	0.68	1.95	0.27	1.823	0.259
Cpx		A	mg_28	592.406	Fine	rim	0.252	1.643	0.425	3.09	1.563	0.564	2.27	0.467	3.23	17.33	0.675	1.905	0.275	1.745	0.249
Cpx		A	mg_29	592.406	Fine	core	0.294	1.706	0.434	3.18	1.609	0.592	2.27	0.477	3.42	18.87	0.712	1.998	0.314	1.917	0.272
Cpx	360_65R5_87	C	mg_30	592.405	Fine	core	0.313	1.722	0.488	3.95	2.06	0.666	3.19	0.633	4.53	25.65	0.959	2.81	0.384	2.49	0.371
Cpx		C	mg_31	592.405	Fine	rim	0.325	1.769	0.491	3.96	2.05	0.65	3.14	0.624	4.61	25.43	0.985	2.84	0.367	2.47	0.364
Cpx		E	mg_32	592.391	Fine	core	0.273	1.369	0.388	3.12	1.656	0.569	2.77	0.555	4.23	23.35	0.943	2.56	0.381	2.34	0.335
Cpx		E	mg_33	592.391	Fine	rim	0.281	1.506	0.432	3.43	1.92	0.632	3.01	0.617	4.72	25.07	0.944	2.76	0.4	2.61	0.371
Cpx		E	mg_34	592.391	Fine	core	0.272	1.442	0.416	3.33	1.805	0.633	2.83	0.554	4.38	23.53	0.943	2.59	0.367	2.26	0.348
Cpx		F	mg_35	592.384	Fine	core	0.206	1.187	0.342	2.63	1.46	0.5	2.38	0.467	3.45	18.74	0.722	2.043	0.288	1.855	0.268
Cpx		F	mg_36	592.384	Fine	rim	0.252	1.434	0.388	3.18	1.698	0.617	2.66	0.565	4.08	22.03	0.872	2.47	0.348	2.16	0.323
Cpx		F	mg_37	592.384	Fine	core	0.265	1.543	0.417	3.44	1.727	0.628	2.8	0.571	4.42	23.02	0.919	2.62	0.363	2.35	0.336

Mineral		Area	Point	Depth (mbsf)	Layer type	Grain area	La	Ce	Pr	Nd	Sm	Eu	Gd	Tb	Dy	Y	Ho	Er	Tm	Yb	Lu
Cpx	360_65R5_91	C	cf_19	592.446	Coarse in	rim	0.377	1.992	0.532	4.32	2.124	0.616	3.6	0.729	5.13	28.34	1.104	3.14	0.444	2.76	0.444
Cpx		C	cf_20	592.446	Coarse in	core	0.533	2.341	0.57	4.42	2.233	0.675	3.44	0.755	5.2	29.07	1.135	3.18	0.477	3.06	0.452
Cpx		A	cf_21	592.445	Coarse in	core	0.296	1.401	0.363	2.73	1.508	0.552	2.26	0.497	3.44	19.25	0.765	2.076	0.311	1.99	0.295
Cpx		A	cf_22	592.445	Coarse in	rim	0.378	2.099	0.565	4.5	2.144	0.691	3.43	0.692	4.88	26.9	1.043	3.04	0.418	2.73	0.389
Cpx		B	cf_23	592.443	Coarse in	core	0.34	1.579	0.363	2.77	1.408	0.524	2.21	0.457	3.36	17.98	0.683	1.967	0.284	1.9	0.272
Cpx		D	cf_25	592.432	Fine	core	0.1918	1.088	0.321	2.84	1.675	0.604	3.06	0.627	4.71	26.58	1.058	2.85	0.421	2.61	0.418
Cpx		E	cf_26	592.428	Fine	core	0.1997	1.227	0.369	3.27	1.822	0.646	3.06	0.608	4.71	24.97	1.02	2.86	0.401	2.57	0.357
Cpx		B	ma_12	592.456	Fine	core	0.2544	1.381	0.379	3.17	1.64	0.54	2.555	0.561	4	21.45	0.848	2.368	0.349	2.053	0.315
Cpx	360_65R5_94	C	ma_25	592.466	Fine	core	0.1903	1.089	0.291	2.321	1.255	0.49	1.9	0.398	2.85	16.19	0.62	1.793	0.245	1.764	0.229
Cpx		C	ma_26	592.466	Fine	rim	0.1964	1.15	0.303	2.349	1.355	0.503	1.921	0.417	3.07	16.73	0.638	1.857	0.255	1.678	0.246
Cpx		C	ma_27	592.466	Fine	core	0.2184	1.227	0.352	2.97	1.564	0.555	2.556	0.533	3.92	21.16	0.791	2.413	0.334	2.123	0.308
Cpx		C	ma_28	592.466	Fine	rim	0.254	1.416	0.4	3.49	1.854	0.678	2.81	0.634	4.64	25.6	1.026	2.82	0.393	2.432	0.37
Cpx		D	ma_29	592.453	Fine	core	0.315	1.666	0.47	3.72	1.958	0.659	3.17	0.638	4.59	25.84	1	2.82	0.401	2.66	0.371
Cpx		D	ma_30	592.453	Fine	rim	0.26	1.482	0.414	3.36	1.889	0.607	2.89	0.594	4.43	24.15	0.928	2.77	0.364	2.386	0.373
Cpx	360_65R5_102	D	cc_21	592.557	Coarse	core	0.548	2.76	0.632	4.71	2.23	0.677	3.72	0.733	5.61	31.08	1.211	3.48	0.513	3.65	0.508
Cpx		D	cc_22	592.557	Coarse	rim	0.563	2.956	0.797	5.8	2.82	0.765	4.39	0.805	5.78	32.53	1.249	3.62	0.505	3.31	0.509
Cpx		B	cc_23	592.550	Coarse	rim	0.602	3.08	0.764	5.53	2.54	0.699	3.66	0.766	5.47	31.66	1.206	3.5	0.529	3.37	0.519
Cpx		B	cc_24	592.550	Coarse	core	0.319	1.515	0.37	2.91	1.45	0.488	2.52	0.483	3.84	20.64	0.812	2.44	0.321	2.116	0.316
Cpx		E	cc_25	592.533	Coarse	rim	0.649	3.37	0.896	7.24	3.55	0.792	5.61	1.069	7.75	41.59	1.652	4.72	0.665	4.03	0.607
Cpx		E	cc_26	592.533	Coarse	core	0.804	3.98	1.08	8.31	3.95	1.006	7.05	1.308	9.47	51.8	1.991	5.58	0.776	5.14	0.752
Cpx		C	cc_27	592.533	Coarse	rim	0.58	2.761	0.752	5.81	2.8	0.742	4.37	0.815	6.25	35.86	1.316	3.66	0.516	3.42	0.489
Cpx		C	cc_28	592.533	Coarse	core	0.464	2.034	0.505	3.94	2.2	0.637	3.63	0.716	5.42	29.4	1.149	3.23	0.457	2.85	0.427
Cpx	360_65R5_111	B	cd_21	592.642	Fine	core	0.283	1.447	0.364	2.777	1.495	0.545	2.238	0.465	3.58	19.57	0.786	2.107	0.315	2.089	0.289
Cpx		B	cd_22	592.642	Fine	rim	0.461	2.633	0.665	4.73	2.203	0.706	3.07	0.663	4.74	25.3	1.01	2.792	0.376	2.596	0.362
Cpx		A	cd_23	592.637	Fine	core	0.407	2.22	0.554	4.12	1.987	0.591	2.737	0.614	4.62	25.5	0.981	2.86	0.399	2.594	0.402
Cpx		A	cd_24	592.637	Fine	rim	0.499	2.541	0.648	4.99	2.389	0.684	3.58	0.755	5.39	30.55	1.191	3.19	0.474	3.03	0.45
Cpx		A	cd_25	592.637	Fine	core	0.534	2.762	0.749	5.62	2.71	0.704	3.95	0.838	5.86	33.17	1.264	3.56	0.509	3.1	0.47
Cpx		C	cd_26	592.631	Fine	rim	0.461	2.459	0.645	4.99	2.529	0.706	3.54	0.768	5.77	31.87	1.245	3.41	0.494	3.23	0.462
Cpx		C	cd_27	592.631	Fine	core	0.507	2.656	0.71	5.29	2.629	0.738	3.94	0.83	6.13	34.52	1.323	3.74	0.559	3.56	0.529
Cpx		D	cd_28	592.627	Fine	core	0.497	2.528	0.643	4.87	2.283	0.611	3.11	0.663	4.73	25.73	1.001	2.87	0.396	2.566	0.385
Cpx		D	cd_29	592.627	Fine	rim	0.379	1.725	0.424	3.11	1.573	0.551	2.456	0.534	3.78	21.5	0.839	2.427	0.329	2.272	0.345

Mineral		Area	Point	Depth (mbsf)	Layer type	Grain area	La	Ce	Pr	Nd	Sm	Eu	Gd	Tb	Dy	Y	Ho	Er	Tm	Yb	Lu
Cpx		E	mf_13	592.695	Coarse	core	0.479	2.398	0.676	5.27	2.58	0.693	3.42	0.749	5.32	28.48	1.113	3.15	0.446	2.924	0.42
Cpx		E	mf_14	592.695	Coarse	rim	0.381	1.855	0.517	3.92	1.797	0.544	2.51	0.534	4.02	21.93	0.834	2.436	0.349	2.241	0.324
Cpx		E	mf_15	592.695	Coarse	core	0.515	2.571	0.726	5.59	2.675	0.692	3.65	0.763	5.65	30.72	1.205	3.42	0.471	3	0.44
Cpx		D	mf_16	592.701	Coarse	core	0.429	1.945	0.501	3.65	1.79	0.594	2.57	0.552	4.24	24.04	0.898	2.672	0.391	2.519	0.39
Cpx		D	mf_17	592.701	Coarse	rim	0.518	2.606	0.737	5.65	2.681	0.763	3.42	0.784	5.69	31.51	1.222	3.46	0.489	3.22	0.465
Cpx		B	mf_18	592.706	Coarse	core	0.447	1.873	0.474	3.57	1.675	0.536	2.44	0.523	3.87	21.98	0.827	2.425	0.363	2.148	0.338
Cpx		B	mf_19	592.706	Coarse	rim	0.602	2.746	0.748	5.59	2.681	0.738	3.51	0.773	5.79	32	1.216	3.44	0.525	3.28	0.486
Cpx		A	mf_20	592.713	Coarse	core	0.298	1.248	0.344	2.855	1.556	0.564	2.279	0.518	3.79	20.94	0.839	2.303	0.329	2.144	0.292
Cpx		A	mf_21	592.713	Coarse	rim	0.579	2.72	0.736	5.37	2.714	0.698	3.38	0.734	5.29	29.42	1.121	3.24	0.46	2.92	0.423
Cpx		A	mf_22	592.713	Coarse	core	0.676	3.2	0.863	6.54	3.12	0.79	4.11	0.866	6.32	34.27	1.346	3.8	0.536	3.41	0.51
Cpx		C	mf_23	592.718	Coarse	core	0.554	3.09	0.739	5	2.31	0.649	2.83	0.624	4.53	24.47	0.947	2.608	0.382	2.537	0.339
Cpx		C	mf_24	592.718	Coarse	rim	0.598	3.69	0.903	5.97	2.651	0.802	3.21	0.694	4.93	25.83	1.014	2.89	0.398	2.599	0.355
Cpx		B	xa_32	592.175	Coarse	rim	0.606	3.68	0.924	6.41	2.957	0.777	4.38	0.851	5.98	32.42	1.213	3.53	0.489	3.18	0.47
Cpx		C	xa_34	592.169	Coarse	core	0.533	2.733	0.646	4.61	2.273	0.656	3.51	0.665	4.81	25.68	1.002	2.833	0.393	2.589	0.377
Cpx		C	xa_36	592.169	Coarse	core	0.497	2.509	0.557	3.89	1.804	0.582	2.85	0.563	4.11	22.65	0.853	2.485	0.364	2.347	0.335
Cpx		D	xa_37	592.171	Coarse	core	0.582	3.5	0.885	6.2	2.928	0.741	4.41	0.833	5.91	31.65	1.222	3.41	0.488	3.1	0.453
Cpx		D	xa_38	592.171	Coarse	rim	0.417	2.487	0.615	4.4	2.068	0.528	3.03	0.567	4.11	22.64	0.876	2.425	0.348	2.29	0.343
Cpx		D	xa_39	592.171	Coarse	core	0.567	2.945	0.68	4.53	2.109	0.608	3.18	0.598	4.44	24.39	0.931	2.602	0.381	2.523	0.364
Cpx		D	xa_41	592.171	Coarse	rim	0.551	3.06	0.687	4.71	2.153	0.63	3.19	0.608	4.51	24.56	0.937	2.757	0.397	2.614	0.383
Cpx		E	xa_42	592.182	Coarse	core	0.51	2.845	0.663	4.51	2.093	0.594	3.05	0.584	4.23	23.75	0.923	2.634	0.378	2.564	0.382
Cpx		E	xa_43	592.182	Coarse	rim	0.603	3.81	0.963	6.79	3.14	0.774	4.61	0.883	6.25	33.77	1.318	3.77	0.541	3.42	0.503
Cpx		E	xa_44	592.182	Coarse	rim	0.577	3.4	0.837	5.97	2.805	0.742	4.24	0.8	5.74	30.93	1.19	3.38	0.489	3.11	0.449
Cpx		G	xa_46	592.178	Coarse	rim	0.553	3.35	0.808	5.63	2.494	0.692	3.84	0.735	5.14	29.12	1.107	3.22	0.461	3.21	0.466
Cpx		N1	xb_25	592.158	Coarse	core	0.823	4.99	1.255	8.53	3.85	0.878	5.76	1.048	7.38	38.61	1.561	4.39	0.602	4.02	0.567
Cpx		N2	xb_27	592.153	Coarse	rim	0.592	3.4	0.823	5.87	2.783	0.753	4.41	0.803	5.8	31.35	1.209	3.53	0.477	3.2	0.467
Cpx		N4	xb_28	592.156	Coarse	core	0.634	3.93	0.962	6.88	3.09	0.821	4.76	0.832	5.95	32.11	1.239	3.47	0.515	3.32	0.5
Cpx		N4	xb_29	592.156	Coarse	core	0.693	4.26	1.056	7.52	3.53	0.849	5.28	0.913	6.49	35.35	1.334	3.88	0.541	3.63	0.519
Cpx		N4	xb_30	592.156	Coarse	core	0.614	3.76	0.916	6.32	2.91	0.771	4.4	0.809	5.91	31.03	1.204	3.33	0.475	3.24	0.444
Cpx		N4	xb_31	592.156	Coarse	core	0.651	3.93	0.95	6.5	2.89	0.789	4.44	0.813	5.88	31.53	1.214	3.47	0.513	3.31	0.48
Cpx		N4	xb_32	592.156	Coarse	rim	0.587	3.68	0.898	6.33	2.88	0.721	4.25	0.755	5.52	29.4	1.142	3.24	0.467	3.16	0.443
Cpx		N5	xb_33	592.154	Coarse	core	0.561	3.37	0.811	5.81	2.713	0.73	4.21	0.767	5.44	28.9	1.154	3.18	0.464	3.03	0.429

360_65R5_117

360_65R5_63B

360_65R5_63A

Mineral	Area	Point	Depth (mbsf)	Layer type	Grain area	La	Ce	Pr	Nd	Sm	Eu	Gd	Tb	Dy	Y	Ho	Er	Tm	Yb	Lu
Cpx	N5	xb_34	592.154	Coarse	rim	0.558	3.33	0.821	5.83	2.69	0.766	4.28	0.78	5.63	29.79	1.161	3.28	0.464	3.1	0.436
BIR	Average (N = 42)					0.58	1.74	0.34	2.22	1.02	0.49	1.43	0.31	2.30	1.56	0.50	1.47	0.22	1.56	0.22
	2SD					0.04	0.16	0.02	0.16	0.11	0.04	0.34	0.04	0.34	0.16	0.08	0.21	0.04	0.16	0.04
	Preferred values ("GeoRem" Jochum et al., 2007)					0.609	1.89	0.37	2.37	1.09	0.517	1.85	0.35	2.55	14.3	0.56	1.7	0.24	1.64	0.25

Appendix 2

Multi-stage development of a magma reservoir at a slow-spreading center (CHAPTER 4)

- **Appendix 2.1**: minerals *in situ* analyses for major elements of olivine (16p), plagioclase (25p) and clinopyroxene (14p - *Table S1*), from ODP Hole 735B (~250 - 550 mbsf).
  55 PAGES

- **Appendix 2.2**: minerals *in situ* analyses for Rare Earth Elements of olivine (5p), plagioclase (7p) and clinopyroxene (6p - *Table S2*) , from ODP Hole 735B (~250 - 550 mbsf).
  18 PAGES

- **Appendix 2.3**: parameters for the fractional crystallization models (MELTS) of (A) the average primitive MORB composition for the Atlantis Bank area, (B) the hybrid melt resulting from assimilation of a troctolitic matrix and crystallization of clinopyroxene. (C) normalization REE values used in this study. (*Table S3*)
  1 PAGE

- **Appendix 2.4**: Parameters of the Assimilation-Fractional Crystallization models (*DePaolo, 1981*) described in the study of the Lower and Upper unit of the igneous reservoir (*Table S4*).
  2 PAGES

Appendix 2.1

In situ major elements concentrations in wt% analyzed by EPMA on a Cameca SX100 at LMV (Clermont-Ferrand, France)

Mineral	Sample	Point	Depth (mbsf)	Grain area	Lithology	SiO2	Al2O3	TiO2	CaO	MnO	MgO	FeO	Cr2O3	NiO	Total
					2 sigma	0.425	0.065	0.055	0.029	0.061	0.445	0.355	0.087	0.054	
Ol		Counting time (s) - per element				10	10	10	10	10	10	10	20	20	
Ol		115 / 1 .	284.353	core	Ol-gabbro	37.07	0.01	0.03	0.04	0.46	31.98	30.15	0.03	0.11	99.9
Ol		116 / 1 .	284.353	core	Ol-gabbro	37.08	0.05	0.00	0.03	0.48	32.29	30.30	0.02	0.12	100.4
Ol		117 / 1 .	284.353	core	Ol-gabbro	36.76	0.04	0.04	0.05	0.41	31.44	30.28	0.00	0.05	99.1
Ol	735B_58R3_108A	119 / 1 .	284.353	core	Ol-gabbro	37.02	0.00	0.01	0.06	0.52	31.94	30.87	0.00	0.05	100.5
Ol		120 / 1 .	284.353	core	Ol-gabbro	37.00	0.00	0.00	0.03	0.49	32.26	30.56	0.00	0.09	100.4
Ol		141 / 1 .	284.332	core	Ol-gabbro	37.14	0.06	0.01	0.01	0.46	32.56	29.32	0.02	0.03	99.6
Ol		142 / 1 .	284.332	core	Ol-gabbro	37.32	0.00	0.00	0.04	0.47	32.97	29.46	0.00	0.03	100.3
Ol		144 / 1 .	284.332	core	Ol-gabbro	37.23	0.01	0.00	0.07	0.50	32.87	29.18	0.00	0.06	99.9
Ol		80 / 1 .	295.3855	core	Ol-gabbro	37.91	0.01	0.03	0.03	0.41	35.77	25.44	0.00	0.11	99.7
Ol		82 / 1 .	295.3855	core	Ol-gabbro	38.05	0.00	0.00	0.05	0.43	35.50	25.92	0.00	0.05	100.0
Ol	735B_60R4_115B	96 / 1 .	295.3975	core	Ol-gabbro	38.51	0.01	0.04	0.05	0.33	36.90	24.68	0.00	0.07	100.6
Ol		3 / 1 .	295.3875	core	Ol-gabbro	38.12	0.00	0.00	0.06	0.37	36.29	25.36	0.07	0.06	100.3
Ol		20 / 1 .	295.388	core	Ol-gabbro	37.82	0.02	0.04	0.04	0.41	35.57	26.34	0.00	0.04	100.3
Ol		32 / 1 .	295.386	core	Ol-gabbro	38.06	0.00	0.01	0.09	0.42	35.39	26.17	0.01	0.13	100.3
Ol		1 / 1 .	336.5455	core	Ol-gabbro	38.47	0.00	0.05	0.04	0.35	38.67	22.25	0.03	0.14	100.0
Ol		3 / 1 .	336.5455	core	Ol-gabbro	39.00	0.01	0.02	0.08	0.32	38.63	21.77	0.00	0.06	99.9
Ol		7 / 1 .	336.5455	core	Ol-gabbro	38.62	0.05	0.00	0.11	0.31	38.52	21.80	0.01	0.12	99.5
Ol		14 / 1 .	336.5435	core	Ol-gabbro	38.54	0.04	0.06	0.07	0.36	38.28	21.88	0.03	0.07	99.3
Ol		20 / 1 .	336.5415	core	Ol-gabbro	38.62	0.02	0.02	0.03	0.36	38.51	21.70	0.00	0.12	99.4
Ol		23 / 1 .	336.5415	core	Ol-gabbro	38.72	0.00	0.00	0.03	0.34	38.59	22.13	0.00	0.13	99.9
Ol	735B_68R2_10.5A	25 / 1 .	336.5415	core	Ol-gabbro	38.98	0.00	0.00	0.02	0.43	38.69	21.94	0.03	0.12	100.2
Ol		30 / 1 .	336.535	core	Ol-gabbro	38.22	0.00	0.00	0.02	0.37	37.36	23.95	0.00	0.09	100.0
Ol		47 / 1 .	336.537	core	Ol-gabbro	38.39	0.03	0.03	0.03	0.30	38.17	22.24	0.00	0.01	99.2
Ol		51 / 1 .	336.547	core	Ol-gabbro	39.06	0.00	0.02	0.04	0.31	38.61	21.96	0.04	0.10	100.1
Ol		52 / 1 .	336.547	core	Ol-gabbro	39.01	0.01	0.03	0.07	0.37	38.88	21.76	0.02	0.04	100.2
Ol		54 / 1 .	336.547	core	Ol-gabbro	38.75	0.00	0.00	0.06	0.30	38.97	21.98	0.02	0.09	100.2
Ol		67 / 1 .	336.535	core	Ol-gabbro	38.60	0.02	0.00	0.02	0.34	37.85	22.96	0.02	0.10	99.9
Ol		3 / 1 .	371.1235	core	Ol-gabbro	38.82	0.00	0.00	0.03	0.26	39.42	21.09	0.02	0.15	99.8
Ol		5 / 1 .	371.1235	core	Ol-gabbro	38.59	0.00	0.00	0.04	0.25	39.67	20.89	0.00	0.09	99.5
Ol		22 / 1 .	371.132	core	Ol-gabbro	38.57	0.01	0.00	0.03	0.39	38.64	21.99	0.00	0.07	99.7
Ol	735B_73R5_9	24 / 1 .	371.132	core	Ol-gabbro	38.54	0.01	0.06	0.06	0.33	38.33	21.54	0.01	0.09	99.0
Ol		36 / 1 .	371.1345	core	Ol-gabbro	38.74	0.00	0.00	0.07	0.26	39.02	21.64	0.00	0.10	99.8
Ol		62 / 1 .	371.15	core	Ol-gabbro	38.42	0.00	0.00	0.08	0.41	38.43	22.32	0.00	0.12	99.8
Ol		63 / 1 .	371.15	core	Ol-gabbro	38.52	0.01	0.00	0.05	0.24	38.90	21.87	0.00	0.11	99.7
Ol		5 / 1 .	390.3575	core	Ol-gabbro	38.79	0.00	0.01	0.05	0.27	39.89	21.32	0.00	0.14	100.5
Ol		16 / 1 .	390.3535	core	Ol-gabbro	38.89	0.00	0.00	0.04	0.28	39.81	21.47	0.00	0.11	100.6
Ol		34 / 1 .	390.353	core	Ol-gabbro	38.57	0.00	0.02	0.03	0.32	39.12	21.85	0.00	0.09	100.0

Mineral		Point	Depth (mbsf)	Grain area	Lithology	SiO2	Al2O3	TiO2	CaO	MnO	MgO	FeO	Cr2O3	NiO	Total
Ol	735B_75R5_27	35 / 1 .	390.353	core	Ol-gabbro	38.72	0.00	0.02	0.09	0.30	39.15	21.59	0.00	0.11	100.0
Ol		50 / 1 .	390.3475	core	Ol-gabbro	38.86	0.01	0.01	0.05	0.32	39.25	21.46	0.02	0.06	100.0
Ol		52 / 1 .	390.3475	core	Ol-gabbro	38.96	0.01	0.02	0.07	0.27	39.52	21.38	0.00	0.10	100.3
Ol		59 / 1 .	390.342	core	Ol-gabbro	39.02	0.00	0.00	0.07	0.29	39.47	20.77	0.00	0.07	99.7
Ol		78 / 1 .	390.3375	core	Ol-gabbro	38.91	0.00	0.02	0.05	0.28	39.40	21.62	0.00	0.09	100.4
Ol		100 / 1 .	390.347	core	Ol-gabbro	39.06	0.01	0.03	0.02	0.30	39.85	21.06	0.01	0.09	100.4
Ol		101 / 1 .	390.347	core	Ol-gabbro	38.98	0.01	0.00	0.02	0.35	39.98	21.55	0.01	0.10	101.0
Ol	735B_69R3_52B	2 / 1 .	344.1285	core	Ol-gabbro	39.26	0.02	0.00	0.08	0.32	38.95	22.10	0.02	0.11	100.9
Ol		25 / 1 .	344.13	core	Ol-gabbro	38.75	0.02	0.02	0.07	0.35	39.01	22.46	0.00	0.05	100.7
Ol		34 / 1 .	344.136	core	Ol-gabbro	38.71	0.00	0.04	0.00	0.32	38.55	22.41	0.00	0.09	100.1
Ol		50 / 1 .	344.141	core	Ol-gabbro	38.51	0.01	0.00	0.08	0.38	37.66	23.14	0.00	0.09	99.9
Ol		51 / 1 .	344.141	core	Ol-gabbro	38.61	0.01	0.03	0.04	0.42	38.53	22.45	0.02	0.11	100.2
Ol		67 / 1 .	344.135	core	Ol-gabbro	38.85	0.03	0.00	0.00	0.34	38.39	22.00	0.00	0.10	99.7
Ol		92 / 1 .	344.127	core	Ol-gabbro	39.07	0.03	0.00	0.06	0.33	38.13	22.57	0.00	0.09	100.3
Ol	735B_58R3_108A	118 / 1 .	284.353	rim	Ol-gabbro	37.00	0.00	0.00	0.05	0.45	31.95	29.91	0.00	0.07	99.4
Ol		121 / 1 .	284.353	rim	Ol-gabbro	36.88	0.00	0.00	0.04	0.52	32.43	29.94	0.01	0.07	99.9
Ol		143 / 1 .	284.332	rim	Ol-gabbro	37.07	0.04	0.00	0.03	0.48	33.22	29.19	0.00	0.08	100.1
Ol	735B_60R4_115B	79 / 1 .	295.3855	rim	Ol-gabbro	38.22	0.00	0.00	0.03	0.41	36.15	25.97	0.01	0.04	100.8
Ol		81 / 1 .	295.3855	rim	Ol-gabbro	37.77	0.00	0.02	0.06	0.40	35.05	26.32	0.00	0.10	99.7
Ol		95 / 1 .	295.3975	rim	Ol-gabbro	38.25	0.01	0.00	0.06	0.41	36.80	24.38	0.01	0.07	100.0
Ol		1 / 1 .	295.3875	rim	Ol-gabbro	38.14	0.02	0.03	0.07	0.37	36.43	25.13	0.02	0.09	100.3
Ol		2 / 1 .	295.3875	rim	Ol-gabbro	38.10	0.00	0.00	0.01	0.43	35.95	25.46	0.00	0.09	100.0
Ol		21 / 1 .	295.388	rim	Ol-gabbro	37.86	0.02	0.00	0.05	0.36	35.63	26.19	0.00	0.06	100.2
Ol		31 / 1 .	295.386	rim	Ol-gabbro	37.95	0.00	0.03	0.02	0.40	35.35	26.18	0.00	0.14	100.1
Ol	735B_68R2_10.5A	2 / 1 .	336.5455	rim	Ol-gabbro	38.63	0.00	0.00	0.06	0.33	38.57	21.83	0.00	0.10	99.5
Ol		4 / 1 .	336.5455	rim	Ol-gabbro	38.66	0.01	0.02	0.03	0.33	38.61	21.97	0.04	0.14	99.8
Ol		5 / 1 .	336.5455	rim	Ol-gabbro	38.85	0.00	0.00	0.02	0.38	38.37	21.99	0.00	0.08	99.7
Ol		6 / 1 .	336.5455	rim	Ol-gabbro	38.62	0.02	0.00	0.02	0.35	38.32	21.96	0.00	0.10	99.4
Ol		12 / 1 .	336.5435	rim	Ol-gabbro	38.42	0.02	0.04	0.01	0.31	38.69	21.87	0.00	0.08	99.4
Ol		13 / 1 .	336.5435	rim	Ol-gabbro	38.56	0.01	0.00	0.05	0.29	38.30	21.70	0.00	0.09	99.0
Ol		21 / 1 .	336.5415	rim	Ol-gabbro	38.89	0.00	0.00	0.04	0.28	38.91	21.14	0.00	0.11	99.4
Ol		22 / 1 .	336.5415	rim	Ol-gabbro	38.90	0.00	0.02	0.03	0.34	38.20	21.64	0.00	0.11	99.3
Ol		24 / 1 .	336.5415	rim	Ol-gabbro	38.66	0.02	0.00	0.02	0.30	38.87	21.77	0.01	0.11	99.8
Ol		48 / 1 .	336.537	rim	Ol-gabbro	38.79	0.00	0.03	0.04	0.38	37.89	22.41	0.01	0.13	99.7
Ol		50 / 1 .	336.547	rim	Ol-gabbro	38.75	0.04	0.04	0.02	0.34	38.54	21.88	0.00	0.09	99.7
Ol		53 / 1 .	336.547	rim	Ol-gabbro	39.08	0.01	0.01	0.03	0.43	38.85	21.63	0.00	0.10	100.1
Ol		68 / 1 .	336.535	rim	Ol-gabbro	38.92	0.02	0.02	0.04	0.29	38.03	22.12	0.00	0.10	99.5
Ol		2 / 1 .	371.1235	rim	Ol-gabbro	39.06	0.01	0.00	0.03	0.29	39.78	19.95	0.01	0.15	99.3
Ol		4 / 1 .	371.1235	rim	Ol-gabbro	38.71	0.02	0.02	0.06	0.31	39.09	21.73	0.04	0.08	100.1
Ol		6 / 1 .	371.1235	rim	Ol-gabbro	38.49	0.00	0.00	0.05	0.29	39.74	21.34	0.00	0.12	100.0

Mineral		Point	Depth (mbsf)	Grain area	Lithology	SiO2	Al2O3	TiO2	CaO	MnO	MgO	FeO	Cr2O3	NiO	Total
Ol	735B_73R5_9	23 / 1 .	371.132	rim	Ol-gabbro	38.70	0.00	0.00	0.06	0.36	39.12	21.41	0.00	0.11	99.8
Ol		37 / 1 .	371.1345	rim	Ol-gabbro	39.01	0.01	0.02	0.06	0.35	38.94	21.90	0.01	0.10	100.4
Ol		40 / 1 .	371.1345	rim	Ol-gabbro	38.44	0.01	0.00	0.06	0.38	38.88	21.48	0.02	0.13	99.4
Ol		64 / 1 .	371.15	rim	Ol-gabbro	38.59	0.02	0.00	0.07	0.33	39.20	21.84	0.00	0.17	100.2
Ol	735B_75R5_27	6 / 1 .	390.3575	rim	Ol-gabbro	39.30	0.00	0.05	0.03	0.30	39.68	21.17	0.01	0.09	100.6
Ol		7 / 1 .	390.3575	rim	Ol-gabbro	39.10	0.02	0.00	0.04	0.28	39.62	21.16	0.00	0.11	100.3
Ol		17 / 1 .	390.3535	rim	Ol-gabbro	39.22	0.02	0.00	0.04	0.26	39.66	21.03	0.00	0.06	100.3
Ol		51 / 1 .	390.3475	rim	Ol-gabbro	38.85	0.01	0.01	0.07	0.34	39.55	21.45	0.01	0.10	100.4
Ol		60 / 1 .	390.342	rim	Ol-gabbro	38.68	0.01	0.04	0.03	0.29	39.82	20.51	0.00	0.10	99.5
Ol		61 / 1 .	390.342	rim	Ol-gabbro	39.34	0.00	0.06	0.00	0.29	40.29	20.63	0.04	0.10	100.8
Ol		62 / 1 .	390.342	rim	Ol-gabbro	38.56	0.00	0.00	0.02	0.33	39.70	20.90	0.05	0.15	99.7
Ol		77 / 1 .	390.3375	rim	Ol-gabbro	39.06	0.00	0.03	0.05	0.24	39.59	21.40	0.00	0.08	100.4
Ol		99 / 1 .	390.347	rim	Ol-gabbro	38.91	0.01	0.00	0.04	0.23	39.53	21.58	0.05	0.05	100.4
Ol	735B_69R3_52B	1 / 1 .	344.1285	rim	Ol-gabbro	38.87	0.00	0.00	0.05	0.32	38.47	22.38	0.03	0.10	100.2
Ol		26 / 1 .	344.13	rim	Ol-gabbro	38.97	0.00	0.01	0.00	0.37	39.03	22.13	0.00	0.10	100.6
Ol		27 / 1 .	344.13	rim	Ol-gabbro	38.73	0.00	0.00	0.03	0.33	38.57	22.55	0.00	0.11	100.3
Ol		33 / 1 .	344.136	rim	Ol-gabbro	38.62	0.02	0.02	0.07	0.28	38.52	22.00	0.01	0.11	99.7
Ol		52 / 1 .	344.141	rim	Ol-gabbro	39.07	0.00	0.00	0.06	0.32	38.25	22.63	0.00	0.11	100.5
Ol		65 / 1 .	344.135	rim	Ol-gabbro	39.05	0.02	0.05	0.06	0.31	38.79	22.51	0.04	0.12	100.9
Ol		66 / 1 .	344.135	rim	Ol-gabbro	38.74	0.01	0.04	0.03	0.24	38.18	22.42	0.00	0.11	99.8
Ol		91 / 1 .	344.127	rim	Ol-gabbro	38.85	0.00	0.00	0.03	0.32	38.40	22.78	0.00	0.16	100.5
Ol	735B_80R1_136	86 / 1 .	425.363	core	Ol-gabbro	33.40	0.02	0.04	0.03	0.82	15.84	49.81	0.00	0.02	100.0
Ol		102 / 1 .	425.3695	core	Ol-gabbro	33.54	0.02	0.06	0.02	0.74	18.77	46.71	0.00	0.00	99.9
Ol		107 / 1 .	425.372	core	Ol-gabbro	34.49	0.01	0.01	0.07	0.73	21.99	42.01	0.02	0.06	99.4
Ol		118 / 1 .	425.3735	core	Ol-gabbro	37.36	0.00	0.00	0.05	0.45	33.88	27.67	0.01	0.06	99.5
Ol		139 / 1 .	425.3815	core	Ol-gabbro	39.28	0.03	0.00	0.09	0.24	42.00	18.22	0.00	0.09	100.0
Ol		165 / 1 .	425.3865	core	Ol-gabbro	39.19	0.00	0.00	0.06	0.32	41.85	18.37	0.02	0.14	100.0
Ol	735B_81R5_7	21 / 1 .	439.2465	core	Ol-gabbro	38.37	0.00	0.00	0.03	0.30	37.87	23.37	0.00	0.11	100.0
Ol		22 / 1 .	439.2465	core	Ol-gabbro	38.63	0.00	0.03	0.05	0.34	37.65	22.96	0.02	0.08	99.8
Ol		37 / 1 .	439.2515	core	Ol-gabbro	38.50	0.00	0.03	0.08	0.30	38.93	21.63	0.00	0.13	99.6
Ol		39 / 1 .	439.2515	core	Ol-gabbro	38.71	0.00	0.07	0.02	0.35	38.66	21.66	0.02	0.06	99.5
Ol		67 / 1 .	439.257	core	Ol-gabbro	38.64	0.02	0.00	0.09	0.29	38.94	21.32	0.00	0.14	99.4
Ol		68 / 1 .	439.258	core	Ol-gabbro	39.10	0.00	0.00	0.07	0.33	39.44	21.20	0.00	0.06	100.2
Ol		69 / 1 .	439.258	core	Ol-gabbro	38.79	0.00	0.02	0.07	0.31	39.25	21.15	0.00	0.13	99.7
Ol	735B_79R3_100	2 / 1 .	418.5075	core	Ol-gabbro	39.57	0.04	0.00	0.02	0.35	40.24	20.08	0.00	0.18	100.5
Ol		5 / 1 .	418.5075	core	Ol-gabbro	39.17	0.04	0.00	0.08	0.28	40.15	19.94	0.02	0.09	99.8
Ol		17 / 1 .	418.5085	core	Ol-gabbro	38.61	0.01	0.00	0.01	0.29	38.64	22.10	0.03	0.15	99.8
Ol		18 / 1 .	418.503	core	Ol-gabbro	38.43	0.02	0.01	0.06	0.30	38.40	22.22	0.02	0.15	99.6
Ol		19 / 1 .	418.503	core	Ol-gabbro	38.67	0.01	0.00	0.05	0.32	38.56	22.31	0.02	0.11	100.0
Ol		33 / 1 .	418.506	core	Ol-gabbro	38.63	0.00	0.00	0.01	0.29	39.68	21.45	0.00	0.13	100.2

Mineral		Point	Depth (mbsf)	Grain area	Lithology	SiO2	Al2O3	TiO2	CaO	MnO	MgO	FeO	Cr2O3	NiO	Total
Ol		61 / 1 .	418.5265	core	Ol-gabbro	38.89	0.00	0.00	0.08	0.30	39.99	20.94	0.04	0.12	100.4
Ol		63 / 1 .	418.5265	core	Ol-gabbro	38.57	0.02	0.04	0.08	0.28	39.06	21.10	0.01	0.10	99.3
Ol		67 / 1 .	418.5265	core	Ol-gabbro	38.98	0.00		0.07		40.20	20.74			100.0
Ol		44 / 1 .	397.581	core	Ol-gabbro	38.94	0.04	0.03	0.03	0.42	38.20	22.78	0.00	0.08	100.5
Ol		53 / 1 .	397.583	core	Ol-gabbro	38.66	0.02	0.05	0.03	0.32	38.84	22.77	0.01	0.07	100.8
Ol	735B_76R3_96	75 / 1 .	397.5851	core	Ol-gabbro	38.56	0.00	0.00	0.02	0.32	37.57	23.58	0.02	0.05	100.1
Ol		96 / 1 .	397.577	core	Ol-gabbro	38.45	0.00	0.00	0.05	0.36	38.30	23.46	0.04	0.09	100.7
Ol		98 / 1 .	397.577	core	Ol-gabbro	38.62	0.01	0.05	0.07	0.32	38.33	22.53	0.04	0.05	100.0
Ol		107 / 1 .	397.575	core	Ol-gabbro	38.34	0.00	0.00	0.02	0.33	37.97	23.16	0.01	0.05	99.9
Ol		105 / 1 .	419.1525	core	Ol-gabbro	39.16	0.02	0.00	0.00	0.31	39.89	20.72	0.00	0.10	100.2
Ol		106 / 1 .	419.1525	core	Ol-gabbro	39.48	0.01	0.00	0.06	0.22	40.07	20.25	0.01	0.15	100.3
Ol		6 / 1 .	419.159	core	Ol-gabbro	39.70	0.01	0.00	0.02	0.29	41.82	18.17	0.00	0.13	100.1
Ol		7 / 1 .	419.159	core	Ol-gabbro	39.70	0.02	0.00	0.03	0.27	42.11	18.18	0.00	0.16	100.5
Ol		9 / 1 .	419.159	core	Ol-gabbro	39.36	0.03	0.03	0.04	0.28	41.62	18.30	0.00	0.14	99.8
Ol		18 / 1 .	419.1585	core	Ol-gabbro	39.88	0.04	0.00	0.03	0.32	41.71	18.43	0.04	0.15	100.6
Ol		33 / 1 .	419.163	core	Ol-gabbro	39.61	0.00	0.08	0.03	0.29	40.83	19.46	0.02	0.18	100.5
Ol	735B_79R4_20	35 / 1 .	419.163	core	Ol-gabbro	39.49	0.00	0.00	0.09	0.28	40.87	19.00	0.00	0.16	99.9
Ol		61 / 1 .	419.172	core	Ol-gabbro	39.39	0.06	0.00	0.04	0.32	40.86	19.09	0.02	0.11	99.9
Ol		63 / 1 .	419.172	core	Ol-gabbro	39.31	0.00	0.00	0.05	0.28	41.97	18.11	0.00	0.11	99.8
Ol		64 / 1 .	419.172	core	Ol-gabbro	39.80	0.00	0.04	0.04	0.21	41.82	18.19	0.00	0.13	100.2
Ol		79 / 1 .	419.1745	core	Ol-gabbro	39.63	0.00	0.00	0.02	0.23	42.00	17.86	0.02	0.12	99.9
Ol		80 / 1 .	419.1745	core	Ol-gabbro	39.64	0.00	0.02	0.02	0.29	42.09	17.60	0.00	0.13	99.8
Ol		86 / 1 .	419.1795	core	Ol-gabbro	39.66	0.00	0.02	0.03	0.28	42.49	18.17	0.00	0.14	100.8
Ol		90 / 1 .	419.1795	core	Ol-gabbro	39.73	0.00	0.00	0.05	0.30	41.91	17.83	0.00	0.10	99.9
Ol		4 / 1 .	461.682	core	Ol-gabbro	39.61	0.00	0.00	0.02	0.32	42.70	18.10	0.00	0.16	100.9
Ol		17 / 1 .	461.6975	core	Ol-gabbro	39.71	0.03	0.02	0.03	0.35	42.02	18.38	0.00	0.17	100.7
Ol		27 / 1 .	461.7005	core	Ol-gabbro	39.90	0.00	0.02	0.04	0.26	42.10	17.86	0.00	0.11	100.3
Ol		29 / 1 .	461.7005	core	Ol-gabbro	39.85	0.02	0.00	0.05	0.22	41.75	18.39	0.02	0.19	100.5
Ol		42 / 1 .	461.6995	core	Ol-gabbro	39.84	0.03	0.00	0.08	0.33	41.46	19.09	0.00	0.12	101.0
Ol		52 / 1 .	461.7015	core	Ol-gabbro	39.58	0.00	0.01	0.05	0.27	41.67	18.29	0.01	0.12	100.0
Ol		54 / 1 .	461.7015	core	Ol-gabbro	39.95	0.01	0.02	0.05	0.33	41.71	18.42	0.00	0.17	100.7
Ol	735B_83R7_43B	56 / 1 .	461.7015	core	Ol-gabbro	39.42	0.00	0.00	0.01	0.27	41.82	18.69	0.02	0.16	100.4
Ol		60 / 1 .	461.6925	core	Ol-gabbro	39.71	0.02	0.00	0.03	0.32	41.80	18.10	0.02	0.17	100.2
Ol		62 / 1 .	461.6925	core	Ol-gabbro	39.54	0.00	0.02	0.07	0.27	42.15	18.41	0.00	0.19	100.7
Ol		73 / 1 .	461.6905	core	Ol-gabbro	39.65	0.00	0.00	0.05	0.27	42.07	18.36	0.02	0.15	100.6
Ol		74 / 1 .	461.6875	core	Ol-gabbro	39.91	0.02	0.00	0.03	0.28	42.43	17.90	0.04	0.13	100.8
Ol		92 / 1 .	461.6905	core	Ol-gabbro	39.54	0.04	0.02	0.00	0.29	41.52	18.60	0.03	0.13	100.2
Ol		100 / 1 .	461.6885	core	Ol-gabbro	39.10	0.00	0.00	0.07	0.25	41.28	18.45	0.01	0.15	99.3
Ol		101 / 1 .	461.6885	core	Ol-gabbro	39.58	0.01	0.01	0.04	0.26	42.29	18.05	0.00	0.16	100.4
Ol		1 / 1 .	425.9865	core	Ol-gabbro	39.46	0.03	0.07	0.06	0.27	42.42	17.73	0.01	0.10	100.1

Mineral		Point	Depth (mbsf)	Grain area	Lithology	SiO2	Al2O3	TiO2	CaO	MnO	MgO	FeO	Cr2O3	NiO	Total
Ol		3 / 1 .	425.9865	core	Ol-gabbro	39.88	0.01	0.00	0.04	0.27	41.79	17.51	0.00	0.12	99.6
Ol		5 / 1 .	425.9865	core	Ol-gabbro	39.82	0.01	0.00	0.05	0.30	41.80	17.58	0.00	0.16	99.7
Ol		15 / 1 .	425.9915	core	Ol-gabbro	39.69	0.01	0.01	0.04	0.26	41.41	17.79	0.01	0.14	99.4
Ol		17 / 1 .	425.9915	core	Ol-gabbro	39.77	0.02	0.02	0.06	0.30	41.57	18.22	0.00	0.14	100.1
Ol		19 / 1 .	425.9915	core	Ol-gabbro	39.79	0.00	0.01	0.03	0.33	41.94	17.90	0.00	0.12	100.1
Ol		20 / 1 .	425.9915	core	Ol-gabbro	39.66	0.01	0.00	0.03	0.28	42.20	18.18	0.01	0.13	100.5
Ol		21 / 1 .	425.9915	core	Ol-gabbro	39.50	0.01	0.00	0.01	0.27	41.41	17.94	0.00	0.13	99.3
Ol	735B_80R2_51	37 / 1 .	425.9985	core	Ol-gabbro	39.52	0.00	0.00	0.05	0.40	41.94	18.67	0.00	0.14	100.7
Ol		39 / 1 .	425.9985	core	Ol-gabbro	39.60	0.01	0.00	0.04	0.25	41.13	18.14	0.00	0.17	99.3
Ol		40 / 1 .	425.9985	core	Ol-gabbro	39.70	0.03	0.07	0.02	0.34	41.32	18.55	0.00	0.16	100.2
Ol		55 / 1 .	425.9935	core	Ol-gabbro	39.27	0.00	0.00	0.01	0.26	40.91	19.31	0.00	0.17	99.9
Ol		56 / 1 .	425.9935	core	Ol-gabbro	39.20	0.01	0.01	0.04	0.32	40.80	18.90	0.01	0.16	99.4
Ol		58 / 1 .	425.9935	core	Ol-gabbro	39.30	0.00	0.02	0.04	0.30	39.80	20.50	0.00	0.16	100.1
Ol		59 / 1 .	425.9935	core	Ol-gabbro	39.26	0.04	0.01	0.02	0.32	40.67	19.35	0.00	0.15	99.8
Ol		74 / 1 .	425.996	core	Ol-gabbro	39.61	0.00	0.02	0.03	0.31	40.90	18.76	0.00	0.11	99.7
Ol		75 / 1 .	425.996	core	Ol-gabbro	39.56	0.00	0.01	0.03	0.25	41.01	18.63	0.04	0.15	99.7
Ol		82 / 1 .	426.002	core	Ol-gabbro	39.38	0.00	0.03	0.04	0.24	41.81	18.15	0.00	0.14	99.8
Ol		85 / 1 .	426.002	core	Ol-gabbro	39.46	0.02	0.00	0.03	0.35	41.43	18.56	0.02	0.15	100.0
Ol		86 / 1 .	426.002	core	Ol-gabbro	39.56	0.03	0.04	0.03	0.31	41.31	18.00	0.00	0.20	99.5
Ol		5	509.49	core	Ol-gabbro	38.90	0.00	0.02	0.05	0.30	42.39	17.51	0.00	0.13	99.3
Ol		15	509.49	core	Ol-gabbro	39.12	0.00	0.02	0.06	0.31	42.51	17.94	0.00	0.13	100.1
Ol		19	509.49	core	Ol-gabbro	39.17	0.00	0.02	0.04	0.25	41.93	17.60	0.00	0.14	99.1
Ol		28	509.49	core	Ol-gabbro	39.16	0.00	0.00	0.04	0.30	42.61	17.82	0.01	0.13	100.1
Ol		38	509.49	core	Ol-gabbro	38.93	0.00	0.02	0.04	0.31	42.29	18.18	0.01	0.17	99.9
Ol	90R-2W-18-20	44	509.49	core	Ol-gabbro	38.91	0.01	0.00	0.04	0.29	41.93	18.45	0.00	0.14	99.8
Ol		45	509.49	core	Ol-gabbro	39.01	0.01	0.00	0.05	0.28	42.58	17.97	0.00	0.16	100.0
Ol		57	509.49	core	Ol-gabbro	39.11	0.00	0.00	0.05	0.30	42.58	17.46	0.02	0.11	99.6
Ol		61	509.49	core	Ol-gabbro	39.06	0.02	0.00	0.05	0.31	42.51	17.46	0.00	0.11	99.5
Ol		67	509.49	core	Ol-gabbro	39.11	0.02	0.00	0.04	0.30	42.48	17.51	0.00	0.15	99.6
Ol		50	510.1	core	Ol-gabbro	39.60	0.00	0.03	0.06	0.27	44.11	15.39	0.02	0.15	99.6
Ol		51	510.1	core	Ol-gabbro	39.67	0.01	0.04	0.05	0.26	44.32	15.23	0.00	0.14	99.7
Ol		80	510.1	core	Ol-gabbro	39.33	0.03	0.01	0.05	0.26	43.19	16.30	0.00	0.13	99.3
Ol		82	510.1	core	Ol-gabbro	39.22	0.02	0.00	0.04	0.25	43.03	16.46	0.03	0.16	99.2
Ol	90R-2W-82-86	93	510.1	core	Ol-gabbro	39.69	0.00	0.01	0.05	0.27	43.20	16.14	0.02	0.15	99.5
Ol		98	510.1	core	Ol-gabbro	39.06	0.03	0.03	0.04	0.31	42.70	17.25	0.01	0.17	99.6
Ol		115	510.1	core	Ol-gabbro	39.37	0.01	0.03	0.05	0.28	42.90	16.40	0.02	0.14	99.2
Ol		123	510.1	core	Ol-gabbro	38.98	0.00	0.01	0.05	0.30	42.50	17.21	0.00	0.14	99.2
Ol		177	510.17	core	Ol-gabbro	39.68	0.00	0.00	0.05	0.28	42.94	16.55	0.00	0.13	99.6
Ol		178	510.17	core	Ol-gabbro	39.59	0.03	0.01	0.06	0.32	43.23	16.57	0.02	0.13	100.0
Ol	90R-2W-84-90	209	510.17	core	Ol-gabbro	39.47	0.01	0.00	0.05	0.27	42.86	17.01	0.02	0.14	99.8

Mineral	90R-2W-84-90	Point	Depth (mbsf)	Grain area	Lithology	SiO2	Al2O3	TiO2	CaO	MnO	MgO	FeO	Cr2O3	NiO	Total
Ol		215	510.17	core	Ol-gabbro	39.17	0.00	0.01	0.06	0.25	42.10	17.11	0.00	0.16	98.9
Ol		5	510.27	core	Ol-gabbro	39.32	0.01	0.00	0.04	0.25	44.40	14.84	0.01	0.18	99.1
Ol		24	510.27	core	Ol-gabbro	39.55	0.03	0.02	0.05	0.27	43.51	16.09	0.02	0.16	99.7
Ol		27	510.27	core	Ol-gabbro	39.53	0.01	0.00	0.04	0.23	44.10	15.26	0.00	0.17	99.3
Ol	90R-2W-94-100b	42	510.27	core	Ol-gabbro	39.62	0.01	0.03	0.05	0.24	44.61	15.04	0.00	0.16	99.8
Ol		51	510.27	core	Ol-gabbro	39.56	0.00	0.01	0.05	0.21	44.24	15.21	0.01	0.18	99.5
Ol		60	510.27	core	Ol-gabbro	39.66	0.01	0.01	0.03	0.23	44.46	14.99	0.00	0.18	99.6
Ol		1	510.27	core	Ol-gabbro	39.22	0.00	0.02	0.05	0.26	44.66	14.96	0.00	0.15	99.3
Ol		82	510.56	core	Ol-gabbro	39.33	0.02	0.00	0.05	0.23	43.43	16.00	0.02	0.16	99.2
Ol		97	510.56	core	Ol-gabbro	39.93	0.02	0.00	0.03	0.24	43.84	15.52	0.02	0.18	99.8
Ol		98	510.56	core	Ol-gabbro	39.51	0.01	0.02	0.03	0.25	43.91	15.60	0.00	0.13	99.5
Ol	90R-2W-123-129	105	510.56	core	Ol-gabbro	39.67	0.00	0.03	0.04	0.28	43.76	15.78	0.05	0.15	99.7
Ol		116	510.56	core	Ol-gabbro	39.48	0.01	0.01	0.04	0.28	43.19	16.44	0.00	0.16	99.6
Ol		123	510.56	core	Ol-gabbro	39.39	0.01	0.01	0.05	0.25	42.98	16.48	0.00	0.16	99.3
Ol		124	510.56	core	Ol-gabbro	39.50	0.00	0.00	0.05	0.28	43.23	16.43	0.00	0.18	99.7
Ol		133	510.56	core	Ol-gabbro	39.58	0.02	0.01	0.03	0.26	44.06	15.70	0.01	0.15	99.8
Ol		136	510.67	core	Ol-gabbro	39.11	0.02	0.03	0.03	0.26	44.00	15.72	0.01	0.15	99.3
Ol	90R-2W-135-139	144	510.67	core	Ol-gabbro	39.65	0.01	0.02	0.05	0.25	44.16	15.32	0.00	0.16	99.6
Ol		145	510.67	core	Ol-gabbro	39.66	0.00	0.02	0.05	0.25	43.94	15.21	0.01	0.13	99.3
Ol		10	510.84	core	Ol-gabbro	39.44	0.00	0.00	0.07	0.26	44.25	15.49	0.01	0.18	99.7
Ol		23	510.84	core	Ol-gabbro	39.30	0.02	0.00	0.05	0.28	43.40	16.46	0.00	0.18	99.7
Ol		27	510.84	core	Ol-gabbro	39.35	0.02	0.03	0.04	0.25	43.96	15.95	0.00	0.17	99.8
Ol		31	510.84	core	Ol-gabbro	39.59	0.02	0.01	0.01	0.24	44.06	15.52	0.00	0.16	99.6
Ol		39	510.84	core	Ol-gabbro	39.35	0.03	0.00	0.03	0.24	43.81	15.21	0.02	0.16	98.8
Ol	90R-3W-6-8	40	510.84	core	Ol-gabbro	39.57	0.01	0.01	0.04	0.26	44.71	15.39	0.02	0.13	100.2
Ol		41	510.84	core	Ol-gabbro	39.72	0.02	0.02	0.05	0.26	44.51	15.08	0.00	0.13	99.8
Ol		45	510.84	core	Ol-gabbro	39.57	0.02	0.03	0.03	0.29	44.45	14.78	0.01	0.16	99.3
Ol		59	510.84	core	Ol-gabbro	39.75	0.02	0.00	0.05	0.29	44.74	14.91	0.03	0.18	100.0
Ol		74	510.84	core	Ol-gabbro	39.41	0.00	0.04	0.05	0.25	44.01	15.31	0.00	0.15	99.2
Ol		106 / 1 .	425.372	rim	Ol-gabbro	34.66	0.00	0.01	0.10	0.72	21.67	43.10	0.00	0.04	100.3
Ol		108 / 1 .	425.372	rim	Ol-gabbro	34.07	0.01	0.01	0.07	0.73	20.43	44.05	0.00	0.03	99.4
Ol		119 / 1 .	425.3735	rim	Ol-gabbro	37.40	0.02	0.00	0.04	0.45	33.76	28.01	0.03	0.08	99.8
Ol	735B_80R1_136	125 / 1 .	425.3795	rim	Ol-gabbro	38.26	0.01	0.01	0.08	0.45	37.06	24.19	0.00	0.06	100.1
Ol		126 / 1 .	425.3795	rim	Ol-gabbro	38.76	0.01	0.00	0.08	0.33	40.05	20.19	0.00	0.11	99.5
Ol		138 / 1 .	425.3815	rim	Ol-gabbro	39.48	0.03	0.02	0.06	0.36	41.41	18.42	0.02	0.08	99.9
Ol		166 / 1 .	425.3865	rim	Ol-gabbro	39.30	0.01	0.00	0.01	0.27	41.37	17.97	0.01	0.14	99.1
Ol		167 / 1 .	425.3865	rim	Ol-gabbro	39.17	0.00	0.00	0.04	0.33	41.59	18.57	0.02	0.15	99.9
Ol		20 / 1 .	439.2465	rim	Ol-gabbro	38.42	0.00	0.02	0.05	0.36	38.09	23.24	0.02	0.08	100.3
Ol		23 / 1 .	439.2465	rim	Ol-gabbro	38.85	0.00	0.04	0.08	0.37	37.46	22.97	0.01	0.12	99.9
Ol		38 / 1 .	439.2515	rim	Ol-gabbro	38.66	0.02	0.00	0.03	0.27	38.97	21.34	0.00	0.14	99.4

Mineral	735B_81R5_7	Point	Depth (mbsf)	Grain area	Lithology	SiO2	Al2O3	TiO2	CaO	MnO	MgO	FeO	Cr2O3	NiO	Total
Ol		40 / 1 .	439.2515	rim	Ol-gabbro	38.52	0.02	0.01	0.06	0.31	39.65	21.31	0.01	0.11	100.0
Ol		66 / 1 .	439.257	rim	Ol-gabbro	38.79	0.00	0.00	0.03	0.32	39.00	21.02	0.00	0.10	99.3
Ol		70 / 1 .	439.258	rim	Ol-gabbro	38.67	0.00	0.01	0.01	0.31	39.57	20.80	0.00	0.10	99.5
Ol	735B_79R3_100	3 / 1 .	418.5075	rim	Ol-gabbro	39.10	0.01	0.00	0.05	0.22	40.00	20.05	0.03	0.12	99.6
Ol		4 / 1 .	418.5075	rim	Ol-gabbro	39.34	0.00	0.00	0.08	0.30	40.61	20.03	0.00	0.18	100.5
Ol		60 / 1 .	418.5255	rim	Ol-gabbro	38.85	0.00	0.01	0.05	0.31	39.10	20.84	0.00	0.11	99.3
Ol		62 / 1 .	418.5265	rim	Ol-gabbro	38.66	0.01	0.02	0.05	0.32	40.15	20.93	0.00	0.13	100.3
Ol		68 / 1 .	418.532	rim	Ol-gabbro	38.79	0.01	0.02	0.06	0.29	39.97	20.11	0.01	0.15	99.4
Ol		69 / 1 .	418.532	rim	Ol-gabbro	39.00	0.03	0.00	0.05	0.25	40.05	20.58	0.00	0.10	100.1
Ol	735B_76R3_96	43 / 1 .	397.581	rim	Ol-gabbro	38.47	0.00	0.01	0.03	0.36	38.24	22.88	0.01	0.07	100.1
Ol		45 / 1 .	397.581	rim	Ol-gabbro	38.83	0.03	0.00	0.05	0.32	38.54	22.42	0.01	0.07	100.3
Ol		52 / 1 .	397.583	rim	Ol-gabbro	38.49	0.00	0.01	0.07	0.35	38.43	23.11	0.01	0.05	100.5
Ol		54 / 1 .	397.583	rim	Ol-gabbro	38.62	0.00	0.00	0.04	0.37	38.06	23.00	0.03	0.12	100.2
Ol		74 / 1 .	397.5851	rim	Ol-gabbro	38.54	0.02	0.00	0.04	0.37	37.68	23.58	0.02	0.09	100.3
Ol		76 / 1 .	397.5851	rim	Ol-gabbro	38.43	0.02	0.01	0.06	0.36	37.04	24.35	0.00	0.09	100.4
Ol		84 / 1 .	397.576	rim	Ol-gabbro	38.31	0.02	0.00	0.06	0.30	37.87	22.99	0.01	0.10	99.7
Ol		95 / 1 .	397.577	rim	Ol-gabbro	38.81	0.00	0.02	0.05	0.41	38.34	23.27	0.01	0.07	101.0
Ol		97 / 1 .	397.577	rim	Ol-gabbro	38.41	0.00	0.00	0.04	0.39	37.90	23.09	0.00	0.08	99.9
Ol		106 / 1 .	397.575	rim	Ol-gabbro	38.48	0.00	0.00	0.02	0.31	37.52	23.43	0.02	0.09	99.9
Ol	735B_79R4_20	8 / 1 .	419.159	rim	Ol-gabbro	39.72	0.00	0.00	0.03	0.30	41.75	18.07	0.02	0.16	100.1
Ol		10 / 1 .	419.159	rim	Ol-gabbro	39.43	0.01	0.00	0.03	0.29	41.55	18.47	0.00	0.16	99.9
Ol		19 / 1 .	419.1585	rim	Ol-gabbro	39.52	0.00	0.00	0.01	0.29	41.01	18.80	0.04	0.16	99.8
Ol		20 / 1 .	419.1585	rim	Ol-gabbro	39.87	0.02	0.00	0.05	0.22	41.99	18.23	0.02	0.13	100.5
Ol		34 / 1 .	419.163	rim	Ol-gabbro	39.31	0.00	0.00	0.03	0.35	40.36	19.64	0.03	0.15	99.9
Ol		36 / 1 .	419.163	rim	Ol-gabbro	39.42	0.01	0.05	0.00	0.30	41.24	19.45	0.00	0.12	100.6
Ol		62 / 1 .	419.172	rim	Ol-gabbro	39.17	0.01	0.00	0.04	0.31	40.89	18.94	0.01	0.13	99.5
Ol		65 / 1 .	419.172	rim	Ol-gabbro	39.63	0.02	0.03	0.02	0.24	41.69	18.29	0.00	0.13	100.1
Ol		87 / 1 .	419.1795	rim	Ol-gabbro	39.91	0.02	0.00	0.04	0.27	42.22	17.74	0.01	0.12	100.3
Ol		89 / 1 .	419.1795	rim	Ol-gabbro	39.74	0.02	0.03	0.01	0.16	42.44	18.31	0.00	0.13	100.8
Ol	735B_83R7_43B	5 / 1 .	461.682	rim	Ol-gabbro	39.49	0.04	0.00	0.03	0.23	41.88	18.00	0.00	0.15	99.8
Ol		6 / 1 .	461.682	rim	Ol-gabbro	39.71	0.04	0.01	0.04	0.24	42.24	18.48	0.04	0.16	100.9
Ol		28 / 1 .	461.7005	rim	Ol-gabbro	39.72	0.01	0.07	0.00	0.22	42.06	18.30	0.00	0.14	100.5
Ol		30 / 1 .	461.7005	rim	Ol-gabbro	39.73	0.01	0.01	0.04	0.25	41.76	18.62	0.00	0.19	100.6
Ol		31 / 1 .	461.7005	rim	Ol-gabbro	39.60	0.00	0.02	0.06	0.26	42.01	18.13	0.01	0.18	100.3
Ol		33 / 1 .	461.7005	rim	Ol-gabbro	39.84	0.01	0.06	0.06	0.28	42.20	17.66	0.01	0.15	100.3
Ol		43 / 1 .	461.6995	rim	Ol-gabbro	39.47	0.01	0.02	0.02	0.26	41.37	18.98	0.05	0.16	100.3
Ol		53 / 1 .	461.7015	rim	Ol-gabbro	39.53	0.00	0.00	0.02	0.28	41.77	18.42	0.02	0.14	100.2
Ol		55 / 1 .	461.7015	rim	Ol-gabbro	39.82	0.00	0.00	0.04	0.29	41.51	18.68	0.01	0.16	100.5
Ol		61 / 1 .	461.6925	rim	Ol-gabbro	39.74	0.02	0.06	0.00	0.27	41.49	18.19	0.00	0.19	100.0
Ol		63 / 1 .	461.6925	rim	Ol-gabbro	39.38	0.00	0.00	0.01	0.30	41.56	18.30	0.01	0.15	99.7

Mineral		Point	Depth (mbsf)	Grain area	Lithology	SiO2	Al2O3	TiO2	CaO	MnO	MgO	FeO	Cr2O3	NiO	Total
Ol		75 / 1 .	461.6875	rim	Ol-gabbro	40.01	0.00	0.00	0.00	0.24	42.32	17.69	0.03	0.14	100.4
Ol		91 / 1 .	461.6905	rim	Ol-gabbro	39.43	0.01	0.00	0.02	0.28	41.29	18.92	0.00	0.15	100.1
Ol		93 / 1 .	461.6905	rim	Ol-gabbro	39.33	0.01	0.00	0.04	0.34	41.02	18.81	0.01	0.12	99.7
Ol		102 / 1 .	461.6885	rim	Ol-gabbro	39.63	0.02	0.00	0.08	0.28	41.56	18.19	0.01	0.12	99.9
Ol		103 / 1 .	461.6885	rim	Ol-gabbro	39.51	0.00	0.00	0.02	0.33	41.53	19.33	0.00	0.16	100.9
Ol		104 / 1 .	461.6885	rim	Ol-gabbro	39.73	0.00	0.03	0.08	0.26	41.60	18.48	0.00	0.17	100.4
Ol	735B_80R2_51	2 / 1 .	425.9865	rim	Ol-gabbro	39.63	0.00	0.04	0.04	0.31	42.02	17.44	0.00	0.14	99.6
Ol		4 / 1 .	425.9865	rim	Ol-gabbro	39.63	0.01	0.04	0.02	0.28	41.74	17.41	0.00	0.13	99.3
Ol		6 / 1 .	425.9865	rim	Ol-gabbro	39.62	0.00	0.00	0.04	0.28	42.49	17.76	0.01	0.14	100.3
Ol		16 / 1 .	425.9915	rim	Ol-gabbro	39.50	0.01	0.00	0.01	0.29	42.07	18.37	0.00	0.13	100.4
Ol		18 / 1 .	425.9915	rim	Ol-gabbro	39.79	0.01	0.03	0.05	0.30	41.71	18.27	0.00	0.13	100.3
Ol		38 / 1 .	425.9985	rim	Ol-gabbro	39.40	0.00	0.00	0.06	0.29	41.51	18.24	0.02	0.16	99.7
Ol		41 / 1 .	425.9985	rim	Ol-gabbro	39.60	0.01	0.00	0.06	0.28	41.66	18.60	0.00	0.11	100.3
Ol		57 / 1 .	425.9935	rim	Ol-gabbro	39.24	0.00	0.00	0.07	0.34	40.85	18.42	0.00	0.14	99.1
Ol		60 / 1 .	425.9935	rim	Ol-gabbro	39.57	0.00	0.00	0.06	0.37	40.61	19.37	0.00	0.15	100.1
Ol		76 / 1 .	425.996	rim	Ol-gabbro	39.51	0.03	0.00	0.04	0.24	40.91	19.03	0.00	0.13	99.9
Ol		83 / 1 .	426.002	rim	Ol-gabbro	39.63	0.00	0.03	0.04	0.26	41.71	18.19	0.00	0.14	100.0
Ol		84 / 1 .	426.002	rim	Ol-gabbro	39.42	0.02	0.04	0.03	0.27	41.35	18.42	0.03	0.11	99.7
Ol	90R-2W-18-20	4	509.49	rim	Ol-gabbro	38.92	0.00	0.01	0.03	0.27	41.89	18.22	0.01	0.16	99.5
Ol		6	509.49	rim	Ol-gabbro	38.67	0.02	0.01	0.04	0.32	42.31	17.84	0.00	0.13	99.3
Ol		16	509.49	rim	Ol-gabbro	39.28	0.00	0.00	0.04	0.28	42.58	17.50	0.02	0.16	99.9
Ol		20	509.49	rim	Ol-gabbro	39.14	0.00	0.03	0.04	0.29	42.31	17.93	0.00	0.16	99.9
Ol		27	509.49	rim	Ol-gabbro	38.95	0.02	0.01	0.04	0.33	42.09	18.07	0.00	0.14	99.7
Ol		29	509.49	rim	Ol-gabbro	39.07	0.00	0.00	0.03	0.26	42.32	17.91	0.00	0.12	99.7
Ol		37	509.49	rim	Ol-gabbro	38.93	0.02	0.01	0.04	0.31	41.40	19.02	0.01	0.14	99.9
Ol		43	509.49	rim	Ol-gabbro	38.72	0.02	0.00	0.04	0.31	41.59	18.28	0.00	0.10	99.1
Ol		46	509.49	rim	Ol-gabbro	39.28	0.00	0.00	0.04	0.30	41.95	18.57	0.00	0.18	100.3
Ol		56	509.49	rim	Ol-gabbro	39.08	0.01	0.04	0.05	0.28	41.86	17.64	0.01	0.15	99.1
Ol		60	509.49	rim	Ol-gabbro	39.35	0.01	0.00	0.04	0.29	42.35	17.50	0.00	0.18	99.7
Ol		66	509.49	rim	Ol-gabbro	39.39	0.01	0.01	0.03	0.26	42.60	17.10	0.00	0.13	99.5
Ol	90R-2W-82-86	53	510.1	rim	Ol-gabbro	39.86	0.00	0.02	0.04	0.29	44.24	14.95	0.01	0.15	99.6
Ol		81	510.1	rim	Ol-gabbro	39.56	0.01	0.02	0.05	0.28	43.04	16.67	0.01	0.16	99.8
Ol		83	510.1	rim	Ol-gabbro	39.36	0.02	0.01	0.08	0.28	43.03	16.51	0.00	0.13	99.4
Ol		92	510.1	rim	Ol-gabbro	39.46	0.00	0.02	0.05	0.28	43.18	16.19	0.00	0.16	99.3
Ol		94	510.1	rim	Ol-gabbro	39.37	0.01	0.01	0.03	0.27	43.17	16.34	0.00	0.17	99.4
Ol		99	510.1	rim	Ol-gabbro	39.44	0.02	0.00	0.04	0.27	42.78	16.61	0.00	0.14	99.3
Ol		114	510.1	rim	Ol-gabbro	39.41	0.00	0.00	0.04	0.26	42.89	16.22	0.00	0.14	99.0
Ol		116	510.1	rim	Ol-gabbro	39.43	0.01	0.00	0.04	0.27	43.22	16.28	0.01	0.17	99.4
Ol		122	510.1	rim	Ol-gabbro	39.45	0.01	0.00	0.04	0.27	42.68	17.02	0.00	0.13	99.6
Ol		124	510.1	rim	Ol-gabbro	39.28	0.00	0.00	0.06	0.30	42.30	17.48	0.00	0.17	99.6

Mineral		Point	Depth (mbsf)	Grain area	Lithology	SiO2	Al2O3	TiO2	CaO	MnO	MgO	FeO	Cr2O3	NiO	Total
Ol		173	510.17	rim	Ol-gabbro	39.70	0.01	0.01	0.05	0.27	43.24	16.36	0.01	0.11	99.8
Ol	90R-2W-84-90	184	510.17	rim	Ol-gabbro	39.58	0.02	0.01	0.05	0.28	42.81	16.43	0.01	0.16	99.3
Ol		208	510.17	rim	Ol-gabbro	39.46	0.03	0.00	0.04	0.28	42.26	17.05	0.00	0.14	99.3
Ol		214	510.17	rim	Ol-gabbro	38.99	0.01	0.00	0.06	0.30	42.68	16.84	0.01	0.14	99.0
Ol		3	510.27	rim	Ol-gabbro	39.46	0.00	0.02	0.04	0.21	44.81	14.45	0.03	0.17	99.2
Ol		4	510.27	rim	Ol-gabbro	39.67	0.00	0.00	0.05	0.26	44.10	15.11	0.00	0.18	99.4
Ol		6	510.27	rim	Ol-gabbro	39.52	0.00	0.00	0.03	0.26	44.01	14.99	0.00	0.15	99.0
Ol		28	510.27	rim	Ol-gabbro	39.48	0.00	0.00	0.05	0.26	44.11	15.38	0.02	0.16	99.5
Ol		41	510.27	rim	Ol-gabbro	39.81	0.02	0.00	0.04	0.24	44.63	14.88	0.03	0.19	99.8
Ol	90R-2W-94-100b	50	510.27	rim	Ol-gabbro	39.60	0.02	0.01	0.04	0.25	44.92	14.74	0.01	0.20	99.8
Ol		52	510.27	rim	Ol-gabbro	39.41	0.00	0.01	0.06	0.25	43.93	15.22	0.04	0.15	99.1
Ol		59	510.27	rim	Ol-gabbro	39.47	0.00	0.00	0.07	0.24	44.87	14.74	0.00	0.17	99.6
Ol		61	510.27	rim	Ol-gabbro	39.56	0.00	0.00	0.03	0.27	44.52	14.70	0.02	0.15	99.2
Ol		2	510.27	rim	Ol-gabbro	39.07	0.00	0.02	0.04	0.26	44.62	15.20	0.05	0.18	99.4
Ol		81	510.56	rim	Ol-gabbro	39.59	0.00	0.00	0.05	0.27	43.19	15.84	0.01	0.15	99.1
Ol		83	510.56	rim	Ol-gabbro	39.75	0.02	0.02	0.03	0.28	43.10	16.05	0.01	0.18	99.4
Ol		88	510.56	rim	Ol-gabbro	39.42	0.02	0.01	0.05	0.26	43.29	16.24	0.03	0.13	99.5
Ol		89	510.56	rim	Ol-gabbro	39.51	0.01	0.02	0.04	0.26	43.58	16.02	0.00	0.17	99.6
Ol		91	510.56	rim	Ol-gabbro	39.70	0.00	0.00	0.04	0.26	43.05	16.18	0.00	0.18	99.4
Ol	90R-2W-123-129	96	510.56	rim	Ol-gabbro	39.41	0.00	0.02	0.03	0.28	43.38	15.87	0.00	0.18	99.2
Ol		99	510.56	rim	Ol-gabbro	39.66	0.00	0.00	0.06	0.28	43.74	15.83	0.02	0.16	99.8
Ol		104	510.56	rim	Ol-gabbro	39.42	0.01	0.04	0.04	0.23	43.71	15.59	0.01	0.14	99.2
Ol		115	510.56	rim	Ol-gabbro	39.40	0.01	0.02	0.05	0.31	42.74	16.93	0.03	0.16	99.7
Ol		122	510.56	rim	Ol-gabbro	39.25	0.02	0.03	0.05	0.25	43.20	16.15	0.01	0.18	99.1
Ol		132	510.56	rim	Ol-gabbro	39.34	0.02	0.00	0.03	0.24	43.40	15.55	0.00	0.15	98.8
Ol		137	510.67	rim	Ol-gabbro	39.46	0.00	0.00	0.02	0.25	44.08	15.81	0.00	0.16	99.8
Ol	90R-2W-135-139	169	510.67	rim	Ol-gabbro	38.95	0.02	0.01	0.10	0.28	42.71	17.06	0.00	0.15	99.3
Ol		224	510.67	rim	Ol-gabbro	39.25	0.00	0.00	0.03	0.26	43.23	16.55	0.00	0.12	99.4
Ol		230	510.67	rim	Ol-gabbro	39.42	0.01	0.02	0.03	0.23	44.00	16.10	0.01	0.19	100.0
Ol		11	510.84	rim	Ol-gabbro	39.65	0.02	0.01	0.03	0.25	44.88	15.30	0.00	0.13	100.3
Ol		12	510.84	rim	Ol-gabbro	39.66	0.01	0.01	0.03	0.25	44.79	15.12	0.00	0.15	100.0
Ol		22	510.84	rim	Ol-gabbro	39.41	0.00	0.01	0.06	0.21	43.38	16.18	0.00	0.14	99.4
Ol		26	510.84	rim	Ol-gabbro	39.41	0.00	0.01	0.03	0.28	43.39	16.06	0.01	0.15	99.4
Ol	90R-3W-6-8	30	510.84	rim	Ol-gabbro	39.92	0.02	0.05	0.04	0.23	43.83	15.77	0.02	0.16	100.0
Ol		38	510.84	rim	Ol-gabbro	39.49	0.02	0.00	0.03	0.25	43.79	15.66	0.00	0.16	99.4
Ol		46	510.84	rim	Ol-gabbro	39.62	0.02	0.00	0.04	0.26	44.44	15.12	0.01	0.13	99.6
Ol		60	510.84	rim	Ol-gabbro	39.47	0.00	0.00	0.05	0.29	44.31	14.86	0.01	0.16	99.2
Ol		75	510.84	rim	Ol-gabbro	39.45	0.01	0.04	0.03	0.25	44.19	15.32	0.02	0.16	99.5
Ol		89 / 1 .	462.554	core	Ol-rich gabbro	40.05	0.02	0.00	0.03	0.27	43.75	15.30	0.06	0.16	99.6
Ol		92 / 1 .	462.554	core	Ol-rich gabbro	39.92	0.00	0.01	0.02	0.27	43.61	15.37	0.01	0.24	99.4

Mineral		Point	Depth (mbsf)	Grain area	Lithology	SiO2	Al2O3	TiO2	CaO	MnO	MgO	FeO	Cr2O3	NiO	Total
Ol		93 / 1 .	462.554	core	Ol-rich gabbro	40.19	0.00	0.01	0.07	0.28	43.26	15.35	0.02	0.18	99.4
Ol		102 / 1 .	462.5685	core	Ol-rich gabbro	40.38	0.00	0.02	0.05	0.24	43.60	15.33	0.00	0.21	99.8
Ol		103 / 1 .	462.5685	core	Ol-rich gabbro	40.04	0.00	0.00	0.04	0.21	44.18	15.20	0.03	0.25	100.0
Ol		110 / 1 .	462.568	core	Ol-rich gabbro	39.91	0.00	0.02	0.08	0.23	43.83	15.37	0.00	0.17	99.6
Ol		111 / 1 .	462.568	core	Ol-rich gabbro	39.93	0.01	0.02	0.08	0.25	43.76	15.41	0.00	0.14	99.6
Ol	735B_83R7_130A	130 / 1 .	462.56	core	Ol-rich gabbro	40.08	0.02	0.00	0.08	0.25	43.93	14.93	0.00	0.13	99.4
Ol		132 / 1 .	462.56	core	Ol-rich gabbro	40.24	0.00	0.04	0.04	0.26	43.75	15.41	0.00	0.23	100.0
Ol		134 / 1 .	462.56	core	Ol-rich gabbro	40.16	0.03	0.00	0.06	0.26	43.74	15.43	0.00	0.17	99.9
Ol		136 / 1 .	462.56	core	Ol-rich gabbro	40.08	0.01	0.00	0.04	0.26	43.60	15.23	0.01	0.16	99.4
Ol		139 / 1 .	462.56	core	Ol-rich gabbro	40.41	0.00	0.01	0.02	0.23	44.07	15.19	0.00	0.20	100.1
Ol		150 / 1 .	462.553	core	Ol-rich gabbro	40.11	0.01	0.00	0.08	0.28	43.78	14.98	0.02	0.21	99.5
Ol		153 / 1 .	462.553	core	Ol-rich gabbro	40.04	0.01	0.00	0.04	0.26	43.95	14.84	0.00	0.21	99.3
Ol		154 / 1 .	462.553	core	Ol-rich gabbro	40.01	0.01	0.00	0.07	0.27	43.56	15.58	0.01	0.17	99.7
Ol		156 / 1 .	462.553	core	Ol-rich gabbro	40.09	0.01	0.04	0.02	0.21	43.98	15.09	0.00	0.20	99.6
Ol		162 / 1 .	462.566	core	Ol-rich gabbro	39.95	0.04	0.00	0.06	0.20	43.78	15.19	0.02	0.14	99.4
Ol		164 / 1 .	462.566	core	Ol-rich gabbro	40.35	0.00	0.06	0.07	0.23	43.97	15.49	0.00	0.17	100.3
Ol		1 / 1 .	461.554	core	Ol-rich gabbro	39.66	0.00	0.04	0.01	0.25	42.46	17.59	0.01	0.16	100.2
Ol		3 / 1 .	461.554	core	Ol-rich gabbro	39.50	0.01	0.00	0.06	0.25	42.48	17.06	0.01	0.16	99.5
Ol		5 / 1 .	461.554	core	Ol-rich gabbro	39.14	0.03	0.04	0.02	0.29	42.18	17.25	0.01	0.10	99.1
Ol		17 / 1 .	461.568	core	Ol-rich gabbro	39.63	0.01	0.03	0.02	0.25	41.98	17.36	0.01	0.12	99.4
Ol		19 / 1 .	461.568	core	Ol-rich gabbro	39.53	0.01	0.01	0.02	0.27	42.16	17.27	0.00	0.08	99.4
Ol		31 / 1 .	461.5685	core	Ol-rich gabbro	39.44	0.00	0.00	0.03	0.25	41.53	18.23	0.02	0.14	99.6
Ol		32 / 1 .	461.5685	core	Ol-rich gabbro	39.19	0.00	0.00	0.04	0.30	42.23	17.44	0.06	0.13	99.4
Ol		34 / 1 .	461.5685	core	Ol-rich gabbro	39.47	0.02	0.00	0.03	0.25	41.87	17.63	0.02	0.11	99.4
Ol	735B_83R7_0	35 / 1 .	461.5685	core	Ol-rich gabbro	39.62	0.00	0.00	0.04	0.27	42.27	17.35	0.00	0.19	99.7
Ol		36 / 1 .	461.563	core	Ol-rich gabbro	39.22	0.00	0.00	0.05	0.24	42.56	17.29	0.04	0.14	99.5
Ol		39 / 1 .	461.563	core	Ol-rich gabbro	39.15	0.02	0.02	0.06	0.22	42.46	17.76	0.02	0.19	99.9
Ol		41 / 1 .	461.563	core	Ol-rich gabbro	39.48	0.01	0.00	0.00	0.28	42.95	16.89	0.00	0.16	99.8
Ol		54 / 1 .	461.565	core	Ol-rich gabbro	39.48	0.00	0.00	0.04	0.28	42.48	17.78	0.00	0.15	100.2
Ol		56 / 1 .	461.565	core	Ol-rich gabbro	39.43	0.02	0.01	0.02	0.20	42.03	17.22	0.01	0.12	99.1
Ol		57 / 1 .	461.563	core	Ol-rich gabbro	39.29	0.00	0.00	0.05	0.24	42.48	17.00	0.00	0.16	99.2
Ol		70 / 1 .	461.5735	core	Ol-rich gabbro	39.88	0.01	0.00	0.08	0.32	42.70	17.31	0.00	0.18	100.5
Ol		73 / 1 .	461.5735	core	Ol-rich gabbro	39.69	0.01	0.06	0.06	0.29	42.23	17.45	0.01	0.14	99.9
Ol		3 / 1 .	462.4	core	Ol-rich gabbro	39.71	0.00	0.02	0.04	0.20	44.28	15.70	0.00	0.20	100.2
Ol		4 / 1 .	462.4	core	Ol-rich gabbro	39.73	0.00	0.05	0.05	0.22	43.97	15.54	0.00	0.22	99.8
Ol		6 / 1 .	462.4	core	Ol-rich gabbro	39.60	0.00	0.02	0.04	0.21	44.18	15.73	0.00	0.21	100.0
Ol		20 / 1 .	462.3885	core	Ol-rich gabbro	39.65	0.00	0.02	0.04	0.27	43.70	15.96	0.01	0.18	99.8
Ol		24 / 1 .	462.3905	core	Ol-rich gabbro	39.70	0.01	0.02	0.03	0.27	43.64	15.44	0.00	0.23	99.3
Ol		25 / 1 .	462.3905	core	Ol-rich gabbro	39.57	0.01	0.00	0.06	0.24	43.94	15.41	0.01	0.19	99.4
Ol		30 / 1 .	462.383	core	Ol-rich gabbro	39.95	0.00	0.02	0.05	0.28	43.12	16.07	0.01	0.20	99.7

Mineral		Point	Depth (mbsf)	Grain area	Lithology	SiO2	Al2O3	TiO2	CaO	MnO	MgO	FeO	Cr2O3	NiO	Total
Ol		32 / 1 .	462.383	core	Ol-rich gabbro	39.47	0.01	0.03	0.04	0.24	43.44	15.86	0.01	0.20	99.3
Ol		44 / 1 .	462.3835	core	Ol-rich gabbro	39.69	0.01	0.00	0.08	0.24	43.23	15.86	0.00	0.22	99.3
Ol	735B_83R7_113A	45 / 1 .	462.3935	core	Ol-rich gabbro	39.70	0.01	0.08	0.07	0.24	43.59	15.90	0.01	0.20	99.8
Ol		48 / 1 .	462.3935	core	Ol-rich gabbro	39.86	0.00	0.00	0.04	0.22	43.71	15.63	0.00	0.15	99.6
Ol		53 / 1 .	462.3915	core	Ol-rich gabbro	39.73	0.02	0.03	0.12	0.21	43.94	15.54	0.00	0.19	99.8
Ol		60 / 1 .	462.3995	core	Ol-rich gabbro	39.95	0.02	0.03	0.03	0.26	43.65	15.62	0.02	0.22	99.8
Ol		61 / 1 .	462.3995	core	Ol-rich gabbro	39.87	0.00	0.00	0.03	0.20	43.90	15.28	0.02	0.20	99.5
Ol		62 / 1 .	462.3925	core	Ol-rich gabbro	39.76	0.00	0.00	0.05	0.21	43.41	15.57	0.01	0.13	99.2
Ol		73 / 1 .	462.395	core	Ol-rich gabbro	39.68	0.00	0.00	0.05	0.24	43.29	15.77	0.00	0.21	99.3
Ol		80 / 1 .	462.394	core	Ol-rich gabbro	39.60	0.00	0.02	0.08	0.23	43.29	15.72	0.00	0.19	99.1
Ol		86 / 1 .	462.393	core	Ol-rich gabbro	39.78	0.00	0.01	0.00	0.21	43.55	15.78	0.00	0.19	99.5
Ol		87 / 1 .	462.393	core	Ol-rich gabbro	39.64	0.01	0.00	0.06	0.20	43.65	16.09	0.00	0.16	99.8
Ol		88 / 1 .	462.393	core	Ol-rich gabbro	39.87	0.00	0.00	0.04	0.24	43.13	15.88	0.00	0.22	99.4
Ol		55 / 1 .	518.3567	core	Ol-rich gabbro	40.11	0.00	0.01	0.08	0.26	43.21	16.01	0.00	0.16	99.8
Ol		56 / 1 .	518.3567	core	Ol-rich gabbro	39.98	0.00	0.00	0.06	0.29	43.29	16.01	0.05	0.14	99.8
Ol		57 / 1 .	518.3567	core	Ol-rich gabbro	40.18	0.01	0.05	0.03	0.26	43.78	15.96	0.05	0.20	100.5
Ol		58 / 1 .	518.3567	core	Ol-rich gabbro	39.94	0.00	0.00	0.05	0.27	43.52	15.82	0.00	0.14	99.7
Ol		65 / 1 .	518.3567	core	Ol-rich gabbro	39.87	0.01	0.03	0.05	0.26	43.66	15.93	0.02	0.24	100.1
Ol		67 / 1 .	518.3567	core	Ol-rich gabbro	40.13	0.01	0.07	0.02	0.24	43.08	16.37	0.02	0.21	100.2
Ol		68 / 1 .	518.3567	core	Ol-rich gabbro	40.28	0.02	0.01	0.03	0.26	43.34	15.74	0.00	0.17	99.9
Ol		69 / 1 .	518.3567	core	Ol-rich gabbro	40.14	0.02	0.07	0.05	0.27	43.50	16.18	0.00	0.19	100.4
Ol		74 / 1 .	518.3572	core	Ol-rich gabbro	40.10	0.00	0.00	0.05	0.31	43.42	15.61	0.02	0.19	99.7
Ol		76 / 1 .	518.3572	core	Ol-rich gabbro	39.96	0.00	0.03	0.05	0.25	43.21	15.99	0.00	0.20	99.7
Ol		78 / 1 .	518.3572	core	Ol-rich gabbro	40.19	0.02	0.01	0.04	0.19	43.81	15.53	0.00	0.21	100.0
Ol		2 / 1 .	518.35	core	Ol-rich gabbro	39.81	0.00	0.00	0.04	0.22	44.10	15.53	0.00	0.19	99.9
Ol		4 / 1 .	518.35	core	Ol-rich gabbro	39.59	0.02	0.01	0.05	0.27	43.47	15.83	0.00	0.19	99.4
Ol		6 / 1 .	518.35	core	Ol-rich gabbro	39.89	0.02	0.01	0.01	0.20	43.32	15.60	0.00	0.16	99.2
Ol		7 / 1 .	518.35	core	Ol-rich gabbro	39.88	0.01	0.03	0.03	0.23	43.39	15.70	0.00	0.17	99.4
Ol		8 / 1 .	518.35	core	Ol-rich gabbro	39.81	0.02	0.04	0.02	0.29	43.46	15.92	0.00	0.17	99.7
Ol		22 / 1 .	518.345	core	Ol-rich gabbro	39.59	0.05	0.05	0.05	0.31	42.38	16.19	0.02	0.20	98.8
Ol		24 / 1 .	518.345	core	Ol-rich gabbro	39.64	0.03	0.00	0.03	0.27	42.80	16.40	0.01	0.19	99.4
Ol		25 / 1 .	518.345	core	Ol-rich gabbro	40.05	0.01	0.05	0.08	0.23	43.14	16.30	0.00	0.20	100.1
Ol	735B_91R1_93A	27 / 1 .	518.345	core	Ol-rich gabbro	39.58	0.04	0.04	0.03	0.28	42.53	16.23	0.00	0.15	98.9
Ol		28 / 1 .	518.345	core	Ol-rich gabbro	39.88	0.03	0.04	0.03	0.21	43.42	15.99	0.05	0.19	99.8
Ol		40 / 1 .	518.3433	core	Ol-rich gabbro	40.00	0.00	0.00	0.04	0.26	43.30	16.07	0.00	0.19	99.9
Ol		41 / 1 .	518.3433	core	Ol-rich gabbro	39.67	0.01	0.06	0.05	0.22	43.50	16.21	0.02	0.21	99.9
Ol		42 / 1 .	518.3433	core	Ol-rich gabbro	39.88	0.01	0.05	0.04	0.22	43.15	15.87	0.02	0.16	99.4
Ol		43 / 1 .	518.3433	core	Ol-rich gabbro	39.85	0.00	0.00	0.06	0.20	42.78	16.20	0.00	0.12	99.2
Ol		51 / 1 .	518.351	core	Ol-rich gabbro	39.87	0.00	0.00	0.00	0.24	43.12	15.75	0.05	0.16	99.2
Ol		52 / 1 .	518.351	core	Ol-rich gabbro	39.86	0.02	0.05	0.03	0.22	43.35	15.96	0.03	0.19	99.7

Mineral		Point	Depth (mbsf)	Grain area	Lithology	SiO2	Al2O3	TiO2	CaO	MnO	MgO	FeO	Cr2O3	NiO	Total
Ol		54 / 1 .	518.351	core	Ol-rich gabbro	39.94	0.03	0.05	0.03	0.21	43.32	16.18	0.00	0.16	99.9
Ol		65 / 1 .	518.3355	core	Ol-rich gabbro	39.41	0.02	0.04	0.04	0.30	42.76	16.89	0.00	0.17	99.6
Ol		66 / 1 .	518.3355	core	Ol-rich gabbro	39.82	0.02	0.06	0.03	0.29	42.82	16.98	0.03	0.19	100.2
Ol		67 / 1 .	518.3355	core	Ol-rich gabbro	39.48	0.01	0.04	0.00	0.29	42.61	16.68	0.00	0.16	99.3
Ol		68 / 1 .	518.3355	core	Ol-rich gabbro	39.77	0.01	0.06	0.04	0.27	42.92	16.18	0.01	0.17	99.4
Ol		69 / 1 .	518.3338	core	Ol-rich gabbro	39.61	0.02	0.04	0.04	0.21	43.26	16.24	0.00	0.17	99.6
Ol		71 / 1 .	518.3338	core	Ol-rich gabbro	39.69	0.03	0.04	0.03	0.30	43.66	16.04	0.01	0.18	100.0
Ol		87 / 1 .	518.3338	core	Ol-rich gabbro	39.68	0.02	0.02	0.03	0.27	42.98	16.26	0.03	0.20	99.5
Ol		88 / 1 .	518.3338	core	Ol-rich gabbro	39.38	0.00	0.00	0.01	0.24	43.23	16.43	0.00	0.22	99.5
Ol		89 / 1 .	518.3338	core	Ol-rich gabbro	39.49	0.00	0.00	0.03	0.26	42.41	16.96	0.01	0.15	99.3
Ol		1 / 1 .	518.1644	core	Ol-rich gabbro	39.62	0.02	0.02	0.06	0.24	43.73	16.19	0.00	0.20	100.1
Ol		2 / 1 .	518.1644	core	Ol-rich gabbro	39.61	0.00	0.02	0.03	0.26	43.86	15.37	0.01	0.16	99.3
Ol		4 / 1 .	518.1644	core	Ol-rich gabbro	39.69	0.01	0.00	0.02	0.25	43.52	15.59	0.00	0.22	99.3
Ol		18 / 1 .	518.1645	core	Ol-rich gabbro	39.57	0.00	0.05	0.06	0.25	42.79	16.68	0.00	0.15	99.6
Ol		19 / 1 .	518.1645	core	Ol-rich gabbro	39.59	0.00	0.01	0.04	0.28	42.80	16.07	0.02	0.19	99.0
Ol		20 / 1 .	518.1645	core	Ol-rich gabbro	39.54	0.00	0.05	0.05	0.28	43.20	16.06	0.00	0.16	99.3
Ol		27 / 1 .	518.1617	core	Ol-rich gabbro	39.80	0.03	0.00	0.03	0.25	43.67	16.29	0.03	0.17	100.3
Ol		28 / 1 .	518.1617	core	Ol-rich gabbro	39.47	0.02	0.02	0.04	0.27	42.82	16.05	0.01	0.18	98.9
Ol		30 / 1 .	518.1617	core	Ol-rich gabbro	39.49	0.00	0.03	0.02	0.23	43.25	16.19	0.03	0.17	99.4
Ol		31 / 1 .	518.1544	core	Ol-rich gabbro	39.67	0.02	0.06	0.06	0.26	43.71	15.99	0.00	0.15	99.9
Ol	735B_91R1_74	33 / 1 .	518.1544	core	Ol-rich gabbro	40.05	0.00	0.00	0.03	0.23	43.12	16.64	0.03	0.14	100.2
Ol		46 / 1 .	518.1522	core	Ol-rich gabbro	39.68	0.01	0.05	0.03	0.20	43.15	16.31	0.01	0.17	99.6
Ol		47 / 1 .	518.1522	core	Ol-rich gabbro	39.63	0.00	0.01	0.05	0.26	42.80	16.64	0.01	0.20	99.6
Ol		48 / 1 .	518.1522	core	Ol-rich gabbro	39.52	0.12	0.00	0.04	0.26	43.00	16.14	0.11	0.17	99.4
Ol		54 / 1 .	518.1455	core	Ol-rich gabbro	39.41	0.01	0.05	0.08	0.26	42.68	16.90	0.00	0.13	99.5
Ol		55 / 1 .	518.1455	core	Ol-rich gabbro	39.16	0.00	0.03	0.02	0.32	42.29	17.35	0.03	0.22	99.4
Ol		63 / 1 .	518.1528	core	Ol-rich gabbro	39.77	0.00	0.02	0.04	0.25	43.13	16.63	0.00	0.20	100.0
Ol		65 / 1 .	518.1528	core	Ol-rich gabbro	39.41	0.01	0.05	0.04	0.28	42.92	16.67	0.02	0.19	99.6
Ol		66 / 1 .	518.1528	core	Ol-rich gabbro	39.58	0.01	0.03	0.04	0.26	43.29	16.33	0.01	0.16	99.7
Ol		75 / 1 .	518.1505	core	Ol-rich gabbro	39.68	0.02	0.12	0.05	0.27	42.78	16.34	0.01	0.14	99.4
Ol		76 / 1 .	518.1505	core	Ol-rich gabbro	39.58	0.05	0.00	0.04	0.20	43.76	16.26	0.00	0.15	100.0
Ol		90 / 1 .	462.554	rim	Ol-rich gabbro	40.28	0.00	0.00	0.02	0.17	44.34	14.92	0.03	0.20	100.0
Ol		91 / 1 .	462.554	rim	Ol-rich gabbro	39.99	0.00	0.00	0.06	0.26	43.86	15.43	0.00	0.17	99.8
Ol		94 / 1 .	462.554	rim	Ol-rich gabbro	40.17	0.00	0.02	0.05	0.27	43.93	15.27	0.00	0.23	99.9
Ol		104 / 1 .	462.5685	rim	Ol-rich gabbro	40.08	0.02	0.00	0.04	0.26	44.17	15.42	0.00	0.20	100.2
Ol		105 / 1 .	462.5685	rim	Ol-rich gabbro	40.01	0.00	0.05	0.05	0.24	43.90	15.38	0.00	0.15	99.8
Ol		106 / 1 .	462.5685	rim	Ol-rich gabbro	40.10	0.03	0.02	0.06	0.21	43.84	15.18	0.02	0.24	99.7
Ol		112 / 1 .	462.568	rim	Ol-rich gabbro	40.27	0.00	0.00	0.06	0.29	43.52	15.32	0.03	0.18	99.7
Ol		113 / 1 .	462.568	rim	Ol-rich gabbro	39.92	0.01	0.00	0.04	0.23	43.57	15.14	0.01	0.14	99.1
Ol		114 / 1 .	462.568	rim	Ol-rich gabbro	40.22	0.00	0.06	0.04	0.26	44.63	14.97	0.00	0.20	100.4

Mineral		Point	Depth (mbsf)	Grain area	Lithology	SiO2	Al2O3	TiO2	CaO	MnO	MgO	FeO	Cr2O3	NiO	Total
Ol	735B_83R7_130A	131 / 1 .	462.56	rim	Ol-rich gabbro	40.19	0.00	0.02	0.02	0.24	42.52	16.68	0.00	0.11	99.8
Ol		133 / 1 .	462.56	rim	Ol-rich gabbro	39.84	0.01	0.04	0.02	0.25	43.43	16.01	0.02	0.18	99.8
Ol		135 / 1 .	462.56	rim	Ol-rich gabbro	40.00	0.03	0.00	0.06	0.21	43.56	14.82	0.03	0.15	98.9
Ol		137 / 1 .	462.56	rim	Ol-rich gabbro	40.08	0.00	0.00	0.04	0.22	43.96	14.83	0.02	0.26	99.4
Ol		138 / 1 .	462.56	rim	Ol-rich gabbro	39.80	0.01	0.02	0.03	0.23	43.84	15.51	0.00	0.22	99.7
Ol		151 / 1 .	462.553	rim	Ol-rich gabbro	40.02	0.03	0.00	0.05	0.25	43.46	16.02	0.04	0.22	100.1
Ol		152 / 1 .	462.553	rim	Ol-rich gabbro	40.15	0.00	0.00	0.03	0.18	43.78	15.22	0.01	0.14	99.5
Ol		155 / 1 .	462.553	rim	Ol-rich gabbro	40.01	0.05	0.02	0.03	0.22	43.89	14.96	0.03	0.19	99.4
Ol		157 / 1 .	462.553	rim	Ol-rich gabbro	40.07	0.00	0.04	0.04	0.23	44.38	14.76	0.00	0.24	99.8
Ol		163 / 1 .	462.566	rim	Ol-rich gabbro	40.05	0.02	0.00	0.05	0.30	43.75	14.93	0.00	0.20	99.3
Ol		165 / 1 .	462.566	rim	Ol-rich gabbro	40.06	0.00	0.06	0.07	0.20	44.21	15.18	0.00	0.16	99.9
Ol	735B_83R7_0	2 / 1 .	461.554	rim	Ol-rich gabbro	39.31	0.04	0.00	0.01	0.29	42.21	17.12	0.04	0.17	99.2
Ol		18 / 1 .	461.568	rim	Ol-rich gabbro	39.63	0.00	0.03	0.07	0.29	42.28	17.08	0.02	0.16	99.5
Ol		33 / 1 .	461.5685	rim	Ol-rich gabbro	39.31	0.03	0.05	0.03	0.32	42.14	17.46	0.05	0.09	99.5
Ol		37 / 1 .	461.563	rim	Ol-rich gabbro	39.60	0.02	0.03	0.03	0.32	42.19	17.21	0.03	0.23	99.7
Ol		38 / 1 .	461.563	rim	Ol-rich gabbro	39.57	0.00	0.00	0.03	0.26	42.74	17.87	0.01	0.12	100.6
Ol		40 / 1 .	461.563	rim	Ol-rich gabbro	39.53	0.01	0.03	0.02	0.33	42.25	17.56	0.01	0.13	99.9
Ol		55 / 1 .	461.565	rim	Ol-rich gabbro	39.48	0.01	0.04	0.05	0.28	42.56	17.59	0.01	0.14	100.2
Ol		58 / 1 .	461.563	rim	Ol-rich gabbro	39.25	0.00	0.00	0.03	0.22	42.55	16.91	0.01	0.12	99.1
Ol		71 / 1 .	461.5735	rim	Ol-rich gabbro	39.63	0.04	0.00	0.03	0.30	42.31	17.04	0.02	0.14	99.5
Ol		72 / 1 .	461.5735	rim	Ol-rich gabbro	39.45	0.02	0.00	0.04	0.27	42.72	17.41	0.00	0.14	100.1
Ol	735B_83R7_113A	1 / 1 .	462.4	rim	Ol-rich gabbro	40.01	0.00	0.00	0.02	0.25	43.66	15.98	0.00	0.16	100.1
Ol		2 / 1 .	462.4	rim	Ol-rich gabbro	39.80	0.03	0.00	0.04	0.25	43.75	15.45	0.02	0.16	99.5
Ol		5 / 1 .	462.4	rim	Ol-rich gabbro	39.73	0.01	0.02	0.03	0.27	43.98	15.99	0.00	0.19	100.2
Ol		7 / 1 .	462.4	rim	Ol-rich gabbro	39.52	0.00	0.00	0.06	0.24	43.06	16.18	0.00	0.17	99.2
Ol		17 / 1 .	462.3885	rim	Ol-rich gabbro	39.98	0.02	0.00	0.04	0.21	44.18	15.00	0.00	0.21	99.6
Ol		18 / 1 .	462.3885	rim	Ol-rich gabbro	39.61	0.00	0.00	0.04	0.25	44.04	15.47	0.00	0.20	99.6
Ol		19 / 1 .	462.3885	rim	Ol-rich gabbro	39.81	0.00	0.00	0.05	0.17	43.93	15.68	0.00	0.19	99.8
Ol		31 / 1 .	462.383	rim	Ol-rich gabbro	39.42	0.00	0.01	0.01	0.30	43.68	16.09	0.01	0.19	99.7
Ol		33 / 1 .	462.383	rim	Ol-rich gabbro	39.91	0.02	0.00	0.05	0.25	43.31	15.60	0.00	0.18	99.3
Ol		34 / 1 .	462.383	rim	Ol-rich gabbro	39.86	0.01	0.00	0.06	0.25	43.70	15.49	0.01	0.19	99.6
Ol		38 / 1 .	462.385	rim	Ol-rich gabbro	39.91	0.00	0.00	0.04	0.26	43.14	15.64	0.02	0.17	99.2
Ol		40 / 1 .	462.385	rim	Ol-rich gabbro	39.89	0.02	0.04	0.07	0.22	43.80	15.50	0.00	0.18	99.7
Ol		46 / 1 .	462.3935	rim	Ol-rich gabbro	39.82	0.02	0.03	0.05	0.27	44.13	15.55	0.00	0.13	100.0
Ol		47 / 1 .	462.3935	rim	Ol-rich gabbro	39.71	0.01	0.00	0.06	0.26	43.25	15.63	0.00	0.21	99.1
Ol		59 / 1 .	462.3995	rim	Ol-rich gabbro	39.90	0.00	0.00	0.06	0.31	43.57	15.74	0.04	0.18	99.8
Ol		63 / 1 .	462.3925	rim	Ol-rich gabbro	39.58	0.00	0.00	0.04	0.22	43.24	15.60	0.01	0.18	98.9
Ol		74 / 1 .	462.395	rim	Ol-rich gabbro	39.55	0.00	0.00	0.03	0.33	42.87	16.04	0.00	0.20	99.0
Ol		79 / 1 .	462.394	rim	Ol-rich gabbro	39.54	0.01	0.00	0.03	0.31	43.36	16.16	0.01	0.15	99.6
Ol		85 / 1 .	462.393	rim	Ol-rich gabbro	40.24	0.01	0.01	0.05	0.26	43.58	15.45	0.00	0.19	99.8

Mineral		Point	Depth (mbsf)	Grain area	Lithology	SiO2	Al2O3	TiO2	CaO	MnO	MgO	FeO	Cr2O3	NiO	Total
Ol		89 / 1 .	462.393	rim	Ol-rich gabbro	39.45	0.00	0.02	0.02	0.22	43.50	15.99	0.01	0.19	99.4
Ol		59 / 1 .	518.3567	rim	Ol-rich gabbro	40.46	0.01	0.00	0.01	0.29	43.93	15.91	0.00	0.15	100.8
Ol		66 / 1 .	518.3567	rim	Ol-rich gabbro	40.11	0.01	0.00	0.04	0.25	43.63	15.89	0.02	0.18	100.1
Ol		75 / 1 .	518.3572	rim	Ol-rich gabbro	40.25	0.01	0.00	0.04	0.27	43.69	15.85	0.00	0.15	100.3
Ol		77 / 1 .	518.3572	rim	Ol-rich gabbro	40.14	0.00	0.00	0.07	0.27	44.07	15.64	0.03	0.22	100.4
Ol		1 / 1 .	518.35	rim	Ol-rich gabbro	39.69	0.04	0.06	0.05	0.21	43.36	15.69	0.02	0.15	99.3
Ol		3 / 1 .	518.35	rim	Ol-rich gabbro	40.00	0.00	0.01	0.06	0.23	43.54	15.44	0.04	0.14	99.5
Ol		5 / 1 .	518.35	rim	Ol-rich gabbro	39.66	0.00	0.02	0.03	0.20	43.48	15.41	0.00	0.14	98.9
Ol		23 / 1 .	518.345	rim	Ol-rich gabbro	39.60	0.01	0.05	0.03	0.28	42.96	16.28	0.00	0.18	99.4
Ol	735B_91R1_93A	29 / 1 .	518.345	rim	Ol-rich gabbro	40.03	0.02	0.00	0.07	0.32	43.26	16.70	0.01	0.16	100.6
Ol		39 / 1 .	518.3433	rim	Ol-rich gabbro	39.95	0.02	0.00	0.02	0.29	43.14	16.22	0.03	0.19	99.9
Ol		44 / 1 .	518.3433	rim	Ol-rich gabbro	39.68	0.01	0.00	0.02	0.23	43.47	15.89	0.00	0.18	99.5
Ol		53 / 1 .	518.351	rim	Ol-rich gabbro	39.79	0.00	0.00	0.06	0.27	43.57	16.07	0.00	0.19	100.0
Ol		55 / 1 .	518.351	rim	Ol-rich gabbro	40.05	0.02	0.00	0.03	0.24	43.94	15.61	0.05	0.21	100.2
Ol		56 / 1 .	518.351	rim	Ol-rich gabbro	39.46	0.01	0.02	0.04	0.30	43.09	16.28	0.01	0.16	99.4
Ol		70 / 1 .	518.3338	rim	Ol-rich gabbro	39.91	0.00	0.00	0.03	0.23	43.61	15.55	0.00	0.18	99.5
Ol		72 / 1 .	518.3338	rim	Ol-rich gabbro	39.88	0.00	0.05	0.04	0.25	43.80	16.18	0.01	0.18	100.4
Ol		3 / 1 .	518.1644	rim	Ol-rich gabbro	39.75	0.01	0.01	0.05	0.18	43.11	15.85	0.00	0.19	99.2
Ol		5 / 1 .	518.1644	rim	Ol-rich gabbro	39.79	0.00	0.00	0.05	0.22	43.64	15.79	0.00	0.22	99.7
Ol		21 / 1 .	518.1645	rim	Ol-rich gabbro	39.41	0.00	0.01	0.05	0.27	43.84	16.04	0.00	0.16	99.8
Ol		29 / 1 .	518.1617	rim	Ol-rich gabbro	39.73	0.03	0.02	0.05	0.21	43.17	15.80	0.00	0.20	99.2
Ol	735B_91R1_74	32 / 1 .	518.1544	rim	Ol-rich gabbro	39.76	0.01	0.00	0.01	0.23	43.26	16.38	0.00	0.22	99.9
Ol		45 / 1 .	518.1522	rim	Ol-rich gabbro	40.00	0.00	0.02	0.08	0.25	42.82	16.26	0.00	0.13	99.6
Ol		56 / 1 .	518.1455	rim	Ol-rich gabbro	39.31	0.00	0.00	0.03	0.30	42.51	17.19	0.03	0.21	99.6
Ol		64 / 1 .	518.1528	rim	Ol-rich gabbro	39.65	0.01	0.00	0.04	0.23	43.05	16.60	0.01	0.15	99.8
Ol		6 / 1 .	499.6325	core	Troctolite	39.46	0.00	0.00	0.05	0.32	42.29	18.16	0.07	0.13	100.5
Ol		8 / 1 .	499.6325	core	Troctolite	39.49	0.01	0.00	0.00	0.31	42.06	17.82	0.00	0.11	99.8
Ol		16 / 1 .	499.6355	core	Troctolite	39.34	0.00	0.02	0.02	0.31	42.10	17.76	0.01	0.21	99.8
Ol		21 / 1 .	499.6355	core	Troctolite	39.41	0.01	0.04	0.09	0.26	41.66	18.20	0.00	0.10	99.8
Ol		34 / 1 .	499.6395	core	Troctolite	39.81	0.00	0.00	0.06	0.22	42.19	17.64	0.06	0.16	100.1
Ol		36 / 1 .	499.6395	core	Troctolite	39.52	0.00	0.07	0.05	0.29	42.03	18.30	0.01	0.17	100.4
Ol	735B_87R7_49	37 / 1 .	499.6395	core	Troctolite	39.39	0.00	0.00	0.04	0.31	42.10	17.94	0.02	0.13	99.9
Ol		42 / 1 .	499.6445	core	Troctolite	40.00	0.00	0.02	0.04	0.24	41.96	17.52	0.00	0.15	99.9
Ol		48 / 1 .	499.6515	core	Troctolite	39.47	0.02	0.05	0.00	0.31	41.96	18.10	0.00	0.15	100.1
Ol		50 / 1 .	499.6515	core	Troctolite	39.81	0.00	0.00	0.05	0.35	41.87	18.01	0.01	0.14	100.2
Ol		59 / 1 .	499.6525	core	Troctolite	39.80	0.00	0.00	0.01	0.30	42.12	17.90	0.05	0.08	100.3
Ol		61 / 1 .	499.6525	core	Troctolite	39.55	0.03	0.02	0.01	0.28	42.34	17.82	0.00	0.06	100.1
Ol		62 / 1 .	499.6575	core	Troctolite	39.58	0.02	0.00	0.03	0.33	42.07	18.21	0.01	0.12	100.4
Ol		2 / 1 .	425.5625	core	Troctolite	39.37	0.01	0.00	0.04	0.26	41.71	18.63	0.02	0.12	100.1
Ol		15 / 1 .	425.561	core	Troctolite	39.71	0.02	0.00	0.09	0.29	42.23	18.30	0.01	0.14	100.8

Mineral		Point	Depth (mbsf)	Grain area	Lithology	SiO2	Al2O3	TiO2	CaO	MnO	MgO	FeO	Cr2O3	NiO	Total
Ol		20 / 1 .	425.562	core	Troctolite	39.37	0.00	0.00	0.03	0.38	40.40	20.48	0.00	0.18	100.8
Ol		32 / 1 .	425.5595	core	Troctolite	39.45	0.01	0.01	0.07	0.26	40.99	19.93	0.00	0.11	100.8
Ol		48 / 1 .	425.557	core	Troctolite	38.95	0.01	0.00	0.06	0.34	41.84	18.79	0.00	0.15	100.1
Ol	735B_80R2_7.5A	50 / 1 .	425.557	core	Troctolite	38.77	0.00	0.00	0.06	0.33	41.48	18.62	0.01	0.16	99.4
Ol		52 / 1 .	425.557	core	Troctolite	39.31	0.01	0.02	0.05	0.28	41.12	18.52	0.00	0.15	99.5
Ol		62 / 1 .	425.5565	core	Troctolite	39.38	0.00	0.00	0.06	0.28	41.93	18.30	0.03	0.12	100.1
Ol		63 / 1 .	425.5565	core	Troctolite	39.24	0.01	0.01	0.00	0.25	40.93	18.75	0.00	0.15	99.3
Ol		72 / 1 .	425.5485	core	Troctolite	39.27	0.04	0.00	0.06	0.27	41.92	18.33	0.02	0.16	100.1
Ol		74 / 1 .	425.5485	core	Troctolite	39.60	0.00	0.00	0.08	0.22	42.32	18.21	0.00	0.14	100.6
Ol		77 / 1 .	425.551	core	Troctolite	39.52	0.02	0.00	0.03	0.30	41.01	19.11	0.03	0.16	100.2
Ol		79 / 1 .	425.551	core	Troctolite	38.99	0.02	0.02	0.04	0.35	40.93	20.08	0.00	0.12	100.5
Ol		1 / 1 .	505.2735	core	Troctolite	39.80	0.01	0.03	0.06	0.25	43.34	16.80	0.03	0.16	100.5
Ol		10 / 1 .	505.2755	core	Troctolite	39.84	0.01	0.00	0.02	0.21	43.38	16.11	0.00	0.14	99.7
Ol		12 / 1 .	505.2755	core	Troctolite	39.68	0.00	0.00	0.06	0.26	43.49	16.55	0.00	0.12	100.2
Ol	735B_89R1_47	22 / 1 .	505.281	core	Troctolite	39.74	0.00	0.01	0.03	0.22	43.20	16.18	0.00	0.13	99.5
Ol		31 / 1 .	505.283	core	Troctolite	39.62	0.02	0.00	0.05	0.32	42.89	16.74	0.00	0.15	99.8
Ol		43 / 1 .	505.291	core	Troctolite	39.90	0.00	0.01	0.07	0.23	43.67	15.91	0.01	0.16	100.0
Ol		46 / 1 .	505.2925	core	Troctolite	40.02	0.02	0.03	0.07	0.29	43.65	16.00	0.01	0.14	100.2
Ol		47 / 1 .	505.298	core	Troctolite	39.89	0.00	0.00	0.05	0.19	43.26	15.87	0.01	0.12	99.4
Ol		1	510.015	core	Troctolite	39.12	0.01	0.05	0.04	0.25	42.69	17.17	0.00	0.14	99.5
Ol		20	510.015	core	Troctolite	39.14	0.01	0.01	0.06	0.25	42.88	16.73	0.02	0.15	99.2
Ol		21	510.015	core	Troctolite	39.41	0.00	0.03	0.03	0.27	42.43	17.24	0.00	0.17	99.6
Ol		26	510.015	core	Troctolite	39.24	0.07	0.00	0.05	0.26	42.69	17.17	0.00	0.16	99.6
Ol		30	510.015	core	Troctolite	39.13	0.00	0.02	0.04	0.28	42.72	17.18	0.02	0.17	99.6
Ol	90R-2W-68-75	31	510.015	core	Troctolite	39.05	0.00	0.02	0.05	0.29	42.88	16.92	0.00	0.13	99.3
Ol		35	510.015	core	Troctolite	39.27	0.02	0.01	0.04	0.29	42.27	16.92	0.02	0.13	99.0
Ol		39	510.015	core	Troctolite	39.01	0.00	0.02	0.05	0.31	42.53	17.25	0.01	0.15	99.3
Ol		43	510.015	core	Troctolite	39.06	0.01	0.01	0.04	0.29	42.48	17.70	0.00	0.12	99.7
Ol		49	510.015	core	Troctolite	39.15	0.00	0.00	0.04	0.28	42.81	17.25	0.01	0.13	99.7
Ol		7 / 1 .	499.6325	rim	Troctolite	39.34	0.02	0.01	0.06	0.31	41.90	18.23	0.00	0.10	100.0
Ol		9 / 1 .	499.6325	rim	Troctolite	39.42	0.00	0.00	0.01	0.28	42.48	17.47	0.00	0.13	99.8
Ol		15 / 1 .	499.6355	rim	Troctolite	39.69	0.02	0.02	0.04	0.28	42.41	17.44	0.00	0.15	100.0
Ol		17 / 1 .	499.6355	rim	Troctolite	39.61	0.00	0.00	0.04	0.29	42.23	17.40	0.01	0.13	99.7
Ol		22 / 1 .	499.6355	rim	Troctolite	39.71	0.03	0.04	0.05	0.31	42.15	17.74	0.04	0.19	100.3
Ol	735B_87R7_49	35 / 1 .	499.6395	rim	Troctolite	39.77	0.00	0.01	0.06	0.27	42.79	17.32	0.03	0.11	100.4
Ol		43 / 1 .	499.6445	rim	Troctolite	39.70	0.00	0.02	0.08	0.35	42.36	17.71	0.00	0.18	100.4
Ol		44 / 1 .	499.6445	rim	Troctolite	39.61	0.00	0.01	0.05	0.31	42.16	17.43	0.02	0.20	99.8
Ol		49 / 1 .	499.6515	rim	Troctolite	39.45	0.00	0.03	0.05	0.24	42.13	17.96	0.00	0.17	100.0
Ol		60 / 1 .	499.6525	rim	Troctolite	39.02	0.00	0.04	0.03	0.28	41.76	17.61	0.01	0.09	98.8
Ol		63 / 1 .	499.6575	rim	Troctolite	39.75	0.01	0.03	0.04	0.29	42.05	17.61	0.00	0.14	99.9

Mineral		Point	Depth (mbsf)	Grain area	Lithology	SiO2	Al2O3	TiO2	CaO	MnO	MgO	FeO	Cr2O3	NiO	Total
Ol		1 / 1 .	425.5625	rim	Troctolite	39.34	0.01	0.00	0.03	0.34	41.17	19.28	0.01	0.19	100.4
Ol		3 / 1 .	425.5625	rim	Troctolite	39.41	0.00	0.03	0.06	0.34	41.82	18.84	0.00	0.18	100.7
Ol		16 / 1 .	425.561	rim	Troctolite	39.63	0.03	0.04	0.04	0.32	41.38	18.59	0.02	0.08	100.1
Ol		33 / 1 .	425.5595	rim	Troctolite	38.96	0.00	0.00	0.06	0.34	40.82	19.66	0.03	0.16	100.0
Ol		34 / 1 .	425.5595	rim	Troctolite	39.47	0.00	0.00	0.01	0.34	41.21	20.04	0.00	0.12	101.2
Ol		49 / 1 .	425.557	rim	Troctolite	39.17	0.00	0.00	0.00	0.27	41.68	18.28	0.00	0.15	99.6
Ol	735B_80R2_7.5A	51 / 1 .	425.557	rim	Troctolite	39.39	0.02	0.00	0.03	0.31	41.09	18.62	0.00	0.15	99.6
Ol		53 / 1 .	425.557	rim	Troctolite	39.42	0.00	0.01	0.01	0.29	42.12	18.62	0.02	0.16	100.7
Ol		61 / 1 .	425.5565	rim	Troctolite	39.28	0.01	0.02	0.05	0.31	41.49	18.46	0.01	0.15	99.8
Ol		73 / 1 .	425.5485	rim	Troctolite	39.38	0.00	0.02	0.05	0.27	41.87	18.43	0.00	0.13	100.2
Ol		75 / 1 .	425.5485	rim	Troctolite	39.35	0.00	0.03	0.03	0.29	42.17	17.86	0.01	0.16	99.9
Ol		76 / 1 .	425.551	rim	Troctolite	39.53	0.00	0.07	0.03	0.29	41.84	18.22	0.01	0.22	100.2
Ol		78 / 1 .	425.551	rim	Troctolite	39.44	0.00	0.01	0.08	0.28	41.33	19.14	0.00	0.16	100.4
Ol		2 / 1 .	505.2735	rim	Troctolite	39.59	0.01	0.08	0.06	0.30	42.89	16.66	0.01	0.11	99.7
Ol		11 / 1 .	505.2755	rim	Troctolite	39.84	0.03	0.00	0.03	0.21	43.83	16.35	0.01	0.13	100.4
Ol		13 / 1 .	505.2755	rim	Troctolite	39.94	0.04	0.00	0.00	0.27	43.39	16.00	0.03	0.13	99.8
Ol	735B_89R1_47	23 / 1 .	505.281	rim	Troctolite	39.84	0.02	0.01	0.00	0.28	43.10	16.41	0.03	0.14	99.8
Ol		30 / 1 .	505.283	rim	Troctolite	39.57	0.00	0.00	0.03	0.26	43.18	16.20	0.00	0.17	99.4
Ol		42 / 1 .	505.291	rim	Troctolite	39.76	0.01	0.05	0.08	0.21	43.16	15.94	0.00	0.14	99.3
Ol		48 / 1 .	505.298	rim	Troctolite	39.83	0.00	0.00	0.07	0.26	43.73	16.10	0.00	0.12	100.1
Ol		2	510.015	rim	Troctolite	39.21	0.00	0.00	0.04	0.27	42.92	16.93	0.02	0.15	99.5
Ol		19	510.015	rim	Troctolite	39.25	0.01	0.00	0.03	0.30	43.00	16.54	0.00	0.15	99.3
Ol		22	510.015	rim	Troctolite	39.06	0.01	0.00	0.04	0.24	42.63	17.30	0.01	0.17	99.5
Ol		25	510.015	rim	Troctolite	39.80	0.03	0.00	0.20	0.28	42.82	17.10	0.00	0.16	100.4
Ol	90R-2W-68-75	29	510.015	rim	Troctolite	38.93	0.00	0.03	0.03	0.31	42.37	17.48	0.00	0.17	99.3
Ol		32	510.015	rim	Troctolite	38.73	0.02	0.00	0.04	0.27	42.37	17.09	0.04	0.12	98.7
Ol		36	510.015	rim	Troctolite	39.22	0.00	0.00	0.04	0.30	42.31	17.32	0.00	0.15	99.3
Ol		40	510.015	rim	Troctolite	38.99	0.03	0.00	0.03	0.25	42.23	17.29	0.05	0.18	99.0
Ol		48	510.015	rim	Troctolite	39.21	0.01	0.01	0.05	0.29	43.22	16.96	0.00	0.16	99.9

Calibration standards	Wollastonite (San Carlos)	Al2O3	Wollastonite	Albite	Orthose	Forsterite	Fayalite

In situ major elements concentrations in wt% analyzed by EPMA on a Cameca SX100 at LMV (Clermont-Ferrand, France)

Mineral	Sample	Point	Depth (mbsf)	Grain area	Lithology	SiO2	Al2O3	CaO	Na2O	K2O	MgO	FeO	Total
					2 sigma	0.545	0.629	0.309	0.343	0.067	0.030	0.039	
Pl		Counting time (s) - per element				10	10	10	10	10	10	20	
Pl		1 / 1 .	480.6835	core	Gabbro	50.76	31.44	13.97	3.73	0.03	0.02	0.12	100.1
Pl		3 / 1 .	480.6835	core	Gabbro	51.44	31.16	13.82	3.94	0.02	0.04	0.09	100.5
Pl		4 / 1 .	480.6835	core	Gabbro	50.11	32.07	14.90	3.00	0.00	0.02	0.13	100.2
Pl		6 / 1 .	480.6835	core	Gabbro	50.07	32.21	14.93	3.14	0.03	0.01	0.13	100.5
Pl		9 / 1 .	480.694	core	Gabbro	51.50	31.25	14.03	3.69	0.00	0.01	0.09	100.6
Pl		11 / 1 .	480.694	core	Gabbro	51.96	30.87	13.52	3.95	0.00	0.00	0.09	100.4
Pl		13 / 1 .	480.694	core	Gabbro	50.14	31.80	14.52	3.25	0.04	0.03	0.13	99.9
Pl		24 / 1 .	480.691	core	Gabbro	51.32	31.53	14.34	3.61	0.01	0.01	0.11	100.9
Pl		26 / 1 .	480.691	core	Gabbro	51.64	31.09	13.62	4.01	0.00	0.03	0.07	100.5
Pl		28 / 1 .	480.6945	core	Gabbro	53.82	29.50	11.83	4.69	0.04	0.00	0.06	99.9
Pl		35 / 1 .	480.698	core	Gabbro	51.79	30.85	13.45	4.01	0.00	0.02	0.11	100.2
Pl		36 / 1 .	480.698	core	Gabbro	51.20	31.23	13.95	3.63	0.00	0.02	0.07	100.1
Pl		38 / 1 .	480.703	core	Gabbro	51.31	31.30	14.01	3.88	0.05	0.01	0.07	100.6
Pl		39 / 1 .	480.703	core	Gabbro	48.36	33.00	16.55	2.49	0.01	0.01	0.18	100.6
Pl		42 / 1 .	480.703	core	Gabbro	51.50	31.12	13.68	3.79	0.07	0.03	0.08	100.3
Pl	735B_85R7_79	47 / 1 .	480.705	core	Gabbro	52.01	30.86	13.53	3.89	0.03	0.02	0.06	100.4
Pl		50 / 1 .	480.705	core	Gabbro	51.60	31.03	13.69	3.91	0.03	0.02	0.12	100.4
Pl		52 / 1 .	480.704	core	Gabbro	52.07	30.42	13.20	4.19	0.04	0.03	0.09	100.0
Pl		59 / 1 .	480.709	core	Gabbro	50.75	31.52	14.24	3.42	0.00	0.07	0.13	100.1
Pl		60 / 1 .	480.709	core	Gabbro	51.44	31.18	13.94	3.74	0.02	0.00	0.08	100.4
Pl		63 / 1 .	480.711	core	Gabbro	49.85	32.24	14.97	2.98	0.00	0.00	0.12	100.2
Pl		2 / 1 .	480.6835	rim	Gabbro	51.34	31.28	13.80	3.77	0.01	0.00	0.08	100.3
Pl		12 / 1 .	480.694	rim	Gabbro	50.95	31.82	14.35	3.39	0.01	0.00	0.11	100.6
Pl		25 / 1 .	480.691	rim	Gabbro	51.32	31.48	14.02	3.73	0.01	0.03	0.09	100.7
Pl		37 / 1 .	480.698	rim	Gabbro	50.85	31.31	14.49	3.43	0.01	0.04	0.13	100.3
Pl		43 / 1 .	480.703	rim	Gabbro	51.50	31.12	13.81	3.73	0.04	0.01	0.05	100.3
Pl		48 / 1 .	480.705	rim	Gabbro	51.12	31.54	14.42	3.38	0.02	0.03	0.06	100.6
Pl		49 / 1 .	480.705	rim	Gabbro	51.65	31.12	13.87	3.80	0.02	0.00	0.06	100.5
Pl		51 / 1 .	480.704	rim	Gabbro	51.70	30.84	13.65	3.92	0.02	0.01	0.10	100.2
Pl		54 / 1 .	480.704	rim	Gabbro	48.93	32.39	15.54	2.77	0.00	0.00	0.12	99.8
Pl		61 / 1 .	480.711	rim	Gabbro	50.81	31.49	14.02	3.68	0.00	0.01	0.08	100.1
Pl		5 / 1 .	274.885	core	Ol-bearing gabbro	56.98	27.53	9.81	6.02	0.06	0.01	0.20	100.6
Pl		7 / 1 .	274.885	core	Ol-bearing gabbro	57.87	27.13	9.35	6.17	0.08	0.00	0.23	100.8
Pl		8 / 1 .	274.885	core	Ol-bearing gabbro	57.01	27.16	9.26	6.00	0.11	0.00	0.17	99.7
Pl		9 / 1 .	274.885	core	Ol-bearing gabbro	57.58	27.37	9.66	6.25	0.08	0.03	0.26	101.2
Pl		13 / 1 .	274.892	core	Ol-bearing gabbro	57.07	27.10	9.35	6.09	0.09	0.01	0.22	99.9
Pl		15 / 1 .	274.892	core	Ol-bearing gabbro	57.37	27.17	9.23	6.07	0.11	0.03	0.18	100.2

Mineral		Point	Depth (mbsf)	Grain area	Lithology	SiO2	Al2O3	CaO	Na2O	K2O	MgO	FeO	Total
Pl		16 / 1 .	274.892	core	Ol-bearing gabbro	56.69	27.33	9.76	5.93	0.09	0.02	0.15	100.0
Pl		33 / 1 .	274.899	core	Ol-bearing gabbro	57.16	27.29	9.54	6.15	0.07	0.02	0.30	100.5
Pl	735B_56R4_61A	35 / 1 .	274.899	core	Ol-bearing gabbro	56.90	27.36	9.54	6.10	0.07	0.02	0.17	100.2
Pl		39 / 1 .	274.9015	core	Ol-bearing gabbro	57.54	27.07	9.17	6.19	0.07	0.02	0.21	100.3
Pl		41 / 1 .	274.904	core	Ol-bearing gabbro	57.03	27.26	9.53	5.91	0.10	0.03	0.21	100.1
Pl		44 / 1 .	274.904	core	Ol-bearing gabbro	57.27	27.15	9.51	6.07	0.13	0.03	0.16	100.3
Pl		45 / 1 .	274.904	core	Ol-bearing gabbro	57.42	27.25	9.54	6.15	0.08	0.00	0.17	100.6
Pl		49 / 1 .	274.903	core	Ol-bearing gabbro	57.69	27.16	9.28	6.26	0.07	0.00	0.11	100.6
Pl		50 / 1 .	274.903	core	Ol-bearing gabbro	57.51	27.27	9.36	6.26	0.09	0.00	0.17	100.7
Pl		51 / 1 .	274.903	core	Ol-bearing gabbro	57.09	27.24	9.31	6.08	0.08	0.01	0.24	100.0
Pl		61 / 1 .	274.9065	core	Ol-bearing gabbro	57.38	26.99	9.09	6.32	0.11	0.03	0.19	100.1
Pl		70 / 1 .	274.9045	core	Ol-bearing gabbro	56.92	27.38	9.29	6.01	0.11	0.03	0.20	100.0
Pl		71 / 1 .	274.9045	core	Ol-bearing gabbro	57.11	27.00	9.29	5.91	0.10	0.02	0.14	99.6
Pl		74 / 1 .	274.904	core	Ol-bearing gabbro	57.24	26.92	9.30	6.14	0.06	0.03	0.19	99.9
Pl		66 / 1 .	274.88	core	Ol-bearing gabbro	63.47	22.92	4.17	9.06	0.44	0.01	0.11	100.2
Pl		67 / 1 .	274.88	core	Ol-bearing gabbro	66.11	21.49	2.19	10.43	0.04	0.00	0.05	100.3
Pl		68 / 1 .	274.88	core	Ol-bearing gabbro	56.02	27.57	9.62	6.32	0.22	0.02	0.11	99.9
Pl		69 / 1 .	274.88	core	Ol-bearing gabbro	62.32	22.79	4.07	9.01	0.32	0.03	0.28	98.8
Pl		70 / 1 .	274.88	core	Ol-bearing gabbro	66.19	21.62	2.15	10.68	0.03	0.01	0.12	100.8
Pl		71 / 1 .	274.88	core	Ol-bearing gabbro	66.40	21.31	2.19	10.50	0.10	0.00	0.14	100.6
Pl	735B_56R4_61B	74 / 1 .	274.88	core	Ol-bearing gabbro	64.60	22.61	3.34	9.90	0.08	0.00	0.15	100.8
Pl		88 / 1 .	274.88	core	Ol-bearing gabbro	55.79	27.58	9.56	6.35	0.08	0.03	0.21	99.7
Pl		91 / 1 .	274.88	core	Ol-bearing gabbro	56.32	27.48	9.47	6.52	0.11	0.07	0.35	100.4
Pl		94 / 1 .	274.88	core	Ol-bearing gabbro	62.71	22.84	4.27	9.12	0.22	0.02	0.13	99.3
Pl		95 / 1 .	274.88	core	Ol-bearing gabbro	56.83	27.57	9.49	6.45	0.14	0.02	0.08	100.7
Pl		98 / 1 .	274.88	core	Ol-bearing gabbro	56.75	27.22	9.36	6.47	0.23	0.00	0.09	100.3
Pl		99 / 1 .	274.88	core	Ol-bearing gabbro	63.28	22.57	3.60	10.01	0.04	0.03	0.04	99.6
Pl		100 / 1 .	274.88	core	Ol-bearing gabbro	63.05	22.96	4.04	9.22	0.48	0.01	0.21	100.0
Pl		6 / 1 .	274.885	rim	Ol-bearing gabbro	56.82	28.06	9.72	6.05	0.05	0.00	0.21	100.9
Pl		10 / 1 .	274.885	rim	Ol-bearing gabbro	57.06	27.73	9.59	6.03	0.03	0.02	0.18	100.6
Pl		14 / 1 .	274.892	rim	Ol-bearing gabbro	57.27	27.47	9.60	5.96	0.11	0.00	0.22	100.6
Pl		17 / 1 .	274.892	rim	Ol-bearing gabbro	57.30	27.31	9.39	6.30	0.06	0.00	0.18	100.5
Pl		34 / 1 .	274.899	rim	Ol-bearing gabbro	57.04	26.97	9.40	6.13	0.07	0.01	0.18	99.8
Pl		36 / 1 .	274.9015	rim	Ol-bearing gabbro	57.33	27.44	9.34	6.13	0.05	0.00	0.18	100.5
Pl		38 / 1 .	274.9015	rim	Ol-bearing gabbro	56.82	27.24	9.38	6.30	0.08	0.00	0.22	100.1
Pl		42 / 1 .	274.904	rim	Ol-bearing gabbro	57.15	27.53	9.63	6.00	0.07	0.03	0.19	100.6
Pl		43 / 1 .	274.904	rim	Ol-bearing gabbro	56.95	27.39	9.71	5.99	0.03	0.03	0.17	100.3
Pl	735B_56R4_61A	46 / 1 .	274.904	rim	Ol-bearing gabbro	57.37	27.45	9.54	6.00	0.12	0.02	0.20	100.7
Pl		48 / 1 .	274.903	rim	Ol-bearing gabbro	56.74	27.53	9.63	6.11	0.05	0.00	0.21	100.3

Mineral		Point	Depth (mbsf)	Grain area	Lithology	SiO2	Al2O3	CaO	Na2O	K2O	MgO	FeO	Total
Pl		62 / 1 .	274.9065	rim	Ol-bearing gabbro	57.25	27.39	9.61	6.21	0.09	0.03	0.20	100.8
Pl		63 / 1 .	274.9065	rim	Ol-bearing gabbro	57.06	27.31	9.31	6.15	0.07	0.04	0.15	100.1
Pl		69 / 1 .	274.9045	rim	Ol-bearing gabbro	56.87	27.61	9.78	5.94	0.08	0.02	0.20	100.5
Pl		72 / 1 .	274.9045	rim	Ol-bearing gabbro	56.47	27.36	9.63	6.20	0.05	0.01	0.22	99.9
Pl		73 / 1 .	274.904	rim	Ol-bearing gabbro	57.43	26.67	9.05	6.36	0.04	0.02	0.14	99.7
Pl		75 / 1 .	274.904	rim	Ol-bearing gabbro	56.69	27.52	9.32	6.13	0.07	0.01	0.14	99.9
Pl		2 / 1 .	275.7355	core	Ol-gabbro	62.52	23.20	4.69	8.47	0.52	0.00	0.20	99.6
Pl		3 / 1 .	275.7355	core	Ol-gabbro	56.35	27.19	9.60	6.11	0.18	0.00	0.16	99.6
Pl		5 / 1 .	275.7355	core	Ol-gabbro	56.72	26.95	9.21	6.16	0.11	0.03	0.23	99.4
Pl		7 / 1 .	275.7355	core	Ol-gabbro	56.70	27.11	9.38	6.19	0.08	0.00	0.14	99.6
Pl		20 / 1 .	275.737	core	Ol-gabbro	56.84	27.22	9.30	6.35	0.17	0.00	0.10	100.0
Pl		21 / 1 .	275.737	core	Ol-gabbro	63.67	23.03	4.31	8.91	0.28	0.01	0.11	100.3
Pl		22 / 1 .	275.737	core	Ol-gabbro	63.16	23.31	4.61	8.76	0.48	0.00	0.14	100.5
Pl		24 / 1 .	275.7385	core	Ol-gabbro	56.65	27.50	9.70	6.07	0.11	0.01	0.09	100.1
Pl		25 / 1 .	275.7385	core	Ol-gabbro	56.77	27.11	9.34	6.25	0.07	0.01	0.20	99.8
Pl	735B_57R1_73	38 / 1 .	275.7445	core	Ol-gabbro	56.55	26.76	9.24	6.37	0.13	0.02	0.19	99.3
Pl		39 / 1 .	275.7445	core	Ol-gabbro	62.82	23.24	4.50	8.76	0.22	0.00	0.15	99.7
Pl		40 / 1 .	275.7445	core	Ol-gabbro	56.72	27.23	9.42	6.16	0.20	0.00	0.14	99.9
Pl		42 / 1 .	275.7445	core	Ol-gabbro	56.72	26.97	9.25	6.17	0.13	0.00	0.13	99.4
Pl		44 / 1 .	275.7445	core	Ol-gabbro	63.23	23.40	4.60	8.87	0.26	0.01	0.14	100.5
Pl		51 / 1 .	275.7455	core	Ol-gabbro	56.42	27.04	9.40	6.23	0.17	0.01	0.27	99.5
Pl		52 / 1 .	275.7455	core	Ol-gabbro	56.90	27.18	9.32	6.25	0.15	0.02	0.12	99.9
Pl		59 / 1 .	275.745	core	Ol-gabbro	56.90	27.10	9.07	6.16	0.15	0.00	0.20	99.6
Pl		67 / 1 .	275.7605	core	Ol-gabbro	56.70	27.43	9.36	6.13	0.19	0.00	0.18	100.0
Pl		71 / 1 .	275.7605	core	Ol-gabbro	56.96	27.28	9.30	6.39	0.11	0.02	0.08	100.1
Pl		80 / 1 .	284.3455	core	Ol-gabbro	55.67	27.52	10.00	5.78	0.09	0.00	0.25	99.3
Pl		82 / 1 .	284.3455	core	Ol-gabbro	55.58	27.51	10.18	5.92	0.07	0.01	0.23	99.5
Pl		84 / 1 .	284.3455	core	Ol-gabbro	54.91	27.99	10.83	5.50	0.11	0.01	0.23	99.6
Pl		87 / 1 .	284.3485	core	Ol-gabbro	55.57	27.46	10.17	5.81	0.08	0.02	0.20	99.3
Pl		99 / 1 .	284.3425	core	Ol-gabbro	55.36	28.23	10.60	5.50	0.04	0.02	0.22	100.0
Pl		102 / 1 .	284.3425	core	Ol-gabbro	52.66	29.81	12.63	4.54	0.07	0.00	0.25	100.0
Pl		105 / 1 .	284.344	core	Ol-gabbro	52.77	29.46	12.73	4.54	0.08	0.02	0.26	99.9
Pl		107 / 1 .	284.35	core	Ol-gabbro	55.27	27.54	10.28	5.55	0.09	0.06	0.27	99.1
Pl		109 / 1 .	284.35	core	Ol-gabbro	54.12	28.48	11.60	4.96	0.08	0.05	0.23	99.5
Pl	735B_58R3_108A	111 / 1 .	284.3505	core	Ol-gabbro	52.86	29.47	12.85	4.30	0.06	0.07	0.39	100.0
Pl		113 / 1 .	284.353	core	Ol-gabbro	52.59	29.33	12.66	4.32	0.06	0.04	0.33	99.3
Pl		126 / 1 .	284.3505	core	Ol-gabbro	56.06	27.19	9.95	5.68	0.10	0.05	0.30	99.3
Pl		128 / 1 .	284.346	core	Ol-gabbro	54.25	28.49	11.56	5.11	0.09	0.03	0.23	99.7
Pl		130 / 1 .	284.346	core	Ol-gabbro	55.32	28.05	10.75	5.47	0.09	0.03	0.26	100.0

Mineral		Point	Depth (mbsf)	Grain area	Lithology	SiO2	Al2O3	CaO	Na2O	K2O	MgO	FeO	Total
Pl		138 / 1 .	284.3405	core	Ol-gabbro	54.18	28.24	10.97	5.18	0.09	0.03	0.30	99.0
Pl		139 / 1 .	284.3405	core	Ol-gabbro	54.98	28.06	11.08	5.18	0.09	0.05	0.27	99.7
Pl		140 / 1 .	284.3385	core	Ol-gabbro	53.24	28.87	11.93	4.75	0.09	0.02	0.30	99.2
Pl		147 / 1 .	284.331	core	Ol-gabbro	53.82	28.85	11.81	4.90	0.06	0.05	0.30	99.8
Pl		76 / 1 .	295.3855	core	Ol-gabbro	53.33	29.51	12.24	4.48	0.04	0.05	0.30	100.0
Pl		86 / 1 .	295.3835	core	Ol-gabbro	52.23	29.74	12.92	4.41	0.08	0.07	0.29	99.7
Pl		87 / 1 .	295.3835	core	Ol-gabbro	52.42	29.96	12.49	4.39	0.06	0.04	0.26	99.6
Pl		100 / 1 .	295.3975	core	Ol-gabbro	52.69	29.91	12.68	4.53	0.02	0.01	0.24	100.1
Pl		102 / 1 .	295.3975	core	Ol-gabbro	53.13	29.83	12.64	4.35	0.04	0.00	0.23	100.2
Pl		104 / 1 .	295.395	core	Ol-gabbro	52.60	29.87	13.03	4.23	0.07	0.05	0.36	100.2
Pl		108 / 1 .	295.391	core	Ol-gabbro	54.19	28.51	11.18	5.11	0.08	0.04	0.31	99.4
Pl		111 / 1 .	295.391	core	Ol-gabbro	52.54	29.85	12.86	4.09	0.04	0.03	0.36	99.8
Pl	735B_60R4_115B	112 / 1 .	295.391	core	Ol-gabbro	52.20	29.55	12.94	4.08	0.02	0.04	0.39	99.2
Pl		8 / 1 .	295.3875	core	Ol-gabbro	52.62	29.76	12.80	4.39	0.03	0.02	0.34	100.0
Pl		10 / 1 .	295.384	core	Ol-gabbro	52.46	29.88	12.87	4.28	0.06	0.05	0.37	100.0
Pl		15 / 1 .	295.3825	core	Ol-gabbro	55.18	28.54	10.68	5.41	0.10	0.02	0.22	100.1
Pl		18 / 1 .	295.3825	core	Ol-gabbro	55.30	28.34	10.93	5.27	0.08	0.02	0.22	100.2
Pl		26 / 1 .	295.388	core	Ol-gabbro	54.17	28.82	11.48	5.06	0.06	0.02	0.33	99.9
Pl		30 / 1 .	295.388	core	Ol-gabbro	52.87	29.66	12.55	4.20	0.03	0.04	0.31	99.7
Pl		39 / 1 .	295.386	core	Ol-gabbro	53.84	29.48	11.77	4.80	0.03	0.02	0.25	100.2
Pl		42 / 1 .	295.386	core	Ol-gabbro	52.92	29.88	12.73	4.45	0.04	0.01	0.29	100.3
Pl		26 / 1 .	336.5415	core	Ol-gabbro	52.41	30.03	13.10	4.17	0.03	0.05	0.23	100.1
Pl		27 / 1 .	336.5415	core	Ol-gabbro	53.15	29.82	12.54	4.43	0.04	0.04	0.29	100.4
Pl		29 / 1 .	336.5415	core	Ol-gabbro	53.30	29.53	12.43	4.46	0.07	0.03	0.25	100.1
Pl		34 / 1 .	336.535	core	Ol-gabbro	54.07	29.26	11.97	4.69	0.04	0.03	0.19	100.3
Pl		36 / 1 .	336.535	core	Ol-gabbro	53.23	29.45	12.35	4.50	0.05	0.03	0.24	99.8
Pl		37 / 1 .	336.535	core	Ol-gabbro	48.68	32.53	15.97	2.59	0.03	0.04	0.24	100.1
Pl	735B_68R2_10.5A	41 / 1 .	336.533	core	Ol-gabbro	52.25	30.15	13.18	4.07	0.05	0.02	0.25	100.0
Pl		42 / 1 .	336.537	core	Ol-gabbro	51.86	30.33	13.76	3.96	0.03	0.02	0.31	100.3
Pl		55 / 1 .	336.547	core	Ol-gabbro	52.44	30.35	13.06	4.31	0.05	0.05	0.26	100.5
Pl		58 / 1 .	336.547	core	Ol-gabbro	52.47	30.14	13.18	4.15	0.05	0.01	0.25	100.2
Pl		59 / 1 .	336.5465	core	Ol-gabbro	52.82	30.05	12.80	4.20	0.08	0.00	0.21	100.2
Pl		62 / 1 .	336.5465	core	Ol-gabbro	52.35	30.21	12.96	4.17	0.02	0.03	0.28	100.0
Pl		72 / 1 .	336.535	core	Ol-gabbro	52.71	30.14	13.02	4.28	0.06	0.05	0.26	100.5
Pl		75 / 1 .	336.535	core	Ol-gabbro	52.87	30.05	12.33	4.46	0.05	0.05	0.26	100.1
Pl		18 / 1 .	371.1235	core	Ol-gabbro	51.70	30.05	13.00	4.05	0.05	0.07	0.17	99.1
Pl		35 / 1 .	371.132	core	Ol-gabbro	52.66	29.76	12.70	4.35	0.02	0.05	0.18	99.7
Pl		39 / 1 .	371.1345	core	Ol-gabbro	51.86	29.99	12.92	4.24	0.03	0.05	0.19	99.3
Pl		45 / 1 .	371.1375	core	Ol-gabbro	51.85	30.24	13.15	4.15	0.05	0.03	0.19	99.7

Mineral		Point	Depth (mbsf)	Grain area	Lithology	SiO2	Al2O3	CaO	Na2O	K2O	MgO	FeO	Total
Pl	735B_73R5_9	48 / 1 .	371.137	core	Ol-gabbro	52.19	30.28	13.19	3.97	0.04	0.04	0.21	99.9
Pl		57 / 1 .	371.145	core	Ol-gabbro	52.86	29.91	12.71	4.32	0.03	0.01	0.14	100.0
Pl		59 / 1 .	371.145	core	Ol-gabbro	52.58	29.75	12.45	4.44	0.03	0.03	0.16	99.4
Pl		61 / 1 .	371.145	core	Ol-gabbro	53.54	29.21	11.80	4.78	0.06	0.03	0.18	99.6
Pl		67 / 1 .	371.15	core	Ol-gabbro	52.68	29.83	12.69	4.28	0.07	0.01	0.17	99.7
Pl		68 / 1 .	371.15	core	Ol-gabbro	52.48	30.03	12.96	4.40	0.05	0.04	0.16	100.1
Pl		1 / 1 .	390.3575	core	Ol-gabbro	53.43	29.52	12.11	4.52	0.07	0.01	0.16	99.8
Pl		22 / 1 .	390.3535	core	Ol-gabbro	52.64	29.99	12.81	4.36	0.06	0.00	0.21	100.1
Pl		24 / 1 .	390.3535	core	Ol-gabbro	52.49	30.07	12.88	4.18	0.05	0.01	0.13	99.8
Pl		38 / 1 .	390.353	core	Ol-gabbro	52.60	29.65	12.86	4.26	0.05	0.04	0.19	99.7
Pl		39 / 1 .	390.353	core	Ol-gabbro	52.09	30.17	13.00	4.27	0.06	0.04	0.21	99.8
Pl		45 / 1 .	390.3505	core	Ol-gabbro	52.55	30.08	12.90	4.27	0.08	0.02	0.22	100.1
Pl		46 / 1 .	390.3505	core	Ol-gabbro	54.40	28.81	11.45	5.01	0.14	0.00	0.14	100.0
Pl		53 / 1 .	390.3475	core	Ol-gabbro	52.67	29.95	12.94	4.19	0.07	0.02	0.19	100.0
Pl		56 / 1 .	390.3475	core	Ol-gabbro	52.72	29.79	12.88	4.33	0.04	0.01	0.19	100.0
Pl		70 / 1 .	390.342	core	Ol-gabbro	52.32	29.85	12.81	4.42	0.07	0.05	0.19	99.7
Pl		71 / 1 .	390.342	core	Ol-gabbro	52.96	30.00	12.69	4.16	0.04	0.03	0.18	100.1
Pl		74 / 1 .	390.342	core	Ol-gabbro	52.41	30.18	13.16	4.19	0.05	0.03	0.23	100.3
Pl	735B_75R5_27	79 / 1 .	390.3375	core	Ol-gabbro	53.12	29.77	12.57	4.34	0.06	0.05	0.18	100.1
Pl		80 / 1 .	390.3375	core	Ol-gabbro	53.01	29.92	12.61	4.47	0.03	0.04	0.22	100.3
Pl		81 / 1 .	390.3375	core	Ol-gabbro	52.86	29.92	12.69	4.55	0.05	0.07	0.28	100.4
Pl		93 / 1 .	390.336	core	Ol-gabbro	53.06	29.63	12.53	4.47	0.04	0.00	0.16	99.9
Pl		94 / 1 .	390.336	core	Ol-gabbro	53.17	29.74	12.54	4.49	0.04	0.01	0.24	100.2
Pl		95 / 1 .	390.336	core	Ol-gabbro	53.15	29.78	12.59	4.27	0.02	0.00	0.18	100.0
Pl		98 / 1 .	390.336	core	Ol-gabbro	53.13	29.75	12.79	4.30	0.06	0.00	0.20	100.2
Pl		108 / 1 .	390.347	core	Ol-gabbro	52.41	30.22	13.01	4.15	0.00	0.02	0.15	100.0
Pl		111 / 1 .	390.347	core	Ol-gabbro	52.45	30.23	13.05	4.20	0.04	0.00	0.17	100.1
Pl		112 / 1 .	390.3445	core	Ol-gabbro	52.72	29.89	12.92	4.36	0.06	0.01	0.14	100.1
Pl		114 / 1 .	390.3445	core	Ol-gabbro	52.52	30.30	12.94	4.09	0.05	0.07	0.21	100.2
Pl		122 / 1 .	390.341	core	Ol-gabbro	52.37	29.98	12.76	4.36	0.05	0.03	0.24	99.8
Pl		123 / 1 .	390.341	core	Ol-gabbro	52.49	29.88	12.75	4.19	0.05	0.03	0.17	99.6
Pl		10 / 1 .	344.1285	core	Ol-gabbro	53.77	29.61	12.42	4.58	0.05	0.02	0.20	100.6
Pl		12 / 1 .	344.1285	core	Ol-gabbro	52.44	30.55	13.01	4.08	0.04	0.03	0.28	100.4
Pl		21 / 1 .	344.13	core	Ol-gabbro	52.85	30.26	12.80	4.21	0.03	0.02	0.19	100.4
Pl		24 / 1 .	344.13	core	Ol-gabbro	53.03	30.00	13.12	4.28	0.03	0.03	0.26	100.8
Pl		29 / 1 .	344.13	core	Ol-gabbro	50.63	31.33	14.61	3.59	0.03	0.01	0.24	100.4
Pl		31 / 1 .	344.13	core	Ol-gabbro	52.97	30.09	12.73	4.19	0.04	0.03	0.20	100.3
Pl		39 / 1 .	344.136	core	Ol-gabbro	52.48	29.98	12.60	4.28	0.01	0.02	0.21	99.6
Pl		41 / 1 .	344.136	core	Ol-gabbro	53.19	30.17	12.79	4.27	0.05	0.04	0.23	100.7

Mineral		Point	Depth (mbsf)	Grain area	Lithology	SiO2	Al2O3	CaO	Na2O	K2O	MgO	FeO	Total
Pl	735B_69R3_52B	44 / 1 .	344.136	core	Ol-gabbro	52.74	30.47	13.15	4.29	0.05	0.03	0.25	101.0
Pl		61 / 1 .	344.141	core	Ol-gabbro	53.00	29.87	12.60	4.57	0.06	0.00	0.22	100.3
Pl		64 / 1 .	344.141	core	Ol-gabbro	52.86	30.32	13.17	4.25	0.04	0.03	0.24	100.9
Pl		71 / 1 .	344.135	core	Ol-gabbro	52.84	30.18	12.85	4.19	0.04	0.02	0.26	100.4
Pl		72 / 1 .	344.135	core	Ol-gabbro	52.31	30.35	13.35	4.07	0.04	0.02	0.26	100.4
Pl		75 / 1 .	344.135	core	Ol-gabbro	53.36	29.73	12.34	4.61	0.05	0.03	0.22	100.3
Pl		81 / 1 .	344.1375	core	Ol-gabbro	52.51	30.45	13.08	4.08	0.04	0.04	0.27	100.5
Pl		82 / 1 .	344.1375	core	Ol-gabbro	53.66	29.58	12.11	4.55	0.07	0.04	0.25	100.2
Pl		85 / 1 .	344.1285	core	Ol-gabbro	52.16	30.21	13.19	4.22	0.04	0.05	0.28	100.1
Pl		90 / 1 .	344.126	core	Ol-gabbro	52.54	29.88	13.03	4.17	0.06	0.04	0.31	100.0
Pl		93 / 1 .	344.127	core	Ol-gabbro	52.91	30.07	13.05	4.41	0.06	0.01	0.20	100.7
Pl		95 / 1 .	344.127	core	Ol-gabbro	54.02	29.19	11.73	4.81	0.03	0.01	0.20	100.0
Pl	735B_57R1_73	6 / 1 .	275.7355	rim	Ol-gabbro	56.51	27.25	9.50	6.30	0.05	0.00	0.26	99.9
Pl		23 / 1 .	275.7385	rim	Ol-gabbro	57.41	27.22	9.43	6.17	0.09	0.00	0.18	100.5
Pl		26 / 1 .	275.7385	rim	Ol-gabbro	56.69	27.05	9.39	6.38	0.07	0.00	0.26	99.8
Pl		37 / 1 .	275.7445	rim	Ol-gabbro	56.48	27.30	9.35	6.26	0.13	0.00	0.23	99.8
Pl		41 / 1 .	275.7445	rim	Ol-gabbro	56.91	27.22	9.47	6.19	0.11	0.00	0.16	100.1
Pl		43 / 1 .	275.7445	rim	Ol-gabbro	56.96	26.96	9.29	6.25	0.11	0.03	0.18	99.8
Pl		53 / 1 .	275.7455	rim	Ol-gabbro	56.71	27.23	9.23	6.28	0.09	0.00	0.21	99.8
Pl		54 / 1 .	275.7455	rim	Ol-gabbro	56.95	27.33	9.30	6.19	0.16	0.00	0.12	100.0
Pl		55 / 1 .	275.7455	rim	Ol-gabbro	63.40	23.24	4.29	8.89	0.18	0.01	0.09	100.1
Pl		69 / 1 .	275.7605	rim	Ol-gabbro	63.29	23.24	4.50	8.63	0.30	0.00	0.17	100.1
Pl		70 / 1 .	275.7605	rim	Ol-gabbro	56.95	27.28	9.37	6.30	0.18	0.02	0.15	100.3
Pl	735B_58R3_108A	79 / 1 .	284.3455	rim	Ol-gabbro	53.36	29.17	11.98	4.79	0.08	0.02	0.23	99.6
Pl		81 / 1 .	284.3455	rim	Ol-gabbro	55.28	28.05	10.58	5.61	0.10	0.06	0.26	99.9
Pl		83 / 1 .	284.3455	rim	Ol-gabbro	54.56	28.42	11.00	5.38	0.11	0.02	0.21	99.7
Pl		85 / 1 .	284.3455	rim	Ol-gabbro	54.39	28.36	10.81	5.29	0.10	0.02	0.26	99.2
Pl		86 / 1 .	284.3485	rim	Ol-gabbro	54.09	28.84	11.20	5.12	0.09	0.01	0.26	99.6
Pl		100 / 1 .	284.3425	rim	Ol-gabbro	54.27	28.17	10.92	5.24	0.01	0.02	0.23	98.9
Pl		101 / 1 .	284.3425	rim	Ol-gabbro	53.15	29.60	12.17	4.76	0.05	0.00	0.20	99.9
Pl		103 / 1 .	284.3425	rim	Ol-gabbro	55.79	27.70	10.48	5.75	0.08	0.02	0.21	100.0
Pl		104 / 1 .	284.3425	rim	Ol-gabbro	55.23	28.25	10.76	5.47	0.10	0.05	0.25	100.1
Pl		106 / 1 .	284.35	rim	Ol-gabbro	53.77	28.55	11.48	5.30	0.07	0.01	0.32	99.5
Pl		108 / 1 .	284.35	rim	Ol-gabbro	54.73	28.58	11.33	5.09	0.09	0.04	0.26	100.1
Pl		110 / 1 .	284.35	rim	Ol-gabbro	53.88	28.74	11.48	4.73	0.07	0.02	0.26	99.2
Pl		112 / 1 .	284.353	rim	Ol-gabbro	53.80	28.48	11.26	5.07	0.08	0.03	0.36	99.1
Pl		125 / 1 .	284.3505	rim	Ol-gabbro	54.74	28.20	10.78	5.46	0.10	0.03	0.21	99.5
Pl		127 / 1 .	284.346	rim	Ol-gabbro	54.26	28.85	11.50	5.08	0.11	0.00	0.25	100.0
Pl		129 / 1 .	284.346	rim	Ol-gabbro	54.19	28.64	11.53	5.24	0.07	0.02	0.25	99.9

Mineral		Point	Depth (mbsf)	Grain area	Lithology	SiO2	Al2O3	CaO	Na2O	K2O	MgO	FeO	Total
Pl		136 / 1 .	284.3405	rim	Ol-gabbro	55.51	27.82	10.31	5.78	0.04	0.02	0.27	99.8
Pl		137 / 1 .	284.3405	rim	Ol-gabbro	55.31	27.74	10.59	5.72	0.10	0.05	0.23	99.7
Pl		146 / 1 .	284.332	rim	Ol-gabbro	55.34	28.35	10.63	5.52	0.05	0.03	0.31	100.2
Pl		77 / 1 .	295.3855	rim	Ol-gabbro	53.79	29.32	11.70	4.58	0.03	0.00	0.28	99.7
Pl		85 / 1 .	295.3835	rim	Ol-gabbro	54.39	29.10	11.47	4.99	0.03	0.02	0.27	100.3
Pl		88 / 1 .	295.3835	rim	Ol-gabbro	53.92	28.91	11.67	4.94	0.06	0.03	0.26	99.8
Pl		101 / 1 .	295.3975	rim	Ol-gabbro	53.31	29.62	12.02	4.79	0.02	0.01	0.34	100.1
Pl		103 / 1 .	295.3975	rim	Ol-gabbro	53.60	29.31	12.05	4.65	0.04	0.04	0.33	100.0
Pl		105 / 1 .	295.4015	rim	Ol-gabbro	52.55	30.07	12.90	4.17	0.00	0.03	0.20	99.9
Pl		109 / 1 .	295.391	rim	Ol-gabbro	54.21	28.84	11.50	4.91	0.04	0.05	0.30	99.8
Pl		110 / 1 .	295.391	rim	Ol-gabbro	54.68	28.83	11.21	5.15	0.05	0.03	0.29	100.2
Pl		113 / 1 .	295.391	rim	Ol-gabbro	53.71	29.18	11.82	4.64	0.03	0.02	0.29	99.7
Pl	735B_60R4_115B	7 / 1 .	295.3875	rim	Ol-gabbro	53.62	29.45	11.98	4.83	0.01	0.00	0.28	100.2
Pl		9 / 1 .	295.384	rim	Ol-gabbro	53.32	29.65	12.43	4.72	0.03	0.05	0.26	100.5
Pl		16 / 1 .	295.3825	rim	Ol-gabbro	54.99	28.18	10.88	5.28	0.01	0.00	0.34	99.7
Pl		17 / 1 .	295.3825	rim	Ol-gabbro	54.42	28.79	11.25	5.03	0.06	0.05	0.28	99.9
Pl		19 / 1 .	295.3825	rim	Ol-gabbro	53.95	28.88	11.65	4.85	0.08	0.03	0.27	99.7
Pl		27 / 1 .	295.388	rim	Ol-gabbro	55.05	28.35	10.93	5.33	0.06	0.00	0.24	100.0
Pl		28 / 1 .	295.388	rim	Ol-gabbro	53.57	29.42	12.16	4.72	0.07	0.02	0.29	100.3
Pl		29 / 1 .	295.388	rim	Ol-gabbro	53.72	28.91	11.52	4.92	0.03	0.02	0.24	99.4
Pl		40 / 1 .	295.386	rim	Ol-gabbro	53.97	29.18	11.90	4.88	0.03	0.01	0.38	100.4
Pl		41 / 1 .	295.386	rim	Ol-gabbro	55.13	28.35	11.04	5.17	0.05	0.04	0.39	100.2
Pl		28 / 1 .	336.5415	rim	Ol-gabbro	53.46	29.61	12.36	4.54	0.07	0.04	0.30	100.4
Pl		35 / 1 .	336.535	rim	Ol-gabbro	49.43	32.21	15.32	2.73	0.03	0.00	0.25	100.0
Pl		38 / 1 .	336.535	rim	Ol-gabbro	53.09	29.78	12.86	4.35	0.00	0.03	0.25	100.4
Pl		39 / 1 .	336.535	rim	Ol-gabbro	53.79	29.01	11.64	4.91	0.08	0.07	0.25	99.8
Pl		40 / 1 .	336.535	rim	Ol-gabbro	51.54	30.41	13.68	3.60	0.04	0.01	0.26	99.5
Pl	735B_68R2_10.5A	43 / 1 .	336.537	rim	Ol-gabbro	52.29	30.23	13.06	4.02	0.06	0.03	0.26	99.9
Pl		56 / 1 .	336.547	rim	Ol-gabbro	51.30	30.64	14.13	3.66	0.04	0.04	0.22	100.0
Pl		57 / 1 .	336.547	rim	Ol-gabbro	52.37	30.02	13.02	4.03	0.06	0.06	0.26	99.8
Pl		60 / 1 .	336.5465	rim	Ol-gabbro	52.04	30.47	13.35	3.98	0.03	0.02	0.24	100.1
Pl		61 / 1 .	336.5465	rim	Ol-gabbro	52.91	29.98	12.89	4.16	0.06	0.03	0.28	100.3
Pl		73 / 1 .	336.535	rim	Ol-gabbro	53.04	29.73	12.45	4.47	0.01	0.02	0.31	100.0
Pl		74 / 1 .	336.535	rim	Ol-gabbro	53.00	29.73	12.88	4.27	0.07	0.01	0.34	100.3
Pl		14 / 1 .	371.1235	rim	Ol-gabbro	52.01	30.23	12.98	4.07	0.05	0.06	0.15	99.6
Pl		16 / 1 .	371.1235	rim	Ol-gabbro	52.33	30.17	12.84	4.06	0.05	0.03	0.21	99.7
Pl		17 / 1 .	371.1235	rim	Ol-gabbro	49.34	31.47	14.97	3.16	0.03	0.05	0.20	99.2
Pl		34 / 1 .	371.132	rim	Ol-gabbro	52.79	29.48	12.66	4.57	0.03	0.04	0.19	99.8
Pl		38 / 1 .	371.1345	rim	Ol-gabbro	52.66	30.19	12.83	4.28	0.04	0.02	0.25	100.3

Mineral		Point	Depth (mbsf)	Grain area	Lithology	SiO2	Al2O3	CaO	Na2O	K2O	MgO	FeO	Total
Pl	735B_73R5_9	44 / 1 .	371.1375	rim	Ol-gabbro	52.70	29.96	12.61	4.40	0.03	0.02	0.20	99.9
Pl		46 / 1 .	371.1375	rim	Ol-gabbro	53.03	29.23	12.20	4.55	0.05	0.02	0.20	99.3
Pl		58 / 1 .	371.145	rim	Ol-gabbro	49.78	31.71	14.84	3.28	0.05	0.02	0.24	99.9
Pl		60 / 1 .	371.145	rim	Ol-gabbro	52.73	30.11	12.87	4.36	0.06	0.04	0.20	100.4
Pl		66 / 1 .	371.15	rim	Ol-gabbro	52.97	29.33	12.57	4.68	0.03	0.04	0.27	99.9
Pl		69 / 1 .	371.15	rim	Ol-gabbro	52.89	29.95	12.78	4.33	0.06	0.02	0.18	100.2
Pl		70 / 1 .	371.15	rim	Ol-gabbro	52.99	29.91	12.57	4.32	0.05	0.02	0.16	100.0
Pl	735B_75R5_27	2 / 1 .	390.3575	rim	Ol-gabbro	51.56	30.76	13.61	3.61	0.02	0.00	0.18	99.8
Pl		3 / 1 .	390.3575	rim	Ol-gabbro	53.65	29.38	11.82	4.67	0.07	0.00	0.15	99.7
Pl		21 / 1 .	390.3535	rim	Ol-gabbro	48.11	32.57	16.19	2.55	0.01	0.01	0.25	99.7
Pl		23 / 1 .	390.3535	rim	Ol-gabbro	52.97	29.49	12.37	4.51	0.03	0.00	0.26	99.6
Pl		36 / 1 .	390.353	rim	Ol-gabbro	53.05	29.60	12.59	4.32	0.05	0.03	0.18	99.8
Pl		40 / 1 .	390.353	rim	Ol-gabbro	50.76	31.30	14.62	3.24	0.02	0.02	0.21	100.2
Pl		44 / 1 .	390.3505	rim	Ol-gabbro	52.04	29.83	12.63	4.17	0.06	0.03	0.24	99.0
Pl		54 / 1 .	390.3475	rim	Ol-gabbro	52.49	30.12	13.10	4.20	0.06	0.06	0.18	100.2
Pl		55 / 1 .	390.3475	rim	Ol-gabbro	50.02	31.61	15.14	3.03	0.04	0.04	0.19	100.1
Pl		72 / 1 .	390.342	rim	Ol-gabbro	52.59	29.83	12.67	4.12	0.04	0.01	0.15	99.4
Pl		73 / 1 .	390.342	rim	Ol-gabbro	52.77	30.03	13.01	4.21	0.05	0.01	0.20	100.3
Pl		96 / 1 .	390.336	rim	Ol-gabbro	50.81	30.92	14.10	3.47	0.07	0.03	0.15	99.5
Pl		97 / 1 .	390.336	rim	Ol-gabbro	52.92	29.88	12.75	4.40	0.06	0.01	0.19	100.2
Pl		109 / 1 .	390.347	rim	Ol-gabbro	52.50	30.13	12.67	4.27	0.07	0.02	0.19	99.8
Pl		110 / 1 .	390.347	rim	Ol-gabbro	51.93	30.50	13.62	3.99	0.01	0.03	0.34	100.4
Pl		113 / 1 .	390.3445	rim	Ol-gabbro	52.64	29.78	12.65	4.13	0.06	0.03	0.14	99.4
Pl		124 / 1 .	390.341	rim	Ol-gabbro	51.29	30.92	13.92	3.60	0.05	0.00	0.25	100.0
Pl		125 / 1 .	390.341	rim	Ol-gabbro	52.81	29.79	12.61	4.22	0.03	0.00	0.17	99.6
Pl	735B_69R3_52B	9 / 1 .	344.1285	rim	Ol-gabbro	50.27	32.24	15.05	2.96	0.04	0.01	0.24	100.8
Pl		11 / 1 .	344.1285	rim	Ol-gabbro	53.16	29.93	12.58	4.23	0.01	0.03	0.23	100.2
Pl		22 / 1 .	344.13	rim	Ol-gabbro	53.26	30.19	12.62	4.41	0.04	0.04	0.19	100.7
Pl		23 / 1 .	344.13	rim	Ol-gabbro	53.56	30.05	12.35	4.43	0.03	0.01	0.20	100.6
Pl		30 / 1 .	344.13	rim	Ol-gabbro	49.62	32.03	14.89	2.93	0.04	0.00	0.30	99.8
Pl		38 / 1 .	344.136	rim	Ol-gabbro	53.41	29.51	12.05	4.46	0.04	0.00	0.22	99.7
Pl		40 / 1 .	344.136	rim	Ol-gabbro	51.35	31.09	14.10	3.62	0.04	0.00	0.21	100.4
Pl		42 / 1 .	344.136	rim	Ol-gabbro	49.99	32.21	14.83	3.19	0.03	0.00	0.18	100.4
Pl		43 / 1 .	344.136	rim	Ol-gabbro	52.83	30.20	12.90	4.40	0.04	0.02	0.22	100.6
Pl		62 / 1 .	344.141	rim	Ol-gabbro	49.90	32.45	15.03	3.09	0.01	0.03	0.22	100.7
Pl		63 / 1 .	344.141	rim	Ol-gabbro	53.13	30.12	12.71	4.48	0.01	0.02	0.26	100.7
Pl		70 / 1 .	344.135	rim	Ol-gabbro	53.40	29.64	11.98	4.59	0.00	0.03	0.30	99.9
Pl		73 / 1 .	344.135	rim	Ol-gabbro	51.53	31.19	13.76	3.89	0.01	0.02	0.23	100.6
Pl		74 / 1 .	344.135	rim	Ol-gabbro	48.23	33.19	16.39	2.39	0.04	0.00	0.24	100.5
Pl		80 / 1 .	344.1375	rim	Ol-gabbro	53.59	29.51	12.18	4.46	0.07	0.04	0.25	100.1

Mineral		Point	Depth (mbsf)	Grain area	Lithology	SiO2	Al2O3	CaO	Na2O	K2O	MgO	FeO	Total
Pl		83 / 1 .	344.1375	rim	Ol-gabbro	53.00	30.05	12.40	4.39	0.03	0.01	0.19	100.1
Pl		84 / 1 .	344.1285	rim	Ol-gabbro	52.81	29.96	12.80	4.23	0.06	0.01	0.20	100.1
Pl		86 / 1 .	344.1285	rim	Ol-gabbro	53.14	29.92	12.26	4.32	0.02	0.04	0.23	99.9
Pl		87 / 1 .	344.1285	rim	Ol-gabbro	53.81	29.41	12.26	4.77	0.08	0.04	0.23	100.6
Pl		94 / 1 .	344.127	rim	Ol-gabbro	53.92	29.67	12.09	4.91	0.04	0.00	0.22	100.8
Pl		89 / 1 .	425.363	core	Ol-gabbro	59.59	25.78	7.42	7.33	0.12	0.03	0.15	100.4
Pl		90 / 1 .	425.363	core	Ol-gabbro	58.78	25.92	7.81	7.40	0.13	0.00	0.15	100.2
Pl		92 / 1 .	425.363	core	Ol-gabbro	59.28	25.87	7.87	7.18	0.16	0.02	0.14	100.5
Pl		104 / 1 .	425.3695	core	Ol-gabbro	58.24	26.06	8.38	6.66	0.11	0.00	0.17	99.6
Pl		113 / 1 .	425.372	core	Ol-gabbro	58.22	26.22	8.07	7.05	0.05	0.00	0.06	99.7
Pl		115 / 1 .	425.372	core	Ol-gabbro	58.94	26.16	7.76	7.07	0.14	0.00	0.11	100.2
Pl		116 / 1 .	425.372	core	Ol-gabbro	50.78	31.01	14.02	3.62	0.08	0.00	0.14	99.6
Pl		121 / 1 .	425.3735	core	Ol-gabbro	51.04	30.90	13.88	3.84	0.04	0.00	0.08	99.8
Pl		122 / 1 .	425.3735	core	Ol-gabbro	51.07	30.81	13.92	3.77	0.02	0.02	0.12	99.7
Pl	735B_80R1_136	124 / 1 .	425.3735	core	Ol-gabbro	49.87	31.46	14.30	3.47	0.04	0.01	0.15	99.3
Pl		129 / 1 .	425.3795	core	Ol-gabbro	50.82	31.09	14.09	3.83	0.02	0.02	0.11	100.0
Pl		130 / 1 .	425.3795	core	Ol-gabbro	50.70	31.10	14.04	3.60	0.00	0.01	0.08	99.5
Pl		132 / 1 .	425.3795	core	Ol-gabbro	53.77	29.14	11.73	5.01	0.09	0.00	0.13	99.9
Pl		133 / 1 .	425.3795	core	Ol-gabbro	49.47	31.80	15.10	2.98	0.06	0.04	0.10	99.5
Pl		137 / 1 .	425.3795	core	Ol-gabbro	58.28	26.42	8.39	6.74	0.09	0.01	0.05	100.0
Pl		149 / 1 .	425.3835	core	Ol-gabbro	47.91	32.89	16.08	2.26	0.00	0.03	0.15	99.3
Pl		159 / 1 .	425.389	core	Ol-gabbro	50.88	31.52	14.20	3.51	0.06	0.02	0.13	100.3
Pl		163 / 1 .	425.389	core	Ol-gabbro	48.38	32.80	16.28	2.54	0.01	0.01	0.08	100.1
Pl		169 / 1 .	425.3865	core	Ol-gabbro	49.30	31.71	14.72	3.14	0.03	0.03	0.11	99.0
Pl		8 / 1 .	439.2455	core	Ol-gabbro	51.44	31.09	13.75	3.75	0.01	0.05	0.11	100.2
Pl		10 / 1 .	439.2455	core	Ol-gabbro	52.92	29.97	12.46	4.52	0.03	0.01	0.11	100.0
Pl		11 / 1 .	439.2455	core	Ol-gabbro	52.79	29.78	12.21	4.58	0.02	0.05	0.09	99.5
Pl		12 / 1 .	439.246	core	Ol-gabbro	53.09	29.65	12.23	4.43	0.06	0.02	0.09	99.6
Pl		30 / 1 .	439.2465	core	Ol-gabbro	52.78	30.25	12.68	4.48	0.05	0.00	0.06	100.3
Pl		34 / 1 .	439.2465	core	Ol-gabbro	52.51	29.96	12.77	4.39	0.04	0.03	0.14	99.8
Pl		44 / 1 .	439.2515	core	Ol-gabbro	52.22	30.40	12.79	4.18	0.02	0.02	0.15	99.8
Pl		45 / 1 .	439.2515	core	Ol-gabbro	52.26	30.10	12.86	4.30	0.03	0.03	0.12	99.7
Pl		47 / 1 .	439.2515	core	Ol-gabbro	52.05	30.41	12.86	4.34	0.04	0.03	0.14	99.9
Pl	735B_81R5_7	50 / 1 .	439.253	core	Ol-gabbro	52.42	30.26	13.09	4.22	0.03	0.02	0.08	100.1
Pl		57 / 1 .	439.255	core	Ol-gabbro	52.33	30.11	12.97	4.05	0.05	0.04	0.22	99.8
Pl		58 / 1 .	439.257	core	Ol-gabbro	52.76	29.47	12.42	4.50	0.06	0.03	0.10	99.3
Pl		60 / 1 .	439.257	core	Ol-gabbro	53.18	29.73	12.16	4.62	0.04	0.05	0.13	99.9
Pl		61 / 1 .	439.257	core	Ol-gabbro	53.40	29.46	12.09	4.57	0.04	0.03	0.10	99.7
Pl		81 / 1 .	439.2645	core	Ol-gabbro	52.05	30.13	13.19	4.19	0.02	0.04	0.15	99.8

Mineral		Point	Depth (mbsf)	Grain area	Lithology	SiO2	Al2O3	CaO	Na2O	K2O	MgO	FeO	Total
Pl		82 / 1 .	439.262	core	Ol-gabbro	52.29	30.64	13.15	4.06	0.03	0.02	0.11	100.3
Pl		83 / 1 .	439.262	core	Ol-gabbro	51.95	30.76	13.23	4.00	0.04	0.03	0.09	100.1
Pl		7 / 1 .	418.5075	core	Ol-gabbro	51.36	31.06	13.82	3.85	0.05	0.07	0.19	100.4
Pl		25 / 1 .	418.503	core	Ol-gabbro	51.20	31.29	13.61	3.81	0.04	0.01	0.14	100.1
Pl		28 / 1 .	418.503	core	Ol-gabbro	52.32	30.16	12.97	4.22	0.05	0.02	0.09	99.8
Pl		30 / 1 .	418.506	core	Ol-gabbro	47.72	33.35	16.66	2.28	0.01	0.00	0.07	100.1
Pl		42 / 1 .	418.515	core	Ol-gabbro	51.28	30.93	13.78	3.67	0.03	0.01	0.13	99.8
Pl		43 / 1 .	418.515	core	Ol-gabbro	51.48	30.71	13.18	4.02	0.04	0.03	0.07	99.5
Pl	735B_79R3_100	47 / 1 .	418.517	core	Ol-gabbro	52.51	30.10	12.62	4.43	0.05	0.00	0.13	99.8
Pl		48 / 1 .	418.517	core	Ol-gabbro	52.14	30.42	13.30	4.15	0.07	0.03	0.11	100.2
Pl		54 / 1 .	418.524	core	Ol-gabbro	49.36	32.30	15.35	2.93	0.03	0.04	0.12	100.1
Pl		58 / 1 .	418.524	core	Ol-gabbro	51.63	30.85	13.83	3.84	0.03	0.02	0.17	100.4
Pl		59 / 1 .	418.5225	core	Ol-gabbro	51.53	30.77	13.65	3.93	0.05	0.02	0.17	100.1
Pl		65 / 1 .	418.5265	core	Ol-gabbro	51.62	30.62	13.46	3.98	0.04	0.05	0.10	99.9
Pl		74 / 1 .	418.532	core	Ol-gabbro	51.75	30.32	13.24	4.07	0.01	0.03	0.16	99.6
Pl		76 / 1 .	418.532	core	Ol-gabbro	51.87	30.95	13.76	4.07	0.05	0.02	0.08	100.8
Pl		46 / 1 .	397.581	core	Ol-gabbro	52.76	30.03	12.71	4.35	0.04	0.04	0.17	100.1
Pl		50 / 1 .	397.581	core	Ol-gabbro	52.50	30.01	13.15	4.22	0.02	0.00	0.17	100.1
Pl		58 / 1 .	397.583	core	Ol-gabbro	52.35	29.98	13.10	4.03	0.02	0.03	0.23	99.8
Pl		60 / 1 .	397.587	core	Ol-gabbro	52.95	29.74	12.48	4.42	0.04	0.01	0.17	99.8
Pl		62 / 1 .	397.587	core	Ol-gabbro	52.18	30.02	13.09	4.23	0.04	0.03	0.22	99.8
Pl		71 / 1 .	397.5865	core	Ol-gabbro	54.07	29.08	11.70	4.84	0.06	0.01	0.19	100.0
Pl		73 / 1 .	397.5865	core	Ol-gabbro	52.23	30.31	13.23	4.22	0.04	0.01	0.20	100.2
Pl		79 / 1 .	397.5851	core	Ol-gabbro	52.89	29.78	12.70	4.37	0.05	0.02	0.25	100.1
Pl		80 / 1 .	397.5851	core	Ol-gabbro	52.85	29.45	12.18	4.67	0.04	0.02	0.20	99.4
Pl	735B_76R3_96	82 / 1 .	397.5851	core	Ol-gabbro	52.87	29.73	12.56	4.47	0.04	0.00	0.16	99.8
Pl		88 / 1 .	397.576	core	Ol-gabbro	52.49	29.83	12.64	4.28	0.03	0.02	0.14	99.4
Pl		91 / 1 .	397.576	core	Ol-gabbro	52.43	29.80	12.75	4.16	0.03	0.00	0.13	99.3
Pl		100 / 1 .	397.577	core	Ol-gabbro	52.95	29.69	12.27	4.80	0.07	0.01	0.15	99.9
Pl		101 / 1 .	397.577	core	Ol-gabbro	53.46	29.67	12.57	4.60	0.05	0.04	0.14	100.5
Pl		103 / 1 .	397.577	core	Ol-gabbro	52.82	30.02	12.64	4.43	0.03	0.02	0.16	100.1
Pl		109 / 1 .	397.575	core	Ol-gabbro	52.65	29.84	12.65	4.40	0.04	0.05	0.21	99.8
Pl		111 / 1 .	397.5715	core	Ol-gabbro	52.36	29.84	12.56	4.36	0.04	0.00	0.20	99.4
Pl		112 / 1 .	397.5715	core	Ol-gabbro	53.08	29.88	12.61	4.43	0.05	0.00	0.15	100.2
Pl		114 / 1 .	397.5715	core	Ol-gabbro	52.10	29.95	13.07	4.19	0.05	0.02	0.13	99.5
Pl		122 / 1 .	397.5625	core	Ol-gabbro	53.02	30.05	12.88	4.24	0.05	0.01	0.09	100.4
Pl		107 / 1 .	419.1525	core	Ol-gabbro	51.18	31.27	14.06	3.53	0.04	0.01	0.05	100.1
Pl		109 / 1 .	419.1525	core	Ol-gabbro	51.43	31.68	13.96	3.73	0.04	0.00	0.06	100.9
Pl		111 / 1 .	419.1525	core	Ol-gabbro	50.94	31.59	14.20	3.23	0.01	0.03	0.07	100.1

Mineral		Point	Depth (mbsf)	Grain area	Lithology	SiO2	Al2O3	CaO	Na2O	K2O	MgO	FeO	Total
Pl		117 / 1 .	419.157	core	Ol-gabbro	51.34	31.21	14.16	3.56	0.03	0.00	0.04	100.3
Pl		119 / 1 .	419.157	core	Ol-gabbro	50.93	31.36	14.27	3.66	0.00	0.02	0.10	100.3
Pl		120 / 1 .	419.157	core	Ol-gabbro	50.70	31.23	13.99	3.63	0.00	0.03	0.09	99.7
Pl		1 / 1 .	419.159	core	Ol-gabbro	51.27	31.01	13.75	3.49	0.01	0.03	0.08	99.6
Pl		5 / 1 .	419.159	core	Ol-gabbro	51.99	30.83	13.34	3.90	0.02	0.00	0.05	100.1
Pl		26 / 1 .	419.1585	core	Ol-gabbro	50.81	31.53	14.14	3.45	0.06	0.02	0.06	100.1
Pl		31 / 1 .	419.1585	core	Ol-gabbro	51.32	31.00	13.81	3.60	0.00	0.00	0.08	99.8
Pl	735B_79R4_20	32 / 1 .	419.1585	core	Ol-gabbro	50.33	31.58	14.66	3.15	0.00	0.00	0.07	99.8
Pl		44 / 1 .	419.163	core	Ol-gabbro	51.33	31.23	13.92	3.60	0.02	0.03	0.08	100.2
Pl		46 / 1 .	419.163	core	Ol-gabbro	51.65	30.73	13.29	4.01	0.00	0.00	0.04	99.7
Pl		48 / 1 .	419.163	core	Ol-gabbro	51.90	30.97	13.55	3.75	0.03	0.00	0.08	100.3
Pl		56 / 1 .	419.168	core	Ol-gabbro	50.95	31.43	14.04	3.40	0.01	0.00	0.05	99.9
Pl		58 / 1 .	419.168	core	Ol-gabbro	51.57	31.05	13.94	3.68	0.02	0.00	0.08	100.3
Pl		60 / 1 .	419.168	core	Ol-gabbro	51.50	30.90	13.78	3.59	0.03	0.01	0.07	99.9
Pl		75 / 1 .	419.172	core	Ol-gabbro	51.40	31.50	14.06	3.46	0.01	0.01	0.06	100.5
Pl		76 / 1 .	419.172	core	Ol-gabbro	50.53	31.75	14.01	3.37	0.00	0.00	0.07	99.7
Pl		78 / 1 .	419.172	core	Ol-gabbro	51.17	31.22	13.80	3.63	0.02	0.02	0.05	99.9
Pl		83 / 1 .	419.1745	core	Ol-gabbro	51.50	31.17	13.77	3.79	0.00	0.01	0.07	100.3
Pl		85 / 1 .	419.1745	core	Ol-gabbro	50.70	31.85	14.45	3.46	0.03	0.01	0.05	100.5
Pl		93 / 1 .	419.1795	core	Ol-gabbro	52.02	30.34	13.45	4.01	0.02	0.00	0.10	99.9
Pl		8 / 1 .	461.682	core	Ol-gabbro	51.09	31.23	14.18	3.62	0.02	0.04	0.19	100.4
Pl		11 / 1 .	461.682	core	Ol-gabbro	51.55	31.04	13.75	3.77	0.04	0.02	0.12	100.3
Pl		13 / 1 .	461.684	core	Ol-gabbro	51.79	30.63	13.63	3.83	0.05	0.00	0.05	100.0
Pl		22 / 1 .	461.6975	core	Ol-gabbro	51.53	30.55	13.12	4.09	0.11	0.00	0.09	99.5
Pl		23 / 1 .	461.6975	core	Ol-gabbro	50.99	31.74	14.77	3.41	0.05	0.02	0.09	101.1
Pl		24 / 1 .	461.6975	core	Ol-gabbro	48.82	33.20	16.10	2.45	0.00	0.01	0.11	100.7
Pl		26 / 1 .	461.6975	core	Ol-gabbro	52.92	30.12	12.47	4.40	0.05	0.00	0.08	100.0
Pl		36 / 1 .	461.7005	core	Ol-gabbro	51.31	31.57	14.55	3.47	0.04	0.03	0.11	101.1
Pl		38 / 1 .	461.7005	core	Ol-gabbro	50.27	31.95	14.87	3.11	0.02	0.01	0.06	100.3
Pl		41 / 1 .	461.7005	core	Ol-gabbro	48.35	33.23	16.29	2.20	0.03	0.03	0.10	100.2
Pl		48 / 1 .	461.6995	core	Ol-gabbro	48.05	33.36	16.69	2.05	0.01	0.01	0.18	100.3
Pl		57 / 1 .	461.7015	core	Ol-gabbro	52.30	30.63	13.39	4.22	0.04	0.02	0.09	100.7
Pl		59 / 1 .	461.7015	core	Ol-gabbro	50.16	31.95	14.92	3.23	0.03	0.03	0.10	100.4
Pl	735B_83R7_43B	68 / 1 .	461.6925	core	Ol-gabbro	49.27	32.66	15.45	2.81	0.05	0.00	0.08	100.3
Pl		70 / 1 .	461.6905	core	Ol-gabbro	49.67	32.54	15.26	2.92	0.00	0.00	0.26	100.7
Pl		72 / 1 .	461.6905	core	Ol-gabbro	51.20	31.45	14.22	3.45	0.02	0.01	0.06	100.4
Pl		80 / 1 .	461.6875	core	Ol-gabbro	51.11	31.00	14.05	3.66	0.03	0.02	0.09	100.0
Pl		82 / 1 .	461.6875	core	Ol-gabbro	47.85	33.25	16.62	2.10	0.00	0.00	0.12	99.9
Pl		86 / 1 .	461.684	core	Ol-gabbro	52.49	30.22	12.78	4.16	0.10	0.07	0.11	99.9

Mineral		Point	Depth (mbsf)	Grain area	Lithology	SiO2	Al2O3	CaO	Na2O	K2O	MgO	FeO	Total
Pl		87 / 1 .	461.684	core	Ol-gabbro	57.79	27.09	9.10	6.38	0.14	0.00	0.05	100.6
Pl		90 / 1 .	461.684	core	Ol-gabbro	50.56	31.50	14.52	3.31	0.03	0.00	0.14	100.1
Pl		99 / 1 .	461.6905	core	Ol-gabbro	50.81	31.44	14.41	3.46	0.01	0.02	0.09	100.2
Pl		108 / 1 .	461.6885	core	Ol-gabbro	50.11	31.87	14.83	3.13	0.02	0.03	0.09	100.1
Pl		109 / 1 .	461.6885	core	Ol-gabbro	51.47	31.14	13.92	3.71	0.01	0.00	0.13	100.4
Pl		9 / 1 .	425.9865	core	Ol-gabbro	49.06	32.65	15.74	2.66	0.02	0.00	0.11	100.2
Pl		13 / 1 .	425.9865	core	Ol-gabbro	49.95	31.81	15.09	3.05	0.05	0.02	0.08	100.0
Pl		14 / 1 .	425.9865	core	Ol-gabbro	50.29	31.68	14.64	3.27	0.05	0.04	0.09	100.1
Pl		24 / 1 .	425.9915	core	Ol-gabbro	51.03	30.78	14.08	3.64	0.02	0.00	0.08	99.6
Pl		26 / 1 .	425.9915	core	Ol-gabbro	51.26	31.20	14.14	3.61	0.00	0.04	0.10	100.3
Pl		29 / 1 .	425.9915	core	Ol-gabbro	51.25	31.39	14.05	3.55	0.01	0.01	0.06	100.3
Pl		42 / 1 .	425.9985	core	Ol-gabbro	51.34	30.67	13.49	3.72	0.04	0.05	0.16	99.5
Pl		44 / 1 .	425.9985	core	Ol-gabbro	51.86	30.51	13.19	3.92	0.00	0.03	0.09	99.6
Pl		45 / 1 .	425.9985	core	Ol-gabbro	49.45	32.27	15.35	2.86	0.04	0.01	0.05	100.0
Pl		47 / 1 .	425.9985	core	Ol-gabbro	51.35	30.91	13.47	3.78	0.04	0.02	0.08	99.7
Pl	735B_80R2_51	61 / 1 .	425.9935	core	Ol-gabbro	50.67	31.11	14.43	3.54	0.03	0.04	0.10	99.9
Pl		62 / 1 .	425.9935	core	Ol-gabbro	51.74	30.53	13.52	3.93	0.02	0.00	0.10	99.8
Pl		63 / 1 .	425.9935	core	Ol-gabbro	51.74	30.96	13.39	3.96	0.07	0.03	0.10	100.2
Pl		65 / 1 .	425.9935	core	Ol-gabbro	50.10	31.33	14.50	3.29	0.01	0.03	0.13	99.4
Pl		66 / 1 .	425.996	core	Ol-gabbro	51.35	30.98	13.85	3.71	0.02	0.03	0.13	100.1
Pl		68 / 1 .	425.996	core	Ol-gabbro	50.51	31.63	14.43	3.27	0.02	0.02	0.07	100.0
Pl		71 / 1 .	425.996	core	Ol-gabbro	49.45	32.39	15.39	2.83	0.03	0.02	0.09	100.2
Pl		72 / 1 .	425.996	core	Ol-gabbro	51.75	30.91	13.34	3.70	0.04	0.03	0.04	99.8
Pl		87 / 1 .	426.002	core	Ol-gabbro	51.64	30.54	13.74	4.04	0.03	0.02	0.15	100.2
Pl		88 / 1 .	426.002	core	Ol-gabbro	45.98	34.57	17.94	1.36	0.03	0.03	0.11	100.0
Pl		90 / 1 .	426.002	core	Ol-gabbro	51.90	30.74	13.20	3.92	0.03	0.03	0.05	99.9
Pl		8	509.49	core	Ol-gabbro	49.87	31.12	14.93	3.85	0.03	0.02	0.20	100.1
Pl		14	509.49	core	Ol-gabbro	49.91	30.89	14.67	3.99	0.04	0.03	0.21	99.8
Pl		25	509.49	core	Ol-gabbro	49.64	31.13	14.92	3.82	0.03	0.12	0.27	99.9
Pl		32	509.49	core	Ol-gabbro	50.14	31.11	14.70	3.86	0.04	0.04	0.14	100.1
Pl	90R-2W-18-20	40	509.49	core	Ol-gabbro	48.19	32.52	16.32	3.16	0.03	0.00	0.15	100.5
Pl		41	509.49	core	Ol-gabbro	50.14	31.24	14.73	4.12	0.04	0.05	0.13	100.5
Pl		48	509.49	core	Ol-gabbro	50.39	31.25	14.66	3.93	0.02	0.02	0.14	100.5
Pl		52	509.49	core	Ol-gabbro	50.65	31.18	14.77	3.78	0.04	0.02	0.18	100.7
Pl		63	509.49	core	Ol-gabbro	50.68	31.05	14.58	4.12	0.03	0.02	0.10	100.6
Pl		64	509.49	core	Ol-gabbro	49.43	32.01	15.62	3.47	0.03	0.00	0.16	100.8
Pl		78	510.1	core	Ol-gabbro	47.29	33.10	17.42	2.40	0.02	0.01	0.23	100.5
Pl		79	510.1	core	Ol-gabbro	47.38	33.23	17.40	2.46	0.02	0.02	0.26	100.8
Pl		87	510.1	core	Ol-gabbro	50.20	31.17	14.96	4.01	0.05	0.03	0.27	100.7

Mineral		Point	Depth (mbsf)	Grain area	Lithology	SiO2	Al2O3	CaO	Na2O	K2O	MgO	FeO	Total
Pl	90R-2W-82-86	89	510.1	core	Ol-gabbro	49.83	31.46	15.24	3.55	0.03	0.02	0.13	100.3
Pl		97	510.1	core	Ol-gabbro	48.32	32.52	16.43	3.07	0.02	0.00	0.08	100.4
Pl		103	510.1	core	Ol-gabbro	50.51	31.11	14.67	4.06	0.04	0.00	0.17	100.6
Pl		108	510.1	core	Ol-gabbro	50.56	30.89	14.62	3.90	0.15	0.00	0.15	100.4
Pl		118	510.1	core	Ol-gabbro	48.81	32.32	16.19	3.19	0.03	0.02	0.12	100.7
Pl		120	510.1	core	Ol-gabbro	49.93	31.53	15.17	3.89	0.04	0.00	0.17	100.8
Pl		127	510.1	core	Ol-gabbro	48.59	32.60	16.29	3.06	0.04	0.02	0.16	100.8
Pl		136	510.1	core	Ol-gabbro	48.41	32.65	16.36	3.02	0.03	0.02	0.18	100.7
Pl	90R-2W-84-90	140	510.17	core	Ol-gabbro	50.58	31.32	14.83	3.76	0.04	0.08	0.27	100.9
Pl		147	510.17	core	Ol-gabbro	48.34	32.83	16.66	2.82	0.02	0.02	0.19	100.9
Pl		148	510.17	core	Ol-gabbro	49.77	31.71	15.34	3.76	0.04	0.02	0.17	100.9
Pl		149	510.17	core	Ol-gabbro	49.94	31.61	15.08	3.61	0.04	0.08	0.31	100.8
Pl		202	510.17	core	Ol-gabbro	48.42	32.31	16.44	3.21	0.02	0.03	0.18	100.7
Pl		217	510.17	core	Ol-gabbro	49.37	31.69	15.47	3.41	0.03	0.01	0.17	100.2
Pl	90R-2W-94-100b	2	510.27	core	Ol-gabbro	50.70	30.96	13.64	3.91	0.03	0.01	0.13	99.4
Pl		11	510.27	core	Ol-gabbro	50.34	31.40	14.05	3.87	0.03	0.02	0.19	99.9
Pl		15	510.27	core	Ol-gabbro	49.13	32.16	15.26	3.43	0.03	0.00	0.13	100.2
Pl		17	510.27	core	Ol-gabbro	48.90	32.44	15.30	3.34	0.03	0.03	0.11	100.2
Pl		19	510.27	core	Ol-gabbro	48.87	32.72	15.56	3.10	0.02	0.00	0.12	100.5
Pl		22	510.27	core	Ol-gabbro	48.81	32.28	15.28	3.32	0.02	0.00	0.11	99.9
Pl		31	510.27	core	Ol-gabbro	50.28	31.04	13.97	4.19	0.02	0.05	0.24	99.9
Pl		37	510.27	core	Ol-gabbro	50.37	30.99	13.86	4.03	0.03	0.03	0.24	99.6
Pl		38	510.27	core	Ol-gabbro	48.98	31.86	15.33	3.20	0.02	0.02	0.16	99.6
Pl		44	510.27	core	Ol-gabbro	47.70	32.79	16.07	2.75	0.03	0.08	0.36	99.8
Pl		58	510.27	core	Ol-gabbro	45.99	34.40	17.66	1.71	0.01	0.03	0.22	100.0
Pl		63	510.27	core	Ol-gabbro	49.68	31.61	14.55	3.55	0.03	0.02	0.12	99.6
Pl		65	510.27	core	Ol-gabbro	48.72	32.21	15.47	3.12	0.01	0.01	0.13	99.7
Pl		67	510.27	core	Ol-gabbro	50.33	31.29	14.24	3.80	0.04	0.04	0.15	99.9
Pl		7	510.27	core	Ol-gabbro	50.16	31.56	14.34	3.70	0.02	0.06	0.13	100.0
Pl		9	510.27	core	Ol-gabbro	50.51	31.10	13.95	4.00	0.04	0.03	0.13	99.8
Pl	90R-2W-123-129	77	510.56	core	Ol-gabbro	49.18	32.07	15.14	3.26	0.02	0.02	0.11	99.9
Pl		87	510.56	core	Ol-gabbro	48.06	32.85	16.03	2.74	0.02	0.04	0.12	99.9
Pl		92	510.56	core	Ol-gabbro	49.32	32.39	15.18	3.26	0.04	0.03	0.13	100.4
Pl		107	510.56	core	Ol-gabbro	48.93	32.32	15.29	3.09	0.03	0.02	0.09	99.8
Pl		109	510.56	core	Ol-gabbro	48.33	32.68	15.98	2.80	0.02	0.02	0.13	100.0
Pl		110	510.56	core	Ol-gabbro	46.66	33.82	17.13	2.21	0.01	0.01	0.11	100.0
Pl		129	510.56	core	Ol-gabbro	48.67	32.27	15.39	3.17	0.03	0.01	0.13	99.7
Pl		135	510.56	core	Ol-gabbro	50.66	31.27	14.11	3.93	0.04	0.02	0.16	100.2
Pl		143	510.67	core	Ol-gabbro	49.21	32.23	15.21	3.23	0.03	0.15	0.20	100.3

Mineral		Point	Depth (mbsf)	Grain area	Lithology	SiO2	Al2O3	CaO	Na2O	K2O	MgO	FeO	Total
Pl		178	510.67	core	Ol-gabbro	50.11	31.46	14.38	3.73	0.03	0.12	0.40	100.3
Pl		179	510.67	core	Ol-gabbro	50.19	31.26	14.32	3.89	0.05	0.04	0.27	100.1
Pl		209	510.67	core	Ol-gabbro	49.48	31.72	15.10	3.15	0.02	0.03	0.23	99.8
Pl		14	510.84	core	Ol-gabbro	48.79	32.41	15.35	3.16	0.02	0.04	0.12	100.0
Pl		16	510.84	core	Ol-gabbro	49.61	31.74	14.65	3.53	0.03	0.02	0.13	99.7
Pl		18	510.84	core	Ol-gabbro	50.50	31.44	14.26	3.66	0.04	0.02	0.19	100.2
Pl		24	510.84	core	Ol-gabbro	50.51	31.16	14.06	3.82	0.06	0.20	0.21	100.1
Pl		28	510.84	core	Ol-gabbro	49.96	31.59	14.61	3.75	0.03	0.04	0.12	100.1
Pl		32	510.84	core	Ol-gabbro	49.46	31.78	14.94	3.21	0.03	0.01	0.14	99.6
Pl	90R-3W-6-8	37	510.84	core	Ol-gabbro	50.11	31.50	14.48	3.74	0.03	0.04	0.13	100.1
Pl		44	510.84	core	Ol-gabbro	47.73	31.94	15.90	2.91	0.03	0.09	0.13	98.8
Pl		50	510.84	core	Ol-gabbro	47.68	32.94	16.23	2.68	0.01	0.01	0.16	99.7
Pl		51	510.84	core	Ol-gabbro	47.88	32.86	16.08	2.83	0.02	0.03	0.15	99.9
Pl		58	510.84	core	Ol-gabbro	48.17	32.64	15.84	2.84	0.02	0.03	0.14	99.7
Pl		62	510.84	core	Ol-gabbro	49.30	32.07	15.06	3.40	0.01	0.00	0.06	99.9
Pl		65	510.84	core	Ol-gabbro	49.88	31.50	14.48	3.77	0.03	0.02	0.18	99.9
Pl		70	510.84	core	Ol-gabbro	49.24	32.07	14.92	3.38	0.02	0.01	0.16	99.9
Pl		91 / 1 .	425.363	rim	Ol-gabbro	59.44	25.54	7.39	7.32	0.12	0.00	0.14	100.0
Pl		103 / 1 .	425.3695	rim	Ol-gabbro	58.82	26.02	8.00	7.26	0.08	0.00	0.25	100.4
Pl		114 / 1 .	425.372	rim	Ol-gabbro	58.70	26.34	7.98	7.08	0.07	0.01	0.19	100.4
Pl		117 / 1 .	425.372	rim	Ol-gabbro	56.06	27.78	9.92	5.95	0.04	0.00	0.21	100.0
Pl		120 / 1 .	425.3735	rim	Ol-gabbro	50.94	30.42	13.67	3.97	0.03	0.01	0.15	99.2
Pl		123 / 1 .	425.3735	rim	Ol-gabbro	50.21	31.43	14.55	3.30	0.05	0.01	0.15	99.7
Pl		131 / 1 .	425.3795	rim	Ol-gabbro	50.93	31.41	13.80	3.81	0.04	0.02	0.08	100.1
Pl		134 / 1 .	425.3795	rim	Ol-gabbro	50.60	31.10	14.12	3.58	0.04	0.00	0.04	99.5
Pl		135 / 1 .	425.3795	rim	Ol-gabbro	49.52	32.19	14.96	3.09	0.03	0.00	0.19	100.0
Pl	735B_80R1_136	141 / 1 .	425.3815	rim	Ol-gabbro	50.03	31.78	15.01	3.28	0.04	0.01	0.11	100.3
Pl		147 / 1 .	425.384	rim	Ol-gabbro	50.43	31.40	14.18	3.51	0.09	0.07	0.14	99.8
Pl		148 / 1 .	425.3835	rim	Ol-gabbro	50.56	31.13	14.23	3.46	0.04	0.00	0.13	99.5
Pl		157 / 1 .	425.39	rim	Ol-gabbro	49.09	32.33	15.15	2.94	0.02	0.00	0.06	99.6
Pl		160 / 1 .	425.389	rim	Ol-gabbro	47.92	33.09	16.63	2.22	0.01	0.00	0.10	100.0
Pl		161 / 1 .	425.389	rim	Ol-gabbro	51.21	30.93	13.78	3.77	0.03	0.00	0.09	99.8
Pl		162 / 1 .	425.389	rim	Ol-gabbro	51.17	30.90	13.79	3.66	0.05	0.03	0.13	99.7
Pl		164 / 1 .	425.389	rim	Ol-gabbro	48.68	32.46	15.56	2.63	0.03	0.01	0.08	99.4
Pl		170 / 1 .	425.3865	rim	Ol-gabbro	49.89	32.07	15.09	3.20	0.02	0.01	0.11	100.4
Pl		9 / 1 .	439.2455	rim	Ol-gabbro	49.88	32.19	14.68	3.23	0.00	0.00	0.07	100.0
Pl		13 / 1 .	439.246	rim	Ol-gabbro	52.39	30.06	12.81	4.16	0.05	0.00	0.10	99.6
Pl		31 / 1 .	439.2465	rim	Ol-gabbro	50.00	31.91	14.74	3.21	0.03	0.04	0.13	100.1
Pl		32 / 1 .	439.2465	rim	Ol-gabbro	49.70	32.03	14.95	3.11	0.01	0.01	0.13	99.9

Mineral		Point	Depth (mbsf)	Grain area	Lithology	SiO2	Al2O3	CaO	Na2O	K2O	MgO	FeO	Total
Pl		33 / 1 .	439.2465	rim	Ol-gabbro	50.00	31.91	14.76	3.12	0.04	0.02	0.10	99.9
Pl	735B_81R5_7	46 / 1 .	439.2515	rim	Ol-gabbro	52.41	29.96	12.90	4.20	0.03	0.03	0.13	99.7
Pl		48 / 1 .	439.253	rim	Ol-gabbro	52.81	30.17	12.56	4.32	0.01	0.03	0.11	100.0
Pl		49 / 1 .	439.253	rim	Ol-gabbro	52.48	29.98	12.62	4.47	0.05	0.01	0.10	99.7
Pl		59 / 1 .	439.257	rim	Ol-gabbro	52.33	30.01	13.06	4.17	0.04	0.01	0.08	99.7
Pl		62 / 1 .	439.257	rim	Ol-gabbro	53.06	29.35	12.24	4.46	0.04	0.02	0.18	99.3
Pl		73 / 1 .	439.2645	rim	Ol-gabbro	52.96	30.01	12.56	4.63	0.04	0.02	0.10	100.3
Pl		74 / 1 .	439.2645	rim	Ol-gabbro	52.79	30.30	12.82	4.35	0.03	0.03	0.13	100.5
Pl		84 / 1 .	439.262	rim	Ol-gabbro	53.14	29.51	12.08	4.53	0.04	0.03	0.13	99.5
Pl		6 / 1 .	418.5075	rim	Ol-gabbro	51.36	30.68	13.82	3.76	0.03	0.03	0.08	99.8
Pl		8 / 1 .	418.5075	rim	Ol-gabbro	49.82	32.08	15.12	3.23	0.02	0.03	0.11	100.4
Pl		26 / 1 .	418.503	rim	Ol-gabbro	50.59	31.41	14.24	3.40	0.03	0.07	0.33	100.1
Pl		27 / 1 .	418.503	rim	Ol-gabbro	51.98	30.68	13.37	4.15	0.04	0.02	0.07	100.3
Pl		29 / 1 .	418.503	rim	Ol-gabbro	51.35	30.70	13.95	3.75	0.03	0.00	0.10	99.9
Pl		41 / 1 .	418.515	rim	Ol-gabbro	51.42	30.56	13.52	3.99	0.05	0.03	0.10	99.7
Pl	735B_79R3_100	44 / 1 .	418.515	rim	Ol-gabbro	51.54	30.87	13.79	4.00	0.03	0.04	0.16	100.4
Pl		55 / 1 .	418.524	rim	Ol-gabbro	49.40	32.38	15.22	2.93	0.05	0.00	0.13	100.1
Pl		56 / 1 .	418.524	rim	Ol-gabbro	52.60	30.18	13.15	4.17	0.02	0.04	0.19	100.3
Pl		57 / 1 .	418.524	rim	Ol-gabbro	52.21	30.37	12.93	4.29	0.03	0.02	0.14	100.0
Pl		64 / 1 .	418.5265	rim	Ol-gabbro	51.01	30.83	13.77	3.68	0.02	0.04	0.17	99.5
Pl		66 / 1 .	418.5265	rim	Ol-gabbro	51.05	31.29	14.11	3.41	0.03	0.04	0.10	100.0
Pl		73 / 1 .	418.532	rim	Ol-gabbro	51.66	30.88	13.89	3.95	0.01	0.03	0.08	100.5
Pl		75 / 1 .	418.532	rim	Ol-gabbro	51.37	30.49	13.60	3.99	0.02	0.06	0.17	99.7
Pl		47 / 1 .	397.581	rim	Ol-gabbro	52.74	30.02	12.79	4.50	0.07	0.03	0.16	100.3
Pl		48 / 1 .	397.581	rim	Ol-gabbro	53.93	29.72	12.17	4.59	0.04	0.02	0.11	100.6
Pl		49 / 1 .	397.581	rim	Ol-gabbro	53.08	29.73	12.86	4.40	0.05	0.04	0.21	100.4
Pl		57 / 1 .	397.583	rim	Ol-gabbro	53.03	29.88	12.43	4.43	0.04	0.03	0.14	100.0
Pl		59 / 1 .	397.587	rim	Ol-gabbro	50.59	31.09	14.09	3.45	0.02	0.00	0.23	99.5
Pl		61 / 1 .	397.587	rim	Ol-gabbro	53.50	29.18	12.21	4.76	0.02	0.01	0.17	99.9
Pl		70 / 1 .	397.5865	rim	Ol-gabbro	53.06	30.42	12.75	4.37	0.04	0.04	0.17	100.9
Pl	735B_76R3_96	72 / 1 .	397.5865	rim	Ol-gabbro	53.02	29.50	12.40	4.41	0.02	0.03	0.18	99.6
Pl		81 / 1 .	397.5851	rim	Ol-gabbro	53.16	29.32	11.95	4.56	0.04	0.07	0.28	99.4
Pl		89 / 1 .	397.576	rim	Ol-gabbro	52.94	29.95	12.59	4.46	0.02	0.01	0.14	100.1
Pl		90 / 1 .	397.576	rim	Ol-gabbro	53.09	29.59	12.23	4.44	0.06	0.02	0.25	99.7
Pl		102 / 1 .	397.577	rim	Ol-gabbro	52.80	29.83	12.38	4.42	0.04	0.04	0.24	99.8
Pl		108 / 1 .	397.575	rim	Ol-gabbro	52.74	29.55	12.54	4.54	0.06	0.01	0.17	99.6
Pl		113 / 1 .	397.5715	rim	Ol-gabbro	53.08	29.97	12.71	4.28	0.03	0.03	0.21	100.3
Pl		121 / 1 .	397.5625	rim	Ol-gabbro	53.16	29.82	12.36	4.36	0.05	0.02	0.17	99.9
Pl		108 / 1 .	419.1525	rim	Ol-gabbro	50.70	32.00	14.20	3.41	0.03	0.00	0.06	100.4

Mineral		Point	Depth (mbsf)	Grain area	Lithology	SiO2	Al2O3	CaO	Na2O	K2O	MgO	FeO	Total
Pl		110 / 1 .	419.1525	rim	Ol-gabbro	51.12	31.37	14.53	3.40	0.00	0.00	0.07	100.5
Pl		116 / 1 .	419.157	rim	Ol-gabbro	51.87	31.08	13.89	3.91	0.02	0.00	0.10	100.9
Pl		118 / 1 .	419.157	rim	Ol-gabbro	51.49	31.25	13.99	3.43	0.03	0.00	0.06	100.3
Pl		2 / 1 .	419.159	rim	Ol-gabbro	50.96	31.37	14.05	3.48	0.02	0.00	0.09	100.0
Pl		4 / 1 .	419.159	rim	Ol-gabbro	51.73	31.14	13.52	3.68	0.00	0.01	0.03	100.1
Pl		27 / 1 .	419.1585	rim	Ol-gabbro	49.81	31.96	15.30	2.88	0.01	0.02	0.14	100.1
Pl	735B_79R4_20	29 / 1 .	419.1585	rim	Ol-gabbro	52.15	30.70	13.33	4.15	0.04	0.01	0.05	100.4
Pl		30 / 1 .	419.1585	rim	Ol-gabbro	51.96	30.66	13.34	3.99	0.01	0.01	0.10	100.1
Pl		45 / 1 .	419.163	rim	Ol-gabbro	51.12	31.11	14.01	3.53	0.00	0.02	0.09	99.9
Pl		47 / 1 .	419.163	rim	Ol-gabbro	49.47	32.41	15.28	2.78	0.02	0.00	0.03	100.0
Pl		49 / 1 .	419.163	rim	Ol-gabbro	51.90	30.29	13.50	3.79	0.01	0.00	0.08	99.6
Pl		57 / 1 .	419.168	rim	Ol-gabbro	50.84	31.54	14.31	3.80	0.04	0.03	0.09	100.7
Pl		59 / 1 .	419.168	rim	Ol-gabbro	51.59	30.96	13.60	3.83	0.02	0.02	0.04	100.0
Pl		73 / 1 .	419.172	rim	Ol-gabbro	51.34	31.32	13.57	3.70	0.02	0.00	0.10	100.1
Pl		74 / 1 .	419.172	rim	Ol-gabbro	51.83	30.70	13.32	3.99	0.02	0.01	0.01	99.9
Pl		77 / 1 .	419.172	rim	Ol-gabbro	51.13	31.35	14.02	3.63	0.03	0.02	0.03	100.2
Pl		84 / 1 .	419.1745	rim	Ol-gabbro	51.51	30.75	13.23	4.06	0.03	0.03	0.04	99.6
Pl		7 / 1 .	461.682	rim	Ol-gabbro	51.69	30.94	13.92	3.83	0.01	0.00	0.10	100.5
Pl		9 / 1 .	461.682	rim	Ol-gabbro	50.09	32.15	15.18	3.04	0.03	0.01	0.07	100.6
Pl		10 / 1 .	461.682	rim	Ol-gabbro	49.13	32.74	15.76	2.68	0.03	0.00	0.08	100.4
Pl		12 / 1 .	461.682	rim	Ol-gabbro	50.92	31.87	14.16	3.28	0.00	0.02	0.13	100.4
Pl		14 / 1 .	461.684	rim	Ol-gabbro	50.96	31.84	14.28	3.50	0.02	0.02	0.12	100.7
Pl		20 / 1 .	461.6975	rim	Ol-gabbro	50.28	32.29	14.94	3.04	0.00	0.01	0.04	100.6
Pl		21 / 1 .	461.6975	rim	Ol-gabbro	51.91	31.03	13.57	4.00	0.00	0.01	0.08	100.6
Pl		25 / 1 .	461.6975	rim	Ol-gabbro	49.88	32.18	14.94	3.05	0.03	0.04	0.05	100.2
Pl		37 / 1 .	461.7005	rim	Ol-gabbro	49.86	32.38	15.25	2.97	0.06	0.05	0.10	100.7
Pl		39 / 1 .	461.7005	rim	Ol-gabbro	50.37	32.29	14.97	3.03	0.04	0.05	0.14	100.9
Pl	735B_83R7_43B	40 / 1 .	461.7005	rim	Ol-gabbro	50.80	31.80	14.53	3.41	0.00	0.00	0.14	100.7
Pl		47 / 1 .	461.6995	rim	Ol-gabbro	52.25	30.49	13.26	4.06	0.03	0.02	0.08	100.2
Pl		58 / 1 .	461.7015	rim	Ol-gabbro	49.83	32.46	15.14	2.99	0.03	0.00	0.10	100.5
Pl		67 / 1 .	461.6925	rim	Ol-gabbro	51.78	31.17	13.58	3.97	0.03	0.01	0.13	100.7
Pl		71 / 1 .	461.6905	rim	Ol-gabbro	50.15	31.94	14.99	3.15	0.04	0.01	0.06	100.3
Pl		79 / 1 .	461.6875	rim	Ol-gabbro	52.20	30.73	13.39	4.07	0.05	0.02	0.07	100.5
Pl		81 / 1 .	461.6875	rim	Ol-gabbro	51.19	31.20	14.22	3.58	0.03	0.01	0.15	100.4
Pl		85 / 1 .	461.684	rim	Ol-gabbro	50.94	31.41	14.36	3.55	0.05	0.02	0.08	100.4
Pl		88 / 1 .	461.684	rim	Ol-gabbro	51.76	30.77	13.41	3.81	0.03	0.00	0.11	99.9
Pl		89 / 1 .	461.684	rim	Ol-gabbro	52.30	30.44	12.65	4.34	0.06	0.01	0.05	99.8
Pl		98 / 1 .	461.6905	rim	Ol-gabbro	50.89	31.41	14.21	3.42	0.03	0.00	0.08	100.0
Pl		107 / 1 .	461.6885	rim	Ol-gabbro	50.67	31.69	14.63	3.33	0.01	0.02	0.15	100.5

Mineral		Point	Depth (mbsf)	Grain area	Lithology	SiO2	Al2O3	CaO	Na2O	K2O	MgO	FeO	Total
Pl		10 / 1 .	425.9865	rim	Ol-gabbro	50.52	30.88	14.18	3.56	0.02	0.05	0.09	99.3
Pl		11 / 1 .	425.9865	rim	Ol-gabbro	50.33	31.64	14.61	3.23	0.03	0.04	0.17	100.0
Pl		12 / 1 .	425.9865	rim	Ol-gabbro	50.11	31.71	14.77	3.21	0.05	0.02	0.07	99.9
Pl		25 / 1 .	425.9915	rim	Ol-gabbro	51.48	30.85	13.74	3.65	0.02	0.02	0.07	99.8
Pl		27 / 1 .	425.9915	rim	Ol-gabbro	50.90	30.95	13.91	3.64	0.04	0.00	0.11	99.6
Pl		28 / 1 .	425.9915	rim	Ol-gabbro	51.67	31.17	13.83	3.94	0.03	0.02	0.08	100.7
Pl	735B_80R2_51	43 / 1 .	425.9985	rim	Ol-gabbro	51.30	30.76	13.78	3.69	0.05	0.02	0.22	99.8
Pl		46 / 1 .	425.9985	rim	Ol-gabbro	51.82	30.58	13.63	3.88	0.07	0.04	0.10	100.1
Pl		64 / 1 .	425.9935	rim	Ol-gabbro	51.41	30.89	13.42	3.85	0.02	0.03	0.17	99.8
Pl		67 / 1 .	425.996	rim	Ol-gabbro	52.11	30.30	13.33	3.95	0.04	0.03	0.08	99.8
Pl		69 / 1 .	425.996	rim	Ol-gabbro	50.57	31.62	14.21	3.45	0.05	0.01	0.31	100.2
Pl		70 / 1 .	425.996	rim	Ol-gabbro	51.53	30.89	13.73	3.76	0.04	0.02	0.09	100.1
Pl		89 / 1 .	426.002	rim	Ol-gabbro	51.49	30.94	13.72	3.77	0.02	0.01	0.10	100.0
Pl		7	509.49	rim	Ol-gabbro	47.80	32.68	16.37	2.89	0.02	0.01	0.15	100.0
Pl		9	509.49	rim	Ol-gabbro	48.74	32.16	15.82	3.41	0.02	0.00	0.15	100.3
Pl		13	509.49	rim	Ol-gabbro	50.06	31.27	14.68	3.83	0.04	0.03	0.18	100.1
Pl		17	509.49	rim	Ol-gabbro	49.44	31.94	15.54	3.55	0.03	0.01	0.14	100.7
Pl		24	509.49	rim	Ol-gabbro	50.02	31.16	14.97	3.94	0.03	0.02	0.18	100.4
Pl		26	509.49	rim	Ol-gabbro	49.27	31.68	15.33	3.66	0.03	0.04	0.19	100.3
Pl		31	509.49	rim	Ol-gabbro	50.00	31.30	14.83	3.94	0.02	0.03	0.16	100.4
Pl	90R-2W-18-20	33	509.49	rim	Ol-gabbro	49.28	31.93	15.57	3.46	0.03	0.01	0.15	100.4
Pl		39	509.49	rim	Ol-gabbro	48.76	32.15	16.01	3.34	0.03	0.01	0.17	100.5
Pl		42	509.49	rim	Ol-gabbro	49.92	31.38	15.14	3.78	0.04	0.04	0.26	100.6
Pl		47	509.49	rim	Ol-gabbro	50.44	30.97	14.47	3.98	0.03	0.03	0.18	100.1
Pl		49	509.49	rim	Ol-gabbro	50.74	30.82	14.43	3.99	0.02	0.00	0.14	100.2
Pl		51	509.49	rim	Ol-gabbro	48.72	32.45	16.06	3.14	0.01	0.00	0.08	100.5
Pl		59	509.49	rim	Ol-gabbro	49.02	31.66	15.41	3.51	0.02	0.05	0.19	99.9
Pl		62	509.49	rim	Ol-gabbro	48.71	32.27	16.01	3.29	0.03	0.02	0.12	100.6
Pl		65	509.49	rim	Ol-gabbro	48.54	32.20	16.06	3.25	0.03	0.02	0.22	100.3
Pl		66	510.1	rim	Ol-gabbro	50.08	29.45	13.12	3.48	0.04	2.55	0.44	99.2
Pl		88	510.1	rim	Ol-gabbro	48.50	32.30	16.27	3.06	0.03	0.00	0.16	100.4
Pl		96	510.1	rim	Ol-gabbro	46.24	33.86	18.05	2.13	0.01	0.01	0.20	100.5
Pl	90R-2W-82-86	102	510.1	rim	Ol-gabbro	48.07	32.80	16.66	2.87	0.03	0.00	0.11	100.6
Pl		107	510.1	rim	Ol-gabbro	48.97	32.27	16.07	3.24	0.02	0.01	0.13	100.8
Pl		119	510.1	rim	Ol-gabbro	47.35	32.76	17.05	2.59	0.02	0.05	0.14	100.0
Pl		121	510.1	rim	Ol-gabbro	50.30	31.44	14.85	3.89	0.04	0.00	0.16	100.7
Pl		135	510.1	rim	Ol-gabbro	49.49	31.77	15.45	3.67	0.04	0.02	0.13	100.6
Pl		139	510.17	rim	Ol-gabbro	48.87	32.00	15.89	3.29	0.02	0.02	0.14	100.3
Pl		141	510.17	rim	Ol-gabbro	48.77	32.41	16.06	3.17	0.03	0.02	0.18	100.7

Mineral		Point	Depth (mbsf)	Grain area	Lithology	SiO2	Al2O3	CaO	Na2O	K2O	MgO	FeO	Total
Pl	90R-2W-84-90	155	510.17	rim	Ol-gabbro	48.55	32.40	16.29	3.06	0.01	0.00	0.15	100.5
Pl		196	510.17	rim	Ol-gabbro	49.08	32.31	16.02	3.15	0.01	0.04	0.14	100.8
Pl		210	510.17	rim	Ol-gabbro	49.24	31.87	15.69	3.45	0.02	0.01	0.12	100.4
Pl		216	510.17	rim	Ol-gabbro	49.33	31.96	15.58	3.51	0.03	0.03	0.19	100.6
Pl	90R-2W-94-100b	1	510.27	rim	Ol-gabbro	47.36	33.36	16.37	2.57	0.01	0.00	0.17	99.9
Pl		10	510.27	rim	Ol-gabbro	49.09	32.55	15.31	3.22	0.03	0.00	0.14	100.3
Pl		14	510.27	rim	Ol-gabbro	48.45	32.75	15.73	3.04	0.02	0.00	0.14	100.2
Pl		16	510.27	rim	Ol-gabbro	49.25	32.31	15.04	3.36	0.02	0.00	0.11	100.1
Pl		18	510.27	rim	Ol-gabbro	49.18	32.38	15.25	3.31	0.03	0.00	0.16	100.4
Pl		23	510.27	rim	Ol-gabbro	49.02	32.41	15.36	3.21	0.01	0.02	0.12	100.2
Pl		29	510.27	rim	Ol-gabbro	47.53	33.05	16.26	2.76	0.01	0.03	0.19	99.9
Pl		30	510.27	rim	Ol-gabbro	48.49	32.46	15.49	3.19	0.02	0.02	0.12	99.8
Pl		36	510.27	rim	Ol-gabbro	46.19	34.20	17.35	2.07	0.00	0.00	0.14	100.0
Pl		43	510.27	rim	Ol-gabbro	49.21	32.01	15.17	3.31	0.01	0.03	0.16	100.0
Pl		62	510.27	rim	Ol-gabbro	47.93	32.91	16.13	2.67	0.02	0.01	0.10	99.8
Pl		64	510.27	rim	Ol-gabbro	47.06	33.54	16.84	2.34	0.02	0.00	0.12	99.9
Pl		66	510.27	rim	Ol-gabbro	48.03	32.64	15.81	2.84	0.02	0.02	0.18	99.5
Pl		6	510.27	rim	Ol-gabbro	49.46	31.88	14.94	3.53	0.02	0.03	0.17	100.0
Pl		8	510.27	rim	Ol-gabbro	48.88	31.94	14.92	3.50	0.02	0.04	0.14	99.5
Pl	90R-2W-123-129	76	510.56	rim	Ol-gabbro	49.57	31.97	14.89	3.65	0.02	0.01	0.09	100.2
Pl		86	510.56	rim	Ol-gabbro	48.13	32.90	16.02	2.83	0.02	0.02	0.13	100.1
Pl		93	510.56	rim	Ol-gabbro	48.84	32.70	15.72	3.00	0.02	0.04	0.21	100.6
Pl		106	510.56	rim	Ol-gabbro	47.53	33.18	16.47	2.44	0.02	0.02	0.14	99.8
Pl		108	510.56	rim	Ol-gabbro	46.40	33.78	17.23	2.04	0.02	0.02	0.20	99.7
Pl		111	510.56	rim	Ol-gabbro	46.49	33.89	17.47	1.92	0.01	0.01	0.13	99.9
Pl		117	510.56	rim	Ol-gabbro	50.01	32.06	14.73	3.61	0.02	0.02	0.11	100.6
Pl		128	510.56	rim	Ol-gabbro	46.68	33.41	16.97	2.07	0.02	0.00	0.09	99.3
Pl		134	510.56	rim	Ol-gabbro	47.36	33.34	16.56	2.47	0.01	0.01	0.13	99.9
Pl		142	510.67	rim	Ol-gabbro	50.48	31.59	14.23	3.80	0.03	0.01	0.15	100.4
Pl		194	510.67	rim	Ol-gabbro	51.44	30.64	13.52	4.26	0.03	0.04	0.14	100.1
Pl		222	510.67	rim	Ol-gabbro	47.13	31.54	14.85	2.84	0.03	2.37	0.45	99.2
Pl	90R-3W-6-8	13	510.84	rim	Ol-gabbro	47.38	33.17	16.19	2.55	0.02	0.03	0.14	99.5
Pl		15	510.84	rim	Ol-gabbro	49.90	31.84	14.72	3.65	0.03	0.03	0.15	100.4
Pl		17	510.84	rim	Ol-gabbro	49.32	31.81	14.80	3.48	0.03	0.08	0.12	99.7
Pl		25	510.84	rim	Ol-gabbro	47.87	33.12	16.11	2.75	0.01	0.00	0.17	100.1
Pl		43	510.84	rim	Ol-gabbro	49.92	31.56	14.56	3.67	0.02	0.02	0.11	99.9
Pl		49	510.84	rim	Ol-gabbro	48.68	32.33	15.41	3.13	0.01	0.01	0.09	99.7
Pl		52	510.84	rim	Ol-gabbro	48.65	32.49	15.67	2.95	0.01	0.00	0.10	99.9
Pl		57	510.84	rim	Ol-gabbro	48.45	32.43	15.70	2.94	0.02	0.02	0.14	99.7

Mineral		Point	Depth (mbsf)	Grain area	Lithology	SiO2	Al2O3	CaO	Na2O	K2O	MgO	FeO	Total
Pl		61	510.84	rim	Ol-gabbro	48.65	32.43	15.71	3.03	0.02	0.02	0.12	100.0
Pl		66	510.84	rim	Ol-gabbro	48.76	32.48	15.63	3.02	0.03	0.03	0.13	100.1
Pl		71	510.84	rim	Ol-gabbro	49.14	32.17	15.43	3.32	0.02	0.02	0.15	100.3
Pl	735B_83R7_130A	95 / 1 .	462.554	core	Ol-rich gabbro	51.59	31.01	13.69	3.82	0.02	0.00	0.07	100.2
Pl		97 / 1 .	462.554	core	Ol-rich gabbro	51.60	31.02	13.75	3.58	0.00	0.04	0.07	100.1
Pl		108 / 1 .	462.5685	core	Ol-rich gabbro	49.89	32.02	14.89	3.04	0.05	0.00	0.02	99.9
Pl		109 / 1 .	462.5685	core	Ol-rich gabbro	49.30	32.31	15.49	2.82	0.01	0.01	0.03	100.0
Pl		115 / 1 .	462.568	core	Ol-rich gabbro	50.63	31.30	14.32	3.49	0.04	0.01	0.17	100.0
Pl		126 / 1 .	462.56	core	Ol-rich gabbro	51.27	30.98	13.81	3.74	0.06	0.02	0.06	99.9
Pl		128 / 1 .	462.56	core	Ol-rich gabbro	48.85	32.67	15.76	2.58	0.03	0.02	0.06	100.0
Pl		142 / 1 .	462.56	core	Ol-rich gabbro	51.52	30.97	13.52	3.92	0.01	0.03	0.06	100.0
Pl		143 / 1 .	462.56	core	Ol-rich gabbro	49.95	32.15	15.08	2.95	0.01	0.00	0.02	100.2
Pl		145 / 1 .	462.553	core	Ol-rich gabbro	51.36	31.01	13.87	3.65	0.02	0.00	0.10	100.0
Pl		147 / 1 .	462.553	core	Ol-rich gabbro	51.81	30.68	13.68	3.89	0.05	0.01	0.06	100.2
Pl		160 / 1 .	462.566	core	Ol-rich gabbro	49.51	31.99	15.10	2.91	0.05	0.05	0.06	99.7
Pl	735B_83R7_0	6 / 1 .	461.554	core	Ol-rich gabbro	52.55	29.87	13.10	4.42	0.06	0.00	0.09	100.1
Pl		8 / 1 .	461.554	core	Ol-rich gabbro	48.21	32.45	16.39	2.57	0.02	0.00	0.09	99.7
Pl		21 / 1 .	461.568	core	Ol-rich gabbro	49.00	32.36	15.51	2.99	0.02	0.02	0.12	100.0
Pl		23 / 1 .	461.568	core	Ol-rich gabbro	51.06	31.06	13.95	3.61	0.01	0.01	0.10	99.8
Pl		30 / 1 .	461.5685	core	Ol-rich gabbro	51.68	30.36	13.47	4.04	0.04	0.02	0.06	99.7
Pl		45 / 1 .	461.563	core	Ol-rich gabbro	51.69	30.96	13.84	3.87	0.06	0.01	0.08	100.5
Pl		47 / 1 .	461.565	core	Ol-rich gabbro	49.48	32.25	15.15	2.90	0.03	0.01	0.10	99.9
Pl		60 / 1 .	461.563	core	Ol-rich gabbro	52.48	29.75	12.68	4.60	0.05	0.00	0.04	99.6
Pl		62 / 1 .	461.563	core	Ol-rich gabbro	49.42	31.94	15.21	3.02	0.00	0.04	0.07	99.7
Pl		64 / 1 .	461.563	core	Ol-rich gabbro	52.12	30.41	13.17	4.20	0.05	0.04	0.09	100.1
Pl		74 / 1 .	461.5735	core	Ol-rich gabbro	52.13	30.31	12.84	4.25	0.03	0.02	0.10	99.7
Pl		75 / 1 .	461.5735	core	Ol-rich gabbro	52.75	29.79	12.72	4.57	0.03	0.02	0.06	99.9
Pl	735B_83R7_113A	13 / 1 .	462.4	core	Ol-rich gabbro	50.61	31.96	14.63	3.12	0.01	0.00	0.03	100.4
Pl		15 / 1 .	462.4	core	Ol-rich gabbro	50.17	32.50	14.97	3.01	0.01	0.00	0.06	100.7
Pl		23 / 1 .	462.3885	core	Ol-rich gabbro	50.09	31.78	14.65	3.33	0.04	0.00	0.15	100.0
Pl		35 / 1 .	462.383	core	Ol-rich gabbro	50.93	31.45	14.47	3.52	0.03	0.01	0.05	100.5
Pl		37 / 1 .	462.383	core	Ol-rich gabbro	50.94	31.24	14.13	3.53	0.01	0.01	0.05	99.9
Pl		43 / 1 .	462.385	core	Ol-rich gabbro	50.49	32.21	14.49	3.02	0.02	0.03	0.08	100.3
Pl		51 / 1 .	462.3935	core	Ol-rich gabbro	51.69	31.08	14.04	3.82	0.03	0.02	0.05	100.7
Pl		52 / 1 .	462.3935	core	Ol-rich gabbro	49.11	32.59	15.51	2.66	0.01	0.01	0.08	100.0
Pl		55 / 1 .	462.3995	core	Ol-rich gabbro	48.55	33.13	15.77	2.48	0.00	0.02	0.06	100.0
Pl		57 / 1 .	462.3995	core	Ol-rich gabbro	49.19	32.79	15.36	2.70	0.00	0.00	0.04	100.1
Pl		64 / 1 .	462.3925	core	Ol-rich gabbro	51.68	30.97	13.82	3.73	0.04	0.00	0.06	100.3
Pl		75 / 1 .	462.395	core	Ol-rich gabbro	50.86	31.93	14.50	3.34	0.00	0.05	0.09	100.8

Mineral		Point	Depth (mbsf)	Grain area	Lithology	SiO2	Al2O3	CaO	Na2O	K2O	MgO	FeO	Total
Pl		77 / 1 .	462.395	core	Ol-rich gabbro	51.17	31.52	14.07	3.46	0.02	0.00	0.09	100.3
Pl		84 / 1 .	462.394	core	Ol-rich gabbro	48.37	33.07	16.43	2.40	0.00	0.00	0.06	100.3
Pl		92 / 1 .	462.393	core	Ol-rich gabbro	50.49	31.98	14.22	3.23	0.04	0.02	0.02	100.0
Pl		94 / 1 .	462.393	core	Ol-rich gabbro	49.52	32.58	15.29	2.76	0.01	0.00	0.06	100.2
Pl		61 / 1 .	518.3567	core	Ol-rich gabbro	49.15	32.76	15.63	2.71	0.03	0.02	0.09	100.4
Pl		62 / 1 .	518.3567	core	Ol-rich gabbro	48.40	33.06	16.40	2.47	0.02	0.04	0.09	100.5
Pl		73 / 1 .	518.3567	core	Ol-rich gabbro	48.62	32.53	15.34	2.57	0.02	0.04	0.08	99.2
Pl		79 / 1 .	518.3572	core	Ol-rich gabbro	48.87	32.67	15.98	2.62	0.02	0.01	0.04	100.2
Pl		1 / 1 .	518.35	core	Ol-rich gabbro	48.45	32.84	15.93	2.49	0.04	0.16	0.08	100.0
Pl		2 / 1 .	518.35	core	Ol-rich gabbro	48.72	32.48	15.67	2.46	0.02	0.08	0.03	99.5
Pl		9 / 1 .	518.345	core	Ol-rich gabbro	49.85	32.15	14.97	2.84	0.04	0.02	0.16	100.0
Pl		10 / 1 .	518.345	core	Ol-rich gabbro	49.13	32.39	15.54	2.77	0.02	0.01	0.30	100.2
Pl		12 / 1 .	518.345	core	Ol-rich gabbro	48.56	32.22	15.38	2.69	0.01	0.03	0.12	99.0
Pl		14 / 1 .	518.345	core	Ol-rich gabbro	48.87	32.67	15.70	2.58	0.01	0.01	0.10	100.0
Pl	735B_91R1_93A	17 / 1 .	518.345	core	Ol-rich gabbro	49.24	32.21	15.22	2.78	0.01	0.00	0.09	99.5
Pl		31 / 1 .	518.3433	core	Ol-rich gabbro	48.59	33.09	15.75	2.48	0.05	0.01	0.10	100.1
Pl		32 / 1 .	518.3433	core	Ol-rich gabbro	48.49	32.70	15.77	2.78	0.01	0.00	0.09	99.9
Pl		34 / 1 .	518.3433	core	Ol-rich gabbro	49.30	32.35	15.41	2.85	0.03	0.02	0.11	100.1
Pl		45 / 1 .	518.351	core	Ol-rich gabbro	48.37	32.77	15.97	2.35	0.04	0.00	0.07	99.6
Pl		57 / 1 .	518.3355	core	Ol-rich gabbro	49.15	32.00	15.09	2.89	0.02	0.00	0.07	99.2
Pl		58 / 1 .	518.3355	core	Ol-rich gabbro	49.61	32.39	15.50	2.78	0.00	0.03	0.15	100.5
Pl		74 / 1 .	518.3338	core	Ol-rich gabbro	48.39	32.71	15.98	2.41	0.00	0.04	0.08	99.6
Pl		76 / 1 .	518.3338	core	Ol-rich gabbro	49.58	32.24	15.35	2.92	0.02	0.06	0.10	100.3
Pl		79 / 1 .	518.3338	core	Ol-rich gabbro	49.35	32.48	15.20	2.64	0.03	0.00	0.08	99.8
Pl		80 / 1 .	518.3338	core	Ol-rich gabbro	49.87	32.19	15.17	2.98	0.02	0.03	0.08	100.3
Pl		81 / 1 .	518.3338	core	Ol-rich gabbro	49.20	32.45	15.58	2.72	0.00	0.01	0.11	100.1
Pl		6 / 1 .	518.1644	core	Ol-rich gabbro	48.53	32.93	16.07	2.47	0.08	0.02	0.09	100.2
Pl		10 / 1 .	518.1644	core	Ol-rich gabbro	49.91	31.78	14.60	3.15	0.03	0.03	0.04	99.5
Pl		11 / 1 .	518.1644	core	Ol-rich gabbro	48.38	32.06	15.52	2.72	0.05	0.00	0.05	98.8
Pl		17 / 1 .	518.1645	core	Ol-rich gabbro	49.13	32.32	15.59	2.78	0.03	0.01	0.10	100.0
Pl		24 / 1 .	518.1617	core	Ol-rich gabbro	49.13	32.24	15.33	2.86	0.00	0.00	0.09	99.7
Pl		26 / 1 .	518.1617	core	Ol-rich gabbro	48.00	33.10	16.43	2.27	0.00	0.02	0.13	100.0
Pl		34 / 1 .	518.1544	core	Ol-rich gabbro	49.86	31.96	14.81	3.07	0.00	0.03	0.04	99.8
Pl		36 / 1 .	518.1544	core	Ol-rich gabbro	49.09	32.34	15.33	2.81	0.02	0.02	0.10	99.7
Pl	735B_91R1_74	41 / 1 .	518.1522	core	Ol-rich gabbro	49.37	32.59	15.24	2.77	0.01	0.00	0.09	100.1
Pl		44 / 1 .	518.1522	core	Ol-rich gabbro	49.00	32.32	15.32	2.78	0.03	0.04	0.15	99.6
Pl		53 / 1 .	518.1455	core	Ol-rich gabbro	47.77	33.02	16.36	2.15	0.04	0.02	0.04	99.4
Pl		57 / 1 .	518.1528	core	Ol-rich gabbro	47.74	33.33	16.51	2.09	0.00	0.02	0.07	99.8
Pl		58 / 1 .	518.1528	core	Ol-rich gabbro	49.10	32.50	15.60	2.83	0.05	0.03	0.06	100.2

Mineral		Point	Depth (mbsf)	Grain area	Lithology	SiO2	Al2O3	CaO	Na2O	K2O	MgO	FeO	Total
Pl		71 / 1 .	518.1505	core	Ol-rich gabbro	49.35	32.25	15.09	2.82	0.03	0.02	0.06	99.6
Pl		74 / 1 .	518.1505	core	Ol-rich gabbro	48.32	32.64	16.14	2.30	0.02	0.02	0.09	99.5
Pl		96 / 1 .	462.554	rim	Ol-rich gabbro	49.75	32.16	15.27	2.97	0.02	0.01	0.06	100.2
Pl		98 / 1 .	462.554	rim	Ol-rich gabbro	50.51	31.72	14.31	3.53	0.02	0.00	0.07	100.2
Pl		116 / 1 .	462.568	rim	Ol-rich gabbro	50.75	31.77	14.56	3.41	0.03	0.00	0.08	100.6
Pl		118 / 1 .	462.568	rim	Ol-rich gabbro	49.12	32.44	15.67	2.72	0.03	0.00	0.07	100.1
Pl	735B_83R7_130A	127 / 1 .	462.56	rim	Ol-rich gabbro	51.31	31.00	13.85	3.82	0.03	0.03	0.06	100.1
Pl		129 / 1 .	462.56	rim	Ol-rich gabbro	50.11	31.97	14.85	3.16	0.06	0.03	0.03	100.2
Pl		144 / 1 .	462.56	rim	Ol-rich gabbro	51.51	31.02	13.64	3.84	0.02	0.01	0.09	100.1
Pl		146 / 1 .	462.553	rim	Ol-rich gabbro	51.04	30.61	13.78	3.81	0.04	0.03	0.03	99.3
Pl		159 / 1 .	462.566	rim	Ol-rich gabbro	50.57	31.55	14.39	3.19	0.03	0.01	0.06	99.8
Pl		161 / 1 .	462.566	rim	Ol-rich gabbro	50.64	31.52	14.65	3.28	0.02	0.02	0.09	100.2
Pl		7 / 1 .	461.554	rim	Ol-rich gabbro	52.38	30.28	12.99	4.23	0.05	0.02	0.16	100.1
Pl		9 / 1 .	461.554	rim	Ol-rich gabbro	50.82	31.03	14.29	3.50	0.04	0.02	0.08	99.8
Pl		22 / 1 .	461.568	rim	Ol-rich gabbro	49.52	31.90	15.25	3.04	0.00	0.00	0.14	99.9
Pl		29 / 1 .	461.5685	rim	Ol-rich gabbro	52.26	30.53	13.64	4.02	0.01	0.01	0.12	100.6
Pl		44 / 1 .	461.563	rim	Ol-rich gabbro	52.94	30.03	12.59	4.51	0.08	0.03	0.08	100.3
Pl	735B_83R7_0	46 / 1 .	461.563	rim	Ol-rich gabbro	51.80	30.35	13.42	4.12	0.01	0.05	0.12	99.9
Pl		48 / 1 .	461.565	rim	Ol-rich gabbro	52.26	30.40	13.13	4.27	0.06	0.03	0.06	100.2
Pl		49 / 1 .	461.565	rim	Ol-rich gabbro	52.57	30.16	12.75	4.43	0.03	0.01	0.09	100.0
Pl		61 / 1 .	461.563	rim	Ol-rich gabbro	49.61	32.10	15.24	3.09	0.00	0.02	0.15	100.2
Pl		63 / 1 .	461.563	rim	Ol-rich gabbro	52.63	29.86	12.70	4.42	0.06	0.02	0.06	99.8
Pl		76 / 1 .	461.5735	rim	Ol-rich gabbro	52.38	29.82	12.83	4.36	0.04	0.00	0.06	99.5
Pl		14 / 1 .	462.4	rim	Ol-rich gabbro	50.78	31.74	14.32	3.30	0.02	0.06	0.13	100.4
Pl		16 / 1 .	462.4	rim	Ol-rich gabbro	50.97	31.41	14.04	3.33	0.02	0.00	0.08	99.9
Pl		54 / 1 .	462.3995	rim	Ol-rich gabbro	51.15	31.47	13.97	3.44	0.02	0.03	0.07	100.2
Pl		56 / 1 .	462.3995	rim	Ol-rich gabbro	49.40	32.44	15.74	2.68	0.01	0.00	0.08	100.4
Pl	735B_83R7_113A	65 / 1 .	462.3925	rim	Ol-rich gabbro	51.81	30.92	13.68	3.64	0.04	0.04	0.08	100.2
Pl		78 / 1 .	462.395	rim	Ol-rich gabbro	50.67	31.87	14.84	3.23	0.04	0.00	0.09	100.7
Pl		83 / 1 .	462.394	rim	Ol-rich gabbro	51.61	31.45	14.05	3.55	0.02	0.03	0.06	100.8
Pl		93 / 1 .	462.393	rim	Ol-rich gabbro	51.80	30.90	13.46	3.77	0.02	0.00	0.13	100.1
Pl		95 / 1 .	462.393	rim	Ol-rich gabbro	51.14	31.71	14.17	3.37	0.05	0.00	0.11	100.6
Pl		60 / 1 .	518.3567	rim	Ol-rich gabbro	49.18	32.46	15.64	2.67	0.01	0.02	0.15	100.1
Pl		63 / 1 .	518.3567	rim	Ol-rich gabbro	49.30	32.77	15.78	2.59	0.03	0.06	0.13	100.7
Pl		72 / 1 .	518.3567	rim	Ol-rich gabbro	49.58	32.45	15.25	2.84	0.03	0.01	0.04	100.2
Pl		80 / 1 .	518.3572	rim	Ol-rich gabbro	49.45	32.61	15.27	2.92	0.01	0.02	0.08	100.4
Pl		3 / 1 .	518.35	rim	Ol-rich gabbro	49.20	32.57	15.79	2.42	0.00	0.21	0.00	100.2
Pl		4 / 1 .	518.35	rim	Ol-rich gabbro	50.43	31.45	14.58	3.06	0.06	0.19	0.00	99.8
Pl		11 / 1 .	518.345	rim	Ol-rich gabbro	48.74	32.56	15.87	2.50	0.01	0.03	0.13	99.8
Pl	735B_91R1_93A	13 / 1 .	518.345	rim	Ol-rich gabbro	48.92	32.67	15.54	2.60	0.00	0.00	0.13	99.9

Mineral	735B_91R1_95A	Point	Depth (mbsf)	Grain area	Lithology	SiO2	Al2O3	CaO	Na2O	K2O	MgO	FeO	Total
Pl		30 / 1 .	518.3433	rim	Ol-rich gabbro	48.02	33.48	16.39	2.14	0.01	0.02	0.16	100.2
Pl		33 / 1 .	518.3433	rim	Ol-rich gabbro	49.28	32.65	15.51	2.65	0.01	0.02	0.08	100.2
Pl		46 / 1 .	518.351	rim	Ol-rich gabbro	49.39	32.00	15.37	2.83	0.04	0.03	0.09	99.8
Pl		73 / 1 .	518.3338	rim	Ol-rich gabbro	48.75	32.55	15.51	2.85	0.02	0.00	0.10	99.8
Pl		75 / 1 .	518.3338	rim	Ol-rich gabbro	49.71	32.09	14.86	2.95	0.00	0.00	0.11	99.7
Pl		78 / 1 .	518.3338	rim	Ol-rich gabbro	48.56	32.90	15.91	2.40	0.02	0.04	0.13	100.0
Pl		7 / 1 .	518.1644	rim	Ol-rich gabbro	50.12	32.26	14.89	3.05	0.00	0.12	0.23	100.7
Pl		8 / 1 .	518.1644	rim	Ol-rich gabbro	48.36	33.09	16.25	2.36	0.02	0.03	0.09	100.2
Pl		9 / 1 .	518.1644	rim	Ol-rich gabbro	49.52	32.13	15.25	3.07	0.05	0.03	0.08	100.1
Pl		16 / 1 .	518.1645	rim	Ol-rich gabbro	49.15	32.11	15.31	2.88	0.01	0.01	0.09	99.6
Pl		25 / 1 .	518.1617	rim	Ol-rich gabbro	49.34	32.48	15.40	2.79	0.02	0.03	0.16	100.2
Pl	735B_91R1_74	35 / 1 .	518.1544	rim	Ol-rich gabbro	49.17	32.58	15.45	2.78	0.00	0.00	0.13	100.1
Pl		37 / 1 .	518.1544	rim	Ol-rich gabbro	49.43	32.24	15.25	2.77	0.01	0.01	0.08	99.8
Pl		42 / 1 .	518.1522	rim	Ol-rich gabbro	49.23	32.41	15.31	2.77	0.01	0.03	0.13	99.9
Pl		52 / 1 .	518.1455	rim	Ol-rich gabbro	49.18	32.41	15.25	2.72	0.04	0.01	0.10	99.7
Pl		59 / 1 .	518.1528	rim	Ol-rich gabbro	49.01	32.50	15.60	2.86	0.02	0.03	0.11	100.1
Pl		72 / 1 .	518.1505	rim	Ol-rich gabbro	49.32	32.42	15.35	2.98	0.00	0.02	0.11	100.2
Pl		73 / 1 .	518.1505	rim	Ol-rich gabbro	48.10	32.85	16.23	2.56	0.01	0.02	0.04	99.8
Pl		2 / 1 .	499.6325	core	Troctolite	51.12	30.93	14.01	3.74	0.00	0.00	0.12	99.9
Pl		5 / 1 .	499.6325	core	Troctolite	50.40	31.63	14.27	3.44	0.02	0.02	0.10	99.9
Pl		20 / 1 .	499.6355	core	Troctolite	51.54	30.89	13.64	3.66	0.03	0.02	0.14	99.9
Pl		24 / 1 .	499.6355	core	Troctolite	51.73	30.76	13.46	4.10	0.04	0.04	0.15	100.3
Pl		25 / 1 .	499.6355	core	Troctolite	52.24	30.60	13.21	4.06	0.04	0.02	0.13	100.3
Pl		33 / 1 .	499.6395	core	Troctolite	51.50	31.20	13.85	3.80	0.01	0.05	0.11	100.5
Pl	735B_87R7_49	45 / 1 .	499.6445	core	Troctolite	51.98	30.81	13.54	4.09	0.00	0.03	0.13	100.6
Pl		52 / 1 .	499.6515	core	Troctolite	50.94	31.13	14.12	3.51	0.02	0.02	0.15	99.9
Pl		55 / 1 .	499.6525	core	Troctolite	51.91	30.70	13.19	3.96	0.03	0.04	0.12	100.0
Pl		58 / 1 .	499.6525	core	Troctolite	52.13	30.38	12.97	4.12	0.01	0.02	0.16	99.8
Pl		65 / 1 .	499.6575	core	Troctolite	50.98	31.07	14.15	3.69	0.05	0.05	0.13	100.1
Pl		67 / 1 .	499.6575	core	Troctolite	50.44	31.28	14.37	3.35	0.01	0.03	0.13	99.6
Pl		8 / 1 .	425.5625	core	Troctolite	49.62	31.52	15.13	3.08	0.01	0.00	0.08	99.4
Pl		11 / 1 .	425.5625	core	Troctolite	51.67	30.79	13.39	3.95	0.01	0.00	0.09	99.9
Pl		14 / 1 .	425.5625	core	Troctolite	50.99	31.47	14.16	3.57	0.04	0.05	0.07	100.3
Pl		18 / 1 .	425.561	core	Troctolite	51.30	30.85	13.63	3.83	0.05	0.03	0.09	99.8
Pl		19 / 1 .	425.561	core	Troctolite	50.72	31.08	14.17	3.41	0.03	0.02	0.11	99.5
Pl		27 / 1 .	425.562	core	Troctolite	51.00	31.11	14.23	3.54	0.00	0.00	0.09	100.0
Pl		28 / 1 .	425.562	core	Troctolite	51.52	31.25	13.92	3.86	0.07	0.03	0.08	100.7
Pl		30 / 1 .	425.5625	core	Troctolite	51.75	30.76	13.35	3.88	0.02	0.01	0.07	99.9
Pl		36 / 1 .	425.5595	core	Troctolite	49.34	32.43	15.62	2.93	0.03	0.01	0.13	100.5

Mineral		Point	Depth (mbsf)	Grain area	Lithology	SiO2	Al2O3	CaO	Na2O	K2O	MgO	FeO	Total
Pl	735B_80R2_7.5A	39 / 1 .	425.5595	core	Troctolite	48.62	32.43	15.98	2.66	0.01	0.03	0.09	99.8
Pl		40 / 1 .	425.5595	core	Troctolite	50.42	31.29	14.09	3.63	0.05	0.03	0.12	99.6
Pl		43 / 1 .	425.554	core	Troctolite	50.93	31.28	14.05	3.59	0.03	0.00	0.07	100.0
Pl		47 / 1 .	425.554	core	Troctolite	50.63	31.16	14.12	3.58	0.01	0.02	0.13	99.6
Pl		55 / 1 .	425.557	core	Troctolite	51.42	30.87	13.53	3.84	0.02	0.01	0.06	99.8
Pl		56 / 1 .	425.557	core	Troctolite	48.06	33.39	16.48	2.16	0.00	0.01	0.16	100.3
Pl		58 / 1 .	425.557	core	Troctolite	50.99	31.06	14.27	3.43	0.02	0.00	0.10	99.9
Pl		60 / 1 .	425.557	core	Troctolite	50.59	31.15	14.32	3.55	0.01	0.01	0.09	99.7
Pl		64 / 1 .	425.5565	core	Troctolite	50.52	31.35	14.47	3.31	0.03	0.00	0.12	99.8
Pl		66 / 1 .	425.5565	core	Troctolite	51.09	31.25	13.83	3.66	0.00	0.00	0.07	99.9
Pl		67 / 1 .	425.5485	core	Troctolite	49.87	32.02	14.94	3.13	0.01	0.05	0.10	100.1
Pl		70 / 1 .	425.5485	core	Troctolite	50.36	31.52	14.45	3.31	0.06	0.05	0.10	99.9
Pl		82 / 1 .	425.551	core	Troctolite	49.18	32.15	15.35	2.82	0.01	0.03	0.10	99.6
Pl	735B_89R1_47	7 / 1 .	505.2735	core	Troctolite	51.37	30.83	13.80	3.83	0.01	0.01	0.09	99.9
Pl		9 / 1 .	505.2735	core	Troctolite	51.98	30.39	13.01	4.16	0.01	0.02	0.02	99.6
Pl		17 / 1 .	505.2755	core	Troctolite	49.16	32.25	15.54	2.80	0.00	0.01	0.08	99.8
Pl		20 / 1 .	505.2755	core	Troctolite	50.90	31.45	14.46	3.67	0.04	0.01	0.16	100.7
Pl		21 / 1 .	505.277	core	Troctolite	50.57	31.18	14.30	3.49	0.02	0.00	0.12	99.7
Pl		27 / 1 .	505.281	core	Troctolite	48.55	32.13	15.80	2.80	0.04	0.04	0.18	99.6
Pl		29 / 1 .	505.281	core	Troctolite	51.75	30.59	13.60	3.84	0.07	0.05	0.14	100.0
Pl		32 / 1 .	505.283	core	Troctolite	50.99	30.80	13.57	3.67	0.04	0.02	0.09	99.2
Pl		37 / 1 .	505.283	core	Troctolite	50.53	31.26	14.25	3.55	0.04	0.05	0.08	99.8
Pl		40 / 1 .	505.291	core	Troctolite	50.71	31.23	14.30	3.58	0.04	0.03	0.11	100.0
Pl		41 / 1 .	505.291	core	Troctolite	48.80	32.28	15.36	2.83	0.00	0.00	0.16	99.4
Pl		50 / 1 .	505.298	core	Troctolite	50.69	31.23	14.10	3.53	0.00	0.02	0.10	99.7
Pl		52 / 1 .	505.3	core	Troctolite	51.03	30.91	13.92	3.69	0.00	0.04	0.24	99.8
Pl	90R-2W-68-75	4	510.015	core	Troctolite	50.58	31.12	14.51	3.94	0.05	0.02	0.15	100.4
Pl		10	510.015	core	Troctolite	50.52	31.05	14.40	4.13	0.04	0.01	0.13	100.4
Pl		14	510.015	core	Troctolite	50.34	31.22	14.34	4.16	0.05	0.02	0.12	100.3
Pl		16	510.015	core	Troctolite	49.01	31.70	15.60	3.29	0.03	0.03	0.20	99.9
Pl		24	510.015	core	Troctolite	49.39	31.83	15.47	3.53	0.04	0.03	0.14	100.5
Pl		27	510.015	core	Troctolite	50.47	31.01	14.47	3.98	0.05	0.01	0.11	100.2
Pl		34	510.015	core	Troctolite	49.81	31.25	14.91	3.74	0.13	0.17	0.25	100.4
Pl		38	510.015	core	Troctolite	49.09	31.85	15.51	3.46	0.02	0.01	0.19	100.2
Pl		42	510.015	core	Troctolite	49.46	32.03	15.60	3.52	0.03	0.01	0.15	100.9
Pl		44	510.015	core	Troctolite	50.28	31.23	14.81	3.96	0.04	0.01	0.14	100.5
Pl		45	510.015	core	Troctolite	51.18	30.55	13.88	4.25	0.05	0.01	0.10	100.1
Pl		46	510.015	core	Troctolite	50.45	31.26	14.71	4.07	0.03	0.02	0.16	100.8
Pl		1 / 1 .	499.6325	rim	Troctolite	51.40	31.40	14.14	3.71	0.02	0.01	0.19	100.9

Mineral		Point	Depth (mbsf)	Grain area	Lithology	SiO2	Al2O3	CaO	Na2O	K2O	MgO	FeO	Total
Pl		3 / 1 .	499.6325	rim	Troctolite	49.30	32.38	15.12	2.81	0.00	0.01	0.14	99.8
Pl		4 / 1 .	499.6325	rim	Troctolite	51.69	31.06	13.57	3.92	0.02	0.00	0.17	100.4
Pl		19 / 1 .	499.6355	rim	Troctolite	51.77	31.02	13.57	3.87	0.04	0.00	0.07	100.3
Pl	735B_87R7_49	23 / 1 .	499.6355	rim	Troctolite	51.43	31.11	13.59	3.99	0.02	0.00	0.15	100.3
Pl		32 / 1 .	499.6395	rim	Troctolite	51.52	31.04	13.81	3.87	0.04	0.02	0.25	100.6
Pl		46 / 1 .	499.6445	rim	Troctolite	48.28	33.03	16.11	2.37	0.00	0.01	0.25	100.1
Pl		51 / 1 .	499.6515	rim	Troctolite	50.79	31.11	14.28	3.56	0.06	0.01	0.19	100.0
Pl		56 / 1 .	499.6525	rim	Troctolite	49.16	32.11	15.14	2.85	0.02	0.00	0.17	99.5
Pl		57 / 1 .	499.6525	rim	Troctolite	51.95	30.55	13.54	4.06	0.01	0.05	0.16	100.3
Pl		64 / 1 .	499.6575	rim	Troctolite	50.40	31.58	14.23	3.54	0.02	0.01	0.09	99.9
Pl		66 / 1 .	499.6575	rim	Troctolite	51.84	30.50	13.27	3.92	0.02	0.00	0.10	99.6
Pl		9 / 1 .	425.5625	rim	Troctolite	50.55	31.49	14.34	3.41	0.00	0.01	0.14	99.9
Pl		10 / 1 .	425.5625	rim	Troctolite	51.18	30.95	13.35	3.69	0.02	0.00	0.09	99.3
Pl		12 / 1 .	425.5625	rim	Troctolite	48.84	32.86	16.19	2.60	0.02	0.00	0.10	100.6
Pl		13 / 1 .	425.5625	rim	Troctolite	52.42	30.46	13.04	4.01	0.05	0.03	0.07	100.1
Pl		17 / 1 .	425.561	rim	Troctolite	50.14	31.80	14.59	3.28	0.00	0.02	0.12	99.9
Pl		26 / 1 .	425.562	rim	Troctolite	51.98	30.37	13.14	4.15	0.03	0.03	0.13	99.8
Pl		29 / 1 .	425.562	rim	Troctolite	48.66	32.72	15.55	2.64	0.00	0.00	0.13	99.7
Pl		31 / 1 .	425.5625	rim	Troctolite	51.37	31.13	13.46	3.62	0.04	0.03	0.07	99.7
Pl		37 / 1 .	425.5595	rim	Troctolite	51.68	30.66	13.58	3.98	0.02	0.03	0.11	100.1
Pl		38 / 1 .	425.5595	rim	Troctolite	51.21	31.16	14.15	3.80	0.02	0.05	0.17	100.6
Pl	735B_80R2_7.5A	44 / 1 .	425.554	rim	Troctolite	51.44	30.91	13.63	3.80	0.02	0.01	0.04	99.9
Pl		45 / 1 .	425.554	rim	Troctolite	51.50	30.72	13.32	3.95	0.06	0.04	0.07	99.7
Pl		46 / 1 .	425.554	rim	Troctolite	50.42	31.44	14.26	3.30	0.04	0.00	0.10	99.6
Pl		54 / 1 .	425.557	rim	Troctolite	51.08	30.86	13.96	3.58	0.04	0.00	0.13	99.6
Pl		57 / 1 .	425.557	rim	Troctolite	50.32	31.57	14.84	3.19	0.01	0.01	0.11	100.1
Pl		59 / 1 .	425.557	rim	Troctolite	50.20	31.90	14.55	3.21	0.00	0.00	0.09	100.0
Pl		65 / 1 .	425.5565	rim	Troctolite	50.32	31.58	14.26	3.31	0.01	0.00	0.13	99.6
Pl		68 / 1 .	425.5485	rim	Troctolite	50.40	31.58	14.76	3.20	0.01	0.03	0.14	100.1
Pl		69 / 1 .	425.5485	rim	Troctolite	50.91	31.30	14.08	3.45	0.00	0.02	0.15	99.9
Pl		71 / 1 .	425.5485	rim	Troctolite	51.04	30.93	13.65	3.75	0.03	0.01	0.11	99.5
Pl		81 / 1 .	425.551	rim	Troctolite	50.29	31.86	14.79	3.20	0.03	0.00	0.04	100.2
Pl		8 / 1 .	505.2735	rim	Troctolite	51.25	30.85	13.54	3.87	0.03	0.04	0.11	99.7
Pl		18 / 1 .	505.2755	rim	Troctolite	49.41	32.53	15.30	2.79	0.01	0.02	0.08	100.1
Pl		19 / 1 .	505.2755	rim	Troctolite	51.38	30.92	13.76	3.96	0.04	0.05	0.14	100.2
Pl		26 / 1 .	505.281	rim	Troctolite	51.22	30.56	13.83	3.66	0.06	0.00	0.11	99.4
Pl		28 / 1 .	505.281	rim	Troctolite	49.74	31.96	15.18	3.14	0.01	0.00	0.10	100.1
Pl	735B_89R1_47	33 / 1 .	505.283	rim	Troctolite	51.31	31.01	13.94	3.52	0.03	0.00	0.09	99.9
Pl		36 / 1 .	505.283	rim	Troctolite	51.01	31.24	13.92	3.71	0.03	0.04	0.14	100.1

Mineral		Point	Depth (mbsf)	Grain area	Lithology	SiO2	Al2O3	CaO	Na2O	K2O	MgO	FeO	Total
Pl		39 / 1 .	505.291	rim	Troctolite	50.53	31.25	13.99	3.25	0.04	0.08	0.19	99.3
Pl		49 / 1 .	505.298	rim	Troctolite	51.08	31.06	13.84	3.50	0.02	0.02	0.17	99.7
Pl		51 / 1 .	505.298	rim	Troctolite	51.06	30.77	13.85	3.74	0.01	0.01	0.09	99.5
Pl		3	510.015	rim	Troctolite	50.22	31.27	14.67	3.85	0.04	0.03	0.15	100.3
Pl		5	510.015	rim	Troctolite	51.08	30.83	14.16	4.19	0.03	0.02	0.13	100.5
Pl		9	510.015	rim	Troctolite	48.37	32.45	16.02	3.00	0.03	0.01	0.13	100.0
Pl		13	510.015	rim	Troctolite	50.79	30.92	14.21	4.04	0.05	0.01	0.17	100.2
Pl		15	510.015	rim	Troctolite	50.87	31.07	14.40	4.11	0.04	0.00	0.11	100.7
Pl	90R-2W-68-75	23	510.015	rim	Troctolite	50.42	31.24	14.48	4.03	0.04	0.01	0.18	100.4
Pl		28	510.015	rim	Troctolite	47.38	33.14	16.98	2.56	0.01	0.01	0.10	100.2
Pl		33	510.015	rim	Troctolite	50.46	30.93	14.49	4.10	0.04	0.02	0.17	100.3
Pl		37	510.015	rim	Troctolite	50.95	31.01	14.49	4.14	0.04	0.01	0.16	100.9
Pl		41	510.015	rim	Troctolite	49.63	31.29	15.03	3.66	0.04	0.01	0.15	99.9
Pl		47	510.015	rim	Troctolite	50.61	31.12	14.54	4.07	0.03	0.02	0.14	100.6

		Calibration standards				Wollastonite (San Carlos)	Al2O3	Wollastonite	Albite	Orthose	Forsterite	Fayalite	

In situ major elements concentrations in wt% analyzed by EPMA on a Cameca SX100 at LMV (Clermont-Ferrand, France)

Mineral	Sample	Point	Depth (mbsf)	Grain area	Lithology	SiO2	Al2O3	TiO2	CaO	Na2O	K2O	MnO	MgO	FeO	Cr2O3	Total
					2 sigma	0.32	0.13	0.06	0.27	0.08	0.04	#VALEUR!	0.17	0.14	0.06	
Cpx		Counting time (s) - per element				10	10	10	10	10	10	10	10	20	10	
Cpx		8 / 1 .	480.68	core	Gabbro	51.91	3.91	0.44	22.97	0.38	0.01	0.13	15.03	3.91	1.19	99.9
Cpx		14 / 1 .	480.69	core	Gabbro	52.36	2.39	0.37	21.70	0.35	0.01	0.14	15.76	5.29	0.62	99.0
Cpx		18 / 1 .	480.69	core	Gabbro	51.92	3.50	0.51	22.88	0.47	0.00	0.14	15.15	4.39	1.15	100.1
Cpx		19 / 1 .	480.69	core	Gabbro	53.34	2.63	0.48	22.26	0.34	0.00	0.13	15.76	4.60	0.63	100.2
Cpx		23 / 1 .	480.69	core	Gabbro	52.30	3.89	0.43	22.47	0.41	0.00	0.17	15.16	3.99	0.96	99.8
Cpx		30 / 1 .	480.69	core	Gabbro	52.17	3.82	0.44	22.11	0.39	0.00	0.16	15.67	4.10	1.00	99.9
Cpx		45 / 1 .	480.71	core	Gabbro	51.44	4.05	0.50	22.64	0.43	0.00	0.14	15.07	4.37	1.18	99.8
Cpx		65 / 1 .	480.71	core	Gabbro	52.52	3.22	0.48	22.73	0.32	0.00	0.12	15.59	4.11	0.83	99.9
Cpx		7 / 1 .	480.68	rim	Gabbro	52.11	3.30	0.52	22.28	0.38	0.00	0.17	15.05	5.13	0.74	99.7
Cpx	735B_85R7_79	15 / 1 .	480.69	rim	Gabbro	51.88	3.52	0.89	21.62	0.50	0.01	0.15	15.00	5.28	0.85	99.7
Cpx		16 / 1 .	480.69	rim	Gabbro	52.43	3.16	0.72	22.65	0.37	0.00	0.16	15.05	4.67	0.51	99.7
Cpx		20 / 1 .	480.69	rim	Gabbro	52.66	3.49	0.32	22.53	0.44	0.00	0.13	15.35	4.31	1.09	100.3
Cpx		22 / 1 .	480.69	rim	Gabbro	52.93	3.13	0.70	21.60	0.46	0.00	0.20	15.82	4.89	0.67	100.4
Cpx		27 / 1 .	480.69	rim	Gabbro	52.34	3.22	0.48	22.13	0.41	0.00	0.12	15.69	4.62	0.99	100.0
Cpx		32 / 1 .	480.7	rim	Gabbro	52.21	3.67	0.60	21.41	0.37	0.01	0.15	15.99	4.76	0.85	100.0
Cpx		33 / 1 .	480.7	rim	Gabbro	52.53	3.35	0.57	22.77	0.37	0.00	0.10	15.54	4.50	0.63	100.4
Cpx		46 / 1 .	480.71	rim	Gabbro	52.85	2.73	0.67	23.15	0.34	0.01	0.16	15.20	4.42	0.56	100.1
Cpx		58 / 1 .	480.71	rim	Gabbro	53.23	1.89	0.37	23.16	0.39	0.00	0.12	15.79	4.69	0.41	100.0
Cpx		66 / 1 .	480.71	rim	Gabbro	52.43	2.44	0.55	22.99	0.37	0.00	0.18	15.23	5.20	0.47	99.9
Cpx		67 / 1 .	480.71	rim	Gabbro	51.56	3.31	0.54	22.74	0.42	0.01	0.12	14.56	4.84	1.00	99.1
Cpx		1 / 1 .	274.89	core	Ol-bearing gabbro	52.21	2.17	0.72	21.09	0.42	0.00	0.34	14.07	9.78	0.03	100.8
Cpx		4 / 1 .	274.89	core	Ol-bearing gabbro	51.44	2.29	0.84	21.12	0.38	0.03	0.24	13.84	10.00	0.00	100.2
Cpx		20 / 1 .	274.89	core	Ol-bearing gabbro	51.61	2.58	0.82	21.12	0.61	0.04	0.26	13.75	8.88	0.05	99.7
Cpx		23 / 1 .	274.89	core	Ol-bearing gabbro	51.64	2.71	0.99	21.31	0.52	0.02	0.36	13.69	9.17	0.01	100.4
Cpx		24 / 1 .	274.89	core	Ol-bearing gabbro	51.98	2.72	0.83	21.23	0.56	0.03	0.21	13.56	9.16	0.00	100.3
Cpx		26 / 1 .	274.9	core	Ol-bearing gabbro	51.75	2.59	0.83	21.35	0.47	0.00	0.27	13.69	9.07	0.04	100.1
Cpx	735B_56R4_61A	28 / 1 .	274.9	core	Ol-bearing gabbro	51.54	2.93	0.84	20.55	0.38	0.02	0.31	13.82	9.48	0.01	99.9
Cpx		53 / 1 .	274.9	core	Ol-bearing gabbro	51.85	2.58	0.94	20.77	0.41	0.01	0.33	13.30	9.13	0.03	99.4
Cpx		56 / 1 .	274.91	core	Ol-bearing gabbro	52.02	2.34	0.78	21.56	0.54	0.01	0.21	13.41	9.43	0.00	100.3
Cpx		58 / 1 .	274.91	core	Ol-bearing gabbro	51.81	2.36	0.84	22.06	0.38	0.00	0.24	13.78	9.24	0.00	100.7
Cpx		59 / 1 .	274.91	core	Ol-bearing gabbro	52.35	2.12	0.62	22.43	0.38	0.02	0.20	14.00	7.95	0.01	100.1
Cpx		60 / 1 .	274.91	core	Ol-bearing gabbro	51.63	2.48	0.83	21.97	0.34	0.01	0.30	13.53	9.39	0.00	100.5
Cpx		65 / 1 .	274.9	core	Ol-bearing gabbro	50.95	2.45	1.57	19.00	0.48	0.00	0.27	14.48	11.11	0.00	100.3
Cpx		68 / 1 .	274.9	core	Ol-bearing gabbro	52.29	2.04	0.64	21.65	0.40	0.02	0.25	13.67	8.85	0.02	99.8
Cpx		65 / 1 .	274.88	core	Ol-bearing gabbro	52.37	1.94	0.48	20.97	0.48	0.01	0.24	14.65	9.84	0.04	101.0
Cpx		73 / 1 .	274.88	core	Ol-bearing gabbro	52.35	1.47	0.05	23.96	0.38	0.01	0.37	13.22	9.81	0.04	101.7
Cpx		75 / 1 .	274.88	core	Ol-bearing gabbro	51.72	2.07	0.62	22.13	0.57	0.03	0.30	14.33	8.98	0.02	100.8

Mineral		Point	Depth (mbsf)	Grain area	Lithology	SiO2	Al2O3	TiO2	CaO	Na2O	K2O	MnO	MgO	FeO	Cr2O3	Total
Cpx		77 / 1 .	274.88	core	Ol-bearing gabbro	52.07	2.21	0.57	21.36	0.62	0.02	0.30	14.76	8.85	0.00	100.8
Cpx	735B_56R4_61B	87 / 1 .	274.88	core	Ol-bearing gabbro	50.77	3.17	0.90	22.01	0.50	0.00	0.23	14.44	8.97	0.03	101.0
Cpx		89 / 1 .	274.88	core	Ol-bearing gabbro	51.07	2.54	0.90	20.57	0.48	0.00	0.44	14.90	10.01	0.00	100.9
Cpx		90 / 1 .	274.88	core	Ol-bearing gabbro	51.26	2.05	0.53	20.89	0.43	0.01	0.22	14.02	9.58	0.00	99.0
Cpx		92 / 1 .	274.88	core	Ol-bearing gabbro	50.55	2.91	0.80	20.66	0.80	0.04	0.24	14.63	9.14	0.00	99.8
Cpx		93 / 1 .	274.88	core	Ol-bearing gabbro	47.87	5.69	1.55	10.78	1.84	0.22	0.32	14.06	15.42	0.00	97.8
Cpx		96 / 1 .	274.88	core	Ol-bearing gabbro	49.38	3.57	0.77	19.58	0.48	0.03	0.30	14.82	10.12	0.02	99.1
Cpx		97 / 1 .	274.88	core	Ol-bearing gabbro	51.31	2.74	0.84	20.94	0.54	0.02	0.32	14.48	9.37	0.00	100.6
Cpx		3 / 1 .	274.89	rim	Ol-bearing gabbro	52.04	2.50	0.91	21.21	0.58	0.01	0.27	13.62	9.10	0.03	100.3
Cpx		21 / 1 .	274.89	rim	Ol-bearing gabbro	52.17	2.46	0.87	21.54	0.43	0.01	0.31	13.30	8.99	0.01	100.1
Cpx		22 / 1 .	274.89	rim	Ol-bearing gabbro	51.73	2.37	0.73	21.88	0.53	0.00	0.30	13.84	9.00	0.00	100.4
Cpx		25 / 1 .	274.89	rim	Ol-bearing gabbro	52.74	1.93	0.54	20.97	0.48	0.00	0.34	13.82	9.21	0.01	100.0
Cpx		27 / 1 .	274.9	rim	Ol-bearing gabbro	51.84	2.38	0.63	21.91	0.53	0.01	0.29	13.49	8.90	0.01	100.0
Cpx	735B_56R4_61A	29 / 1 .	274.9	rim	Ol-bearing gabbro	51.64	2.32	0.87	21.86	0.43	0.02	0.22	13.93	8.91	0.03	100.2
Cpx		40 / 1 .	274.9	rim	Ol-bearing gabbro	51.87	2.45	0.77	21.37	0.40	0.00	0.31	13.99	8.83	0.05	100.0
Cpx		52 / 1 .	274.9	rim	Ol-bearing gabbro	51.96	2.29	0.89	21.55	0.41	0.01	0.37	12.90	9.38	0.00	99.8
Cpx		54 / 1 .	274.9	rim	Ol-bearing gabbro	52.07	2.28	0.61	21.31	0.49	0.01	0.28	13.98	8.67	0.02	99.7
Cpx		57 / 1 .	274.91	rim	Ol-bearing gabbro	51.92	2.31	0.62	21.23	0.48	0.00	0.31	14.08	9.24	0.00	100.2
Cpx		66 / 1 .	274.9	rim	Ol-bearing gabbro	52.09	2.36	0.74	20.84	0.44	0.03	0.26	14.03	9.44	0.05	100.3
Cpx		2 / 1 .	274.89	exsol	Ol-bearing gabbro	52.24	2.41	0.86	20.84	0.48	0.01	0.22	13.61	9.51	0.00	100.2
Cpx		18 / 1 .	275.74	core	Ol-gabbro	51.51	2.30	0.68	22.13	0.45	0.01	0.25	13.43	9.16	0.03	99.9
Cpx		28 / 1 .	275.74	core	Ol-gabbro	51.45	2.42	0.96	19.32	0.39	0.02	0.27	14.20	10.50	0.05	99.6
Cpx		30 / 1 .	275.74	core	Ol-gabbro	51.25	2.66	0.81	21.72	0.51	0.01	0.27	13.92	8.69	0.02	99.9
Cpx	735B_57R1_73	32 / 1 .	275.74	core	Ol-gabbro	51.46	2.58	0.86	21.23	0.58	0.00	0.26	13.90	8.81	0.04	99.7
Cpx		48 / 1 .	275.75	core	Ol-gabbro	51.35	2.44	0.90	21.29	0.57	0.00	0.28	13.46	8.94	0.00	99.2
Cpx		57 / 1 .	275.75	core	Ol-gabbro	51.24	2.53	0.75	20.64	0.53	0.00	0.26	13.79	9.03	0.01	98.8
Cpx		61 / 1 .	275.76	core	Ol-gabbro	51.31	2.54	0.97	20.93	0.65	0.00	0.30	13.70	8.82	0.01	99.2
Cpx		74 / 1 .	284.35	core	Ol-gabbro	51.14	3.35	0.98	19.86	0.39	0.02	0.22	15.22	8.02	0.04	99.2
Cpx		76 / 1 .	284.35	core	Ol-gabbro	51.62	2.68	0.84	21.70	0.44	0.00	0.22	13.98	7.95	0.05	99.5
Cpx	735B_58R3_108A	94 / 1 .	284.34	core	Ol-gabbro	52.39	2.62	0.63	21.39	0.46	0.01	0.17	15.30	6.61	0.15	99.7
Cpx		132 / 1 .	284.34	core	Ol-gabbro	51.77	3.11	0.84	20.52	0.49	0.00	0.16	15.79	6.25	0.13	99.1
Cpx		134 / 1 .	284.35	core	Ol-gabbro	52.45	2.79	0.44	20.72	0.32	0.01	0.14	16.65	5.26	0.14	98.9
Cpx		83 / 1 .	295.39	core	Ol-gabbro	52.15	3.24	0.50	20.93	0.46	0.00	0.16	16.17	5.72	0.21	99.5
Cpx		91 / 1 .	295.38	core	Ol-gabbro	52.36	2.80	0.67	21.94	0.50	0.01	0.19	14.53	6.74	0.13	99.9
Cpx		93 / 1 .	295.38	core	Ol-gabbro	51.98	3.13	0.58	21.94	0.36	0.01	0.15	16.17	5.50	0.21	100.0
Cpx		97 / 1 .	295.4	core	Ol-gabbro	52.49	3.07	0.52	22.43	0.46	0.01	0.20	16.00	5.37	0.19	100.8
Cpx		107 / 1 .	295.4	core	Ol-gabbro	52.49	3.23	0.58	21.61	0.36	0.00	0.10	16.17	4.69	0.18	99.4
Cpx		5 / 1 .	295.39	core	Ol-gabbro	52.63	2.82	0.44	21.98	0.31	0.00	0.12	16.24	5.00	0.18	99.7
Cpx	735B_60R4_115B	6 / 1 .	295.39	core	Ol-gabbro	52.79	3.07	0.57	21.37	0.32	0.00	0.11	16.29	5.22	0.20	99.9
Cpx		23 / 1 .	295.39	core	Ol-gabbro	52.84	2.66	0.49	19.37	0.33	0.00	0.22	16.65	7.87	0.16	100.6

Mineral		Point	Depth (mbsf)	Grain area	Lithology	SiO2	Al2O3	TiO2	CaO	Na2O	K2O	MnO	MgO	FeO	Cr2O3	Total
Cpx		25 / 1 .	295.39	core	Ol-gabbro	51.58	2.74	1.09	20.05	0.38	0.00	0.23	15.39	8.34	0.11	99.9
Cpx		35 / 1 .	295.39	core	Ol-gabbro	51.93	2.67	1.20	19.53	0.33	0.00	0.26	15.74	8.89	0.18	100.7
Cpx		36 / 1 .	295.39	core	Ol-gabbro	52.39	2.76	0.72	18.12	0.36	0.01	0.24	16.39	9.05	0.22	100.2
Cpx		9 / 1 .	336.55	core	Ol-gabbro	51.86	3.06	0.65	22.20	0.40	0.02	0.17	15.03	5.83	0.31	99.5
Cpx		10 / 1 .	336.55	core	Ol-gabbro	51.98	3.09	0.49	21.98	0.40	0.00	0.09	14.78	5.68	0.38	98.9
Cpx	735B_68R2_10.5A	16 / 1 .	336.54	core	Ol-gabbro	51.97	3.45	0.61	20.73	0.40	0.00	0.16	15.55	6.26	0.46	99.6
Cpx		32 / 1 .	336.54	core	Ol-gabbro	51.52	2.95	1.05	20.58	0.31	0.02	0.22	15.67	7.44	0.04	99.8
Cpx		46 / 1 .	336.54	core	Ol-gabbro	52.49	2.83	0.46	22.32	0.41	0.03	0.15	15.56	5.55	0.31	100.1
Cpx		70 / 1 .	336.54	core	Ol-gabbro	52.13	3.27	0.58	19.68	0.29	0.02	0.28	16.06	7.10	0.51	99.9
Cpx		7 / 1 .	371.12	core	Ol-gabbro	52.59	2.52	0.74	20.16	0.29	0.03	0.21	16.94	5.93	0.20	99.6
Cpx		8 / 1 .	371.12	core	Ol-gabbro	52.41	2.76	0.34	20.81	0.31	0.00	0.21	16.41	6.10	0.22	99.6
Cpx		10 / 1 .	371.12	core	Ol-gabbro	52.53	2.83	0.52	22.02	0.38	0.01	0.20	15.60	5.61	0.20	99.9
Cpx		26 / 1 .	371.13	core	Ol-gabbro	51.68	2.41	0.85	22.05	0.33	0.02	0.20	15.37	5.53	0.07	98.5
Cpx	735B_73R5_9	28 / 1 .	371.13	core	Ol-gabbro	52.49	2.66	0.33	18.95	0.26	0.01	0.16	18.13	6.06	0.23	99.3
Cpx		43 / 1 .	371.14	core	Ol-gabbro	52.59	2.72	0.44	20.59	0.32	0.01	0.19	16.36	6.07	0.17	99.5
Cpx		49 / 1 .	371.13	core	Ol-gabbro	52.52	2.78	0.34	20.59	0.29	0.02	0.18	17.04	5.47	0.23	99.5
Cpx		53 / 1 .	371.15	core	Ol-gabbro	52.35	2.70	0.43	20.79	0.39	0.00	0.18	16.01	5.77	0.17	98.8
Cpx		55 / 1 .	371.15	core	Ol-gabbro	52.62	2.82	0.39	20.68	0.39	0.00	0.15	16.61	5.77	0.24	99.7
Cpx		72 / 1 .	371.15	core	Ol-gabbro	52.63	2.91	0.49	20.42	0.36	0.00	0.13	16.66	7.12	0.23	101.0
Cpx		8 / 1 .	390.36	core	Ol-gabbro	53.29	2.62	0.47	17.08	0.29	0.04	0.14	18.96	7.50	0.21	100.6
Cpx		12 / 1 .	390.36	core	Ol-gabbro	52.85	2.71	0.45	19.95	0.34	0.00	0.17	17.22	6.29	0.16	100.2
Cpx		26 / 1 .	390.35	core	Ol-gabbro	52.65	2.77	0.59	20.28	0.31	0.01	0.16	16.29	6.60	0.13	99.8
Cpx		30 / 1 .	390.35	core	Ol-gabbro	52.53	2.68	0.49	20.24	0.30	0.00	0.17	17.18	6.43	0.13	100.1
Cpx		32 / 1 .	390.35	core	Ol-gabbro	52.71	2.77	0.56	21.96	0.31	0.02	0.20	15.58	5.67	0.16	99.9
Cpx		42 / 1 .	390.35	core	Ol-gabbro	52.98	2.60	0.54	19.49	0.30	0.00	0.18	17.03	6.90	0.10	100.1
Cpx		48 / 1 .	390.35	core	Ol-gabbro	52.52	2.78	0.55	22.39	0.33	0.00	0.12	15.62	5.20	0.22	99.7
Cpx		58 / 1 .	390.35	core	Ol-gabbro	52.24	2.56	0.75	22.44	0.30	0.00	0.18	15.92	5.51	0.18	100.1
Cpx		63 / 1 .	390.34	core	Ol-gabbro	52.52	2.56	0.58	21.86	0.29	0.02	0.13	15.94	5.75	0.15	99.8
Cpx		66 / 1 .	390.34	core	Ol-gabbro	52.35	2.71	0.51	20.71	0.31	0.00	0.22	16.24	6.05	0.17	99.3
Cpx		83 / 1 .	390.34	core	Ol-gabbro	52.17	2.84	0.54	21.28	0.37	0.00	0.19	15.97	5.96	0.20	99.5
Cpx		87 / 1 .	390.34	core	Ol-gabbro	52.65	2.80	0.50	20.55	0.36	0.00	0.23	15.94	6.35	0.24	99.6
Cpx	735B_75R5_27	88 / 1 .	390.34	core	Ol-gabbro	52.89	2.30	0.61	22.38	0.18	0.00	0.09	16.23	5.27	0.21	100.2
Cpx		89 / 1 .	390.34	core	Ol-gabbro	52.39	2.71	0.47	22.25	0.39	0.00	0.16	15.56	5.87	0.21	100.0
Cpx		91 / 1 .	390.34	core	Ol-gabbro	52.58	2.54	0.64	16.82	0.26	0.03	0.16	18.65	8.32	0.07	100.1
Cpx		103 / 1 .	390.35	core	Ol-gabbro	53.31	2.64	0.42	19.04	0.29	0.00	0.19	17.96	6.24	0.26	100.3
Cpx		105 / 1 .	390.35	core	Ol-gabbro	52.37	2.66	0.58	22.43	0.43	0.02	0.16	15.68	5.35	0.20	99.9
Cpx		106 / 1 .	390.35	core	Ol-gabbro	52.66	2.63	0.41	20.56	0.40	0.03	0.20	16.67	6.27	0.18	100.0
Cpx		116 / 1 .	390.34	core	Ol-gabbro	52.72	2.81	0.46	18.75	0.32	0.01	0.20	17.20	7.29	0.30	100.1
Cpx		117 / 1 .	390.34	core	Ol-gabbro	52.49	2.51	0.63	22.21	0.47	0.01	0.15	15.42	5.89	0.14	99.9
Cpx		118 / 1 .	390.34	core	Ol-gabbro	52.23	2.44	0.59	21.49	0.43	0.06	0.15	15.61	5.98	0.24	99.2

Mineral		Point	Depth (mbsf)	Grain area	Lithology	SiO2	Al2O3	TiO2	CaO	Na2O	K2O	MnO	MgO	FeO	Cr2O3	Total
Cpx		119 / 1 .	390.34	core	Ol-gabbro	52.65	2.72	0.52	19.82	0.32	0.00	0.19	16.95	7.04	0.25	100.5
Cpx		120 / 1 .	390.34	core	Ol-gabbro	52.67	2.68	0.47	21.89	0.33	0.00	0.21	15.67	5.96	0.19	100.1
Cpx		121 / 1 .	390.34	core	Ol-gabbro	52.82	2.66	0.56	18.57	0.29	0.02	0.27	17.20	7.13	0.16	99.7
Cpx		4 / 1 .	344.13	core	Ol-gabbro	52.69	3.05	0.47	21.97	0.36	0.01	0.11	15.57	5.43	0.32	100.0
Cpx		5 / 1 .	344.13	core	Ol-gabbro	52.31	3.02	0.69	22.29	0.43	0.01	0.18	15.74	5.81	0.32	100.8
Cpx		6 / 1 .	344.13	core	Ol-gabbro	52.61	2.86	0.58	21.37	0.32	0.02	0.15	15.77	5.99	0.20	99.9
Cpx		17 / 1 .	344.13	core	Ol-gabbro	52.68	3.48	0.51	20.89	0.36	0.00	0.14	16.70	5.49	0.35	100.6
Cpx		18 / 1 .	344.13	core	Ol-gabbro	52.39	3.29	0.54	21.64	0.35	0.01	0.16	16.07	5.44	0.32	100.2
Cpx		20 / 1 .	344.13	core	Ol-gabbro	52.22	3.20	0.62	22.16	0.38	0.00	0.15	15.41	5.60	0.32	100.0
Cpx	735B_69R3_52B	55 / 1 .	344.14	core	Ol-gabbro	51.88	3.15	1.06	19.35	0.39	0.00	0.20	15.98	7.39	0.22	99.6
Cpx		58 / 1 .	344.14	core	Ol-gabbro	52.27	2.74	0.79	19.92	0.39	0.00	0.17	16.41	7.05	0.14	99.9
Cpx		59 / 1 .	344.14	core	Ol-gabbro	52.00	2.88	0.78	20.78	0.40	0.00	0.19	15.96	6.62	0.25	99.8
Cpx		77 / 1 .	344.14	core	Ol-gabbro	52.85	2.73	0.50	19.92	0.32	0.00	0.16	16.77	6.78	0.12	100.2
Cpx		89 / 1 .	344.13	core	Ol-gabbro	52.17	3.16	0.55	20.12	0.37	0.00	0.18	15.99	6.68	0.33	99.5
Cpx		97 / 1 .	344.13	core	Ol-gabbro	53.28	2.42	0.36	20.98	0.31	0.01	0.14	16.01	6.08	0.25	99.8
Cpx		98 / 1 .	344.13	core	Ol-gabbro	52.23	2.84	0.63	22.34	0.35	0.00	0.17	15.31	6.02	0.23	100.1
Cpx		29 / 1 .	275.74	rim	Ol-gabbro	51.72	2.19	0.77	20.78	0.46	0.00	0.26	13.95	9.56	0.05	99.7
Cpx	735B_57R1_73	34 / 1 .	275.74	rim	Ol-gabbro	52.18	1.68	0.49	22.49	0.44	0.00	0.35	13.45	8.40	0.01	99.5
Cpx		50 / 1 .	275.75	rim	Ol-gabbro	51.45	2.60	0.85	21.60	0.46	0.00	0.30	13.86	8.60	0.05	99.8
Cpx		58 / 1 .	275.75	rim	Ol-gabbro	50.98	2.58	0.70	21.34	0.59	0.00	0.21	13.61	8.77	0.00	98.8
Cpx		72 / 1 .	284.35	rim	Ol-gabbro	50.96	2.63	0.87	21.29	0.34	0.00	0.24	14.33	8.33	0.08	99.1
Cpx		75 / 1 .	284.35	rim	Ol-gabbro	51.41	2.60	0.86	18.87	0.37	0.01	0.26	15.62	9.85	0.07	99.9
Cpx	735B_58R3_108A	77 / 1 .	284.35	rim	Ol-gabbro	51.44	2.73	0.85	21.59	0.39	0.01	0.30	13.95	8.04	0.11	99.4
Cpx		131 / 1 .	284.35	rim	Ol-gabbro	51.11	2.63	0.91	21.36	0.39	0.00	0.20	14.76	7.55	0.13	99.0
Cpx		135 / 1 .	284.35	rim	Ol-gabbro	51.88	2.57	0.83	21.55	0.39	0.02	0.23	14.83	6.84	0.09	99.2
Cpx		84 / 1 .	295.39	rim	Ol-gabbro	51.82	2.88	0.93	22.02	0.57	0.01	0.18	14.92	6.38	0.07	99.8
Cpx		89 / 1 .	295.38	rim	Ol-gabbro	51.53	3.12	1.03	20.94	0.46	0.00	0.20	14.92	7.06	0.11	99.4
Cpx		90 / 1 .	295.38	rim	Ol-gabbro	51.30	3.08	0.90	21.94	0.43	0.00	0.27	14.96	6.94	0.11	99.9
Cpx		92 / 1 .	295.38	rim	Ol-gabbro	51.70	2.93	1.04	21.63	0.52	0.00	0.22	15.45	6.41	0.12	100.0
Cpx		98 / 1 .	295.4	rim	Ol-gabbro	52.88	2.69	0.72	19.77	0.41	0.00	0.22	16.75	6.86	0.20	100.5
Cpx	735B_60R4_115B	99 / 1 .	295.4	rim	Ol-gabbro	52.20	3.10	0.58	21.11	0.40	0.00	0.24	15.57	6.64	0.19	100.0
Cpx		4 / 1 .	295.39	rim	Ol-gabbro	52.44	2.68	0.65	20.22	0.32	0.04	0.21	16.01	7.10	0.15	99.8
Cpx		22 / 1 .	295.39	rim	Ol-gabbro	52.11	2.73	0.91	20.50	0.31	0.01	0.19	15.64	7.44	0.15	100.0
Cpx		24 / 1 .	295.39	rim	Ol-gabbro	51.36	2.81	0.95	21.45	0.43	0.02	0.19	14.87	7.57	0.15	99.8
Cpx		34 / 1 .	295.39	rim	Ol-gabbro	51.79	2.69	1.02	21.67	0.54	0.00	0.25	14.99	7.18	0.13	100.3
Cpx		37 / 1 .	295.39	rim	Ol-gabbro	51.98	2.82	0.74	19.87	0.39	0.00	0.23	15.90	7.69	0.14	99.8
Cpx		11 / 1 .	336.55	rim	Ol-gabbro	51.44	2.86	0.90	22.41	0.35	0.02	0.19	14.93	5.52	0.30	98.9
Cpx		17 / 1 .	336.54	rim	Ol-gabbro	51.77	2.77	0.88	22.71	0.34	0.00	0.17	15.51	5.53	0.15	99.8
Cpx		18 / 1 .	336.54	rim	Ol-gabbro	52.61	2.79	0.65	22.17	0.37	0.01	0.16	15.35	6.02	0.13	100.3
Cpx		31 / 1 .	336.54	rim	Ol-gabbro	51.10	3.13	1.19	21.47	0.34	0.02	0.22	14.68	7.05	0.06	99.3

Mineral		Point	Depth (mbsf)	Grain area	Lithology	SiO2	Al2O3	TiO2	CaO	Na2O	K2O	MnO	MgO	FeO	Cr2O3	Total
Cpx	735B_68R2_10.5A	33 / 1 .	336.54	rim	Ol-gabbro	51.31	3.13	1.32	22.07	0.39	0.00	0.19	14.64	6.72	0.04	99.8
Cpx		45 / 1 .	336.54	rim	Ol-gabbro	51.99	2.84	0.99	22.27	0.37	0.01	0.19	15.07	6.19	0.08	100.0
Cpx		63 / 1 .	336.55	rim	Ol-gabbro	51.31	2.90	1.25	20.85	0.37	0.00	0.18	15.15	6.39	0.19	98.6
Cpx		64 / 1 .	336.55	rim	Ol-gabbro	51.58	2.84	0.82	21.60	0.32	0.01	0.23	15.30	6.13	0.27	99.1
Cpx		65 / 1 .	336.55	rim	Ol-gabbro	52.46	2.77	0.72	18.18	0.33	0.01	0.22	16.94	7.65	0.28	99.6
Cpx		71 / 1 .	336.54	rim	Ol-gabbro	52.58	2.63	0.75	19.78	0.27	0.00	0.23	16.47	7.31	0.23	100.2
Cpx		11 / 1 .	371.12	rim	Ol-gabbro	52.53	2.58	0.68	21.80	0.33	0.01	0.19	15.73	5.65	0.17	99.7
Cpx		29 / 1 .	371.13	rim	Ol-gabbro	52.43	2.65	0.89	18.34	0.25	0.00	0.20	17.53	7.25	0.13	99.7
Cpx		41 / 1 .	371.14	rim	Ol-gabbro	50.92	3.23	1.26	22.34	0.37	0.00	0.17	14.81	5.83	0.11	99.0
Cpx	735B_73R5_9	42 / 1 .	371.14	rim	Ol-gabbro	51.55	2.84	1.06	20.69	0.31	0.01	0.34	15.50	6.45	0.11	98.9
Cpx		52 / 1 .	371.15	rim	Ol-gabbro	51.69	2.69	1.10	22.14	0.36	0.02	0.20	15.17	5.94	0.12	99.4
Cpx		54 / 1 .	371.15	rim	Ol-gabbro	52.16	3.27	0.64	20.93	0.38	0.00	0.18	16.35	5.74	0.18	99.8
Cpx		56 / 1 .	371.15	rim	Ol-gabbro	52.39	2.68	0.63	17.99	0.33	0.01	0.22	17.21	7.82	0.10	99.4
Cpx		71 / 1 .	371.15	rim	Ol-gabbro	51.56	2.87	1.11	22.41	0.36	0.01	0.14	14.95	5.81	0.11	99.3
Cpx		9 / 1 .	390.36	rim	Ol-gabbro	52.32	2.62	0.74	21.13	0.32	0.01	0.16	16.49	6.06	0.13	100.0
Cpx		10 / 1 .	390.36	rim	Ol-gabbro	52.97	2.59	0.61	18.10	0.26	0.01	0.17	17.59	7.18	0.15	99.6
Cpx		11 / 1 .	390.36	rim	Ol-gabbro	52.52	2.59	0.73	19.95	0.29	0.02	0.22	16.62	6.43	0.16	99.5
Cpx		27 / 1 .	390.35	rim	Ol-gabbro	52.25	2.69	0.80	22.49	0.32	0.03	0.20	15.18	5.82	0.13	99.9
Cpx		28 / 1 .	390.35	rim	Ol-gabbro	52.37	2.81	0.80	22.22	0.34	0.00	0.18	15.64	5.81	0.09	100.3
Cpx		29 / 1 .	390.35	rim	Ol-gabbro	52.25	2.60	0.84	20.43	0.28	0.00	0.17	16.55	6.31	0.20	99.6
Cpx		31 / 1 .	390.35	rim	Ol-gabbro	52.44	2.78	0.69	20.15	0.37	0.03	0.19	16.48	6.55	0.14	99.8
Cpx		41 / 1 .	390.35	rim	Ol-gabbro	52.32	2.82	0.97	22.20	0.38	0.01	0.12	14.97	5.84	0.09	99.7
Cpx		43 / 1 .	390.35	rim	Ol-gabbro	52.17	2.68	0.96	22.50	0.33	0.01	0.20	15.59	5.87	0.11	100.4
Cpx		47 / 1 .	390.35	rim	Ol-gabbro	52.37	2.75	0.64	19.57	0.30	0.01	0.21	16.66	6.62	0.04	99.2
Cpx	735B_75R5_27	49 / 1 .	390.35	rim	Ol-gabbro	52.38	2.48	0.90	22.12	0.36	0.03	0.17	15.21	5.64	0.13	99.4
Cpx		64 / 1 .	390.34	rim	Ol-gabbro	52.44	2.53	0.58	22.11	0.37	0.02	0.16	15.81	5.66	0.17	99.8
Cpx		67 / 1 .	390.34	rim	Ol-gabbro	52.81	2.63	0.71	20.11	0.27	0.01	0.17	16.88	6.31	0.14	100.0
Cpx		84 / 1 .	390.34	rim	Ol-gabbro	52.65	2.32	0.68	22.00	0.41	0.01	0.17	15.88	5.78	0.12	100.0
Cpx		86 / 1 .	390.34	rim	Ol-gabbro	53.03	2.45	0.56	19.95	0.33	0.00	0.19	16.85	6.80	0.13	100.3
Cpx		90 / 1 .	390.34	rim	Ol-gabbro	52.86	2.68	0.63	22.33	0.33	0.02	0.17	15.53	6.19	0.11	100.8
Cpx		92 / 1 .	390.34	rim	Ol-gabbro	52.38	2.69	0.63	19.57	0.44	0.05	0.22	16.67	6.88	0.14	99.7
Cpx		102 / 1 .	390.35	rim	Ol-gabbro	52.79	2.77	0.47	18.92	0.34	0.00	0.20	17.31	6.96	0.17	99.9
Cpx		104 / 1 .	390.35	rim	Ol-gabbro	52.13	2.70	0.74	21.12	0.49	0.03	0.18	16.07	6.00	0.17	99.6
Cpx		115 / 1 .	390.34	rim	Ol-gabbro	52.68	2.60	0.56	21.18	0.32	0.00	0.15	16.17	6.04	0.21	99.9
Cpx		3 / 1 .	344.13	rim	Ol-gabbro	52.73	2.68	0.67	21.95	0.43	0.02	0.15	15.83	5.53	0.19	100.2
Cpx		7 / 1 .	344.13	rim	Ol-gabbro	52.61	2.54	0.76	21.30	0.30	0.00	0.17	15.85	6.04	0.25	99.8
Cpx		15 / 1 .	344.13	rim	Ol-gabbro	52.08	3.15	0.91	21.64	0.55	0.03	0.17	15.56	5.88	0.23	100.2
Cpx		16 / 1 .	344.13	rim	Ol-gabbro	51.52	3.04	1.09	22.64	0.62	0.04	0.22	15.00	5.58	0.27	100.0
Cpx		35 / 1 .	344.14	rim	Ol-gabbro	52.86	2.84	0.49	20.37	0.37	0.01	0.17	16.62	6.12	0.18	100.0
Cpx		54 / 1 .	344.14	rim	Ol-gabbro	51.51	3.22	1.08	21.83	0.46	0.00	0.22	15.01	6.11	0.18	99.6

Mineral	735B_69R3_52B	Point	Depth (mbsf)	Grain area	Lithology	SiO2	Al2O3	TiO2	CaO	Na2O	K2O	MnO	MgO	FeO	Cr2O3	Total
Cpx		56 / 1 .	344.14	rim	Ol-gabbro	51.85	3.11	1.15	19.93	0.48	0.01	0.19	15.91	6.78	0.19	99.6
Cpx		57 / 1 .	344.14	rim	Ol-gabbro	51.59	3.13	1.09	21.39	0.40	0.00	0.12	15.50	6.18	0.26	99.7
Cpx		76 / 1 .	344.14	rim	Ol-gabbro	52.15	2.86	0.87	22.09	0.36	0.00	0.17	15.39	6.17	0.14	100.2
Cpx		88 / 1 .	344.13	rim	Ol-gabbro	51.94	2.90	0.95	21.91	0.44	0.00	0.17	15.16	6.01	0.12	99.6
Cpx		96 / 1 .	344.13	rim	Ol-gabbro	52.22	2.72	0.71	19.63	0.36	0.01	0.20	16.36	7.30	0.17	99.7
Cpx		95 / 1 .	425.37	core	Ol-gabbro	51.50	1.80	0.64	20.02	0.42	0.00	0.45	12.24	12.50	0.00	99.6
Cpx		97 / 1 .	425.37	core	Ol-gabbro	51.79	1.63	0.51	19.32	0.35	0.00	0.39	12.80	13.09	0.04	99.9
Cpx		98 / 1 .	425.37	core	Ol-gabbro	51.34	1.89	0.59	20.00	0.49	0.00	0.39	12.38	12.66	0.03	99.8
Cpx	735B_80R1_136	100 / 1 .	425.37	core	Ol-gabbro	51.70	1.62	0.57	20.31	0.45	0.00	0.37	12.63	12.27	0.00	99.9
Cpx		109 / 1 .	425.37	core	Ol-gabbro	51.55	1.61	0.49	20.06	0.38	0.01	0.43	12.56	12.30	0.00	99.4
Cpx		142 / 1 .	425.38	core	Ol-gabbro	52.23	3.80	0.40	22.08	0.35	0.01	0.10	16.22	3.70	0.95	99.8
Cpx		143 / 1 .	425.38	core	Ol-gabbro	52.11	3.77	0.46	20.75	0.37	0.00	0.11	16.92	3.59	0.87	98.9
Cpx		150 / 1 .	425.38	core	Ol-gabbro	51.08	4.31	0.63	20.89	0.53	0.01	0.16	16.11	3.91	1.12	98.7
Cpx		1 / 1 .	439.25	core	Ol-gabbro	52.53	3.45	0.47	21.34	0.37	0.00	0.19	15.84	5.00	0.32	99.5
Cpx		4 / 1 .	439.25	core	Ol-gabbro	51.89	3.29	0.53	22.03	0.32	0.03	0.21	15.32	5.25	0.33	99.2
Cpx		16 / 1 .	439.25	core	Ol-gabbro	52.13	3.09	0.73	22.39	0.46	0.01	0.15	15.62	5.42	0.21	100.2
Cpx		18 / 1 .	439.25	core	Ol-gabbro	52.49	2.43	0.51	22.72	0.37	0.01	0.19	15.53	5.25	0.17	99.7
Cpx		19 / 1 .	439.25	core	Ol-gabbro	52.49	2.59	0.76	20.55	0.31	0.01	0.23	15.92	6.73	0.16	99.8
Cpx		26 / 1 .	439.25	core	Ol-gabbro	52.75	2.20	0.60	22.44	0.41	0.00	0.21	15.64	5.43	0.24	99.9
Cpx		28 / 1 .	439.25	core	Ol-gabbro	52.88	2.38	0.71	22.27	0.36	0.03	0.20	15.68	5.23	0.18	99.9
Cpx	735B_81R5_7	29 / 1 .	439.25	core	Ol-gabbro	53.05	2.41	0.62	20.28	0.29	0.04	0.16	16.63	6.25	0.17	99.9
Cpx		36 / 1 .	439.25	core	Ol-gabbro	52.04	2.88	0.73	21.51	0.41	0.02	0.18	15.88	5.57	0.24	99.5
Cpx		41 / 1 .	439.25	core	Ol-gabbro	52.59	2.77	0.43	22.09	0.34	0.00	0.16	16.14	4.99	0.23	99.7
Cpx		52 / 1 .	439.25	core	Ol-gabbro	52.80	2.87	0.62	18.76	0.33	0.01	0.27	16.84	7.51	0.19	100.2
Cpx		56 / 1 .	439.25	core	Ol-gabbro	52.41	2.61	0.39	20.65	0.37	0.00	0.21	16.41	6.09	0.25	99.4
Cpx		72 / 1 .	439.26	core	Ol-gabbro	52.54	2.77	0.52	19.23	0.30	0.00	0.21	16.98	6.19	0.27	99.0
Cpx		80 / 1 .	439.26	core	Ol-gabbro	51.58	2.84	1.04	21.52	0.39	0.00	0.18	15.77	5.92	0.21	99.4
Cpx		85 / 1 .	439.26	core	Ol-gabbro	51.67	3.09	0.89	21.97	0.38	0.00	0.19	15.13	5.48	0.21	99.0
Cpx		88 / 1 .	439.26	core	Ol-gabbro	52.01	2.76	0.44	21.83	0.39	0.02	0.18	15.70	5.66	0.21	99.2
Cpx		12 / 1 .	418.51	core	Ol-gabbro	52.01	3.22	0.63	22.46	0.33	0.01	0.17	15.67	4.62	0.60	99.7
Cpx		23 / 1 .	418.5	core	Ol-gabbro	51.75	3.04	1.14	22.29	0.38	0.00	0.21	14.93	5.63	0.17	99.5
Cpx	735B_79R3_100	35 / 1 .	418.52	core	Ol-gabbro	51.81	3.03	0.66	22.22	0.33	0.00	0.20	15.67	5.29	0.48	99.7
Cpx		38 / 1 .	418.52	core	Ol-gabbro	51.91	3.12	0.67	21.23	0.35	0.02	0.14	15.93	5.51	0.47	99.3
Cpx		45 / 1 .	418.52	core	Ol-gabbro	52.57	3.21	0.44	17.88	0.22	0.03	0.18	18.58	7.19	0.47	100.8
Cpx		56 / 1 .	397.58	core	Ol-gabbro	52.51	3.16	0.51	21.26	0.32	0.02	0.17	16.64	5.60	0.19	100.4
Cpx		64 / 1 .	397.59	core	Ol-gabbro	52.32	2.61	0.75	19.33	0.32	0.01	0.25	16.29	7.90	0.02	99.8
Cpx		78 / 1 .	397.59	core	Ol-gabbro	52.43	2.78	0.66	21.21	0.41	0.02	0.14	15.86	6.47	0.16	100.1
Cpx		86 / 1 .	397.58	core	Ol-gabbro	52.26	3.10	0.47	21.45	0.34	0.01	0.18	15.74	6.14	0.30	100.0
Cpx		87 / 1 .	397.58	core	Ol-gabbro	52.39	2.89	0.57	19.55	0.26	0.01	0.20	16.66	7.44	0.19	100.1
Cpx		94 / 1 .	397.58	core	Ol-gabbro	52.54	3.15	0.50	20.96	0.33	0.00	0.16	16.51	5.75	0.30	100.2

Mineral	735B_76R3_96	Point	Depth (mbsf)	Grain area	Lithology	SiO2	Al2O3	TiO2	CaO	Na2O	K2O	MnO	MgO	FeO	Cr2O3	Total
Cpx		104 / 1 .	397.58	core	Ol-gabbro	52.83	2.80	0.60	19.65	0.34	0.00	0.24	16.51	7.09	0.21	100.3
Cpx		105 / 1 .	397.58	core	Ol-gabbro	52.24	2.81	0.74	21.21	0.32	0.00	0.16	15.98	6.54	0.12	100.1
Cpx		115 / 1 .	397.57	core	Ol-gabbro	52.43	2.90	0.63	20.73	0.35	0.01	0.22	15.85	6.60	0.19	99.9
Cpx		118 / 1 .	397.57	core	Ol-gabbro	53.33	2.24	0.38	19.97	0.34	0.00	0.17	17.70	5.92	0.23	100.3
Cpx		120 / 1 .	397.56	core	Ol-gabbro	52.54	2.77	0.44	20.56	0.32	0.00	0.13	17.20	6.14	0.25	100.4
Cpx		123 / 1 .	397.56	core	Ol-gabbro	52.69	3.17	0.51	18.60	0.35	0.01	0.14	17.59	6.38	0.27	99.7
Cpx		103 / 1 .	419.15	core	Ol-gabbro	52.71	2.86	0.41	20.47	0.62	0.03	0.20	16.65	5.04	0.63	99.6
Cpx		114 / 1 .	419.16	core	Ol-gabbro	52.06	3.68	0.57	21.05	0.78	0.00	0.11	15.78	4.84	0.79	99.7
Cpx		115 / 1 .	419.16	core	Ol-gabbro	52.51	2.76	0.53	23.13	0.48	0.01	0.16	15.09	4.33	0.70	99.7
Cpx		11 / 1 .	419.16	core	Ol-gabbro	53.77	1.91	0.25	23.56	0.29	0.01	0.17	16.25	3.71	0.43	100.4
Cpx		25 / 1 .	419.16	core	Ol-gabbro	50.71	4.88	0.65	19.81	1.05	0.03	0.14	15.78	4.67	0.87	98.6
Cpx	735B_79R4_20	37 / 1 .	419.16	core	Ol-gabbro	52.48	3.42	0.48	21.53	0.72	0.02	0.13	16.15	4.21	0.70	99.8
Cpx		41 / 1 .	419.16	core	Ol-gabbro	52.46	3.53	0.42	21.19	0.62	0.00	0.16	16.12	4.64	0.70	99.9
Cpx		54 / 1 .	419.17	core	Ol-gabbro	52.66	3.40	0.39	20.71	0.41	0.00	0.15	16.63	4.66	0.60	99.6
Cpx		67 / 1 .	419.17	core	Ol-gabbro	53.63	1.83	0.37	22.65	0.30	0.01	0.16	15.85	4.37	0.57	99.8
Cpx		68 / 1 .	419.17	core	Ol-gabbro	53.23	1.96	0.24	22.58	0.51	0.00	0.13	16.20	4.18	0.59	99.6
Cpx		82 / 1 .	419.17	core	Ol-gabbro	53.46	2.31	0.54	23.05	0.39	0.00	0.18	15.79	3.87	0.33	99.9
Cpx		15 / 1 .	461.68	core	Ol-gabbro	52.39	3.60	0.44	20.20	0.35	0.00	0.12	17.31	5.30	0.91	100.6
Cpx		16 / 1 .	461.68	core	Ol-gabbro	52.60	3.57	0.41	19.48	0.31	0.00	0.15	17.53	5.44	0.79	100.3
Cpx		45 / 1 .	461.7	core	Ol-gabbro	53.16	2.51	0.64	21.65	0.31	0.00	0.14	16.37	4.63	0.34	99.7
Cpx	735B_83R7_43B	64 / 1 .	461.69	core	Ol-gabbro	53.08	3.08	0.62	22.76	0.47	0.00	0.23	15.78	4.25	0.32	100.6
Cpx		83 / 1 .	461.69	core	Ol-gabbro	52.36	3.31	0.34	18.00	0.31	0.01	0.13	18.13	6.04	0.80	99.4
Cpx		84 / 1 .	461.69	core	Ol-gabbro	51.60	3.70	0.34	22.10	0.43	0.03	0.14	15.83	4.41	0.95	99.5
Cpx		95 / 1 .	461.69	core	Ol-gabbro	53.21	2.75	0.30	17.55	0.27	0.01	0.16	19.36	6.40	0.32	100.3
Cpx		23 / 1 .	425.99	core	Ol-gabbro	52.04	3.22	1.48	22.48	0.36	0.00	0.15	15.54	4.01	0.20	99.5
Cpx		33 / 1 .	426	core	Ol-gabbro	52.28	3.24	1.18	22.06	0.45	0.02	0.14	15.90	4.13	0.18	99.6
Cpx	735B_80R2_51	48 / 1 .	425.99	core	Ol-gabbro	52.46	3.38	0.83	20.94	0.41	0.00	0.19	16.13	5.06	0.24	99.6
Cpx		51 / 1 .	425.99	core	Ol-gabbro	52.88	3.17	0.58	22.60	0.45	0.04	0.18	15.59	4.60	0.27	100.4
Cpx		79 / 1 .	426	core	Ol-gabbro	53.52	2.39	0.67	19.78	0.27	0.02	0.15	17.36	5.45	0.13	99.7
Cpx		1	509.49	core	Ol-gabbro	51.31	2.99	0.66	21.71	0.24	0.00	0.19	16.85	5.57	0.31	99.8
Cpx	90R-2W-18-20	11	509.49	core	Ol-gabbro	49.92	3.17	1.07	22.11	0.36	0.00	0.18	15.99	4.98	0.42	98.2
Cpx		22	509.49	core	Ol-gabbro	51.04	2.73	0.93	24.65	0.28	0.00	0.16	15.57	4.24	0.29	99.9
Cpx		54	509.49	core	Ol-gabbro	50.79	3.10	0.84	21.99	0.44	0.02	0.18	15.91	5.78	0.31	99.3
Cpx		59	510.1	core	Ol-gabbro	51.70	3.52	0.36	21.20	0.32	0.01	0.13	16.51	4.21	1.16	99.1
Cpx		91	510.1	core	Ol-gabbro	52.58	2.96	0.40	17.11	0.24	0.00	0.17	19.81	6.44	0.71	100.4
Cpx		101	510.1	core	Ol-gabbro	50.82	3.46	0.94	21.63	0.38	0.01	0.17	16.53	5.21	0.58	99.7
Cpx		105	510.1	core	Ol-gabbro	51.64	3.11	0.48	19.50	0.36	0.00	0.19	17.29	6.79	0.51	99.9
Cpx		110	510.1	core	Ol-gabbro	51.20	3.03	0.84	19.89	0.33	0.01	0.21	17.79	6.44	0.53	100.3
Cpx	90R-2W-82-86	111	510.1	core	Ol-gabbro	51.30	3.17	0.66	22.48	0.27	0.01	0.19	16.61	4.75	0.39	99.8
Cpx		126	510.1	core	Ol-gabbro	50.71	3.23	1.20	23.75	0.45	0.00	0.16	16.11	4.26	0.27	100.1

Mineral		Point	Depth (mbsf)	Grain area	Lithology	SiO2	Al2O3	TiO2	CaO	Na2O	K2O	MnO	MgO	FeO	Cr2O3	Total
Cpx		129	510.1	core	Ol-gabbro	52.12	3.02	0.57	19.65	0.23	0.01	0.20	17.98	6.54	0.26	100.6
Cpx		133	510.1	core	Ol-gabbro	50.68	3.21	0.90	23.84	0.35	0.00	0.21	15.33	5.22	0.38	100.1
Cpx		137	510.17	core	Ol-gabbro	50.82	3.59	0.64	24.09	0.36	0.00	0.16	15.66	4.18	0.83	100.3
Cpx		145	510.17	core	Ol-gabbro	50.87	3.77	0.45	22.98	0.40	0.01	0.16	15.98	4.19	1.04	99.9
Cpx		162	510.17	core	Ol-gabbro	52.22	3.43	0.35	21.55	0.34	0.00	0.12	17.29	4.50	1.04	100.8
Cpx	90R-2W-84-90	163	510.17	core	Ol-gabbro	51.74	3.46	0.36	20.72	0.30	0.00	0.12	17.41	4.60	1.07	99.8
Cpx		190	510.17	core	Ol-gabbro	51.27	3.56	0.46	23.60	0.33	0.01	0.15	15.98	4.34	0.85	100.5
Cpx		204	510.17	core	Ol-gabbro	50.99	3.99	0.60	20.83	0.59	0.00	0.21	16.91	5.35	0.85	100.3
Cpx		213	510.17	core	Ol-gabbro	51.59	3.37	0.44	22.92	0.25	0.00	0.14	16.48	4.76	0.74	100.7
Cpx		9	510.27	core	Ol-gabbro	51.06	3.49	0.48	22.94	0.39	0.00	0.14	15.70	4.03	0.69	98.9
Cpx		13	510.27	core	Ol-gabbro	51.13	3.42	0.52	22.75	0.43	0.02	0.15	15.25	4.33	0.78	98.8
Cpx		21	510.27	core	Ol-gabbro	51.88	2.92	0.60	20.11	0.39	0.00	0.25	15.73	5.95	0.44	98.3
Cpx		25	510.27	core	Ol-gabbro	51.40	3.41	0.50	22.64	0.38	0.00	0.13	16.10	4.08	0.60	99.3
Cpx		34	510.27	core	Ol-gabbro	51.24	3.26	0.42	21.69	0.29	0.00	0.14	16.34	4.63	0.71	98.7
Cpx	90R-2W-94-100b	40	510.27	core	Ol-gabbro	51.26	3.58	0.54	20.80	0.49	0.00	0.17	16.71	4.55	0.58	98.7
Cpx		47	510.27	core	Ol-gabbro	51.53	3.57	0.45	22.36	0.33	0.00	0.12	16.21	4.22	0.74	99.5
Cpx		48	510.27	core	Ol-gabbro	52.01	3.11	0.33	18.28	0.20	0.00	0.13	18.85	5.72	0.79	99.4
Cpx		55	510.27	core	Ol-gabbro	51.97	3.38	0.29	14.85	0.34	0.00	0.18	20.69	6.75	0.88	99.3
Cpx		56	510.27	core	Ol-gabbro	51.57	3.78	0.69	19.24	0.55	0.01	0.15	17.86	4.32	0.66	98.8
Cpx		4	510.27	core	Ol-gabbro	51.15	3.31	0.38	20.33	0.30	0.00	0.11	18.21	4.59	1.04	99.4
Cpx		85	510.56	core	Ol-gabbro	51.78	2.93	0.53	21.56	0.21	0.01	0.17	16.81	4.87	0.43	99.3
Cpx		94	510.56	core	Ol-gabbro	51.86	3.27	0.43	19.71	0.29	0.01	0.17	17.42	5.30	0.71	99.2
Cpx	90R-2W-123-129	102	510.56	core	Ol-gabbro	51.48	3.78	0.41	20.41	0.31	0.00	0.17	16.75	5.14	1.01	99.5
Cpx		120	510.56	core	Ol-gabbro	52.16	3.33	0.56	18.82	0.29	0.00	0.15	18.00	5.32	0.66	99.3
Cpx		126	510.56	core	Ol-gabbro	51.19	3.34	0.48	22.14	0.41	0.00	0.13	16.05	4.29	1.11	99.1
Cpx		130	510.56	core	Ol-gabbro	51.88	3.44	0.43	20.64	0.31	0.01	0.16	16.98	4.88	0.61	99.3
Cpx		139	510.67	core	Ol-gabbro	51.96	2.97	0.45	19.23	0.23	0.00	0.15	18.02	5.40	0.47	98.9
Cpx	90R-2W-135-139	208	510.67	core	Ol-gabbro	51.45	3.43	0.50	22.24	0.36	0.00	0.17	16.27	4.32	0.52	99.2
Cpx		234	510.67	core	Ol-gabbro	52.76	2.66	0.37	21.87	0.19	0.00	0.15	17.40	4.42	0.51	100.3
Cpx		235	510.67	core	Ol-gabbro	52.08	3.00	0.42	20.18	0.25	0.00	0.17	18.05	5.27	0.55	100.0
Cpx		20	510.84	core	Ol-gabbro	51.74	3.15	0.61	21.46	0.26	0.00	0.16	16.68	4.88	0.57	99.5
Cpx	90R-3W-6-8	54	510.84	core	Ol-gabbro	51.40	3.72	0.46	22.56	0.29	0.00	0.15	15.80	4.16	0.77	99.3
Cpx		56	510.84	core	Ol-gabbro	51.35	3.33	0.60	22.45	0.42	0.01	0.14	16.12	3.79	0.75	98.9
Cpx		68	510.84	core	Ol-gabbro	51.18	3.70	0.42	19.67	0.37	0.01	0.19	17.12	5.14	0.74	98.5
Cpx		83 / 1 .	425.36	rim	Ol-gabbro	51.80	1.18	0.34	19.93	0.37	0.01	0.45	12.15	13.43	0.00	99.7
Cpx		84 / 1 .	425.36	rim	Ol-gabbro	51.68	1.23	0.28	20.11	0.40	0.01	0.41	11.94	12.90	0.00	99.0
Cpx		96 / 1 .	425.37	rim	Ol-gabbro	51.25	1.74	0.53	20.42	0.46	0.02	0.39	12.20	11.96	0.00	99.0
Cpx		99 / 1 .	425.37	rim	Ol-gabbro	52.01	1.31	0.33	20.68	0.29	0.02	0.37	12.78	11.66	0.00	99.5
Cpx		110 / 1 .	425.37	rim	Ol-gabbro	51.67	1.59	0.52	20.46	0.40	0.01	0.41	12.39	12.38	0.04	99.9
Cpx	735B_80R1_136	112 / 1 .	425.37	rim	Ol-gabbro	51.19	1.49	0.47	20.58	0.32	0.02	0.42	12.55	12.04	0.02	99.1

Mineral		Point	Depth (mbsf)	Grain area	Lithology	SiO2	Al2O3	TiO2	CaO	Na2O	K2O	MnO	MgO	FeO	Cr2O3	Total
Cpx		144 / 1 .	425.38	rim	Ol-gabbro	52.15	3.16	0.47	22.18	0.49	0.00	0.14	15.03	4.92	0.85	99.4
Cpx		155 / 1 .	425.39	rim	Ol-gabbro	51.76	3.40	0.68	22.37	0.56	0.01	0.15	15.22	4.62	0.91	99.7
Cpx		2 / 1 .	439.25	rim	Ol-gabbro	53.04	1.99	0.53	22.25	0.27	0.04	0.16	15.83	5.55	0.14	99.8
Cpx		3 / 1 .	439.25	rim	Ol-gabbro	52.58	2.66	0.66	21.91	0.37	0.03	0.18	16.18	4.95	0.22	99.7
Cpx		15 / 1 .	439.25	rim	Ol-gabbro	52.47	2.57	0.68	22.27	0.34	0.00	0.18	15.62	5.58	0.18	99.9
Cpx		27 / 1 .	439.25	rim	Ol-gabbro	52.75	2.37	0.60	22.13	0.34	0.01	0.16	15.77	5.24	0.17	99.5
Cpx		42 / 1 .	439.25	rim	Ol-gabbro	51.99	2.90	0.77	22.27	0.34	0.00	0.15	15.33	5.43	0.19	99.4
Cpx	735B_81R5_7	43 / 1 .	439.25	rim	Ol-gabbro	52.56	2.70	0.76	22.42	0.41	0.01	0.14	15.49	4.74	0.10	99.3
Cpx		53 / 1 .	439.25	rim	Ol-gabbro	52.06	2.75	0.92	22.09	0.34	0.00	0.18	15.17	5.63	0.13	99.3
Cpx		55 / 1 .	439.25	rim	Ol-gabbro	51.76	3.17	1.14	21.94	0.40	0.00	0.15	14.92	5.87	0.15	99.5
Cpx		71 / 1 .	439.26	rim	Ol-gabbro	52.32	2.76	0.85	21.89	0.34	0.00	0.18	16.14	5.15	0.18	99.8
Cpx		77 / 1 .	439.26	rim	Ol-gabbro	52.33	2.97	0.83	22.12	0.35	0.01	0.17	15.15	5.76	0.19	99.9
Cpx		78 / 1 .	439.26	rim	Ol-gabbro	52.03	3.17	0.59	21.70	0.37	0.00	0.17	15.66	5.37	0.21	99.3
Cpx		11 / 1 .	418.51	rim	Ol-gabbro	52.35	3.14	0.43	22.13	0.35	0.00	0.17	15.85	4.57	0.52	99.5
Cpx		13 / 1 .	418.51	rim	Ol-gabbro	52.82	3.34	0.48	19.83	0.33	0.01	0.26	17.16	5.62	0.56	100.4
Cpx		14 / 1 .	418.51	rim	Ol-gabbro	52.02	3.38	0.67	21.99	0.43	0.01	0.16	15.51	4.58	0.65	99.4
Cpx	735B_79R3_100	34 / 1 .	418.51	rim	Ol-gabbro	51.45	3.22	0.57	22.02	0.32	0.00	0.14	15.78	5.24	0.54	99.3
Cpx		36 / 1 .	418.52	rim	Ol-gabbro	52.46	2.93	0.65	20.88	0.33	0.04	0.22	16.15	5.55	0.58	99.8
Cpx		37 / 1 .	418.52	rim	Ol-gabbro	52.13	3.26	0.58	21.35	0.35	0.00	0.19	15.79	5.91	0.50	100.1
Cpx		72 / 1 .	418.53	rim	Ol-gabbro	51.80	3.61	0.44	22.07	0.36	0.00	0.14	15.62	5.19	0.85	100.1
Cpx		55 / 1 .	397.58	rim	Ol-gabbro	52.03	2.92	0.91	22.09	0.42	0.04	0.18	15.24	5.75	0.13	99.7
Cpx		63 / 1 .	397.59	rim	Ol-gabbro	51.22	3.02	1.22	20.97	0.42	0.00	0.21	15.61	6.98	0.09	99.7
Cpx		65 / 1 .	397.59	rim	Ol-gabbro	51.86	2.68	0.94	22.60	0.39	0.00	0.14	14.92	6.36	0.04	99.9
Cpx		77 / 1 .	397.59	rim	Ol-gabbro	52.35	2.88	1.00	21.42	0.40	0.01	0.23	15.69	6.61	0.09	100.7
Cpx	735B_76R3_96	85 / 1 .	397.58	rim	Ol-gabbro	51.94	2.83	1.02	21.85	0.32	0.00	0.21	15.52	6.13	0.16	100.0
Cpx		93 / 1 .	397.58	rim	Ol-gabbro	52.06	2.75	0.78	21.83	0.33	0.00	0.22	16.08	6.14	0.15	100.3
Cpx		116 / 1 .	397.57	rim	Ol-gabbro	52.57	2.91	0.86	22.08	0.43	0.01	0.13	15.17	5.71	0.18	100.1
Cpx		117 / 1 .	397.57	rim	Ol-gabbro	52.05	2.99	0.68	20.57	0.32	0.00	0.15	16.37	6.16	0.19	99.5
Cpx		119 / 1 .	397.56	rim	Ol-gabbro	52.53	2.88	0.66	22.27	0.34	0.01	0.16	15.73	5.82	0.14	100.5
Cpx		101 / 1 .	419.15	rim	Ol-gabbro	53.26	2.53	0.38	22.92	0.45	0.00	0.19	16.03	3.80	0.53	100.1
Cpx		102 / 1 .	419.15	rim	Ol-gabbro	53.26	2.27	0.31	22.72	0.48	0.00	0.16	15.88	4.54	0.62	100.2
Cpx		113 / 1 .	419.16	rim	Ol-gabbro	52.61	2.75	0.40	22.30	0.57	0.02	0.18	15.86	4.45	0.66	99.8
Cpx		23 / 1 .	419.16	rim	Ol-gabbro	52.74	2.80	0.40	22.36	0.52	0.01	0.11	15.29	4.39	0.71	99.3
Cpx	735B_79R4_20	38 / 1 .	419.16	rim	Ol-gabbro	52.54	3.15	0.52	21.12	0.52	0.01	0.19	16.47	4.59	0.61	99.7
Cpx		40 / 1 .	419.16	rim	Ol-gabbro	53.05	2.95	0.41	21.70	0.53	0.00	0.11	16.00	4.36	0.76	99.9
Cpx		50 / 1 .	419.17	rim	Ol-gabbro	52.28	3.64	0.48	20.59	0.76	0.01	0.13	15.94	4.86	0.77	99.5
Cpx		55 / 1 .	419.17	rim	Ol-gabbro	53.49	2.74	0.42	21.37	0.57	0.00	0.20	16.18	4.45	0.57	100.0
Cpx		66 / 1 .	419.17	rim	Ol-gabbro	52.91	2.94	0.29	21.84	0.53	0.02	0.12	15.89	4.08	0.62	99.2
Cpx		91 / 1 .	419.18	rim	Ol-gabbro	52.88	2.80	0.55	22.16	0.53	0.03	0.16	15.90	4.33	0.53	99.9
Cpx		1 / 1 .	461.68	rim	Ol-gabbro	52.45	2.82	0.58	22.89	0.41	0.01	0.15	15.45	3.87	0.62	99.2

Mineral		Point	Depth (mbsf)	Grain area	Lithology	SiO2	Al2O3	TiO2	CaO	Na2O	K2O	MnO	MgO	FeO	Cr2O3	Total
Cpx		2 / 1 .	461.68	rim	Ol-gabbro	52.41	3.53	0.74	21.38	0.50	0.00	0.14	15.74	4.95	0.70	100.1
Cpx		44 / 1 .	461.7	rim	Ol-gabbro	52.82	2.61	0.70	23.17	0.32	0.00	0.15	15.47	4.19	0.36	99.8
Cpx		46 / 1 .	461.7	rim	Ol-gabbro	52.86	2.92	0.72	23.00	0.43	0.04	0.14	15.86	4.10	0.41	100.5
Cpx		65 / 1 .	461.69	rim	Ol-gabbro	52.68	2.86	0.70	22.97	0.41	0.01	0.15	15.42	3.82	0.71	99.7
Cpx	735B_83R7_43B	66 / 1 .	461.69	rim	Ol-gabbro	53.13	2.47	0.44	23.44	0.35	0.00	0.16	16.04	3.78	0.57	100.4
Cpx		76 / 1 .	461.69	rim	Ol-gabbro	53.07	2.47	0.48	22.61	0.39	0.00	0.20	15.98	3.97	0.62	99.8
Cpx		77 / 1 .	461.69	rim	Ol-gabbro	53.08	3.13	0.80	18.79	0.48	0.01	0.19	17.30	5.87	0.27	99.9
Cpx		78 / 1 .	461.69	rim	Ol-gabbro	52.53	2.93	0.47	22.01	0.45	0.01	0.19	15.94	4.99	0.62	100.1
Cpx		94 / 1 .	461.69	rim	Ol-gabbro	53.08	2.15	0.31	22.59	0.38	0.00	0.20	15.73	4.66	0.57	99.7
Cpx		96 / 1 .	461.69	rim	Ol-gabbro	52.70	3.06	0.60	20.51	0.36	0.01	0.16	16.51	5.26	0.52	99.7
Cpx		105 / 1 .	461.69	rim	Ol-gabbro	52.42	3.40	0.42	21.45	0.45	0.01	0.22	15.95	4.96	0.67	100.0
Cpx		106 / 1 .	461.69	rim	Ol-gabbro	52.14	3.35	0.41	21.87	0.37	0.01	0.15	15.68	4.41	0.72	99.1
Cpx		30 / 1 .	426	rim	Ol-gabbro	52.39	3.14	1.07	22.49	0.48	0.00	0.17	15.94	3.94	0.14	99.8
Cpx		32 / 1 .	426	rim	Ol-gabbro	52.22	3.15	1.13	22.79	0.39	0.00	0.10	15.59	3.65	0.10	99.1
Cpx		34 / 1 .	426	rim	Ol-gabbro	52.55	2.81	1.04	22.85	0.39	0.03	0.12	16.00	4.01	0.09	99.9
Cpx		50 / 1 .	425.99	rim	Ol-gabbro	52.53	2.54	0.89	23.04	0.47	0.01	0.17	15.91	4.02	0.15	99.7
Cpx	735B_80R2_51	52 / 1 .	425.99	rim	Ol-gabbro	52.64	2.74	0.88	22.62	0.41	0.01	0.19	15.89	4.22	0.21	99.8
Cpx		53 / 1 .	425.99	rim	Ol-gabbro	52.21	3.11	1.02	22.77	0.44	0.05	0.14	15.68	3.83	0.11	99.4
Cpx		77 / 1 .	426	rim	Ol-gabbro	52.33	2.84	1.00	22.70	0.36	0.00	0.14	16.02	4.83	0.11	100.3
Cpx		78 / 1 .	426	rim	Ol-gabbro	52.41	2.99	1.01	20.45	0.45	0.01	0.14	16.71	5.16	0.10	99.4
Cpx		80 / 1 .	426	rim	Ol-gabbro	52.25	2.95	1.06	22.34	0.53	0.02	0.12	15.76	4.54	0.09	99.6
Cpx		2	509.49	rim	Ol-gabbro	50.54	3.13	0.88	23.28	0.38	0.00	0.15	16.04	4.67	0.29	99.4
Cpx		3	509.49	rim	Ol-gabbro	50.84	3.14	1.01	22.80	0.33	0.00	0.16	16.47	4.64	0.32	99.7
Cpx		10	509.49	rim	Ol-gabbro	51.14	2.71	0.81	24.11	0.28	0.01	0.15	15.74	4.53	0.30	99.8
Cpx		12	509.49	rim	Ol-gabbro	50.83	2.81	0.81	24.14	0.31	0.01	0.16	15.43	4.84	0.31	99.7
Cpx	90R-2W-18-20	21	509.49	rim	Ol-gabbro	50.32	3.37	1.32	22.33	0.41	0.01	0.15	16.48	4.58	0.15	99.1
Cpx		34	509.49	rim	Ol-gabbro	50.17	3.84	1.16	23.07	0.56	0.02	0.16	15.45	5.10	0.33	99.9
Cpx		35	509.49	rim	Ol-gabbro	51.04	2.67	0.81	24.58	0.25	0.01	0.15	15.55	4.56	0.26	99.9
Cpx		36	509.49	rim	Ol-gabbro	52.12	2.15	0.64	24.56	0.22	0.01	0.14	16.21	4.24	0.20	100.5
Cpx		55	509.49	rim	Ol-gabbro	51.16	2.67	0.89	24.47	0.32	0.00	0.18	15.23	5.05	0.30	100.3
Cpx		54	510.1	rim	Ol-gabbro	51.54	3.50	0.62	21.68	0.33	0.00	0.16	16.83	4.59	0.95	100.2
Cpx		65	510.1	rim	Ol-gabbro	51.51	3.39	0.48	21.20	0.41	0.00	0.17	16.97	5.18	1.12	100.4
Cpx		84	510.1	rim	Ol-gabbro	51.76	3.32	0.62	23.05	0.37	0.01	0.15	16.28	3.94	0.74	100.2
Cpx		85	510.1	rim	Ol-gabbro	50.80	3.28	0.59	23.20	0.28	0.00	0.14	15.94	4.97	0.67	99.9
Cpx		100	510.1	rim	Ol-gabbro	50.56	3.10	0.77	23.31	0.36	0.00	0.17	16.85	4.38	0.64	100.1
Cpx		106	510.1	rim	Ol-gabbro	51.58	2.92	0.83	20.22	0.32	0.00	0.21	17.23	6.57	0.34	100.2
Cpx	90R-2W-82-86	109	510.1	rim	Ol-gabbro	50.64	3.58	1.11	24.25	0.43	0.00	0.13	15.64	3.78	0.69	100.2
Cpx		125	510.1	rim	Ol-gabbro	50.97	3.67	1.30	24.16	0.45	0.02	0.14	15.86	4.02	0.25	100.8
Cpx		130	510.1	rim	Ol-gabbro	50.03	3.42	1.28	23.57	0.48	0.01	0.18	14.99	5.39	0.27	99.6
Cpx		131	510.1	rim	Ol-gabbro	52.38	1.82	0.50	24.55	0.26	0.00	0.15	15.79	4.90	0.15	100.5

Mineral		Point	Depth (mbsf)	Grain area	Lithology	SiO2	Al2O3	TiO2	CaO	Na2O	K2O	MnO	MgO	FeO	Cr2O3	Total
Cpx		134	510.1	rim	Ol-gabbro	50.88	3.13	0.93	24.05	0.36	0.01	0.17	15.38	5.20	0.40	100.5
Cpx		138	510.17	rim	Ol-gabbro	50.32	4.17	0.72	22.33	0.73	0.05	0.14	16.35	4.59	0.56	99.9
Cpx		142	510.17	rim	Ol-gabbro	51.10	3.13	0.60	22.16	0.32	0.00	0.17	16.47	5.21	0.85	100.0
Cpx		143	510.17	rim	Ol-gabbro	50.95	3.43	0.53	21.59	0.38	0.00	0.24	15.43	5.91	0.81	99.3
Cpx		157	510.17	rim	Ol-gabbro	51.49	3.65	0.50	24.00	0.35	0.01	0.13	15.63	3.92	1.00	100.7
Cpx	90R-2W-84-90	186	510.17	rim	Ol-gabbro	51.53	3.33	0.65	20.73	0.36	0.01	0.20	17.73	4.83	0.77	100.1
Cpx		195	510.17	rim	Ol-gabbro	50.76	3.39	0.50	23.81	0.32	0.00	0.16	16.36	4.47	0.98	100.7
Cpx		206	510.17	rim	Ol-gabbro	50.55	3.27	0.97	23.78	0.34	0.00	0.19	14.99	4.98	0.50	99.6
Cpx		207	510.17	rim	Ol-gabbro	50.71	3.43	0.78	21.91	0.47	0.00	0.19	16.17	5.00	0.67	99.3
Cpx		212	510.17	rim	Ol-gabbro	51.32	3.24	0.56	23.31	0.42	0.00	0.14	16.26	4.18	0.71	100.1
Cpx		7	510.27	rim	Ol-gabbro	51.02	3.52	0.65	22.89	0.33	0.00	0.13	16.14	3.70	0.71	99.1
Cpx		8	510.27	rim	Ol-gabbro	50.89	3.82	0.48	22.42	0.45	0.00	0.13	16.30	3.76	0.92	99.2
Cpx		12	510.27	rim	Ol-gabbro	51.78	2.31	0.54	23.24	0.30	0.01	0.16	15.73	4.24	0.55	98.9
Cpx		20	510.27	rim	Ol-gabbro	51.42	2.99	0.91	23.15	0.44	0.00	0.14	15.53	4.09	0.53	99.2
Cpx		26	510.27	rim	Ol-gabbro	51.48	3.36	0.59	23.02	0.34	0.00	0.16	16.04	3.84	0.83	99.7
Cpx		33	510.27	rim	Ol-gabbro	51.08	3.45	0.65	22.98	0.41	0.00	0.13	16.01	3.53	0.77	99.0
Cpx	90R-2W-94-100b	39	510.27	rim	Ol-gabbro	51.65	3.14	0.64	21.34	0.35	0.00	0.15	16.45	4.85	0.76	99.3
Cpx		46	510.27	rim	Ol-gabbro	52.22	2.65	0.39	22.14	0.37	0.01	0.13	17.24	3.59	0.59	99.3
Cpx		49	510.27	rim	Ol-gabbro	51.03	3.30	0.68	22.60	0.30	0.00	0.11	16.61	3.77	0.77	99.2
Cpx		53	510.27	rim	Ol-gabbro	50.82	4.66	0.76	21.07	0.65	0.02	0.13	16.24	3.85	0.97	99.2
Cpx		57	510.27	rim	Ol-gabbro	52.04	2.56	0.69	23.87	0.24	0.00	0.12	16.39	3.18	0.72	99.8
Cpx		3	510.27	rim	Ol-gabbro	51.24	3.29	0.71	22.99	0.32	0.00	0.12	16.12	3.65	0.89	99.3
Cpx		5	510.27	rim	Ol-gabbro	50.21	3.83	0.71	22.47	0.34	0.00	0.13	15.80	4.33	0.97	98.8
Cpx		78	510.56	rim	Ol-gabbro	51.27	3.26	0.86	23.47	0.35	0.01	0.14	15.45	3.95	0.58	99.3
Cpx		80	510.56	rim	Ol-gabbro	51.15	3.24	0.88	23.27	0.38	0.01	0.15	15.66	3.85	0.68	99.3
Cpx		84	510.56	rim	Ol-gabbro	51.49	3.07	0.63	21.65	0.24	0.00	0.18	17.00	4.48	0.59	99.3
Cpx		95	510.56	rim	Ol-gabbro	51.49	3.14	0.65	21.72	0.31	0.01	0.14	16.74	4.20	0.85	99.2
Cpx		101	510.56	rim	Ol-gabbro	51.39	3.53	0.58	20.36	0.44	0.00	0.16	16.89	4.63	0.99	99.0
Cpx	90R-2W-123-129	103	510.56	rim	Ol-gabbro	51.82	2.46	0.47	23.59	0.30	0.00	0.15	15.92	3.42	0.78	98.9
Cpx		114	510.56	rim	Ol-gabbro	51.43	3.17	0.81	23.28	0.26	0.00	0.14	15.74	3.82	0.77	99.4
Cpx		119	510.56	rim	Ol-gabbro	51.38	3.23	0.87	20.87	0.28	0.00	0.17	16.87	4.65	0.65	99.0
Cpx		121	510.56	rim	Ol-gabbro	51.08	3.15	0.89	23.42	0.24	0.00	0.15	15.94	3.87	0.67	99.4
Cpx		125	510.56	rim	Ol-gabbro	51.71	3.01	0.54	22.66	0.26	0.00	0.15	16.20	3.97	0.95	99.5
Cpx		127	510.56	rim	Ol-gabbro	50.98	3.74	0.62	22.77	0.40	0.01	0.17	15.14	4.54	1.20	99.6
Cpx		131	510.56	rim	Ol-gabbro	51.22	3.30	0.61	23.12	0.27	0.00	0.14	16.05	3.75	0.78	99.2
Cpx		138	510.67	rim	Ol-gabbro	51.15	3.32	0.92	23.24	0.31	0.01	0.14	15.94	3.81	0.63	99.5
Cpx		140	510.67	rim	Ol-gabbro	51.25	3.10	0.73	23.17	0.20	0.00	0.14	15.76	4.23	0.49	99.1
Cpx		141	510.67	rim	Ol-gabbro	50.98	3.23	1.12	23.26	0.31	0.01	0.16	15.65	3.96	0.48	99.2
Cpx	90R-2W-135-139	195	510.67	rim	Ol-gabbro	51.43	3.29	0.78	21.69	0.30	0.00	0.15	16.40	4.95	0.52	99.5
Cpx		231	510.67	rim	Ol-gabbro	51.07	3.13	0.99	23.62	0.25	0.00	0.13	15.99	3.56	0.58	99.3

Mineral		Point	Depth (mbsf)	Grain area	Lithology	SiO2	Al2O3	TiO2	CaO	Na2O	K2O	MnO	MgO	FeO	Cr2O3	Total
Cpx		238	510.67	rim	Ol-gabbro	51.12	3.18	0.81	21.46	0.32	0.00	0.16	16.71	4.81	0.62	99.2
Cpx		21	510.84	rim	Ol-gabbro	51.91	2.97	0.77	20.61	0.30	0.00	0.18	17.66	4.98	0.53	99.9
Cpx		34	510.84	rim	Ol-gabbro	51.49	2.89	0.83	23.36	0.26	0.00	0.14	16.05	3.80	0.43	99.3
Cpx		36	510.84	rim	Ol-gabbro	50.93	3.33	0.60	21.90	0.33	0.00	0.12	16.42	4.10	0.50	98.2
Cpx		47	510.84	rim	Ol-gabbro	51.34	3.35	0.62	22.99	0.39	0.00	0.13	16.11	3.52	0.85	99.3
Cpx	90R-3W-6-8	53	510.84	rim	Ol-gabbro	51.50	2.95	0.48	21.61	0.28	0.00	0.17	16.80	4.43	0.73	99.0
Cpx		55	510.84	rim	Ol-gabbro	51.34	3.61	0.58	20.18	0.46	0.00	0.15	17.11	4.54	0.77	98.7
Cpx		67	510.84	rim	Ol-gabbro	51.81	2.81	0.45	20.57	0.25	0.00	0.18	17.50	4.98	0.64	99.2
Cpx		69	510.84	rim	Ol-gabbro	51.10	3.33	0.71	22.34	0.33	0.00	0.16	15.51	4.34	0.87	98.7
Cpx		73	510.84	rim	Ol-gabbro	50.91	3.72	0.54	20.65	0.34	0.00	0.16	17.12	4.39	1.26	99.1
Cpx		99 / 1 .	462.55	core	Ol-rich gabbro	52.60	3.39	0.43	21.52	0.46	0.02	0.16	16.43	4.11	1.18	100.3
Cpx		120 / 1 .	462.57	core	Ol-rich gabbro	52.46	3.40	0.48	20.63	0.36	0.01	0.15	17.04	4.28	0.95	99.8
Cpx		121 / 1 .	462.57	core	Ol-rich gabbro	52.32	3.43	0.47	21.21	0.31	0.01	0.16	16.31	4.48	0.86	99.6
Cpx	735B_83R7_130A	123 / 1 .	462.56	core	Ol-rich gabbro	52.18	3.12	0.91	23.73	0.39	0.03	0.12	15.53	3.24	0.56	99.8
Cpx		125 / 1 .	462.56	core	Ol-rich gabbro	52.31	2.77	0.93	23.16	0.44	0.01	0.09	16.03	3.18	0.56	99.5
Cpx		141 / 1 .	462.56	core	Ol-rich gabbro	52.51	3.37	0.80	22.44	0.38	0.03	0.15	15.79	3.77	0.62	99.9
Cpx		149 / 1 .	462.55	core	Ol-rich gabbro	52.15	3.42	0.59	22.31	0.36	0.00	0.14	15.70	4.14	0.53	99.3
Cpx		13 / 1 .	461.55	core	Ol-rich gabbro	52.25	2.94	0.91	22.80	0.33	0.00	0.16	15.80	3.51	0.27	99.0
Cpx		28 / 1 .	461.57	core	Ol-rich gabbro	52.53	3.17	0.51	21.49	0.49	0.02	0.14	16.32	4.41	0.40	99.5
Cpx	735B_83R7_0	52 / 1 .	461.57	core	Ol-rich gabbro	52.66	3.14	0.54	22.15	0.37	0.03	0.15	16.19	4.46	0.41	100.1
Cpx		68 / 1 .	461.57	core	Ol-rich gabbro	52.07	3.14	1.07	22.38	0.48	0.01	0.14	15.62	3.98	0.40	99.3
Cpx		69 / 1 .	461.57	core	Ol-rich gabbro	52.07	3.38	0.80	22.24	0.51	0.00	0.17	15.87	4.18	0.65	99.9
Cpx		9 / 1 .	462.4	core	Ol-rich gabbro	52.06	3.68	0.73	22.10	0.51	0.00	0.15	15.88	4.22	0.86	100.2
Cpx		21 / 1 .	462.39	core	Ol-rich gabbro	52.93	3.59	0.42	19.59	0.44	0.00	0.16	17.15	5.28	1.20	100.8
Cpx		26 / 1 .	462.39	core	Ol-rich gabbro	53.25	3.18	0.52	19.53	0.30	0.00	0.17	17.57	5.06	0.56	100.1
Cpx		28 / 1 .	462.38	core	Ol-rich gabbro	52.09	3.33	0.63	22.49	0.40	0.01	0.15	15.81	4.15	0.86	99.9
Cpx		41 / 1 .	462.39	core	Ol-rich gabbro	52.41	3.63	0.57	21.30	0.44	0.01	0.12	15.83	4.20	1.02	99.5
Cpx	735B_83R7_113A	49 / 1 .	462.39	core	Ol-rich gabbro	52.95	2.97	0.38	20.10	0.43	0.00	0.19	17.12	5.02	0.79	100.0
Cpx		58 / 1 .	462.4	core	Ol-rich gabbro	52.25	3.41	0.78	22.70	0.52	0.02	0.13	15.78	3.95	0.74	100.3
Cpx		66 / 1 .	462.39	core	Ol-rich gabbro	52.41	3.73	0.96	22.24	0.64	0.00	0.13	15.52	3.86	0.68	100.2
Cpx		69 / 1 .	462.4	core	Ol-rich gabbro	51.78	3.89	0.63	20.24	0.74	0.03	0.17	16.64	4.29	0.95	99.4
Cpx		72 / 1 .	462.4	core	Ol-rich gabbro	52.51	3.17	0.46	22.07	0.39	0.00	0.12	15.93	4.26	0.84	99.7
Cpx		90 / 1 .	462.39	core	Ol-rich gabbro	52.84	2.56	0.71	23.11	0.42	0.01	0.12	15.86	3.21	0.53	99.4
Cpx		71 / 1 .	518.36	core	Ol-rich gabbro	51.89	4.05	0.47	22.47	0.38	0.00	0.18	15.25	4.38	1.03	100.1
Cpx		81 / 1 .	518.36	core	Ol-rich gabbro	51.82	3.42	1.11	23.47	0.42	0.00	0.07	15.84	3.25	0.81	100.2
Cpx		82 / 1 .	518.36	core	Ol-rich gabbro	52.20	3.25	1.03	22.68	0.45	0.00	0.15	15.39	3.52	0.74	99.4
Cpx		18 / 1 .	518.35	core	Ol-rich gabbro	51.86	3.79	0.37	20.87	0.34	0.01	0.08	16.20	4.60	1.30	99.4
Cpx		20 / 1 .	518.35	core	Ol-rich gabbro	51.50	4.23	0.38	22.44	0.45	0.00	0.09	15.04	4.24	1.42	99.8
Cpx	735B_91R1_93A	48 / 1 .	518.35	core	Ol-rich gabbro	51.26	3.93	0.50	22.44	0.46	0.00	0.14	14.88	3.94	1.29	98.8
Cpx		61 / 1 .	518.34	core	Ol-rich gabbro	51.18	4.33	0.49	22.07	0.46	0.00	0.15	15.07	4.01	1.34	99.1

Mineral		Point	Depth (mbsf)	Grain area	Lithology	SiO2	Al2O3	TiO2	CaO	Na2O	K2O	MnO	MgO	FeO	Cr2O3	Total
Cpx		62 / 1 .	518.34	core	Ol-rich gabbro	50.93	4.50	0.36	21.21	0.39	0.00	0.11	15.54	4.15	1.42	98.6
Cpx		82 / 1 .	518.33	core	Ol-rich gabbro	52.14	3.98	0.42	21.30	0.38	0.00	0.11	15.82	4.45	1.28	99.9
Cpx		83 / 1 .	518.33	core	Ol-rich gabbro	51.36	3.89	0.48	22.60	0.44	0.00	0.13	15.39	3.78	1.28	99.3
Cpx		13 / 1 .	518.16	core	Ol-rich gabbro	51.40	3.85	0.50	21.54	0.40	0.01	0.15	16.23	4.63	0.91	99.6
Cpx		22 / 1 .	518.16	core	Ol-rich gabbro	52.66	3.32	0.47	22.16	0.36	0.00	0.18	16.01	4.26	0.83	100.2
Cpx	735B_91R1_74	51 / 1 .	518.15	core	Ol-rich gabbro	51.83	3.79	0.44	23.02	0.44	0.02	0.17	15.44	4.23	0.91	100.3
Cpx		61 / 1 .	518.15	core	Ol-rich gabbro	52.01	3.55	0.50	23.08	0.38	0.00	0.15	15.34	3.78	1.06	99.9
Cpx		67 / 1 .	518.15	core	Ol-rich gabbro	52.49	3.25	0.41	21.76	0.36	0.01	0.16	16.75	4.45	1.03	100.7
Cpx		100 / 1 .	462.55	rim	Ol-rich gabbro	52.15	3.20	0.89	23.09	0.46	0.00	0.14	15.66	3.56	0.97	100.1
Cpx	735B_83R7_130A	119 / 1 .	462.57	rim	Ol-rich gabbro	52.80	2.86	0.65	23.01	0.44	0.00	0.14	15.75	3.12	0.74	99.5
Cpx		140 / 1 .	462.56	rim	Ol-rich gabbro	52.61	3.15	1.00	22.31	0.44	0.00	0.16	15.82	3.56	0.57	99.6
Cpx		148 / 1 .	462.55	rim	Ol-rich gabbro	52.13	3.41	1.08	22.23	0.48	0.01	0.17	15.92	3.74	0.63	99.8
Cpx		15 / 1 .	461.57	rim	Ol-rich gabbro	52.85	2.56	0.52	23.34	0.36	0.00	0.10	16.03	3.72	0.41	99.9
Cpx		16 / 1 .	461.57	rim	Ol-rich gabbro	52.44	3.07	0.57	22.29	0.42	0.00	0.16	15.81	4.09	0.45	99.3
Cpx	735B_83R7_0	27 / 1 .	461.57	rim	Ol-rich gabbro	52.61	3.21	0.66	22.59	0.45	0.00	0.14	15.84	4.06	0.57	100.1
Cpx		50 / 1 .	461.57	rim	Ol-rich gabbro	52.50	2.59	0.73	22.75	0.37	0.02	0.16	16.07	4.08	0.31	99.6
Cpx		51 / 1 .	461.57	rim	Ol-rich gabbro	52.78	2.65	0.47	18.62	0.33	0.00	0.21	18.53	5.62	0.30	99.5
Cpx		8 / 1 .	462.4	rim	Ol-rich gabbro	52.23	3.56	0.65	22.27	0.56	0.00	0.13	15.62	3.89	0.77	99.7
Cpx		22 / 1 .	462.39	rim	Ol-rich gabbro	52.77	2.88	0.64	23.87	0.32	0.02	0.07	15.78	3.14	0.80	100.3
Cpx		27 / 1 .	462.39	rim	Ol-rich gabbro	52.87	3.28	0.50	19.03	0.32	0.01	0.18	18.02	5.46	0.53	100.2
Cpx	735B_83R7_113A	29 / 1 .	462.38	rim	Ol-rich gabbro	52.32	3.57	0.76	22.35	0.43	0.00	0.17	15.72	3.94	0.78	100.0
Cpx		42 / 1 .	462.39	rim	Ol-rich gabbro	52.88	3.43	0.68	19.69	0.40	0.00	0.18	17.18	4.77	0.95	100.1
Cpx		50 / 1 .	462.39	rim	Ol-rich gabbro	52.21	3.52	0.60	20.53	0.49	0.00	0.15	16.72	4.66	0.96	99.8
Cpx		70 / 1 .	462.4	rim	Ol-rich gabbro	52.70	3.42	0.68	22.58	0.50	0.02	0.14	15.43	3.58	0.91	100.0
Cpx		71 / 1 .	462.4	rim	Ol-rich gabbro	51.99	3.72	0.70	22.21	0.60	0.01	0.08	15.68	3.59	1.10	99.7
Cpx		70 / 1 .	518.36	rim	Ol-rich gabbro	52.09	3.41	0.96	22.01	0.40	0.02	0.15	15.91	3.80	0.93	99.7
Cpx		83 / 1 .	518.36	rim	Ol-rich gabbro	51.96	3.65	1.45	23.06	0.51	0.00	0.13	15.70	3.25	0.84	100.6
Cpx		19 / 1 .	518.35	rim	Ol-rich gabbro	51.31	3.82	0.90	22.67	0.47	0.00	0.14	15.41	3.44	1.26	99.4
Cpx		21 / 1 .	518.35	rim	Ol-rich gabbro	51.86	3.63	1.03	22.33	0.51	0.01	0.12	15.87	3.38	0.92	99.7
Cpx	735B_91R1_93A	35 / 1 .	518.34	rim	Ol-rich gabbro	51.25	3.89	1.38	22.40	0.61	0.01	0.11	15.50	3.61	1.00	99.8
Cpx		36 / 1 .	518.34	rim	Ol-rich gabbro	51.33	3.86	1.44	22.99	0.41	0.00	0.09	15.56	3.42	1.08	100.2
Cpx		47 / 1 .	518.35	rim	Ol-rich gabbro	50.96	4.35	1.49	22.23	0.55	0.01	0.12	15.01	3.30	1.12	99.1
Cpx		59 / 1 .	518.34	rim	Ol-rich gabbro	51.28	3.82	1.36	22.46	0.62	0.01	0.10	15.24	3.61	1.04	99.5
Cpx		60 / 1 .	518.34	rim	Ol-rich gabbro	51.87	4.09	0.53	21.06	0.34	0.00	0.11	16.05	4.40	1.42	99.9
Cpx		84 / 1 .	518.33	rim	Ol-rich gabbro	51.27	3.82	1.15	22.82	0.58	0.03	0.11	15.18	3.31	1.19	99.5
Cpx		14 / 1 .	518.16	rim	Ol-rich gabbro	51.66	3.56	1.08	22.87	0.40	0.01	0.15	15.52	3.48	0.78	99.5
Cpx		15 / 1 .	518.16	rim	Ol-rich gabbro	51.38	3.24	1.23	23.11	0.28	0.00	0.13	15.49	3.49	0.69	99.0
Cpx		23 / 1 .	518.16	rim	Ol-rich gabbro	51.83	3.37	0.66	22.34	0.41	0.01	0.14	15.55	4.04	0.80	99.1
Cpx		39 / 1 .	518.15	rim	Ol-rich gabbro	50.94	3.80	1.22	22.19	0.75	0.03	0.10	15.84	3.51	0.88	99.3
Cpx	735B_91R1_74	50 / 1 .	518.15	rim	Ol-rich gabbro	51.37	4.03	1.25	22.60	0.48	0.01	0.14	15.21	3.80	1.00	99.9

Mineral	[illegible]	Point	Depth (mbsf)	Grain area	Lithology	SiO2	Al2O3	TiO2	CaO	Na2O	K2O	MnO	MgO	FeO	Cr2O3	Total
Cpx		60 / 1 .	518.15	rim	Ol-rich gabbro	51.96	3.80	0.72	21.69	0.37	0.00	0.14	16.22	4.37	1.00	100.3
Cpx		68 / 1 .	518.15	rim	Ol-rich gabbro	51.62	3.94	0.98	22.70	0.43	0.00	0.14	15.51	3.78	0.93	100.0
Cpx		70 / 1 .	518.15	rim	Ol-rich gabbro	51.84	3.65	0.98	23.02	0.42	0.02	0.10	15.60	3.50	0.88	100.0
Cpx		13 / 1 .	499.63	core	Troctolite	52.42	3.46	0.57	22.39	0.39	0.00	0.15	15.61	4.18	0.78	100.0
Cpx	735B_87R7_49	29 / 1 .	499.64	core	Troctolite	52.85	2.86	0.81	21.28	0.41	0.00	0.17	16.90	4.28	0.30	99.8
Cpx		30 / 1 .	499.64	core	Troctolite	52.27	2.99	1.12	21.98	0.35	0.00	0.16	16.44	4.32	0.36	100.0
Cpx		4 / 1 .	505.27	core	Troctolite	51.70	3.48	1.28	23.34	0.28	0.00	0.10	15.56	3.78	0.44	100.0
Cpx	735B_89R1_47	6 / 1 .	505.27	core	Troctolite	51.46	3.70	1.37	21.62	0.48	0.00	0.16	15.81	4.66	0.28	99.6
Cpx		14 / 1 .	505.28	core	Troctolite	51.96	2.88	0.85	22.64	0.45	0.01	0.14	16.52	3.46	0.36	99.3
Cpx	90R-2W-68-75	8	510.02	core	Troctolite	50.65	3.35	1.27	23.58	0.39	0.00	0.16	15.58	4.87	0.14	100.0
Cpx		11	510.02	core	Troctolite	51.45	3.06	1.11	19.23	0.29	0.00	0.22	18.04	6.67	0.15	100.2
Cpx		12 / 1 .	499.63	rim	Troctolite	51.49	3.58	1.03	21.86	0.66	0.00	0.14	15.63	4.32	0.65	99.4
Cpx	735B_87R7_49	31 / 1 .	499.64	rim	Troctolite	53.07	2.66	0.94	23.21	0.29	0.00	0.13	16.21	4.00	0.26	100.8
Cpx		53 / 1 .	499.65	rim	Troctolite	52.68	3.13	0.94	19.99	0.42	0.03	0.18	17.02	5.94	0.24	100.6
Cpx		54 / 1 .	499.65	rim	Troctolite	51.80	3.21	1.21	22.96	0.33	0.00	0.14	15.74	3.89	0.32	99.6
Cpx		21 / 1 .	425.56	rim	Troctolite	51.08	3.93	1.52	22.62	0.47	0.01	0.17	15.25	4.60	0.05	99.7
Cpx		22 / 1 .	425.56	rim	Troctolite	50.96	3.96	1.62	22.94	0.50	0.04	0.12	14.70	4.91	0.10	99.8
Cpx	735B_80R2_7.5A	23 / 1 .	425.56	rim	Troctolite	50.98	4.11	1.74	22.89	0.42	0.03	0.18	14.64	4.91	0.07	100.0
Cpx		35 / 1 .	425.56	rim	Troctolite	51.44	4.05	1.78	22.50	0.41	0.02	0.14	15.38	4.12	0.02	99.9
Cpx		41 / 1 .	425.55	rim	Troctolite	51.48	3.33	1.05	21.78	0.50	0.00	0.20	15.61	5.55	0.09	99.6
Cpx		42 / 1 .	425.55	rim	Troctolite	50.97	3.62	1.80	23.18	0.44	0.00	0.17	14.68	5.28	0.03	100.2
Cpx	735B_89R1_47	5 / 1 .	505.27	rim	Troctolite	51.65	3.46	1.21	23.18	0.35	0.01	0.17	15.54	3.92	0.43	99.9
Cpx	90R-2W-68-75	6	510.02	rim	Troctolite	50.91	2.77	0.96	24.12	0.30	0.00	0.16	15.37	4.73	0.15	99.5
Cpx		12	510.02	rim	Troctolite	50.43	3.09	1.11	23.74	0.32	0.01	0.18	15.53	4.91	0.20	99.5

Calibration standards	Wollastonite (San Carlos)	Al2O3	TiMnO3	Wollastonite	Albite	Orthose	TiMnO3	Forsterite	Fayalite	Crr2O3

Appendix 2.2

In situ trace elements concentrations in ppm analyzed by LA-ICP-MS on a ThermoFisher Element XR at GM (Montpellier, France)

Mineral	Sample	Area	Point	Depth (mbsf)	Grain area	Lithology	La	Ce	Pr	Nd	Sm	Eu	Gd	Tb	Dy	Y	Ho	Er	Tm	Yb	Lu
Ol	735B_60R4_115B	A	ag_2	295.408	core	Ol-gabbro						0.000			0.002	0.048	0.000	0.009	0.003	0.052	0.018
Ol	735B_60R4_115B	B	ag_4	295.421	core	Ol-gabbro									0.003	0.028	0.001	0.006	0.003	0.033	0.013
Ol	735B_60R4_115B	E	ag_6	295.4105	core	Ol-gabbro	0.000	0.001	0.000							0.034	0.001	0.007	0.003	0.036	0.013
Ol	735B_60R4_115B	G	ag_7	295.412	core	Ol-gabbro										0.043	0.001	0.007	0.003	0.049	0.015
Ol	735B_60R4_115B	G	ag_10	295.412	core	Ol-gabbro				0.000	0.000	0.000	0.002	0.000	0.004	0.044	0.002	0.012	0.003	0.053	0.016
Ol	735B_58R3_108A	I	ai_1	284.333	core	Ol-gabbro					0.000		0.000			0.021	0.000	0.006	0.003	0.070	0.031
Ol	735B_58R3_108A	I	ai_3	284.333	core	Ol-gabbro		0.001					0.000		0.003	0.106	0.003	0.024	0.012	0.160	0.046
Ol	735B_58R3_108A	E	ai_4	284.3515	core	Ol-gabbro										0.013	0.000	0.003	0.003	0.045	0.019
Ol	735B_58R3_108A	E	ai_5	284.3515	core	Ol-gabbro		0.000				0.000			0.004	0.129	0.003	0.038	0.013	0.162	0.049
Ol	735B_58R3_108A	E	ai_6	284.3515	core	Ol-gabbro	0.000	0.001			0.000		0.000	0.000	0.004	0.138	0.003	0.035	0.012	0.146	0.041
Ol	735B_75R5_27	B	aj_1	390.354	core	Ol-gabbro	0.000	0.001					0.001		0.002	0.029	0.001	0.007	0.002	0.025	0.009
Ol	735B_75R5_27	D	aj_3	390.342	core	Ol-gabbro		0.000		0.000		0.000			0.001	0.030	0.001	0.009	0.002	0.028	0.009
Ol	735B_75R5_27	E	aj_5	390.3375	core	Ol-gabbro	0.000			0.000	0.000			0.000		0.033	0.001	0.005	0.002	0.030	0.008
Ol	735B_75R5_27	G	aj_6	390.3465	core	Ol-gabbro	0.000			0.000	0.000	0.000				0.008		0.001	0.001	0.019	0.007
Ol	735B_69R3_52B	A	al_1	344.1515	core	Ol-gabbro	0.000			0.000	0.000			0.000		0.011	0.000	0.002	0.001	0.025	0.010
Ol	735B_69R3_52B	B	al_2	344.153	core	Ol-gabbro				0.000	0.000			0.000	0.002	0.060	0.001	0.014	0.004	0.054	0.019
Ol	735B_69R3_52B	EF	al_7	344.159	core	Ol-gabbro				0.000		0.000			0.001	0.040	0.001	0.013	0.003	0.053	0.016
Ol	735B_69R3_52B	H	al_8	344.15	core	Ol-gabbro		0.000			0.000					0.028	0.001	0.007	0.002	0.038	0.012
Ol	735B_68R2_10,5A	AB	pa_3	336.546	core	Ol-gabbro									0.005	0.072	0.002	0.017	0.005	0.069	0.018
Ol	735B_68R2_10,5A	C	pa_5	336.5415	core	Ol-gabbro		0.001			0.000				0.002	0.047	0.001	0.009	0.003	0.048	0.014
Ol	735B_68R2_10,5A	F	pa_10	336.5465	core	Ol-gabbro				0.000	0.000				0.002	0.034	0.001	0.006	0.003	0.046	0.016
Ol	735B_68R2_10,5A	F	pa_11	336.5465	core	Ol-gabbro				0.000		0.000	0.000		0.002	0.032	0.001	0.009	0.003	0.043	0.016
Ol	735B_68R2_10,5A	F	pa_12	336.5465	core	Ol-gabbro	0.001	0.001	0.000						0.002	0.030	0.001	0.007	0.003	0.053	0.016
Ol	735B_60R4_115B	A	ag_1	295.408	rim	Ol-gabbro				0.000	0.000			0.000	0.004	0.044	0.001	0.009	0.004	0.045	0.016
Ol	735B_60R4_115B	B	ag_3	295.421	rim	Ol-gabbro			0.000		0.000					0.036	0.001	0.010	0.003	0.042	0.013
Ol	735B_60R4_115B	E	ag_5	295.4105	rim	Ol-gabbro			0.000					0.000		0.016	0.000	0.005	0.002	0.023	0.007
Ol	735B_60R4_115B	G	ag_8	295.412	rim	Ol-gabbro						0.000			0.002	0.049	0.002	0.012	0.003	0.045	0.015
Ol	735B_60R4_115B	G	ag_9	295.412	rim	Ol-gabbro								0.000	0.000	0.011	0.000		0.001	0.024	0.009
Ol	735B_58R3_108A	I	ai_2	284.333	rim	Ol-gabbro				0.000		0.000	0.000	0.000		0.028	0.001	0.007	0.005	0.082	0.026
Ol	735B_58R3_108A	E	ai_7	284.3515	rim	Ol-gabbro	0.000	0.000		0.000		0.000			0.002	0.052	0.001	0.014	0.005	0.089	0.028
Ol	735B_58R3_108A	E	ai_8	284.3515	rim	Ol-gabbro		0.000	0.000						0.004	0.104	0.002	0.024	0.009	0.132	0.039
Ol	735B_75R5_27	B	aj_2	390.354	rim	Ol-gabbro	0.000		0.000	0.000	0.000			0.000		0.029	0.001	0.007	0.002	0.021	0.008
Ol	735B_75R5_27	D	aj_4	390.342	rim	Ol-gabbro			0.000							0.033	0.001	0.006	0.003	0.033	0.010
Ol	735B_75R5_27	G	aj_7	390.3465	rim	Ol-gabbro		0.001	0.000						0.001	0.023	0.001	0.005	0.002	0.027	0.007
Ol	735B_69R3_52B	B	al_3	344.153	rim	Ol-gabbro										0.015		0.003	0.001	0.019	0.009
Ol	735B_69R3_52B	C	al_4	344.1585	rim	Ol-gabbro					0.000	0.000				0.004	0.000	0.002	0.001	0.014	0.008
Ol	735B_69R3_52B	EF	al_6	344.159	rim	Ol-gabbro			0.000	0.000		0.000				0.011		0.002	0.001	0.014	0.009
Ol	735B_68R2_10,5A	AB	pa_2	336.546	rim	Ol-gabbro	0.014	0.030	0.005	0.014					0.004	0.044	0.001	0.006	0.003	0.047	0.016

Mineral	Sample	Area	Point	Depth (mbsf)	Grain area	Lithology	La	Ce	Pr	Nd	Sm	Eu	Gd	Tb	Dy	Y	Ho	Er	Tm	Yb	Lu
Ol	735B_68R2_10,5A	AB	pa_4	336.546	rim	Ol-gabbro		0.001	0.000						0.004	0.033	0.002	0.009	0.004	0.057	0.013
Ol	735B_68R2_10,5	C	pa_6	336.5415	rim	Ol-gabbro				0	0					0.0246	0.001	0.0067	0.002	0.027	0.0102
Ol	735B_68R2_10,5A	E	pa_8	336.5365	rim	Ol-gabbro	0.000	0.001							0.003	0.040	0.001	0.013	0.005	0.046	0.016
Ol	735B_68R2_10,5A	F	pa_9	336.5465	rim	Ol-gabbro				0.000					0.001	0.024	0.000	0.005	0.003	0.046	0.014
Ol	735B_79R4_20	C	ak_1	419.159	core	Ol-gabbro	0.001	0.002	0.000	0.000	0.000			0.000	0.001	0.016		0.001	0.001	0.022	0.010
Ol	735B_79R4_20	C	ak_2	419.159	core	Ol-gabbro	0.001	0.002	0.000	0.001	0.000	0.000		0.000	0.001	0.025	0.000	0.004	0.002	0.029	0.010
Ol	735B_79R4_20	C	ak_3	419.159	core	Ol-gabbro		0.001			0.000					0.013	0.000	0.003	0.001	0.021	0.010
Ol	735B_79R4_20	D	ak_4	419.163	core	Ol-gabbro		0.001	0.000	0.000	0.000	0.000	0.000	0.000		0.021		0.002	0.001	0.021	0.006
Ol	735B_79R4_20	FG	ak_5	419.173	core	Ol-gabbro	0.000									0.009	0.000		0.001	0.014	0.005
Ol	735B_79R4_20	FG	ak_6	419.173	core	Ol-gabbro			0.000	0.000	0.000	0.000				0.012		0.002	0.001	0.008	0.003
Ol	735B_79R4_20	H	ak_8	419.179	core	Ol-gabbro		0.001	0.000		0.000					0.012		0.003	0.001	0.012	0.007
Ol	735B_79R4_20	H	ak_9	419.179	core	Ol-gabbro	0.000	0.001	0.000	0.000	0.000	0.000	0.000		0.001	0.012		0.004	0.001	0.016	0.005
Ol	735B_79R3_100	A	am_3	418.507	core	Ol-gabbro									0.005	0.113	0.004	0.020	0.005	0.101	0.024
Ol	735B_79R3_100	B	am_4	418.505	core	Ol-gabbro		0.000	0.000	0.000		0.000		0.001	0.006	0.085	0.003	0.014	0.004	0.074	0.020
Ol	735B_79R3_100	B	am_5	418.505	core	Ol-gabbro	0.000	0.001						0.000	0.010	0.106	0.003	0.028	0.008	0.090	0.027
Ol	735B_79R3_100	F	am_9	418.526	core	Ol-gabbro		0.000		0.000		0.000		0.000	0.007	0.133	0.004	0.026	0.009	0.114	0.031
Ol	735B_79R3_100	F	am_11	418.526	core	Ol-gabbro				0.001	0.000			0.001	0.009	0.140	0.005	0.030	0.010	0.121	0.031
Ol	735B_79R3_100	G	am_12	418.5315	core	Ol-gabbro	0.000	0.001			0.000		0.000		0.007	0.116	0.004	0.023	0.008	0.106	0.026
Ol	735B_76R3_96	C	pb_2	397.5745	core	Ol-gabbro	0.001	0.001							0.002	0.032	0.001	0.005	0.001	0.027	0.011
Ol	735B_76R3_96	D	pb_3	397.576	core	Ol-gabbro		0.001	0.000							0.035	0.002	0.009	0.002	0.037	0.013
Ol	735B_76R3_96	D	pb_4	397.576	core	Ol-gabbro		0.001	0.000							0.036	0.001	0.005	0.002	0.035	0.012
Ol	735B_76R3_96	D	pb_6	397.576	core	Ol-gabbro		0.001								0.030	0.001	0.006	0.002	0.049	0.012
Ol	735B_76R3_96	G	pb_9	397.5815	core	Ol-gabbro				0.000					0.004	0.045	0.001	0.009	0.003	0.051	0.014
Ol	735B_76R3_96	G	pb_10	397.5815	core	Ol-gabbro			0.000	0.002						0.045	0.001	0.011	0.003	0.053	0.017
Ol	735B_91R1_74	B	ab_3	518.167	core	Ol-gabbro	0.001			0.000					0.004	0.057	0.002	0.011	0.004	0.059	0.017
Ol	735B_91R1_74	C	ab_5	518.164	core	Ol-gabbro		0.001						0.000	0.007	0.071	0.002	0.011	0.005	0.057	0.017
Ol	735B_91R1_74	C	ab_6	518.164	core	Ol-gabbro	0.002	0.004								0.030		0.006	0.002	0.037	0.011
Ol	735B_91R1_74	D	ab_7	518.154	core	Ol-gabbro		0.002								0.046	0.002	0.008	0.003	0.040	0.011
Ol	735B_91R1_74	D	ab_10	518.154	core	Ol-gabbro		0.003	0.000							0.048	0.001	0.006	0.003	0.040	0.013
Ol	735B_91R1_74	E	ab_11	518.1465	core	Ol-gabbro		0.001					0.002		0.005	0.080	0.003	0.018	0.004	0.075	0.020
Ol	735B_91R1_74	G	ab_14	518.1535	core	Ol-gabbro		0.001	0.000						0.003	0.049	0.001	0.008	0.003	0.041	0.011
Ol	735B_91R1_74	A	ab_16	518.168	core	Ol-gabbro	0.001	0.003	0.000	0.002				0.000	0.003	0.053	0.002	0.015	0.004	0.053	0.017
Ol	735B_83R7_43B	B	qb_2	461.722	core	Ol-gabbro									0.001	0.037	0.001	0.011	0.002	0.045	0.013
Ol	735B_83R7_43B	B	qb_4	461.722	core	Ol-gabbro		0.001							0.003	0.041	0.001	0.010	0.003	0.045	0.012
Ol	735B_83R7_43B	C	qb_6	461.7225	core	Ol-gabbro	0.000	0.000			0.000	0.000			0.002	0.032	0.001	0.006	0.002	0.030	0.009
Ol	735B_83R7_43B	D	qb_7	461.725	core	Ol-gabbro			0.000							0.028	0.000	0.004	0.002	0.033	0.013
Ol	735B_83R7_43B	E	qb_9	461.7155	core	Ol-gabbro					0.000			0.000	0.006	0.080	0.002	0.016	0.006	0.091	0.025
Ol	735B_83R7_43B	F	qb_11	461.71	core	Ol-gabbro		0.001							0.002	0.031	0.001	0.007	0.002	0.025	0.010
Ol	735B_83R7_43B	I	qb_13	461.712	core	Ol-gabbro					0.000				0.002	0.023	0.001	0.004	0.002	0.024	0.010
Ol	81R5-7/11	C	SMPABC	439.2515	core	Ol-gabbro	0.001	0.001								0.037	0.002	0.008	0.002	0.036	0.011

Mineral	Sample	Area	Point	Depth (mbsf)	Grain area	Lithology	La	Ce	Pr	Nd	Sm	Eu	Gd	Tb	Dy	Y	Ho	Er	Tm	Yb	Lu
Ol	81R5-7/11	C	SMPABC	439.2515	core	Ol-gabbro		0.002	0.000	0.004				0.000	0.004	0.051	0.002	0.013	0.004	0.040	0.012
Ol	81R5-7/11	E	SMPABC	439.257	core	Ol-gabbro	0.001	0.001	0.000						0.005	0.056	0.002	0.011	0.003	0.032	0.011
Ol	81R5-7/11	E	untSM	439.257	core	Ol-gabbro	0.0005	0.0014							0.0028	0.0334	0.0012	0.0073	0.0025	0.0412	0.0105
Ol	90R2-84/90	-90_a2_	wc_14	510.17	core	Ol-gabbro	0.000	0.009	0.000	0.000	0.000	0.000	0.010	0.000	0.003	0.068	0.001	0.011	0.004	0.042	0.012
Ol	90R2-84/90	-90_a3	wc_16	510.17	core	Ol-gabbro	0.002	0.000	0.000	0.000	0.000	0.000	0.000	0.000	0.006	0.041	0.001	0.005	0.004	0.042	0.010
Ol	90R2-94/100B	100B_a	wc_10	510.27	core	Ol-gabbro	0.000	0.000	0.001	0.000	0.000	0.000	0.000	0.000	0.000	0.045	0.001	0.010	0.002	0.029	0.011
Ol	90R2-94/100B	100B_a	wc_12	510.27	core	Ol-gabbro	0.000	0.000	0.000	0.000	0.000	0.000	0.000	0.000	0.004	0.026	0.001	0.006	0.003	0.020	0.007
Ol	90R2-123/129	-129_a	wc_6	510.56	core	Ol-gabbro	0.000	0.000	0.000	0.000	0.000	0.000	0.000	0.000	0.000	0.030	0.000	0.004	0.002	0.021	0.009
Ol	90R2-123/129	-129_a	wc_8	510.56	core	Ol-gabbro	0.000	0.003	0.000	0.000	0.000	0.000	0.000	0.000	0.000	0.039	0.001	0.006	0.002	0.027	0.007
ol	90R3-6/8	-8_a3_	wc_2	510.84	core	Ol-gabbro	0.000	0.000	0.000	0.000	0.000	0.000	0.011	0.000	0.000	0.025	0.000	0.006	0.004	0.025	0.008
ol	90R3-6/8	-8_a4_	wc_3	510.84	core	Ol-gabbro	0.000	0.004	0.000	0.000	0.000	0.000	0.000	0.001	0.000	0.025	0.000	0.005	0.001	0.024	0.006
Ol	735B_79R4_20	H	ak_7	419.179	rim	Ol-gabbro				0.000	0.000					0.013	0.000	0.003	0.001	0.011	0.005
Ol	735B_79R3_100	A	am_1	418.507	rim	Ol-gabbro		0.001							0.004	0.076	0.002	0.016	0.007	0.081	0.021
Ol	735B_79R3_100	A	am_2	418.507	rim	Ol-gabbro		0.000			0.000		0.000		0.006	0.110	0.002	0.021	0.008	0.097	0.027
Ol	735B_79R3_100	B	am_6	418.505	rim	Ol-gabbro		0.002		0.002	0.000	0.000		0.000	0.005	0.095	0.003	0.016	0.006	0.081	0.026
Ol	735B_79R3_100	B	am_7	418.505	rim	Ol-gabbro						0.000			0.005	0.081	0.002	0.016	0.005	0.070	0.022
Ol	735B_79R3_100	F	am_8	418.526	rim	Ol-gabbro	0.000	0.000		0.000				0.000	0.006	0.118	0.003	0.025	0.008	0.114	0.030
Ol	735B_79R3_100	F	am_10	418.526	rim	Ol-gabbro	0.000	0.001		0.001				0.000	0.005	0.082	0.003	0.017	0.008	0.091	0.026
Ol	735B_79R3_100	G	am_13	418.5315	rim	Ol-gabbro		0.001		0.000	0.000				0.004	0.092	0.003	0.013	0.008	0.107	0.025
Ol	735B_76R3_96	C	pb_1	397.5745	rim	Ol-gabbro		0.001		0.000						0.020		0.003	0.002	0.018	0.009
Ol	735B_76R3_96	D	pb_5	397.576	rim	Ol-gabbro		0.002								0.034	0.001	0.008	0.003	0.043	0.013
Ol	735B_76R3_96	E	pb_8	397.585	rim	Ol-gabbro	0.001	0.001							0.002	0.032	0.000	0.006	0.002	0.039	0.010
Ol	735B_76R3_96	G	pb_11	397.5815	rim	Ol-gabbro		0.001	0.000							0.037	0.001	0.008	0.003	0.047	0.015
Ol	735B_91R1_74	A	ab_1	518.168	rim	Ol-gabbro		0.002	0.000						0.003	0.049	0.001	0.010	0.004	0.049	0.015
Ol	735B_91R1_74	B	ab_4	518.167	rim	Ol-gabbro	0.001	0.002	0.000	0.002		0.000		0.000	0.004	0.036	0.001	0.008	0.002	0.038	0.012
Ol	735B_91R1_74	D	ab_8	518.154	rim	Ol-gabbro	0.003	0.002								0.037		0.010	0.003	0.032	0.010
Ol	735B_91R1_74	F	ab_13	518.1545	rim	Ol-gabbro	0.000	0.001	0.000						0.006	0.029		0.007	0.003	0.037	0.010
Ol	735B_91R1_74	G	ab_15	518.1535	rim	Ol-gabbro	0.001	0.002								0.035	0.001	0.008	0.002	0.031	0.010
Ol	735B_83R7_43B	A	qb_1	461.7055	rim	Ol-gabbro							0.002			0.022	0.000	0.003	0.001	0.017	0.007
Ol	735B_83R7_43B	B	qb_3	461.722	rim	Ol-gabbro		0.001						0.000		0.023	0.001	0.005	0.002	0.034	0.013
Ol	735B_83R7_43B	B	qb_5	461.722	rim	Ol-gabbro										0.020	0.001	0.004	0.002	0.027	0.010
Ol	735B_83R7_43B	D	qb_8	461.725	rim	Ol-gabbro	0.000	0.001		0.001						0.021	0.000	0.003	0.002	0.033	0.011
Ol	735B_83R7_43B	E	qb_10	461.7155	rim	Ol-gabbro	0.004	0.006	0.000						0.004	0.069	0.002	0.015	0.004	0.060	0.019
Ol	735B_83R7_43B	F	qb_12	461.71	rim	Ol-gabbro		0.001							0.002	0.020	0.001	0.005	0.002	0.025	0.008
Ol	735B_83R7_43B	I	qb_14	461.712	rim	Ol-gabbro		0.002							0.002	0.035	0.001	0.004	0.002	0.038	0.011
Ol	735B_83R7_43B	I	qb_15	461.712	rim	Ol-gabbro				0.000						0.013	0.000	0.004	0.002	0.030	0.007
Ol	81R5-7/11	E	SMPABC	439.257	rim	Ol-gabbro	0.001	0.002			0.003					0.030	0.001	0.006	0.002	0.023	0.009
Ol	90R2-84/90	-90_a2_	wc_13	510.17	rim	Ol-gabbro	0.003	0.000	0.000	0.015	0.000	0.000	0.000	0.000	0.000	0.045	0.000	0.010	0.002	0.037	0.012
Ol	90R2-84/90	-90_a3	wc_15	510.17	rim	Ol-gabbro	0.000	0.004	0.001	0.014	0.000	0.000	0.000	0.001	0.003	0.065	0.001	0.005	0.004	0.044	0.012
Ol	90R2-94/100B	100B_a	wc_9	510.27	rim	Ol-gabbro	0.000	0.000	0.000	0.000	0.000	0.000	0.000	0.000	0.003	0.038	0.002	0.009	0.002	0.030	0.010

Mineral	Sample	Area	Point	Depth (mbsf)	Grain area	Lithology	La	Ce	Pr	Nd	Sm	Eu	Gd	Tb	Dy	Y	Ho	Er	Tm	Yb	Lu
Ol	90R2-94/100B	100B_a	wc_11	510.27	rim	Ol-gabbro	0.000	0.000	0.001	0.000	0.000	0.001	0.000	0.000	0.000	0.023	0.001	0.002	0.002	0.014	0.008
Ol	90R2-123/129	-129_a	wc_5	510.56	rim	Ol-gabbro	0.000	0.000	0.000	0.000	0.000	0.000	0.000	0.002	0.008	0.029	0.001	0.005	0.002	0.034	0.007
Ol	90R2-123/129	-129_a	wc_7	510.56	rim	Ol-gabbro	0.000	0.000	0.000	0.000	0.000	0.000	0.000	0.001	0.000	0.039	0.002	0.009	0.003	0.044	0.008
Ol	90R3-6/8	6-	wc_1	510.84	rim	Ol-gabbro	0	0	0	0	0	0	0	0	0	0.0279	0.0013	0.0046	0.0022	0.0239	0.0064
Ol	90R3-6/8	-8_a4_	wc_4	510.84	rim	Ol-gabbro	0.000	0.000	0.000	0.008	0.000	0.000	0.000	0.000	0.003	0.016	0.001	0.000	0.000	0.014	0.005
Ol	735B_83R7_113A	A	ae_2	462.399	core	Ol-rich gabbro		0.000	0.000					0.000		0.033	0.001	0.007	0.002	0.034	0.011
Ol	735B_83R7_113A	B	ae_4	462.3875	core	Ol-rich gabbro	0.001	0.001	0.000		0.000			0.000	0.002	0.074	0.002	0.017	0.005	0.079	0.020
Ol	735B_83R7_113A	CD	ae_6	462.385	core	Ol-rich gabbro			0.000	0.000	0.000	0.000		0.000	0.004	0.036	0.001	0.007	0.003	0.037	0.010
Ol	735B_83R7_113A	CD	ae_9	462.385	core	Ol-rich gabbro		0.000		0.000	0.000				0.003	0.065	0.002	0.013	0.005	0.063	0.015
Ol	735B_83R7_113A	EG	ae_11	462.393	core	Ol-rich gabbro	0.000	0.001			0.001	0.000	0.000		0.002	0.043	0.000	0.013	0.004	0.055	0.014
Ol	735B_83R7_113A	EG	ae_13	462.393	core	Ol-rich gabbro					0.000		0.000		0.003	0.034	0.001	0.008	0.002	0.038	0.009
Ol	735B_83R7_113A	F	ae_15	462.399	core	Ol-rich gabbro	0.001	0.003	0.000		0.000			0.000		0.033		0.005	0.002	0.037	0.012
Ol	735B_83R7_113A	I	ae_16	462.3875	core	Ol-rich gabbro	0.000	0.001	0.000	0.000	0.000	0.000		0.000	0.004	0.034	0.000	0.006	0.003	0.039	0.012
Ol	735B_83R7_0	A	oc_3	461.2535	core	Ol-rich gabbro				0.000						0.041	0.001	0.006	0.002	0.036	0.013
Ol	735B_83R7_0	BC	oc_4	461.2675	core	Ol-rich gabbro	0.000	0.002							0.008	0.066	0.001	0.012	0.004	0.060	0.016
Ol	735B_83R7_0	BC	oc_6	461.2675	core	Ol-rich gabbro	0.001	0.003	0.001					0.000	0.005	0.056	0.003	0.014	0.004	0.044	0.014
Ol	735B_83R7_0	BC	oc_7	461.2675	core	Ol-rich gabbro		0.001	0.000						0.002	0.033	0.001	0.005	0.002	0.029	0.012
Ol	735B_83R7_0	D	oc_8	461.2625	core	Ol-rich gabbro	0.001	0.002	0.000						0.002	0.055	0.002	0.011	0.004	0.050	0.016
Ol	735B_83R7_0	D	oc_10	461.2625	core	Ol-rich gabbro				0.000					0.004	0.040	0.001	0.011	0.003	0.043	0.012
Ol	735B_83R7_0	D	oc_11	461.2625	core	Ol-rich gabbro	0.000	0.000	0.000							0.019	0.000	0.005	0.002	0.039	0.012
Ol	735B_83R7_0	E	oc_13	461.265	core	Ol-rich gabbro	0.002	0.005	0.001	0.004						0.037	0.001	0.008	0.004	0.031	0.010
Ol	735B_83R7_0	F	oc_14	461.264	core	Ol-rich gabbro	0.001	0.002							0.002	0.035	0.001	0.005	0.003	0.042	0.011
Ol	735B_83R7_0	G	oc_15	461.2745	core	Ol-rich gabbro				0.000		0.000		0.000	0.005	0.051	0.001	0.012	0.003	0.041	0.012
Ol	735B_83R7_0	G	oc_17	461.2745	core	Ol-rich gabbro		0.001		0.002				0.000	0.002	0.036	0.001	0.009	0.003	0.038	0.009
Ol	735B_83R7_113A	A	ae_1	462.399	rim	Ol-rich gabbro	0.000	0.002	0.000	0.001				0.000	0.002	0.041	0.001	0.009	0.003	0.044	0.014
Ol	735B_83R7_113A	B	ae_3	462.3875	rim	Ol-rich gabbro	0.000		0.000		0.000	0.000			0.004	0.041	0.001	0.008	0.003	0.040	0.012
Ol	735B_83R7_113A	CD	ae_5	462.385	rim	Ol-rich gabbro	0.001	0.001	0.000			0.000			0.004	0.035	0.001	0.007	0.002	0.028	0.009
Ol	735B_83R7_113A	CD	ae_7	462.385	rim	Ol-rich gabbro				0.000				0.000		0.025	0.001	0.004	0.002	0.026	0.008
Ol	735B_83R7_113A	CD	ae_8	462.385	rim	Ol-rich gabbro		0.000						0.000	0.002	0.031	0.001	0.007	0.002	0.037	0.010
Ol	735B_83R7_113A	EG	ae_10	462.393	rim	Ol-rich gabbro	0.000			0.000	0.000		0.001		0.002	0.038	0.001	0.009	0.003	0.037	0.011
Ol	735B_83R7_113A	EG	ae_12	462.393	rim	Ol-rich gabbro		0.001	0.000	0.001	0.000	0.000	0.000	0.000		0.020	0.001	0.003	0.002	0.030	0.010
Ol	735B_83R7_113A	I	ae_17	462.3875	rim	Ol-rich gabbro		0.003	0.000		0.000	0.000	0.001	0.000	0.003	0.032	0.001	0.009	0.002	0.035	0.012
Ol	735B_83R7_0	A	oc_2	461.2535	rim	Ol-rich gabbro		0.001							0.003	0.030	0.001	0.009	0.002	0.034	0.011
Ol	735B_83R7_0	BC	oc_5	461.2675	rim	Ol-rich gabbro	0.001	0.003		0.002	0.000				0.002	0.029	0.001	0.005	0.002	0.032	0.011
Ol	735B_83R7_0	D	oc_9	461.2625	rim	Ol-rich gabbro									0.002	0.033	0.001	0.007	0.003	0.044	0.012
Ol	735B_83R7_0	E	oc_12	461.265	rim	Ol-rich gabbro			0.000				0.002		0.002	0.022	0.001	0.005	0.002	0.030	0.008
Ol	735B_83R7_0	G	oc_16	461.2745	rim	Ol-rich gabbro		0.001	0.000		0.001					0.016	0.001	0.003	0.002	0.023	0.007
Ol	735B_89R1_47	B	ah_1	505.2765	core	Troctolite	0.000	0.001	0.000					0.000	0.004	0.074	0.002	0.016	0.005	0.075	0.020
Ol	735B_89R1_47	B	ah_2	505.2765	core	Troctolite		0.001			0.000	0.000		0.001	0.010	0.130	0.004	0.030	0.011	0.097	0.026
Ol	735B_89R1_47	D	ah_4	505.2835	core	Troctolite	0.001	0.002	0.000	0.001				0.000	0.005	0.121	0.004	0.024	0.008	0.115	0.030

Mineral	Sample	Area	Point	Depth (mbsf)	Grain area	Lithology	La	Ce	Pr	Nd	Sm	Eu	Gd	Tb	Dy	Y	Ho	Er	Tm	Yb	Lu
Ol	735B_89R1_47	E	ah_6	505.291	core	Troctolite		0.002						0.001	0.007	0.106	0.003	0.023	0.010	0.103	0.029
Ol	735B_89R1_47	F	ah_7	505.2935	core	Troctolite		0.002						0.001	0.013	0.189	0.006	0.034	0.013	0.160	0.039
Ol	735B_80R2_7,5A	A	qa_1	425.563	core	Troctolite	0.001	0.001	0.000				0.000		0.000	0.041	0.001	0.009	0.006	0.089	0.032
Ol	735B_80R2_7,5A	A	qa_2	425.563	core	Troctolite	0.001	0.000	0.000	0.000	0.000			0.000	0.002	0.064	0.002	0.014	0.008	0.110	0.032
Ol	735B_80R2_7,5A	B	qa_4	425.56	core	Troctolite			0	0					0.0023	0.0458	0.001	0.0065	0.0043	0.0483	0.0183
Ol	735B_80R2_7,5A	D	qa_7	425.556	core	Troctolite										0.064	0.002	0.019	0.007	0.099	0.029
Ol	735B_80R2_7,5A	E	qa_9	425.5555	core	Troctolite		0.001	0.000	0.000			0.001		0.000	0.029	0.001	0.008	0.005	0.064	0.022
Ol	735B_80R2_7,5A	F	qa_11	425.5485	core	Troctolite		0.002								0.016	0.000		0.002	0.041	0.018
Ol	735B_80R2_7,5A	F	qa_13	425.5485	core	Troctolite				0.000	0.000				0.003	0.073	0.002	0.016	0.007	0.089	0.028
Ol	735B_89R1_47	D	ah_3	505.2835	rim	Troctolite	0.002	0.002	0.000	0.002				0.001	0.008	0.100	0.004	0.020	0.008	0.105	0.027
Ol	735B_89R1_47	E	ah_5	505.291	rim	Troctolite					0.000			0.000	0.002	0.062	0.002	0.015	0.007	0.084	0.023
Ol	735B_89R1_47	G	ah_8	505.2975	rim	Troctolite		0.001						0.001	0.007	0.052	0.002	0.016	0.007	0.070	0.018
Ol	735B_80R2_7,5A	B	qa_5	425.56	rim	Troctolite		0.001		0.001					0.003	0.042	0.001	0.004	0.003	0.044	0.016
Ol	735B_80R2_7,5A	D	qa_6	425.556	rim	Troctolite		0.001								0.008		0.002	0.002	0.031	0.013
Ol	735B_80R2_7,5A	E	qa_8	425.5555	rim	Troctolite	0.000		0.000							0.022	0.001	0.008	0.002	0.058	0.019
Ol	735B_80R2_7,5A	F	qa_10	425.5485	rim	Troctolite		0.000								0.027	0.001	0.008	0.003	0.053	0.014
BIR	Average (N = 81)						0.58	1.87	0.35	2.25	1.01	0.49	1.59	0.31	2.31	12.89	0.51	1.48	0.22	1.54	0.23
	2SD						0.11	0.27	0.04	0.28	0.11	0.06	0.26	0.05	0.30	2.04	0.08	0.25	0.04	0.24	0.04
	Preferred values ("Georem" Jochum et al., 2007)						0.61	1.89	0.37	2.37	1.09	0.52	1.85	0.35	2.55	14.30	0.56	1.70	0.24	1.64	0.25

In situ trace elements concentrations in ppm analyzed by LA-ICP-MS on a ThermoFisher Element XR at GM (Montpellier, France)

Mineral	Sample	Area	Point	Depth (mbsf)	Grain area	Lithology	La	Ce	Pr	Nd	Sm	Eu	Gd	Tb	Dy	Y	Ho	Er	Tm	Yb	Lu
Pl	85R7-79/83	J	IPABC001	480.694	core	Gabbro	0.434	0.944	0.111	0.442	0.053	0.470	0.040	0.005		0.088	0.004				
Pl	85R7-79/83	K	IPABC007	480.684	core	Gabbro	0.187	0.528	0.079	0.379	0.091	0.353	0.094	0.011	0.048	0.229	0.007	0.013			0.001
Pl	85R7-79/83	K	IPABC008	480.684	core	Gabbro	0.317	0.704	0.084	0.348	0.067	0.433	0.045	0.006	0.024	0.090	0.004				
Pl	85R7-79/83	F	IPABC009	480.698	core	Gabbro	0.234	0.675	0.100	0.475	0.112	0.373	0.081	0.011	0.038	0.202	0.008	0.011			0.001
Pl	85R7-79/83	C	IPABC012	480.704	core	Gabbro	0.210	0.564	0.080	0.384	0.099	0.401	0.094	0.011	0.065	0.351	0.015	0.034	0.003	0.027	0.003
Pl	85R7-79/83	A	IPABC013	480.711	core	Gabbro	0.180	0.490	0.073	0.358	0.083	0.385	0.070	0.009	0.048	0.224	0.008	0.018	0.002		0.001
Pl	85R7-79/83	E	IPABC015	480.703	core	Gabbro	2.750	5.000	0.478	1.585	0.195	0.760	0.135	0.012	0.048	0.233	0.009	0.016	0.001	0.005	
Pl	85R7-79/83	J	IPABC004	480.694	rim	Gabbro	0.359	0.913	0.116	0.460	0.073	0.436	0.041	0.006	0.023	0.137	0.005	0.011		0.007	0.001
Pl	85R7-79/83	F	IPABC010	480.698	rim	Gabbro	0.384	0.823	0.101	0.415	0.059	0.430	0.055	0.006	0.022	0.087	0.002			0.005	0.001
Pl	85R7-79/83	C	IPABC011	480.704	rim	Gabbro	0.750	2.077	0.268	1.067	0.167	0.577	0.137	0.016	0.061	0.293	0.009	0.021	0.002	0.011	0.002
Pl	85R7-79/83	A	IPABC014	480.711	rim	Gabbro	0.480	1.052	0.122	0.471	0.074	0.455	0.043	0.005	0.022	0.110	0.003	0.012		0.006	
Pl	735B_56R4_61A	F2	aa_2	274.904	core	l-bearing gabbı	0.494	1.021	0.124	0.477	0.084	0.604	0.082	0.012	0.059	0.264	0.010	0.013	0.003	0.013	
Pl	735B_56R4_61A	E	aa_5	274.906	core	l-bearing gabbı	0.455	0.955	0.115	0.472	0.089	0.580	0.090	0.007	0.043	0.153	0.008	0.006	0.000	0.000	
Pl	735B_56R4_61A	D	aa_6	274.904	core	l-bearing gabbı	0.431	0.914	0.105	0.443	0.076	0.606	0.049	0.007	0.024	0.110	0.004	0.005			
Pl	735B_56R4_61A	Dbis	aa_7	274.903	core	l-bearing gabbı	0.458	0.977	0.119	0.479	0.086	0.626	0.062	0.007	0.038	0.193	0.006	0.015	0.002	0.009	0.001
Pl	735B_56R4_61A	D	aa_9	274.904	core	l-bearing gabbı	0.453	0.980	0.119	0.474	0.081	0.605	0.074	0.010	0.039	0.185	0.008	0.010	0.001	0.008	
Pl	735B_56R4_61A	C2	aa_11	274.902	core	l-bearing gabbı	0.398	0.911	0.118	0.491	0.093	0.583	0.086	0.010	0.061	0.238	0.009	0.019	0.001	0.012	0.001
Pl	735B_56R4_61A	B	aa_12	274.893	core	l-bearing gabbı	0.816	1.463	0.147	0.502	0.065	0.657	0.056	0.005	0.023	0.080	0.003	0.005		0.000	
Pl	735B_56R4_61A	B	aa_14	274.893	core	l-bearing gabbı	0.451	0.996	0.128	0.504	0.102	0.661	0.081	0.007	0.041	0.183	0.004	0.021	0.002	0.006	
Pl	735B_56R4_61A	F2	aa_1	274.904	rim	l-bearing gabbı	0.440	0.868	0.095	0.370	0.056	0.577	0.039	0.005	0.018	0.076	0.003	0.007		0.000	
Pl	735B_56R4_61A	F2	aa_3	274.904	rim	l-bearing gabbı	0.437	0.859	0.098	0.392	0.062	0.588	0.045	0.008	0.026	0.096	0.003	0.006	0.000	0.004	0.000
Pl	735B_56R4_61A	E	aa_4	274.906	rim	l-bearing gabbı	0.520	1.003	0.112	0.398	0.078	0.609	0.076	0.007	0.044	0.251	0.010	0.013	0.003	0.013	0.001
Pl	735B_56R4_61A	D	aa_8	274.904	rim	l-bearing gabbı	0.445	0.922	0.108	0.425	0.072	0.626	0.048	0.004	0.032	0.114	0.004	0.007	0.001	0.005	0.001
Pl	735B_56R4_61A	C2	aa_10	274.902	rim	l-bearing gabbı	0.424	0.892	0.101	0.410	0.057	0.560	0.052	0.004	0.014	0.088	0.003	0.005			
Pl	735B_56R4_61A	B	aa_13	274.893	rim	l-bearing gabbı	0.835	1.558	0.157	0.534	0.087	0.682	0.072	0.009	0.027	0.151	0.005	0.007	0.001	0.005	
Pl	735B_57R1_73	A	ac_2	275.735	core	Ol-gabbro	6.810	11.720	1.015	3.000	0.311	2.047	0.218	0.019	0.083	0.358	0.014	0.009	0.003	0.013	0.001
Pl	735B_57R1_73	A	ac_3	275.735	core	Ol-gabbro	8.700	12.590	0.924	2.321	0.214	1.518	0.143	0.013	0.065	0.268	0.008	0.015	0.001	0.008	0.002
Pl	735B_57R1_73	A	ac_4	275.735	core	Ol-gabbro	7.800	12.560	1.009	2.743	0.302	1.837	0.193	0.016	0.072	0.401	0.016	0.028	0.003	0.015	0.002
Pl	735B_57R1_73	B	ac_6	275.738	core	Ol-gabbro	0.272	0.682	0.086	0.402	0.078	0.607	0.062	0.009	0.034	0.165	0.006	0.016	0.001	0.005	0.001
Pl	735B_57R1_73	B	ac_7	275.738	core	Ol-gabbro	0.548	1.186	0.126	0.469	0.074	0.600	0.064	0.007	0.035	0.142	0.004	0.007			0.000
Pl	735B_57R1_73	C	ac_8	275.743	core	Ol-gabbro	0.576	1.235	0.135	0.532	0.090	0.719	0.053	0.008	0.043	0.178	0.007	0.016	0.002	0.011	0.001
Pl	735B_57R1_73	C	ac_9	275.743	core	Ol-gabbro	0.324	0.842	0.112	0.525	0.098	0.610	0.081	0.010	0.065	0.363	0.011	0.028	0.005	0.025	0.005
Pl	735B_57R1_73	C	ac_11	275.743	core	Ol-gabbro	7.230	11.700	1.000	2.730	0.301	1.982	0.167	0.016	0.080	0.319	0.014	0.033	0.002		
Pl	735B_57R1_73	D	ac_13	275.745	core	Ol-gabbro	0.619	1.362	0.147	0.572	0.092	0.676	0.116	0.012	0.038	0.197	0.006	0.015	0.001	0.006	0.001
Pl	735B_57R1_73	C	ac_17	275.743	core	Ol-gabbro	0.287	0.724	0.094	0.417	0.085	0.620	0.088	0.012	0.058	0.259	0.009	0.025	0.002	0.003	0.001
Pl	735B_60R4_115B	A	ag_11	295.408	core	Ol-gabbro	0.664	1.656	0.200	0.780	0.130	0.460	0.090	0.010	0.053	0.250	0.010	0.015	0.003	0.008	0.001
Pl	735B_60R4_115B	B	ag_12	295.421	core	Ol-gabbro	0.591	1.155	0.129	0.504	0.081	0.372	0.073	0.008	0.033	0.143	0.004	0.010	0.000	0.003	0.000
Pl	735B_60R4_115B	B	ag_14	295.421	core	Ol-gabbro	0.193	0.465	0.066	0.291	0.063	0.399	0.055	0.009	0.046	0.227	0.008	0.019	0.002	0.017	0.002
Pl	735B_60R4_115B	D	ag_18	295.415	core	Ol-gabbro	0.591	1.323	0.164	0.684	0.113	0.478	0.086	0.007	0.033	0.113	0.003	0.006	0.000		0.000

Mineral	Sample	Area	Point	Depth (mbsf)	Grain area	Lithology	La	Ce	Pr	Nd	Sm	Eu	Gd	Tb	Dy	Y	Ho	Er	Tm	Yb	Lu
Pl	735B_60R4_115B	E	ag_21	295.411	core	Ol-gabbro	0.189	0.483	0.067	0.283	0.066	0.388	0.053	0.004	0.029	0.142	0.005	0.010	0.002	0.000	0.000
Pl	735B_60R4_115B	F	ag_23	295.407	core	Ol-gabbro	0.621	1.430	0.168	0.674	0.108	0.474	0.094	0.009	0.055	0.242	0.010	0.024	0.003	0.014	0.001
Pl	735B_60R4_115B	F	ag_24	295.407	core	Ol-gabbro	0.495	1.173	0.147	0.667	0.103	0.477	0.053	0.008	0.036	0.103	0.004	0.002			
Pl	735B_60R4_115B	G	ag_27	295.412	core	Ol-gabbro	0.602	1.496	0.179	0.800	0.125	0.456	0.118	0.009	0.034	0.165	0.005	0.009	0.001		
Pl	735B_60R4_115B	G	ag_28	295.412	core	Ol-gabbro	0.637	1.258	0.143	0.545	0.087	0.433	0.062	0.006	0.030	0.124	0.005	0.008	0.001	0.005	0.001
Pl	735B_58R3_108A	A	ai_12	284.346	core	Ol-gabbro	0.760	1.810	0.219	0.846	0.141	0.600	0.125	0.013	0.062	0.267	0.011	0.018	0.002	0.008	0.001
Pl	735B_58R3_108A	D	ai_15	284.35	core	Ol-gabbro	0.776	2.009	0.267	1.155	0.157	0.587	0.138	0.015	0.063	0.268	0.009	0.025	0.001	0.005	0.001
Pl	735B_58R3_108A	D	ai_17	284.35	core	Ol-gabbro	0.183	0.495	0.070	0.343	0.079	0.525	0.061	0.009	0.043	0.219	0.007	0.014	0.002	0.018	0.000
Pl	735B_58R3_108A	E	ai_19	284.352	core	Ol-gabbro	0.408	0.993	0.137	0.607	0.110	0.646	0.103	0.012	0.058	0.272	0.011	0.024	0.002	0.013	0.001
Pl	735B_58R3_108A	F	ai_21	284.345	core	Ol-gabbro	1.089	2.460	0.302	1.273	0.230	0.699	0.163	0.018	0.077	0.331	0.013	0.026	0.002	0.011	0.001
Pl	735B_58R3_108A	H	ai_23	284.34	core	Ol-gabbro	0.276	0.661	0.099	0.451	0.098	0.636	0.098	0.015	0.078	0.352	0.013	0.032	0.004	0.021	0.002
Pl	735B_58R3_108A	H	ai_25	284.34	core	Ol-gabbro	0.209	0.526	0.070	0.339	0.070	0.473	0.071	0.008	0.032	0.162	0.005	0.013	0.001	0.005	0.001
Pl	735B_58R3_108A	I	ai_26	284.333	core	Ol-gabbro	0.240	0.605	0.088	0.362	0.080	0.502	0.075	0.011	0.045	0.225	0.008	0.017	0.002	0.007	0.001
Pl	735B_75R5_27	B	aj_9	390.354	core	Ol-gabbro	0.342	0.841	0.113	0.429	0.078	0.383	0.065	0.007	0.026	0.175	0.005	0.010	0.001	0.013	0.001
Pl	735B_75R5_27	C	aj_12	390.352	core	Ol-gabbro	0.163	0.432	0.063	0.330	0.066	0.400	0.069	0.012	0.046	0.247	0.009	0.021	0.002	0.012	0.001
Pl	735B_75R5_27	C	aj_14	390.352	core	Ol-gabbro	0.224	0.524	0.072	0.367	0.079	0.428	0.081	0.010	0.049	0.237	0.010	0.022	0.002	0.015	0.002
Pl	735B_75R5_27	C	aj_15	390.352	core	Ol-gabbro	0.420	0.635	0.069	0.277	0.046	0.401	0.035	0.003	0.024	0.094	0.002	0.003		0.003	
Pl	735B_75R5_27	D	aj_16	390.342	core	Ol-gabbro	0.267	0.619	0.082	0.371	0.067	0.355	0.063	0.007	0.035	0.156	0.005	0.012	0.001	0.004	0.001
Pl	735B_75R5_27	D	aj_18	390.342	core	Ol-gabbro	0.138	0.377	0.062	0.306	0.076	0.331	0.066	0.009	0.061	0.232	0.008	0.020	0.002	0.010	0.001
Pl	735B_75R5_27	E	aj_19	390.338	core	Ol-gabbro	0.299	0.652	0.072	0.326	0.054	0.355	0.046	0.005	0.022	0.095	0.002	0.008	0.001	0.004	
Pl	735B_75R5_27	F	aj_20	390.335	core	Ol-gabbro	0.286	0.683	0.087	0.377	0.070	0.374	0.065	0.007	0.034	0.158	0.005	0.008		0.005	0.001
Pl	735B_75R5_27	G	aj_23	390.347	core	Ol-gabbro	0.237	0.606	0.074	0.347	0.085	0.367	0.070	0.008	0.034	0.162	0.007	0.011	0.001	0.004	0.001
Pl	735B_75R5_27	G	aj_24	390.347	core	Ol-gabbro	0.251	0.632	0.087	0.381	0.077	0.361	0.065	0.007	0.040	0.148	0.005	0.008	0.001	0.006	0.000
Pl	735B_75R5_27	H	aj_25	390.341	core	Ol-gabbro	0.292	0.611	0.075	0.304	0.061	0.378	0.051	0.004	0.027	0.108	0.004	0.008	0.001	0.004	0.001
Pl	735B_75R5_27	H	aj_26	390.341	core	Ol-gabbro	0.288	0.639	0.074	0.317	0.066	0.384	0.033	0.006	0.035	0.102	0.005	0.012	0.001	0.004	
Pl	735B_69R3_52B	A	al_11	344.152	core	Ol-gabbro	0.900	1.884	0.212	0.802	0.123	0.412	0.106	0.010	0.048	0.228	0.007	0.018	0.002	0.009	0.001
Pl	735B_69R3_52B	A	al_13	344.152	core	Ol-gabbro	0.160	0.392	0.055	0.278	0.055	0.411	0.057	0.009	0.039	0.210	0.007	0.019	0.002	0.011	0.001
Pl	735B_69R3_52B	B	al_15	344.153	core	Ol-gabbro	0.171	0.436	0.062	0.337	0.072	0.456	0.080	0.011	0.061	0.292	0.012	0.019	0.002	0.013	0.002
Pl	735B_69R3_52B	C	al_18	344.159	core	Ol-gabbro	0.234	0.686	0.086	0.401	0.091	0.427	0.069	0.008	0.044	0.151	0.006	0.010	0.001	0.005	0.000
Pl	735B_69R3_52B	D	al_19	344.164	core	Ol-gabbro	0.757	1.620	0.177	0.698	0.107	0.410	0.074	0.009	0.037	0.160	0.006	0.014	0.001	0.006	0.001
Pl	735B_69R3_52B	EF	al_20	344.159	core	Ol-gabbro	0.538	1.450	0.194	0.823	0.159	0.437	0.120	0.012	0.062	0.250	0.011	0.020	0.002	0.009	0.001
Pl	735B_69R3_52B	G	al_24	344.15	core	Ol-gabbro	0.629	1.406	0.165	0.705	0.110	0.468	0.081	0.008	0.039	0.204	0.006	0.013	0.001	0.005	0.001
Pl	735B_69R3_52B	G	al_25	344.15	core	Ol-gabbro	0.153	0.380	0.056	0.279	0.057	0.410	0.067	0.008	0.050	0.247	0.008	0.020	0.002	0.018	0.002
Pl	735B_69R3_52B	H	al_26	344.15	core	Ol-gabbro	0.295	0.660	0.083	0.355	0.063	0.376	0.046	0.005	0.031	0.127	0.005	0.010		0.009	0.001
Pl	735B_68R2_10,5A	C	pa_14	336.542	core	Ol-gabbro	0.612	1.397	0.180	0.826	0.170	0.393	0.127	0.014	0.078	0.367	0.011	0.023	0.002	0.012	0.001
Pl	735B_68R2_10,5A	D	pa_16	336.534	core	Ol-gabbro	0.202	0.500	0.072	0.339	0.088	0.399	0.078	0.013	0.063	0.372	0.012	0.036	0.005	0.022	0.003
Pl	735B_68R2_10,5A	D	pa_17	336.534	core	Ol-gabbro	0.635	1.504	0.211	0.878	0.160	0.455	0.111	0.014	0.058	0.333	0.012	0.026	0.003	0.014	0.002
Pl	735B_68R2_10,5A	E	pa_19	336.537	core	Ol-gabbro	0.232	0.622	0.095	0.461	0.098	0.418	0.115	0.016	0.076	0.393	0.015	0.037	0.004	0.027	0.004
Pl	735B_68R2_10,5A	F	pa_21	336.547	core	Ol-gabbro	0.615	1.370	0.166	0.663	0.131	0.398	0.075	0.008	0.044	0.216	0.006	0.011	0.002	0.009	0.001
Pl	735B_68R2_10,5A	F	pa_24	336.547	core	Ol-gabbro	0.463	1.123	0.147	0.559	0.120	0.386	0.081	0.008	0.058	0.240	0.009	0.024	0.003	0.013	0.001

Mineral	Sample	Area	Point	Depth (mbsf)	Grain area	Lithology	La	Ce	Pr	Nd	Sm	Eu	Gd	Tb	Dy	Y	Ho	Er	Tm	Yb	Lu
Pl	735B_68R2_10,5A	G	pa_25	336.547	core	Ol-gabbro	0.615	1.230	0.144	0.569	0.076	0.390	0.065	0.008	0.036	0.154	0.006	0.011	0.002	0.006	0.001
Pl	735B_68R2_10,5A	G	pa_27	336.547	core	Ol-gabbro	0.335	0.869	0.125	0.579	0.118	0.383	0.113	0.014	0.073	0.379	0.016	0.025	0.003	0.019	0.003
Pl	735B_68R2_10,5A	H	pa_28	336.615	core	Ol-gabbro	0.663	1.545	0.193	0.824	0.141	0.412	0.106	0.015	0.054	0.278	0.010	0.015	0.002	0.006	0.001
Pl	735B_57R1_73	A	ac_1	275.735	rim	Ol-gabbro	7.380	11.730	0.924	2.428	0.229	1.852	0.206	0.013	0.082	0.337	0.012	0.029	0.001	0.011	0.001
Pl	735B_57R1_73	B	ac_5	275.738	rim	Ol-gabbro	0.489	1.094	0.128	0.496	0.089	0.623	0.068	0.007	0.028	0.151	0.006	0.011		0.007	0.001
Pl	735B_57R1_73	D	ac_12	275.745	rim	Ol-gabbro	0.609	1.208	0.140	0.515	0.071	0.657	0.080	0.008	0.040	0.149	0.005	0.011	0.002	0.008	0.001
Pl	735B_57R1_73	C	ac_16	275.743	rim	Ol-gabbro	0.500	1.063	0.122	0.481	0.091	0.615	0.064	0.006	0.021	0.095	0.003			0.002	0.000
Pl	735B_57R1_73	D	ac_18	275.745	rim	Ol-gabbro	0.585	1.160	0.129	0.498	0.087	0.629	0.062	0.008	0.034	0.163	0.005	0.011	0.002	0.009	0.001
Pl	735B_57R1_73	A	ac_19	275.735	rim	Ol-gabbro	7.150	11.210	0.895	2.367	0.259	1.854	0.147	0.015	0.072	0.313	0.011	0.036	0.001	0.016	0.001
Pl	735B_60R4_115B	B	ag_13	295.421	rim	Ol-gabbro	0.558	1.187	0.145	0.559	0.084	0.352	0.076	0.007	0.027	0.136	0.004	0.000	0.001	0.000	0.000
Pl	735B_60R4_115B	C	ag_15	295.425	rim	Ol-gabbro	0.219	0.505	0.067	0.312	0.056	0.295	0.049	0.004	0.027	0.131	0.005	0.009	0.001	0.003	0.000
Pl	735B_60R4_115B	D	ag_16	295.415	rim	Ol-gabbro	0.598	1.357	0.167	0.709	0.102	0.467	0.088	0.010	0.045	0.213	0.006	0.015	0.001	0.005	0.001
Pl	735B_60R4_115B	D	ag_17	295.415	rim	Ol-gabbro	0.579	1.287	0.156	0.606	0.092	0.475	0.080	0.008	0.047	0.215	0.009	0.018	0.002	0.008	0.001
Pl	735B_60R4_115B	D	ag_19	295.415	rim	Ol-gabbro	0.230	0.574	0.088	0.411	0.062	0.430	0.071	0.012	0.050	0.280	0.012	0.024	0.001	0.025	0.003
Pl	735B_60R4_115B	E	ag_22	295.411	rim	Ol-gabbro	0.386	0.983	0.117	0.512	0.090	0.428	0.079	0.006	0.019	0.121	0.006	0.007	0.000	0.000	
Pl	735B_60R4_115B	F	ag_25	295.407	rim	Ol-gabbro	0.734	1.706	0.201	0.837	0.136	0.471	0.117	0.014	0.065	0.326	0.012	0.029	0.004	0.015	0.002
Pl	735B_60R4_115B	G	ag_26	295.412	rim	Ol-gabbro	0.689	1.513	0.169	0.702	0.100	0.466	0.093	0.009	0.041	0.169	0.006	0.010	0.001	0.006	0.000
Pl	735B_58R3_108A	A	ai_9	284.346	rim	Ol-gabbro	0.653	1.448	0.165	0.642	0.119	0.601	0.049	0.007	0.042	0.139	0.004		0.000		0.000
Pl	735B_58R3_108A	A	ai_11	284.346	rim	Ol-gabbro	0.631	1.466	0.174	0.689	0.104	0.575	0.077	0.008	0.042	0.177	0.007	0.012	0.002	0.007	0.000
Pl	735B_58R3_108A	A	ai_13	284.346	rim	Ol-gabbro	0.675	1.553	0.185	0.740	0.133	0.602	0.096	0.010	0.041	0.185	0.007	0.009	0.001	0.004	0.001
Pl	735B_58R3_108A	D	ai_14	284.35	rim	Ol-gabbro	0.793	1.957	0.235	0.946	0.148	0.598	0.116	0.013	0.045	0.206	0.007	0.011	0.001		
Pl	735B_58R3_108A	D	ai_16	284.35	rim	Ol-gabbro	0.684	1.831	0.236	0.954	0.168	0.611	0.131	0.013	0.064	0.236	0.010	0.015	0.001	0.006	0.001
Pl	735B_58R3_108A	E	ai_18	284.352	rim	Ol-gabbro	0.761	1.823	0.232	0.991	0.172	0.671	0.114	0.011	0.042	0.176	0.007	0.011	0.000	0.006	0.001
Pl	735B_58R3_108A	F	ai_20	284.345	rim	Ol-gabbro	0.890	1.852	0.217	0.839	0.127	0.669	0.106	0.011	0.051	0.222	0.008	0.013	0.001	0.005	0.001
Pl	735B_58R3_108A	H	ai_22	284.34	rim	Ol-gabbro	0.849	1.960	0.243	1.050	0.177	0.652	0.138	0.015	0.061	0.300	0.010	0.019	0.002	0.008	0.001
Pl	735B_58R3_108A	H	ai_24	284.34	rim	Ol-gabbro	0.970	2.160	0.274	1.131	0.217	0.675	0.163	0.017	0.076	0.355	0.011	0.027	0.001	0.007	0.001
Pl	735B_75R5_27	B	aj_8	390.354	rim	Ol-gabbro	0.409	0.876	0.101	0.398	0.064	0.366	0.039	0.004	0.024	0.103	0.004	0.007	0.001	0.003	0.000
Pl	735B_75R5_27	B	aj_10	390.354	rim	Ol-gabbro	0.412	0.878	0.105	0.436	0.075	0.387	0.044	0.008	0.032	0.130	0.004	0.011	0.001	0.006	0.001
Pl	735B_75R5_27	C	aj_11	390.352	rim	Ol-gabbro	0.420	0.812	0.092	0.399	0.059	0.418	0.046	0.005	0.022	0.108	0.004	0.006	0.001	0.003	0.000
Pl	735B_75R5_27	C	aj_13	390.352	rim	Ol-gabbro	0.418	0.849	0.098	0.422	0.081	0.391	0.058	0.005	0.028	0.117	0.004	0.014		0.000	0.001
Pl	735B_75R5_27	D	aj_17	390.342	rim	Ol-gabbro	0.261	0.618	0.080	0.328	0.056	0.365	0.056	0.007	0.030	0.125	0.003	0.009	0.001	0.000	
Pl	735B_75R5_27	F	aj_21	390.335	rim	Ol-gabbro	0.273	0.631	0.073	0.347	0.062	0.354	0.056	0.004	0.026	0.115	0.004	0.007	0.001	0.003	
Pl	735B_75R5_27	G	aj_22	390.347	rim	Ol-gabbro	0.256	0.621	0.077	0.361	0.070	0.353	0.062	0.005	0.031	0.147	0.006	0.007	0.001	0.005	0.001
Pl	735B_69R3_52B	A	al_12	344.152	rim	Ol-gabbro	0.559	1.133	0.118	0.490	0.066	0.412	0.049	0.007	0.020	0.115	0.004	0.008	0.000		0.000
Pl	735B_69R3_52B	B	al_14	344.153	rim	Ol-gabbro	0.640	1.239	0.132	0.529	0.069	0.418	0.068	0.006	0.019	0.112	0.003	0.005	0.000	0.000	0.000
Pl	735B_69R3_52B	C	al_16	344.159	rim	Ol-gabbro	0.699	1.395	0.148	0.566	0.080	0.399	0.056	0.005	0.025	0.088	0.004	0.005			
Pl	735B_69R3_52B	C	al_17	344.159	rim	Ol-gabbro	0.598	1.396	0.160	0.667	0.112	0.417	0.075	0.007	0.033	0.162	0.005	0.009	0.001	0.003	0.000
Pl	735B_69R3_52B	EF	al_21	344.159	rim	Ol-gabbro	0.739	1.485	0.165	0.607	0.082	0.356	0.053	0.005	0.023	0.107	0.004	0.004	0.001	0.003	
Pl	735B_69R3_52B	EF	al_22	344.159	rim	Ol-gabbro	1.000	2.195	0.250	1.006	0.142	0.443	0.115	0.013	0.059	0.269	0.010	0.016	0.003	0.012	0.001
Pl	735B_69R3_52B	G	al_23	344.15	rim	Ol-gabbro	0.633	1.224	0.130	0.569	0.076	0.393	0.053	0.006	0.028	0.125	0.005	0.010	0.001	0.004	

Mineral	Sample	Area	Point	Depth (mbsf)	Grain area	Lithology	La	Ce	Pr	Nd	Sm	Eu	Gd	Tb	Dy	Y	Ho	Er	Tm	Yb	Lu
Pl	735B_68R2_10,5A	C	pa_13	336.542	rim	Ol-gabbro	0.642	1.524	0.192	0.868	0.142	0.456	0.099	0.012	0.090	0.276	0.009	0.026	0.002	0.000	0.003
Pl	735B_68R2_10,5A	D	pa_15	336.534	rim	Ol-gabbro	0.409	0.994	0.146	0.623	0.144	0.422	0.113	0.011	0.061	0.288	0.011	0.024	0.002	0.007	0.000
Pl	735B_68R2_10,5A	D	pa_18	336.534	rim	Ol-gabbro	0.682	1.479	0.179	0.700	0.145	0.399	0.084	0.009	0.045	0.174	0.007	0.011	0.002		0.001
Pl	735B_68R2_10,5A	E	pa_20	336.537	rim	Ol-gabbro	0.422	1.100	0.154	0.698	0.129	0.417	0.123	0.014	0.064	0.349	0.013	0.025	0.003	0.007	0.002
Pl	735B_68R2_10,5A	F	pa_22	336.547	rim	Ol-gabbro	0.615	1.301	0.156	0.599	0.099	0.397	0.061	0.007	0.030	0.155	0.006	0.007	0.002		
Pl	735B_68R2_10,5A	F	pa_23	336.547	rim	Ol-gabbro	0.529	1.302	0.174	0.785	0.139	0.407	0.111	0.014	0.056	0.292	0.009	0.013	0.002	0.011	0.001
Pl	735B_68R2_10,5A	G	pa_26	336.547	rim	Ol-gabbro	0.516	1.237	0.149	0.642	0.098	0.402	0.079	0.009	0.055	0.249	0.006	0.015	0.001	0.006	0.001
Pl	735B_68R2_10,5A	H	pa_29	336.615	rim	Ol-gabbro	0.666	1.575	0.201	0.872	0.149	0.424	0.113	0.013	0.061	0.270	0.009	0.018	0.002	0.009	0.002
Pl	735B_79R4_20	E	ak_19	419.168	core	Ol-gabbro	0.485	0.930	0.100	0.415	0.067	0.453	0.056	0.006	0.033	0.246	0.010	0.014	0.000	0.000	
Pl	735B_79R4_20	E	ak_21	419.168	core	Ol-gabbro	0.215	0.546	0.082	0.308	0.074	0.306	0.070	0.009	0.043	0.167	0.005	0.011		0.000	0.000
Pl	735B_79R3_100	A	ob_1	418.507	core	Ol-gabbro	0.405	1.023	0.128	0.569	0.087	0.371	0.085	0.007	0.031	0.159	0.006	0.009	0.001	0.005	0.001
Pl	735B_79R3_100	B	ob_4	418.505	core	Ol-gabbro	0.362	0.928	0.127	0.607	0.110	0.360	0.107	0.013	0.059	0.277	0.009	0.025	0.001	0.009	0.001
Pl	735B_76R3_96	A	pb_12	397.563	core	Ol-gabbro	0.298	0.792	0.109	0.503	0.088	0.374	0.087	0.009	0.049	0.222	0.010	0.018	0.002	0.004	0.000
Pl	735B_76R3_96	B	pb_14	397.571	core	Ol-gabbro	0.451	0.989	0.118	0.515	0.076	0.389	0.057	0.007	0.042	0.165	0.005	0.015	0.001	0.011	
Pl	735B_76R3_96	B	pb_16	397.571	core	Ol-gabbro	0.274	0.728	0.096	0.457	0.079	0.370	0.078	0.011	0.051	0.297	0.012	0.023	0.003	0.010	0.002
Pl	735B_76R3_96	E	pb_17	397.585	core	Ol-gabbro	0.358	0.811	0.095	0.442	0.060	0.414	0.044	0.005	0.027	0.149	0.004	0.013	0.001	0.004	0.001
Pl	735B_76R3_96	E	pb_19	397.585	core	Ol-gabbro	0.297	0.706	0.096	0.383	0.098	0.421	0.047	0.004	0.029	0.111	0.004	0.000			0.000
Pl	735B_76R3_96	E	pb_21	397.585	core	Ol-gabbro	0.178	0.439	0.060	0.330	0.060	0.387	0.061	0.009	0.048	0.227	0.007	0.017	0.002	0.009	0.001
Pl	735B_76R3_96	F	pb_25	397.587	core	Ol-gabbro	0.175	0.429	0.063	0.297	0.058	0.376	0.052	0.006	0.037	0.194	0.007	0.008	0.001	0.017	
Pl	735B_76R3_96	G	pb_26	397.582	core	Ol-gabbro	0.178	0.452	0.064	0.338	0.061	0.395	0.068	0.006	0.055	0.202	0.009	0.009	0.003	0.008	0.001
Pl	735B_76R3_96	G	pb_29	397.582	core	Ol-gabbro	0.215	0.502	0.066	0.296	0.081	0.415	0.058	0.008	0.048	0.244	0.004	0.012	0.001	0.011	0.001
Pl	735B_91R1_74	A	ab_17	518.168	core	Ol-gabbro	0.507	1.444	0.198	0.802	0.172	0.354	0.137	0.015	0.076	0.387	0.014	0.026	0.004	0.020	0.002
Pl	735B_91R1_74	A	ab_19	518.168	core	Ol-gabbro	0.658	1.726	0.225	0.894	0.152	0.339	0.098	0.008	0.064	0.236	0.010	0.016	0.003	0.005	0.001
Pl	735B_91R1_74	B	ab_20	518.167	core	Ol-gabbro	0.830	1.915	0.221	0.851	0.113	0.402	0.077	0.008	0.041	0.174	0.006	0.012	0.001	0.007	0.001
Pl	735B_91R1_74	C	ab_21	518.164	core	Ol-gabbro	0.768	1.908	0.238	0.931	0.167	0.362	0.122	0.013	0.065	0.282	0.011	0.019	0.002	0.008	0.001
Pl	735B_91R1_74	D	ab_23	518.154	core	Ol-gabbro	0.715	1.696	0.204	0.756	0.123	0.321	0.075	0.008	0.035	0.171	0.005	0.011	0.001	0.000	
Pl	735B_91R1_74	D	ab_25	518.154	core	Ol-gabbro	0.722	1.609	0.194	0.725	0.085	0.352	0.067	0.008	0.024	0.142	0.007	0.008		0.005	0.000
Pl	735B_91R1_74	E	ab_28	518.147	core	Ol-gabbro	0.675	1.704	0.207	0.900	0.134	0.376	0.120	0.012	0.062	0.250	0.008	0.018	0.001	0.009	0.001
Pl	735B_91R1_74	F	ab_29	518.155	core	Ol-gabbro	0.751	1.740	0.186	0.733	0.100	0.336	0.079	0.007	0.039	0.177	0.005	0.004	0.002	0.000	0.000
Pl	735B_91R1_74	G	ab_31	518.154	core	Ol-gabbro	0.653	1.662	0.199	0.796	0.139	0.349	0.077	0.009	0.051	0.190	0.010			0.000	
Pl	735B_83R7_43B	A	qb_17	461.706	core	Ol-gabbro	0.231	0.587	0.086	0.436	0.113	0.335	0.094	0.014	0.055	0.278	0.011	0.026	0.001	0.009	0.001
Pl	735B_83R7_43B	A	qb_18	461.706	core	Ol-gabbro	0.287	0.694	0.099	0.429	0.084	0.326	0.078	0.009	0.043	0.189	0.007	0.009	0.001	0.006	
Pl	735B_83R7_43B	B	qb_22	461.722	core	Ol-gabbro	0.447	1.126	0.156	0.714	0.125	0.344	0.121	0.011	0.060	0.222	0.007	0.018	0.002	0.012	0.002
Pl	735B_83R7_43B	B	qb_24	461.722	core	Ol-gabbro	0.210	0.603	0.091	0.533	0.141	0.331	0.149	0.018	0.094	0.446	0.017	0.035	0.003	0.020	0.003
Pl	735B_83R7_43B	D	qb_27	461.725	core	Ol-gabbro	0.560	1.340	0.178	0.725	0.085	0.316	0.064	0.004	0.020	0.084	0.003	0.004	0.000		0.000
Pl	735B_83R7_43B	G	qb_31	461.707	core	Ol-gabbro	0.310	0.788	0.118	0.582	0.108	0.343	0.114	0.011	0.046	0.249	0.008	0.020	0.001	0.010	0.001
Pl	735B_83R7_43B	I	qb_34	461.712	core	Ol-gabbro	0.303	0.815	0.127	0.541	0.090	0.319	0.087	0.010	0.038	0.217	0.007	0.027	0.001	0.000	0.001
Pl	735B_83R7_43B	I	qb_35	461.712	core	Ol-gabbro	0.329	0.788	0.103	0.426	0.068	0.274	0.045	0.005	0.019	0.111	0.003	0.008	0.001	0.000	0.000
Pl	81R5-7/11	E	IPABC010	439.257	core	Ol-gabbro	0.400	0.980	0.129	0.555	0.090	0.440	0.071	0.009	0.036	0.179	0.006	0.012			0.001
Pl	81R5-7/11	E	IPABC012	439.257	core	Ol-gabbro	0.481	1.065	0.129	0.534	0.087	0.452	0.071	0.008	0.030	0.135	0.005	0.012	0.001	0.007	

Mineral	Sample	Area	Point	Depth (mbsf)	Grain area	Lithology	La	Ce	Pr	Nd	Sm	Eu	Gd	Tb	Dy	Y	Ho	Er	Tm	Yb	Lu
Pl	81R5-7/11	B	IPABC016	439.247	core	Ol-gabbro	0.176	0.462	0.072	0.333	0.090	0.416	0.087	0.011	0.055	0.262	0.011	0.024	0.001	0.011	0.001
Pl	81R5-7/11	C	IPABC017	439.252	core	Ol-gabbro	0.488	1.065	0.124	0.508	0.078	0.507	0.062	0.006	0.025	0.126	0.005	0.008	0.001	0.004	0.001
Pl	81R5-7/11	D	IPABC018	439.253	core	Ol-gabbro	0.599	1.257	0.140	0.527	0.084	0.559	0.048	0.006	0.028	0.128	0.005	0.007		0.006	0.001
Pl	90R2-18/20	a4_4	wa_22	509.49	core	Ol-gabbro	0.167	0.487	0.074	0.375	0.106	0.429	0.108	0.014	0.100	0.480	0.015	0.040	0.004	0.021	0.002
Pl	90R2-18/20	a3_4	wa_12	509.49	nt-core	Ol-gabbro	0.205	0.569	0.087	0.454	0.091	0.388	0.139	0.017	0.087	0.426	0.013	0.039	0.003	0.018	0.003
Pl	90R2-18/20	a3_11	wa_14	509.49	core	Ol-gabbro	0.184	0.609	0.085	0.389	0.130	0.393	0.073	0.021	0.085	0.454	0.021	0.039	0.003	0.017	0.002
Pl	90R2-18/20	a2_8	wa_5	509.49	core	Ol-gabbro	0.189	0.536	0.082	0.453	0.108	0.382	0.150	0.018	0.110	0.478	0.019	0.035	0.004	0.017	0.002
Pl	90R2-18/20	a1_8	wa_8	509.49	core	Ol-gabbro	0.387	1.181	0.173	0.857	0.204	0.356	0.135	0.018	0.074	0.261	0.008	0.009	0.001	0.000	0.000
Pl	90R2-18/20	a1_9	wa_9	509.49	core	Ol-gabbro	0.245	0.708	0.099	0.486	0.131	0.431	0.105	0.019	0.104	0.493	0.021	0.056	0.006	0.016	0.003
Pl	90R2-82/86	a4_1	wa_47	510.1	core	Ol-gabbro	0.249	0.764	0.121	0.542	0.157	0.337	0.148	0.020	0.119	0.627	0.030	0.049	0.005	0.043	0.005
Pl	90R2-82/86	a3_15	wa_42	510.1	core	Ol-gabbro	0.151	0.453	0.061	0.316	0.058	0.326	0.090	0.010	0.032	0.224	0.008	0.000	0.003	0.012	0.000
Pl	90R2-82/86	a3_17	wa_46	510.1	core	Ol-gabbro	0.384	1.105	0.171	0.793	0.176	0.335	0.151	0.015	0.074	0.291	0.014	0.022	0.003	0.000	0.000
Pl	90R2-82/86	a2_6	wa_31	510.1	core	Ol-gabbro	0.376	1.188	0.174	0.741	0.203	0.390	0.242	0.019	0.092	0.487	0.017	0.027	0.003	0.000	0.003
Pl	90R2-82/86	a1_1	wa_23	510.1	core	Ol-gabbro	0.268	0.758	0.119	0.565	0.167	0.478	0.165	0.022	0.120	0.561	0.022	0.056	0.006	0.034	0.004
Pl	90R2-84/90	a1_4	wa_53	510.17	core	Ol-gabbro	0.369	1.013	0.140	0.642	0.111	0.352	0.122	0.014	0.038	0.183	0.005	0.011	0.000	0.006	0.000
Pl	90R2-84/90	a2_p1	wa_57	510.17	core	Ol-gabbro	0.305	0.841	0.125	0.592	0.147	0.308	0.110	0.011	0.049	0.217	0.010	0.021	0.000	0.006	0.000
Pl	90R2-84/90	a5_6	wb_7	510.17	core	Ol-gabbro	0.405	1.232	0.183	0.824	0.158	0.395	0.225	0.020	0.109	0.448	0.022	0.027	0.002	0.008	0.002
Pl	90R2-94/100B	a1_11	wb_11	510.27	core	Ol-gabbro	0.279	0.713	0.106	0.406	0.112	0.308	0.100	0.010	0.052	0.229	0.010	0.017	0.002	0.000	0.000
Pl	90R2-94/100B	a3_7	wb_21	510.27	core	Ol-gabbro	0.241	0.633	0.094	0.480	0.110	0.295	0.103	0.012	0.091	0.384	0.015	0.025	0.005	0.014	0.002
Pl	90R2-123/129	a1_12	wb_26	510.56	core	Ol-gabbro	0.522	1.363	0.177	0.676	0.116	0.340	0.093	0.007	0.030	0.147	0.004	0.006	0.000	0.000	0.000
Pl	90R3-6/8	a3_12	wb_42	510.84	core	Ol-gabbro	0.346	0.997	0.141	0.568	0.081	0.325	0.097	0.000	0.055	0.202	0.015	0.016	0.000	0.000	0.000
Pl	735B_79R4_20	D	ak_11	419.163	rim	Ol-gabbro	0.277	0.626	0.077	0.351	0.049	0.306	0.048	0.002	0.014	0.078	0.001	0.000	0.000		
Pl	735B_79R4_20	D	ak_18	419.163	rim	Ol-gabbro	0.450	0.854	0.101	0.371	0.064	0.353	0.086	0.005	0.048	0.232	0.004		0.000	0.016	0.000
Pl	735B_79R3_100	A	ob_2	418.507	rim	Ol-gabbro	0.399	0.855	0.104	0.439	0.065	0.372	0.051	0.004	0.024	0.127	0.005	0.010	0.001	0.007	0.001
Pl	735B_79R3_100	B	ob_3	418.505	rim	Ol-gabbro	0.262	0.750	0.108	0.531	0.111	0.397	0.137	0.014	0.085	0.342	0.014	0.026	0.001	0.015	0.001
Pl	735B_76R3_96	A	pb_13	397.563	rim	Ol-gabbro	0.334	0.768	0.107	0.492	0.073	0.415	0.104	0.007	0.026	0.168	0.005			0.000	
Pl	735B_76R3_96	B	pb_15	397.571	rim	Ol-gabbro	0.362	0.832	0.106	0.472	0.082	0.407	0.068	0.011	0.044	0.204	0.008	0.027	0.003	0.016	0.002
Pl	735B_76R3_96	E	pb_18	397.585	rim	Ol-gabbro	0.364	0.792	0.099	0.363	0.050	0.417	0.048	0.003	0.016	0.088	0.003	0.005			
Pl	735B_76R3_96	E	pb_20	397.585	rim	Ol-gabbro	0.358	0.823	0.103	0.448	0.070	0.414	0.058	0.006	0.039	0.138	0.004	0.007		0.000	0.001
Pl	735B_76R3_96	F	pb_22	397.587	rim	Ol-gabbro	0.388	0.878	0.114	0.484	0.083	0.410	0.058	0.007	0.026	0.137	0.004	0.005	0.001	0.000	
Pl	735B_76R3_96	F	pb_24	397.587	rim	Ol-gabbro	0.347	0.807	0.099	0.432	0.091	0.395	0.061	0.006	0.030	0.142	0.004	0.009	0.001		0.001
Pl	735B_76R3_96	G	pb_27	397.582	rim	Ol-gabbro	0.356	0.826	0.110	0.495	0.084	0.406	0.068	0.004	0.027	0.163	0.006	0.008			
Pl	735B_76R3_96	G	pb_28	397.582	rim	Ol-gabbro	0.292	0.755	0.104	0.524	0.085	0.407	0.102	0.009	0.069	0.286	0.012	0.023	0.001	0.019	0.001
Pl	735B_91R1_74	A	ab_18	518.168	rim	Ol-gabbro	0.617	1.652	0.197	0.764	0.136	0.356	0.105	0.009	0.042	0.221	0.005	0.015	0.001	0.008	0.001
Pl	735B_91R1_74	C	ab_22	518.164	rim	Ol-gabbro	0.779	1.722	0.186	0.699	0.111	0.371	0.057	0.007	0.030	0.156	0.006	0.008	0.001	0.010	0.001
Pl	735B_91R1_74	D	ab_24	518.154	rim	Ol-gabbro	0.737	1.732	0.212	0.772	0.117	0.316	0.082	0.009	0.028	0.165	0.008	0.012	0.001	0.010	0.000
Pl	735B_91R1_74	E	ab_27	518.147	rim	Ol-gabbro	0.697	1.686	0.205	0.796	0.107	0.396	0.098	0.011	0.045	0.213	0.006	0.013	0.002	0.003	0.001
Pl	735B_91R1_74	F	ab_30	518.155	rim	Ol-gabbro	0.624	1.568	0.191	0.766	0.124	0.352	0.072	0.008	0.035	0.196	0.007	0.017	0.001	0.000	
Pl	735B_91R1_74	G	ab_32	518.154	rim	Ol-gabbro	0.707	1.784	0.200	0.852	0.116	0.327	0.104	0.009	0.052	0.205	0.006	0.014	0.002	0.004	

Mineral	Sample	Area	Point	Depth (mbsf)	Grain area	Lithology	La	Ce	Pr	Nd	Sm	Eu	Gd	Tb	Dy	Y	Ho	Er	Tm	Yb	Lu
Pl	735B_83R7_43B	B	qb_21	461.722	rim	Ol-gabbro	0.431	1.072	0.154	0.716	0.134	0.356	0.076	0.009	0.040	0.180	0.007	0.009	0.001	0.005	0.001
Pl	735B_83R7_43B	B	qb_23	461.722	rim	Ol-gabbro	0.455	1.168	0.152	0.646	0.113	0.332	0.074	0.007	0.029	0.155	0.005	0.010	0.001	0.000	0.001
Pl	735B_83R7_43B	C	qb_25	461.723	rim	Ol-gabbro	0.313	0.796	0.108	0.497	0.098	0.359	0.079	0.010	0.049	0.209	0.006	0.009	0.002	0.005	
Pl	735B_83R7_43B	G	qb_30	461.707	rim	Ol-gabbro	1.032	2.530	0.286	0.971	0.138	0.363	0.105	0.014	0.065	0.375	0.014	0.027	0.004	0.025	0.001
Pl	735B_83R7_43B	I	qb_33	461.712	rim	Ol-gabbro	0.289	0.797	0.101	0.484	0.108	0.293	0.082	0.008	0.034	0.164	0.005	0.011	0.001	0.004	0.001
Pl	81R5-7/11	E	IPABC011	439.257	rim	Ol-gabbro	0.442	1.038	0.137	0.581	0.097	0.448	0.086	0.009	0.043	0.185	0.007	0.013	0.001	0.008	0.001
Pl	81R5-7/11	B	IPABC013	439.247	rim	Ol-gabbro	0.434	0.841	0.095	0.374	0.065	0.535	0.053	0.006	0.023	0.098	0.003	0.008			
Pl	81R5-7/11	B	IPABC014	439.247	rim	Ol-gabbro	0.344	0.833	0.111	0.478	0.083	0.456	0.082	0.008	0.030	0.146	0.005	0.007	0.001		
Pl	90R2-18/20	a4_3	wa_21	509.49	rim	Ol-gabbro	0.537	1.503	0.222	0.888	0.173	0.392	0.144	0.016	0.091	0.349	0.017	0.024	0.000	0.018	0.002
Pl	90R2-18/20	a3_3	wa_11	509.49	rim	Ol-gabbro	0.495	1.391	0.193	0.905	0.170	0.398	0.106	0.013	0.074	0.298	0.013	0.015	0.001	0.009	0.002
Pl	90R2-18/20	a3_10	wa_13	509.49	rim	Ol-gabbro	0.505	1.324	0.171	0.637	0.109	0.448	0.077	0.010	0.040	0.190	0.008	0.008	0.000	0.000	0.000
Pl	90R2-18/20	a3_12	wa_15	509.49	rim	Ol-gabbro	0.507	1.272	0.180	0.817	0.140	0.487	0.111	0.012	0.035	0.187	0.006	0.025	0.000	0.006	0.000
Pl	90R2-18/20	a2_7	wa_6	509.49	rim	Ol-gabbro	0.551	1.358	0.192	0.708	0.159	0.400	0.107	0.013	0.075	0.265	0.008	0.035	0.001	0.014	0.002
Pl	90R2-18/20	a2_9	wa_4	509.49	rim	Ol-gabbro	0.544	1.344	0.191	0.815	0.163	0.477	0.175	0.014	0.066	0.291	0.012	0.027	0.000	0.018	0.005
Pl	90R2-18/20	a1_7	wa_7	509.49	rim	Ol-gabbro	0.584	1.577	0.213	0.920	0.136	0.436	0.080	0.010	0.034	0.122	0.003	0.008	0.000	0.014	0.000
Pl	90R2-18/20	a1_10	wa_10	509.49	rim	Ol-gabbro	0.575	1.555	0.205	0.966	0.167	0.405	0.169	0.018	0.093	0.379	0.014	0.022	0.002	0.015	0.000
Pl	90R2-82/86	a4_1	wa_48	510.1	rim	Ol-gabbro	0.264	0.681	0.091	0.401	0.074	0.288	0.047	0.012	0.040	0.179	0.006	0.007	0.000	0.013	0.000
Pl	90R2-82/86	a3_16	wa_45	510.1	rim	Ol-gabbro	0.472	1.163	0.132	0.552	0.089	0.382	0.050	0.007	0.034	0.102	0.004	0.000	0.002	0.000	0.001
Pl	90R2-82/86	a2_5	wa_30	510.1	rim	Ol-gabbro	0.538	1.336	0.173	0.756	0.141	0.459	0.117	0.008	0.056	0.174	0.006	0.010	0.000	0.000	0.000
Pl	90R2-82/86	a1_2	wa_24	510.1	rim	Ol-gabbro	0.616	1.562	0.201	0.912	0.140	0.463	0.081	0.009	0.061	0.244	0.008	0.022	0.001	0.000	0.001
Pl	90R2-84/90	a1_3	wa_51	510.17	rim	Ol-gabbro	0.309	0.719	0.086	0.483	0.082	0.335	0.094	0.003	0.037	0.166	0.005	0.012	0.000	0.005	0.000
Pl	90R2-84/90	a1_5	wa_54	510.17	rim	Ol-gabbro	0.341	0.790	0.098	0.416	0.061	0.319	0.080	0.003	0.017	0.100	0.001	0.000	0.000	0.000	0.000
Pl	90R2-84/90	a2_p1	wa_58	510.17	rim	Ol-gabbro	0.388	0.955	0.116	0.505	0.094	0.337	0.064	0.006	0.048	0.198	0.008	0.000	0.000	0.000	0.000
Pl	90R2-84/90	a3_8	wb_3	510.17	rim	Ol-gabbro	0.515	1.376	0.192	0.840	0.151	0.433	0.179	0.015	0.073	0.291	0.014	0.018	0.002	0.000	0.000
Pl	90R2-84/90	a5_5	wb_6	510.17	rim	Ol-gabbro	0.600	1.457	0.178	0.783	0.094	0.360	0.079	0.007	0.031	0.128	0.005	0.008	0.000	0.000	0.000
Pl	90R2-94/100B	a1_10	wb_10	510.27	rim	Ol-gabbro	0.292	0.696	0.088	0.412	0.062	0.338	0.074	0.012	0.036	0.147	0.004	0.008	0.000	0.000	0.000
Pl	90R2-94/100B	a2_10	wb_18	510.27	rim	Ol-gabbro	0.313	0.812	0.114	0.405	0.079	0.365	0.066	0.007	0.039	0.208	0.010	0.020	0.000	0.010	0.000
Pl	90R2-94/100B	a3_6	wb_20	510.27	rim	Ol-gabbro	0.296	0.714	0.087	0.416	0.066	0.281	0.048	0.007	0.035	0.120	0.004	0.012	0.000	0.000	0.000
Pl	90R2-123/129	a1_11	wb_25	510.56	rim	Ol-gabbro	0.519	1.170	0.146	0.576	0.066	0.332	0.068	0.006	0.019	0.110	0.003	0.005	0.000	0.000	0.000
Pl	90R2-123/129	a3_8	wb_35	510.56	rim	Ol-gabbro	0.448	0.989	0.124	0.506	0.061	0.355	0.111	0.009	0.041	0.100	0.002	0.005	0.001	0.007	0.000
Pl	90R3-6/8	a3_11	wb_41	510.84	rim	Ol-gabbro	0.276	0.718	0.085	0.386	0.061	0.391	0.034	0.005	0.031	0.097	0.004	0.009	0.000	0.000	0.000
Pl	735B_83R7_113A	A	ae_18	462.399	core	Ol-rich gabbro	0.402	1.026	0.124	0.506	0.082	0.374	0.063	0.006	0.023	0.137	0.005	0.011	0.000		0.000
Pl	735B_83R7_113A	CD	ae_20	462.385	core	Ol-rich gabbro	0.369	0.868	0.103	0.419	0.083	0.386	0.070	0.005	0.029	0.138	0.004	0.009	0.000	0.003	0.000
Pl	735B_83R7_113A	CD	ae_21	462.385	core	Ol-rich gabbro	0.356	0.840	0.094	0.369	0.057	0.381	0.044	0.005	0.020	0.088	0.003	0.005	0.000		0.000
Pl	735B_83R7_113A	F	ae_25	462.399	core	Ol-rich gabbro	0.189	0.588	0.085	0.450	0.134	0.343	0.098	0.015	0.064	0.322	0.012	0.019	0.002	0.011	0.001
Pl	735B_83R7_113A	F	ae_27	462.399	core	Ol-rich gabbro	0.390	0.969	0.127	0.532	0.086	0.376	0.064	0.008	0.036	0.158	0.006	0.008		0.006	0.001
Pl	735B_83R7_113A	H	ae_29	462.395	core	Ol-rich gabbro	0.244	0.725	0.106	0.532	0.118	0.355	0.127	0.012	0.066	0.268	0.011	0.020	0.002	0.005	
Pl	735B_83R7_113A	I	ae_30	462.388	core	Ol-rich gabbro	0.269	0.746	0.104	0.431	0.070	0.329	0.059	0.005	0.033	0.125	0.002	0.007	0.001	0.006	
Pl	735B_83R7_0	BC	oc_19	461.268	core	Ol-rich gabbro	0.299	0.828	0.097	0.454	0.087	0.331	0.102	0.010	0.043	0.187	0.007	0.004	0.002	0.007	0.001
Pl	735B_83R7_0	BC	oc_20	461.268	core	Ol-rich gabbro	0.513	1.212	0.156	0.609	0.114	0.359	0.077	0.008	0.042	0.156	0.008	0.011	0.001	0.006	

Min	Sample	Area	Point	Depth	Grain	Lithology	La	Ce	Pr	Nd	Sm	Eu	Gd	Tb	Dy	Y	Ho	Er	Tm	Yb	Lu
Pl	735B_83R7_0	E	oc_27	461.265	core	Ol-rich gabbro	0.298	0.847	0.111	0.514	0.105	0.318	0.100	0.010	0.047	0.202	0.008	0.014	0.001	0.005	0.001
Pl	735B_83R7_0	G	oc_30	461.275	core	Ol-rich gabbro	0.582	1.305	0.155	0.645	0.109	0.404	0.078	0.009	0.035	0.169	0.006	0.015	0.001	0.000	0.001
Pl	735B_83R7_113A	A	ae_19	462.399	rim	Ol-rich gabbro	0.367	1.008	0.126	0.597	0.103	0.345	0.073	0.007	0.034	0.153	0.005	0.019	0.001	0.003	0.001
Pl	735B_83R7_113A	F	ae_26	462.399	rim	Ol-rich gabbro	0.357	0.954	0.128	0.529	0.102	0.333	0.064	0.009	0.050	0.225	0.009	0.024	0.003	0.013	0.002
Pl	735B_83R7_113A	H	ae_28	462.395	rim	Ol-rich gabbro	0.324	0.815	0.100	0.455	0.061	0.334	0.052	0.005	0.024	0.143	0.004	0.002	0.001	0.006	0.001
Pl	735B_83R7_0	E	oc_28	461.265	rim	Ol-rich gabbro	0.396	0.959	0.120	0.462	0.077	0.398	0.060	0.008	0.031	0.152	0.004	0.011	0.001		
Pl	735B_83R7_0	G	oc_29	461.275	rim	Ol-rich gabbro	0.540	1.233	0.155	0.620	0.105	0.385	0.058	0.007	0.037	0.150	0.004	0.006	0.001		
Pl	735B_89R1_47	A	ah_9	505.274	core	Troctolite	0.304	0.963	0.149	0.668	0.184	0.350	0.141	0.022	0.103	0.500	0.017	0.047	0.006	0.023	0.002
Pl	735B_89R1_47	B	ah_13	505.277	core	Troctolite	0.271	0.923	0.140	0.666	0.156	0.349	0.114	0.013	0.054	0.311	0.010	0.019	0.001	0.004	
Pl	735B_89R1_47	B	ah_14	505.277	core	Troctolite	0.138	0.393	0.059	0.288	0.081	0.343	0.081	0.012	0.070	0.341	0.011	0.035	0.005	0.021	0.003
Pl	735B_89R1_47	C	ah_16	505.281	core	Troctolite	0.248	0.695	0.107	0.542	0.148	0.352	0.142	0.021	0.116	0.603	0.021	0.048	0.005	0.022	0.003
Pl	735B_89R1_47	D	ah_18	505.284	core	Troctolite	0.270	0.764	0.118	0.585	0.171	0.366	0.171	0.021	0.103	0.577	0.019	0.040	0.005	0.028	0.002
Pl	735B_89R1_47	E	ah_20	505.291	core	Troctolite	0.231	0.749	0.117	0.575	0.149	0.343	0.152	0.020	0.116	0.556	0.019	0.051	0.006	0.029	0.004
Pl	735B_89R1_47	G	ah_21	505.298	core	Troctolite	0.564	1.492	0.184	0.812	0.123	0.332	0.107	0.009	0.043	0.216	0.007	0.015	0.002	0.006	0.001
Pl	735B_89R1_47	G	ah_23	505.298	core	Troctolite	0.505	1.435	0.203	0.916	0.173	0.340	0.137	0.014	0.061	0.258	0.010	0.015	0.002	0.006	0.001
Pl	735B_89R1_47	G	ah_25	505.298	core	Troctolite	0.195	0.537	0.080	0.395	0.098	0.331	0.107	0.015	0.073	0.364	0.013	0.030	0.003	0.015	0.002
Pl	735B_80R2_7,5A	A	qa_15	425.563	core	Troctolite	0.177	0.462	0.068	0.314	0.083	0.308	0.093	0.011	0.080	0.368	0.013	0.019	0.005	0.017	0.002
Pl	735B_80R2_7,5A	A	qa_16	425.563	core	Troctolite	0.473	1.164	0.171	0.711	0.148	0.289	0.136	0.014	0.073	0.405	0.013	0.028	0.003	0.027	0.002
Pl	735B_80R2_7,5A	B	qa_20	425.56	core	Troctolite	0.373	0.954	0.135	0.538	0.112	0.344	0.091	0.011	0.060	0.274	0.012	0.024	0.004	0.018	0.002
Pl	735B_80R2_7,5A	B	qa_22	425.56	core	Troctolite	0.184	0.459	0.068	0.304	0.085	0.330	0.085	0.011	0.070	0.374	0.014	0.037	0.001	0.029	0.003
Pl	735B_80R2_7,5A	B	qa_24	425.56	core	Troctolite	0.273	0.761	0.120	0.569	0.116	0.316	0.113	0.014	0.071	0.354	0.014	0.022	0.003	0.013	
Pl	735B_80R2_7,5A	C	qa_27	425.553	core	Troctolite	0.363	0.931	0.129	0.653	0.106	0.327	0.088	0.009	0.049	0.176	0.007	0.010	0.001	0.000	
Pl	735B_80R2_7,5A	E	qa_32	425.556	core	Troctolite	0.340	0.889	0.130	0.562	0.092	0.341	0.064	0.007	0.043	0.152	0.008	0.006	0.000	0.000	
Pl	735B_80R2_7,5A	E	qa_34	425.556	core	Troctolite	0.204	0.536	0.092	0.437	0.124	0.296	0.115	0.014	0.066	0.291	0.009	0.017	0.002	0.000	0.000
Pl	735B_80R2_7,5A	F	qa_36	425.549	core	Troctolite	0.201	0.595	0.095	0.474	0.136	0.328	0.142	0.019	0.104	0.471	0.016	0.037	0.003	0.007	0.001
Pl	735B_89R1_47	A	ah_10	505.274	rim	Troctolite	1.053	2.462	0.267	0.940	0.148	0.381	0.077	0.010	0.063	0.211	0.007	0.017	0.002	0.014	0.001
Pl	735B_89R1_47	B	ah_12	505.277	rim	Troctolite	0.547	1.438	0.180	0.732	0.118	0.363	0.090	0.009	0.052	0.194	0.008	0.020	0.002	0.010	0.001
Pl	735B_89R1_47	D	ah_17	505.284	rim	Troctolite	0.760	2.088	0.279	1.206	0.247	0.374	0.187	0.020	0.108	0.434	0.015	0.032	0.003	0.015	0.002
Pl	735B_89R1_47	E	ah_19	505.291	rim	Troctolite	0.604	1.560	0.191	0.824	0.130	0.335	0.084	0.009	0.040	0.190	0.005	0.014	0.002	0.007	0.001
Pl	735B_89R1_47	E	ah_22	505.291	rim	Troctolite	0.545	1.407	0.176	0.680	0.105	0.335	0.074	0.007	0.039	0.173	0.005	0.013	0.001	0.007	0.001
Pl	735B_89R1_47	G	ah_24	505.298	rim	Troctolite	0.352	1.046	0.158	0.719	0.166	0.341	0.148	0.014	0.074	0.306	0.012	0.021	0.002	0.010	0.001
Pl	735B_80R2_7,5A	A	qa_14	425.563	rim	Troctolite	0.333	0.845	0.119	0.532	0.106	0.311	0.084	0.009	0.047	0.219	0.007	0.015	0.001	0.005	0.001
Pl	735B_80R2_7,5A	A	qa_18	425.563	rim	Troctolite	0.370	0.920	0.131	0.659	0.140	0.325	0.115	0.014	0.079	0.398	0.014	0.032	0.004	0.017	0.003
Pl	735B_80R2_7,5A	B	qa_21	425.56	rim	Troctolite	0.284	0.725	0.109	0.542	0.125	0.331	0.097	0.015	0.076	0.375	0.012	0.030	0.003	0.015	0.002
Pl	735B_80R2_7,5A	B	qa_23	425.56	rim	Troctolite	0.345	0.914	0.120	0.608	0.118	0.321	0.097	0.011	0.061	0.255	0.010	0.019	0.002	0.009	0.001
Pl	735B_80R2_7,5A	C	qa_25	425.553	rim	Troctolite	0.352	0.884	0.125	0.566	0.115	0.332	0.084	0.009	0.043	0.185	0.008	0.011	0.001	0.007	
Pl	735B_80R2_7,5A	D	qa_31	425.556	rim	Troctolite	0.314	0.815	0.122	0.591	0.127	0.324	0.127	0.015	0.060	0.331	0.013	0.024	0.002	0.016	0.002
Pl	735B_80R2_7,5A	E	qa_33	425.556	rim	Troctolite	0.299	0.751	0.102	0.474	0.090	0.313	0.069	0.007	0.026	0.109	0.004	0.003	0.001		
	Average (N = 81)						0.58	1.87	0.35	2.25	1.01	0.49	1.59	0.31	2.31	12.89	0.51	1.48	0.22	1.54	0.23
BIR	2SD						0.11	0.27	0.04	0.28	0.11	0.06	0.26	0.05	0.30	2.04	0.08	0.25	0.04	0.24	0.04
	Preferred values ("Georem" Jochum et al., 2007)						0.61	1.89	0.37	2.37	1.09	0.52	1.85	0.35	2.55	14.30	0.56	1.70	0.24	1.64	0.25

In situ trace elements concentrations in ppm analyzed by LA-ICP-MS on a ThermoFisher Element XR at GM (Montpellier, France)

Mineral	Sample	Area	Point	Depth (mbsf)	Grain area	Lithology	La	Ce	Pr	Nd	Sm	Eu	Gd	Tb	Dy	Y	Ho	Er	Tm	Yb	Lu
Cpx	85R7-79/83	F	'ABC018	480.698	core	Gabbro	0.259	1.699	0.400	2.780	1.380	0.511	2.035	0.402	2.739	14.740	0.578	1.652	0.224	1.472	0.207
Cpx	85R7-79/83	G	'ABC019	480.695	core	Gabbro	0.201	1.141	0.278	1.943	1.056	0.443	1.676	0.320	2.179	11.540	0.473	1.311	0.177	1.176	0.169
Cpx	85R7-79/83	B	'ABC025	480.709	core	Gabbro	0.244	1.357	0.319	2.222	1.088	0.473	1.785	0.340	2.348	11.950	0.483	1.403	0.186	1.289	0.185
Cpx	85R7-79/83	F	'ABC017	480.698	rim	Gabbro	0.228	1.492	0.361	2.552	1.275	0.484	1.992	0.381	2.602	13.950	0.551	1.579	0.211	1.470	0.209
Cpx	85R7-79/83	I	'ABC020	480.695	rim	Gabbro	0.228	1.341	0.305	2.112	1.117	0.456	1.680	0.314	2.125	11.860	0.448	1.252	0.166	1.152	0.164
Cpx	85R7-79/83	J	'ABC021	480.694	rim	Gabbro	0.347	2.494	0.557	3.720	1.817	0.502	2.569	0.487	3.430	18.430	0.746	2.109	0.294	2.049	0.282
Cpx	85R7-79/83	K	'ABC022	480.684	rim	Gabbro	0.288	1.731	0.411	2.845	1.456	0.502	2.095	0.406	2.755	14.410	0.592	1.688	0.239	1.551	0.213
Cpx	85R7-79/83	K	'ABC023	480.684	rim	Gabbro	0.213	1.189	0.301	2.087	1.085	0.476	1.880	0.326	2.327	11.520	0.483	1.380	0.185	1.186	0.171
Cpx	85R7-79/83	A	'ABC024	480.711	rim	Gabbro	0.180	1.129	0.284	2.043	1.095	0.437	1.761	0.336	2.277	11.690	0.482	1.376	0.181	1.204	0.169
Cpx	735B_56R4_61A	F	aa_17	274.905	core	Ol-bearing gabbro	0.603	3.330	0.848	6.170	3.180	1.045	5.190	0.936	7.000	37.530	1.490	4.300	0.605	3.930	0.563
Cpx	735B_56R4_61A	E	aa_19	274.906	core	Ol-bearing gabbro	0.540	3.240	0.785	6.000	3.070	1.004	4.940	0.946	6.820	36.340	1.477	4.340	0.604	4.040	0.551
Cpx	735B_56R4_61A	D	aa_21	274.904	core	Ol-bearing gabbro	0.584	3.150	0.765	5.890	2.900	0.932	4.860	0.860	6.510	34.720	1.357	3.930	0.550	3.670	0.538
Cpx	735B_56R4_61A	C	aa_22	274.899	core	Ol-bearing gabbro	0.509	3.061	0.764	5.840	3.040	0.927	5.060	0.915	6.850	36.970	1.452	4.110	0.579	3.710	0.556
Cpx	735B_56R4_61A	C	aa_24	274.899	core	Ol-bearing gabbro	0.518	3.150	0.769	5.710	2.930	0.917	5.040	0.867	6.680	35.990	1.398	3.790	0.563	3.830	0.561
Cpx	735B_56R4_61A	B	aa_25	274.893	core	Ol-bearing gabbro	0.891	3.950	0.862	5.910	2.970	0.994	4.860	0.908	6.570	35.090	1.388	3.940	0.552	3.900	0.550
Cpx	735B_56R4_61A	A	aa_28	274.884	core	Ol-bearing gabbro	0.561	3.130	0.777	5.740	2.710	0.970	4.800	0.851	6.530	34.700	1.375	4.000	0.560	3.750	0.559
Cpx	735B_56R4_61A	F	aa_15	274.905	rim	Ol-bearing gabbro	0.438	2.805	0.744	5.400	2.870	0.925	4.570	0.855	6.390	33.740	1.334	3.810	0.533	3.470	0.487
Cpx	735B_56R4_61A	F	aa_16	274.905	rim	Ol-bearing gabbro	0.518	3.016	0.747	5.630	2.880	0.895	4.640	0.849	6.340	34.010	1.346	3.740	0.534	3.580	0.516
Cpx	735B_56R4_61A	E	aa_18	274.906	rim	Ol-bearing gabbro	0.525	3.043	0.751	5.730	2.830	0.881	4.820	0.903	6.580	35.560	1.395	4.070	0.584	3.870	0.537
Cpx	735B_56R4_61A	D	aa_20	274.904	rim	Ol-bearing gabbro	0.534	3.006	0.761	5.780	2.960	0.959	4.850	0.909	6.650	35.330	1.341	4.000	0.574	3.830	0.533
Cpx	735B_56R4_61A	C	aa_23	274.899	rim	Ol-bearing gabbro	0.470	2.799	0.713	5.440	2.660	0.862	4.570	0.863	6.150	33.190	1.289	3.660	0.515	3.400	0.496
Cpx	735B_56R4_61A	B	aa_26	274.893	rim	Ol-bearing gabbro	0.934	4.360	0.935	6.340	3.000	0.886	4.960	0.917	6.590	35.400	1.410	4.080	0.573	3.710	0.550
Cpx	735B_56R4_61A	A	aa_27	274.884	rim	Ol-bearing gabbro	0.515	3.030	0.766	5.740	2.840	0.885	4.450	0.877	6.270	33.680	1.330	3.570	0.536	3.470	0.522
Cpx	735B_57R1_73	A	ac_20	275.735	core	Ol-gabbro	1.751	6.530	1.175	7.260	3.430	1.105	5.360	0.998	7.560	39.830	1.588	4.390	0.655	4.390	0.633
Cpx	735B_57R1_73	B	ac_21	275.738	core	Ol-gabbro	0.677	3.840	0.924	6.680	3.190	0.975	5.080	0.912	6.760	35.240	1.387	3.950	0.573	3.690	0.530
Cpx	735B_57R1_73	B	ac_23	275.738	core	Ol-gabbro	0.693	4.210	1.023	7.550	3.660	1.078	5.290	1.045	7.790	39.890	1.601	4.610	0.650	4.330	0.598
Cpx	735B_57R1_73	C	ac_24	275.743	core	Ol-gabbro	0.642	3.710	0.909	6.290	3.060	0.970	5.030	0.938	6.870	36.760	1.430	4.200	0.618	3.970	0.566
Cpx	735B_57R1_73	D	ac_25	275.745	core	Ol-gabbro	1.043	4.150	0.950	6.690	3.370	1.044	5.370	1.001	7.420	39.810	1.569	4.460	0.638	4.240	0.619
Cpx	735B_57R1_73	E	ac_27	275.759	core	Ol-gabbro	1.227	5.010	1.020	6.880	3.340	1.054	5.120	1.004	7.310	39.980	1.551	4.460	0.658	4.460	0.641
Cpx	735B_60R4_115E	A	ag_30	295.408	core	Ol-gabbro	0.320	1.887	0.471	3.320	1.474	0.599	2.299	0.414	2.990	15.430	0.596	1.756	0.242	1.491	0.216
Cpx	735B_60R4_115E	A	ag_32	295.408	core	Ol-gabbro	0.259	1.614	0.421	2.980	1.535	0.592	2.308	0.421	3.060	15.450	0.620	1.679	0.227	1.514	0.232
Cpx	735B_60R4_115E	B	ag_33	295.421	core	Ol-gabbro	0.259	1.446	0.366	2.983	1.479	0.559	2.503	0.434	3.270	17.010	0.684	1.862	0.269	1.775	0.251
Cpx	735B_60R4_115E	C	ag_34	295.425	core	Ol-gabbro	0.272	1.512	0.390	3.000	1.545	0.581	2.469	0.462	3.380	17.610	0.692	1.926	0.283	1.746	0.263
Cpx	735B_60R4_115E	E	ag_36	295.411	core	Ol-gabbro	0.241	1.417	0.378	2.777	1.361	0.524	2.173	0.407	2.910	14.880	0.594	1.582	0.229	1.480	0.212
Cpx	735B_60R4_115E	G	ag_38	295.412	core	Ol-gabbro	0.245	1.444	0.360	2.811	1.350	0.511	2.157	0.384	3.070	15.780	0.618	1.724	0.251	1.566	0.239
Cpx	735B_60R4_115E	G	ag_39	295.412	core	Ol-gabbro	0.687	4.140	1.028	7.290	3.440	0.886	5.200	0.953	6.790	35.960	1.429	3.990	0.548	3.710	0.524
Cpx	735B_60R4_115E	G	ag_41	295.412	core	Ol-gabbro	0.556	3.060	0.694	4.910	2.293	0.740	3.660	0.685	4.990	26.380	1.048	3.010	0.430	2.820	0.404
Cpx	735B_58R3_108A	A	ai_28	284.346	core	Ol-gabbro	0.252	1.451	0.339	2.418	1.122	0.342	1.633	0.303	2.284	12.380	0.488	1.390	0.204	1.390	0.194

Mineral	Sample	Area	Point	Depth (mbsf)	Grain area	Lithology	La	Ce	Pr	Nd	Sm	Eu	Gd	Tb	Dy	Y	Ho	Er	Tm	Yb	Lu
Cpx	735B_58R3_108A	B	ai_31	284.339	core	Ol-gabbro	0.148	0.755	0.191	1.402	0.719	0.273	1.076	0.209	1.541	8.050	0.321	0.911	0.129	0.860	0.123
Cpx	735B_58R3_108	F	ai_33	284.345	core	Ol-gabbro	0.1585	0.822	0.2108	1.702	0.871	0.283	1.378	0.2562	1.855	9.64	0.395	1.073	0.154	1.011	0.1453
Cpx	735B_58R3_108A	G	ai_34	284.348	core	Ol-gabbro	0.072	0.433	0.115	0.924	0.502	0.189	0.808	0.156	1.148	5.950	0.241	0.669	0.095	0.620	0.087
Cpx	735B_75R5_27	B	aj_28	390.354	core	Ol-gabbro	0.291	1.666	0.401	3.280	1.624	0.581	2.550	0.505	3.540	19.220	0.783	2.133	0.304	1.976	0.298
Cpx	735B_75R5_27	B	aj_31	390.354	core	Ol-gabbro	0.355	2.030	0.477	3.390	1.546	0.542	2.449	0.454	3.370	17.770	0.711	1.933	0.282	1.886	0.249
Cpx	735B_75R5_27	C	aj_32	390.352	core	Ol-gabbro	0.311	1.626	0.404	2.895	1.559	0.493	2.423	0.469	3.460	18.680	0.740	2.125	0.293	1.897	0.278
Cpx	735B_75R5_27	C	aj_34	390.352	core	Ol-gabbro	0.342	1.660	0.399	3.020	1.462	0.549	2.620	0.482	3.520	18.970	0.745	2.173	0.307	1.933	0.290
Cpx	735B_75R5_27	D	aj_35	390.342	core	Ol-gabbro	0.272	1.674	0.453	3.440	1.777	0.543	2.830	0.546	3.960	21.130	0.856	2.305	0.336	2.169	0.313
Cpx	735B_75R5_27	E	aj_37	390.338	core	Ol-gabbro	0.311	1.861	0.467	3.350	1.625	0.592	2.810	0.520	3.790	20.280	0.797	2.214	0.316	2.104	0.323
Cpx	735B_75R5_27	E	aj_39	390.338	core	Ol-gabbro	0.282	1.520	0.385	2.735	1.463	0.519	2.390	0.465	3.290	17.900	0.720	1.950	0.274	1.921	0.264
Cpx	735B_75R5_27	F	aj_40	390.335	core	Ol-gabbro	0.296	1.663	0.399	3.050	1.564	0.556	2.440	0.468	3.500	18.800	0.748	2.085	0.297	2.015	0.276
Cpx	735B_75R5_27	F	aj_42	390.335	core	Ol-gabbro	0.274	1.566	0.409	2.944	1.516	0.508	2.480	0.443	3.230	17.430	0.685	1.916	0.277	1.750	0.255
Cpx	735B_75R5_27	G	aj_43	390.347	core	Ol-gabbro	0.292	1.645	0.409	3.120	1.532	0.575	2.540	0.486	3.550	19.110	0.754	2.090	0.293	1.912	0.282
Cpx	735B_75R5_27	G	aj_44	390.347	core	Ol-gabbro	0.232	1.298	0.310	2.466	1.290	0.494	2.180	0.395	2.980	15.910	0.639	1.789	0.257	1.700	0.251
Cpx	735B_75R5_27	G	aj_45	390.347	core	Ol-gabbro	0.253	1.365	0.342	2.455	1.354	0.472	2.045	0.409	2.890	16.010	0.631	1.740	0.260	1.657	0.236
Cpx	735B_75R5_27	H	aj_48	390.341	core	Ol-gabbro	0.278	1.707	0.427	3.360	1.615	0.584	2.620	0.488	3.640	19.750	0.773	2.245	0.286	2.100	0.301
Cpx	735B_69R3_52B	A	al_27	344.152	core	Ol-gabbro	0.490	2.457	0.553	3.910	1.749	0.579	2.660	0.505	3.580	19.330	0.755	2.174	0.316	2.052	0.285
Cpx	735B_69R3_52B	A	al_28	344.152	core	Ol-gabbro	0.561	2.902	0.651	4.380	1.970	0.621	2.980	0.551	3.900	20.550	0.818	2.274	0.313	2.061	0.305
Cpx	735B_69R3_52B	B	al_31	344.153	core	Ol-gabbro	0.219	1.164	0.321	2.550	1.434	0.527	2.350	0.453	3.370	18.010	0.718	2.109	0.291	1.856	0.268
Cpx	735B_69R3_52B	B	al_32	344.153	core	Ol-gabbro	0.335	1.596	0.386	2.740	1.377	0.543	2.390	0.439	3.210	16.880	0.686	1.802	0.254	1.725	0.242
Cpx	735B_69R3_52B	B	al_33	344.153	core	Ol-gabbro	0.547	2.826	0.701	4.920	2.315	0.685	3.520	0.649	4.440	24.720	0.965	2.700	0.392	2.563	0.365
Cpx	735B_69R3_52B	D	al_34	344.164	core	Ol-gabbro	0.672	3.700	0.840	5.590	2.477	0.664	3.390	0.647	4.620	24.130	0.919	2.654	0.397	2.647	0.370
Cpx	735B_69R3_52B	D	al_36	344.164	core	Ol-gabbro	0.754	4.320	1.016	6.720	2.930	0.807	4.230	0.755	5.490	28.820	1.143	3.190	0.458	3.020	0.429
Cpx	735B_69R3_52B	EF	al_38	344.159	core	Ol-gabbro	0.293	1.440	0.358	2.670	1.330	0.500	2.200	0.408	2.970	15.840	0.625	1.774	0.254	1.676	0.236
Cpx	735B_69R3_52B	H	al_40	344.15	core	Ol-gabbro	0.260	1.366	0.327	2.360	1.145	0.436	1.860	0.362	2.630	13.960	0.537	1.489	0.212	1.492	0.215
Cpx	735B_69R3_52B	H	al_41	344.15	core	Ol-gabbro	0.637	3.330	0.789	5.360	2.280	0.671	3.420	0.613	4.410	22.840	0.900	2.600	0.368	2.309	0.337
Cpx	735B_68R2_10,5A	AB	pa_30	336.546	core	Ol-gabbro	0.467	2.832	0.636	4.280	1.959	0.637	3.130	0.563	4.090	22.340	0.864	2.600	0.390	2.670	0.370
Cpx	735B_68R2_10,5A	AB	pa_32	336.546	core	Ol-gabbro	0.327	1.692	0.426	2.830	1.383	0.518	2.267	0.412	2.940	15.760	0.640	1.748	0.257	1.798	0.261
Cpx	735B_68R2_10,5A	D	pa_35	336.534	core	Ol-gabbro	0.617	3.740	0.896	6.380	3.120	0.741	4.890	0.892	6.400	34.490	1.398	3.860	0.578	3.860	0.525
Cpx	735B_68R2_10,5A	E	pa_37	336.537	core	Ol-gabbro	0.306	1.683	0.398	2.900	1.366	0.501	2.155	0.398	2.910	14.940	0.601	1.646	0.240	1.613	0.226
Cpx	735B_68R2_10,5A	H	pa_40	336.615	core	Ol-gabbro	0.374	2.002	0.441	2.960	1.344	0.497	2.103	0.384	2.809	15.310	0.598	1.730	0.252	1.854	0.260
Cpx	735B_57R1_73	B	ac_22	275.738	rim	Ol-gabbro	0.654	3.730	0.922	6.490	3.080	0.923	4.950	0.899	6.520	33.720	1.401	3.750	0.545	3.640	0.503
Cpx	735B_57R1_73	D	ac_26	275.745	rim	Ol-gabbro	0.733	3.810	0.909	6.580	3.190	1.045	5.350	1.008	7.650	40.980	1.617	4.540	0.671	4.530	0.641
Cpx	735B_60R4_115B	A	ag_31	295.408	rim	Ol-gabbro	0.561	3.740	0.942	6.520	3.110	0.840	4.520	0.825	5.930	30.950	1.246	3.480	0.496	3.470	0.498
Cpx	735B_60R4_115B	E	ag_35	295.411	rim	Ol-gabbro	0.223	1.351	0.326	2.253	1.092	0.350	1.644	0.312	2.270	12.420	0.488	1.375	0.199	1.365	0.192
Cpx	735B_60R4_115B	G	ag_37	295.412	rim	Ol-gabbro	0.521	3.190	0.785	5.680	2.691	0.777	4.280	0.772	5.600	29.700	1.204	3.320	0.500	3.170	0.445
Cpx	735B_60R4_115B	G	ag_40	295.412	rim	Ol-gabbro	0.601	3.400	0.837	6.040	2.930	0.904	4.330	0.860	5.970	31.970	1.265	3.460	0.504	3.280	0.443
Cpx	735B_58R3_108A	A	ai_29	284.346	rim	Ol-gabbro	0.249	1.473	0.364	2.530	1.182	0.346	1.746	0.324	2.369	12.480	0.498	1.396	0.197	1.358	0.193
Cpx	735B_58R3_108A	A	ai_30	284.346	rim	Ol-gabbro	0.177	0.875	0.202	1.444	0.733	0.264	1.083	0.206	1.514	7.700	0.308	0.897	0.123	0.815	0.112

Mineral	Sample	Area	Point	Depth (mbsf)	Grain area	Lithology	La	Ce	Pr	Nd	Sm	Eu	Gd	Tb	Dy	Y	Ho	Er	Tm	Yb	Lu
Cpx	735B_58R3_108A	F	ai_32	284.345	rim	Ol-gabbro	0.272	1.524	0.380	2.750	1.361	0.391	2.117	0.395	2.830	15.090	0.594	1.676	0.240	1.554	0.227
Cpx	735B_58R3_108A	G	ai_35	284.348	rim	Ol-gabbro	0.298	1.655	0.397	2.950	1.352	0.412	2.123	0.397	2.866	15.090	0.594	1.640	0.248	1.480	0.218
Cpx	735B_75R5_27	B	aj_29	390.354	rim	Ol-gabbro	0.347	1.966	0.511	3.600	1.905	0.584	2.920	0.549	3.980	21.210	0.852	2.402	0.333	2.294	0.307
Cpx	735B_75R5_27	B	aj_30	390.354	rim	Ol-gabbro	0.393	2.136	0.52	3.83	1.827	0.59	2.73	0.527	3.76	20.18	0.812	2.233	0.32	2.147	0.293
Cpx	735B_75R5_27	C	aj_33	390.352	rim	Ol-gabbro	0.380	2.120	0.532	3.890	1.993	0.560	3.010	0.590	4.140	21.740	0.867	2.417	0.346	2.215	0.323
Cpx	735B_75R5_27	D	aj_36	390.342	rim	Ol-gabbro	0.256	1.631	0.434	3.350	1.734	0.547	2.920	0.538	3.950	21.050	0.848	2.340	0.330	2.109	0.316
Cpx	735B_75R5_27	E	aj_38	390.338	rim	Ol-gabbro	0.280	1.660	0.418	3.260	1.594	0.524	2.570	0.474	3.370	17.910	0.732	1.998	0.280	1.821	0.276
Cpx	735B_75R5_27	F	aj_41	390.335	rim	Ol-gabbro	0.317	1.924	0.503	3.720	1.823	0.610	2.950	0.549	4.080	21.720	0.866	2.442	0.349	2.161	0.318
Cpx	735B_75R5_27	H	aj_46	390.341	rim	Ol-gabbro	0.273	1.785	0.457	3.510	1.869	0.575	2.970	0.570	4.030	21.250	0.854	2.336	0.348	2.218	0.314
Cpx	735B_75R5_27	H	aj_47	390.341	rim	Ol-gabbro	0.270	1.599	0.414	3.070	1.462	0.550	2.370	0.465	3.470	18.550	0.721	2.036	0.289	1.808	0.276
Cpx	735B_69R3_52B	A	al_29	344.152	rim	Ol-gabbro	0.564	2.917	0.681	4.830	2.281	0.622	3.260	0.590	4.320	22.380	0.906	2.425	0.350	2.262	0.312
Cpx	735B_69R3_52B	B	al_30	344.153	rim	Ol-gabbro	0.598	3.230	0.752	5.200	2.381	0.715	3.620	0.672	4.900	27.430	1.074	3.120	0.459	3.070	0.433
Cpx	735B_69R3_52B	D	al_35	344.164	rim	Ol-gabbro	0.706	4.160	1.003	6.770	3.000	0.750	4.080	0.748	5.390	27.750	1.109	3.030	0.456	2.860	0.404
Cpx	735B_69R3_52B	EF	al_37	344.159	rim	Ol-gabbro	0.593	3.340	0.804	5.750	2.670	0.768	4.110	0.764	5.380	28.010	1.114	3.180	0.444	3.000	0.412
Cpx	735B_69R3_52B	H	al_39	344.15	rim	Ol-gabbro	0.466	2.425	0.553	3.890	1.890	0.558	2.830	0.524	3.970	21.260	0.816	2.416	0.347	2.206	0.343
Cpx	735B_68R2_10,5A	AB	pa_31	336.546	rim	Ol-gabbro	0.594	3.760	0.918	6.460	2.970	0.756	4.710	0.837	6.310	33.310	1.309	3.870	0.570	3.850	0.566
Cpx	735B_68R2_10,5A	AB	pa_33	336.546	rim	Ol-gabbro	0.523	3.200	0.777	5.450	2.459	0.667	3.940	0.708	5.100	27.390	1.079	3.240	0.484	3.250	0.482
Cpx	735B_68R2_10,5A	D	pa_34	336.534	rim	Ol-gabbro	0.700	4.710	1.260	8.700	4.170	0.833	6.330	1.085	8.070	41.620	1.678	4.680	0.679	4.610	0.634
Cpx	735B_68R2_10,5A	E	pa_36	336.537	rim	Ol-gabbro	0.591	3.930	0.932	6.580	2.900	0.763	4.400	0.802	5.720	30.450	1.225	3.420	0.493	3.230	0.465
Cpx	735B_68R2_10,5A	G	pa_38	336.547	rim	Ol-gabbro	1.319	8.170	1.957	13.310	6.290	1.671	8.980	1.649	12.030	65.040	2.547	6.990	1.050	6.990	1.018
Cpx	735B_68R2_10,5A	G	pa_39	336.547	rim	Ol-gabbro	0.520	3.280	0.786	5.700	2.574	0.644	3.790	0.703	4.890	26.180	1.034	2.990	0.421	2.780	0.407
Cpx	735B_79R4_20	A	ak_27	419.153	core	Ol-gabbro	0.285	1.485	0.366	2.629	1.324	0.491	2.025	0.389	2.880	15.260	0.599	1.650	0.236	1.575	0.221
Cpx	735B_79R4_20	B	ak_29	419.157	core	Ol-gabbro	0.346	1.830	0.394	2.800	1.233	0.368	2.041	0.395	2.950	15.850	0.591	1.792	0.247	1.697	0.237
Cpx	735B_79R4_20	C	ak_31	419.159	core	Ol-gabbro	0.200	1.114	0.287	2.111	1.147	0.400	1.822	0.334	2.464	12.670	0.505	1.416	0.195	1.304	0.183
Cpx	735B_79R4_20	D	ak_32	419.163	core	Ol-gabbro	0.433	1.710	0.345	2.505	1.174	0.403	1.866	0.364	2.750	14.980	0.584	1.701	0.252	1.681	0.240
Cpx	735B_79R4_20	E	ak_35	419.168	core	Ol-gabbro	0.175	1.007	0.268	2.173	1.209	0.454	2.046	0.388	2.820	14.700	0.612	1.653	0.240	1.499	0.204
Cpx	735B_79R4_20	FG	ak_38	419.173	core	Ol-gabbro	0.229	1.480	0.368	2.900	1.483	0.479	2.427	0.456	3.420	17.160	0.692	1.931	0.278	1.853	0.259
Cpx	735B_79R3_100	A	ob_18	418.507	core	Ol-gabbro	0.214	1.154	0.281	2.230	1.052	0.443	2.023	0.373	2.480	12.550	0.522	1.455	0.210	1.333	0.205
Cpx	735B_79R3_100	A	ob_20	418.507	core	Ol-gabbro	0.339	2.102	0.497	3.310	1.680	0.529	2.754	0.488	3.790	20.530	0.811	2.257	0.320	2.314	0.320
Cpx	735B_79R3_100	C	ob_21	418.514	core	Ol-gabbro	0.353	1.984	0.459	2.860	1.473	0.527	2.399	0.426	3.140	17.390	0.646	1.863	0.263	1.867	0.267
Cpx	735B_76R3_96	A	pb_34	397.563	core	Ol-gabbro	0.234	1.280	0.323	2.560	1.273	0.499	2.121	0.398	2.930	15.460	0.605	1.726	0.241	1.568	0.223
Cpx	735B_76R3_96	B	pb_36	397.571	core	Ol-gabbro	0.181	1.043	0.269	2.114	1.127	0.433	1.834	0.341	2.676	13.720	0.545	1.514	0.224	1.430	0.205
Cpx	735B_76R3_96	D	pb_37	397.576	core	Ol-gabbro	0.269	1.504	0.348	2.550	1.310	0.498	2.279	0.418	2.990	16.420	0.679	1.786	0.249	1.821	0.237
Cpx	735B_76R3_96	D	pb_38	397.576	core	Ol-gabbro	0.283	1.772	0.426	3.030	1.497	0.531	2.560	0.460	3.310	17.970	0.716	2.034	0.280	1.924	0.265
Cpx	735B_76R3_96	E	pb_42	397.585	core	Ol-gabbro	0.360	2.076	0.489	3.620	1.681	0.598	2.840	0.529	3.770	21.370	0.845	2.320	0.337	2.380	0.334
Cpx	735B_76R3_96	F	pb_43	397.587	core	Ol-gabbro	0.437	2.673	0.645	4.870	2.473	0.629	3.730	0.667	5.030	25.800	1.022	2.860	0.393	2.670	0.384
Cpx	735B_76R3_96	G	pb_45	397.582	core	Ol-gabbro	0.243	1.339	0.344	2.539	1.220	0.487	2.065	0.377	2.751	14.970	0.571	1.654	0.223	1.520	0.209
Cpx	735B_91R1_74	B	ad_1	518.167	core	Ol-gabbro	0.348	1.631	0.368	2.536	1.299	0.502	2.163	0.399	2.920	15.390	0.616	1.755	0.244	1.663	0.231
Cpx	735B_91R1_74	C	ad_3	518.164	core	Ol-gabbro	0.370	1.758	0.377	2.479	1.133	0.439	2.079	0.382	2.770	14.870	0.585	1.683	0.247	1.580	0.228

Mineral	Sample	Area	Point	Depth (mbsf)	Grain area	Lithology	La	Ce	Pr	Nd	Sm	Eu	Gd	Tb	Dy	Y	Ho	Er	Tm	Yb	Lu
Cpx	735B_91R1_74	D	ad_4	518.154	core	Ol-gabbro	0.670	4.190	1.020	7.100	3.050	0.536	4.470	0.814	5.750	30.340	1.196	3.410	0.488	3.210	0.474
Cpx	735B_91R1_74	E	ad_6	518.147	core	Ol-gabbro	0.345	1.578	0.355	2.445	1.243	0.480	2.030	0.381	2.736	14.760	0.578	1.644	0.233	1.504	0.225
Cpx	735B_91R1_74	F	ad_7	518.155	core	Ol-gabbro	0.523	2.473	0.495	3.260	1.374	0.483	2.183	0.407	2.970	16.300	0.622	1.814	0.260	1.896	0.251
Cpx	735B_91R1_74	G	ad_8	518.154	core	Ol-gabbro	0.439	2.002	0.401	2.432	1.047	0.400	1.643	0.314	2.302	12.680	0.495	1.433	0.204	1.456	0.197
Cpx	735B_83R7_43B	A	qb_39	461.706	core	Ol-gabbro	0.147	0.836	0.242	1.940	1.012	0.398	1.940	0.370	2.720	14.890	0.586	1.730	0.240	1.560	0.215
Cpx	735B_83R7_43B	C	qb_40	461.723	core	Ol-gabbro	0.317	2.2	0.62	4.68	2.62	0.479	4.2	0.797	6.08	32.1	1.289	3.63	0.517	3.41	0.501
Cpx	735B_83R7_43B	E	ra_1	461.716	core	Ol-gabbro	0.536	2.893	0.641	4.300	2.007	0.594	3.250	0.612	4.550	25.050	0.983	2.990	0.417	2.960	0.419
Cpx	735B_83R7_43B	F	ra_5	461.71	core	Ol-gabbro	0.139	0.762	0.182	1.546	0.804	0.319	1.362	0.257	1.899	9.780	0.386	1.110	0.139	1.050	0.142
Cpx	735B_83R7_43B	I	ra_7	461.712	core	Ol-gabbro	0.170	1.045	0.267	2.057	1.087	0.399	1.842	0.326	2.530	13.350	0.512	1.440	0.200	1.431	0.200
Cpx	81R5-7/11	A1	SMPABC	439.246	core	Ol-gabbro	0.168	1.136	0.282	2.078	1.137	0.474	1.859	0.367	2.570	13.980	0.546	1.632	0.214	1.444	0.212
Cpx	81R5-7/11	D	SMPABC	439.253	core	Ol-gabbro	0.378	2.379	0.523	3.310	1.585	0.473	2.269	0.424	2.910	16.260	0.625	1.793	0.247	1.683	0.245
Cpx	81R5-7/11	D	SMPABC	439.253	core	Ol-gabbro	0.277	1.500	0.328	2.156	1.119	0.434	1.831	0.345	2.424	13.480	0.546	1.506	0.216	1.511	0.216
Cpx	81R5-7/11	F	SMPABC	439.265	core	Ol-gabbro	0.188	1.275	0.306	2.245	1.230	0.501	2.040	0.376	2.690	14.270	0.593	1.660	0.224	1.488	0.211
Cpx	81R5-7/11	F	SMPABC	439.265	core	Ol-gabbro	0.349	1.995	0.440	2.870	1.429	0.543	2.185	0.427	2.960	15.290	0.615	1.776	0.253	1.652	0.239
Cpx	81R5-7/11	G	SMPABC	439.262	core	Ol-gabbro	0.435	2.499	0.542	3.400	1.595	0.574	2.530	0.497	3.360	18.690	0.752	2.157	0.288	2.070	0.290
Cpx	90R2-18/20	-20_a4	wa_20	509.49	core	Ol-gabbro	0.339	1.995	0.485	3.540	1.747	0.557	3.067	0.560	4.229	22.710	0.919	2.891	0.401	2.670	0.396
Cpx	90R2-18/20	-20_a3	wa_18	509.49	core	Ol-gabbro	0.568	4.020	1.080	7.850	4.170	0.700	7.122	1.309	9.344	49.820	2.068	6.020	0.833	5.461	0.751
Cpx	90R2-18/20	20_a2	wa_2	509.49	core	Ol-gabbro	0.409	2.620	0.641	4.230	2.180	0.508	3.683	0.723	5.487	29.420	1.182	3.465	0.485	3.270	0.460
Cpx	90R2-82/86	-86_a4	wa_50	510.1	core	Ol-gabbro	0.157	1.021	0.248	1.870	0.956	0.435	1.730	0.323	2.290	11.920	0.492	1.401	0.192	1.288	0.195
Cpx	90R2-82/86	86_a3	wa_41	510.1	core	Ol-gabbro	0.107	0.664	0.168	1.346	0.710	0.297	1.227	0.231	1.623	8.290	0.350	0.965	0.128	0.831	0.118
Cpx	90R2-82/86	-86_a2	wa_29	510.1	core	Ol-gabbro	0.465	3.100	0.749	5.150	2.480	0.579	4.214	0.792	5.662	30.220	1.227	3.682	0.528	3.170	0.472
Cpx	90R2-82/86	86_a2	wa_32	510.1	core	Ol-gabbro	0.339	2.390	0.587	4.220	2.052	0.495	3.577	0.675	4.682	24.840	1.033	3.086	0.414	2.730	0.382
Cpx	90R2-82/86	-86_a1	wa_25	510.1	core	Ol-gabbro	0.575	4.140	1.084	7.730	3.870	0.741	6.432	1.192	8.447	42.620	1.801	5.284	0.731	4.731	0.656
Cpx	90R2-82/86	86_a1	wa_26	510.1	core	Ol-gabbro	0.258	1.492	0.360	2.570	1.372	0.519	2.558	0.470	3.362	17.710	0.711	2.046	0.294	1.950	0.277
Cpx	90R2-84/90	-90_a1	wa_55	510.17	core	Ol-gabbro	0.225	1.530	0.360	2.630	1.357	0.518	2.324	0.431	3.032	15.320	0.631	1.848	0.249	1.610	0.235
Cpx	90R2-84/90	90_a2	wa_60	510.17	core	Ol-gabbro	0.273	1.011	0.217	1.613	0.872	0.358	1.528	0.273	1.918	10.010	0.404	1.200	0.159	0.997	0.148
Cpx	90R2-84/90	-90_a3	wb_2	510.17	core	Ol-gabbro	0.377	2.230	0.455	3.020	1.433	0.482	2.342	0.464	3.364	18.680	0.739	2.293	0.349	2.372	0.369
Cpx	90R2-94/100B	l00B_a	wb_9	510.27	core	Ol-gabbro	0.186	1.066	0.270	2.119	1.132	0.461	1.954	0.380	2.649	13.180	0.542	1.575	0.195	1.326	0.194
Cpx	90R2-94/100B	00B_a	wb_14	510.27	core	Ol-gabbro	0.276	1.829	0.470	3.440	1.762	0.484	3.123	0.594	4.107	21.140	0.892	2.591	0.353	2.310	0.333
Cpx	90R2-94/100B	l00B_a	wb_15	510.27	core	Ol-gabbro	0.172	1.090	0.286	2.126	1.159	0.491	2.208	0.393	2.737	13.700	0.583	1.584	0.224	1.412	0.202
Cpx	90R2-94/100B	00B_a	wb_23	510.27	core	Ol-gabbro	0.123	0.724	0.199	1.471	0.760	0.336	1.481	0.267	1.961	9.210	0.388	1.110	0.155	0.971	0.144
Cpx	90R2-123/129	-129_a	wb_28	510.56	core	Ol-gabbro	0.114	0.676	0.163	1.157	0.618	0.239	1.037	0.196	1.358	7.030	0.295	0.844	0.117	0.733	0.113
Cpx	90R2-123/129	129_a	wb_31	510.56	core	Ol-gabbro	0.208	1.186	0.290	2.075	1.014	0.445	1.781	0.318	2.432	12.090	0.513	1.502	0.200	1.311	0.186
Cpx	90R2-123/129	129_a	wb_38	510.56	core	Ol-gabbro	0.347	2.278	0.577	4.020	1.802	0.483	2.972	0.569	4.011	20.440	0.864	2.562	0.368	2.290	0.320
cpx	90R3-6/8	8_a4_	wb_48	510.84	core	Ol-gabbro	0.203	1.251	0.298	2.173	1.124	0.479	1.931	0.381	2.663	13.570	0.560	1.642	0.231	1.554	0.225
Cpx	735B_79R4_20	A	ak_26	419.153	rim	Ol-gabbro	0.306	1.718	0.402	2.810	1.292	0.363	2.031	0.402	2.930	15.760	0.607	1.732	0.257	1.712	0.256
Cpx	735B_79R4_20	B	ak_28	419.157	rim	Ol-gabbro	0.288	1.388	0.321	2.248	1.087	0.316	1.731	0.325	2.434	12.860	0.515	1.424	0.200	1.373	0.206
Cpx	735B_79R4_20	C	ak_30	419.159	rim	Ol-gabbro	0.305	1.622	0.362	2.675	1.265	0.361	1.973	0.367	2.720	14.070	0.559	1.584	0.215	1.534	0.205
Cpx	735B_79R4_20	D	ak_33	419.163	rim	Ol-gabbro	0.348	1.562	0.360	2.640	1.369	0.382	2.266	0.411	3.090	16.580	0.671	1.852	0.268	1.688	0.262

Mineral	Sample	Area	Point	Depth (mbsf)	Grain area	Lithology	La	Ce	Pr	Nd	Sm	Eu	Gd	Tb	Dy	Y	Ho	Er	Tm	Yb	Lu
Cpx	735B_79R4_20	E	ak_34	419.168	rim	Ol-gabbro	0.572	2.193	0.434	2.740	1.309	0.379	2.135	0.388	2.960	15.290	0.600	1.644	0.239	1.657	0.228
Cpx	735B_79R4_20	E	ak_36	419.168	rim	Ol-gabbro	0.406	1.638	0.359	2.610	1.323	0.418	2.252	0.422	3.090	16.740	0.654	1.813	0.270	1.689	0.245
Cpx	735B_79R4_20	FG	ak_37	419.173	rim	Ol-gabbro	0.204	1.205	0.322	2.446	1.321	0.397	2.046	0.379	2.830	14.170	0.575	1.587	0.229	1.465	0.208
Cpx	735B_79R3_100	A	ob_19	418.507	rim	Ol-gabbro	0.259	1.451	0.394	2.720	1.277	0.483	2.255	0.419	3.030	17.040	0.638	2.020	0.292	1.939	0.285
Cpx	735B_79R3_100	C	ob_22	418.514	rim	Ol-gabbro	0.319	1.906	0.443	3.060	1.582	0.424	2.355	0.407	3.180	16.070	0.646	1.742	0.245	1.635	0.232
Cpx	735B_76R3_96	A	pb_33	397.563	rim	Ol-gabbro	0.290	1.828	0.432	3.160	1.518	0.576	2.475	0.474	3.570	18.870	0.766	2.125	0.303	1.918	0.294
Cpx	735B_76R3_96	B	pb_35	397.571	rim	Ol-gabbro	0.339	1.849	0.437	3.230	1.676	0.567	2.690	0.506	3.720	18.910	0.794	2.138	0.292	1.991	0.295
Cpx	735B_76R3_96	D	pb_39	397.576	rim	Ol-gabbro	0.388	2.33	0.597	4.09	2.095	0.628	3.27	0.616	4.5	23.07	0.963	2.69	0.394	2.53	0.376
Cpx	735B_76R3_96	D	pb_40	397.576	rim	Ol-gabbro	0.272	1.425	0.357	2.711	1.253	0.523	2.370	0.444	3.070	15.630	0.633	1.825	0.257	1.714	0.244
Cpx	735B_76R3_96	E	pb_41	397.585	rim	Ol-gabbro	0.348	2.256	0.557	4.060	2.064	0.609	3.170	0.569	4.520	23.420	0.933	2.677	0.395	2.700	0.376
Cpx	735B_76R3_96	G	pb_44	397.582	rim	Ol-gabbro	0.371	2.283	0.585	4.200	1.946	0.684	3.360	0.569	4.380	23.440	0.940	2.617	0.358	2.340	0.343
Cpx	735B_91R1_74	B	ad_2	518.167	rim	Ol-gabbro	0.823	5.090	1.233	8.380	3.480	0.677	5.200	0.930	6.520	35.420	1.426	3.900	0.583	3.830	0.540
Cpx	735B_91R1_74	E	ad_5	518.147	rim	Ol-gabbro	0.625	3.760	0.915	6.280	2.723	0.589	4.090	0.738	5.320	28.210	1.113	3.170	0.446	2.838	0.415
Cpx	735B_91R1_74	G	ad_9	518.154	rim	Ol-gabbro	0.745	4.280	0.959	6.120	2.394	0.580	3.540	0.631	4.600	24.760	0.971	2.750	0.398	2.491	0.384
Cpx	735B_83R7_43B	A	qb_38	461.706	rim	Ol-gabbro	0.234	1.550	0.417	3.200	1.630	0.382	2.690	0.485	3.600	18.530	0.769	2.120	0.302	1.890	0.290
Cpx	735B_83R7_43B	C	qb_41	461.723	rim	Ol-gabbro	0.329	2.340	0.666	4.950	2.700	0.544	4.810	0.883	6.360	34.090	1.400	3.870	0.547	3.500	0.507
Cpx	735B_83R7_43B	E	ra_2	461.716	rim	Ol-gabbro	0.467	3.150	0.763	5.600	2.890	0.481	4.610	0.875	6.420	34.560	1.395	3.970	0.551	3.680	0.495
Cpx	735B_83R7_43B	F	ra_3	461.71	rim	Ol-gabbro	0.285	1.850	0.486	3.520	1.754	0.511	3.040	0.548	3.960	21.730	0.870	2.470	0.343	2.356	0.324
Cpx	735B_83R7_43B	F	ra_4	461.71	rim	Ol-gabbro	0.222	1.542	0.421	3.120	1.583	0.439	2.710	0.490	3.490	19.020	0.762	2.106	0.303	1.919	0.274
Cpx	735B_83R7_43B	I	ra_6	461.712	rim	Ol-gabbro	0.201	1.300	0.311	2.270	1.148	0.443	1.887	0.364	2.640	14.810	0.568	1.699	0.221	1.606	0.230
Cpx	81R5-7/11	A1	SMPABC	439.246	rim	Ol-gabbro	0.259	1.609	0.386	2.735	1.412	0.504	2.266	0.433	3.000	16.810	0.653	1.894	0.266	1.773	0.254
Cpx	81R5-7/11	F	SMPABC	439.265	rim	Ol-gabbro	0.493	3.340	0.766	5.140	2.392	0.554	3.610	0.651	4.410	23.380	0.950	2.720	0.360	2.430	0.349
Cpx	90R2-18/20	-20_a4	wa_19	509.49	rim	Ol-gabbro	0.437	3.100	0.826	6.280	3.380	0.573	5.933	1.086	7.549	38.140	1.570	4.634	0.610	3.851	0.530
Cpx	90R2-18/20	20_a3_	wa_16	509.49	rim	Ol-gabbro	0.619	4.450	1.176	8.590	4.460	0.698	7.621	1.428	10.066	52.730	2.114	6.313	0.849	5.491	0.746
Cpx	90R2-18/20	20_a3_	wa_17	509.49	rim	Ol-gabbro	0.520	3.770	1.053	7.700	4.050	0.591	6.963	1.301	9.313	48.180	2.018	5.923	0.790	5.051	0.705
Cpx	90R2-18/20	20_a2_	wa_3	509.49	rim	Ol-gabbro	0.489	3.210	0.805	5.720	2.750	0.602	4.638	0.915	6.436	35.010	1.446	4.277	0.582	3.871	0.561
Cpx	90R2-82/86	-86_a4	wa_49	510.1	rim	Ol-gabbro	0.191	1.311	0.327	2.430	1.273	0.421	2.208	0.397	2.826	14.040	0.582	1.684	0.221	1.444	0.209
Cpx	90R2-82/86	-86_a3	wa_39	510.1	rim	Ol-gabbro	0.237	1.581	0.397	2.860	1.446	0.431	2.590	0.483	3.434	17.810	0.738	2.137	0.289	1.870	0.267
Cpx	90R2-82/86	-86_a3	wa_40	510.1	rim	Ol-gabbro	0.292	1.840	0.462	3.310	1.732	0.498	3.142	0.565	3.981	21.240	0.889	2.685	0.374	2.420	0.343
Cpx	90R2-82/86	-86_a2	wa_28	510.1	rim	Ol-gabbro	0.419	2.710	0.709	4.920	2.530	0.596	4.171	0.772	5.446	29.130	1.200	3.671	0.507	3.200	0.464
Cpx	90R2-82/86	86_a1_	wa_27	510.1	rim	Ol-gabbro	0.549	3.900	0.973	7.150	3.580	0.768	6.336	1.140	7.838	41.190	1.663	4.840	0.648	4.291	0.604
Cpx	90R2-84/90	-90_a1	wa_56	510.17	rim	Ol-gabbro	0.273	1.820	0.481	3.650	1.794	0.532	3.057	0.575	3.806	19.310	0.814	2.393	0.334	2.020	0.293
Cpx	90R2-84/90	90_a2_	wa_59	510.17	rim	Ol-gabbro	0.270	1.680	0.428	3.040	1.577	0.472	2.781	0.508	3.486	17.850	0.793	2.166	0.294	1.900	0.266
Cpx	90R2-84/90	-90_a3	wb_1b	510.17	edge	Ol-gabbro	0.452	2.812	0.680	4.740	2.193	0.533	3.683	0.688	4.902	25.200	1.052	3.085	0.441	2.867	0.413
Cpx	90R2-94/100B	l00B_a	wb_8	510.27	rim	Ol-gabbro	0.246	1.547	0.384	2.940	1.620	0.518	2.905	0.533	3.841	19.840	0.835	2.419	0.343	2.259	0.333
Cpx	90R2-94/100B	l00B_a	wb_17	510.27	rim	Ol-gabbro	0.232	1.317	0.327	2.310	1.210	0.508	2.352	0.430	3.152	16.320	0.699	2.035	0.276	1.875	0.267
Cpx	90R2-94/100B	l00B_a	wb_22	510.27	rim	Ol-gabbro	0.226	1.364	0.327	2.426	1.192	0.433	2.065	0.420	2.950	14.550	0.610	1.808	0.251	1.562	0.226
Cpx	90R2-94/100B	00B_a	wb_24	510.27	rim	Ol-gabbro	0.222	1.481	0.383	2.780	1.402	0.477	2.399	0.451	3.152	15.780	0.677	1.927	0.253	1.627	0.245
Cpx	90R2-123/129	-129_a	wb_27	510.56	rim	Ol-gabbro	0.382	2.717	0.684	4.920	2.179	0.504	3.521	0.631	4.382	22.090	0.921	2.736	0.382	2.382	0.359

Mineral	Sample	Area	Point	Depth (mbsf)	Grain area	Lithology	La	Ce	Pr	Nd	Sm	Eu	Gd	Tb	Dy	Y	Ho	Er	Tm	Yb	Lu
Cpx	90R2-123/129	129_a	wb_32	510.56	rim	Ol-gabbro	0.259	1.742	0.416	2.980	1.521	0.539	2.584	0.466	3.385	16.420	0.694	2.091	0.287	1.799	0.261
Cpx	90R2-123/129	129_a	wb_37	510.56	rim	Ol-gabbro	0.386	2.627	0.654	4.530	2.123	0.541	3.381	0.657	4.605	23.150	0.977	2.899	0.380	2.553	0.356
cpx	90R3-6/8	-8_a3_	wb_43	510.84	rim	Ol-gabbro	0.291	2.158	0.555	4.160	2.123	0.570	3.650	0.689	4.881	23.960	1.043	3.128	0.406	2.607	0.387
cpx	90R3-6/8	-8_a3_	wb_44	510.84	rim	Ol-gabbro	0.275	1.829	0.468	3.300	1.642	0.532	2.983	0.548	3.863	19.700	0.828	2.474	0.338	2.184	0.325
cpx	90R3-6/8	-8_a4_	wb_47	510.84	rim	Ol-gabbro	0.193	1.280	0.304	2.320	1.162	0.421	2.042	0.383	2.589	13.020	0.556	1.550	0.212	1.468	0.212
Cpx	735B_83R7_113A	A	af_2	462.399	core	Ol-rich gabbro	0.320	1.952	0.466	3.460	1.748	0.571	2.650	0.527	3.860	21.140	0.842	2.386	0.331	2.243	0.327
Cpx	735B_83R7_113A	B	af_3	462.388	core	Ol-rich gabbro	0.209	1.080	0.264	2.006	1.066	0.428	1.726	0.345	2.582	13.900	0.536	1.501	0.212	1.468	0.204
Cpx	735B_83R7_113A	B	af_5	462.388	core	Ol-rich gabbro	0.217	1.233	0.338	2.521	1.347	0.469	2.148	0.420	3.170	16.780	0.673	1.927	0.268	1.682	0.250
Cpx	735B_83R7_113	CD	af_6	462.385	core	Ol-rich gabbro	0.362	2.242	0.548	4	1.997	0.625	3.02	0.578	4.23	22.52	0.913	2.575	0.368	2.47	0.342
Cpx	735B_83R7_113A	CD	af_8	462.385	core	Ol-rich gabbro	0.268	1.514	0.354	2.625	1.405	0.525	2.165	0.434	3.230	16.820	0.680	1.950	0.260	1.953	0.278
Cpx	735B_83R7_113A	EG	af_9	462.393	core	Ol-rich gabbro	0.157	0.891	0.229	1.874	1.099	0.439	1.765	0.370	2.689	14.360	0.571	1.540	0.238	1.428	0.217
Cpx	735B_83R7_113A	EG	af_11	462.393	core	Ol-rich gabbro	0.398	2.367	0.632	4.710	2.570	0.705	3.940	0.751	5.470	28.020	1.123	3.090	0.434	2.940	0.400
Cpx	735B_83R7_113A	EG	af_12	462.393	core	Ol-rich gabbro	0.238	1.327	0.329	2.470	1.357	0.498	2.243	0.438	3.290	17.840	0.694	1.992	0.282	1.902	0.278
Cpx	735B_83R7_113A	EG	af_14	462.393	core	Ol-rich gabbro	0.324	1.983	0.515	3.840	2.000	0.645	3.130	0.616	4.780	25.710	0.977	2.940	0.402	2.840	0.429
Cpx	735B_83R7_0	A	oc_33	461.254	core	Ol-rich gabbro	0.325	2.434	0.637	4.270	1.985	0.368	3.070	0.532	3.830	20.470	0.831	2.404	0.360	2.514	0.332
Cpx	735B_83R7_0	BC	oc_36	461.268	core	Ol-rich gabbro	0.356	1.891	0.393	2.742	1.366	0.502	2.223	0.419	3.180	16.620	0.664	1.860	0.278	1.903	0.268
Cpx	735B_83R7_113A	A	af_1	462.399	rim	Ol-rich gabbro	0.388	2.351	0.581	4.210	2.171	0.615	2.960	0.572	4.450	23.720	0.912	2.648	0.379	2.720	0.376
Cpx	735B_83R7_113A	B	af_4	462.388	rim	Ol-rich gabbro	0.367	2.210	0.564	4.140	2.006	0.598	3.150	0.624	4.800	26.170	1.029	2.970	0.452	2.910	0.425
Cpx	735B_83R7_113A	CD	af_7	462.385	rim	Ol-rich gabbro	0.332	2.114	0.524	3.760	1.938	0.565	2.860	0.553	4.190	22.470	0.891	2.602	0.369	2.560	0.366
Cpx	735B_83R7_113A	EG	af_10	462.393	rim	Ol-rich gabbro	0.256	1.577	0.387	2.855	1.509	0.533	2.490	0.486	3.670	19.800	0.775	2.210	0.325	2.227	0.300
Cpx	735B_83R7_113A	EG	af_13	462.393	rim	Ol-rich gabbro	0.309	1.821	0.475	3.550	1.944	0.606	2.950	0.593	4.270	23.890	0.984	2.690	0.390	2.590	0.368
Cpx	735B_83R7_0	BC	oc_34	461.268	rim	Ol-rich gabbro	0.346	2.125	0.474	3.390	1.690	0.437	2.657	0.521	3.910	21.330	0.857	2.488	0.362	2.527	0.359
Cpx	735B_83R7_0	BC	oc_35	461.268	rim	Ol-rich gabbro	0.447	2.642	0.608	4.100	1.902	0.504	2.896	0.538	4.030	22.850	0.894	2.532	0.394	2.643	0.381
Cpx	735B_83R7_0	E	oc_37	461.265	rim	Ol-rich gabbro	0.354	2.228	0.574	4.030	1.801	0.558	2.970	0.515	3.780	20.890	0.844	2.295	0.340	2.192	0.339
Cpx	735B_83R7_0	E	oc_38	461.265	rim	Ol-rich gabbro	0.290	1.728	0.426	3.010	1.477	0.462	2.226	0.424	3.110	16.540	0.645	1.845	0.277	1.857	0.264
Cpx	735B_89R1_47	A	ah_27	505.274	core	Troctolite	1.056	6.160	1.345	8.960	4.180	0.621	6.360	1.167	8.580	45.700	1.813	5.320	0.750	4.920	0.690
Cpx	735B_80R2_7,5A	B	qa_37	425.56	core	Troctolite	0.370	2.775	0.775	5.800	3.170	0.358	5.180	0.937	6.930	37.170	1.534	4.310	0.614	4.100	0.606
Cpx	735B_80R2_7,5A	C	qa_39	425.553	core	Troctolite	0.448	2.892	0.729	5.440	2.720	0.538	4.510	0.848	6.290	34.310	1.381	3.990	0.575	3.780	0.511
Cpx	735B_89R1_47	A	ah_26	505.274	rim	Troctolite	1.407	8.780	2.068	12.990	5.590	0.568	7.910	1.478	10.700	56.820	2.310	6.500	0.900	6.180	0.814
Cpx	735B_80R2_7,5A	B	qa_38	425.56	rim	Troctolite	0.434	3.350	0.955	7.150	3.800	0.392	6.190	1.134	8.430	44.160	1.831	5.180	0.700	4.690	0.649
BIR	Average (N = 81)						0.58	1.87	0.35	2.25	1.01	0.49	1.59	0.31	2.31	12.89	0.51	1.48	0.22	1.54	0.23
	2SD						0.11	0.27	0.04	0.28	0.11	0.06	0.26	0.05	0.30	2.04	0.08	0.25	0.04	0.24	0.04
Preferred values ("Georem" Jochum et al., 2007)							0.61	1.89	0.37	2.37	1.09	0.52	1.85	0.35	2.55	14.30	0.56	1.70	0.24	1.64	0.25

Appendix 2.3

A/ MELTs parameters - Primitive MORB crystallization

Starting composition - Primitive MORB AB (after Coogan et al., 2004)

SiO2	Al2O3	TiO2	Fe2O3t	MgO	MnO	CaO	Na2O	K2O	P2O5*	Cr2O3	total
47.860	16.300	1.330	10.560	9.840	0.200	10.860	2.770	0.100	0.100	0.050	100

* from Godard et al., 2009

Conditions

P (bar)	Start T (°C)	Stop T (°C)	Inc. T (°C)	H2O (wt%)	deltaQFM	Liquidus (°C)	Mode
2000	1300	900	5	0.2	0	1257.62	Fractional

B/ MELTs parameters - Hybrid melt crystallization

Starting composition - Hybride melt (assimilation troctolitic matrix - crystallization clinopyroxene)

SiO2	Al2O3	TiO2	FeO	MgO	MnO	CaO	Na2O	K2O	total
45.680	15.630	0.970	11.890	15.750	0.210	7.280	2.490	0.080	100

Conditions

P (bar)	Start T (°C)	Stop T (°C)	Inc. T (°C)	H2O (wt%)	deltaQFM	Mode
2000	1300	900	5	0.2	0	Fractional

C/ Normalization values - Rare Earth Elements

La	Ce	Pr	Nd	Sm	Eu	Gd	Tb	Dy	Ho	Er	Tm	Yb	Lu
Av. primitive MORBs - Atlantis Bank (from Coogan et al., 2004)													
2.759	8.107	1.586	8.431	2.876	1.082	3.269	0.663	4.262	0.941	2.780	0.457	2.651	0.408
CI (McDonough & Sun, 1995)													
0.237	0.613	0.093	0.457	0.148	0.056	0.199	0.036	0.246	0.055	0.160	0.025	0.161	0.025

Appendix 2.4

AFC modeling - Lower unit N°1														
Percoalting liquid composition	La	Ce	Pr	Nd	Sm	Eu	Gd	Tb	Dy	Ho	Er	Tm	Yb	Lu
Av. primitive MORB (from Coogan et al., 2004)	2.759	8.312	1.346	7.076	2.436	0.933	3.322	0.613	4.208	0.917	2.702	0.421	2.716	0.408
Mush composition	La	Ce	Pr	Nd	Sm	Eu	Gd	Tb	Dy	Ho	Er	Tm	Yb	Lu
Equivalent prim. - Troctolitic	0.113	0.318	0.046	0.212	0.052	0.226	0.050	0.008	0.045	0.009	0.026	0.004	0.029	0.005
Partition coefficients	La	Ce	Pr	Nd	Sm	Eu	Gd	Tb	Dy	Ho	Er	Tm	Yb	Lu
Pl	0.055	0.052	0.046	0.040	0.028	0.378	0.019	0.015	0.012	0.009	0.007	0.006	0.005	0.004
Cpx	0.111	0.167	0.236	0.314	0.452	0.502	0.539	0.561	0.566	0.556	0.536	0.509	0.479	0.448
Ol	0.000	0.000	0.000	0.000	0.000	0.000	0.001	0.001	0.003	0.004	0.006	0.009	0.013	0.016
Crystallization steps														
F (%)	0.0	0.2	0.4	0.6	0.7	0.8	0.8	0.9	0.9	1.0				
Ratio Assimilated / Fractionated)														
r	0.9	1.0	1.0	1.0	1.0									
Mineral proportions	Ol	Pl	Cpx											
% Assimilated	45	55	0											
% Crystallized	0	100	0											
AFC modeling - Lower unit N°2														
Percoalting liquid composition	La	Ce	Pr	Nd	Sm	Eu	Gd	Tb	Dy	Ho	Er	Tm	Yb	Lu
Av. Pl equilibrium melt composition	2.954	9.475	1.546	9.194	3.808	0.907	4.700	0.870	5.618	1.252	3.618	0.590	3.315	0.428
Mush composition	La	Ce	Pr	Nd	Sm	Eu	Gd	Tb	Dy	Ho	Er	Tm	Yb	Lu
Equivalent prim. - Troctolitic	0.113	0.318	0.046	0.212	0.052	0.226	0.050	0.008	0.045	0.009	0.026	0.004	0.029	0.005
Partition coefficients	La	Ce	Pr	Nd	Sm	Eu	Gd	Tb	Dy	Ho	Er	Tm	Yb	Lu
Pl	0.055	0.052	0.046	0.040	0.028	0.378	0.019	0.015	0.012	0.009	0.007	0.006	0.005	0.004
Cpx	0.111	0.167	0.236	0.314	0.452	0.502	0.539	0.561	0.566	0.556	0.536	0.509	0.479	0.448
Ol	0.000	0.000	0.000	0.000	0.000	0.000	0.001	0.001	0.003	0.004	0.006	0.009	0.013	0.016
Crystallization steps														
F (%)	0.0	0.2	0.4	0.6	0.7	0.8	0.8	0.9	0.9	1.0				
Ratio Assimilated / Fractionated)														
r	0.5	0.7	0.8	0.9	1.0									
Mineral proportions	Ol	Pl	Cpx											
% Assimilated	45	55	0											
% Crystallized	5	50	45											

AFC modeling - Upper unit N°1														
Percoalting liquid composition	La	Ce	Pr	Nd	Sm	Eu	Gd	Tb	Dy	Ho	Er	Tm	Yb	Lu
Av. Pl equilibrium melt composition	1.989	5.604	0.885	5.309	1.688	1.298	2.343	0.426	2.810	0.654	1.479	0.255	2.154	0.165
Mush composition	La	Ce	Pr	Nd	Sm	Eu	Gd	Tb	Dy	Ho	Er	Tm	Yb	Lu
Equivalent prim. - Troctolitic	0.109	0.268	0.037	0.174	0.034	0.199	0.027	0.003	0.003	0.003	0.006	0.001	0.011	0.004
Partition coefficients	La	Ce	Pr	Nd	Sm	Eu	Gd	Tb	Dy	Ho	Er	Tm	Yb	Lu
Pl	0.089	0.083	0.074	0.064	0.045	0.378	0.030	0.024	0.019	0.014	0.011	0.009	0.007	0.006
Cpx	0.105	0.162	0.232	0.314	0.461	0.515	0.557	0.583	0.591	0.583	0.563	0.536	0.505	0.474
Ol	0.000	0.000	0.000	0.000	0.000	0.000	0.001	0.001	0.003	0.004	0.007	0.010	0.013	0.017
Crystallization steps														
F (%)	0.0	0.2	0.4	0.6	0.7	0.8	0.8	0.9	0.9	1.0				
Ratio Assimilated / Fractionated)														
r	0.6	0.7	0.8	0.9	1.0									
Mineral proportions	Ol	Pl	Cpx											
% Assimilated	45	55	0											
% Crystallized	0	55	45											

AFC modeling - Upper unit N°2														
Percoalting liquid composition	La	Ce	Pr	Nd	Sm	Eu	Gd	Tb	Dy	Ho	Er	Tm	Yb	Lu
Reactive melt - Lower	6.856	19.241	2.878	13.864	4.118	0.929	5.223	0.967	6.890	1.612	5.230	0.913	6.682	1.141
Mush composition	La	Ce	Pr	Nd	Sm	Eu	Gd	Tb	Dy	Ho	Er	Tm	Yb	Lu
Equivalent prim. - Troctolitic	0.109	0.268	0.037	0.174	0.034	0.199	0.027	0.003	0.003	0.003	0.006	0.001	0.011	0.004
Partition coefficients	La	Ce	Pr	Nd	Sm	Eu	Gd	Tb	Dy	Ho	Er	Tm	Yb	Lu
Pl	0.089	0.083	0.074	0.064	0.045	0.378	0.030	0.024	0.019	0.014	0.011	0.009	0.007	0.006
Cpx	0.105	0.162	0.232	0.314	0.461	0.515	0.557	0.583	0.591	0.583	0.563	0.536	0.505	0.474
Ol	0.000	0.000	0.000	0.000	0.000	0.000	0.001	0.001	0.003	0.004	0.007	0.010	0.013	0.017
Crystallization steps														
F (%)	0.0	0.2	0.4	0.6	0.7	0.8	0.8	0.9	0.9	1.0				
Ratio Assimilated / Fractionated)														
r	0.7	0.8	0.9	0.9	0.9									
Mineral proportions	Ol	Pl	Cpx											
% Assimilated	45	55	0											
% Crystallized	0	55	45											

Appendix 3

Implications for magma evolution at slow-spreading ridges (CHAPTER 5)

- **Appendix 3.1**: minerals *in situ* analyses for major elements of olivine (7p), plagioclase (17p) and clinopyroxene (12p), from IODP Hole U1473A (372 - 740.6 mbsf).
  36 PAGES

- **Appendix 3.2**: minerals *in situ* analyses for Rare Earth Elements of plagioclase (4p) and clinopyroxene (4p), from IODP Hole U1473A (372 - 740.6 mbsf).
  8 PAGES

- **Appendix 3.3**: Figure describing the textural characteristics of the finer "F" and coarser "G" grains for plagioclases analyzed in the lower ~400m of IODP Hole U1473A.
  1 PAGE

- **Appendix 3.4**: Figure representing minerals *in situ* major element contents in An (pl), Mg# (cpx) and Cr_2O_3 (wt% - cpx) with depth of IODP Hole U1309A (data from Miller et al., 2009).
  1 PAGE

Appendix 3.1

In situ majot elements concentrations in wt% analyzed by EPMA on a Cameca SX at LMV (Clermont-Ferrand, France)

Mineral	Sample	Point	Depth (mbsf)	Grain size	Grain area	SiO2	Al2O3	TiO2	CaO	Na2O	MnO	MgO	FeO	Cr2O3	NiO	Total
2 sigma						0.453	0.045	0.035	0.124	0.056	0.068	0.391	0.401	0.074	0.047	
Pl	Counting time (s) - per element					10	10	10	10	10	10	10	10	20	20	
Ol	360_60R1_26_D	18 / 1 .	538.8185	G	rim	37.73	0.03	0.00	0.02		0.42	36.07	25.90	0.00	0.08	100.2
Ol	360_60R1_26_G	19 / 1 .	538.8215	G	core	37.77	0.01	0.03	0.04		0.44	35.90	26.23	0.00	0.07	100.5
Ol	360_60R1_26_G	19 / 2 .	538.8215	F	core	37.84	0.00	0.00	0.03		0.42	36.25	26.12	0.01	0.04	100.7
Ol	360_60R1_26_G	19 / 3 .	538.8215	G	rim	37.82	0.00	0.00	0.03		0.35	36.32	26.13	0.00	0.12	100.8
Ol	360_60R1_26_E	22 / 1 .	538.8285	G	core	37.72	0.00	0.00	0.10		0.34	36.43	25.41	0.00	0.10	100.1
Ol	360_60R1_26_E	22 / 2 .	538.8285	G	rim	37.70	0.02	0.05	0.09		0.36	36.22	25.63	0.03	0.06	100.1
Ol	360_62R4_62_B	3 / 1 .	561.879	G	core	37.37	0.00	0.00	0.09		0.45	32.96	29.45	0.00	0.00	100.3
Ol	360_62R4_62_C	7 / 1 .	561.8765	F	core	37.23	0.00	0.03	0.07		0.46	33.26	29.33	0.00	0.08	100.5
Ol	360_64R5_39_A	4 / 2 .	579.658	G	rim	37.58	0.01	0.00	0.03		0.40	36.80	24.95	0.00	0.04	99.8
Ol	360_64R5_39_A	4 / 3 .	579.658	G	core	38.17	0.00	0.00	0.05		0.38	37.00	24.69	0.03	0.11	100.4
Ol	360_64R5_39_A	4 / 4 .	579.658	G	rim	37.82	0.01	0.00	0.04		0.36	37.07	24.54	0.00	0.07	99.9
Ol	360_64R5_39_C	9 / 1 .	579.654	G	core	37.49	0.03	0.00	0.05		0.37	36.89	24.52	0.00	0.09	99.4
Ol	360_64R5_39_C	9 / 2 .	579.654	G	rim	37.83	0.00	0.00	0.02		0.38	36.87	24.77	0.00	0.05	99.9
Ol	360_64R5_39_D	12 / 1 .	579.6645	G	core	38.01	0.00	0.01	0.03		0.31	37.18	24.40	0.01	0.09	100.0
Ol	360_64R5_39_D	12 / 2 .	579.6645	G	rim	37.93	0.00	0.01	0.00		0.38	37.08	24.86	0.02	0.05	100.3
Ol	360_64R5_39_D	12 / 3 .	579.6645	G	core	37.97	0.01	0.02	0.06		0.41	36.84	24.41	0.00	0.10	99.8
Ol	360_64R5_39_D	12 / 4 .	579.6645	G	core	37.95	0.01	0.00	0.06		0.33	37.19	24.52	0.00	0.09	100.2
Ol	360_64R5_39_D	12 / 5 .	579.6645	G	rim	38.19	0.00	0.02	0.01		0.42	37.47	24.62	0.01	0.05	100.8
Ol	360_64R5_39_E	5 / 1 .	579.6725	G	rim	37.81	0.02	0.01	0.01		0.39	36.78	24.41	0.02	0.05	99.5
Ol	360_64R5_39_E	5 / 2 .	579.6725	G	core	38.32	0.03	0.00	0.08		0.41	37.00	24.50	0.05	0.06	100.5
Ol	360_64R5_39_E	5 / 3 .	579.6725	G	rim	38.02	0.00	0.00	0.01		0.31	36.98	24.27	0.04	0.07	99.7
Ol	360_64R5_39_F	6 / 1 .	579.674	G	rim	37.83	0.00	0.06	0.03		0.42	37.03	24.92	0.05	0.09	100.4
Ol	360_64R5_39_F	6 / 2 .	579.674	G	core	37.71	0.03	0.00	0.08		0.38	37.11	24.75	0.02	0.06	100.2
Ol	360_64R5_39_F	6 / 3 .	579.674	G	rim	37.81	0.00	0.00	0.03		0.38	37.12	24.87	0.04	0.08	100.3
Ol	360_67R1_91a_B	5 / 1 .	604.5375	G	rim	38.42	0.00	0.00	0.02		0.35	38.69	22.34	0.02	0.04	99.9
Ol	360_67R1_91a_B	5 / 2 .	604.5375	G	rim	38.35	0.01	0.01	0.05		0.30	39.07	22.04	0.00	0.07	99.9
Ol	360_67R1_91a_B	5 / 3 .	604.5375	G	core	38.23	0.00	0.00	0.08		0.31	38.78	22.45	0.00	0.07	99.9
Ol	360_67R1_91a_C	8 / 1 .	604.5425	G	rim	38.13	0.00	0.02	0.02		0.33	39.36	22.02	0.03	0.10	100.0
Ol	360_67R1_91a_C	8 / 2 .	604.5425	G	rim	38.38	0.01	0.00	0.03		0.26	38.71	22.25	0.04	0.01	99.7
Ol	360_67R1_91a_C	8 / 3 .	604.5425	G	core	38.27	0.04	0.02	0.00		0.28	39.01	21.92	0.00	0.11	99.6
Ol	360_67R1_91a_E	15 / 1 .	604.5485	G	rim	38.16	0.00	0.00	0.02		0.34	39.16	21.91	0.00	0.09	99.7
Ol	360_67R1_91a_E	15 / 2 .	604.5485	G	core	38.37	0.00	0.01	0.04		0.30	39.21	22.04	0.02	0.10	100.1
Ol	360_67R1_91a_E	15 / 3 .	604.5485	G	rim	38.61	0.02	0.00	0.03		0.32	39.42	21.98	0.02	0.10	100.5
Ol	360_67R1_91a_E	15 / 4 .	604.5485	G	core	38.13	0.00	0.06	0.08		0.35	39.27	21.91	0.01	0.09	99.9
Ol	360_67R1_91a_E	15 / 5 .	604.5485	G	rim	38.29	0.01	0.00	0.05		0.31	39.20	21.79	0.00	0.09	99.7
Ol	360_70R7_58a_A	3 / 1 .	642.2885	F	core	38.58	0.00	0.04	0.03		0.37	38.50	22.37	0.00	0.08	100.0

Mineral	Sample	Point	Depth (mbsf)	Grain size	Grain area	SiO2	Al2O3	TiO2	CaO	Na2O	MnO	MgO	FeO	Cr2O3	NiO	Total
Ol	360_70R7_58a_A	3 / 2 .	642.2885	G	core	38.35	0.00	0.00	0.03		0.35	38.67	22.60	0.00	0.09	100.1
Ol	360_70R7_58a_A	3 / 3 .	642.2885	G	rim	38.07	0.02	0.00	0.02		0.40	38.87	22.18	0.02	0.09	99.7
Ol	360_70R7_58a_A	3 / 4 .	642.2885	F	core	38.30	0.01	0.01	0.08		0.37	37.95	23.11	0.00	0.12	99.9
Ol	360_70R7_58a_A	3 / 5 .	642.2885	G	core	38.10	0.02	0.08	0.04		0.34	38.68	22.67	0.04	0.11	100.1
Ol	360_70R7_58a_A	3 / 6 .	642.2885	G	rim	38.41	0.00	0.03	0.02		0.28	38.66	23.03	0.01	0.10	100.5
Ol	360_70R7_58a_C	9 / 1 .	642.288	G	core	38.10	0.00	0.03	0.02		0.31	38.42	22.97	0.00	0.11	100.0
Ol	360_70R7_58a_C	9 / 2 .	642.288	G	rim	38.02	0.00	0.00	0.03		0.33	38.39	22.37	0.00	0.09	99.2
Ol	360_70R7_58a_C	9 / 3 .	642.288	F	core	38.04	0.02	0.00	0.05		0.38	38.33	22.72	0.00	0.06	99.6
Ol	360_70R7_58a_E	14 / 1 .	642.2975	G	core	37.98	0.00	0.01	0.05		0.35	38.41	22.83	0.02	0.04	99.7
Ol	360_70R7_58a_E	14 / 2 .	642.2975	G	rim	38.13	0.02	0.00	0.07		0.31	38.76	22.46	0.00	0.03	99.8
Ol	360_70R7_58a_E	14 / 3 .	642.2975	G	core	38.44	0.00	0.00	0.03		0.34	38.82	22.47	0.00	0.08	100.2
Ol	360_70R7_58a_E	14 / 4 .	642.2975	F	rim	38.36	0.02	0.00	0.02		0.31	38.72	22.38	0.00	0.09	99.9
Ol	360_74R6_27_A	3 / 2 .	659.623	F	rim	37.94	0.00	0.06	0.02		0.36	37.10	24.15	0.00	0.07	99.7
Ol	360_74R6_27_B	7 / 1 .	659.6265	G	core	37.57	0.00	0.05	0.03		0.32	35.97	25.73	0.00	0.07	99.7
Ol	360_74R6_27_B	7 / 2 .	659.6265	G	rim	38.09	0.00	0.05	0.01		0.41	36.49	25.03	0.01	0.10	100.2
Ol	360_74R6_27_D	10 / 1 .	659.633	G	core	37.71	0.00	0.03	0.04		0.42	35.82	25.67	0.00	0.07	99.8
Ol	360_74R6_27_D	10 / 2 .	659.633	G	rim	37.94	0.00	0.01	0.01		0.40	36.29	25.60	0.00	0.04	100.3
Ol	360_74R6_27_D	10 / 3 .	659.633	G	rim	37.67	0.00	0.05	0.03		0.34	36.27	25.31	0.00	0.08	99.7
Ol	360_74R6_27_E	14 / 1 .	659.639	G	core	37.69	0.00	0.00	0.03		0.36	36.50	25.31	0.00	0.10	100.0
Ol	360_74R6_27_E	14 / 2 .	659.639	G	rim	38.17	0.00	0.01	0.01		0.40	36.58	25.52	0.00	0.04	100.7
Ol	360_75R7_56_A	3 / 1 .	671.1955	G	core	38.63	0.00	0.00	0.02		0.27	38.91	22.12	0.05	0.10	100.1
Ol	360_75R7_56_A	3 / 2 .	671.1955	G	rim	38.21	0.00	0.00	0.04		0.26	38.97	22.19	0.02	0.07	99.8
Ol	360_75R7_56_F	15 / 1 .	671.218	G	core	38.38	0.02	0.00	0.04		0.28	39.53	21.87	0.00	0.07	100.2
Ol	360_75R7_56_F	15 / 2 .	671.218	G	rim	38.37	0.01	0.06	0.05		0.31	39.48	21.89	0.02	0.08	100.3
Ol	360_75R7_56_G	18 / 1 .	671.2165	F	core	38.54	0.02	0.01	0.02		0.30	38.98	22.49	0.01	0.05	100.4
Ol	360_75R7_56_G	18 / 2 .	671.2165	F	core	38.05	0.00	0.05	0.01		0.31	38.31	22.83	0.00	0.04	99.6
Ol	360_79R6_1a_A	3 / 1 .	699.004	G	rim	37.73	0.00	0.00	0.02		0.40	35.96	25.70	0.03	0.07	99.9
Ol	360_79R6_1a_A	3 / 2 .	699.004	G	core	37.91	0.00	0.03	0.09		0.41	36.81	24.75	0.03	0.07	100.1
Ol	360_79R6_1a_A	3 / 3 .	699.004	G	rim	37.71	0.00	0.00	0.07		0.38	36.49	24.95	0.02	0.05	99.7
Ol	360_79R6_1a_B	5 / 1 .	699.0065	F	core	37.92	0.00	0.03	0.04		0.33	36.94	25.15	0.02	0.08	100.5
Ol	360_79R6_1a_B	5 / 2 .	699.0065	F	rim	37.72	0.00	0.01	0.00		0.34	36.50	24.85	0.01	0.06	99.5
Ol	360_79R6_1a_C	9 / 1 .	699.014	G	core	37.59	0.02	0.01	0.03		0.37	36.84	24.68	0.06	0.09	99.7
Ol	360_79R6_1a_C	9 / 2 .	699.014	G	rim	37.99	0.00	0.02	0.05		0.35	36.48	25.01	0.02	0.06	100.0
Ol	360_79R6_1a_C	9 / 3 .	699.014	G	core	37.60	0.00	0.01	0.06		0.37	36.32	25.02	0.01	0.05	99.4
Ol	360_79R6_1a_D	14 / 1 .	699.022	G	rim	37.42	0.00	0.00	0.04		0.45	37.03	24.67	0.00	0.06	99.7
Ol	360_79R6_1a_D	14 / 2 .	699.022	G	core	37.94	0.01	0.02	0.10		0.30	36.95	24.44	0.01	0.10	99.9
Ol	360_79R6_1a_D	14 / 3 .	699.022	G	rim	37.66	0.01	0.00	0.04		0.39	37.05	25.31	0.02	0.06	100.5
Ol	360_79R6_1a_D	14 / 4 .	699.022	G	core	37.94	0.03	0.00	0.04		0.33	36.89	24.75	0.04	0.08	100.1
Ol	360_79R6_1a_D	14 / 5 .	699.022	G	rim	37.87	0.00	0.00	0.04		0.32	36.49	24.71	0.01	0.09	99.5

Mineral	Sample	Point	Depth (mbsf)	Grain size	Grain area	SiO2	Al2O3	TiO2	CaO	Na2O	MnO	MgO	FeO	Cr2O3	NiO	Total
Ol	360_82R3_19a_C	7 / 1 .	723.537	G	core	38.10	0.00	0.00	0.01		0.36	37.51	23.80	0.02	0.02	99.8
Ol	360_82R3_19a_C	7 / 2 .	723.537	G	rim	37.85	0.04	0.04	0.04		0.34	37.35	24.18	0.00	0.07	99.9
Ol	360_82R3_19a_C	7 / 3 .	723.537	G	core	37.71	0.00	0.02	0.07		0.37	37.84	23.66	0.00	0.07	99.8
Ol	360_82R3_19a_C	7 / 4 .	723.537	G	core	37.89	0.00	0.01	0.05		0.37	37.72	23.82	0.03	0.05	99.9
Ol	360_82R3_19a_C	7 / 5 .	723.537	G	rim	38.10	0.00	0.03	0.02		0.31	37.73	23.78	0.00	0.04	100.0
Ol	360_82R3_19a_D	10 / 1 .	723.548	G	rim	38.37	0.00	0.05	0.04		0.37	37.54	24.87	0.00	0.03	101.3
Ol	360_82R3_19a_D	10 / 2 .	723.548	G	core	38.13	0.00	0.02	0.06		0.34	37.27	24.05	0.00	0.06	99.9
Ol	360_82R3_19a_D	10 / 3 .	723.548	G	rim	38.00	0.02	0.02	0.02		0.36	37.63	24.49	0.00	0.04	100.6
Ol	360_82R3_19a_F	15 / 1 .	723.5605	F	core	37.88	0.04	0.00	0.04		0.36	36.17	25.71	0.03	0.07	100.3
Ol	360_82R3_19a_F	15 / 2 .	723.5605	F	core	37.77	0.00	0.00	0.04		0.40	36.39	25.57	0.00	0.08	100.3
Ol	360_82R3_19a_G	18 / 1 .	723.562	F	core	38.03	0.02	0.04	0.07		0.34	36.24	25.92	0.04	0.12	100.8
Ol	360_82R3_19a_G	18 / 2 .	723.562	F	core	37.58	0.00	0.03	0.03		0.37	36.50	25.71	0.00	0.13	100.3
Ol	360_82R3_19a_G	18 / 3 .	723.562	F	core	37.72	0.00	0.02	0.03		0.33	36.28	25.95	0.02	0.07	100.4
Ol	360_82R3_19a_D	21 / 96 .	723.548			38.06	0.03	0.00	0.02		0.39	37.56	24.12	0.04	0.08	100.3
Ol	360_80R6_64b_A	4 / 1 .	707.954	G	rim	37.96	0.01	0.00	0.02		0.36	35.98	25.33	0.02	0.05	99.7
Ol	360_80R6_64b_B	6 / 1 .	707.958	G	core	37.72	0.01	0.01	0.07		0.35	35.22	26.28	0.00	0.10	99.8
Ol	360_80R6_64b_B	6 / 2 .	707.958	G	rim	37.54	0.02	0.01	0.05		0.40	35.70	26.23	0.03	0.10	100.1
Ol	360_80R6_64b_C	10 / 1 .	707.962	G	core	37.50	0.01	0.03	0.07		0.38	36.09	25.78	0.00	0.09	99.9
Ol	360_80R6_64b_C	10 / 2 .	707.962	G	rim	37.76	0.00	0.02	0.06		0.35	36.07	25.78	0.00	0.05	100.1
Ol	360_80R6_64b_C	10 / 3 .	707.962	G	rim	37.51	0.02	0.01	0.09		0.48	35.90	26.02	0.02	0.16	100.2
Ol	360_80R6_64b_C	10 / 4 .	707.962	G	core	37.50	0.02	0.04	0.07		0.37	36.12	26.47	0.00	0.10	100.7
Ol	360_80R6_64b_C	10 / 5 .	707.962	G	rim	37.82	0.01	0.00	0.07		0.38	35.55	26.46	0.02	0.09	100.4
Ol	360_80R6_64b_F	17 / 1 .	707.9795	G	core	37.71	0.01	0.01	0.03		0.35	35.64	26.45	0.02	0.07	100.3
Ol	360_80R6_64b_F	17 / 2 .	707.9795	G	rim	37.66	0.02	0.08	0.02		0.38	35.55	26.59	0.04	0.11	100.5
Ol	360_80R6_64b_F	17 / 3 .	707.9795	G	rim	37.71	0.00	0.03	0.01		0.46	35.61	26.55	0.00	0.10	100.5
Ol	360_44R5_0_E	24 / 1 .	406.389	G	core	37.49	0.01	0.04	0.06	0.00	0.40	34.53	27.87	0.03	0.02	100.5
Ol	360_44R5_0_E	24 / 2 .	406.389	G	rim	37.25	0.00	0.05	0.02	0.02	0.37	35.30	27.31	0.00	0.03	100.4
Ol	360_44R5_0_E	24 / 3 .	406.389	G	rim	37.04	0.00	0.00	0.02	0.01	0.40	34.20	27.42	0.00	0.07	99.2
Ol	360_44R5_0_E	24 / 4 .	406.389	F	core	37.06	0.03	0.00	0.02	0.00	0.39	34.87	27.25	0.00	0.07	99.7
Ol	360_44R5_0_F	32 / 1 .	406.396	G	core	37.35	0.00	0.02	0.03	0.00	0.42	35.33	26.87	0.00	0.03	100.1
Ol	360_44R5_0_F	32 / 2 .	406.396	G	rim	36.99	0.00	0.05	0.03	0.00	0.43	34.45	27.90	0.00	0.03	99.9
Ol	360_44R5_0_F	32 / 3 .	406.396	F	core	37.33	0.02	0.03	0.02	0.00	0.42	34.85	28.03	0.01	0.05	100.8
Ol	360_43R1_105_A	4 / 1 .	390.486	G	core	37.74	0.02	0.01	0.05	0.00	0.40	36.26	25.39	0.07	0.05	100.0
Ol	360_43R1_105_A	4 / 2 .	390.486	G	core	38.02	0.00	0.02	0.06	0.00	0.41	36.30	25.33	0.00	0.05	100.2
Ol	360_43R1_105_A	4 / 3 .	390.486	G	rim	37.69	0.00	0.02	0.05	0.01	0.39	35.83	25.55	0.03	0.07	99.7
Ol	360_43R1_105_A	4 / 4 .	390.486	G	rim	37.76	0.00	0.00	0.00	0.00	0.36	36.24	25.23	0.00	0.07	99.7
Ol	360_43R1_105_E	18 / 1 .	390.511	G	rim	37.81	0.00	0.04	0.10	0.01	0.37	36.36	25.07	0.00	0.04	99.8
Ol	360_43R1_105_Ebis	21 / 1 .	390.509	G	core	37.81	0.01	0.02	0.05	0.00	0.38	36.35	24.90	0.00	0.06	99.6
Ol	360_43R1_105_Ebis	21 / 2 .	390.509	G	rim	37.91	0.01	0.05	0.04	0.01	0.31	36.21	25.09	0.00	0.07	99.7

Mineral	Sample	Point	Depth (mbsf)	Grain size	Grain area	SiO2	Al2O3	TiO2	CaO	Na2O	MnO	MgO	FeO	Cr2O3	NiO	Total
Ol	360_43R1_105_Ebis	21 / 3 .	390.509	G	rim	37.56	0.00	0.00	0.04	0.05	0.33	36.83	24.99	0.08	0.00	99.9
Ol	360_41R2_1_A	1 / 1 .	372.854	G	rim	37.07	0.00	0.01	0.00	0.00	0.48	33.50	29.38	0.01	0.09	100.5
Ol	360_41R2_1_A	2 / 1 .	372.854	G	rim	37.39	0.01	0.00	0.00	0.00	0.45	33.16	29.66	0.00	0.10	100.8
Ol	360_41R2_1_A	2 / 2 .	372.854	G	core	37.32	0.00	0.03	0.03	0.02	0.45	33.35	28.93	0.01	0.05	100.2
Ol	360_41R2_1_A	2 / 3 .	372.854	F	core	36.86	0.00	0.03	0.05	0.00	0.47	32.17	30.56	0.00	0.05	100.2
Ol	360_41R2_1_B	7 / 1 .	372.855	G	core	37.41	0.00	0.00	0.06	0.01	0.51	33.73	28.67	0.03	0.04	100.5
Ol	360_41R2_1_B	7 / 2 .	372.855	G	rim	37.65	0.00	0.00	0.00	0.00	0.41	33.99	28.45	0.00	0.05	100.5
Ol	360_41R2_1_B	7 / 3 .	372.855	G	rim	37.18	0.02	0.01	0.02	0.03	0.48	32.93	29.18	0.13	0.02	100.0
Ol	360_41R2_1_C	10 / 1 .	372.8655	G	core	36.91	0.00	0.01	0.07	0.01	0.46	33.26	29.72	0.00	0.07	100.5
Ol	360_41R2_1_C	10 / 2 .	372.8655	G	rim	37.03	0.00	0.00	0.01	0.01	0.49	33.01	29.24	0.00	0.06	99.9
Ol	360_41R2_1_C	10 / 3 .	372.8655	G	rim	36.99	0.00	0.00	0.04	0.00	0.41	33.45	29.40	0.02	0.06	100.4
Ol	360_41R2_1_C	10 / 4 .	372.8655	F	rim	37.00	0.00	0.03	0.03	0.00	0.40	33.84	28.69	0.00	0.04	100.0
Ol	360_41R2_1_E	21 / 1 .	372.873	G	rim	37.00	0.02	0.01	0.06	0.00	0.50	32.91	29.60	0.00	0.02	100.1
Ol	360_41R2_1_E	21 / 2 .	372.873	G	core	37.07	0.01	0.03	0.02	0.01	0.51	33.02	29.81	0.01	0.04	100.5
Ol	360_41R2_1_E	21 / 3 .	372.873	G	rim	36.92	0.00	0.01	0.03	0.02	0.45	33.06	29.72	0.04	0.04	100.3
Ol	360_50R1_73_B	29 / 1 .	449.6093	F	core	37.90	0.00	0.01	0.06	0.00	0.32	35.23	26.51	0.02	0.05	100.1
Ol	360_50R1_73_B	29 / 2 .	449.6093	F	rim	37.11	0.01	0.00	0.03	0.01	0.37	34.49	27.51	0.00	0.06	99.6
Ol	360_50R1_73_B	29 / 3 .	449.6093	F	core	37.52	0.01	0.00	0.04	0.00	0.43	34.85	27.54	0.00	0.05	100.4
Ol	360_50R1_73_B	29 / 4 .	449.6093	F	core	37.58	0.00	0.00	0.00	0.02	0.36	34.56	27.26	0.00	0.06	99.9
Ol	360_50R1_73_C	2 / 1 .	449.6115	F	core	37.77	0.00	0.09	0.03	0.01	0.45	34.44	27.97	0.00	0.09	100.8
Ol	360_50R1_73_D	7 / 1 .	449.615	F	core	37.57	0.02	0.00	0.02	0.02	0.41	35.11	27.11	0.00	0.07	100.3
Ol	360_50R1_73_D	7 / 2 .	449.615	F	core	37.26	0.01	0.00	0.01	0.00	0.41	34.69	27.64	0.06	0.06	100.1
Ol	360_50R1_73_D	7 / 3 .	449.615	F	core	37.51	0.00	0.01	0.06	0.00	0.40	34.81	27.34	0.00	0.10	100.2
Ol	360_50R1_73_F	14 / 1 .	449.622	G	core	38.22	0.01	0.02	0.05	0.00	0.37	36.51	24.65	0.00	0.03	99.9
Ol	360_50R1_73_F	14 / 2 .	449.622	G	core	37.68	0.00	0.00	0.07	0.00	0.38	36.99	24.72	0.00	0.10	99.9
Ol	360_50R1_73_F	14 / 3 .	449.622	G	rim	38.07	0.00	0.00	0.04	0.01	0.33	37.15	24.78	0.00	0.04	100.4
Ol	360_50R1_73_F	14 / 4 .	449.622	G	core	38.21	0.00	0.03	0.05	0.00	0.37	37.16	24.65	0.03	0.05	100.5
Ol	360_50R1_73_F	14 / 5 .	449.622	G	rim	37.85	0.00	0.06	0.06	0.00	0.36	37.11	24.51	0.00	0.02	100.0
Ol	360_50R1_73_G	17 / 1 .	449.627	F	core	37.93	0.01	0.03	0.03	0.00	0.35	37.07	24.88	0.02	0.08	100.4
Ol	360_50R1_73_G	17 / 2 .	449.627	F	rim	38.14	0.00	0.02	0.03	0.00	0.39	36.93	24.98	0.05	0.09	100.6
Ol	360_60R2_69_C	27 / 1 .	539.8613	G	core	37.65	0.04	0.03	0.03	0.00	0.38	36.59	24.97	0.02	0.05	99.8
Ol	360_60R2_69_C	27 / 2 .	539.8613	G	rim	37.51	0.00	0.02	0.04	0.00	0.41	36.74	24.98	0.00	0.08	99.8
Ol	360_60R2_69_C	27 / 3 .	539.8613	F	core	37.51	0.01	0.02	0.04	0.01	0.36	36.38	25.41	0.00	0.05	99.8
Ol	360_60R2_69_D	2 / 1 .	539.8674	F	core	37.91	0.01	0.08	0.02	0.02	0.32	35.91	25.43	0.02	0.10	99.8
Ol	360_60R2_69_D	2 / 2 .	539.8674	F	rim	37.79	0.00	0.00	0.05	0.01	0.33	36.31	24.75	0.00	0.11	99.4
Ol	360_60R2_69_E	5 / 1 .	539.874	F	core	37.85	0.00	0.04	0.03	0.02	0.38	36.46	24.69	0.02	0.08	99.6
Ol	360_60R2_69_E	5 / 2 .	539.874	F	rim	37.92	0.01	0.03	0.02	0.02	0.31	36.61	24.56	0.00	0.05	99.5
Ol	360_60R2_69_E	5 / 3 .	539.874	F	core	37.95	0.04	0.00	0.00	0.00	0.39	36.38	24.99	0.00	0.08	99.8
Ol	360_66R3_29_A	12 / 1 .	598.438	G	rim	38.13	0.00	0.04	0.03	0.04	0.29	39.86	21.71	0.04	0.06	100.2

Mineral	Sample	Point	Depth (mbsf)	Grain size	Grain area	SiO2	Al2O3	TiO2	CaO	Na2O	MnO	MgO	FeO	Cr2O3	NiO	Total
Ol	360_66R3_29_A	12 / 2 .	598.438	G	core	38.70	0.03	0.02	0.06	0.02	0.29	39.48	22.09	0.04	0.10	100.8
Ol	360_66R3_29_A	12 / 3 .	598.438	F	rim	38.43	0.02	0.00	0.04	0.04	0.33	39.42	21.74	0.00	0.10	100.1
Ol	360_66R3_29_B	16 / 1 .	598.434	F	rim	38.62	0.01	0.05	0.00	0.00	0.25	39.68	21.56	0.02	0.06	100.2
Ol	360_66R3_29_B	16 / 2 .	598.434	F	core	38.37	0.03	0.01	0.03	0.01	0.30	39.69	21.47	0.00	0.06	100.0
Ol	360_66R3_29_B	16 / 3 .	598.434	G	core	38.62	0.02	0.00	0.05	0.01	0.33	39.67	21.52	0.00	0.03	100.3
Ol	360_66R3_29_B	16 / 4 .	598.434	G	rim	38.88	0.01	0.00	0.04	0.01	0.30	39.37	21.56	0.00	0.14	100.3
Ol	360_66R3_29_C	19 / 1 .	598.4405	G	core	38.80	0.00	0.00	0.07	0.00	0.33	39.58	21.71	0.03	0.08	100.6
Ol	360_66R3_29_C	19 / 2 .	598.4405	G	rim	38.84	0.00	0.02	0.01	0.02	0.28	40.07	21.47	0.03	0.06	100.8
Ol	360_66R3_29_C	19 / 3 .	598.4405	G	rim	38.72	0.01	0.08	0.05	0.04	0.33	39.30	21.86	0.00	0.07	100.4
Ol	360_66R3_29_D	25 / 1 .	598.4495	G	core	38.56	0.00	0.05	0.04	0.00	0.28	39.62	22.11	0.00	0.04	100.7
Ol	360_66R3_29_D	25 / 2 .	598.4495	G	rim	38.45	0.00	0.05	0.02	0.01	0.31	39.41	21.79	0.00	0.09	100.1
Ol	360_66R3_29_D	25 / 3 .	598.4495	G	rim	38.72	0.00	0.00	0.04	0.00	0.32	39.26	22.19	0.00	0.06	100.6
Ol	360_66R3_29_D	25 / 4 .	598.4495	F	core	38.42	0.00	0.03	0.03	0.00	0.31	39.11	22.33	0.00	0.11	100.4
Ol	360_66R3_29_D	25 / 5 .	598.4495	F	rim	38.51	0.01	0.00	0.02	0.02	0.27	39.38	21.69	0.04	0.10	100.0
Ol	360_66R3_29_E	2 / 1 .	598.4545	F	core	38.45	0.00	0.01	0.05	0.00	0.28	39.02	22.11	0.04	0.06	100.0
Ol	360_66R3_29_E	2 / 2 .	598.4545	F	core	38.25	0.01	0.02	0.00	0.00	0.32	38.69	22.21	0.02	0.07	99.6
Ol	360_66R3_29_E	2 / 3 .	598.4545	G	core	38.50	0.01	0.00	0.02	0.02	0.31	39.13	22.27	0.01	0.14	100.4
Ol	360_66R3_29_E	2 / 4 .	598.4545	G	rim	38.37	0.00	0.02	0.02	0.01	0.27	39.46	21.92	0.03	0.08	100.2
Ol	360_66R3_29_F	7 / 1 .	598.4595	G	core	38.35	0.00	0.04	0.04	0.00	0.28	39.60	21.20	0.00	0.05	99.6
Ol	360_66R3_29_F	7 / 2 .	598.4595	G	rim	38.31	0.00	0.00	0.08	0.03	0.31	39.09	22.04	0.00	0.06	99.9
Ol	360_66R3_29_F	7 / 3 .	598.4595	G	rim	38.03	0.05	0.08	0.01	0.01	0.34	39.37	21.68	0.02	0.08	99.7
Ol	360_67R8_50_Cbis	14 / 1 .	614.0225	G	core	38.28	0.01	0.02	0.03	0.03	0.29	39.03	22.39	0.00	0.06	100.1
Ol	360_67R8_50_Cbis	14 / 2 .	614.0225	G	rim	38.43	0.00	0.01	0.04	0.00	0.30	38.61	22.64	0.00	0.13	100.2
Ol	360_67R8_50_Cbis	14 / 3 .	614.0225	G	core	38.31	0.00	0.07	0.05	0.00	0.37	38.45	22.50	0.00	0.03	99.8
Ol	360_67R8_50_Cbis	14 / 4 .	614.0225	G	rim	38.28	0.01	0.02	0.08	0.03	0.32	38.67	22.02	0.04	0.09	99.6
Ol	360_67R8_50_D	20 / 1 .	614.029	G	rim	38.46	0.02	0.00	0.03	0.03	0.31	38.96	22.54	0.01	0.06	100.4
Ol	360_67R8_50_D	20 / 2 .	614.029	G	rim	38.43	0.01	0.03	0.03	0.01	0.36	38.73	21.81	0.02	0.13	99.6
Ol	360_67R8_50_D	20 / 3 .	614.029	G	core	38.17	0.00	0.04	0.02	0.01	0.25	39.34	22.03	0.01	0.10	100.0
Ol	360_67R8_50_D	20 / 4 .	614.029	G	core	38.82	0.02	0.00	0.03	0.02	0.31	39.16	22.19	0.00	0.10	100.6
Ol	360_67R8_50_D	20 / 5 .	614.029	G	rim	38.57	0.03	0.00	0.04	0.01	0.34	38.85	22.06	0.00	0.15	100.1
Ol	360_67R8_50_E	23 / 1 .	614.034	G	rim	38.67	0.02	0.05	0.04	0.04	0.34	39.58	21.35	0.00	0.06	100.1
Ol	360_67R8_50_E	23 / 2 .	614.034	G	core	38.31	0.00	0.00	0.06	0.00	0.30	39.58	21.54	0.00	0.12	99.9
Ol	360_67R8_50_E	23 / 3 .	614.034	G	rim	38.60	0.02	0.01	0.05	0.00	0.29	39.02	21.67	0.01	0.07	99.8
Ol	360_67R8_50_F	26 / 1 .	614.041	F	core	38.30	0.00	0.00	0.02	0.00	0.30	39.80	21.27	0.00	0.08	99.8
Ol	360_67R8_50_F	26 / 2 .	614.041	F	core	38.74	0.00	0.01	0.02	0.01	0.39	39.78	21.21	0.06	0.11	100.3
Ol	360_67R8_50_F	26 / 3 .	614.041	G	rim	38.88	0.00	0.06	0.05	0.00	0.25	39.67	21.12	0.03	0.10	100.2
Ol	360_67R8_50_F	26 / 4 .	614.041	G	core	38.51	0.00	0.02	0.04	0.00	0.25	39.78	20.71	0.00	0.05	99.4
Ol	360_67R8_50_G	29 / 1 .	614.038	F	core	38.21	0.00	0.00	0.04	0.02	0.31	38.22	22.93	0.01	0.09	99.8
Ol	360_67R8_50_G	29 / 2 .	614.038	G	rim	38.06	0.02	0.00	0.03	0.01	0.27	38.77	22.43	0.00	0.10	99.7

Mineral	Sample	Point	Depth (mbsf)	Grain size	Grain area	SiO2	Al2O3	TiO2	CaO	Na2O	MnO	MgO	FeO	Cr2O3	NiO	Total
Ol	360_67R8_50_G	29 / 3 .	614.038	G	core	38.09	0.00	0.00	0.10	0.00	0.29	38.74	22.28	0.00	0.06	99.6
Ol	360_78R7_97b_D	15 / 1 .	689.7035	F	core	37.78	0.00	0.02	0.03	0.02	0.35	36.89	25.19	0.03	0.07	100.4
Ol	360_78R7_97b_D	15 / 2 .	689.7035	F	rim	37.88	0.00	0.03	0.04	0.01	0.41	36.66	24.67	0.00	0.09	99.8
Ol	360_78R7_97b_D	15 / 3 .	689.7035	F	core	37.87	0.03	0.00	0.07	0.00	0.42	36.74	25.10	0.00	0.05	100.3
Ol	360_78R7_97b_D	15 / 4 .	689.7035	F	rim	37.72	0.00	0.00	0.03	0.02	0.37	36.83	25.10	0.06	0.06	100.2
Ol	360_78R7_97b_D	15 / 5 .	689.7035	G	core	37.99	0.02	0.00	0.08	0.00	0.37	36.84	25.11	0.04	0.09	100.5
Ol	360_78R7_97b_D	15 / 6 .	689.7035	G	core	37.84	0.00	0.00	0.04	0.03	0.38	36.73	24.87	0.02	0.11	100.0
Ol	360_78R7_97b_D	15 / 7 .	689.7035	G	rim	37.74	0.00	0.03	0.05	0.00	0.36	36.78	25.02	0.07	0.05	100.1
Ol	360_78R7_97b_F	25 / 1 .	689.712	F	core	38.13	0.00	0.08	0.02	0.00	0.35	38.16	23.44	0.04	0.07	100.3
Ol	360_78R7_97b_F	25 / 2 .	689.712	G	rim	37.72	0.01	0.02	0.05	0.00	0.39	37.08	25.19	0.00	0.04	100.5
Ol	360_78R7_97b_F	25 / 3 .	689.712	G	rim	38.09	0.02	0.00	0.05	0.00	0.40	36.75	25.35	0.03	0.04	100.7
Ol	360_78R7_97b_Fbis	29 / 1 .	689.712	G	core	37.77	0.00	0.03	0.08	0.00	0.42	36.76	25.52	0.01	0.06	100.7
Ol	360_78R7_97b_Fbis	29 / 2 .	689.712	G	core	38.32	0.00	0.00	0.06	0.00	0.31	36.45	25.86	0.03	0.08	101.1
Ol	360_78R7_97b_Fbis	29 / 3 .	689.712	G	core	37.69	0.01	0.00	0.07	0.01	0.30	36.53	25.55	0.01	0.04	100.2
Ol	360_77R2_60_C	5 / 1 .	680.5615	G	core	36.17	0.01	0.00	0.05	0.00	0.51	28.38	35.76	0.02	0.03	100.9
Ol	360_77R2_60_C	5 / 2 .	680.5615	G	rim	35.60	0.01	0.00	0.07	0.00	0.57	28.17	35.96	0.00	0.10	100.5
Ol	360_77R2_60_C	5 / 3 .	680.5615	G	core	35.96	0.00	0.00	0.05	0.00	0.56	27.71	35.98	0.03	0.06	100.3
Ol	360_77R2_60_D	9 / 1 .	680.5625	G	rim	35.66	0.01	0.00	0.04	0.00	0.63	27.91	35.53	0.04	0.00	99.8
Ol	360_77R2_60_D	9 / 2 .	680.5625	G	core	36.13	0.01	0.00	0.00	0.00	0.57	28.32	35.32	0.00	0.00	100.4
Ol	360_77R2_60_D	9 / 3 .	680.5625	G	rim	36.23	0.00	0.03	0.06	0.00	0.52	27.82	35.49	0.03	0.02	100.2
Ol	360_77R2_60_H	22 / 1 .	680.578	F	core	35.63	0.00	0.08	0.05	0.03	0.66	26.42	37.81	0.00	0.02	100.7
Ol	360_84R1_20_A	28 / 1 .	740.6555	F	rim	37.79	0.00	0.08	0.05	0.00	0.36	37.16	24.22	0.02	0.08	99.8
Ol	360_84R1_20_A	28 / 2 .	740.6555	F	core	37.77	0.02	0.00	0.04	0.02	0.34	38.24	23.66	0.00	0.07	100.2
Ol	360_84R1_20_A	28 / 3 .	740.6555	F	core	37.92	0.02	0.02	0.06	0.00	0.42	37.92	23.35	0.00	0.07	99.8
Ol	360_84R1_20_A	28 / 4 .	740.6555	G	rim	38.15	0.00	0.00	0.02	0.02	0.38	37.75	23.42	0.00	0.07	99.8
Ol	360_84R1_20_A	28 / 5 .	740.6555	G	core	38.29	0.01	0.03	0.05	0.02	0.30	37.28	23.96	0.01	0.05	100.0
Ol	360_84R1_20_A	28 / 6 .	740.6555	G	rim	38.44	0.00	0.00	0.02	0.02	0.40	37.30	23.64	0.00	0.10	99.9
Ol	360_84R1_20_B	32 / 1 .	740.658	G	core	37.58	0.00	0.02	0.04	0.02	0.40	37.44	23.94	0.00	0.04	99.5
Ol	360_84R1_20_B	32 / 2 .	740.658	G	rim	38.23	0.03	0.07	0.01	0.02	0.37	37.25	23.75	0.03	0.09	99.8
Ol	360_84R1_20_B	32 / 3 .	740.658	G	core	38.28	0.01	0.00	0.03	0.00	0.37	37.58	24.00	0.01	0.12	100.4
Ol	360_84R1_20_B	32 / 4 .	740.658	G	rim	38.15	0.01	0.04	0.04	0.01	0.33	37.41	24.05	0.02	0.07	100.1
Ol	360_84R1_20_E	10 / 1 .	740.667	F	core	37.95	0.02	0.00	0.00	0.00	0.33	37.50	23.98	0.03	0.09	99.9
Ol	360_84R1_20_F	12 / 1 .	740.68	F	core	37.99	0.00	0.00	0.07	0.00	0.30	38.20	23.32	0.03	0.08	100.0
Ol	360_84R1_20_F	12 / 2 .	740.68	F	rim	38.35	0.00	0.02	0.01	0.01	0.35	38.16	23.14	0.01	0.12	100.2
Ol	360_84R1_20_F	12 / 3 .	740.68	F	core	37.95	0.02	0.00	0.06	0.00	0.28	38.30	22.59	0.00	0.13	99.3
Ol	360_84R1_20_F	12 / 4 .	740.68	G	core	38.32	0.00	0.05	0.02	0.03	0.38	38.35	23.28	0.01	0.09	100.5
Ol	360_84R1_20_F	12 / 5 .	740.68	G	rim	37.75	0.02	0.03	0.05	0.00	0.35	38.32	23.36	0.00	0.06	99.9
Ol	360_84R1_20_F	12 / 6 .	740.68	G	rim	37.86	0.01	0.00	0.01	0.00	0.34	38.28	23.14	0.00	0.08	99.7
Ol	360_84R1_20_G	17 / 1 .	740.674	G	core	37.77	0.01	0.01	0.06	0.00	0.31	38.14	23.01	0.00	0.12	99.4

Mineral	Sample	Point	Depth (mbsf)	Grain size	Grain area	SiO2	Al2O3	TiO2	CaO	Na2O	MnO	MgO	FeO	Cr2O3	NiO	Total
Ol	360_84R1_20_G	17 / 2 .	740.674	G	rim	38.12	0.00	0.05	0.08	0.01	0.34	38.12	23.02	0.00	0.09	99.8
Ol	360_84R1_20_G	17 / 3 .	740.674	F	core	38.31	0.02	0.01	0.03	0.02	0.32	38.36	22.95	0.05	0.08	100.1
Calibration standards						Wollastonite (San Carlos)	Al2O3	TiMnO3	Wollastonite	Albite	TiMnO3	Forsterite	Fayalite	Cr2O3	NiO	

In situ majot elements concentrations in wt% analyzed by EPMA on a Cameca SX at LMV (Clermont-Ferrand, France)

Mineral	Sample	Area	Point	Depth (mbsf)	Grain size	Grain area	SiO2	Al2O3	CaO	Na2O	K2O	MnO	MgO	FeO	Total
			2 sigma				0.512	0.595	0.279	0.365	0.074	0.029	0.021	0.058	
Pl			Counting time (s) - per element				10	10	10	10	10	10	10	20	
Pl		A	1 / 1 .	538.8035	G	core	51.97	30.49	13.18	3.98	0.07		0.02	0.24	100.0
Pl		A	2 / 1 .	538.8035	G	rim	52.35	30.42	13.76	4.14	0.07		0.03	0.32	101.1
Pl		A	5 / 1 .	538.8035	G	rim	55.12	28.61	11.20	5.13	0.08		0.03	0.24	100.4
Pl		A	5 / 2 .	538.8035	G	core	54.21	29.01	11.50	4.98	0.06		0.03	0.23	100.0
Pl		A	5 / 3 .	538.8035	G	rim	53.67	29.11	11.94	4.84	0.10		0.03	0.43	100.1
Pl		A	5 / 4 .	538.8035	F	core	53.96	29.16	11.75	4.81	0.06		0.02	0.27	100.0
Pl		B	10 / 1 .	538.804	G	rim	52.71	30.34	13.15	4.17	0.07		0.03	0.16	100.6
Pl		B	10 / 2 .	538.804	G	core	52.26	29.99	13.02	4.05	0.04		0.03	0.33	99.7
Pl		B	10 / 3 .	538.804	G	Rim	53.32	29.80	12.36	4.59	0.06		0.01	0.27	100.4
Pl		B	10 / 4 .	538.804	F	core	52.47	29.98	12.99	4.17	0.04		0.02	0.23	99.9
Pl	360_60R1_26	B	10 / 5 .	538.804	F	rim	53.78	29.76	12.26	4.62	0.01		0.00	0.21	100.6
Pl		B	10 / 6 .	538.804	G	core	53.03	29.79	12.98	4.15	0.05		0.01	0.19	100.2
Pl		B	10 / 7 .	538.804	G	rim	53.40	29.97	12.59	4.48	0.08		0.01	0.19	100.7
Pl		C	12 / 1 .	538.8115	G	core	53.66	29.21	11.84	4.75	0.08		0.01	0.20	99.8
Pl		C	12 / 2 .	538.8115	G	rim	54.38	28.92	11.56	4.94	0.05		0.01	0.31	100.2
Pl		C	12 / 3 .	538.8115	F	core	53.65	29.50	11.99	4.88	0.06		0.02	0.30	100.4
Pl		G	20 / 1 .	538.8215	G	core	53.25	29.88	12.69	4.31	0.05		0.03	0.28	100.5
Pl		G	20 / 2 .	538.8215	G	rim	53.25	29.86	12.55	4.55	0.06		0.03	0.32	100.6
Pl		G	20 / 3 .	538.8215	F	rim	53.63	29.58	12.03	4.69	0.01		0.01	0.29	100.2
Pl		E	23 / 1 .	538.8285	G	core	52.03	30.26	13.22	4.16	0.00		0.02	0.22	99.9
Pl		E	23 / 2 .	538.8285	G	rim	52.04	29.74	12.57	4.28	0.06		0.02	0.38	99.1
Pl		E	23 / 3 .	538.8285	F	core	53.53	29.33	12.22	4.59	0.10		0.02	0.26	100.0
Pl		F	25 / 1 .	538.831	F	core	53.33	29.41	12.41	4.53	0.02		0.01	0.30	100.0
Pl		F	25 / 3 .	538.831	G	core	52.37	30.07	13.36	4.07	0.05		0.05	0.31	100.3
Pl		F	25 / 4 .	538.831	G	rim	52.94	29.57	12.30	4.59	0.07		0.01	0.21	99.7
Pl		A	1 / 1 .	561.8725	G	core	55.61	27.74	10.30	5.63	0.10		0.06	0.28	99.7
Pl		A	2 / 1 .	561.8725	G	rim	56.11	27.94	10.27	5.73	0.02		0.03	0.26	100.4
Pl		A	2 / 2 .	561.8725	G	core	56.28	27.84	10.18	5.75	0.07		0.05	0.24	100.4
Pl		A	2 / 3 .	561.8725	F	core	56.07	28.00	10.39	5.79	0.05		0.02	0.27	100.6
Pl		A1	2 / 4 .	561.8745	G	core	55.52	28.16	10.90	5.32	0.05		0.05	0.31	100.3
Pl		A1	2 / 5 .	561.8745	G	rim	56.20	28.06	10.62	5.63	0.08		0.06	0.20	100.8
Pl		C	6 / 1 .	561.8765	G	core	55.19	28.25	10.89	5.37	0.09		0.01	0.22	100.0
Pl		C	6 / 2 .	561.8765	G	rim	55.75	28.50	11.10	5.50	0.05		0.02	0.33	101.2

Mineral		Area	Point	Depth (mbsf)	Grain size	Grain area	SiO2	Al2O3	CaO	Na2O	K2O	MnO	MgO	FeO	Total
Pl	360_62R4_62	D	10 / 1 .	561.8845	F	core	55.77	28.17	10.55	5.75	0.06		0.01	0.29	100.6
Pl		D	10 / 2 .	561.8845	F	core	55.49	28.39	10.62	5.45	0.06		0.02	0.18	100.2
Pl		D	10 / 3 .	561.8845	F	core	55.43	28.40	11.06	5.54	0.09		0.02	0.21	100.7
Pl		D	10 / 4 .	561.8845	G	core	55.70	28.37	10.65	5.44	0.08		0.01	0.37	100.6
Pl		D	10 / 5 .	561.8845	G	rim	55.74	28.31	10.84	5.61	0.01		0.01	0.28	100.8
Pl		E	12 / 1 .	561.8905	G	core	55.39	28.35	11.08	5.61	0.09		0.01	0.24	100.8
Pl		E	12 / 2 .	561.8905	G	rim	54.49	28.75	11.01	5.29	0.10		0.01	0.28	99.9
Pl		E	12 / 3 .	561.8905	F	core	55.95	27.71	10.35	5.46	0.13		0.02	0.29	99.9
Pl		E	12 / 4 .	561.8905	F	core	55.31	28.31	10.73	5.51	0.04		0.02	0.21	100.1
Pl		F	13 / 1 .	561.8985	G	rim	56.49	27.68	10.43	5.83	0.08		0.00	0.20	100.7
Pl		F	13 / 2 .	561.8985	G	core	55.21	28.48	10.99	5.41	0.06		0.01	0.22	100.4
Pl		F	13 / 3 .	561.8985	F	core	55.05	28.49	10.72	5.42	0.04		0.02	0.22	100.0
Pl		F	13 / 4 .	561.8985	F	core	55.55	28.24	10.67	5.59	0.03		0.00	0.16	100.2
Pl		G	16 / 1 .	561.8965	G	core	55.84	28.01	10.42	5.79	0.08		0.02	0.15	100.3
Pl		G	16 / 2 .	561.8965	G	rim	55.46	28.01	10.50	5.58	0.03		0.01	0.18	99.8
Pl		G	16 / 3 .	561.8965	G	core	55.85	28.09	10.63	5.66	0.09		0.02	0.18	100.5
Pl		G	16 / 4 .	561.8965	F	core	56.37	27.95	10.56	5.72	0.02		0.01	0.16	100.8
Pl		A	1 / 1 .	579.658	F	core	52.48	30.20	13.34	4.09	0.04		0.00	0.19	100.3
Pl		A	2 / 1 .	579.658	F	core	54.39	28.86	11.39	5.17	0.08		0.03	0.22	100.2
Pl		A	2 / 2 .	579.658	F	rim	53.23	29.86	12.56	4.57	0.04		0.02	0.24	100.5
Pl		A	2 / 3 .	579.658	F	core	54.08	29.06	12.02	4.78	0.03		0.02	0.22	100.2
Pl		A	2 / 4 .	579.658	F	core	50.09	32.29	15.15	3.07	0.02		0.02	0.40	101.0
Pl		B	8 / 2 .	579.6575	F	rim	53.74	29.40	12.19	4.95	0.05		0.04	0.23	100.6
Pl		B	8 / 3 .	579.6575	F	rim	53.73	29.16	12.13	4.61	0.03		0.01	0.19	99.9
Pl		B	8 / 4 .	579.6575	F	core	54.28	29.31	11.74	4.97	0.03		0.02	0.26	100.6
Pl		B	8 / 5 .	579.6575	G	rim	53.59	29.44	12.04	4.81	0.03		0.01	0.29	100.2
Pl		B	8 / 6 .	579.6575	G	core	53.74	29.11	12.07	4.73	0.06		0.02	0.23	100.0
Pl		B	8 / 7 .	579.6575	G	core	53.93	29.21	12.20	4.69	0.09		0.04	0.30	100.5
Pl	360_64R5_39	C	11 / 1 .	579.654	F	core	53.69	29.36	12.09	4.84	0.05		0.02	0.15	100.2
Pl		C	11 / 2 .	579.654	G	rim	53.73	29.24	12.12	4.75	0.06		0.01	0.24	100.1
Pl		C	11 / 3 .	579.654	G	core	53.71	29.37	12.04	4.86	0.05		0.04	0.24	100.3
Pl		C	11 / 4 .	579.654	G	rim	53.67	29.28	12.03	4.75	0.09		0.03	0.29	100.2
Pl		C	11 / 5 .	579.654	G	core	53.77	29.16	12.03	4.75	0.07		0.03	0.27	100.1
Pl		C	11 / 6 .	579.654	G	rim	52.40	30.18	13.02	4.20	0.04		0.02	0.17	100.0
Pl		D	15 / 1 .	579.6645	F	core	54.54	28.92	11.31	5.15	0.06		0.01	0.25	100.2
Pl		D	15 / 2 .	579.6645	G	core	54.42	28.88	11.66	4.90	0.05		0.03	0.28	100.2

Mineral		Area	Point	Depth (mbsf)	Grain size	Grain area	SiO2	Al2O3	CaO	Na2O	K2O	MnO	MgO	FeO	Total
Pl		D	15 / 3 .	579.6645	G	rim	54.55	29.01	11.52	4.94	0.05		0.01	0.20	100.3
Pl	360_64R5_	E	1 / 1 .	579.6725	F	core	53.60	29.13	12.18	4.72	0.07		0.01	0.23	99.9
Pl		E	2 / 1 .	579.6725	F	rim	53.51	29.46	12.33	4.53	0.00		0.01	0.31	100.2
Pl		E	2 / 2 .	579.6725	G	rim	53.34	30.12	12.69	4.36	0.04		0.01	0.20	100.8
Pl		E	2 / 3 .	579.6725	G	core	53.85	29.32	12.17	4.59	0.04		0.03	0.27	100.3
Pl		A	4 / 1 .	604.537	F	core	52.44	29.49	12.48	4.31	0.04		0.02	0.35	99.1
Pl		A	4 / 2 .	604.537	G	rim	50.08	31.53	14.66	3.24	0.01		0.01	0.25	99.8
Pl		A	4 / 3 .	604.537	G	core	54.13	28.96	11.60	5.02	0.07		0.02	0.23	100.0
Pl		A	4 / 4 .	604.537	G	core	52.32	29.83	12.66	4.19	0.06		0.02	0.22	99.3
Pl		A	4 / 5 .	604.537	G	rim	51.28	31.05	13.62	3.57	0.03		0.00	0.23	99.8
Pl		B	7 / 1 .	604.5375	F	core	53.25	29.14	12.18	4.57	0.04		0.03	0.19	99.4
Pl		B	7 / 2 .	604.5375	F	rim	48.03	32.75	16.24	2.19	0.01		0.03	0.29	99.5
Pl		B	7 / 3 .	604.5375	G	core	52.18	29.85	13.28	4.21	0.02		0.03	0.29	99.9
Pl		B	7 / 4 .	604.5375	G	rim	53.14	29.65	12.58	4.48	0.06		0.04	0.34	100.3
Pl		B	7 / 5 .	604.5375	F	core	54.28	28.78	11.63	4.94	0.06		0.00	0.18	99.9
Pl		B	7 / 6 .	604.5375	F	core	53.36	29.32	12.28	4.45	0.05		0.04	0.29	99.8
Pl		C	10 / 1 .	604.5425	F	core	52.75	29.45	12.07	4.64	0.05		0.01	0.25	99.2
Pl		C	10 / 2 .	604.5425	F	core	53.73	29.30	11.98	4.75	0.04		0.01	0.25	100.0
Pl		C	10 / 3 .	604.5425	G	rim	49.49	31.70	15.06	2.98	0.03		0.02	0.30	99.6
Pl		C	10 / 4 .	604.5425	G	core	53.99	28.81	11.63	4.85	0.06		0.03	0.23	99.6
Pl		D	13 / 1 .	604.5415	F	rim	53.63	29.49	11.96	4.69	0.03		0.02	0.19	100.0
Pl	360_67R1_91a	D	13 / 2 .	604.5415	F	core	53.42	29.38	11.80	4.74	0.05		0.02	0.22	99.6
Pl		D	13 / 3 .	604.5415	F	core	52.57	29.21	12.27	4.53	0.06		0.03	0.26	98.9
Pl		D	13 / 4 .	604.5415	G	rim	52.93	29.72	12.76	4.40	0.06		0.01	0.25	100.1
Pl		E	17 / 1 .	604.5485	F	core	53.59	29.24	11.86	4.81	0.05		0.01	0.28	99.8
Pl		E	17 / 2 .	604.5485	F	rim	50.15	31.01	14.38	3.54	0.05		0.04	0.36	99.5
Pl		E	17 / 3 .	604.5485	F	core	52.60	29.55	12.47	4.39	0.04		0.03	0.39	99.5
Pl		E	17 / 4 .	604.5485	G	core	52.99	29.33	12.27	4.34	0.06		0.03	0.30	99.3
Pl		E	17 / 5 .	604.5485	G	rim	54.59	29.07	11.70	4.83	0.06		0.03	0.32	100.6
Pl		F	19 / 1 .	604.5575	F	core	53.17	29.50	12.16	4.62	0.06		0.03	0.26	99.8
Pl		F	19 / 2 .	604.5575	G	rim	53.75	29.33	12.42	4.72	0.04		0.04	0.22	100.5
Pl		F	19 / 3 .	604.5575	G	core	53.32	29.57	12.14	4.48	0.01		0.02	0.24	99.8
Pl		G	20 / 1 .	604.5605	G	core	53.69	28.92	11.94	4.68	0.04		0.01	0.23	99.5
Pl		G	20 / 2 .	604.5605	G	rim	51.63	30.26	13.44	3.89	0.02		0.01	0.29	99.5
Pl		G	20 / 3 .	604.5605	F	core	53.29	29.24	12.14	4.67	0.01		0.00	0.23	99.6
Pl		G	20 / 4 .	604.5605	F	core	52.59	29.71	12.47	4.32	0.02		0.00	0.30	99.4

Mineral		Area	Point	Depth (mbsf)	Grain size	Grain area	SiO2	Al2O3	CaO	Na2O	K2O	MnO	MgO	FeO	Total
Pl		G	20 / 5 .	604.5605	G	core	53.03	29.58	12.33	4.49	0.02		0.01	0.24	99.7
Pl		G	20 / 6 .	604.5605	G	rim	53.72	29.38	11.83	4.82	0.01		0.00	0.20	99.9
Pl		A	1 / 1 .	642.2885	F	core	52.83	29.81	12.41	4.56	0.05		0.03	0.27	100.0
Pl		A	2 / 1 .	642.2885	F	rim	48.91	32.55	15.47	2.56	0.00		0.03	0.33	99.8
Pl		A	2 / 2 .	642.2885	F	core	53.31	29.54	11.84	4.56	0.05		0.02	0.20	99.5
Pl		A	2 / 3 .	642.2885	G	rim	53.00	29.57	12.46	4.41	0.03		0.03	0.20	99.7
Pl		A	2 / 4 .	642.2885	G	core	52.80	30.01	12.89	4.18	0.06		0.04	0.21	100.2
Pl		A	2 / 5 .	642.2885	F	core	49.42	31.74	15.09	2.84	0.01		0.01	0.27	99.4
Pl		B	7 / 1 .	642.2865	G	core	52.80	29.36	12.52	4.48	0.06		0.04	0.20	99.5
Pl		B	7 / 2 .	642.2865	G	rim	53.26	29.32	12.13	4.65	0.05		0.02	0.16	99.6
Pl		B	7 / 3 .	642.2865	G	core	52.14	29.84	12.70	4.18	0.03		0.02	0.17	99.1
Pl		B	7 / 4 .	642.2865	G	rim	52.11	30.11	13.16	3.96	0.05		0.02	0.17	99.6
Pl	360_70R7_58a	B	7 / 5 .	642.2865	F	core	53.64	29.81	12.38	4.49	0.03		0.03	0.27	100.6
Pl		B	7 / 6 .	642.2865	F	core	51.08	31.09	14.19	3.58	0.04		0.02	0.26	100.3
Pl		C	11 / 1 .	642.288	F	core	52.97	29.66	12.59	4.46	0.09		0.01	0.21	100.0
Pl		C	11 / 2 .	642.288	F	rim	53.46	29.04	12.12	4.47	0.07		0.02	0.19	99.4
Pl		C	11 / 3 .	642.288	G	core	52.77	29.67	12.78	4.20	0.06		0.01	0.20	99.7
Pl		C	11 / 4 .	642.288	G	rim	52.50	29.62	12.58	4.40	0.06		0.03	0.23	99.4
Pl		D	13 / 2 .	642.298	G	rim	53.08	29.50	12.36	4.41	0.05		0.02	0.16	99.6
Pl		D	13 / 3 .	642.298	G	core	52.82	29.62	12.46	4.58	0.08		0.02	0.22	99.8
Pl		D	13 / 4 .	642.298	F	core	51.45	30.82	13.51	3.80	0.05		0.00	0.28	99.9
Pl		D	13 / 5 .	642.298	G	rim	53.61	29.09	11.99	4.78	0.01		0.01	0.19	99.7
Pl		D	13 / 6 .	642.298	G	core	52.63	30.17	12.86	4.19	0.05		0.03	0.21	100.2
Pl		E	17 / 1 .	642.2975	G	rim	53.06	29.85	12.26	4.48	0.04		0.03	0.31	100.0
Pl		E	17 / 2 .	642.2975	G	core	53.68	29.04	11.98	4.65	0.06		0.03	0.30	99.7
Pl		E	17 / 3 .	642.2975	F	core	53.44	29.67	12.23	4.46	0.06		0.03	0.19	100.1
Pl		E	17 / 4 .	642.2975	F	rim	49.26	32.02	15.12	3.01	0.05		0.02	0.20	99.7
Pl		A	4 / 1 .	659.623	F	core	53.99	29.16	11.72	4.78	0.07		0.02	0.27	100.0
Pl		A	4 / 2 .	659.623	F	rim	53.58	29.35	11.95	4.79	0.04		0.03	0.28	100.0
Pl		A	4 / 3 .	659.623	G	core	52.77	29.78	12.54	4.37	0.09		0.03	0.28	99.9
Pl		A	4 / 4 .	659.623	G	rim	54.86	28.59	11.06	5.37	0.11		0.01	0.27	100.3
Pl		A	4 / 5 .	659.623	G	rim	53.70	29.03	11.85	4.86	0.05		0.02	0.32	99.8
Pl		B	6 / 2 .	659.6265	F	core	53.49	29.21	12.03	4.65	0.04		0.01	0.28	99.7
Pl		B	6 / 3 .	659.6265	F	core	53.24	29.32	11.96	4.60	0.06		0.00	0.22	99.4
Pl		B	6 / 4 .	659.6265	G	core	54.27	28.63	11.23	4.99	0.08		0.03	0.21	99.4
Pl		B	6 / 5 .	659.6265	G	rim	53.02	29.64	12.33	4.41	0.10		0.01	0.21	99.7

Mineral		Area	Point	Depth (mbsf)	Grain size	Grain area	SiO2	Al2O3	CaO	Na2O	K2O	MnO	MgO	FeO	Total
Pl	360_74R6_27	B	6 / 6 .	659.6265	G	rim	53.28	29.57	12.31	4.51	0.07		0.02	0.30	100.1
Pl		B	6 / 7 .	659.6265	G	core	52.67	29.60	13.04	4.26	0.04		0.02	0.30	99.9
Pl		C	8 / 1 .	659.624	G	core	52.55	29.94	12.73	4.18	0.02		0.02	0.25	99.7
Pl		C	8 / 2 .	659.624	G	core	53.65	29.23	11.90	4.69	0.07		0.02	0.29	99.9
Pl		C	8 / 3 .	659.624	F	core	53.29	29.18	12.04	4.55	0.06		0.02	0.21	99.3
Pl		C	8 / 4 .	659.624	G	rim	53.86	29.08	11.63	4.95	0.09		0.02	0.23	99.9
Pl		C	8 / 5 .	659.624	F	core	53.54	29.39	12.14	4.66	0.02		0.00	0.24	100.0
Pl		D	12 / 2 .	659.633	G	rim	53.89	29.24	11.79	4.84	0.08		0.01	0.24	100.1
Pl		D	12 / 3 .	659.633	G	core	53.93	28.90	11.50	5.02	0.09		0.04	0.25	99.7
Pl		D	12 / 4 .	659.633	G	core	53.90	28.88	11.47	5.00	0.08		0.03	0.24	99.6
Pl		E	17 / 1 .	659.639	G	core	52.68	29.75	12.59	4.40	0.10		0.03	0.23	99.8
Pl		E	17 / 2 .	659.639	G	rim	53.83	29.29	11.97	4.76	0.10		0.04	0.25	100.2
Pl		E	17 / 3 .	659.639	G	rim	54.35	28.50	11.41	5.15	0.08		0.03	0.32	99.8
Pl		E	17 / 4 .	659.639	G	core	52.70	29.70	12.80	4.34	0.08		0.02	0.24	99.9
Pl		F	19 / 2 .	659.646	F	core	53.78	29.34	11.76	4.89	0.08		0.02	0.24	100.1
Pl		F	19 / 3 .	659.646	F	rim	52.03	30.13	13.26	4.10	0.04		0.02	0.29	99.9
Pl		F	19 / 4 .	659.646	G	rim	54.06	28.90	11.42	4.99	0.07		0.02	0.21	99.7
Pl		F	19 / 5 .	659.646	G	core	53.02	29.85	12.75	4.25	0.07		0.04	0.29	100.3
Pl		A	1 / 1 .	671.1955	G	core	53.71	29.35	12.20	4.69	0.06		0.02	0.17	100.2
Pl		A	2 / 1 .	671.1955	G	rim	53.45	29.50	12.19	4.55	0.05		0.01	0.19	99.9
Pl		A	2 / 3 .	671.1955	F	core	53.31	29.30	12.13	4.54	0.06		0.05	0.18	99.6
Pl		A	2 / 4 .	671.1955	F	rim	50.41	30.86	14.23	3.31	0.05		0.02	0.20	99.1
Pl		A	2 / 5 .	671.1955	G	core	53.56	29.45	12.10	4.59	0.04		0.03	0.17	99.9
Pl		A	2 / 6 .	671.1955	G	rim	50.75	31.44	14.52	3.34	0.02		0.01	0.13	100.2
Pl		B	7 / 2 .	671.1985	F	core	53.18	29.19	12.17	4.65	0.03		0.03	0.16	99.4
Pl		B	7 / 3 .	671.1985	G	core	52.34	29.65	12.41	4.27	0.09		0.04	0.33	99.1
Pl		B	7 / 4 .	671.1985	F	core	53.09	29.17	11.97	4.78	0.04		0.03	0.18	99.3
Pl		B	7 / 5 .	671.1985	G	rim	53.24	29.65	12.28	4.44	0.06		0.01	0.16	99.8
Pl		C	8 / 1 .	671.197	G	rim	54.08	29.06	11.56	4.90	0.06		0.03	0.17	99.9
Pl		C	8 / 2 .	671.197	G	core	52.76	29.70	12.43	4.30	0.04		0.03	0.25	99.5
Pl		C	8 / 3 .	671.197	F	rim	53.54	29.52	12.04	4.65	0.03		0.04	0.22	100.0
Pl		C	8 / 4 .	671.197	F	core	53.84	28.65	11.63	4.95	0.08		0.02	0.15	99.3
Pl		C	8 / 6 .	671.197	F	core	53.55	29.17	11.95	4.60	0.02		0.01	0.14	99.4
Pl		D	11 / 1 .	671.2055	F	core	53.35	29.52	12.14	4.60	0.05		0.01	0.17	99.8
Pl	7_56	D	11 / 2 .	671.2055	F	core	53.47	29.63	12.37	4.60	0.07		0.03	0.20	100.4
Pl		D	11 / 3 .	671.2055	F	core	53.93	29.00	12.00	4.78	0.03		0.03	0.18	99.9

Mineral	360_75R	Area	Point	Depth (mbsf)	Grain size	Grain area	SiO2	Al2O3	CaO	Na2O	K2O	MnO	MgO	FeO	Total
Pl		D	11 / 4 .	671.2055	F	core	53.43	29.48	12.05	4.61	0.06		0.03	0.17	99.8
Pl		D	11 / 5 .	671.2055	G	core	53.05	29.30	12.21	4.68	0.05		0.03	0.17	99.5
Pl		E	14 / 1 .	671.212	G	rim	52.13	29.64	12.97	4.26	0.04		0.01	0.11	99.2
Pl		E	14 / 2 .	671.212	G	core	53.48	29.38	12.25	4.41	0.07		0.04	0.19	99.8
Pl		E	14 / 3 .	671.212	G	rim	50.66	30.96	14.07	3.39	0.04		0.02	0.21	99.3
Pl		E	14 / 4 .	671.212	G	core	52.99	29.43	12.31	4.35	0.08		0.03	0.15	99.3
Pl		F	17 / 1 .	671.218	F	core	53.23	29.55	12.31	4.41	0.05		0.03	0.17	99.8
Pl		F	17 / 2 .	671.218	G	core	53.59	29.14	11.93	4.88	0.07		0.04	0.19	99.8
Pl		F	17 / 3 .	671.218	G	rim	53.82	29.20	11.73	4.81	0.06		0.04	0.15	99.8
Pl		F	17 / 4 .	671.218	F	core	53.01	29.50	12.68	4.45	0.05		0.01	0.16	99.9
Pl		F	17 / 5 .	671.218	F	core	53.13	29.11	12.09	4.47	0.09		0.04	0.25	99.2
Pl		F	17 / 6 .	671.218	F	core	49.86	31.81	15.05	3.01	0.01		0.05	0.23	100.0
Pl		G	20 / 2 .	671.2165	F	core	49.76	31.83	15.13	2.88	0.05		0.03	0.23	99.9
Pl		G	20 / 3 .	671.2165	F	core	53.94	29.05	11.60	4.94	0.07		0.01	0.17	99.8
Pl		G	20 / 4 .	671.2165	F	core	51.61	30.38	13.67	3.80	0.06		0.04	0.17	99.7
Pl		G	20 / 5 .	671.2165	F	core	53.19	29.66	12.14	4.53	0.05		0.02	0.17	99.8
Pl		A	4 / 1 .	699.004	F	core	53.10	29.47	12.61	4.37	0.06		0.02	0.26	99.9
Pl		A	4 / 2 .	699.004	F	rim	50.55	30.97	13.97	3.49	0.03		0.00	0.37	99.4
Pl		A	4 / 3 .	699.004	G	rim	53.47	28.92	11.85	4.56	0.08		0.04	0.49	99.4
Pl		A	4 / 4 .	699.004	G	core	52.48	29.95	13.05	4.26	0.05		0.04	0.32	100.2
Pl		B	8 / 1 .	699.0065	G	rim	53.25	29.17	12.01	4.63	0.08		0.03	0.22	99.4
Pl		B	8 / 2 .	699.0065	G	core	54.00	28.79	11.55	4.99	0.08		0.04	0.25	99.7
Pl		B	8 / 3 .	699.0065	F	core	52.46	29.72	12.68	4.10	0.04		0.01	0.19	99.2
Pl	360_79R6_1a	C	12 / 1 .	699.014	F	core	53.90	28.98	11.70	4.67	0.07		0.02	0.24	99.6
Pl		C	12 / 2 .	699.014	F	rim	53.87	28.96	11.96	4.70	0.07		0.03	0.27	99.9
Pl		C	12 / 3 .	699.014	G	rim	54.05	28.70	11.48	4.95	0.06		0.04	0.23	99.5
Pl		C	12 / 4 .	699.014	G	core	53.84	28.35	11.51	4.95	0.07		0.04	0.28	99.0
Pl		C	12 / 5 .	699.014	G	core	51.93	30.35	13.57	3.99	0.04		0.03	0.27	100.2
Pl		D	13 / 1 .	699.022	F	core	53.85	28.72	11.62	4.80	0.08		0.03	0.20	99.3
Pl		D	13 / 2 .	699.022	F	core	53.80	28.76	11.81	4.71	0.07		0.03	0.23	99.4
Pl		D	13 / 3 .	699.022	F	core	53.61	28.82	11.73	4.83	0.08		0.04	0.28	99.4
Pl		D	13 / 4 .	699.022	G	core	51.65	29.83	13.03	4.07	0.09		0.04	0.28	99.0
Pl		D	13 / 5 .	699.022	G	rim	54.80	28.09	10.94	5.41	0.05		0.02	0.19	99.5
Pl		D	13 / 6 .	699.022	F	core	52.29	29.88	13.01	4.03	0.03		0.04	0.27	99.5
Pl		D	13 / 7 .	699.022	F	rim	52.22	30.14	13.30	4.07	0.04		0.04	0.30	100.1
Pl		A	1 / 1 .	723.533	F	core	52.37	29.63	12.46	4.36	0.07		0.02	0.18	99.1

Mineral		Area	Point	Depth (mbsf)	Grain size	Grain area	SiO2	Al2O3	CaO	Na2O	K2O	MnO	MgO	FeO	Total
Pl		A	2 / 1 .	723.533	G	rim	53.13	29.60	12.42	4.68	0.08		0.01	0.15	100.1
Pl		A	2 / 2 .	723.533	G	core	52.05	30.12	13.05	4.15	0.07		0.04	0.18	99.7
Pl		A	2 / 3 .	723.533	G	rim	52.34	30.25	13.05	4.04	0.06		0.02	0.18	99.9
Pl		A	2 / 4 .	723.533	F	core	50.92	30.98	14.20	3.65	0.03		0.01	0.36	100.2
Pl		B	5 / 1 .	723.5395	F	core	52.98	29.71	12.54	4.42	0.04		0.01	0.19	99.9
Pl		B	5 / 2 .	723.5395	F	core	53.08	29.88	12.57	4.36	0.04		0.03	0.18	100.2
Pl		B	5 / 3 .	723.5395	F	core	53.03	29.81	12.25	4.26	0.03		0.02	0.19	99.6
Pl		B	5 / 4 .	723.5395	F	core	51.82	30.68	13.59	3.82	0.00		0.01	0.34	100.3
Pl		B	5 / 5 .	723.5395	G	core	53.34	29.58	12.08	4.65	0.07		0.01	0.07	99.8
Pl		B	5 / 6 .	723.5395	G	rim	52.98	30.11	12.38	4.36	0.04		0.02	0.16	100.0
Pl		B	5 / 7 .	723.5395	G	rim	52.24	30.24	13.37	4.06	0.01		0.02	0.14	100.1
Pl		B	5 / 8 .	723.5395	G	core	52.53	30.04	12.88	4.18	0.02		0.01	0.21	99.9
Pl		B	5 / 9 .	723.5395	G	rim	52.94	29.38	12.30	4.58	0.08		0.01	0.17	99.5
Pl		C	9 / 1 .	723.537	F	rim	52.80	29.86	12.21	4.48	0.01		0.03	0.28	99.7
Pl	360_82R3_19a	C	9 / 2 .	723.537	F	core	52.48	30.33	13.19	4.15	0.06		0.04	0.18	100.4
Pl		C	9 / 3 .	723.537	G	rim	53.50	29.49	12.17	4.60	0.05		0.03	0.19	100.0
Pl		C	9 / 4 .	723.537	G	core	53.58	29.53	11.98	4.81	0.05		0.01	0.12	100.1
Pl		D	12 / 2 .	723.548	F	core	53.19	29.34	12.27	4.64	0.03		0.03	0.23	99.7
Pl		D	12 / 3 .	723.548	F	core	51.50	30.82	13.70	3.76	0.06		0.02	0.21	100.1
Pl		D	12 / 4 .	723.548	G	rim	51.72	30.62	13.62	3.93	0.01		0.03	0.19	100.1
Pl		D	12 / 5 .	723.548	G	core	53.96	29.06	11.85	4.83	0.01		0.04	0.19	99.9
Pl		D	12 / 6 .	723.548	G	rim	51.84	30.07	13.05	4.25	0.04		0.03	0.19	99.5
Pl		E	14 / 1 .	723.552	F	core	52.93	29.67	12.49	4.54	0.02		0.03	0.17	99.9
Pl		E	14 / 2 .	723.552	G	core	52.36	30.27	13.02	4.18	0.04		0.02	0.16	100.0
Pl		E	14 / 3 .	723.552	G	rim	52.68	29.94	12.77	4.29	0.05		0.02	0.15	99.9
Pl		G	20 / 1 .	723.562	F	core	53.21	29.36	12.05	4.56	0.03		0.01	0.22	99.4
Pl		G	20 / 2 .	723.562	G	core	54.24	28.79	11.15	5.08	0.05		0.04	0.21	99.5
Pl		G	20 / 3 .	723.562	G	rim	54.06	28.77	11.48	5.12	0.06		0.02	0.15	99.7
Pl		A	1 / 1 .	707.954	G	rim	52.75	29.81	12.46	4.37	0.04		0.02	0.19	99.7
Pl		A	2 / 1 .	707.954	G	core	51.97	30.09	13.06	4.14	0.03		0.03	0.24	99.6
Pl		B	8 / 1 .	707.958	F	core	53.25	29.57	12.54	4.56	0.06		0.02	0.18	100.2
Pl		B	8 / 2 .	707.958	F	core	52.50	29.77	12.68	4.26	0.06		0.02	0.21	99.5
Pl		B	8 / 3 .	707.958	G	core	53.33	29.57	12.48	4.48	0.03		0.03	0.22	100.1
Pl		B	8 / 4 .	707.958	G	rim	53.47	28.71	11.44	4.87	0.01		0.04	0.18	98.7
Pl		C	12 / 1 .	707.962	G	rim	52.60	29.71	12.26	4.40	0.00		0.01	0.21	99.2
Pl		C	12 / 3 .	707.962	G	core	51.77	30.18	12.95	4.19	0.01		0.04	0.22	99.4

Mineral		Area	Point	Depth (mbsf)	Grain size	Grain area	SiO2	Al2O3	CaO	Na2O	K2O	MnO	MgO	FeO	Total
Pl	360_80R6_64b	C	12 / 4 .	707.962	G	rim	52.22	30.03	12.93	4.03	0.05		0.04	0.21	99.5
Pl		D	14 / 3 .	707.967	G	core	54.05	28.35	11.23	5.18	0.04		0.03	0.22	99.1
Pl		D	14 / 4 .	707.967	G	rim	51.93	30.34	13.15	4.05	0.05		0.03	0.24	99.8
Pl		D	14 / 5 .	707.967	G	core	53.31	29.35	12.06	4.50	0.04		0.03	0.18	99.5
Pl		E	16 / 1 .	707.97	F	core	52.05	30.08	13.20	4.13	0.02		0.02	0.18	99.7
Pl		E	16 / 2 .	707.97	G	core	52.30	30.04	13.12	4.06	0.03		0.03	0.23	99.8
Pl		E	16 / 3 .	707.97	G	rim	52.90	29.33	12.18	4.41	0.07		0.03	0.22	99.1
Pl		E	16 / 4 .	707.97	G	core	51.52	30.14	12.99	4.10	0.06		0.01	0.22	99.0
Pl		F	20 / 1 .	707.9795	F	rim	54.77	28.41	10.93	5.24	0.07		0.04	0.25	99.7
Pl		F	20 / 2 .	707.9795	F	rim	54.47	28.99	11.12	5.14	0.06		0.02	0.22	100.0
Pl		F	20 / 4 .	707.9795	G	rim	53.57	29.00	11.60	4.76	0.09		0.02	0.22	99.3
Pl		F	20 / 5 .	707.9795	G	core	51.95	30.25	13.02	3.97	0.08		0.02	0.20	99.5
Pl		G	21 / 1 .	707.977	G	rim	53.51	28.85	11.36	4.97	0.04		0.04	0.21	99.0
Pl		G	21 / 3 .	707.977	G	rim	53.31	28.95	11.72	4.90	0.05		0.04	0.20	99.2
Pl		G	21 / 4 .	707.977	G	core	52.25	30.17	13.09	3.97	0.02		0.01	0.25	99.8
Pl		G	21 / 5 .	707.977	G	rim	53.80	28.73	11.12	5.06	0.04		0.03	0.21	99.0
Pl		G	21 / 6 .	707.977	G	core	53.64	29.15	11.66	4.99	0.07		0.03	0.26	99.8
Pl		G	21 / 7 .	707.977	G	rim	54.29	28.27	10.97	5.13	0.07		0.04	0.21	99.0
Pl		A	1 / 1 .	406.374	G	core	55.25	28.03	10.77	5.43	0.09		0.02	0.22	99.8
Pl		A	1 / 2 .	406.374	G	rim	54.41	28.77	11.46	4.95	0.04		0.02	0.19	99.8
Pl		A	2 / 1 .	406.374	F	core	55.13	28.08	10.79	5.51	0.10	0.00		0.21	99.8
Pl		A	2 / 2 .	406.374	F	core	55.95	27.90	10.88	5.35	0.10	0.01		0.24	100.4
Pl		A	2 / 3 .	406.374	F	rim	54.60	28.19	11.21	5.12	0.08	0.00		0.22	99.4
Pl		A	2 / 4 .	406.374	F	core	55.04	27.94	10.57	5.39	0.08	0.03		0.34	99.4
Pl		A	2 / 5 .	406.374	F	rim	54.80	27.99	10.91	5.31	0.08	0.02		0.33	99.4
Pl		A	3 / 1 .	406.374	G	core	55.06	27.96	10.71	5.47	0.09	0.00		0.27	99.6
Pl		A	3 / 2 .	406.374	G	rim	54.92	28.68	11.02	5.25	0.07	0.00		0.22	100.2
Pl		B	7 / 2 .	406.382	F	core	55.60	27.76	10.70	5.33	0.09		0.04	0.25	99.8
Pl		B	10 / 1 .	406.382	F	rim	55.05	28.25	11.16	5.20	0.09		0.03	0.29	100.1
Pl		B	11 / 1 .	406.382	G	core	54.37	28.35	11.36	5.01	0.10	0.00		0.30	99.5
Pl		B	11 / 2 .	406.382	G	rim	54.99	27.82	10.47	5.16	0.12	0.00		0.34	98.9
Pl		B	11 / 3 .	406.382	F	core	55.81	27.71	10.40	5.39	0.13	0.03		0.29	99.8
Pl		B	11 / 4 .	406.382	F	rim	54.67	28.27	11.20	5.13	0.06	0.03		0.33	99.7
Pl		C	16 / 1 .	406.3815	G	core	54.61	28.50	11.35	4.90	0.06		0.02	0.22	99.7
Pl		C	16 / 2 .	406.3815	G	rim	54.09	29.11	11.67	4.88	0.05		0.01	0.26	100.1
Pl		C	17 / 1 .	406.3815	G	rim	53.85	28.48	11.80	4.95	0.08	0.01		0.27	99.4

Mineral		Area	Point	Depth (mbsf)	Grain size	Grain area	SiO2	Al2O3	CaO	Na2O	K2O	MnO	MgO	FeO	Total
Pl	360_44R5_0	C	17 / 2 .	406.3815	G	core	54.40	28.57	11.30	5.11	0.05	0.03		0.17	99.6
Pl		C	17 / 3 .	406.3815	F	core	54.48	28.90	11.79	4.97	0.05	0.01		0.30	100.5
Pl		C	17 / 4 .	406.3815	F	rim	54.48	28.62	11.49	4.98	0.05	0.00		0.23	99.8
Pl		Cbis	19 / 1 .	406.3815	F	core	54.76	28.61	11.26	5.05	0.09	0.04		0.23	100.0
Pl		Cbis	19 / 2 .	406.3815	F	rim	54.59	28.68	11.16	5.28	0.09	0.02		0.12	99.9
Pl		Cbis	19 / 3 .	406.3815	F	core	54.58	28.52	11.13	5.17	0.07	0.00		0.23	99.7
Pl		Cbis	19 / 4 .	406.3815	F	rim	54.31	28.68	11.52	5.00	0.09	0.04		0.26	99.9
Pl		Cbis	19 / 5 .	406.3815	F	core	54.65	28.37	11.00	5.16	0.07	0.02		0.23	99.5
Pl		D	22 / 1 .	406.3905	F	core	54.79	28.38	11.12	5.18	0.07		0.03	0.19	99.8
Pl		D	22 / 2 .	406.3905	F	rim	54.82	28.53	11.01	5.19	0.14		0.01	0.22	99.9
Pl		D	23 / 1 .	406.3905	G	rim	54.86	28.92	11.37	4.93	0.05	0.00		0.21	100.3
Pl		D	23 / 2 .	406.3905	G	core	54.72	28.66	11.45	5.14	0.05	0.00		0.21	100.2
Pl		D	23 / 3 .	406.3905	F	core	54.25	28.28	11.35	4.98	0.07	0.00		0.19	99.1
Pl		D	23 / 4 .	406.3905	F	rim	54.65	28.39	11.24	5.13	0.11	0.01		0.26	99.8
Pl		E	26 / 1 .	406.389	F	core	54.24	28.55	11.53	4.77	0.08	0.00		0.24	99.4
Pl		E	26 / 2 .	406.389	F	rim	53.10	29.04	12.24	4.41	0.04	0.02		0.34	99.2
Pl		E	26 / 3 .	406.389	F	core	54.75	27.74	10.67	5.40	0.06	0.02		0.46	99.1
Pl		E	26 / 4 .	406.389	F	rim	54.97	28.23	10.74	5.17	0.06	0.00		0.25	99.4
Pl		E	26 / 5 .	406.389	F	core	54.38	28.29	11.06	5.05	0.05	0.03		0.25	99.1
Pl		E	27 / 1 .	406.389	F	core	54.48	28.20	11.30	5.13	0.11		0.02	0.25	99.5
Pl		Ebis	31 / 1 .	406.3905	G	core	54.50	28.41	11.17	5.01	0.05	0.01		0.33	99.5
Pl		Ebis	31 / 2 .	406.3905	G	rim	54.49	28.49	11.24	4.92	0.07	0.00		0.18	99.4
Pl		F	34 / 1 .	406.396	G	core	54.90	28.43	11.15	5.14	0.08	0.00		0.27	100.0
Pl		F	34 / 2 .	406.396	G	rim	54.00	28.80	12.03	4.62	0.04	0.00		0.23	99.7
Pl		F	34 / 3 .	406.396	F	core	54.36	28.58	11.52	4.76	0.05	0.00		0.23	99.5
Pl		F	34 / 4 .	406.396	F	rim	53.12	29.00	12.26	4.58	0.07	0.00		0.21	99.2
Pl		F	35 / 1 .	406.396	F	core	53.75	28.60	11.42	4.74	0.09		0.02	0.25	98.9
Pl		Abis	1 / 1 .	390.484	F	core	54.86	28.44	11.02	5.09	0.05	0.03		0.22	99.7
Pl		Abis	2 / 1 .	390.484	F	rim	54.38	28.47	10.94	4.90	0.06	0.02		0.18	98.9
Pl		Abis	2 / 2 .	390.484	G	rim	53.54	29.09	12.02	4.61	0.02	0.01		0.26	99.6
Pl		Abis	2 / 3 .	390.484	G	core	53.98	29.21	12.06	4.67	0.07	0.01		0.16	100.2
Pl		Abis	2 / 4 .	390.484	F	core	54.06	29.22	11.43	4.82	0.06	0.01		0.21	99.8
Pl		A	5 / 1 .	390.486	G	rim	53.82	28.77	11.88	4.74	0.05	0.00		0.18	99.4
Pl		A	5 / 2 .	390.486	G	rim	55.05	28.42	10.64	5.31	0.09	0.04		0.21	99.8
Pl		A	5 / 3 .	390.486	F	core	54.45	28.83	11.68	4.85	0.03	0.01		0.24	100.1
Pl		A	5 / 4 .	390.486	F	rim	55.05	28.16	11.19	5.10	0.05	0.01		0.26	99.8

Mineral		Area	Point	Depth (mbsf)	Grain size	Grain area	SiO2	Al2O3	CaO	Na2O	K2O	MnO	MgO	FeO	Total
Pl		A	5 / 5 .	390.486	G	core	53.64	29.10	12.39	4.62	0.06	0.00		0.17	100.0
Pl		A	5 / 6 .	390.486	G	rim	53.75	29.00	12.05	4.55	0.06	0.01		0.20	99.6
Pl		A	6 / 2 .	390.486	G	rim	53.52	29.24	12.09	4.47	0.06		0.02	0.20	99.6
Pl		B	8 / 2 .	390.4975	G	rim	54.61	28.56	11.46	5.08	0.04	0.00		0.13	99.9
Pl		B	8 / 3 .	390.4975	G	core	54.65	28.24	11.32	4.93	0.08	0.00		0.13	99.3
Pl	360_43R1_105	Cbis	12 / 1 .	390.4965	F	rim	54.00	28.57	11.55	4.88	0.08	0.01		0.24	99.3
Pl		Cbis	12 / 2 .	390.4965	F	core	54.43	28.43	11.59	5.00	0.09	0.00		0.17	99.7
Pl		C	14 / 1 .	390.498	F	core	54.66	28.44	11.09	5.15	0.08	0.02		0.28	99.7
Pl		C	14 / 2 .	390.498	F	core	54.09	28.67	11.58	4.79	0.09	0.04		0.17	99.4
Pl		C	15 / 1 .	390.498	F	core	53.75	28.93	12.08	4.59	0.06		0.00	0.25	99.7
Pl		C	15 / 2 .	390.498	F	core	54.17	28.41	11.60	4.94	0.02		0.01	0.13	99.3
Pl		C	15 / 4 .	390.498	F	core	54.24	28.31	11.38	4.90	0.06		0.03	0.39	99.3
Pl		D	17 / 2 .	390.495	G	rim	54.60	28.62	11.34	5.03	0.08	0.02		0.17	99.9
Pl		D	17 / 3 .	390.495	G	core	54.05	28.46	11.74	4.80	0.04	0.01		0.30	99.4
Pl		D	17 / 4 .	390.495	G	rim	53.96	28.63	11.55	4.84	0.05	0.00		0.21	99.2
Pl		D	17 / 5 .	390.495	F	rim	54.81	28.65	11.53	5.01	0.06	0.00		0.16	100.2
Pl		D	17 / 6 .	390.495	F	core	54.62	28.26	11.64	5.12	0.07	0.03		0.20	99.9
Pl		E	20 / 1 .	390.511	F	core	54.72	27.94	10.89	5.31	0.05	0.03		0.17	99.1
Pl		E	20 / 2 .	390.511	F	rim	55.19	28.25	10.79	5.31	0.10	0.02		0.42	100.1
Pl		Ebis	22 / 1 .	390.509	F	core	54.05	28.48	11.53	5.04	0.04	0.02		0.26	99.4
Pl		Ebis	22 / 2 .	390.509	F	rim	53.11	29.18	12.13	4.34	0.03	0.00		0.35	99.1
Pl		Ebis	22 / 3 .	390.509	F	rim	54.76	28.89	11.82	4.73	0.04	0.02		0.23	100.5
Pl		Ebis	22 / 4 .	390.509	F	core	53.86	28.75	12.08	4.60	0.03	0.00		0.24	99.6
Pl		Ebis	23 / 1 .	390.509	F	rim	54.20	28.89	11.76	4.95	0.04		0.04	0.24	100.1
Pl		Ebis	23 / 2 .	390.509	F	core	53.93	28.64	11.44	4.72	0.06		0.03	0.21	99.0
Pl		F	24 / 1 .	390.503	G	core	54.27	28.50	11.39	4.89	0.06	0.00		0.20	99.3
Pl		F	24 / 2 .	390.503	G	rim	54.12	28.55	11.46	4.87	0.06	0.00		0.18	99.2
Pl		A	4 / 1 .	372.854	G	core	54.90	28.66	11.30	4.92	0.04	0.00		0.19	100.0
Pl		A	4 / 2 .	372.854	G	rim	55.30	28.24	10.69	5.18	0.08	0.02		0.20	99.7
Pl		A	4 / 3 .	372.854	G	rim	55.49	28.08	10.74	5.36	0.04	0.03		0.08	99.8
Pl		A	4 / 4 .	372.854	F	core	54.92	28.25	10.87	5.07	0.10	0.00		0.16	99.4
Pl		A	4 / 5 .	372.854	F	rim	55.88	27.43	10.35	5.51	0.02	0.01		0.19	99.4
Pl		A	4 / 7 .	372.854	F	core	54.84	28.46	11.29	5.06	0.10	0.03		0.22	100.0
Pl		A	5 / 1 .	372.854	F	core	55.23	28.22	11.27	5.38	0.11		0.01	0.23	100.4
Pl		B	9 / 1 .	372.855	F	core	55.69	27.93	10.53	5.43	0.06	0.00		0.16	99.8
Pl		B	9 / 2 .	372.855	F	core	54.54	28.50	11.23	5.01	0.08	0.03		0.14	99.5

Mineral		Area	Point	Depth (mbsf)	Grain size	Grain area	SiO2	Al2O3	CaO	Na2O	K2O	MnO	MgO	FeO	Total
Pl		B	9 / 3 .	372.855	G	rim	54.62	28.76	11.15	4.99	0.11	0.00		0.15	99.8
Pl		B	9 / 4 .	372.855	G	core	54.66	28.36	11.32	4.98	0.08	0.00		0.20	99.6
Pl		B	9 / 5 .	372.855	G	rim	54.48	28.69	11.32	4.93	0.08	0.00		0.15	99.7
Pl		B	9 / 6 .	372.855	F	core	55.30	28.86	11.26	5.08	0.06	0.00		0.21	100.8
Pl	360_41R2_1	C	12 / 1 .	372.8655	F	core	55.02	28.41	11.12	5.29	0.08	0.00		0.14	100.1
Pl		C	12 / 2 .	372.8655	F	rim	55.56	28.01	10.63	5.26	0.10	0.00		0.19	99.8
Pl		C	12 / 3 .	372.8655	F	core	55.87	27.94	10.38	5.57	0.09	0.00		0.15	100.0
Pl		C	13 / 1 .	372.8655	F	core	55.12	28.22	10.97	5.15	0.05		0.01	0.15	99.7
Pl		C	13 / 2 .	372.8655	F	rim	55.43	28.15	10.82	5.37	0.08		0.02	0.17	100.0
Pl		Cbis	17 / 1 .	372.868	F	core	55.47	28.23	10.93	5.25	0.06	0.04		0.17	100.1
Pl		Cbis	17 / 2 .	372.868	F	rim	55.49	28.16	10.85	5.25	0.09	0.00		0.22	100.1
Pl		Cbis	18 / 1 .	372.868	F	core	55.01	28.24	10.93	5.19	0.05		0.01	0.12	99.6
Pl		D	20 / 1 .	372.8745	G	rim	55.03	28.03	10.95	5.25	0.06	0.03		0.18	99.5
Pl		D	20 / 2 .	372.8745	G	core	55.09	28.50	11.18	4.98	0.06	0.00		0.22	100.0
Pl		D	20 / 3 .	372.8745	G	rim	54.70	28.42	11.06	4.96	0.06	0.08		0.18	99.5
Pl		D	20 / 4 .	372.8745	F	core	55.95	28.19	10.77	5.28	0.08	0.01		0.15	100.4
Pl		E	24 / 1 .	372.873	G	rim	54.83	28.62	11.63	5.06	0.09	0.00		0.15	100.4
Pl		E	24 / 2 .	372.873	G	core	54.52	28.61	11.25	4.96	0.08	0.02		0.21	99.7
Pl		E	24 / 3 .	372.873	F	core	55.77	28.10	10.49	5.37	0.07	0.01		0.14	99.9
Pl		A	27 / 1 .	449.604	G	core	53.06	29.82	12.60	4.34	0.08	0.00		0.30	100.2
Pl		A	27 / 2 .	449.604	G	rim	54.08	29.31	12.02	4.64	0.06	0.01		0.19	100.3
Pl		A	27 / 3 .	449.604	F	core	54.86	28.78	11.32	5.06	0.08	0.01		0.19	100.3
Pl		A	27 / 4 .	449.604	F	core	54.75	28.63	11.42	4.96	0.07	0.00		0.18	100.0
Pl		A	28 / 1 .	449.604	G	core	53.66	29.62	12.28	4.39	0.05		0.02	0.22	100.2
Pl		A	28 / 2 .	449.604	G	rim	54.02	29.30	12.06	4.73	0.01		0.01	0.22	100.4
Pl		B	31 / 1 .	449.6093	G	core	52.85	29.73	12.63	4.28	0.03	0.02		0.22	99.8
Pl		B	31 / 2 .	449.6093	G	rim	54.42	29.23	11.59	4.79	0.04	0.00		0.26	100.3
Pl		B	31 / 3 .	449.6093	F	core	55.02	28.54	10.91	5.08	0.07	0.00		0.21	99.8
Pl		B	31 / 4 .	449.6093	F	rim	55.02	28.38	11.30	5.12	0.07	0.00		0.37	100.2
Pl		B	31 / 5 .	449.6093	F	core	54.81	28.60	11.36	5.09	0.05	0.00		0.22	100.1
Pl		C	5 / 1 .	449.6115	G	core	55.20	28.20	10.75	5.18	0.06		0.03	0.22	99.6
Pl		C	5 / 2 .	449.6115	G	rim	53.96	29.32	11.73	4.74	0.04		0.00	0.24	100.0
Pl		C	6 / 1 .	449.6115	G	core	55.43	28.40	10.77	5.31	0.07	0.00		0.18	100.2
Pl		C	6 / 2 .	449.6115	G	rim	53.74	29.46	12.27	4.67	0.03	0.00		0.30	100.5
Pl		C	6 / 3 .	449.6115	F	core	54.91	29.07	11.32	5.00	0.04	0.00		0.12	100.5
Pl	360_50R1_73	C	6 / 4 .	449.6115	F	core	54.59	29.00	11.59	4.80	0.03	0.00		0.15	100.2

Mineral		Area	Point	Depth (mbsf)	Grain size	Grain area	SiO2	Al2O3	CaO	Na2O	K2O	MnO	MgO	FeO	Total
Pl		D	11 / 1 .	449.615	F	core	55.50	28.46	10.70	5.48	0.07	0.03		0.17	100.4
Pl		D	11 / 2 .	449.615	F	core	54.51	28.64	11.31	4.89	0.08	0.00		0.30	99.7
Pl		D	11 / 3 .	449.615	F	rim	54.75	28.63	11.35	5.12	0.04	0.00		0.17	100.1
Pl		E	13 / 1 .	449.624	F	core	55.02	28.62	11.18	5.15	0.05	0.02		0.26	100.3
Pl		E	13 / 2 .	449.624	F	core	54.71	28.82	11.30	4.85	0.05	0.01		0.14	99.9
Pl		E	13 / 3 .	449.624	F	rim	54.59	28.88	11.82	4.91	0.02	0.05		0.18	100.4
Pl		E	13 / 4 .	449.624	G	rim	54.06	29.25	11.60	4.71	0.04	0.00		0.15	99.8
Pl		E	13 / 5 .	449.624	G	core	52.87	29.83	12.82	4.35	0.06	0.00		0.22	100.2
Pl		G	19 / 1 .	449.627	F	core	53.79	29.29	12.35	4.45	0.02	0.05		0.22	100.2
Pl		G	19 / 2 .	449.627	F	core	52.97	30.12	12.94	4.21	0.04	0.02		0.24	100.5
Pl		A	21 / 1 .	539.8535	F	core	54.56	28.70	11.47	4.95	0.06	0.05		0.17	100.0
Pl		A	21 / 2 .	539.8535	F	core	54.17	28.75	11.51	4.87	0.03	0.00		0.27	99.6
Pl		A	21 / 3 .	539.8535	F	core	54.26	28.77	11.42	4.91	0.03	0.01		0.16	99.6
Pl		A	21 / 4 .	539.8535	F	rim	54.12	29.01	11.72	4.66	0.06	0.00		0.15	99.7
Pl		B	25 / 1 .	539.8587	F	core	53.54	28.98	11.64	4.69	0.03	0.02		0.22	99.1
Pl		B	25 / 2 .	539.8587	F	rim	53.64	28.90	11.98	4.72	0.06	0.00		0.26	99.6
Pl		B	25 / 3 .	539.8587	G	rim	54.01	28.73	11.88	4.83	0.05	0.00		0.19	99.7
Pl		B	25 / 4 .	539.8587	G	core	53.94	29.21	11.66	4.76	0.06	0.00		0.21	99.8
Pl		B	26 / 1 .	539.8587	G	core	54.14	29.00	11.71	4.78	0.08		0.02	0.18	99.9
Pl		B	26 / 2 .	539.8587	G	rim	54.99	28.21	11.01	5.10	0.04		0.01	0.17	99.5
Pl		C	29 / 1 .	539.8613	F	core	54.23	28.75	11.62	4.98	0.03	0.00		0.21	99.8
Pl		C	29 / 2 .	539.8613	F	rim	52.81	29.89	13.28	4.20	0.06	0.00		0.28	100.5
Pl		C	29 / 3 .	539.8613	G	rim	54.11	28.67	11.98	4.87	0.01	0.01		0.22	99.9
Pl		C	29 / 4 .	539.8613	G	core	54.07	28.71	11.59	4.84	0.09	0.00		0.49	99.8
Pl		D	1 / 1 .	539.8674	F	core	54.27	28.78	11.61	4.85	0.05	0.00		0.17	99.7
Pl		D	4 / 1 .	539.8674	F	core	53.98	28.42	11.58	4.83	0.03	0.01		0.18	99.0
Pl		D	4 / 2 .	539.8674	F	core	54.20	28.61	12.05	4.90	0.05	0.00		0.21	100.0
Pl		D	4 / 3 .	539.8674	F	rim	54.27	28.84	11.77	4.75	0.03	0.00		0.29	100.0
Pl		E	7 / 1 .	539.874	F	core	54.54	28.45	11.40	4.98	0.05	0.00		0.14	99.6
Pl		E	7 / 2 .	539.874	F	rim	54.32	28.37	11.47	5.04	0.08	0.00		0.30	99.6
Pl		E	7 / 3 .	539.874	G	core	54.12	28.63	11.75	4.82	0.07	0.02		0.19	99.6
Pl		E	7 / 4 .	539.874	G	rim	54.34	28.67	11.65	4.78	0.08	0.00		0.28	99.8
Pl		F	9 / 1 .	539.8767	F	core	54.49	28.72	11.28	4.88	0.07	0.03		0.38	99.8
Pl		F	9 / 2 .	539.8767	G	core	54.16	28.31	11.87	4.89	0.04	0.04		0.21	99.5
Pl		F	9 / 3 .	539.8767	G	rim	53.90	29.01	11.65	4.84	0.03	0.00		0.18	99.6
Pl		F	9 / 4 .	539.8767	G	core	54.04	28.62	11.66	4.94	0.05	0.01		0.24	99.6

Mineral		Area	Point	Depth (mbsf)	Grain size	Grain area	SiO2	Al2O3	CaO	Na2O	K2O	MnO	MgO	FeO	Total
Pl		F	9 / 5 .	539.8767	G	rim	53.84	28.59	11.85	4.60	0.07	0.00		0.19	99.1
Pl		F	10 / 1 .	539.8767	G	core	54.07	28.79	11.72	4.83	0.05		0.01	0.32	99.8
Pl		F	10 / 2 .	539.8767	G	rim	54.31	28.80	11.88	4.92	0.11		0.02	0.20	100.2
Pl		A	14 / 1 .	598.438	F	core	53.14	29.73	12.40	4.24	0.07	0.03		0.12	99.7
Pl		A	14 / 2 .	598.438	F	core	53.16	29.36	12.55	4.39	0.06	0.00		0.16	99.7
Pl		A	14 / 3 .	598.438	F	rim	52.76	29.74	12.79	4.33	0.08	0.01		0.22	99.9
Pl		A	14 / 4 .	598.438	G	rim	53.30	29.57	12.67	4.29	0.05	0.00		0.24	100.1
Pl		A	14 / 5 .	598.438	G	rim	52.96	29.47	12.61	4.26	0.08	0.00		0.15	99.5
Pl		B	15 / 1 .	598.434	F	core	53.01	29.57	12.43	4.33	0.01		0.03	0.19	99.6
Pl		B	15 / 2 .	598.434	F	rim	53.29	29.67	12.48	4.40	0.06		0.03	0.19	100.1
Pl		B	18 / 1 .	598.434	F	core	53.09	29.37	12.54	4.31	0.05	0.00		0.15	99.5
Pl		B	18 / 2 .	598.434	F	rim	51.14	30.58	13.90	3.57	0.04	0.00		0.11	99.3
Pl		B	18 / 3 .	598.434	F	core	53.04	29.48	12.71	4.14	0.03	0.00		0.17	99.6
Pl		B	18 / 4 .	598.434	F	rim	53.54	29.73	12.41	4.25	0.05	0.02		0.15	100.1
Pl		B	18 / 5 .	598.434	G	core	53.05	29.74	12.42	4.32	0.08	0.00		0.15	99.8
Pl		B	18 / 6 .	598.434	G	rim	52.83	30.09	12.81	4.12	0.06	0.01		0.22	100.1
Pl		C	21 / 1 .	598.4405	F	core	53.71	28.91	11.91	4.51	0.06	0.02		0.24	99.4
Pl		C	21 / 2 .	598.4405	F	core	53.25	29.82	12.46	4.50	0.05	0.05		0.22	100.3
Pl		C	21 / 3 .	598.4405	F	rim	52.99	29.19	12.51	4.32	0.01	0.01		0.37	99.4
Pl	360_66R3_29	C	21 / 4 .	598.4405	F	core	52.78	29.85	12.83	4.04	0.05	0.00		0.15	99.7
Pl		C	21 / 5 .	598.4405	F	rim	53.33	29.48	12.47	4.26	0.07	0.06		0.31	100.0
Pl		C	21 / 6 .	598.4405	G	core	53.73	29.85	12.12	4.44	0.07	0.00		0.19	100.4
Pl		C	21 / 7 .	598.4405	G	rim	53.92	29.49	11.97	4.57	0.03	0.00		0.11	100.1
Pl		D	27 / 2 .	598.4495	F	rim	49.74	32.05	15.18	2.76	0.11	0.00		0.28	100.1
Pl		D	27 / 3 .	598.4495	G	core	53.04	29.23	12.57	4.38	0.05	0.00		0.14	99.4
Pl		D	27 / 4 .	598.4495	G	rim	53.18	29.06	12.22	4.41	0.04	0.00		0.45	99.4
Pl		E	1 / 1 .	598.4545	F	core	53.46	29.41	12.16	4.51	0.08	0.01		0.17	99.8
Pl		E	4 / 1 .	598.4545	F	core	53.31	29.86	12.48	4.27	0.05	0.00		0.10	100.1
Pl		E	4 / 2 .	598.4545	F	rim	53.19	29.67	12.56	4.17	0.02	0.01		0.17	99.8
Pl		E	4 / 3 .	598.4545	G	core	53.01	29.80	12.78	4.35	0.06	0.01		0.16	100.2
Pl		E	4 / 4 .	598.4545	G	rim	53.31	29.47	12.39	4.35	0.05	0.00		0.27	99.8
Pl		E	5 / 1 .	598.4545	G	core	53.16	29.56	12.53	4.16	0.06		0.02	0.16	99.7
Pl		E	5 / 2 .	598.4545	G	rim	52.79	29.74	12.61	4.17	0.07		0.02	0.27	99.7
Pl		F	9 / 1 .	598.4595	F	core	52.97	29.68	12.68	4.33	0.05	0.04		0.14	99.9
Pl		F	9 / 2 .	598.4595	F	rim	51.93	30.32	13.55	3.79	0.02	0.00		0.26	99.9
Pl		F	9 / 3 .	598.4595	G	core	52.89	29.97	12.93	4.18	0.05	0.01		0.20	100.2

Mineral	Area	Point	Depth (mbsf)	Grain size	Grain area	SiO2	Al2O3	CaO	Na2O	K2O	MnO	MgO	FeO	Total
Pl	F	9 / 4 .	598.4595	G	rim	52.05	29.94	13.24	4.07	0.06	0.02		0.20	99.6
Pl	A	11 / 1 .	614.0135	F	core	54.21	28.99	11.66	4.95	0.04	0.00		0.18	100.0
Pl	A	11 / 2 .	614.0135	F	rim	53.45	29.39	12.36	4.45	0.05	0.00		0.21	99.9
Pl	A	11 / 3 .	614.0135	F	core	52.93	29.73	12.29	4.51	0.05	0.00		0.16	99.7
Pl	A	11 / 4 .	614.0135	G	rim	53.21	29.08	11.66	4.54	0.05	0.03		0.23	98.8
Pl	A	11 / 5 .	614.0135	G	core	53.37	28.61	11.73	4.83	0.05	0.05		0.23	98.9
Pl	B	13 / 1 .	614.016	F	core	53.41	29.45	12.20	4.68	0.04	0.00		0.15	99.9
Pl	B	13 / 2 .	614.016	F	core	53.26	29.47	12.31	4.56	0.07	0.00		0.20	99.9
Pl	B	13 / 3 .	614.016	G	core	52.62	29.46	12.48	4.30	0.03	0.00		0.23	99.1
Pl	B	13 / 4 .	614.016	G	rim	53.09	29.68	12.55	4.32	0.09	0.00		0.23	100.0
Pl	B	13 / 5 .	614.016	G	rim	53.15	29.45	12.60	4.52	0.10	0.03		0.16	100.0
Pl	B	13 / 6 .	614.016	G	core	52.66	29.87	12.96	4.38	0.06	0.00		0.19	100.1
Pl	Cbis	16 / 1 .	614.0225	G	core	53.56	29.66	12.12	4.61	0.06	0.00		0.29	100.3
Pl	Cbis	16 / 2 .	614.0225	G	rim	52.43	29.99	13.10	3.92	0.03	0.02		0.18	99.7
Pl	Cbis	16 / 3 .	614.0225	G	core	53.35	29.42	12.58	4.38	0.06	0.00		0.19	100.0
Pl	C	18 / 1 .	614.0235	G	core	52.97	29.06	12.42	4.41	0.06	0.00		0.24	99.2
Pl	C	18 / 2 .	614.0235	G	rim	53.36	29.14	12.27	4.48	0.06	0.03		0.16	99.5
Pl	C	18 / 3 .	614.0235	F	core	53.07	29.58	12.49	4.33	0.07	0.00		0.21	99.7
Pl	C	19 / 1 .	614.0235	F	core	52.66	29.33	12.59	4.39	0.04		0.02	0.19	99.2
Pl	D	22 / 1 .	614.029	F	core	53.29	29.41	12.21	4.58	0.10	0.00		0.29	99.9
Pl	D	22 / 2 .	614.029	F	core	52.66	29.71	12.91	4.19	0.05	0.03		0.26	99.8
Pl	D	22 / 3 .	614.029	F	rim	53.47	29.71	12.38	4.48	0.04	0.02		0.19	100.3
Pl	D	22 / 4 .	614.029	F	core	53.08	29.61	12.03	4.52	0.08	0.00		0.20	99.5
Pl	D	22 / 5 .	614.029	G	rim	52.80	29.35	12.37	4.41	0.07	0.00		0.20	99.2
Pl	D	22 / 6 .	614.029	G	core	53.75	29.37	11.93	4.64	0.06	0.00		0.22	100.0
Pl	E	25 / 1 .	614.034	F	core	53.05	29.33	12.20	4.57	0.03	0.02		0.15	99.3
Pl	E	25 / 2 .	614.034	F	rim	52.96	29.66	12.62	4.20	0.06	0.00		0.25	99.7
Pl	E	25 / 3 .	614.034	G	rim	52.25	30.23	13.35	3.84	0.07	0.00		0.31	100.1
Pl	E	25 / 4 .	614.034	G	core	53.36	28.93	12.44	4.47	0.05	0.00		0.29	99.5
Pl	E	25 / 5 .	614.034	F	core	53.17	28.89	12.11	4.54	0.03	0.00		0.22	99.0
Pl	F	28 / 1 .	614.041	F	core	53.22	29.45	12.20	4.23	0.06	0.04		0.26	99.5
Pl	F	28 / 2 .	614.041	F	core	53.23	29.46	12.20	4.41	0.06	0.00		0.16	99.5
Pl	F	28 / 3 .	614.041	F	rim	53.25	29.43	12.78	4.57	0.03	0.00		0.16	100.2
Pl	F	28 / 4 .	614.041	F	core	53.24	29.42	12.59	4.41	0.06	0.01		0.14	99.9
Pl	F	28 / 5 .	614.041	G	rim	53.19	29.69	12.78	4.24	0.03	0.02		0.20	100.2
Pl	F	28 / 6 .	614.041	G	core	53.39	29.24	12.27	4.53	0.11	0.00		0.22	99.8

Mineral	Area	Point	Depth (mbsf)	Grain size	Grain area	SiO2	Al2O3	CaO	Na2O	K2O	MnO	MgO	FeO	Total
Pl	G	31 / 1 .	614.038	F	core	53.44	29.01	12.11	4.59	0.05	0.03		0.21	99.4
Pl	G	31 / 2 .	614.038	F	rim	53.08	29.72	12.52	4.30	0.00	0.00		0.22	99.8
Pl	G	31 / 3 .	614.038	G	core	53.05	29.21	12.60	4.32	0.08	0.00		0.18	99.5
Pl	G	31 / 4 .	614.038	G	rim	52.98	29.35	12.44	4.36	0.06	0.00		0.14	99.3
Pl	G	31 / 5 .	614.038	F	core	53.21	29.31	12.25	4.55	0.05	0.01		0.27	99.7
Pl	G	31 / 6 .	614.038	F	rim	50.64	31.41	14.33	3.07	0.04	0.00		0.23	99.7
Pl	A	5 / 1 .	689.695	F	rim	54.68	28.77	11.62	4.94	0.06	0.01		0.25	100.3
Pl	A	5 / 2 .	689.695	F	core	55.46	28.06	10.63	5.18	0.07	0.00		0.15	99.6
Pl	A	5 / 3 .	689.695	G	core	54.89	28.12	10.95	5.07	0.09	0.00		0.16	99.3
Pl	A	5 / 4 .	689.695	G	rim	53.47	29.33	12.29	4.56	0.06	0.00		0.21	99.9
Pl	B	8 / 1 .	689.6995	G	rim	53.83	29.19	11.85	4.74	0.03	0.02		0.23	99.9
Pl	B	8 / 2 .	689.6995	G	rim	54.22	28.71	11.78	4.75	0.05	0.01		0.24	99.8
Pl	B	9 / 1 .	689.6995	G	rim	53.60	29.09	12.21	4.54	0.00		0.02	0.25	99.7
Pl	Bbis	10 / 1 .	689.6995	G	core	52.99	28.73	12.50	4.26	0.05	0.03		0.26	98.8
Pl	Bbis	11 / 1 .	689.6995	G	core	53.35	29.01	12.21	4.41	0.07		0.06	0.30	99.4
Pl	C	13 / 1 .	689.702	F	core	54.17	28.71	11.84	4.95	0.07	0.00		0.18	99.9
Pl	C	13 / 2 .	689.702	G	rim	53.94	29.21	12.24	4.43	0.06	0.00		0.23	100.1
Pl	C	14 / 1 .	689.702	G	rim	54.01	28.89	12.15	4.50	0.05		0.03	0.20	99.8
Pl	E	19 / 1 .	689.717	F	core	54.04	28.73	11.47	4.65	0.05	0.00		0.21	99.1
Pl	E	19 / 2 .	689.717	F	rim	53.85	28.68	11.92	4.67	0.04	0.02		0.15	99.3
Pl	E	20 / 1 .	689.717	F	core	53.99	29.08	11.87	4.76	0.07		0.03	0.21	100.0
Pl	E	20 / 2 .	689.717	F	rim	53.77	28.80	11.95	4.89	0.03		0.02	0.21	99.7
Pl	E	20 / 3 .	689.717	G	rim	54.24	28.67	11.15	5.07	0.06		0.03	0.27	99.5
Pl	E	21 / 1 .	689.717	G	core	53.78	29.01	11.84	4.77	0.04		0.05	0.28	99.8
Pl	E	22 / 1 .	689.717	G	core	53.83	28.84	12.11	4.70	0.04		0.05	0.28	99.9
Pl	E	23 / 2 .	689.717	F	core	54.01	29.24	11.92	4.61	0.10	0.01	0.04	0.19	100.2
Pl	E	23 / 4 .	689.717	F	core	54.14	29.12	11.71	4.78	0.04	0.00	0.01	0.16	100.1
Pl	F	28 / 1 .	689.712	F	core	54.70	28.52	11.28	5.03	0.05	0.00		0.12	99.7
Pl	F	28 / 2 .	689.712	F	rim	54.30	28.63	11.48	5.01	0.06	0.03		0.18	99.7
Pl	F	28 / 3 .	689.712	G	rim	54.31	28.54	11.61	4.96	0.04	0.00		0.16	99.6
Pl	F	28 / 4 .	689.712	G	core	53.79	29.06	11.80	4.52	0.06	0.02		0.24	99.5
Pl	A	33 / 2 .	680.5545	F	rim	57.35	27.12	9.24	6.16	0.07	0.02		0.23	100.2
Pl	A	33 / 3 .	680.5545	F	core	57.28	27.25	9.46	6.20	0.05	0.00		0.16	100.4
Pl	A	33 / 4 .	680.5545	G	rim	57.03	27.08	9.67	5.94	0.11	0.01		0.17	100.0
Pl	A	33 / 5 .	680.5545	G	core	56.22	27.36	10.32	5.70	0.10	0.00		0.23	99.9
Pl	B	3 / 1 .	680.5555	F	core	57.01	26.75	9.31	6.08	0.09	0.01		0.14	99.4

Mineral		Area	Point	Depth (mbsf)	Grain size	Grain area	SiO2	Al2O3	CaO	Na2O	K2O	MnO	MgO	FeO	Total
Pl		B	3 / 2 .	680.5555	F	rim	57.03	26.76	9.43	6.02	0.07	0.00		0.26	99.6
Pl		B	3 / 3 .	680.5555	F	core	57.55	26.83	9.05	6.40	0.11	0.00		0.20	100.1
Pl		B	3 / 4 .	680.5555	G	rim	56.54	27.19	9.45	5.96	0.10	0.00		0.16	99.4
Pl		B	4 / 1 .	680.5555	F	core	57.19	27.14	9.29	5.91	0.11		0.00	0.19	99.8
Pl		B	4 / 2 .	680.5555	F	rim	57.41	27.03	9.53	6.01	0.14		0.00	0.26	100.4
Pl		D	11 / 1 .	680.5625	G	core	57.20	27.02	9.45	6.02	0.11	0.00		0.16	100.0
Pl		D	11 / 2 .	680.5625	G	rim	56.33	27.70	9.95	5.77	0.09	0.02		0.31	100.2
Pl	360_77R2_60	D	11 / 3 .	680.5625	G	core	57.87	26.59	8.85	6.54	0.15	0.06		0.16	100.2
Pl		D	11 / 4 .	680.5625	G	rim	58.16	26.80	8.76	6.55	0.16	0.02		0.26	100.7
Pl		Dbis	12 / 1 .	680.5625	G	core	55.36	27.74	10.56	5.39	0.10	0.00		0.19	99.3
Pl		Dbis	13 / 1 .	680.5625	G	core	55.55	27.64	10.32	5.66	0.09		0.03	0.22	99.5
Pl		E	16 / 1 .	680.569	G	core	57.26	26.99	9.54	6.05	0.10	0.00		0.22	100.2
Pl		E	16 / 2 .	680.569	G	rim	56.79	27.05	9.61	5.95	0.10	0.00		0.20	99.7
Pl		E	16 / 3 .	680.569	F	core	57.04	27.11	9.43	5.98	0.10	0.00		0.19	99.9
Pl		E	16 / 4 .	680.569	F	core	57.11	27.11	9.43	6.16	0.11	0.00		0.18	100.1
Pl		G	19 / 1 .	680.582	F	rim	56.77	27.06	9.55	6.09	0.09	0.05		0.17	99.8
Pl		G	19 / 2 .	680.582	F	core	57.18	26.99	9.21	6.20	0.12	0.02		0.17	99.9
Pl		G	19 / 3 .	680.582	F	core	57.05	27.46	9.64	5.98	0.12	0.00		0.18	100.4
Pl		G	20 / 1 .	680.582	F	rim	56.87	27.13	9.79	5.98	0.08		0.02	0.18	100.0
Pl		G	20 / 2 .	680.582	F	core	56.76	27.43	9.49	5.94	0.10		0.01	0.18	99.9
Pl		H	25 / 1 .	680.578	F	core	56.27	27.47	9.81	5.81	0.08	0.01		0.23	99.7
Pl		H	25 / 2 .	680.578	F	core	56.69	27.39	9.55	5.76	0.08	0.02		0.11	99.6
Pl		H	25 / 3 .	680.578	F	rim	57.07	27.43	9.67	5.90	0.09	0.00		0.17	100.3
Pl		I	27 / 1 .	680.583	F	rim	56.90	27.08	9.83	5.91	0.08	0.02		0.16	100.0
Pl		I	27 / 2 .	680.583	F	core	57.08	26.82	9.48	5.92	0.09	0.02		0.16	99.6
Pl		I	27 / 3 .	680.583	F	core	57.29	27.11	9.35	6.01	0.08	0.02		0.14	100.0
Pl		A	30 / 1 .	740.6555	F	core	53.28	29.35	12.59	4.65	0.04	0.01		0.19	100.1
Pl		A	30 / 2 .	740.6555	F	core	53.83	29.16	12.16	4.55	0.06	0.00		0.18	99.9
Pl		A	30 / 3 .	740.6555	F	rim	53.07	29.68	12.73	4.21	0.06	0.00		0.17	99.9
Pl		A	30 / 4 .	740.6555	G	rim	53.43	29.27	12.57	4.39	0.04	0.00		0.28	100.0
Pl		A	30 / 5 .	740.6555	G	core	52.72	29.38	12.57	4.30	0.03	0.00		0.23	99.2
Pl		A	31 / 1 .	740.6555	G	core	52.63	29.76	12.86	4.31	0.05		0.04	0.20	99.9
Pl		A	31 / 2 .	740.6555	G	rim	53.87	28.74	11.87	4.76	0.05		0.03	0.16	99.5
Pl		B	34 / 1 .	740.658	F	core	52.75	29.76	12.81	4.09	0.05	0.03		0.14	99.6
Pl		B	34 / 2 .	740.658	F	rim	52.73	29.72	12.75	4.19	0.06	0.00		0.18	99.6
Pl		B	34 / 3 .	740.658	F	core	52.49	29.92	13.10	4.06	0.01	0.00		0.10	99.7

Mineral	Area	Point	Depth (mbsf)	Grain size	Grain area	SiO2	Al2O3	CaO	Na2O	K2O	MnO	MgO	FeO	Total
Pl	B	34 / 4 .	740.658	G	core	51.92	29.93	13.24	4.00	0.05	0.01		0.22	99.4
Pl	B	34 / 5 .	740.658	G	rim	53.88	29.26	12.19	4.78	0.06	0.00		0.20	100.4
Pl	C	2 / 1 .	740.6675	F	core	52.76	29.60	12.88	3.98	0.04	0.00	0.03	0.19	99.5
Pl	C	4 / 1 .	740.6675	G	core	51.85	30.01	13.32	3.91	0.06	0.01		0.19	99.4
Pl	C	4 / 2 .	740.6675	G	rim	53.06	29.38	12.60	4.35	0.03	0.02		0.14	99.6
Pl	C	4 / 3 .	740.6675	G	rim	52.78	29.45	12.42	4.47	0.06	0.00		0.20	99.4
Pl	C	4 / 4 .	740.6675	G	core	52.03	29.92	13.09	4.01	0.06	0.03		0.25	99.4
Pl	D	7 / 1 .	740.667	F	core	53.63	28.88	12.03	4.46	0.04	0.00		0.25	99.3
Pl	D	7 / 2 .	740.667	G	core	51.69	30.17	13.59	3.69	0.01	0.03		0.26	99.4
Pl	D	7 / 3 .	740.667	G	rim	53.47	28.68	11.68	4.63	0.05	0.00		0.25	98.8
Pl	D	7 / 4 .	740.667	G	rim	54.12	28.87	11.77	4.88	0.06	0.01		0.09	99.8
Pl	D	7 / 5 .	740.667	G	core	53.83	28.85	11.80	4.75	0.04	0.00		0.16	99.4
Pl	D	7 / 6 .	740.667	G	rim	52.98	29.47	12.49	4.34	0.07	0.00		0.15	99.5
Pl	D	8 / 1 .	740.667	G	rim	53.67	29.04	12.47	4.53	0.05		0.03	0.19	100.0
Pl	D	8 / 2 .	740.667	G	core	53.55	29.04	11.75	4.64	0.05		0.03	0.17	99.2
Pl	E	9 / 6 .	740.667	F	core	52.64	30.25	13.64	3.79	0.00	0.00	0.00	0.28	100.7
Pl	E	11 / 1 .	740.667	F	core	52.98	29.50	12.56	4.10	0.05	0.04		0.21	99.4
Pl	E	11 / 2 .	740.667	F	rim	53.34	29.02	12.06	4.44	0.08	0.00		0.25	99.2
Pl	E	11 / 3 .	740.667	F	core	51.70	30.17	13.40	3.77	0.03	0.00		0.28	99.4
Pl	E	11 / 4 .	740.667	G	rim	53.63	29.32	12.16	4.61	0.08	0.03		0.24	100.1
Pl	E	11 / 5 .	740.667	G	core	52.63	29.37	12.66	4.24	0.04	0.00		0.16	99.1
Pl	F	15 / 1 .	740.68	F	core	51.70	30.04	13.48	3.79	0.06	0.05		0.20	99.3
Pl	F	15 / 2 .	740.68	F	rim	52.61	29.38	12.59	4.30	0.02	0.00		0.40	99.3
Pl	F	15 / 3 .	740.68	G	core	51.87	30.22	13.33	3.97	0.07	0.01		0.21	99.7
Pl	F	15 / 4 .	740.68	G	rim	53.12	29.30	12.16	4.50	0.06	0.00		0.17	99.3
Pl	F	16 / 1 .	740.68	G	core	51.89	29.92	12.94	3.99	0.05		0.02	0.20	99.0
Pl	F	16 / 2 .	740.68	G	rim	53.61	28.94	12.33	4.59	0.05		0.03	0.21	99.8
Pl	G	19 / 1 .	740.674	F	core	52.78	29.46	12.52	4.25	0.05	0.00		0.19	99.2
Pl	G	19 / 2 .	740.674	F	rim	52.97	29.31	12.50	4.29	0.06	0.01		0.36	99.5
Pl	G	19 / 3 .	740.674	G	core	51.93	30.24	13.52	3.73	0.04	0.01		0.20	99.7
Pl	G	19 / 4 .	740.674	G	rim	52.87	29.76	12.95	4.31	0.07	0.02		0.20	100.2

Calibration standards	Wollastonite (San Carlos)	Al2O3	Wollastonite	Albite	Orthose	TiMnO3	Forsterite	Fayalite

In situ majot elements concentrations in wt% analyzed by EPMA on a Cameca SX at LMV (Clermont-Ferrand, France)

mineral	sample	Point	Depth (mbsf)	Grain size	Grain area	SiO2	Al2O3	TiO2	CaO	Na2O	K2O	MnO	MgO	FeO	Cr2O3	Total
		2 sigma				0.486	0.184	0.093	0.427	0.124	0.063	0.064	0.251	0.245	0.103	
Cpx		Counting time (s) - per element				10	10	10	10	10	10	10	10	20	10	
Cpx	360_60R1_26_A	6 / 1 .	538.8035	F	core	51.36	3.03	1.15	18.83	0.40	0.00	0.24	15.49	9.17	0.07	99.7
Cpx	360_60R1_26_A	6 / 2 .	538.8035	F	core	51.40	3.08	1.01	21.46	0.41	0.00	0.17	14.18	7.87	0.10	99.7
Cpx	360_60R1_26_A	6 / 4 .	538.8035	G	rim	51.40	2.78	0.86	21.86	0.37	0.00	0.19	14.23	7.94	0.12	99.7
Cpx	360_60R1_26_A	6 / 5 .	538.8035	G	core	51.41	3.36	0.58	22.00	0.47	0.00	0.19	14.79	6.60	0.47	99.9
Cpx	360_60R1_26_A	6 / 6 .	538.8035	G	rim	51.71	2.65	0.74	22.31	0.38	0.00	0.29	14.55	7.44	0.13	100.2
Cpx	360_60R1_26_B	11 / 1 .	538.804	G	rim	51.40	3.25	0.69	20.69	0.37	0.03	0.16	16.13	6.75	0.33	99.8
Cpx	360_60R1_26_B	11 / 2 .	538.804	G	core	51.88	3.28	0.66	22.58	0.41	0.00	0.18	15.15	5.38	0.28	99.8
Cpx	360_60R1_26_B	11 / 3 .	538.804	G	core	51.88	3.05	0.79	21.89	0.42	0.00	0.15	15.24	5.84	0.40	99.7
Cpx	360_60R1_26_B	11 / 5 .	538.804	G	rim	51.67	2.77	0.78	21.57	0.43	0.01	0.20	15.39	6.70	0.26	99.8
Cpx	360_60R1_26_B	11 / 6 .	538.804	G	rim	52.19	3.30	0.72	21.42	0.41	0.00	0.22	15.29	6.64	0.42	100.6
Cpx	360_60R1_26_C	13 / 1 .	538.8115	G	rim	51.06	3.17	1.08	21.50	0.42	0.00	0.23	14.26	7.96	0.13	99.8
Cpx	360_60R1_26_C	13 / 2 .	538.8115	F	core	52.17	2.41	0.58	21.98	0.38	0.02	0.22	14.92	7.10	0.13	99.9
Cpx	360_60R1_26_C	13 / 3 .	538.8115	G	core	52.24	2.85	0.72	17.86	0.36	0.01	0.29	16.55	9.26	0.21	100.4
Cpx	360_60R1_26_C	13 / 4 .	538.8115	G	rim	51.42	3.03	1.05	22.08	0.39	0.02	0.27	14.09	7.56	0.13	100.0
Cpx	360_60R1_26_D	17 / 1 .	538.8185	G	core	52.19	2.80	0.41	18.81	0.28	0.01	0.23	16.96	7.73	0.48	99.9
Cpx	360_60R1_26_D	17 / 2 .	538.8185	G	rim	52.15	2.90	0.85	18.31	0.42	0.00	0.24	16.93	9.06	0.14	101.0
Cpx	360_60R1_26_G	21 / 1 .	538.8215	G	core	53.58	2.62	0.31	20.30	0.34	0.01	0.15	18.24	5.22	0.49	101.3
Cpx	360_60R1_26_G	21 / 2 .	538.8215	G	rim	52.24	3.29	0.70	21.91	0.44	0.00	0.18	15.29	6.13	0.41	100.6
Cpx	360_60R1_26_G	21 / 3 .	538.8215	F	core	51.45	3.35	0.67	21.70	0.44	0.00	0.22	15.11	6.46	0.75	100.2
Cpx	360_60R1_26_G	21 / 4 .	538.8215	F	core	51.80	2.68	0.71	22.26	0.45	0.00	0.14	15.15	6.48	0.28	99.9
Cpx	360_60R1_26_F	26 / 1 .	538.831	F	rim	51.10	3.29	1.11	22.07	0.42	0.00	0.20	14.52	6.67	0.25	99.6
Cpx	360_60R1_26_F	26 / 2 .	538.831	G	core	52.84	2.72	0.38	11.30	0.23	0.00	0.29	20.64	11.54	0.34	100.3
Cpx	360_62R4_62_B	4 / 2 .	561.879	G	core	52.18	2.50	0.78	19.13	0.38	0.00	0.28	15.44	9.40	0.01	100.1
Cpx	360_62R4_62_B	4 / 3 .	561.879	G	core	52.02	2.64	0.80	20.33	0.40	0.00	0.27	15.11	8.71	0.02	100.3
Cpx	360_62R4_62_C	8 / 1 .	561.8765	G	rim	52.13	2.32	0.48	22.30	0.32	0.00	0.21	14.48	7.42	0.00	99.7
Cpx	360_62R4_62_C	8 / 2 .	561.8765	G	core	52.05	2.76	0.81	18.00	0.37	0.00	0.20	16.44	9.54	0.07	100.2
Cpx	360_62R4_62_D	9 / 1 .	561.8845	G	rim	51.79	2.55	0.96	21.17	0.46	0.00	0.26	14.29	8.55	0.00	100.0
Cpx	360_62R4_62_E	11 / 1 .	561.8905	F	core	52.01	2.50	0.83	21.25	0.46	0.02	0.24	14.35	8.36	0.00	100.0
Cpx	360_62R4_62_E	11 / 2 .	561.8905	F	rim	52.01	2.52	0.85	21.55	0.45	0.01	0.22	14.76	8.04	0.04	100.5
Cpx	360_62R4_62_E	11 / 3 .	561.8905	F	core	51.28	2.73	0.98	21.64	0.45	0.00	0.23	14.07	8.11	0.00	99.5
Cpx	360_62R4_62_E	11 / 4 .	561.8905	F	rim	51.78	2.44	0.76	21.83	0.38	0.02	0.25	14.58	7.92	0.00	100.0
Cpx	360_62R4_62_F	14 / 3 .	561.8985	G	core	51.64	2.62	1.06	20.66	0.39	0.06	0.25	14.57	8.49	0.01	99.7
Cpx	360_62R4_62_F	14 / 4 .	561.8985	G	rim	52.11	2.64	1.00	20.95	0.48	0.00	0.28	14.54	8.29	0.04	100.3
Cpx	360_62R4_62_F	14 / 5 .	561.8985	G	core	52.49	2.41	0.74	20.43	0.41	0.00	0.21	15.51	8.37	0.03	100.6
Cpx	360_62R4_62_G	15 / 3 .	561.8965	F	core	52.03	2.64	0.88	21.36	0.52	0.00	0.28	14.50	8.39	0.03	100.6
Cpx	360_62R4_62_G	15 / 4 .	561.8965	F	core	52.07	2.74	0.95	21.09	0.49	0.00	0.30	14.05	9.03	0.06	100.8
Cpx	360_62R4_62_G	15 / 5 .	561.8965	G	rim	52.54	2.01	0.48	22.42	0.33	0.00	0.22	14.59	7.99	0.03	100.6

mineral	sample	Point	Depth (mbsf)	Grain size	Grain area	SiO2	Al2O3	TiO2	CaO	Na2O	K2O	MnO	MgO	FeO	Cr2O3	Total
Cpx	360_64R5_39_A	3 / 4 .	579.658	G	rim	52.05	2.68	0.90	21.97	0.42	0.00	0.21	15.13	6.74	0.02	100.1
Cpx	360_64R5_39_A	3 / 5 .	579.658	F	core	51.46	2.82	1.02	21.96	0.42	0.00	0.20	14.89	6.77	0.09	99.6
Cpx	360_64R5_39_A	3 / 6 .	579.658	G	core	51.35	3.05	0.85	21.80	0.44	0.00	0.20	15.32	6.66	0.08	99.7
Cpx	360_64R5_39_B	7 / 1 .	579.6575	G	rim	52.37	2.57	0.76	20.64	0.36	0.03	0.24	16.01	7.19	0.07	100.2
Cpx	360_64R5_39_B	7 / 3 .	579.6575	G	core	52.98	2.40	0.54	18.88	0.34	0.00	0.17	16.90	7.90	0.10	100.2
Cpx	360_64R5_39_B	7 / 4 .	579.6575	F	core	51.73	2.75	0.96	20.74	0.41	0.03	0.21	15.51	6.83	0.05	99.2
Cpx	360_64R5_39_C	10 / 2 .	579.654	G	core	51.72	2.69	0.76	20.70	0.37	0.00	0.24	15.69	7.20	0.09	99.5
Cpx	360_64R5_39_C	10 / 4 .	579.654	G	rim	52.00	2.85	0.97	20.26	0.35	0.01	0.27	15.72	7.50	0.10	100.0
Cpx	360_64R5_39_D	13 / 4 .	579.6645	G	core	51.97	2.65	0.74	21.61	0.36	0.00	0.26	15.32	7.27	0.06	100.2
Cpx	360_64R5_39_E	3 / 1 .	579.6725	F	core	52.47	2.69	0.78	22.11	0.37	0.00	0.20	15.42	6.15	0.05	100.3
Cpx	360_64R5_39_E	3 / 2 .	579.6725	G	core	52.03	2.96	0.65	20.68	0.43	0.00	0.25	15.96	6.73	0.08	99.8
Cpx	360_64R5_39_E	3 / 3 .	579.6725	G	rim	52.75	2.45	0.47	17.39	0.23	0.00	0.22	17.72	9.02	0.07	100.3
Cpx	360_64R5_39_E	3 / 4 .	579.6725	G	rim	52.30	2.43	0.57	18.56	0.30	0.03	0.20	16.88	7.50	0.03	98.8
Cpx	360_64R5_39_F	7 / 2 .	579.674	G	rim	52.02	2.75	0.78	22.51	0.42	0.00	0.16	14.43	6.51	0.03	99.6
Cpx	360_64R5_39_F	7 / 3 .	579.674	G		52.31	2.90	0.75	20.26	0.42	0.00	0.20	15.81	7.22	0.09	100.0
Cpx	360_67R1_91a_A	3 / 1 .	604.537	G	rim	51.80	2.78	1.10	21.48	0.40	0.00	0.17	15.51	6.68	0.06	100.0
Cpx	360_67R1_91a_A	3 / 2 .	604.537	G	core	53.44	2.85	0.54	19.77	0.39	0.00	0.13	16.82	5.41	0.09	99.4
Cpx	360_67R1_91a_A	3 / 4 .	604.537	G	core	52.32	2.65	0.63	19.63	0.33	0.01	0.18	17.01	6.92	0.11	99.8
Cpx	360_67R1_91a_A	3 / 5 .	604.537	G	rim	51.85	2.74	0.98	22.06	0.38	0.01	0.19	14.99	6.23	0.11	99.5
Cpx	360_67R1_91a_C	9 / 1 .	604.5425	G	rim	52.16	2.79	1.06	20.38	0.35	0.00	0.24	16.37	6.83	0.09	100.3
Cpx	360_67R1_91a_C	9 / 2 .	604.5425	G	core	53.12	2.33	0.48	17.44	0.29	0.02	0.20	18.05	7.81	0.01	99.7
Cpx	360_67R1_91a_D	14 / 2 .	604.5415	G	core	52.81	2.62	0.64	19.42	0.31	0.00	0.20	16.99	7.05	0.08	100.1
Cpx	360_67R1_91a_D	14 / 3 .	604.5415	G	rim	52.08	2.64	0.90	20.67	0.32	0.00	0.18	16.14	6.52	0.12	99.6
Cpx	360_67R1_91a_D	14 / 5 .	604.5415	G	core	52.24	2.68	0.54	19.10	0.29	0.01	0.24	17.03	7.06	0.06	99.3
Cpx	360_67R1_91a_F	18 / 1 .	604.5575	G	core	52.41	2.83	0.54	21.99	0.41	0.00	0.18	15.34	6.08	0.07	99.9
Cpx	360_67R1_91a_F	18 / 2 .	604.5575	G	rim	52.11	2.78	0.81	21.57	0.41	0.00	0.15	15.62	6.08	0.08	99.6
Cpx	360_67R1_91a_F	18 / 3 .	604.5575	G	rim	52.03	2.80	0.69	19.94	0.47	0.02	0.20	16.07	6.75	0.10	99.1
Cpx	360_67R1_91a_F	18 / 4 .	604.5575	F		51.92	2.94	0.63	21.23	0.38	0.00	0.15	15.94	6.52	0.11	99.8
Cpx	360_67R1_91a_F	18 / 6 .	604.5575	G	core	52.29	2.51	0.62	20.63	0.37	0.00	0.20	16.19	6.45	0.06	99.3
Cpx	360_67R1_91a_F	18 / 7 .	604.5575	G	rim	51.90	2.57	0.94	21.98	0.35	0.00	0.20	15.42	6.12	0.13	99.6
Cpx	360_67R1_91a_G	21 / 2 .	604.5605	G	rim	52.48	2.27	0.78	17.69	0.35	0.00	0.22	17.06	8.11	0.10	99.1
Cpx	360_67R1_91a_G	21 / 3 .	604.5605	G	core	51.86	2.91	0.63	20.53	0.39	0.00	0.18	15.92	6.81	0.09	99.3
Cpx	360_67R1_91a_G	21 / 4 .	604.5605	G	core	51.77	2.78	0.77	22.16	0.40	0.01	0.17	15.38	5.91	0.08	99.4
Cpx	360_67R1_91a_G	21 / 5 .	604.5605	G	rim	52.74	2.33	0.81	17.46	0.34	0.01	0.22	17.47	8.55	0.11	100.0
Cpx	360_67R1_91a_G	21 / 6 .	604.5605	F	core	51.91	2.65	0.73	21.70	0.40	0.00	0.20	15.26	6.25	0.16	99.3
Cpx	360_67R1_91a_G	21 / 7 .	604.5605	F	rim	51.89	2.30	1.14	18.47	0.35	0.00	0.20	17.37	8.17	0.12	100.0
Cpx	360_67R1_91a_G	21 / 8 .	604.5605	F	rim	51.84	2.62	0.87	22.35	0.39	0.04	0.22	15.22	6.18	0.17	99.9
Cpx	360_70R7_58a_B	6 / 1 .	642.2865	G	rim	51.84	2.67	0.89	22.27	0.40	0.01	0.20	15.18	6.17	0.13	99.8
Cpx	360_70R7_58a_B	6 / 2 .	642.2865	G	core	51.83	2.97	0.95	21.15	0.43	0.00	0.23	14.94	6.56	0.29	99.3
Cpx	360_70R7_58a_B	6 / 3 .	642.2865	G	core	53.02	2.20	0.43	16.56	0.27	0.00	0.23	18.27	9.04	0.18	100.2

mineral	sample	Point	Depth (mbsf)	Grain size	Grain area	SiO2	Al2O3	TiO2	CaO	Na2O	K2O	MnO	MgO	FeO	Cr2O3	Total
Cpx	360_70R7_58a_B	6 / 4 .	642.2865	G	rim	51.70	2.71	0.91	21.96	0.43	0.00	0.16	15.13	6.22	0.17	99.4
Cpx	360_70R7_58a_B	6 / 6 .	642.2865	G	core	51.40	3.20	1.16	21.44	0.42	0.00	0.21	15.14	6.54	0.26	99.8
Cpx	360_70R7_58a_C	10 / 1 .	642.288	G	core	52.62	2.80	0.48	11.33	0.23	0.01	0.30	20.54	11.66	0.15	100.1
Cpx	360_70R7_58a_C	10 / 2 .	642.288	G	rim	52.23	2.71	0.86	21.12	0.37	0.00	0.17	15.59	6.73	0.11	99.9
Cpx	360_70R7_58a_D	12 / 1 .	642.298	G	core	52.55	2.81	0.44	21.92	0.42	0.00	0.14	15.56	6.10	0.20	100.1
Cpx	360_70R7_58a_D	12 / 2 .	642.298	G	rim	51.51	2.96	1.02	21.31	0.41	0.00	0.23	14.92	6.58	0.07	99.0
Cpx	360_70R7_58a_D	12 / 3 .	642.298	F	core	51.10	3.24	1.20	22.04	0.41	0.03	0.20	14.77	6.28	0.10	99.4
Cpx	360_70R7_58a_D	12 / 4 .	642.298	G	core	52.28	2.56	0.44	19.42	0.34	0.00	0.23	16.35	7.36	0.24	99.2
Cpx	360_70R7_58a_E	15 / 3 .	642.2975	G	core	51.68	2.61	0.69	20.86	0.38	0.00	0.21	16.34	6.65	0.07	99.5
Cpx	360_70R7_58a_E	15 / 4 .	642.2975	G	rim	51.41	2.92	1.05	21.69	0.48	0.00	0.22	15.21	6.44	0.08	99.5
Cpx	360_74R6_27_A	1 / 1 .	659.623	G	core	51.34	3.05	1.01	20.72	0.38	0.02	0.13	15.33	7.52	0.19	99.7
Cpx	360_74R6_27_A	2 / 1 .	659.623	G	rim	51.11	2.94	1.17	21.25	0.39	0.00	0.17	15.01	7.51	0.05	99.6
Cpx	360_74R6_27_B	5 / 2 .	659.6265	G	rim	52.26	2.43	0.75	18.41	0.27	0.00	0.21	16.97	8.04	0.10	99.4
Cpx	360_74R6_27_B	5 / 5 .	659.6265	G	rim	51.88	2.74	0.91	22.33	0.42	0.00	0.20	14.82	7.01	0.07	100.4
Cpx	360_74R6_27_B	5 / 6 .	659.6265	G		51.74	2.82	0.88	21.79	0.43	0.01	0.25	14.90	6.80	0.10	99.7
Cpx	360_74R6_27_C	9 / 1 .	659.624	G	rim	52.10	2.71	0.97	19.63	0.41	0.01	0.22	16.17	7.96	0.03	100.2
Cpx	360_74R6_27_C	9 / 2 .	659.624	G	core	52.58	2.91	0.58	20.36	0.38	0.00	0.15	15.90	6.72	0.13	99.7
Cpx	360_74R6_27_C	9 / 3 .	659.624	G	core	52.09	2.87	0.63	20.63	0.39	0.00	0.18	15.85	6.77	0.17	99.6
Cpx	360_74R6_27_D	11 / 1 .	659.633	G	core	51.38	3.15	1.19	21.14	0.51	0.02	0.16	14.97	6.85	0.17	99.5
Cpx	360_74R6_27_D	11 / 2 .	659.633	G	rim	51.44	3.01	1.14	21.38	0.40	0.00	0.23	14.65	7.33	0.12	99.7
Cpx	360_74R6_27_E	15 / 2 .	659.639	F	core	50.99	3.14	0.96	21.34	0.39	0.00	0.16	15.04	7.29	0.12	99.4
Cpx	360_74R6_27_E	15 / 3 .	659.639	G	core	52.16	2.54	0.44	21.16	0.43	0.01	0.20	15.42	6.78	0.17	99.3
Cpx	360_74R6_27_E	15 / 4 .	659.639	G	rim	51.45	2.75	0.69	21.04	0.31	0.00	0.18	15.27	7.08	0.04	98.8
Cpx	360_74R6_27_F	18 / 1 .	659.646	F	core	51.12	3.08	1.03	21.68	0.38	0.00	0.20	14.99	6.96	0.13	99.6
Cpx	360_74R6_27_F	18 / 2 .	659.646	G	core	52.40	2.92	0.52	18.35	0.32	0.00	0.23	17.07	7.30	0.17	99.3
Cpx	360_74R6_27_F	18 / 3 .	659.646	G	rim	51.99	2.85	1.02	21.95	0.36	0.00	0.24	15.03	6.46	0.12	100.0
Cpx	360_74R6_27_F	18 / 4 .	659.646	G	core	51.73	3.11	0.60	20.52	0.45	0.00	0.17	15.39	7.07	0.18	99.2
Cpx	360_74R6_27_F	18 / 5 .	659.646	G	rim	51.36	2.89	0.93	22.39	0.41	0.01	0.11	14.91	6.55	0.14	99.7
Cpx	360_74R6_27_F	18 / 6 .	659.646	F	core	51.34	2.59	0.84	22.11	0.37	0.01	0.24	14.86	7.01	0.14	99.5
Cpx	360_74R6_27_F	18 / 7 .	659.646	G	core	52.14	2.62	0.71	21.46	0.41	0.00	0.23	15.38	7.18	0.14	100.3
Cpx	360_74R6_27_F	18 / 8 .	659.646	G	core	52.10	2.53	0.55	20.73	0.41	0.00	0.26	15.59	7.31	0.21	99.7
Cpx	360_74R6_27_F	18 / 9 .	659.646	G	rim	51.91	2.83	0.91	21.26	0.39	0.00	0.18	15.14	7.24	0.14	100.0
Cpx	360_75R7_56_A	5 / 2 .	671.1955	F	core	51.89	3.06	0.79	22.04	0.35	0.00	0.15	15.42	5.73	0.15	99.6
Cpx	360_75R7_56_A	5 / 4 .	671.1955	G	rim	52.51	2.64	0.81	22.06	0.41	0.00	0.22	15.62	6.02	0.12	100.4
Cpx	360_75R7_56_A	5 / 5 .	671.1955	G	core	53.03	2.85	0.53	14.86	0.32	0.00	0.26	19.76	9.18	0.15	100.9
Cpx	360_75R7_56_A	5 / 6 .	671.1955	F	core	52.40	2.43	0.79	19.47	0.33	0.00	0.21	16.97	7.67	0.07	100.3
Cpx	360_75R7_56_B	6 / 1 .	671.1985	G	core	52.69	2.67	0.59	19.85	0.33	0.00	0.23	16.52	6.77	0.11	99.8
Cpx	360_75R7_56_B	6 / 2 .	671.1985	G	rim	52.06	2.60	1.04	19.79	0.33	0.00	0.22	16.14	7.30	0.08	99.6
Cpx	360_75R7_56_B	6 / 6 .	671.1985	G	rim	51.99	2.53	0.90	17.35	0.34	0.00	0.22	17.80	8.15	0.06	99.3
Cpx	360_75R7_56_B	6 / 7 .	671.1985	G	core	52.09	2.73	0.61	20.80	0.36	0.00	0.17	16.01	6.04	0.11	98.9

mineral	sample	Point	Depth (mbsf)	Grain size	Grain area	SiO2	Al2O3	TiO2	CaO	Na2O	K2O	MnO	MgO	FeO	Cr2O3	Total
Cpx	360_75R7_56_C	9 / 3 .	671.197	F	rim	51.00	3.07	1.28	21.57	0.39	0.03	0.24	15.00	6.32	0.08	99.0
Cpx	360_75R7_56_C	9 / 4 .	671.197	F	core	51.45	3.01	1.24	19.62	0.41	0.02	0.18	16.13	7.07	0.10	99.2
Cpx	360_75R7_56_C	9 / 6 .	671.197	G	rim	51.54	2.99	1.15	21.03	0.39	0.00	0.22	15.73	6.59	0.05	99.7
Cpx	360_75R7_56_C	9 / 7 .	671.197	G	core	53.22	2.34	0.50	16.98	0.22	0.00	0.24	19.05	7.60	0.11	100.3
Cpx	360_75R7_56_D	10 / 1 .	671.2055	G	rim	51.63	2.52	0.92	21.19	0.37	0.00	0.17	15.73	6.61	0.13	99.3
Cpx	360_75R7_56_D	10 / 2 .	671.2055	G	core	52.24	3.45	0.71	21.52	0.46	0.01	0.19	15.15	6.18	0.16	100.1
Cpx	360_75R7_56_D	10 / 3 .	671.2055	G	core	51.89	3.09	0.97	21.92	0.49	0.00	0.20	15.14	6.00	0.16	99.9
Cpx	360_75R7_56_D	10 / 4 .	671.2055	G	rim	52.10	2.64	1.05	22.05	0.39	0.00	0.18	15.22	6.17	0.13	99.9
Cpx	360_75R7_56_D	10 / 5 .	671.2055	G	core	52.19	2.69	0.81	20.60	0.32	0.01	0.17	15.91	7.20	0.13	100.0
Cpx	360_75R7_56_D	10 / 8 .	671.2055	F	core	52.00	2.54	0.79	22.39	0.44	0.00	0.17	15.26	5.92	0.18	99.7
Cpx	360_75R7_56_E	13 / 3 .	671.212	G	rim	52.08	2.78	0.92	21.26	0.39	0.00	0.18	15.81	6.18	0.07	99.7
Cpx	360_75R7_56_E	13 / 4 .	671.212	G	core	51.96	3.21	0.64	20.49	0.43	0.00	0.15	16.06	6.10	0.16	99.2
Cpx	360_75R7_56_E	13 / 6 .	671.212	G	rim	51.79	2.98	0.97	19.84	0.31	0.01	0.15	16.55	6.95	0.04	99.6
Cpx	360_75R7_56_E	13 / 7 .	671.212	G	core	52.64	2.47	0.55	21.96	0.38	0.03	0.17	16.45	5.53	0.12	100.3
Cpx	360_75R7_56_F	16 / 2 .	671.218	G	core	52.11	3.17	0.68	20.70	0.41	0.02	0.20	15.72	6.35	0.15	99.5
Cpx	360_75R7_56_F	16 / 3 .	671.218	G	rim	52.64	2.53	0.68	18.70	0.27	0.01	0.21	17.02	7.77	0.14	100.0
Cpx	360_75R7_56_F	16 / 4 .	671.218	G	core	52.34	2.92	0.60	18.20	0.35	0.00	0.26	17.72	7.42	0.15	100.0
Cpx	360_75R7_56_F	16 / 5 .	671.218	G	rim	52.08	2.87	0.97	21.21	0.33	0.00	0.20	15.81	6.39	0.09	99.9
Cpx	360_75R7_56_G	19 / 3 .	671.2165	G	core	52.25	2.73	0.75	19.75	0.37	0.00	0.16	16.70	6.71	0.13	99.5
Cpx	360_75R7_56_G	19 / 4 .	671.2165	G	rim	52.55	2.42	0.73	22.09	0.33	0.00	0.19	15.44	6.01	0.10	99.9
Cpx	360_75R7_56_G	19 / 5 .	671.2165	F	core	52.14	2.47	0.81	21.92	0.35	0.00	0.17	15.60	6.17	0.13	99.7
Cpx	360_79R6_1a_A	1 / 1 .	699.004	G	rim	51.60	2.41	0.83	21.60	0.40	0.00	0.23	14.75	7.12	0.04	99.0
Cpx	360_79R6_1a_A	2 / 1 .	699.004	G	core	50.62	3.29	1.21	20.54	0.37	0.00	0.22	14.88	7.69	0.00	98.8
Cpx	360_79R6_1a_B	6 / 5 .	699.0065	G	core	52.63	3.21	0.47	21.09	0.40	0.00	0.15	16.43	4.95	0.30	99.6
Cpx	360_79R6_1a_B	6 / 6 .	699.0065	G	rim	51.06	3.05	1.21	21.83	0.39	0.00	0.22	14.50	7.31	0.14	99.7
Cpx	360_79R6_1a_B	6 / 7 .	699.0065	F	core	51.16	3.08	1.16	22.02	0.41	0.00	0.18	14.61	6.92	0.07	99.6
Cpx	360_79R6_1a_D	15 / 3 .	699.022	G	core	52.00	3.53	0.54	21.82	0.47	0.02	0.14	15.96	4.84	0.39	99.7
Cpx	360_79R6_1a_D	15 / 4 .	699.022	G	rim	51.96	2.73	0.98	20.40	0.38	0.00	0.24	15.66	7.48	0.13	100.0
Cpx	360_82R3_19a_A	3 / 1 .	723.533	G	core	52.12	3.83	0.60	21.82	0.38	0.00	0.20	15.17	5.51	0.50	100.1
Cpx	360_82R3_19a_A	3 / 4 .	723.533	G	rim	51.28	3.11	1.02	20.95	0.46	0.01	0.20	15.22	6.33	0.29	98.9
Cpx	360_82R3_19a_B	6 / 1 .	723.5395	G	core	52.28	3.13	0.54	18.06	0.32	0.02	0.19	16.33	8.07	0.35	99.3
Cpx	360_82R3_19a_B	6 / 2 .	723.5395	G	rim	51.09	3.14	1.07	21.61	0.36	0.00	0.18	14.88	6.64	0.30	99.3
Cpx	360_82R3_19a_B	6 / 4 .	723.5395	G	core	51.11	3.60	1.36	21.20	0.54	0.00	0.14	14.98	6.89	0.35	100.2
Cpx	360_82R3_19a_B	6 / 5 .	723.5395	G	rim	51.39	3.02	1.21	20.87	0.39	0.00	0.20	15.19	7.01	0.28	99.5
Cpx	360_82R3_19a_B	6 / 6 .	723.5395	G	rim	52.32	2.19	0.70	21.86	0.29	0.00	0.20	15.44	6.60	0.20	99.8
Cpx	360_82R3_19a_B	6 / 7 .	723.5395	F	core	52.35	2.78	0.78	21.78	0.42	0.03	0.18	15.26	6.36	0.14	100.1
Cpx	360_82R3_19a_B	6 / 8 .	723.5395	G	core	52.44	3.17	0.41	19.75	0.31	0.00	0.18	16.42	6.88	0.35	99.9
Cpx	360_82R3_19a_B	6 / 9 .	723.5395	G	rim	52.01	2.90	0.74	21.38	0.43	0.01	0.20	15.37	6.19	0.27	99.5
Cpx	360_82R3_19a_C	8 / 1 .	723.537	F	core	52.49	2.81	0.44	18.61	0.32	0.00	0.22	16.77	7.96	0.20	99.8
Cpx	360_82R3_19a_C	8 / 2 .	723.537	G	core	52.52	3.17	0.50	18.66	0.27	0.00	0.18	17.54	6.54	0.38	99.8

mineral	sample	Point	Depth (mbsf)	Grain size	Grain area	SiO2	Al2O3	TiO2	CaO	Na2O	K2O	MnO	MgO	FeO	Cr2O3	Total
Cpx	360_82R3_19a_C	8 / 3 .	723.537	G	rim	51.58	3.11	0.65	21.22	0.39	0.00	0.24	15.35	6.55	0.35	99.4
Cpx	360_82R3_19a_C	8 / 4 .	723.537	G	rim	52.43	2.63	0.50	18.97	0.26	0.00	0.16	17.08	7.28	0.36	99.7
Cpx	360_82R3_19a_C	8 / 5 .	723.537	G	core	51.36	2.88	1.22	21.53	0.33	0.02	0.22	15.35	6.40	0.19	99.5
Cpx	360_82R3_19a_D	11 / 1 .	723.548	F	rim	52.56	2.81	0.65	19.46	0.35	0.00	0.21	16.20	7.94	0.27	100.4
Cpx	360_82R3_19a_D	11 / 2 .	723.548	G	core	51.40	3.90	0.67	21.18	0.50	0.01	0.19	15.64	5.56	0.58	99.6
Cpx	360_82R3_19a_D	11 / 3 .	723.548	G	rim	52.02	3.14	1.02	21.58	0.50	0.00	0.14	15.10	6.42	0.43	100.4
Cpx	360_82R3_19a_E	13 / 1 .	723.552	F	core	51.55	2.89	1.10	19.57	0.40	0.00	0.28	15.65	8.02	0.24	99.7
Cpx	360_82R3_19a_E	13 / 2 .	723.552	G	core	51.82	3.17	0.49	21.47	0.38	0.01	0.27	14.77	7.04	0.43	99.8
Cpx	360_82R3_19a_E	13 / 5 .	723.552	G	rim	52.77	2.87	0.38	20.15	0.35	0.00	0.19	16.84	6.39	0.26	100.2
Cpx	360_82R3_19a_E	13 / 6 .	723.552	G	core	52.06	3.09	0.74	21.02	0.35	0.01	0.23	15.78	7.12	0.30	100.7
Cpx	360_82R3_19a_F	16 / 1 .	723.5605	G	core	51.77	3.50	0.49	21.86	0.36	0.00	0.19	14.96	5.61	0.41	99.2
Cpx	360_82R3_19a_F	16 / 2 .	723.5605	G	rim	51.52	3.30	1.18	17.90	0.53	0.00	0.25	16.57	8.61	0.24	100.1
Cpx	360_82R3_19a_F	16 / 3 .	723.5605	F	core	51.89	2.67	1.05	15.09	0.29	0.01	0.23	18.12	10.46	0.23	100.1
Cpx	360_82R3_19a_F	16 / 4 .	723.5605	F	core	51.28	3.13	1.10	21.87	0.41	0.01	0.20	14.88	6.59	0.29	99.8
Cpx	360_82R3_19a_G	19 / 2 .	723.562	G	core	51.54	3.03	0.70	19.86	0.44	0.00	0.22	15.56	7.73	0.35	99.4
Cpx	360_82R3_19a_G	19 / 3 .	723.562	G	rim	51.45	3.09	1.06	19.82	0.38	0.00	0.23	15.52	7.42	0.27	99.2
Cpx	360_80R6_64b_A	5 / 1 .	707.954	G	rim	51.84	2.74	0.59	19.76	0.32	0.02	0.24	15.79	7.58	0.19	99.1
Cpx	360_80R6_64b_A	5 / 2 .	707.954	G	core	52.37	3.49	0.64	20.08	0.35	0.02	0.22	16.75	5.72	0.40	100.0
Cpx	360_80R6_64b_A	5 / 5 .	707.954	G	rim	51.68	3.07	0.73	21.91	0.35	0.01	0.17	15.20	6.06	0.25	99.4
Cpx	360_80R6_64b_B	7 / 3 .	707.958	G	rim	51.71	2.71	0.86	19.54	0.28	0.01	0.22	15.83	8.20	0.17	99.5
Cpx	360_80R6_64b_B	7 / 4 .	707.958	G	core	51.89	3.59	0.54	19.52	0.39	0.00	0.22	16.50	6.29	0.41	99.4
Cpx	360_80R6_64b_B	7 / 5 .	707.958	G	rim	52.20	2.78	0.80	21.00	0.35	0.04	0.19	15.55	6.73	0.26	99.9
Cpx	360_80R6_64b_B	7 / 6 .	707.958	G	core	52.85	2.98	0.47	20.30	0.40	0.03	0.16	17.36	5.72	0.28	100.6
Cpx	360_80R6_64b_B	7 / 7 .	707.958	G	rim	52.20	2.59	0.76	20.33	0.32	0.01	0.21	15.55	7.16	0.19	99.3
Cpx	360_80R6_64b_B	7 / 8 .	707.958	F	core	52.25	3.26	0.46	21.87	0.32	0.00	0.13	15.69	5.10	0.42	99.5
Cpx	360_80R6_64b_C	11 / 1 .	707.962	F	core	51.12	4.04	0.59	21.17	0.50	0.02	0.20	14.81	6.22	0.59	99.3
Cpx	360_80R6_64b_C	11 / 2 .	707.962	F	rim	51.27	3.20	0.91	19.25	0.36	0.00	0.22	16.00	8.11	0.28	99.6
Cpx	360_80R6_64b_C	11 / 4 .	707.962	G	core	51.26	3.44	0.50	18.52	0.34	0.02	0.19	17.13	7.46	0.37	99.2
Cpx	360_80R6_64b_C	11 / 5 .	707.962	G	rim	51.16	3.23	0.69	21.40	0.44	0.02	0.17	15.03	6.92	0.34	99.4
Cpx	360_80R6_64b_C	11 / 8 .	707.962	G	core	51.46	2.85	0.76	21.21	0.30	0.00	0.21	15.32	6.86	0.19	99.2
Cpx	360_80R6_64b_D	13 / 1 .	707.967	G	rim	52.43	3.26	0.43	16.21	0.29	0.00	0.21	18.47	8.83	0.39	100.5
Cpx	360_80R6_64b_D	13 / 2 .	707.967	G	core	51.20	3.67	0.60	21.37	0.53	0.00	0.18	15.14	6.96	0.37	100.0
Cpx	360_80R6_64b_D	13 / 3 .	707.967	G	core	51.62	2.89	1.06	20.97	0.39	0.00	0.23	14.75	7.50	0.09	99.5
Cpx	360_80R6_64b_D	13 / 5 .	707.967	G	rim	51.99	2.70	0.83	19.94	0.30	0.03	0.20	15.94	7.60	0.09	99.6
Cpx	360_80R6_64b_D	13 / 6 .	707.967	G	core	51.77	3.04	0.46	20.46	0.32	0.03	0.15	15.54	7.14	0.28	99.2
Cpx	360_80R6_64b_E	15 / 1 .	707.97	G	core	52.77	2.56	0.42	19.94	0.31	0.00	0.16	17.45	5.77	0.29	99.7
Cpx	360_80R6_64b_E	15 / 2 .	707.97	G	rim	52.26	2.62	0.64	20.02	0.31	0.00	0.23	16.67	6.78	0.24	99.8
Cpx	360_80R6_64b_E	15 / 4 .	707.97	F	rim	52.08	2.76	0.90	18.60	0.32	0.00	0.24	16.44	8.44	0.24	100.0
Cpx	360_80R6_64b_E	15 / 5 .	707.97	F	rim	51.43	2.74	0.90	18.57	0.46	0.03	0.29	16.39	7.94	0.16	98.9
Cpx	360_80R6_64b_E	15 / 6 .	707.97	G	rim	51.10	3.18	1.04	21.20	0.39	0.02	0.16	14.96	6.86	0.25	99.1

mineral	sample	Point	Depth (mbsf)	Grain size	Grain area	SiO2	Al2O3	TiO2	CaO	Na2O	K2O	MnO	MgO	FeO	Cr2O3	Total
Cpx	360_80R6_64b_E	15 / 7 .	707.97	G	rim	51.70	2.51	0.54	21.41	0.30	0.00	0.21	15.86	6.37	0.33	99.2
Cpx	360_80R6_64b_F	18 / 1 .	707.9795	G	core	52.04	3.03	0.47	20.16	0.28	0.02	0.12	16.79	5.97	0.20	99.1
Cpx	360_80R6_64b_F	18 / 2 .	707.9795	G	rim	51.90	2.55	0.78	19.54	0.33	0.03	0.25	16.19	8.17	0.11	99.9
Cpx	360_80R6_64b_F	18 / 5 .	707.9795	F	core	51.48	2.97	1.23	22.09	0.36	0.03	0.24	14.86	7.00	0.09	100.3
Cpx	360_80R6_64b_F	18 / 7 .	707.9795	G	core	52.30	3.02	0.60	21.19	0.32	0.00	0.20	15.91	7.52	0.12	101.2
Cpx	360_44R5_0_A	4 / 1 .	406.374	G	core	51.45	2.69	1.03	21.83	0.44	0.02	0.16	14.17	7.32	0.05	99.2
Cpx	360_44R5_0_A	4 / 2 .	406.374	G	rim	51.45	2.65	1.05	21.40	0.39	0.02	0.24	14.61	8.00	0.04	99.8
Cpx	360_44R5_0_A	4 / 3 .	406.374	G	core	50.96	2.70	1.16	21.58	0.52	0.01	0.22	13.99	7.90	0.01	99.0
Cpx	360_44R5_0_A	4 / 4 .	406.374	G	rim	51.68	2.21	0.69	20.80	0.39	0.01	0.22	14.57	8.44	0.00	99.0
Cpx	360_44R5_0_A	4 / 5 .	406.374	F	core	51.18	2.64	0.92	22.04	0.41	0.00	0.29	13.89	7.93	0.05	99.4
Cpx	360_44R5_0_B	12 / 1 .	406.382	G	core	51.75	2.52	0.64	20.05	0.36	0.01	0.22	15.50	8.48	0.01	99.5
Cpx	360_44R5_0_B	12 / 3 .	406.382	G	rim	51.74	2.46	0.73	22.24	0.38	0.00	0.23	14.34	7.83	0.01	100.0
Cpx	360_44R5_0_B	12 / 4 .	406.382	G	core	51.69	2.55	0.76	18.85	0.32	0.00	0.29	16.23	9.10	0.02	99.8
Cpx	360_44R5_0_B	12 / 5 .	406.382	G	rim	52.12	2.55	0.84	20.13	0.37	0.06	0.26	14.95	9.48	0.01	100.8
Cpx	360_44R5_0_C	15 / 1 .	406.3815	G	core	51.43	3.13	0.77	21.41	0.38	0.00	0.23	14.93	6.61	0.03	98.9
Cpx	360_44R5_0_C	15 / 2 .	406.3815	G	rim	53.15	1.98	0.59	17.49	0.34	0.00	0.25	17.49	9.33	0.06	100.7
Cpx	360_44R5_0_Cbis	18 / 1 .	406.3815	G	rim	51.95	2.75	1.03	21.47	0.40	0.00	0.22	14.36	8.28	0.00	100.4
Cpx	360_44R5_0_Cbis	18 / 2 .	406.3815	G	rim	52.26	2.52	0.63	16.99	0.32	0.00	0.27	16.59	9.38	0.05	99.0
Cpx	360_44R5_0_D	21 / 1 .	406.3905	G	core	51.39	3.14	0.79	21.19	0.48	0.02	0.25	14.58	7.18	0.00	99.0
Cpx	360_44R5_0_D	21 / 2 .	406.3905	G	rim	52.41	2.83	0.78	18.67	0.40	0.03	0.22	17.07	8.01	0.07	100.5
Cpx	360_44R5_0_D	21 / 5 .	406.3905	F	core	51.67	2.56	0.90	19.81	0.37	0.02	0.23	15.66	8.88	0.06	100.1
Cpx	360_44R5_0_E	25 / 4 .	406.389	F	rim	51.62	2.69	0.96	21.71	0.49	0.00	0.22	14.34	7.73	0.02	99.8
Cpx	360_44R5_0_E	25 / 5 .	406.389	G	rim	51.79	2.44	0.91	21.74	0.39	0.01	0.27	14.43	7.66	0.03	99.7
Cpx	360_44R5_0_E	25 / 6 .	406.389	G	rim	51.73	2.62	1.02	21.72	0.45	0.00	0.24	14.48	7.89	0.01	100.2
Cpx	360_44R5_0_E	25 / 7 .	406.389	G	rim	51.70	2.65	0.92	21.31	0.40	0.00	0.29	14.76	8.26	0.00	100.3
Cpx	360_44R5_0_Ebis	30 / 1 .	406.3905	G	core	51.49	3.22	0.73	20.25	0.46	0.00	0.23	15.64	7.45	0.00	99.5
Cpx	360_44R5_0_Ebis	30 / 2 .	406.3905	G	core	51.41	2.74	0.89	21.85	0.46	0.00	0.18	14.45	7.38	0.07	99.4
Cpx	360_44R5_0_F	33 / 3 .	406.396	G	core	52.32	2.52	0.73	17.55	0.27	0.00	0.26	16.91	10.29	0.04	100.9
Cpx	360_44R5_0_F	33 / 4 .	406.396	G	rim	52.33	2.32	0.75	13.35	0.25	0.01	0.31	18.50	12.63	0.04	100.5
Cpx	360_44R5_0_F	33 / 5 .	406.396	F	core	51.34	2.79	1.05	21.70	0.45	0.00	0.29	14.30	7.84	0.00	99.7
Cpx	360_44R5_0_F	33 / 6 .	406.396	F	core	51.37	3.02	0.92	21.01	0.48	0.00	0.22	14.26	8.46	0.01	99.8
Cpx	360_43R1_105_Abis	3 / 1 .	390.484	G	core	51.93	2.64	0.64	20.23	0.28	0.00	0.22	15.55	7.83	0.06	99.4
Cpx	360_43R1_105_Abis	3 / 2 .	390.484	G	rim	52.72	2.52	0.65	19.21	0.35	0.00	0.24	16.24	8.37	0.05	100.3
Cpx	360_43R1_105_Abis	3 / 3 .	390.484	G	rim	51.98	2.62	0.90	22.10	0.39	0.00	0.22	14.78	6.82	0.02	99.8
Cpx	360_43R1_105_B	7 / 1 .	390.4975	G	rim	52.88	2.64	0.68	15.92	0.26	0.00	0.28	18.17	9.36	0.05	100.2
Cpx	360_43R1_105_B	7 / 2 .	390.4975	G	rim	51.71	2.94	0.88	20.23	0.31	0.01	0.21	15.84	7.79	0.06	100.0
Cpx	360_43R1_105_B	7 / 5 .	390.4975	F	core	51.67	2.87	0.91	21.85	0.33	0.00	0.21	15.21	6.94	0.04	100.0
Cpx	360_43R1_105_Cbis	11 / 1 .	390.4965	G	core	52.30	2.44	0.59	18.76	0.36	0.00	0.26	17.04	7.87	0.01	99.6
Cpx	360_43R1_105_Cbis	11 / 3 .	390.4965	G	core	52.51	2.65	0.59	17.92	0.32	0.01	0.25	17.36	7.93	0.06	99.6
Cpx	360_43R1_105_C	13 / 1 .	390.498	G	rim	51.06	2.96	1.25	21.54	0.50	0.00	0.25	14.39	7.41	0.02	99.4

mineral	sample	Point	Depth (mbsf)	Grain size	Grain area	SiO2	Al2O3	TiO2	CaO	Na2O	K2O	MnO	MgO	FeO	Cr2O3	Total
Cpx	360_43R1_105_C	13 / 2 .	390.498	G	rim	51.73	2.59	0.94	22.39	0.38	0.02	0.20	14.78	6.77	0.03	99.8
Cpx	360_43R1_105_D	16 / 1 .	390.495	F	core	50.95	2.79	1.00	21.86	0.38	0.00	0.25	14.12	7.41	0.04	98.8
Cpx	360_43R1_105_E	19 / 1 .	390.511	G	rim	52.32	2.70	0.70	22.17	0.38	0.01	0.20	15.12	6.55	0.05	100.2
Cpx	360_43R1_105_E	19 / 2 .	390.511	G	core	51.94	2.81	0.68	21.71	0.37	0.02	0.17	15.12	6.71	0.02	99.5
Cpx	360_43R1_105_F	25 / 1 .	390.503	G	core	52.43	2.78	0.71	22.06	0.45	0.00	0.19	15.02	6.81	0.06	100.5
Cpx	360_43R1_105_F	25 / 2 .	390.503	G	rim	52.00	2.60	0.85	22.01	0.44	0.02	0.16	14.84	6.98	0.05	100.0
Cpx	360_43R1_105_F	25 / 3 .	390.503	G	rim	52.31	2.55	1.02	20.90	0.34	0.02	0.19	15.41	7.48	0.03	100.3
Cpx	360_43R1_105_F	25 / 4 .	390.503	G	core	52.18	2.56	0.77	21.10	0.34	0.00	0.22	15.33	7.58	0.03	100.1
Cpx	360_43R1_105_F	25 / 5 .	390.503	F	core	52.48	2.62	0.86	22.02	0.38	0.00	0.23	14.86	6.64	0.02	100.1
Cpx	360_43R1_105_F	25 / 6 .	390.503	G	core	51.88	2.72	0.69	21.81	0.36	0.00	0.22	14.89	6.54	0.05	99.2
Cpx	360_41R2_1_A	3 / 1 .	372.854	F	core	52.85	2.48	0.88	10.73	0.34	0.00	0.33	19.25	14.07	0.05	101.0
Cpx	360_41R2_1_A	3 / 2 .	372.854	F	rim	52.49	2.35	0.69	21.96	0.38	0.00	0.26	14.64	7.60	0.01	100.4
Cpx	360_41R2_1_A	3 / 5 .	372.854	G	rim	51.56	2.61	1.04	21.92	0.42	0.00	0.24	14.49	7.67	0.01	100.0
Cpx	360_41R2_1_A	3 / 6 .	372.854	G	rim	51.74	2.80	1.12	20.76	0.45	0.00	0.19	14.66	8.14	0.04	99.9
Cpx	360_41R2_1_A	3 / 7 .	372.854	G	core	51.46	2.79	1.00	22.01	0.39	0.00	0.28	14.33	7.49	0.05	99.8
Cpx	360_41R2_1_B	8 / 2 .	372.855	G	rim	52.48	2.12	0.50	22.43	0.31	0.00	0.23	15.38	6.63	0.01	100.1
Cpx	360_41R2_1_B	8 / 3 .	372.855	G	core	52.44	2.41	0.54	16.29	0.25	0.02	0.24	17.58	10.29	0.04	100.1
Cpx	360_41R2_1_B	8 / 4 .	372.855	G	core	52.14	2.78	0.67	18.55	0.38	0.00	0.30	15.81	9.27	0.04	99.9
Cpx	360_41R2_1_B	8 / 5 .	372.855	G	rim	52.58	2.31	0.60	21.29	0.33	0.00	0.21	15.36	7.63	0.03	100.3
Cpx	360_41R2_1_B	8 / 6 .	372.855	F	core	53.05	2.09	0.58	21.70	0.30	0.02	0.21	15.00	7.45	0.04	100.4
Cpx	360_41R2_1_B	8 / 7 .	372.855	F	core	51.98	2.61	0.85	21.87	0.36	0.00	0.24	14.66	7.43	0.00	100.0
Cpx	360_41R2_1_C	11 / 1 .	372.8655	G	core	51.60	2.58	0.80	21.18	0.37	0.00	0.22	14.42	7.65	0.03	98.9
Cpx	360_41R2_1_C	11 / 2 .	372.8655	G	rim	52.39	2.54	0.74	19.74	0.33	0.00	0.22	15.40	8.37	0.05	99.8
Cpx	360_41R2_1_C	11 / 3 .	372.8655	G	core	52.25	2.55	0.77	21.15	0.39	0.02	0.24	14.87	8.41	0.08	100.7
Cpx	360_41R2_1_C	11 / 4 .	372.8655	G	rim	52.14	2.75	1.01	19.42	0.40	0.02	0.24	15.66	9.37	0.00	101.0
Cpx	360_41R2_1_C	11 / 5 .	372.8655	G	rim	51.88	2.71	0.96	19.87	0.33	0.01	0.31	15.29	9.16	0.04	100.5
Cpx	360_41R2_1_Cbis	16 / 1 .	372.868	F	core	52.91	2.27	0.86	17.07	0.28	0.00	0.28	16.06	10.81	0.00	100.5
Cpx	360_41R2_1_Cbis	16 / 2 .	372.868	F	core	51.56	2.71	0.98	20.78	0.45	0.00	0.23	14.83	8.38	0.03	100.0
Cpx	360_41R2_1_Cbis	16 / 3 .	372.868	G	core	52.16	2.68	0.60	20.06	0.39	0.04	0.18	15.75	7.69	0.01	99.6
Cpx	360_41R2_1_Cbis	16 / 4 .	372.868	G	rim	52.52	2.06	0.56	13.96	0.28	0.01	0.37	18.06	12.03	0.00	99.8
Cpx	360_41R2_1_D	19 / 1 .	372.8745	G	rim	52.52	2.48	0.76	18.04	0.32	0.00	0.28	15.65	10.58	0.01	100.6
Cpx	360_41R2_1_D	19 / 2 .	372.8745	G	rim	51.41	2.85	1.07	20.72	0.47	0.01	0.23	14.47	8.66	0.08	100.0
Cpx	360_41R2_1_D	19 / 3 .	372.8745	G	core	52.24	2.75	0.77	20.92	0.39	0.01	0.25	15.03	7.61	0.00	100.0
Cpx	360_41R2_1_D	19 / 4 .	372.8745	G	core	52.06	2.32	0.83	18.94	0.38	0.01	0.22	15.11	9.67	0.03	99.6
Cpx	360_41R2_1_D	19 / 5 .	372.8745	G	rim	51.75	2.54	1.03	19.52	0.34	0.02	0.25	15.25	9.63	0.02	100.4
Cpx	360_41R2_1_E	22 / 1 .	372.873	F	core	52.43	1.94	0.50	21.59	0.33	0.01	0.25	14.64	8.04	0.03	99.8
Cpx	360_41R2_1_E	22 / 2 .	372.873	G	rim	52.08	2.46	0.82	21.40	0.32	0.02	0.17	14.59	7.93	0.04	99.8
Cpx	360_41R2_1_E	22 / 3 .	372.873	G	rim	51.80	2.75	0.95	21.02	0.39	0.00	0.24	14.50	8.08	0.02	99.7
Cpx	360_41R2_1_E	22 / 4 .	372.873	G	core	52.14	2.46	0.81	21.20	0.37	0.00	0.29	14.96	7.70	0.00	99.9
Cpx	360_41R2_1_E	22 / 5 .	372.873	G	rim	51.46	2.69	0.83	21.52	0.44	0.00	0.26	14.20	7.77	0.00	99.2

mineral	sample	Point	Depth (mbsf)	Grain size	Grain area	SiO2	Al2O3	TiO2	CaO	Na2O	K2O	MnO	MgO	FeO	Cr2O3	Total
Cpx	360_41R2_1_F	25 / 1 .	372.879	G	core	52.50	2.83	0.61	19.50	0.39	0.00	0.24	16.09	7.86	0.02	100.0
Cpx	360_41R2_1_F	25 / 2 .	372.879	G	rim	51.66	2.84	0.98	21.17	0.39	0.00	0.27	14.39	7.90	0.00	99.6
Cpx	360_41R2_1_F	25 / 3 .	372.879	G	core	52.07	2.65	0.75	21.70	0.39	0.04	0.21	14.97	7.30	0.05	100.1
Cpx	360_41R2_1_F	25 / 6 .	372.879	G	rim	51.94	2.84	0.95	21.42	0.38	0.00	0.30	14.52	8.10	0.06	100.5
Cpx	360_50R1_73_A	26 / 1 .	449.604	G	core	52.02	2.76	0.59	20.98	0.44	0.00	0.20	15.12	7.88	0.11	100.1
Cpx	360_50R1_73_A	26 / 2 .	449.604	G	rim	51.68	2.70	0.77	21.31	0.46	0.00	0.31	14.64	7.81	0.08	99.8
Cpx	360_50R1_73_A	26 / 3 .	449.604	F	core	52.82	2.18	0.55	22.32	0.38	0.02	0.24	14.82	7.06	0.06	100.4
Cpx	360_50R1_73_A	26 / 4 .	449.604	F	rim	51.86	2.61	0.75	21.87	0.41	0.00	0.19	14.72	7.29	0.15	99.8
Cpx	360_50R1_73_A	26 / 5 .	449.604	F	core	52.25	2.61	0.83	19.18	0.37	0.02	0.22	15.67	8.74	0.07	100.0
Cpx	360_50R1_73_B	30 / 3 .	449.6093	F	core	52.56	2.43	0.80	16.32	0.32	0.01	0.24	17.42	10.23	0.07	100.4
Cpx	360_50R1_73_B	30 / 4 .	449.6093	F	core	52.03	2.85	0.96	21.42	0.41	0.01	0.22	14.77	7.55	0.05	100.3
Cpx	360_50R1_73_C	1 / 1 .	449.6115	F	core	52.49	2.14	0.66	20.34	0.36	0.00	0.25	16.01	7.85	0.08	100.2
Cpx	360_50R1_73_C	3 / 2 .	449.6115	G	rim	51.79	2.75	0.80	21.36	0.43	0.01	0.23	14.77	7.34	0.14	99.6
Cpx	360_50R1_73_C	3 / 3 .	449.6115	G	rim	51.57	2.70	0.87	21.00	0.36	0.01	0.27	15.06	7.53	0.12	99.5
Cpx	360_50R1_73_C	3 / 4 .	449.6115	F	core	52.40	2.77	1.15	18.79	0.39	0.01	0.30	15.55	8.96	0.02	100.3
Cpx	360_50R1_73_C	3 / 5 .	449.6115	F	rim	50.49	3.26	1.04	21.00	0.45	0.00	0.15	14.68	8.06	0.07	99.2
Cpx	360_50R1_73_D	8 / 1 .	449.615	F	core	52.07	2.58	0.73	19.45	0.38	0.00	0.26	15.34	8.73	0.15	99.7
Cpx	360_50R1_73_D	8 / 2 .	449.615	F	rim	51.56	2.64	0.98	21.91	0.37	0.00	0.22	14.56	7.06	0.12	99.4
Cpx	360_50R1_73_D	8 / 3 .	449.615	F	rim	51.92	2.61	0.95	22.03	0.39	0.01	0.25	14.49	7.19	0.10	99.9
Cpx	360_50R1_73_E	12 / 1 .	449.624	F	core	52.18	2.82	0.70	21.13	0.45	0.00	0.21	15.05	7.52	0.07	100.1
Cpx	360_50R1_73_E	12 / 2 .	449.624	F	core	52.15	2.62	0.67	21.94	0.36	0.00	0.23	14.82	7.31	0.10	100.2
Cpx	360_50R1_73_E	12 / 3 .	449.624	F	core	51.53	3.12	0.87	22.25	0.43	0.00	0.19	14.49	6.97	0.14	100.0
Cpx	360_50R1_73_E	12 / 4 .	449.624	F	core	51.47	2.85	1.01	21.13	0.43	0.01	0.16	14.80	7.63	0.12	99.6
Cpx	360_50R1_73_E	12 / 5 .	449.624	G	rim	52.06	2.72	0.89	20.41	0.40	0.00	0.21	15.21	7.50	0.09	99.5
Cpx	360_50R1_73_E	12 / 6 .	449.624	G	core	52.42	2.55	0.46	19.87	0.38	0.00	0.18	16.20	7.04	0.05	99.2
Cpx	360_50R1_73_E	12 / 7 .	449.624	G	core	51.68	2.90	1.06	21.23	0.45	0.00	0.24	14.72	7.29	0.08	99.7
Cpx	360_50R1_73_F	15 / 1 .	449.622	G	core	52.76	2.63	0.50	17.24	0.32	0.00	0.26	17.63	8.65	0.12	100.1
Cpx	360_50R1_73_F	15 / 2 .	449.622	G	rim	52.62	2.54	0.75	19.00	0.30	0.02	0.29	16.71	8.28	0.10	100.6
Cpx	360_50R1_73_F	15 / 4 .	449.622	G	core	52.12	2.84	0.59	21.87	0.43	0.01	0.21	15.45	6.44	0.04	100.0
Cpx	360_50R1_73_F	15 / 5 .	449.622	G	rim	52.35	2.62	0.67	19.85	0.40	0.02	0.24	15.77	7.07	0.09	99.1
Cpx	360_50R1_73_G	18 / 2 .	449.627	F	core	52.87	2.79	0.62	18.35	0.38	0.03	0.17	16.89	7.94	0.13	100.2
Cpx	360_50R1_73_G	18 / 3 .	449.627	F	rim	52.41	2.40	0.69	20.10	0.43	0.01	0.24	16.06	7.12	0.10	99.5
Cpx	360_50R1_73_G	18 / 4 .	449.627	G	core	51.66	3.08	0.58	21.40	0.37	0.00	0.19	15.60	6.41	0.23	99.5
Cpx	360_50R1_73_G	18 / 5 .	449.627	G	rim	52.28	2.88	0.85	21.47	0.41	0.01	0.20	14.90	6.89	0.15	100.0
Cpx	360_60R2_69_A	20 / 1 .	539.8535	G	core	52.10	2.90	0.89	21.53	0.43	0.01	0.19	14.87	6.85	0.10	99.9
Cpx	360_60R2_69_A	20 / 2 .	539.8535	G	rim	51.91	2.69	0.90	21.44	0.43	0.00	0.16	15.15	6.79	0.04	99.5
Cpx	360_60R2_69_A	20 / 3 .	539.8535	F	core	52.05	2.51	0.95	19.78	0.43	0.00	0.21	15.98	8.07	0.05	100.0
Cpx	360_60R2_69_A	20 / 4 .	539.8535	F	rim	52.26	2.46	0.88	17.98	0.38	0.00	0.23	16.81	9.34	0.08	100.4
Cpx	360_60R2_69_A	20 / 5 .	539.8535	G	core	52.44	2.34	0.88	21.61	0.42	0.00	0.21	15.00	7.00	0.04	99.9
Cpx	360_60R2_69_B	24 / 1 .	539.8587	F	core	51.82	2.44	0.79	21.73	0.42	0.00	0.15	14.94	6.74	0.01	99.0

mineral	sample	Point	Depth (mbsf)	Grain size	Grain area	SiO2	Al2O3	TiO2	CaO	Na2O	K2O	MnO	MgO	FeO	Cr2O3	Total
Cpx	360_60R2_69_B	24 / 2 .	539.8587	G	rim	51.85	2.55	0.78	20.81	0.32	0.01	0.17	15.47	7.37	0.05	99.4
Cpx	360_60R2_69_B	24 / 3 .	539.8587	G	core	52.27	3.05	0.61	21.70	0.45	0.00	0.22	15.06	6.61	0.12	100.1
Cpx	360_60R2_69_B	24 / 4 .	539.8587	F	rim	51.82	2.63	0.87	21.67	0.43	0.01	0.21	14.86	6.85	0.05	99.4
Cpx	360_60R2_69_B	24 / 5 .	539.8587	F	core	51.66	2.81	0.96	21.42	0.44	0.01	0.23	14.78	7.07	0.04	99.4
Cpx	360_60R2_69_B	24 / 6 .	539.8587	F	core	51.73	2.71	0.68	21.92	0.45	0.00	0.25	14.94	6.81	0.01	99.5
Cpx	360_60R2_69_C	28 / 1 .	539.8613	F	core	52.02	2.58	0.83	20.21	0.41	0.00	0.20	15.84	7.64	0.06	99.8
Cpx	360_60R2_69_C	28 / 2 .	539.8613	F	core	51.91	2.79	0.89	22.02	0.45	0.01	0.19	14.63	6.76	0.08	99.7
Cpx	360_60R2_69_D	3 / 2 .	539.8674	F	core	52.31	2.82	0.68	18.77	0.37	0.00	0.21	16.37	7.94	0.01	99.5
Cpx	360_60R2_69_D	3 / 3 .	539.8674	F	rim	52.09	2.80	0.77	21.66	0.42	0.00	0.24	14.81	7.09	0.05	99.9
Cpx	360_60R2_69_D	3 / 4 .	539.8674	F	core	51.64	2.87	0.91	21.88	0.43	0.00	0.23	14.74	6.91	0.11	99.7
Cpx	360_60R2_69_D	3 / 5 .	539.8674	F	core	52.24	2.50	0.83	21.70	0.40	0.00	0.20	15.05	6.81	0.03	99.8
Cpx	360_60R2_69_D	3 / 7 .	539.8674	F	core	52.60	2.55	0.81	21.93	0.43	0.00	0.23	15.03	6.81	0.04	100.4
Cpx	360_60R2_69_D	3 / 8 .	539.8674	F	rim	52.23	2.32	0.86	20.52	0.43	0.00	0.24	15.87	7.63	0.04	100.1
Cpx	360_60R2_69_E	6 / 1 .	539.874	F	core	52.57	2.72	0.83	21.77	0.35	0.00	0.16	15.28	6.82	0.03	100.5
Cpx	360_60R2_69_E	6 / 2 .	539.874	F	rim	51.96	2.60	0.86	21.76	0.43	0.01	0.15	15.01	6.78	0.03	99.6
Cpx	360_60R2_69_E	6 / 3 .	539.874	F	core	52.42	2.38	0.79	19.58	0.36	0.00	0.21	15.82	7.90	0.03	99.5
Cpx	360_60R2_69_F	8 / 1 .	539.8767	G	rim	51.95	2.61	1.14	19.20	0.45	0.00	0.18	15.88	8.13	0.09	99.6
Cpx	360_60R2_69_F	8 / 2 .	539.8767	G	core	52.49	2.33	0.51	20.96	0.39	0.00	0.22	15.61	7.10	0.08	99.7
Cpx	360_60R2_69_F	8 / 3 .	539.8767	F	core	51.71	2.81	1.00	22.05	0.39	0.00	0.23	14.65	6.86	0.04	99.7
Cpx	360_60R2_69_F	8 / 4 .	539.8767	F	rim	51.77	2.64	1.00	21.72	0.46	0.00	0.15	14.77	7.14	0.06	99.7
Cpx	360_60R2_69_F	8 / 7 .	539.8767	F	core	51.71	2.80	1.05	22.04	0.42	0.00	0.21	14.52	7.07	0.04	99.9
Cpx	360_66R3_29_A	13 / 1 .	598.438	G	core	52.72	3.12	0.55	21.12	0.39	0.00	0.23	16.00	6.02	0.19	100.3
Cpx	360_66R3_29_A	13 / 2 .	598.438	G	rim	52.78	3.06	0.80	21.69	0.39	0.00	0.21	15.76	6.19	0.14	101.0
Cpx	360_66R3_29_A	13 / 3 .	598.438	F	core	52.66	2.58	0.48	22.42	0.29	0.00	0.21	15.74	5.64	0.24	100.3
Cpx	360_66R3_29_A	13 / 4 .	598.438	G	rim	52.86	2.76	0.79	20.28	0.31	0.00	0.17	16.49	7.18	0.14	101.0
Cpx	360_66R3_29_A	13 / 5 .	598.438	G	rim	52.45	2.64	0.81	22.21	0.35	0.00	0.21	15.40	5.86	0.15	100.1
Cpx	360_66R3_29_A	13 / 6 .	598.438	G	core	52.79	2.73	0.85	19.67	0.33	0.00	0.20	17.02	7.57	0.11	101.3
Cpx	360_66R3_29_B	17 / 3 .	598.434	G	core	52.86	3.25	0.57	21.15	0.36	0.00	0.22	16.26	6.34	0.17	101.2
Cpx	360_66R3_29_B	17 / 5 .	598.434	G	rim	52.33	2.69	0.81	22.26	0.31	0.00	0.20	15.47	5.87	0.12	100.1
Cpx	360_66R3_29_C	20 / 2 .	598.4405	F	core	53.15	2.57	0.55	20.86	0.34	0.00	0.20	16.29	6.02	0.15	100.1
Cpx	360_66R3_29_C	20 / 3 .	598.4405	F	rim	52.40	2.70	0.67	22.49	0.34	0.00	0.23	15.49	5.64	0.08	100.0
Cpx	360_66R3_29_Cbis	24 / 2 .	598.442	F	rim	52.59	2.55	0.87	19.50	0.29	0.03	0.16	16.91	7.08	0.16	100.1
Cpx	360_66R3_29_Cbis	24 / 4 .	598.442	G	core	53.26	2.28	0.44	19.90	0.25	0.00	0.19	17.02	6.53	0.19	100.1
Cpx	360_66R3_29_Cbis	24 / 5 .	598.442	G	rim	52.65	2.58	0.60	21.71	0.34	0.00	0.18	16.12	5.92	0.11	100.2
Cpx	360_66R3_29_D	26 / 2 .	598.4495	F	core	53.06	2.60	0.64	20.05	0.29	0.00	0.21	16.75	7.47	0.18	101.3
Cpx	360_66R3_29_D	26 / 3 .	598.4495	F	rim	53.25	2.27	0.70	18.55	0.34	0.02	0.19	17.51	7.16	0.12	100.1
Cpx	360_66R3_29_D	26 / 4 .	598.4495	F	rim	52.66	2.48	0.84	19.88	0.25	0.00	0.21	16.86	6.76	0.14	100.1
Cpx	360_66R3_29_D	26 / 5 .	598.4495	F	core	52.50	2.84	0.65	19.18	0.30	0.00	0.15	17.10	6.69	0.22	99.6
Cpx	360_66R3_29_E	3 / 1 .	598.4545	F	rim	52.63	2.53	0.96	20.54	0.32	0.00	0.22	16.24	6.55	0.08	100.1
Cpx	360_66R3_29_E	3 / 3 .	598.4545	G	rim	52.23	2.75	0.82	22.53	0.37	0.00	0.14	15.23	5.29	0.16	99.5

mineral	sample	Point	Depth (mbsf)	Grain size	Grain area	SiO2	Al2O3	TiO2	CaO	Na2O	K2O	MnO	MgO	FeO	Cr2O3	Total
Cpx	360_66R3_29_E	3 / 4 .	598.4545	G	core	53.03	2.52	0.47	21.56	0.31	0.00	0.18	15.88	5.78	0.25	100.0
Cpx	360_66R3_29_E	3 / 5 .	598.4545	G	rim	52.62	2.69	0.70	22.43	0.38	0.00	0.14	15.51	5.64	0.16	100.3
Cpx	360_66R3_29_F	8 / 2 .	598.4595	F	core	52.62	2.49	0.75	22.41	0.33	0.04	0.23	15.50	5.44	0.08	99.9
Cpx	360_66R3_29_F	8 / 4 .	598.4595	G	core	53.05	2.48	0.49	19.57	0.25	0.00	0.16	17.25	6.85	0.20	100.3
Cpx	360_66R3_29_F	8 / 5 .	598.4595	G	rim	52.68	2.54	0.76	19.29	0.29	0.01	0.20	17.01	6.91	0.06	99.7
Cpx	360_67R8_50_A	10 / 1 .	614.0135	G	core	52.12	3.13	0.98	22.01	0.42	0.01	0.22	15.35	5.97	0.15	100.4
Cpx	360_67R8_50_A	10 / 2 .	614.0135	G	rim	51.59	2.99	0.91	22.13	0.41	0.00	0.17	15.20	6.26	0.13	99.8
Cpx	360_67R8_50_A	10 / 3 .	614.0135	G	rim	52.06	2.81	0.88	22.33	0.29	0.00	0.16	15.39	6.22	0.15	100.3
Cpx	360_67R8_50_B	12 / 1 .	614.016	G	core	52.22	3.16	0.53	22.02	0.44	0.00	0.18	15.10	5.91	0.17	99.7
Cpx	360_67R8_50_B	12 / 2 .	614.016	G	rim	51.90	2.81	1.09	21.84	0.42	0.04	0.20	15.04	6.43	0.05	99.8
Cpx	360_67R8_50_B	12 / 5 .	614.016	G	rim	52.69	2.58	0.83	22.43	0.39	0.01	0.19	15.06	5.87	0.16	100.2
Cpx	360_67R8_50_C	17 / 1 .	614.0235	G	rim	52.32	2.94	0.87	22.33	0.40	0.00	0.19	15.49	5.83	0.08	100.5
Cpx	360_67R8_50_C	17 / 2 .	614.0235	G	core	52.72	3.16	0.50	22.29	0.41	0.00	0.15	15.55	5.58	0.15	100.5
Cpx	360_67R8_50_C	17 / 3 .	614.0235	G	rim	52.67	2.94	0.53	21.15	0.32	0.02	0.18	16.69	5.67	0.14	100.3
Cpx	360_67R8_50_C	17 / 5 .	614.0235	G	rim	52.11	2.89	0.91	21.99	0.40	0.00	0.18	15.36	6.12	0.07	100.0
Cpx	360_67R8_50_C	17 / 6 .	614.0235	G	rim	52.17	2.67	0.82	22.30	0.35	0.01	0.14	15.51	5.82	0.06	99.8
Cpx	360_67R8_50_C	17 / 7 .	614.0235	G	rim	52.55	2.79	0.45	22.36	0.33	0.00	0.13	15.68	5.48	0.11	99.9
Cpx	360_67R8_50_C	17 / 9 .	614.0235	G	core	52.64	2.87	0.63	22.44	0.37	0.00	0.17	15.26	5.74	0.15	100.3
Cpx	360_67R8_50_E	24 / 1 .	614.034	F	core	53.08	2.51	0.72	20.57	0.28	0.00	0.20	16.70	6.29	0.14	100.5
Cpx	360_67R8_50_E	24 / 3 .	614.034	F	core	52.12	2.84	0.60	22.21	0.34	0.00	0.26	15.29	5.49	0.14	99.3
Cpx	360_67R8_50_E	24 / 5 .	614.034	G	rim	52.83	2.87	0.59	19.05	0.31	0.00	0.18	17.05	6.83	0.13	99.8
Cpx	360_67R8_50_E	24 / 6 .	614.034	G	rim	52.07	2.57	0.75	22.06	0.34	0.01	0.25	15.36	5.63	0.11	99.2
Cpx	360_67R8_50_E	24 / 7 .	614.034	G	rim	52.22	2.75	0.57	19.93	0.26	0.01	0.27	16.45	7.51	0.11	100.1
Cpx	360_67R8_50_E	24 / 8 .	614.034	G	core	52.70	2.74	0.53	21.40	0.36	0.00	0.17	15.76	6.28	0.10	100.0
Cpx	360_67R8_50_F	27 / 1 .	614.041	F	core	52.91	2.37	0.76	21.68	0.38	0.00	0.14	15.96	5.63	0.12	99.9
Cpx	360_67R8_50_F	27 / 3 .	614.041	G	rim	52.72	2.36	0.69	21.66	0.28	0.00	0.15	16.24	5.81	0.11	100.0
Cpx	360_67R8_50_F	27 / 4 .	614.041	G	core	53.08	2.42	0.81	22.14	0.40	0.00	0.18	15.70	5.65	0.11	100.5
Cpx	360_67R8_50_G	30 / 1 .	614.038	F	core	52.05	2.74	0.84	20.53	0.31	0.00	0.22	16.17	5.93	0.08	98.9
Cpx	360_67R8_50_G	30 / 2 .	614.038	G	core	52.30	2.59	0.73	19.26	0.39	0.00	0.22	17.40	7.63	0.12	100.6
Cpx	360_67R8_50_G	30 / 3 .	614.038	G	rim	52.35	2.74	0.74	20.37	0.34	0.01	0.19	16.35	6.69	0.11	99.9
Cpx	360_67R8_50_G	30 / 4 .	614.038	G	rim	52.23	2.62	0.93	20.66	0.37	0.00	0.25	15.92	6.67	0.15	99.8
Cpx	360_67R8_50_G	30 / 5 .	614.038	G	rim	51.83	2.63	0.93	22.12	0.35	0.00	0.19	15.24	5.71	0.11	99.1
Cpx	360_67R8_50_G	30 / 8 .	614.038	F	core	51.83	2.47	0.92	22.02	0.38	0.00	0.22	15.14	6.09	0.07	99.1
Cpx	360_78R7_97b_A	1 / 1 .	689.695	G	core	52.68	2.59	0.67	17.72	0.33	0.00	0.25	16.94	8.05	0.09	99.3
Cpx	360_78R7_97b_A	2 / 3 .	689.695	G	rim	51.83	2.67	0.99	22.36	0.41	0.00	0.22	14.73	6.62	0.05	99.9
Cpx	360_78R7_97b_A	2 / 4 .	689.695	G	rim	52.24	2.56	0.64	20.45	0.35	0.01	0.28	15.77	7.15	0.06	99.5
Cpx	360_78R7_97b_A	2 / 5 .	689.695	G	core	52.16	2.56	0.73	22.01	0.38	0.00	0.21	15.07	6.64	0.07	99.8
Cpx	360_78R7_97b_Abis	6 / 1 .	689.695	G	core	52.87	2.75	0.57	19.28	0.42	0.00	0.22	16.66	7.18	0.07	100.0
Cpx	360_78R7_97b_Abis	6 / 3 .	689.695	G	core	52.41	2.74	0.55	21.60	0.36	0.00	0.20	15.61	5.78	0.06	99.3
Cpx	360_78R7_97b_Abis	6 / 4 .	689.695	G	core	52.66	2.90	0.61	22.16	0.33	0.00	0.24	15.00	5.52	0.09	99.5

mineral	sample	Point	Depth (mbsf)	Grain size	Grain area	SiO2	Al2O3	TiO2	CaO	Na2O	K2O	MnO	MgO	FeO	Cr2O3	Total
Cpx	360_78R7_97b_B	7 / 1 .	689.6995	G	core	52.75	2.53	0.64	18.26	0.29	0.00	0.20	17.55	7.91	0.09	100.2
Cpx	360_78R7_97b_B	7 / 2 .	689.6995	G	rim	53.01	2.32	0.65	17.13	0.25	0.00	0.24	17.74	8.54	0.07	100.0
Cpx	360_78R7_97b_B	7 / 3 .	689.6995	G	rim	51.74	2.72	0.99	22.01	0.33	0.01	0.23	15.17	6.64	0.06	99.9
Cpx	360_78R7_97b_B	7 / 4 .	689.6995	G	rim	52.05	2.69	1.16	19.36	0.27	0.00	0.26	16.30	8.34	0.04	100.5
Cpx	360_78R7_97b_C	12 / 1 .	689.702	G	core	52.97	2.21	0.55	18.29	0.30	0.00	0.18	17.80	7.34	0.06	99.7
Cpx	360_78R7_97b_C	12 / 2 .	689.702	G	rim	51.81	2.95	1.14	21.76	0.41	0.00	0.12	15.24	6.55	0.05	100.0
Cpx	360_78R7_97b_C	12 / 3 .	689.702	G	core	52.90	2.51	0.63	20.03	0.28	0.01	0.20	16.73	6.81	0.08	100.2
Cpx	360_78R7_97b_C	12 / 4 .	689.702	G	rim	51.98	2.66	0.75	21.60	0.28	0.02	0.24	15.33	6.48	0.08	99.4
Cpx	360_78R7_97b_C	12 / 6 .	689.702	F	core	52.80	2.57	0.56	22.21	0.31	0.01	0.16	15.33	6.12	0.04	100.1
Cpx	360_78R7_97b_D	16 / 2 .	689.7035	G	core	52.30	2.67	0.68	21.37	0.31	0.00	0.16	15.48	6.83	0.06	99.9
Cpx	360_78R7_97b_D	16 / 3 .	689.7035	G	rim	51.72	2.68	0.73	20.90	0.35	0.00	0.24	15.92	6.93	0.07	99.5
Cpx	360_78R7_97b_E	18 / 1 .	689.717	G	core	52.67	2.54	0.61	19.70	0.39	0.00	0.18	16.78	6.97	0.06	99.9
Cpx	360_78R7_97b_E	18 / 2 .	689.717	G	rim	52.26	2.63	0.69	21.02	0.30	0.00	0.25	15.80	7.62	0.09	100.7
Cpx	360_78R7_97b_E	23 / 1 .	689.717	G	core	52.72	2.86	0.56	21.18	0.35	0.00	0.21	15.96	6.20	0.05	100.1
Cpx	360_78R7_97b_F	26 / 2 .	689.712	G	rim	52.17	2.61	0.85	19.41	0.41	0.03	0.22	15.85	7.87	0.04	99.4
Cpx	360_78R7_97b_F	26 / 3 .	689.712	G	core	52.04	2.67	0.61	21.09	0.36	0.00	0.18	15.62	6.68	0.00	99.3
Cpx	360_78R7_97b_F	26 / 4 .	689.712	G	core	51.97	2.70	0.64	21.96	0.39	0.00	0.20	15.52	6.42	0.04	99.8
Cpx	360_77R2_60_A	30 / 1 .	680.5545	G	core	51.42	2.62	0.95	20.54	0.51	0.00	0.29	13.45	9.99	0.01	99.8
Cpx	360_77R2_60_A	30 / 3 .	680.5545	G	rim	51.72	2.33	0.90	20.06	0.45	0.01	0.31	13.81	10.25	0.00	99.8
Cpx	360_77R2_60_A	30 / 4 .	680.5545	F	rim	51.47	2.16	0.79	20.14	0.43	0.01	0.25	13.70	10.26	0.08	99.3
Cpx	360_77R2_60_A	30 / 5 .	680.5545	F	rim	51.92	1.92	0.68	19.31	0.39	0.00	0.31	14.53	11.02	0.01	100.1
Cpx	360_77R2_60_A	30 / 6 .	680.5545	F	core	51.78	2.08	0.78	20.54	0.44	0.02	0.25	13.70	9.93	0.01	99.5
Cpx	360_77R2_60_A	30 / 7 .	680.5545	F	core	51.83	2.37	0.90	20.71	0.45	0.00	0.33	13.39	9.78	0.02	99.8
Cpx	360_77R2_60_B	1 / 1 .	680.5555	F	core	51.44	2.44	0.81	20.42	0.45	0.00	0.34	13.44	9.89	0.00	99.2
Cpx	360_77R2_60_B	2 / 2 .	680.5555	F	rim	52.16	1.96	0.63	20.84	0.40	0.00	0.30	13.99	9.66	0.01	99.9
Cpx	360_77R2_60_B	2 / 3 .	680.5555	F	rim	51.49	2.00	0.70	21.00	0.40	0.01	0.33	13.91	10.06	0.00	99.9
Cpx	360_77R2_60_B	2 / 5 .	680.5555	F	core	51.85	2.12	0.63	20.91	0.35	0.00	0.25	13.63	10.06	0.04	99.8
Cpx	360_77R2_60_B	2 / 7 .	680.5555	F	core	51.71	2.20	0.82	20.99	0.39	0.00	0.33	13.70	9.56	0.04	99.7
Cpx	360_77R2_60_C	6 / 2 .	680.5615	G	core	51.70	2.68	1.03	21.11	0.44	0.00	0.31	14.29	8.89	0.02	100.5
Cpx	360_77R2_60_C	6 / 5 .	680.5615	G	rim	51.99	2.20	0.77	20.23	0.46	0.01	0.28	13.69	10.64	0.06	100.3
Cpx	360_77R2_60_C	6 / 6 .	680.5615	G	rim	51.62	2.62	0.85	20.98	0.56	0.01	0.33	13.57	9.95	0.03	100.5
Cpx	360_77R2_60_Cbis	8 / 1 .	680.5615	G	core	51.64	2.60	0.92	20.48	0.56	0.00	0.31	13.83	9.22	0.01	99.6
Cpx	360_77R2_60_D	10 / 1 .	680.5625	F	core	52.07	2.13	0.68	20.28	0.33	0.00	0.28	14.34	10.04	0.03	100.2
Cpx	360_77R2_60_E	14 / 1 .	680.569	G	rim	51.81	2.07	0.80	20.73	0.43	0.00	0.31	13.82	9.88	0.03	99.9
Cpx	360_77R2_60_E	14 / 5 .	680.569	G	rim	51.82	2.12	0.74	21.37	0.42	0.00	0.29	13.48	9.65	0.03	99.9
Cpx	360_77R2_60_F	17 / 1 .	680.573	G	core	52.03	2.52	0.82	20.57	0.43	0.00	0.22	14.98	7.86	0.04	99.5
Cpx	360_77R2_60_F	17 / 2 .	680.573	G	rim	52.10	2.57	0.77	20.74	0.43	0.01	0.22	14.93	7.95	0.03	99.8
Cpx	360_77R2_60_G	18 / 1 .	680.582	F	rim	52.80	1.81	0.56	16.03	0.35	0.01	0.39	15.63	13.58	0.00	101.2
Cpx	360_77R2_60_G	18 / 2 .	680.582	F	core	52.08	2.19	0.83	17.71	0.33	0.01	0.28	14.87	12.05	0.01	100.4
Cpx	360_77R2_60_G	18 / 3 .	680.582	F	rim	51.72	2.16	0.75	21.25	0.45	0.00	0.30	13.82	9.38	0.03	99.8

mineral	sample	Point	Depth (mbsf)	Grain size	Grain area	SiO2	Al2O3	TiO2	CaO	Na2O	K2O	MnO	MgO	FeO	Cr2O3	Total
Cpx	360_77R2_60_G	18 / 5 .	680.582	F	core	52.30	1.61	0.44	20.73	0.40	0.00	0.34	14.36	9.90	0.00	100.1
Cpx	360_77R2_60_G	18 / 6 .	680.582	F	rim	52.86	1.68	0.36	21.70	0.37	0.02	0.30	14.02	9.17	0.00	100.5
Cpx	360_77R2_60_H	21 / 1 .	680.578	F	rim	51.97	2.18	0.71	20.58	0.37	0.00	0.28	13.80	9.89	0.05	99.8
Cpx	360_77R2_60_I	26 / 1 .	680.583	G	core	51.74	2.52	0.93	19.67	0.43	0.01	0.21	15.03	9.74	0.04	100.3
Cpx	360_77R2_60_I	26 / 3 .	680.583	F	core	52.65	1.65	0.48	19.71	0.38	0.00	0.31	14.62	10.77	0.00	100.6
Cpx	360_77R2_60_I	26 / 4 .	680.583	F	core	51.87	2.08	0.96	21.17	0.44	0.00	0.30	13.45	9.94	0.00	100.2
Cpx	360_84R1_20_A	29 / 1 .	740.6555	G	rim	51.70	3.05	0.93	21.53	0.48	0.03	0.21	15.16	6.25	0.32	99.7
Cpx	360_84R1_20_A	29 / 2 .	740.6555	G	core	52.43	2.58	0.46	20.16	0.32	0.00	0.17	16.19	6.95	0.43	99.7
Cpx	360_84R1_20_A	29 / 3 .	740.6555	G	rim	51.82	3.21	1.25	20.22	0.37	0.00	0.20	15.78	6.85	0.17	99.9
Cpx	360_84R1_20_B	33 / 1 .	740.658	G	rim	51.76	2.84	0.83	20.46	0.35	0.00	0.21	15.72	6.97	0.33	99.5
Cpx	360_84R1_20_B	33 / 3 .	740.658	G	core	51.39	4.17	0.60	21.87	0.41	0.02	0.22	14.72	5.59	0.72	99.7
Cpx	360_84R1_20_C	3 / 1 .	740.6675	G	core	52.24	3.28	0.43	21.97	0.45	0.01	0.20	15.49	5.40	0.45	99.9
Cpx	360_84R1_20_C	3 / 2 .	740.6675	G	rim	51.38	2.95	1.28	19.70	0.37	0.02	0.24	15.54	8.02	0.13	99.7
Cpx	360_84R1_20_C	3 / 5 .	740.6675	F	core	52.05	2.88	1.07	21.04	0.41	0.01	0.16	15.29	7.52	0.08	100.5
Cpx	360_84R1_20_E	9 / 1 .	740.667	G	core	52.82	3.22	0.53	19.32	0.33	0.01	0.19	17.50	6.00	0.49	100.4
Cpx	360_84R1_20_E	9 / 2 .	740.667	G	rim	51.55	3.39	1.21	20.50	0.45	0.01	0.20	16.08	6.78	0.22	100.4
Cpx	360_84R1_20_E	9 / 3 .	740.667	G	rim	51.58	2.90	1.02	17.30	0.35	0.01	0.23	17.63	7.77	0.27	99.0
Cpx	360_84R1_20_E	9 / 4 .	740.667	F	core	52.08	2.67	0.59	21.59	0.38	0.01	0.12	15.43	5.61	0.53	99.0
Cpx	360_84R1_20_E	9 / 7 .	740.667	G	core	52.17	3.28	0.41	21.84	0.43	0.00	0.15	15.65	5.50	0.47	99.9
Cpx	360_84R1_20_E	9 / 8 .	740.667	G	rim	52.47	2.97	0.58	22.41	0.41	0.00	0.15	15.24	5.35	0.45	100.0
Cpx	360_84R1_20_F	13 / 2 .	740.68	F	core	51.20	3.40	1.37	21.68	0.41	0.02	0.20	15.00	5.86	0.18	99.3
Cpx	360_84R1_20_F	13 / 3 .	740.68	G	rim	51.22	3.34	1.25	20.99	0.38	0.00	0.22	15.87	6.56	0.22	100.0
Cpx	360_84R1_20_F	13 / 4 .	740.68	G	core	52.66	2.96	0.68	17.37	0.29	0.00	0.24	17.54	8.34	0.23	100.3
Cpx	360_84R1_20_G	18 / 1 .	740.674	G	core	52.00	2.98	0.48	21.89	0.36	0.00	0.18	15.60	6.18	0.49	100.2
Cpx	360_84R1_20_G	18 / 2 .	740.674	G	rim	52.49	2.80	0.60	21.18	0.31	0.00	0.19	15.99	6.01	0.33	99.9
Calibration standards						Wollastonite (San Carlos)	Al2O3	TiMnO3	Wollastonite	Albite	Orthose	TiMnO3	Forsterite	Fayalite	Cr2O3	

Appendix 3.2

In situ trace elements concentrations in ppm analyzed by LA-ICP-MS on Thermo Fisher Element XR in GM (Montpellier, France)

Mineral	Sample	Area	Point	depth (mbsf)	Grain size	Grain area	La	Ce	Pr	Nd	Sm	Eu	Gd	Tb	Dy	Y	Ho	Er	Tm	Yb	Lu
Pl	Analytical error average				1 sigma		0.058	0.126	0.014	0.062	0.016	0.044	0.016	0.002	0.01	0.018	0.002	0.006	0.0008	0.004	0.0006
Pl		A+A	xj_6	390.484	G	core	0.287	0.784	0.1156	0.51	0.128	0.486	0.106	0.0101	0.0544	0.252	0.0087	0.0205	0.0015	<0.00	0.00155
Pl		A+A	xj_7	390.484	G	rim	0.634	1.445	0.1756	0.736	0.1172	0.479	0.1107	0.0108	0.0518	0.2274	0.0082	0.0168	0.00168	0.0042	<0.00024
Pl		A+A	xj_8	390.484	F	core	0.711	1.336	0.1396	0.584	0.08	0.489	0.0479	0.0057	0.0261	0.122	0.00317	0.0021	<0.00039	0.0026	<0.00020
Pl		B+B	xj_9	390.497	G	rim	0.607	1.399	0.169	0.657	0.114	0.475	0.0783	0.0114	0.0469	0.239	0.0068	0.0122	0.00133	0.0066	0.00077
Pl	360_43R1_105	C+C	xj_12	390.4965	F	rim	0.1444	0.314	0.0384	0.1647	0.0337	0.1089	0.0225	0.00278	0.0162	0.0585	0.00206	0.00528	0.00022	0.00112	0.00008
Pl		D	xj_13	390.495	G	rim	0.1729	0.356	0.0393	0.1545	0.0266	0.1084	0.0143	0.00222	0.0107	0.0383	0.00115	0.00287	0.00024	<0.00042	0.00012
Pl		D	xj_14	390.495	G	core	0.09	0.2534	0.0321	0.1611	0.0325	0.1218	0.0234	0.00328	0.0186	0.0823	0.00303	0.0073	0.00083	0.00251	0.00053
Pl		D	xj_15	390.495	F	core	0.1766	0.385	0.0468	0.1801	0.0271	0.1197	0.0271	0.00233	0.0115	0.0472	0.00207	0.002	0.00027	<0.00017	0.00021
Pl		E+E	xj_16	390.509	F	core	0.1406	0.2347	0.0247	0.1052	0.018	0.1005	0.0132	0.00172	0.0091	0.0342	0.00126	0.0035	0.00033	0.00202	0.00008
Pl		A	xi_6	538.8035	G	core	0.1563	0.42	0.0594	0.312	0.0753	0.483	0.0694	0.0122	0.0608	0.327	0.0107	0.0262	0.00374	0.0204	0.00238
Pl		A	xi_7	538.8035	G	rim	0.698	1.613	0.2031	0.882	0.153	0.559	0.134	0.0127	0.0849	0.342	0.0118	0.0176	0.00356	0.0142	0.00188
Pl		A	xi_8	538.8035	G	core	0.2345	0.712	0.1039	0.453	0.139	0.481	0.104	0.0132	0.076	0.408	0.0124	0.0192	0.0057	0.0222	0.00172
Pl		B	xi_9	538.804	G	rim	0.569	1.316	0.1411	0.604	0.0946	0.366	0.0784	0.00809	0.0422	0.1685	0.00544	0.0135	0.00193	0.0059	0.00048
Pl		B	xi_10	538.804	G	core	0.382	1.061	0.1368	0.557	0.1121	0.394	0.0848	0.0119	0.053	0.2313	0.0099	0.0118	<0.00026	0.0107	0.00103
Pl		B	xi_11	538.804	F	core	0.643	1.193	0.1203	0.426	0.0687	0.386	0.0377	0.00559	0.019	0.1062	0.00217	0.0017	0.00058	0.0036	0.00027
Pl	360_60R1_26	C	xi_12	538.8115	G	core	0.924	1.917	0.2151	0.879	0.1388	0.594	0.1101	0.0118	0.0473	0.2327	0.00662	0.0102	0.00196	0.0087	0.00034
Pl		C	xi_14	538.8115	F	core	0.967	1.988	0.2234	0.829	0.1175	0.569	0.1145	0.0103	0.0464	0.2366	0.00732	0.0145	0.00108	0.0066	0.00073
Pl		E	xi_17	538.8285	F	core	0.93	1.949	0.2266	0.879	0.139	0.522	0.131	0.0104	0.0479	0.245	0.0056	0.0142	0.00255	0.0097	0.00157
Pl		G1	xi_19	538.8215	G	core	0.914	2.152	0.2473	0.916	0.15	0.54	0.1156	0.0124	0.0743	0.286	0.00723	0.0177	0.00196	0.0149	0.0015
Pl		G1	xi_20	538.8215	G	rim	1.376	3.21	0.351	1.248	0.15	0.519	0.127	0.0105	0.0561	0.26	0.0089	0.0171	<0.00029	0.003	0.00108
Pl		A	ba_9	372.854	G	core	0.842	2.029	0.2272	0.982	0.1635	0.606	0.1289	0.01538	0.0733	0.31	0.01095	0.0216	0.00198	0.0143	0.00112
Pl		A	ba_10	372.854	G	rim	0.829	1.636	0.1601	0.594	0.0608	0.587	0.0668	0.00487	0.0217	0.0987	0.00325	0.0067	0.00055	0.00124	0.00022
Pl		A	ba_11	372.854	F	core	0.862	1.88	0.215	0.761	0.1138	0.642	0.0844	0.0064	0.0298	0.1329	0.00396	0.008	0.00071	0.0049	0.00073
Pl		B	ba_12	372.855	G	rim	0.752	1.554	0.1631	0.574	0.0967	0.574	0.0757	0.00639	0.0215	0.1018	0.00433	0.0044	0.00113	0.0029	0.00058
Pl		B	ba_13	372.855	G	core	0.624	1.502	0.1768	0.765	0.1144	0.602	0.0952	0.00882	0.0322	0.1322	0.0047	0.0076	0.00043	0.0045	0.00029
Pl		C	ba_14	372.8655		rim	0.811	1.49	0.157	0.599	0.0891	0.513	0.095	0.0135	0.0929	0.511	0.0165	0.0649	0.0079	0.0598	0.00798
Pl		C	ba_15	372.8655	F	rim	0.985	2.01	0.223	0.846	0.1275	0.635	0.112	0.01093	0.0447	0.1962	0.00618	0.0122	0.00163	0.0097	0.00107
Pl		C	ba_16	372.8655	F	core	1.03	2.1	0.233	0.877	0.135	0.608	0.097	0.01	0.0367	0.17	0.0068	0.0122	0.00249	0.007	0.00088
Pl		Cbis	ba_17	372.868	F	core	0.963	1.93	0.208	0.802	0.1192	0.665	0.0936	0.0101	0.0409	0.207	0.00743	0.0131	0.0013	0.0057	0.00121
Pl		D	ba_18	372.8745	G	core	0.241	0.669	0.0864	0.427	0.1053	0.672	0.0876	0.01251	0.0633	0.273	0.00956	0.0211	0.00218	0.0116	0.00113
Pl	360_41R2_1	D	ba_19	372.8745	G	rim	0.842	1.814	0.1957	0.776	0.1168	0.64	0.0973	0.00979	0.0311	0.1462	0.00502	0.0088	0.00097	0.0039	0.00036
Pl		D	ba_20	372.8745	F	core	0.778	1.56	0.168	0.615	0.0741	0.603	0.066	0.00645	0.028	0.1148	0.00411	0.0076	0.00079	0.0027	<0.00024
Pl		E	ba_21	372.873	G	core	0.899	1.89	0.217	0.842	0.129	0.646	0.112	0.0089	0.0326	0.1487	0.00441	0.0131	0.00102	0.007	<0.00024
Pl		E	ba_23	372.873	F	core	0.796	1.574	0.1537	0.616	0.0823	0.625	0.0586	0.0058	0.0188	0.0868	0.00356	0.0051	0.00037	0.00234	<0.00017
Pl		A	bb_8	406.374	F	core	0.638	1.535	0.1801	0.692	0.122	0.544	0.0943	0.0095	0.0379	0.1851	0.00551	0.0099	0.00099	0.0077	<0.00027
Pl		A	bb_9	406.374	F	rim	0.633	1.502	0.1728	0.717	0.1217	0.559	0.0817	0.0082	0.0451	0.1903	0.00537	0.0158	0.002	0.0067	0.00061
Pl		B	bb_10	406.382	G	core	0.511	1.332	0.1762	0.765	0.1445	0.574	0.1181	0.01394	0.0654	0.305	0.00996	0.0294	0.0022	0.0087	0.00204

Mineral		Area	Point	depth (mbsf)	Grain size	Grain area	La	Ce	Pr	Nd	Sm	Eu	Gd	Tb	Dy	Y	Ho	Er	Tm	Yb	Lu
Pl		B	bb_11	406.382	G	rim	0.629	1.479	0.1733	0.714	0.1125	0.575	0.0948	0.00894	0.0493	0.1993	0.00618	0.0133	0.00156	0.0056	0.00094
Pl		B	bb_12	406.382	F	rim	0.625	1.484	0.1853	0.759	0.1266	0.58	0.095	0.01217	0.0455	0.2094	0.00806	0.0195	0.00073	0.0078	0.00091
Pl		C	bb_13	406.3815	G	core	0.3001	0.656	0.0799	0.361	0.0743	0.36	0.0705	0.00539	0.0328	0.1603	0.00691	0.0128	0.00138	0.0043	0.00079
Pl		C	bb_14	406.3815	G	rim	0.322	0.674	0.0799	0.383	0.058	0.377	0.0442	0.00596	0.0269	0.1456	0.00512	0.0087	0.00109	0.0116	0.00126
Pl		C	bb_15	406.3815	F	core	0.314	0.662	0.0831	0.379	0.0524	0.372	0.0641	0.00706	0.0356	0.1483	0.00488	0.0091	0.00151	0.0027	0.00075
Pl		Cbis	bb_16	406.3815	F	core	0.775	1.667	0.1939	0.777	0.1138	0.568	0.114	0.0102	0.059	0.258	0.00605	0.0185	0.00171	0.0141	0.00135
Pl		Cbis	bb_17	406.3815	F	rim	0.792	1.6	0.1844	0.736	0.125	0.524	0.0935	0.0083	0.0584	0.239	0.0084	0.0174	0.00101	0.0095	0.00106
Pl		D	bb_18	406.3905	G	rim	0.719	1.471	0.17	0.645	0.1208	0.52	0.1008	0.01001	0.0543	0.227	0.00811	0.0162	0.00115	0.0098	0.00169
Pl	360_44R5_0	D	bb_19	406.3905	G	core	0.684	1.533	0.1767	0.729	0.1329	0.514	0.1049	0.0107	0.0538	0.2182	0.00754	0.0151	0.00124	0.0052	0.00083
Pl		F	bb_20	406.396	G	core	0.66	1.521	0.1832	0.69	0.109	0.554	0.0832	0.00854	0.0329	0.1673	0.00588	0.0105	0.00066	0.0059	0.00077
Pl		F	bb_21	406.396	G	rim	0.704	1.62	0.1879	0.781	0.13	0.564	0.0866	0.0116	0.0493	0.2013	0.0088	0.0126	0.00202	0.0073	0.0014
Pl		F	bb_22	406.396	F	core	0.761	1.732	0.2055	0.816	0.1362	0.587	0.0969	0.01281	0.0573	0.2245	0.00876	0.0134	0.00171	0.006	0.00092
Pl		A	bc_6	680.5545	F	rim	1.034	2.119	0.233	0.87	0.1351	0.916	0.1034	0.0113	0.0592	0.2354	0.00731	0.0174	0.00154	0.0069	0.00113
Pl		A	bc_7	680.5545	F	core	1.056	2.183	0.2434	0.92	0.148	0.908	0.1163	0.01219	0.0544	0.2633	0.00771	0.0136	0.00147	0.0103	0.00072
Pl		D	bc_8	680.5625	G	rim	1.027	2.302	0.2512	1.028	0.1302	0.871	0.0975	0.0109	0.0512	0.2224	0.00936	0.0145	0.00128	0.0083	0.00118
Pl		D	bc_9	680.5625	G	core	1.145	2.434	0.2553	0.974	0.1363	0.908	0.0938	0.00834	0.0426	0.1645	0.00489	0.0123	0.00083	0.0039	0.00076
Pl		D	bc_10	680.5625	G	rim	1.137	2.296	0.2582	0.864	0.135	0.959	0.0564	0.0101	0.0305	0.1742	0.00534	0.0104	0.00167	0.005	0.0006
Pl		Dbis	bc_11	680.5625	G	core	0.492	1.372	0.1771	0.817	0.191	0.785	0.1474	0.02	0.0936	0.486	0.0173	0.0329	0.00294	0.0177	0.00232
Pl		E	bc_12	680.569	G	core	1.158	2.37	0.2564	0.971	0.1402	0.872	0.112	0.00935	0.0465	0.1993	0.00668	0.0106	0.00196	0.0083	<0.00022
Pl		E	bc_13	680.569	G	rim	1.164	2.28	0.2416	0.834	0.115	0.813	0.0746	0.00884	0.0331	0.1565	0.00584	0.0149	0.00048	0.0061	0.00096
Pl		E	bc_14	680.569	F	core	0.907	1.917	0.209	0.746	0.1041	0.808	0.0782	0.0082	0.0326	0.1625	0.00478	0.0094	0.00034	0.008	0.00102
Pl		G	bc_15	680.582	F	rim	0.91	1.894	0.2066	0.801	0.1144	0.774	0.0871	0.00643	0.0511	0.2025	0.00789	0.0149	0.00112	0.0095	<0.00034
Pl	360_77R2_60	G	bc_16	680.582	F	core	0.849	1.77	0.1809	0.614	0.1043	0.779	0.0707	0.00686	0.0332	0.1243	0.00365	0.0099	0.00074	0.0043	<0.00036
Pl		G	bc_17	680.582		rim	0.899	1.908	0.2113	0.748	0.1242	0.807	0.0826	0.00934	0.0364	0.2075	0.0086	0.0134	0.00172	0.0059	0.00089
Pl		I	bc_18	680.583	F	rim	0.861	1.852	0.2035	0.746	0.1074	0.829	0.0955	0.0085	0.0397	0.1979	0.00675	0.0137	0.00147	0.0026	0.0004
Pl		I	bc_19	680.583	F	core	0.823	1.782	0.1845	0.7	0.0956	0.816	0.0684	0.00711	0.0363	0.1269	0.00411	0.009	<0.00031	0.0058	0.00078
Pl		I	bc_20	680.583	F	core	0.935	1.859	0.1869	0.705	0.0991	0.852	0.0605	0.00563	0.0245	0.114	0.00217	0.0079	0.00118	0.0067	0.00084
Pl		A1	bd_3	561.8745	G	core	0.256	0.629	0.0864	0.401	0.0764	0.486	0.0651	0.011	0.0417	0.2164	0.00683	0.0124	0.00261	0.0122	0.00122
Pl		A1	bd_4	561.8745	G	rim	0.412	1.097	0.1422	0.605	0.1082	0.533	0.0921	0.0091	0.0581	0.208	0.00644	0.0094	0.0009	0.003	0.00074
Pl		A2	bd_5	561.8725	G	core	0.472	1.135	0.1377	0.617	0.0755	0.538	0.0771	0.0063	0.0261	0.1146	0.00358	0.0109	0.00076	0.0024	<0.00037
Pl		D	bd_6	561.8845	F	core	0.516	1.118	0.1331	0.542	0.0897	0.526	0.0793	0.0094	0.0398	0.1938	0.00699	0.0142	0.00138	0.0095	0.00046
Pl		D	bd_7	561.8845	G	core	0.522	1.098	0.1227	0.581	0.0974	0.549	0.081	0.00721	0.038	0.1707	0.00643	0.0114	0.00046	0.0075	0.00144
Pl		E	bd_8	561.8905	G	core	0.571	1.207	0.1512	0.616	0.0821	0.526	0.0759	0.0097	0.0608	0.216	0.0083	0.0118	0.00192	0.0054	0.00113
Pl		E	bd_9	561.8905	G	rim	0.526	1.097	0.1318	0.526	0.1007	0.578	0.0702	0.0082	0.0384	0.1511	0.00527	0.0142	0.00099	0.0058	0.00084
Pl	360_62R4_62	E	bd_10	561.8905	F	core	0.513	1.111	0.1407	0.54	0.0968	0.553	0.079	0.0067	0.0428	0.1669	0.0079	0.0075	0.00115	0.0071	<0.00047
Pl		F	bd_11	561.8985	G	rim	0.383	0.871	0.1111	0.481	0.0861	0.54	0.0618	0.0078	0.0303	0.1469	0.00442	0.0155	0.00168	0.0033	0.00091
Pl		F	bd_12	561.8985	G	core	0.273	0.768	0.1104	0.44	0.1	0.526	0.072	0.0083	0.0477	0.166	0.0047	0.0171	0.00062	0.0058	0.00129
Pl		F	bd_13	561.8985	F	core	0.433	1.031	0.1279	0.552	0.0959	0.515	0.0869	0.00821	0.0409	0.173	0.00684	0.0187	0.00087	0.0065	0.00075
Pl		A	bf_3	598.438	F	core	0.554	1.237	0.1444	0.589	0.0918	0.414	0.0735	0.00956	0.044	0.1845	0.00658	0.0147	0.00203	0.0058	0.0007

Mineral		Area	Point	depth (mbsf)	Grain size	Grain area	La	Ce	Pr	Nd	Sm	Eu	Gd	Tb	Dy	Y	Ho	Er	Tm	Yb	Lu
Pl		A	bf_4	598.438	G	rim	0.395	0.927	0.1083	0.47	0.0823	0.388	0.0609	0.00552	0.0298	0.1497	0.00422	0.0093	0.00098	0.008	0.00068
Pl		A	bf_5	598.438	G	core	0.2515	0.699	0.0969	0.425	0.0965	0.419	0.071	0.00729	0.0557	0.2008	0.00846	0.0132	0.00128	0.0067	0.00124
Pl		B	bf_6	598.434		rim	0.386	0.908	0.1099	0.444	0.0668	0.373	0.0534	0.00449	0.0248	0.109	0.00512	0.0125	0.00049	0.0068	0.00074
Pl		C	bf_7	598.4405	F	core	0.381	0.79	0.0892	0.355	0.0549	0.347	0.0429	0.00471	0.016	0.0857	0.00522	0.0065	0.00091	<0.00196	0.00052
Pl		C	bf_8	598.4405	F	core	0.393	0.936	0.1024	0.442	0.0855	0.355	0.0532	0.00752	0.0313	0.1495	0.00436	0.0117	0.00126	0.0049	0.00091
Pl	360_66R3_29	C	bf_9	598.4405	F	rim	0.38	0.889	0.1069	0.428	0.0803	0.383	0.0629	0.00591	0.031	0.1395	0.00371	0.0083	0.00126	0.0061	0.00077
Pl	360_66R3_29	D	bf_10	598.4495	F	core	0.408	0.849	0.1008	0.381	0.056	0.385	0.0494	0.00544	0.0175	0.1079	0.00369	0.0101	0.00114	0.0039	0.00043
Pl	360_66R3_29	E	bf_11	598.4545	G	core	0.254	0.713	0.0953	0.425	0.0741	0.377	0.0787	0.00933	0.0397	0.1828	0.00636	0.011	0.00085	0.0036	0.00129
Pl	360_66R3_29	E	bf_12	598.4545	G	rim	0.325	0.816	0.1016	0.447	0.0783	0.386	0.0629	0.0056	0.0286	0.1229	0.00377	0.0079	0.00039	0.0055	0.00038
Pl	360_66R3_29	E	bf_13	598.4545	F	core	0.442	1.023	0.1245	0.506	0.0773	0.406	0.0719	0.00629	0.0563	0.1609	0.00596	0.0123	0.00135	0.0064	0.00045
Pl	360_66R3_29	B	bg_13	614.016	F	core	0.677	1.535	0.1647	0.6	0.0803	0.455	0.0742	0.00909	0.0349	0.1661	0.00576	0.0151	0.00153	0.0066	0.00064
Pl	360_66R3_29	B	bg_14	614.016	G	core	0.625	1.484	0.1746	0.699	0.1164	0.434	0.0895	0.0098	0.0426	0.218	0.00872	0.0178	0.00132	0.0059	0.00073
Pl	360_66R3_29	B	bg_15	614.016	G	rim	0.602	1.42	0.1598	0.635	0.0932	0.459	0.0677	0.0091	0.0521	0.1675	0.00622	0.0094	0.00127	0.004	0.00071
Pl	360_66R3_29	B	bg_16	614.016	G	rim	0.69	1.464	0.1562	0.563	0.0663	0.438	0.054	0.00803	0.0256	0.1239	0.00388	0.0088	0.00142	<0.0016	0.00061
Pl	360_66R3_29	B	bg_17	614.016	G	core	0.435	1.255	0.1484	0.646	0.107	0.457	0.0787	0.00819	0.0429	0.1989	0.00734	0.0123	0.0015	0.0086	0.00088
Pl	360_66R3_29	D	bg_19	614.029	F	rim	0.631	1.351	0.1542	0.619	0.0861	0.446	0.0749	0.00888	0.0344	0.1569	0.00545	0.0196	0.00186	0.0104	0.0011
Pl	360_66R3_29	D	bg_20	614.029	F	core	0.662	1.423	0.1612	0.666	0.113	0.45	0.0904	0.0099	0.0362	0.1863	0.0079	0.0121	0.00187	0.0089	0.00064
Pl	360_67R8_50	E	bg_21	614.034	F	core	0.391	0.864	0.0989	0.396	0.0688	0.378	0.0565	0.00385	0.0253	0.1035	0.00312	0.0095	0.00109	0.0027	0.0005
Pl	360_67R8_50	E	bg_22	614.034	G	core	0.367	0.869	0.1007	0.421	0.0686	0.376	0.0519	0.00609	0.0348	0.1365	0.00551	0.0089	0.00102	0.0055	0.00037
Pl	360_67R8_50	E	bg_23	614.034	G	rim	0.395	0.88	0.0977	0.358	0.0422	0.357	0.0541	0.00541	0.0203	0.109	0.00495	0.0049	0.00088	0.0083	0.00061
Pl	360_67R8_50	G	bg_24	614.038	F	core	0.471	1.021	0.1161	0.483	0.0704	0.422	0.0488	0.00642	0.0222	0.1178	0.00387	0.0085	0.00074	0.0043	0.00055
Pl	360_67R8_50	G	bg_26	614.038	G	rim	0.356	0.908	0.1168	0.492	0.078	0.393	0.0755	0.0095	0.0406	0.179	0.00715	0.0107	0.00178	0.0093	0.00091
Pl		A	bi_8	659.623	G	core	0.2193	0.603	0.088	0.427	0.1139	0.544	0.0923	0.01284	0.067	0.337	0.01022	0.025	0.00312	0.0174	0.00206
Pl		A	bi_9	659.623	G	rim	0.67	1.705	0.2166	0.883	0.165	0.583	0.132	0.011	0.0538	0.252	0.0091	0.0163	0.00127	0.0081	0.0009
Pl		A	bi_10	659.623	F	core	0.871	1.753	0.184	0.681	0.0959	0.53	0.0642	0.00639	0.0201	0.1211	0.00464	0.0093	<0.00016	0.0037	0.0004
Pl		B	bi_11	659.6265	G	rim	0.907	1.916	0.2064	0.82	0.1104	0.536	0.0771	0.00804	0.0305	0.1503	0.00497	0.0072	0.00091	0.0035	0.00059
Pl		B	bi_12	659.6265	G	core	0.932	2.011	0.2321	0.874	0.1434	0.571	0.1009	0.01011	0.0409	0.1907	0.00816	0.0059	0.0012	0.004	0.00036
Pl		C	bi_13	659.624	G	core	0.419	1.272	0.1689	0.714	0.1528	0.547	0.1297	0.0163	0.0723	0.326	0.01083	0.0208	0.00161	0.016	0.0018
Pl		C	bi_14	659.624	G	rim	0.526	1.519	0.1894	0.765	0.138	0.565	0.1039	0.0101	0.0439	0.2252	0.0079	0.0153	0.00169	0.0067	0.00096
Pl		D	bi_15	659.633	G	rim	0.856	1.899	0.2042	0.747	0.1165	0.552	0.0777	0.00766	0.0374	0.1304	0.00455	0.0112	0.00067	0.003	<0.00016
Pl		D	bi_16	659.633	G	core	1.011	2.34	0.275	1.132	0.1591	0.556	0.1319	0.01	0.0561	0.246	0.00838	0.0202	0.00198	0.0075	0.00115
Pl		D	bi_17	659.633	G	core	0.886	1.977	0.2184	0.816	0.1361	0.574	0.0856	0.00872	0.0454	0.2047	0.00771	0.017	0.00128	0.0103	0.00099
Pl	360_74R6_27	E	bi_18	659.639	G	core	0.288	0.813	0.1211	0.547	0.1263	0.565	0.1196	0.01284	0.0661	0.315	0.01151	0.0205	0.00194	0.0066	0.00045
Pl	360_74R6_27	E	bi_19	659.639	G	rim	0.679	1.564	0.1949	0.809	0.139	0.565	0.0972	0.0132	0.055	0.2099	0.0081	0.0088	0.00192	0.0049	0.00086
Pl	360_74R6_27	E	bi_20	659.639	G	core	0.939	2.1	0.2498	0.993	0.177	0.56	0.1115	0.0121	0.0629	0.256	0.0116	0.0222	0.00207	0.0078	0.00084
Pl	360_74R6_27	F	bi_21	659.646		rim	0.754	1.555	0.1667	0.652	0.1074	0.52	0.0791	0.00756	0.0328	0.1678	0.00517	0.0112	0.00107	0.0074	0.00092
Pl	360_74R6_27	F	bi_22	659.646	G	core	0.226	0.659	0.0941	0.464	0.1024	0.526	0.1008	0.0128	0.0689	0.297	0.0123	0.0219	0.0023	0.0102	0.00133
Pl		B1	bj_11	699.0065	G	rim	1.3	2.95	0.33	1.231	0.165	0.54	0.144	0.0137	0.0644	0.276	0.0117	0.0226	0.00224	0.0058	0.00125
Pl		B1	bj_12	699.0065	G	core	0.519	1.421	0.1919	0.833	0.1461	0.546	0.1113	0.0124	0.0589	0.2336	0.01011	0.0142	0.00146	0.0056	0.00031

Mineral		Area	Point	depth (mbsf)	Grain size	Grain area	La	Ce	Pr	Nd	Sm	Eu	Gd	Tb	Dy	Y	Ho	Er	Tm	Yb	Lu
Pl	360_79R6_1	B2	bj_13	699.0065	F	core	1.227	3.101	0.353	1.26	0.182	0.477	0.1241	0.0155	0.0634	0.2434	0.01005	0.0187	0.00214	0.0084	0.0008
Pl		C	bj_14	699.014	G	core	0.56	1.705	0.238	1.092	0.217	0.581	0.192	0.026	0.1472	0.689	0.0246	0.0572	0.00662	0.0333	0.00391
Pl		C	bj_15	699.014	G	rim	1.162	2.92	0.353	1.418	0.229	0.567	0.185	0.0217	0.0959	0.46	0.0176	0.0342	0.00432	0.0248	0.00246
Pl		D1	bj_16	699.022	F	core	1.626	3.4	0.359	1.337	0.188	0.565	0.1349	0.0141	0.069	0.305	0.00993	0.0241	0.00372	0.0103	0.00136
Pl		D1	bj_18	699.022	G	rim	1.304	2.59	0.266	0.908	0.1266	0.549	0.101	0.01004	0.0387	0.1758	0.00588	0.0157	0.00134	0.0102	0.00082
Pl		D2	bj_19	699.022	F	core	0.848	2.46	0.315	1.304	0.247	0.553	0.188	0.0195	0.0926	0.413	0.0147	0.0301	0.00407	0.0194	0.00178
Pl		A	bk_8	723.533	G	rim	0.633	1.422	0.1631	0.639	0.083	0.454	0.0769	0.00649	0.0284	0.1585	0.00436	0.0082	0.00095	0.0045	0.00029
Pl		A	bk_9	723.533	G	core	0.223	0.676	0.092	0.454	0.0955	0.485	0.084	0.0116	0.075	0.299	0.01	0.0189	0.00182	0.0113	0.00108
Pl		B	bk_10	723.5395	G	core	0.2243	0.642	0.0881	0.401	0.0884	0.472	0.0891	0.01094	0.0611	0.2702	0.00998	0.0178	0.00285	0.0176	0.00141
Pl		B	bk_11	723.5395	G	rim	0.717	1.582	0.1856	0.705	0.0896	0.483	0.0803	0.0077	0.0364	0.1567	0.0067	0.0125	0.00114	0.0061	0.00064
Pl		C	bk_12	723.537	G	rim	0.563	1.387	0.175	0.678	0.1265	0.473	0.0849	0.0104	0.0408	0.211	0.00553	0.0121	0.00183	0.0075	0.00153
Pl		C	bk_13	723.537	G	core	0.7	1.592	0.1914	0.756	0.1097	0.472	0.0947	0.00901	0.0348	0.1796	0.00496	0.0115	0.0011	0.0097	0.00096
Pl		D	bk_14	723.548	G	core	0.469	1.153	0.1585	0.712	0.151	0.493	0.1123	0.0124	0.0688	0.343	0.0124	0.0244	0.00254	0.0096	0.00105
Pl		D	bk_15	723.548	G	rim	0.629	1.483	0.1878	0.711	0.1308	0.498	0.0994	0.00788	0.0507	0.2219	0.00809	0.0171	0.00139	0.006	0.00074
Pl	360_82R3_19	E	bk_17	723.552	G	core	0.327	0.988	0.1333	0.635	0.127	0.482	0.1132	0.0132	0.0669	0.289	0.00922	0.0228	0.00291	0.0101	0.00158
Pl		E	bk_18	723.552	G	rim	0.638	1.477	0.1612	0.651	0.1081	0.481	0.0862	0.00747	0.0434	0.1587	0.00437	0.0133	0.00172	0.0079	0.0009
Pl		G	bk_19	723.562	F	core	0.632	1.396	0.1507	0.612	0.074	0.502	0.063	0.0086	0.0303	0.1432	0.0062	0.0134	0.0007	0.0091	0.0011
Pl		G	bk_20	723.562	G	core	0.636	1.525	0.1949	0.849	0.1475	0.487	0.1023	0.0106	0.0532	0.1866	0.00572	0.015	0.00111	0.0084	0.0003
Pl		G	bk_21	723.562	G	rim	0.51	1.244	0.1523	0.635	0.1156	0.458	0.0849	0.0079	0.0473	0.1931	0.00796	0.0135	0.00081	0.0059	0.00065
				Average			0.585	1.870	0.352	2.239	1.026	0.493	1.578	0.319	2.368	13.5797	0.523	1.531	0.231	1.597	0.234
BIR				2SD			0.04445	0.1306	0.0307	0.14676	0.07959	0.04115	0.20821	0.02665	0.21231	1.23459	0.05035	0.16688	0.02231	0.14982	0.02099
		referred values ("Georem" Jochum et al., 200					0.609	1.89	0.37	2.37	1.09	0.517	1.85	0.35	2.55	14.3	0.56	1.7	0.24	1.64	0.25

In situ trace elements concentrations in ppm analyzed by LA-ICP-MS on Thermo Fisher Element XR in GM (Montpellier, France)

Mineral	Sample	Area	Point	depth (mbsf)	Grain size	Grain area	La	Ce	Pr	Nd	Sm	Eu	Gd	Tb	Dy	Y	Ho	Er	Tm	Yb	Lu
Cpx		Analytical error average			1 sigma		0.022	0.119	0.03	0.211	0.103	0.028	0.173	0.031	0.227	1.01	0.048	0.137	0.021	0.127	0.019
Cpx		A	xj_18	390.486	G	core	0.374	1.958	0.47	3.43	1.745	0.609	2.785	0.528	3.88	20.94	0.838	2.357	0.316	2.147	0.317
Cpx	360_43R1_105	A	xj_19	390.486	G	rim	0.439	2.383	0.545	3.79	1.737	0.603	3.04	0.536	4.07	22.3	0.844	2.359	0.366	2.366	0.342
Cpx		B	xj_20	390.4975	F	core	0.701	3.93	0.959	6.71	3.09	0.834	4.88	0.894	6.63	35.4	1.388	3.94	0.573	3.64	0.529
Cpx		B	xj_21	390.4975	G	rim	0.36	1.605	0.356	2.494	1.213	0.46	2.04	0.377	2.702	14.81	0.571	1.69	0.2316	1.562	0.2174
Cpx		B	xj_22	390.4975	G	core	0.348	1.666	0.38	2.691	1.353	0.481	2.27	0.411	3.21	17.26	0.678	1.93	0.277	1.696	0.2534
Cpx		C	xj_23	390.498	G	rim	0.768	4.23	1.023	6.92	3.3	0.845	5.16	0.954	7.04	38.72	1.508	4.23	0.631	4.03	0.582
Cpx		C	xj_24	390.498	G	core	0.3	1.543	0.376	2.91	1.584	0.577	2.614	0.475	3.61	19.49	0.75	2.285	0.311	1.982	0.278
Cpx		B	xi_21	538.804	G	rim	0.403	1.778	0.357	2.415	1.19	0.449	1.924	0.371	2.782	15.52	0.601	1.691	0.2463	1.654	0.2308
Cpx		B	xi_22	538.804	G	core	0.581	3.21	0.759	5.28	2.415	0.693	3.52	0.651	4.76	26.01	0.989	2.822	0.393	2.471	0.362
Cpx		B	xi_23	538.804	G	core	0.555	3.08	0.741	4.84	2.141	0.67	3.22	0.593	4.14	22.57	0.863	2.381	0.336	2.229	0.322
Cpx	360_60R1_26	D	xi_25	538.8185	G	core	0.323	1.565	0.333	2.224	0.999	0.374	1.624	0.324	2.376	13.53	0.508	1.457	0.2089	1.452	0.2125
Cpx		D	xi_26	538.8185	G	rim	0.447	2.411	0.561	3.91	1.963	0.558	2.94	0.563	4.14	23.78	0.921	2.708	0.374	2.506	0.367
Cpx		F	xi_27	538.831	G	core	0.347	1.858	0.416	2.676	1.163	0.362	1.759	0.331	2.411	13.93	0.526	1.578	0.2276	1.536	0.2353
Cpx		G2	xi_28	538.8215	G	core	0.1489	0.843	0.2274	1.694	0.912	0.354	1.551	0.292	2.188	11.35	0.457	1.32	0.172	1.148	0.1602
Cpx		G2	xi_29	538.8215	G	rim	0.627	3.51	0.82	5.53	2.547	0.757	3.73	0.706	5.04	26.99	1.022	2.93	0.426	2.76	0.4
Cpx		A	ba_24	372.854	F	core	0.454	2.705	0.646	4.37	1.911	0.513	2.641	0.523	3.69	20.66	0.793	2.252	0.325	2.188	0.325
Cpx		A	ba_25	372.854	F	rim	0.739	4.48	1.106	7.55	3.49	0.871	4.92	0.969	6.83	36.83	1.437	3.96	0.565	3.83	0.55
Cpx		B	ba_26	372.855	G	rim	0.498	2.812	0.639	4.16	1.854	0.597	2.698	0.539	3.84	21.54	0.835	2.381	0.352	2.431	0.365
Cpx		B	ba_27	372.855	G	core	0.543	2.86	0.639	4.26	1.93	0.64	3.15	0.576	4.14	22.58	0.887	2.48	0.381	2.52	0.37
Cpx		C	ba_28	372.8655	G	core	0.746	3.83	0.827	5.51	2.436	0.76	3.61	0.711	5.14	28.67	1.099	3.115	0.455	3.044	0.454
Cpx	360_41R2_1	C	ba_29	372.8655	G	rim	0.706	4.05	0.97	6.61	3.096	0.824	4.48	0.888	6.29	33.67	1.326	3.74	0.536	3.48	0.507
Cpx		D	ba_30	372.8745	G	rim	0.638	3.62	0.82	5.4	2.425	0.729	3.41	0.67	4.77	26.16	1.014	2.875	0.415	2.758	0.396
Cpx		D	ba_31	372.8745	G	core	0.601	3.24	0.754	5.16	2.32	0.825	3.93	0.693	4.92	26.88	1.07	3	0.445	3.02	0.435
Cpx		E	ba_32	372.873	G	rim	0.729	4.5	1.127	8.06	3.84	1.003	5.64	1.073	7.71	41.77	1.659	4.7	0.673	4.24	0.621
Cpx		E	ba_33	372.873	G	core	0.684	4.22	1.059	7.49	3.46	0.922	5.14	0.972	6.98	38.41	1.498	4.27	0.619	3.98	0.606
Cpx		F	ba_34	372.879	G	core	0.28	1.45	0.383	3.06	1.65	0.617	3.33	0.55	3.97	21.66	0.862	2.35	0.35	2.24	0.326
Cpx		F	ba_35	372.879	G	rim	0.592	3.22	0.808	5.95	2.86	0.933	5.37	0.882	6.3	34.45	1.38	3.83	0.562	3.6	0.535
Cpx		A	bb_23	406.374	G	rim	0.746	4.6	1.126	7.78	3.51	0.975	4.97	0.922	6.47	34.91	1.368	3.83	0.554	3.65	0.511
Cpx		A	bb_24	406.374	F	rim	0.768	4.9	1.204	8.38	3.75	1.038	5.31	0.961	6.87	37.09	1.455	4	0.559	3.89	0.539
Cpx		B	bb_25	406.382	G	core	0.5	2.999	0.708	4.95	2.302	0.688	3.33	0.649	4.61	25.64	0.96	2.774	0.418	2.636	0.39
Cpx		C	bb_26	406.3815	G	core	0.347	1.833	0.488	3.79	2.013	0.706	3.28	0.616	4.42	24.36	0.942	2.619	0.366	2.382	0.348
Cpx		C	bb_27	406.3815	G	core	0.2712	1.394	0.335	2.533	1.35	0.462	2.187	0.411	2.988	16.36	0.638	1.752	0.2515	1.65	0.2447
Cpx		Cbis	bb_28	406.3815	G	rim	0.68	4.06	1.009	7.16	3.4	0.938	5.51	0.989	7.1	39.29	1.533	4.12	0.6	3.84	0.564
Cpx	360_44R5_0	E	bb_29	406.389	G	rim	0.66	3.78	0.936	6.44	2.982	0.846	4.39	0.816	5.98	32.63	1.259	3.54	0.511	3.36	0.489
Cpx		E	bb_30	406.389	G	core	0.614	3.211	0.74	5.04	2.36	0.791	3.69	0.703	5.25	29.47	1.149	3.32	0.484	3.26	0.474
Cpx		E	bb_31	406.389	F	rim	0.655	4.12	1.046	7.59	3.61	0.972	5.51	1.005	7.28	39.6	1.539	4.35	0.609	4	0.572
Cpx		Ebis	bb_33	406.3905	G	rim	0.609	3.65	0.861	6.18	2.794	0.87	4.35	0.811	5.79	31.58	1.215	3.43	0.493	3.2	0.466

Mineral		Area	Point	depth (mbsf)	Grain size	Grain area	La	Ce	Pr	Nd	Sm	Eu	Gd	Tb	Dy	Y	Ho	Er	Tm	Yb	Lu
Cpx		F	bb_34	406.396	G	core	0.537	3.5	0.881	6.41	2.853	0.782	4.34	0.792	5.78	31.99	1.253	3.48	0.509	3.34	0.478
Cpx		F	bb_35	406.396	G	rim	0.411	2.717	0.702	4.97	2.321	0.608	3.57	0.653	4.71	26.2	1.005	2.814	0.4	2.64	0.367
Cpx		G	bc_5	680.582	F	core	0.926	5.49	1.35	8.95	4.02	0.918	5.66	1.132	7.93	43.56	1.712	4.68	0.689	4.44	0.669
Cpx		A	bc_21	680.5545	F	rim	0.95	5.69	1.398	10.1	4.64	1.003	7.11	1.311	9.59	50.43	1.98	5.67	0.816	5.35	0.792
Cpx		A	bc_22	680.5545	F	core	1.074	6.38	1.558	11.2	5.24	1.078	7.68	1.498	10.61	57.44	2.28	6.37	0.939	6.01	0.9
Cpx		B	bc_23	680.5555		core	1.092	6.98	1.707	11.49	4.99	1.114	7.23	1.377	9.78	53.88	2.11	5.91	0.889	5.98	0.859
Cpx		B	bc_24	680.5555	F	rim	0.945	6.01	1.52	10.52	4.72	0.991	7.13	1.333	9.45	51.27	2.01	5.7	0.834	5.4	0.793
Cpx		C	bc_25	680.5615	G	core	0.67	3.04	0.692	5.05	2.56	0.852	4.21	0.827	5.9	32.38	1.293	3.61	0.504	3.26	0.499
Cpx	360_77R2_60	C	bc_26	680.5615	G	rim	1.206	6.97	1.77	13.02	6.16	1.148	9.48	1.8	12.79	68.71	2.76	7.98	1.152	7.54	1.119
Cpx		C	bc_27	680.5615	G	core	1.151	6.69	1.675	12.23	5.69	1.061	8.73	1.66	12.07	65.03	2.57	7.53	1.102	7.28	1.085
Cpx		D	bc_28	680.5625	F	core	1.195	7.75	1.98	14.48	6.58	1.045	9.82	1.83	13.23	69.87	2.81	7.96	1.155	7.78	1.108
Cpx		E	bc_30	680.569	G	rim	1.119	6.91	1.779	12.84	6.12	1.202	9.42	1.75	12.55	70.26	2.65	7.48	1.094	7.13	1.027
Cpx		F	bc_31	680.573	G	core	0.325	1.932	0.502	3.69	1.91	0.719	3.08	0.594	4.27	22.69	0.883	2.47	0.359	2.29	0.335
Cpx		G	bc_32	680.582	F	rim	0.63	3.88	0.98	7	3.1	0.705	4.99	0.913	6.43	35.26	1.36	3.8	0.544	3.61	0.518
Cpx		G	bc_33	680.582	F	rim	0.954	5.94	1.426	9.87	4.43	1.02	6.74	1.26	9.1	49.15	1.92	5.49	0.784	5.24	0.752
Cpx		I	bc_34	680.583	G	core	0.441	2.23	0.515	3.78	1.84	0.681	2.97	0.56	3.93	21.47	0.838	2.42	0.347	2.18	0.329
Cpx		I	bc_35	680.583	G	rim	0.825	4.7	1.088	7.19	3.14	0.887	4.56	0.896	6.44	34.86	1.35	3.92	0.563	3.84	0.536
Cpx		I	bc_36	680.583	F	core	0.76	4.59	1.107	7.73	3.52	0.787	5.04	0.938	6.8	35.56	1.42	3.96	0.569	3.77	0.555
Cpx		B	bd_14	561.879	G	core	0.398	2.17	0.542	3.96	2.094	0.719	3.54	0.66	4.89	26.84	1.042	2.93	0.409	2.724	0.41
Cpx		B	bd_15	561.879	G	core	0.584	3.177	0.766	5.49	2.74	0.848	4.28	0.807	5.83	32.66	1.262	3.64	0.503	3.38	0.494
Cpx		C	bd_16	561.8765	G	core	0.35	1.946	0.484	3.79	2.025	0.699	3.13	0.578	4.32	23.58	0.916	2.664	0.384	2.448	0.357
Cpx		C	bd_17	561.8765	G	rim	0.523	3.197	0.785	5.86	2.87	0.894	4.52	0.838	6.06	33.25	1.297	3.66	0.514	3.42	0.504
Cpx	360_62R4_62	D	bd_18	561.8845	G	rim	0.494	2.809	0.699	5.15	2.65	0.852	4.44	0.808	5.95	33.35	1.292	3.57	0.53	3.4	0.497
Cpx		D	bd_19	561.8845	G	core	0.396	2.092	0.525	4.08	2.136	0.774	3.65	0.7	5.16	27.84	1.074	2.96	0.44	2.88	0.424
Cpx		E	bd_20	561.8905	F	core	0.548	3.28	0.844	6.44	3.24	0.928	5.1	0.934	6.99	38.22	1.504	4.21	0.605	4.01	0.579
Cpx		E	bd_21	561.8905	F	rim	0.537	3.218	0.855	6.62	3.35	0.926	5.39	1.022	7.41	39.69	1.571	4.35	0.623	4.14	0.598
Cpx		F	bd_22	561.8985	G	rim	0.394	2.417	0.635	4.69	2.48	0.763	3.86	0.735	5.43	29.07	1.125	3.18	0.466	3.02	0.454
Cpx		F	bd_23	561.8985	G	rim	0.393	2.055	0.519	3.84	1.941	0.698	3.19	0.603	4.45	24.42	0.955	2.634	0.371	2.55	0.379
Cpx		A	bf_14	598.438	G	core	0.2638	1.429	0.348	2.748	1.421	0.546	2.327	0.443	3.21	17.25	0.675	1.849	0.2583	1.695	0.2364
Cpx		A	bf_15	598.438	G	rim	0.477	2.583	0.581	4.14	1.924	0.612	2.808	0.554	3.86	21.81	0.855	2.362	0.335	2.189	0.325
Cpx		A	bf_16	598.438	F	core	0.329	1.772	0.412	2.841	1.367	0.495	2.147	0.426	3.025	16.93	0.631	1.785	0.2493	1.699	0.2392
Cpx		B	bf_17	598.434	G	core	0.348	1.9	0.457	3.19	1.529	0.523	2.315	0.441	3.25	17.85	0.694	1.907	0.285	1.853	0.2673
Cpx		B	bf_18	598.434	G	rim	0.348	2.033	0.489	3.45	1.613	0.535	2.442	0.459	3.24	18.4	0.684	2.03	0.274	1.977	0.285
Cpx		C	bf_19	598.4405	F	rim	0.2616	1.445	0.349	2.623	1.327	0.487	2.13	0.424	3.058	17.28	0.67	1.87	0.2582	1.741	0.2587
Cpx		Cbis	bf_20	598.442	F	core	0.251	1.261	0.2965	2.26	1.22	0.478	2.022	0.39	2.833	16.16	0.62	1.759	0.2437	1.633	0.2433
Cpx		Cbis	bf_21	598.442	G	core	0.2428	1.225	0.2948	2.185	1.174	0.434	1.952	0.376	2.731	15	0.586	1.624	0.2357	1.482	0.2298
Cpx		Cbis	bf_22	598.442	G	rim	0.333	1.893	0.469	3.37	1.593	0.578	2.613	0.503	3.64	20.18	0.757	2.2	0.312	2.098	0.307
Cpx	360_66R3_29	D	bf_23	598.4495	F	core	0.347	2.048	0.512	3.77	1.844	0.549	2.86	0.556	4.09	22.19	0.844	2.44	0.35	2.268	0.325
Cpx		D	bf_24	598.4495	F	rim	0.3015	1.732	0.426	3.17	1.527	0.486	2.499	0.475	3.51	19.45	0.751	2.128	0.298	2.029	0.301

Mineral		Area	Point	depth (mbsf)	Grain size	Grain area	La	Ce	Pr	Nd	Sm	Eu	Gd	Tb	Dy	Y	Ho	Er	Tm	Yb	Lu
Cpx		E	bf_25	598.4545	G	core	0.2709	1.472	0.342	2.372	1.208	0.458	1.927	0.367	2.62	14.83	0.566	1.616	0.2387	1.526	0.2232
Cpx		E	bf_26	598.4545	G	rim	0.335	1.86	0.448	3.15	1.492	0.55	2.292	0.449	3.29	18.24	0.698	1.987	0.286	1.881	0.281
Cpx		B	bg_27	614.016	G	core	0.37	1.673	0.367	2.54	1.266	0.506	2.071	0.383	2.73	14.94	0.581	1.695	0.2303	1.576	0.2218
Cpx		B	bg_28	614.016	G	rim	0.725	4.22	0.928	6.02	2.565	0.728	3.59	0.669	4.6	24.91	0.968	2.668	0.373	2.574	0.365
Cpx		C	bg_29	614.0235	G	rim	0.589	3.27	0.758	5.31	2.348	0.667	3.55	0.653	4.62	25.5	0.999	2.74	0.395	2.483	0.371
Cpx		C	bg_30	614.0235	G	core	0.36	1.688	0.384	2.738	1.369	0.521	2.254	0.413	3.03	16.44	0.635	1.766	0.258	1.699	0.2324
Cpx		C	bg_31	614.0235	G	core	0.551	3.25	0.831	5.88	2.824	0.712	4.36	0.822	5.81	31.32	1.217	3.39	0.467	3.12	0.442
Cpx		C	bg_32	614.0235	G	rim	0.491	2.435	0.533	3.58	1.695	0.591	2.636	0.495	3.54	19.43	0.756	2.122	0.294	1.97	0.285
Cpx		E	bg_33	614.034	F	rim	0.328	1.978	0.481	3.41	1.596	0.562	2.53	0.482	3.43	18.97	0.71	2.1	0.305	1.993	0.288
Cpx	360_67R8_50	E	bg_34	614.034	G	core	0.303	1.773	0.411	2.97	1.425	0.508	2.192	0.411	2.96	15.72	0.616	1.734	0.256	1.661	0.24
Cpx		E	bg_36	614.034	F	core	0.343	2.124	0.519	3.56	1.689	0.561	2.652	0.489	3.48	19.13	0.75	2.153	0.295	2.047	0.294
Cpx		G	bg_37	614.038	G	core	0.476	2.733	0.639	4.48	1.929	0.607	3.11	0.578	4.22	23.69	0.915	2.62	0.386	2.53	0.387
Cpx		G	bg_38	614.038	G	rim	0.446	2.788	0.676	4.8	2.255	0.642	3.38	0.641	4.54	25.09	0.974	2.8	0.4	2.61	0.396
Cpx		G	bg_39	614.038	G	rim	0.459	2.819	0.712	5.02	2.357	0.674	3.68	0.684	5	26.58	1.047	2.9	0.427	2.8	0.413
Cpx		A	bh_1	659.623	G	core	0.571	3.001	0.695	5.06	2.384	0.711	3.76	0.717	5.23	28.79	1.101	3.17	0.475	3.056	0.459
Cpx		B	bh_2	659.6265	G	core	0.611	3.39	0.778	5.06	2.197	0.639	3.31	0.631	4.67	25.35	0.988	2.736	0.421	2.748	0.413
Cpx		B	bh_3	659.6265	G	rim	0.659	4.08	0.976	6.75	2.984	0.744	4.24	0.788	5.66	31.03	1.189	3.39	0.503	3.31	0.489
Cpx		C	bh_4	659.624	G	rim	0.555	3.119	0.74	5.18	2.447	0.732	3.78	0.704	5.1	27.8	1.068	3.037	0.445	2.88	0.408
Cpx		C	bh_5	659.624	G	core	0.36	1.711	0.368	2.463	1.242	0.466	1.842	0.356	2.608	14.21	0.545	1.528	0.2239	1.46	0.2094
Cpx		D	bh_6	659.633	G	core	0.942	5.87	1.449	10.27	4.59	0.993	6.49	1.181	8.26	43.82	1.715	4.95	0.69	4.55	0.653
Cpx		E	bh_7	659.639	G	rim	0.699	3.9	0.904	6.45	2.892	0.78	4.39	0.81	5.8	30.79	1.224	3.34	0.486	3.17	0.454
Cpx	360_74R6_27	F	bh_8	659.646	G	rim	0.699	3.7	0.804	5.25	2.337	0.693	3.48	0.654	4.85	27.12	1.011	3	0.448	2.934	0.446
Cpx		F	bh_9	659.646	G	core	0.746	4.23	0.986	6.76	2.99	0.784	4.31	0.83	5.86	32.02	1.235	3.6	0.504	3.22	0.462
Cpx		F	bh_10	659.646	G	core	0.724	3.94	0.879	6.07	2.589	0.738	3.79	0.691	4.98	27.22	1.041	3.13	0.437	2.827	0.41
Cpx		F	bh_11	659.646	G	core	0.541	2.642	0.561	3.79	1.762	0.596	2.66	0.523	3.7	20.81	0.812	2.405	0.357	2.382	0.343
Cpx		F	bh_12	659.646	G	rim	0.728	4.18	1.022	7.26	3.25	0.859	5.08	0.921	6.46	34.34	1.378	3.81	0.529	3.4	0.488
Cpx		F	bh_13	659.646	G	rim	0.669	3.78	0.893	6.03	2.685	0.751	4.13	0.737	5.4	28.56	1.116	3.16	0.45	2.92	0.433
Cpx		F	bh_14	659.646	G	rim	0.783	4.42	1.05	7.26	3.24	0.803	4.76	0.864	6.2	33.77	1.319	3.63	0.518	3.43	0.508
Cpx		F	bh_15	659.646	G	core	0.55	2.708	0.592	4.01	1.789	0.579	2.764	0.521	3.62	19.93	0.772	2.189	0.317	2.052	0.298
Cpx		A1	bj_20	699.004	G	rim	1.303	7.99	1.87	12.18	5.05	0.773	7.09	1.346	9.78	54.24	2.152	6.34	0.965	6.38	0.874
Cpx		B2	bj_21	699.0065	G	core	0.2165	1.248	0.313	2.224	1.107	0.444	1.71	0.318	2.271	12.34	0.493	1.325	0.185	1.204	0.1741
Cpx		B2	bj_22	699.0065	G	rim	1.411	8.9	2.028	13.21	5.63	0.929	7.54	1.425	9.95	54.37	2.136	6.01	0.903	5.78	0.814
Cpx	360_79R6_1	D1	bj_23	699.022	G	core	0.398	2.173	0.51	3.62	1.713	0.597	2.576	0.496	3.45	18.23	0.739	1.962	0.286	1.825	0.2666
Cpx		D1	bj_24	699.022	G	rim	0.824	4.18	0.932	6.18	2.732	0.733	4.06	0.755	5.55	28.84	1.159	3.19	0.445	3.07	0.436
Cpx		A	bk_22	723.533	G	core	0.358	1.808	0.421	2.92	1.418	0.557	2.29	0.427	3.06	16.69	0.653	1.786	0.2549	1.655	0.2481
Cpx		B	bk_24	723.5395	G	core	0.436	2.183	0.466	2.861	1.27	0.461	1.863	0.34	2.54	14.42	0.543	1.618	0.233	1.577	0.2249
Cpx		B	bk_25	723.5395	G	rim	0.574	3.37	0.782	5.22	2.262	0.602	3.37	0.626	4.52	24.34	0.953	2.632	0.381	2.463	0.362
Cpx		C	bk_26	723.537	G	core	0.2047	1.09	0.2696	2.038	1.034	0.403	1.663	0.3	2.212	12.15	0.465	1.311	0.1812	1.21	0.1707
Cpx	9	C	bk_27	723.537	G	rim	0.619	3.53	0.795	5.25	2.268	0.601	3.28	0.606	4.54	26.07	0.981	2.845	0.413	2.79	0.403

Mineral	360_82R3_1	Area	Point	depth (mbsf)	Grain size	Grain area	La	Ce	Pr	Nd	Sm	Eu	Gd	Tb	Dy	Y	Ho	Er	Tm	Yb	Lu
Cpx		D	bk_28	723.548	F	rim	0.448	2.48	0.564	3.92	1.658	0.543	2.568	0.491	3.63	20.3	0.783	2.226	0.322	2.192	0.307
Cpx		D	bk_29	723.548	G	core	0.353	1.701	0.397	2.892	1.467	0.548	2.203	0.427	3.07	16.26	0.652	1.745	0.25	1.602	0.2278
Cpx		D	bk_30	723.548	G	rim	0.583	3.3	0.77	5.24	2.233	0.642	3.32	0.615	4.48	24.7	0.953	2.641	0.401	2.631	0.373
Cpx		E	bk_31	723.552	F	rim	0.535	3.245	0.74	4.85	2.096	0.575	2.94	0.551	3.96	21.77	0.831	2.33	0.346	2.335	0.333
Cpx		E	bk_32	723.552	G	core	0.445	2.326	0.475	3.07	1.338	0.501	2.001	0.39	2.89	16.39	0.606	1.784	0.263	1.947	0.2802
Cpx		E	bk_33	723.552	G	core	0.296	1.562	0.34	2.292	1.103	0.43	1.595	0.314	2.186	12.31	0.482	1.339	0.1998	1.283	0.1852
			Average				0.585	1.870	0.352	2.239	1.026	0.493	1.578	0.319	2.368	13.58	0.523	1.531	0.231	1.597	0.234
BIR			2SD				0.0444	0.1306	0.0307	0.1468	0.0796	0.0412	0.2082	0.0266	0.2123	1.2346	0.0503	0.1669	0.0223	0.1498	0.021
		Preferred values ("Georem" Jochum et al., 2007)					0.609	1.89	0.37	2.37	1.09	0.517	1.85	0.35	2.55	14.3	0.56	1.7	0.24	1.64	0.25

Appendix 3.3

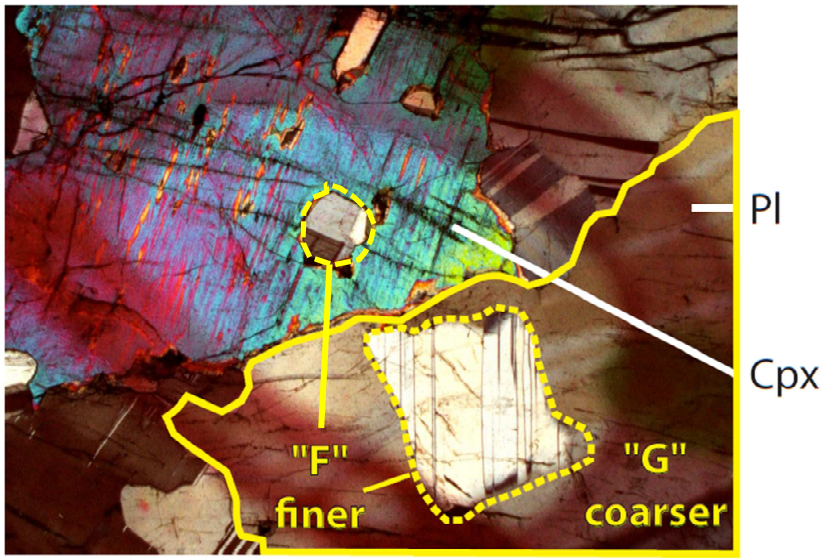

Sample 360-U1473A-67R8 (50cm)

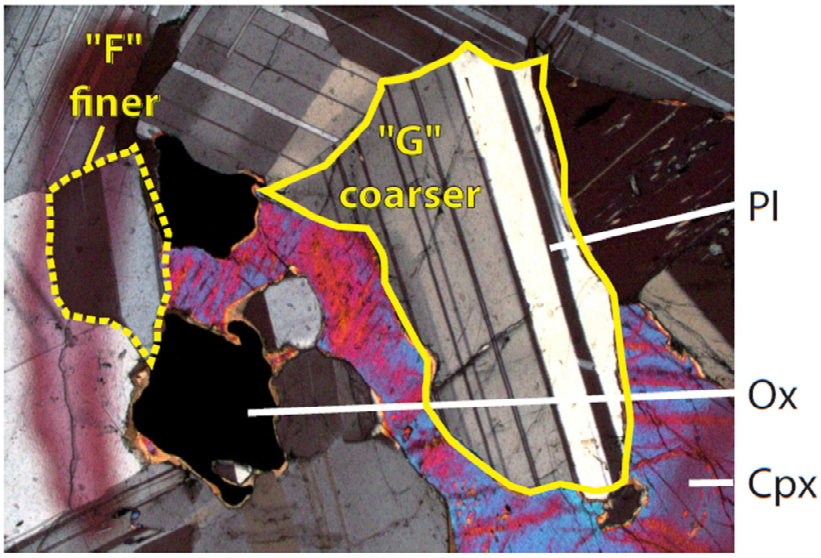

Sample 360-U1473A-80R6 (64bcm)

Appendix 3.3 - Example of arbitrary characterization of the minerals analyzed into the fine "F" or the coarse "G" grain category for the analyses of the bottom 400m of IODP Hole U14773A. The limit between the "F" and the "G" category is roughly per sample half the maximum grain size encountered. The finer grains here either represent actual smaller grains or outer crosscut portions of larger minerals.

Appendix 3.4

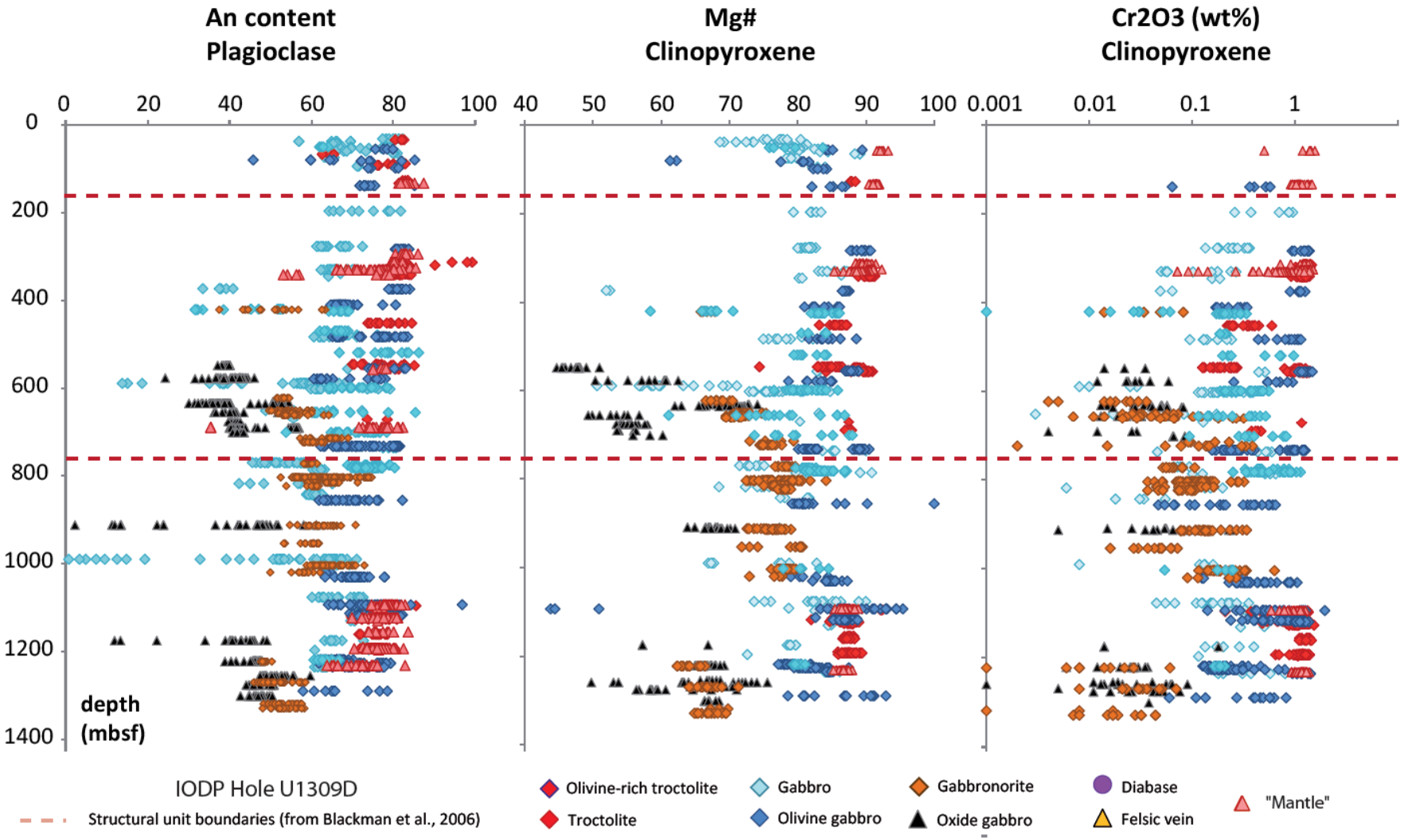

Appendix 3.4 -*In situ* An contents of plagioclases (left), Mg# (middle) and Cr_2O_3 (wt% - right) of clinopyroxenes from IODP Hole U1309A (Atlantis Massif OCC, Mid Atlantic Ridge). Data from the compilation of Miller et al. (2009).

Appendix 4

Experimental constraints on the evolution of tholeiitic magmas at Atlantis Bank (CHAPTER 6)

- **Appendix 4.1**: average *in situ* analyses for major elements of the different phases present in the crystallization experiments products.
  2 PAGES

- **Appendix 4.2**: *In situ* major element analyses of the run products or the partition coefficient project.
  4 PAGES

- **Appendix 4.3**: *In situ* trace element analyses of the run products or the partition coefficient project.
  6 PAGES

Appendix 4.1

Average in situ major element concentrations in wt% analyzed by EPMA on a Cameca SX100 at Institut für Mineralogie (Hannover, Germnay)

Name	Exp. Series	Water	T (°C)	N	Phase	SiO2	TiO2	Al2O3	FeO	MnO	MgO	CaO	Na2O	K2O	P2O5	Cr2O3	NiO	Total	Mg#	Fo	An	final H2O (wt%)
SG01		Dry - H_2O	1200		Melt	48.58	1.50	16.18	9.85	0.17	8.93	11.40	3.06	0.20	0.12			100	61.8	61.4	66.4	
MB04	Equi. - Frac.	Dry	1150	10	Melt	49.20	1.63	16.82	9.78	0.20	6.92	11.76	3.33	0.22	0.14			100	55.8	55.3	65.1	
MB04	Equi. - Frac.	Dry	1150	5	Ol	40.15	0.04	0.07	13.69	0.29	45.29	0.44	0.03	0.00				100	85.5	85.2	88.7	0.17
MB04	Equi. - Frac.	Dry	1150	6	Pl	50.90	0.17	30.07	1.01	0.02	0.63	14.14	3.00	0.07				100	52.5	52.1	72.0	
MB05	Equilibrium	Dry	1125	9	Melt	48.08	1.99	16.51	12.87	0.20	5.83	10.52	3.55	0.26	0.19			100	44.6	44.3	61.0	
MB05	Equilibrium	Dry	1125	6	Ol	39.36	0.06	0.05	17.20	0.28	42.58	0.44	0.03	0.00				100	81.5	81.3	87.5	
MB05	Equilibrium	Dry	1125	4	Pl	52.31	0.28	29.12	1.24	0.00	0.53	12.70	3.70	0.11				100	43.3	43.3	65.1	
MB05	Equilibrium	Dry	1125	6	Px	51.09	0.99	4.27	6.87	0.17	15.21	20.95	0.43	0.01				100	79.8	79.4	96.3	
MB06	Equilibrium	H2O	1125	10	Melt	49.37	1.63	17.04	9.55	0.17	6.94	11.70	3.24	0.21	0.15			100	56.4	56.0	65.7	1.45
MB06	Equilibrium	H2O	1125	6	Ol	40.04	0.03	0.03	12.98	0.23	46.32	0.35	0.00	0.01				100	86.4	86.2	95.8	
MB07	Fractional	Dry	1125	10	Melt	48.75	1.94	15.78	12.92	0.23	5.94	10.53	3.50	0.25	0.16			100	45.0	44.6	61.4	
MB07	Fractional	Dry	1125	6	Ol	39.48	0.08	0.25	16.68	0.33	42.53	0.58	0.06	0.00				100	82.0	81.7	83.2	
MB07	Fractional	Dry	1125	5	Pl	51.66	0.59	27.71	2.41	0.02	1.17	12.97	3.35	0.13				100	46.3	46.1	67.6	
MB07	Fractional	Dry	1125	6	Px	51.30	0.98	7.77	6.98	0.21	13.11	18.70	0.89	0.06				100	77.0	76.5	91.8	
MB08	Fractional	H2O	1125	10	Melt	49.71	1.56	16.99	9.55	0.17	7.03	11.75	2.93	0.20	0.11			100	56.8	56.3	67.9	1.72
MB08	Fractional	H2O	1125	3	Ol	39.75	0.06	0.31	13.08	0.28	45.94	0.52	0.06	0.00				100	86.2	86.0	82.6	
MB09	Equilibrium	Dry	1100	6	Melt	48.42	2.70	15.74	13.40	0.20	4.82	9.72	4.33	0.40	0.27			100	39.0	38.7	53.9	
MB09	Equilibrium	Dry	1100	6	Ol	38.23	0.08	0.05	23.13	0.38	37.61	0.49				0.01	0.01	100	74.3	74.0	100	
MB09	Equilibrium	Dry	1100	7	Pl	52.94	0.00	28.37	1.25	0.00	0.37	12.50	4.47	0.10				100	34.5	34.5	60.4	
MB09	Equilibrium	Dry	1100	6	Cpx	49.71	1.55	5.05	8.43	0.21	14.01	20.40	0.58	0.03		0.02		100	74.8	74.3	94.9	
MB10	Equilibrium	H2O	1100	6	Melt	49.75	1.72	17.08	10.24	0.11	6.09	11.32	3.32	0.24	0.12			100	51.4	51.1	64.3	
MB10	Equilibrium	H2O	1100	6	Ol	39.67	0.05	0.07	16.62	0.29	42.88	0.38				0.01	0.02	100	82.1	81.9	100	1.41
MB10	Equilibrium	H2O	1100	5	Pl	47.65		32.26	0.94		0.33	16.76	2.04	0.02				100	38.6	38.6	81.8	
MB10	Equilibrium	H2O	1100	6	Cpx	50.16	1.00	5.10	6.53	0.14	14.95	21.70	0.37	0.01		0.04		100	80.3	80.0	96.9	
MB11	Fractional	Dry	1100	6	Melt	47.65	3.04	13.37	17.96	0.35	4.36	8.93	3.70	0.42	0.22			100	30.2	29.8	55.4	
MB11	Fractional	Dry	1100	7	Ol	36.83	0.09	0.05	30.73	0.58	31.22	0.45				0.01	0.01	100	64.4	64.0	100	
MB11	Fractional	Dry	1100	5	Pl	53.34	0.00	28.66	0.98		0.14	12.29	4.52	0.08				100	20.1	20.1	59.8	
MB11	Fractional	Dry	1100	7	Cpx	50.86	1.06	3.48	10.54	0.30	14.33	18.96	0.41	0.02		0.04	0.00	100	70.8	70.2	96.1	
MB12	Fractional	H2O	1100	6	Melt	50.37	1.77	16.22	11.17	0.20	5.87	10.93	3.00	0.26	0.22			100	48.3	47.9	65.6	
MB12	Fractional	H2O	1100	6	Ol	39.051	0.0149	0.0345	19.514	0.2939	40.733	0.317	0.0244	0		0.0141	0.0039	100	78.81	78.56	87.78	1.49
MB12	Fractional	H2O	1100	5	Pl	49.793	0	30.467	1.2618	0	0.4454	15.037	2.9375	0.058				100	38.61	38.61	73.63	
MB12	Fractional	H2O	1100	6	Cpx	50.264	0.9148	4.6406	7.1364	0.1923	15.466	20.998	0.3178	0.0168		0.0531		100	79.43	78.99	97.24	
MB13	Equilibrium	Dry	1070	5	Melt	48.46	3.15	15.90	14.18	0.26	4.21	8.70	4.18	0.56	0.40			100	34.6	34.2	51.4	
MB13	Equilibrium	Dry	1070	10	Ol	38.21	0.09	0.17	24.21	0.39	36.32	0.54	0.04	0.01				100	72.8	72.5	85.1	1.43
MB13	Equilibrium	Dry	1070	5	Pl	52.84	0.26	29.01	1.33	0.02	0.36	12.01	4.05	0.14				100	32.3	32.0	61.6	
MB13	Equilibrium	Dry	1070	7	Cpx	49.41	1.62	5.79	9.36	0.21	13.39	19.52	0.64	0.05				100	71.8	71.4	94.1	
MB14	Equilibrium	H2O	1070	5	Ol	37.85	0.14	0.46	27.56	0.51	32.70	0.68	0.08	0.02				100	67.9	67.5	79.6	
MB14	Equilibrium	H2O	1070	6	Pl	53.61	0.34	27.81	1.17	0.01	1.12	11.51	4.22	0.22				100	63.2	63.0	59.3	
MB14	Equilibrium	H2O	1070	6	Cpx	49.64	2.02	5.35	9.10	0.21	12.65	20.33	0.66	0.03		0.01	0.01	100	71.3	70.8	94.3	

Name	Exp. Series	Water	T (°C)	N	Phase	SiO2	TiO2	Al2O3	FeO	MnO	MgO	CaO	Na2O	K2O	P2O5	Cr2O3	NiO	Total	Mg#	Fo	An	
MB14	Equilibrium	H2O	1070	3	Ilm	3.50	42.94	1.90	45.44	0.46	4.23	1.07	0.39	0.03		0.01	0.03	100	14.2	14.1	59.2	
MB15	Fractional	Dry	1070	10	Melt	49.01	2.80	13.84	17.15	0.33	3.88	8.81	3.51	0.42	0.26			100	28.7	28.3	56.3	
MB15	Fractional	Dry	1070	7	Cpx	49.42	1.23	3.84	12.96	0.31	13.03	18.67	0.51	0.02				100	64.2	63.6	95.1	1.76
MB15	Fractional	Dry	1070	7	Ox	0.31	17.32		77.45	0.53	4.02	0.38						100	8.5	8.4	100	
MB16	Fractional	H2O	1070	10	Melt	50.65	1.94	16.44	13.01	0.22	4.74	9.46	3.04	0.28	0.21			100	39.4	39.0	61.9	
MB16	Fractional	H2O	1070	6	Pl	50.60	0.24	30.22	1.42	0.01	0.32	14.14	2.98	0.07				100	28.7	28.5	72.1	1.67
MB16	Fractional	H2O	1070	8	Cpx	50.43	0.91	4.24	9.24	0.23	14.82	19.72	0.33	0.01		0.05	0.01	100	74.1	73.6	97.0	
MB17	Equilibrium	Dry	1030	6	Melt	49.48	1.95	19.49	13.01	0.14	2.36	8.12	4.35	0.58	0.52	-0.01	0.05	100	24.4	24.2	48.7	
MB17	Equilibrium	Dry	1030	8	Ol	37.02	0.12	0.38	26.56	0.43	34.76	0.55	0.13	0.01	0.05	0.00	0.00	100	70.0	69.6	69.4	
MB17	Equilibrium	Dry	1030	8	Pl	53.02	0.21	28.14	1.21	-0.01	0.44	11.84	4.79	0.12	0.22	-0.02	0.03	100	39.4	39.5	57.4	
MB17	Equilibrium	Dry	1030	8	Cpx	48.71	1.75	5.92	8.73	0.23	13.49	19.85	0.85	0.06	0.37	0.03	0.01	100	73.4	72.8	92.5	
MB17	Equilibrium	Dry	1030	9	Ilm	7.31	16.09	7.16	61.23	0.39	5.26	1.70	0.73	0.06	0.01	0.08	-0.03	100	13.3	13.2	54.9	
MB17	Equilibrium	Dry	1030	3	Ilm+	3.43	40.90	1.90	45.10	0.47	6.71	1.17	0.23	0.01	-0.03	0.10	0.00	100	21.0	20.8	73.2	
MB18	Equilibrium	H2O	1030	9	Melt	50.04	2.07	18.18	10.76	0.12	4.58	9.36	4.23	0.34	0.33	0.03	-0.01	100	43.1	42.9	53.7	
MB18	Equilibrium	H2O	1030	7	Ol	38.00	0.03	0.05	22.09	0.32	38.99	0.38	0.05	0.01	0.04	0.02	0.00	100	75.9	75.6	78.3	
MB18	Equilibrium	H2O	1030	7	Pl	48.09	0.26	31.38	1.37	0.01	0.49	15.65	2.51	0.07	0.27	-0.02	-0.08	100	39.0	38.9	77.2	
MB18	Equilibrium	H2O	1030	6	Cpx	48.70	1.37	5.67	7.67	0.18	14.65	20.85	0.51	0.03	0.37	0.02	-0.02	100	77.3	76.9	95.6	
MB19	Fractional	Dry	1030	8	Melt	51.64	1.99	13.70	18.45	0.33	2.73	7.26	2.66	0.66	0.58	0.03	0.06	100	20.9	20.6	56.4	
MB19	Fractional	Dry	1030	5	Pl	55.24	0.20	26.60	1.51	0.00	0.19	10.37	5.50	0.17	0.20	0.01	0.02	100	18.5	18.5	50.5	
MB19	Fractional	Dry	1030	6	Cpx	49.62	0.85	2.52	15.19	0.54	13.15	17.47	0.35	0.02	0.27	0.01	0.02	100	60.7	59.8	96.4	
MB19	Fractional	Dry	1030	4	Ilm	0.63	19.22	3.67	72.34	0.58	2.94	0.38	0.10	0.02	0.02	0.07	0.03	100	6.7	6.7	64.8	
MB20	Fractional	H2O	1030	8	Melt	51.10	2.22	15.48	14.14	0.28	4.11	8.80	3.11	0.34	0.41	0.03	-0.17	100	34.1	33.7	59.3	
MB20	Fractional	H2O	1030	6	Ol	36.29	0.04	0.24	30.46	0.38	32.21	0.30	0.01	0.01	0.04	0.01	0.00	100	65.3	65.0	90.1	
MB20	Fractional	H2O	1030	5	Pl	50.73	0.21	29.26	1.50	0.03	0.43	13.83	3.63	0.08	0.27	0.00	0.03	100	33.7	33.3	67.5	
MB20	Fractional	H2O	1030	6	Cpx	49.03	1.35	4.35	10.86	0.32	14.52	18.69	0.40	0.03	0.34	0.06	0.05	100	70.4	69.8	96.1	

N : number of analyses averaged; An = molar ratio Ca / Ca+Na+K; Mg# = molar ratio Mg / Mg + Fe; Fo = molar ratio Mg / Mg + Fe + Mn

Ol : olivine, Pl : plagioclase, Cpx : clinopyroxene, Ilm : Ilménite, Ilm+ : Ti-rich Ilménite ; Dry : "Nominally dry" (see Chapter 6 for complements); H2O : 1.5 wt% initial H2O content

Appendix 4.2

Average in situ major element concentrations in wt% analyzed by EPMA on a Cameca SX100 at Institut für Mineralogie (Hannover, Germnay)

Name	Exp. Series	Water	Phase	SiO2	TiO2	Al2O3	FeO	MnO	MgO	CaO	Na2O	K2O	P2O5	Cr2O3	NiO	Total	Mg#	Fo	An
				46.88	2.38	15.29	10.38	0.39	5.10	9.44	3.91	0.37	0.46			94.6	46.7	45.7	55.7
				49.34	2.51	16.28	10.45	0.42	5.14	9.63	4.19	0.34	0.36			98.7	46.7	45.7	54.7
				47.94	2.40	15.46	10.64	0.29	5.10	10.12	3.88	0.35	0.27			96.4	46.1	45.4	57.6
				48.15	2.39	15.46	10.69	0.29	4.96	10.00	3.76	0.33	0.56			96.6	45.3	44.6	58.2
				48.25	2.29	15.71	10.29	0.26	4.96	9.86	3.85	0.35	0.24			96.0	46.2	45.6	57.2
				48.45	2.35	15.86	10.34	0.23	5.13	10.26	4.10	0.33	0.35			97.4	46.9	46.4	56.8
				48.06	2.37	15.13	10.85	0.35	6.14	9.51	4.17	0.34	0.41			97.3	50.2	49.4	54.4
			Melt	48.36	2.34	15.51	10.44	0.27	5.07	10.32	3.86	0.36	0.32			96.8	46.4	45.7	58.2
				48.23	2.37	15.30	10.08	0.30	5.03	9.62	3.88	0.34	0.21			95.3	47.1	46.3	56.5
				48.54	2.27	15.83	10.43	0.24	5.05	10.20	4.03	0.36	0.21			97.1	46.3	45.7	56.9
				48.58	2.37	15.66	10.64	0.19	5.02	9.47	4.02	0.36	0.44			96.8	45.7	45.2	55.2
				47.98	2.45	15.26	10.49	0.30	5.01	9.64	3.64	0.42	0.21			95.4	46.0	45.3	57.6
				48.00	2.28	15.49	10.13	0.16	4.98	9.84	3.99	0.34	0.32			95.5	46.7	46.3	56.3
				47.94	2.32	15.95	10.30	0.27	5.22	9.38	3.88	0.31	0.18			95.7	47.4	46.8	55.9
				47.97	2.46	15.63	10.45	0.31	5.05	9.90	3.91	0.37	0.26			96.3	46.3	45.6	56.9
				38.89	0.06	0.05	18.92	0.36	40.02	0.39	0.01	0.01		0.01	0.03	98.7	79.0	78.7	93.9
				38.76	0.06	0.06	19.38	0.38	39.59	0.38	0.00	0.01		0.02	0.03	98.6	78.4	78.1	97.3
				38.46	0.09	0.05	19.51	0.32	39.78	0.41	0.03	0.00		0.01	0.07	98.6	78.4	78.1	87.4
				38.58	0.08	0.02	19.69	0.39	39.85	0.35	0.00	0.00		0.01	0.02	98.9	78.3	78.0	99.0
				38.41	0.06	0.02	19.67	0.32	39.89	0.40	0.00	0.00		0.02	0.06	98.8	78.3	78.0	100.0
				38.52	0.06	0.07	19.77	0.44	39.33	0.41	0.04	0.00		0.00	0.00	98.6	78.0	77.6	85.1
				38.37	0.04	0.09	19.69	0.37	39.90	0.42	0.01	0.00		0.02	0.09	98.9	78.3	78.0	96.8
			Ol	38.37	0.06	0.03	19.74	0.37	39.89	0.43	0.03	0.01		0.02	0.06	98.9	78.3	77.9	87.4
				38.41	0.05	0.02	19.68	0.31	39.83	0.42	0.01	0.02		0.00	0.03	98.7	78.3	78.0	91.0
				38.59	0.02	0.03	19.83	0.34	39.46	0.47	0.00	0.01		0.01	0.04	98.7	78.0	77.7	98.7
				38.71	0.06	0.08	19.69	0.32	39.44	0.51	0.02	0.01		0.00	0.11	98.8	78.1	77.8	91.4
				38.61	0.05	0.05	19.71	0.40	39.81	0.39	0.04	0.00		0.00	0.08	99.0	78.3	77.9	86.0
				38.30	0.03	0.05	19.65	0.35	40.10	0.41	0.06	0.01		0.02	0.05	99.0	78.4	78.1	76.7
				38.55	0.05	0.05	19.74	0.35	40.06	0.41	0.11	0.00		0.01	0.00	99.3	78.3	78.0	67.6
				38.74	0.04	0.05	19.43	0.35	39.48	0.38	0.02	0.00		0.00	0.01	98.5	78.4	78.0	90.2
MBPC-ed	Equilibrium	"nominally dry"		50.78	0.22	30.47	0.89	0.00	0.28	14.04	3.19	0.09				100.0	35.8	35.8	70.5
				51.48	0.16	30.34	1.08	0.00	0.18	13.76	3.18	0.09				100.3	23.2	23.2	70.1
				51.13	0.15	30.71	0.78	0.04	0.13	13.79	3.04	0.08				99.8	22.2	21.4	71.1
				51.02	0.17	30.91	0.87	0.00	0.14	13.85	3.25	0.10				100.3	22.3	22.3	69.7
				50.96	0.16	31.03	0.82	0.00	0.16	13.76	3.14	0.08				100.1	25.8	25.8	70.4
				51.44	0.11	30.70	0.84	0.05	0.12	13.46	3.22	0.08				100.0	20.5	19.6	69.4
				53.20	0.20	28.93	1.13	0.04	0.26	12.13	4.03	0.13				100.0	28.8	28.2	62.0
			Pl	53.00	0.27	28.70	1.22	0.04	0.54	12.44	3.83	0.13				100.2	44.2	43.5	63.8
				51.04	0.11	31.14	0.81	0.00	0.13	13.57	3.21	0.09				100.1	22.6	22.6	69.6
				51.38	0.12	30.47	0.78	0.00	0.16	13.86	3.33	0.08				100.2	26.4	26.4	69.3

	SiO2	TiO2	Al2O3	FeO	MnO	MgO	CaO	Na2O	K2O	P2O5	Cr2O3	NiO	Total	Mg#	Fo	An
	51.79	0.19	29.77	0.95	0.05	0.29	13.06	3.49	0.11				99.7	35.2	34.1	67.0
	50.98	0.20	30.52	0.99	0.02	0.28	13.72	3.22	0.13				100.1	33.4	33.0	69.6
	50.90	0.17	30.67	0.93	0.00	0.23	14.01	3.13	0.11				100.1	31.0	31.0	70.7
	51.14	0.33	30.23	1.07	0.03	0.41	13.40	3.26	0.12				100.0	40.4	39.7	68.9
	52.88	0.18	29.30	0.97	0.02	0.22	12.35	3.90	0.15				100.0	28.9	28.4	63.1
	50.10	1.07	4.56	6.96	0.11	15.13	21.10	0.40	0.00		0.35	0.00	99.4	79.5	79.2	96.7
	51.41	0.90	3.25	7.22	0.16	15.73	20.66	0.32	0.02		0.18	0.02	99.7	79.5	79.2	97.2
	49.44	1.19	4.60	7.30	0.15	14.75	21.15	0.46	0.00		0.28	0.02	99.0	78.3	77.9	96.3
	49.08	1.29	4.85	7.74	0.12	14.52	20.80	0.40	0.01		0.17	0.05	98.8	77.0	76.7	96.6
	49.78	1.20	4.60	7.55	0.09	14.59	21.18	0.39	0.01		0.16	0.03	99.4	77.5	77.3	96.7
	49.33	1.21	4.60	7.60	0.16	14.70	21.10	0.42	0.00		0.16	0.00	99.1	77.5	77.1	96.5
	50.11	1.18	4.47	7.23	0.18	15.02	21.36	0.36	0.00		0.33	0.00	99.9	78.7	78.3	97.0
Cpx	49.96	1.00	3.76	7.30	0.11	15.30	20.53	0.48	0.00		0.17	0.01	98.4	78.9	78.6	96.0
	49.62	1.15	4.41	7.42	0.16	14.67	21.11	0.35	0.01		0.20	0.04	98.9	77.9	77.5	97.1
	51.34	0.88	3.06	7.24	0.11	15.91	21.01	0.32	0.00		0.13	0.01	99.9	79.7	79.4	97.3
	50.13	0.99	3.98	7.22	0.11	15.32	20.84	0.39	0.00		0.25	0.00	99.0	79.1	78.8	96.7
	49.87	1.16	4.65	7.23	0.12	14.88	21.00	0.52	0.00		0.30	0.06	99.4	78.6	78.3	95.7
	51.68	0.77	2.82	7.25	0.19	16.17	20.64	0.36	0.00		0.16	0.02	99.9	79.9	79.5	97.0
	49.43	1.08	4.55	6.94	0.12	14.98	20.90	0.44	0.00		0.30	0.00	98.4	79.4	79.1	96.4
	48.04	1.43	5.89	8.72	0.15	14.14	20.27	0.47	0.00		0.19	0.00	99.1	74.3	74.0	96.0
	47.99	2.16	14.79	12.11	0.47	4.93	9.66	3.54	0.32	0.03			96.0	42.0	41.1	58.7
	49.74	2.18	15.51	13.04	0.26	4.96	9.50	3.91	0.29	0.27			99.7	40.4	39.9	56.1
	47.96	2.16	15.01	12.02	0.37	4.76	10.00	3.52	0.30	0.20			96.3	41.4	40.6	59.8
	48.12	2.16	15.27	12.46	0.33	4.78	9.45	3.66	0.28	0.12			96.6	40.6	40.0	57.6
	47.91	2.22	14.71	12.46	0.41	4.99	9.62	3.68	0.29	0.38			96.7	41.6	40.8	57.9
	48.22	2.14	15.11	12.52	0.42	4.90	9.62	3.70	0.25	0.44			97.3	41.1	40.3	57.9
	48.31	2.10	15.28	12.31	0.29	4.84	9.67	3.77	0.29	0.18			97.0	41.2	40.6	57.4
Melt	48.40	2.05	14.98	11.88	0.42	4.95	9.64	3.79	0.31	0.29			96.7	42.6	41.7	57.2
	48.79	2.13	14.78	12.66	0.48	4.90	9.95	3.63	0.30	0.35			98.0	40.8	39.9	58.9
	48.42	2.15	14.88	12.36	0.47	4.96	9.67	3.41	0.32	0.21			96.8	41.7	40.8	59.6
	49.24	2.07	14.86	12.43	0.25	5.01	9.55	3.87	0.29	0.12			97.7	41.8	41.3	56.5
	48.71	2.06	15.19	12.54	0.42	4.89	9.85	3.61	0.27	0.26			97.8	41.0	40.2	59.0
	48.34	2.17	15.07	11.80	0.36	4.90	10.00	3.61	0.25	0.35			96.9	42.5	41.8	59.4
	48.64	2.08	15.25	12.16	0.31	5.07	9.68	3.64	0.30	0.24			97.4	42.6	42.0	58.2
	48.61	2.15	14.85	12.15	0.53	5.16	9.65	3.54	0.28	0.41			97.3	43.1	42.0	58.9
	37.66	0.03	0.04	23.00	0.41	37.32	0.33	0.00	0.00		0.04	0.09	98.8	74.3	74.0	98.6
	37.85	0.06	0.04	23.21	0.46	37.41	0.38	0.01	0.00		0.01	0.01	99.4	74.2	73.8	97.6
	37.58	0.07	0.04	23.25	0.52	37.13	0.41	0.00	0.01		0.01	0.03	99.0	74.0	73.6	96.6
	37.75	0.04	0.05	23.71	0.42	37.36	0.43	0.00	0.01		0.01	0.08	99.8	73.7	73.4	98.4
	38.00	0.03	0.02	23.43	0.46	36.87	0.44	0.01	0.00		0.05	0.03	99.3	73.7	73.3	96.4
Ol	37.74	0.05	0.09	23.24	0.39	37.18	0.40	0.02	0.00		0.01	0.08	99.1	74.0	73.7	93.2

				SiO2	TiO2	Al2O3	FeO	MnO	MgO	CaO	Na2O	K2O	P2O5	Cr2O3	NiO	Total	Mg#	Fo	An
				38.06	0.04	0.02	23.26	0.39	37.22	0.34	0.00	0.00		0.00	0.10	99.3	74.0	73.7	99.0
				37.59	0.05	0.03	23.14	0.41	37.41	0.34	0.00	0.02		0.00	0.07	99.0	74.2	73.9	93.2
				37.65	0.07	0.02	22.82	0.45	36.71	0.38	0.03	0.01		0.05	0.12	98.1	74.1	73.8	86.5
				37.89	0.05	0.01	23.14	0.43	36.85	0.38	0.02	0.00		0.01	0.00	98.8	73.9	73.6	90.9
MBPC-fd	Fractional	"nominally dry"		52.20	0.09	29.99	0.84	0.00	0.14	12.96	3.57	0.10				99.9	22.9	22.9	66.3
				51.38	0.11	30.51	0.84	0.08	0.13	13.57	3.47	0.09				100.2	22.2	20.7	68.0
				52.11	0.10	30.35	0.81	0.01	0.18	13.36	3.51	0.08				100.5	28.7	28.4	67.5
				51.58	0.09	30.42	0.81	0.04	0.62	13.36	3.56	0.12				100.6	57.8	56.5	67.0
				51.74	0.10	29.91	0.74	0.01	0.13	12.73	3.57	0.09				99.0	24.0	23.8	66.0
				51.23	0.12	30.27	0.75	0.00	0.12	13.63	3.40	0.09				99.6	22.6	22.6	68.5
				51.09	0.09	30.96	0.76	0.00	0.18	13.88	3.30	0.08				100.3	29.6	29.6	69.6
			Pl	51.20	0.10	30.74	0.77	0.00	0.12	13.70	3.27	0.08				100.0	21.1	21.1	69.5
				52.02	0.12	30.15	0.79	0.01	0.14	13.01	3.53	0.09				99.9	24.1	23.8	66.7
				52.38	0.08	30.32	0.81	0.00	0.16	12.87	3.63	0.08				100.3	25.4	25.3	65.9
				51.38	0.11	29.96	0.76	0.02	0.68	13.19	3.33	0.10				99.5	61.4	60.8	68.2
				51.64	0.10	30.36	0.95	0.04	0.18	13.31	3.37	0.09				100.0	25.3	24.6	68.2
				51.42	0.12	30.66	0.85	0.00	0.14	13.57	3.38	0.06				100.2	23.2	23.2	68.7
				51.56	0.12	30.16	0.89	0.00	0.15	13.48	3.27	0.08				99.7	23.4	23.4	69.2
				52.03	0.12	30.10	0.81	0.01	0.18	12.86	3.65	0.09				99.9	28.5	28.2	65.7
				47.85	1.48	5.91	9.77	0.25	14.10	19.28	0.42	0.00		0.23	0.05	99.1	72.0	71.5	96.2
				49.76	0.99	4.16	9.43	0.22	15.22	18.91	0.39	0.01		0.21	0.01	99.1	74.2	73.7	96.4
				51.48	0.75	2.92	8.86	0.22	15.94	19.04	0.37	0.00		0.24	0.03	99.6	76.2	75.8	96.6
				49.73	1.01	4.54	8.83	0.18	14.75	19.98	0.41	0.01		0.42	0.02	99.4	74.8	74.5	96.3
				49.58	1.07	4.54	8.91	0.18	14.73	19.59	0.40	0.00		0.33	0.00	99.0	74.7	74.3	96.4
				50.04	1.01	4.35	9.12	0.18	14.63	19.70	0.37	0.00		0.47	0.00	99.4	74.1	73.7	96.7
				50.96	0.69	3.09	8.47	0.18	15.55	19.89	0.42	0.00		0.37	0.00	99.2	76.6	76.2	96.4
			Cpx	50.96	0.64	2.85	8.73	0.21	15.56	19.21	0.33	0.01		0.46	0.00	98.5	76.1	75.6	96.9
				51.35	0.70	3.09	8.94	0.13	15.77	19.23	0.33	0.01		0.44	0.00	99.5	75.9	75.6	96.9
				51.78	0.63	3.01	8.47	0.23	15.83	19.61	0.28	0.00		0.43	0.03	99.8	76.9	76.4	97.4
				50.10	0.90	3.92	9.12	0.20	15.08	19.66	0.36	0.00		0.50	0.02	99.3	74.7	74.2	96.8
				51.38	0.70	3.06	9.14	0.24	15.67	19.19	0.38	0.01		0.30	0.00	99.8	75.3	74.9	96.5
				50.55	0.81	3.65	9.19	0.18	15.36	19.45	0.39	0.00		0.37	0.00	99.6	74.8	74.5	96.5
				50.78	0.78	3.32	8.97	0.19	15.91	18.95	0.28	0.00		0.25	0.00	99.2	76.0	75.6	97.4
				50.08	0.94	3.98	8.91	0.19	15.23	19.06	0.35	0.00		0.26	0.05	98.7	75.3	74.9	96.8
				48.55	1.65	17.10	7.61	0.15	6.69	11.05	3.59	0.24	0.47	0.00	0.00	97.1	61.0	60.6	62.0
				46.94	1.64	16.77	7.64	0.00	6.75	11.42	3.03	0.25	0.49	0.01	0.08	95.0	61.2	61.2	66.4
				46.53	1.59	15.76	7.05	0.00	6.46	10.83	3.16	0.21	0.39	0.01	0.00	92.0	62.0	62.0	64.5
				46.03	1.54	16.62	7.70	0.27	6.19	11.24	3.38	0.26	0.46	0.00	0.00	93.7	58.9	58.0	63.6
				48.50	1.67	16.89	7.69	0.00	6.74	11.30	3.42	0.26	0.35	0.00	0.00	96.8	61.0	61.0	63.5
				47.19	1.57	16.79	6.54	0.07	6.77	11.41	3.37	0.25	0.31	0.05	0.00	94.3	64.8	64.6	64.1
				48.19	1.58	16.90	7.35	0.27	6.67	11.01	2.59	0.27	0.42	0.00	0.00	95.3	61.8	60.9	68.7

				SiO2	TiO2	Al2O3	FeO	MnO	MgO	CaO	Na2O	K2O	P2O5	Cr2O3	NiO	Total	Mg#	Fo	An
MBPC-fw	Fractional	water-bearing	Melt	45.99	1.60	16.64	6.78	0.07	6.69	11.32	3.25	0.24	0.52	0.00	0.00	93.1	63.7	63.5	64.7
				48.02	1.54	16.67	7.58	0.12	6.51	11.07	3.20	0.24	0.33	0.00	0.02	95.3	60.5	60.1	64.6
				46.70	1.60	16.07	7.54	0.16	6.36	11.03	3.12	0.24	0.33	0.09	0.00	93.2	60.0	59.5	65.0
				48.97	1.65	16.83	7.36	0.17	6.68	11.36	3.31	0.25	0.46	0.00	0.01	97.1	61.8	61.2	64.4
				47.73	1.63	16.89	7.45	0.17	6.80	11.34	3.05	0.25	0.47	0.00	0.00	95.8	61.9	61.4	66.1
				49.26	1.61	16.66	7.58	0.18	6.65	11.34	3.05	0.25	0.19	0.02	0.00	96.8	61.0	60.4	66.1
				46.96	1.55	16.49	7.98	0.30	6.53	11.31	3.31	0.25	0.32	0.02	0.00	95.0	59.3	58.4	64.3
				49.11	1.65	16.93	7.90	0.02	6.86	11.59	3.22	0.20	0.42	0.03	0.00	97.9	60.7	60.7	65.6
				48.37	1.68	16.94	8.33	0.30	6.71	11.89	3.53	0.25	0.47	0.05	0.00	98.5	58.9	58.1	64.0
			Ol	39.44	0.02	0.00	14.23	0.28	46.38	0.31	0.02	0.01	0.04	0.04	0.08	100.9	85.3	85.1	86.6
				40.32	0.02	0.36	14.54	0.22	45.78	0.37	0.00	0.02	0.00	0.00	0.04	101.7	84.9	84.7	94.0
				40.02	0.01	0.00	14.42	0.24	45.91	0.31	0.00	0.00	0.00	0.01	0.01	100.9	85.0	84.8	100.0
				40.16	0.01	0.05	14.11	0.20	45.69	0.28	0.02	0.01	0.01	0.01	0.00	100.6	85.2	85.0	85.3
				39.21	0.01	0.02	14.19	0.33	45.84	0.30	0.00	0.01	0.00	0.00	0.06	100.0	85.2	84.9	96.2
				39.72	0.02	0.19	14.30	0.25	45.53	0.31	0.02	0.00	0.00	0.00	0.03	100.4	85.0	84.8	89.5
				38.91	0.03	0.10	14.63	0.24	46.09	0.35	0.04	0.00	0.01	0.00	0.00	100.4	84.9	84.7	82.9
				39.41	0.01	0.07	14.38	0.27	45.46	0.29	0.01	0.00	0.00	0.00	0.09	100.0	84.9	84.7	94.1
				40.08	0.03	0.00	14.31	0.34	45.62	0.28	0.00	0.01	0.00	0.02	0.08	100.8	85.0	84.7	95.9
				39.06	0.01	0.00	13.57	0.26	45.51	0.33	0.02	0.01	0.00	0.02	0.03	98.8	85.7	85.4	87.3
				39.90	0.00	0.00	14.60	0.29	46.58	0.29	0.03	0.02	0.00	0.01	0.00	101.7	85.0	84.8	78.8
				39.92	0.01	0.00	15.01	0.32	46.08	0.34	0.02	0.00	0.00	0.05	0.08	101.8	84.5	84.3	90.4
				39.70	0.03	0.11	14.69	0.22	46.22	0.35	0.00	0.00	0.03	0.03	0.04	101.4	84.9	84.7	100.0
				40.02	0.02	0.05	14.18	0.27	46.71	0.34	0.00	0.01	0.03	0.00	0.00	101.6	85.4	85.2	96.6
				40.16	0.00	0.00	13.96	0.42	46.84	0.32	0.00	0.00	0.00	0.05	0.00	101.8	85.7	85.3	100.0
				40.29	0.00	0.00	13.54	0.21	46.71	0.27	0.06	0.00	0.03	0.02	0.05	101.2	86.0	85.8	71.3
			Cpx	48.80	1.09	6.33	4.54	0.08	15.85	22.37	0.29	0.00	0.33	0.57	0.00	100.3	86.1	85.9	97.7
				50.94	0.74	4.69	4.69	0.21	16.28	22.01	0.27	0.00	0.34	0.47	0.00	100.6	86.1	85.5	97.8
				49.79	1.03	5.16	4.64	0.09	15.73	21.95	0.32	0.02	0.33	0.81	0.06	99.9	85.8	85.6	97.3
				48.32	1.24	7.15	4.77	0.09	15.18	21.82	0.35	0.00	0.35	0.55	0.00	99.8	85.0	84.8	97.2
				49.76	1.08	5.72	4.80	0.08	15.84	22.00	0.27	0.01	0.36	0.80	0.06	100.8	85.5	85.3	97.8
				50.20	0.98	4.74	5.31	0.17	16.74	21.53	0.32	0.02	0.35	0.43	0.05	100.8	84.9	84.5	97.3
				49.98	0.96	5.19	4.98	0.15	15.77	21.92	0.33	0.00	0.37	0.33	0.01	100.0	84.9	84.6	97.3
				48.38	1.36	6.38	5.17	0.01	15.10	22.52	0.43	0.00	0.40	0.44	0.00	100.2	83.9	83.9	96.7
				51.69	0.66	3.00	4.55	0.09	17.56	22.10	0.25	0.01	0.32	0.41	0.04	100.7	87.3	87.1	97.9
				51.34	0.61	3.24	4.39	0.30	17.15	21.68	0.22	0.00	0.31	0.45	0.05	99.7	87.4	86.7	98.2
				49.97	1.02	5.16	4.92	0.00	16.11	22.12	0.31	0.00	0.35	0.86	0.00	100.8	85.4	85.4	97.5
				52.17	0.56	2.63	4.14	0.00	17.61	22.56	0.20	0.00	0.44	0.54	0.02	100.9	88.3	88.3	98.4
				49.27	1.09	5.86	5.06	0.26	15.26	22.41	0.30	0.01	0.43	0.65	0.04	100.6	84.3	83.6	97.6
				48.99	1.36	6.43	5.47	0.12	15.70	22.30	0.31	0.00	0.46	0.36	0.00	101.5	83.6	83.3	97.5
				51.42	0.70	3.34	4.73	0.18	17.34	22.11	0.28	0.02	0.50	0.40	0.01	101.0	86.7	86.3	97.7
				48.58	1.47	6.93	4.76	0.22	15.21	22.64	0.31	0.00	0.40	0.46	0.00	101.0	85.1	84.5	97.6

				SiO2	TiO2	Al2O3	FeO	MnO	MgO	CaO	Na2O	K2O	P2O5	Cr2O3	NiO	Total	Mg#	Fo	An
MBPC-ew	Equilibrium	water-bearing	Melt	51.10	2.67	15.41	8.47	0.26	5.85	9.24	3.51	0.44	0.53	0.08	0.00	97.6	55.2	54.4	57.3
				51.96	2.77	16.11	8.44	0.46	5.82	9.45	3.62	0.46	0.59	0.00	0.05	99.7	55.1	53.8	57.1
				49.10	2.62	14.94	8.43	0.40	5.67	9.03	3.49	0.42	0.43	0.00	0.04	94.6	54.5	53.3	57.0
				49.62	2.68	14.51	8.49	0.05	5.54	9.53	3.25	0.41	0.61	0.01	0.04	94.7	53.8	53.6	59.9
				49.76	2.48	15.54	8.60	0.40	5.57	9.13	3.39	0.40	0.35	0.00	0.00	95.6	53.6	52.4	58.0
				49.17	2.58	15.31	8.61	0.17	5.58	9.40	3.37	0.36	0.38	0.06	0.00	95.0	53.6	53.1	59.0
				50.49	2.57	15.25	8.35	0.17	5.71	9.19	3.18	0.43	0.61	0.01	0.03	96.0	54.9	54.4	59.5
				50.25	2.55	15.45	9.39	0.32	5.63	9.40	3.48	0.38	0.49	0.00	0.01	97.4	51.6	50.8	58.2
			Ol	39.60	0.04	0.00	17.44	0.46	43.24	0.34	0.03	0.02	0.03	0.01	0.00	101.2	81.5	81.1	81.3
				39.43	0.04	0.16	17.65	0.51	43.39	0.40	0.00	0.01	0.05	0.03	0.06	101.7	81.4	81.0	97.1
				39.24	0.05	0.08	18.30	0.47	42.87	0.34	0.00	0.01	0.07	0.01	0.00	101.4	80.7	80.3	96.6
				39.31	0.05	0.01	18.24	0.47	42.81	0.27	0.06	0.01	0.05	0.00	0.00	101.3	80.7	80.3	69.1
				39.25	0.02	0.08	18.09	0.58	43.25	0.38	0.02	0.00	0.04	0.02	0.03	101.8	81.0	80.5	91.3
				39.11	0.05	0.14	18.13	0.50	43.10	0.32	0.00	0.00	0.01	0.00	0.00	101.4	80.9	80.5	100.0
				39.56	0.02	0.33	18.53	0.41	42.79	0.35	0.01	0.00	0.01	0.02	0.00	102.0	80.4	80.1	95.1
				39.69	0.05	0.15	18.55	0.37	42.56	0.55	0.00	0.01	0.00	0.00	0.10	102.0	80.3	80.0	97.9
				41.41	0.23	0.93	16.16	0.47	37.54	3.49	0.14	0.00	0.10	0.00	0.00	100.5	80.5	80.1	93.2
				38.91	0.04	0.31	19.29	0.36	41.79	0.33	0.03	0.00	0.05	0.00	0.06	101.2	79.4	79.1	85.9
				38.89	0.05	0.07	18.82	0.56	42.04	0.32	0.03	0.00	0.03	0.03	0.06	100.9	79.9	79.4	85.5
			Pl	51.89	0.08	29.90	0.35	0.06	0.20	13.23	3.91	0.10	0.20	0.00	0.03	100.0	50.4	46.5	64.8
				51.86	0.11	29.71	0.49	0.10	0.36	13.49	3.98	0.06	0.29	0.00	0.00	100.5	56.7	52.0	65.0
				51.30	0.07	29.98	0.75	0.15	0.17	13.45	4.03	0.08	0.19	0.05	0.04	100.3	28.8	25.1	64.5
				52.07	0.10	29.26	0.62	0.00	0.39	12.80	4.30	0.06	0.25	0.00	0.02	99.9	52.8	52.8	62.0
				52.27	0.12	30.40	0.52	0.09	0.16	13.54	4.06	0.07	0.21	0.04	0.02	101.5	35.4	31.8	64.6
				52.00	0.10	29.81	0.86	0.07	0.69	13.33	4.02	0.05	0.20	0.00	0.00	101.1	58.8	56.9	64.5
				51.99	0.10	29.52	0.58	0.06	0.43	13.15	4.11	0.06	0.20	0.06	0.00	100.3	56.9	54.5	63.7
				51.25	0.10	29.90	0.73	0.00	0.13	13.48	3.84	0.05	0.26	0.00	0.00	99.7	24.1	24.1	65.8
			Cpx	50.35	1.18	3.44	6.63	0.49	16.63	20.46	0.31	0.00	0.30	0.15	0.05	100.0	81.7	80.6	97.3
				51.02	1.09	3.53	6.25	0.23	16.56	20.40	0.30	0.00	0.36	0.22	0.03	100.0	82.5	82.0	97.4
				51.26	1.09	3.37	7.04	0.26	16.82	20.47	0.41	0.00	0.39	0.21	0.00	101.3	81.0	80.4	96.5
				50.88	1.18	3.80	6.75	0.35	16.45	20.75	0.31	0.01	0.39	0.20	0.06	101.1	81.3	80.5	97.3
				51.05	0.98	3.33	6.73	0.13	16.66	20.57	0.32	0.00	0.36	0.16	0.06	100.4	81.5	81.2	97.3
				51.20	1.05	3.37	6.35	0.20	17.00	20.55	0.31	0.00	0.36	0.22	0.00	100.6	82.7	82.2	97.3
				52.21	0.81	2.67	6.78	0.29	17.20	20.10	0.29	0.01	0.30	0.24	0.12	101.0	81.9	81.2	97.4

Appendix 4.3

In situ trace element concentrations in ppm analyzed by LA-ICP-MS at LMV (Clermont-Ferrand, France)

Name	Phase	Point	La	Ce	Pr	Nd	Sm	Eu	Gd	Tb	Dy	Ho	Er	Tm	Yb	Lu
		untSMPABC001	220.75	227.35	216.70	215.35	211.66	211.18	204.56	202.59	207.99	208.64	206.90	205.41	209.69	207.78
		untSMPABC008	218.52	228.13	216.38	213.28	212.05	210.83	201.38	200.79	205.23	206.86	203.80	203.74	204.34	205.58
		untSMPABC009	218.24	226.83	216.05	214.16	210.08	210.90	202.95	199.27	203.97	206.20	204.04	201.73	205.14	203.51
		untSMPABC010	217.24	226.68	214.05	212.30	208.75	210.05	201.39	198.42	204.32	205.50	202.42	202.82	202.61	204.02
		untSMPABC011	215.24	224.04	214.40	210.71	209.13	206.49	199.95	196.44	202.05	205.08	199.68	199.34	203.43	200.38
MBPC fw	Melt	untSMPABC012	215.04	220.55	210.75	208.39	207.06	206.23	199.78	195.15	199.93	200.68	199.53	197.61	198.76	198.52
		untSMPABC013	212.69	219.75	207.29	206.71	205.24	203.80	195.76	194.12	198.37	199.27	197.04	195.75	196.70	197.66
		untSMPABC014	218.66	224.61	214.70	212.32	210.95	209.78	202.27	200.38	207.29	206.96	203.00	202.49	205.22	206.46
		untSMPABC015	218.02	226.82	213.64	213.23	210.97	210.42	201.95	199.61	204.56	205.55	202.60	202.68	204.04	205.24
		untSMPABC016	218.16	226.70	213.45	211.55	211.00	209.93	203.03	200.60	205.63	206.63	203.37	203.25	206.16	204.86
		untSMPABC017	219.46	227.64	216.45	213.94	211.53	209.71	202.81	199.94	206.73	207.17	203.78	203.47	204.59	205.25
		untSMPABC020	238.74	245.60	240.71	235.02	230.99	226.32	221.83	218.19	223.72	226.98	223.09	223.26	225.76	225.80
		untSMPABC021	236.38	242.46	236.97	230.72	228.89	221.95	218.22	215.24	220.77	221.65	219.08	219.11	220.71	221.33
		untSMPABC022	230.50	233.49	229.43	224.92	225.09	218.63	213.57	211.13	215.66	217.31	215.28	214.14	216.23	216.16
		untSMPABC023	221.82	226.01	221.29	216.43	215.23	211.94	207.06	202.07	206.00	208.94	204.91	206.09	207.67	208.31
		untSMPABC024	223.05	229.32	224.37	218.71	218.54	214.49	209.06	205.04	210.23	211.92	208.03	207.90	208.31	208.93
MBPC fd	Melt	untSMPABC025	229.49	231.42	227.71	222.85	224.65	219.29	214.36	212.89	215.38	216.81	213.50	213.80	214.53	216.50
		untSMPABC026	226.52	231.03	223.74	218.59	219.52	216.11	209.24	206.97	211.72	212.16	210.30	209.46	210.89	210.95
		untSMPABC027	227.27	231.92	226.75	221.76	220.46	215.39	209.89	209.95	213.71	214.64	212.35	212.53	213.77	213.36
		untSMPABC028	226.88	232.82	229.14	222.85	224.71	216.74	211.33	211.72	215.02	216.10	214.29	211.79	214.73	213.80
		untSMPABC029	232.83	237.72	233.99	224.75	225.45	220.65	213.97	212.25	217.12	218.58	215.83	214.84	215.65	217.06
		untSMPABC030	232.33	236.68	229.53	223.77	222.50	220.61	212.67	208.48	215.59	214.08	214.04	212.81	215.92	214.96
		untSMPABC007	351.70	347.09	314.60	332.17	310.16	275.31	301.63	289.69	310.56	306.98	315.49	293.25	303.05	298.78
		untSMPABC009	358.15	358.51	332.31	330.83	319.25	307.75	306.65	306.12	317.85	327.05	313.59	308.91	324.78	321.49
		untSMPABC011	383.99	368.01	346.95	335.11	322.71	292.79	309.47	308.50	305.33	316.33	313.08	305.50	335.24	317.61
		untSMPABC013	355.44	342.43	322.91	317.34	284.48	268.66	303.09	282.89	313.76	307.47	302.10	297.51	306.32	296.86
		untSMPABC015	364.70	390.21	350.72	363.04	325.79	311.71	319.46	299.04	335.30	328.96	333.13	306.47	335.76	319.92
		untSMPABC019	396.70	376.97	358.68	341.66	327.15	332.39	342.02	322.71	325.93	348.04	331.09	327.94	372.42	362.63
MBPC ed	Melt	untSMPABC021	377.27	401.75	354.40	353.05	352.40	324.40	311.97	337.27	344.35	345.91	342.67	325.42	351.46	344.72
		untSMPABC023	397.19	396.11	378.44	351.85	332.86	326.79	358.26	326.77	361.21	339.29	369.28	335.18	333.08	363.41
		untSMPABC025	357.97	377.94	358.16	362.49	320.87	311.03	323.88	314.90	325.08	335.73	326.86	320.63	334.07	333.36
		untSMPABC027	361.87	390.18	362.89	348.23	306.14	315.26	330.23	297.11	333.39	342.21	326.99	324.98	335.96	339.73
		untSMPABC019	336.77	357.75	319.38	323.32	322.71	277.76	301.71	295.66	302.85	311.77	299.67	304.40	301.86	318.93
		untSMPABC027	319.37	379.34	316.80	295.70	319.57	280.38	278.60	289.18	285.52	304.47	294.53	286.75	281.63	313.81
		untSMPABC029	356.59	377.61	312.56	306.67	316.35	293.54	281.80	313.84	322.42	311.23	292.85	283.50	305.14	306.52

Name	Phase	Point	L	Ce	Pr	Nd	Sm	Eu	Gd	Tb	Dy	Ho	Er	Tm	Yb	Lu
MBPC fw	Ol	untSMPABC007	0.10	0.08	0.08	n.d.	n.d.	0.26	n.d.	0.56	1.31	1.40	2.85	3.62	5.94	8.37
		untSMPABC008	n.d.	n.d.	0.06	n.d.	n.d.	0.11	n.d.	0.43	0.84	1.35	2.23	3.81	6.01	8.70
		untSMPABC009	0.13	0.06	0.09	n.d.	0.19	0.14	0.53	0.56	0.85	1.48	2.10	4.22	5.70	8.96
		untSMPABC010	n.d.	n.d.	n.d.	n.d.	n.d.	0.09	n.d.	0.42	0.85	1.51	2.43	3.70	5.50	8.80
MBPC fw	Ol	untSMPABC011	n.d.	n.d.	n.d.	n.d.	n.d.	0.07	0.30	0.42	0.86	1.22	2.18	3.35	5.41	8.08
MBPC fd	Ol	untSMPABC014	0.07	n.d.	0.03	n.d.	0.18	0.14	0.53	0.57	1.49	1.92	2.83	4.92	8.16	11.37
		untSMPABC015	n.d.	n.d.	n.d.	0.22	0.18	0.22	n.d.	0.80	1.42	2.14	3.58	6.00	8.49	13.00
		untSMPABC016	n.d.	n.d.	n.d.	n.d.	0.14	0.10	0.68	0.77	1.19	2.18	3.28	5.77	8.62	13.24
		untSMPABC017	n.d.	n.d.	0.02	n.d.	n.d.	0.13	0.30	0.67	1.08	2.40	3.44	5.74	8.88	13.50
MBPC ed	Ol	untSMPABC007	n.d.	0.81	1.54	n.d.	n.d.	2.42	n.d.	3.90	3.78	5.16	7.56	10.77	14.77	26.69
		untSMPABC008	n.d.	n.d.	n.d.	n.d.	n.d.	0.72	n.d.	1.25	n.d.	2.59	4.76	7.14	12.22	16.18
		untSMPABC009	n.d.	n.d.	n.d.	n.d.	n.d.	n.d.	5.65	1.03	2.65	3.53	3.78	7.35	12.50	17.86
		untSMPABC010	n.d.	n.d.	n.d.	n.d.	n.d.	n.d.	n.d.	1.50	n.d.	3.14	3.65	8.95	13.35	19.36
		untSMPABC011	n.d.	n.d.	0.30	n.d.	n.d.	n.d.	n.d.	1.12	3.16	2.38	6.41	7.32	12.87	18.51
		untSMPABC012	n.d.	n.d.	n.d.	n.d.	n.d.	n.d.	n.d.	0.94	n.d.	2.62	3.97	6.54	10.56	17.64
		untSMPABC014	n.d.	0.62	n.d.	n.d.	n.d.	n.d.	n.d.	0.62	n.d.	2.68	3.68	7.64	13.51	17.97
		untSMPABC015	n.d.	0.77	n.d.	n.d.	n.d.	n.d.	n.d.	1.27	n.d.	3.22	7.33	7.03	12.01	17.96
		untSMPABC016	n.d.	n.d.	n.d.	3.40	n.d.	0.64	n.d.	0.79	3.81	3.56	5.09	6.45	10.72	16.65
MBPC fd	Pl	untSMPABC005	13.79	10.16	7.92	6.46	3.95	51.16	3.09	1.90	1.40	1.29	0.92	0.82	0.70	0.38
		untSMPABC006	13.80	10.41	7.84	6.70	3.74	52.97	3.45	1.92	1.25	1.31	0.80	0.60	0.52	0.43
		untSMPABC007	11.34	7.64	6.52	5.60	3.09	46.65	2.89	1.79	1.84	0.99	1.13	0.51	n.d.	0.38
		untSMPABC008	11.74	8.48	7.07	6.79	5.33	48.89	3.01	2.38	0.88	1.27	1.00	0.67	0.44	0.46
		untSMPABC009	11.29	7.70	6.40	5.85	4.21	46.77	2.50	1.71	1.58	1.22	0.94	0.51	n.d.	0.34
		untSMPABC010	11.97	8.56	7.01	6.35	3.58	50.41	2.93	1.87	1.00	1.10	0.76	0.63	0.61	0.41
		untSMPABC011	12.51	8.56	7.11	5.94	3.68	47.64	3.23	1.72	1.36	1.10	n.d.	0.65	0.46	0.35
MBPC ed	Pl	untSMPABC020	27.83	26.11	16.91	18.72	8.65	64.59	n.d.	5.55	n.d.	3.35	n.d.	3.41	n.d.	1.34
		untSMPABC023	39.73	43.94	30.89	22.21	22.15	65.25	16.13	17.84	15.90	12.84	8.93	15.93	11.31	14.21
		untSMPABC025	54.81	42.97	28.35	n.d.	n.d.	71.64	57.11	5.53	n.d.	11.23	n.d.	5.57	n.d.	6.70
		untSMPABC026	21.70	24.35	16.08	n.d.	12.21	60.39	37.95	3.69	30.89	5.99	n.d.	5.50	n.d.	1.49
MBPC fw	Cpx	untSMPABC007	14.58	26.02	40.63	60.44	94.11	96.33	122.66	121.56	131.12	135.43	132.22	118.27	117.89	112.61
		untSMPABC009	19.63	35.38	51.53	76.95	116.53	111.39	145.55	145.52	159.10	150.16	146.07	133.78	124.87	124.56
		untSMPABC010	15.14	25.69	42.64	55.94	99.60	97.25	105.99	107.47	117.71	115.46	109.07	99.16	98.79	90.17
		untSMPABC011	14.66	26.13	39.80	59.47	94.03	92.97	117.99	118.67	127.50	122.67	115.25	107.46	103.16	99.46
		untSMPABC012	17.12	29.97	44.81	64.74	101.67	97.86	126.42	127.43	137.13	134.17	126.45	114.01	113.89	106.70
		untSMPABC013	16.59	28.23	44.01	65.87	105.39	103.26	132.30	131.45	146.13	138.07	131.56	118.09	114.60	113.79
		untSMPABC014	19.76	35.03	52.83	78.35	122.15	117.00	154.15	153.48	166.76	158.66	156.44	141.53	137.34	130.80
		untSMPABC015	15.90	27.91	41.71	64.29	102.46	100.42	125.29	127.89	138.52	135.61	129.47	120.24	115.27	111.71

		Point	L	Ce	Pr	Nd	Sm	Eu	Gd	Tb	Dy	Ho	Er	Tm	Yb	Lu
		untSMPABC016	13.66	23.47	36.19	54.88	92.76	91.79	121.06	124.05	135.60	130.85	128.69	115.68	117.24	112.54
MBPC fd	Cpx	untSMPABC019	14.97	25.94	40.74	61.02	103.56	99.95	133.97	141.08	153.35	151.71	152.72	142.37	137.56	139.23
		untSMPABC020	18.56	32.18	49.96	73.60	119.45	113.76	151.69	152.13	168.34	167.49	161.86	153.45	148.60	148.73
		untSMPABC021	13.53	24.36	39.01	58.43	102.37	100.11	135.48	142.17	157.86	158.74	153.48	145.22	143.03	143.30
		untSMPABC022	15.72	26.21	40.14	58.88	98.83	93.18	122.22	124.35	135.53	135.03	128.78	121.97	120.58	120.33
		untSMPABC023	18.35	31.34	49.38	70.01	116.72	115.67	147.69	149.56	162.97	159.07	153.31	144.13	141.53	139.15
		untSMPABC025	18.06	28.37	46.04	67.50	109.50	109.59	139.88	142.77	155.55	152.85	148.65	137.69	141.71	135.73
MBPC fd	Cpx	untSMPABC026	14.78	25.50	40.37	59.88	101.48	98.57	125.42	133.50	148.20	143.02	136.69	126.51	134.43	121.89
		untSMPABC027	14.98	25.48	39.09	58.16	97.47	93.68	122.03	125.60	136.57	132.46	130.28	120.91	117.73	119.57
		untSMPABC028	17.59	29.13	45.57	65.42	112.07	109.62	145.82	145.93	156.06	155.15	151.33	145.13	137.78	142.09
		untSMPABC029	19.64	32.17	49.04	62.21	111.00	106.90	129.97	130.19	144.84	136.52	133.00	122.53	128.31	123.82
		untSMPABC030	18.55	31.37	48.02	69.51	117.24	114.64	149.76	153.12	166.73	160.13	157.17	149.81	148.45	148.75
MBPC ed	Cpx	untSMPABC008	22.16	37.72	64.95	93.14	141.58	117.52	131.44	161.53	156.14	157.50	137.73	134.93	150.36	143.20
		untSMPABC010	34.18	59.15	80.75	101.32	157.60	149.90	204.55	179.51	187.79	202.17	194.19	168.83	173.16	155.38
		untSMPABC014	40.22	67.21	80.69	119.24	163.39	155.19	203.26	205.56	205.60	210.08	200.79	178.16	172.03	181.80
		untSMPABC016	54.60	76.88	96.02	125.70	176.05	166.83	186.22	186.08	224.41	199.61	188.47	191.14	194.15	182.56
		untSMPABC020	34.07	70.03	81.61	119.01	152.61	156.37	176.66	190.45	212.43	191.24	181.71	173.33	165.22	155.03
		untSMPABC022	35.50	62.98	83.40	117.72	184.67	167.81	193.06	187.27	221.07	225.85	215.95	181.91	173.40	184.53
		untSMPABC026	27.42	57.01	73.88	111.79	146.17	152.25	169.61	184.00	193.82	185.28	170.92	160.55	156.41	154.77
		untSMPABC028	33.51	60.41	86.13	112.26	145.69	158.89	193.55	182.30	200.08	196.08	185.59	169.22	161.32	157.63
		untSMPABC028	68.72	84.80	106.37	125.66	183.61	157.40	198.19	200.51	216.39	197.15	191.12	172.45	184.60	191.90
		untSMPABC030	25.47	45.88	50.47	68.62	99.55	80.23	96.76	109.09	112.98	95.81	104.65	93.82	93.73	94.58
Average BCR			24.70	53.11	6.62	27.43	6.36	1.93	6.19	0.91	5.77	1.19	3.46	0.47	3.05	0.45
2SD			0.73	3.21	0.46	0.77	0.31	0.08	1.06	0.12	0.58	0.17	0.18	0.08	0.58	0.06
Ref. value ()			24.70	53.30	6.70	28.90	6.59	1.97	6.71	1.02	6.44	1.27	3.70	0.51	3.39	0.50

Name	Phase	Point	Sc	Ti	V	Co	Rb	Sr	Zr	Ba
		untSMPABC001	184.10	9900.08	217.72	73.02	225.56	252.02	38.15	311.14
		untSMPABC008	183.55	9852.30	218.28	71.23	225.25	250.06	38.58	308.59
		untSMPABC009	186.85	9791.62	218.40	73.83	225.75	251.20	39.02	309.10
		untSMPABC010	187.12	9784.13	220.27	73.17	224.03	248.94	38.50	305.51
		untSMPABC011	185.25	9830.17	218.63	73.47	219.41	247.54	38.19	310.87
MBPC fw	Melt	untSMPABC012	186.73	9751.59	221.67	73.03	221.36	245.33	39.26	301.58
		untSMPABC013	182.18	9809.84	217.86	70.19	220.50	244.95	38.13	300.68
		untSMPABC014	185.93	9936.56	219.03	73.70	231.35	249.09	39.59	306.44
		untSMPABC015	183.85	9799.18	217.67	70.02	228.79	249.13	38.77	306.30
		untSMPABC016	181.59	9836.54	217.63	66.63	228.05	251.49	38.86	307.58
		untSMPABC017	183.33	9770.30	220.20	61.05	224.62	248.84	39.07	309.15
		untSMPABC020	168.35	14013.29	228.48	94.67	251.48	216.59	4.44	247.26
		untSMPABC021	171.83	13756.05	229.13	100.42	248.50	217.53	4.55	244.60
		untSMPABC022	174.83	13512.11	228.90	105.88	251.77	214.56	4.20	240.27
		untSMPABC023	174.25	13590.53	227.57	108.59	240.91	211.52	4.19	229.79
		untSMPABC024	174.26	13407.00	227.55	112.68	244.80	213.52	4.38	234.39
MBPC fd	Melt	untSMPABC025	177.90	13544.01	227.22	115.74	247.19	215.24	4.02	234.68
		untSMPABC026	175.33	13643.68	224.89	112.35	241.01	215.16	4.32	232.13
		untSMPABC027	175.11	13463.92	224.92	112.76	243.30	213.59	4.28	237.92
		untSMPABC028	174.50	13455.20	226.45	110.11	243.01	211.56	3.98	236.62
		untSMPABC029	177.01	13742.89	228.52	107.28	248.22	216.94	4.22	238.82
		untSMPABC030	171.49	13503.63	224.19	103.75	242.39	215.52	4.52	242.31
		untSMPABC007	185.85	14419.18	258.77	110.17	340.98	214.18	51.17	423.00
		untSMPABC009	173.48	15452.40	268.73	93.09	356.09	227.10	30.64	453.93
		untSMPABC011	189.49	15514.95	275.83	113.08	352.85	226.38	42.50	467.69
		untSMPABC013	175.97	15061.40	284.97	111.54	380.72	206.45	n.d.	457.68
		untSMPABC015	166.46	15658.75	255.07	91.30	368.55	220.65	n.d.	456.56
		untSMPABC019	144.93	14963.51	302.39	38.69	390.06	252.84	n.d.	455.95
MBPC ed	Melt	untSMPABC021	185.20	15367.48	295.50	114.61	389.99	235.32	44.02	434.62
		untSMPABC023	188.64	15535.52	307.27	129.70	406.24	260.27	77.51	407.50
		untSMPABC025	153.81	14512.76	284.33	76.22	382.51	220.33	75.28	431.40
		untSMPABC027	161.78	14987.76	290.94	78.25	380.33	226.86	n.d.	430.21
		untSMPABC019	140.81	13785.39	263.04	60.17	313.90	205.12	n.d.	458.15
		untSMPABC027	247.11	14013.13	239.72	76.57	257.20	218.30	36.77	440.09
		untSMPABC029	180.20	14305.13	277.86	79.00	350.84	209.94	n.d.	505.65

Name	Phase	Point	Sc	Ti	V	Co	Rb	Sr	Zr	Ba
MBPC fw	Ol	untSMPABC007	55.12	90.56	11.90	444.42	n.d.	0.46	n.d.	n.d.
		untSMPABC008	57.01	69.97	9.13	444.43	n.d.	n.d.	n.d.	n.d.
		untSMPABC009	59.64	102.78	11.00	440.00	n.d.	n.d.	n.d.	n.d.
		untSMPABC010	55.96	71.14	9.59	427.11	n.d.	n.d.	n.d.	n.d.
MBPC fw	Ol	untSMPABC011	56.72	51.78	8.94	327.47	n.d.	n.d.	n.d.	n.d.
MBPC fd	Ol	untSMPABC014	65.92	124.61	11.63	591.12	n.d.	n.d.	n.d.	n.d.
		untSMPABC015	70.88	125.66	10.65	613.19	n.d.	0.43	n.d.	n.d.
		untSMPABC016	70.64	148.02	11.11	628.38	n.d.	n.d.	n.d.	n.d.
		untSMPABC017	70.36	124.40	11.41	582.02	n.d.	n.d.	n.d.	n.d.
MBPC ed	Ol	untSMPABC007	n.d.	218.55	8.92	488.53	n.d.	n.d.	n.d.	n.d.
		untSMPABC008	44.80	91.94	n.d.	465.31	n.d.	n.d.	n.d.	n.d.
		untSMPABC009	57.58	156.38	8.04	532.83	n.d.	n.d.	n.d.	n.d.
		untSMPABC010	46.27	181.13	10.28	526.61	n.d.	n.d.	n.d.	n.d.
		untSMPABC011	56.17	101.91	13.15	470.02	n.d.	n.d.	n.d.	n.d.
		untSMPABC012	61.86	78.13	12.87	487.98	n.d.	n.d.	n.d.	n.d.
		untSMPABC014	44.26	141.06	n.d.	415.08	n.d.	n.d.	n.d.	n.d.
		untSMPABC015	65.81	129.12	10.75	440.04	n.d.	n.d.	n.d.	n.d.
		untSMPABC016	69.01	68.67	16.05	433.77	n.d.	n.d.	n.d.	n.d.
MBPC fd	Pl	untSMPABC005	n.d.	428.55	2.69	n.d.	4.17	456.09	n.d.	85.06
		untSMPABC006	n.d.	440.46	2.59	n.d.	3.51	467.16	n.d.	81.05
		untSMPABC007	n.d.	404.80	1.76	n.d.	2.85	400.34	n.d.	54.18
		untSMPABC008	n.d.	398.62	3.43	n.d.	3.02	452.89	n.d.	56.64
		untSMPABC009	n.d.	367.50	2.14	n.d.	3.00	415.99	n.d.	52.79
		untSMPABC010	n.d.	431.72	1.62	n.d.	3.62	439.65	n.d.	63.68
		untSMPABC011	n.d.	457.76	1.14	5.33	3.99	397.95	n.d.	57.72
MBPC ed	Pl	untSMPABC020	n.d.	732.16	n.d.	n.d.	n.d.	466.50	n.d.	186.24
		untSMPABC023	n.d.	1467.86	28.16	n.d.	21.80	504.89	n.d.	141.21
		untSMPABC025	n.d.	1333.94	n.d.	n.d.	n.d.	451.03	n.d.	167.51
		untSMPABC026	n.d.	798.11	n.d.	n.d.	15.81	355.53	n.d.	120.79
MBPC fw	Cpx	untSMPABC007	709.73	3704.24	282.46	54.78	0.17	15.08	8.23	n.d.
		untSMPABC009	740.64	5414.61	364.11	51.60	n.d.	18.04	12.26	n.d.
		untSMPABC010	660.10	4683.26	281.85	45.59	n.d.	16.58	4.56	n.d.
		untSMPABC011	721.18	4459.69	317.78	67.66	0.24	17.93	6.91	n.d.
		untSMPABC012	761.30	5022.24	342.44	54.82	n.d.	17.18	10.26	n.d.
		untSMPABC013	742.45	5014.64	320.99	52.41	0.25	16.01	10.46	n.d.
		untSMPABC014	761.10	5574.86	344.44	57.49	n.d.	16.11	11.32	n.d.
		untSMPABC015	734.95	4518.70	325.84	70.30	0.43	16.78	11.14	n.d.

		Point	Sc	Ti	V	Co	Rb	Sr	Zr	Ba
		untSMPABC016	745.98	3512.66	267.48	55.24	0.27	15.18	6.38	n.d.
MBPC fd	Cpx	untSMPABC019	775.45	4984.35	298.49	114.92	n.d.	14.79	n.d.	n.d.
		untSMPABC020	783.20	6225.83	339.97	111.40	n.d.	14.45	n.d.	n.d.
		untSMPABC021	787.30	4815.93	255.73	118.74	n.d.	13.22	n.d.	n.d.
		untSMPABC022	744.90	5227.96	296.08	111.05	1.56	15.99	n.d.	1.70
		untSMPABC023	757.29	5792.20	330.76	105.86	0.34	16.07	n.d.	n.d.
		untSMPABC025	770.48	5739.69	313.96	99.99	0.29	15.50	n.d.	n.d.
		untSMPABC026	760.85	5415.33	325.06	114.94	0.25	15.05	n.d.	n.d.
MBPC fd	Cpx	untSMPABC027	726.00	5051.38	289.53	111.83	0.98	16.52	n.d.	1.03
		untSMPABC028	798.70	5880.10	328.81	106.36	0.18	16.83	n.d.	n.d.
		untSMPABC029	719.01	6227.37	304.95	83.43	2.23	19.02	n.d.	1.80
		untSMPABC030	830.30	6684.98	335.83	107.89	n.d.	16.34	n.d.	n.d.
		untSMPABC008	692.26	6398.07	344.54	118.61	n.d.	19.46	34.96	n.d.
		untSMPABC010	814.85	7982.05	398.53	171.19	4.58	24.44	n.d.	n.d.
		untSMPABC014	702.43	7602.20	385.81	161.57	15.97	28.77	55.29	16.39
		untSMPABC016	746.69	8226.13	429.97	145.48	24.70	30.60	n.d.	19.21
MBPC ed	Cpx	untSMPABC020	739.53	7499.42	384.08	154.77	7.89	25.98	n.d.	n.d.
		untSMPABC022	729.62	7385.17	415.98	175.04	n.d.	19.60	38.46	n.d.
		untSMPABC026	732.59	6291.38	367.93	163.90	4.61	21.57	n.d.	n.d.
		untSMPABC028	755.84	7362.10	470.15	146.93	7.72	27.17	n.d.	8.48
		untSMPABC028	836.63	8145.33	346.40	188.91	32.75	35.07	n.d.	31.41
		untSMPABC030	533.15	4713.44	263.15	62.58	14.32	17.97	n.d.	11.42
	Average BCR		30.79	13179.03	447.31	39.61	48.24	335.40	169.23	687.81
	2SD		2.30	687.39	33.38	7.66	5.70	8.47	17.01	25.69
	Ref. value ()		33	14100	425	38	47	342	184	683

Le devenir des liquides au sein de la croûte océanique des dorsales à expansion lente

Nouveaux apports de l'étude d'Atlantis Bank (dorsale Sud-Ouest Indienne)

Les processus magmatiques qui régissent l'accrétion crustale au niveau des dorsales médio-océaniques à expansion lente restent à l'heure actuelle mal contraints. Parmi les processus potentiellement impliqués dans l'évolution des réservoirs de magma de la croûte inférieure, les réactions associées à des écoulements poreux réactifs au travers de bouillies cristallines - ou mush - tendent à supplanter les processus classiques de cristallisation simple des magmas. La part de ces processus dans la formation des gabbros cumulatifs de base de croûte est dépendante des modes de migration des liquides, qui sont eux-mêmes corrélés à la géométrie des réservoirs considérés. En combinant des études structurales, pétrographiques et géochimiques à haute résolution de sections *in situ* forées dans un corps complexe océanique de la dorsale Sud-Ouest indienne, j'ai pu apporter de nouvelles contraintes sur les modes de formation et d'évolution des réservoirs magmatiques impliqués lors de l'accrétion crustale. Le modèle de réservoir développé est généralisable, au moins en partie, à d'autres portions de croûte inférieure océanique. Ce modèle, ainsi que les nouvelles contraintes de l'étude expérimentale couplée des processus de cristallisation, ouvre la voie vers de nouvelles quantifications des processus d'interaction liquides-roches dans la différenciation des lithologies gabbroïques, et de manière plus générale dans l'évolution des liquides magmatiques de la croûte océanique. Ces développements vont de pair avec l'évolution au cours des dernières décennies de la vision des systèmes magmatiques crustaux, passant de chambres magmatiques constituées de liquides vers des modèles de réservoirs magmatiques majoritairement constitués de mush cristallins.

Mots-clés : dorsales océaniques à expansion lente, dorsale Sud-Ouest Indienne, Atlantis Bank, croûte inférieure océanique, corps complexe océanique, intrusion magmatique, flux poreux réactif, Assimilation-Cristallisation Fractionnée, analyses *in situ*, pétrologie expérimentale, autoclave

The fate of melts within the slow-spreading lower oceanic crust

New insights from Atlantis Bank (Southwest Indian Ridge)

Magmatic processes that govern crustal accretion at mid-ocean ridges still need to be better constrained. Among the processes potentially involved in the evolution of the lower crust magma reservoirs, reactions associated with reactive porous flow through crystal mushes tend to be considered as one of the predominant processes together with simple crystallization of magmas. The share of these processes during magma differentiation is dependent on the modes of melt migration and is thus correlated to the geometry of the reservoirs considered. By combining high-resolution structural, petrographic and geochemical studies of *in situ* sections drilled in an oceanic core complex of the Southwest Indian Ridge, I was able to bring new constraints on the formation and evolution of magmatic reservoirs involved in crustal accretion. All or part of the igneous reservoir model developed herein can be applied to other sections of lower oceanic crust. This model, together with additional constraints obtained by the coupled experimental petrology study of crystallization processes, paves the way for new quantifications of the involvement of melt-rock reactions in the differentiation of gabbroic lithologies, and more generally in the evolution of melts within the oceanic crust. Those developments are consistent with the constant evolution in recent decades of the understanding of crustal magmatic systems, which shifted from melt-filled magma chambers to igneous reservoir models mostly composed of crystal mushes.

Keywords: slow-spreading ridges, Southwest Indian Ridge, Atlantis Bank, lower oceanic crust, oceanic core complexes, magma intrusion, reactive porous flow, Assimilation-Fractional Crystallization, *in situ* analyses, experimental petrology, Internally Heated Pressure Vessels